Proceedings of the International Symposium on Engineering under Uncertainty: Safety Assessment and Management (ISEUSAM - 2012)

Subrata Chakraborty • Gautam Bhattacharya
Editors

Proceedings of the International Symposium on Engineering under Uncertainty: Safety Assessment and Management (ISEUSAM - 2012)

Springer

Editors
Subrata Chakraborty
Civil Engineering
Bengal Engineering and Science University
Howrah, India

Gautam Bhattacharya
Civil Engineering
Bengal Engineering and Science University
Howrah, India

Printed in 2 Volumes
ISBN 978-81-322-0756-6 ISBN 978-81-322-0757-3 (eBook)
DOI 10.1007/978-81-322-0757-3
Springer New Delhi Heidelberg New York Dordrecht London

Library of Congress Control Number: 2012944989

Printed on acid-free paper

Springer is part of Springer Science+Business Media (www.springer.com)

Preface

In engineering applications, it is important to model and treat adequately all the available information during the analysis and design phase. Typically, the information is originated from different sources like field measurements, experts' judgments, objective and subjective considerations. Over these features, the influences originated from the human errors, imperfections in the construction techniques and production process and influence of the boundary and environmental conditions are added. All these aspects can be brought under one common denominator: that is, "presence of uncertainty." Thus, reliability and safety are the core issues which need to be addressed during the analysis, design, construction and operation of engineering systems under such uncertainties. In this backdrop, the aim of ISEUSAM 2012 is to facilitate the discussion for a better understanding and management of uncertainty and risk, encompassing various aspects of safety and reliability of engineering systems. To be specific, the overall theme of the symposium is modelling, analysis and design of engineering systems and decision-making under uncertainties relevant to all engineering disciplines.

The symposium, being the first of its kind organized in India, received overwhelming response from national as well as international scholars, experts and delegates from different parts of the world. Papers were received from authors from several parts of the world including Australia, Canada, China, Germany, Italy, Sharjah, the UK and the USA, besides India. More than 200 authors from India and abroad have shown their interest in the symposium, out of which a total of 90 papers were presented in various technical sessions comprising 4 plenary sessions and 12 parallel technical sessions.

The proceedings began on January 4, 2012, on a grand scale amidst rousing welcome to the delegates and great enthusiasm amongst the organizers and the participants with the opening ceremony hosting, amongst other dignitaries, Dr. Rakesh Kumar Bhandari, Director, Variable Energy Cyclotron Centre, Kolkata, who inaugurated the 3-day international event, Professor Ajoy Kumar Ray, Vice Chancellor, Bengal Engineering and Science University,

Shibpur, who presided over the opening session, and Professor Arun Kumar Majumdar, Deputy Director, Indian Institute of Technology Kharagpur, who graced the occasion as the guest of honour.

The inaugural keynote address, delivered by Achintya Haldar, Emeritus Professor, University of Arizona, USA, on *Past, Present and Future of Engineering under Uncertainty: Safety Assessment and Management,* set the tone for the rest of the proceedings. This was followed by a series of technical sessions including plenary sessions on numerous sub-themes spread over all three days. The other keynote addresses include *Techniques of Analysis of Imprecision in Engineering Systems* by Ajoy K. Ray, Vice Chancellor, BESU, Shibpur; *Uncertainty Quantification in System Risk Assessment and Decision-Making* by Sankaran Mahadevan, John R. Murray Sr. Chair in Engineering, Vanderbilt University, USA; *Advancing Geotechnics in the Twenty-First Century – Dealing with Uncertainty and Other Challenges* by Robin Chowdhury, Emeritus Professor, University of Wollongong, Australia; *State of the Art on Stochastic Control of Structures for Seismic Excitation* by T.K. Datta, Emeritus Professor, IIT Delhi; *Discovering Hidden Structural Degradations* by Abhijit Mukherjee, Director, Thapar University; *SHM of Prestressed Concrete Girder Bridge* by Pradipta Banerji, Director, IIT Roorkee; *Nanotoxicology: A Threat to the Environment and to Human Beings* by D. Dutta Majumder, Professor Emeritus, Indian Statistical Institute, Kolkata; *Uncertainty in Interpreting the Scale Effect of Plate Load Tests in Unsaturated Soils* by Sai K. Vanapalli, Professor and Chair, Civil Engineering Department, University of Ottawa, Canada; and *Response Control of Tall Buildings Using Tuned Liquid Damper* by S. K. Bhattacharyya, Director, CBRI, Roorkee. Two other eminent personalities who had accepted the invitation to deliver keynote lectures, but due to unavoidable circumstances could not be present on the occasion, also sent their contributions for inclusion in the symposium proceedings. These are *Uncertainties in Transportation Infrastructure Development and Management* by Kumares C. Sinha, Olson Distinguished Professor of Civil Engineering, Purdue University, USA, and *Physical Perspective Towards Stochastic Optimal Controls of Engineering Structures* by Jie Li, State Key Laboratory of Disaster Reduction in Civil Engineering, Tongji University, Shanghai, China.

In order to accommodate a wide spectrum of highly relevant sub-themes across the major engineering disciplines, presentations of the invited and the contributory papers were held in two parallel technical sessions. Amongst the presenters were senior professors and chairs from reputed universities from India and abroad, most of the IITs and the IISc Bangalore on the one hand, and experts from the R&D organizations such as BARC, AERB, DRDO, CBRI, CRRI, SERC and leading industry houses such as UltraTech Cement, M.N. Dastur & Company (P) Ltd., Petrofac International Ltd., UAE, and L&T on the other. All the technical sessions invariably concluded with a highly animated discussion session which enthralled the participants and brought their applause in appreciation.

The closing ceremony marked a fitting finale to the 3-day event. Professor Achintya Haldar summed up the proceedings over the last 3 days. He also spelt out the future direction of the symposium by mooting a proposal of organizing it on a regular basis. Dr. Milan Kumar Sanyal, Director, Saha Institute of Nuclear Physics, Kolkata, in his role as the chief guest, enlightened the audience about the uncertainties involved in a nuclear project. Dr. T. K. Datta, Professor Emeritus, IIT Delhi, was the Guest of Honour on the occasion. "Death is certain, yet, when, is uncertain. . ." echoed Dr. Datta on a philosophical note and went on to applaud the Department of Civil Engineering, BESU, for putting in such a wonderful effort in organizing this symposium on uncertainty, the first of its kind in India. Representatives from the delegates, including the well-known academician Professor G. Venkatachalam, expressed that they had found the sessions truly engrossing and also that they were highly satisfied with the arrangements. It thus appears that the symposium could at least partly fulfil the objective with which it was organized.

The organizers sincerely regret that this volume could not be made ready well in advance, and, therefore, at the time of the symposium, the delegates and the participants could be handed over only a CD version of their contributions. But, better late than never, that the proceedings could eventually be published, is a matter of some satisfaction.

Professor of Civil Engineering — Subrata Chakraborty
Bengal Engineering and Science University, Shibpur
Organizing Secretary, ISEUSAM-2012

Professor of Civil Engineering — Gautam Bhattacharya
Bengal Engineering and Science University, Shibpur
Joint Organizing Secretary, ISEUSAM-2012

About the Editors

Dr. Subrata Chakraborty is currently a Professor at the Bengal Engineering and Science University, Shibpur. He is a fellow of the Indian National Academy Engineering and the Institution of Engineers (India). He has obtained his Ph.D. in structural engineering from IIT Kharagpur in 1995. He was postdoctoral researcher at University of Cambridge, UK and University of Arizona, USA and Technical University of Aachen, Germany. In general, Prof. Chakraborty's research interest lies in the field of computational mechanics under uncertainty, structural health monitoring, vibration control, composite mechanics etc. While his inspiring teaching coupled with innate urge for intensive research has already established him as a distinguished academician at the national level, several awards and laurels have come his way. The Humboldt Fellowship for Experienced Researchers, the INAE Young Engineer Award, the BOYSCAST Fellowship, and the Young Faculty Research Award deserve special mention.

Dr. Gautam Bhattacharya, an experienced academic and researcher, is one of the senior Professors of Civil Engineering at the Bengal Engineering and Science University, Shibpur, and currently the Vice-Chairman, Kolkata chapter of the Indian Geotechnical Society. Having obtained his B.E. and M.E. in Civil Engineering from the erstwhile B.E. College, Shibpur, he went to IIT Kanpur to pursue his Doctoral study during which (1985–1990) he developed great interest in the subject of slope stability, and worked on the application of advanced numerical methods in slope analysis for his PhD thesis. He has since been engaged in teaching soil mechanics and foundation engineering and in pursuing research on both deterministic and probabilistic approaches of analysis of unreinforced and reinforced slopes, retaining structures and foundations under static and seismic conditions. He has published several scientific articles in peer reviewed journals and also co-authored a book with the CRC Press/Balkema. He has teaching, research and consultancy experience in the field of geotechnical engineering for about three decades.

Contents of Volume I

Contents of Volume II

Past, Present, and Future of Engineering under Uncertainty: Safety Assessment and Management

Achintya Haldar

Abstract The author's perspective of engineering under uncertainty is presented. In the first part of this chapter, past, present, and future trends of reliability assessment methods, applicable to many branches of engineering, are presented. The discussions cover the cases for both explicit and implicit limit state functions. Finite element-based reliability evaluation methods for large structures satisfying underlying physics are emphasized. The necessity of estimating risks for both strength and serviceability limit states is documented. Concept of several energy dissipation mechanisms recently introduced to improve performance and reduce risk during seismic excitations can be explicitly incorporated in the formulation. Reliability evaluation of very large structures requiring over several hours of continuous running of a computer for one deterministic evaluation is briefly presented. Since major sources of uncertainty cannot be completely eliminated from the analysis and design of an engineering system, the risk needs to be managed appropriately. Risk management in the context of decision analysis framework is also briefly presented. In discussing future directions, the use of artificial neural networks and soft computing, incorporation of cognitive sources of uncertainty, developing necessary computer programs, and education-related issues are discussed.

Keywords Reliability analysis • Seismic analysis • Nonlinear response • Partially restrained connections • Shear walls • Post-Northridge connections • Computer programs • Education • Uncertainty management

A. Haldar (✉)
Department of Civil Engineering and Engineering Mechanics,
University of Arizona, Tucson, AZ, USA
e-mail: Haldar@u.arizona.edu

S. Chakraborty and G. Bhattacharya (eds.), *Proceedings of the International Symposium on Engineering under Uncertainty: Safety Assessment and Management (ISEUSAM - 2012)*,
DOI 10.1007/978-81-322-0757-3_1,

1 Introduction

Uncertainty must have been present from the beginning of time. Our forefathers must have experienced it through observations and experiences. In engineering practices, the probability concept is essentially an attempt to incorporate uncertainty in the formulation. The probability concept can be defined in two ways: (1) an expression of relative frequency and (2) degree of belief. The underlying mathematics of probability are based on three axioms, well developed and accepted by experts; however, sometimes it is used in a philosophical sense. Since the relative frequency concept is almost never used [22], a measure of confidence in expressing uncertain events leads to the degree of belief statements. Laplace (1749–1827), a famous mathematician in "A Philosophical Essay on Probabilities," wrote "It is seen in this essay that the theory of probabilities is at bottom only common sense reduced to calculus; it makes us appreciate with exactitude that which exact minds feel by a sort of instinct without being able ofttimes to give a reason for it. It leaves no arbitrariness in the choice of opinions and sides to be taken; and by its use can always be determined the most advantageous choice. Thereby, it supplements most happily the ignorance and weakness of the human mind" (translation, [25]).

These timeless remarks sum up the importance of probability, reliability, and uncertainty concepts in human endeavor. In my way of thinking, I will try to give my understanding or assessment of "Engineering under Uncertainty – Past, Present, and Future." Obviously, the time lines when past meets present and present becomes future are very difficult to establish. According to Albert Einstein, "People like us, who believe in physics, know that the distinction between past, present, and future is only a stubbornly persistent illusion."

Although the area of probability has a glorious past, I will try to emphasize the present and future in reliability assessment and management in this chapter. I believe that structural engineering provided leadership in developing these areas, and I will emphasize it in my presentation.

2 Reliability Assessment: Past

Many brilliant scholars such as Einstein did not believe in probability. His famous comment that "I am convinced that He (God) does not play dice" is known to most present scholars. On the other hand, the Rev. Thomas Bayes (1702–1761), a Presbyterian Minister at Tunbridge Wells, wrote the Bayes' theorem in 1763 in "An Essay towards Solving a Problem in the Doctrine of Chances" [14]. It has become one of the most important branches of statistics in the modern time. Please note that the paper was published 2 years after his death. One of Bayes' friends, Richard Price, sent the paper for publication by adding an introduction, examples, and figures. Most likely, Bayes was not confident about the paper. At present, the

Bayesian approach provides a mechanism to incorporate uncertainty information in cases of inadequate reliable data by combining experience and judgment.

It is reasonable to state that Freudenthal [15] formally introduced the structural reliability discipline. Obviously, it has gone through monumental developments since then under the leadership of many scholars ([2, 3, 6, 13, 18–20, 33, 34, 42], and many others). A more complete list can be found in Haldar and Mahadevan [18].

2.1 Available Reliability Evaluation Methods

It will be informative to discuss very briefly how the reliability evaluation methods evolved in the past few decades. After four decades of extensive work in different engineering disciplines, several reliability evaluation procedures of various degrees of complexity and sophistication are now available. First-generation structural design guidelines and codes are being developed and promoted worldwide using some of these procedures. Obviously, depending upon the procedure being used, the estimated risk could be different. The engineering profession has not yet officially accepted a particular risk evaluation method. Thus, design of structures satisfying an underlying risk can be debated; even the basic concept of acceptable risk is often openly debated in the profession. Moreover, uncertainty introduced due to human error is not yet understood and thus cannot be explicitly introduced in the available reliability assessment methods. Also, risk or reliability estimated using these methods may not match actual observations. Sometimes, to be more accurate, scholars denote the estimated risk as the notional or relative risk. The main idea is if risk can be estimated using a reasonably acceptable procedure, the design alternatives will indicate different levels of relative risk. When the information is used consistently, it may produce a risk-aversive appropriate design.

Before introducing the reliability-based design concept, it may be informative to study different deterministic structural design concepts used in the recent past and their relationship with the reliability-based concept. The fundamental concept behind any design is that the resistance or capacity or supply should at least satisfy demand with some conservatism or safety factor built in it. The level of conservatism is introduced in the design in several ways depending on the basic design concept being used. In structural design using the allowable stress design (ASD) approach, the basic concept is that the allowable stresses should be greater than the unfactored nominal loads or load combinations expected during the lifetime of a structure. The allowable stresses are calculated using safety factors. In other words, the nominal resistance R_n is divided by a safety factor to compute the allowable resistance R_a, and safe design requires that the nominal load effect S_n is less than R_a. In the ultimate strength design (USD) method, the loads are multiplied by load factors to determine the ultimate load effects, and the members are required to resist the ultimate load. In this case, the safety factors are used in the loads and load combinations. Since the predictabilities of different types of load are expected to

be different, the USD significantly improved the ASD concept. In the current risk-based design concept, widely known as the load and resistance factor design (LRFD), safety factors are introduced to both load and resistance under the constraint of an underlying risk, producing improved designs. It should be pointed out that LRFD-based designs are calibrated with the old time-tested ASD designs. Thus, the final design may be very similar but LRFD design is expected to be more risk consistent.

2.2 Fundamental Concept of Reliability-Based Design

Without losing any generality, suppose R and S represent the resistance or capacity and demand or load effect, respectively, and both are random variables since they are functions of many other random variables. The uncertainty in R and S can be completely defined by their corresponding probability density functions (PDFs) denoted as $f_R(r)$ and $f_S(s)$, respectively. Then the probability of failure of the structural element can be defined as the probability of the resistance being less than the load effect or simply $P(R < S)$. Mathematically, it can be expressed as [18]

$$P(\text{failure}) = P(R \langle S) = \int_0^\infty \left[\int_0^s f_R(r)\mathrm{d}r \right] f_S(s)\mathrm{d}s = \int_0^\infty F_R(s) f_S(s)\mathrm{d}s \qquad (1)$$

where $F_R(s)$ is the cumulative distribution function (CDF) of R evaluated at s. Conceptually, Eq. (1) states that for a particular value of the random variable $S = s$, $F_R(s)$ is the probability of failure. However, since S is also a random variable, the integration needs to be carried out for all possible values of S, with their respective likelihood represented by the corresponding PDF. Equation (1) can be considered as the fundamental equation of the reliability-based design concept. It is shown in Fig. 1. In Fig. 1, the nominal values of resistance and load effect are denoted as R_n and S_n, respectively, and the corresponding PDFs of R and S are shown. The overlapped (dashed) area between the two PDFs provides a *qualitative measure* of the probability of failure. Controlling the size of the overlapped area is essentially the idea behind reliability-based design. Haldar and Mahadevan [18] pointed out that the area could be controlled by changing the relative locations of the two PDFs by separating the mean values of R and S (μ_R and μ_S), the uncertainty expressed in terms of their standard deviations (σ_R and σ_S), and the shape of the PDFs ($f_R(r)$ and $f_S(s)$).

In general, the CDF and the PDF of S may not be available in explicit forms, and the integration of Eq. (1) may not be practical. However, Eq. (1) can be evaluated, without performing the integration if R and S are both statistically independent normal [11] or lognormal [41] random variables. Considering the practical aspects of a design, since R and S can be linear and nonlinear functions of many other

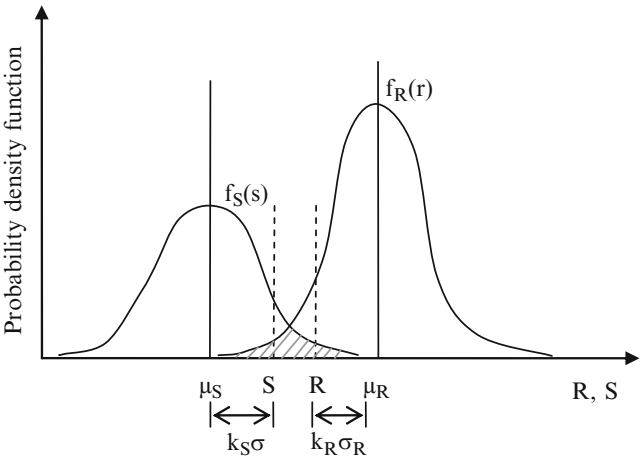

Fig. 1 Reliability-based design concept [18]

random variables, their normality or log normality assumptions can rarely be satisfied.

If the risk cannot be evaluated in closed form, it needs to be evaluated in approximate ways. This led to the development of several reliability analysis techniques. Initially, in the late 1960s, the first-order second-moment (FOSM) method, also known as the mean value first-order second-moment (MVFOSM), was proposed neglecting the distributional information on the random variables present in the problem. This important deficiency was overcome by the advanced first-order second-moment (AFOSM) method applicable when all the variables are assumed to be normal and independent [20]. A more general formulation applicable to different types of distribution was proposed by Rackwitz and Fiessler [34]. In the context of AFOSM, the probability of failure can be estimated using two types of approximations to the limit state at the design point: first order (leading to the name FORM) and second order (leading to the name SORM). Since FORM is a major reliability evaluation technique commonly used in the profession, it is discussed in more detail below.

The basic idea behind reliability-based design is to design satisfying several performance criteria and considering the uncertainties in the relevant load- and resistance-related random variables, called the basic variables X_i. Since the R and S random variables in Eq. (1) are functions of many other load- and resistance-related random variables, they are generally treated as basic random variables. The relationship between the basic random variables and the performance criterion, known as the performance or limit state function, can be mathematically represented as

$$Z = g(X_1, X_2, \ldots, X_n) \tag{2}$$

The failure surface or the limit state of interest can then be defined as $Z = 0$. The limit state equation plays an important role in evaluating reliability using

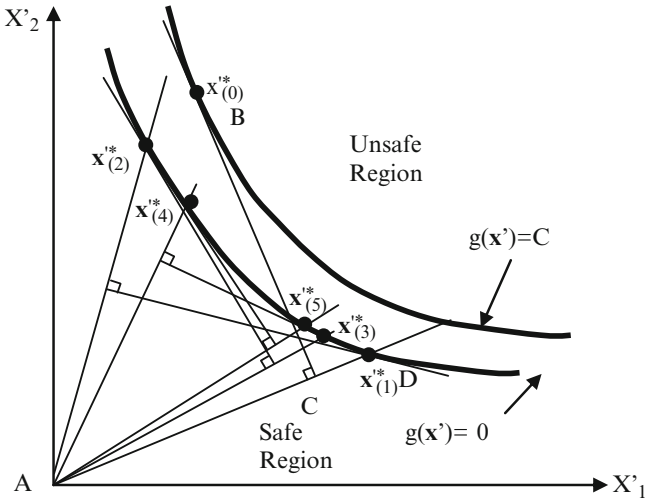

Fig. 2 Limit state concept [18, 19]

FORM/SORM. It represents the boundary between the safe and unsafe regions and a state beyond which a structure can no longer fulfill the function for which it was designed. Assuming R and S are the two basic random variables, the limit state equation and the safe and unsafe regions are shown in Fig. 2.

A limit state equation can be an explicit or implicit function of the basic random variables and can be linear or nonlinear. For nonlinear limit state functions, an iterative strategy is required to estimate the probability of failure as discussed by Haldar and Mahadevan [18], elsewhere. Two types of performance functions are generally used in engineering: strength and serviceability. Strength performance functions relate to the safety of the structures, and serviceability performance functions are related to the serviceability (deflection, vibration, etc.) of the structure. The reliabilities underlying the strength and serviceability performance functions are expected to be different.

2.3 Reliability Assessment: Implicit Limit State Functions

Reliability evaluation using FORM is relatively simple if the limit state function is explicit in terms of design variables. In this case, the derivatives of the limit state functions with respect to design variables are readily available; the iterative process necessary for the reliability evaluation becomes very straightforward. However, in many cases of practical importance, particularly for complicated large systems, the explicit expressions for the limit state functions may not be available. For such systems, the required functions need to be generated numerically such as the finite element analysis. In such cases, the derivatives are not readily available. Their numerical evaluation could be time-consuming. Some alternatives are necessary.

Several computational approaches can be pursued for reliability analysis of systems with implicit performance functions. They can be broadly divided in to three categories, based on their essential philosophy, as (1) Monte Carlo simulation (MCS), (2) response surface method (RSM), and (3) sensitivity-based analysis. Monte Carlo simulation uses randomly generated samples of input variables for each deterministic analysis. Its efficiency can be increased using intelligent schemes, as will be discussed later. It can be used for both explicit and implicit limit state functions. The RSM approximately constructs a polynomial (mainly first or second order) using a few selected deterministic analyses and in some cases regression analysis of these results. The approximate closed-form expression thus obtained is then used to estimate reliability using FORM/SORM. In the sensitivity-based approach, the sensitivity of the structural response to the input variables is computed, and it can be integrated with the FORM approach to extract the information on the underlying reliability. The value of the performance function is evaluated using deterministic structural analysis. The gradient is computed using sensitivity analysis. When the limit state function is implicit, the sensitivities can be computed in three different ways: (1) through a finite difference approach, (2) through classical perturbation methods that apply the chain rule of differentiation to finite element analysis, and (3) through iterative perturbation analysis techniques [19]. The sensitivity-based reliability analysis approach is more elegant and in general more efficient than the simulation and response surface methods. Haldar and Mahadevan [19] suggested the use of the iterative perturbation technique in the context of the basic nonlinear stochastic finite element method (SFEM)-based algorithm.

2.4 *Unified Stochastic Finite Element Method*

Without losing any generality, the limit state function can be expressed in terms of the set of basic random variables **x** (e.g., loads, material properties, and structural geometry), the set of displacements **u,** and the set of load effects **s** (except the displacements) such as internal forces and stresses. The displacement $\mathbf{u} = \mathbf{QD}$, where **D** is the global displacement vector and **Q** is a transformation matrix. The limit state function can be expressed as$g(\mathbf{x}, \mathbf{u}, \mathbf{s}) = 0$. For reliability computation, it is convenient to transform **x** into the standard normal space $\mathbf{y} = \mathrm{y}(\mathbf{x})$ such that the elements of **y** are statistically independent and have a standard normal distribution. An iteration algorithm can be used to locate the design point (the most likely failure point) on the limit state function using the first-order approximation. During each iteration, the structural response and the response gradient vectors are calculated using finite element models. The following iteration scheme can be used for finding the coordinates of the design point:

$$\mathbf{y}_{i+1} = \left[\mathbf{y}_i^t \alpha_i + \frac{g(\mathbf{y}_i)}{|\nabla g(\mathbf{y}_i)|}\right] \alpha_i \tag{3}$$

where

$$\nabla g(\mathbf{y}) = \left[\frac{\partial g(\mathbf{y})}{\partial y_1}, \ldots, \frac{\partial g(\mathbf{y})}{\partial y_n}\right]^t \quad \text{and} \quad \alpha_i = -\frac{\nabla g(\mathbf{y}_i)}{\left|\nabla g(\mathbf{y}_i)\right|} \tag{4}$$

To implement the algorithm, the gradient $\nabla g(\mathbf{y})$of the limit state function in the standard normal space can be derived as [19]:

$$\nabla g(\mathbf{y}) = \left[\frac{\partial g(\mathbf{y})}{\partial \mathbf{s}}\,\mathbf{J}_{s,x} + \left(\mathbf{Q}\frac{\partial g(\mathbf{y})}{\partial \mathbf{u}} + \frac{\partial g(\mathbf{y})}{\partial \mathbf{s}}\,\mathbf{J}_{s,D}\right)\mathbf{J}_{D,x} + \frac{\partial g(\mathbf{y})}{\partial \mathbf{x}}\right]\mathbf{J}_{y,x}^{-1} \tag{5}$$

where $\mathbf{J}_{i,j}$'s are the Jacobians of transformation (e.g., $\mathbf{J}_{s,x} = \partial \mathbf{s}/\partial \mathbf{x}$) and y_i's are statistically independent random variables in the standard normal space. The evaluation of the quantities in Eq. (5) will depend on the problem under consideration (linear or nonlinear, two- or three-dimensional, etc.) and the performance functions used. The essential numerical aspect of SFEM is the evaluation of three partial derivatives, $\partial g/\partial \mathbf{s}$, $\partial g/\partial \mathbf{u}$, and $\partial g/\partial \mathbf{x}$, and four Jacobians, $\mathbf{J}_{s,x}$, $\mathbf{J}_{s,D}$, $\mathbf{J}_{D,x}$, and $\mathbf{J}_{y,x}$. They can be evaluated by procedures suggested by Haldar and Mahadevan [19] for linear and nonlinear, two- or three-dimensional structures. Once the coordinates of the design point $\mathbf{y}^*$ are evaluated with a preselected convergence criterion, the reliability index β can be evaluated as

$$\beta = \sqrt{(\mathbf{y}^*)^t(\mathbf{y}^*)} \tag{6}$$

The evaluation of Eq. (5) will depend on the problem under consideration and the limit state functions used. The probability of failure, P_f, can be calculated as

$$P_f = \Phi(-\beta) = 1.0 - \Phi(\beta) \tag{7}$$

where Φ is the standard normal cumulative distribution function. Equation (7) can be considered as a notational failure probability. When the reliability index is larger, the probability of failure will be smaller. The author and his team published numerous papers to validate the above procedure.

3 Reliability Assessment: Present

3.1 Available Risk Evaluation Methods for Large Structures

As mentioned earlier, one of the alternatives for reliability analysis of large structures with implicit limit state functions is the use of the RSM [7]. The primary purpose of applying RSM in reliability analysis is to approximate the original

complex and implicit limit state function using a simple and explicit polynomial [8, 24, 46]. Three basic weaknesses of RSM that limits its application potential are (1) it cannot incorporate distribution information of random variables; (2) if the response surface (RS) is not generated in the failure region, it may not be directly applicable; and (3) for large systems, it may not give the optimal sampling points. Thus, a basic RSM-based reliability method may not be applicable for large structures.

Before suggesting strategies on how to remove deficiencies in RSM, it is necessary to briefly discuss other available methods to generate RS. In recent past, several methods with the general objective of approximately developing multivariate expressions for RS for mechanical engineering applications were proposed. One such method is high-dimensional model representation (HDMR) [9, 37, 45]. It is also referred to as "decomposition method," "univariate approximation," "bivariate approximation," "S – variate approximation," etc. HDMR captures the high-dimensional relationships between sets of input and output model variables in such a way that the component functions of the approximation are ordered starting from a constant and adding terms such as first order, second order, and so on. The concept appears to be reasonable if higher-order variable correlations are weak, allowing the physical model to be captured by the first few lower-order terms.

Another major work is known as the explicit design space decomposition (EDSD). It can be used when responses can be classified into two classes, e.g., safe and unsafe. The classification is performed using explicitly defined boundaries in space. A machine learning technique known as support vector machines (SVM) [5] is used to construct the boundaries separating distinct classes. The failure regions corresponding to different modes of failure are represented with a single SVM boundary, which is refined through adaptive sampling.

3.2 Improvement of RSM

To bring distributional information of random variables and to efficiently locate the failure region for large complicated systems, the author proposed to integrate RSM and FORM. The integration can be carried out with the help of following tasks.

3.2.1 Degree of Polynomial

The degree of polynomial used to generate a response surface (RS) should be kept to a minimum to increase efficiency. At present, second-order polynomial without and with cross terms are generally used to generate response surfaces. Recently, Li et al. [27] proposed high-order response surface method (HORSM). The method employs Hermite polynomials and the one-dimensional Gaussian points as sampling points to determine the highest power of each variables. Considering the fact that higher-order polynomial may result in ill-conditional system of equations for

unknown coefficients and exhibit irregular behavior outside of the domain of samples, for complicated large systems, second-order polynomial, without and with cross terms, can be used. They can be represented as

$$\hat{g}(\mathbf{X}) = b_0 + \sum_{i=1}^{k} b_i X_i + \sum_{i=1}^{k} b_{ii} X_i^2 \tag{8}$$

$$\hat{g}(\mathbf{X}) = b_0 + \sum_{i=1}^{k} b_i X_i + \sum_{i=1}^{k} b_{ii} X_i^2 + \sum_{i=1}^{k-1} \sum_{j>1}^{k} b_{ij} X_i X_j \tag{9}$$

where X_i ($i = 1, 2, \ldots, k$) is the ith random variable and b_0, b_i, b_{ii}, and b_{ij} are unknown coefficients to be determined; they need to be estimated using the response information at the sampling points by conducting several deterministic FE analyses, and k represents the total number of sensitive random variables after making less sensitive variables constants at their mean values, by conducting sensitivity analyses [18]. The numbers of coefficients necessary to define Eqs. (8 and 9) are $p = 2k + 1$ and $= (k + 1)(k + 2)/2$, respectively. The coefficients can be fully defined either by solving a set of linear equations or from regression analysis using responses at specific data points called experimental sampling points around a center point.

3.2.2 Detection of Failure Region

In the context of iterative scheme of FORM, to locate the coordinates of the most probable failure point and the corresponding reliability index, the initial center point $\mathbf{x}_{C_1}$ can be selected to be the mean values of the random variable X_i's. The response surface $\hat{g}(\mathbf{X})$ can be generated explicitly in terms of the random variables $X_i's$ by conducting deterministic FE analyses at all the experimental sampling points, as will be discussed next. Once an explicit expression of the limit state function $\hat{g}(\mathbf{X})$ is obtained, the coordinates of the checking point $\mathbf{x}_{D_1}$ (iterative process to identify the coordinates of the most probable failure point) can be estimated using FORM, using all the statistical information on X_i's. The actual response can be evaluated again at the checking point $\mathbf{x}_{D_1}$, i.e., $g(\mathbf{x}_{D_1})$ and a new center point $\mathbf{x}_{C_2}$ can be selected using a linear interpolation [8, 36] as

$$\mathbf{x}_{C_2} = \mathbf{x}_{C_1} + (\mathbf{x}_{D_1} - \mathbf{x}_{C_1}) \frac{g(\mathbf{x}_{C_1})}{g(\mathbf{x}_{C_1}) - g(\mathbf{x}_{D_1})} \quad \text{if } g(\mathbf{x}_{D_1}) \geq g(\mathbf{x}_{C_1}) \tag{10}$$

$$\mathbf{x}_{C_2} = \mathbf{x}_{D_1} + (\mathbf{x}_{C_1} - \mathbf{x}_{D_1}) \frac{g(\mathbf{x}_{D_1})}{g(\mathbf{x}_{D_1}) - g(\mathbf{x}_{C_1})} \quad \text{if } g(\mathbf{x}_{D_1}) < g(\mathbf{x}_{C_1}) \tag{11}$$

A new center point $\mathbf{x}_{C_2}$ then can be used to develop an explicit performance function for the next iteration. This iterative scheme can be repeated until a preselected convergence criterion of $(\mathbf{x}_{C_{i+1}} - \mathbf{x}_{C_i})/\mathbf{x}_{C_i} \leq \varepsilon$ is satisfied. ε can be considered to be |0.05|. The second deficiency of RSM will be removed by locating the failure region using the above scheme.

3.2.3 Selection of Sampling Points

Saturated design (SD) and central composite design (CCD) are the two most promising schemes that can be used to generate experimental sampling points around the center point. SD is less accurate but more efficient since it requires only as many sampling points as the total number of unknown coefficients to define the response surface. CCD is more accurate but less efficient since a regression analysis needs to be carried out to evaluate the unknown coefficients. The details of experimental design procedures can be found in [7, 24]. In any case, the use of SD or CCD will remove the third deficiency of RSM.

Since the proposed algorithm is iterative and the basic SD and CCD require different amounts of computational effort, considering efficiency without compromising accuracy, several schemes can be followed. Among numerous schemes, one basic and two promising schemes are:

Scheme 0 – Use SD with second-order polynomial without the cross terms throughout all the iterations.
Scheme 1 – Use Eq. (8) and SD for the intermediate iterations and Eq. (9) and full SD for the final iteration.
Scheme 2 – Use Eq. (8) and SD for the intermediate iterations and Eq. (9) and CCD for the final iteration.

To illustrate the computational effort required for the reliability evaluation of large structural system, suppose the total number of sensitive random variables present in the formulation is, $k = 40$. The total number of coefficients necessary to define Eq. (8) will be $2 \times 40 + 1 = 81$ and to define Eq. (9) will be $(40 + 1)(40 + 2)/2 = 861$. It can also be shown that if Eq. (8) and SD scheme are used to generate the response surface, the total number of sampling points, essentially the total number of deterministic FE-based response analyses, will be 81. However, if Eq. (9) and full SD scheme are used, the corresponding deterministic analyses will be 861. If Eq. (9) and CCD scheme are used, the corresponding deterministic analyses will be $2^{40} + 2 \times 40 + 1 = 1{,}099{,}511{,}160{,}081$.

3.2.4 Mathematical Representation of Large Systems for Reliability Evaluation

The phrase "probability of failure" implies that the risk needs to be evaluated just before failure in the presence of several sources of nonlinearities. Finite element

(FE)-based formulations are generally used to realistically consider different sources of nonlinearity and other performance-enhancing features with improved energy dissipation mechanism now being used after the Northridge earthquake of 1994. Thus, for appropriate reliability evaluation, it is essential that structures are represented realistically by FEs and all major sources of nonlinearity and uncertainty are appropriately incorporated in the formulation.

To study the behavior of frame structures satisfying underlying physics, consideration of appropriate rigidities of connections is essential. In a typical design, all connections are considered to be fully restrained (FR), i.e., the angles between the girders and columns, before and after the application of loads, will remain the same. However, extensive experimental studies indicate that they are essentially partially restrained (PR) connection with different rigidities. In a deterministic analysis, PR connections add a major source of nonlinearity. In a dynamic analysis, it adds a major source of energy dissipation. In reliability analysis, it adds a major source of uncertainty. In general, the relationship between the moment M, transmitted by the connection, and the relative rotation angle θ is used to represent the flexible behavior. Among the many alternatives (Richard model, piecewise linear model, polynomial model, exponential model, B-Spline model, etc.), the Richard four-parameter moment-rotation model is chosen here to represent the flexible behavior of a connection. It is expressed as [39]

$$M = \frac{(k - k_{\mathrm{p}})\theta}{\left(1 + \left|\frac{(k - k_{\mathrm{p}})\theta}{M_0}\right|^{N}\right)^{\frac{1}{N}}} + k_{\mathrm{p}}\theta \tag{12}$$

where M is the connection moment, θ is the relative rotation between the connecting elements, k is the initial stiffness, k_{p} is the plastic stiffness, M_0 is the reference moment, and N is the curve shape parameter. These parameters are identified in Fig. 3. To incorporate flexibility in the connections, a beam-column element can be introduced to represent each connection. However, its stiffness needs to be updated at each iteration since the stiffness representing the partial rigidity depends on θ. The tangent stiffness of the connection element, $K_{\mathrm{C}}(\theta)$, can be shown to be

$$K_{\mathrm{C}}(\theta) = \frac{\mathrm{d}M}{\mathrm{d}\theta} = \frac{(k - k_{\mathrm{p}})}{\left(1 + \left|\frac{(k - k_{\mathrm{p}})\theta}{M_0}\right|^{\mathrm{N}}\right)^{\frac{N+1}{N}}} + k_{\mathrm{p}} \tag{13}$$

The Richard model discussed above represents only the monotonically increasing loading portion of the M-θ curves. However, the unloading and reloading behavior of the M-θ curves is also essential for any nonlinear seismic analysis [10]. Using the Masing rule and the Richard model, Huh and Haldar [21]

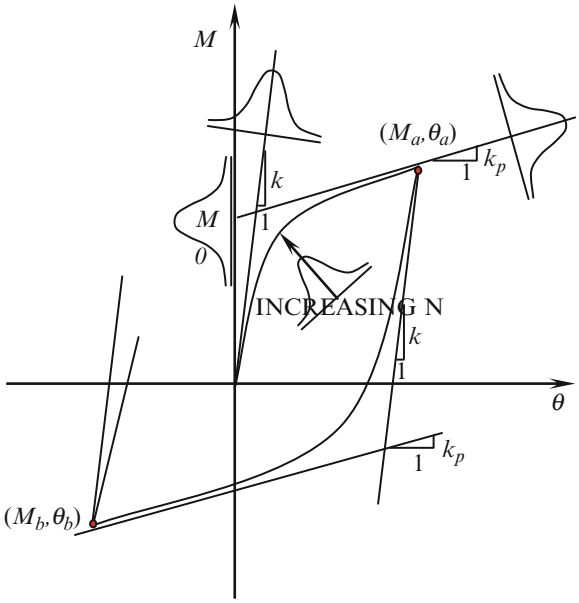

Fig. 3 M-θ curve using the Richard model, Masing rule, and uncertainty

theoretically developed the unloading and reloading parts of the M-θ curves. The tangent stiffness for the unloading and reloading behavior of a PR connection can be represented as

$$K_{\mathrm{C}}(\theta) = \frac{\mathrm{d}M}{\mathrm{d}\theta} = \frac{\left(k - k_{\mathrm{p}}\right)}{\left(1 + \left|\frac{\left(k - k_{\mathrm{p}}\right)(\theta_{\mathrm{a}} - \theta)}{2M_0}\right|^N\right)^{\frac{N+1}{N}}} + k_{\mathrm{p}} \tag{14}$$

As shown in Fig. 3, this represents hysteretic behavior at the PR connections. The basic FE formulation of the structure remains unchanged.

3.2.5 Pre- and Post-Northridge PR Connections

During the Northridge earthquake of 1994, several connections in steel frames fractured in a brittle and premature manner. A typical connection, shown in Fig. 4, was fabricated with the beam flanges attached to the column flanges by full penetration welds (field-welded) and with the beam web bolted (field-bolted) to single plate shear tabs [40], denoted hereafter as the pre-NC.

In the post-Northridge design practices, the thrusts were to make the connections more flexible than the pre-NC and to move the location of formation of any plastic hinge away from the connection and to provide more ductility to increase the energy absorption capacity. Several improved connections can be found in the literature

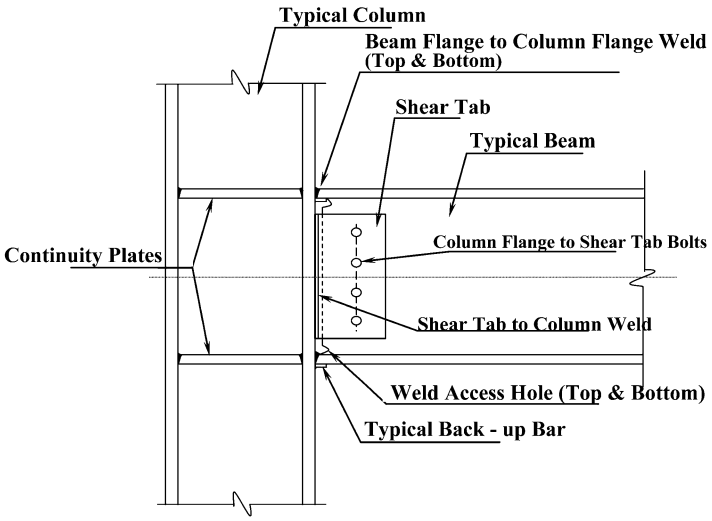

Fig. 4 A typical pre-NC

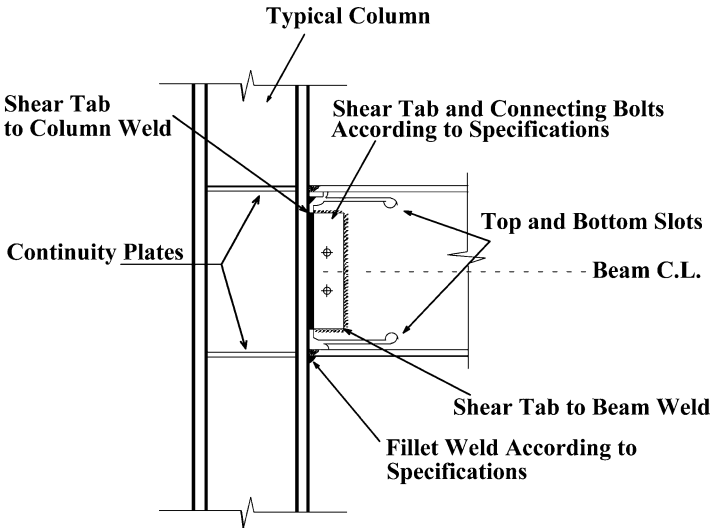

Fig. 5 A typical post-NC

including cover-plated connections, spliced beam connections, side-plated connections, bottom haunch connections, connections with vertical ribs, and connections with a reduced beam sections (RBS) or dog-boned (FEMA 350-3). Seismic Structural Design Associates, Inc. (SSDA) proposed a unique proprietary slotted web (SSDA SlottedWeb^{TM}) moment connection (Richard et al. [40]), as shown in Fig. 5, denoted hereafter as the post-NC. The author was given access to some of the actual SSDA

full-scale test results. Using the four-parameter Richard model, the research team first proposed a mathematical model to represent moment-relative rotation (M-θ) curves for this type of connections [30].

4 Examples

A three-story three-bay steel frame, as shown in Fig. 6, is considered. Section sizes of beams and columns, using A36 steel, are also shown in the figure. It was excited by a seismic time history shown in Fig. 7 [17, 21].

The four parameters of the Richard model are calculated by PRCONN [38], a commercially available computer program for both pre-NC and post-NC connections. For the example under consideration, considering the sizes of columns and beams, three types of connection are necessary. They are denoted as types A, B, and C, hereafter. Four Richard parameters for both pre-NC and post-NC connections are summarized in Table 1.

4.1 Limit States or Performance Functions

In structural engineering, both strength and serviceability limit states are used for reliability estimation. The strength limit states mainly depend on the failure modes. Most of the elements in the structural system considered are beam columns. The interaction equations suggested by the American Institute of Steel Construction's

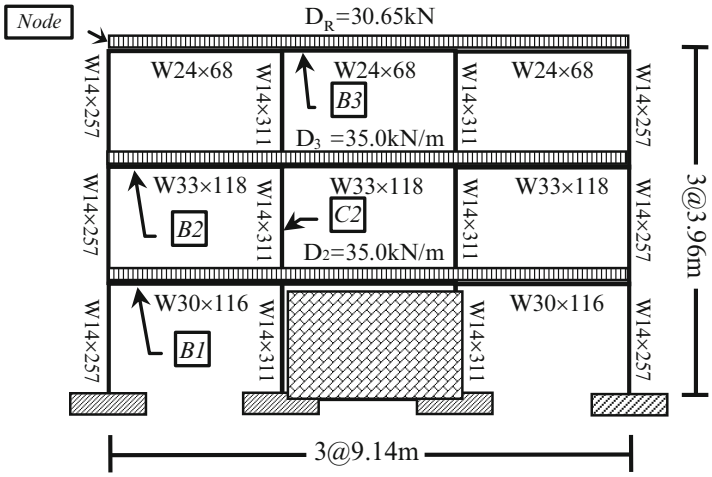

Fig. 6 A 3-story 3-bay SMRF structure

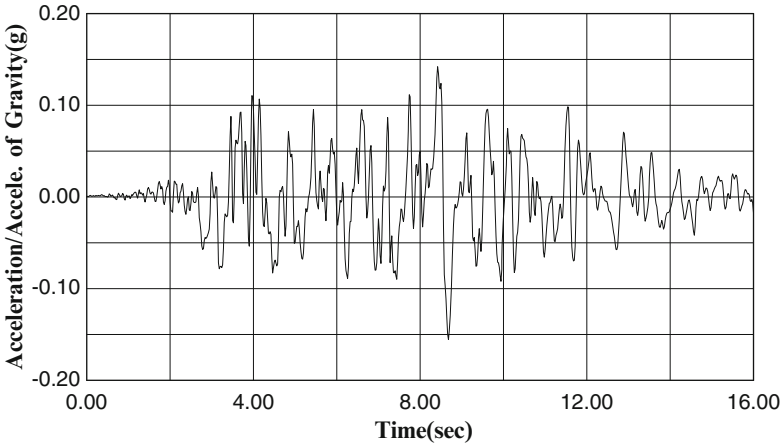

Fig. 7 Earthquake time history

Table 1 Parameters of Richard equation for M-θ curves

Connection assembly type				Connection parameters			
ID.		Beam	Column	k[a]	k_p[a]	M_0[b]	N
Pre-NC	A	W24 × 68	W14 × 257	2.51E7	5.56E5	4.16E4	1.1
		W24 × 68	W14 × 311				
	B	W33 × 118	W14 × 257	5.08E7	1.14E5	6.79E4	1.1
		W33 × 118	W14 × 311				
	C	W30 × 116	W14 × 257	3.95E7	9.19E5	5.65E4	1.1
		W30 × 116	W14 × 311				
Post-NC	A	W24 × 68	W14 × 257	1.00E9	4.52E5	9.64E4	1.0
		W24 × 68	W14 × 311				
	B	W33 × 118	W14 × 257	2.34E9	4.52E5	2.44E5	1.0
		W33 × 118	W14 × 311				
	C	W30 × 116	W14 × 257	2.14E9	4.52E5	2.21E5	1.0
		W30 × 116	W14 × 311				

[a]kN cm/rad
[b]kN cm

Load and Resistance Factor Design [1] manual for two-dimensional structures are used in this study. The serviceability limit states can be represented as

$$g(\mathbf{X}) = \delta_{\text{allow}} - y_{\max}(\mathbf{X}) = \delta_{\text{allow}} - \hat{g}(\mathbf{X}) \tag{15}$$

where δ_{allow} is the allowable interstory drift or overall lateral displacement specified in codes and $y_{\max}(\mathbf{X})$ is the corresponding the maximum interstory drift or overall lateral displacement estimated.

Table 2 Statistical information on the design variables

	Item	Random variable	Mean value	COV	Dist.
Member	All	E(kN/m^2)	2.0E+8	0.06	Ln
		F_y(kN/m^2)	2.48E+5	0.10	Ln
	Column	I_x^{C1}(m^4)	1.42E-3	0.05	Ln
	W14 × 257	Z_x^{C1}(m^3)	7.98E-3	0.05	Ln
	Column	A^{C2}(m^2)	5.90E-2	0.05	Ln
	W14 × 311	I_x^{C2}(m^4)	1.80E-3	0.05	Ln
	Beam	I_x^{B2}(m^4)	2.46E-3	0.05	Ln
	W33 × 118				
	Beam	I_x^{B3}(m^4)	2.05E-3	0.05	Ln
	W30 × 116	Z_x^{B3}(m^3)	6.19E-3	0.05	Ln
Seismic load		ξ	0.05	0.15	Type I
		g_e	1.0	0.20	Type I
Connection	Richard model parameter	K^a	Refer to values in Table 3	0.15	N
		$k_p{}^a$		0.15	N
		$M_0{}^b$		0.15	N
		N		0.05	N
Shear wall[c]		E_C(kN/m^2)	2.14E+7	0.18	Ln
		v	0.17	0.10	Ln

Ln lognormal distribution
[a]kN cm/rad
[b]kN cm
[c]$f_C' = 2.068 \times 10^4$ (kN/m^2)

4.2 *Reliability Evaluations of Frame with Different Connection Conditions, Without RC Shear Wall*

The statistical characteristics of all the design variables used in the formulation are summarized in Table 2. The probabilities of failure of the frame for the lateral deflection at the top of the frame for serviceability limit state and the strength limit state of the weakest members are estimated assuming all the connections are of FR type. The results are summarized in Table 3. To verify the results, 20,000 MCS for the serviceability and 30,000 MCS for the strength limit states were carried out. The results clearly indicate that the bare steel frame will not satisfy the serviceability requirement. Then, the reliabilities of the frame are estimated assuming all the connections are post-NC and pre-NC types, and the results are summarized in Table 4. The behavior of the frame in the presence of FR and post-NC for both serviceability and strength limit states are very similar. This was also observed during the full-scale experimental investigations. This observation clearly indicates that the method can predict realistic behavior of complex structural systems. In any case, the lateral stiffness of the frame needs to be increased.

Table 3 Reliability evaluation of FR frame

		Service-ability	Strength limit state	
Limit state		Node at 1	Beam ($B1$)	Column ($C1$)
MCS	P_f	0.08740	N/A[a]	N/A[a]
	$\beta \approx \Phi^{-1}(1 - P_f)$	1.357	N/A	N/A
	NOS[b]	20,000	30,000	30,000
Proposed algorithm	No. of RV	8	6	6
	Scheme	1	2	2
	β	1.330	4.724	5.402
	Error w.r.t β	1.99%	N/A	N/A
	TNSP[c]	79	103	103

[a]Not a single failure observed for 30,000cycles of simulation since large reliability indexes are expected in the strength limit state
[b]Number of simulation for deterministic FEM analyses
[c]Total number of sampling points (total number of deterministic FEM analyses)

Table 4 Reliability evaluations of frame without and with shear wall

Steel frame without shear wall					Steel frame with shear wall			
		Connection type				Connection type		
		FR	Post-NC	Pre-NC		FR	Post-NC	Pre-NC
Serviceability limit state (node 1)								
	β	1.330	1.329	0.463	β	3.667	3.534	1.685
	$P_f \approx \Phi(-\beta)$	0.092	0.092	0.322	$P_f \approx \Phi(-\beta)$	1.2E-4	2.0E-4	4.6E-2
	No. of R.V.	8	20	20	No. of R.V.	10	22	22
	TNSP	79	313	313	TNSP	108	366	366
Strength limit state								
	β	4.724	4.756	3.681	β	6.879	6.714	4.467
Beam	$P_f \approx \Phi(-\beta)$	1.16E-6	9.87E-7	1.16E-4	$P_f \approx \Phi(-\beta)$	3.01E-12	9.477E-12	3.97E-6
	No. of R.V.	6	18	18	No. of R.V.	8	20	20
	TNSP	103	264	264	TNSP	79	313	313
Column	β	5.402	5.376	4.154	β	6.879	6.714	4.467
	$P_f \approx \Phi(-\beta)$	3.30E-8	3.81E-8	1.63E-5	$P_f \approx \Phi(-\beta)$	3.01E-12	9.47E-12	3.97E-6
	No. of R.V.	6	18	18	No. of R.V.	8	20	20
	TNSP	103	264	264	TNSP	79	313	313

4.3 Reliability Evaluations of Frames with Different Connection Conditions with RC Shear Wall

To increase the lateral stiffness, the steel frame is strengthened with a reinforced concrete (RC) shear wall at the first floor level, as shown in Fig. 6. For the steel and concrete dual system, all the steel elements in the frame are modeled as beam-column elements. A four-node plane stress element is introduced for the shear wall in the frame. To consider the presence of RC shear wall, the modulus of elasticity, E_C, and the Poisson ratio of concrete,v, are necessary in the deterministic formulation. Cracking may develop at a very early stage of loading. It was observed that the

degradation of the stiffness of the shear walls occurs after cracking and can be considered effectively by reducing the modulus of elasticity of the shear walls [26]. The rupture strength of concrete, f_r, is assumed to be $f_r = 7.5 \times \sqrt{f'_c}$, where f_c' is the compressive strength of concrete. After the tensile stress of each shear wall exceeds the prescribed tensile stress of concrete, the degradation of the shear wall stiffness is assumed to be reduced to 40% of the original stiffness [26]. The uncertainty in all the variables considered for the bare steel frame will remain the same. However, two additional sources of uncertainty, namely, in E_C and v, need to be considered, as given in Table 2.

The frame is again excited by the same earthquake time history as shown in Fig. 7. The probabilities of failure for the combined dual system in presence of FR, post-NC, and pre-NC connections are calculated using the proposed algorithm for the strength and serviceability limit states. The results are summarized in Table 4. The results indicate that the presence of shear wall at the first floor level significantly improves both the serviceability and strength behavior of the steel frame. If the probabilities of failure need to be reduced further, RC shear walls can be added in the second and/or third floor. Again, this improved behavior can be observed and quantified by carrying out about hundred deterministic evaluations instead of thousands of MCS. The improved behavior of the frame in the presence of RC shear wall is expected; however, the proposed algorithm can quantify the amount of improvement in terms of probability of failure for different design alternatives.

5 Reliability Assessment: Future

5.1 Reliability Evaluation of Large Structural Systems

In some studies considered by the author, one deterministic nonlinear dynamic analysis of large structures may take over 10 h of computer time. If one has to use very small, say only 100 simulations, it may take 1,000 h or over 41 days of uninterrupted running of a computer. The author proposed to estimate reliability of such systems using only tens instead of hundreds or thousands of deterministic evaluations at intelligently selected points to extract the reliability information. The procedure is still under development. The concept is briefly discussed below.

Scheme M1: To improve the efficiency of Scheme 1 discussed earlier, the cross terms (edge points), $k\ (k-1)$, are suggested to be added only for the most important variables in the last iteration. Since the proposed algorithm is an integral part of FORM, all the random variables in the formulation can be arranged in descending order of their sensitivity indexes $\alpha(X_i)$, i.e., $\alpha(X_1) > \alpha(X_2) > \alpha(X_3) \ldots\ldots\ldots > \alpha(X_k)$. The sensitivity of a variable X, $\alpha(X)$, is the directional cosines of the unit normal vector at the design point. In the last iteration, the cross terms are added only for the sensitive random variables, m, and the corresponding reliability index is calculated. The total number of FEM analyses required for Scheme 1 and *M1* is $(k+1)(k+2)/2$ and $2k+1+m(2k-m-1)/2$, respectively. For an example, suppose for a large

structural system, $k = 40$ and $m = 3$. The total number of required FEM analyses will be 861 and 195, respectively, for the two schemes.

Scheme M2: Instead of using full factorial plan in CCD, Myers et al. [31] recently proposed quarter factorial plan. This improved and efficient version of Scheme 2 will be denoted hereafter as Scheme M2. In Scheme M2, it is proposed that only quarter of the factorial points corresponding to the most sensitive random variables are to be considered. In other words, in the last iteration, the variables are to be arranged in descending order according to their sensitivity indexes $\alpha(X_i)$, i.e., $\alpha(X_1) > \alpha(X_2) > \alpha(X_3) \ldots\ldots > \alpha(X_k)$. Then, the factorial sampling points are determined by using the values +1 and −1, in the coded space, for $X_1, X_2, X_3, \ldots$, until the number of quarter of factorial sampling $= 0.25 \times 2^k = 2^{k-2}$.

6 Risk Management

Since risk cannot be completely eliminated in engineering analysis and design, it needs to be managed appropriately. It is undesirable and uneconomical, if not impossible, to design a risk-free structure. According to Raiffa [35], the decision or management can be subdivided in to risk or data analysis, inference, and decision. Risk analysis is discussed in the first part of this chapter. Inference attempts to incorporate additional scientific knowledge in the formulation that may have been ignored in the previous data analysis. The decision is the final outcome of any risk-based engineering design. For a given structure, the risks for different design alternatives can be estimated. The information on risk and the corresponding consequences of failure, including the replacement cost, can be combined using a decision analysis framework to obtain the best alternative. Thus, the probability concept provides a unified framework for quantitative analysis of risk as well as the formulation of trade-off studies for decision-making, planning, and design considering economic aspects of the problem.

The relevant components of a decision analysis are generally described in the form of a decision tree [16]. The decision tree helps to organize all necessary information in a systematic manner suitable for analytical evaluation of the optimal alternative. A decision-making process starts by choosing an action, a, from among the available alternatives actions $(a_1, a_2, \ldots, a_n)$, called decision variables. They branch out from a square node or a decision node. Once a decision has been made, a natural outcome θ from among all possible states, $\theta_1, \theta_2, \ldots, \theta_n$, would materialize. All possible states are beyond the control of a decision-maker; they are shown to originate from a circular node, called the chance node. Each natural outcome based on the action taken is expected to have a different risk of success or failure and expressed in terms of probability $P(\theta i|ai)$. As a result of having taken action a and having found true state θ, a decision-maker will obtain a utility value $u(a, \theta)$, a numerical measure of the consequences of this action-state pair. A general decision analysis framework may contain the following necessary components: (1) decision variables, (2) consequence, (3) risk associated with each alternative, and (4) identification of the decision-maker and the decision criteria.

7 Future Directions

7.1 Artificial Neural Networks and Soft Computing

The application of artificial neural networks (ANN), the more generic term used by the research community as soft computing, in civil engineering has been significant in the very recent past [23]. In addition to ANN, the other soft computing techniques include genetic algorithm, evolutionary computation, machine learning, organic computing, probabilistic reasoning, etc. The applicability of these techniques could be problem specific, some of them can be combined, or one technique can be used when another failed to meet the objectives of the study. Soft computing differs from conventional hard computing. Unlike hard computing, soft computing is tolerant of imprecision, uncertainty, partial truth, and approximation. To some extent, it essentially plays a role similar to human mind.

7.2 Incorporation of Cognitive Sources of Uncertainty

Being a reliability person, I feel I should address this subject very briefly. Most of the works on reliability-based structural engineering incorporate noncognitive (quantitative) sources of uncertainty using crisp set theory. Cognitive or qualitative sources of uncertainty are also important. They come from the vagueness of the problem arising from the intellectual abstractions of reality. To incorporate cognitive sources of uncertainty, fuzzy set theory [4] is generally used.

7.3 Education

Lack of education could be a major reason for avoidance of using the reliability-based design concept by the profession. If closed-form reliability analysis is not possible and the design codes do not cover the design of a particular structure, at the minimum, simulation can be used to satisfy the intent of the codes. In Europe, highway and railway companies are using simulation for assessment purposes. In the USA, the general feeling is that we are safe if we design according to the design code. Designers should use all available means to satisfy performance requirements, according to a judge. The automotive industry satisfied the code requirements in one case. However, according to a judge, they should have used simulation to address the problem more comprehensively.

Some of the developments in the risk-based design using simulation are very encouraging. Simulation could be used in design in some countries, but it is also necessary to look at its legal ramification. Unlike in Europe, in the USA, a code is not a government document. It is developed by the profession and its acceptance is voted by the users and developers. It was pointed out that in some countries, code

guidelines must be followed to the letters, and other countries permit alternative methods if they are better. In Europe, two tendencies currently exist: Anglo-Saxon – more or less free to do anything, and middle-European – fixed or obligatory requirements. Current Eurocode is obligatory. We need to change the mentality and laws to implement simulation or reliability-based design concept in addressing real problems.

In the context of education of future structural engineers, the presence of uncertainty must be identified in design courses. Reliability assessment methods can contribute to the transition from deterministic to probabilistic way of thinking of students as well as designers. In the USA, the Accreditation Board of Engineering and Technology (ABET) now requires that all civil engineering undergraduate students demonstrate knowledge of the application of probability and statistics to engineering problems, indicating its importance in civil engineering education. Most of the risk-based design codes are the by-product of education and research at the graduate level. In summary, the profession is moving gradually in accepting the reliability-based design concept.

7.4 Computer Programs

The state of the art in reliability estimation is quite advanced; however, it is not popular with the practicing engineers. One issue could be the lack of availability of the user-friendly software. Two types of issues need to be addressed at this stage. Reliability-based computer software should be developed for direct applications, or the reliability-based design feature should be added to the commercially available deterministic software. Some of the commercially available reliability-based computer software is briefly discussed next.

NESSUS (Numerical Evaluation of Stochastic Structures Under Stress) was developed by the Southwest Research Institute [43] under the sponsorship of NASA Lewis Research Center. It combines probabilistic analysis with a general-purpose finite element/boundary element code. The probabilistic analysis features an advanced mean value (AMV) technique. The program also includes techniques such as fast convolution and curvature-based adaptive importance sampling.

PROBAN (PROBability ANalysis) was developed at Det Norske Veritas, Norway, through A.S. Veritas Research [44]. PROBAN was designed to be a general-purpose probabilistic analysis tool. It is capable of estimating the probability of failure using FORM and SORM for a single event, unions, intersections, and unions of intersections. The approximate FORM/SORM results can be updated through importance sampling simulation scheme. The probability of general events can be computed by Monte Carlo simulation and directional sampling.

CALREL (CAL-RELiability) is a general-purpose structural reliability analysis program designed to compute probability integrals [28]. It incorporates four general techniques for computing the probability of failure: FORM, SORM, directional simulation with exact or approximate surfaces, and Monte Carlo simulation. It has a library of probability distributions of independent as well as dependent random variables.

Under the sponsorship of the Pacific Earthquake Engineering Research (PEER), McKenna et al. [29] have developed a finite element reliability code within the framework of OpenSees.

Structural engineers without formal education in risk-based design may not be able to use the computer programs mentioned above. They need to be retrained with very little effort. They may be very knowledgeable using exiting deterministic analysis software including commercially available finite element packages. This expertise needs to be integrated with risk-based design concept. Thus, probabilistic features may need to be added to the deterministic finite element packages. Proppe et al. [32] discussed the subject in great detail. For proper interface of deterministic software, they advocated for graphical user interface, communication interface which must be flexible enough to cope with different application programming interfaces and data format, and the reduction of the problem sizes before undertaking reliability analysis. COSSAN [12] software attempted to implement the concept.

The list of computer programs given here may not be exhaustive. However, they are being developed and are expected to play a major role in implementing reliability-based engineering analysis and design in the near future.

8 Conclusions

Engineering under uncertainty has evolved in the past several decades. It has attracted multidisciplinary research interest. A brief overview of the past, present, and future in the author's assessment is given here. Albert Einstein stated that "The important thing is not to stop questioning. Curiosity has its own reason for existing." The profession is very curious on the topic, and there is no doubt that future analysis and design of engineering structures will be entirely conducted using probability concept.

Acknowledgments I would like to thank all my teachers for teaching me subjects that helped to develop my career and understanding of my life in a broader sense. I also would like to thank all my former and current students who taught me subjects for which I did not have any formal education. They helped me explore some of the unchartered areas. I also appreciate financial support I received from many funding agencies to explore several challenging and risky research areas. I would also like to thank the organizing committee of the International Symposium on Engineering Under Uncertainty: Safety Assessment and Management (ISEUSAM-2012) for inviting me to give the inaugural keynote speech.

References

1. American Institute of Steel Construction (2005) Manual of steel construction: load and resistance factor design. Illinois, Chicago
2. Ang AH-S, Cornell CA (1974) Reliability bases of structural safety and design. J Struct Eng ASCE 100(ST9):1755–1769

3. Ang AH-S, Tang WH (1975) Probability concepts in engineering design, vol. I: Basic principles. Wiley, New York
4. Ayyub BM, Klir GJ (2006) Uncertainty modeling and analysis in engineering and the sciences. Chapman and Hall/CRC, Boca Raton
5. Basudhar A, Missoum S, Harrison Sanchez A (2008) Limit state function identification using support vector machines for discontinuous responses and disjoint failure domains. Probab Eng Mech 23(1):1–11
6. Benjamin JR, Cornell CA (1970) Probability, statistics, and decision for civil engineers. McGraw-Hill, New York
7. Box GP, William GH, Hunter JS (1978) Statistics for experimenters: an introduction to design, data analysis and modeling building. Wiley, New York
8. Bucher CG, Bourgund U (1990) A fast and efficient response surface approach for structural reliability problems. Struct Saf 7:57–66
9. Chowdhury R, Rao BN, Prasad AM (2008) High dimensional model representation for piece wise continuous function approximation. Commun Numer Methods Eng 24(12):1587–1609
10. Colson A (1991) Theoretical modeling of semi-rigid connection behavior. J Construct Steel Res 19:213–224
11. Cornell CA (1969) A probability-based structural code. J Am Concr Inst 66(12):974–985
12. COSSAN (Computational Stochastic Structural Analysis) – Stand – Alone Toolbox (1996) User's manual. IfM – Nr: A, Institute of Engineering Mechanics, Leopold – Franzens University, Innsbruck
13. Ellingwood BR, Galambos TV, MacGregor JG, Cornell CA (1980) Development of probability based load criterion for American National Standard A58. NBS special publication 577. U.S. Department of Commerce, Washington, DC
14. Fisher RA (1959) Statistical methods and scientific inference. Hafner, New York
15. Freudenthal AM (1947) Safety of structures. Trans ASCE 112:125–180
16. Haldar A (1980) Liquefaction study – a decision analysis framework. J Geotech Eng Div ASCE 106(GT12): 1297–1312
17. Haldar A, Farag R, Huh J (2010) Reliability evaluation of large structural systems. Keynote lecture. International symposium on reliability engineering and risk management (ISRERM2010), Shanghai, China, pp. 131–142
18. Haldar A, Mahadevan S (2000) Probability, reliability and statistical methods in engineering design. Wiley, New York
19. Haldar A, Mahadevan S (2000) Reliability assessment using stochastic finite element analysis. Wiley, New York
20. Hasofar AM, Lind NC (1974) Exact and invariant second moment code format. J Eng Mech ASCE 100(EM1):111–121
21. Huh J, Haldar A (2011) A novel risk assessment method for complex structural systems. IEEE Trans Reliab 60(1):210–218
22. Jeffreys H (1961) Theory of probability. Oxford University Press, New York
23. Kartam N, Flood I, Garrett JH (1997) Artificial neural networks for civil engineers. American Society of Civil Engineers, New York
24. Khuri AI, Cornell CA (1996) Response surfaces designs and analyses. Marcel Dekker, New York
25. Laplace PSM (1951) A philosophical essay on probabilities (translated from the sixth French edition by Truscott FW and Emory FL). Dover Publications, New York
26. Lefas D, Kotsovos D, Ambraseys N (1990) Behavior of reinforced concrete structural walls: strength, deformation characteristics, and failure mechanism. ACI Struct J 87(1):23–31
27. Li H, Lu Z, Qiao H (2008) A new high-order response surface method for structural reliability analysis, 2008, personal communication
28. Liu P-L, Lin H-Z, Der Kiureghian A (1989) CALREL. University of California, Berkeley
29. McKenna F, Fenves GL, Scott MH (2002) Open system for earthquake engineering simulation. Pacific Earthquake Engineering Research Center, Berkeley. http://opensees.berkeley.edu/

30. Mehrabian A, Haldar A, Reyes AS (2005) Seismic response analysis of steel frames with post-Northridge connection. Steel Comp Struct 5(4):271–287
31. Myers RH, Montgomery DC, Anderson-Cook CM (2009) Response surface methodology: process and product optimization using designed experiments. Wiley, New York
32. Proppe C, Pradlwarter HJ, Schueller GI (2001) Software for stochastic structural analysis – needs and requirements. In: Corotis RB, Schueller GI, Shinizuka M (eds) Proceedings of the 4th international conference on structural safety and reliability, AA Balkema Publishers, The Netherlands
33. Rackwitz R (1976) Practical probabilistic approach to design. Bulletin No. 112, Comite European du Beton, Paris
34. Rackwitz R, Fiessler B (1978) Structural reliability under combined random load sequences. Comput Struct 9(5):484–494
35. Raiffa H (1968) Decision analysis. Addison-Wesley, Reading
36. Rajashekhar MR, Ellingwood BR (1993) A new look at the response surface approach for reliability analysis. Struct Saf 12:205–220
37. Rao BN, Chowdhury R (2009) Enhanced high dimensional model representation for reliability analysis. Int J Numer Methods Eng 77(5):719–750
38. Richard RM (1993) PRCONN manual. RMR Design Group, Tucson
39. Richard RM, Abbott BJ (1975) Versatile elastic-plastic stress-strain formula. J Eng Mech ASCE 101(EM4):511–515
40. Richard RM, Allen CJ, Partridge JE (1997)Proprietary slotted beam connection designs. Mod Steel Constr 37(3):28–35
41. Richard RM, Radau RE (1998) Force, stress and strain distribution in FR bolted welded connections. In: Proceedings of structural engineering worldwide, San Francisco, CA
42. Rosenbleuth E, Esteva L (1972) Reliability bases for some Mexican codes. ACI Publ SP-31:1–41
43. Shinozuka M (1983) Basic analysis of structural safety. J Struct Eng ASCE 109(3):721–740
44. Southwest Research Institute (1991) NEUSS, San Antonio, Texas
45. Veritas Sesam Systems (1991) *PROBAN*, Houston, Texas
46. Xu H, Rahman S (2005) Decomposition methods for structural reliability analysis. Probab Eng Mech 20:239–250
47. Yao TH-J, Wen YK (1996) Response surface method for time-variant reliability analysis. J Struct Eng ASCE 122(2):193–201

Geotechnics in the Twenty-First Century, Uncertainties and Other Challenges: With Particular Reference to Landslide Hazard and Risk Assessment

Robin Chowdhury, Phil Flentje, and Gautam Bhattacharya

Abstract This chapter addresses emerging challenges in geotechnics in the context of the significant challenges posed by hazards, both natural and human-induced. The tremendous importance of dealing with uncertainties in an organized and systematic way is highlighted. The chapter includes reflections on responding to the need for multidisciplinary approaches. While the concepts and ideas are pertinent to diverse applications of geotechnics or to the whole of geotechnical engineering, illustrative examples will be limited to research trends in slope stability and landslide management.

From time to time, researchers, academics, and practicing engineers refer to the need for interdisciplinary approaches in geotechnical engineering. However, surveys of the relevant literature reveal few examples of documented research studies based within an interdisciplinary framework. Meanwhile there is a broad acceptance of the significant role of uncertainties in geotechnics.

This chapter includes reflections on what steps might be taken to develop better approaches for analysis and improved strategies for managing emerging challenges in geotechnical engineering. For example, one might start with the need to highlight different types of uncertainties such as geotechnical, geological, and hydrological. Very often, geotechnical engineers focus on variability of soil properties such as shear strength parameters and on systematic uncertainties. Yet there may be more important factors in the state of nature which are ignored because of the lack of a multidisciplinary focus. For example, the understanding of the potential for

Robin Chowdhury, Invited Keynote Speaker, ISEUSAM-2012 Conference, January 2012, BESU, Shibpur, India

R. Chowdhury (✉) • P. Flentje
University of Wollongong, New South Wales, Australia
e-mail: robin@uow.edu.au; pflentje@uow.edu.au

G. Bhattacharya
Bengal Engineering & Science University, Shibpur, Howrah, West Bengal 711103, India
e-mail: gautam@civil.becs.ac.in

S. Chakraborty and G. Bhattacharya (eds.), *Proceedings of the International Symposium on Engineering under Uncertainty: Safety Assessment and Management (ISEUSAM - 2012)*,
DOI 10.1007/978-81-322-0757-3_2,

progressive failure within a soil mass or a slope may require careful consideration of the geological context and of the history of stress and strain. The latter may be a consequence of previous seismic activity and fluctuations in rainfall and groundwater flow.

The frequency and consequences of geotechnical failures involving soil and rock continue to increase globally. The most significant failures and disasters are often associated with major natural events but not exclusively so.

It is expected that climate change will lead to even more unfavorable conditions for geotechnical projects and thus to increasing susceptibility and hazard of landsliding. This is primarily because of the expected increase in the variability of rainfall and the expected increase in sea levels. Responding to the effects of climate change will thus require more flexible and robust strategies for assessment of landslide susceptibility and to innovative engineering solutions.

Keywords Geotechnics • Uncertainty • Hazards • Risk • Landslide

1 Introduction

There are significant challenges for the future development and application of geotechnical engineering. Developments in research, analysis, and practice have taken place to advance knowledge and practice. While the scope of the profession and its discipline areas is already vast, significant extension is required in the areas of hazard and risk assessment and management. In particular, the field of natural disaster reduction requires the development of innovative approaches within a multidisciplinary framework. Very useful and up-to-date information on the occurrence frequency and impact of different natural disasters is being assessed and analyzed by a number of organizations around the world. However, geotechnical engineers have not played a prominent part in such activities so far. Reference may be made to the research and educational materials developed on a regular basis by the Global Alliance for Disaster Reduction (GADR) with the aim of information dissemination and training for disaster reduction. Some selected illustrations from GADR are presented in an Appendix to this chapter. The role of geotechnical engineers in implementing such goals is obvious from these illustrations.

The variability of soil and rock masses and other uncertainties have always posed unique challenges to geotechnical engineers. In the last few decades, the need to identify and quantify uncertainties on a systematic basis has been widely accepted. Methods for inclusion of such data in formal ways include reliability analysis within a probabilistic framework. Considerable progress has been made in complementing traditional deterministic methods with probabilistic studies. Nevertheless, the rate of consequent change to geotechnical practice has been relatively slow and sometimes halfhearted. Reviewing all the developments in geotechnical engineering which have taken place over the last 30 years or more would require painstaking and critical reviews from a team of experts over a considerable

period of time and the subsequent reporting of the findings in a series of books. In comparison, the scope of this keynote chapter is humble. Experienced academics who have been engaged in serious scholarship, research, and consulting over several decades should be able to reflect on recent and continuing trends as well as warning signs of complacency or lack of vision. In this spirit, an attempt is made to highlight some pertinent issues and challenges for the assessment and management of geotechnical risk with particular reference to slope stability and landslides.

The writers of the present chapter present some highlights of their own research through case study examples. These relate to aspects of regional slope stability and hazard assessment such as a landslide inventory map, elements of a relational database, rainfall intensity duration for triggering landslides, continuous monitoring of landslide sites in near-real time, landslide susceptibility, and hazard maps. The chapter concludes with reflections on continuing and emerging challenges. For further details, the reader may refer to Chowdhury and Flentje [5] and Flentje et al. [11, 12], and a comprehensive book [8].

In order to get a sense of global trends in geotechnical analysis and the assessment and management of risk, reference may be made to the work of experts and professionals in different countries as reported in recent publications. The applications include the safety of foundations, dams, and slopes against triggering events such as rainstorms, floods earthquakes, and tsunamis.

The following is a sample of five papers from a 2011 conference related to geotechnical risk assessment and management, GeoRisk 2011. Despite covering a wide range of topics and techniques, it is interesting that GIS-based regional analysis for susceptibility and hazard zoning is not included among these publications. Such gaps are often noted and reveal that far greater effort is required to establish multidisciplinary focus in geotechnical research. This is clearly a continuing challenge for geotechnics in the twenty-first century.

- A comprehensive paper on geohazard assessment and management involving the need for integration of hazard, vulnerability, and consequences and the consideration of acceptable and tolerable risk levels [16].
- Risk assessment of Success Dam, California, is discussed by Bowles et al. [2] with particular reference to the evaluation of operating restrictions as an interim measure to mitigate earthquake risk. The potential modes of failure related to earthquake events and flood events are discussed in two companion papers.
- The practical application of risk assessment in dam safety (the practice in USA) is discussed in a paper by Scott [23].
- Unresolved issues in Geotechnical Risk and Reliability [9].
- Development of a risk-based landslide warning system [24].

The first paper [16] has a wide scope of topics and discusses the following six case studies:

Hazard assessment and early warning for a rock slope over a fjord arm on the west coast of Norway – the slope is subject to frequent rockslides usually with volumes in the range 0.5–5 million cubic meters.

Vulnerability assessment – Norwegian clay slopes in an urban area on the south coast of Norway
Risk assessment – 2004 tsunami in the Indian Ocean
Risk mitigation – quick clay in the city of Drammen along the Drammensfjord and the Drammen River.
Risk mitigation – Early Warning System for landslide dams, Lake Sarez in the Pamir Mountain Range in eastern Tajikistan
Risk of tailings dam break – probability of nonperformance of a tailings management facility at Rosia Montana in Romania

2 Uncertainties Affecting Geotechnics

The major challenges in geotechnical engineering arise from uncertainties and the need to incorporate them in analysis, design, and practice. The geotechnical performance of a specific site, facility, system, or regional geotechnical project may be affected by different types of uncertainty such as the following (with examples in brackets):

- Geological uncertainty (geological details)
- Geotechnical parameter uncertainty (variability of shear strength parameters and of pore water pressure)
- Hydrological uncertainty (aspects of groundwater flow)
- Uncertainty related to historical data (frequency of slides, falls, or flows)
- Uncertainty related to natural or external events (magnitude, location and timing of rainstorm, flood, earthquake, and tsunami)
- Project uncertainty (construction quality, construction delays)
- Uncertainty due to unknown factors (effects of climate change)

On some projects, depending on the aims, geotechnical engineers may be justified in restricting their attention to uncertainties arising from geological, geotechnical, and hydrological factors. For example, the limited aim may be to complement deterministic methods of analysis with probabilistic studies to account for imperfect knowledge of geological details and limited data concerning measured soil properties and pore water pressures. It is necessary to recognize that often pore pressures change over time, and therefore, pore pressure uncertainty has both spatial and temporal aspects which can be critically important.

During the early development of probabilistic analysis methods, researchers often focused on the variability of soil properties in order to develop the tools for probabilistic analysis. It was soon realized that natural variability of geotechnical parameters such as shear strength must be separated from systematic uncertainties such as measurement error and limited number of samples. Another advance in understanding has been that the variability of a parameter, measured by its standard deviation, is a function of the spatial dimension over which the variability is

considered. In some problems, consideration of spatial variability on a formal basis is important and leads to significant insights.

An important issue relates to the choice of geotechnical parameters and their number for inclusion in an uncertainty analysis. The selection is often based on experience and can be justified by performing sensitivity studies. A more difficult issue is the consideration of "new" geotechnical parameters not used in traditional deterministic or even in probabilistic studies. Thus, one must think "outside the box" for "new" parameters which might have significant influence on geotechnical reliability. Otherwise, the utility and benefits of reliability analyses may not be fully realized. As an example, the "residual factor" (defined as proportion of a slip surface over which shear strength has decreased to a residual value) is rarely used as a variable in geotechnical slope analysis. Recently, interesting results have been revealed from a consideration of "residual factor" in slope stability as a random variable [1, 4]. Ignoring the residual factor can lead to overestimate of reliability and thus lead to unsafe or unconservative practice.

For regional studies such as zoning for landslide susceptibility and hazard assessment, historical data about previous events are very important. Therefore, uncertainties with respect to historical data must be considered and analyzed carefully. Such regional studies are different in concept and implementation from traditional site-specific deterministic and probabilistic studies and often make use of different datasets. A successful knowledge-based approach for assessment of landslide susceptibility and hazard has been described by Flentje [10].

If the aim of a geotechnical project is to evaluate geotechnical risk, it is necessary to consider the uncertainty related to the occurrence of an external event or events that may affect the site or the project over an appropriate period of time such as the life of the project.

Consideration of project uncertainty would require consideration of economic, financial, and administrative factors in addition to the relevant technical factors considered above. In this regard, the reader may refer to a recent paper on georisks in the business environment by Brumund [3]; the paper also makes reference to unknown risk factors.

For projects which are very important because of their size, location, economic significance, or environmental impact, efforts must be made to consider uncertainty due to unknown factors. Suitable experts may be co-opted by the project team for such an exercise.

3 Slope Analysis Methods

3.1 Limit Equilibrium and Stress-Deformation Approaches

Deterministic methods can be categorized as limit equilibrium methods and stress-deformation methods. Starting from simple and approximate limit equilibrium

methods based on simplifying assumptions, several advanced and relatively rigorous methods have been developed.

The use of advanced numerical methods for stress-deformation analysis is essential when the estimation of strains and deformations within a slope is required. In most cases, two-dimensional (2D) stress-deformation analyses would suffice. However, there are significant problems which need to be modeled and analyzed in three dimensions. Methods appropriate for 3D stress-deformation analysis have been developed and used successfully. Advanced stress-deformation approaches include the finite difference method, the finite element method, the boundary element method, the distinct element method, and the discontinuous deformation analysis method.

3.2 Progressive Failure

Progressive failure of natural slopes, embankment dams, and excavated slopes is a consequence of nonuniform stress and strain distribution and the strain-softening behavior of earth masses. Thus, shear strength of a soil element, or the shear resistance along a discontinuity within a soil or rock mass, may decrease from a peak to a residual value with increasing strain or increasing deformation. Analysis and simulation of progressive failure require that strain-softening behavior be taken into consideration within the context of changing stress or strain fields. This may be done by using advanced methods such as an initial stress approach or a sophisticated stress-deformation approach. Of the many historical landslides in which progressive failure is known to have played an important part, perhaps the most widely studied is the catastrophic Vaiont slide which occurred in Italy in 1964. The causes and mechanisms have not been fully explained by any one study, and there are still uncertainties concerning both the statics and dynamics of the slide. For further details and a list of some relevant references, the reader may refer to Chowdhury et al. [8].

3.3 Probabilistic Approaches and Simulation of Progressive Failure

A probabilistic approach should not be seen simply as the replacement of a calculated "factor of safety" as a performance index by a calculated "probability of failure." It is important to consider the broader perspective and greater insight offered by adopting a probabilistic framework. It enables a better analysis of observational data and enables the modeling of the reliability of a system. Updating of reliability on the basis of observation becomes feasible, and innovative approaches can be used for the modeling of progressive failure probability and

for back-analysis of failed slopes. Other innovative applications of a probabilistic approach with pertinent details and references are discussed by Chowdhury et al. [8].

An interesting approach for probabilistic seismic landslide analysis which incorporates the traditional infinite slope limit equilibrium model as well as the rigid block displacement model has been demonstrated by Jibson et al. [15].

A probabilistic approach also facilitates the communication of uncertainties concerning hazard assessment and slope performance to a wide range of end-users including planners, owners, clients, and the general public.

3.4 Geotechnical Slope Analysis in a Regional Context

Understanding geology, geomorphology, and groundwater flow is of key importance. Therefore, judicious use must be made of advanced methods of modeling in order to gain the best possible understanding of the geological framework and to minimize the role of uncertainties on the outcome of analyses [17, 21].

Variability of ground conditions, spatial and temporal, is important in both regional and site-specific analysis. Consequently, probability concepts are very useful in both cases although they may be applied in quite different ways.

Spatial and temporal variability of triggering factors such as rainfall have a marked influence on the occurrence and distribution of landslides in a region [8, 18]

This context is important for understanding the uncertainties in the development of critical pore water pressures. Consequently, it helps in the estimation of rainfall threshold for onset of landsliding. Regional and local factors both would have a strong influence on the combinations of rainfall magnitude and duration leading to critical conditions.

Since earthquakes trigger many landslides which can have a devastating impact, it is important to understand the causative and influencing factors. The occurrence, reach, volume, and distribution of earthquake-induced landslides are related to earthquake magnitude and other regional factors. For further details and a list of some relevant references, the reader may refer to Chowdhury et al. [8].

4 Regional Slope Stability Assessments

4.1 Basic Requirements

Regional slope stability studies are often carried out within the framework of a Geographical Information System (GIS) and are facilitated by the preparation of relevant datasets relating to the main influencing factors such as geology, topography, and drainage characteristics and by developing a comprehensive inventory of existing landslides. The development of a Digital Elevation Model (DEM)

facilitates GIS-based modeling of landslide susceptibility, hazard, and risk within a GIS framework. Regional slope stability and hazard studies facilitate the development of effective landslide risk management strategies in an urban area. The next section of this chapter is devoted to a brief discussion of GIS as a versatile and powerful system for spatial and even temporal analysis. This is followed by a section providing a brief overview of sources and methods for obtaining accurate spatial data. The data may relate to areas ranging from relatively limited zones to very large regions. Some of these resources and methods have a global reach and applicability. Such data are very valuable for developing Digital Elevation Models (DEMs) of increasing accuracy. For regional analysis, a DEM is, of course, a very important and powerful tool.

4.2 Landslide Inventory

The development of comprehensive databases including a landslide inventory is most desirable if not essential especially for the assessment of slope stability in a regional context. It is important to study the occurrence and spatial distribution of first-time slope failures as well as reactivated landslides.

Identifying the location of existing landslides is just the beginning of a systematic and sustained process with the aim of developing a comprehensive landslide inventory. Among other features, it should include the nature, size, mechanism, triggering factors, and date of occurrence of existing landslides. While some old landslide areas may be dormant, others may be reactivated by one or more regional triggering factors such as heavy rainfall and earthquakes.

One comprehensive study of this type has been discussed in some detail in Chapter 11 of Chowdhury et al. [8]. This study was made for the Greater Wollongong region, New South Wales, Australia, by the University of Wollongong (UOW) Landslide Research Team (LRT). In this chapter, this study is also referred to as the Wollongong Regional Study.

A small segment for the Wollongong Landslide Inventory for the Wollongong Regional Study is shown in Fig. 1. The elements of a Landslide Relational Database are shown in Fig. 2. Some details of the same are shown in Figs. 3 and 4. A successful knowledge-based approach for assessment of landslide susceptibility and hazard has been described by Flentje [10] and is covered in some detail in a separate section of this chapter.

4.3 Role of Geographical Information Systems (GIS)

GIS enables the collection, organization, processing, managing, and updating of spatial and temporal information concerning geological, geotechnical, topographical, and other key parameters. The information can be accessed and applied by a

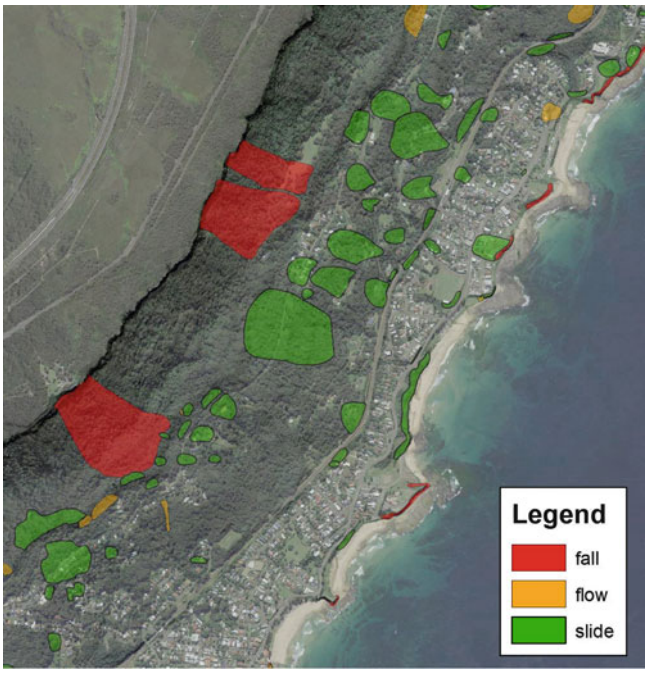

Fig. 1 Segment of the University of Wollongong Landslide Inventory

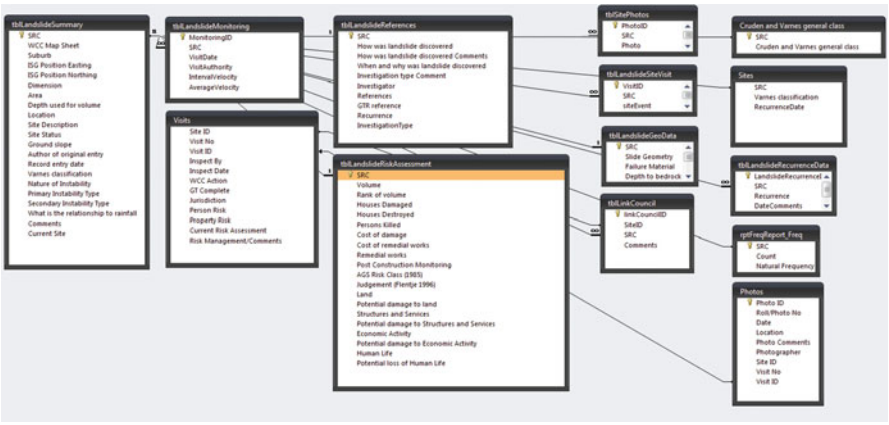

Fig. 2 Elements of a Landslide Relational Database

range of professionals such as geotechnical engineers, engineering geologists, civil engineers, and planners for assessing hazard of landsliding as well as for risk management. Traditional slope analysis must, therefore, be used within the context of a modern framework which includes GIS. Among the other advantages of GIS

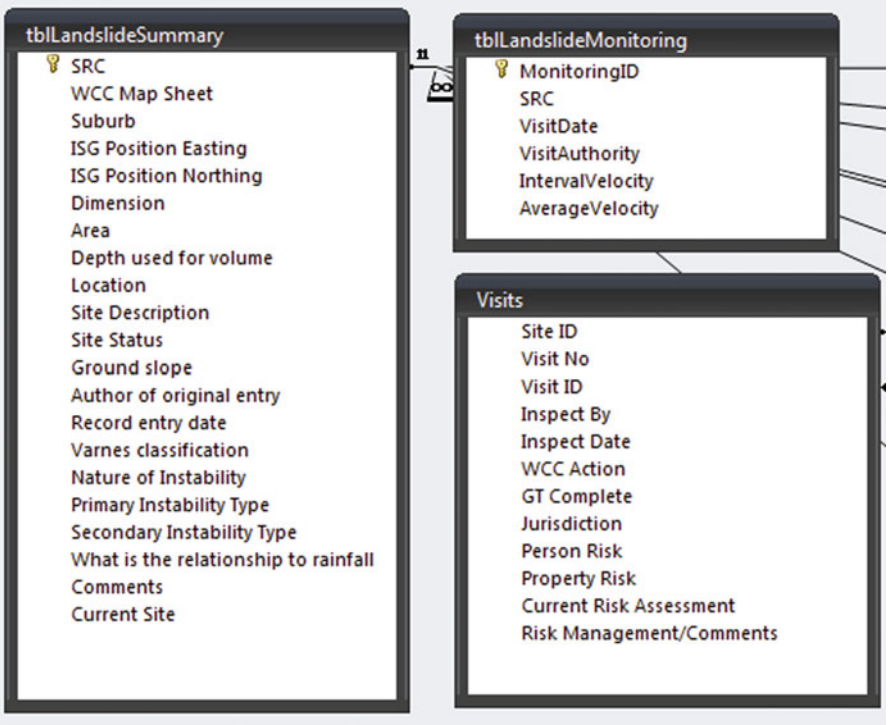

Fig. 3 Details of main tables of relational database shown above

are the ability to deal with multiple hazards, the joining of disparate data, and the ability to include decision support and warning systems [13].

Papers concerning the application of basic, widely available, GIS systems as well as about the development of advanced GIS systems continue to be published. For instance, Reeves and West [22], covering a conference session on "Geodata for the urban environment," found that 11 out of 30 papers were about the "Development of Geographic Information Systems" while Gibson and Chowdhury [13] pointed out that the input of engineering geologists (and, by implication, geotechnical engineers) to urban geohazards management is increasingly through the medium of GIS.

Consequently, 3D geological models have been discussed by a number of authors such as Rees et al. [21] who envisage that such models should be the basis for 4D process modeling in which temporal changes and factors can be taken into consideration. They refer, in particular, to time-series data concerning precipitation, groundwater, sea level, and temperature. Such data, if and when available, can be integrated with 3D spatial modeling.

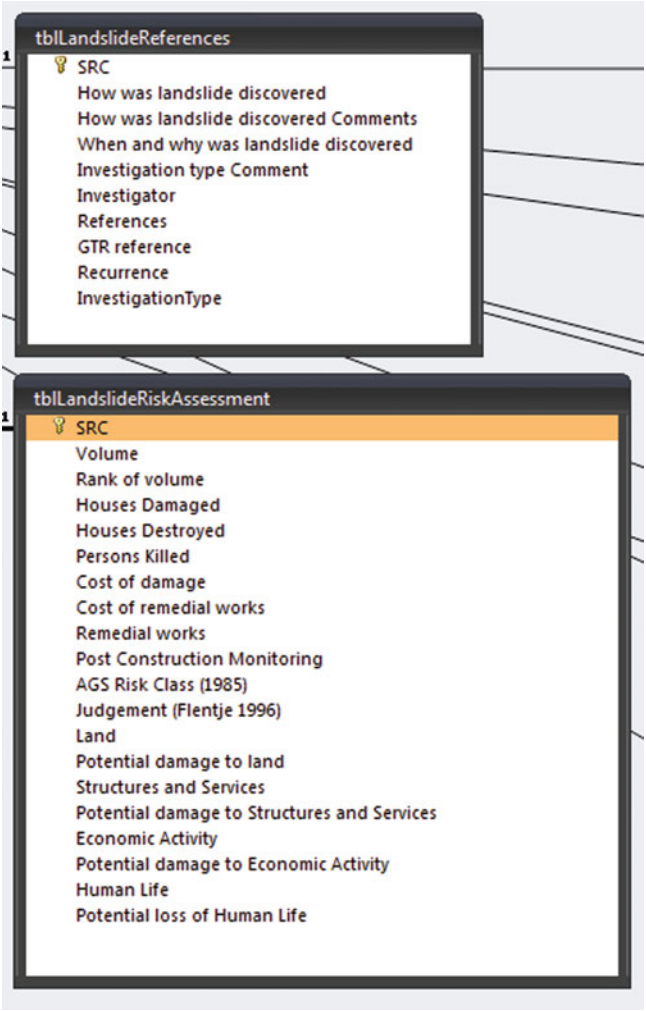

Fig. 4 Details of selected tables of relational database shown above

4.4 Sources of Accurate Spatial Data Relevant to the Development of Digital Elevation Models

Over the last decade, Airborne Laser Scan (ALS) or Light Detection and Ranging (LiDAR) techniques are increasingly being applied across Australia to collect high-resolution terrain point datasets. When processed and used to develop Geographic Information System (GIS) Digital Elevation Models (DEMs), the data provides high-resolution contemporary terrain models that form fundamental GIS datasets. Prior to the advent of this technology, DEMs were typically derived from

10- to 50-year-old photogrammetric contour datasets. When processed, ALS datasets can comprise point clouds of many millions of ground-reflected points covering large areas up to hundreds of square kilometers, with average point densities exceeding one point per square meter. Collection, processing, and delivery of these data types are being enhanced and formalized over time. Increasingly, this data is also being collected in tandem with high-resolution geo-referenced imagery.

Airborne and Satellite-Derived Synthetic Aperture Radar (SAR) techniques are also being increasingly developed and applied internationally to develop terrain models and specifically differential models between return visits over the same area in order to highlight the changes in ground surfaces with time. This is being used to monitor landslide movement, ground subsidence, and other environmental change.

NASA and the Japan Aerospace Exploration Society have just recently (mid-October 2011) and freely released via the Internet the Advanced Spaceborne Thermal Emission and Reflection Radiometer (ASTER) Global Digital Elevation Model (GDEM) – ASTER GDEM v2 global 30 m Digital Elevation Model as an update to the year 2000 vintage NASA SRTM Global DEM at 90 and 30 m pixel resolutions. This global data release means moderately high-resolution global Digital Elevation Model data are available to all.

The development of ALS terrain models and the free release of the global ASTER GDEM v2 have important implications for the development of high-resolution landslide inventories and zoning maps worldwide. These datasets mean one of the main barriers in the development of this work has been eliminated.

4.5 Observational Approach: Monitoring and Alert Systems

Geotechnical analysis should not be considered in isolation since a good understanding of site conditions and field performance is essential. This is particularly important for site-specific as well as regional studies of slopes and landslides. Observation and monitoring of slopes are very important for understanding all aspects of performance: from increases in pore water pressures to the evidence of excessive stress and strain, from the development of tension cracks and small shear movements to initiation of progressive failure, and from the development of a complete landslide to the postfailure displacement of the landslide mass.

Observation and monitoring also facilitate an understanding of the occurrence of multiple slope failures or widespread landsliding within a region after a significant triggering event such as rainfall of high magnitude and intensity [10, 12]. Observational approaches facilitate accurate back-analyses of slope failures and landslides. Moreover, geotechnical analysis and the assessment of hazard and risk can be updated with the availability of additional observational data on different parameters such as pore water pressure and shear strength. The availability of continuous monitoring data obtained in near-real time will also contribute to more accurate assessments and back-analyses. Consequently, such continuous monitoring will lead to further advancement in the understanding of slope behavior.

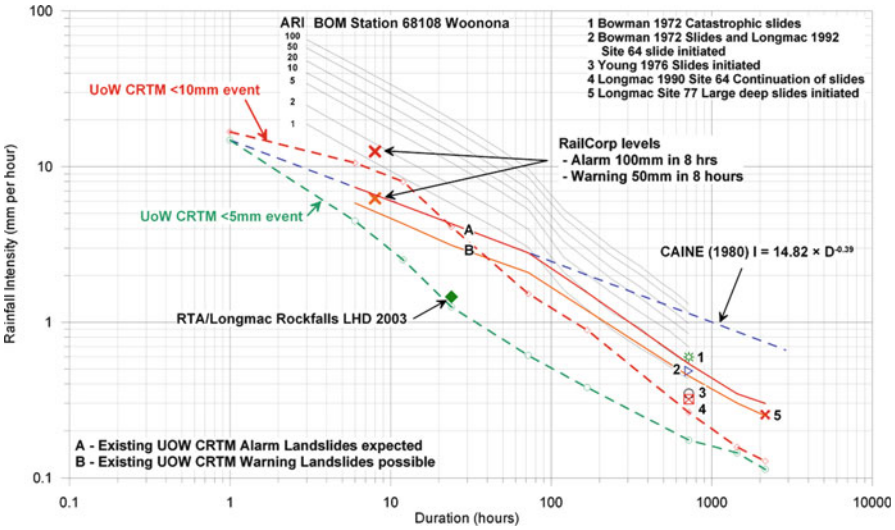

Fig. 5 Interpreted threshold curves for landsliding in Wollongong, superimposed on annual recurrence interval curves for a selected rainfall station

One part of the Wollongong Regional Study is the development of rainfall-intensity-duration curves for the triggering of landslides overlaid with historical rainfall average recurrence interval (ARI) curves as shown in Fig. 5. From the very beginning of this research, the potential use of such curves for alert and warning systems was recognized. In fact, this research facilitated risk management in the Wollongong study area during intense rainfalls of August 1998 when widespread landsliding occurred.

More recent improvement and extension of this work involves the use of data from our growing network of continuous real-time monitoring stations where we are also introducing the magnitude of displacement as an additional parameter. Aspects of this research are shown in Fig. 5, and as more data become available from continuous monitoring, additional displacement (magnitude)-based curves can be added to such a plot.

Two examples of continuous landslide performance monitoring are shown in Figs. 6 and 7. Figure 6 relates to a coastal urban landslide site (43,000 m^3) with limited trench drains installed. The relationship between rainfall, pore water pressure rise, and displacement is clearly evident at two different time intervals in this figure. Figure 7 shows data from a complex translational landslide system (720,000 m^3) which is located on a major highway in NSW Australia. In the 1970s, landsliding severed this artery in several locations resulting in road closures and significant losses arising from damage to infrastructure and from traffic disruptions.

After comprehensive investigations, remedial measures were installed. At this site, a dewatering pump system was installed, which continues to operate to this day. However, this drainage system has been reviewed and upgraded from time to

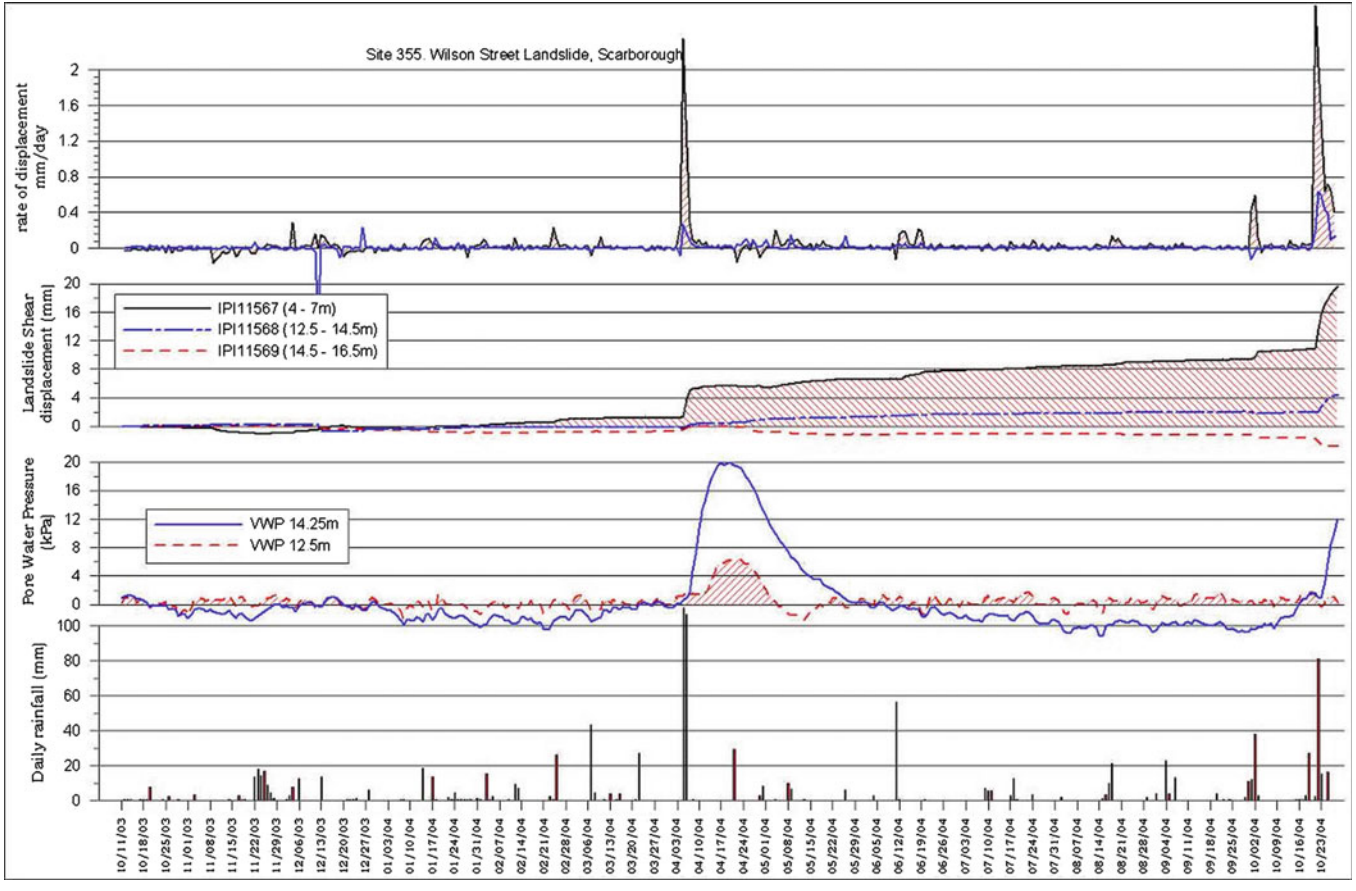

Fig. 6 Hourly logged continuously recorded rainfall, pore water pressure, landslide displacement, and rate of displacement data for a 43,000 m^3 urban landslide site in Wollongong

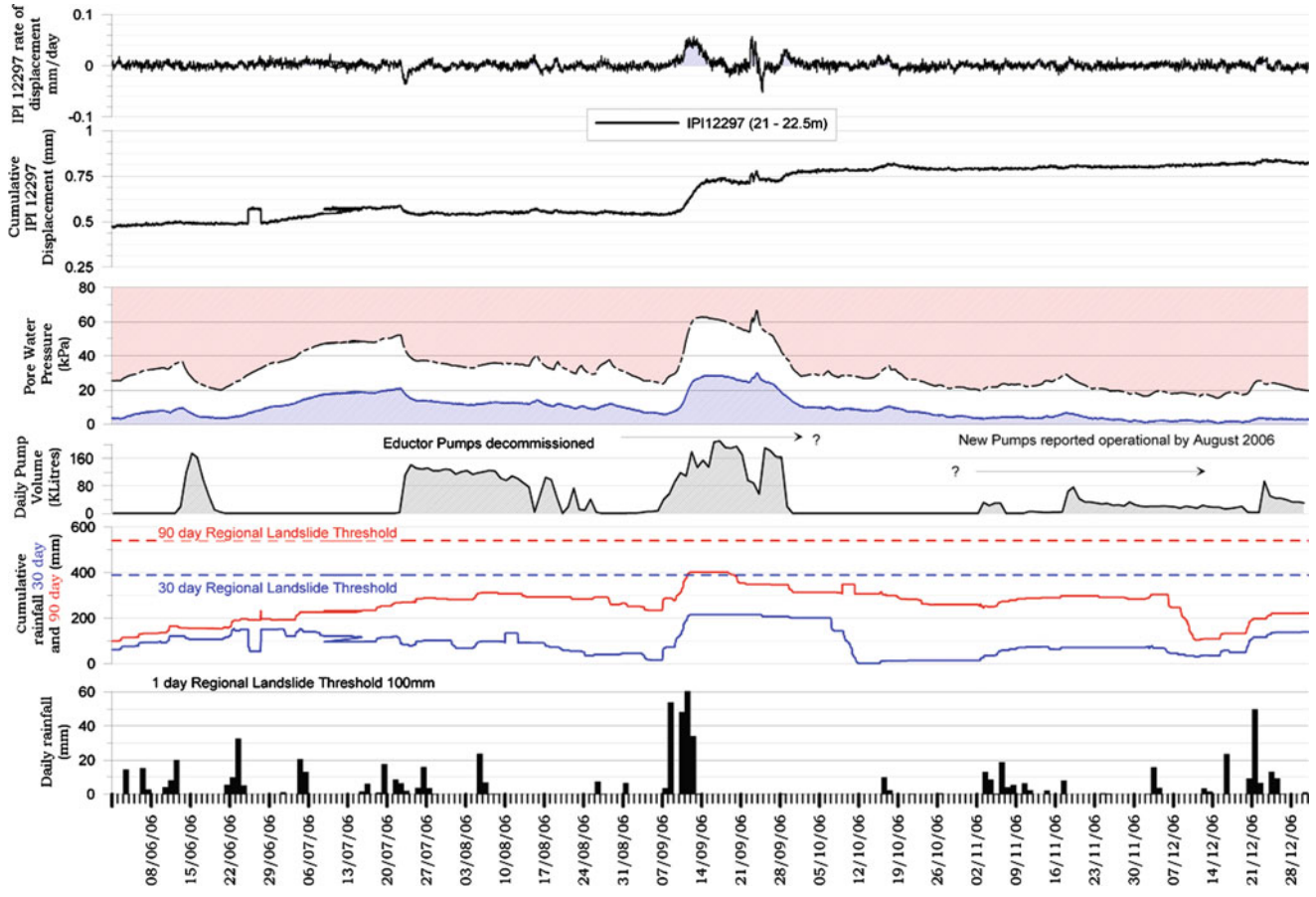

Fig. 7 Hourly logged, continuously recorded rainfall, groundwater pump volumes, pore water pressure, landslide displacement, and rate of displacement data for a 720,000 m^3 landslide affecting a major transport artery in Wollongong

time. Since 2004, this site has been connected to the Continuous Monitoring Network of the University of Wollongong Landslide Research Team. Interpretation of the monitoring data shows that movement has been limited to less than 10 mm since the continuous monitoring commenced as shown in Fig. 7 [11]. However, the occurrence of events of this small movement was considered unacceptable by the authorities. Hence, pump and monitoring system upgrades commenced in 2006 and have been completed in 2011.

4.6 Susceptibility and Hazard Assessment (Wollongong Regional Study)

4.6.1 The Susceptibility Model Area and the Datasets

The area chosen within the Wollongong Region for modeling landslide susceptibility (Susceptibility Model Area) is 188 km^2 in extent and contains 426 slide category landslides.

The datasets used for this study include:

- Geology (mapped geological formations, 21 variables)
- Vegetation (mapped vegetation categories, 15 variables)
- Slope inclination (continuous floating point distribution)
- Slope aspect (continuous floating point distribution)
- Terrain units (buffered water courses, spur lines, and other intermediate slopes)
- Curvature (continuous floating point distribution)
- Profile curvature (continuous floating point distribution)
- Plan curvature (continuous floating point distribution)
- Flow accumulation (continuous integer)
- Wetness index (continuous floating point distribution)

4.6.2 Landslide Inventory

The landslide inventory for this study has been developed over a 15-year period and comprises a relational MS Access and ESRI ArcGIS Geodatabase with 75 available fields of information for each landslide site. It contains information on a total of 614 landslides (falls, flows, and slides) including 480 slides. Among the 426 landslides within the Susceptibility Model Area, landslide volumes have been calculated for 378 of these sites. The average volume is 21,800 m^3 and the maximum volume is 720,000 m^3.

4.6.3 Knowledge-Based Approach Based on Data Mining Model

The specific knowledge-based approach used for analysis and synthesis of the datasets for this study is the data mining (DM) process or model. The DM learning process is facilitated by the software "See5" which is a fully developed application of "C4.5" [20]. The DM learning process helps extract patterns from the databases related to the study. Known landslide areas are used for one half of the model training, the other half comprising randomly selected points from within the model area but outside the known landslide boundaries. Several rules are generated during the process of modeling. Rules which indicate potential landsliding are assigned positive confidence values and those which indicate potential stability (no-landsliding) are assigned negative confidence values. The rule set is then reapplied within the GIS software using the ESRI ModelBuilder extension to produce the susceptibility grid. The complete process of susceptibility and hazard zoning is described in Flentje [10] and in Chapter 11 of Chowdhury et al. [8].

4.6.4 Susceptibility and Hazard Zones

On the basis of the analysis and synthesis using the knowledge-based approach, it has been possible to demarcate zones of susceptibility and hazard into four categories:

1. Very low susceptibility (or hazard) of landsliding (VL)
2. Low susceptibility (or hazard) of landsliding (L)
3. Moderate susceptibility (or hazard) of landsliding (M)
4. High susceptibility (or hazard) of landsliding (H)

A segment of the landslide susceptibility map is shown in Fig. 8 below. A segment of the landslide hazard map, an enlarged portion from the bottom left of Fig. 8, is reproduced as Fig. 9. Relative likelihoods of failure in different zones, estimated from the proportion of total landslides which occurred in each zone over a period of 126 years, are presented in columns 1 and 2 of Table 1 below. This information is only a part of the full table presented as Table 11.3 in Chowdhury et al. [8].

5 Estimated Reliability Indices and Factors of Safety

An innovative concept has been proposed by Chowdhury and Flentje [7] for quantifying failure susceptibility from zoning maps developed on the basis of detailed knowledge-based methods and techniques within a GIS framework. The procedure was illustrated with reference to the results of the Wollongong Regional Study and the relevant tables are reproduced here. Assuming that the factor of safety has a normal distribution, the reliability index was calculated for each zone

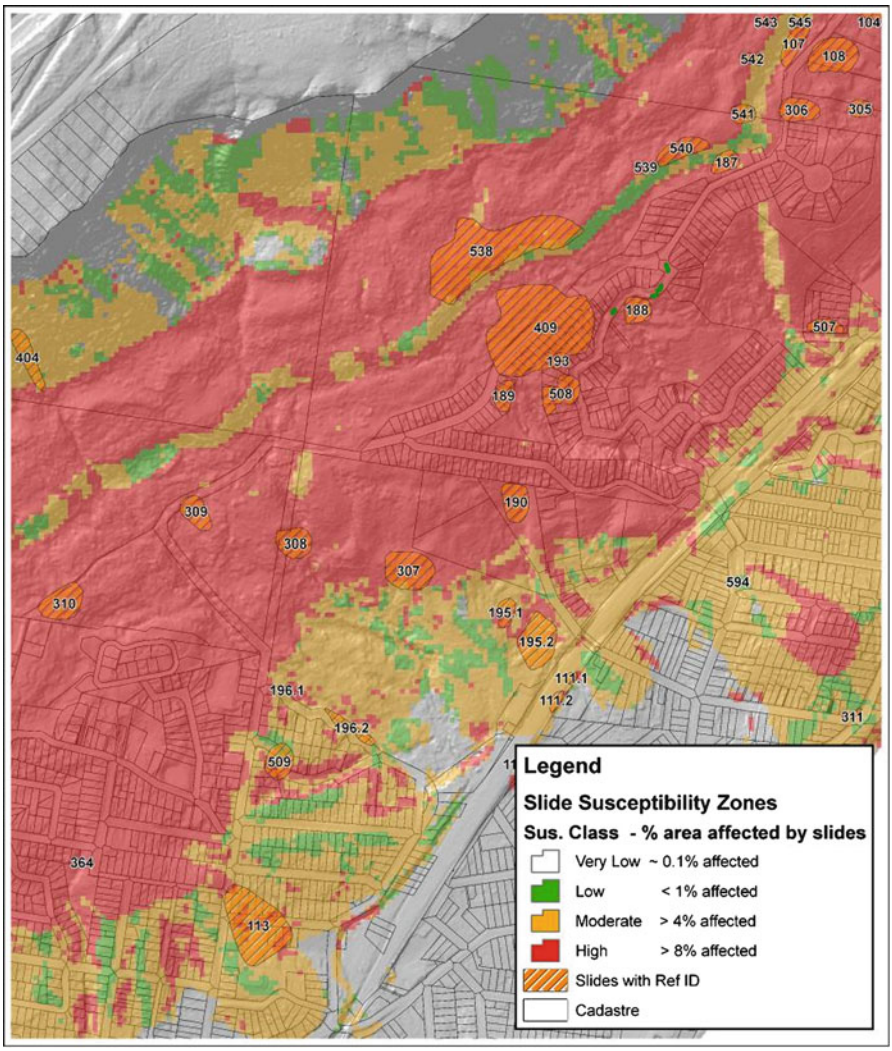

Fig. 8 Segment of landslide inventory and susceptibility zoning map, Wollongong Local Government Area, New South Wales, Australia

based on the associated failure likelihood which is assumed to represent the probability of failure. These results are presented in the third or last column of Table 1.

Assuming that the coefficient of variation of the factor of safety is 10%, the typical values of mean factor of safety for each zone are shown in Table 2. The results were also obtained for other values of the coefficient of variation of the factor of safety (5, 10, 15, and 20%). These results are shown in Table 3.

Most of the landslides have occurred during very high rainfall events. It is assumed here, in the first instance, that most failures are associated with a pore

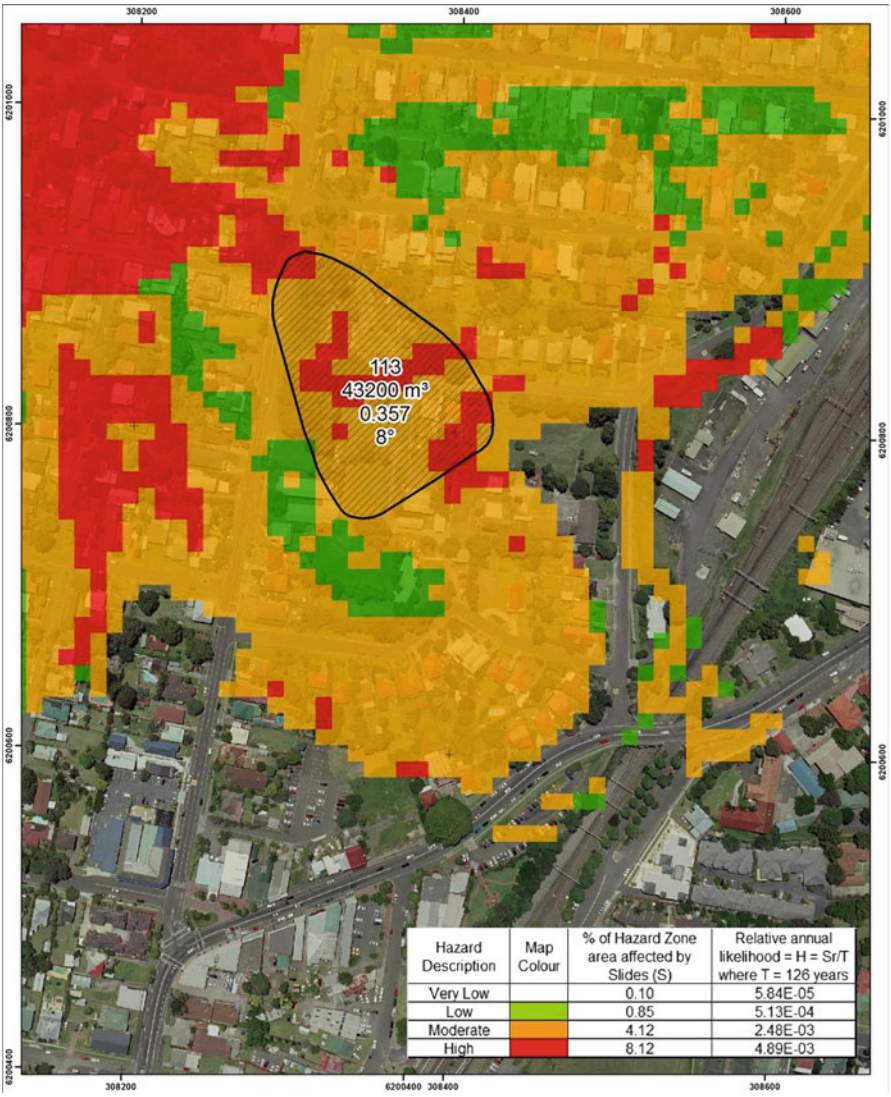

Fig. 9 Segment of landslide hazard zoning map from the *bottom left* corner of Fig.8, Wollongong Local Government Area, New South Wales, Australia. Landslide label shows four important particulars of each landslide stacked vertically. These are (1) site reference code, (2) landslide volume, (3) annual frequency of reactivation derived from inventory, and (4) landslide profile angle. Hazard zoning in legend shows relative annual likelihood as explained in the text

Table 1 Failure likelihood and reliability index for each hazard zone (After Chowdhury et al. [8])

Hazard zone description	Failure likelihood	Reliability index
Very low	7.36×10^{-3}	2.44
Low	6.46×10^{-2}	1.51
Moderate	3.12×10^{-1}	0.49
High	6.16×10^{-1}	−0.30

Table 2 Typical mean value of factor of safety (F) for each hazard zone considering coefficient of variation to be 10% (After Chowdhury and Flentje [7])

Hazard zone description	Reliability index	Mean of factor of safety, F ($V_F = 10\%$)
Very low	2.44	1.32
Low	1.51	1.18
Moderate	0.49	1.05
High	−0.3	0.97

Table 3 Typical mean values of factor of safety for different values of coefficient of variation (After Chowdhury and Flentje [7])

	Mean of F for different hazard zones			
V_F%	Very low	Low	Moderate	High
5	1.14	1.08	1.02	0.98
10	1.32	1.18	1.05	0.97
15	1.57	1.29	1.08	0.96
20	1.95	1.43	1.11	0.94

Table 4 Typical mean factor of safety with different values of pore pressure ratio (slope inclination $i = 12°$, $V_F = 10\%$) (After Chowdhury and Flentje [7])

	Mean of F for different hazard zones			
Pore water pressure ratio	Very low	Low	Moderate	High
0.5	1.32	1.18	1.05	0.97
0.4	1.61	1.44	1.28	1.18
0.3	1.90	1.70	1.51	1.40
0.2	2.19	1.95	1.74	1.61

water pressure ratio of about 0.5 (full seepage condition in a natural slope). Furthermore, assuming that the "infinite slope" model applies to most natural slopes and that cohesion intercept is close to zero, the values of factor of safety can be calculated for other values of the pore pressure ratio (0.2, 0.3, and 0.4) for any assumed value of the slope inclination. The results shown below in Table 4 are for a slope with an inclination of 12 degrees for pore pressure ratios in the range 0.2–0.5.

5.1 Discussion on the Proposed Concept and Procedure

The above results were obtained as a typical F value or a set of F values referring to each hazard zone. However, taking into consideration the spatial variation of slope angle, shear strength, and other factors, this approach may facilitate the calculation F at individual locations. Well-documented case studies of site-specific analysis would be required for such an extension of the procedure. Other possibilities include estimation of the variation of local probability of failure. The approach

may also be used for scenario modeling relating to the effects of climate change. If reliable data concerning pore pressure changes become available, failure susceptibility under those conditions can be modeled, and the likelihood and impact of potential catastrophic slope failures can be investigated.

6 Discussion, Specific Lessons or Challenges

The focus of this chapter has been on hazard and risk assessment in geotechnical engineering. Advancing geotechnical engineering requires the development and use of knowledge which facilitates increasingly reliable assessments even when the budgets are relatively limited. Because of a variety of uncertainties, progress requires an astute combination of site-specific and regional assessments. For some projects, qualitative assessments within the framework of a regional study may be sufficient. In other projects, quantitative assessments, deterministic and probabilistic, may be essential.

In this chapter, different cases have been discussed in relation to the Wollongong Regional Study. Firstly, reference was made to the basis of an alert and warning system for rainfall-induced landsliding based on rainfall-intensity-duration plots supplemented by continuous monitoring. The challenges here are obvious. How do we use the continuous pore pressure data from monitoring to greater advantage? How do we integrate all the continuous monitoring data to provide better alert and warning systems? This research has applications in geotechnical projects generally well beyond slopes and landslides.

The examples concerning continuous monitoring of two case studies discussed in this chapter illustrate the potential of such research for assessing remedial and preventive measures. The lesson from the case studies is that, depending on the importance of a project, even very low hazard levels may be unacceptable. As emphasized earlier, the decision to upgrade subsurface drainage at the cost of hundreds of thousands of dollars over several years was taken and implemented despite the shear movements being far below disruptive magnitudes as revealed by continuous monitoring. The challenge in such problems is to consolidate this experience for future applications so that costs and benefits can be rationalized further.

The last example from the Wollongong Regional Study concerned the preparation of zoning maps for landslide susceptibility and hazard. Reference was made to an innovative approach for quantitative interpretation of such maps in terms of well-known performance indicators such as “factor of safety” under a variety of pore pressure conditions. The challenge here is to develop this methodology further to take into consideration the spatial and temporal variability within the study region.

7 Challenges Due to External Factors

Beyond the scope of this chapter, what are the broad challenges in geotechnical hazard and risk assessment? How do we deal with the increasing numbers of geotechnical failures occurring globally including many disasters and how do we mitigate the increasingly adverse consequences of such events? What strategies, preventive, remedial, and others, are necessary?

Often catastrophic landslides are caused by high-magnitude natural events such as rainstorms and earthquakes. It is also important to consider the contribution of human activities such as indiscriminate deforestation and rapid urbanization to landslide hazard. There is an increasing realization that poor planning of land and infrastructure development has increased the potential for slope instability in many regions of the world.

Issues concerned with increasing hazard and vulnerability are very complex and cannot be tackled by geotechnical engineers alone. Therefore, the importance of working in interdisciplinary teams must again be emphasized. Reference has already been made to the use of geological modeling (2D, 3D, and potentially 4D) and powerful tools such as GIS which can be used in combination with geotechnical and geological models.

At the level of analysis methods and techniques, one of the important challenges for the future is to use slope deformation (or slip movement) as a performance indicator rather than the conventional factor of safety. Also, at the level of analysis, attention needs to be given to better description of uncertainties related to construction of slopes including the quality of supervision.

Research into the effects of climate change and, in particular, its implications for geotechnical engineering is urgently needed [19, 21]. The variability of influencing factors such as rainfall and pore water pressure can be expected to increase. However, there will be significant uncertainties associated with estimates of variability in geotechnical parameters and other temporal and spatial factors. Consequently, geotechnical engineers need to be equipped with better tools for dealing with variability and uncertainty. There may also be other changes in the rate at which natural processes like weathering and erosion occur. Sea level rise is another important projected consequence of global warming and climate change, and it would have adverse effects on the stability of coastal slopes.

8 Concluding Remarks

A wide range of methods, from the simplest to the most sophisticated, are available for the geotechnical analysis of slopes. This includes both static and dynamic conditions and a variety of conditions relating to the infiltration, seepage, and drainage of water. Considering regional slope stability, comprehensive databases and powerful geological models can be combined within a GIS framework to assess

and use information and data relevant to the analysis of slopes and the assessment of the hazard of landsliding. The use of knowledge-based systems for assessment of failure susceptibility, hazard, or performance can be facilitated by these powerful tools. However, this must all be based on a thorough fieldwork ethic.

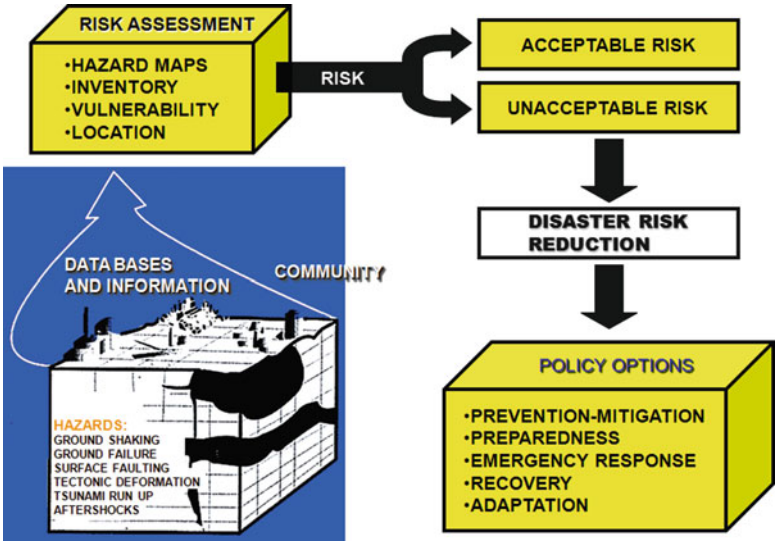

Fig. A.1 Elements of risk assessment and management for natural disasters (Courtesy of Walter Hays [14])

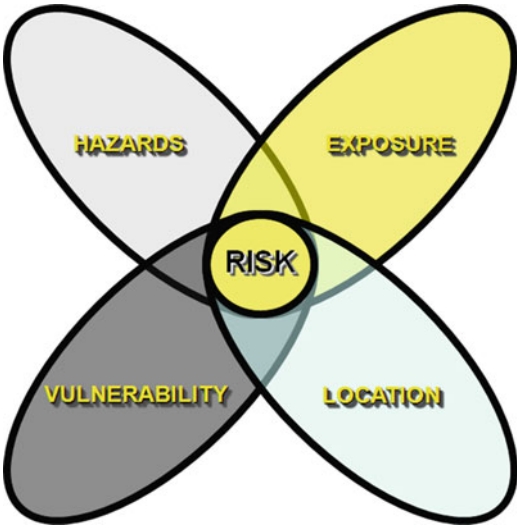

Fig. A.2 Components of risk (Courtesy of Walter Hays [14])

It is important to understand the changes in geohazards with time. In particular, geotechnical engineers and engineering geologists will face long-term challenges due to climate change. Research is required to learn about the effects of climate change in greater detail so that methods of analysis and interpretation can be improved and extended. Exploration of such issues will be facilitated by a proper understanding of the basic concepts of geotechnical slope analysis and the fundamental principles on which the available methods of analysis are based.

Appendix A: Selected Figures from PowerPoint Slide Set Entitled "Understanding Risk and Risk Reduction" [14]

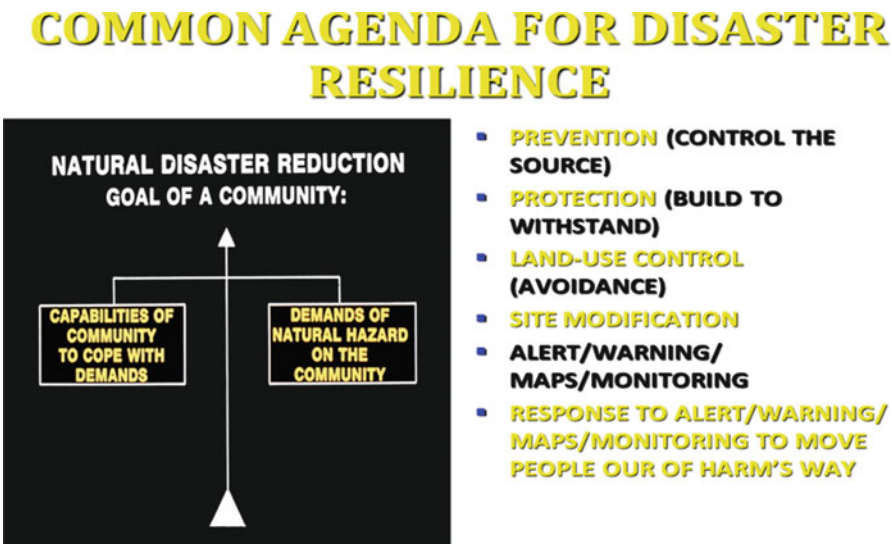

Fig. A.3 Common agenda for natural disaster resilience (Courtesy of Walter Hays [14])

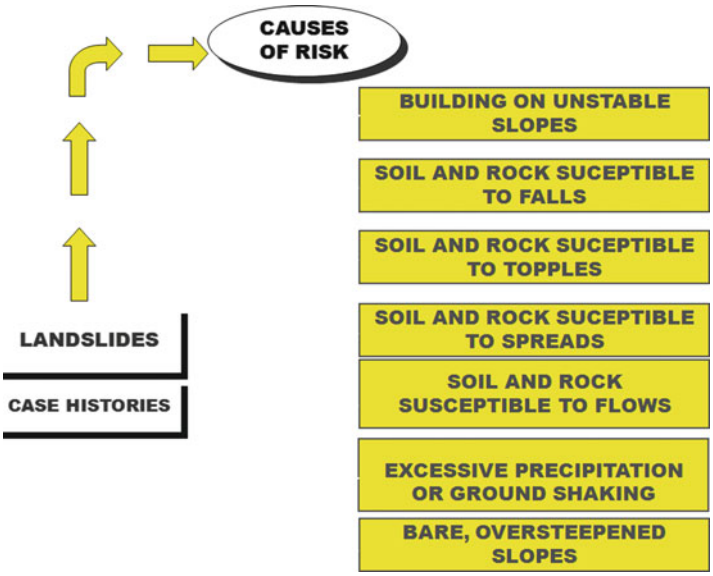

Fig. A.5 Some causes of risk for landslides (Courtesy of Walter Hays [14])

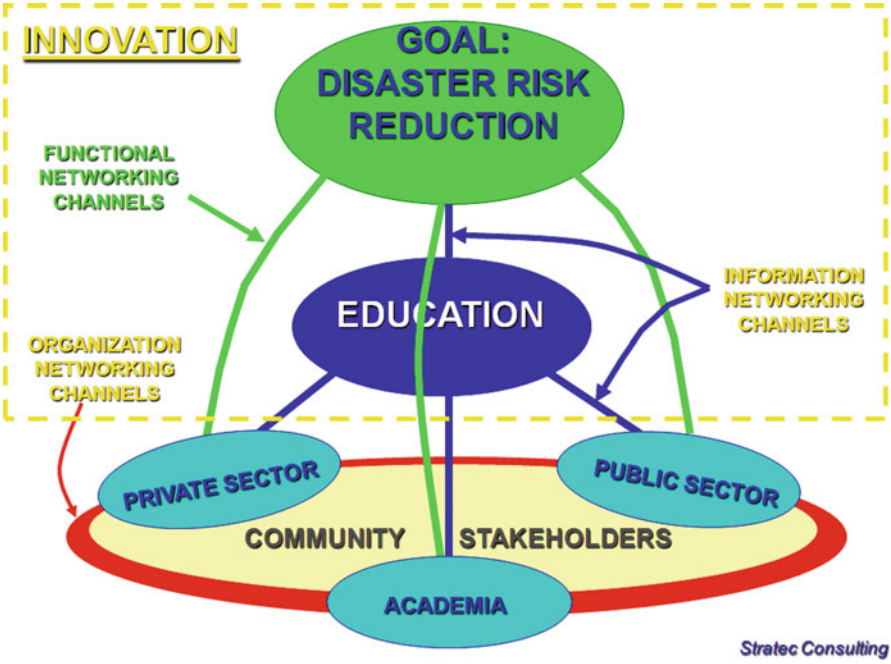

Fig. A.4 The overall context for innovation in disaster management and reduction (Courtesy of Walter Hays [14])

References

1. Bhattacharya G, Chowdhury R (2011) Continuing research concerning the residual factor as a random variable. Progress report, September 2011
2. Bowles D, Rutherford M, Anderson L (2011) Risk assessment of success Dam, California: evaluating of operating restrictions as an interim measure to mitigate earthquake risk. In: Juang CH, Phoon KK, Puppala AJ, Green RA, Fenton GA (eds) Proceedings of GeoRisk 2011. Geotechnical risk assessment and management, Geo-Institute, A.S.C.E
3. Brumund F (2011) Geo – risks in the business environment. In: Juang CH, Phoon KK, Puppala AJ, Green RA, Fenton GA (eds) Proceedings of GeoRisk 2011. Geotechnical risk assessment and management, Geo-Institute, A.S.C.E
4. Chowdhury R, Bhattacharya G (2011) Reliability analysis of strain-softening slopes. In: Proceedings of the 13th international conference of IACMAG, Melbourne, Australia, May, 2011, vol II, pp. 1169–1174
5. Chowdhury R, Flentje P (2008) Strategic approaches for the management of risk in geomechanics. Theme paper. In: Proceedings of the 12 IACMAG conference, Goa, India, CD-ROM, pp 3031–3042
6. Chowdhury R, Flentje P (2010) Geotechnical analysis of slopes and landslides: achievements and challenges (Paper number 10054). In: Proceedings of the 11th IAEG congress of the international association of engineering geology and the environment, Auckland, New Zealand, 6 pp
7. Chowdhury R, Flentje P (2011) Practical reliability approach to urban slope stability. Proceedings of the ICASP11, the 11th international conference on application of statistics and probability in civil engineering, 1–4 August. ETH, Zurich, 5 pp
8. Chowdhury R, Flentje P, Bhattacharya G (2010) Geotechnical slope analysis, CRC Press, Balkema, Taylor and Francis Group, Boca Raton, 746 pp
9. Christian JT, Baecher GB (2011) Unresolved problems in geotechnical risk and reliability. In: Juang CH, Phoon KK, Puppala AJ, Green RA, Fenton GA (eds) Proceedings of GeoRisk 2011. Geotechnical risk assessment and management, Geo-Institute, A.S.C.E
10. Flentje P (2009) Landslide inventory development and landslide susceptibility zoning in the Wollongong City Council Local Government Area. Unpublished report to Industry Partners-Wollongong City Council, RailCorp and the Roads and Traffic Authority, University of Wollongong, Australia, 73 pp
11. Flentje P, Chowdhury R, Miner AS, Mazengarb C (2010) Periodic and continuous monitoring to assess landslide frequency-selected Australian examples. In: Proceedings of the 11th IAEG congress of the international association of engineering geology and the environment, Auckland, New Zealand, 6 pp.
12. Flentje P, Stirling D, Chowdhury R (2007) Landslide susceptibility and hazard derived from a Landslide Inventory using data mining – an Australian case study. In: Proceedings of the first North American landslide conference, landslides and society: integrated science, engineering, management, and mitigation, Vail, Colorado, 3–8 June 2007, 10 pp. CD, Paper number 17823–024,
13. Gibson AD, Chowdhury R (2009) Planning and geohazards. In: Culshaw MG, Reeves HJ, Jefferson I, Spink TW (eds) Engineering geology for tomorrow's cities, vol 22. Engineering Geology Special Publication, London, pp 113–123
14. Hays W (2011) Understanding risk and risk reduction- a set of power point slides. Global Alliance for Disaster Reduction (GADR)
15. Jibson RW, Harp EL, Michael JA (2000) A method for producing digital probabilistic seismic landslide hazard maps. Eng Geol 58(3–4):271–289
16. Lacasse S, Nadim F (2011) Learning to live with geohazards: from research to practice. In: Juang CH, Phoon KK, Puppala AJ, Green RA, Fenton GA (eds) Proceedings of GeoRisk 2011. Geotechnical risk assessment and management, Geo-Institute, A.S.C.E

17. Marker BR (2009) Geology of mega-cities and urban areas. In: Culshaw MG, Reeves HJ, Jefferson I, Spink TW (eds) Engineering geology for tomorrow's cities, vol 22, Engineering Geology Special Publication. Geological Society, London, pp 33–48
18. Murray E (2001) Rainfall thresholds for landslide initiation in the Wollongong Region. Internal report to Australian Geological Survey Organisation and SPIRT Project Team at the University of Wollongong
19. Nathanail J, Banks V (2009) Climate change: implications for engineering geology practice 2009. In: Culshaw MG, Reeves HJ, Jefferson I, Spink TW (eds) Engineering geology for tomorrow's cities, vol 22, Engineering Geology Special Publication. Geological Society, London, pp 65–82
20. Quilan R (1993) C 4.5: programs for machine learning. Morgan, San Mateo
21. Rees JG, Gibson AD, Harrison M, Hughes A, Walsby JC (2009) Regional modeling of geohazards change. In: Culshaw MG, Reeves HJ, Jefferson I, Spink TW (eds) Engineering geology for tomorrow's cities, vol 22, Engineering Geology Special Publication. Geological Society, London, pp 49–64
22. Reeves HJ, West TR (2009) Geodata for the urban environment. In: Culshaw MG, Reeves HJ, Jefferson I, Spink TW (eds) Engineering geology for tomorrow's cities, vol 22, Engineering Geology Special Publication. Geological Society, London, pp 209–213
23. Scott GA (2011) The practical application of risk assessment to Dam safety. In: Juang CH, Phoon KK, Puppala AJ, Green RA, Fenton GA (eds) Proceedings of GeoRisk 2011. Geotechnical risk assessment and management, Geo-Institute, A.S.C.E
24. Tang WH, Zhang LM (2011) Development of a risk-based landslide warning system. In: Juang CH, Phoon KK, Puppala AJ, Green RA, Fenton GA (eds) Proceedings of GeoRisk 2011. Geotechnical risk assessment and management, Geo-Institute, A.S.C.E

Uncertainties in Transportation Infrastructure Development and Management

Kumares C. Sinha, Samuel Labi, and Qiang Bai

Abstract The development and management of transportation infrastructure is a continuous process that includes the phases of planning and design, construction, operations, maintenance, preservation, and reconstruction. Uncertainties at each phase include variability in demand estimation, reliability of planning and design parameters, construction cost overruns and time delay, unexpected outcomes of operational policies and maintenance and preservation strategies, and risks of unintended disruption due to incidents or sudden extreme events. These variabilities, which are due to inexact levels of natural and anthropogenic factors in the system environment, are manifest ultimately in the form of variable outcomes of specific performance measures established for that phase. Transportation infrastructure managers seek to adequately identify and describe these uncertainties through a quantitative assessment of the likelihood and consequence of each of possible level of the performance outcome and to incorporate these uncertainties into the decision-making process. This chapter identifies major sources of uncertainties at different phases of transportation infrastructure development and management and examines the methods of their measurements. Finally, this chapter presents several approaches to incorporate uncertainties in transportation infrastructure decision-making and provides future directions for research.

Keywords Transportation infrastructure • Uncertainty • Extreme events • Decision-making

K.C. Sinha (✉) • S. Labi • Q. Bai
School of Civil Engineering, Purdue University, 550 Stadium Mall Drive,
West Lafayette, IN 47907, USA
e-mail: ksinha@purdue.edu; labi@purdue.edu; qbai@purdue.edu

S. Chakraborty and G. Bhattacharya (eds.), *Proceedings of the International Symposium on Engineering under Uncertainty: Safety Assessment and Management (ISEUSAM - 2012)*,
DOI 10.1007/978-81-322-0757-3_3,

1 Introduction

> The future is uncertain. . .but this uncertainty is at the very heart of human creativity.
> Ilya Prigogine (1917–2003)

The *Oxford English Dictionary* [25] defines uncertainty as "the quality of being uncertain in respect of duration, continuance, occurrence, etc.; the state of not being definitely known or perfectly clear; or the amount of variation in a numerical result that is consistent with observation." As it is in everyday life, the uncertainty is an inevitable aspect of transportation infrastructure development and management and is receiving much attention because of several recent catastrophic events. For instance, the collapses of the Autoroute 19 bridge in Laval of Quebec, Canada, in 2006 and the Minnesota I-35W Mississippi River bridge in 2007 caused many deaths and injuries and created severe travel disruptions. Also, in the earthquake/tsunami of the Pacific coast of Tohoku in Japan in 2011, the sole bridge connecting to Miyatojima was destroyed, which isolated the island's residents; many sections of Tōhoku Expressway were damaged; and the Sendai Airport was flooded and partially damaged. In fact, almost all similar extreme events, such as earthquakes and flooding, always cause damages to transportation infrastructures. In addition to catastrophic collapses and damages due to extreme events, there are other inherent uncertainties in transportation infrastructure development, such as variability in demand estimation, reliability in planning, and construction cost and time estimation. These uncertainties create not only tremendous economic and property losses, but also cause loss of human lives, and pose a serious public health and safety problem. Inability to identify the sources of uncertainty and inadequate assessment of its degree of occurrence introduces significant unreliability in infrastructure decisions. The process of infrastructure development and management could be greatly enhanced if potential uncertainties could be identified and explicitly incorporated in decision-making, in order to minimize potential risks.

2 Transportation Infrastructure Development and Management Process

2.1 Phases of Infrastructure Development and Management

Transportation infrastructure development and management is a multiphase process, which can be divided into four key phases: (1) planning and design, (2) construction, (3) operations, maintenance, and preservation, and (4) reconstruction caused by obsolescence/disruption. At the planning and design phase, the infrastructure need is assessed through demand estimation and the anticipated cost and performance impacts associated with alternative locations and designs are evaluated. The construction phase carries the infrastructure to its physical realization. The longest phase – operations, maintenance, and preservation – simply involves

the use of the system and is carried out continually. Reconstruction is done in response to the physical failure of the system either due to deterioration or due to natural or man-made disasters. At each phase, uncertainties arise from variabilities in natural factors in system environment and anthropogenic factors such as inputs of the infrastructure decision-makers and are manifest ultimately in the form of variable levels of relevant performance measures established for that phase.

2.2 Sources of Uncertainties at Each Phase

2.2.1 The Planning and Design Phase

Transportation infrastructure planning and design is an inherently complex process that is inextricably tied to social, economic, environmental, and political concerns, each of which is associated with significant uncertainty. At the planning stage, possible sources of uncertainty are associated mainly with travel demand and land-use and environmental impacts.

Transportation Demand Uncertainty

Transportation demand is a basic input for establishing the capacity or sizing of an infrastructure. For instance, future traffic volume is an important factor for determining highway geometrics, design speed, and capacity; passenger volume is a prerequisite to design airport terminals; and expected ridership is the key variable for the design of the routing stock and other features of urban transit. Also, transportation demand is the key determinant of the financial viability of projects [26, 27]. In fact, the level of anticipated travel demand serves as the basis for impact analysis of transportation infrastructure investments from social, environmental, and economic perspectives. In practice, however, demand estimation is plagued with a very significant degree of uncertainty in spite of multiple, sustained efforts to enhance demand estimation ([17]). Flyvbjerg et al. [13] conducted a survey on the differences between forecast and actual travel demand of the first year of the operation by examining 210 transportation projects (27 rail projects and 183 road projects) around the world. It was found that in 72% of rail projects, passenger forecasts were overestimated by more than 67%; 50% of road projects had a difference between actual and forecasted traffic of more than ±20% and 25% of projects had the difference more than ±40%. Major sources of these variabilities are shown in Fig. 1.

It is seen that the trip distribution part of travel demand modeling was one of the main sources for the discrepancy in both rail and highway projects, while land-use development had more effect on highway projects than on rail projects. It is also seen that the “deliberately slanted forecast” was a major cause of rail travel demand inaccuracy, which indicates that political influences can introduce significant uncertainty in some project types.

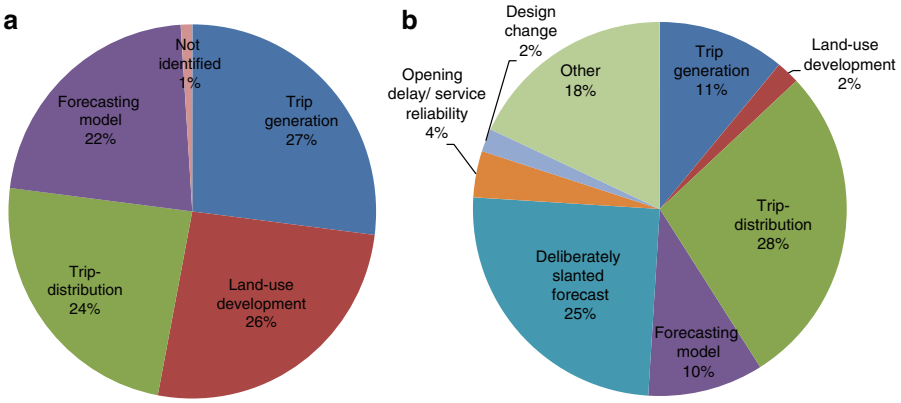

Fig. 1 Causes of uncertainties in traffic forecasts in transportation projects. (**a**) Highway projects and (**b**) Rail projects (Derived from Flyvbjerg et al. [13])

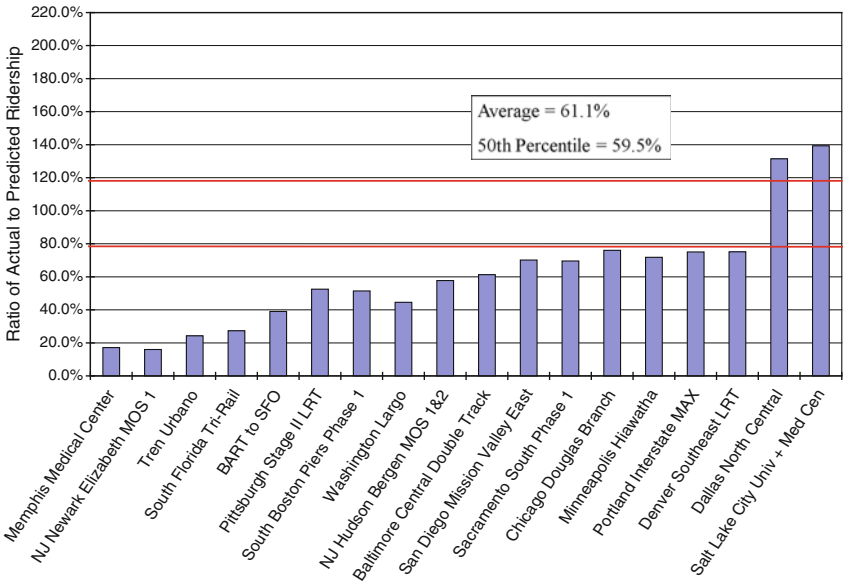

Fig. 2 Transit actual ridership versus predicted ridership (Source: Workman [35])

Figure 2 presents the ratios of the actual ridership to the predicted ridership for 17 urban rail projects in USA. In most cases, actual values were much lower than predicted values. Consequences of travel demand uncertainty can be significant. Overestimation of demand would lead to excess supply and its underutilization, resulting lower revenue and financial problem to the operating agencies.

Underestimation of demand, on the other hand, would cause congestion and excessive user delay and might require expensive upgrading. For instance, the Shenyang-Dalian Freeway, China's first freeway, was completed in 1990 with four lanes, two in each direction. According to the initial planning, the travel demand was not expected to reach the design traffic volume before 2010, the design year of the freeway. However, due to the high traffic volume, the freeway had to be upgraded to eight lanes in 2002, 8 years before the design year. There are many similar cases in China, including the Guangzhou-Qinagyuan Freeway (constructed with four lanes in 1999, expanded to eight lanes in 2009), Fuzhou-Quanzhou Freeway (constructed with four lanes in 1999, expanded to eight lanes in 2010), and Xi'an-Baoji Freeway (constructed with four lanes in 1995, expanded to eight lanes in 2011). If the forecasted traffic volume has less uncertainty, the construction and the upgrading could be done in a more cost-efficient and timely way. For public-private partnership projects, the consequences of demand uncertainty can be severe; if the actual travel demand is far less than as predicted, the investor fails to breakeven, and the investment may run into a loss.

Environmental Impact Uncertainty

Uncertainty associated with environmental impacts of transportation projects is another source of great concern to transportation decision-makers and the general public. To comply with the National Environmental Policy Act (NEPA) of 1969, transportation agencies in the USA evaluate the potential impacts of projects on social and natural environments, and projects are planned and designed accordingly including the provision of appropriate mitigation measures. However, because of the largely unpredictable nature of the climate, weather, traffic characteristics, and emission volumes, the estimation of expected environmental impacts with high degree of uncertainty becomes a challenge.

2.2.2 The Construction Phase

At the construction phase, the uncertainty is mainly associated with construction duration and cost. Table 1 presents results from a study of highway projects in several states in the USA [4], indicating that high percentages of projects had cost and time overruns.

The *Engineering News Record* [11] also reported that for most large transportation infrastructure projects, the final costs significantly exceeded the estimated costs. For example, the San Francisco Bay Bridge replacement project had a 30% cost overrun [10], the Tokyo Oedo Subway in Japan 105% [35], and the Springfield Interchange project in Northern Virginia 180% [11].

Based on data from 708 Florida highway projects during 1999–2001, Vidalis and Najafi [33] found that the construction time overruns could be attributed to unexpected site conditions such as poor geotechnical conditions, utility relocations, and

Table 1 Cost and time overruns at selected states (Source: Bordat et al. [4])

State	Period	Percentage of projects with cost overruns (%)	Percentage of projects with time overruns (%)
Idaho	1997–2001	55–67	–
Indiana	1996–2002	55	12
Missouri	1999–2002	60–64	–
New Mexico	2002	62	10
Ohio	1994–2001	80–92	44–56
Oregon	1998–2002	18–33	15–65
Tennessee	1998–2002	61	14
Texas	1998–2002	66–75	52–55

other environmental problems; deviations between design drawings and actual site conditions; and inclement weather, while cost overruns were due to errors and omissions in plans and modifications and subsequent change orders. Majid and McCaffer [21] found that the top five causes of construction time overrun were (1) late delivery or slow mobilization, (2) damaged materials, (3) poor planning, (4) equipment breakdown, and (5) improper equipment. In Indiana, Bhargava et al. [2] observed that the factors that caused cost overrun mostly included changes in project scope and site conditions. Consequences of construction cost and time overruns can lead to delayed use of the facility, defer the economic development, and cause financial problems for transportation agencies. In most cases, cost and time overruns worsen each other interactively.

2.2.3 The Operations, Maintenance, and Preservation Phase

This phase involves the estimation of annual maintenance and operating costs and timing and cost of periodic preservation. The factors that affect these items are the prevailing infrastructure physical conditions/performances and traffic characteristics. Operational strategies, including traffic management decisions, are typically based on average traffic and the typical pattern of traffic changes during a certain period. However, both the traffic and the change pattern are not deterministic and often exhibit marked variations. These variations may render the operational strategies ineffective. Also, the uncertainty associated with user behavior may cause uncertainty in infrastructure operations, safety, and security. For tolled facilities, one of the serious concerns has been the uncertainty in demand which leads to uncertainty in toll revenue.

With regard to infrastructure maintenance and preservation, a key context of decision-making is to identify specific maintenance and rehabilitation (M&R) treatments at a given time or specific M&R activity profile or schedule that optimizes the cost efficiency within performance constraints. In these contexts, the optimal solution is heavily influenced by prevailing infrastructure attributes such as physical condition, rate of deterioration, M&R cost and effectiveness, amount of traffic, climatic

severity, and prices of raw materials, labor, and equipment use. Variabilities in condition inspection outcomes, the stochastic nature of the infrastructure deterioration, the uncertainty in M&R cost and effectiveness, and variation of traffic levels and distribution all introduce a great deal of uncertainty in the treatment/schedule selection processes. Uncertainties associated with infrastructure deterioration rates and processes have been very extensively studied. In maintenance management, infrastructure performance models are usually applied to simulate the infrastructure deterioration process and to predict the future performance for optimal maintenance decision-making. Often Markov chain process is used for this purpose as it can incorporate the stochastic property [16, 23, 20, 37, 15].

2.2.4 Obsolescence/Disruption and Reconstruction Phase

There can be four types of processes which make an infrastructure facility obsolete: (1) natural deterioration, (2) the changed demand, (3) catastrophic physical failure, and (4) extreme events such as natural and man-made disasters. A transportation facility usually deteriorates gradually over time. When the physical condition reaches a certain level that does not allow cost-effective maintenance and preservation, it requires reconstruction. The uncertainty associated with this type of obsolescence arises from the lack of precise knowledge of the deterioration process of the facility. The causes of the deterioration may include weather, traffic load, and the infrastructure design itself. Often a facility requires reconstruction because the change in demand characteristics, such as vehicle size and weight, makes the geometrics and structural aspects of the facility obsolete. Even though most infrastructure facilities are reconstructed before their failure, there are some cases where infrastructures experience sudden catastrophic failures. This type of disruption is of high uncertainty and is very hard to predict. While better inspection and monitoring of facility conditions might minimize such failures, there will still be a certain degree of uncertainty because of the lack of precise knowledge of the deterioration process.

Extreme events constitute another important source of uncertainty. Extreme events can be defined as occurrences that, relative to some class of related occurrences, are either notable, rare, unique, profound, or otherwise significant in terms of its impacts, effects, or outcomes [29]. Common extreme events that can cause catastrophic disruptions can be categorized into natural disasters, such as the earthquake, tsunami, flooding, landslide, hurricane; and man-made events, such as terrorism attacks and collisions. Figure 3 presents examples of extreme events. The degree of uncertainty associated with infrastructure disruption/destruction due to extreme events depends on both the uncertainty of extreme events themselves as well as the uncertainty of infrastructure resilience/vulnerability. While it is difficult to prevent the occurrence of extreme events, the resilience of the transportation infrastructure can be strengthened to decrease the level of damages and network disruptions under such events.

Fig. 3 Example consequences of extreme events. (**a**) Chehalis River flooding (Source: Blogspot.com [3]), (**b**) Japanese earthquake (Source: Buzzfeed.com [6]), (**c**) California highway landslide (Source: Cbslocal.com [7]), and (**d**) Jintang Bridge collision in China (Source: Xinhuanet.com [36])

3 Measurement of Uncertainty

In order to incorporate the effect of uncertainty in transportation decision-making, it is important to establish a yardstick that could serve as a basis for quantifying the level of uncertainty from each source. As indicated in the definition of uncertainty, the possible outcome of the consequence is unknown in an uncertainty situation. In practice, uncertainty can be further categorized into two cases: (1) risk case where the probability distribution of the outcome is known, and (2) total uncertainty case where the distribution or even the range of the outcome is not known [19]. In past research, several objective approaches, such as the use of expected value, probability distribution, likelihood value, and confidence interval, were developed to quantify uncertainties in the risk situation. In a total uncertainty situation, approaches based on uncertainty or vulnerability ratings are often used. The choice of a specific approach or technique depends on the availability of data and the context of decision-making, which, in turn, is influenced by the phase of transportation infrastructure development in question. There is no universal method to quantify all types of uncertainties. In this section, a number of common methods are presented.

3.1 Probability Distributions

For some parameters associated with infrastructure development and management, such as the pavement condition rating, bridge remaining service life, and construction cost, probability distributions, rather than fixed values (as it is implicitly assumed in deterministic decision-making), are widely used to describe or measure the degree of uncertainty. From the probability distribution of the parameter of interest, a number of statistical measures can help quantify the degree of uncertainty:

(a) The statistical range of values (minimum and maximum values of the parameter).
(b) The standard deviation or variance.
(c) The coefficient of variation (ratio of the mean to the standard deviation).
(d) A visual examination of the shape of the distribution. This can provide clues regarding the degree of uncertainty of the parameter of interest. For example, there is greater certainty when the distribution is compact compared to a diffused distribution.
(e) Confidence interval. In practice, the decision-maker may be relatively unconcerned about the value of even the exact distribution of the investment outcome and may be more concerned about what the range of the outcome will be under a certain confidence level or conversely, at what confidence level the outcome can be expected to fall within a certain range.
(f) The probability that the outcome is more/less than a certain specified value. The greater the probability, the lower the uncertainty associated with that parameter; the smaller the probability, the greater the uncertainty associated with that parameter. Thus, such probabilities can serve as a measure of uncertainty and they can be determined from the cumulative probability function of the outcome.

In practice, the probability distribution of a parameter can be obtained through several ways. If available, the probability distribution can be developed from the historical data. In some cases, when historical data is not available, expert opinions can be used to assign a distribution to the parameter of interest. Also, the distribution of the consequence can be generated using such techniques as Monte Carlo simulation.

The probability distribution approach has been widely used to measure uncertainty of some parameters in transportation infrastructure development and management. For instance, Li and Sinha [19] applied binomial distribution to quantify the uncertainty of bridge condition ratings and beta distributions to measure the uncertainty of construction expenditure, delay time, and crash rate, in the development of a comprehensive highway infrastructure management system. Ford et al. [14] applied probability distribution to measure the uncertainty in bridge replacement needs assessment.

3.2 Uncertainty Rating

In some situations, there may exist certain parameters which are qualitative in nature, or there are inappropriate, inadequate, or unreliable data for probability distributions to be developed. For instance, it is hard to evaluate the probability that an in-service bridge will be destroyed in an earthquake since we cannot do real experiment to obtain the data. In such a case, ratings based on the structure and current condition of the bridge may be useful. In some other situations, particularly where human perspectives are involved, objective attempts to quantify uncertainties on a numerical scale may not be possible. In these cases, expert opinions could be used to develop a representative description of the degree of uncertainty. An example of this approach is Shackle's surprise function [30] to evaluate the subjective degree of uncertainty as perceived by decision-makers. NYSDOT (24) applied infrastructure vulnerability rating to capture the uncertainty associated with infrastructure resilience to sudden disruption through disaster, threat or likelihood of such disaster events, exposure to disaster (or consequence), or any two or all three of these attributes.

4 Incorporating Uncertainty into Decision-Making

With the realization that the parameters involved in transportation infrastructure development process are highly variable and subject to significant uncertainty, the importance of incorporating such uncertainty in decision-making cannot be overemphasized. A number of researchers have attempted, to varying degrees of success, to develop procedures that duly account for uncertainty, as discussed below.

4.1 Probability Models

Of the probability models, Markov chain models probably are the most widely used, particularly for modeling the time-related performance of infrastructure. A Markov chain, which describes the transition from one state to another in a chain-like manner stochastically, is a random and memoryless process, in which the next state depends only on the current state and not on the entire past. A transportation facility at a certain current condition can transform subsequently, due to deterioration, to any one of several possible condition states each with a specific probability. Figure 4 presents a simple example of transition probability matrix for superstructure rating of steel bridges in Indiana [32]. From the figure, it is seen that the probability of a new bridge with superstructure rating of 9 remaining in the same condition in the next period is 0.976 while the probability of transferring to the next lower condition state of 8 is 0.024.

Condition States

Condition States	9	8	7	6	5	4	3	2
9	0.976	0.024						
8		0.936	0.064					
7			0.89	0.11				
6				0.885	0.115			
5					0.92	0.08		
4						0.93	0.07	
3							0.92	0.08
2								1

Fig. 4 Example of Markov transition probability matrix for bridge superstructure rating (Source: Sinha et al. [32])

Weaknesses of this method are that the subsequent condition states actually are influenced by past states and that there is an assumption of time homogeneity. Nevertheless, Markov chain models have been extensively used, with appropriate modifications, in transportation infrastructure performance modeling for pavements [5], bridges [16], harbors and coastal structures [38], and railroads [1, 28].

4.2 Monte Carlo Simulation

Figure 5 presents the process of Monte Carlo simulation. Distributions of the parameters are the basic inputs; the output is the distribution of the outcome for evaluation or decision-making. A randomly generated number from each parameter's distribution is used to yield the final evaluation outcome in each iteration. Thousands of iterations are typically conducted and thus thousands of potential final outcomes are generated and their distribution is determined. Monte Carlo simulation has been widely used in transportation area, including life-cycle cost analysis in pavement design [34], the variability of construction cost escalation pattern [2], and others [9, 12, 22].

4.3 Stochastic Dominance

Using the distribution of the evaluation outcome, the decision-maker can calculate the mean value of the outcome and then make a decision based on the mean value. For example, if the outcome mean value of alternative *A* is superior to that of alternative *B*, then alternative *A* is preferred. However, if the two outcomes are described by a probability distribution, then the mean alone cannot guarantee that *A* is always superior to *B*. For instance, in the case 1 of Fig. 6, distribution *A* has a higher mean value (30) than that of *B* (25). However, from the cumulative probability function, when the value of the input parameter is less than 22, the probability

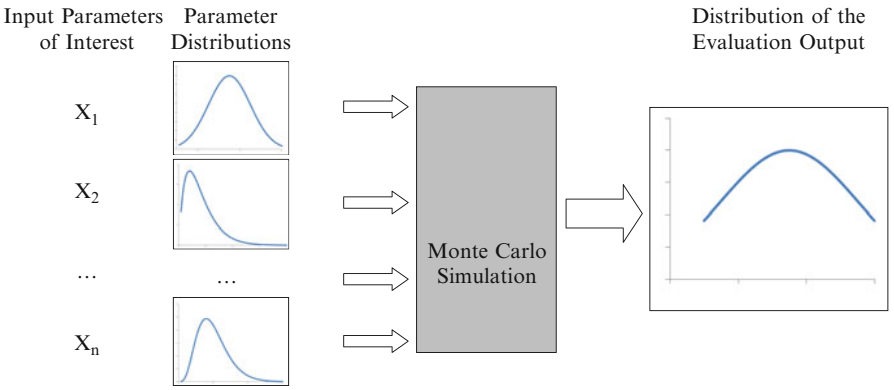

Fig. 5 Illustration of Monte Carlo simulation process

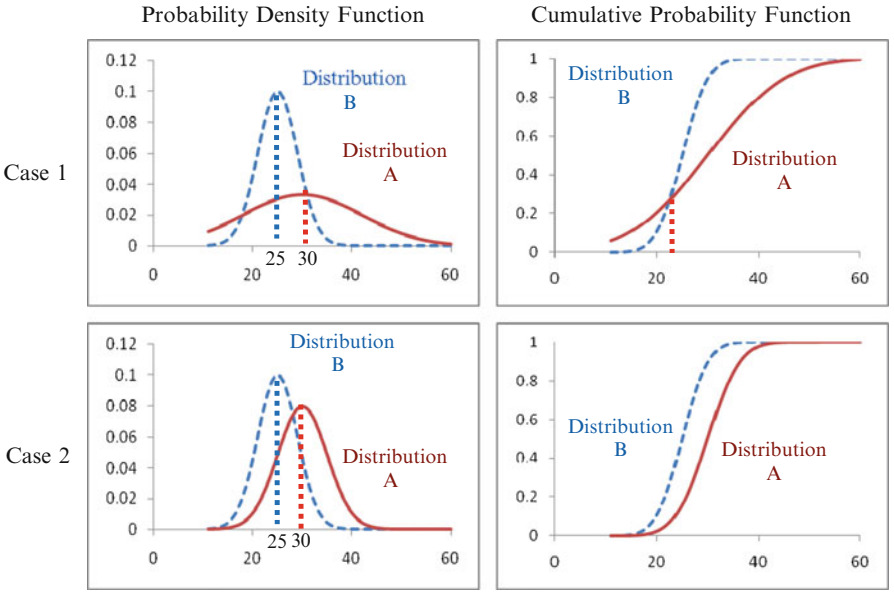

Fig. 6 The concept of stochastic dominance

that *A*'s outcome is less than a certain value is greater than the probability that *B*'s outcome is less than that value; this means that when the outcome is less than 22, alternative *B* is superior to alternative *A* under conditions of uncertainty. As this example demonstrates, using the expected value of probability distributions corresponding to each alternative is not reliable. Stochastic dominance is a method to compare two distributions [8]. In the case 2 of Fig. 6, *A* and *B* have different distributions, not all the possible values of *A* are superior than the value of *B*, but from their cumulative functions, it is seen that for any given outcome level, the

probability that A is smaller than the given level is equal or less than the probability that B is smaller than the given level. Obviously, A is superior to B. In other words, A stochastically dominates B. Thus, it is seen that if the expected value of A is greater than B, that situation does not guarantee that A stochastically dominates B, but if A stochastically dominates B, then the expected value of A is greater than B for sure.

The concept of stochastic dominance avoids the possible bias of just using the expected value in comparing two alternatives. It can yield a more robust evaluation result. Cope et al. [9] applied stochastic dominance to evaluate the effectiveness of using stainless steel as the bridge deck reinforcement. It can also be used in multicriteria decision-making [39].

4.4 Expected Utility Theory

In order to incorporate both parameter uncertainty and decision-maker preferences, Keeney and Raiffa [18] developed the expected utility theory, where a utility function $u(x)$ is first developed as a function of the outcome (x) in its original unit, to represent the degree of preference on different values of the outcome. Then the probability density function of x, i.e., $f(x)$, is used to calculate the expected utility, i.e., $\mathrm{EU} = \int_{x_{\min}}^{x_{\max}} u(x) * f(x)\mathrm{d}x$. The alternative with the highest expected utility becomes the preferred choice. Expected utility theory has been used in numerous studies in transportation infrastructure development. For example, Li and Sinha [19] applied expected utility theory to deal with the uncertainty in transportation asset management for Indiana Department of Transportation.

4.5 Shackle's Model

As seen in previous sections, if the distribution of a parameter is known, it is relatively easy to use the expected value, expected utility value, or stochastic dominance concepts to make a decision. But in practice, it may not be possible to get the distribution. In this case, Shackle's model [30] can be applied to incorporate uncertainties in the decision-making process [19]. There are three main steps in this approach.

1. Establish the degree of surprise function. Degree of surprise is used to measure the decision-maker's degree of uncertainty with gains (positive returns) and losses (negative returns) from the expectation. Usually, the values of degree of surprise range from 0 (no surprise) to 10 (extremely surprised).
2. Develop priority function and focus values. Priority function is developed to evaluate the weighting index of each pair outcome and its degree of surprise.

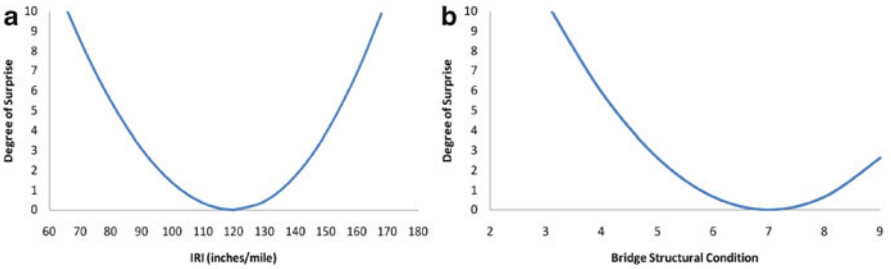

Fig. 7 Examples of surprise function. (**a**) IRI (expectation: 120 in./mile). (**b**) Bridge Structural condition (expectation: 7)

The priority function is usually from 0 (lowest priority) to 10 (highest priority). Based on the priority function, the focus gain (G), the gain with the maximum priority value, and the focus loss (L), the loss with the maximum priority value can be found.

3. Calculate standardized focus gain-over-loss ratio. The degrees of surprise of the focus gain and focus loss are usually nonzero. Then, there is a need to find out the standardized gain and loss values, which are the values of the outcomes that on the same priority indifference curves that have zero degree of surprise. Next, the standardized focus gain-over-loss ratio can be calculated. Usually, the project with the higher standardized focus gain-over-loss ratio is more desirable to decision-makers.

Surprise and priority functions are developed from surveys of potential decision-makers. As an example, Fig. 7 presents the surprise functions for the pavement International Roughness Index (IRI) and the structural condition rating for bridges developed by Li and Sinha [19] for their study to incorporate uncertainty in highway asset management. It is seen that the further the parameter is from its expectation, the larger is the level of surprise the decision-maker experiences.

In addition to the methods discussed above, there are a host of other methods that can be used to incorporate uncertainty into decision-making process, such as sensitivity analysis, fuzzy set theory, mean-variance utility theory, and Bayes' method. Sensitivity analysis is the most widely used approach; it examines the degree of changes in the outcome if there are some changes in the input/dependent variables. Also, fuzzy set theory has been extensively used to deal with uncertainty in transportation infrastructure management. For example, Shoukry et al. [31] developed a universal measure capable of formally assessing the condition of a pavement section based on fuzzy set theory.

The choice of an approach to deal with uncertainty in transportation infrastructure development and management will depend on the specific context of the decision being made. As mentioned earlier, there is no single method that can be applied universally to all problem types and contexts. Also, not all types of uncertainties can be successfully incorporated into the decision-making process.

5 Summary and Conclusions

The development and management of transportation infrastructure is characterized by significant uncertainty at each of its phase. To make optimal and robust decisions at each phase, it is critical not only to be aware of the possible sources of uncertainty, but also to quantify these uncertainties and more importantly, to incorporate them in decision-making processes. While much information is already in existence, further work is necessary to apply the information in infrastructure development and management process so that improved decisions can be made. Some possible research directions include:

1. Extreme events related research. There is an urgent need to address the uncertainty associated with infrastructure disruptions due to sudden catastrophic failures and natural or man-made disasters in order to provide appropriate resilience and sustainability in future infrastructure facilities.
2. Vulnerability assessment related to climate changes, network resilience, and sustainability evaluation and vulnerability management, including how to minimize the effect of network disruption.
3. The integration of optimization and Monte Carlo simulation to incorporate uncertainty in infrastructure investment decision-making. Optimization and Monte Carlo simulation are both computationally time-consuming processes and novel heuristic algorithms are necessary to solve the integration problem.
4. Future research is needed on the development of methods for quantifying uncertainty associated with human input. Decision-makers' preference structure and their perception of uncertainty are important in an effective decision-making process.
5. Trade-off between uncertainty/risk and benefit/return. In most situations, high benefit/return is associated with high risk. There is a need to develop a robust trade-off methodology to reach a balance between uncertainty/risk and benefit/return.

References

1. Bell MGH, Schmoecker JD, Iida Y, Lam WHK (2002) Transit network reliability: an application of absorbing Markov chains. Transportation and traffic theory in the 21st century. In: Proceedings of the 15th international symposium on transportation and traffic theory. University of South Australia, Adelaide, Australia. Accessed 10 Oct 2011
2. Bhargava A, Labi S, Sinha KC (2010) Development of a framework for Ex Post Facto evaluation of highway project costs in Indiana. Publication# FHWA/IN/JTRP-2009/33. Joint Transportation Research Program, Indiana Department of Transportation and Purdue University, West Lafayette, IN
3. Blogspot.com (2007) Light rail will save us. http://victoriataftkpam.blogspot.com/2007/12/light-rail-will-save-us.html. Accessed October 10 2011

4. Bordat C, McCullouch BG, Sinha KC, Labi S (2004) An Analysis of Cost Overruns and Time Delays of INDOT Projects. Joint Transportation Research Program, Indiana Department of Transportation and Purdue University, West Lafayette, Indiana
5. Butt AA, Shahin MY, Feighan KJ, Carpenter SH (1987) Pavement performance prediction model using the Markov process. Transportation research record no. 1123, pp 12–19
6. Buzzfeed.com (2011) Road split in two by Japanese earthquake. http://www.buzzfeed.com/burnred/road-split-in-two-by-japanese-earthquake-281t. Accessed 10 Oct 2011
7. Cbslocal.com (2011) Third mudslide closes Highway 1 on Big Sur coast. http://sanfrancisco.cbslocal.com/2011/03/28/third-mudslide-closes-highway-1-on-big-sur-coast/. Accessed 10 Oct 2011
8. Clemen RT (1996) Making hard decisions. Duxbury Press, Pacific Grove
9. Cope A, Bai Q, Samdariya A, Labi S (2011) Assessing the efficacy of stainless steel for bridge deck reinforcement under uncertainty using Monte Carlo simulation. Struct Infrastruct Eng. doi:10.1080/15732479.2011.602418
10. ENR (2001) Bay bridge replacement comes in above estimate. ENR, p. 5, Dec. 31, 2001
11. ENR (2002) Virginia's big 'mixing bowl' is 180% over budget. ENR, p. 7, Dec. 2, 2002
12. Ersahin T, McCabe B, Doyle M (2003) Monte Carlo simulation analysis at Lester B Pearson International Airport development project. Construction Research Congress. Winds of change: integration and innovation in construction. Proceedings of the Congress, Honolulu, Hawaii, United States
13. Flyvbjerg B, Holm MKS, Buhl SL (2006) Inaccuracy in traffic forecasts. Transp Rev 26(1):1–24
14. Ford K, Arman M, Labi S, Sinha KC, Shirole A, Thompson P, Li Z (2011) Methodology for estimating life expectancies of highway assets (draft). School of Civil Engineering, Purdue University, West Lafayette
15. Fu G, Devaraj D (2008) Methodology of Homogeneous and Non-Homogeneous Markov Chains for Modeling Bridge Element Deterioration. Wayne State University, Detroit, MI
16. Jiang Y, Sinha KC (1989) Bridge service life prediction model using the Markov chain. Transportation research record no. 1223, pp 24–30
17. Kanafani A (1981) Transportation Demand Analysis. John Wiley and Sons, New York, NY
18. Keeney RL, Raiffa H (1993) Decisions with multiple objectives: Preferences and value tradeoffs. Cambridge University Press, New York
19. Li Z, Sinha KC (2004) Methodology for the development of a highway asset management system for Indiana. Purdue University, West Lafayette
20. Li N, Xie WC, Haas R (1996) Reliability-based processing of Markov chains for modeling pavement network deterioration. Transportation research record no. 1524, pp 203–213
21. Majid MZA, McCaffer R (1998) Factors of Non-Excusable Delays that Influence Contractors' Performance. J Manag Eng 14(3):42–48
22. Nagai K, Tomita Y, Fujimoto Y (1985) A fatigue crack initiation model and the life estimation under random loading by Monte Carlo method. J Soc Naval Archit Jpn 158(60):552–564
23. Nesbitt DM, Sparks GA, Neudorf RD (1993) A semi-Markov formulation of the pavement maintenance optimization problem. Can J Civil Eng XX(III):436–447
24. NYSDOT (2002) Vulnerability manuals. Bridge Safety Program, New York State DOT
25. Oxford University Press (2011) Uncertainty. In: Oxford English Dictionary Online. http://dictionary.oed.com. Accessed October 10 2011
26. Pickrell DH (1990) Urban rail transit projects: forecast versus actual ridership and cost. US Department of Transportation, Washington, DC
27. Richmond JED (1998) New rail transit investments: a review. John F. Kennedy School of Government, Harvard University, Cambridge, MA
28. Riddell WT, Lynch J (2005) A Markov chain model for fatigue crack growth, inspection and repair: the relationship between probability of detection, reliability and number of repairs in fleets of railroad tank cars. In: Proceedings of the ASME pressure vessels and piping conference 2005 – operations, applications and components, Denver, Colorado, United States

29. Sarewitz D, Pielke RA (2001) Extreme events: a research and policy framework for disasters in context, Int Geol Rev, 43(5):406–418
30. Shackle GLS (1949) Expectation in economics, 2nd edn. Cambridge University Press, Cambridge
31. Shoukry SN, Martinelli DR, Reigle JA (1997) Universal pavement distress evaluator based on fuzzy sets. Transportation research record, no. 1592, pp 180–186
32. Sinha KC, Labi S, McCullouch B, Bhargava A, Bai Q (2009) Updating and enhancing the Indiana Bridge Management System (IBMS). Joint Transportation Research Program, Purdue University, West Lafayette
33. Vidalis SM, Najafi FT (2002) Cost and time overruns in highway construction. In: 4th transportation specialty conference of the Canadian Society for Civil Engineering, Montréal, QC, Canada, 5–8 June 2002
34. Walls J, Smith MR (1998) Life-cycle cost analysis in pavement design – interim technical bulletin. Federal Highway Administration, SW Washington, DC
35. Workman SL (2008) Predicted vs. actual costs and ridership of new starts projects. In: 88th annual meeting of Transportation Research Board, Washington, DC
36. Xinhuanet.com (2008) Four missing after cargo vessel hits bridge in China. http://news.xinhuanet.com/english/2008-03/27/content_7868845.htm. Accessed 10 Oct 2011
37. Yang JD, Lu JJ, Gunaratne M, Dietrich B (2006) Modeling crack deterioration of flexible pavements: comparison of recurrent Markov chains and artificial neural networks. Transportation research record no. 1974, pp 18–25
38. Yokota H, Komure K (2004) Estimation of structural deterioration process by Markov-chain and costs for rehabilitation. Life-cycle performance of deteriorating structures. Third IABMAS workshop on life-cycle cost analysis and design of civil infrastructure systems and the JCSS workshop on probabilistic modeling of deterioration processes in concrete structures. Lausanne, Switzerland, pp 424–431
39. Zhang Y, Fan ZP, Liu Y (2010) A method based on stochastic dominance degrees for stochastic multiple criteria decision making. Comput Ind Eng 58:544–552

Physical Perspective Toward Stochastic Optimal Controls of Engineering Structures

Jie Li and Yong-Bo Peng

Abstract In the past few years, starting with the thought of physical stochastic systems and the principle of preservation of probability, a family of probability density evolution methods (PDEM) has been developed. It provides a new perspective toward the accurate design and optimization of structural performance under random engineering excitations such as earthquake ground motions and strong winds. On this basis, a physical approach to structural stochastic optimal control is proposed in the present chapter. A family of probabilistic criteria, including the criterion based on mean and standard deviation of responses, the criterion based on Exceedance probability, and the criterion based on global reliability of systems, is elaborated. The stochastic optimal control of a randomly base-excited single-degree-of-freedom system with active tendon is investigated for illustrative purposes. The results indicate that the control effect relies upon control criteria of which the control criterion in global reliability operates efficiently and gains the desirable structural performance. The results obtained by the proposed method are also compared against those by the LQG control, revealing that the PDEM-based stochastic optimal control exhibits significant benefits over the classical LQG control. Besides, the stochastic optimal control, using the global reliability

J. Li (✉)
State Key Laboratory of Disaster Reduction in Civil Engineering,
Tongji University, Shanghai 200092, China

School of Civil Engineering, Tongji University, Shanghai 200092, China
e-mail: lijie@tongji.edu.cn

Y.-B. Peng
State Key Laboratory of Disaster Reduction in Civil Engineering,
Tongji University, Shanghai 200092, China

Shanghai Institute of Disaster Prevention and Relief, Tongji University,
Shanghai 200092, China
e-mail: pengyongbo@tongji.edu.cn

S. Chakraborty and G. Bhattacharya (eds.), *Proceedings of the International Symposium on Engineering under Uncertainty: Safety Assessment and Management (ISEUSAM - 2012)*,
DOI 10.1007/978-81-322-0757-3_4,

criterion, of an eight-story shear frame structure is carried out. The numerical example elucidates the validity and applicability of the developed physical stochastic optimal control methodology.

Keywords Probability density evolution method • Stochastic optimal control • Control criteria • Global reliability • LQG control

1 Introduction

Stochastic dynamics has gained increasing interests and has been extensively studied. However, although the original thought may date back to Einstein [4] and Langevin [11] and then studied in rigorous formulations by mathematicians [8, 10, 37], the random vibration theory, a component of stochastic dynamics, was only regarded as a branch of engineering science until the early of 1960s (Crandall [2]; Lin [28]). Till early 1990s, the theory and pragmatic approaches for random vibration of linear structures were well developed. Meanwhile, researchers were challenged by nonlinear random vibration, despite great efforts devoted coming up with a variety of methods, including the stochastic linearization, equivalent nonlinearization, stochastic averaging, path-integration method, FPK equation, and the Monte Carlo simulation (see, e.g., [29, 30, 41]). The challenge still existed. On the other hand, investigations on stochastic structural analysis (or referred to stochastic finite element method by some researchers), as a critical component of stochastic dynamics, in which the randomness of structural parameters is dealt with, started a little later from the late 1960s. Till middle 1990s, a series of approaches were presented, among which three were dominant: the Monte Carlo simulation [32, 33], the random perturbation technique [6, 9], and the orthogonal polynomial expansion [5, 12]. Likewise with the random vibration, here the analysis of nonlinear stochastic structures encountered huge challenges as well [31].

In the past 10 years, starting with the thought of physical stochastic systems [13] and the principle of preservation of probability [19], a family of probability density evolution methods (PDEM) has been developed, in which a generalized density evolution equation was established. The generalized density evolution equation profoundly reveals the essential relationship between the stochastic and deterministic systems. It is successfully employed in stochastic dynamic response analysis of multi-degree-of-freedom systems [20] and therefore provides a new perspective toward serious problems such as the dynamic reliability of structures, the stochastic stability of dynamical systems, and the stochastic optimal control of engineering structures.

In this chapter, the application of PDEM on the stochastic optimal control of structures will be summarized. Therefore, the fundamental theory of the generalized density evolution equation is firstly revisited. A physical approach to stochastic optimal control of structures is then presented. The optimal control criteria, including those based on mean and standard deviation of responses and those based on exceedance probability and global reliability of systems, are elaborated. The stochastic optimal

control of a randomly base-excited single-degree-of-freedom system with active tendon is investigated for illustrative purposes. Comparative studies of these probabilistic criteria and the developed control methodology against the classical LQG control are carried out. The optimal control strategy is then further employed in the investigation of the stochastic optimal control of an eight-story shear frame. Some concluding remarks are included.

2 Principle Equation

2.1 Principle of Preservation of Probability Revisited

It is noted that the probability evolution in a stochastic dynamical system admits the principle of preservation of probability, which can be stated as the following: if the random factors involved in a stochastic system are retained, the probability will be preserved in the evolution process of the system. Although this principle may be faintly cognized quite long ago (see, e.g., [36]), the physical meaning has been only clarified in the past few years from the state description and random event description, respectively [16–19]. The fundamental logic position of the principle of preservation of probability was then solidly established with the development of a new family of generalized density evolution equations that integrates the ever-proposed probability density evolution equations, including the classic Liouville equation, Dostupov-Pugachev equation, and the FPK equation [20].

To revisit the principle of preservation of probability, consider an n-dimensional stochastic dynamical system governed by the following state equation:

$$\dot{\mathbf{Y}} = \mathbf{A}(\mathbf{Y}, t), \mathbf{Y}(t_0) = \mathbf{Y}_0 \tag{1}$$

where $\mathbf{Y} = (Y_1, Y_2, \cdots, Y_n)^{\mathrm{T}}$ denotes the n-dimensional state vector, $\mathbf{Y}_0 = (Y_{0,1}, Y_{0,2}, \cdots, Y_{0,n})^{\mathrm{T}}$ denotes the corresponding initial vector, and $\mathbf{A}(\cdot)$ is a deterministic operator vector. Evidently, in the case that $\mathbf{Y}_0$ is a random vector, $\mathbf{Y}(t)$ will be a stochastic process vector.

The state equation (1) essentially establishes a mapping from $\mathbf{Y}_0$ to $\mathbf{Y}(t)$, which can be expressed as

$$\mathbf{Y}(t) = g(\mathbf{Y}_0, t) = \mathrm{G}_t(\mathbf{Y}_0) \tag{2}$$

where $g(\cdot), \mathrm{G}_t(\cdot)$ are both mapping operators from $\mathbf{Y}_0$ to $\mathbf{Y}(t)$.

Since $\mathbf{Y}_0$ denotes a random vector, $\{\mathbf{Y}_0 \in \Omega_{t_0}\}$ is a random event. Here Ω_{t_0} is any arbitrary domain in the distribution range of $\mathbf{Y}_0$. According to the stochastic state equation (1), $\mathbf{Y}_0$ will be changed to $\mathbf{Y}(t)$ at time t. The domain Ω_{t_0} to which $\mathbf{Y}_0$

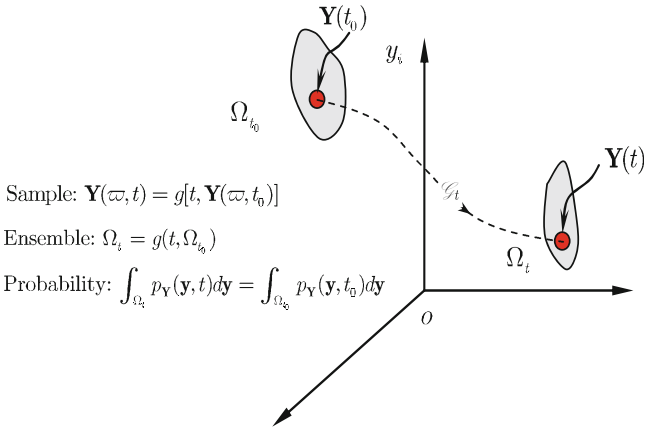

Fig. 1 Dynamical system, mapping, and probability evolution

belongs at time t_0 is accordingly changed to $\boldsymbol{\Omega}_t$ to which $\mathbf{Y}(t)$ belongs at time t; see Fig. 1.

$$\boldsymbol{\Omega}_t = g(\boldsymbol{\Omega}_{t_0}, t) = \mathrm{G}_t(\boldsymbol{\Omega}_{t_0}) \tag{3}$$

Since the probability is preserved in the mapping of any arbitrary element events, we have

$$\int_{\boldsymbol{\Omega}_{t_0}} p_{\mathbf{Y}_0}(\mathbf{y}, t_0)d\mathbf{y} = \int_{\boldsymbol{\Omega}_t} p_{\mathbf{Y}}(\mathbf{y}, t)d\mathbf{y} \tag{4}$$

It is understood that Eq. (4) also holds at $t + \Delta t$, which will then result in

$$\frac{\mathrm{D}}{\mathrm{D}t}\int_{\boldsymbol{\Omega}_t} p_{\mathbf{Y}}(\mathbf{y}, t)d\mathbf{y} = 0 \tag{5}$$

where $\mathrm{D}(\,\cdot\,)/\mathrm{D}t$ operates its arguments with denotation of total derivative.

Equation (5) is clearly the mathematical formulation of the principle of preservation of probability in a stochastic dynamical system. Since the fact of probability invariability of a random event is recognized here, we refer to Eq. (5) as the random event description of the principle of preservation of probability. The meaning of the principle of preservation of probability can also be clarified from the state-space description. These two descriptions are somehow analogous to the Lagrangian and Eulerian descriptions in the continuum mechanics, although there also some distinctive properties particularly in whether overlapping is allowed. For details, refer to Li and Chen [17, 19].

2.2 Generalized Density Evolution Equation (GDEE)

Without loss of generality, consider the equation of motion of a multi-degree-of-freedom (MDOF) system as follows:

$$\mathbf{M}(\eta)\ddot{\mathbf{X}} + \mathbf{C}(\eta)\dot{\mathbf{X}} + \mathbf{f}(\eta, \mathbf{X}) = \Gamma\xi(t) \tag{6}$$

where $\eta = (\eta_1, \eta_2, \cdots, \eta_{s_1})$ are the random parameters involved in the physical properties of the system. If the excitation is a stochastic ground accelerogram $\xi(t) = \ddot{X}_{\mathrm{g}}(t)$, for example, then $\Gamma = -\mathbf{M1}$, $\mathbf{1} = (1, 1, \cdots, 1)^{\mathrm{T}}$. Here $\ddot{\mathbf{X}}, \dot{\mathbf{X}}, \mathbf{X}$ are the accelerations, velocities, and displacements of the structure relative to ground. $\mathbf{M}(\cdot), \mathbf{C}(\cdot), \mathbf{f}(\cdot)$ denote the mass, damping, and stiffness matrices of the structural system, respectively.

In the modeling of stochastic dynamic excitations such as earthquake ground motions, strong winds, and sea waves, the thought of physical stochastic process can be employed [14, 15, 27]. For general stochastic processes or random fields, the double-stage orthogonal decomposition can be adopted such that the excitation could be represented by a random function [22]

$$\ddot{X}_{\mathrm{g}}(t) = \ddot{X}_{\mathrm{g}}(\zeta, t) \tag{7}$$

where $\zeta = (\zeta_1, \zeta_2, \cdots, \zeta_{s_2})$.

For notational consistency, denote

$$\Theta = (\eta, \zeta) = (\eta_1, \eta_2, \cdots, \eta_{s_1}, \zeta_1, \zeta_2, \cdots, \zeta_{s_2}) = (\Theta_1, \Theta_2, \cdots, \Theta_s) \tag{8}$$

in which $s = s_1 + s_2$ is the total number of the basic random variables involved in the system. Equation (6) can thus be rewritten into

$$\mathbf{M}(\Theta)\ddot{\mathbf{X}} + \mathbf{C}(\Theta)\dot{\mathbf{X}} + \mathbf{f}(\Theta, \mathbf{X}) = \mathbf{F}(\Theta, t) \tag{9}$$

where $\mathbf{F}(\Theta, t) = \Gamma\ddot{\mathbf{X}}_{\mathrm{g}}(\zeta, t)$.

This is the equation to be resolved in which all the randomness from the initial conditions, excitations, and system parameters is involved and exposed in a unified manner. Such a stochastic equation of motion can be further rewritten into a stochastic state equation which was firstly formulated by Dostupov and Pugachev [3].

If, besides the displacements and velocities, we are also interested in other physical quantities $\mathbf{Z} = (Z_1, Z_2, \cdots, Z_m)^{\mathrm{T}}$ in the system (e.g., the stress, internal forces), then the augmented system $(\mathbf{Z}, \Theta)$ is probability preserved because all the random factors are involved; thus, according to Eq. (5), we have [19]

$$\frac{\mathrm{D}}{\mathrm{D}t}\int_{\Omega_t \times \Omega_\theta} p_{\mathbf{Z}\Theta}(\mathbf{z}, \theta, t)d\mathbf{z}d\theta = 0 \tag{10}$$

where $\Omega_t \times \Omega_\theta$ is any arbitrary domain in the augmented state space $\Omega \times \Omega_\Theta$, Ω_Θ is the distribution range of the random vector Θ, and $p_{\mathbf{Z}\Theta}(\mathbf{z}, \theta, t)$ is the joint probability density function (PDF) of $(\mathbf{Z}(t), \Theta)$.

After a series of mathematical manipulations, including the use of Reynolds' transfer theorem, we have

$$\int_{\Omega_{t_0} \times \Omega_\theta} \left(\frac{\partial p_{\mathbf{Z}\Theta}(\mathbf{z}, \theta, t)}{\partial t} + \sum_{j=1}^{m} \dot{Z}_j(\theta, t) \frac{\partial p_{\mathbf{Z}\Theta}(\mathbf{z}, \theta, t)}{\partial z_j} \right) d\mathbf{z} d\theta = 0 \tag{11}$$

which holds for any arbitrary $\Omega_{t_0} \times \Omega_\theta \in \Omega \times \Omega_\Theta$. Thus, we have for any arbitrary $\Omega_\theta \in \Omega_\Theta$

$$\int_{\Omega_\theta} \left(\frac{\partial p_{\mathbf{Z}\Theta}(\mathbf{z}, \theta, t)}{\partial t} + \sum_{j=1}^{m} \dot{Z}_j(\theta, t) \frac{\partial p_{\mathbf{Z}\Theta}(\mathbf{z}, \theta, t)}{\partial z_j} \right) d\theta = 0 \tag{12}$$

and also the following partial differential equation:

$$\frac{\partial p_{\mathbf{Z}\Theta}(\mathbf{z}, \theta, t)}{\partial t} + \sum_{j=1}^{m} \dot{Z}_j(\theta, t) \frac{\partial p_{\mathbf{Z}\Theta}(\mathbf{z}, \theta, t)}{\partial z_j} = 0 \tag{13}$$

Specifically, as $m = 1$, Eqs. (12) and (13) become, respectively,

$$\int_{\Omega_\theta} \left(\frac{\partial p_{Z\Theta}(z, \theta, t)}{\partial t} + \dot{Z}(\theta, t) \frac{\partial p_{Z\Theta}(z, \theta, t)}{\partial z} \right) d\theta = 0 \tag{14}$$

and

$$\frac{\partial p_{Z\Theta}(z, \theta, t)}{\partial t} + \dot{Z}(\theta, t) \frac{\partial p_{Z\Theta}(z, \theta, t)}{\partial z} = 0 \tag{15}$$

which is a one-dimensional partial differential equation.

Equations (13) and (15) are referred to as generalized density evolution equations (GDEEs). They reveal the intrinsic connections between a stochastic dynamical system and its deterministic counterpart. It is remarkable that the dimension of a GDEE is not relevant to the dimension (or degree-of-freedom) of the original system; see Eq. (9). This distinguishes GDEEs from the traditional probability density evolution equations (e.g., Liouville, Dostupov-Pugachev, and FPK equations), of which the dimension must be identical to the dimension of the original state equation (twice the degree-of-freedom).

Clearly, Eq. (14) is mathematically equivalent to Eq. (15). But it will be seen later that Eq. (14) itself may provide additional insight into the problem. Particularly, if the physical quantity Z of interest is the displacement X of the system, Eq. (15) becomes

$$\frac{\partial p_{X\Theta}(x,\theta,t)}{\partial t} = -\dot{X}(\theta,t)\frac{\partial p_{X\Theta}(x,\theta,t)}{\partial x} \tag{16}$$

Here we can see the rule clearly revealed by the GDEE: in the evolution of a general dynamical system, the time variant rate of the joint PDF of displacement and source random parameters is proportional to the space variant rate with the coefficient being instantaneous velocity. In other words, the flow of probability is determined by the change of physical states. This demonstrates strongly that the evolution of probability density is not disordered but admits a restrictive physical law. Clearly, this holds for the general physical system with underlying randomness. This rule could not be exposed in such an explicit way in the traditional probability density evolution equations.

Although in principle the GDEE holds for any arbitrary dimension, in most cases, one- or two-dimensional GDEEs are adequate. For simplicity and clarity, in the following sections, we will be focused on the one-dimensional GDEE. Generally, the boundary condition for Eq. (15) is

$$p_{Z\Theta}(z,\theta,t)|_{z\to\pm\infty} = 0 \quad \text{or} \quad p_{Z\Theta}(z,\theta,t) = 0, z \in \Omega_{\mathrm{f}} \tag{17}$$

the latter of which is usually adopted in first-passage reliability evaluation where Ω_{f} is the failure domain, while the initial condition is usually

$$p_{Z\Theta}(z,\theta,t)|_{t=t_0} = \delta(z-z_0)p_{\Theta}(\theta) \tag{18}$$

where z_0 is the deterministic initial value.

Solving Eq. (15), the instantaneous PDF of $Z(t)$ can be obtained by

$$p_Z(z,t) = \int_{\Omega_\Theta} p_{Z\Theta}(z,\theta,t)d\theta \tag{19}$$

The GDEE was firstly obtained as the uncoupled version of the parametric Liouville equation for linear systems [16]. Then for nonlinear systems, the GDEE was reached when the formal solution was employed [18]. It is from the above derivation that the meanings of the GDEE were thoroughly clarified and a solid physical foundation was laid [19].

2.3 Point Evolution and Ensemble Evolution

Since Eq. (14) holds for any arbitrary $\Omega_\theta \in \Omega_\Theta$, then for any arbitrary partition of probability-assigned space [1], of which the sub-domains are Ω_q's, $q = 1, 2, \cdots, n_{\mathrm{pt}}$

satisfying $\Omega_i \cap \Omega_j = \varnothing, \forall i \neq j$ and $\bigcup_{q=1}^{n_{\text{pt}}} \Omega_q = \Omega_\Theta$, Eq. (14) constructed in the subdomain then becomes

$$\int_{\Omega_q} \left(\frac{\partial p_{Z\Theta}(z,\theta,t)}{\partial t} + \dot{Z}(\theta,t) \frac{\partial p_{Z\Theta}(z,\theta,t)}{\partial z} \right) d\theta = 0, q = 1, 2, \cdots, n_{\text{pt}} \tag{20}$$

It is noted that

$$P_q = \int_{\Omega_q} p_\Theta(\theta) d\theta, \quad q = 1, 2, \cdots, n_{\text{pt}} \tag{21}$$

is the assigned probability over Ω_q [1], and

$$p_q(z,t) = \int_{\Omega_q} p_{Z\Theta}(z,\theta,t) d\theta, \quad q = 1, 2, \cdots, n_{\text{pt}} \tag{22}$$

then Eq. (20) becomes

$$\frac{\partial p_q(z,t)}{\partial t} + \int_{\Omega_q} \left[\dot{Z}(\theta,t) \frac{\partial p_{Z\Theta}(z,\theta,t)}{\partial z} \right] d\theta = 0, q = 1, 2, \cdots, n_{\text{pt}} \tag{23}$$

According to Eq. (19), it follows that

$$p_Z(z,t) = \sum_{q=1}^{n_{\text{pt}}} p_q(z,t) \tag{24}$$

There are two important properties that can be observed here:

1. Partition of probability-assigned space and the property of independent evolution The functions $p_q(z,t)$ defined in Eq. (22) themselves are not probability density functions because $\int_{-\infty}^{\infty} p_q(z,t) dz = P_q \neq 1$, that is, the consistency condition is not satisfied. However, except for this violation, they are very similar to probability density functions in many aspects. Actually, a normalized function $\tilde{p}_q(z,t) = p_q(z,t)/P_q$ meets all the conditions of a probability density function, which might be called the partial-probability density function over Ω_q. Equation (24) can then be rewritten into

$$p_Z(z,t) = \sum_{q=1}^{n_{\text{pt}}} P_q \cdot \tilde{p}_q(z,t) \tag{25}$$

It is noted that P_q's are specified by the partition and are time invariant. Thus, the probability density function of $Z(t)$ could be regarded as the weighted sum of a set of partial-probability density functions. What is interesting regarding the partial-probability density functions is that they are in a sense mutually independent, that is, once a partition of probability-assigned space is determined (consequently Ω_q's are specified), then a partial-probability density function $\tilde{p}_q(z,t)$ is completely governed by Eq. (23) (it is of course true if the function $p_q(z,t)$ is substituted by $\tilde{p}_q(z,t)$); the evolution of other partial-probability density functions, $\tilde{p}_r(z,t), r \neq q$, has no effects on the evolution of $\tilde{p}_q(z,t)$. This property of independent evolution of partial-probability density function means that the original problem can be partitioned into a series of independent subproblems, which are usually easier than the original problem. Thus, the possibility of new approaches is implied but still to be explored. It is also stressed that such a property of independent evolution is not conditioned on any assumption of mutual independence of basic random variables.

2. Relationship between point evolution and ensemble evolution
The second term in Eq. (23) usually cannot be integrated explicitly. It is seen from this term that to capture the partial-probability density function $\tilde{p}_q(z,t)$ over Ω_q, the exact information of the velocity dependency on $\theta \in \Omega_q$ is required. This means that the evolution of $\tilde{p}_q(z,t)$ depends on all the exact information in Ω_q; in other words, the evolution of $\tilde{p}_q(z,t)$ is determined by the evolution of information of the ensemble over Ω_q. This manner could be called ensemble evolution.

To uncouple the second term in Eq. (23), we can assume

$$\dot{X}(\theta,t) \doteq \dot{X}(\theta_q,t), \text{ for } \theta \in \Omega_q \tag{26}$$

where $\theta_q \in \Omega_q$ is a representative point of Ω_q. For instance, θ_q could be determined by the Voronoi cell [1], by the average $\theta_q = \frac{1}{P_q}\int_{\Omega_q} \theta p_\Theta(\theta) d\theta$, or in some other appropriate manners. By doing this, Eq. (23) becomes

$$\frac{\partial p_q(z,t)}{\partial t} + \dot{Z}(\theta_q,t)\frac{\partial p_q(z,t)}{\partial z} = 0, \quad q = 1,2,\cdots,n_{\text{pt}} \tag{27}$$

The meaning of Eq. (26) is clear that the ensemble evolution in Eq. (23) is represented by the information of a representative point in the sub-domain, that is, the ensemble evolution in a sub-domain is represented by a point evolution. Another possible manner of uncoupling the second term in Eq. (23) implies a small variation of $p_{Z\Theta}(z,\theta,t)$ over the sub-domain Ω_q. In this case, it follows that

$$\frac{\partial p_q(z,t)}{\partial t} + E_q[\dot{Z}(\theta,t)]\frac{\partial p_q(z,t)}{\partial z} = 0, \ q = 1,2,\cdots,n_{\text{pt}} \tag{28}$$

where $E_q[\dot{Z}(\theta,t)] = \frac{1}{P_q}\int_{\Omega_q}\dot{Z}(\theta,t)p_\Theta(\theta)d\theta$ is the average of $\dot{Z}(\theta,t)$ over Ω_q. In some cases, $E_q[\dot{Z}(\theta,t)]$ might be close to $\dot{Z}(\theta_q,t)$, and thus, Eqs. (27) and (28) coincide.

2.4 Numerical Procedure for the GDEE

In the probability density evolution method, Eq. (9) is the physical equation, while Eq. (15) is the GDEE with initial and boundary conditions specified by Eqs. (17) and (18). Hence, solving the problem needs to incorporate physical equations and the GDEE. For some very simple cases, a closed-form solution might be obtained, say, by the method of characteristics [18]. While for most practical engineering problems, numerical method is needed. To this end, we start with Eq. (14) instead of Eq. (15) because from the standpoint of numerical solution, usually an equation in the form of an integral may have some advantages over an equation in the form of a differential.

According to the discussions in the preceding section, Eqs. (23), (27), or (28) could be adopted as the governing equation for numerical solution. Equation (23) is an exact equation equivalent to the original Eqs. (14) and (15). In the present stage, numerical algorithms for Eq. (27) were extensively studied and will be outlined here.

It is seen that Eq. (27) is a linear partial differential equation. To obtain the solution, the coefficients should be determined first, while these coefficients are time rates of the physical quantity of interest as $\{\Theta = \theta\}$ and thus can be obtained through solving Eq. (9). Therefore, the GDEE can be solved in the following steps:

Step 1: Select representative points (RPs for short) in the probability-assigned space and determine their assigned probability. Select a set of representative points in the distribution domain Ω_Θ. Denote them by $\theta_q = (\theta_{q,1}, \theta_{q,2}, \cdots, \theta_{q,s})$; $q = 1, 2, \cdots, n_{\text{pt}}$, where n_{pt} is the number of the selected points. Simultaneously, determine the assigned probability of each point according to Eq. (22) using the Voronoi cells [1].

Step 2: Solve deterministic dynamical systems. For the specified $\Theta = \theta_q, q = 1, 2, \cdots, n_{\text{pt}}$, solve the physical equation (Eq. 9) to obtain time rate (velocity) of the physical quantities $\dot{Z}(\theta_q, t)$. Through steps 1 and 2, the ensemble evolution is replaced by point evolution as representatives.

Step 3: Solve the GDEE (Eq. 27) under the initial condition, as a discretized version of Eq. (18),

$$p_q(z,t)\big|_{t=t_0} = \delta(z - z_0)P_q \tag{29}$$

by the finite difference method with TVD scheme to acquire the numerical solution of $p_q(z,t)$.

Step 4: Sum up all the results to obtain the probability density function of $Z(t)$ via the Eq. (24).

It is seen clearly that the solving process of the GDEE is to incorporate a series of deterministic analysis (point evolution) and numerical solving of partial differential equations, which is just the essential of the basic thought that the physical mechanism of probability density evolution is the evolution of the physical system.

3 Performance Evolution of Controlled Systems

Extensive studies have been done on the structural optimal control, which serves as one of the most effective measures to mitigate damage and loss of structures induced by disastrous actions such as earthquake ground motions and strong winds [7]. However, the randomness inherent in the dynamics of the system or its operational environment and coupled with the nonlinearity of structural behaviors should be taken into account so as to gain a precise control of structures. The reliability of structures, otherwise, associated with structural performance still cannot be guaranteed even if the responses are greatly reduced compared to the uncontrolled counterparts. Thus, the methods of stochastic optimal control have usually been relied upon to provide a rational mathematical context for analyzing and describing the problem.

Actually, pioneering investigations of stochastic optimal control by mathematician were dated back to semi-century ago and resulted in fruitful theorems and approaches [39]. These advances mainly hinge on the models of Itô stochastic differential equations (e.g., LQG control). They limit themselves in application to white noise or filtered white noise that is quite different from practical engineering excitations. The seismic ground motion, for example, exhibits strongly nonstationary and non-Gaussian properties. In addition, stochastic optimal control of multi-dimensional nonlinear systems is still a challenging problem in open. It is clear that the above two challenges both stem from the classical framework of stochastic dynamics. Therefore, a revolutionary scheme through physical control methodology based on PDEM is developed in the last few years [23–26].

Consider the multi-degree-of-freedom (MDOF) system represented by Eq. (9) is exerted a control action, of which the equation of motion is given by

$$\mathbf{M}(\Theta)\ddot{\mathbf{X}} + \mathbf{C}(\Theta)\dot{\mathbf{X}} + \mathbf{f}(\Theta, \mathbf{X}) = \mathbf{B}_s\mathbf{U}(\Theta, t) + \mathbf{D}_s\mathbf{F}(\Theta, t) \tag{30}$$

where $\mathbf{U}(\Theta, t)$ is the control gain vector provided by the control action, $\mathbf{B}_s$ is a matrix denoting the location of controllers, and $\mathbf{D}_s$ is a matrix denoting the location of excitations.

In the state space, Eq. (30) becomes

$$\dot{Z}(t) = \mathbf{A}\mathbf{Z}(t) + \mathbf{B}\mathbf{U}(t) + \mathbf{D}\mathbf{F}(\Theta, t) \tag{31}$$

where $\mathbf{A}$ is a system matrix, $\mathbf{B}$ is a controller location matrix, and $\mathbf{D}$ is a excitation location vector.

In most cases, Eq. (30) is a well-posed equation, and relationship between the state vector $\mathbf{Z}(t)$ and control gain $\mathbf{U}(t)$ can be determined uniquely. Clearly, it is a function of Θ and might be assumed to take the form

$$\mathbf{Z}(t) = \mathbf{H}_{\mathbf{Z}}(\Theta, t) \tag{32}$$

$$\mathbf{U}(t) = \mathbf{H}_{\mathbf{U}}(\Theta, t) \tag{33}$$

It is seen that all the randomness involved in this system comes from Θ; thus, the augmented systems of components of state and control force vectors $(Z(t), \Theta)$, $(U(t), \Theta)$ are both probability preserved and satisfy the GDEEs, respectively, as follows [25]:

$$\frac{\partial p_{Z\Theta}(z,\theta,t)}{\partial t} + \dot{Z}(\theta,t)\frac{\partial p_{Z\Theta}(z,\theta,t)}{\partial z} = 0 \tag{34}$$

$$\frac{\partial p_{U\Theta}(u,\theta,t)}{\partial t} + \dot{U}(\theta,t)\frac{\partial p_{U\Theta}(u,\theta,t)}{\partial u} = 0 \tag{35}$$

The corresponding instantaneous PDFs of $Z(t)$ and $U(t)$ can be obtained by solving the above partial differential equations with given initial conditions

$$p_Z(z,t) = \int_{\Omega_\Theta} p_{Z\Theta}(z,\theta,t)d\theta \tag{36}$$

$$p_U(u,t) = \int_{\Omega_\Theta} p_{U\Theta}(u,\theta,t)d\theta \tag{37}$$

where Ω_Θ is the distribution domain of Θ and the joint PDFs $p_{Z\Theta}(z,\theta,t)$ and $p_{U\Theta}(u,\theta,t)$ are the solutions of Eqs. (34) and (35), respectively.

As mentioned in the previous sections, the GDEEs reveal the intrinsic relationship between stochastic systems and deterministic systems via the random event description of the principle of preservation of probability. It is thus indicated, according to the relationship between point evolution and ensemble evolution, that the structural stochastic optimal control can be implemented through a collection of representative deterministic optimal controls and their synthesis on evolution of probability densities. Distinguished from the classical stochastic optimal control scheme, the control methodology based on the PDEM is termed as the physical scheme of structural stochastic optimal control.

Figure 2 shows the discrepancy among the deterministic control (DC), the LQG control, and the physical stochastic optimal control (PSC) tracing the performance evolution of optimal control systems. One might realize that the performance trajectory of the deterministic control is point to point, and obviously, it lacks the ability of governing the system performance due to the randomness of external

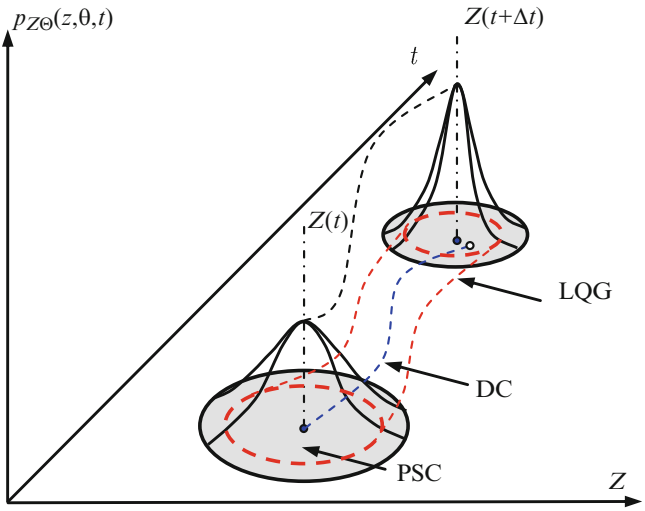

Fig. 2 Performance evolution of optimal control systems: comparison of determinate control (*DC*), LQG control, and physical stochastic optimal control (*PSC*)

excitations. The performance trajectory of the LQG control, meanwhile, is circle to circle. It is remarked here that the classical stochastic optimal control is essentially to govern the system statistics to the general stochastic dynamical systems since there still lacks of efficient methods to solve the response process of the stochastic systems with strong nonlinearities in the context of classical random mechanics. The LQG control, therefore, just holds the system performance in mean-square sense and cannot reach its high-order statistics. The performance trajectory of the PSC control, however, is domain to domain, which can achieve the accurate control of the system performance since the system quantities of interest all admit the GDEEs, Eqs. (34) and (35).

4 Probabilistic Criteria of Structural Stochastic Optimal Control

The structural stochastic optimal control involves maximizing or minimizing the specified cost function, whose generalized form is typically the quadratic combination of displacement, velocity, acceleration and control force. A standard quadratic cost function is given by the following expression [34]:

$$J_1(\mathbf{Z},\mathbf{U},\Theta,t)=\frac{1}{2}\mathbf{Z}^T(t_f)\mathbf{P}(t_f)\mathbf{Z}(t_f)+\frac{1}{2}\int_{t_0}^{t_f}\left[\mathbf{Z}^T(t)\mathbf{Q}\mathbf{Z}(t)+\mathbf{U}^T(t)\mathbf{R}\mathbf{U}(t)\right]dt \quad (38)$$

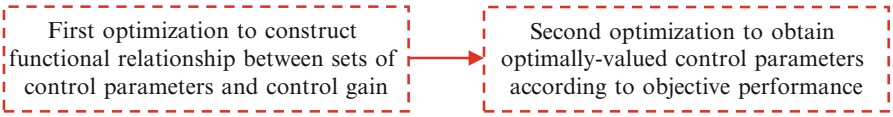

Fig. 3 Two step optimizations included in the physical stochastic optimal control

where $\mathbf{Q}$ is a positive semi-definite matrix, $\mathbf{R}$ is a positive definite matrix, and t_f is the terminal time, usually longer than that of the excitation. As should be noted, the cost function of the classical LQG control is defined as the ensemble-expected formula of Eq. (38) that is a deterministic function in dependence upon the time argument. Its minimization is to obtain the minimum second-order statistics of the state as the given parameters of control policy and construct the corresponding control gain under Gaussian process assumptions. In many cases of practical interests, the probability distribution function of the state related to structural performance is unknown, and the control gain essentially relies on second-order statistics, while the cost function represented by Eq. (38) is a stochastic process, of which minimization is to make the representative solution of the system state globally optimized in case of the given parameters of control policy. This treatment would result in a minimum second-order statistics or the optimum shape of the PDF of system quantities of interests. It is thus practicable to construct a control gain relevant to a predetermined performance of engineering structures since the procedure developed in this chapter adapts to the optimal control of general stochastic systems. In brief, the procedure involves two step optimizations; see Fig. 3. In the first step, for each realization θ_q of the stochastic parameter Θ, the minimization of the cost function Eq. (38) is carried out to build up a functional mapping from the set of parameters of control policy to the set of control gains. In the second step, the specified parameters of control policy to be used are obtained by optimizing the control gain according to the objective structural performance.

Therefore, viewed from representative realizations, the minimum of J_1 results in a solution of the conditional extreme value of cost function. The functional mapping, for a closed-loop control system, from the set of control parameters to the set of control gains is yield by [25]

$$\mathbf{U}(\Theta, t) = -\mathbf{R}^{-1}\mathbf{B}^T\mathbf{P}\mathbf{Z}(\Theta, t) \tag{39}$$

where P is the Riccati matrix function.

As indicated previously, the control effectiveness of stochastic optimal control relies on the specified control policy related to the objective performance of the structure. The critical procedure of designing control system actually is the determination of parameters of control policy, that is, weighting matrices $\mathbf{Q}$ and $\mathbf{R}$ in Eq. (38). There were a couple of strategies regarding to the weighting matrix choice in the context of classical LQG control such as system statistics assessment based on the mathematical expectation of the quantity of interest [40], system robustness analysis in probabilistic optimal sense [35], and comparison of weighting matrices in the context of Hamilton theoretical framework [42]. We are attempting to,

nevertheless, develop a family of probabilistic criteria of weight matrices optimization in the context of the physical stochastic optimal control of structures.

4.1 System Second-Order Statistics Assessment (SSSA)

A probabilistic criterion of weight matrices optimization based on the system second-order statistics assessment, including constraint quantities and assessment quantities, is proposed as follows:

$$\min(J_2) = \arg\min_{Q,R} \{E[\tilde{Y}] \ or \ \sigma[\tilde{Y}] \big| F[\tilde{X}] \leq \tilde{X}_{\text{con}}\} \tag{40}$$

Where J_2 denotes a performance function, $\tilde{Y} = \max_t [\max_i |Y_i(\Theta, t)|]$ is the equivalent extreme-value vector of the quantities to be assessed, $\tilde{X} = \max_t [\max_i |X_i(\Theta, t)|]$ is the equivalent extreme-value vector of the quantities to be used as the constraint, $\tilde{X}_{\text{con}}$ is the threshold of the constraint, the hat "~" on symbols indicates the equivalent extreme-value vector or equivalent extreme-value process [21], and $F[\cdot]$ is the characteristic value function indicating confidence level. The employment of the control criterion of Eq. (40) is to seek the optimal weighting matrices such that the mean or standard deviation of the assessment quantity $\tilde{Y}$ is minimized when the characteristic value of constraint quantity $\tilde{X}$ less than its threshold $\tilde{X}_{\text{con}}$.

4.2 Minimum of Exceedance Probability of Single System Quantity (MESS)

An exceedance probability criterion in the context of first-passage failure of single system quantity can be specified as follows:

$$\min(J_2) = \arg\min_{\text{Q,R}} \left\{ \Pr\left(\tilde{Y} - \tilde{Y}_{\text{thd}} > 0\right) + \left(H(\tilde{X}_{\max} - \tilde{X}_{\text{con}})\right) \right\} \tag{41}$$

where $\Pr(\cdot)$ operates its arguments with denotation of exceedance probability, equivalent extreme-value vector $\tilde{Y}$ is the objective system quantity, and $H(\cdot)$ is the Heaviside step function. The physical meaning of this criterion is that the exceedance probability of the system quantity is minimized [26].

4.3 Minimum of Exceedance Probability of Multiple System Quantities (MEMS)

An exceedance probability criterion in the context of global failure of multiple system quantities is defined as follows:

$$\min(J_2) = \arg\min_{\mathrm{Q,R}} \left\{ \begin{array}{l} \frac{1}{2}\left[\Pr_{\tilde{Z}}^{T}(\tilde{Z} - \tilde{Z}_{\mathrm{thd}} > \mathbf{0}) \Pr_{\tilde{Z}}(\tilde{Z} - \tilde{Z}_{\mathrm{thd}} > 0) + \Pr_{\tilde{U}}^{T}(\tilde{U} - \tilde{U}_{\mathrm{thd}} > \mathbf{0}) \right. \\ \left. \Pr_{\tilde{U}}(\tilde{U} - \tilde{U}_{\mathrm{thd}} > \mathbf{0})\right] + \left(H(\tilde{X}_{\max} - \tilde{X}_{\mathrm{con}})\right) \end{array} \right\} \tag{42}$$

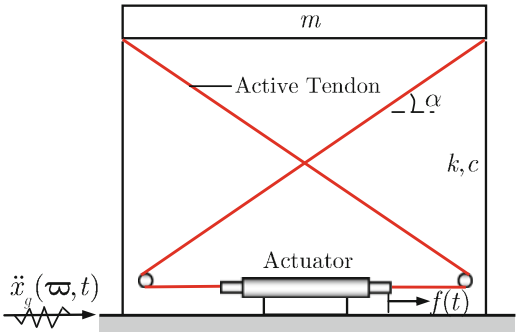

Fig. 4 Base-excited single-story structure with active tendon control system

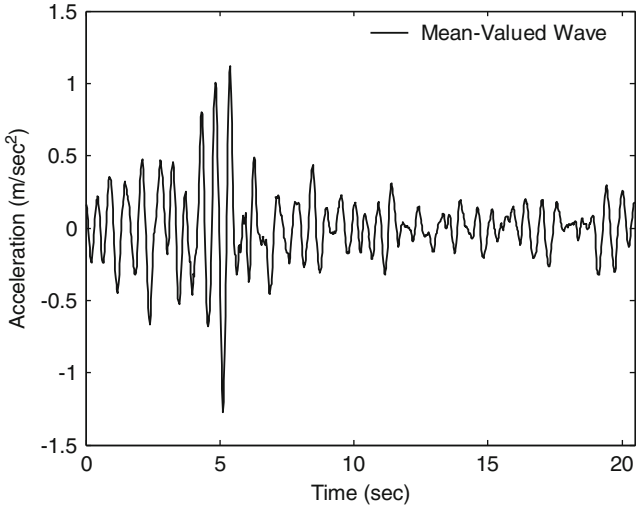

Fig. 5 Mean-valued time history of ground motion

where equivalent extreme-value vectors of state and control force $\tilde{Z}, \tilde{U}$ are the objective system quantities. It is indicated that this control criterion characterizes system safety (indicated in the controlled inter-story drift), system serviceability (indicated in the controlled inter-story velocity), system comfortability (indicated in the constrained story acceleration), controller workability (indicated in the limit control force), and their trade-off.

5 Comparative Studies

A base-excited single-story structure with an active tendon control system (see Fig. 4) is considered as a case for comparative studies of the control policies deduced from the above probabilistic criteria and the developed control methodology against the classical LQG. The properties of the system are as follows: the mass of the story is $m = 1 \times 10^5$ kg; the natural circular frequency of the uncontrolled structural system is $\omega_0 = 11.22$ rad/s; the control force of the actuator is denoted by $f(t)$, α representing the inclination angle of the tendon with respect to the base, and the acting force $u(t)$ on the structure is simulated; and the damping ratio is assumed to be 0.05. A stochastic earthquake ground motion model is used in this case [15], and the mean-valued time history of ground acceleration with peak 0.11 g is shown in Fig. 5.

The objective of stochastic optimal control is to limit the inter-story drift such that the system locates the reliability state, to limit the inter-story velocity such that the system provides the desired serviceability, to limit the story acceleration such that the system provides the desired comfortability, and to limit the control force such that the controller sustains its workability. The thresholds/constraint values of the inter-story drift, of the inter-story velocity, of the story acceleration, and of the control force are 10 mm, 100 mm/s, 3,000 mm/s, and 200 kN, respectively.

5.1 Advantages in Global Reliability-Based Probabilistic Criterion

For the control criterion of system second-order statistics assessment (SSSA), the inter-story drift is set as the constraint, and the assessment quantities include the inter-story drift, the story acceleration, and the control force. The characteristic value function is defined as mean plus three times of standard deviation of equivalent extreme-value variables. For the control criterion of minimum of exceedance probability of single system quantity (MESS), the inter-story drift is set as the objective system quantity, and the constraint quantities include the story acceleration and the control force. For the control criterion of minimum of exceedance probability of multiple system quantities (MEMS), the inter-story drift, inter-story

Table 1 Comparison of control policies

Ext. values	SSSA: Q = diag {80,80}, $R = 10^{-12}$	MESS: Q = diag {101.0,195.4}, $R = 10^{-10}$	MEMS: Q = diag {1073.6,505.0}, $R = 10^{-10}$
Dis-Mn (mm)	28.47[a]	28.47	28.47
	1.16[b]	6.23	4.15
	95.93%[c]	78.12	85.42%
Dis-Std (mm)	13.78	13.78	13.78
	0.20	1.41	0.81
	98.55%	89.77%	94.12%
Acc-Mn (mm/s)	3602.66	3602.66	3602.66
	1069.79	1235.60	1141.00
	70.31%	65.70%	68.33%
Acc-Std (mm/s)	1745.59	1745.59	1745.59
	360.81	348.92	331.78
	79.33%	80.01%	80.99%
CF-Mn (kN)	105.56	86.55	94.93
CF-Std (kN)	35.59	30.71	32.46

[a]Indicates the uncontrolled system quantities
[b]Indicates the controlled system quantities
[c]Indicates the control efficiency defined as $(a - b)/a$

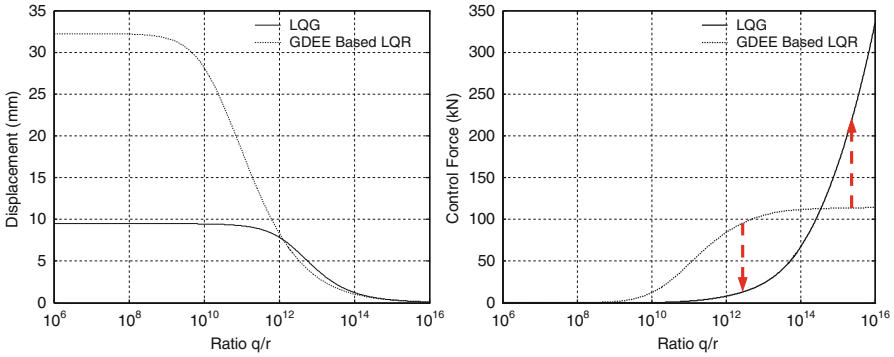

Fig. 6 Comparison of root-mean-square equivalent-extreme quantity vs. weight ratio between PSC and LQG (**a**) Equivalent-extreme relative displacement (**b**) Equivalent-extreme control force

velocity, and control force are set as the objective system quantities, while the constraint quantity is the story acceleration.

The comparison between the three control policies is investigated. The numerical results are listed in Table 1. It is seen that the effectiveness of response control hinges on the physical meanings of the optimal control criteria. As indicated in this case, the control criterion SSSA exhibits the larger control force due to the inter-story drift being only considered as the constraint quantity, which thus has lower inter-story drift. The control criterion MESS, however, exhibits the smaller control force due to the story acceleration and control force being simultaneously considered as the constraint quantities that result in a less reduction on the inter-story drift.

The control criterion MEMS, as seen from Table 1, achieves the best trade-off between control effectiveness and economy in that the objective system quantities include the inter-story drift, together with inter-story velocity and control force. It thus has reason to believe that the multi-objective criterion in the global reliability sense is the primary criterion of structural performance controls.

5.2 *Control Gains Against the Classical LQG*

It is noted that the classical stochastic optimal control strategies also could be applied to a class of stochastic dynamical systems and synthesize the moments or the PDFs of the controlled quantities. The class of systems is typically driven by independent additive Gaussian white noise and usually modeled as the Itô stochastic differential equations. The response processes, meanwhile, exhibit Markov property, of which the transition probabilities are governed by the Fokker-Planck-Kolmogorov equation (FPK equation). It remains an open challenge in the civil engineering system driven by non-Gaussian noise. The proposed physical stochastic optimal control methodology, however, occupies the validity and applicability to the civil engineering system. As a comparative study, Fig. 6 shows the discrepancy of root-mean-square quantity vs. weight ratio, using the control criterion of SSSA, between the advocated method and the LQG control.

One could see that the LQG control would underestimate the desired control force when the coefficient ratio of weighting matrices locates at the lower value, and it would overestimate the desired control force when the coefficient ratio of weighting matrices locates at the higher value. It is thus remarked that the LQG control using the nominal Gaussian white noise as the input cannot design the rational control system for civil engineering structures.

6 Numerical Example

An eight-story single-span shear frame fully controlled by active tendons is taken as a numerical example, of which the properties of the uncontrolled structure are identified according to Yang et al. [38]. The floor mass of each story unit is $m = 3.456 \times 10^5$ kg; the elastic stiffness of each story is $k = 3.404 \times 10^2$ kN/mm; and the internal damping coefficient of each story unit $c = 2.937$ kN $\times$ sec/mm,

Table 2 Optimization results of example

Parameters	Q_d	Q_v	R_u
Initial value	100	100	10^{-12}
Optimal value	102.8	163.7	10^{-12}
Objective value	11.22×10^{-6} ($P_{f,d}$ =0.0023, $P_{f,v} = 0.0035$, $P_{f,u} = 0.0022$)		

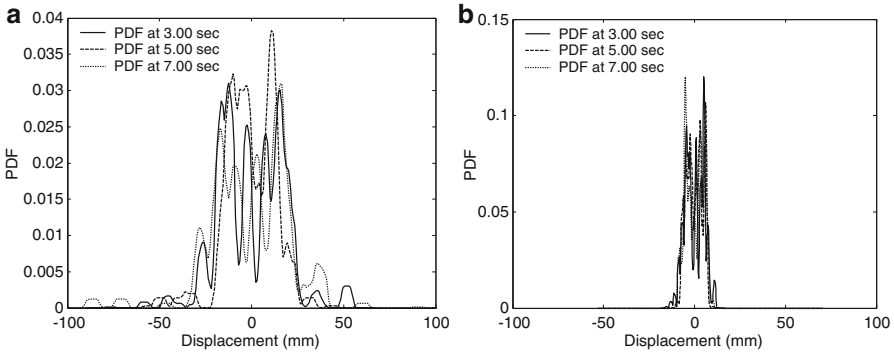

Fig. 7 Typical PDFs of inter-0-1 drift at typical instants of time (**a**) Without control (**b**) With control

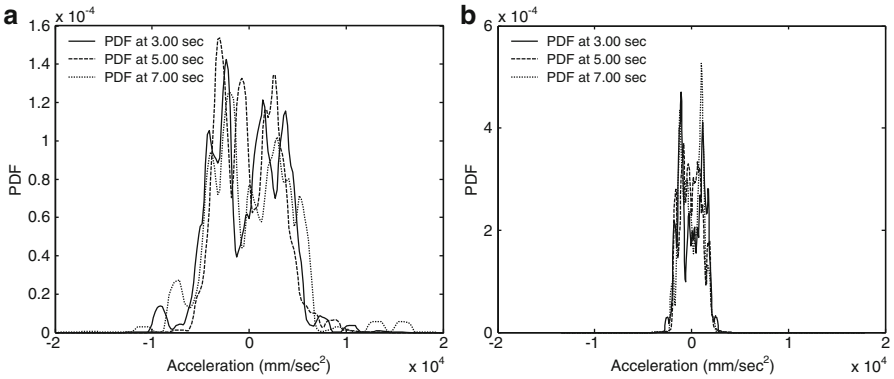

Fig. 8 Typical PDFs of the 8th story acceleration at typical instants of time (**a**) Without control (**b**) With control

which corresponds to a 2% damping ratio for the first vibrational mode of the entire building. The external damping is assumed to be zero. The computed natural frequencies are 5.79, 17.18, 27.98, 37.82, 46.38, 53.36, 58.53, and 61.69 rad/s, respectively. The earthquake ground motion model is the same as that of the preceding SDOF system, and the peak acceleration is 0.30 g. The control criterion MEMS is employed, and the thresholds/constraint values of the structural inter-story drifts, inter-story velocities, story acceleration, and the control forces are 15 mm, 150 mm/s, 2,000 kN, and 8,000 mm/s, respectively. For simplicity, the form of the weighting matrices in this case takes

$$\mathbf{Q} = \text{diag}\{Q_d, ..., Q_d; Q_v, ..., Q_v\}, \quad R = \text{diag}\{R_u, ..., R_u\} \tag{43}$$

The optimization results of the numerical example are shown in Table 2. It is seen that the exceedance probability of system quantities, rather than the ratio of reduction of responses, is provided when the objective value of performance function reaches to the minimum, indicating an accurate control of structural performance implemented. The optimization results also show that the stochastic optimal control achieves a best trade-off between effectiveness and economy.

Figure 7 shows typical PDFs of the inter-0-1-story drift of the controlled/uncontrolled structures at typical instants of time. One can see that the variation of the inter-story drift is obviously reduced. Likewise, the PDFs of the eight-story acceleration at typical instants show a reduction of system response since that distribution of the story acceleration has been narrowed (see Fig. 8). It is indicated that the seismic performance of the structure is improved significantly in case that the stochastic optimal control employing the exceedance probability criterion is applied.

7 Concluding Remarks

In this chapter, the fundamental theory of the generalized density evolution equation is firstly revisited. Then, a physical scheme of structural stochastic optimal control based on the probability density evolution method is presented for the stochastic optimal controls of engineering structures excited by general nonstationary and non-Gaussian processes. It extends the classical stochastic optimal control approaches, such as the LQG control, of which the random dynamic excitations are exclusively assumed as independent white noises or filter white noises. A family of optimal control criteria for designing the controller parameter, including the criterion based on mean and standard deviation of responses, the criterion based on Exceedance probability, and the criterion based on global reliability of systems, is elaborated by investigating the stochastic optimal control of a base-excited single-story structure with an active tendon control system. It is indicated that the control effect relies upon the probabilistic criteria of which the control criterion in global reliability operates efficiently and gains the desirable structural performance. The proposed stochastic optimal control scheme, meanwhile, of structures exhibits significant benefits over the classical LQG control. An eight-story shear frame controlled by active tendons is further investigated, employing the control criterion in global reliability of the system quantities. It is revealed in the numerical example that the seismic performance of the structure is improved significantly, indicating the validity and applicability of the developed PDEM-based stochastic optimal control methodology for the accurate control of structural performance.

Acknowledgements The supports of the National Natural Science Foundation of China (Grant Nos. 50621062, 51108344) and the Exploratory Program of State Key Laboratory of Disaster Reduction in Civil Engineering at Tongji University (Grant No. SLDRCE11-B-04) are highly appreciated.

References

1. Chen JB, Ghanem R, Li J (2009) Partition of the probability-assigned space in probability density evolution analysis of nonlinear stochastic structures. Probab Eng Mech 24(1):27–42
2. Crandall SH (1958) Random Vibration. Technology Press of MIT; John Wiley and Sons, New York
3. Dostupov BG, Pugachev VS (1957) The equation for the integral of a system of ordinary differential equations containing random parameters. Automatikai Telemekhanika 18:620–630
4. Einstein A (1905) Über Die Von Der Molecular-Kinetischen Theorie Der Wärme Geforderte Bewegung Von in Rhuenden Flüssigkeiten Sus-Pendierten Teilchen. Ann Phys (Leipzig) 17:549–560
5. Ghanem RG, Spanos PD (1991) Stochastic finite elements: a spectral approach. Springer, Berlin
6. Halder A, Mahadevar S (2000) Reliability assessment using stochastic finite element analysis. Wiley, New York
7. Housner GW, Bergman LA, Caughey TK et al (1997) Structural control: past, present, and future. J Eng Mech 123(9):897–971
8. Itô K (1942) Differential equations determining a Markoff process. Zenkoku Sizyo Sugaku Danwakasi, 1077
9. Kleiber M, Hien TD (1992) The stochastic finite element method. Wiley, Chichester
10. Kolmogorov A (1931) über die analytischen Methoden in der Wahrscheinlichkeitsrechnung. Math Ann 104(1):415–458
11. Langevin P (1908) Sur La Theorie Du Mouvement Brownien. C. R. Acad. Sci, Paris, pp 530–532
12. Li J (1996) Stochastic structural systems: analysis and modeling. Science Press, Beijing (in Chinese)
13. Li J (2006) A physical approach to stochastic dynamical systems. Sci Paper Online 1(2):93–104 (in Chinese)
14. Li J (2008) Physical stochastic models for the dynamic excitations of engineering structures. In: Advances in theory and applications of random vibration, 119–132, Tongji University Press, Shanghai (in Chinese)
15. Li J, Ai XQ (2006) Study on random model of earthquake ground motion based on physical process. Earthq Eng Eng Vib 26(5):21–26 (in Chinese)
16. Li J, Chen JB (2003) Probability density evolution method for dynamic response analysis of stochastic structures. In: Proceeding of the fifth international conference on stochastic structural dynamics, Hangzhou, China, pp 309–316
17. Li J, Chen JB (2006) Generalized density evolution equations for stochastic dynamical systems. Prog Nat Sci 16(6):712–719
18. Li J, Chen JB (2006) The probability density evolution method for dynamic response analysis of non-linear stochastic structures. Int J Numer Methods Eng 65:882–903
19. Li J, Chen JB (2008) The principle of preservation of probability and the generalized density evolution equation. Struct Saf 30:65–77
20. Li J, Chen JB (2009) Stochastic dynamics of structures. Wiley, Singapore
21. Li J, Chen JB, Fan WL (2007) The equivalent extreme-value event and evaluation of the structural system reliability. Struct Saf 29(2):112–131
22. Li J, Liu ZJ (2006) Expansion method of stochastic processes based on normalized orthogonal bases. J Tongji Univ (Nat Sci) 34(10):1279–1283
23. Li J, Peng YB (2007) Stochastic optimal control of earthquake-excited linear systems. In: Proceedings of 8th Pacific conference on earthquake engineering, Singapore, 5–7 Dec 2007
24. Li J, Peng YB, Chen JB (2008) GDEE-based stochastic control strategy of MR damping systems. In: Proceedings of 10th international symposium on structural engineering for young experts, Changsha, China, pp 1207–1212

25. Li J, Peng YB, Chen JB (2010) A physical approach to structural stochastic optimal controls. Probabilistic Engineering Mechanics 25(1):127–141
26. Li J, Peng YB, Chen JB (2011) Probabilistic criteria of structural stochastic optimal controls. Probab Eng Mech 26(2):240–253
27. Li J, Yan Q, Chen JB (2011) Stochastic modeling of engineering dynamic excitations for stochastic dynamics of structures. Probab Eng Mech 27:19–28
28. Lin YK (1967) Probabilistic Theory of Structural Dynamics. McGraw-Hill, New York
29. Lin YK, Cai GQ (1995) Probabilistic structural dynamics: advanced theory and applications. McGraw-Hill, New York
30. Lutes LD, Sarkani S (2004) Random vibrations: analysis of structural and mechanical systems. Butterworth-Heinemann, Amsterdam
31. Schenk CA, Schuëller GI (2005) Uncertainty assessment of large finite element systems. Springer, Berlin
32. Shinozuka M, Deodatis G (1991) Simulation of stochastic processes by spectral representation. Appl Mech Rev 44(4):191–204
33. Shinozuka M, Jan CM (1972) Digital simulation of random processes and its applications. J Sound Vib 25:111–128
34. Soong TT (1990) Active structural control: theory and practice. Longman Scientific & Technical, New York
35. Stengel RF, Ray LR, Marrison CI (1992) Probabilistic evaluation of control system robustness. IMA workshop on control systems design for advanced engineering systems: complexity, uncertainty, information and organization, Minneapolis, MN, 12–16 Oct 1992
36. Syski R (1967) Stochastic differential equations. Chapter 8. In: Saaty TL (ed) Modern nonlinear equations. McGraw-Hill, New York
37. Wiener N (1923) Differential space. J Math Phys 2(13):131–174
38. Yang JN, Akbarpour A, Ghaemmaghami P (1987) New optimal control algorithms for structural control. J Eng Mech 113(9):1369–1386
39. Yong JM, Zhou XY (1999) Stochastic controls: Hamiltonian systems and HJB equations. Springer, New York
40. Zhang WS, Xu YL (2001) Closed form solution for along-wind response of actively controlled tall buildings with LQG controllers. J Wind Eng Ind Aerodyn 89:785–807
41. Zhu WQ (1992) Random vibration. Science Press, Beijing (in Chinese)
42. Zhu WQ, Ying ZG, Soong TT (2001) An optimal nonlinear feedback control strategy for randomly excited structural systems. Nonlinear Dyn 24:31–51

Uncertainty Quantification for Decision-Making in Engineered Systems

Sankaran Mahadevan

Abstract This chapter discusses current research and opportunities for uncertainty quantification in performance prediction and risk assessment of engineered systems. Model-based simulation becomes attractive for systems that are too large and complex for full-scale testing. However, model-based simulation involves many approximations and assumptions, and thus, confidence in the simulation result is an important consideration in risk-informed decision-making. Sources of uncertainty are both aleatory and epistemic, stemming from natural variability, information uncertainty, and modeling approximations. The chapter draws on illustrative problems in aerospace, mechanical, civil, and environmental engineering disciplines to discuss (1) recent research on quantifying various types of errors and uncertainties, particularly focusing on data uncertainty and model uncertainty (both due to model form assumptions and solution approximations); (2) framework for integrating information from multiple sources (models, tests, experts), multiple model development activities (calibration, verification, validation), and multiple formats; and (3) using uncertainty quantification in risk-informed decision-making throughout the life cycle of engineered systems, such as design, operations, health and risk assessment, and risk management.

Keywords Uncertainty quantification • Model based simulation • Surrogate models

1 Introduction

Uncertainty quantification is important in the assessing and predicting performance of complex engineering systems, especially given limited experimental or real-world data. Simulation of complex physical systems involves multiple levels of

S. Mahadevan (✉)
John R. Murray Sr. Professor of Civil and Environmental Engineering, Vanderbilt University, Nashville, TN, USA
e-mail: sankaran.mahadevan@vanderbilt.edu

S. Chakraborty and G. Bhattacharya (eds.), *Proceedings of the International Symposium on Engineering under Uncertainty: Safety Assessment and Management (ISEUSAM - 2012)*,
DOI 10.1007/978-81-322-0757-3_5,

modeling, ranging from the material to component to subsystem to system. Interacting models and simulation codes from multiple disciplines (multiple physics) may be required, with iterative analyses between some of the codes. As the models are integrated across multiple disciplines and levels, the problem becomes more complex, and assessing the predictive capability of the overall system model becomes more difficult. Many factors contribute to the uncertainty in the prediction of the system model including inherent variability in model input parameters, sparse data, measurement error, modeling errors, assumptions, and approximations.

The various sources of uncertainty in performance prediction can be grouped into three categories:

- Physical variability
- Data uncertainty
- Model error

1.1 Physical Variability

This type of uncertainty also referred to as aleatory or irreducible uncertainty arises from natural or inherent random variability of physical processes and variables, due to many factors such as environmental and operational variations, construction processes, and quality control. This type of uncertainty is present both in system properties (e.g., material strength, porosity, diffusivity, geometry variations, chemical reaction rates) and external influences and demands on the system (e.g., concentration of chemicals, temperature, humidity, mechanical loads). As a result, in model-based prediction of system behavior, there is uncertainty regarding the precise values for model parameters and model inputs, leading to uncertainty about the precise values of the model output. Such quantities are represented in engineering analysis as random variables, with statistical parameters, such as mean values, standard deviations, and distribution types, estimated from observed data or in some cases assumed. Variations over space or time are modeled as random processes.

1.2 Data Uncertainty

This type of uncertainty falls under the category of epistemic uncertainty (i.e., knowledge or information uncertainty) or reducible uncertainty (i.e., the uncertainty is reduced as more information is obtained). Data uncertainty occurs in different forms. In the case of a quantity treated as a random variable, the accuracy of the statistical distribution parameters depends on the amount of data available. If the data is sparse, the distribution parameters themselves are uncertain and may need to be treated as random variables. Alternatively, information may be imprecise or qualitative, or as a range of values, based on expert opinion. Both probabilistic and non-probabilistic methods have been explored to represent epistemic uncertainty. Measurement error (either in the laboratory or in the field) is another important source of data uncertainty.

1.3 Model Error

This results from approximate mathematical models of the system behavior and from numerical approximations during the computational process, resulting in two types of error in general – solution approximation error and model form error. The performance assessment of a complex system involves the use of several analysis models, each with its own assumptions and approximations. The errors from the various analysis components combine in a complicated manner to produce the overall model error (described by both bias and uncertainty).

The roles of several types of uncertainty in the use of model-based simulation for performance assessment can be easily seen in the case of reliability analysis. Consider the probability of an undesirable event denoted by $g(\mathbf{X}) < k$, which can be computed from Eq. (1):

$$P(g(\mathbf{X})<k) = \int_{g(\mathbf{X})<k} f_{\mathbf{X}}(\mathbf{x})\mathrm{d}\mathbf{x} \tag{1}$$

where $\mathbf{X}$ is the vector of input random variables, $f_{\mathbf{X}}(\mathbf{x})$ is the joint probability density function of $\mathbf{X}$, $g(\mathbf{X})$ is the model output, and k is the regulatory requirement in performance assessment. Every term on the right-hand side of Eq. (1) has uncertainty. There is inherent variability represented by the vector of random variables $\mathbf{X}$, data uncertainty (due to inadequate data) regarding the distribution type and distribution parameters of $f_{\mathbf{X}}(\mathbf{x})$, and model errors in the computation of $g(\mathbf{X})$. Thus, it is necessary to systematically identify the various sources of uncertainty and develop the framework for including them in the overall uncertainty quantification in the performance assessment of engineering systems.

The uncertainty analysis methods covered in this chapter are grouped by sections along the four major groups of analysis activities that are needed for performance assessment under uncertainty:

1. Input uncertainty quantification
2. Uncertainty propagation analysis (includes model error quantification)
3. Model calibration, verification, validation, and extrapolation
4. Probabilistic performance assessment

A brief summary of the analysis methods covered in the four groups is as follows:

Input uncertainty quantification: Physical variability of parameters can be quantified through random variables by statistical analysis. Parameters that vary in time or space are modeled as random processes or random fields with appropriate correlation structure. Data uncertainty that leads to uncertainty in the distribution parameters and distribution types can be addressed using confidence intervals and Bayesian statistics. Recent methods to include several sources of data uncertainty, namely, sparse data, interval data, and measurement error, are discussed in this chapter.

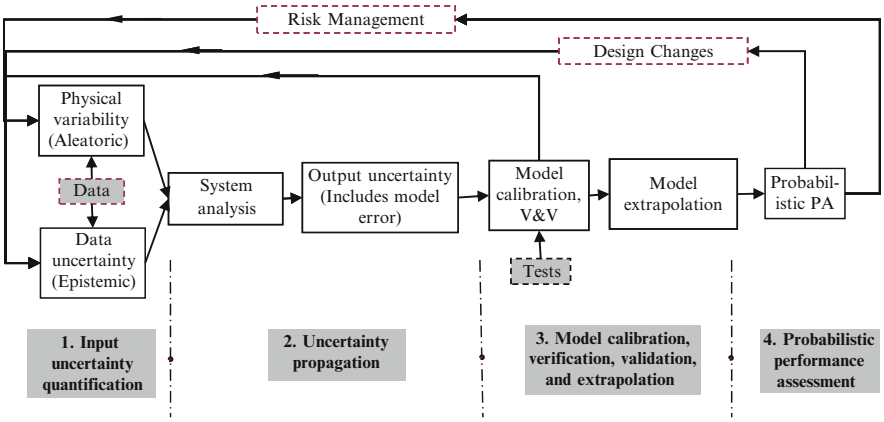

Fig. 1 Uncertainty quantification, propagation, and management

Uncertainty propagation analysis: Both classical and Bayesian probabilistic approaches can be investigated to propagate inherent variability and data uncertainty through individual sub-models and the overall system model. To reduce the computational expense, surrogate models can be constructed using several different techniques. Methods for sensitivity analyses in the presence of uncertainty are discussed. The uncertainty in the overall model output also includes model errors and approximations in each step of the analysis; therefore, approaches to quantify model error are included in the discussion.

Model calibration, verification, validation, and extrapolation: Model calibration is the process of adjusting model parameters to obtain good agreement between model predictions and experimental observations. Both classical and Bayesian statistical methods are discussed for model calibration with available data. One particular concern is how to properly integrate different types of data, available at different levels of the model hierarchy. Assessment of the "correct" implementation of the model is called verification, and assessment of the degree of agreement of the model response with the available physical observation is called validation. Model verification and validation activities help to quantify model error (both model form error and solution approximation error). A Bayesian network framework is discussed for quantifying the confidence in model prediction based on data, models, and activities at various levels of the system hierarchy. Such information is available in heterogeneous formats from multiple sources, and a consistent framework to integrate such disparate information is important.

Performance assessment: Limit state-based reliability analysis methods are available to help quantify the assessment results in a probabilistic manner. Monte Carlo simulation with high-fidelity analyses modules is computationally expensive; hence, surrogate (or abstracted) models are frequently used with Monte Carlo simulation. In that case, the uncertainty or error introduced by the surrogate model also needs to be quantified.

Figure 1 shows the four groups of activities within a conceptual framework for systematic quantification, propagation, and management of various types of

uncertainty. The methods discussed in this chapter address all the four steps shown in Fig. 1. The different steps of analysis in Fig. 1 are not strictly sequential. While uncertainty has been dealt with using probabilistic as well as non-probabilistic (e.g., fuzzy sets, possibility theory, evidence theory) formats in the literature, this chapter will only focus on probabilistic analysis.

In Fig. 1, the box "Data" in the input uncertainty quantification step includes laboratory data, historical field data, literature sources, and expert opinion. The box "Design changes" may refer to conceptual, preliminary, or detailed design, depending on the development stage. The boxes "Design changes" and "Risk management" are outside the scope of this chapter, although they are part of the overall uncertainty management framework.

2 Input Uncertainty Quantification

2.1 Physical Variability

Examples of model input variables with physical variability (i.e., inherent, natural variability) include:

(a) Material properties (e.g., mechanical and thermal properties, soil properties, chemical properties)
(b) Geometrical properties (e.g., Structural dimensions, concrete cover depth)
(c) External conditions (e.g., mechanical loading, boundary conditions, physical processes such as freeze-thaw, chemical processes such as carbonation, chloride, or sulfate attack)

Many uncertainty quantification studies have only focused on quantifying and propagating the inherent variability in the input parameters. Well-established statistical (both classical and Bayesian) methods are available for this purpose.

In probabilistic analysis, the sample to sample variations (random variables) in the parameters are addressed by defining them as random variables with probability density functions (PDFs). Some parameters may vary not only from sample to sample (as is the case for random variables) but also in spatial or time domain. Parameter variation over time and space can be modeled as *random processes or random fields*.

Some well-known methods for simulating random processes are spectral representation (SR) [13], Karhunen-Loeve expansion (KLE) ([10, 18, 30]), and polynomial chaos expansion (PCE) ([18, 30, 37]). The PCE method has been used to represent the stochastic model output as a function of stochastic inputs.

Consider an example of representing a random process using KLE, expressed as

$$\varpi(x,\chi) = \varpi(x) + \sum_{i=1}^{\infty} \sqrt{\lambda_i}\xi_i(\chi)f_i(x) \tag{2}$$

where $\varpi(x)$ is the mean of the random process $\varpi(x,\chi)$, λ_i and $f_i(x)$ are eigenvalues and eigenfunctions of $C(x_1,x_2)$, and $\xi_i(\chi)$ is a set of uncorrelated standard normal random variables (x is a space or time coordinate, and χ is an index representing different realizations of the random process). Using Eq. (2), realizations of the random process $\varpi(x,\chi)$ can be easily simulated by generating samples of the random variables $\xi_i(\chi)$, and these realizations of $\varpi(x,\chi)$ can be used in the reliability analysis.

Some boundary conditions (e.g., temperature and moisture content) might exhibit a recurring pattern over shorter periods and also a trend over longer periods. Both can be numerically represented by a seasonal model using an autoregressive integrated moving average (ARIMA) method generally used for linear[1] nonstationary[2] processes [5]. This method can be used to predict the temperature or the rainfall magnitudes in the future so that it can be used in the durability analysis of the structures under future environmental conditions.

It may also be important to quantify the statistical correlations between some of the input random variables. Many previous studies on uncertainty quantification simply assume either zero or full correlation, in the absence of adequate data. A Bayesian approach may be pursued for this purpose, as described in Sect. 2.2.

2.2 Data Uncertainty

This section discusses methods to quantify uncertainty due to limited statistical data and measurement errors (ε_{exp}). Data may also be available in interval format (e.g., expert opinion). A Bayesian approach, consistent with the framework proposed in Fig. 1, can be used in the presence of data uncertainty. The prior distributions of different physical variables and their distribution parameters can be based on available data and expert judgment, and these are updated as more data becomes available through experiments, analysis, or real-world experience.

Data qualification is an important step in the consideration of data uncertainty. All data points may not have equal weight; a careful investigation of data quality will help to assign appropriate weights to different data sets.

2.2.1 Sparse Statistical Data

For any random variable that is quantitatively described by a probability density function, there is always uncertainty in the corresponding distribution parameters due to small sample size. As testing and data collection activities are performed, the state of knowledge regarding the uncertainty changes and a Bayesian updating

[1] The current observation can be expressed as a linear function of past observations.

[2] A process is said to be nonstationary if its probability structure varies with the time or space coordinate.

approach can be implemented. The Bayesian approach also applies to joint distributions of multiple random variables, which also helps to include the uncertainty in correlations between the variables. A prior joint distribution is assumed (or individual distributions and correlations are assumed) and then updated as data becomes available.

Instead of assuming a well-known prior distribution form (e.g., uniform, normal) for sparse data sets, either empirical distribution functions or flexible families of distributions based on the data can be constructed. A bootstrapping[3] technique can then be used to quantify the uncertainty in the distribution parameters. The *empirical distribution function* is constructed by ranking the observations from lowest to highest value and assigning a probability value to each observation. Examples of flexible distribution families include the Johnson family, Pearson family, gamma distribution, and stretched exponential distribution (e.g., [48]). Recently, Sankararaman and Mahadevan [43] developed a likelihood-based approach to construct nonparametric probability distributions in the presence of both sparse and interval data.

Transformations have been proposed from a non-probabilistic to probabilistic format, through the maximum likelihood approach [25, 40]. Such transformations have attracted the criticism that information is either added or lost in the process. Two ways to address the criticism are to (1) construct empirical distribution functions based on interval data collected from multiple experts or experiments [9] and (2) construct flexible families of distributions with bounds on distribution parameters based on the interval data, without forcing a distribution assumption (McDonald et al. 2008). These can then be treated as random variables with probability distribution functions and combined with other random variables in a Bayesian framework to quantify the overall system model uncertainty. The use of families of distributions will result in multiple probability distributions for the output, representing the contributions of both physical variability and data uncertainty. The nonparametric approach of Sankararaman and Mahadevan [43] also has the ability to quantify the contributions of aleatory and epistemic uncertainty to the probabilistic representation of an uncertain variable.

2.2.2 Measurement Error

The measurement error in each input variable in many studies (e.g., [1]) is assumed to be independent and identically distributed (IID) normal with zero mean and an assumed variance, i.e., $\varepsilon_{\text{exp}} \sim N\left(0, \sigma_{\text{exp}}^2\right)$. Due to the measurement uncertainty, the distribution parameter σ_{exp} cannot be obtained as a deterministic value. Instead, it is a random variable with a prior density $\tau(\sigma_{\text{exp}})$. Thus, when new data is available

[3] Bootstrapping is a data-based simulation method for statistical inference by resampling from an existing data set [7].

after testing, the distribution of σ_{exp} can be easily updated using the Bayesian theorem. Another way to represent measurement error ε_{exp} is through an interval only, and not as a random variable.

3 Uncertainty Propagation Analysis

In this section, methods to quantify the contributions of different sources of uncertainty and error as they propagate through the system analysis model, including the contribution of model error, are discussed, in order to quantify the overall uncertainty in the system model output.

This section covers two issues: (1) quantification of model output uncertainty, given input uncertainty (both physical variability and data uncertainty), and (2) quantification of model error (due to both model form selection and solution approximations).

Several uncertainty analysis studies, including a study with respect to the proposed Yucca Mountain high-level waste repository, have recognized the distinction between physical variability and data uncertainty [16, 17]. As a result, these methods evaluate the variability in an inner loop calculation and data uncertainty in an outer loop calculation.

3.1 Propagation of Physical Variability

Various probabilistic methods (e.g., Monte Carlo simulation and first-order or second-order analytical approximations) have been studied for the propagation of physical variability in model inputs and model parameters [14] expressed through random variables and random process or fields. Stochastic finite element methods (e.g., [10, 15]) have been developed for single discipline problems, in structural, thermal, and fluid mechanics. An example of such propagation is shown in Fig. 2. Several types of combinations of system analysis model and statistical analysis techniques are available:

- Monte Carlo simulation with the deterministic system analysis as a black-box (e.g., [39]) to estimate model output statistics or probability of regulatory compliance
- Monte Carlo simulation with a surrogate model to replace the deterministic system analysis model (e.g., [10, 18, 19, 47]), to estimate model output statistics or probability of regulatory compliance
- Local sensitivity analysis using finite difference, perturbation, or adjoint analyses, leading to estimates of the first-order or second-order moments of the output (e.g., [3])
- Global sensitivity and effects analysis and analysis of variance in the output (e.g., [4])

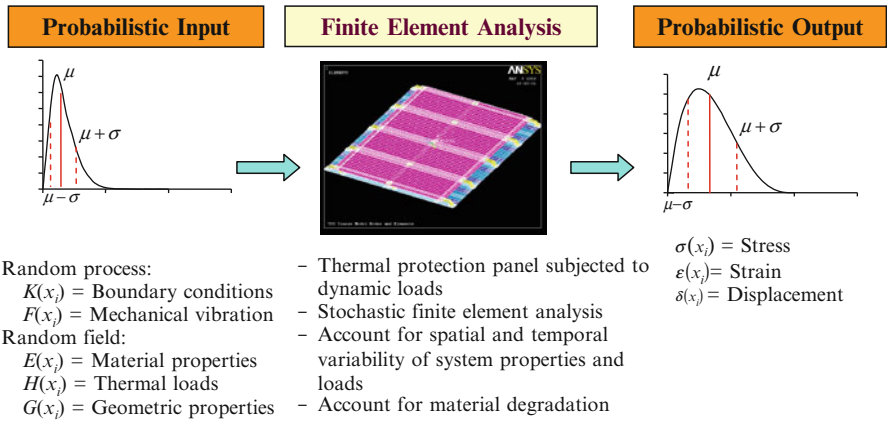

Fig. 2 Example of physical variability propagation

These techniques are generic and can be applied to engineering systems with multiple component modules and multiple physics. However, most applications of these techniques have only considered physical variability. The techniques need to include the contribution of data uncertainty and model error to the overall model prediction uncertainty. Computational effort is a significant issue in practical applications, since these techniques involve a number of repeated runs of the system analysis model. The system analysis may be replaced with an inexpensive surrogate model in order to achieve computational efficiency; this is discussed in Sect. 3.3 of this report. Efficient Monte Carlo techniques have also been pursued to reduce the number of system model runs, including *Latin hypercube sampling* (LHS) [8, 32] and *importance sampling* [28, 50].

When multiple requirements are defined, computation of the overall probability of satisfying multiple performance criteria requires integration over a multidimensional space defined by unions and intersections of individual events (of satisfaction or violation of individual criteria).

3.2 Propagation of Data Uncertainty

Three types of data uncertainty were discussed in Sect. 2. Sparse point data results in uncertainty about the parameters of the probability distributions describing quantities with physical variability. In that case, uncertainty propagation analysis takes a nested implementation. In the outer loop, samples of the distribution parameters are randomly generated, and for each set of sampled distribution parameter values, probabilistic propagation analysis is carried out as in Sect. 3.1. This results in the computation of multiple probability distributions of the output or confidence intervals for the estimates of probability of failure.

In the case of measurement error, choice of the uncertainty propagation technique depends on how the measurement error is represented. If the measurement error is represented as a random variable, it is simply added to the measured quantity, which is also a random variable due to physical variability. Thus, a sum of two random variables may be used to include both physical variability and measurement error in a quantity of interest. If the measurement error is represented as an interval, one way to implement probabilistic analysis is to represent the interval through families of distributions or upper and lower bounds on probability distributions, as discussed in Sect. 2.2.1. In that case, multiple probabilistic analyses, using the same nested approach as in the case of sparse data, can be employed to generate multiple output distributions or confidence intervals for the model output. The same approach is possible for interval variables that are only available as a range of values, as in the case of expert opinion.

Propagation of uncertainty is conceptually very simple but computationally quite expensive to implement, especially when both physical variability and data uncertainty are to be considered. The presence of both types of uncertainty requires a nested implementation of uncertainty propagation analysis (simulation of data uncertainty in the outer loop and simulation of physical variability in the inner loop). If the system model runs are time-consuming, then uncertainty propagation analysis could be prohibitively expensive. One way to overcome the computational hurdle is to use an inexpensive surrogate model to replace the detailed system model, as discussed next.

3.3 Surrogate Models

Surrogate models (also known as response surface models) are frequently used to replace the expensive system model and used for multiple simulations to quantify the uncertainty in the output. Many types of surrogate modeling methods are available, such as linear and nonlinear regression, polynomial chaos expansion, Gaussian process modeling (e.g., Kriging model), splines, moving least squares, support vector regression, relevance vector regression, neural nets, or even simple lookup tables. For example, Goktepe et al. [12] used neural network and polynomial regression models to simulate expansion of concrete specimens under sulfate attack. All surrogate models require training or fitting data, collected by running the full-scale system model repeatedly for different sets of input variable values. Selecting the sets of input values is referred to as statistical design of experiments, and there is extensive literature on this subject. Two types of surrogate modeling methods are discussed below that might achieve computational efficiency while maintaining high accuracy in output uncertainty quantification. The first method expresses the model output in terms of a series expansion of special polynomials such as Hermite polynomials and is referred to as a stochastic response surface method (SRSM). The second method expresses the model output through a Gaussian process and is referred to as Gaussian process modeling.

3.3.1 Stochastic Response Surface Method (SRSM)

The common approach for building a surrogate or response surface model is to use least squares fitting based on polynomials or other mathematical forms based on physical considerations. In SRSM, the response surface is constructed by approximating both the input and output random variables and fields through series expansions of standard random variables (e.g., [18, 19, 47]). This approach has been shown to be efficient, stable, and convergent in several structural, thermal, and fluid flow problems. A general procedure for SRSM is as follows:

(a) Representation of random inputs (either random variables or random processes) in terms of Standard Random Variables (SRVs) by *K-L* expansion, as in Eq. (2).
(b) Expression of model outputs in chaos series expansion. Once the inputs are expressed as functions of the selected SRVs, the output quantities can also be represented as functions of the same set of SRVs. If the SRVs are Gaussian, the output can be expressed a Hermite polynomial chaos series expansion in terms of Gaussian variables. If the SRVs are non-Gaussian, the output can be expressed by a general Askey chaos expansion in terms of non-Gaussian variables [10].
(c) Estimation of the unknown coefficients in the series expansion. The improved probabilistic collocation method [19] is used to minimize the residual in the random dimension by requiring the residual at the collocation points equal to zero. The model outputs are computed at a set of collocation points and used to estimate the coefficients. These collocation points are the roots of the Hermite polynomial of a higher order. This way of selecting collocation points would capture points from regions of high probability [45].
(d) Calculation of the statistics of the output that has been cast as a response surface in terms of a chaos expansion. The statistics of the response can be estimated with the response surface using either Monte Carlo simulation or analytical approximation.

3.3.2 Kriging or Gaussian Process Models

Gaussian process (GP) models have several features that make them attractive for use as surrogate models. The primary feature of interest is the ability of the model to "account for its own uncertainty." That is, each prediction obtained from a Gaussian process model also has an associated variance or uncertainty. This prediction variance primarily depends on the closeness of the prediction location to the training data, but it is also related to the functional form of the response. For example, see Fig. 3, which depicts a one-dimensional Gaussian process model. Note how the uncertainty bounds are related to both the closeness to the training points, as well as the shape of the curve.

The basic idea of the GP model is that the output quantities are modeled as a group of multivariate normal random variables. A parametric covariance function is

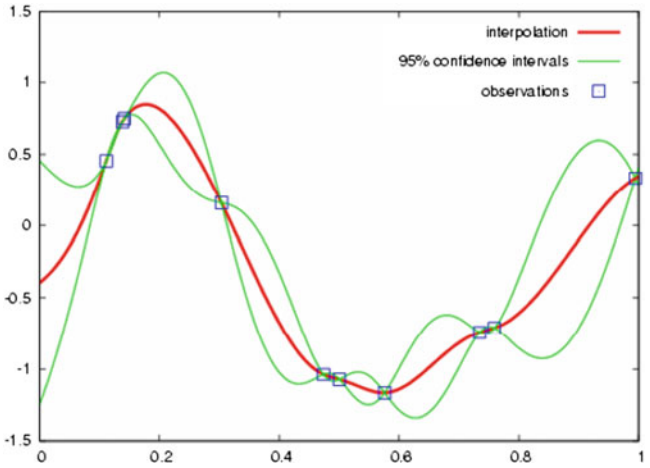

Fig. 3 Gaussian process model with uncertainty bounds

then constructed as a function of the inputs. The covariance function is based on the idea that when the inputs are close together, the correlation between the outputs will be high. As a result, the uncertainty associated with the model prediction is small for input values that are close to the training points and large for input values that are not close to the training points. In addition, the GP model may incorporate a systematic trend function, such as a linear or quadratic regression of the inputs (in the notation of Gaussian process models, this is called the mean function, while in Kriging, it is often called a trend function). The effect of the mean function on predictions which interpolate the training data is small, but when the model is used for extrapolation, the predictions will follow the mean function very closely.

Within the GP modeling technique, it is also possible to adaptively select the design of experiments to achieve very high accuracy. The method begins with an initial GP model built from a very small number of samples, and then one intelligently chooses where to generate subsequent samples to ensure the model is accurate in the vicinity of the region of interest. Since the GP model provides the expected value and variance of the output quantity, the next sample may be chosen in the region of highest variance, if the objective is to minimize the prediction variance. The method has been shown to be both accurate and computationally efficient for arbitrarily shaped functions [2].

3.4 Sensitivity Analysis

Sensitivity analysis serves several important functions: (1) identification of dominant variables or sub-models, thus helping to focus data collection resources efficiently; (2) identification of insignificant variables or sub-models of limited

significance, helping to reduce the size of the problem and computational effort; and (3) quantification of the contribution of solution approximation error. Both local and global sensitivity analysis techniques are available to investigate the quantitative effect of different sources of variation (physical parameters, models, and measured data) on the variation of the model output. The primary benefit of sensitivity analysis to uncertainty analysis is to enable the identification of which physical parameters have the greatest influence on the output [6, 42]).

Sensitivity analysis can be local or global. Local sensitivity analysis utilizes first-order derivatives of system output quantities with respect to the parameters. It is usually performed for a nominal set of parameter values. Global sensitivity analysis typically uses statistical sampling methods, such as Latin Hypercube Sampling, to determine the total uncertainty in the system output over the entire range of the input uncertainty and to apportion that uncertainty among the various parameters.

3.5 Model Error Quantification

Model errors may relate to governing equations, boundary and initial condition assumptions, loading description, and approximations or errors in solution algorithms (e.g., truncation of higher order terms, finite element discretization, curve-fitting models for material damage such as *S-N* curve). Overall model error may be quantified by comparing model prediction and experimental observation, properly accounting for uncertainties in both. This overall error measure combines both model form and solution approximation errors, so it needs to be considered in two parts. Numerical errors in the model prediction can be quantified first, using sensitivity analysis, uncertainty propagation analysis, discretization error quantification, and truncation (residual) error quantification. The measurement error in the input variables can be propagated to the prediction of the output. The error in the prediction of the output due to the measurement error in the input variables is approximated by using a first-order sensitivity analysis [36]. Then the model form error can be quantified based on all the above errors, following the approach illustrated for a heat transfer problem by Rebba et al. [36].

3.5.1 Solution Approximation Error

Several components of prediction error, such as discretization error (denoted by ε_d) and uncertainty propagation analysis error (ε_s) can be considered. Several methods to quantify the discretization error in finite element analysis are available in the literature. However, most of these methods do not quantify the actual error; instead, they only quantify some indicator measures to facilitate adaptive mesh refinement. The Richardson extrapolation (RE) method comes closest to quantifying the actual

discretization error [38]. (In some applications, the model is run with different levels of resolution, until an acceptable level of accuracy is achieved; formal error quantification may not be required).

Errors in uncertainty propagation analysis (ε_s) are method-dependent, i.e., sampling error occurs in Monte Carlo methods and truncation error occurs in response surface methods (either conventional or polynomial chaos-based). For example, sampling error could be assumed to be a Gaussian random variable with zero mean and variance given by σ^2/N where N is the number of Monte Carlo runs and σ^2 is the original variance of the model output [41]. The truncation error is simply the residual error in the response surface.

Rebba et al. [36] and Liang and Mahadevan [26] used the above concept to construct a surrogate model for finite element discretization error in structural analysis, using the stochastic response surface method (SRSM). Gaussian process models may also be employed for this purpose. Both options are helpful in quantifying the solution approximation error.

3.5.2 Model form Error

The overall prediction error is a combination of errors resulting from numerical solution approximations and model form selection. A simple way is to express the total observed error (difference between prediction and observation) as the sum of the following error sources:

$$\varepsilon_{obs} = \varepsilon_{num} + \varepsilon_{model} - \varepsilon_{exp} \tag{3}$$

where ε_{num}, ε_{model}, and ε_{exp} represent numerical solution error, model form error, and output measurement error, respectively. However, solution approximation error results from multiple sources and is probably a nonlinear combination of various errors such as discretization error, round-off and truncation errors, and stochastic analysis errors. One option is to construct a regression model consisting of the individual error components [36]. The residual of such a regression analysis will include the model form error (after subtracting the experimental error effects). By denoting ε_{obs} as the difference between the data and prediction, i.e., $\varepsilon_{obs} = y_{exp} - y_{pred}$, we can construct the following relation by considering a few sources of numerical solution error [36]:

$$\varepsilon_{obs} = f(\varepsilon_h, \varepsilon_d, \varepsilon_s) + \varepsilon_{model} - \varepsilon_{exp} \tag{4}$$

where ε_h, ε_d, and ε_s represent output error due to input parameter measurement error, finite element discretization error, and uncertainty propagation analysis error, respectively, all of which contribute to numerical solution error. Rebba et al. [36] illustrated the estimation of model form error using the above concept for a one-dimensional heat conduction problem, using a polynomial chaos expansion for the

input-output model as well as numerical solution error. Kennedy and O'Hagan [24] calibrated Gaussian process surrogate models for both the input-output model and the model form error (which is also referred to as model discrepancy or model inadequacy term). Both approaches incorporate the dependence of model error on input values.

4 Model Calibration, Validation and Extrapolation

After quantifying and propagating the physical variability, data uncertainty, and model error for individual components of the overall system model, the probability of meeting performance requirements (and our confidence in the model prediction) needs to be assessed based on extrapolating the model to field conditions (which are uncertain as well), where sometimes very limited or no experimental data is available. Rigorous verification, validation, and calibration methods are needed to establish credibility in the modeling and simulation. Both classical and Bayesian statistical methodologies have been investigated during recent years. The methods have the capability to consider multiple output quantities or a single model output at different spatial and temporal points.

This section discusses methods for (1) calibration of model parameters, based on observation data; (2) validation assessment of the model, based on observation data; and (3) estimation of confidence in the extrapolation of model prediction from laboratory conditions to field conditions.

4.1 Model Calibration

Two types of statistical techniques may be pursued for model calibration uncertainty, the least squares approach and the Bayesian approach. The least squares approach estimates the values of the calibration parameters that minimize the discrepancy between model prediction and experimental observation. This approach can also be used to calibrate surrogate models or low-fidelity models, based on high-fidelity runs, by treating the high-fidelity results similar to experimental data.

The second approach is Bayesian calibration [24] using Gaussian process surrogate models. This approach is flexible and allows different forms for including the model errors during calibration of model parameters [31]. Recently, Sankararaman and Mahadevan [43] extended least squares, likelihood and Bayesian calibration approaches to include imprecise and unpaired input-output data sets, a commonly occurring situation when using historical data or data from the literature, where all the inputs to the model may not be reported.

Markov Chain Monte Carlo (MCMC) simulation is used for numerical implementation of the Bayesian updating analysis. Several efficient sampling techniques are available for MCMC, such as Gibbs sampling, the Metropolis algorithm, and the Metropolis-Hastings algorithm [11].

4.2 Model Validation

Model validation involves comparing prediction with observation data (either historical or experimental) when both have uncertainty. Since there is uncertainty in both model prediction and experimental observation, it is necessary to pursue rigorous statistical techniques to perform model validation assessment rather than simple graphical comparisons, provided data is even available for such comparisons. Statistical hypothesis testing is one approach to quantitative model validation under uncertainty, and both classic and Bayesian statistics have been explored. Classical hypothesis testing is a well-developed statistical method for accepting or rejecting a model based on an error statistic (see e.g., [46]). Validation metrics have been investigated in recent years based on Bayesian hypothesis testing [29, 33, 34, 49], reliability-based methods [35], and risk-based decision analysis [22, 23]. Ling and Mahadevan [27] provide detailed discussion of the interpretations of various metrics, their mathematical relationships, and implementation issues, with the example of a MEMS device reliability prediction problem and validation data.

In Bayesian hypothesis testing, we assign prior probabilities for the null and alternative hypotheses; let these be denoted as $P(H_0)$ and $P(H_a)$ such that $P(H_0) + P(H_a) = 1$. Here, H_0: model error $<$ allowable limit, and H_a: model error $>$ allowable limit. When data D is obtained, the probabilities are updated as $P(H_0 \mid D)$ and $P(H_a \mid D)$ using the Bayesian theorem. Then, a Bayesian factor [20] B is defined as the ratio of likelihoods of observing D under H_0 and H_a; i.e., the first term in the square brackets on the right-hand side of Eq. (5):

$$\frac{P(H_0|D)}{P(H_a|D)} = \left[\frac{P(D|H_0)}{P(D|H_a)}\right] \frac{P(H_0)}{P(H_a)} \tag{5}$$

If $B > 1$, the data gives more support to H_0 than H_a. Also, the confidence in H_0, based on the data, comes from the posterior null probability $P(H_0 \mid D)$, which can be rearranged from the above equation as $\frac{P(H_0)B}{P(H_0)B+1-P(H_0)}$. Typically, in the absence of prior knowledge, we may assign equal probabilities to each hypothesis, and thus, $P(H_0) = P(H_a) = 0.5$. In that case, the posterior null probability can be further simplified to $B/(B + 1)$. Thus, a B value of 1.0 represents 50 % confidence in the null hypothesis being true.

The Bayesian hypothesis testing is also able to account for uncertainty in the distribution parameters (mentioned in Sect. 2). For such problems, the validation metric (Bayesian factor) itself becomes a random variable. In that case, the probability of the Bayesian factor exceeding a specified value can be used as the decision criterion for model acceptance/rejection.

Notice that model validation only refers to the situation when controlled, target experiments are performed to evaluate model prediction, and both the model runs and experiments are done under the same set of input and boundary conditions. The validation is done only by comparing the outputs of the model and the experiment.

Once the model is calibrated, verified, and validated, it may be investigated for confidence in extrapolating to field conditions different from laboratory conditions. This is discussed in the next section.

4.3 Overall Uncertainty Quantification

While individual methods for calibration, verification, and validation have been developed as mentioned above, it is necessary to integrate the results from these activities for the purpose of overall uncertainty quantification in the model prediction. This is not trivial because of several reasons. First, the solution approximation errors calculated as a result of the verification process need to be accounted for during calibration, validation, and prediction. Second, the result of validation may lead to a binary result, i.e., the model is accepted or rejected; however, even when the model is accepted, it is not completely correct. Hence, it is necessary to account for the degree of correctness of the model in the prediction. Third, calibration and validation are performed using independent data sets, and it is not straightforward to compute their combined effect on the overall uncertainty in the response.

The issue gets further complicated when system-level behavior is predicted based on a hierarchy of models. As the complexity of the system under study increases, there may be several components and subsystems at multiple levels of hierarchy, which integrate to form the overall multilevel system. Each of these components and subsystems is represented using component-level and subsystem-level models which are mathematically connected to represent the overall system model which is used to study the underlying system. In each level, there is a computational model with inputs, parameters, outputs, experimental data (hopefully available for calibration and validation separately), and several sources of uncertainty – physical variability, data uncertainty (sparse or imprecise data, measurement errors, expert opinion), and model uncertainty (parameter uncertainty, solution approximation errors, and model form error).

Recent studies by the author and coworkers have demonstrated that the Bayesian network methodology provides an efficient and powerful tool to integrate multiple levels of models, associated sources of uncertainty and error, and available data at multiple levels and in multiple formats. While the Bayesian approach can be used to perform calibration and validation individually for each model in the multilevel system, it is not straightforward to integrate the information from these activities in order to compute the overall uncertainty in the system-level prediction. Sankararaman and Mahadevan [44] extend the Bayesian approach to integrate and propagate information from verification, calibration, and validation activities in order to quantify the margins and uncertainties in the overall system-level prediction.

Bayesian networks [21] are directed acyclic graphical representations with nodes to represent the random variables and arcs to show the conditional dependencies among the nodes. Data in any one node can be used to update the statistics of all

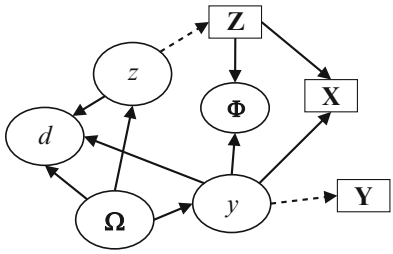

Fig. 4 Bayes network

other nodes. This property makes the Bayesian network a powerful tool to integrate information generated from multiple activities and to quantify the uncertainty in prediction under actual usage conditions [29].

Figure 4 shows an illustrative Bayesian network for confidence extrapolation. An ellipse represents a random variable, and a rectangle represents observed data. A solid line arrow represents a conditional probability link, and a dashed line arrow represents the link of a variable to its observed data if available. The probability densities of the variables $\mathbf{\Omega}$, z, and y are updated using the validated data $\mathbf{Y}$. The updated statistics of $\mathbf{\Omega}$, z, and y are then used to estimate the updated statistics of the decision variable d (i.e., assessment metric). In addition, both model prediction and predictive experiments are related to input variables $\mathbf{X}$ via physical parameters Φ. Note that there is no observed data available for d; yet we are able to calculate the confidence in the prediction of d, by making use of observed data in several other nodes and propagation of posterior statistics through the Bayesian network.

The Bayesian network thus links the various simulation codes and corresponding experimental observations to facilitate two objectives: (1) uncertainty quantification and propagation and (2) confidence assessment in system behavior prediction in the application domain, based on data from the laboratory domain, expert opinion, and various computational models at different levels of the system hierarchy.

5 Conclusion

Uncertainty quantification in performance assessment involves consideration of three sources of uncertainty – inherent variability, information uncertainty, and model errors. This chapter surveyed probabilistic methods to quantify the uncertainty in model-based prediction due to each of these sources and addressed them in four stages – input characterization based on data; propagation of uncertainties and errors through the system model; model calibration, validation, and extrapolation; and performance assessment. Flexible distribution families as well as a nonparametric Bayesian approach were discussed to handle sparse data and interval data. Methods to quantify model errors resulting from both model form selection and solution approximation were discussed. Bayesian methods were discussed for model calibration,

validation, and extrapolation. An important issue is computational expense, when iterative analysis between multiple codes is necessary. Uncertainty quantification multiplies the computational effort of deterministic analysis by an order of magnitude. Therefore, the use of surrogate models, sensitivity and screening analyses, and first-order approximations of overall output uncertainty are available to reduce the computational expense.

Many of the methods described in the chapter have been applied to mechanical systems that are small in size or time-independent, and the uncertainties considered were not very large. None of these simplifications are available in the case of long-term performance assessment of civil infrastructure systems, and real-world data to validate long-term model predictions are not available. Thus, the extrapolations are based on laboratory data or limited term observations and come with large uncertainty. The application of the methods described in this chapter to such complex systems needs to be investigated. However, it should be recognized that the benefit of uncertainty quantification is not so much in predicting the actual failure probability or similar measures but in facilitating engineering decision-making, such as comparing different design and analysis options, performing sensitivity analyses, and allocating resources for uncertainty reduction through further data collection and/or model refinement.

Acknowledgement The research described in this chapter by the author and his students/colleagues has been funded by many sources during the past decade. A partial listing of the recent sources includes the following: (1) National Science Foundation (IGERT project on Reliability and Risk Assessment and Management at Vanderbilt University), (2) Sandia National Laboratories (Bayesian framework for model validation, calibration, and error estimation), (3) US Department of Energy (uncertainty quantification in micro-electro-mechanical systems (MEMS) reliability prediction, long-term durability of cementitious barriers), (4) National Aeronautics and Space Administration (space vehicle performance uncertainty quantification, uncertainty quantification in diagnosis and prognosis, Bayesian network development for testing resource allocation), (5) US Air Force Office of Scientific Research (multidisciplinary uncertainty analysis of aircraft components), and (6) Federal Aviation Administration (uncertainty quantification in fracture mechanics simulation of rotorcraft components). The support is gratefully acknowledged.

References

1. Barford NC (1985) Experimental measurements: precision, error, and truth. Wiley, New York
2. Bichon, BJ, Eldred, MS, Swiler, LP, Mahadevan, S, McFarland, JM (2007) Multimodal reliability assessment for complex engineering applications using efficient global optimization. In: Proceedings of 9th AIAA non-deterministic approaches conference, Waikiki, HI
3. Blischke WR, Murthy DNP (2000) Reliability: modeling, prediction, and optimization. Wiley, New York
4. Box GEP, Hunter WG, Hunter JS (1978) Statistics for experimenters, an introduction to design, data analysis, and model building. Wiley, New York
5. Box GEP, Jenkins GM, Reinsel GC (1994) Time series analysis forecasting and control, 3rd edn. Prentice Hall, Englewood Cliffs

6. Campolongo F, Saltelli A, Sorensen T, Tarantola S (2000) Hitchhiker's guide to sensitivity analysis. In: Saltelli A, Chan K, Scott EM (eds) Sensitivity analysis. Wiley, New York, pp 15–47
7. Efron B, Tibshirani RJ (1994) An introduction to the bootstrap. Chapman & Hall/CRC, New York/Boca Raton
8. Farrar CR, Sohn H, Hemez FM, Anderson MC, Bement MT, Cornwell PJ, Doebling SW, Schultze JF, Lieven N, Robertson AN (2003) Damage prognosis: current status and future needs. Technical report LA–14051–MS, Los Alamos National Laboratory, Los Alamos, New Mexico
9. Ferson S, Kreinovich V, Hajagos J, Oberkampf W, Ginzburg L (2007) Experimental uncertainty estimation and statistics for data having interval uncertainty. Sandia National Laboratories technical report, SAND2003-0939, Albuquerque, New Mexico
10. Ghanem R, Spanos P (2003) Stochastic finite elements: a spectral approach. Springer, New York
11. Gilks WR, Richardson S, Spiegelhalter DJ (1996) Markov Chain Monte Carlo in practice, Interdisciplinary statistics series. Chapman and Hall, Boca Raton
12. Goktepe AB, Inan G, Ramyar K, Sezer A (2006) Estimation of sulfate expansion level of pc mortar using statistical and neural approaches. Constr Build Mater 20:441–449
13. Gurley KR (1997) Modeling and simulation of non-Gaussian processes. Ph.D. thesis, University of Notre Dame, April
14. Haldar A, Mahadevan S (2000) Probability, reliability and statistical methods in engineering design. Wiley, New York
15. Haldar A, Mahadevan S (2000) Reliability analysis using the stochastic finite element method. Wiley, New York
16. Helton JC, Sallabery CJ (2009) Conceptual basis for the definition and calculation of expected dose in performance assessments for the proposed high-level radioactive waste repository at Yucca Mountain, Nevada. Reliab Eng Syst Saf 94:677–698
17. Helton JC, Sallabery CJ (2009) Computational implementation of sampling-based approaches to the calculation of expected dose in performance assessments for the proposed high-level radioactive waste repository at Yucca Mountain, Nevada. Reliab Eng Syst Saf 94:699–721
18. Huang S, Mahadevan S, Rebba R (2007) Collocation-based stochastic finite element analysis for random field problems, Probab Eng Mech 22:194–205
19. Isukapalli SS, Roy A, Georgopoulos PG (1998) Stochastic response surface methods (SRSMs) for uncertainty propagation: application to environmental and biological systems. Risk Anal 18(3):351–363
20. Jeffreys H (1961) Theory of probability, 3rd edn. Oxford University Press, London
21. Jensen FV, Jensen FB (2001) Bayesian networks and decision graphs. Springer, New York
22. Jiang X, Mahadevan S (2007) Bayesian risk-based decision method for model validation under uncertainty. Reliab Eng Syst Saf 92(6):707–718
23. Jiang X, Mahadevan S (2008) Bayesian validation assessment of multivariate computational models. J Appl Stat 35(1):49–65
24. Kennedy MC, O'Hagan A (2001) Bayesian calibration of computer models (with discussion). JR Stat Soc Ser B 63(3):425–464
25. Langley RS (2000) A unified approach to the probabilistic and possibilistic analysis of uncertain systems. ASCE J Eng Mech 126:1163–1172
26. Liang B, Mahadevan S (2011) Error and uncertainty quantification and sensitivity analysis of mechanics computational models. Int J Uncertain Quantif 1:147–161
27. Ling Y, Mahadevan S (2012) Intepretations, relationships, and application issues in model validation. In: Proceedings, 53rd AIAA/ASME/ASCE Structures, Dynamics and Materials (SDM) conference, paper no. AIAA-2012-1366, Honolulu, Hawaii, April 2012
28. Mahadevan S, Raghothamachar P (2000) Adaptive simulation for system reliability analysis of large structures. Comput Struct 77(6):725–734

29. Mahadevan S, Rebba R (2005) Validation of reliability computational models using Bayes networks. Reliab Eng Syst Saf 87(2):223–232
30. Mathelin L, Hussaini MY, Zang TA (2005) Stochastic approaches to uncertainty quantification in CFD simulations. Numer Algorithm 38:209–236
31. McFarland JM (2008) Uncertainty analysis for computer simulations through validation and calibration. Ph.D. dissertation, Vanderbilt University, Nashville, TN
32. Mckay MD, Conover WJ, Beckman RJ (1979) A comparison of three methods for selecting values of input variables in the analysis of output from a computer code. Technometrics 21:239–245
33. Rebba R (2005) Model validation and design under uncertainty. Ph.D. dissertation, Vanderbilt University, Nashville, TN, USA
34. Rebba R, Mahadevan S (2006) Model predictive capability assessment under uncertainty. AIAA J 44(10):2376–2384
35. Rebba R, Mahadevan S (2008) Computational methods for model reliability assessment. Reliab Eng Syst Saf 93:1197–1207
36. Rebba R, Mahadevan S, Huang S (2006) Validation and error estimation of computational models. Reliab Eng Syst Saf 91(10–11):1390–1397
37. Red-Horse JR, Benjamin AS (2004) A probabilistic approach to uncertainty quantification with limited information. Reliab Eng Syst Saf 85:183–190
38. Richards SA (1997) Completed Richardson extrapolation in space and time. Commun Numer Methods Eng 13(7):558–573
39. Robert CP, Casella G (2004) Monte Carlo statistical methods, 2nd edn. Springer, New York
40. Ross TJ, Booker JM, Parkinson WJ (2002) Fuzzy logic and probability applications: bridging the gap. SIAM, Philadelphia
41. Rubinstein RY (1981) Simulation and the Monte Carlo method. Wiley, New York
42. Saltelli A, Chan K, Scott EM (2000) Sensitivity analysis. Wiley, West Sussex
43. Sankararaman S, Mahadevan S (2011) Likelihood-based representation of epistemic uncertainty due to sparse point data and interval data. Reliab Eng Syst Saf 96:814–824
44. Sankararaman S, Mahadevan S (2012) Roll-up of calibration and validation results towards system-level QMU. In: Proceedings of 15th AIAA non-deterministic approaches conference, Honolulu, Hawaii
45. Tatang MA, Pan W, Prinn RG, McRae GJ (1997) An efficient method for parametric uncertainty analysis of numerical geophysical models. J Geophys Res 102(D18):21925–21932
46. Trucano TG, Easterling RG, Dowding KJ, Paez TL, Urbina A, Romero VJ, Rutherford BM, Hills RG (2001) Description of the Sandia validation metrics project. Sandia National Laboratories technical report, SAND2001-1339, Albuquerque, New Mexico
47. Xiu D, Karniadakis GE (2003) Modeling uncertainty in flow simulations via generalized polynomial chaos. J Comput Phys 187(1):137–167
48. Zaman K, McDonald M, Mahadevan S (2011) A probabilistic approach for representation of interval uncertainty. Reliab Eng Syst Saf 96(1):117–130
49. Zhang R, Mahadevan S (2003) Bayesian methodology for reliability model acceptance. Reliab Eng Syst Saf 80(1):95–103
50. Zou T, Mahadevan S, Mourelatos Z (2003) Reliability-based evaluation of automotive wind noise quality. Reliab Eng Syst Saf 82(2):217–224

A Brief Review of Stochastic Control of Structures

T.K. Datta

Abstract Stochastic control of structures is a relatively new area of research. Despite enormous amount of work on deterministic structural control and its application on many civil engineering structures, stochastic structural control is evolving as a promising subject of investigation. The main reason for choosing a stochastic control theory is that most of the feedback and excitation measurements are polluted with noises which are inherently random. Further, environmental dynamic excitations are more realistically modeled as stochastic processes. In this presentation, stochastic control of structures is briefly reviewed in order to highlight different types of researches being carried out in this area in recent years. The review includes linear and nonlinear stochastic control of linear systems, nonlinear stochastic control of nonlinear systems, stochastic control of hysteretic systems, and stochastic control of structures using stochastic linearization technique. A number of interesting applications of stochastic control theory to structures such as stochastic control of hysteretic column, semiactive control of building frame using MR-TLCD, and active control of coupled buildings are discussed. Finally, future scopes of research in this area emerging from the literature review are outlined.

Keywords Structures • Linear and nonlinear stochastic control • Linear systems • Nonlinear systems • Hysteretic system

T.K. Datta (✉)
Department of Civil Engineering, Indian Institute of Technology Delhi,
Hauz Khas, New Delhi 110 016, India
e-mail: tushar_k_datta@yahoo.com

S. Chakraborty and G. Bhattacharya (eds.), *Proceedings of the International Symposium on Engineering under Uncertainty: Safety Assessment and Management (ISEUSAM - 2012)*,
DOI 10.1007/978-81-322-0757-3_6,

1 Introduction

Stochastic optimal control is a topic of considerable interest in different fields of engineering since uncertainties are inherent in all types of control problems. These uncertainties include uncertainties of modeling, estimation of parameters, measurements, disturbances, etc. In the field of structural engineering, stochastic optimal control of structures becomes necessary when the structures are subjected to random excitations and the system states are estimated from measurements with random noises. Further, it is also required because uncertainties are also present in the stiffness and damping of the system. As a result, the stochastic optimal control should also be robust, i.e., its stability should be guaranteed.

Mathematical theory of stochastic optimal control is quite well developed. However, only linear quadratic Gaussian control strategy has been used so far for structural control problems mainly because of its simplicity. In recent years, nonlinear stochastic control of structures has attracted the attention of researchers mainly because the nonlinearities are present in most practical control problems. Even without considering the nonlinearities of the system or even after linearizing them, nonlinear control algorithm may be applied to control the system. It is found that more effective control is obtained by applying nonlinear control theory. A number of papers dealing with linear and nonlinear stochastic control of structures are available in the literature [1–14]. A survey of these papers reveals the current state of the art on the subject including the application problems that have been solved.

In this chapter, different types of work which have been carried out on the stochastic control of structures are briefly reviewed. The review includes (1) stochastic optimal control for linear systems with or without observer, (2) stochastic nonlinear optimal control for linear systems with or without observer, (3) stochastic optimal control for nonlinear system using linearization technique, (4) nonlinear optimal control for nonlinear systems, (5) stochastic control using stability criterion, (6) H_α stochastic control for linearized hysteretic system, and (7) stochastic control using stochastic averaging technique. A number of applications such as stochastic seismic control of hysteretic columns, coupled buildings, semiactive control of buildings using MR-TLCD, and MR dampers are also discussed. At the end, future scope of the work in this area is outlined.

2 Stochastic Control Problem

The control problem is mathematically defined as

$$\text{System} \qquad \dot{X} = f(x, u, k, t) \tag{1}$$

$$\text{Observation} \qquad Y = h(x, t) + \eta \tag{2}$$

$$\text{Performance Index} \qquad J = E\left[\int_0^{t_f} F(x,u,t)\mathrm{d}t\right] \tag{3}$$

in which f could be a linear or nonlinear function with or without uncertain system dynamics and noise/excitation (k), η is additive linear or nonlinear noisy component associated with the measurements, u is the control force, F is a nonlinear function of finite or infinite duration, and E denotes expectation. Complexity of the problem increases with increasing nonlinearity in the system and with less availability of measured responses. The minimization of the performance function which provides the control force becomes complex for nonlinear systems. Observed states are determined using some filters. The problem can be formulated with continuous variable or variables described in discrete form. Algorithms of the computations can be derived for both.

3 Linear Stochastic Control

The linear stochastic control takes the following forms [9]:

$$\text{System} \qquad \dot{X} = AX + bu \tag{4}$$

$$\text{Observation} \qquad Y = HX + \eta \tag{5}$$

$$\text{Performance Index} \qquad J = E\left[\int_0^{t_f} \left[X^T QX + ru^2\right]\mathrm{d}t\right] \tag{6}$$

Initial state of the system is normally distributed with mean X_0 and covariance P_0. Observation error η is assumed to be Gaussian white noise with mean zero and mean square value $N(t)$, i.e., $E[\eta(t)\eta(\tau)] = N(t)\delta(t-\tau)$. The conditional mean and covariance of the state $X(t)$ are given by

$$\mu(t) = E[X(t)|Y(\tau)] \tag{7}$$

$$P(t) = E\left[(X-\mu)(X-\mu)^T|Y(\tau)\right] \tag{8}$$

These quantities are governed by Kalman filter equation

$$\dot{\mu} = A\mu + bu + PH^T N^{-1}(Y - H\mu) \tag{9}$$

$$\dot{P} = AP + PA^T - PH^T N^{-1} HP \tag{10}$$

With initial conditions as

$$\mu(0) = X_0 \quad P(0) = P_0$$

$u(t)$ is obtained by minimizing J [1]

$$u(t) = -\frac{1}{r}\mu^T Bb \tag{11}$$

where B satisfies the Riccati equation

$$\dot{B} + BA + A^T B - \frac{1}{r}Bbb^T b + Q = 0 \tag{12}$$

with $B(t_f) = 0$

Discrete state-space model of linear stochastic control system is given by [2]

$$X_{K+1} = AX_K + Bu_K + w_K \tag{13}$$

$$Y_K = CX_K + \eta_K \tag{14}$$

$$MinJ = Min_{u_K \cdots u_N} E\left[X_{N+1}^T Q_0 X_{N+1} + \sum_{S=K}^{N} X_S^T Q_1 X_S + u_S^T Q_2 u_S\right] \tag{15}$$

$$u_K = -L_K \widehat{X}_{K|K}; \quad L_K = \left[Q_2 + B^T S_{K+1} B\right]^{-1} B^T S_{K+1} A \tag{16}$$

$$S_K = Q_1 + A^T S_{K+1}(A - BL_K); \quad S_{N+1} = Q_0 \tag{17}$$

For fully measured state, $\widehat{X}_{K|K} \to X_K$, i.e., observed state, is the same as the measured state. A backward step computational algorithm is developed without the solution of any Riccati equation. Kalman filter equation in discrete form is used for state estimation, i.e.,

$$\widehat{X}_{K+1} = A\widehat{X}_K + Bu_K + R_K\left(Y_K - C\widehat{X}_K\right) \tag{18}$$

$$R_K = A\sum\nolimits_K C^T\left(C\sum\nolimits_K C^T + N\right)^{-1} \tag{19}$$

$$\sum\nolimits_{K+1} = W + (A - R_K C)\sum\nolimits_K A^T \tag{20}$$

$$\sum\nolimits_K = \mathrm{cov}\widehat{X}_K \tag{21}$$

in which N is defined earlier and W is the covariance matrix of the white noise $w(t)$.

4 Nonlinear Optimal Control

For explaining the nonlinear optimal control for linear system, a linear structure under random ground motion is considered [14]:

$$M\ddot{X} + C\dot{X} + KX = -Mr\ddot{x}_g + PU \tag{22}$$

The solution is carried out in modal coordinate with n modal equations as

$$\ddot{q}_i + 2\eta\omega_i\dot{q}_i + \omega_i^2 q_i = -\beta_i\ddot{x}_g + u_i \,(i = 1 \cdot \cdots \cdot n) \tag{23}$$

in which β_i is the mode participation factor and u_i is the ith modal control force. Assuming $\ddot{x}_g$ to be a uniformly modulated stationary process,

$$S_{\ddot{x}_g}(\tau) = \sigma^2(\tau) S_{\ddot{x}_g} \tag{24}$$

The uniformly modulated stationary process is considered as filtered white noise with following transformation:

$$\ddot{x}_g = \left(\sum_{j=0}^{r-1} d_j \frac{\mathrm{d}^j}{\mathrm{d}t^j}\right) f \left(\sum c_j \frac{\mathrm{d}^j}{\mathrm{d}t^j}\right) f = \sigma(\tau) w(t) \tag{25}$$

in which $w(t)$ is the white noise process.

With this transformation, a combined Ito equation is formulated as

$$dZ = (AZ + Bu)\mathrm{d}t + CdB(t) \tag{26}$$

$$Z = \left[q^T, \dot{q}^T, f^T\right]^T$$

Observation equations are formed with measured quantities expressed as modal responses and noises. They are converted into equation as

$$\mathrm{d}v = (DZ + Gu)\mathrm{d}t + \sigma_1(\tau) dB_1(t) \tag{27}$$

in which $\dfrac{dv}{dt} = \left[a^T, d^T\right]$ and $\sigma_1(\tau)$ is the accuracy matrix. a and d denote vectors of measured accelerations and floor drifts.

Objective function is taken as

$$J = \lim_{T\to\infty} \frac{1}{T_f} \int_0^{t_f} L(q, \dot{q}, u) dt \tag{28}$$

It is assumed that σ and σ_1 are constants, and as $T \to \infty$, the response of the controlled system is stationary and ergodic. Both system and observation equations are linear. If L is nonquadratic, nonlinear feedback control is formed.

Let state vector estimate be denoted by $\widehat{Z}$. Ito equation with estimated $\widehat{Z}$ is governed by

$$\mathrm{d}\widehat{Z} = \left(A\widehat{Z} + Bu\right)\mathrm{d}t + f(t)\sigma_1(\tau)\widehat{B}(t) \tag{29}$$

$$\widehat{Z}(0) = \widehat{Z}_0 \tag{30}$$

$$f(t) = R_C(t)D^T S_a^{-1} \tag{31}$$

$R_C(t)$ is the covariance matrix of error $\bar{Z} = Z - \widehat{Z}$ which satisfies the Riccati type matrix equation. The objective function is written in the form of

$$\widehat{J} = \int \widehat{L}\left(\widehat{q}, \dot{\widehat{q}}, u\right)dt \tag{32}$$

in which $\widehat{L} = \int Lp\left(Z - \widehat{Z}\right)\mathrm{d}z$; p is Gaussian distribution.

Using Hamiltonian as the variable for performance function,

$$\widehat{H}_i = \frac{\dot{\widehat{q}}_i^2 + \omega_i^2 \widehat{q}_i^2}{2} \tag{33}$$

and using Vanderpol transformation and stochastic averaging, the Ito equation is formed as

$$\mathrm{d}\widehat{H}_i = \left[m_i\left(\widehat{H}_i, \tau\right) + \frac{d\widehat{H}_i}{d\widehat{q}_i}u_i\right]\mathrm{d}t + \sigma_i\left(\widehat{H}_i, \tau\right)dB_i(t) \tag{34}$$

Dynamic programming is used to minimize $\widehat{J}$, and optimal $\widehat{u}^*$ is obtained in the form

$$\widehat{u}^* = -\frac{1}{2}R^{-1}P^T \sum_{i=1}^{m} \widehat{q}_i \dot{\widehat{q}}_i \frac{\mathrm{d}v}{\mathrm{d}H_i} \tag{35}$$

$\dfrac{\mathrm{d}v}{\mathrm{d}H_i}$ is obtained from a separate equation, i.e., dynamic programming equation for ergodic control problem [4, 13]

$$\lambda = g(\bar{H}) + \sum_{i=1}^{n_1} \left[m_i\left(\widehat{H}_i\right) \frac{\mathrm{d}v}{\mathrm{d}\widehat{H}_i} - \frac{1}{4}\phi_i^T P_u \phi_i H_i \left(\frac{\mathrm{d}v}{\mathrm{d}\widehat{H}_i}\right)^2 + \frac{1}{2}\sigma_i^2\left(\widehat{H}_i\right) \frac{\mathrm{d}^2 v}{\mathrm{d}\widehat{H}_i^2} \right] \tag{36}$$

$$P_u = PR^{-1}P^T \tag{37}$$

Substituting for $\bar{u}^*$, Ito equation turns out to be

$$\mathrm{d}\widehat{H}_i = \left[m_i\left(\widehat{H}_i\right) + m_i^u(\bar{H}_i) \right] \mathrm{d}t + \sigma_i\left(\widehat{H}_i\right) \mathrm{d}\bar{B}_i(t) \tag{38a}$$

in which $m_i^u(\bar{H}_i)$ is given by

$$m_i^u(\bar{H}_i) = \left\{ \begin{array}{cc} -\frac{1}{2}\phi_i^T P_u \phi_i \widehat{H}_i \dfrac{\mathrm{d}v}{d\widehat{H}_i} & i = 1 \ldots n_1 \\ 0 & i = n_1 + 1 \ldots n \end{array} \right\} \tag{38b}$$

in which n_1 is the dominant modes to be controlled.

Solving the associated FPK provides

$$p\left(\widehat{H}_i\right) \text{ and } p\left(\widehat{q}, \dot{\widehat{q}}\right), \text{and then, } E\left[\widehat{q}^2\right] \text{ and } E\left[\dot{\widehat{q}}^2\right] \text{ are obtained.} \tag{39}$$

5 Nonlinear Stochastic Control with Sliding Mode Control

System is represented by [6]

$$\mathrm{d}X = [AX + Bu]\mathrm{d}t + f(X, \xi)\mathrm{d}t + G_x(X)\mathrm{d}v(t) \tag{40}$$

Observer equation is given by

$$\mathrm{d}Y = CX\mathrm{d}t + G_y(X)\mathrm{d}w(t) \tag{41}$$

in which $\mathrm{d}w(t)$ and $\mathrm{d}v(t)$ are Weiner process noises and $\xi(t)$ is deterministic process disturbance which cannot be measured; f is nonlinear uncertain dynamics. It is assumed that A and C are observable and an observer gain matrix K_0 exists. Further, $f(X, \xi)$ consists of two parts, i.e.,

$$f(X, \xi) = f_1(X) + f_2(X, t) \text{ [Nonlinear + unmeasured]} \tag{42}$$

The function and matrices satisfy following conditions: $(A - K_0C)$ satisfies Hurwitz condition, $f_1(X)$ satisfies Lipschitz condition, and $f_2(X,t)$ satisfies matching condition given by $P^{-1}C^T\xi(Y(t),t)$ in which P is obtained by the solution of the following equation [6]:

$$PA_0 + A_0^T P = -Q; \quad A_0 = A - K_0C \tag{43}$$

Lipschitz constant α satisfies

$$\alpha < \frac{1}{2}\frac{\lambda(Q)}{\lambda(P)} \tag{44}$$

Observer is designed based on sliding mode control

$$\mathrm{d}\bar{X} = [A\bar{X} + Bu + f_1(\bar{X})]\mathrm{d}t + K_0(Y - C\bar{X})\mathrm{d}t + S_0(\bar{X}, Y, \bar{\eta}_i)\mathrm{d}t \tag{45}$$

S_0 is defined as

$$S_0 = P^{-1}C^T \sum_{i=0}^{N} \bar{\eta}_i l_i(Y) \frac{Y - C\bar{X}}{\|Y - C\bar{X}\|\|-\phi\|} \tag{46}$$

$$\phi = h_1 h_2 \left[\sum_{i=0}^{N} \bar{\eta}_i l_i\right] \tag{47}$$

Convergence of observation error is proved using Lyapunov technique. Sliding MDOF controller is designed as $S_c = \sigma + G\bar{X}$ with $\mathrm{d}\sigma = [GBK_c\bar{X} - GA\bar{X}]\mathrm{d}t$. G is selected such that GB is nonsingular and $A - BK_c = A_c$ satisfies Hurwitz condition with K_c as the coefficient matrix and $S_c = 0$ is the sliding surface. The control law is based on

$$u(t) = -\gamma S_c - K_c\bar{X} - \rho(t)\mathrm{sgn}(S_0) \tag{48}$$

in which ρ is switching gain defined by some norm.

Reachability and subsequent stay of the state on sliding surface are proved. The sliding mode dynamics is governed by

$$\mathrm{d}\bar{X} = A_c\bar{X}\mathrm{d}t + \left[I - B(GB)^{-1}G\right][K_c(Y - C\bar{X} + f(\bar{X},t)) + S_0]\mathrm{d}t \tag{49}$$

Stability of the closed-loop system is proved by Lyapunov technique.

6 Nonlinear Stochastic Control Using State Dependant Riccati Equation

The control equation is given by

$$\mathrm{d}X = F(X,u)\mathrm{d}t + G(X,t)\mathrm{d}Bt \tag{50}$$

In discrete form, the equation can be written as

$$X_{K+1} = f_K(X, w_k) \tag{51}$$

The observer equation is given by

$$Y = h(X,t) + v; \quad Y_K = h_K(X, v_K) \tag{52}$$

For estimation of the state of nonlinear systems, extended Kalman filter and simulation-based methods are generally used. The particle filter is based on the latter scheme and has many variants. Using simulation, filter obtains conditional mean and variance of the *k-th* state estimate. Applying separation principle, and state-dependent Riccati equation, *k-th* optimal control force is u_k and is determined as [8]

$$u_k = -R^{-1}(X_K)B^T(X_K)P(X_K)X_K \tag{53}$$

in which the state equation which is used as constraint for minimizing the cost function is

$$\dot{X} = A(X)X + B(X)u \tag{54}$$

Ito-Taylor expansion is utilized to formulate the problem in discrete form and solves the problem in discrete steps with

$$u_{K+1} = u_K + \dot{u}_K h \tag{55}$$

7 Nonlinear Stochastic Control Using Optimal Controller

The system to be controlled is defined by

$$\dot{X} = f(X,u,k,t) \tag{56}$$

The observer equation with uncertainty is given by

$$Y = h(x,t) + \eta \tag{57}$$

The objective function takes the form

$$J = \underset{t\to\infty}{E}\left[\int_0^t F(x,u,t)\mathrm{d}t\right] \tag{58}$$

For the problem, separation rule is employed and nonlinear Kalman is employed for state estimation [9]

$$\dot{\widehat{X}} = f\left(\widehat{X},u,k,t\right) + Ph_y^T M(Y - h(x,t)) \tag{59}$$

$$\dot{P} = f_x P + Pf_x^T + P^T\left[h_y^T M(Y - h(x,t))\right]P \tag{60}$$

in which $\widehat{X}$ is the least square estimate.

P and $M\left(\approx N^{-1}\right)$ are similar to those used in linear quadratic case with μ defined as minimum variance estimate of $X(t)$

Filtering can be used to find the unknown parameters k; $\bar{\eta} = 0$

The state equation can be written as

$$\dot{Z} = g(x,u,t) \text{ or } \dot{\bar{Z}} = g\left(\widehat{x},u,t\right) \tag{61}$$

The controlled design is based on a target response X^d and instantaneous deviation with

$$F\left(\widehat{X}\right) = \left(\widehat{X} - X^d\right)^T Q\left(\widehat{X} - X^d\right) \quad \text{with} \quad u^* \geq u \geq u_* \tag{62}$$

Minimization of the above function provides maximum rate of movement of $\widehat{X}$ to X^d. This leads to a maximum control force

$$u = \begin{cases} u^*{}_i & \beta_i \leq 0 \\ u_{*i} & \beta_i \geq 0 \end{cases} \quad \beta_i = 2S(x,u,t)^T Q\left(x - x^d\right) \tag{63}$$

For minimization, it is assumed that

$$\dot{x} = f(x,u,k,t) = W(x,u,k,t) + S(x,k,t)u \tag{64}$$

8 Nonlinear Stochastic Control Using Partially Observable Quasi-Hamiltonian

System is described as

$$dX = [AX + G(X)]\mathrm{d}t + \bar{U}_2\mathrm{d}t + c_1\mathrm{d}B \tag{65}$$

Observation equation is given by

$$\mathrm{d}Y = [DX + E(X)]\mathrm{d}t + F\bar{U}_2\mathrm{d}t + c_2\mathrm{d}B + c_3\mathrm{d}B_1 \tag{66}$$

Objective function is

$$J = \lim_{T\to\infty}\frac{1}{T}\int_0^T L(X, U_2)\mathrm{d}t \tag{67}$$

$$\begin{gathered}\text{in which } X = \left[Q^T, P^T\right]^T, \quad Q = \frac{\partial H'}{\partial P}, \quad \text{and} \\ P' = -\frac{\partial H'}{\partial Q} - C'_0\frac{\partial H'}{\partial P} + U + K'_0 w(t)\end{gathered} \tag{68}$$

H' is the unperturbed Hamiltonian, U is the control force, C'_0 is the damping coefficient matrix, K'_0 is the stochastic excitation amplitude matrix, and $w(t)$ is the Gaussian white noise vector with intensity matrix 2D. Using Wong-Zakai correction, a modified Hamiltonian H is obtained which transforms $\frac{\partial H'}{\partial P}$ to $\frac{\partial H}{\partial P}$, $\frac{\partial H'}{\partial Q}$ to $\frac{\partial H}{\partial Q}$, and K' to K_0 through $2K'_0DK'_0T = K_0K_0^T$ [11].

$\bar{U}$ is split into

$$\bar{U} = \begin{bmatrix}0 & U\end{bmatrix}^T \quad \bar{U} = \bar{U}_1 + \bar{U}_2 \tag{69}$$

$\bar{U}_1$ is combined with uncontrolled system and observation so that original equations

$$\mathrm{d}X = \bar{A}X\mathrm{d}t + \bar{U}\mathrm{d}t + c_1\mathrm{d}B(t) \tag{70}$$

$$\mathrm{d}Y = \bar{D}Xdt + F\bar{U}\mathrm{d}t + c_2\mathrm{d}B(t) + c_3\mathrm{d}B_1(t) \tag{71}$$

are converted to Eqs. (65 and 66). In the above equations,

$$\bar{A} = \begin{bmatrix} \dfrac{\partial H}{\partial P} \\ -\dfrac{\partial H}{\partial Q} - C_0 \dfrac{\partial H}{\partial P} \end{bmatrix}, \quad \bar{U} = \begin{bmatrix} 0 \\ U \end{bmatrix}, \quad C_1 = \begin{bmatrix} 0 \\ K_0 \end{bmatrix}, \tag{72}$$

$$G(X) = \bar{A} + \bar{U}_1 - AX, \quad D = \frac{\mathrm{d}}{\mathrm{d}x}[\bar{D}(0) + F\bar{U}_1(0)], \tag{73}$$

$$E(X) = \bar{D}(X) + F\bar{U}_1 - D(X), \quad \text{and}$$

$$A = \begin{bmatrix} \dfrac{\partial \bar{H} Q}{\partial Q \partial P} & \dfrac{\partial^2 \bar{H}(0)}{\partial P^2} \\ \dfrac{\partial^2 \bar{H}(0)}{\partial Q^2} - \dfrac{\partial}{\partial Q} C_0(0) \dfrac{\partial \bar{H}(0)}{\partial P} & -\dfrac{\partial^2 \bar{H}(0)}{\partial P \partial Q} - \dfrac{\partial}{\partial P} C_0(0) \dfrac{\partial \bar{H}(0)}{\partial P} \end{bmatrix} \tag{74}$$

With these, the problem is finally converted to completely observable linear problem [11]

$$\mathrm{d}\widehat{X} = \left(A\widehat{X} + \bar{U}_2\right)\mathrm{d}t + \left(R_C D^T + C_1 C_2^T\right) C_1^{-1} \mathrm{d}V_1 \tag{75}$$

$$\mathrm{d}V_1 = \mathrm{d}Y - D\widehat{X}\mathrm{d}t \tag{76}$$

$$J_2 = \lim_{T \to \infty} \frac{1}{T} \int_0^T L_2\left(\widehat{X}, U_2\right)\mathrm{d}t \tag{77}$$

R_C satisfies Riccati equation

$$AR_C + R_C A^T - \left(R_C D^T + C_1 C_2^T\right) C^{-1} \left(DR_C + C_2 C_1^T\right) + C_1 C_1^T = 0 \tag{78}$$

$$U_2^* = -\frac{1}{2} R^{-1} \frac{\mathrm{d}\widehat{H}}{\mathrm{d}\widehat{P}} \frac{\mathrm{d}V}{\mathrm{d}\widehat{H}} \tag{79}$$

$$U^* = U_1 + U_2^* \tag{80}$$

$\dfrac{\mathrm{d}V}{\mathrm{d}H}$ is separately obtained from the dynamical programming equation [4, 13]. Using stochastic averaging, corresponding FPK gives the controlled responses.

9 Control of Hysteretic Structures Using H_α

The equation of motion is written in the form

$$M\ddot{x} + C\dot{x} + K_{eL}x + K_{in}v = DU - ME\ddot{x}_g \tag{81}$$

The Bouc-Wen model relates x and v. The state-space formulation gives [7]

$$\dot{X}_1 = g(X_1) + B_1U + G_1\ddot{X}_g; \quad g(X_1) = \left[\{\dot{x}\} - M^{-1}(c\dot{x} + K_{el}x + K_{in}v)\{\dot{V}\}\right]^T;$$

$$X_1 = [x \quad \dot{x} \quad \dot{v}]^T \tag{82}$$

H_α norm is given by

$$\|TF\| = Sup\frac{\|x_1\|_2}{\|W\|_2} \quad H_\alpha \rightarrow < \gamma \tag{83}$$

The gain matrix K is obtained based on this norm. One of the variants of the K matrix is given by

$$K = K_f\Theta^+ \tag{84}$$

in which K_f is obtained by keeping H_α norm as less than γ and K_f is given by [7]

$$K_f = -R^{-1}S^T + R^{-1/2}\psi(-N_1)^{1/2} \tag{85}$$

Θ^+ is the pseudo-inverse of Θ. ψ is given by

$$\psi = R^{-1/2}S^T\left(I - \Theta^+\Theta\right)(-N_1)^{1/2} \tag{86}$$

$$N_1 = A^TP + PA + \gamma^{-2}PGG^TP + H_1^TH_1 - SR^{-1}S^T + Q < 0 \tag{87}$$

in which P is obtained by solving the Riccati equation $N_1 + Q = 0$

$$R = H_2^TH_2 + \delta I \quad (\delta > 0) \tag{88}$$

$$S = PB + H_1^TH_2 \tag{89}$$

H_1, H_2, etc., are associated with the following linear control problem [7]:

$$\dot{X} = AX + BU + Gw \tag{90}$$

$$Z = H_1 X + H_2 U \tag{91}$$

$$Y = QX \tag{92}$$

$$U = KY = K\Theta X \tag{93}$$

For stochastic disturbance $\ddot{x}_g$, it is expressed as filtered white noise. Solution of the Lyapunov equation is used to obtained the responses

$$LV^T + VL^T + \bar{F} = 0 \tag{94}$$

$$\bar{F}_{ij} = 0 \qquad \text{except} \quad \bar{F}_{last,last} = 2\pi S_0 \tag{95}$$

When filter variables η are included, the following state-space equation results:

$$\dot{\phi} = L\phi + F \tag{96}$$

$$\phi = \left[X, \dot{X}, u, \eta, \dot{\eta}\right]^T; \quad \eta \text{ are filter variables} \tag{97}$$

V represents covariance matrix of ϕ. Iteration is required as L contains K_e, C_e; the elements K_{ei}, C_{ei} require $E(\dot{x}_i v_i)/\sigma v_i$ to be known. Note that K_e and C_e appear because of the linearization form of Bouc-Wen model as

$$v = -K_e v - C_e \dot{x} \tag{98}$$

10 Semiactive Stochastic Control with MR Damper

For semiactive control of structure with MR damper, the control force is split into [12]

$$\begin{aligned} U_r(Q,P) &= U_r(Q,P) + U_{ra}(Q,P) \\ &= -c_r b_{ir} \dot{Q}_i - F_r \mathrm{sgn}\left(b_{ir}\dot{Q}_i\right) \\ &= -c_r b_{ir} \dot{Q}_i - c_{ra} V_{re}^{\infty} \mathrm{sgn}\left(b_{ir}\dot{Q}_i\right) \end{aligned}$$

$$\text{in which} \quad \dot{Q} = \frac{\mathrm{d}H''}{\mathrm{d}P_i}, \quad \dot{P}_i = -\frac{\mathrm{d}H''}{\mathrm{d}Q_i} - c''_{ij}\frac{\mathrm{d}H''}{\mathrm{d}P_j} + b_{ir}U_{ra} + f_{ik}\xi_k \tag{100}$$

H'' and C'' are the Hamiltonian and damping coefficients modified by the conservative and dissipative part of the passive control of MR dampers $\left(U_{rp}\right)$. If $\xi(t)$ is the

Gaussian white noise with intensities $2D_{ke}$, then Eq. (100) can be converted into a Ito differential equation by adding Wong-Zakai correction $D_{kl}f_{je}\dfrac{\partial f_{ik}}{\partial P_j}$.

Once modified Hamiltonian with overall conservative force $-\partial H/\partial Q_i$ and dissipative force $-c_{ij}\partial H/\partial P_j$ are obtained, rest of the formulation remains the same as that given before. The state equation takes the form

$$\mathrm{d}Q_i = \frac{\mathrm{d}H}{\mathrm{d}P_i}\mathrm{d}t \tag{101}$$

$$\mathrm{d}P_i = -\left[\frac{\mathrm{d}H}{\mathrm{d}Q_i} + c_{ij}\frac{\mathrm{d}H}{\mathrm{d}P_j} - b_{ir}U_{ra}\right]\mathrm{d}t + \bar{\sigma}_{ik}\mathrm{d}B_k \tag{102}$$

with $\bar{\sigma}\bar{\sigma}^T = 2fDf^T$.

The control force U_{ra} is given by [12]

$$U_{ra}^* = -\frac{1}{2R_{rr}}\frac{\partial V}{\partial H_i}\left|b_{ir}\dot{Q}_i\right|\mathrm{sgn}\left(b_{ir}\dot{Q}_i\right) \tag{103}$$

in which V is the value function of the dynamic programming and R_{rr} is a positive definite diagonal matrix.

11 Application Problems

Three application problems on stochastic active and semiactive control are presented here which use some of the above control methods. These applications include both linear and nonlinear control problems.

11.1 Nonlinear Semiactive Stochastic Control of Hysteretic Column Using MR Damper

The MR damper is modeled by Bouc-Wen model. The same model is used for hysteretic behavior of the column also [12]

$$\dot{Z}_i = A_i\dot{X} - \beta_i\dot{X}|Z_i|^{n_i} - \gamma_i\left|\dot{X}\right|Z_i|Z_i|^{n_i-1} \tag{104}$$

in which Z_i denotes the hysteretic force and $\dot{X}$ denotes the relative velocity between the two ends of the damper.

The damper force is given by

$$F = c_1\dot{x} + \alpha_1 Z_i \tag{105}$$

Both α_1 and c_1 are functions of filtered voltage u, i.e.,

$$c_1 = c_p + c_s u \quad \alpha_1 = \alpha_p + \alpha_s u \tag{106}$$

c_p, c_s, etc., are constants, and filtered voltage u is determined from applied voltage v as [3]

$$\dot{u} = -\eta(u - v) \tag{107}$$

The damper force can be split in two parts

$$F_p = c_p\dot{x} + \alpha_p Z_i \tag{108}$$

$$F_s = (c_s\dot{x} + \alpha_s Z_i)u \tag{109}$$

F_p is the passive part, and F_s is the semiactive part depending on the filtered voltage u. Integration of Eq. (107) gives

$$u = e^{-\eta t}\int_0^t v\mathrm{d}e^{nt}; \quad v \geq 0 \quad \text{denotes clippings} \tag{110}$$

The equation of motion of the column is given by

$$\ddot{X} + 2\xi\dot{X} + [\alpha - k_1 - k_2\eta(t)]X + (1 - \alpha)Z_1 = \xi(t) - F \tag{111}$$

$\xi(t)$ and $\eta(t)$ are horizontal and vertical random ground acceleration acting as external and parametric excitations. They are Gaussian white noise with intensities of $2D_1$ and $2D_2$, respectively. Restoring force of the column is modeled by the same Bouc-Wen model.

To apply the stochastic averaging method of energy envelop, the hysteretic forces are to be separated as nonlinear elastic forces and nonlinear damping forces.

After doing this, equation is replaced by the following non hysteretic system [3]

$$\begin{aligned}\ddot{X} + \left[C + 2\xi_1(H) + 2\xi_{2p}(H)\right]\dot{X} + \mathrm{d}U(X)/\mathrm{d}X \\ = \xi(t) + k_2 X\eta(t) - \left[(c_s + 2\xi_{2s}(H))\dot{X} + \mathrm{d}U_{2s}(X)\right]u\end{aligned} \tag{112}$$

$$H = \frac{\dot{X}^2}{2} + U(X) \tag{113}$$

The nonlinear damping coefficients $2\xi_1$ and $2\xi_{2p}$ are related to the areas of hysteretic loop. The Ito equation finally takes the form

$$\mathrm{d}H = \left\{ m(H) - \left\langle \left[(c_s + 2\xi_{2s}(H)) \left(\frac{\mathrm{d}H}{\mathrm{d}\dot{X}} \right)^2 + \frac{\mathrm{d}U_2}{\mathrm{d}X} \right] u \right\rangle \right\} + \sigma(H)\mathrm{d}B(t) \tag{114}$$

The optimal filtered voltage is given by

$$u^* = \frac{1}{2R}[c_s + 2\xi_{2s}(H)] \frac{\mathrm{d}V}{\mathrm{d}H} \tag{115}$$

Optimal semiactive control force

$$F_s^* = \frac{1}{2R}\left(c_s\dot{X} + \alpha_s Z_i\right)[c_s + 2\xi_{2s}(H)] \frac{\mathrm{d}V}{\mathrm{d}H} \tag{116}$$

A suitable value of R may be selected along with $g(H)$ so that $\mathrm{d}V/\mathrm{d}H \geq 0$ $\frac{\mathrm{d}V}{\mathrm{d}H}$ is obtained from the dynamic programming equation. Solution of the corresponding FPK equation gives the controlled responses.

11.2 Stochastic Control by MR-TLCD for Controlling Wind-Induced Vibration

The equation of motion of the MR-TLCD can be written as [5]

$$m_D\ddot{y} + u(\dot{y}) + k_D y = -\lambda m_D \ddot{y}_0 \tag{117}$$

in which $m_D = \rho A_D L_D, k_D = 2\rho g A_D, \lambda = \frac{B_D}{L_D}, B_D$ is the width of the tube and L_D is the effective fluid length. Magnetic field passes across the bottom part of the tube over length L_p. The damping force can be split into passive and semiactive parts:

$$u(\dot{y}) = u_p(\dot{y}) + u_s(\dot{y}) \tag{118}$$

$$u_p(\dot{y}) = \frac{1}{2}\rho\delta A_D \dot{y}^2 \mathrm{sgn}(\dot{y}) \tag{119}$$

$$u_s(\dot{y}) = \tau_y \left(cA_D \frac{L_p}{h} \right) \mathrm{sgn}(\dot{y}) \tag{120}$$

in which h is the depth of flow between the fixed poles.

$$\delta = \frac{48}{R_c \left(1 + \frac{H}{W} \right)^2} \frac{L_D}{H} + \sum \xi_i \tag{121}$$

δ is the overall head loss coefficient; W is the width of the flow; H is the depth of tube; R_c is Reynolds's number; $\sum \xi_i$ is the coefficient of minor head losses.

The equation of motion of the MR-TLCD fitted building in state space is given by

$$\dot{Z} = AZ + F(t) + U \tag{122}$$

A is an appropriate matrix consisting of A_L and A_N. A_N contains a C_{eq} (equivalent linearized damping) term given by [5]

$$C_{eq} = \zeta^{\delta} A_D \sqrt{\frac{2E[\dot{y}]^2}{\pi}} \tag{123}$$

$$U = -Bu_s(\dot{y}) \tag{124}$$

Semiactive part of the control force is obtained through dynamic programming. If LQR is used, the Lagrangian L and value function V are represented such that the control damping face u_s becomes Riccati solution based. It is given as

$$u_s = R^{-1}B^T PZ \tag{125}$$

$$u_s^* = \begin{cases} F^* \text{sgn}(\dot{y}) & F^* \geq 0 \\ 0 & F^* \leq 0 \end{cases} \tag{126}$$

$$\text{with} \quad F^* = R^{-1}B^T PZ\text{sgn}(\dot{y}) \tag{127}$$

The solution of the equation of motion is obtained using spectral analysis. A statistical linearization is required to obtain the solutions as described by Eq. (123).

11.3 Stochastic Control of Coupled Structures Under Random Excitation

For the coupled buildings (shear type) under lateral excitation and the control forces through n number of interconnected control devices, equations of motion are represented as

$$M_1\ddot{x}_1 + C_1\dot{x}_1 + K_1x_1 = -\ddot{x}_g M_1E_1 + P_1U \tag{128}$$

$$M_2\ddot{x}_2 + C_2\dot{x}_2 + K_2x_2 = -\ddot{x}_g M_2E_2 + P_2U \tag{129}$$

in which $\ddot{x}_g$ is the random ground motion which is modeled as Gaussian process and having Kanai Tajimi PSDF. Other vector and matrices are self-explanatory.

Assuming the system to be fully observed and making use of modal transformation, the modal equations take the form

$$\ddot{q}_{1i} + 2\zeta_{1i}\omega_{1i}\dot{q}_{1i} + \omega_{1i}^2 q_{1i} = -\beta_{1i}\ddot{x}_g(t) + v_{1i} \quad (i = 1 \cdot \cdots \cdot m_3) \tag{130}$$

$$\ddot{q}_{2i} + 2\zeta_{2i}\omega_{2i}\dot{q}_{2i} + \omega_{2i}^2 q_{2i} = -\beta_{2i}\ddot{x}_g(t) + v_{2i} \quad (i = 1 \cdot \cdots \cdot m_4) \tag{131}$$

The Hamiltonian in modal coordinate system is

$$\bar{H}_j = \sum H_{ji} \tag{132}$$

$$\text{where} \quad H_{ji} = \left(\dot{q}_{ji}^2 + \omega_{ji}^2 q_{ji}^2\right)/2 \tag{133}$$

The Ito stochastic differential equation for modal vibrational energy after stochastic averaging method is given by [10]

$$\mathrm{d}\bar{H} = \left[\bar{m}(\bar{H}) + \left\langle \frac{\mathrm{d}\bar{H}}{\mathrm{d}Q}\bar{U}_i \right\rangle_t\right]\mathrm{d}t + \bar{\sigma}(\bar{H})\mathrm{d}\bar{w}(t) \tag{134}$$

$$\text{in which} \quad \bar{m} = [\bar{m}_1, \bar{m}_2]^T = [m_{11}, m_{12} \cdot \cdots \cdot m_{21}, m_{22} \cdot \cdots \cdot]^T \tag{135}$$

$$\bar{\sigma} = \mathrm{diag}\{\bar{\sigma}_1, \bar{\sigma}_2\} = \mathrm{diag}\{\sigma_{11}, \sigma_{12} \cdot \cdots \cdot \sigma_{21}, \sigma_{22} \cdot \cdots \cdot\}^T \tag{136}$$

$$\bar{\omega} = [\omega_{11}, \omega_{12} \cdot \cdots \cdot \omega_{21}, \omega_{22} \cdot \cdots \cdot]^T \tag{137}$$

$$\bar{m}_{1i}(\bar{H}_{1i}) = -2\zeta_{1i}\omega_{1i}H_{1i} + \frac{1}{2}\beta_{1i}^2 S_g(\omega_{1i}) \tag{138}$$

$$\bar{n}_{2i}(\bar{H}_{2i}) = -2\zeta_{2i}\omega_{2i}H_{2i} + \frac{1}{2}\beta_{2i}^2 S_g(\omega_{2i}) \tag{139}$$

$$\bar{\sigma}_{1i}^2(\bar{H}_{1i}) = \beta_{1i}^2 \bar{H}_{1i} S_g(\omega_{1i}); \quad \bar{\sigma}_{2i}^2(\bar{H}_{2i}) = \beta_{2i}^2 \bar{H}_{2i} S_g(\omega_{2i}) \tag{140}$$

Using dynamic programming technique, the optimal control force vector is given by [10]

$$U^* = -\frac{1}{2}R_p^{-1}\left(P_1^T\bar{\phi}_1\frac{\partial\bar{H}_1}{\partial\dot{\bar{Q}}_1}\frac{\partial V}{\partial\bar{H}_1} + P_2^T\bar{\phi}_2\frac{\partial\bar{H}_2}{\partial\dot{\bar{Q}}_2}\frac{\partial V}{\partial\bar{H}_2}\right) \tag{141}$$

The solution of value function provides $\dfrac{\mathrm{d}V}{\mathrm{d}\bar{H}_i}$

Substituting for U^* and performing stochastic averaging leads to

$$\mathrm{d}\bar{H} = [m(\bar{H}) + m_u(\bar{H})]\mathrm{d}t + \sigma(\bar{H})\mathrm{d}w(t) \tag{142}$$

in which

$$m_{u1} = -\frac{1}{2}\left\{\phi_{11}^T P_u \phi_{11} \bar{H}_{11} \frac{\partial V}{\partial \bar{H}_{11}} \cdots\cdots \phi_{1m3}^T P_u \phi_{1m3} \bar{H}_{1m3} \frac{\partial V}{\partial \bar{H}_{1m3}}\right\}^T \tag{143}$$

$$m_{u2} = -\frac{1}{2}\left\{\phi_{21}^T P_u \phi_{21} \bar{H}_{21} \frac{\partial V}{\partial \bar{H}_{21}} \cdots\cdots \phi_{2m4}^T P_w \phi_{2m4} \bar{H}_{2m4} \frac{\partial V}{\partial \bar{H}_{2m4}}\right\}^T \tag{144}$$

$$P_u = P_1 R_p^{-1} P_1^T \quad P_w = P_2 R_p^{-1} P_2^T \tag{145}$$

12 Conclusions

Stochastic control of structures for environmental excitations is a relatively new area of research. It is also the realistic way of tackling the structural control problems as both environmental excitations and uncertainties associated with the problem are best modeled as stochastic processes. The literature search shows that a number of problems in this area have remained unattempted such as:

1. ANN-based stochastic control of structures
2. Application of fuzzy (stochastic) rule base in developing control algorithms
3. Verification of stochastic control algorithms by real time simulation in on-line control
4. More exhaustive studies on the application of stochastic control using MR and VE dampers
5. Use of different control devices for semiactive and hybrid stochastic control like AMD – TMD, spring-connected MR-TLCD, and base isolated – semiactive dampers, friction damper, and adjacent connectors
6. Stochastic control in post yield state of structures
7. Stochastic control in aeroelastic vibrations of structures
8. Application in the vibration control of offshore structures
9. Application in the vibration control of bridges
10. Stability analysis/robustness of stochastic control strategies

References

1. Ariaratnam ST, Loh NK (1968) Optimal control and filtering of linear stochastic systems. Int J Control 7(5):433–445
2. Astrom KJ (1970) Introduction to stochastic control theory. Academic, New York

3. Cheng H, Zhu WQ, Ying ZG (2006) Stochastic optimal semi-active control of hysteretic systems by using a magneto-rheological damper. Smart Mater Struct 15:711–718
4. Fleming WH, Rishel RW (1975) Deterministic and stochastic optimal control. Springer, New York
5. Ni YQ, Ying ZG, Wang JY, Ko JM, Spencer BF Jr (2004) Stochastic optimal control of wind-excited tall buildings using semi-active MR-TLCDs. Probab Eng Mech 19:269–277
6. Qiao F, Zhu MQ, Liu J, Zhang F (2004) Adaptive observer-based non-linear stochastic system control with sliding mode schemes. J Syst Control Eng 222(1):681–690
7. Sadek F, Ftima MB, El-Borgi S, McCormick J, Riley MA (1994) Control of hysteretic structures using H∞ algorithm and stochastic linearization techniques. J Sound Vib 210(5):540–548
8. Sajeeb R, Manohar CS, Roy D (2007) Use of particle filters in active control algorithm for noisy nonlinear structural dynamical systems. J Sound Vib 306:111–135
9. Seinfeld JH (1970) Optimal stochastic control of nonlinear systems. AICHE J 16:1016–1022
10. Ying ZG, Ni YQ, Ko JM (2004) Non-linear stochastic optimal control for coupled-structures system of multi-degree-of-freedom. J Sound Vib 274:843–861
11. Ying ZG, Zhu WQ (2008) A stochastic optimal control strategy for partially observable nonlinear quasi-Hamiltonian systems. J Sound Vib 310:184–196
12. Ying ZG, Zhu WQ (2003) A stochastic optimal semi-active control strategy for ER/MR dampers. J Sound Vib 259(1):45–62
13. Yong JM, Zhou XY (1999) Stochastic control, Hamiltonian systems and HJB equations. Springer, New York
14. Zhu WQ, Ying ZG (2002) Nonlinear stochastic optimal control of partially observable linear structures. Eng Struct 24:333–342

Uncertainties in Interpreting the Scale Effect of Plate Load Tests in Unsaturated Soils

Sai K. Vanapalli and Won Taek Oh

Abstract The applied stress versus surface settlement (*SVS*) behavior from in situ plate load tests (*PLT*s) is valuable information that can be used for the reliable design of shallow foundations (*SF*s). In situ *PLT*s are commonly conducted on the soils that are typically in a state of unsaturated condition. However, in most cases, the influence of matric suction is not taken into account while interpreting the *SVS* behavior of *PLT*s. In addition, the sizes of plates used for load tests are generally smaller in comparison to real sizes of footings used in practice. Therefore, in situ *PLT* results should be interpreted taking account of not only matric suction but also the scale effects. In the present study, discussions associated with the uncertainties in interpreting the *SVS* behavior of *PLT*s taking account of matric suction and scale effects are detailed and discussed.

Keywords Plate load test • Unsaturated soil • Matric suction • Shallow foundation • Bearing capacity • Settlement

1 Introduction

Bearing capacity and settlement are two key parameters required in the design of foundations. There are several techniques available today to determine or estimate both the bearing capacity and settlement behavior of foundations based on experimental methods, in situ tests, and numerical models including finite element analysis. In addition, there are different ground improvement methods to increase the bearing capacity and reduce the settlements. However, in spite of these advancements, various types of damages still can be caused to the superstructures placed on shallow foundations (hereafter referred to as *SF*s) due to the problems

S.K. Vanapalli (✉) • W.T. Oh
Civil Engineering Department, University of Ottawa, Ottawa, ON, Canada
e-mail: vanapall@eng.uottawa.ca; oh.wontaek@gmail.com

S. Chakraborty and G. Bhattacharya (eds.), *Proceedings of the International Symposium on Engineering under Uncertainty: Safety Assessment and Management (ISEUSAM - 2012)*,
DOI 10.1007/978-81-322-0757-3_7,

associated with the settlements leading to cracks, tilts, differential settlements, or displacements. This is particularly true for coarse-grained soils such as sands in which foundation settlements occur quickly after construction. Due to this reason, the settlement behavior is regarded as a governing parameter in the design of *SF*s in coarse-grained soils [25, 26, 34]. Foundation design codes suggest restricting the settlement of *SF*s placed in coarse-grained soils to 25 mm and also limit their differential settlements (e.g., [13]). Such design code guidelines suggest that the rational design of *SF*s can be achieved by estimating the applied stress versus surface settlement (hereafter referred to as *SVS*) behavior of *SF*s reliably instead of estimating the bearing capacity and settlement separately.

The most reliable testing method to estimate the *SVS* behaviors of *SF*s is in situ plate load tests (hereafter referred to as *PLTs)*. In situ *PLT*s are commonly performed on the soils that are typically in a state of unsaturated condition. This is particularly true in arid or semiarid regions where the natural groundwater table is deep. Hence, the stresses associated with the constructed infrastructures such as *SF*s are distributed in the zone above the groundwater table, where the pore water pressures are negative with respect to the atmospheric pressure (i.e., matric suction). Several researchers showed that the *SVS* behaviors from model footings [35, 40, 42, 45] or in situ *PLTs* [16, 39] are significantly influenced by matric suction. However, in most cases, the in situ *PLT* results are interpreted without taking account of the negative pore water pressure above groundwater table. In other words, the influence of capillary stress or matric suction toward the *SVS* behavior is ignored in engineering practice. Moreover, the *PLT*s are generally conducted with small sizes of plates (either steel or concrete) in comparison to the real sizes of foundations. Due to this reason, the scale effect has been a controversial issue in implementing the *PLT* results into the design of *SF*s. These details suggest that the reliability of the design of *SF*s based on the *PLT* results can be improved by taking account of the influence of not only matric suction but also plate size on the *SVS* behaviors.

In this present study, two sets of in situ plate and footing load test results in unsaturated sandy and clayey soils available in the literature are revisited. Based on the results of these studies, an approach is presented such that the uncertainties associated with the scale effects are reduced or eliminated. In addition, discussions on how to interpret the in situ *PLT* results taking account of matric suction are also presented and discussed. Moreover, a methodology to estimate the variation of *SVS* behavior with respect to matric suction using finite element analysis (hereafter referred as *FEA*) is introduced.

2 Plate Load Test

In situ *PLT*s are generally conducted while designing *SF*s [3] or pavement structures [4, 5, 11] to estimate the reliable design parameters (i.e., bearing capacity and displacement) or to confirm the design assumptions. Figure 1 shows typical "applied stress" versus "surface settlement" (*SVS*) behavior from a *PLT*. The peak

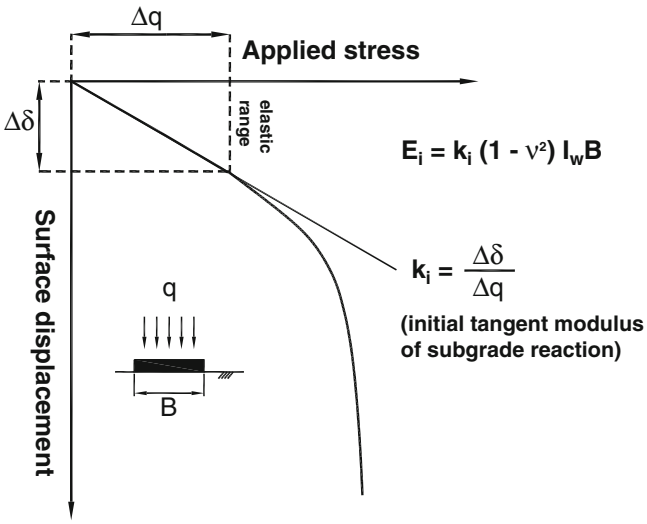

Fig. 1 Typical stress versus displacement behavior from plate load test

stress is defined as ultimate bearing capacity, q_{ult}, for general failure; however, in the case where well-defined failure is not observed (i.e., local or punching failure), the stress corresponding to the 10% of the width of a foundation (ASTM D1194-94) or the stress corresponding to the intersection of elastic and plastic lines of the *SVS* behavior is regarded as q_{ult} [16, 42, 48].

The elastic modulus can be estimated based on the modulus of subgrade reaction, k, that is a slope of *SVS* behavior (i.e., δ versus q) using the theory of elasticity as shown in Eq. (1). The maximum elastic modulus (i.e., initial tangent elastic modulus, E_i) can be computed using the k_i value in the elastic range of *SVS* behavior (initial tangent modulus of subgrade reaction):

$$E = \frac{(1 - v^2)}{(\delta/q)} B I_w = k(1 - v^2) I_w B \tag{1}$$

where E = elastic modulus, v = Poisson's ratio, δ, q = settlement and corresponding stress, B = width (or diameter) of bearing plate, I_w = factor involving the influence of shape and flexibility of loaded area, and k = modulus of subgrade reaction.

Ultimate bearing capacity, q_{ult}, and elastic modulus, E, estimated based on the *SVS* behavior from a *PLT* are representative of soils within a depth zone which is approximately 1.5*B*–2.0*B* [38]. Agarwal and Rana [1] performed model footing tests in sands to study the influence of groundwater table on settlement. The results of the study showed that the settlement behavior of relatively dry sand is similar to that of sand with a groundwater table at a depth of 1.5*B* below the model footing. These results indirectly support that the increment of stress due to the load applied

on the model footing is predominant in the range of 0–1.5*B* below model footing. These observations are also consistent with the modeling studies results by Oh and Vanapalli [31]. This fact also indicates that the *SVS* behavior from *PLT* is influenced by plate (or footing) size since different plate sizes result in different sizes of stress bulbs and mean stresses in soils. This phenomenon which is conventionally defined as "scale effect" needs to be investigated more rigorously to rationally design the shallow foundations.

3 Scale Effect in Plate Load Test

3.1 Scale Effect and Critical State Line

The Terzaghi's bearing capacity factor, N_γ, decreases with an increase in the width of footings [18]. Various attempts have been made by several researchers to understand the causes of scale effects. Three main explanations for the scale effect that generally accepted are as follows:

1. Reduction in the internal friction angle, ϕ', with increasing footing size (i.e., nonlinearity of the Mohr–Coulomb failure envelop) [7, 18, 21]
2. Progressive failure (i.e., different ϕ' along the slip surfaces below a footing) [43, 49]
3. Particle size effect (i.e., the ratio of soil particles to footing size) [41, 43]

According to Hettler and Gudehus [21], there is lack of consistent theory to explain the progressive failure mechanism in the soils below different sizes of footings. In addition, the particle size effect for the in situ plate (or footing) load test (hereafter the term "plate" is used to indicate both steel plate and concrete footing) can be neglected since the ratio of plate size, *B* to d_{50} (i.e., grain size corresponding to 50% finer from the grain size distribution curve), for in situ *PLT*s are mostly greater than 50–100 [24]. The focus of the present study is to better understand the scale effects of *PLT* results and suggest some guidelines of how they can be used in practice.

The reduction in ϕ' with an increasing footing size is attributed to the fact that the larger footing size contributes to a higher mean stress in the soils. In other words, the larger footing induces higher mean stress that contributes to lower ϕ' due to the nonlinearity of the Mohr–Coulomb failure envelop when tested rigorously over a large stress range. This phenomenon can be better explained using the critical state concept ([19]; Fig. 2).

In Fig. 2, the points plotted on the lines *a–b*, *c–d*, and *e–f* simulate the following scenarios:

1. Line *a–b*: Different sizes of footings placed at different depths in sand that have the same initial void ratio value, but the distances to the critical state line are different.

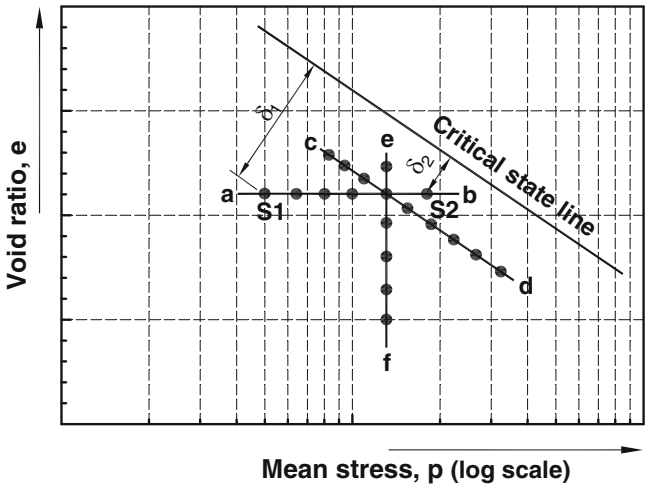

Fig. 2 Relationship between the initial states (i.e., void ratio and mean stress) of soils below footings and critical state line (After Fellenius and Altaee [19])

2. Line *c–d*: Same sizes of footings places at the same depth in sand that have different initial void ratio values, but the distances to the critical state line are the same.
3. Line *e–f*: Different sizes of footings placed at different depths in sands that have different void ratio values, but the distances to the critical state line are the same.

The main concept shown in Fig. 2 is that the behavior of sand below a footing is governed by a distance from the initial state to the critical state line. In other words, the initial states plotted on the line *e–f* will show the same *SVS* behaviors regardless of footing size since the distance to the critical state line for each initial state is the same. On the other hand, the sand below a larger footing (e.g., *S*1 in Fig. 2) will have larger displacement at a certain applied stress in comparison to a smaller footing (e.g., *S*2 in Fig. 2) due to the greater mean stress (i.e., closer to the critical state line) even though the initial void ratio is the same.

3.2 Plate Load Test Results

In this present study, two sets of in situ *PLT*s in sandy and clayey soils available in the literature are revisited to discuss scale effect of *PLT*s.

The Federal Highway Administration (*FHWA*) has encouraged investigators to study the performance of *SF*s by providing research funding. As part of this research project, several series of in situ footing (i.e., 1, 2, 2.5, and 3 m) load tests were conducted on sandy soils. These studies were summarized in a symposium held at the Texas A&M University in 1994 [9] (Fig. 3). Consoli et al. [15]

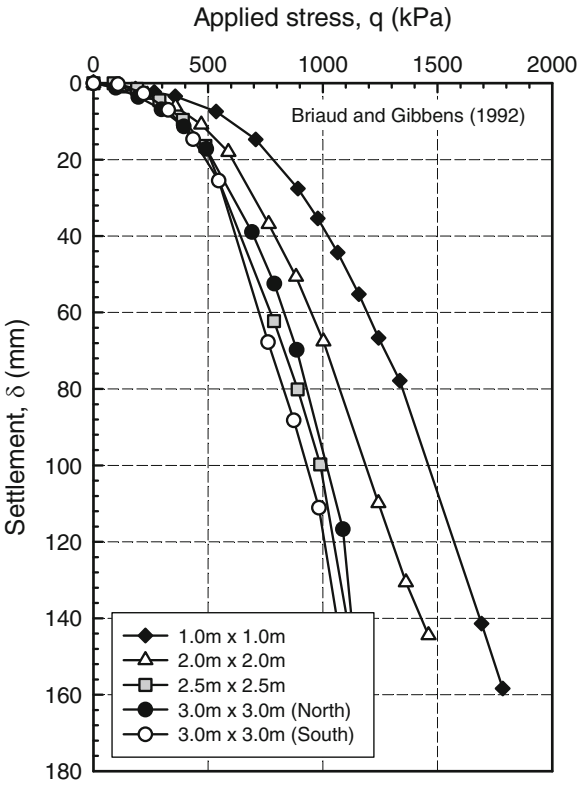

Fig. 3 Stress versus displacement behavior from in situ footing load tests (After Briaud and Gibbens [9])

conducted in situ *PLT*s in unsaturated clayey soils using three steel circular plates (i.e., 0.3, 0.45, and 0.6 m; *PLT*) and three concrete square footings (i.e., 0.4, 0.7, and 1.0 m; *FLT*) (Fig. 4).

As can be seen in Figs. 3 and 4, the bearing capacity increases with decreasing plate size, and different displacement values are observed under different stresses. The *SVS* behaviors clearly show that the *SVS* behavior is dependent of plate size (i.e., scale effect). These observations are consistent with the *SVS* behaviors along the line *a–b* shown in Fig. 2. In other words, the soil below a larger footing induces higher mean stress; therefore, the initial state is closer to the critical state. This phenomenon makes the soil below a larger footing behave as if it is loose soil compared to a smaller footing [12].

3.3 Elimination of Scale Effect of Shallow Foundations

Briaud [8] suggested that scale effect (Fig. 3) can be eliminated by plotting the *SVS* behaviors as "applied stress" versus "settlement/width of footing" (i.e., δ/B) curves

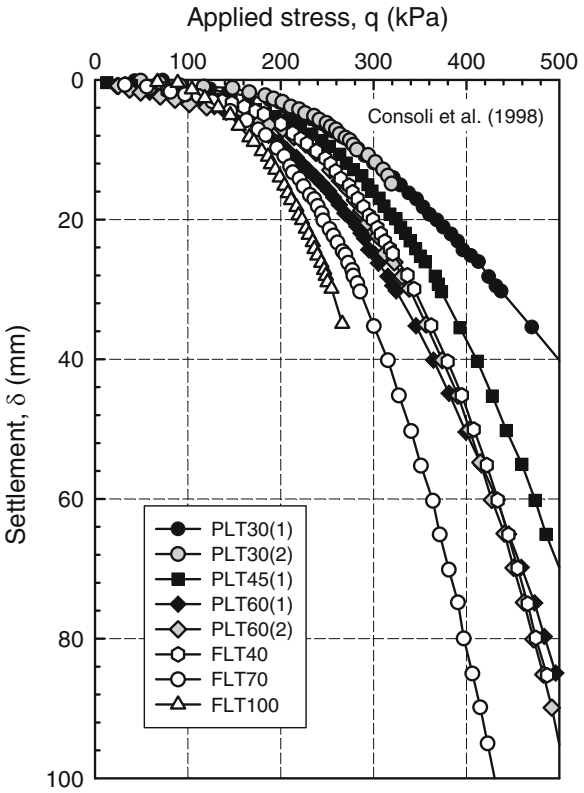

Fig. 4 Stress versus displacement behavior from in situ plate (*PLT*) and footing (*FLT*) load tests (After Consoli et al. [15])

(i.e., normalized settlement; Eq. (2)). Similar trends of results were reported by Osterberg [36] and Palmer [37]:

$$\frac{\delta}{B} = \frac{q(1-v^2)}{E} I_w \tag{2}$$

According to the report published by *FHWA* [10], this behavior can be explained using triaxial test analogy (Fig. 5). If triaxial tests are conducted for identical sand samples under the same confining pressure where the top platens are different sizes of footings, the stress versus strain behaviors for the samples are unique regardless of the diameter of the samples (i.e., the same stress for the same strain). This concept is similar to relationship between q and δ/B from *PLT*s since the term δ/B can be regarded as strain.

Consoli et al. [15] suggested that the scale effect of *PLT*s (Fig. 4) can be eliminated when the applied stress and displacement are normalized with unconfined compressive strength, q_u, and footing width, B, respectively, as shown in Eq. (3). They also analyzed *PLT*s results available in literature [17, 22] and

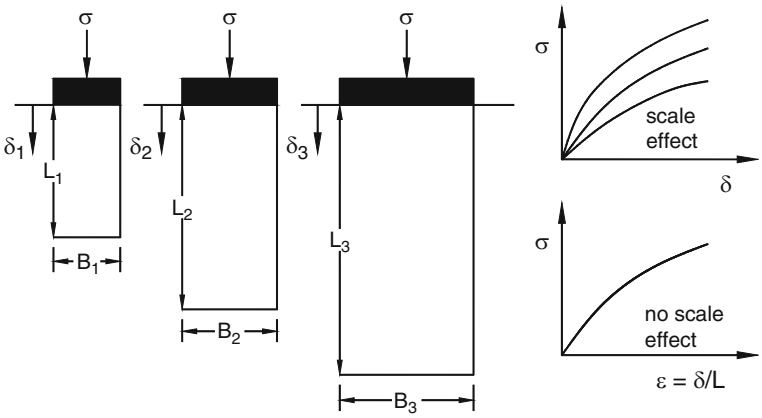

Fig. 5 Triaxial test/shallow foundation analogy [10]

showed that the concept in Eq. (3) can be extended to the *PLT* results in sandy soils as well:

$$\left(\frac{q}{q_u}\right) = \left(\frac{1}{q_u}\right)\left(\frac{E}{1-\nu^2}\right)\left(\frac{1}{C_s}\right)\left(\frac{\delta}{B}\right) = \left\{\frac{C_d}{q_u C_s}\right\}\left(\frac{\delta}{B}\right) \tag{3}$$

where q = applied stress, q_u = unconfined compressive strength at the depth of embedment, δ = surface settlement, B = width of footing, C_s = coefficient involving shape and stiffness of loaded area (I_w in Eq. 1), and C_d = coefficient of deformation ($=E/(1-\nu^2)$).

As can be seen in Figs. 6 and 7, the curves (δ/B versus q) fall in a narrow range. From an engineering practice point of view, these curves can be considered to be unique. Consoli et al. [15] suggested that uniqueness of the normalized curves can be observed at sites where the soils are homogeneous and isotropic in nature.

4 Scale Effect of Plate Size in Unsaturated Soils

The critical state concept discussed above can be effectively used to explain the scale effect of *SF*s in saturated or dry sands. However, this concept may not be applicable to interpret the scale effect of plate size in unsaturated soils since the *SVS* behaviors in unsaturated soils are influenced not only by footing size but also by matric suction value. The influence of matric suction however is typically ignored in conventional engineering practice.

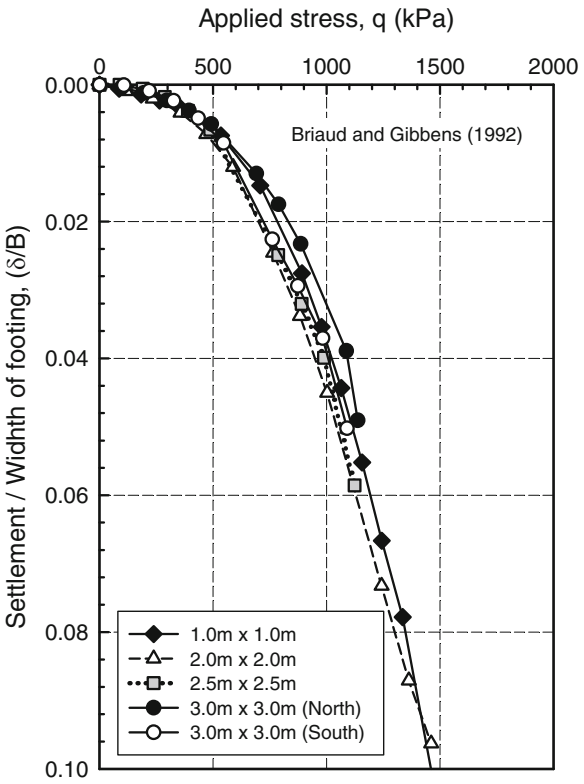

Fig. 6 Normalized in situ footing load test results [9]

4.1 Average Matric Suction Value

Matric suction distribution profile is mostly not uniform with depth in fields. In this case, the concept of "average matric suction" [45] can be used as a representative matric suction value to interpret mechanical properties of a soil at a certain matric suction distribution profile. The average matric suction value, Ψ, is defined as a matric suction value corresponding to the centroid of the suction distribution diagram from 0 to 1.5*B* depth (Fig. 8).

As discussed earlier, the stress increment in a soil due to a load or a stress act on a *SF* is predominant in the range of 0–1.5*B*. Hence, when loads are applied on two different sizes of footings, the sizes of stress bulbs (in the depth zone of 0–1.5*B*) are different (Fig. 9). In other words, the stress bulb for the smaller footing (i.e., B_1) is shallower in comparison to that of the larger footing (i.e., B_2). These facts indicate that the *SVS* behaviors from *PLT*s are governed by *E* and *v* values within the stress bulb. If a matric suction distribution profile is uniform with depth, the average matric suction value is the same regardless of footing size. However, if the matric suction distribution profile is nonuniform, the average matric suction value is dependent on the footing size. For example, the average matric suction value for

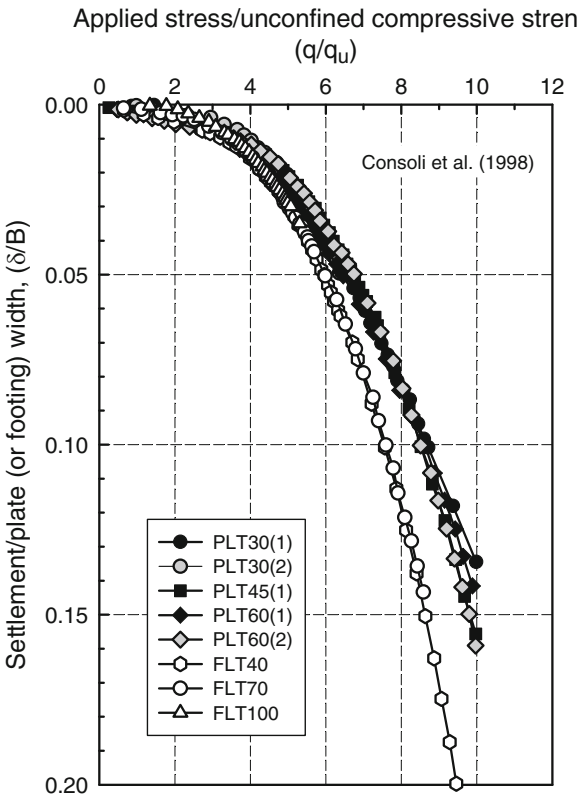

Fig. 7 Normalized in situ plate and footing load test results [15]

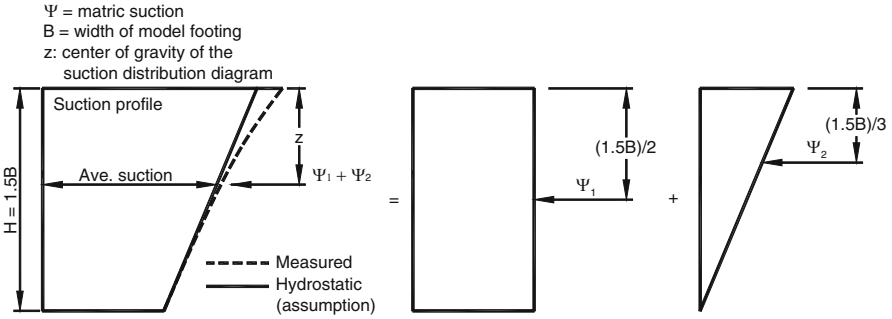

Fig. 8 Estimation of average matric suction value using the centroid of suction distribution diagram

the smaller plate, B_1, (i.e., Ψ_1) is greater than that of larger plate, B_2, (i.e., Ψ_2). In this case, the concept shown in Eqs. (2) and (3) cannot be used to eliminate the scale effect of plate since q_u [29], E_i [34], and v [30, 32, 33] are not constant but vary with respect to matric suction. More discussions are summarized in later sections.

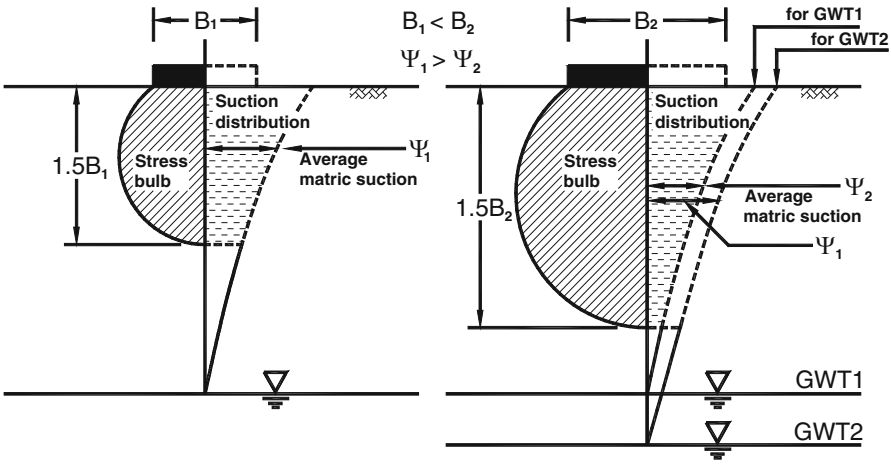

Fig. 9 Average matric suction values for different footing sizes under nonconstant matric suction distribution profile

4.2 *Variation of E_i with Respect to Matric Suction for Coarse-Grained Soils*

Oh et al. [34] analyzed three sets of model footing test results in unsaturated sands [28, 42] and showed that the initial tangent elastic modulus, E_i, is significantly influenced by matric suction. Based on the analyses, they proposed a semiempirical model to estimate the variation of E_i with respect to matric suction using the soil–water characteristic curve (*SWCC*) and the E_i for saturated condition along with two fitting parameters, α and β:

$$E_{i(\text{unsat})} = E_{i(\text{sat})}\left[1 + \alpha \frac{(u_a - u_w)}{(P_a/101.3)}\left(S^{\beta}\right)\right] \tag{4}$$

where $E_{i(\text{sat})}$ and $E_{i(\text{unsat})}$ = initial tangent elastic modulus for saturated and unsaturated conditions, respectively, P_a = atmospheric pressure (i.e., 101.3 kPa), and α, β = fitting parameters.

They suggested that the fitting parameter, $\beta = 1$, is required for coarse-grained soils (i.e., $I_p = 0\%$; *NP*). The fitting parameter, α, is a function of footing size, and the values between 1.5 and 2 were recommended for large sizes of footings in field conditions to reliably estimate E_i (Fig. 10) and elastic settlement (Fig. 11). Vanapalli and Oh [46] analyzed model footing [47], and in situ *PLT* [16, 39] results in unsaturated fine-grained soils and suggested that the fitting parameter, $\beta = 2$, is required for fine-grained soils. The analyses results also showed that the inverse of α (i.e., $1/\alpha$) nonlinearly increases with increasing I_p and the upper and the lower boundary relationship can be used for low and high matric suction values, respectively, at a certain I_p (Fig. 12).

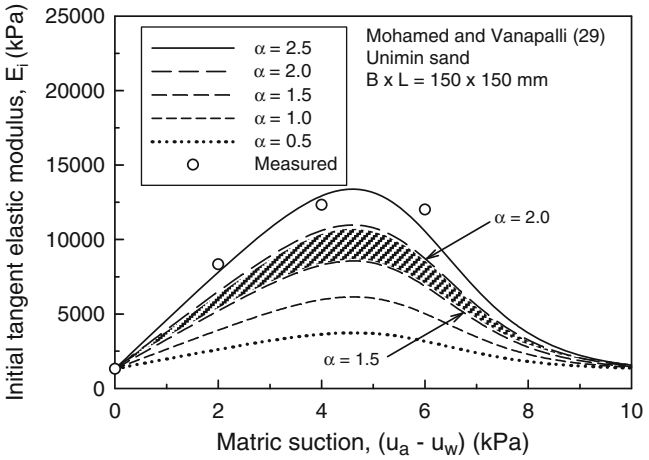

Fig. 10 Variation of modulus of elasticity with the parameter, α, for the 150 mm × 150 mm (Using data from Mohamed and Vanapalli [28])

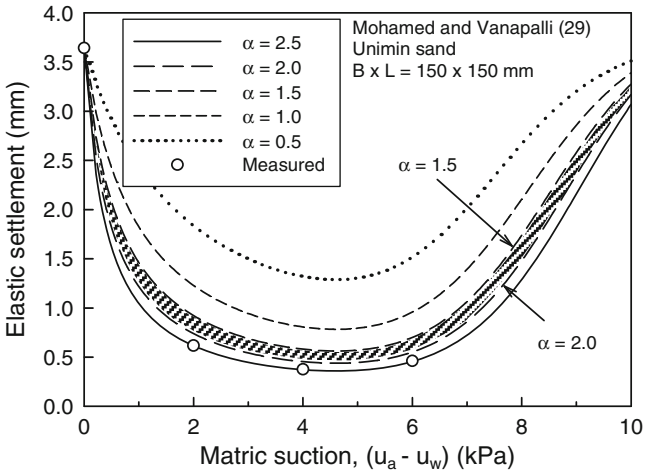

Fig. 11 Variation of elastic settlement with the parameter, α, for the 150 mm × 150 mm footing (Using data from Mohamed and Vanapalli [28])

4.3 Variation of q_u with Respect to Matric Suction for Fine-Grained Soils

Oh and Vanapalli [29] analyzed six sets of unconfined compression test results and showed that the q_u value is a function of matric suction (Figs. 13 and 14). Based on the analyses, they proposed a semiempirical model to estimate the variation of undrained shear strength of unsaturated soils using the *SWCC* and undrained shear

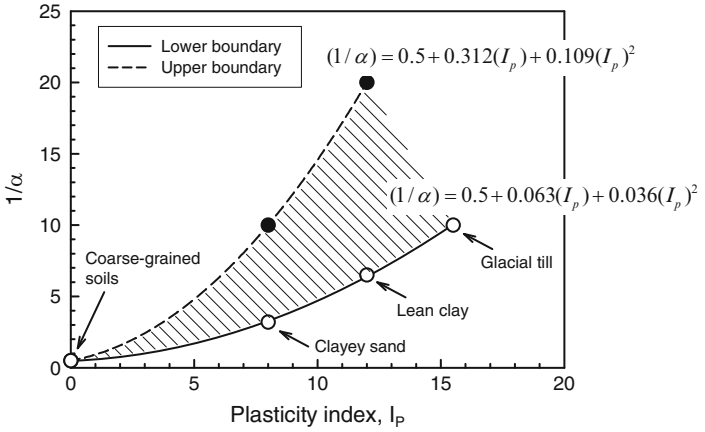

Fig. 12 Relationship between $(1/\alpha)$ and plasticity index, I_p

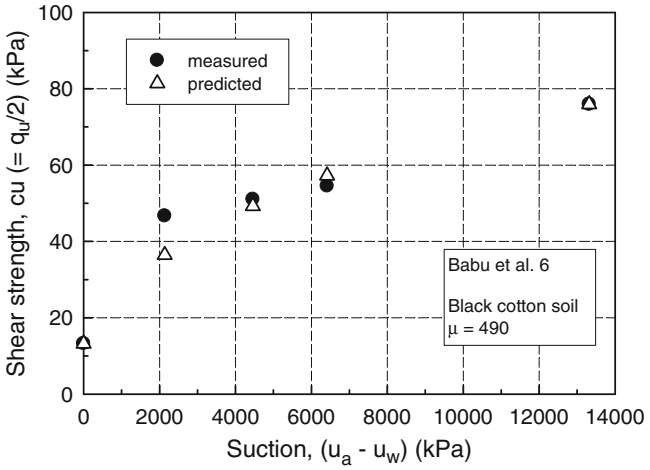

Fig. 13 Comparison between the measured and the estimated shear strength using the data by Babu et al. [6]

strength under saturated condition along with two fitting parameters, v and μ (Eq. 5). Equation (5) is the same in form as Eq. (4):

$$c_{u(unsat)} = c_{u(sat)}\left[1 + \frac{(u_a - u_w)}{(P_a/101.3)}\frac{(S^v)}{\mu}\right] \tag{5}$$

where $c_{u(sat)}$, $c_{u(unsat)}$ = shear strength under saturated and unsaturated condition, respectively, P_a = atmospheric pressure (i.e., 101.3 kPa) and v, μ = fitting parameters.

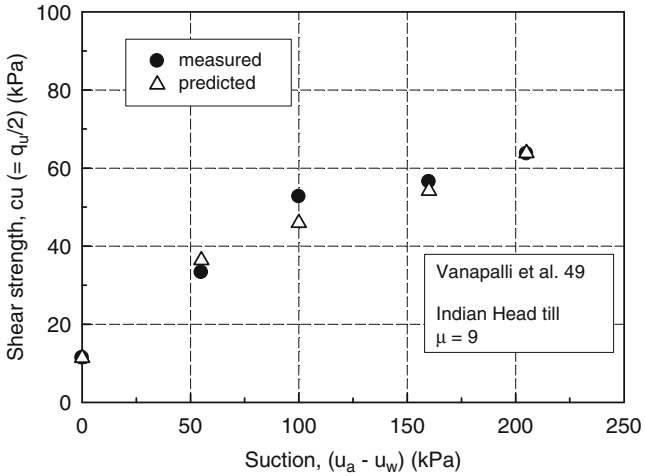

Fig. 14 Comparison between the measured and the estimated shear strength using the data by Vanapalli et al. [47]

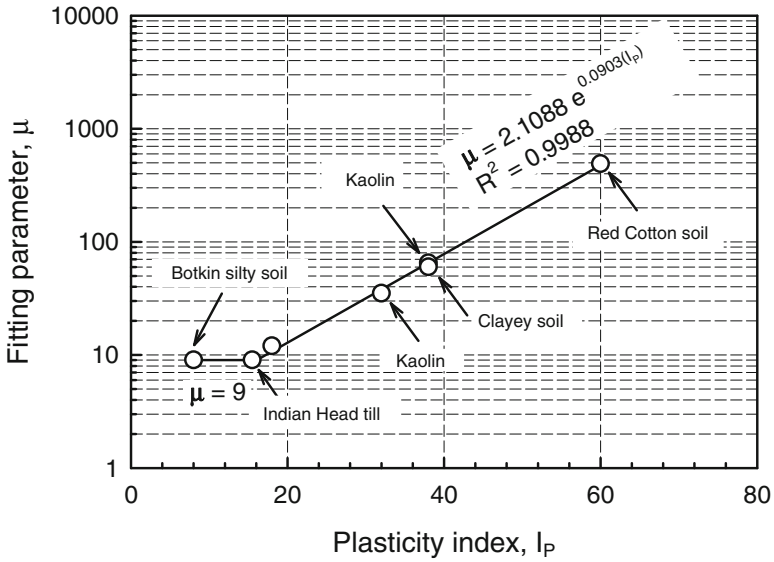

Fig. 15 Relationship between plasticity index, I_p, and the fitting parameter, μ

The fitting parameter, $v = 2$, is required for unsaturated fine-grained soils. Figure 15 shows the relationship between the fitting parameter, μ, and plasticity index, I_p, on semilogarithmic scale for the soils used for the analysis. The fitting parameter, μ, was found to be constant with a value of "9" for the soils that have I_p values in the range of 8 and 15.5%. The value of μ however increases linearly on semilogarithmic scale with increasing I_p.

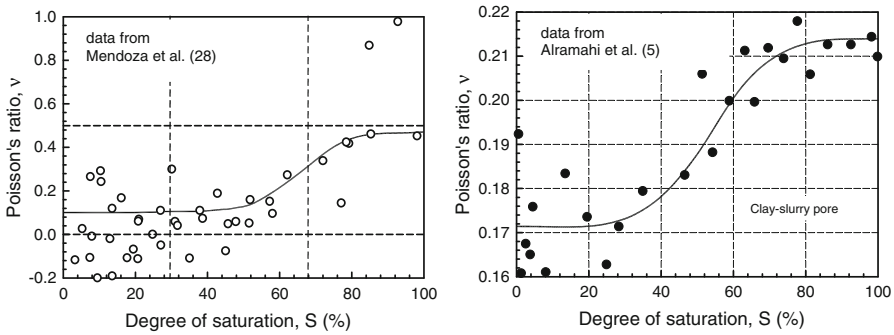

Fig. 16 Variation of Poisson's ratio, v, with respect to degree saturation

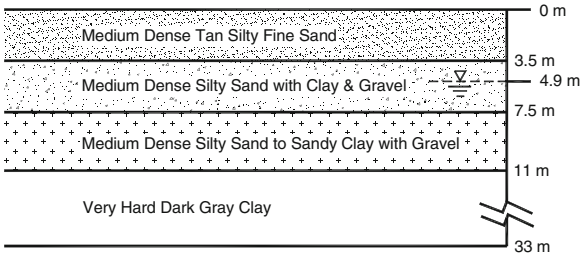

Fig. 17 The average soil profile at the test site (After Briaud and Gibbens [9])

4.4 Variation of v with Respect to Matric Suction

The Poisson's ratio, v, is typically considered to be a constant value in the elastic settlement analysis of soils. This section briefly highlights how v varies with matric suction by revisiting published data from the literature. Mendoza et al. [27] and Alramahi et al. [2] conducted bender element tests to investigate the variation of small-strain elastic and shear modulus with respect to degree of saturation for kaolinite and mixture of glass beads and kaolin clay, respectively. Oh and Vanapalli [33] reanalyzed the results and back calculated the Poisson's ratio, v, with respect to degree of saturation. The analyses of the results show that v is not constant but varies with the degree of saturation as shown in Fig. 16.

5 Reanalysis of Footing Load Test Results in Briaud and Gibbens [9]

The site selected for the in situ footing load tests was predominantly sand (mostly medium dense silty sand) from 0 to 11 m overlain by hard clay layer (Fig. 17). The groundwater table was observed at a depth of 4.9 m, and the soil above the groundwater table was in a state of unsaturated condition. In this case, different

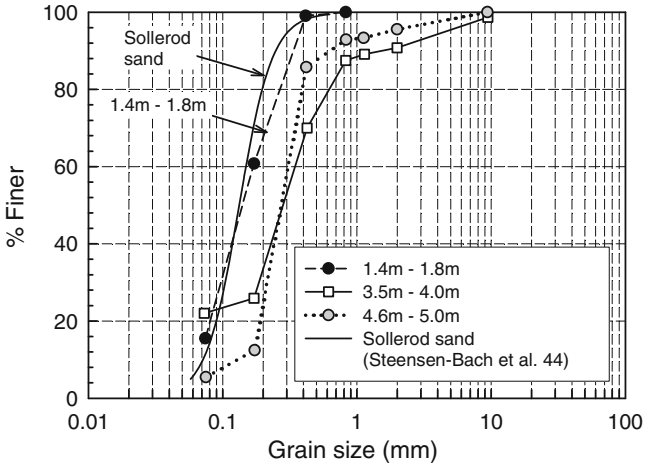

Fig. 18 Grain size distribution curves for the soil samples collected from three different depths [9] and Sollerod sand [42]

Table 1 Summary of the soil properties (From Briaud and Gibbens [9])

Property	Sand (0.6 m)	Sand (3.0 m)
Specific gravity, G_s	2.64	2.66
Water content, w (%)	5.0	5.0
Void ratio, e	0.78	0.75
Effective cohesion, c' (kPa)	0	0
Effective internal friction angle, ϕ' (°)	35.5	34.2

footing sizes may result in different average matric suction values. In other words, scale effect cannot be eliminated with normalized settlement since the soils at the site are not "homogenous and isotropic." Despite this fact, as can be seen in Fig. 6, the *SVS* behaviors from different sizes of footing fall in a narrow range. This behavior can be explained by investigating the variation of matric suction with depth at the site as follows.

Figure 18 shows the grain size distribution curves for the soil samples collected from three different depths (i.e., 1.4–1.8 m, 3.5–4.0 m, and 4.6–5.0 m). The grain size distribution curve the Sollerod sand shown in Fig. 18 is similar to the sand sample collected at the depth of 1.4–1.8 m. The reasons associated with showing the *GSD* curve of Sollerod sand will be discussed later in this chapter. The soil properties used in the analysis are summarized in Table 1.

As shown in Table 1, the water content at the depths of 0.6 and 3.0 m is 5%. This implies that the matric suction value can be assumed to be constant up to the depth of approximately 3.0 m. The field matric suction distribution profile is consistent with the typical matric suction distribution profile above groundwater table for the coarse-grained soils. In other words, matric suction increases gradually (which is close to hydrostatic conditions) up to residual matric suction value and thereafter

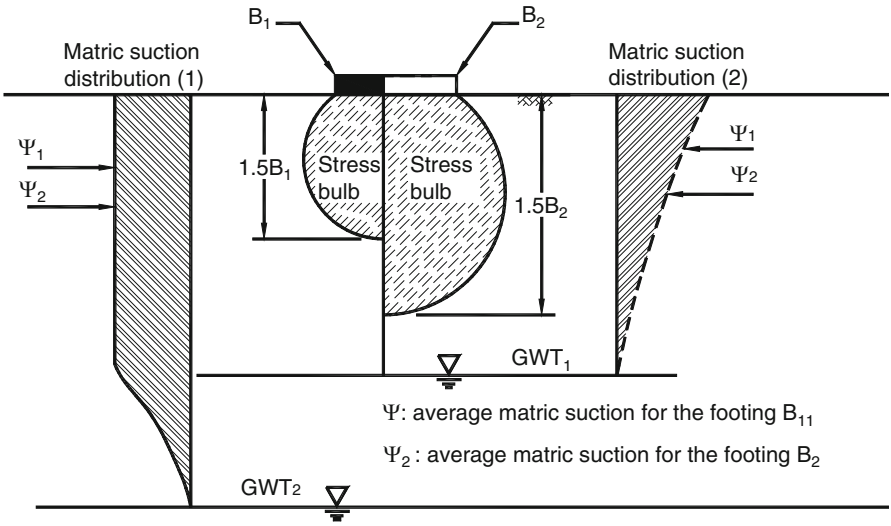

Fig. 19 Average matric suction for different sizes of footing under uniform and nonuniform matric suction distribution

remains close to constant conditions (i.e., matric suction distribution (1) in Fig. 19). This matric suction distribution profile resulted in the same average matric suction value regardless of footing size (for this study). However, it also should be noted that the average matric suction value for each footing can be different if a nonuniform matric suction distribution profile is available below the footings (i.e., matric suction distribution (2) in Fig. 19).

6 Variation of *SVS* Behaviors with Respect to Matric Suction

After construction of *SF*s, the soils below them typically experience wetting–drying cycles due to the reasons mostly associated with the climate (i.e., rain infiltration or evaporation). Hence, it is also important to estimate the variation of *SVS* behaviors with respect to matric suction.

Oh and Vanapalli [32, 33] conducted finite element analysis (*FEA*) using the commercial finite element software SIGMA/W (Geo-Slope 2007; [23]) to simulate *SVS* behavior of in situ footing ($B \times L = 1\text{ m} \times 1\text{ m}$) load test results ([9]; Fig. 3) on unsaturated sandy soils. The *FEA* was performed using elastic–perfectly plastic model [14] extending the approach proposed by Oh and Vanapalli [30]. The square footing was modeled as a circular footing with an equivalent area (i.e., 1.13 m in diameter, axisymmetric problem).

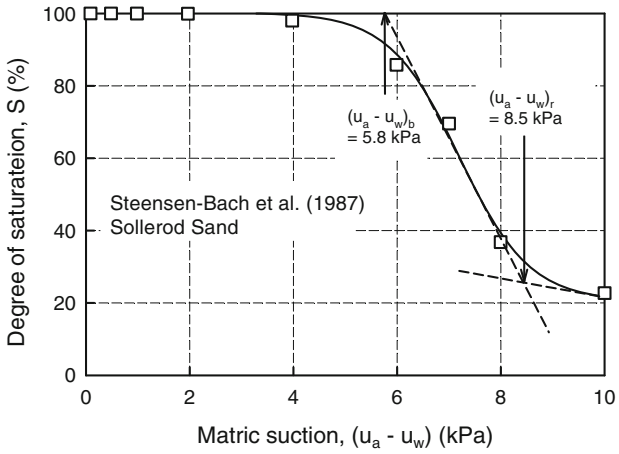

Fig. 20 *SWCC* used for the analysis (Date from Steensen-Bach et al. [42])

The soil–water characteristic curve (*SWCC*) can be used as a tool to estimate the variation of total cohesion, c, (Eq. 6; [44]) and initial tangent elastic modulus, E_i, (Eq. 4) with respect to matric suction:

$$c = c' + (u_a - u_w)(S^{\kappa}) \tan \phi' \tag{6}$$

where c = total cohesion, c' and ϕ' = effective cohesion and internal friction angle for saturated condition, respectively, $(u_a - u_w)$ = matric suction, S = degree of saturation, and κ = fitting parameter ($\kappa = 1$ for sandy soils (i.e. $I_p = 0\%$); [20]).

Information on the *SWCC* was not available in the literature for the site where the in situ footing load test was carried out. Hence, the *SWCC* for the Sollerod sand (Fig. 20) used for the analysis as an alternative based on the following justifications. Among the grain size distribution (hereafter referred as *GSD*) curves shown in Fig. 18, the grain size distribution curve for the range of depth 1.4–1.8 m can be chosen as a representative *GSD* curve since the stress below the footing 1 m × 1 m is predominant in the range of 0–1.5 m (i.e., 1.5*B*) below the footing. This *GSD* curve is similar to that of Sollerod sand (see Fig. 18) used by Steensen-Bach et al. [42] to conduct model footing tests in a sand to understand influence of matric suction on the load carrying capacity. In addition, the shear strength parameters for the Sollerod sand ($c' = 0.8$ kPa and $\phi' = 35.8°$) are also similar to those of the sand where the in situ footing load tests were conducted (see Table 1). The influence of wetting–drying cycles (i.e., hysteresis) and external stresses on the *SWCC* is not taken into account in the analysis due to the limited information.

The variation of *SVS* behavior with respect to matric suction from the *FEA* is shown in Fig. 21. Figure 22a, b shows the variation of settlement under the same stress of 344 kPa and the variation of stress that can cause 25-mm settlement for different matric suction values, respectively. The stress 344 kPa is chosen since the

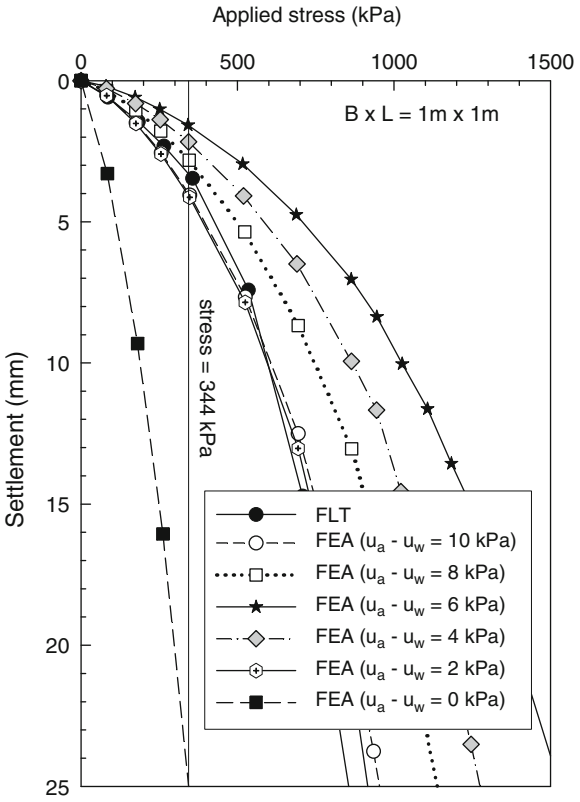

Fig. 21 Variation of *SVS* behavior with respect to matric suction

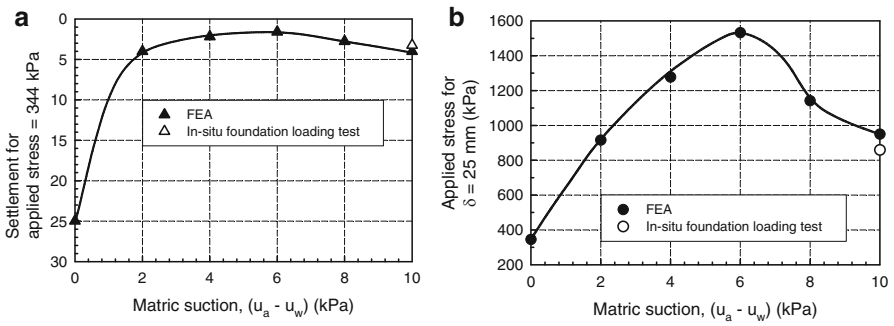

Fig. 22 Variation of (**a**) settlement under the applied stress of 344 kPa and (**b**) stress that can cause 25-mm settlement with respect to matric suction

settlement for saturated condition at this stress is 25 mm. The settlement at the matric suction of 10 kPa (i.e., field condition) is approximately 4 mm and then increases up to 25 mm (i.e., permissible settlement) as the soil approaches saturated conditions under the constant stress (i.e., 344 kPa). The permissible settlement,

25 mm, can be induced at 2.7 times less stress as the soil approaches saturated conditions (i.e., from 10 to 0 kPa). The results imply that settlements can increase due to decrease in matric suction. It is also of interest to note that such a problem can be alleviated if the matric suction of the soil is maintained at 2-kPa value.

7 Summary and Conclusions

Plate load test (*PLT*) is regarded as the most reliable testing method to estimate the applied stress versus surface settlement (*SVS*) behavior of shallow foundations. However, there are uncertainties in interpreting the *PLT* results for soils that are in a state of unsaturated condition. This is mainly attributed to the fact that the *SVS* behavior from the *PLT*s is significantly influenced by both footing size and the capillary stresses (i.e., matric suction). Previous studies showed that the scale effect can be eliminated by normalizing settlement with footing size. This methodology is applicable to the soils that are homogeneous and isotropic with depth in nature such as saturated or dry soils. In case of unsaturated soils, matric suction distribution profile with depth should be taken into account to judge whether or not this methodology is applicable. This is because if the matric suction distribution profile is nonuniform with depth, different plate sizes lead to different average matric suction values. In other words, the soil below the plates cannot be regarded as homogeneous and isotropic since strength, initial tangent elastic modulus, and the Poisson's ratio are function of matric suction. These facts indicate that the reliable deign of shallow foundations based on the *PLT* results can be obtained only when the results are interpreted taking account of the matric suction distribution profile with depth and influence of average matric suction value on the *SVS* behavior.

In case of the shallow foundations resting on unsaturated sandy soils, it is also important to estimate the variation of *SVS* behavior with respect to matric suction. This can be achieved by conducting finite element analysis using the methodology presented in this chapter. According to the finite element analysis for the in situ footing (1 m $\times$ 1 m) load test results discussed in this chapter [9], unexpected problems associated with settlement are likely due to decrease in matric suction. Such a problem can be alleviated if the matric suction of the soil is maintained at a low of 2 kPa.

References

1. Agarwal KB, Rana MK (1987) Effect of ground water on settlement of footing in sand. In: Proceedings of the 9th European conference on soil mechanics and foundation engineering, Dublin, pp 751–754.
2. Alramahi B, Alshibli KA, Fratta D (2010) Effect of fine particle migration on the small-strain stiffness of unsaturated soils. J Geotech Geoenviron Eng 136(4):620–628

3. ASTM D1194-94 (2003) Standard test method for bearing capacity of soil for static load and spread footings. American Society for Testing Materials, Philadelphia
4. ASTM D1195-93 (2004) Standard test method for repetitive static plate load tests of soils and flexible pavement components, for use in evaluation and design of airport and highway pavements. American Society for Testing Materials, Philadelphia
5. ASTM D1196 – 93 (2004) Standard test method for nonrepetitive static plate load tests of soils and flexible pavement components, for use in evaluation and design of airport and highway pavements. American Society for Testing Materials, Philadelphia
6. Babu GLS, Rao RS, Peter J (2005) Evaluation of shear strength functions based on soil water characteristic curves. J Test Eval 33(6):461–465
7. Bolton MD, Lau CK (1989) Scale effects in the bearing capacity of granular soils. In: Proceedings of the 12th international conference of soil mechanics and foundation engineering, vol 2. Balkema Publishers, Rotterdam, pp 895–898
8. Briaud J-L (2007) Spread footings in sand: load settlement curve approach. J Geotech Geoenviron Eng 133(8):905–920
9. Briaud J-L, Gibbens R (1994) Predicted and measured behavior of five large spread footings on sand. In: Proceedings of a prediction symposium, ASCE, GSP41
10. Briaud JL, Gibbens RM (1997) Large scale load tests and data base of spread footings on sand. Publication no. FHWA-RD-97-068. Federal Highway Administration, Washington, DC
11. BS 1377–9:1990 Methods for test for soils for civil engineering purposes. In-situ tests, British Standards Institution, 31 Aug 1990, 70 pp
12. Cerato AB, Lutenegger AJ (2007) Scale effects of shallow foundation bearing capacity on granular material. J Geotech Geoenviron Eng 133(3):1192–1202
13. CFEM (2006) Canadian foundation engineering manual, 4th edn. Canadian Geotechnical Society, Toronto
14. Chen WF, Zhang H (1991) Structural plasticity: theory, problems, and CAE software. Springer, New York
15. Consoli NC, Schnaid F, Milititsky J (1998) Interpretation of plate load tests on residual soil site. J Geotech Geoenviron Eng 124(9):857–867
16. Costa YD, Cintra JC, Zornberg JC (2003) Influence of matric suction on the results of plate load tests performed on a lateritic soil deposit. Geotech Test J 26(2):219–226
17. D'Appolonia DJ, D'Appolonia E, Brisette RF (1968) Settlement of spread footings on sand. J Soil Mech Found Div ASCE 3:735–760
18. De Beer EE (1965) The scale effect on the phenomenon of progressive rupture in cohesionless soils. In: Proceedings of the 6th international conference on soil mechanics and foundation engineering, vol 2(3–6), pp 13–17
19. Fellenius BH, Altaee A (1994) Stress and settlement of footings in sand. In: Proceedings of the conference on vertical and horizontal deformations of foundations and embankments, ASCE, GSP40, College Station, vol 2, pp 1760–1773
20. Garven E, Vanapalli SK (2006) Evaluation of empirical procedures for predicting the shear strength of unsaturated soils. In: Proceedings of the 4th international conference on unsaturated soils, ASCE, GSP147, Arizona, vol 2, pp 2570–2581
21. Hettler A, Gudehus G (1988) Influence of the foundation width on the bearing capacity factor. Soils Found 28(4):81–92
22. Ismael NF (1985) Allowable pressure from loading tests on Kuwaiti soils. Can Geotech J 22(2):151–157
23. Krahn J (2007) Stress and deformation modelling with SIGMA/W. Goe-slope International Ltd.
24. Kusakabe O (1995) Foundations. In: Taylor RN (ed) Geotechnical centrifuge technology. Blackie Academic & Professional, London, pp 118–167
25. Lee J, Salgado R (2001) Estimation of footing settlement in sand. Int J Geomech 2(1):1–28

26. Maugeri M, Castelli F, Massimino MR, Verona G (1998) Observed and computed settlements of two shallow foundations on sand. J Geotech Geoenviron Eng 124(7):595–605
27. Mendoza CE, Colmenares JE, Merchan VE (2005) Stiffness of an unsaturated compacted clayey soil at very small strains. In: Proceedings of the international symposium on advanced experimental unsaturated soil mechanics, Trento, Italy, pp 199–204
28. Mohamed FMO, Vanapalli SK (2006) Laboratory investigations for the measurement of the bearing capacity of an unsaturated coarse-grained soil. In: Proceedings of the 59th Canadian geotechnical conference, Vancouver
29. Oh WT, Vanapalli SK (2009) A simple method to estimate the bearing capacity of unsaturated fine-grained soils. In: Proceedings of the 62nd Canadian geotechnical conference, Hailfax, Canada, pp 234–241
30. Oh WT, Vanapalli SK (2010) The relationship between the elastic and shear modulus of unsaturated soils. In: Proceedings of the 5th international conference on unsaturated soils, Barcelona, Spain, pp 341–346.
31. Oh WT, Vanapalli SK (2011) Modelling the applied vertical stress and settlement relationship of shallow foundations in saturated and unsaturated sands. Can Geotech J 48(3): 425–438
32. Oh WT, Vanapalli SK (2011) Modelling the stress versus displacement behavior of shallow foundations in unsaturated coarse-grained soils. In: Proceedings of the 5th international symposium on deformation characteristics of geomaterials, Seoul, Korea, pp 821–828
33. Oh WT, Vanapalli SK (2012) Modelling the settlement behaviour of in-situ shallow foundations in unsaturated sands. In: Proceedings of the geo-congress 2012 (Accepted for publication)
34. Oh WT, Vanapalli SK, Puppala AJ (2009) Semi-empirical model for the prediction of modulus of elasticity for unsaturated soils. Can Geotech J 46(8):903–914
35. Oloo SY (1994) A bearing capacity approach to the design of low-volume traffics roads. Ph.D. thesis, University of Saskatchewan, Saskatoon, Canada
36. Osterberg JS (1947) Discussion in symposium on load tests of bearing capacity of soils. ASTM STP 79. ASTM, Philadelphia, pp 128–139
37. Palmer LA (1947) Field loading tests for the evaluation of the wheel load capacities of airport pavements. ASTM STP 79. ASTM, Philadelphia, pp 9–30
38. Poulos HD, Davis EH (1974) Elastic solutions for soil and rock mechanics. Wiley, New York
39. Rojas JC, Salinas LM, Seja C (2007) Plate-load tests on an unsaturated lean clay. Experimental unsaturated soil mechanics, Springer proceedings in physics, vol 112, pp 445–452
40. Schanz T, Lins Y, Vanapalli SK (2010) Bearing capacity of a strip footing on an unsaturated sand. In: Proceedings of the 5th international conference on unsaturated soils, Barcelona, Spain, pp 1195–1220.
41. Steenfelt JS (1977) Scale effect on bearing capacity factor N_γ. In: Proceeding of the 9th international conference of soil mechanics and foundations engineering, vol 1. Balkema Publishers, Rotterdam, pp 749–752
42. Steensen-Bach JO, Foged N, Steenfelt JS (1987) Capillary induced stresses–fact or fiction? In: Proceedings of the 9th European conference on soil mechanics and foundation engineering, Dublin, pp 83–89
43. Tatsuoka F, Okahara M, Tanaka T, Tani K, Morimoto T, Siddiquee MSA (1991) Progressive failure and particle size effect in bearing capacity of a footing on sand, GSP27, vol 2, pp 788–802
44. Vanapalli SK, Fredlund DG, Pufahl DE, Clifton AW (1996) Model for the prediction of shear strength with respect to soil suction. Can Geotech J 33(3):379–392
45. Vanapalli SK, Mohamed FMO (2007) Bearing capacity of model footings in unsaturated soils. In: Proceedings of the experimental unsaturated soil mechanics, Springer proceedings in physics, vol 112, pp 483–493

46. Vanapalli SK, Oh WT (2010) A model for predicting the modulus of elasticity of unsaturated soils using the soil-water characteristic curves. Int J Geotech Eng 4(4):425–433
47. Vanapalli SK, Oh WT, Puppala AJ (2007) Determination of the bearing capacity of unsaturated soils under undrained loading conditions. In: Proceedings of the 60th Canadian geotechnical conference, Ottawa, Canada, pp 1002–1009
48. Xu YF (2004) Fractal approach to unsaturated shear strength. J Geotech Geoenviron Eng 130(3):264–273
49. Yamaguchi H, Kimura T, Fuji N (1976) On the influence of progressive failure on the bearing capacity of shallow foundations in dense sand. Soils Found 16(4):11–22

An Approach for Creating Certainty in Uncertain Environment: A Case Study for Rebuilding a Major Equipment Foundation

Abhijit Dasgupta and Suvendu Dey

Abstract The only thing that makes life possible is permanent, intolerable uncertainty; not knowing what comes next – Ursula Le Guin

To the common man, uncertainty is being in doubt or the state of being unsure about something. In scientific parlance, it is the unpredictable difference between the observed data and the model output. Sources of uncertainty may be many including material, manufacturing, environment, experiments, human factors, assumptions and lack of knowledge. Any one of these or a combination may lead to a significant loss of performance, that is, a large variation in output due to a small variation in the input parameters. The human being craves for certainty because the first priority for every individual on this planet is survival and the process of living contains many risks. This chapter deals with the various uncertainties that confronted a team of engineers during the course of rebuilding and upgrading an existing major equipment in an integrated steel plant. There were multiple challenges and uncertainties involved in every step of the rebuilding process.

Keywords Uncertainty • Equipment • Blasting • Shutdown • Rebuilding • Upgradation

1 Introduction

The potentiality of perfection outweighs actual contradictions. Existence in itself is here to prove that it cannot be an evil – Rabindranath Tagore

The terms risk and uncertainty are intertwined and somewhat complex to analyse and differentiate. Risk can be defined as a state of uncertainty where some of the possibilities involve a loss, catastrophe or other undesirable outcome.

A. Dasgupta • S. Dey (✉)
M.N. Dastur & Company (P) Ltd., Kolkata, West Bengal, India
e-mail: Abhijit.DG@dasturco.com; Suvendu.D@dasturco.com

S. Chakraborty and G. Bhattacharya (eds.), *Proceedings of the International Symposium on Engineering under Uncertainty: Safety Assessment and Management (ISEUSAM - 2012)*,
DOI 10.1007/978-81-322-0757-3_8,

Uncertainty, on the other hand, may be defined as the lack of complete certainty, that is, the existence of more than one possibility. The true outcome/state/result/value is not known. Human endeavour has always been to try and minimise risks even if it means working in uncertain conditions. Accordingly, 'one may have uncertainty without risk but not risk without uncertainty'. This chapter presents a case study where uncertainties and contradictions were overcome by the sheer will to achieve perfection and minimise potential risks.

In any integrated steel plant, one of the most important and major equipment is where iron ore, flux and fuel are burned in oxygen-enriched air to produce molten metal and slag. In a premier steel plant of India, such an equipment was first blown in the late 1950s. It was due for relining in the new millennium when the owners decided to upgrade it as well, from the existing 0.64–1.0 MTPA capacity. This was no mean task as every stage of engineering involved uncertainties and risks that had to be mitigated and solutions found.

In this chapter, an effort has been made to identify the uncertainties involved for this rebuilding and upgradation process. This chapter also describes how each uncertainty was analysed and dealt with in a rational manner to reach a level of relative certainty. Some explanatory sketches have also been included for a better understanding of the problem and the solutions.

2 Uncertainties

There were multiple challenges and uncertainties involved in every step of the rebuilding and upgradation process of the equipment. Some of the major uncertainties were:

- Knowledge of the existing foundation system
- Geotechnical data
- Load-carrying capacity
- Time constraint for shutdown of the equipment
- Developing model of foundation and subsequent blasting of part of foundation to simulate results
- Dismantling part of existing foundation by controlled blasting
- Restriction of energy propagation to the base raft of foundation
- Part load transfer through tower and part through existing foundation after partial rebuilding

Each of the above uncertainty has been elaborated in the following sections of this chapter, and steps to overcome them have also been described.

2.1 Existing Foundation System

Since the actual engineering of the equipment was done more than four decades ago, very limited and scanty data could be located from the client's archives. A few

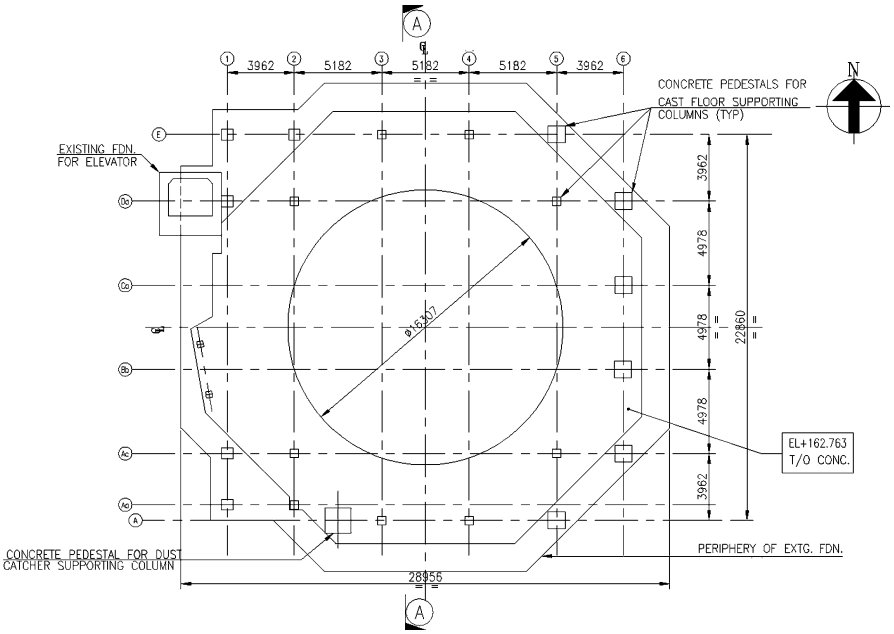

Fig. 1 Plan of existing equipment foundation

old drawings and an article, published in an in-house journal, were all that could be unearthed. Thus, credible information was limited and grossly insufficient. From the very limited data, it was understood that the main equipment shell was supported on a 52-ft.-diameter cylindrical concrete pedestal over a 13-ft.-thick octagonal concrete mat. The mat itself was supported on 28 nos. concrete columns, of size 5 sq. ft, founded on hard mica-schist rock. The column foundations were designed with safe bearing capacity of 4.0–9.0 t/sq. ft. Schematic sketches of the existing equipment foundation are shown in Figs. 1 and 2 below.

The above was the basis of a study undertaken by Dasturco to judge the feasibility of the proposed rebuilding and upgradation of the equipment.

2.2 Geotechnical Data

No soil investigation/geotechnical data could be found catering to the location of the existing equipment. From an old publication, as indicated earlier, it could be inferred that the foundation was designed with a safe bearing capacity between 4.0 and 9.0 t/sq. ft. Due to lack of data in the concerned area, it was decided to use existing geotechnical information from the neighbouring areas. Accordingly, from available soil investigation reports and test data of a nearby mill area, the gross safe bearing capacity of competent rock was estimated to be about 75.0 t/m^2. This corroborated well with the data obtained earlier from the technical article.

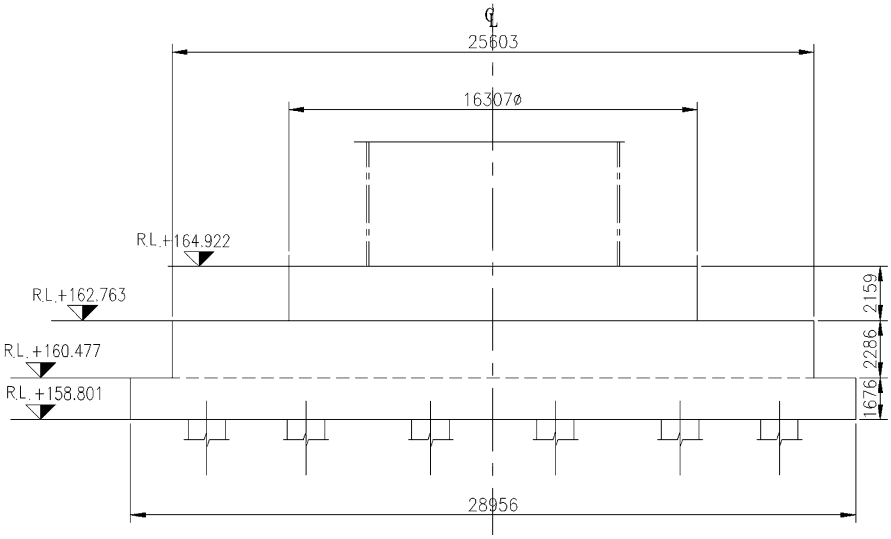

Fig. 2 Sectional view of existing equipment foundation

2.3 Load-Carrying Capacity

From the unearthed documents, no detailed load data on foundation could be found except an indicative vertical load of 21,000 Kips (9,258 tons) from the shell and cast house. However, there were necessarily other loads imposed on the foundation proper, and these had to be estimated to study the adequacy of the foundation system. A thorough reassessment of load was done considering additional loading from the elevator and one leg of dust catcher. Moreover, the equipment had undergone intermediate relining and modification works over the years. These would have increased the loading substantially. Considering all these factors, the vertical load on the existing foundation was reassessed and estimated to be of the order of 10,186 tons.

It was decided that the upgraded equipment would be free standing with four (4) tower legs around the shell proper. The design load from the shell and the tower legs considering all possible vertical loads for upgradation of the equipment for capacity enhancement were estimated to be to the tune of 13,000 tons. The existing foundation was not found to be adequate to carry the additional loads. Moreover, some cracks were noted on the foundation shaft and on top of the existing mat indicating signs of distress possibly due to flow of some molten iron on the foundation top. Based on the above, it was decided to get a thorough health study of the existing foundation done. Accordingly, the following studies were carried out:

- Cover metre test
- Carbonation test and pH
- Crack-width measurement and mapping
- Half-cell corrosion potential test
- Schmidt's rebound hammer test
- Ultrasonic pulse velocity test
- Core cutting and crushing tests

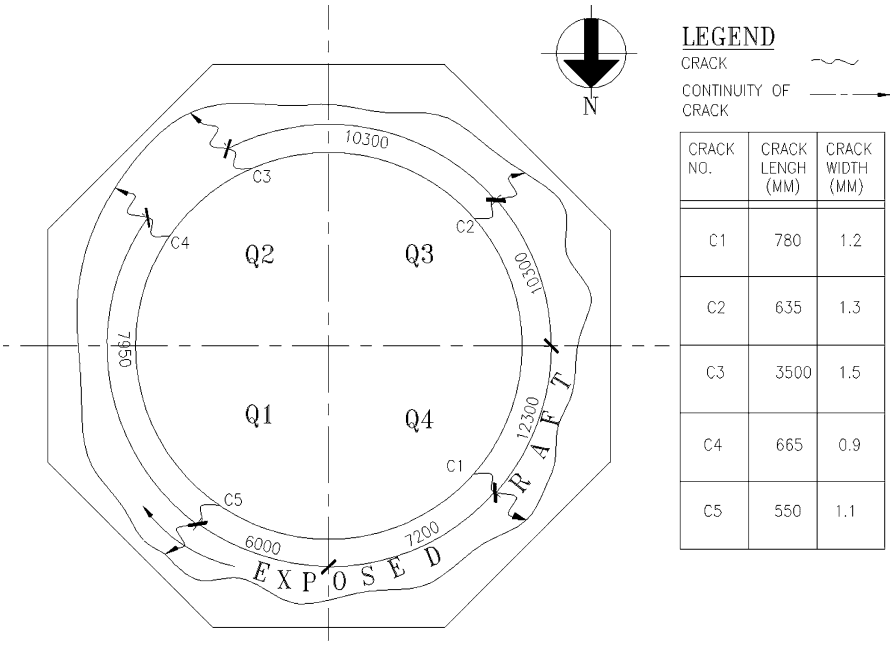

CRACK NO.	CRACK LENGH (MM)	CRACK WIDTH (MM)
C1	780	1.2
C2	635	1.3
C3	3500	1.5
C4	665	0.9
C5	550	1.1

Fig. 3 Crack mapping on existing foundation

Results of the health study indicated that the concrete grade of the existing reinforced concrete foundation was between M15 and M20 (M15 grade shown in drawing/document). Mild steel reinforcement was provided and found to be in excellent condition with no signs of corrosion. Low degree of carbonation and residual alkalinity were also inferred from the tests. Moreover, vertical cracks on outer face of pedestal and horizontal cracks on top surface of mat could be observed. The crack widths were measured and mapped. This is presented in Fig. 3 below.

Thus, it was evident that the structure was under distress for quite some time. Accordingly, Dasturco made the following major recommendations in the feasibility report:

- The proposed four (4) towers, around the shell proper, must be independently supported on 1,000-mm-diameter pile foundations.
- Top pedestal and part of the main foundation raft must be dismantled and rebuilt with heat-resistant concrete (M30 grade) along with new holding down bolts to fix the upgraded equipment base and additional reinforcements, wherever required.
- After modification, the vertical load on the equipment foundation from the shell of the upgraded equipment must not exceed the original design load, that is, 21,000 Kips (9,258 tons).

2.4 Time Constraint for Shutdown of the Equipment

The entire rebuilding and upgradation process had to be done under a very tight time schedule. Since the work involved dismantling and rebuilding of part of the existing foundation, temporary shutdown of the equipment was necessary. However, in a running plant, shutdown of a major equipment is directly related to a loss in production and hence revenue. Thus, it was essential to minimise the shutdown period as far as practicable. A micro schedule was prepared to target a total shutdown period of 100 days, consisting of rebuilding of the furnace shell and other accessories to cater to the capacity enhancement. This period also included erection of steel tower and rebuilding of foundation. Period for dismantling and rebuilding of foundation proper was restricted to 14 days only.

To optimise the shutdown period to a minimum, it was decided to adopt controlled blasting technique for breaking/dismantling part of the foundation, as manual breaking would have taken an enormous amount of time. At the same time, one had to be extremely careful to ensure that the blasting process did not cause any distress or damage to the remaining portion of the structure, proposed to be retained intact. Based on these considerations and to address the uncertainties involved with the after-effects of blasting, it was decided to construct a model of the foundation system and carry out controlled blasting to simulate the actual conditions.

2.5 Model Foundation with Blasting to Simulate Results

As described in the preceding section, it was decided to carry out the trial blasting on a model foundation, similar to the actual equipment foundation, to have hands-on information about the effects of blasting on the portion of the foundation to be retained and reused. Accordingly, the following course of action was decided upon:

- To construct a scaled model foundation based on information gathered from unearthed data about the existing equipment foundation, that is, shape, size, grade of concrete and reinforcements.
- To carry out controlled blasting through 32-mm-diameter vertical holes, at 500-mm centres, circumferentially, in ring formations, with three (3) such rings at radial distance of 500 mm. Sequence of blasting would be from the outer to inner rings with suitable delay per charge.
- To drill 32-mm-diameter horizontal through holes, at 500-mm centres, at 250 mm above the octagonal mat for easy separation and arresting shock wave propagation down below.
- To record shock wave intensities during blasting, near the dismantling level of the model block, engaging suitable sensors.
- To carry out non-destructive/partial destructive tests on balance portion of model foundation block, intended to be retained, before and after blasting, to check for possible health deterioration.

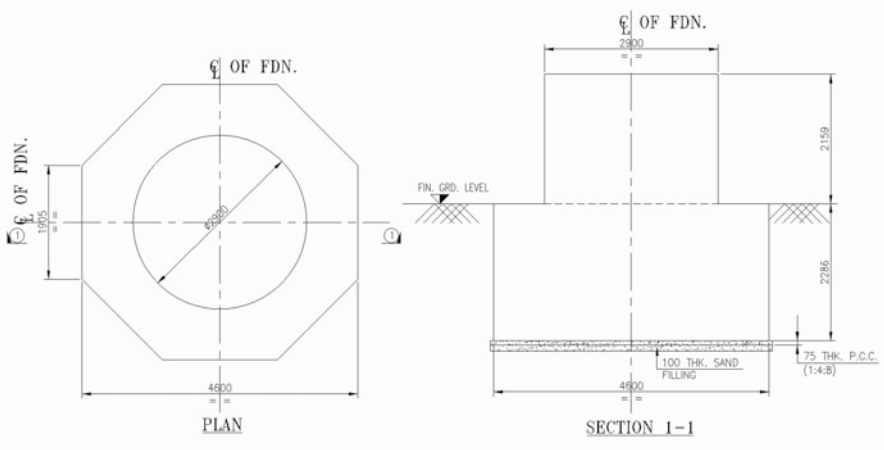

Fig. 4 Details of model foundation

- To simulate all recorded data on model foundation block with the prototype foundation block to ascertain different parameters for controlled blasting of the same and to restrict the disturbance below dismantling level to within acceptable limits.

Details of the model foundation are indicated schematically in Fig. 4 above.

Based on the above guidelines, controlled blasting was successfully carried out, on a model foundation, with extensive recording of data. Analyses of all recorded data led to the following conclusions:

- Results of core samples from octagonal mat before and after blasting did not indicate any deterioration of concrete strength due to the effect of blasting.
- Fragmentation of concrete was less in the area with reduced explosive charge, and the overburden on the pedestal was less than sufficient to contain the fragments from ejecting.
- The mat experienced mainly symmetric compression and a marginal amount of tension due to the effect of blasting. The compressive stresses were well within the allowable limits of concrete, and chances of cracking were remote due to insignificant tensile stresses.
- High vibration levels and high momentary shock-wave velocities were recorded, due to blasting, which were higher than the permissible values. However, these would actually subside to low levels due to attenuation characteristics of the soil surrounding the foundation.

The above observations and analyses of results were found to be quite encouraging thereby emboldening the concerned engineers to finalise dismantling of part of the actual equipment foundation by controlled blasting.

2.6 Dismantling Part of Existing Foundation

Based on the results and simulation studies of blasting of model foundation, actual controlled blasting of the prototype equipment foundation was done. To carry out this work, it was decided to maintain the disposition of vertical and horizontal holes and sequence of blasting in line with the model study. To minimise the critical shutdown period of the equipment, some activities were carried out in the pre-shutdown period, as preparatory work. These mainly included:

- Developing a plain cement-concrete horizontal base on which the reinforcement cage of the foundation pedestal was fabricated with erection framework, bolt sleeves and bolt boxes
- Fabricating lower erection framework followed by fabrication of the upper framework
- Providing permanent steel shuttering with 10-mm-thick steel plates and fixing the same with the reinforcement by welding arrangement
- Providing lifting hooks to each segment of the upper erection frame and strengthening the upper and lower erection frames by bracings to prevent buckling during lifting and transporting

During the initial phase of shutdown, some more preparatory works were done like construction of an RCC overlay on the vertical side of upper octagonal mat with dowel bars and bonding agent, horizontal drilling to create a cut-off plane and drilling about 10% of vertical holes on top of circular pedestal to facilitate blasting.

Dismantling of part of the existing foundation was done during the period allotted for rebuilding of the foundation that was limited to 14 days only to adhere to the schedule for total shutdown period of the furnace. During this period, the balance vertical holes were drilled, in staggered fashion, in a grid of 650 mm square. A temporary safety deck was also erected to act as a barrier for accidental fall of any object during activity above the deck. These were followed by installing the requisite explosive charge in the vertical holes (between 125 and 250 g per hole) and carrying out controlled blasting.

Blasting was carried out in four volleys with the total charge of the explosives being 42.5 kg. Adequate safety precautions were taken by placing sand bags all around the foundation as the operations were done within an existing plant. During blasting, the cylindrical pedestal was loaded with overburden weight of about 100 kg/m^2 to prevent the fragmented pieces from being ejected.

Controlled blasting proved to be a very successful venture. After the operation, it was noted that the total concrete above the octagonal raft could be removed easily leaving a smooth top surface of the octagonal mat. This was because the continuity of reinforcement was limited only along the periphery of the circular shaft and the central portion was actually filled with lean concrete. The resulting debris, post blasting, was cleaned by excavators and disposed to designated dump areas.

A sectional view of the equipment foundation proposed to be partly dismantled and rebuilt is shown in Fig. 5 below. The scheme of blasting along with disposition of blasting holes, sequence of blasting and details of charge placement in each hole is presented in Fig. 6 below.

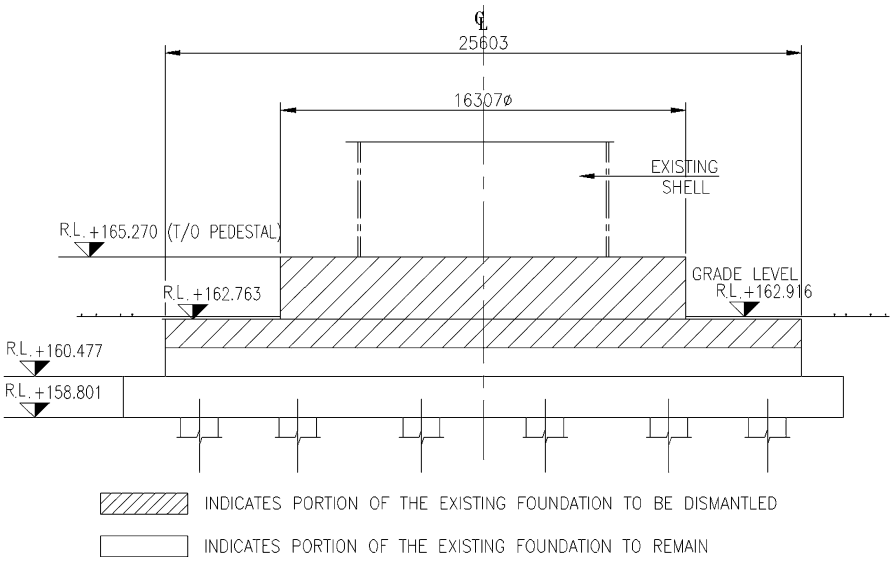

Fig. 5 Sectional view of foundation proposed to be partly dismantled and rebuilt

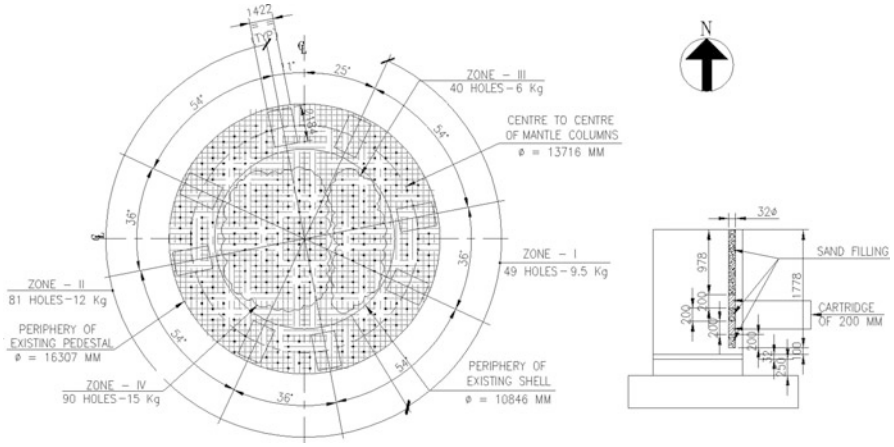

Fig. 6 Disposition of blasting holes, sequence of blasting and details of charge placement

2.7 Restricting Energy Propagation to the Base Raft

A major concern while planning the blasting activities was the propagation of shock waves to the lower portion of the foundation mat, intended to be retained and reused. To restrict wave propagation and avoid possible distress to the lower portion of the foundation mat, some kind of cut-off had to be planned. As indicated earlier, this was planned to be facilitated by drilling horizontal holes, through the

cylindrical pedestal, at a suitable height above the top of the octagonal mat. This was implemented during the model study to simulate the actual conditions with extensive measurement of shock-induced strains in the concrete.

The model studies indicated that due to blasting, the vertical reinforcement bars of the cylindrical pedestal had bent outwards from the level of the horizontal holes. The bars held with them chunks of pedestal concrete in the lower portion near the horizontal holes. As a result of this, the level of separation was formed at 200–300 mm above the desired level. As a result of this experience, the vertical reinforcements of the pedestal were cut at the level of the horizontal holes before blasting to facilitate proper separation and fragmentation. Based on the above, a series of 32-mm-diameter horizontal holes were drilled, at 500-mm centres, at 250 mm above the octagonal mat for easy separation and arresting shock wave propagation down below.

After the actual controlled blasting of the prototype equipment foundation took place, the results were there for everyone to see. There were absolutely no signs of distress or crack on the lower portion of the octagonal mat that was planned to be retained. This proved that the series horizontal drill holes, provided at cardinal locations, were indeed effective in creating a cut-off plane for energy dissipation and preventing the shock waves to travel below.

2.8 Load Transfer Through Tower and Existing Foundation

As indicated earlier, an assessment of loading on the existing equipment foundation was done to gauge its present condition. It worked out that the foundation was already overstressed in excess of what it was designed for. Some telltale cracks on the foundation mat also bore testimony to this fact. Thus, there was no way the foundation could be loaded further as per the requirement of upgradation. The engineering solution that was needed to be developed was to design a system that would effectively transfer the enhanced load, from the upgraded equipment, without causing any distress to the foundation. The solution suggested was the following:

- The proposed upgraded equipment should be free-standing type accompanied by four (4) tower legs around the shell proper.
- The entire shell would carry its self-weight including the weight of refractories and weight of offtake, uptake, downcomer and the Compact Bell Less (CBLT) Top charging system.
- The four tower legs would carry, besides their self-weight, the weight of skip bridge, top structure and platforms at different levels.
- To facilitate the above, the main octagonal mat foundation was partly dismantled and rebuilt, as described in the preceding sections. The four (4) towers, on the other hand, were independently supported on 1,000-mm-diameter bored cast-in-situ piles of 300-t capacity each.

Sketches showing the plan and sectional elevations of the rebuilt equipment foundation are shown in Figs. 7, 8, and 9, respectively.

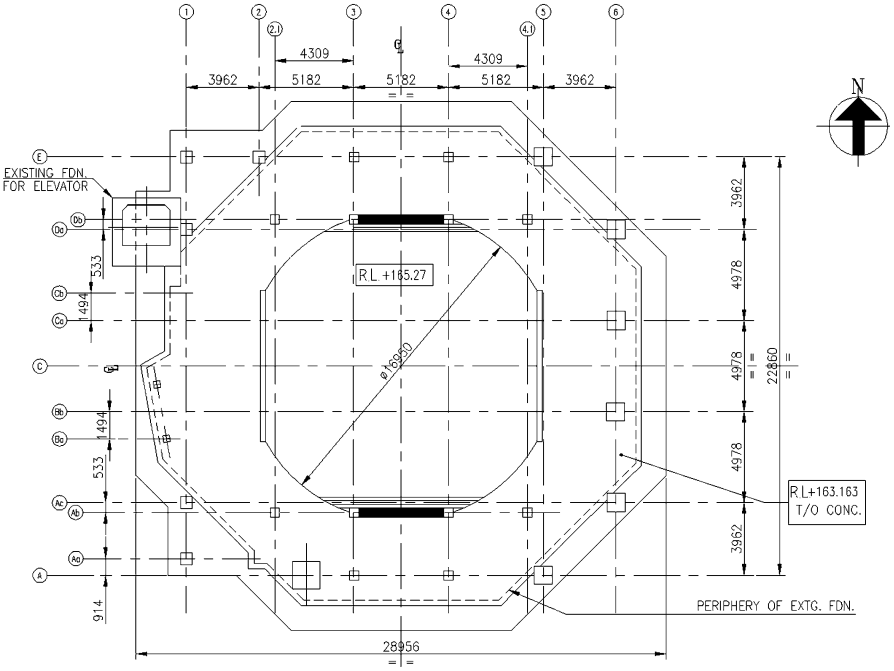

Fig. 7 Plan showing rebuilt equipment foundation

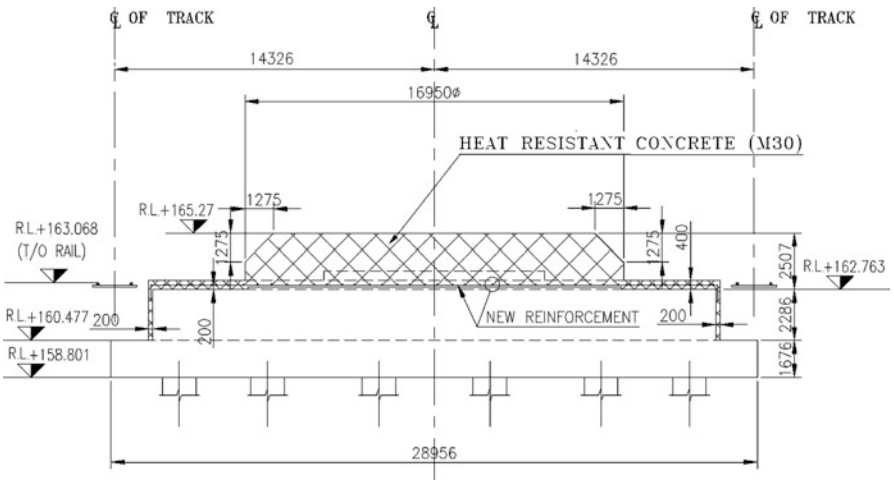

Fig. 8 View from west side showing rebuilt equipment foundation

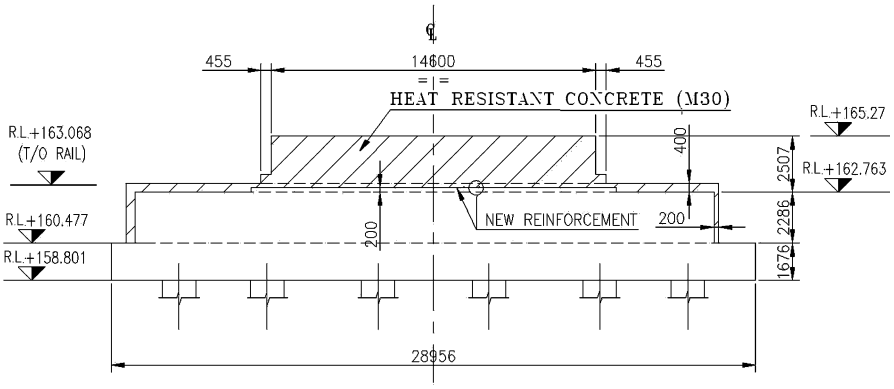

Fig. 9 View from south side showing rebuilt equipment foundation

3 Mitigating Uncertainties in Record Time

There were a number of uncertainties in every step of the rebuilding process that confronted the engineering team. Some of them have been highlighted in the preceding sections of this chapter. However, the biggest and by far the most challenging task was the race against time. As the work was being done in a running plant, any rebuilding and upgradation process necessarily required an optimum period of shutdown of the concerned equipment and some of the associated facilities. It goes without saying that shutting down of a major unit in a running plant hampers production and, consequently, has a direct bearing on revenue. To be fair to the clients, the shutdown period allowed for the work was extremely tight. It seemed impossible and somewhat improbable to complete all the activities within the very stringent time period that was allowed. However, with a dedicated design and construction team working in unison and perfect harmony, the target was achieved a couple of days before the scheduled completion date. The feat was duly recognised and appreciated by the clients in no uncertain terms.

An isometric view of the rebuilt and upgraded equipment foundation is shown in Fig. 10.

4 Conclusion

In a premier integrated steel plant of our country, a major production equipment was due for relining and refurbishment during the early part of the new millennium. However, the clients desired to upgrade the equipment at the same time to enhance their production capacity. This called for a detailed study of the existing foundation

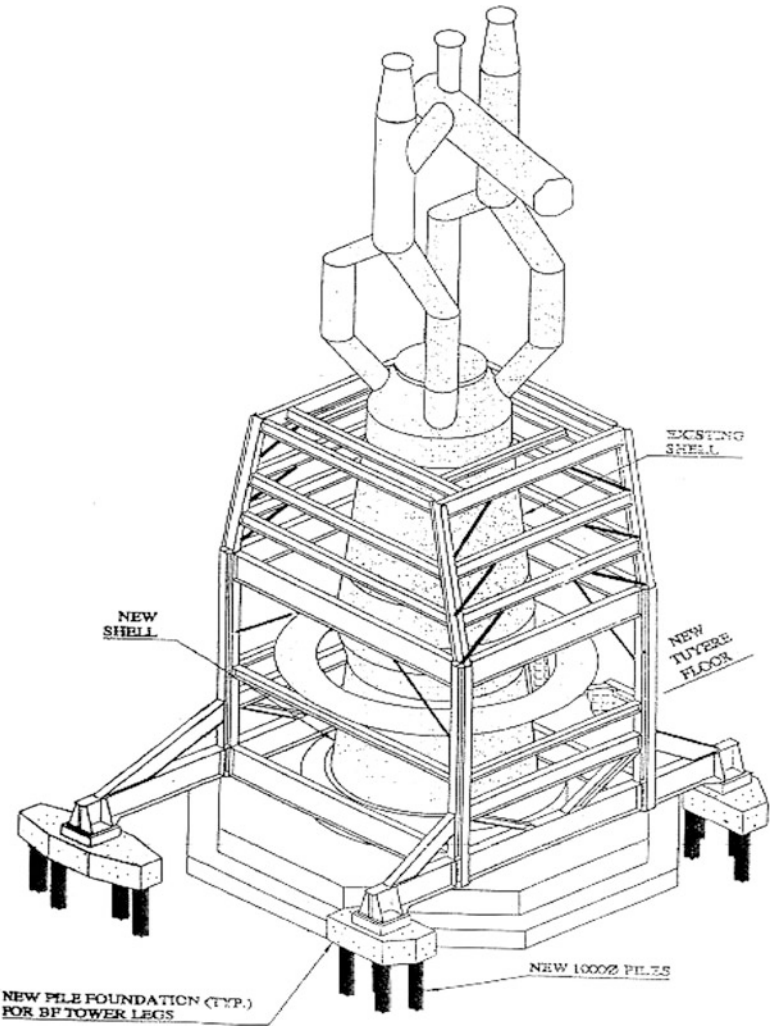

Fig. 10 View of rebuilt and upgraded blast furnace

system of the equipment to assess its feasibility of upgradation. Being constructed and commissioned more than four decades ago, there were very few data available regarding the foundation system of the equipment. A thorough search of the client's archives yielded rather insufficient and scanty data related to the equipment foundation. A team of engineers did a feasibility study based on whatever data could be unearthed and some innovative engineering to develop a workable scheme of rebuilding and upgrading the equipment. There were multiple uncertainties involved in every stage of the work. However, through meticulous planning,

brain storming and model studies to simulate results and some innovative engineering, these uncertainties were overcome to reach levels of relative certainty in each and every stage. The equipment was rebuilt and upgraded in record time and handed over to the clients to start production to its planned enhanced capacity.

> So what do we do? Anything. Something. So long as we just don't sit there. If we screw it up, start over. Try something else. If we wait until we've satisfied all the uncertainties, it may be too late. Lee Iacocca

Discovering Hidden Structural Degradations

S. Sharma, S. Sharma, and A. Mukherjee

Abstract Structures degrade due to a variety of reasons such as environmental actions, overloading, and natural calamities. Inspection, diagnosis, and prognosis of damage in installations are imperative for avoiding their catastrophic failures. However, a reliable tool for early detection of damages in large structures has remained elusive. The ability ultrasonic guided waves to travel long distances and pick up the signatures The ability of structural damage makes them most promising among the handful of techniques available. Yet, there are formidable challenges in theoretical understanding and field implementations. In this chapter, we describe some recent developments in utilizing ultrasonic guided waves in discovering hidden damages.

Keywords Ultrasonic • Utilizing • Guided waves • Corrosion • Concrete • Plates

1 Introduction

Many nondestructive evaluation (NDE) techniques such as liquid penetrant dye, radiography, holography, eddy current, magnetic flux, and thermography are available for investigating the insides of a structure, the large size of the installations makes use of these unrealistic techniques. For discovering deep structural degradations, ultrasonic guided waves offer a potentially effective solution since they can travel long distances and pick up signals of early deterioration. It involves introducing a high-frequency stress pulse or "wave packet" into a material and observing the subsequent propagation and reflection of the pulse. The wave characteristics change due to the deterioration in the structure and these are sensitive to the location, extent, and character of damage.

S. Sharma (✉) • S. Sharma • A. Mukherjee
Thapar University, Patiala, Punjab, India
e-mail: shruti.sharma@thapar.edu; sksharma@thapar.edu; abhijit@thapar.edu

S. Chakraborty and G. Bhattacharya (eds.), *Proceedings of the International Symposium on Engineering under Uncertainty: Safety Assessment and Management (ISEUSAM - 2012)*,
DOI 10.1007/978-81-322-0757-3_9,

In this work, suitable ultrasonic guided waves have been used for damage detection of embedded and submerged structures. For embedded systems, suitable guided wave modes have been identified through modeling which are sensitive to different types of corrosion-induced damages encountered in reinforcing bars embedded in concrete. Corrosion of reinforcing steel in concrete is one of the major durability problems faced by civil engineers. Ultrasonic guided waves have been used to develop a non-intrusive corrosion monitoring technique for early detection of corrosion-induced damages in steel embedded in concrete. Corrosion manifests itself in debond and pitting steel bars. But it is imperative to excite the right mode for detection of a particular type of corrosion. A guided wave excited in the reinforcing bar in concrete would be reflected from the defects simulating area reduction due to pitting caused as a result of corrosion, thus facilitating the detection of these defects accurately. Amplitude and time of arrival of these reflections can be used to identify or locate defects. Ultrasonic pulse transmission utilizing two piezoelectric transducers at the two ends of the reinforcing bars is also used in conjunction with pulse echo testing method to quantify the extent of corrosion-induced defects in embedded bars.

On the other hand, many structures like ship hulls, oil storage tanks, and off shore oil platforms are assemblies of large plate like components which are prone to deterioration and damages due to environmental degradation, excessive loads, material fatigue, corrosion, etc. Criticality in such cases is further compounded due to economic constraints like high out of service costs associated with frequent health monitoring checkup schedules. The ultrasonic guided wave methodology is also applied for damage detection in such plate structures seeded with defects like notches especially in submerged states like ship hulls in water. Submerged nature of the specimens also limits the use of available and conventional NDT techniques. Guided waves are a successful means for detection of deterioration of such structures.

2 Guided Waves for Corrosion Monitoring in Reinforcing Bars in Concrete

Reinforced concrete (RC) is the most popular, economical, and versatile construction material as it can be molded into any shape. It has proven to be successful in terms of both structural performance and durability. But in humid conditions, atmospheric pollutants percolate through the concrete cover and cause corrosion of steel reinforcements. The formation of the corrosion products on the surface of the reinforcing bar having higher volume than the corresponding volume of steel results in an outward pressure on concrete. Corrosion, in the form of pitting, may also reduce the ductility of the steel bar by introducing crevices on the surface. But the size and limited accessibility of civil engineering installations prevent adoption of many currently used nondestructive testing methods such as radiography and

acoustic emission. Hence, there is a need for nonintrusive, in situ, and real-time corrosion monitoring system for RC structures. In this study, guided waves have been used to develop a non-intrusive corrosion monitoring technique for early detection of corrosion-induced damages in steel embedded in concrete.

Corrosion manifests itself in debond and pitting steel bars. But it is imperative to excite the right mode for detection of a particular type of corrosion. This study investigates the effect of local loss of material and loss of bond on the propagation of ultrasonic waves through the reinforcing bars. Simulated pitting effects were created by notches on the surface of the bar in varying percentages of its cross sectional area. Simulated debond was generated by wrapping a double-sided tape of varying length on the bar embedded in concrete. Conventional techniques of pulse echo and pulse transmission have been used in combination to predict the presence, location, and magnitude of the damages. An experiment is carried out to create accelerated actual corrosion in RC samples. Both the simulated and actual corrosion samples were ultrasonically monitored using guided waves. The results have been compared to estimate the suitability of simulation techniques [1]. The effect of degradation due to corrosion on the ultrasonic signals is reported [2]. Effective combination of suitable guided wave modes could relate to the state of reinforcing bar corrosion [3].

2.1 Description of Experiments

For simulating corrosion in reinforcing bars in concrete, concrete with proportions of cement, sand, and stone aggregates as 1:1.5:2.96 was taken (w/c ratio = 0.45). RC beam specimens of dimensions 150 mm × 150 mm × 700 mm were cast. 12-mm-diameter plain mild steel bars of 1.1 m length were placed at the center of cross section of the beams at the time of casting with a projection of 200 mm on each side of beam. One set of bars with simulated damages in the form of notches (with symmetrical 0, 20, 40, and 60% diameter reduction) were introduced in the middle of the bar before casting them in concrete. Another set of bars were wrapped with a double-sided tape in varying percentages of 0, 12.5, 25, 50,75, and 100% simulating delamination and were then cast in concrete.

The RC beams were ultrasonically monitored using the standard UT setup consisting of a pulser-receiver and transducers. Contact transducers ACCUSCAN "S" series with center frequency of 3.5 MHz is used for the 12-mm bars. The transducers were attached at the two ends of the bars by means of a holder and a coupling gel between the bar and the transducer. Driven by the pulser, the compressional transducer generates a compressive spike pulse that propagates through the embedded bar in the form of longitudinal waves. In a reinforcing bar, different modes can be excited selectively by choosing a frequency bound. To determine the frequency band, standard software, Disperse [4] was used. Only longitudinal modes were considered for excitation since they are least attenuative. They were produced by keeping compressional transducers parallel to the guiding configuration at the

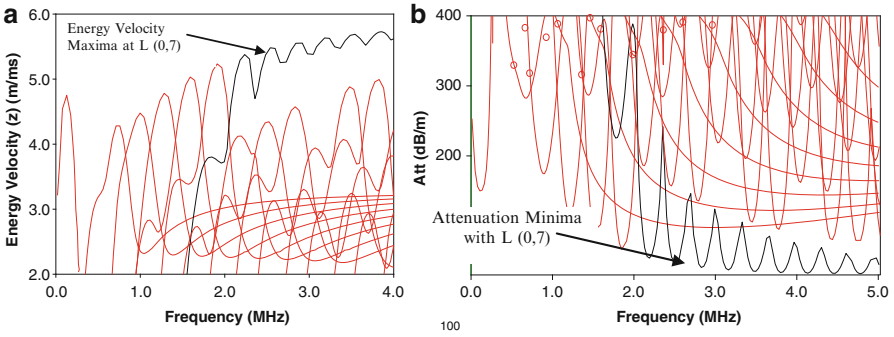

Fig. 1 Dispersion curves for a 12-mm bar in concrete [4]. (**a**) Energy velocity (z) versus frequency. (**b**) Attenuation versus frequency

two ends of the embedded bars by varying the excitation frequencies. The selection of frequencies for testing was done based on the phase velocity dispersion curves and validated by experimentally confirming the signal fidelity. High-frequency low-loss modes as identified by Pavlakovic [5] were chosen. L (0, 7) mode corresponding to maximum energy velocity (Fig. 1a) and minimum attenuation (Fig. 1b) was chosen for study at a frequency of 3.5 MHz. Testing of the embedded bar was done in both pulse echo and transmission modes.

To determine the suitability of the simulated corrosion experiments by ultrasonic guided waves, another set of beam specimens were subjected to actual accelerated corrosion. The projected bar was made an anode by connecting it to a positive terminal of a DC power supply. The middle 300 mm of the beam was selected for exposure to corrosive environment. A thick cotton gauge was placed in this region wrapped with a stainless steel wire mesh around with a dripping mechanism of 5% NaCl fitted on top of it. The negative terminal was connected to the wire mesh and a constant voltage of 30 V was applied between the two terminals. Beams undergoing accelerated chloride corrosion were ultrasonically monitored both in pulse echo and pulse transmission modes. The pulse transmission signatures disappeared in 8 days. Then the corroded beams were taken out and the extracted bars were tested for mass loss and tensile strength. The ultrasonic test results were compared to the actual state of the bar.

3 Results and Discussions

3.1 Simulated Notch Damage Study

Pulse echo records for a 12-mm bar in concrete show the notch echo (NE) as well as the back wall echo (BWE). In a healthy specimen, the peak is the BWE (Fig. 2a).

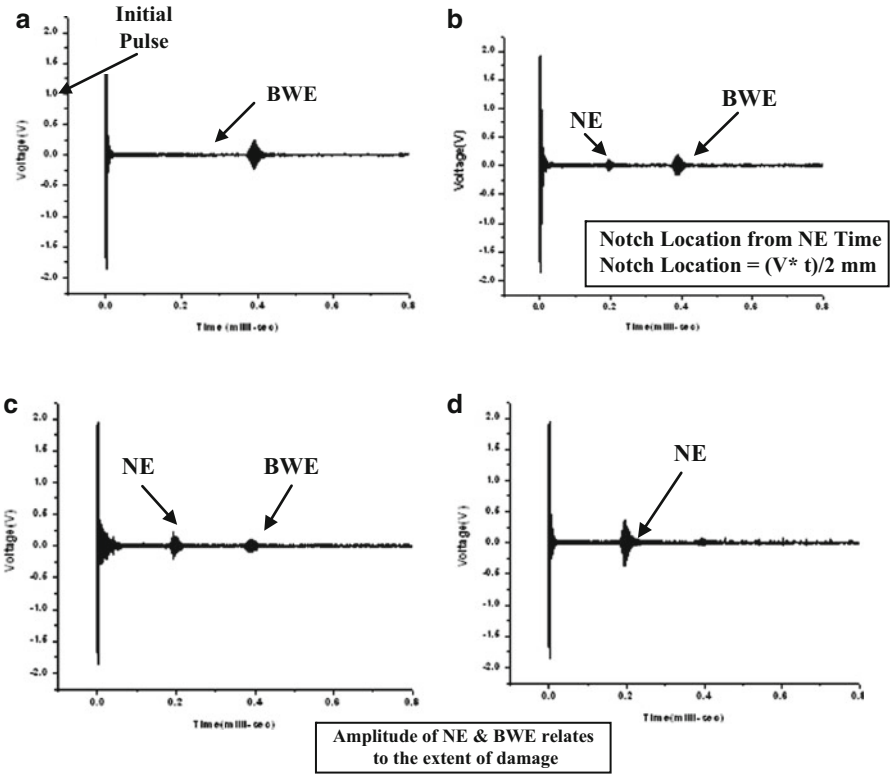

Fig. 2 Pulse echo signatures of a 12-mm, 1.1-m bar embedded in 700 mm of concrete [4]. (**a**) Healthy specimen. (**b**) 20% notch in embedded bar. (**c**) 40% notch in embedded bar. (**d**) 60% notch in embedded bar

In a notched specimen, the first peak is NE and the second peak is BWE (Fig. 2b). Appearance of NE indicates presence of the defect in the embedded bar. By knowing the time of flight of this echo, the location of the damage can be calculated. The magnitude of damage can be directly related to the magnitude of NE as well as BWE. It is observed that the amplitude of NE increased and that of BWE reduced with the increase in the notch dimensions (Fig. 2). As the magnitude of notch increased, more signal energy is reflected back from the notch and less of it is travels to the back wall.

In the pulse transmission signatures, the peaks observed (Fig. 3) are the transmitted peaks obtained after traveling length L of the embedded bar. It may be noted that the arrival time of the pulse is not affected by the presence of the notch. Thus, the notch location is not discernible through pulse transmission. However, studying the relative change in the amplitude of input pulse and the transmitted pulse (P/T-Notch), an assessment of the severity of the damage can be made.

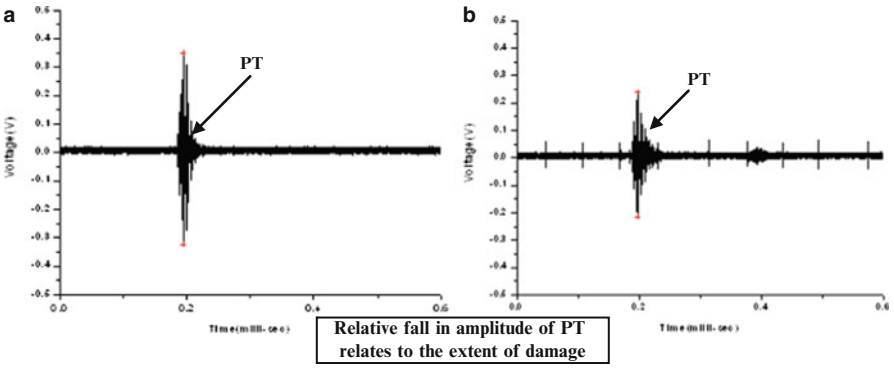

Fig. 3 Pulse transmission signatures of a 12-mm bar embedded in concrete [4]. (**a**) Healthy specimen. (**b**) 60% notch in embedded bar

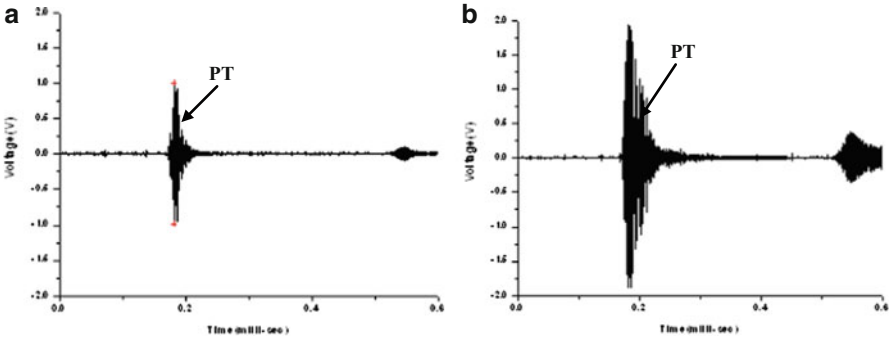

Fig. 4 Pulse transmission signatures in simulated delamination [4]. (**a**) 12.5% delamination. (**b**) 100% delamination

3.2 Simulated Debond Damage Study

In simulated debond specimens, as the percentage of delamination increases, the transmitted signal strength (P/T-Debond) keeps on rising (Fig. 4). This is due to decrease in the amount of energy leaking into the surrounding concrete with increase in percentage delamination. Hence, an increase in P/T-Debond can successfully relate to the presence as well as extent of delamination.

3.3 Comparison of Notch and Debond

As the percent of damage increased from 0 to 60%, the magnitude of P/T-Notch reduces. This is because as the notch dimensions increased, more energy is reflected

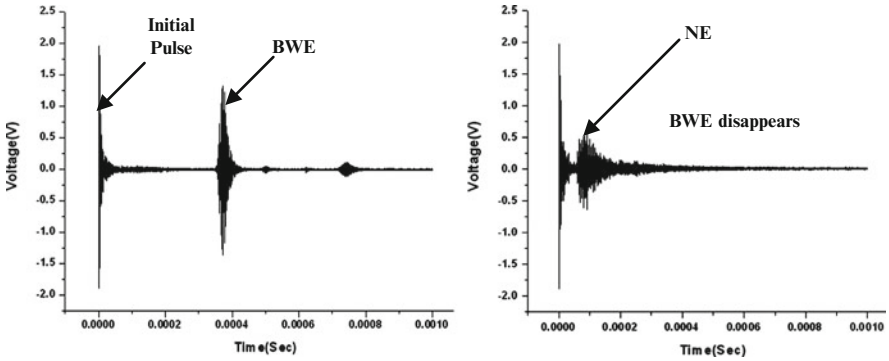

Fig. 5 Pulse echo signatures during accelerated corrosion [5]. (**a**) First day signature. (**b**) Seventh day signature

back and less of it travels through the bar to reach the other end. The counter-balancing effect of the two manifestations of corrosion – debonding and pitting – is clear. Pitting that is similar to a notch reduces the strength of the transmitted pulse (P/T-Notch) while debonding increases the strength of the transmitted pulse (P/T-Debond). Thus, it would be interesting to compare the simulated corrosion with the actual corrosion.

3.4 Actual Corrosion Study

Beams undergoing accelerated chloride corrosion showed reddish brown patches of corrosion products. A longitudinal crack appeared parallel to the bar within 3 days. With the increase in the volume of corrosion products, another crack parallel to the bar appeared on another face of the beam after 6 days. A reddish brown liquid oozed out of the cracks and the ends of the beam. The crack length and width increased with the increase in exposure. At 8 days of exposure, there were two large and wide longitudinal cracks that divided the entire beam into wedges.

Ultrasonic pulse echo signatures were monitored everyday during the exposure to the corrosive environment. In the healthy bar, the signature is characterized by a strong BWE (Fig. 5a). As the exposure proceeds, BWE attenuates rapidly and disappeared completely on fourth day. This is contrary to the expectation if corrosion is manifested through delamination only. Due to the nonuniform loss of material from the bar caused by chlorides, the waveguide is disturbed, thus resulting in scattering of waves. The scattering reduces the strength of the transmitted pulse further.

Another significant observation was the appearance of a peak between the initial pulse and BWE on the second day (Fig. 5b). This indicates that pulses are reflecting from a localized neck formed in the bar due to corrosion. From the time of flight of

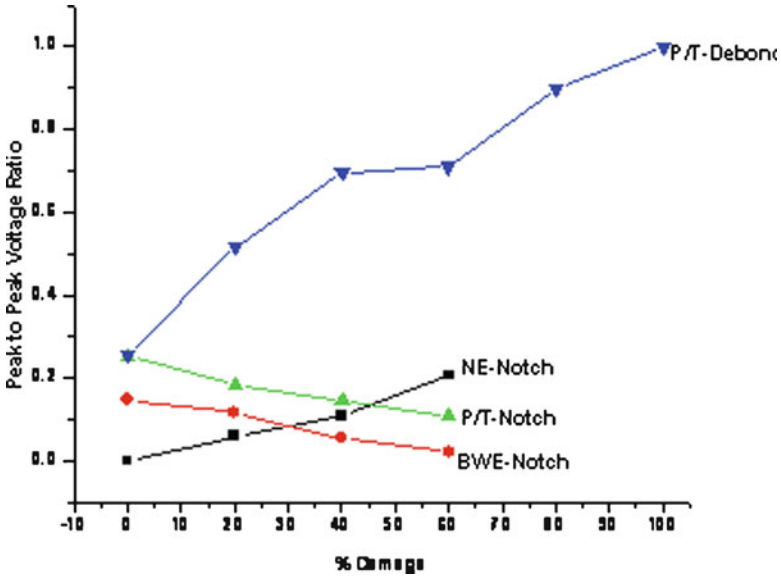

Fig. 6 Peak-peak voltage ratio trends of reflected and transmitted peaks [4]

the peak, the location of the neck was estimated at the bar-beam interface. After completion of the corrosion process, concrete was removed and the extracted bar was observed. A large notch was indeed seen at the estimated location. As corrosion increased, amplitude of this peak increased indicating further loss of area from the interface. Figures 6 and 7 compare the pulse echo results of simulated and actual corrosion. It is observed that corrosion in the presence of chlorides is characterized by localized loss of material similar to notches. In the present sample, one major notch developed due to corrosion resulting in a close match.

The pulse transmission studies where corrosion has been simulated as the loss of bond indicate that the transmitted signal strength goes up. Contrary to this observation, the transmitted pulse steadily lost strength as the corrosion progressed. It disappeared completely on the seventh day (Fig. 8). As discussed, the most likely cause of this phenomenon is the development of large pitting that further restricts the passage of waves. While notches restrict the passage of the waves, smooth delamination would facilitate the passage. Thus, pitting and delamination counteract each other. Figure 9 compares the peak-peak voltage ratios of simulated and actually corroded bars. Clearly, the results of notch specimens are in closer agreement with the actual chloride corrosion. Thus, chloride corrosion is simulated better as notches rather than delamination.

The bars were subjected to a series to destructive tests after the period of exposure was completed. After 8 days, the bar was removed from concrete and its mass loss and tensile strength were calculated. The bar had lost 18.6% of its mass. In tensile test, the bar failed in the region where a huge area loss was observed. The tensile strength reduced to 20% of that of undamaged bar.

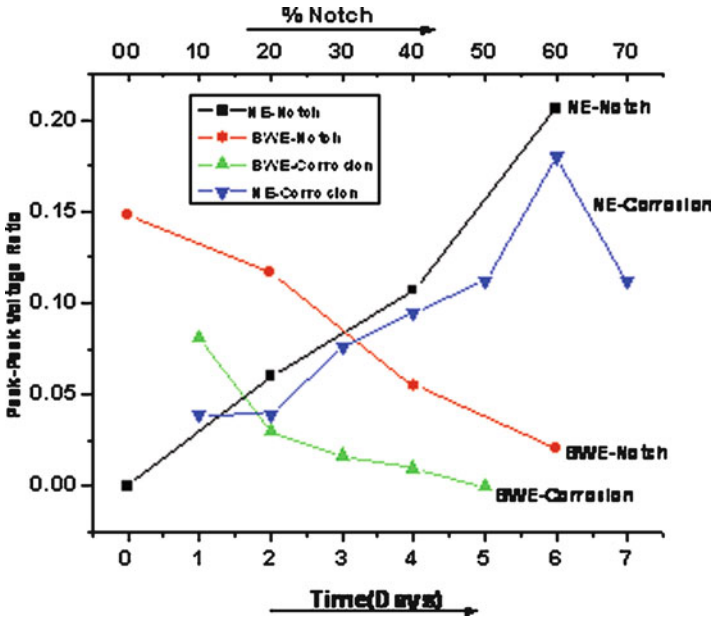

Fig. 7 Peak to peak voltage ratio in pulse echo [5]

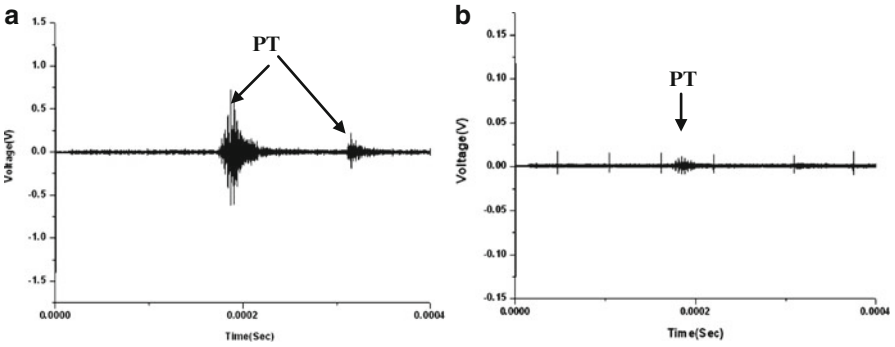

Fig. 8 Pulse transmission signatures during corrosion [5]. (**a**) Second day signature. (**b**) Fifth day signature

These reductions in mass and ultimate tensile strengths correlate well with the ultrasonic monitoring results wherein the signal experiences huge attenuation both in pulse echo and pulse transmission techniques. So the methodology established in the study using ultrasonic pulse echo and pulse transmission can be applied for in situ monitoring of embedded reinforcements undergoing corrosion.

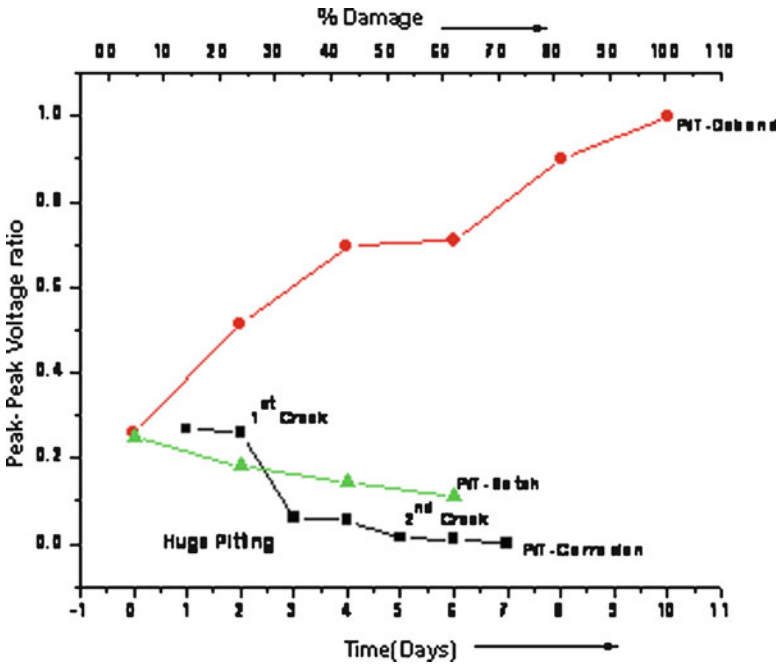

Fig. 9 Peak to peak voltage ratio in pulse transmission [5]

4 Guided Waves for Damage Monitoring in Submerged Structures

Many structures like ship hulls, oil storage tanks, off shore oil platforms are assemblies of large platelike components which are prone to deterioration and damages due to environmental degradation, excessive loads, fatigue loads, corrosion, etc. Criticality in such cases is further compounded due to economic constraints like high out of service costs associated with frequent health monitoring checkup schedules. The ultrasonic guided wave methodology is further applied for damage detection in such plate structures seeded with defects like notches and holes where structure remains in submerged state. Presence of water makes it all the more challenging as water loaded structures exhibit higher attenuative behavior due to comparatively lesser impedance mismatch, but on the other hand, it can be used to an advantage as a natural couplant. This obviates the subjectivity that may creep in while using direct contact techniques. Similar UT setup is used for damage detection in submerged plate specimens with the scanning setup as shown in Fig. 10.

Symmetric Lamb wave modes in plates were preferred because of ease of excitation. Selection of a particular mode is dependent on the type of damage to be monitored. For guided waves in plates, not many studies exist. Basically, two types of Lamb wave modes can exist in isotropic, homogeneous plates – symmetric

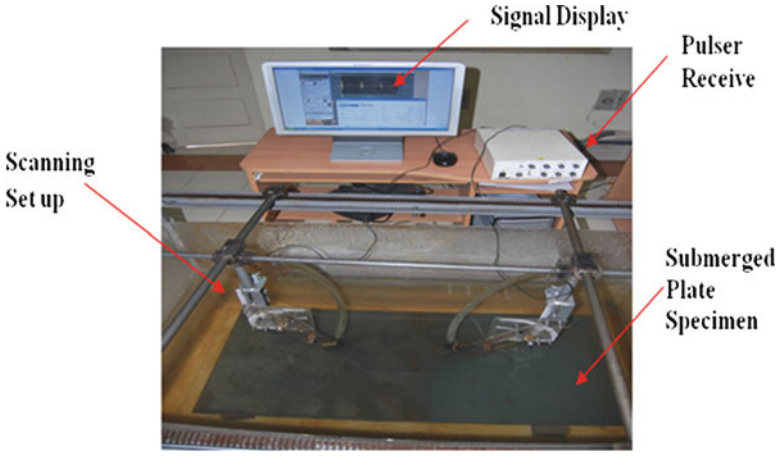

Fig. 10 Experimental setup for submerged specimen

and antisymmetric. Fundamental symmetric and antisymmetric modes describe a longitudinal wave and bending motion of the plate, respectively. As compared to the bulk waves used in UT, these modes are dispersive in nature, i.e., propagation velocity depends on the frequency. Guided waves may be produced by varying the excitation frequency or by changing the angle of incidence. Placing a transducer on the specimen, a guided wave can be excited that interrogates the whole structure.

The ultrasonic guided waves have been used for damage detection in plated steel structures using frequencies of the order of 1–3-MHz ultrasonic techniques of pulse echo and pulse transmission can be effectively used in combination to detect the presence, exact location, and quantification of the damage. Steel plate specimens with simulated defects in the form of localized area reduction were monitored in damaged state and compared with healthy specimens. Guided waves were generated by varying the input frequencies of the transducer. Different modes are excited at different frequencies and the suitable mode was chosen relevant to the defect to be characterized and ones corresponding to highest signal fidelities. Comparison of the wave signatures in healthy and simulated damaged state can easily reveal the existence, location, and extent of damage with reasonable accuracy.

Plate geometry results in the generation of multimode dispersive guided waves which are again obtained using software Disperse [4]. Different modes (symmetric and antisymmetric) of varying orders can be selectively excited by offering subject structure at various critical angles to the incident energy. Different modes have varying levels of sensitivities to different types of defects like notch, dent, and holes. Suitable modes are selected by testing the specimen implanted with a particular defect of varying degree in pulse transmission mode and observing the corresponding response of the received signal for various modes. Then specimen is tested in pulse transmission technique to ascertain the presence of the defect and subsequently pulse echo technique is employed to localize the same. The data obtained from these two techniques can be used to obtain the defect terrain of the specimen in the form of nice tomograms as shown in Fig. 11.

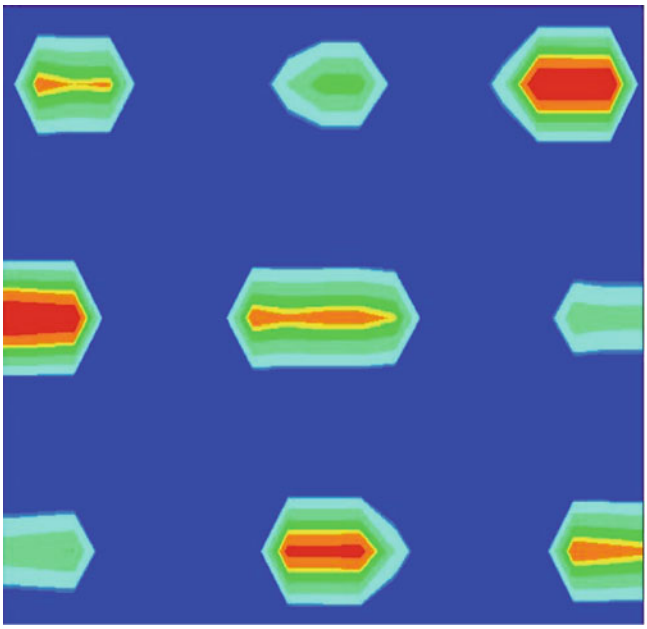

Fig. 11 Defect terrain on a 4-mm-thick submerged steel plate

5 Conclusions

Ultrasonic guided waves can be effectively used for monitoring corrosion damages in reinforcing bars embedded in concrete as well as in submerged steel plates by utilizing its wave guide effects. Corrosion in reinforcing bars has been simulated as loss of bond and loss of area. The results have been compared with that of a bar undergoing accelerated chloride corrosion. The notch specimens had a closer agreement with the corroded bars than the debonded specimens. Chloride corrosion roughens up the surface of the bar and creates large pitting. While it is desirable to perform ultrasonic monitoring when actual corrosion is taking place it is extremely time consuming. This chapter highlights that a judicious contribution of delamination and notch would be essential to closely simulate the corroded bar. It has also been successfully applied to steel plates submerged in water simulating ship hulls and other hidden plate geometries. Guided waves offer a potentially attractive and a practically viable solution to discovering hidden structural degradations in civil and mechanical infrastructural systems.

Acknowledgements The fund received from the Department of Science and Technology, Government of India, Naval Research Board, and All India Council of Technical Education is gratefully acknowledged.

References

1. Sharma S, Mukherjee A (2010) Longitudinal guided waves for monitoring corrosion in reinforcing bars in concrete. Struct Health Monit 13:555–567
2. Sharma S, Mukherjee A (2011) Monitoring corrosion in oxide and chloride environments using ultrasonic guided waves. ASCE J Mater Civil Eng 23(2):207–211
3. Sharma S, Mukherjee A (2012) Non-Destructive Evaluation of Corrosion in varying environments using guided waves. RNDE,. Available Online
4. Pavlakovic BN, Cawley P (2000) DISPERSE user's manual version 2.0.1.1. Imperial College, University of London, London
5. Sharma S, Mukherjee A (2010) Propagating ultrasonic guided waves through concrete reinforcements with simulated and actual corrosion. CINDE J 31(2):6–12

Stochastic Structural Dynamics Using Frequency Adaptive Basis Functions

A. Kundu and S. Adhikari

Abstract A novel Galerkin subspace projection scheme for structural dynamic systems with stochastic parameters is developed in this chapter. The fundamental idea is to solve the discretised stochastic damped dynamical system in the frequency domain by projecting the solution into a reduced subspace of eigenvectors of the underlying deterministic operator. The associated complex random coefficients are obtained as frequency-dependent quantities, termed as spectral functions. Different orders of spectral functions are proposed depending on the order of the terms retained in the expression. Subsequently, Galerkin weighting coefficients are employed to minimise the error induced due to the reduced basis and finite order spectral functions. The complex response quantity is explicitly expressed in terms of the spectral functions, eigenvectors and the Galerkin weighting coefficients. The statistical moments of the solution are evaluated at all frequencies including the resonance and antiresonance frequencies for a fixed value of damping. Two examples involving a beam and a plate with stochastic properties subjected to harmonic excitations are considered. The results are compared to direct Monte Carlo simulation and polynomial chaos expansion for different correlation lengths and variability of randomness.

Keywords Stochastic dynamics • Random field • Spectral decomposition • Karhunen-Loeve Expansion • Stochastic subspace

1 Introduction

The framework of the present work is the parametric uncertainty that is inherent in the mathematical models laid out to describe the governing equations of physical systems. These uncertainties may be intrinsic variability of physical quantities or a

A. Kundu (✉) • S. Adhikari
College of Engineering, Swansea University, Singleton Park SA2 8PP, UK
e-mail: a.kundu.577613@swansea.ac.uk

S. Chakraborty and G. Bhattacharya (eds.), *Proceedings of the International Symposium on Engineering under Uncertainty: Safety Assessment and Management (ISEUSAM - 2012)*,
DOI 10.1007/978-81-322-0757-3_10,

lack of knowledge about the physical behaviours of certain systems. As a result, though the recent advances in computational hardware has enabled the solution of very high resolution problems and even the sophisticated techniques of *a posteriori* error estimation [3], mesh adaptivity or the modelling error analysis has improved the confidence on results, yet these are not enough to determine the credibility of the numerical model.

There has been an increasing amount of research activities over the past three decades to model the governing partial differential equations within the framework of stochastic equations. We refer to few recent review papers [1, 8, 9]. After the discretisation of random fields and displacement fields, the equation of motion can be expressed by [2, 4, 5] a set of stochastic ordinary differential equations

$$\mathbf{M}(\theta)\,\ddot{\mathbf{u}}\,(\theta,\,t) + \mathbf{C}(\theta)\,\dot{\mathbf{u}}\,(\theta,\,t) + \mathbf{K}(\theta)\,\mathbf{u}(\theta,\,t) = \mathbf{f}_0(t) \tag{1}$$

where $\mathbf{M}(\theta) = \mathbf{M}_0 + \sum_{i=1}^{p_1} \mu i(\theta)\mathbf{M}_i \in \mathbb{R}^{n\times n}$ is the random mass matrix and $\mathbf{K}(\theta) = \mathbf{K}_0 + \sum_{i=1}^{p_2} vi(\theta)\mathbf{K}_i \in \mathbb{R}^{n\times n}$ is the random stiffness matrix along with $\mathbf{C}(\theta) \in \mathbb{R}^{n\times n}$ as the random damping matrix. The notation θ is used to denote the random sample space. Here, the mass and stiffness matrices have been expressed in terms of their deterministic components ($\mathbf{M_0}$ and $\mathbf{K_0}$) and the corresponding random contributions ($\mathbf{M_i}$ and $\mathbf{K}_i$) obtained from discretising the stochastic field with a finite number of random variables ($\mu_i(\theta)$ and $v_i(\theta)$) and their corresponding spatial basis functions. In the present work proportional damping is considered for which $\mathbf{C}(\theta) = \varsigma_1\mathbf{M}(\theta) + \varsigma_2\mathbf{K}(\theta)$, where ς_1 and ς_2 are deterministic scalars. For the harmonic analysis of the structural system considered in Eq. (1), it is represented in the frequency domain as

$$\left[-\omega^2\mathbf{M}(\theta) + i\omega\mathbf{C}(\theta) + \mathbf{K}(\theta)\right]\tilde{\mathbf{u}}(\theta,\,\omega) = \tilde{\mathbf{f}}_0(\omega) \tag{2}$$

where $\tilde{\mathbf{u}}(\theta,\,\omega)$ is the complex frequency domain system response amplitude and $\tilde{\mathbf{f}}_0(\omega)$ is the amplitude of the harmonic force.

Now we group the random variables associated with the mass and damping matrices of Eq. (1) as

$$\xi_i(\theta) = \mu_i(\theta) \quad for \quad i = 1, 2, \ldots, p_1$$
$$\text{and} \quad \xi_{i+p_1}(\theta) = v_i(\theta) \quad for \quad i = 1, 2, \ldots, p_2$$

Thus, the total number of random variables used to represent the mass and the stiffness matrices becomes $p = p_1 + p_2$. Following this, the expression for the linear structural system in Eq. (2) can be expressed as

$$\left(\mathbf{A}_0(\omega) + \sum_{i=1}^{p} \xi_i(\theta)\mathbf{A}_i(\omega)\right)\tilde{\mathbf{u}}(\omega,\theta) = \tilde{\mathbf{f}}_0(\omega) \tag{3}$$

where $\mathbf{A_o}$ and $\mathbf{A}_i \in \mathbb{C}^{n\times n}$ represent the complex deterministic and stochastic parts, respectively, of the mass, the stiffness and the damping matrices ensemble. For the case of proportional damping, the matrices $\mathbf{A}_o$ and $\mathbf{A}_i$ can be written as

$$\mathbf{A}_0(\omega) = \left[-\omega^2 + i\omega\varsigma_1\right]\mathbf{M}_0 + [i\omega\varsigma_2 + 1]\mathbf{K}_0 \tag{4}$$

and

$$\begin{aligned}\mathbf{A}_i(\omega) &= \left[-\omega^2 + i\omega\varsigma_1\right]\mathbf{M}_i \quad \text{for} \quad i = 1, 2, ..., p_1\\ \mathbf{A}_{i+p_1}(\omega) &= [i\omega\varsigma_2 + 1]\mathbf{K}_i \quad \textit{for} \quad i = 1, 2, ..., p_2\end{aligned} \tag{5}$$

The chapter has been arranged as follows. The projection theory in the vector space is developed in Sect. 2. In Sect. 3 an error minimisation approach in the Hilbert space is proposed. The idea of the reduced orthonormal vector basis is introduced in Sect. 4. Based on the theoretical results, a simple computational approach is shown in Sect. 5 where the proposed method of reduced orthonormal basis is applied to the stochastic mechanics of a Euler-Bernoulli beam. From the theoretical developments and numerical results, some conclusions are drawn in Sect. 6.

2 Spectral Decomposition in the Vector Space

Following the spectral stochastic finite-element method, or otherwise, an approximation to the solution stochastic system can be expressed as a linear combination of functions of random variables and deterministic vectors. Recently Nouy [6, 7] discussed the possibility of an optimal spectral decomposition. The aim is to use small number of terms to reduce the computation without losing the accuracy. We use the eigenvectors $\phi_k \in \mathbb{R}^n$ of the generalised eigenvalue problem

$$\mathbf{K}_0\phi_k = \lambda_k\mathbf{M}_0\phi_k; \quad k = 1, 2, ...n \tag{6}$$

Since the matrices $\mathbf{K_0}$ and $\mathbf{M_0}$ are symmetric and generally non-negative definite, the eigenvectors ϕ_k for $k = 1, 2, ...n$ form an orthonormal basis. Note that in principle, any orthonormal basis can be used. This choice is selected due to the analytical simplicity as will be seen later. For notational convenience, define the matrix of eigenvalues and eigenvectors

$$\lambda_0 = \text{diag}[\lambda_1, \lambda_2, \ldots, \lambda_n] \in \mathbb{R}^{n\times n} \quad \text{and} \quad \Phi = [\phi_1, \phi_2, \ldots, \phi_n] \in \mathbb{R}^{n\times n} \tag{7}$$

Eigenvalues are ordered in the ascending order so that $\lambda_1 < \lambda_2 < \ldots < \lambda_n$. Since Φ is an orthonormal matrix, we have $\Phi^{-1} = \Phi^T$ so that the following identities can easily be established:

$$\begin{aligned}\Phi^T\mathbf{A}_0\Phi &= \Phi^T\left(\left[-\omega^2 + i\omega\varsigma_1\right]\mathbf{M}_0 + [i\omega\varsigma_2 + 1]\mathbf{K}_0\right)\Phi\\ &= \left(-\omega^2 + i\omega\varsigma_1\right)\mathbf{I} + (i\omega\varsigma_2 + 1)\lambda_0\end{aligned}$$

which gives

$$\Phi^T \mathbf{A}_0 \Phi = \Lambda_0; \quad \mathbf{A}_0 = \Phi^{-T} \Lambda_0 \Phi^{-1} \quad \text{and} \quad \mathbf{A}_0^{-1} = \Phi \Lambda_0^{-1} \Phi^{-T} \tag{8}$$

where $\Lambda_0 = (-\omega^2 + i\omega\varsigma_1)\mathbf{I} + (i\omega\varsigma_2 + 1)\lambda_0$ and $\mathbf{I}$ is the identity matrix. Hence, Λ_0 can also be written as

$$\Lambda_0 = \text{diag}\left[\lambda_{0_1}, \lambda_{0_2}, \ldots, \lambda_{0_n}\right] \in \mathbb{C}^{n \times n} \tag{9}$$

where $\lambda_{0_j} = (-\omega^2 + i\omega\varsigma_1) + (i\omega\varsigma_2 + 1)\lambda_j$ and λ_j is defined in Eq. (7). We also introduce the transformations

$$\tilde{\mathbf{A}}_i = \Phi^T \mathbf{A}_i \Phi \in \mathbb{C}^{n \times n}; i = 0, 1, 2, \ldots, M \tag{10}$$

Note that $\tilde{\mathbf{A}}_i = \Lambda_0$ is a diagonal matrix and

$$\tilde{\mathbf{A}}_i = \Phi^{-T} \tilde{\mathbf{A}}_i \Phi^{-1} \in \mathbb{C}^{n \times n}; i = 0, 1, 2, \ldots, M \tag{11}$$

Suppose the solution of Eq. (3) is given by

$$\hat{\mathbf{u}}(\omega, \theta) = \left[\mathbf{A}_0(\omega) + \sum_{i=1}^{M} \xi_i(\theta) \mathbf{A}_i(\omega)\right]^{-1} \mathbf{f}_0(\omega) \tag{12}$$

Using Eqs. (7), (8), (9), (10), and (11) and the orthonormality of Φ, one has

$$\begin{aligned} \hat{\mathbf{u}}(\omega, \theta) &= \left[\Phi^{-T} \Lambda_0(\omega) \Phi^{-1} + \sum_{i=1}^{M} \xi_i(\theta) \Phi^{-T} \tilde{\mathbf{A}}_i \Phi^{-1}\right]^{-1} \mathbf{f}_0(\omega) \\ &= \Phi \Psi(\omega, \xi(\theta)) \Phi^{-T} \mathbf{f}_0(\omega) \end{aligned} \tag{13}$$

where

$$\Psi(\omega, \xi(\theta)) = \left[\Lambda_0(\omega) + \sum_{i=1}^{M} \xi_i(\theta) \tilde{\mathbf{A}}_i(\omega)\right]^{-1} \tag{14}$$

and the M-dimensional random vector

$$\xi(\theta) = \{\xi_1(\theta), \xi_2(\theta), \ldots, \xi_M(\theta)\}^T \tag{15}$$

Now we separate the diagonal and off-diagonal terms of the $\tilde{\mathbf{A}}_i$ matrices as

$$\tilde{\mathbf{A}}_i = \Lambda_i + \Delta_i, \quad i = 1, 2, \ldots, M \tag{16}$$

Here, the diagonal matrix

$$\Lambda_i = \text{diag}\left[\tilde{\mathbf{A}}_i\right] = \text{diag}\left[\lambda_{i_1}, \lambda_{i_2}, \ldots, \lambda_{i_n}\right] \in \mathbb{C}^{n\times n} \tag{17}$$

and the matrix containing only the off-diagonal elements $\Delta_i = \tilde{\mathbf{A}}_i - \Lambda_i$ is such that Trace $(\Delta_i) = 0$. Using these, from Eq. (14) one has

$$\Psi(\omega, \xi(\theta)) = \left[\underbrace{\Lambda_0(\omega) + \sum_{i=1}^{M} \xi_i(\theta)\Lambda_i(\omega)}_{\Lambda(\omega,\boldsymbol{\xi}(\theta))} + \underbrace{\sum_{i=1}^{M} \xi_i(\theta)\Delta_i(\omega)}_{\Delta(\omega,\boldsymbol{\xi}(\theta))}\right]^{-1} \tag{18}$$

where $\Lambda(\omega, \boldsymbol{\xi}(\theta)) \in \mathbb{C}^{n\times n}$ is a diagonal matrix and $\Delta(\omega, \boldsymbol{\xi}(\theta))$ is an off-diagonal only matrix. In the subsequent expressions, we choose to omit the inclusion of frequency dependence of the individual matrices for the sake of notational simplicity, so that $\Psi(\omega, \boldsymbol{\xi}(\theta)) \equiv \Psi(\boldsymbol{\xi}(\theta))$ and so on. Hence, we rewrite Eq. (18) as

$$\Psi(\boldsymbol{\xi}(\theta)) = \left[\Lambda(\boldsymbol{\xi}(\theta))\left[\mathbf{I}_n + \Lambda^{-1}(\boldsymbol{\xi}(\theta))\Delta(\boldsymbol{\xi}(\theta))\right]\right]^{-1} \tag{19}$$

The above expression can be represented using a Neumann type of matrix series [10] as

$$\Psi(\boldsymbol{\xi}(\theta)) = \sum_{s=0}^{\infty} (-1)^s \left[\Lambda^{-1}(\boldsymbol{\xi}(\theta))\Delta(\boldsymbol{\xi}(\theta))\right]^s \Lambda^{-1}(\boldsymbol{\xi}(\theta)) \tag{20}$$

Taking an arbitrary r-th element of $\hat{\mathbf{u}}(\theta)$, Eq. (13) can be rearranged to have

$$\hat{u}_r(\theta) = \sum_{k=1}^{n} \Phi_{rk} \left(\sum_{j=1}^{n} \Psi_{kj}(\boldsymbol{\xi}(\theta)) \left(\phi_j^T \mathbf{f}_0 \right) \right) \tag{21}$$

Defining

$$\Gamma_k(\xi(\theta)) = \sum_{j=1}^{n} \Psi_{kj}(\boldsymbol{\xi}(\theta)) \left(\phi_j^T \mathbf{f}_0 \right) \tag{22}$$

and collecting all the elements in Eq. (21) for $r = 1,2,\ldots,n$, one has

$$\hat{\mathbf{u}}(\theta) = \sum_{k=1}^{n} \Gamma_k(\boldsymbol{\xi}(\theta))\phi_k \tag{23}$$

This shows that the solution vector $\hat{\mathbf{u}}(\theta)$ can be projected in the space spanned by ϕ_k.

3 Error Minimisation Using the Galerkin Approach

In Sec. 2 we derived the spectral functions such that a projection in an orthonormal basis converges to the exact solution in probability 1. The spectral functions are expressed in terms of a convergent infinite series. First, second- and higher-order spectral functions obtained by truncating the infinite series have been derived. We have also showed that they have the same functional form as the exact solution of Eq. (3). This motivates us to use these functions as 'trial functions' to construct the solution. The idea is to minimise the error arising due to the truncation. A Galerkin approach is proposed where the error is made orthogonal to the spectral functions.

We express the solution vector by the series representation

$$\hat{\mathbf{u}}(\theta) = \sum_{k=1}^{n} c_k \widehat{\Gamma}_k(\boldsymbol{\xi}(\theta))\phi_k \tag{24}$$

Here, the functions $\widehat{\Gamma}_k : \mathbb{C}^M \to \mathbb{C}$ are the spectral functions, and the constants $c_k \in \mathbb{C}$ need to be obtained using the Galerkin approach. The functions $\widehat{\Gamma_k}(\xi(\theta))$ can be the first-order, second-order or any higher-order spectral function (depending on the order of the expansion s in Eq. (20)) and are the complex frequency adaptive weighting coefficient of the eigenvectors introduced earlier in Eq. (6). Substituting the expansion of $\hat{\mathbf{u}}(\theta)$ in the linear system equation (3), the error vector can be obtained as

$$\varepsilon(\theta) = \left(\sum_{i=0}^{M} \mathbf{A}_i \xi_i(\theta)\right)\left(\sum_{k=1}^{n} c_k \widehat{\Gamma_k}(\boldsymbol{\xi}(\theta))\phi_k\right) - \mathbf{f}_0 \in \mathbb{C}^n \tag{25}$$

where $\xi_0 = 1$ is used to simplify the first summation expression. The expression (24) is viewed as a projection where $\left\{\widehat{\Gamma_k}(\boldsymbol{\xi}(\theta))\phi_k\right\} \in \mathbb{C}^n$ are the basis functions and c_k are the unknown constants to be determined. We wish to obtain the coefficients c_k using the Galerkin approach so that the error is made orthogonal to the basis functions, that is, mathematically

$$\varepsilon(\theta) \perp \left(\widehat{\Gamma}_j(\boldsymbol{\xi}(\theta))\phi_j\right) \quad \text{or} \quad \left\langle \widehat{\Gamma}_j(\boldsymbol{\xi}(\theta))\phi_j, \varepsilon(\theta) \right\rangle = 0 \; \forall \, j = 1, 2, \ldots, n \tag{26}$$

Here, $\langle \mathbf{u}(\theta), \mathbf{v}(\theta) \rangle = \int P(d\theta \mathbf{u}(\theta)\mathbf{v}(\theta))$ defines the inner product norm. Imposing this condition and using the expression of $\varepsilon(\theta)$ from Eq. (25), one has

$$E\left[\left(\widehat{\Gamma}_j(\boldsymbol{\xi}(\theta))\phi_j\right)^T \left(\sum_{i=0}^{M} \mathbf{A}_i \xi_i(\theta)\right)\left(\sum_{k=1}^{n} c_k \widehat{\Gamma_k}(\boldsymbol{\xi}(\theta))\phi_k\right) - \left(\widehat{\Gamma}_j(\boldsymbol{\xi}(\theta))\phi_j\right)^T \mathbf{f}_0\right] = 0 \tag{27}$$

Interchanging the $E[\bullet]$ and summation operations, this can be simplified to

$$\sum_{k=1}^{n}\left(\sum_{i=0}^{M}\left(\phi_j^T\mathbf{A}_i\phi_k\right)E\left[\xi_i(\theta)\widehat{\Gamma}_j^T(\boldsymbol{\xi}(\theta))\widehat{\Gamma}_k(\boldsymbol{\xi}(\theta))\right]\right)c_k = E\left[\widehat{\Gamma}_j^T(\boldsymbol{\xi}(\theta))\right]\left(\phi_j^T\mathbf{f}_o\right) \quad (28)$$

or

$$\sum_{k=1}^{n}\left(\sum_{i=0}^{M}\widetilde{A}_{i_{jk}}D_{ijk}\right)c_k = b_j \quad (29)$$

Defining the vector $\mathbf{c} = \{c_1, c_2, \ldots, c_n\}^T$, these equations can be expressed in a matrix form as

$$\mathbf{S}\,\mathbf{c} = \mathbf{b} \quad (30)$$

with

$$S_{jk} = \sum_{i=0}^{M}\widetilde{A}_{i_{jk}}D_{ijk}; \quad \forall j,k = 1,2,\ldots,n \quad (31)$$

where

$$\widetilde{A}_{i_{jk}} = \phi_j^T\mathbf{A}_i\phi_k, \quad (32)$$

$$D_{ijk} = E\left[\xi_i(\theta)\widehat{\Gamma}_j^T(\boldsymbol{\xi}(\theta))\widehat{\Gamma}_k(\boldsymbol{\xi}(\theta))\right] \quad (33)$$

and

$$b_j = E\left[\widehat{\Gamma}_j^T(\boldsymbol{\xi}(\theta))\right]\left(\phi_j^T\mathbf{f}_o\right) \quad (34)$$

Higher-order spectral functions can be used to improve the accuracy and convergence of the series (24). This will be demonstrated in the numerical examples later in the chapter.

4 Model Reduction Using a Reduced Number of Basis

The Galerkin approach proposed in the previous section requires the solution of $n \times n$ algebraic equations. Although in general this is smaller compared to the polynomial chaos approach, the computational cost can still be high for large n as the coefficient matrix is in general a dense matrix. The aim of this section is to reduce it further so that, in addition to large number of random variables, problems with large degrees of freedom can also be solved efficiently.

Suppose the eigenvalues of $\mathbf{A}_0$ are arranged in an increasing order such that

$$\lambda_{01} < \lambda_{02} < \ldots < \lambda_{0n} \tag{35}$$

From the expression of the spectral functions, observe that the eigenvalues appear in the denominator:

$$\widehat{\Gamma}_k^{(1)}(\boldsymbol{\xi}(\theta)) = \frac{\phi_k^T \mathbf{f}_0}{\lambda_{0k} + \sum_{i=1}^{M} \xi_i(\theta)\lambda_{i_k}} \tag{36}$$

The numerator $\left(\phi_k^T \mathbf{f}_0\right)$ is the projection of the force on the deformation mode. Since the eigenvalues are arranged in an increasing order, the denominator of $\left|\Gamma_{k+r}^{(1)}(\boldsymbol{\xi}(\theta))\right|$ is larger than the denominator of $\left|\Gamma_k^{(1)}(\boldsymbol{\xi}(\theta))\right|$ according a suitable measure. The numerator $\left(\phi_k^T \mathbf{f}_0\right)$ depends on the nature of forcing and the eigenvectors. Although this quantity is deterministic, in general an ordering cannot be easily established for different values of k. Because all the eigenvectors are normalised to unity, it is reasonable to consider that $\left(\phi^T{}_k f_0\right)$ does not vary significantly for different values of k. Using the ordering of the eigenvalues, one can select a small number ϵ such that $\lambda_1/\lambda_q < \epsilon$ for some value of q, where λ_j is the eigenvalue of the generalised eigenvalue problem defined in Eq. (6). Based on this, we can approximate the solution using a truncated series as

$$\hat{\mathbf{u}}(\theta) \approx \sum_{k=1}^{q} c_k \widehat{\Gamma_k}(\boldsymbol{\xi}(\theta))\phi_k \tag{37}$$

where c_k, $\widehat{\Gamma}_k(\boldsymbol{\xi}(\theta))$ and are obtained following the procedure described in the previous section by letting the indices j, k only up to q in Eqs. (31) and (32). The accuracy of the series (37) can be improved in two ways, namely, (a) by increasing the number of terms q or (b) by increasing the order of the spectral functions $\widehat{\Gamma_k}(\boldsymbol{\xi}(\theta))$. Once the samples of $\mathbf{u} = (\theta)$ are generated, the statistics can be obtained using standard procedures.

5 Illustrative Application: The Stochastic Mechanics of a Euler-Bernoulli Beam

In this section we apply the computational method to a cantilever beam with stochastic bending modulus. We assume that the bending modulus is a homogeneous stationary Gaussian random field of the form

$$EI(x,\theta) = EI_0(1 + a(x,\theta)) \tag{38}$$

where x is the coordinate along the length of the beam, EI_0 is the estimate of the mean bending modulus and $a(x,\theta)$ is a zero mean stationary Gaussian random field. The autocorrelation function of this random field is assumed to be

$$C_a(x_1, x_2) = \sigma_a^2 e^{\frac{-(|x_1 - x_2|)}{\mu_a}} \tag{39}$$

where μ_a is the correlation length and σ_a is the standard deviation. We use the baseline parameters as the length $L = 1$ m, cross section $(b \times h)$ 39×5.93 mm^2 and Young's modulus $E = 2 \times 10^{11}$ Pa.

In study we consider deflection of the tip of the beam under harmonic loads of amplitude $\tilde{f}_0 = 1.0N$. The correlation length considered in this numerical study is $\mu_a = L/2$. The number of terms retained (M) in the Karhunen-Loeve expansion is selected such that $v_M/v_1 = 0.01$ in order to retain 90% of the variability. For this correlation length, the number of terms M comes to 18. For the finite element discretisation, the beam is divided into 40 elements. Standard four degrees of freedom Euler-Bernoulli beam model is used [11]. After applying the fixed boundary condition at one edge, we obtain the number of degrees of freedom of the model to be $n = 80$.

5.1 Results

The proposed method has been compared with a direct Monte Carlo simulation (MCS), where both have been performed with 10,000 samples. For the direct MCS, Eq. (12) is solved for each sample, and the mean and standard deviation is derived by assembling the responses. The calculations have been performed for all the four values of σ_a to simulate increasing uncertainty. This is done to check the accuracy of the proposed method against the direct MCS results for varying degrees of uncertainty.

Figure 1a presents the ratio of the eigenvalues of the generalised eigenvalue problem (6) for which the ratio of the eigenvalues is taken with the first eigenvalue. We choose the reduced basis of the problem based on $\lambda_1/\lambda_q < \in$, where $e = 0.01$, and they are highlighted in the figure. Figure 1b shows the frequency domain response of the deterministic system for both damped and undamped conditions. We have applied a constant modal damping matrix with the damping coefficient $\alpha = 0.02$ (which comes to 1% damping). It is also to be noted that the mass and damping matrices are assumed to be deterministic in nature, while it has to be emphasised that the approach is equally valid for random mass, stiffness and damping matrices. The frequency range of interest for the present study is 0–600 Hz with an interval of 2 Hz. In Fig. 1b, the tip deflection is shown on a log scale for a unit amplitude harmonic force input. The resonance peak amplitudes of the response of the undamped system definitely depend on the frequency resolution of the plot.

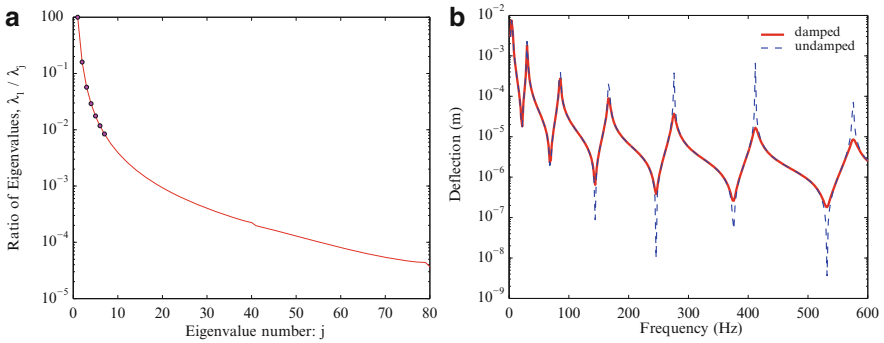

Fig. 1 The eigenvalues of the generalised eigenvalue problem involving the mass and stiffness matrices given in Eq. (6). For $e = 0.01$, the number of reduced eigenvectors $q = 7$ such that $\lambda_1/\lambda_j < \in$. (**a**) Ratio of eigenvalues of the generalised eigenvalue problem. (**b**) Frequency domain response of the tip of the beam under point load for the undamped and damped conditions (constant modal damping)

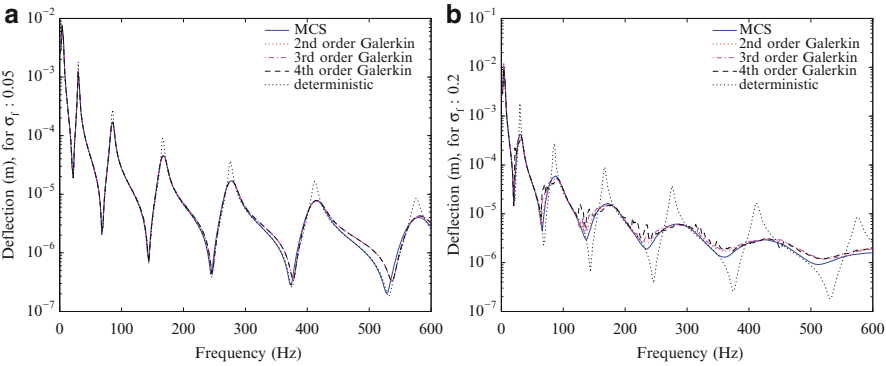

Fig. 2 The frequency domain response of the deflection of the tip of the Euler-Bernoulli beam under unit amplitude harmonic point load at the free end. The response is obtained with 10,000 sample MCS and for $\sigma_a = \{0.05, 0.10, 0.15, 0.20\}$. The proposed Galerkin approach needs solution of a 7×7 linear system of equations only. (**a**) Beam deflection for $\sigma_a = 0.05$. (**b**) Beam deflection for $\sigma_a = 0.2$

The frequency response of the mean deflection of the tip of the beam is shown in Fig. 2 for the cases of $\sigma_a = \{0.05, 0.10, 0.15, 0.20\}$. The figures show a comparison of the direct MCS simulation results with different orders of the solution following Eq. (20), where the orders $s = 2, 3, 4$. A very good agreement between the MCS simulation and the proposed spectral approach can be observed in the figures. All the results have been compared with the response of the deterministic system which shows that the uncertainty has an added damping effect at the resonance peaks. This can be explained by the fact that the parametric variation

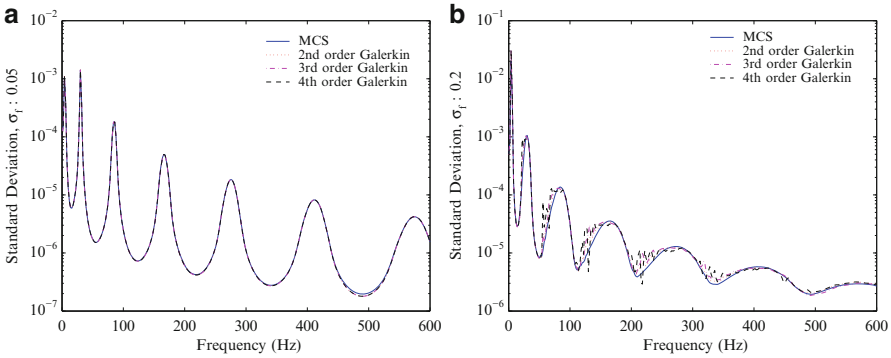

Fig. 3 The standard deviation of the tip deflection of the Euler-Bernoulli beam under unit amplitude harmonic point load at the free end. The response is obtained with 10,000 sample MCS and for $\sigma_a = \{0.05, 0.10, 0.15, 0.20\}$. (**a**) Standard deviation for the reference σ_a=0.05. (**b**) Standard deviation for the reference $\sigma_a = 0.2$

of the beam results in its peak response for the different samples to get distributed around the resonance frequency zones instead of being concentrated at a particular frequency, and when the subsequent averaging is applied, it smoothes out the response peaks to a fair degree. The same explanation holds for the antiresonance frequencies. It can also be observed that increased variability of the parametric uncertainties (as is represented by the increasing value of σ_a) results in an increase of this added damping effect which is consistent with the previous explanation.

The standard deviation of the frequency domain response of the tip deflection for different spectral order of solution of the reduced basis approach is compared with the direct MCS and is shown in Fig. 3, for different values of σ_a. We find that the standard deviation is maximum at the resonance frequencies, which is expected due to the differences in the resonance peak of each sample. It is again observed that the direct MCS solution and the reduced-order approach give almost identical results, which demonstrate the effectiveness of the proposed approach.

The probability density function of the deflection of the tip of the cantilever beam for different degrees of variability of the random field is shown in Fig. 4. The probability density functions have been calculated at the frequency of 412 Hz, which is a resonance frequency of the beam. The results indicate that with the increase in the degree of uncertainty (variance) of the random system, we have long-tailed the density functions which is consistent with the standard deviation curve shown in Fig. 3 and the mean deflection of the stochastic system with the deterministic response in Fig. 2. This shows that the increase in the variability of the stochastic system has a damping effect on the response.

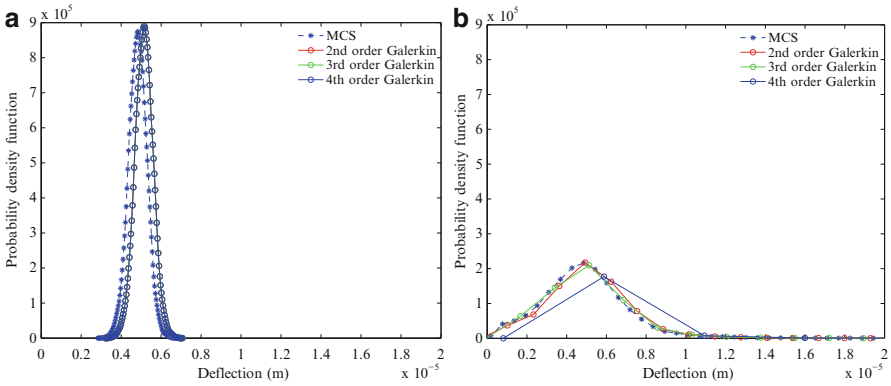

Fig. 4 The probability density function (*PDF*) of the tip deflection of the Euler-Bernoulli beam at 210 Hz under unit amplitude harmonic point load at the free end. The response is obtained with 10,000 samples and for $\sigma_a = \{0.05, 0.10, 0.15, 0.20\}$. (**a**) PDF of the response 210 Hz for $\sigma_a = 0.05$. (**b**) PDF of the response 210 Hz for $\sigma_a = 0.2$

6 Conclusions

Here, we have considered the discretised stochastic partial differential equation for structural systems with generally non-Gaussian random fields. In the classical spectral stochastic finite element approach, the solution is projected into an infinite dimensional orthonormal basis functions, and the associated constant vectors are obtained using the Galerkin type of error minimisation approach. Here an alternative approach is proposed. The solution is projected into a finite dimensional reduced vector basis, and the associated coefficient functions are obtained. The coefficient functions, called as the *spectral functions*, are expressed in terms of the spectral properties of the matrices appearing in the discretised governing equation. It is shown that then the resulting series converge to the exact solution in probability 1. This is a stronger convergence compared to the classical polynomial chaos which converges in the mean-square sense in the Hilbert space. Using an analytical approach, it is shown that the proposed spectral decomposition has the same functional form as the exact solution, which is not a polynomial, but a ratio of polynomials where the denominator has a higher degree than the numerator.

The computational efficiency of the proposed reduced spectral approach has been demonstrated for large linear systems with non-Gaussian random variables. It may be possible to extend the underlying idea to the class of non-linear problems. For example, the proposed spectral approach can be used for every linearisation step or every time step. Further research is necessary in this direction.

Acknowledgement A. Kundu acknowledges the financial support from the Swansea University through the award for Zienkiewicz scholarship. S. Adhikari acknowledges the financial support from the Royal Society of London through the Wolfson Research Merit Award.

References

1. Charmpis DC, Schueeller GI, Pellissetti MF (2007) The need for linking micromechanics of materials with stochastic finite elements: a challenge for materials science. Comput Mater Sci 41(1):27–37
2. Ghanem R, Spanos PD (1991) Stochastic finite elements: a spectral approach. Springer, New York
3. Kelly DW, De SR, Gago JP, Zienkiewicz OC, Babuska I (1983) A posteriori error analysis and adaptive processes in the finite element method: Part I: Error analysis. Int J Numer Methods Eng 19(11):1593–1619
4. Kleiber M, Hien TD (1992) The stochastic finite element method. Wiley, Chichester
5. Matthies HG, Brenner CE, Bucher CG, Soares CG (1997) Uncertainties in probabilistic numerical analysis of structures and solids – stochastic finite elements. Struct Saf 19(3):283–336
6. Nouy A (2007) A generalized spectral decomposition technique to solve a class of linear stochastic partial differential equations. Comput Methods Appl Mech Eng 196(45-48): 4521–4537
7. Nouy A (2008) Generalized spectral decomposition method for solving stochastic finite element equations: invariant subspace problem and dedicated algorithms. Comput Methods Appl Mech Eng 197(51–52):4718–4736
8. Nouy A (2009) Recent developments in spectral stochastic methods for the numerical solution of stochastic partial differential equations. Arch Comput Methods Eng 16:251–285. URL http://dx.doi.org/10.1007/s11831-009-9034-5
9. Stefanou G (2009) The stochastic finite element method: past, present and future. Comput Methods Appl Mech Eng 198(9–12):1031–1051
10. Yamazaki F, Shinozuka M, Dasgupta G (1988) Neumann expansion for stochastic finite element analysis. J Eng Mech ASCE 114(8):1335–1354
11. Zienkiewicz OC, Taylor RL (1991) The finite element method, 4th edn. McGraw-Hill, London

Uncertainties in Transportation Analysis

Partha Chakroborty

Abstract Like in most engineering disciplines, so also in transportation engineering, one often faces situations where the behaviour of the system is stochastic. Given the wide range of situations that comes under transportation engineering, the use of probability theory ranges from simple representation of variability through density functions to complex birth and death processes observed at intersection approaches, parking lots, toll booths, etc.

Unlike in most engineering disciplines, however, one of the basic elements of transportation systems is the human being. Sometimes, they are present as drivers controlling the units that make up a traffic stream, while at other times, they act as users who create demand for a transportation facility (like roads and airports). The uncertainties that human involvement brings to the transport systems often cannot be represented using the theory of probability. One has to look at other means of set descriptions and measures like possibility.

This note outlines the types of uncertainties that arise in the various systems that make up the field of transportation engineering and analysis and suggests appropriate paradigms to deal with them.

Keywords Probability • Fuzzy sets • Possibility • Transportation system

1 Introduction

Transportation is replete with situations which demand analysis through incorporation of uncertainties. However, uncertainties arise in different forms. In order to understand these different forms, the best way is to look at how one can evaluate the truth of the statement "x is A." Here, A is the description of some situation and x is a variable

P. Chakroborty (✉)
Department of Civil Engineering, Indian Institute of Technology Kanpur,
Kanpur 208 016, India
e-mail: partha@iitk.ac.in

S. Chakraborty and G. Bhattacharya (eds.), *Proceedings of the International Symposium on Engineering under Uncertainty: Safety Assessment and Management (ISEUSAM - 2012)*,
DOI 10.1007/978-81-322-0757-3_11,

which can sometimes be A. For example, (1) x can be queue length, while A could be "greater than 5" or "large," or (2) x can be estimated arrival time at a station, while A could be "before departure of the train" or "desired arrival time."

If x is known deterministically and A can be defined precisely, then the truth of the statement is either 0 or 1. In the simplest and most naïve form, even today, engineering is practiced based on such deterministic evaluations of supposedly precise notions. For example, routinely one would declare that the level of service prevailing on a road section is C even though neither the roads conditions which lead to a particular level of service is deterministic nor the definition of level of service is precise. Engineering analysis can only mature if attempt is made to better understand and model the uncertainties in the processes. Only with a better understanding of these uncertainties and their incorporation in the analysis can tolerances improve and reliance on large "factors of safety" reduce.

In transportation, different situations lead to different types of x and A and consequently to different types of uncertainties. In this short note, a brief description of different types of uncertainty handling paradigms which find a place in transportation is described. This note is divided into five brief sections of which this is the first. The next section describes some situations in transportation engineering which require probability theory and probability theory-based modelling techniques to handle the inherent uncertainties. The third section describes scenarios where the assumption that a situation (like A, above) can be precisely described is no longer tenable. This section looks at how the concept of fuzzy sets can be used in such scenarios. The fourth section dwells briefly on the applicability of possibility theory in transportation problems. The last section summarizes this chapter.

2 Probability Theory and Transportation

In transportation engineering, probability theory and its models are used whenever the chances of occurrences of precisely defined events or sets are sought to be determined. In the following, few situations are described which require use of probabilistic analysis:

- Variation in speeds of vehicles in a traffic stream needs to be represented using probability density functions.
- Birth processes (or inter-birth times), like arrival of vehicles at a section on a road or to a parking lot, must be represented through appropriate means.
- Death processes (or inter-death times), like departure of vehicles from a toll booth or an unsignalized intersection approach, must be represented through appropriate means.
- Combined birth and death processes (i.e. the queueing processes), like the queueing at an intersection, or at a toll plaza or at a parking lot, need to be modelled as proper queues. Note that some queueing systems could be simple single-server queues with Poisson arrival and Poisson departures, while others could be more complicated in terms of the departure process (like at unsignalized intersections), yet others are as complicated as coupled multiple queues (like at toll plazas).

- Choice processes like drivers choosing particular destinations or modes over others or drivers choosing particular toll booths while approaching a plaza over others need to be properly understood and modelled. Often these are modelled using discrete choice analysis which is based on the principles of random utility. Of course, given that this is a human choice process, the use of random utility principles can be questioned.

There are many more examples, but the purpose here is not to list them but to give the reader an idea about the variety of situations that arise in transportation which require probabilistic modelling. A quick survey of the literature will yield many references where probability models have been used to analyse transportation problems.

Yet, at the same time, all the cases that arise in transportation, on a closer scrutiny indicate that they are not fit cases for probabilistic analysis. The next section gives some examples where uncertainty arises due to lack of clarity in defining concepts and discusses how this type of uncertainty needs to be handled.

3 Fuzzy Sets and Transportation

It often happens that a concept is defined using terms which are inherently vague. For example, the level of service (an important design parameter for traffic facilities) is defined using expressions like “slightly and quickly.” The highway capacity manual [2–4], from which this concept has originated, undoubtedly considers level of service as a qualitative measure of the driving conditions. Yet, the same manual and various other manuals around the world continue to evaluate the level of service through deterministic means which yield precise levels of service for given stream parameters. Kikuchi and Chakroborty [6] point this out and suggest how this can be corrected.

The problem in the example given here is that of how one defines a set for a concept like level of service A or level of service B. Even if one accepts the proposition that somehow density of the traffic stream is a good indicator of the level of service, the definition of level of service implies that one cannot draw precise or crisp boundaries in the universe of density to indicate different sets representing different levels of service. A more appropriate description would be where the boundaries are not precise and allow elements of the universe to be partial members of a set or that of a set and its complement. Such sets are called fuzzy sets and are defined through membership functions which map the elements of a universe to a unit real scale [0,1] indicating membership to that set.

There are other examples in transportation where the concepts one deals with, ideally, should not be described though traditional sets or crisp sets. This is so because human inference often proceeds with concepts which are perceived (rather than measured) and classified linguistically; typically, such classification does not lend itself to precise boundaries. For example, the concept of “tall” cannot be

represented as a set where only people whose heights are greater than, say, 6 ft are members and others are not. This is because a person who is 5 ft 11 in. is also, in the mind of humans, not not-tall.

In transportation, human inference plays a big role. For example, the process of driving is a system where the human driver (or controller) perceives the relevant parameters from the surroundings (like speed, distance headway and relative speed) and infers what action should be taken in terms of acceleration. Theories which describe this inference mechanism through differential equations make the sweeping and reasonably untenable assumption that drivers perceive and infer precisely. Although such analysis has a place in developing the theory of traffic flow, it is important to realize that a fuzzy inference (or control) system will be a truer model of the real-world system. In such models, among other things, concepts are represented as fuzzy sets. Kikuchi and Chakroborty [5] and Chakroborty and Kikuchi [1] highlight these points in terms of the theory of car-following—an essential element of the theory of traffic flow.

Interested readers may refer to Klir and Folger [9], Zimmermann [12] and various other texts for a better understanding of fuzzy sets and other theories built on fuzzy sets.

4 Possibility Theory and Transportation

The first section introduced the concept of looking at the truth of the statement "x is A" as a way to understanding the different types of uncertainty that may exist in a system. The second section described situations in transportation where x is random (or stochastic) while the concept A, that one wish to evaluate, can be precisely defined. For example, in this situation, meaningful questions could be "queue length is greater than 7" or "number of vehicles arriving (in a 5-min interval) is more than 10 but less than 15." As can be seen, what gives rise to the uncertainty in evaluating the truth of the statement "x is A" is the stochastic nature of queue length or number of vehicles arriving (i.e. the x) and not "greater than 7," or "more than 10 but less than 15" (i.e. the A).

In the third section, situations were presented where the source of uncertainty was the way A was defined. For example, concepts like "large delay" or "closing-in quickly" could only be represented, respectively, in the universe of time or relative speed through fuzzy sets which do not have crisp or precise boundaries. Hence, even if x is known precisely, there would be uncertainty associated with the truth of the statement x is A because of how A is defined.

In this section, those cases are considered where the information which helps in determining the nature of x (i.e. whether it is known precisely or it can be best described through a probability density function) is such that a probability density function cannot be used to describe x.

Both probability and possibility are measures which assign to a set a number in the range [0,1] that indicates the strength of the belief that a given element is in the

set. This, of course, is a very coarse and naïve definition of measures. The interested reader may refer to Klir and Folger [9] for a simple description of measures. Suffice it to say that probability is but one measure which tries to capture this strength of belief. In fact, it is understood that if the evidence is arranged in a particular way (referred to as *conflicting*) can the associated measure be referred to as probability. While if the evidence is arranged in a different way (referred to as *consonant*), then the associated measure is referred to as a possibility measure. In transportation, often situations arise where the evidence is arranged in a manner which is consonant. Interestingly, Zadeh [11] drew analogies between the theories of fuzzy sets and possibility.

Kikuchi and Chakroborty [7] list many situations where possibility distribution and possibilistic analysis are more relevant; some of them are:

- Representing desire, for example, desired departure time and desired arrival time.
- Representing notion of satisfaction and acceptability, for example, satisfactory cost, acceptable toll and acceptable delay.
- Representing perceived quantities or quantities based on experience, for example, estimated travel time, expected delay and value of time.
- Situations where quantities are represented using possibility measure require analysis using the theory of possibility; a detailed description of this can be found in Kikuchi and Chakroborty [7].

The interested reader may refer to Klir [8] and Klir and Wierman [10] among many others for a comprehensive understanding of how to analyse uncertainty.

5 Conclusion

In this short note, an attempt is made to highlight the different types of uncertainties that exist in transportation and how these types can be handled by using appropriate paradigms. Specifically, the use of theories of probability, possibility and fuzzy sets is described here.

References

1. Chakroborty P, Kikuchi S (1999) Evaluation of general motors' based car-following models and a proposed fuzzy inference model. Transp Res Part C 7:209–235
2. Highway Capacity Manual (1965) HRB. Special report 87. National Research Council, Washington, DC
3. Highway Capacity Manual (1985) TRB. Special report 209, 3rd edn. National Research Council, Washington, DC
4. Highway Capacity Manual (2000) TRB. National Research Council, Washington, DC

5. Kikuchi S, Chakroborty P (1992) Car-following model based on fuzzy inference system. Transp Res Rec 1365:82–91
6. Kikuchi S, Chakroborty P (2006) Frameworks to represent uncertainty when level of service is determined. Transp Res Rec 1968:53–62
7. Kikuchi S, Chakroborty P (2006) Place of possibility theory in transportation analysis. Transp Res Part B 40:595–615
8. Klir GJ (1999) On fuzzy set interpretation of possibility theory. Fuzzy Sets Syst 108:263–273
9. Klir GJ, Folger TA (1988) Fuzzy sets, uncertainty, and information. Prentice-Hall, Englewood Cliffs
10. Klir G, Wierman M (2000) Uncertainty-based Information: elements of generalized information theory. Physica-Verlag, Heidelberg/New York
11. Zadeh LA (1978) Fuzzy sets as basis for a theory of possibility. Fuzzy Sets Syst 1:3–28
12. Zimmermann H-J (1991) Fuzzy set theory and its applications, 2nd edn. Kluwer Academic Publishers, Boston

Reliability Analysis of Municipal Solid Waste Settlement

Sandeep K. Chouksey and G.L. Sivakumar Babu

Abstract It is well-known that the disposal of municipal solid waste (MSW) has become one of the challenges in landfill engineering. It is very important to consider mechanical processes that occur in settlement response of MSW with time. In the recent years, most of the researchers carried out different tests to understand the complex behavior of municipal solid waste and based on the observations and proposed different models for the analysis of stress-strain, time-dependent settlement response of MSW. However, in most of the cases, the variability of MSW is not considered. For the analysis of MSW settlement, it is very important to account for the variability of different parameters representing primary compression, mechanical creep, and effect of biodegradation. In this chapter, an approach is used to represent the complex behavior of municipal solid waste using response surface method constructed based on a newly developed constitutive model for MSW. The variability associated with parameters relating to primary compression, mechanical creep, and biodegradation are used to analyze MSW settlement using reliability analysis framework.

Keywords Municipal solid waste • Mechanical creep • Biodegradation • Response surface method • Reliability analysis

1 Introduction

Landfilling is still the most common treatment and disposal technique for Municipal Solid Waste (MSW) worldwide. In every country, millions of tons of wastes are produced annually and it became one of the mammoth tasks to overcome it. Recently, MSW landfilling has significantly improved and has achieved a stage

S.K. Chouksey • G.L.S. Babu (✉)
Department of Civil Engineering, Indian Institute of Science, Bangalore 560012, India
e-mail: choukseysandeep@gamil.com; gls@civil.iisc.ernet.in

S. Chakraborty and G. Bhattacharya (eds.), *Proceedings of the International Symposium on Engineering under Uncertainty: Safety Assessment and Management (ISEUSAM - 2012)*,
DOI 10.1007/978-81-322-0757-3_12,

of highly engineered sanitary landfills in the most developed and developing countries. Evaluation of settlement is one of the critical components in landfill design. The contribution of engineered landfilling requires extensive knowledge of the different processes which occur simultaneously in MSW during settlement. The settlement in MSW is mainly attributed to (1) physical and mechanical processes that include the reorientation of particles, movement of the fine materials into larger voids, and collapse of void spaces; (2) chemical processes that include corrosion, combustion, and oxidation; (3) dissolution processes that consist of dissolving soluble substances by percolating liquids and then forming leachate; and (4) biological decomposition of organics with time depending on humidity and the amount of organics present in the waste.

Due to heterogeneity in the material of MSW, the analysis becomes more complicated because degradation process on MSW is time-dependent phenomena and continuously undergoes degradation with time. In the degradation process, two major mechanisms of biodegradation may occur: aerobic (in the presence of oxygen) and anaerobic (in the absence of oxygen) processes. The production of landfill biogas is a consequence of organic MSW biodegradation. This process is caused by the action of bacteria and other microorganisms that degrade the organic fraction of MSW in wet conditions. To capture this phenomenon in the prediction of settlement and stress-strain response of MSW, several researchers have proposed different models based on the different assumptions [1–3, 7, 8, 10, 12].

Marques et al. [10] presented a model to obtain the compression of MSW in terms of primary compression in response to applied load, secondary mechanical creep, and time-dependent biological decomposition. The model performance was assessed using data from the Bandeirantes landfill, which is a well-documented landfill located in Sao Paulo, Brazil, in which an instrumented test fill was constructed. Machado et al. [8] presented a constitutive model for MSW based on elastoplasticity considering that the MSW contains two component groups: the paste and the fibers. The effect of biodegradation is included in the model using a first-order decay model to simulate gas generation process through a mass-balance approach while the degradation of fibers is related to the decrease of fiber properties with time. The predictions of stress-strain response from the model and observations from the experiments were compared, and guidelines for the use of the model are suggested. Babu et al. [1, 3] proposed constitutive model based on the critical state soil mechanics concept. The model gives the prediction of stress-strain and pore water pressure response and the predicted results were compared with the experimental results. In addition, the model was used to calculate the time-settlement response of simple landfill case. The predicted settlements are compared with the results obtained from the model of Marques et al. [9, 10].

1.1 Settlement Predictive Model

Babu et al. [1] proposed a constitutive model which can be used to determine settlement of MSW landfills based on constitutive modeling approach. In this

model, the elastic and plastic behavior as well as mechanical creep and biological decomposition is used to calculate the total volumetric strain of the MSW under loading as follows:

$$d\varepsilon_v = d\varepsilon_v^e + d\varepsilon_v^p + d\varepsilon_v^c + d\varepsilon_v^b \tag{1}$$

where $d\varepsilon_v^e$, $d\varepsilon_v^p$, $d\varepsilon_v^c$, and $d\varepsilon_v^b$ are the increments of volumetric strain due elastic, plastic, time-dependent mechanical creep, and biodegradation effects, respectively. The increment in elastic volumetric strain $d\varepsilon_v^e$ can be written as:

$$d\varepsilon_v^e = -\frac{de^e}{1+e} = \frac{\kappa}{1+e}\frac{dp'}{p'} \tag{2}$$

And increment in plastic volumetric strain can be written as

$$d\varepsilon_v^p = \left(\frac{\lambda-\kappa}{1+e}\right)\left[\frac{dp'}{p'} + \frac{2\eta d\eta}{M^2+\eta^2}\right] \tag{3}$$

The above formulations for increments in volumetric strain due to elastic and plastic are well established in critical state soil mechanics literature.

The mechanical creep is a time-dependent phenomenon proposed by Gibson and Lo's [6] model, in exponential function, is given by

$$\varepsilon_v^c = b\Delta p'\left(1 - e^{-ct'}\right) \tag{4}$$

where b is the coefficient of mechanical creep, $\Delta p'$ is the change in mean effective stress, c is the rate constant for mechanical creep, and t' is the time since application of the stress increment. The biological degradation is a function of time and is related to the total amount of strain that can occur due to biological decomposition and the rate of degradation. The time-dependent biodegradation proposed by Park and Lee [12] is given by

$$\varepsilon_v^b = E_{dg}\left(1 - e^{-dt''}\right) \tag{5}$$

where E_{dg} is the total amount of strain that can occur due to biological decomposition, d is the rate constant for biological decomposition, and t'' is the time since placement of the waste in the landfill.

From Eq. (4), increment in volumetric strain due to creep is written as

$$d\varepsilon_v^c = cb\Delta p' e^{-ct'} dt' \tag{6}$$

From Eq. (5), increment in volumetric strain due to biodegradation effect is written as

$$d\varepsilon_v^b = E_{dg} e^{-dt''} dt'' \tag{7}$$

In the present case, t' time since application of the stress increment and t'' time since placement of the waste in the landfill are considered equal to "t."

Using Eqs. (2), (3), (6), and (7) and substituting in Eq. (1), total increment in strain is given by

$$d\varepsilon_v = \frac{\kappa}{1+e}\frac{dp'}{p'} + \left(\frac{\lambda-\kappa}{1+e}\right)\left[\frac{dp'}{p'} + \frac{2\eta d\eta}{M^2+\eta^2}\right] + cb\Delta\sigma' e^{-ct}dt + E_{dg}e^{-dt}dt \quad (8)$$

Calculation procedure of settlement response of MSW using above equations is given in Babu et al. [2].

1.2 Variability of MSW Parameters

Settlement models of Marques et al. [10] and Babu et al. [1, 3] have parameters such as compressibility index, coefficient of mechanical creep (b), creep constant (c), biodegradation constant (E_{dg}) and rate of biodegradation (d). All these parameters are highly variable in nature due to heterogeneity of MSW. For any engineering design of landfill, these parameters are design parameters, and their variability plays vital role in design. Literature review indicates that the influence of all these parameters and their variations have significant effects on prediction of MSW settlement. Based on experimental and field observations, various researchers reported different range of values and percentage of coefficient of variations (COV). For example, Sowers [13] reported that the compression index (c_c) is related to the initial void ratio (e_0) and can vary between 0.15 e_0 and 0.55 e_0 and the value of secondary compression index (c_a) varied between 0.03 e_0 and 0.09 e_0. The upper limit corresponds to MSW containing large quantities of food waste and high decomposable materials. Results of Gabr and Valero [5] indicated c_c values varying from 0.4 to 0.9, and c_a values varying from 0.03 to 0.009 for the initial void ratios (e_0) in the range of approximately 1.0–3.0. Machado et al. [7] obtained the values of primary compression index which varied between 0.52 and 0.92. Marques et al. [10] reported c_c values varying from 0.073 to 1.32 with a coefficient of variation (COV) of 12.6%. The coefficient of mechanical creep (b) was reported in the range of 0.000292–0.000726 and COV of 17.7% and creep constant varying from 0.000969 to 0.00257 with COV of 26.9%. The time-dependent strain due to biodegradation is expressed by equation which uses E_{dg}, the parameter related to total amount of strain that can occur due to biodegradation, and d is the rate constant for biological decomposition. Biodegradation constant depends upon the organic content present in MSW. Marques et al. [10] gave typical range of E_{dg} varying from 0.131 to 0.214 and COV of 12.7% and biodegradation rate constant d varying from 0.000677 to 0.00257 and COV of 42.3%. Foye and Zhao [4] used random field model to analyze differential settlement of existing landfills. They used c_c values 0.22 and 0.29 with COV of 36% and E_{dg} time-dependent strain due to biodegradation equal to 0.03724 and rate constant due to biodegradation (d) equal to

0.00007516. These variables are not certain; their values depend upon the variation conditions like site conditions, initial moisture content, and quantity of biodegradable material present in the existing MSW. Therefore, it is very important to perform settlement analysis of MSW with consideration of variability and their influence on reliability index or probability of failure. In order to simplify the settlement calculations, the above settlement evaluation procedure is used with reference to a typical landfill condition using response surface method (RSM).

1.3 Response Surface Method

RSM is a collection of statistical and mathematical techniques useful for developing, improving, and optimizing process. In the practical application of response surface methodology (RSM), it is necessary to develop an approximating model for the true response surface. A first-order (multilinear) response surface model is given by

$$y_i = \beta_0 + \beta_1 x_1 + \beta_2 x_2 + \cdots\cdots\cdots\cdots\cdots + \beta_n x_n + \varepsilon \tag{9}$$

Here, y_i is the observed settlement of MSW; the term "linear" is used because Eq. (9) is a linear function of the unknown parameters $\beta_1, \beta_2, \beta_3, \beta_4$, and β_5 that are called the regression coefficients, and $x_1, x_2, x_3, \cdots\cdots\cdots\cdots\cdots x_n$ are coded variables which are usually defined to be dimensionless with mean zero and same standard deviation. In the multiple linear regression model, natural variables $\left(b, c, d, E_{dg}, \lambda\right)$ are converted into coded variable by relationship

$$x_{i1} = \frac{\xi_{i1} - [\max(\xi_{i1}) + \min(\xi_{i1})]/2}{[\max(\xi_{i1}) - \min(\xi_{i1})]/2}$$

In the present study, RSM analysis is performed using single replicate 2^n factorial design to fit first-order linear regression model, where n is the total number of input variables involved in the analysis and corresponding to these variables the number of sample point required is 2^n. For example, in the present case five variables are considered; here, n is equal to 5 and number of sample points required is 32. These 32 sample points are generated using "+"and "−" notation to represent the high and low levels of each factor, the 32 runs in the 2^5 design in the tabular format shown in Table 1.

For the analysis, the maximum and minimum values are assigned based on the one-sigma, two-sigma, and three-sigma rule, i.e., $\sigma \pm \mu, \sigma \pm 2\mu$, and $\sigma \pm 3\mu$, where μ is the mean value and σ is the standard deviation of variables given in Table 2. In order to account the variability of different parameters in the settlement analysis of MSW, five major parameters are used under the loading conditions (from bottom to top) as shown in Fig. 1; the following variable parameters are used for the study.

Table 1 Generation +'s and −'s for generation of response surface equation

S. No.	$b\ (m^2/kN)$	$c\ (day^{-1})$	$d\ (day^{-1})$	E_{dg}	λ
1.	+	+	+	+	+
2.	+	+	+	+	−
3.	+	+	+	−	+
4.	+	+	+	−	−
5.	+	+	−	+	+
6.	+	+	−	+	−
7.	+	+	−	−	+
8.	+	+	−	−	−
9.	+	−	+	+	+
10.	+	−	+	+	−
11.	+	−	+	−	+
12.	+	−	+	−	−
13.	+	−	−	+	+
14.	+	−	−	+	−
15.	+	−	−	−	+
16.	+	−	−	−	−
17.	−	+	+	+	+
18.	−	+	+	+	−
19.	−	+	+	−	+
20.	−	+	+	−	−
21.	−	+	−	+	+
22.	−	+	−	+	−
23.	−	+	−	−	+
24.	−	+	−	−	−
25.	−	−	+	+	+
26.	−	−	+	+	−
27.	−	−	+	−	+
28.	−	−	+	−	−
29.	−	−	−	+	+
30.	−	−	−	+	−
31.	−	−	−	−	+
32.	−	−	−	−	−

Table 2 Parameters used for the regression analysis [10]

	λ	$b\ (m^2/kN)$	$c\ (day^{-1})$	$d\ (day^{-1})$	E_{dg}
Average	0.046	5.27E-04	1.79E-03	1.14E-03	0.15
Standard deviation	0.0059	9.5793E-05	0.000492	0.00049	0.020
COV	12.93	1.82E+01	2.75E+01	4.35E+01	12.99

They are coefficient of time-dependent mechanical creep (b), time-dependent mechanical creep rate constant (c), rate of biodegradation (d), biodegradation constant (E_{dg}), and the slope of normally consolidate line (λ). In the literature, it was reported that they are highly variable in nature, and it is very important to account these variation during the prediction of MSW settlement.

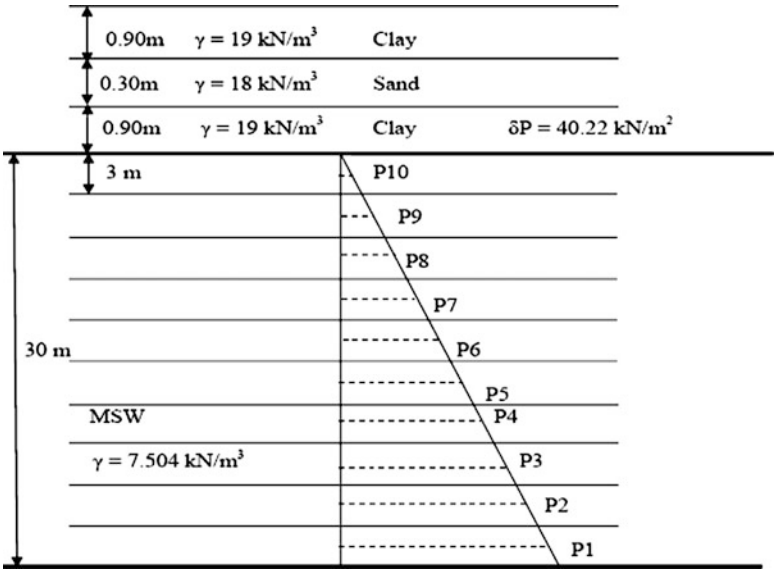

Fig. 1 MSW landfill scenario for estimation of settlement versus time

One-sigma (standard deviation) rule considers about 68%, and two sigma (standard deviations) consider almost 95% of sample variation assuming normal distribution, whereas three sigma (standard deviations) account for 99.7% of the sample variations, assuming the normal distribution. Using one-, two-, and three-sigma rules, the sample points are generated, and corresponding settlements are calculated using proposed model by Babu et al. [1].

The method of least squares is typically used to estimate the regression coefficients in a multiple linear regression model for the simple case of landfill as shown in Fig. 1. Myers and Montgomery [11] gave the multilinear regression in the form of matrix.

$$y = X\beta + \varepsilon \tag{10a}$$

where,

$$\beta = (X'X)^{-1}X'y \tag{10b}$$

Using above method, regression coefficients are calculated, and least square fit with the regression coefficients in terms of natural variables corresponding to the different COVs is presented in Table 3. Settlements are obtained from first-order regression model and from Babu et al. [1]. It is always necessary to examine the fitted model to ensure that it provides an adequate approximation to the true system and verify that none of the least square regression assumptions are violated. To ensure the adequacy of the regression equations, coefficient of regression (R^2 and R^2_{adj}) is calculated. Table 4 presents regression coefficients for the different standard deviations and at different COV.

Table 3 Regression equation in natural variables

(a) One-sigma deviation	
COV 10%	$1.90b + 12.29c + 303.96d + 8.13d + 203.26\lambda - 1.70$
COV 14%	$-11.38b + 16.76c + 426.07d + 11.38d + 284.67\lambda - 6.10$
COV 18%	$-30.35b + 21.78c + 549.94d + 14.62d + 36.20\lambda - 10.50$
COV 20%	$-41.73b + 24.57c + 612.32d + 16.24d + 407\lambda - 12.70$
(b) Two-sigma deviations	
COV 10%	$-41.73b + 25.13c + 613.24d + 16.24d + 407\lambda - 12.70$
COV 14%	$-108.11b + 35.20c + 866.20d + 22.67d + 570.6\lambda - 21.51$
COV 18%	$-201.10b + 47.47c + 1132.40d + 28.98d + 734.94\lambda - 30.33$
COV 20%	$-257.94b + 53.62c + 1273.83d + 32.10d + 817.41\lambda - 34.74$
(c) Three-sigma deviations	
COV 10%	$-127b + 38.54c + 932.10d + 24.26d + 611.62\lambda - 23.71$
COV 14%	$-290.18b + 56.41c + 1346.75d + 33.61d + 858.71\lambda - 36.95$
COV 18%	$-515.88b + 77.63c + 1847.50d + 42.26d + 1107.40\lambda - 50.22$
COV 20%	$-652.44b + 88.80c + 2167.27d + 46.03d + 1231.83\lambda - 56.84$

Table 4 Coefficients of regression (R^2) and R^2_{adj} for 1σ, 2σ, and 3σ for different COVs

COV %	R^2 (1σ)	$R^2_{adj}(1\sigma)$	R^2 (2σ)	R^2_{adj} (2σ)	$R^2(3\sigma)$	$R^2_{adj}(3\sigma)$
10	0.999	0.998	0.999	0.999	0.998	0.998
14	0.998	0.998	0.999	0.998	0.996	0.996
18	0.998	0.997	0.998	0.997	0.994	0.993
20	0.997	0.996	0.997	0.996	0.993	0.992

1.4 Reliability Index Formulation

The reliability index β for the independent variables in n-dimensional space is given as:

$$g(X) = c_0 + \sum_{i=1}^{n} c_i x_i \tag{11}$$

$$\mu_g = c_0 + c_1\mu_{x_1} + c_2\mu_{x_2} + \cdots\cdots + c_n\mu_{x_n} \tag{12}$$

$$\sigma_g = \sqrt{\sum_{i=1}^{n} c_i^2\sigma_{x_i}^2} \tag{13}$$

$$\beta = \frac{\mu_{\tilde{g}}}{\sigma_{\tilde{g}}} \tag{14}$$

In the present study, using deterministic analysis, with mean values given in Table 2, an ultimate settlement of 9.3 m for 30 years is obtained using the proposed

Table 5 Variation of reliability index with COVs at one-, two-, and three-sigma deviations

COV %	One sigma (β)	Two sigma (β)	Three sigma (β)
10	9.71	2.43	0.81
14	4.96	1.24	0.56
18	2.99	0.75	0.33
20	2.42	0.61	0.28

model as well as the response surface equations. To ascertain the probability of ultimate settlement reaching this value, the limit state function is defined as

$$g(x_i) = 9.3 - y_i \tag{15}$$

2 Methodology

In order to evaluate the reliability index or probability of failure considering variability of different parameters in the calculation of MSW settlement, the settlement given by the model is converted into Eq. (9) to using the procedure described earlier. In this chapter, settlement is evaluated for the one, two, and three standard deviations. Using the mean and standard deviation given in Table 2 and with "+" and "−" or maximum or minimum, values are calculated for all the variables. Table 1 shows the generation of sample points for the one standard deviation considering the normal distribution. These values are used to evaluate performance function based on the multilinear regression analysis as discussed previously for one, two, and three standard deviations at all the percentages of COV. Table 3 present the performance functions for the one, two, and three standard deviation at different percentages (10, 14, 18, and 20%) of COV. The performance functions are in the form of multilinear equations that include all the contributing variables used for the prediction of MSW settlement in the form of natural variables $\left(b, c, d, E_{dg}, \lambda\right)$. Equations (12) and (13) are used to calculate mean and standard deviation of the approximated limit state function. Knowing approximated mean (μ_g) and standard deviation (σ_g), reliability index is calculated using relation given in Eq. (14). Table 5 presents the summary of variation of reliability index values for the one, two, and three standard deviations at different COV. It is observed from Table 5 that the reliability index is inversely proportional to the COV of design variables decreases with increase in percentage of COVs of the design variables and also with increase in standard deviations.

3 Results and Discussion

Using RSM, multilinear equations are developed and these equations are considered as performance functions for the calculation of reliability index using Eqs. (12), (13), and (14) for MSW settlement. It is noted that the reliability index of MSW settlement is inversely related to the coefficient of variation of design variable

parameters. The results clearly depict that with increase in percentages of COV, reliability index decreases and probability of failure increases. For example, in case of 10% COV reliability index is calculated 9.71, whereas for the 20% COV this reliability index reduced to 2.42, which is reduction in 75% for one standard deviation. Similar results are observed for other cases. This indicates that probability of failure or reliability index is highly dependent upon COV of variable parameters. It is well-known that the MSW composition is highly heterogenous in nature which leads to higher percentages of COV, and hence, the chance of failure is very high. On the other hand, reliability index of MSW is highly dependent on sampling variations. It is observed that reliability index for 10% COV is 9.71 for one standard deviation, 2.42 for two standard deviations and 0.8078 for the three standard deviations. From one standard deviation to two standard deviation 75% reduction and for three standard deviations approximately 91% reduction in reliability index was observed. These results clearly point out the significance of sampling in the landfilling design for longer time periods.

4 Conclusions

The objective of this chapter is to demonstrate the influence of variability in the estimation of MSW settlement. Settlement is calculated based on the response surface method for the five design variables. Sample points are generated using "+" and "−" method for the one, two, and three standard deviations. Using these sample points, multilinear equations are developed for the estimation of MSW settlement. Based on these equations, reliability index is calculated for all percentages of COV. The results indicate that reliability index is highly dependent upon variability of the design variables and sample variations.

References

1. Babu Sivakumar GL, Reddy KR, Chouksey SK (2010) Constitutive model for municipal solid waste incorporating mechanical creep and biodegradation-induced compression. Waste Manage J 30(1):11–22
2. Babu Sivakumar GL, Reddy KR, Chouksey SK (2011) Parametric study of parametric study of MSW landfill settlement model. Waste Manage J 31(1):1222–1231
3. Babu Sivakumar GL, Reddy KR, Chouksey SK, Kulkarni H (2010) Prediction of long-term municipal solid waste landfill settlement using constitutive model. Pract Period Hazard Toxic Radioact Waste Manage ASCE 14(2):139–150
4. Foye KC, Zhao X (2011) Design criteria for the differential settlement of landfill foundations modeled using random fields. GeoRisk ASCE, Atlanta, GA, 26–28 June
5. Gabr MA, Valero SN (1995) Geotechnical properties of solid waste. ASTM Geotech Test J 18(2):241–251
6. Gibson RE, Lo KY (1961) A theory of soils exhibiting secondary compression. Acta Polytech Scand C-10:1–15

7. Machado SL, Carvalho MF, Vilar OM (2002) Constitutive model for municipal solid waste. J Geotech Geoenviron Eng ASCE 128(11):942–951
8. Machado SL, Vilar OM, Carvalho MF (2008) Constitutive model for long – term municipal solid waste mechanical behavior. Comput Geotech 35:775–790
9. Marques ACM (2001) Compaction and compressibility of municipal solid waste. Ph.D. thesis, Sao Paulo University, Sao Carlos, Brazil
10. Marques ACM, Filz GM, Vilar OM (2003) Composite compressibility model for municipal solid waste. J Geotech Geoenviron Eng 129(4):372–378
11. Myers RH, Montgomery DC (2002) Response surface methodology, process and product optimization using designed experiments, 2nd edn. Wiley, New York
12. Park HI, Lee SR (1997) Long-term settlement behavior of landfills with refuse decomposition. J Resour Manage Technol 24(4):159–165
13. Sowers F (1973) Settlement of waste disposal fills. In: Proceedings of 3rd international conference on soil mechanics and foundation engineering, vol 2, Moscow, pp 207–210

Uncertainty Evaluation in Integrated Risk-Based Engineering

P.V. Varde

Abstract Uncertainty evaluation is one of the important areas that needs to be strengthened toward effective implementation risk-based approach. At the outset, this chapter introduces the broad concepts in respect of integrated risk-based engineering and examines the capability of the current approaches for uncertainty modeling as applicable to integrated risk-based engineering. A brief overview of state of the art in uncertainty analysis for nuclear plants and the limitation of the current approaches in quantitative characterization of uncertainties have been discussed. Role of qualitative or cognitive-based approaches has also been discussed to address the scenario where quantitative approach is not adequate.

Keywords Uncertainty characterization • Risk-based engineering • Probabilistic safety assessment • Nuclear plants • Safety assessment

1 Introduction

Existing literature in safety assessment for nuclear plants deals with two terms, viz., "risk-based decisions" and "risk-informed decisions," for dealing with regulatory cases. In the context of nuclear plant safety evaluation, risk-based engineering deals with the evaluation of safety cases using probabilistic safety assessment (PSA) methods alone, while risk-informed approach decisions are based on, primarily, deterministic methods including design and operational insights, and PSA results either complement or supplement the deterministic findings [1]. These approaches intuitively consider that probabilistic and deterministic methods are two explicit domains. However, ideally speaking, any problem or modeling

P.V. Varde (✉)
Life Cycle Reliability Engineering Lab, Safety Evaluation and Manpower Training & Development Section, Research Reactor Services Division, Bhabha Atomic Research Centre, Mumbai 400 085, India
e-mail: varde@barc.gov.in

S. Chakraborty and G. Bhattacharya (eds.), *Proceedings of the International Symposium on Engineering under Uncertainty: Safety Assessment and Management (ISEUSAM - 2012)*,
DOI 10.1007/978-81-322-0757-3_13,

requires considerations of deterministic as well as probabilistic methods together. Otherwise, the salutation is not adequate and complete. Even though the risk-informed approach that requires considerations of deterministic as primary approach and probabilistic as supplementary/complimentary approach deals with the issues in explicit manner. The fact is that even deterministic variables, like design parameters, process, and nuclear parameters, are often random in nature and require probabilistic treatment. Defense-in-depth along with other principles, viz., redundancy, diversity, and fail-safe design, forms the basic framework of deterministic approach. It will help to characterize the reliability of various barriers of protection – the basic instrument of defense-in-depth. Similarly, probabilistic methods cannot work in isolation and require deterministic input in terms of plant configurations, failure criteria, design inputs, etc. Hence, it can be argued that a holistic approach is required where deterministic and probabilistic methods have to work in an integrated manner in support of decisions related to design, operation, and regulatory review of nuclear plants. The objective should be to remove overconservatism and prescriptive nature of current approach and bring in rationales and make the overall process of safety evaluation scientific, systematic, effective, and integrated in nature.

Integrated risk-based engineering is a new paradigm that is being introduced through this chapter. In this approach, the deterministic as well as probabilistic methods are integrated to form a holistic framework to address the safety issues. However, the key issues that need to be considered for applications are characterization of uncertainty, assessment of safety margins, and requirements of dynamic models for assessment of accident sequence evolution in time domain.

Another significant feature of this chapter is that it is perhaps for the first time that the term "risk-based engineering" has been used and not the traditional "risk-based decisions." The reason is that traditionally the terms "risk-based" and "risk-informed" have been associated with regulatory decisions. However, keeping in view the knowledge base that is available and the tools and methods that have been developed along these years makes the case for risk-based approach to qualify as a discipline as "risk-based engineering." Hence, it is proposed that the term "integrated risk-based engineering" has relevance to any area of engineering, be it design, operations including regulatory reviews.

Keeping in view the theme of this conference, the aspects related to uncertainty have been discussed. Included here is a brief overview of uncertainty evaluation methods in risk-based applications and requirements related to epistemic and aleatory uncertainty. Further, the aspects related to qualitative or cognitive aspects of uncertainty have also been discussed. This chapter treats the subject in a philosophical manner, and there is conscious decision not to cover the specifics that can be found in the referred literature.

2 Integrated Risk-Based Engineering: A Historical Perspective

It is generally felt that the traditional approach to safety assessment is purely deterministic in nature. It is true that most of the cases evaluated as part of safety assessment employ deterministic models and methods. However, if we look at the

assumptions, boundary conditions, factors of safety, data, and model, it can be argued that there is a good deal of probabilistic element even as part of traditional safety analysis. These elements or variables had qualitative notions for bounding situations and often provided comparative or relative aspects of two or more prepositions. To understand this point further, let us review the traditional safety analysis report(s) and have a fresh look at the broader aspect of this methodology. The major feature of the traditional safety analysis was based on the maximum credible accident, and for nuclear plants, it was mainly loss-of-coolant accident, loss-of-regulation accident scenario, etc. It was assumed that plant design should consider LOCA and other scenario like station blackout scenario to demonstrate that plant is safe enough. A reference to a safety report will make clear that there is an element of probability in a qualitative manner. Like (a) the possibility of two-out-of-three train failure is very low, (b) possibility of a particular scenario involving multiple failure is very unlikely or low, and (c) series of assumptions that will form bounding conditions. These aspects provided definite observation that probabilistic aspects were part of deterministic methods. These aspects were qualitative in nature. Keeping in view the above and considerations of factor of safety in the design as part of deterministic methods bring out the fact that safety analysis approach was integrated right since inception. This background along with current safety requirements, like process of safety evaluation, should (a) be more rational based and not prescriptive in nature, (b) remove overconservative, (c) be holistic in nature, (d) provide improved framework for addressing uncertainty, (e) allow realistic safety margins, and (f) provide framework for dynamic aspect of the accident scenario evaluation.

The integrated risk-based approach as mentioned above is expected to provide an improved framework for safety engineering. Here, the deterministic and probabilistic approaches treat the issues in an implicit manner unlike risk-informed approach where these two approaches have been employed in explicit manner. In this approach, issues are addressed in an integrated manner employing deterministic and probabilistic approaches. From the point of uncertainty characterization, in this approach, the random phenomenon is addressed as aleatory uncertainty while the model- and data-related uncertainty as epistemic uncertainty. There are host of issues in safety analysis where handling of uncertain issue is more important than quantification. These rather qualitative aspects of uncertainty or cognitive uncertainty need to be addressed by having safety provisions in the plant. The integrated risk-based framework proposes to address these issues.

3 Major Issues for Implementation of Integrated Risk-Based Engineering Approach

One of the major issues that forms the bottleneck to realize application of risk-based engineering is characterization of uncertainty associated with data and model. Even though for internal events there exist reasonable data, characterization of external

events poses major challenges. Apart from this availability of probabilistic criteria and safety margins as nation policy for regulation, issues related to new and advanced features of the plants like passive system modeling, digital system reliability in general, and software system reliability pose special challenges. Relatively large uncertainties associated with common cause failures of hardware systems and human action considerations particularly with accident scenarios are one of the major issues.

It can be argued that reduction of uncertainty associated with data and model in and characterization of uncertainties particularly for rare events where data and model are either not available or inadequate is one of the major challenges in implementation of integrated risk-based applications.

4 Uncertainty Analysis in Support of Integrated Risk-Based Decisions: A Brief Overview

Even though there are many definitions of uncertainty given in literature, the one which suits the risk assessment or rather the risk-informed/risk-based decisions has been given by ASME as "representation of the confidence in the state of knowledge about the parameter values and models used in constructing the PSA" [2]. Uncertainty characterization in the form of qualitative assessment and assumptions has been inherent part of risk assessment. However, as the data, tools, and statistical methods developed over the years, the quantitative methods for risk assessment came into being. The uncertainty in estimates has been recognized as inherent part of any analysis results. The actual need of uncertainty characterization was felt while addressing many real-time decisions related to assessment of realistic safety margin.

The major development has been in respect of classification/categorizing uncertainty based on the nature of uncertainty, viz., aleatory uncertainty and epistemic uncertainty. Uncertainty associated due to randomness (chance phenomenon) in the system/process is referred as aleatory uncertainty. This type of uncertainty arises due to inherent characteristic of the system/process and data. Aleatory uncertainty cannot be reduced as it is inherent part of the system. This is the reason aleatory uncertainty is also called irreducible uncertainty [3]. The nature of this uncertainty can be explained further by some examples like results of flipping a coin – head or tail it is matter of chance. Chances of diesel set to start on demand it could be success or failure, etc. On the other hand, the uncertainty associated due to lack of knowledge is referred as epistemic uncertainty. This uncertainty can be reduced either by performing additional number of experiments, more data, and information about the system. This uncertainty is more of subjective in nature.

If we look at the modeling and analysis methods in statistical distributions, we will note that probability distributions provide one of the important and fundamental mechanisms to characterize uncertainty in data by estimating upper bound

and lower bounds of the data [4, 5]. Hence, various probability distributions are central to characterization of uncertainty. Apart from this, fuzzy logic approach also provides an important tool to handle uncertainty where the information is imprecise and where probability approach is not adequate to address the issues [6]. Like in many situations, the performance data on system and components is not adequate, and the only input that is available is opinion of the domain experts. Apart from this, there are many situations where it is required to use linguistic variables as an input. Fuzzy approach suits these requirements.

There are many approaches for characterization/modeling of uncertainty. Keeping in the nature of problem is being solved; a judicious selection of applicable method has to be made [7]. Even though the list of approaches listed here is not exhaustive, commonly, the following methods can be reviewed as possible candidate for uncertainty modeling:

1. Probabilistic approach
   - Frequentist approach
   - Bayesian approach
2. Evidence theory – imprecise probability approach
   - Dempster-Shafer theory
   - Possibility theory – fuzzy approach
3. Structural reliability approach (application oriented)
   - First-order reliability method
   - Stochastic response surface method
4. Other nonparametric approaches (application specific)
   - Wilk's method
   - Bootstrap method

Each of the above methods has some merits and limitations. The available literature shows that general practice for uncertainty modeling in PSA is through the probabilistic approach [8–11]. Application of probabilistic distributions to address aleatory as well as epistemic uncertainty forms the fundamentals of this approach. There are two major basic models, classical model which is also referred as frequentist models and subjective model. Frequentist model tends to characterize uncertainty using probability bounds at component level. This approach has some limitations like no information on characterization of distribution and nonavailability of data and information for tail ends. The most popular approach is subjective approach implemented through Bayes theorem called Bayesian approach which allows subjective opinion of the analysts as "prior" knowledge to be integrated with the data or evidence that is available to provide with the estimate of the event called "posteriori" estimate [12]. Even though this approach provides an improved framework for uncertainty characterization in PSA modeling compared to frequentist approach, there are arguments against this approach. The subjectivity that this

approach carries with it has become the topic of debate in respect of regulatory decisions. Hence, there are arguments in favor of application of methods that use evidence theory which works on to address "imprecise probabilities" to characterize uncertainty [13–18]. Among the existing approach for imprecise probability, the one involving "coherent imprecise probability" which provides upper and lower bound reliability estimates has been favored by many researchers[19].

Among other methods listed above, each one has its merit for specific applications like response surface method, and FORMs (first-order reliability methods) are used generally for structural reliability modeling [20]. There are some application-specific requirements, like problems involving nonparametric tests where it is not possible to assume any particular distribution (as is the case with probabilistic methods); in such cases, bootstrap nonparametric approach is employed [21]. Even though this method has certain advantages, like it can draw inference even from small samples, estimation of standard error, it is computationally intensive and may become prohibitive for complex problems that are encountered in risk-based applications. Other nonparametric methods that find only limited application in risk-based engineering do not form the scope of this chapter.

From the above, it could be concluded that the probabilistic methods that include classical statistical methods and Bayesian approach form the major approaches for uncertainty characterization in risk-based approach. At times, fuzzy-based approach is used as part where the data deals with imprecise input in the form of linguistic variables. However, fuzzy logic applications need to be scrutinized for methodology that is used to design the membership functions as membership functions have found to introduce subjectivity to final estimates.

5 Major Features of RB Approach Relevant Uncertainty Characterization

Keeping in view the subject of this chapter, i.e., uncertainty characterization for risk-based approach, it is required to understand the nature of major issues that need to be addressed in risk-based characterization and accordingly look for the appropriate approach. At the outset, there appears general consensus that on a case to case basis most of the above listed approaches may provide efficient solution for the specific domain. However, here the aim is to focus on the most appropriate approach that suits the risk-based applications. The PSA in general and Level 1 PSA in particular, as part of risk-based approaches, have following major features [22–25]:

(a) The probabilistic models basically characterize randomness in data and model, and hence, the model at integrated level requires aleatory uncertainty characterization.
(b) The probabilistic models are basically complex and relatively large in size compared to the models developed for other engineering applications.

(c) The uncertainty characterization for PSA models requires an efficient simulation tool/method.
(d) The approach should allow characterization epistemic component of data as well as model.
(e) Confidence intervals for the component, human errors, etc., estimated using statistical analysis form the input for the probabilistic models.
(f) Major part of modeling is performed using fault tree and event tree approaches; hence, the uncertainty modeling approach should be effective for these models.
(g) There should be provision to integrate the prior knowledge about the event for getting the posteriori estimates, i.e., the approach should be able to handle subjective probabilities.
(h) Often, instead of quantitative estimates, the analysts come across situations where it becomes necessary to derive quantitative estimates through "linguistic" inputs. Hence, the framework should enable estimation of variables based on qualitative inputs.
(i) Evaluation of deterministic variable forms part of risk assessment. Hence, provision should exist to characterize uncertainty for structural, thermal hydraulic, and neutronics assessment.
(j) Sensitivity analysis for verifying impact of assumptions, data, etc., forms the fundamental requirements.
(k) The PSA offers improved framework for assessment of safety margin – a basic requirement for risk-based applications.
(l) Even though PSA provides an improved methodology for assessment of common cause failure and human factor data, keeping in view the requirements of risk-based applications further consolidation of data and model is required.

Apart from this, there are specific requirements, like modeling for chemical, environmental, geological, and radiological dose evaluation, which also need to be modeled. As can be seen above, the uncertainty characterization for risk assessment is a complex issue.

5.1 Uncertainty Propagation

The other issue in characterizing uncertainty is consideration of effective methodology for propagation of uncertainty. Here, the literature shows that Monte Carlo simulation and Latin hypercube approach form the most appropriate approach for uncertainty propagation [26]. Even though these approaches are primarily been used for probabilistic methods, there are applications where simulations have been performed in evidence theory or application where the priori has been presented as interval estimates [27]. The risk-based models are generally very complex in terms of (a) size of the model, (b) interconnections of nodes and links, (c) interpretation of results, etc. The available literature shows that the Monte Carlo simulation approach is extensively being used in many applications; it also labeled this method as computationally intensive and approximate in natures. Even with these

complexities, the risk-based applications, both Latin hypercube and Monte Carlo, have been working well. Even though it is always expected that higher efficiency in uncertainty modeling is required for selected cases, for overall risk-based models, these approaches can be termed as adequate. In fact, we have developed a risk-based configuration system in which the uncertainty characterization for core damage frequency has been performed using Monte Carlo simulation [28].

6 Uncertainty Characterization: Risk-Informed/Risk-Based Requirements

The scope and objective of risk-informed/risk-based applications determine the major element of Level 1 PSA. However, for the purpose of this chapter, let us consider that development of base Level 1 PSA for regulatory review as the all-encompassing study. The scope of this study includes full-scope PSA which means considerations of (a) internal event (including loss of off-site power and interfacing loss of coolant accident, internal floods, and internal fire); (b) external event, like seismic events, external impacts, and flood; (c) full-power and shut-down PSA; and (d) reactor core as the source of radioactivity (fuel storage pool not included) [25].

The point to be remembered here is that uncertainty characterization should be performed keeping in view the nature of applications [2, 29]. For example, if the application deals with the estimation of surveillance test interval, then the focus will start right from uncertainty in initiating event that demands automatic action of a particular safety system, unavailability for safety significant component, human actions, deterministic parameters that determine failure/success criteria, assumptions which determine the boundary condition for the analysis, etc.

An important reference that deals with uncertainty modeling is USNRC (United State Nuclear Regulatory Commission) document NUREG-1856 (USNRC, 2009) which provides guidance on the treatment of uncertainties in PSA as part of risk-informed decisions [29]. Though the scope of this document is limited to light water reactors, the guidelines with little modification can be adopted for uncertainty modeling in either CANDU (CA-Nadian Deuterium Uranium reactor)/PHWR (pressurized heavy water reactor) or any other Indian nuclear plants. In fact, even though this document provides guidelines on risk-informed decisions, requirements related to risk-based applications can be easily be modeled giving due considerations to the emphasis being placed on the risk metrics used in PSA. Significant contribution of ASME/ANS framework includes incorporation of "state-of-knowledge correlation" [2] which means the correlation that arises between sample values when performing uncertainty analysis for cut sets consisting of basic events using a sampling approach such as the Monte Carlo method; when taken into account, this results, for each sample, in the same value being used for all basic event probabilities to which the same data applies.

As for the standardization of risk-assessment procedure and dealing with uncertainty issues concerned, the PSA community finds itself in relatively comfortable position. The reason is that there is a consensus at international level as to which uncertainty aspects need to be addressed to realize certain quality criteria in PSA applications. The three major references that take care of this aspect are (a) ASME (American Society of Mechanical Engineers)/ANS (American Nuclear Society) Standard on PSA Applications [2], (b) IAEA-TECDOC-1120 (International Atomic Energy Agency-Technical Document) on Quality Attribute of PSA applications [30], and (c) various NEA (Nuclear Energy Agency) documents on PSA [24]. Any PSA applications to qualify as "Quality PSA" need to conform to these quality attributes as laid out for various elements of PSA. For example, the ASME/ANS code provides a very structured framework, wherein there are higher level attributes for an element of PSA, then there are specific attributes that support the higher level attributes, etc. These attributes enable formulating a program in the form of checklists that need to be fulfilled in terms of required attributes to achieve conformance quality level for PSAs. The examples of quality attributes that are required to assure uncertainty analysis requirements following are some examples from ASME/ANS in respect of the PSA element – Initiating event (IE) Modeling.

Examples of some lower level specific attributes from ASME/ANS include:

ASME/ANS attribute IE-C4: "When combining evidence from generic and plant-specific data, USE a Bayesian update process or equivalent statistical process. JUSTIFY the selection of any informative prior distribution used on the basis of industry experience."

Similarly,

ASME/ANS attribute IE-C3: *CALCULATE the initiating event frequency accounting for relevant generic and plant-specific data unless it is justified that there are adequate plant-specific data to characterize the parameter value and its uncertainty*.

Also, the lower support requirement IE-D3 documents the sources of model uncertainty and related assumptions.

The USNRC guide as mentioned above summarizes in details the uncertainty related to supporting requirements of ASME/ANS documents systematically. For details, these documents may be referred. Availability of this ASME/ANS standard, NEA documents, and IAEA-TECDOC is one of the important milestones for risk-based/risk-informed applications as these documents provide an important tool toward standardization of and harmonization of risk-assessment process in general and capturing of important uncertainty assessment aspects that impact the results and insights of risk assessment.

7 Decisions Under Uncertainty

At this point, it is important to understand that the uncertainty in engineering systems creeps basically from two sources, viz., noncognitive generally referred as quantitative uncertainty and cognitive referred as qualitative uncertainty [31].

The major part of this chapter has so far dealt with the noncognitive part of the uncertainty, i.e., uncertainty due to inherent randomness (aleatory) and uncertainty due to lack of knowledge (epistemic). We had enough discussions on this type of uncertainty. However, unless we address the sources of uncertainty due to cognitive aspects, the topic of uncertainty has not been fully addressed. The cognitive uncertainty caused due to inadequate definition of parameters, such as structural performance, safety culture, deterioration/degradation in system functions, level of skill/knowledge base, and experience staff (design, construction, operation, and regulation) [32]. The fact is that dealing with uncertainty using statistical modeling or any other evidence-based approach including approaches that deal with precise or imprecise probabilities has their limitations and cannot address issues involving vagueness of the problem arising from missing information and lack of intellectual abstraction of real-time scenario, be it regulatory decisions, design-related issues, or operational issues. The reason for this is that traditional probabilistic and evidence-based methods for most of the time deal with subjectivities, perceptions, and assumptions that may not form part of the real-time scenarios that require to address cognitive part of the uncertainty. Following subsections bring out the various aspects of cognitive/qualitative part of the uncertainty and methods to address these issues.

7.1 Engineering Design and Analysis

The issues related to "uncertainty" have been part of engineering design and analysis. The traditional working stress design (WSD)/allowable stress design (ASD) in civil engineering deal with uncertainty by defining "suitable factor." The same factor of safety is used for mechanical design to estimate the allowable stress (AS = Yield Stress/FS). This FS accounts for variation in material properties, quality-related issues, degradation during the design life, modeling issues and variation in life cycle loads, and lack of knowledge about the system being designed. The safety factor is essentially based on past experience but does not guarantee safety. Another issue is this approach is highly conservative in nature.

It is expected that an effective design approach should facilitate trade-off between maximizing safety and minimizing cost. Probabilistic- or reliability-based design allows this optimization in an efficient manner. The design problems require treatment of both cognitive and noncognitive sources of uncertainty. It should be recognized that the designer's personal preferences or subjective choices can be source of uncertainties which bring in cognitive aspect of uncertainty. Statistical aspects like variability in assessment of loads, variation in material properties, and extreme loading cycles are the source of noncognitive uncertainties.

In probabilistic-based design approach, considerations of uncertainty when modeled as stress-strength relation for reliability-based design form an integral part of design methodology. The Load and Resistance Factor Design (LRFD), first-order reliability methods (FORM), and second-order reliability methods (SORM)

are some of the application of probabilistic approach structural design and analysis. Many of civil engineering codes are based on probabilistic considerations. The available literature shows that design and analysis using probabilistic-based structural reliability approach have matured into an "engineering discipline" [20], and new advances and research have further strengthened this area [32].

The Level 1 PSA models are often utilized in support of design evaluation. During design stage, often complete information and data are not available. This leads to higher level of uncertainty in estimates. On the other hand, the traditional approach using deterministic design methodology involves use of relatively higher safety factors to compensate for the lack of knowledge. The strength of PSA framework is that it provides a systematic framework that allows capturing of uncertainties in data, model, and uncertainty due to missing or fuzzy inputs. Be it probabilistic or evidence-based tools and methods, it provides an improved framework for treatment of uncertainty. Another advantage of PSA framework is that it allows propagation of uncertainty from component level to system level and further up to plant level in terms of confidence bounds in for system unavailability/initiating event frequency and core damage frequency, respectively.

7.2 Management of Operational Emergencies

If we take lessons from the history of nuclear accidents in general and the three major accidents, viz., TMI (Three Mile Island) in 1979, Chernobyl in 1986, and the recent one Fukushima in 2011, it is clear that real-time scenario always require some emergency aids that respond to the actual plant parameters in a given "time window." Even though probabilistic risk analysis framework may address these scenarios, it can only addresses the modeling part of the safety analysis. It is also required to consider the qualitative or cognitive uncertainty aspects and its characteristics for operational emergency scenario.

The major characteristics of the operational emergencies can include:

(a) Deviation of plant condition from normal operations that require safety actions, it could be plant shutdown, actuation of shutdown cooling, etc.
(b) Flooding of plant parameters which include process parameters crossing its preset bounds, parameter trends and indications
(c) Available "time window" for taking a grasp of the situation and action by the operator toward correcting the situation
(d) Feedback in terms of plant parameters regarding the improved/deteriorated situations
(e) Decisions regarding restorations of systems and equipments status if the situation is moving toward normalcy
(f) Decision regarding declaration of emergency which requires a good understanding whether the situation requires declaration of plant emergency, site emergency, or off-site emergency
(g) Interpretation of available safety margins in terms of time window that can be used for designing the emergency operator aids

As the literature shows, that responding to accident/off-normal situations as characterized above calls for modeling that should have following attributes:

(a) Modeling of the anticipated transients and accident conditions in advance such that knowledge-based part is captured in terms of rules/heuristics as far as possible.
(b) Adequate provision to detect and alert plant staff for threat to safety functions in advance.
(c) Unambiguous and automatic plant symptoms based on well-defined criterion like plant safety limits and emergency procedures that guide the operators to take the needed action to arrest further degradation in plant condition.
(d) Considering the plant limits of plant parameters assessment of actual time window that is available for applicable scenarios.
(e) The system for dealing with emergency should take into plant-specific attributes, distribution of manpower, laid down line of communications, other than the standard provisions, the tools, methods, and procedures that can be applied for planned and long-term or extreme situations.
(f) Heuristics on system failure criteria using available safety margins.

Obviously, ball is out of "uncertainty modeling" domain and requires to address the scenarios from other side, i.e., taking decisions such that action part in real-time scenario compensates for the missing knowledge base and brings plant to safe state.

The answer to the above situation is development of knowledge-based systems that not only capture the available knowledge base but also provide advice to maintain plant safety under uncertain situation by maintaining plant safety functions. It may please be noted that here we are not envisaging any role for "risk-monitor" type of systems. We are visualizing an operator support system which can fulfill the following requirements (the list is not exhaustive and only presents few major requirements):

1. Detection of plant deviation based on plant symptoms.
2. The system should exhibit intelligent behavior, like reasoning, learning from the new patterns, conflict resolution capability, pattern recognition capability, and parallel processing of input and information.
3. The system should be able to predict the time window that is available for the safety actions.
4. Takes into account operator training and optimizes the graphic user interface (GUI).
5. The system should be effective in assessment of plant transients – it calls for parallel processing of plant symptoms to present the correct plant deviation.
6. The system should have adequate provision to deal with uncertain and incomplete data.
7. The presentation of results of the reasoning with confidence limits.
8. It should have an efficient diagnostics capability for capturing the basic cause (s) of the failures/transients.
9. The advice should be presented with adequate line of explanations.
10. The system should be interactive and use graphics to present the results.

11. Provisions for presentation of results at various levels, like abstract level advice (like open MV-3001 and Start P-2) to advise with reasonable details (like Open ECCS Valve MV-3001 located in reactor basement area and Start Injection Pump P-2, it can be started from control room L panel).

Even though there are many examples of R&D efforts on development of intelligent operator advisory systems for plant emergencies, readers may refer to the paper by Varde et al. for further details [33]. Here, the probabilistic safety assessment framework is used for knowledge representation. The fault tree models of PSA are used for generating the diagnostics, while the event tree models are used to generate procedure synthesis for evolving emergencies. The intelligent tools like artificial neural network approach are used for identification of transients, while the knowledge-based approach is used for performing diagnostics.

As can be seen above, the uncertain scenarios can be modeled by capturing either from the lessons learned from the past records for anticipated events. Even for the rare events where uncertainty could be of higher levels, the symptom-based models which focus on maintaining the plant safety functions can be used as model plant knowledge base.

8 Regulatory Reviews

In fact, the available literature on decisions under uncertainty has often focused on the regulatory aspects [29]. One of the major differences between operational scenarios and regulatory reviews or risk-informed decisions is that there generally is no preset/specified time window for decisions that directly affect plant safety. The second difference is that in regulatory or risk-informed decisions requires collective decisions and basically a deliberative process unlike operational emergencies where the decisions are taken often by individuals or between a limited set of plant management staff where the available time window and some time resources are often the constraints. Expert elicitation and treatment of the same often form part of the risk-informed decisions. Here, the major question is "what is the upper limit of spread of confidence bounds" that can be tolerated in the decision process. In short, "how much uncertainty in the estimates" can be absorbed in the decision process? It may be noted that the decisions problem should be evaluated using an integrated approach where apart from probabilistic variables even deterministic variables should be subjected to uncertainty analysis. One major aspect of risk assessment from the uncertainty point of view is updating the plant-specific estimates with generic prior data available either in literature or from other plants. This updating brings in subjectivity to the posteriori estimates. Therefore, it is required to justify and document the prior inputs. Bayesian method coupled with Monte Carlo simulation is the conventional approach for uncertainty analysis. The regulatory reviews often deal with inputs in the form of linguistic variables or "perceptions" which require perception-based theory of probabilistic reasoning with imprecise probabilities [13]. In such scenarios, the classical probabilistic

approach alone does not work. The literature shows that application of fuzzy logic offers an effective tool to address qualitative and imprecise inputs [34].

The assumptions often form part of any risk-assessment models. These assumptions should be validated by performing the sensitivity analysis. Here, apart from independent parameter assessment, sensitivity analysis should also be carried out for a set of variables. The formations of set of variables require a systematic study of the case under considerations.

The USNRC document NUREG-1855 on "Guidance on the treatment of Uncertainties Associated with PSAs in Risk-informed Decision Making" deals with the subject in details, and readers are recommended to refer to this document for details [29].

9 Conclusions

The available literature shows that there is an increasing trend toward the use of risk assessment or PSA insights in support of decisions. This chapter proposes a new approach called integrated risk-based engineering for dealing with safety of nuclear plants in an integrated and systematic manner. It is explained that this approach is a modification of the existing risk-informed/risk-based approach. Apart from application of PSA models, probabilistic treatment to traditional deterministic variables, success, and failure criteria, assessment of safety margins in general and treatment uncertainties in particular, forms part of the integrated risk-based approach.

There is general consensus that strengthening of uncertainty evaluation is a must for realizing risk-based application. It is expected that integrated risk-based approach will provide the required framework to implement the decisions. This chapter also argues that apart from probabilistic methods, evidence-based approaches need to be used to deal with "imprecise probabilities" which often form important input for the risk-based decisions.

Further other issue that this chapter discusses is that various methods, be it probabilistic or evidence based, cannot provide complete solution for issues related to uncertainty. There are qualitative or cognitive issues that need to be addressed by incorporating management tools for handling real-time situations. This is true for operational applications.

Finally, this chapter drives the point that both the quantitative and quantitative aspects need to be addressed to get toward more holistic solutions. Further research is needed to deal with imprecise probability, while cognitive aspects form the cornerstone of uncertainty evaluation.

Acknowledgments I sincerely thank Shri R. C. Sharma, Head, RRSD, BARC, for his constant support, guidance, and help without which Reliability and PSA activities in Life Cycle Reliability Engineering Lab would not have been possible. I also thank my SE&MTD Section colleagues Mr. Preeti Pal, Shri N. S. Joshi, Shri A. K. Kundu, Shri D. Mathur, and Shri Rampratap for their cooperation and help. I also thank Shri Meshram, Ms Nutan Bhosale, and Shri M. Das for their assistance in various R&D activities in the LCRE lab.

References

1. Chapman JR et al (1999) Challenges in using a probabilistic safety assessment in risk-informed process. Reliab Eng Syst Saf 63:251–255
2. American Society of Mechanical Engineers/American Nuclear Society (2009) Standards for level 1 large early release frequency in probabilistic risk assessment for nuclear power plant applications. ASME/ANS RA-Sa-2009, March 2009
3. Parry GW (1996) The characterization of uncertainty in probabilistic risk assessments of complex systems. Reliab Eng Syst Saf 54:119–126
4. Modarres M (2006) Risk analysis in engineering – techniques, tools and trends. CRC-Taylor & Francis Publication, Boca Raton
5. Modarres M, Mark K, Vasiliy K (2010) Reliability engineering and risk analysis – a practical guide. CRC Press Taylor & Francis Group, Boca Raton
6. Mishra KB, Weber GG (1990) Use of fuzzy set theory for level 1 studies in probabilistic risk assessment. Fuzzy Sets Syst 37(2):139–160
7. Kushwaha HS (ed) (2009) Uncertainty modeling and analysis. A Bhabha Atomic Research Centre Publication, Mumbai
8. Weisman J (1972) Uncertainty and risk in nuclear power plant. Nucl Eng Des 21 (1972):396–405. North–Holland Publishing Company
9. Gábor Lajtha (VEIKI Institute for Electric Power Research, Budapest, Hungary), Attila Bareith, Előd Holló, Zoltán Karsa, Péter Siklóssy, Zsolt Téchy (VEIKI Institute for Electric Power Research, Budapest, Hungary) "Uncertainty of the Level 2 PSA for NPP Paks"
10. Pate-Cornell ME (1986) Probability and uncertainty in nuclear safety decisions. Nucl Eng Des 93:319–327
11. Nilsen T, Aven T (2003) Models and model uncertainty in the context of risk analysis. Reliab Eng Syst Saf 79:309–317
12. Siu NO, Kelly DL (1998) Bayesian parameter estimation in probabilistic risk assessment. Reliab Eng Syst Saf 62:89–116
13. Zadeh LA (2002) Towards a perception-based theory of probabilistic reasoning with imprecise probabilities. J Stat Plan Inference 105:233–264
14. Peter W, Lyle G, Paul B (1996) Analysis of clinical data using imprecise prior probabilities. The Statistician 45(4):457–485
15. Peter W (2000) Towards a unified theory of imprecise probability. Int J Approx Reason 24:125–148
16. Troffaes MCM (2007) Decision making under uncertainty using imprecise probabilities. Int J Approx Reason 45:17–29
17. George KJ (1999) Uncertainty and information measures for imprecise probabilities: an overview. First international symposium on imprecise probabilities and their applications, Belgium, 29 June–2 July 1999
18. Caselton FW, Wuben L (1992) Decision making with imprecise probabilities: Dempster-Shafer theory and application. AGU: Water Resour Res 28(12):3071–3083
19. Kozine IO, Filimonov YV (2000) Imprecise reliabilities: experience and advances. Reliab Eng Syst Saf 67(1):75–83
20. Ranganathan R (1999) Structural reliability analysis and design. Jaico Publishing House, Mumbai
21. Davison AC et al (1997) Bootstrap methods and their applications. Cambridge University Press, Cambridge
22. Winkler RL (1996) Uncertainty in probabilistic risk assessment. Reliab Eng Syst Saf 54:127–132
23. Daneshkhah AR. Uncertainty in probabilistic risk assessment: a Review
24. Nuclear Energy Agency (2007) Use and development of probabilistic safety assessment. Committee on Safety of Nuclear Installations, NEA/CSNI/R(2007)12, November 2007

25. IAEA (2010) Development and application of level 1 probabilistic safety assessment for nuclear power plants. IAEA safety standards – specific safety guide no. SSG-3, Vienna
26. Atomic Energy Regulatory Board (2005) Probabilistic safety assessment for nuclear power plants and research reactors. AERB draft manual. AERB/NF/SM/O-1(R-1)
27. Weichselberger K (2000) The theory of interval-probability as a unifying concept for uncertainty. Int J Approx Reason 24:149–170
28. Agarwal M, Varde PV (2011) Risk-informed asset management approach for nuclear plants. 21st international conference on structural mechanics in reactor technology (SMiRT-21), India, 6–11 Nov 2011
29. Drouin M, Parry G, Lehner J, Martinez-GuridiG, LaChance J, Wheeler T (2009) Guidance on the treatment of uncertainties associated with PSAs in risk-informed decision making (Main report). NUREG-1855 (Vol.1). Office of Nuclear Regulatory Research Office of Nuclear Reactor Regulation, USNRC, USA.
30. International Atomic Energy Agency. Quality attributes for PSA applications. IAEA-TECDOC-1120. IAEA, Vienna
31. Assakkof I. Modeling for uncertainty: ENCE-627 decision analysis for engineering. Making hard decisions. Dept. of Civil Engineering, University of Maryland, College Park
32. Haldar A, Mahadevan S (2000) Probability reliability and statistical methods i±n engineering design. Wiley, New York
33. Varde PV et al (1996) An integrated approach for development of operator support system for research reactor operations and fault diagnosis. Reliab Eng Syst Saf 56
34. Iman K, Hullermeier E (2007) Risk assessment system of natural hazards: a new approach based on fuzzy probability. Fuzzy Set Syst 158:987–999

Past, Resent, and Future of Structural Health Assessment

Achintya Haldar and Ajoy Kumar Das

Abstract Past, present, and future of structural health assessment (SHA) concepts and related areas, as envisioned by the authors, are briefly reviewed in this chapter. The growth in the related areas has been exponential covering several engineering disciplines. After presenting the basic concept, the authors discussed its growth from infancy, that is, hitting something with a hammer and listening to sound, to the use of most recent development of wireless sensors and the associated advanced signal processing algorithms. Available SHA methods are summarized in the first part of this chapter. The works conducted by the research team of the authors are emphasized. Later, some of the future challenges in SHA areas are identified. Since it is a relatively new multidisciplinary area, the education component is also highlighted at the end.

Keywords Structural health assessment • Kalman filter • Substructure • System identification • Uncertainty analysis • Sensors

1 Introduction

The nature and quality of infrastructure have always been one of the indicators of sophistication of a civilization. There is no doubt that we are now at a historical peak. However, keeping the infrastructure at its present level has been a major challenge due to recent financial strain suffered by the global community. We do not have adequate resources to build new infrastructure or replace the aged ones that are over their design lives. The most economical alternative is found to be extending the life of existing infrastructure without compromising our way of living

A. Haldar (✉) • A.K. Das
Department of Civil Engineering and Engineering Mechanics,
University of Arizona, Tucson, AZ, USA
e-mail: haldar@u.arizona.edu; akdas@email.arizona.edu

S. Chakraborty and G. Bhattacharya (eds.), *Proceedings of the International Symposium on Engineering under Uncertainty: Safety Assessment and Management (ISEUSAM - 2012)*,
DOI 10.1007/978-81-322-0757-3_14,

and without exposing public to increased risk. This has been one of the major challenges to the engineering profession and attracted multidisciplinary research interests. The main thrust has been to locate defects in structures at the local element level and then repair them or replace the defective elements, instead of replacing the whole structure. Several advanced theoretical concepts required to detect defects have been proposed. At the same time, improved and smart sensing technologies, high-resolution data acquisition systems, digital communications, and high-performance computational technologies have been developed for implementing these concepts. The general area is now commonly known as structural health assessment (SHA) or structural health monitoring (SHM). In spite of these developments in analytical and sensor technologies, the implementations of these concepts in assessing structural health have been limited due to several reasons. An attempt has been made here to identify some of the major works (emphasizing analytical), their merits and demerits, contributions made by the research team of the authors, and future challenges.

2 Concept of Structural Health Assessment

All civil engineering structures, new and old, may not totally satisfy the intents of the designers. Minor temperature cracks in concrete or lack of proper amount of pretension in bolts cannot completely be eliminated. In that sense, all structures can be assessed as defective. Our past experiences indicate that presence of minor defects that do not alter the structural behavior may not be of interest to engineers. Considering only major defects, all of them are not equally important. Their locations, numbers, and severities will affect the structural behavior. Thus, the concept behind SHA can be briefly summarized as locating major defects, their numbers, and severities in a structure at the local element level. For the sake of completeness of this discussion, available SHA procedures are classified into four levels as suggested by Rytter [39]. They are as follows: level 1 – determination if damage is present in a structure, level 2 – determination of geometric location of the damage, level 3 – assessment of severity of the damage, and level 4 – prediction of remaining life of the structure.

3 Structural Health Assessment: Past

Structural health assessment has been practiced for centuries. Ever since pottery was invented, cracks and cavities in them were detected by listening to the sound generated when tapped by fingers. A similar sonic technique was used by blacksmiths to establish the soundness of the metals they were shaping. Even today, it is not uncommon to observe that inspectors assess structural health by hitting structures with a hammer and listening to the sounds they produce. These types of inspections, with various levels of sophistication, can be broadly termed as nondestructive evaluation (NDE) of health of a structure.

3.1 Early Developments in SHA

Although the awareness of the scientific concepts of many NDE technologies began during 1920s, they experienced major growth during and after the Second World War. However, there had been always problems in the flow of NDE research to everyday use [4]. Besides the use of visual testing (VT), early developments of instrument-based nondestructive detection of defects include penetrate testing (PT), magnetic particle testing (MPT), radiographic testing (RT), ultrasonic testing (UT), Eddy current testing (ET), thermal infrared testing (TIR), and acoustic emission testing (AE). Many of them required the damage/irregularity to be exposed to the surface or within small depth from the open surface. Some of them required direct contact of sensors with the test surface [22]. They mainly focussed on the "hot spot" areas or objects readily available for testing. For instance, RT has been routinely used for detection of internal physical imperfections such as voids, cracks, flaws, segregations, porosities, and inclusions in material at selective location(s). Most of these methods are non-model based, that is, the structure need not be mathematically modeled to identify location and severity of defects.

3.2 Transition from Past to Present: New Challenges

For most large civil infrastructure, the location(s), numbers, and severity of defect(s) may not be known in advance, although sometimes they can be anticipated using past experiences. Also, sometimes, defects may be hidden behind obstructions, for example, cracks in steel members hidden behind fire-proofing materials. Thus, instrument-based nondestructive testing (NDT) may not be practical if the inspector does not know what to inspect or the location of defect is not known *a priori*. During 1970s, detection of cracks was a major thrust. Subsequently, determination of crack size in order to compare with the critical crack size added another level of challenge to the engineering profession. In any case, inspection of "hot spot" areas limited their application potential. Subsequently, a consensus started developing about the use of measured responses to assess current structural health, as discussed next.

3.3 Model-Based SHA

Some of the deficiencies in non-model-based approaches can be removed by using model-based techniques. The aim of this approach is to predict the parameters of the assumed mathematical model of a physical system; that is, the system is considered to behave in predetermined manner represented in algorithmic form using the governing differential equations, finite element (FE) discretization, etc.

The changes in the parameters should indicate the presence of defects. To implement the concept, responses need to be measured by exciting the structure statically or dynamically.

3.3.1 SHA Using Static Responses

Because of its simplicity, initially SHA using static responses were attempted. Static responses are generally measured in terms of displacements, rotations, or strains, and the damage detection problems are generally formulated in an optimization framework employing minimization of error between the analytical and measured quantities. They mostly use FE model for structural representation. Three classes of error functions are reported in the literature: displacement equation error function, output error function, and strain output error function [41]. Recently, Bernal [3] proposed flexibility-based damage localization method, denoted as the damage locating vector (DLV) method. The basic approach is the determination of a set of vectors (i.e., the DLVs), which when applied as static forces at the sensor locations, no stress will be induced in the damaged elements. The method can be a promising damage detection tool as it allows locating damages using limited number of sensor responses. It was verified for truss elements, where axial force remains constant through its length. However, the verification of the procedure for real structures using noise-contaminated responses has yet to be completed.

There are several advantages of SHA using static responses including that the amount of data needed to be stored is relatively small and simple, and no assumption on the mass or damping characteristics is required. Thus, less errors and uncertainties are introduced into the model. However, there are several disadvantages including that the number of measurement points should be larger than the number of unknown parameters to assure a proper solution. Civil engineering structures are generally large and complex with extremely high overall stiffness. It may require extremely large static load to obtain measurable deflections. Fixed reference locations are required to measure deflections which might be impractical to implement for bridges, offshore platforms, etc. Also, static response-based methods are sensitive to measurement errors [1, 2].

3.3.2 SHA Using Dynamic Responses

Recent developments in SHA are mostly based on dynamic responses. There are several advantages of this approach. It is possible to excite structures by dynamic loadings of small amplitude relative to static loadings. In some cases, ambient responses caused by natural sources, for example, wind, earthquake, and moving vehicle, can be used. If acceleration responses are measured, they eliminate the need for fixed physical reference locations. They perform well in presence of high measurement errors [14].

Earlier works on SHA using dynamic responses are mostly modal information based [5, 15, 16, 38, 42]. Changes in modal properties, that is, natural frequencies, damping, and mode shape vectors, or properties derived from these quantities are used as damage indicators. Doebling et al. [15] presented various methods for damage identification including methods based on changes in frequency, mode shapes, mode shape curvature, and modal strain energy. Sohn et al. [42] updated the above report and discussed procedures based on damping, antiresonance, Ritz vectors, a family of autoregressive moving average (ARMA) models, canonical variate analysis, nonlinear features, time-frequency analysis, empirical mode decomposition, Hilbert transform, singular value decomposition, wave propagation, autocorrelation functions, etc. More complete information on them can be found in the literature cited above.

Natural frequency-based methods use change in the natural frequency as the primary feature for damage identification. They are generally categorized as forward problem or inverse problem. The forward problems deal with determination of changes in frequency based on location and severity of damage, whereas the inverse problems deal with determination of damage location and size based on natural frequency measurement. Among the mode shape-based procedures for damage detection, the mode shape/curvature methods generally use two approaches: traditional analysis of mode shape or curvature and modern signal processing methods using mode shapes or curvature. Modal strain energy-based procedures consider fractal modal energy for damage detection [16]. Methods based on damping have the advantage that a larger change in damping can be observed due to small cracks. Also, it is possible to trace nonlinear, dissipative effects produced by the cracks. However, damping properties have not been studied as extensively as natural frequencies and mode shapes [42]. Methods based on dynamically measured flexibility detect damages by comparing flexibility matrix synthesized using the modes of damaged structure to that of undamaged structure or flexibility matrix from FE analysis. The flexibility matrix is most sensitive to changes in the lower frequencies [15].

Modal-based approaches have many desirable features. Instead of using enormous amount of data, the modal information can be expressed in countable form in terms of frequencies and mode shape vectors. Since structural global properties are evaluated, there may be an averaging effect, reducing the effect of noise in the measurements. However, the general consensus is that modal-based approaches fail to evaluate the health of individual structural elements; they indicate overall effect, that is, whether the structure is defective or not [18, 26, 37]. For complicated structural systems, the higher-order calculated modes are unreliable, and the minimum numbers of required modes to identify the system parameters is problem dependent, limiting their applicability. The mode shape vectors may be more sensitive to defects than the frequencies, but the fact remains that they will be unable to predict which element(s) caused the changes. It was reported that even when a member breaks, the natural frequency may not change more than 5%. This type of change can be caused by the noises in the measured responses. A time-domain approach will be preferable.

3.3.3 Damages Initiated During Observations

A considerable amount of work also reported is on damages initiation time, commonly known as time-frequency methods for damage identification. The time-frequency localization capability has been applied for damage feature extractions from sudden changes, breakdown points, discontinuity in higher derivatives of responses, etc. They circumvent the modeling difficulty as they do not require the system to be identified, and the health assessment strategy often reduces to the evaluation of symptoms reflecting the presence and nature of defect [6]. Extensive study on short-time Fourier transform (STFT), Wigner-Ville distribution (WVD), pseudo Wigner-Ville distribution (PWVD), Choi-Williams distribution (CWD), wavelet transform (WT), Hilbert transform (HT), and Hilbert-Huang transform (HHT) for analyzing any nonstationary events localized in time domain has been reported in the literature. STFT is an extension of the Fourier transform allowing for the analysis of nonstationary signals by dividing it into small-time windows and analyzing each using the fast Fourier transform (FFT). The formulation provides localization in time as well as capturing frequency information simultaneously. WT has greater flexibility than STFT in terms of choosing different basis functions or mother wavelets. The wavelets have finite duration, and their energy is localized around a point in time. The WVD gives the energy distribution of a signal as a function of time and frequency; however, it has major shortcoming for multicomponent signals in terms of cross-terms. The CWD provides filtered/smoothed version of the WVD by removing the cross-terms [40].

These studies are very interesting, but there is no general consensus about the most suitable technique. Recently, Yadav et al. [48] studied some of the time-frequency procedures for defect characterization in a wave-propagation problem. However, the fundamental limitation of STFT, WVD, PWVD, CWD, and CWT is due to the fact that they are based on Fourier analysis and can accommodate only nonstationary phenomena in the data driven from linear systems; they are not suitable to capture nonlinear distortion. In this context, the HT and HHT are suitable for nonlinear and nonstationary data. Application of Hilbert transform to nonlinear data requires the signal to be decomposed to "mono-component" condition without any smaller, riding waves. The real advantage of HT is implemented in HHT proposed by Huang et al. [25]. The procedure consists of empirical mode decomposition (EMD) and Hilbert spectral analysis (HSA). HHT clearly define nonlinearly deformed waveforms; this definition can be the first indication of the existence of damage [24]. They applied the concept for bridge health monitoring using two criteria: nonlinear characteristics of the intra-wave frequency modulations of the bridge response and frequency downshift as an indication of structural yield. Yang et al. [51] proposed two HHT-based procedures for identifying damage time instances, damage locations, and natural frequencies and damping ratios before and after occurrence of damage.

4 Structural Health Assessment: Present

In an attempt to develop an ideal SHA technique for the rapid assessment of structural health, the research team at the University of Arizona identified several desirable features considering theoretical as well as implementation issues. The team concluded that a system identification (SI)-based approach using measured dynamic response information in time domain will have the most desirable attributes. A basic SI-based approach has three essential components: (a) the excitation force(s); (b) the system to be identified, generally represented by some equations in algorithmic form such as by FEs; and (c) the output response information measured by sensors. Using the excitation and response information, the third component, that is, the system, can be identified. The basic concept is that the dynamic responses will change as the structure degrades. Since the structure is represented by FEs, by tracking the changes in the stiffness parameter of the elements, the location and severity of defects can be established.

For a structure with N dynamic degrees of freedom (DDOF), the dynamic governing equation can be written as

$$\mathbf{M}\ddot{\mathbf{x}}(t) + \mathbf{C}\dot{\mathbf{x}}(t) + \mathbf{K}\mathbf{x}(t) = \mathbf{f}(t) \tag{1}$$

where $\mathbf{K}$, $\mathbf{M}$, and $\mathbf{C}$ are $N \times N$ stiffness, mass, and damping matrix, respectively; $\mathbf{x}(t)$, $\dot{\mathbf{x}}(t)$, $\ddot{\mathbf{x}}(t)$, and $\mathbf{f}(t)$ are $N \times 1$ displacement, velocity, acceleration, and load vector, respectively, at time t. The acceleration time histories at the FE node points are expected to be measured by accelerometers. The velocity and displacement time histories can be generated by successively integrating the acceleration time histories, as suggested by Vo and Haldar [44]. Assuming mass is known, $\mathbf{K}$ matrix at the time of inspection can be evaluated. Using the information on the current elements' stiffness properties and comparing them with the "as built" or expected properties or deviation from the previous values if periodic inspections were conducted**,** the structural health can be assessed.

4.1 General Challenges in Time-Domain SHA

Referring to the SI concept discussed earlier, structural stiffness parameters will be estimated by using information on excitation and measured responses. It is interesting to point out that according to Maybeck [36], deterministic mathematical model and control theories do not appropriately represent the behavior of a physical system, and thus, the SI-based method may not be appropriate for SHA. He correctly pointed out three basic reasons: (a) a mathematical model is incapable of incorporating various sources of uncertainties and thus does not represent true behavior of a system, (b) dynamic systems are driven not only by controlled inputs but also by disturbances that can neither be controlled nor modeled using deterministic formulations, and (c) sensors used for data measurements cannot be perfectly devised to provide

complete and perfect data about a system. These concerns and other implementation issues must be addressed before developing a SI-based SHA procedure.

Outside the controlled laboratory environment, measuring input excitation force(s) can be very expensive and problematic during health assessment of an existing structure. In the context of a SI-based approach, it will be desirable if a system can be identified using only measured response information and completely ignoring the excitation information. This task is expected to be challenging since two of the three basic components of SI process will be unknown. Responses, even measured by smart sensors, are expected to be noise contaminated. Depending on the amount of noise, the SI-based approach may be inapplicable. The basic concept also assumes that responses will be available at all DDOFs. For large structural systems, it may be practically impossible or uneconomical to instrument the whole structure; only a part can be instrumented. Thus, the basic challenge is to identify stiffness parameters of a large structural system using limited noise-contaminated response information measured at a small part of the structure. The research team successfully developed such a method in steps, as discussed next.

4.2 SHA Using Responses at All DDOFs

Using noisy responses measured at all DDOFs, Wang and Haldar [46] proposed a procedure, popularly known as iterative least squares with unknown input (ILS-UI). They used viscous damping and verified it for shear buildings. The efficiency of the numerical algorithm was improved later by introducing Rayleigh-type proportional damping, known as modified ILS-UI or MILS-UI [32]. Later, Katkhuda et al. [29] improved the concept further and called it generalized ILS-UI or GILS-UI. All these are least-squares procedures. They were extensively verified using computer-generated response information for shear buildings, two-dimensional trusses, and frames. They added artificially generated white noises in the computer-generated noise-free responses and showed that the methods could assess health of defect-free and defective structures. Recently, the concept has been verified for three-dimensional (3D) structures, denoted as 3D-GILS-UI [11, 12].

For the sake of completeness, other recently proposed least-squares-based SHA procedures need a brief review. Yang et al. [54] proposed a recursive least-squares estimation procedure with unknown inputs (RLSE-UI) for the identification of stiffness, damping, and other nonlinear parameters, and the unmeasured excitations. They implemented an adaptive technique [52] in RLSE-UI to track the variations of structural parameters due to damages. Then, Yang et al. [50, 53] proposed a new data analysis method, denoted as the sequential nonlinear least-square (SNLSE) approach, for the on-line identification of structural parameters. Later, Yang and Huang [49] extended the procedure for unknown excitations and reduce number of sensors (SNLSE-UI-UO). They verified the procedures for simple linear and nonlinear structures. Several other methods based on least squares can be found in Choi et al. [10], Chase et al. [8, 9], and Garrido and Rivero-Angeles [17].

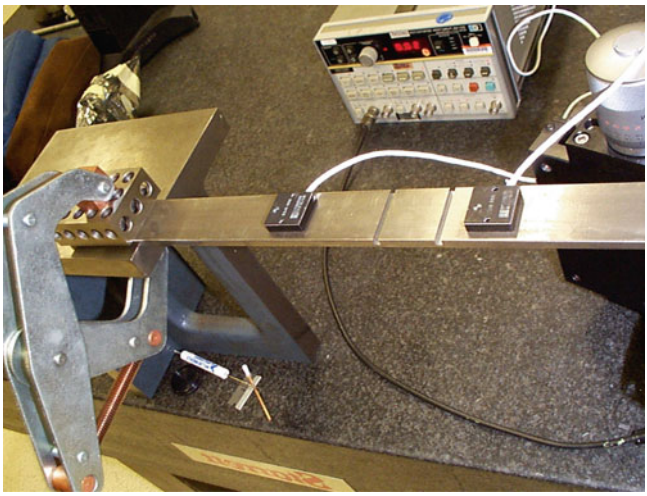

Fig. 1 Laboratory test of defective beams

After analytically establishing the concept that a structure can be identified using only noise-contaminated response information, completely ignoring the excitation information, the research team at the University of Arizona tested a one-dimensional beam [45] and a two-dimensional frame built to one-third scale in the laboratory [34, 35]. The test setups for the two studies are shown in Figs. 1 and 2, respectively. Both studies conclusively confirmed the validity of the basic SI concept without excitation information.

4.3 SHA Using Limited Response Information: Measured at a Small Part of the Structure

It is now established that least-squares concept can be used for SHA without using excitation information, but response information must be available at all DDOFs. This led the team to study cases when response information is available only at a part of the structure. Kalman filter-based algorithm is commonly used when the system is uncertain and the responses are noise-contaminated and not available at all DDOFs.

4.3.1 Kalman Filter

Application of Kalman filter (KF) for assessing health for civil engineering structures is relatively recent. Various forms of Kalman filter can be found in the literature including extended Kalman filter (EKF), unscented Kalman filter (UKF),

Fig. 2 Experimental verification of a scaled 2D frame

particle filter, and ensemble Kalman filter (EnKF). In mathematical sense, the basic KF is a nondeterministic, recursive computational procedure to provide best estimate of the states by minimizing the mean of squared error for a process governed by linear stochastic differential equation expressed as [47]

$$\mathbf{x}(k+1) = \mathbf{F}(k)\mathbf{x}(k) + \mathbf{G}(k)\mathbf{u}(k) + \mathbf{w}(k) \tag{4}$$

with the measurement model of the form:

$$\mathbf{z}(k+1) = \mathbf{H}(k+1)\mathbf{x}(k+1) + \mathbf{v}(k+1) \tag{5}$$

where $\mathbf{x}(k+1)$ and $\mathbf{x}(k)$ are the state vectors at time instant $k+1$ and k, respectively; vectors $\mathbf{w}(k)$ and $\mathbf{v}(k)$ represent the process and measurement noises, respectively; $\mathbf{F}(k)$ relates the two state vectors in absence of either a driving function or process noise; $\mathbf{G}(k)$ relates the optimal control input $\mathbf{u}(k)$ to the state; and $\mathbf{H}(k+1)$ in the measurement model relates the state vector to the measurement vector $\mathbf{z}(k+1)$. $\mathbf{w}(k)$ and $\mathbf{v}(k)$ are considered to be independent, zero-mean, white random vectors with normal probability distributions. Kalman filter is very powerful in several ways. It incorporates the (1) knowledge of the system, (2) statistical description of the system noises, measurement errors and uncertainty in the dynamic models, and (3) any available information on the initial conditions of the variables of interest [36].

The basic KF is essentially applicable for linear structural behavior. For SHA of civil engineering structures, the behavior may not be linear. Moderate to high level of excitation may force the structure to behave nonlinearly. Presence of defects may also cause nonlinearity, even when the excitation is at the low level. This leads to the development of the extended Kalman filter (EKF) concept. For EKF, Eq. (4) is expressed in the following form [47]:

$$\mathbf{x}(k+1) = f[\mathbf{x}(k), \mathbf{u}(k), \mathbf{w}(k)] \tag{6}$$

and the measurement equation, Eq. (5), is modified as

$$\mathbf{z}(k+1) = h[\mathbf{x}(k+1), \mathbf{v}(k+1)] \tag{7}$$

where nonlinear function f relates the states at time k to the current states at time $k + 1$, and it includes the state vector $\mathbf{x}(k)$, driving force $\mathbf{u}(k)$, and process noise $\mathbf{w}(k)$. The nonlinear function h relates the state vector $\mathbf{x}(k + 1)$ to the measurement vector $\mathbf{z}(k + 1)$. Again, $\mathbf{w}(k)$ and $\mathbf{v}(k)$ are the independent, zero-mean, white random vectors with normal distribution, representing the process and measurement noises, respectively. The EKF estimates the state by linearizing the process and measurement equations about the current states and covariances. KF or EKF attempts to predict responses and the model parameters and then updates them at each time point using current measurements. The procedure involving prediction and updating at each time point is generally known as *local iteration*. Completion of local iteration processes covering all time instances in the entire time-history of responses is generally known as first *global iteration*. The global iterations need to be repeated to satisfy the preselected convergence criterion of system parameters. Hoshiya and Saito [23] proposed a weighted global iteration (WGI) procedure with an objective function after the first global iteration to obtain convergence in an efficient way. The entire procedure is denoted as EKF-WGI. Recently, several researchers have improved computational aspects of EKF-WGI [14]. Koh and See [31] proposed an adaptive EKF (AEKF) to estimate both the parameter values and associated uncertainties in the identification. Yang et al. [50, 53] proposed an adaptive tracking technique based on EKF to identify structural parameters and their variation during damage events. Ghosh et al. [19] developed two novel forms of EKF-based parameter identification techniques; these are based on variants of the derivative-free locally transversal linearization (LTL) and multistep transverse linearization (MTrL) procedures. Liu et al. [33] proposed multiple model adaptive estimators (MMAE) that consist of bank of EKF designed in the modal domain (MOKF) and incorporated fuzzy logic-based block in EKF to estimate variance of measurement noise.

When KF or EKF is used to identify a structure using dynamic response information satisfying the governing equation represented by Eq. (1), it requires that the excitation information and the initial values of unknown state vector. As mentioned earlier, to improve implementation potential, the proposed approach needs to identify a structure without using excitation information, and the information on

the state vector will be available only at the completion of the identification, not at the beginning. The discussions clearly indicate that the basic KF or EKF cannot be used to identify a structure. To overcome these challenges, the research team proposed a two-stage approach by combining GILS-UI and EKF-WGI procedures. Based on the available measured responses, a substructure can be selected that will satisfy all the requirements to implement the GILS-UI procedure in stage 1. At the completion of stage 1, the information on the unknown excitation and the damping and stiffness parameters of all the elements in the substructure will be available. The identified damping can be assumed to be applicable for the whole structure. Structural members in a structure are expected to have similar cross-sectional properties. Suppose the substructure consists of one beam and one column. The identified stiffness parameters of the beam in the substructure can be assigned to all the beams in the structure. Similarly, the identified stiffness parameters of the column can be assigned to all the columns. This will give information on the initial state vector. With the information on initial state vector and excitation information, the EKF-WGI procedure can be initiated to identify the whole structure in stage 2. This novel concept was developed in stages; they are known as ILS-EKF-UI [47], MILS-EKF-UI [32], and GILS-EKF-UI [28]. These procedures were successfully verified using analytically generated responses, primarily for two-dimensional structures [21, 27]. Martinez-Flores et al. [35] then successfully verified GILS-EKF-UI in the laboratory for a two-dimensional frame shown in Fig. 2. They considered defect-free and several defective states with different levels of severities, including broken members, loss of cross-sectional area over the entire length of members, loss of area over small length of a member, and presence of one or multiple cracks in a member; Das and Haldar [13] recently extended the method to assess structural health for 3D structures.

5 Future of Structural Health Assessment

Future directions of the SHA area, as foreseen by the authors, are presented in the following sections. In the previous sections, the authors emphasized analytical concepts used for SHA and their contributions. In developing their methods, they observed many challenges yet to be resolved. Some issues are related to explicit consideration of uncertainty in describing the system and noises in the measured responses. Selection of initial state vector for large structure is also expected to be challenging. Although EKF can be used in presence of nonlinearity, the threshold nonlinearity is not known, that is, when it will fail to identify a structure. The methods proposed by the authors can identify structures with less information, but the absolute minimum number of required responses for acceptable identification needs further study. Issues related to the stability, convergence, and acceptable error in prediction need further works. Although the information of excitation is not required, characteristics of excitations need some attentions.

At the beginning of this chapter, the authors mentioned that SHA is a multidisciplinary research area. This chapter will not be complete without the discussions

on sensors, intelligent sensing technologies and signal processing, next generation structural health monitoring strategies, etc. Since SHA is a relatively new area and not covered in the existing curriculum of major branches of engineering, it is necessary to emphasize education aspect of SHA. The authors are not expert in some of these areas; however, they expect that the discussions will prompt future engineers to explore them. The first author is in the process of editing a book with contributions from experts covering all these areas [20].

5.1 *Transition from Present to Future: Local Level SHA Using Global Responses*

SHA procedures are developed generally assuming that measured responses will be altered in presence of defects. Obviously, minor defects may not alter the responses and thus cannot be detected. A structure is expected to be inspected several times during its lifetime. Minor defects such as initiation and development of cracks and corrosion of reinforcements in concrete are expected to grow over time. The basic assumption is that when they become major, they will be detected during the periodic inspections. Environmental influences on structural behavior, for example, effect of temperature on measured responses, are not completely understood at this time. Similar comments can be made for exposure to chemicals or high-pressure gradients. Smart sensors are now being developed to detect damage for various applications. Not all sensors are equally sensitive, and noises in the measurements cannot be avoided. Depending upon to noise to signal ratios, the output of a sensor can be misleading. The discussions clearly indicate that besides analytical developments, industrial research is also going to be critical in implementing a particular health assessment strategy. Hopefully, advances in technologies, digital computing, and data processing will remove some of these hurdles.

5.2 *SHA in Presence of Nonlinearity*

One major assumption in most SI-based SHA procedures is that the responses are linear or mildly nonlinear. Major nonlinearities are not expected to show up in the responses during ambient excitation or when the level of excitation is relatively small. However, in real situations, the nonlinearity in the responses cannot be avoided. To understand and develop robust mathematical model of the dynamical system, the distinct effects of nonlinearities must be realistically accounted for. At the same time, it will be important to use the available resources in a very systematic manner for successful implementation of the SHA procedures. To identify a highly nonlinear structure, it is important first to identify the level of nonlinearity and establish whether available methods are appropriate or not.

Next, it will be important to determine the location, type, and form of nonlinearity and how to model them in the optimum way. Another important task will be the selection of parameters/coefficients that need to be tracked for damage assessment. The area of nonlinear system identification is still in its infancy. An extensive discussion on the related areas and future directions in nonlinear SI is discussed by Kerschen et al. [30].

5.3 *Intelligent Sensing Technologies and Signal Processing*

Development of new sensor technologies for various applications is expanding in an exponential scale. Use of smart wireless sensors is becoming very common. The placements of sensors, density, sources of power for their operation, calibration for maintaining them in good operating condition, acquisition of signals, advanced signal processing algorithms considering increased signal-to-noise ratio, well-developed numerical procedure for post-processing of signal, integration of software and hardware, realistic mathematical model for structures and their components, etc., are being actively studied by various researchers. Smart sensors are wireless and equipped with on-board microprocessors; they are small in size and can be procured at a lower cost. However, there are several hardware aspects such as efficient data acquisition, synchronization, limited memory, encryption and secured data transmission, and limited bandwidth that need further attention. They should be operational throughout the life of the structure, if continuous-time SHA is performed [7]. It is expected that distributed computational framework and use of agents-based architecture will expand the possibility of intelligent infrastructure maintenance in future [43].

5.4 *Next Generation Structural Health Monitoring Strategy*

Structural systems always change due to inevitable deterioration processes. Assessment of current state of a structure cannot be complete without taking into account the uncertainties at every step of the assessment process. Even ignoring uncertainties, monitoring a structure continuously throughout its life may not be an optimum use of available resources. Next generation structural health monitoring research needs to be performance based. Using information from the most recent assessment, mathematical model to represent the structure, placement of sensors, data collection, and interpretation methods need to be modified or updated. The integration of past and present information on structural health needs to be carried out for the cost-efficient assessment. Risk-based nondestructive evaluation concept is expected to optimize the frequency of inspection.

5.5 SHA Curriculum in Education

The authors sincerely hope that the previous discussions provided a flavor of multidisciplinary nature of SHA areas. Both authors are civil engineers. Their formal education in civil engineering did not train them to undertake the research discussed here. Most engineering colleges do not offer courses related to SHA. NDE mostly belongs to mechanical engineering, whereas sensors and signal processing belong to electrical engineering. So far, the SHA/SHM education for professional engineers is limited to web-based resources or short course modules. Recently, several universities in Europe are collaboratively offering an Advanced Master's in Structural Analysis of Monuments and Historical Constructions (SAMHC) funded by the European Commission. In the USA, University of California, San Diego, has started M.S. program with specialization in SHM.

There is no doubt that the SHA/SHM areas will grow exponentially in near future all over the world. Trained engineers will be essential to carry out the necessary works. A severe shortage of trained professionals is expected. It will be highly desirable if we introduce a multidisciplinary engineering discipline in SHA/SHM by integrating civil, electrical, material, and mechanical engineering departments.

6 Conclusions

Structural health assessment has become an important research topic and attracted multidisciplinary research interests. Its growth has been exponential in the recent past. Past and present developments in the related areas are briefly reviewed in this chapter. Because of their academic background, the authors emphasized the structural health assessment for civil infrastructures. Some of the future challenges are also identified. Advancements in sensor technology and signal processing techniques are also reviewed briefly. An upcoming edited book on the subject by the first author is expected to provide more information on the related areas. Because of the newness of the area, there is a major gap in current engineering curriculum. In the near future, a severe shortage is expected for experts with proper training in SHA/SHM. The authors advocate for a new multidisciplinary engineering discipline in SHA/SHM by integrating, civil, electrical, material, and mechanical engineering departments.

References

1. Aditya G, Chakraborty S (2008) Sensitivity based health monitoring of structures with static responses. Scientia Iranica 15(3):267–274
2. Anh TV (2009) Enhancements to the damage locating vector method for structural health monitoring. Ph. D. dissertation, National University of Singapore, Singapore

3. Bernal D (2002) Load vectors for damage localization. J Eng Mech ASCE 128(1):7–14
4. Bray DE (2000) Historical review of technology development in NDE. In: 15th world conference on nondestructive testing, Roma, Italy, 15–21 Oct 2000
5. Carden EP, Fanning P (2004) Vibration based condition monitoring: a review. Struct Health Monit 3(4):355–377
6. Ceravolo R (2009) Time–frequency analysis. Chapter 26. In: Boller C, Chang F-K, Fuzino Y (eds) Encyclopedia of structural health monitoring. Wiley, Chichester
7. Chang PC, Flatau A, Liu SC (2003) Review paper: health monitoring of civil infrastructure. Struct Health Monit 2(3):257–267
8. Chase JG, Begoc V, Barroso LR (2005) Efficient structural health monitoring for benchmark structure using adaptive RLS filters. Comput Struct 83:639–647
9. Chase JG, Spieth HA, Blome CF, Mandler JB (2005) LMS-based structural health monitoring of a non-linear rocking structure. Earthq Eng Struct Dyn 34:909–930
10. Choi YM, Cho HN, Kim YB, Hwang YK (2001) Structural identification with unknown input excitation. KSCE J Civil Eng 5(3):207–213
11. Das AK, Haldar A (2010) Structural integrity assessment under uncertainty for three dimensional offshore structures. Int J Terraspace Sci Eng (IJTSE) 2(2):101–111
12. Das AK, Haldar A (2010) Structural health assessment of truss-type bridges using noise-contaminated uncertain dynamic response information. Int J Eng under Uncertainity: Hazards, Assessment, and Mitigation 2(3–4):75–87
13. Das AK, Haldar A (2012) Health assessment of three dimensional large structural systems – a novel approach. Int J Life Cycle Reliab Saf Eng (in press)
14. Das AK, Haldar A, Chakraborty S (2012) Health assessment of large two dimensional structures using minimum information – recent advances. Adv Civil Eng. Article ID 582472. doi:10.1155/2012/582472
15. Doebling SW, Farrar CR, Prime MB, Shevitz DW (1996) Damage identification and health monitoring of structural and mechanical systems from changes in their vibration characteristics: a literature review, Los Alamos National Laboratory. Report no. LA-13070-MS
16. Fan W, Qiao P (2010) Vibration-based damage identification methods: a review and comparative study. Struct Health Monit 10(14):1–29
17. Garrido R, Rivero-Angeles FJ (2006) Hysteresis and parameter estimation of MDOF systems by a continuous-time least-squares method. J Earthq Eng 10(2):237–264
18. Ghanem R, Ferro G (2006) Health monitoring for strongly non-linear systems using the ensemble Kalman filter. Struct Control Health Monit 13:245–259
19. Ghosh S, Roy D, Manohar CS (2007) New forms of extended Kalman filter via transversal linearization and applications to structural system identification. Comput Methods Appl Mech Eng 196:5063–5083
20. Haldar A (ed) (2012) Health assessment of engineered structures: bridges, buildings and other infrastructures. World Scientific Publishing Co
21. Haldar A, Das AK (2010) Prognosis of structural health – nondestructive methods. Int J Perform Eng. Special Issue on Prognostics and Health Management (PHM) 6(5):487–498
22. Hellier CJ (2003) Handbook of nondestructive evaluation. The McGraw-Hill Companies, Inc, New York
23. Hoshiya M, Saito E (1984) Structural identification by extended Kalman filter. J Eng Mech ASCE 110(12):1757–1770
24. Huang NE, Huang K, Chiang W-L (2005) HHT-based bridge structural-health monitoring. Chapter 12. In: Huang NE, Shen SS (eds) Hilbert-Huang transform and its applications. World Scientific Publishing Co. Pte. Ltd., Singapore
25. Huang NE, Shen Z, Long SR, Wu MC, Shih HH, Zheng Q, Yen N-C, Tung CC, Liu HH (1998) The empirical mode decomposition and the Hilbert spectrum for nonlinear and non-stationary time series analysis. Proc R Soc Lond A 454:903–995
26. Ibanez P (1973) Identification of dynamic parameters of linear and non-linear structural models from experimental data. Nucl Eng Design 25:30–41

27. Katkhuda H (2004) In-service health assessment of real structures at the element level with unknown input and limited global responses. Ph. D. thesis, University of Arizona, Tucson, USA
28. Katkhuda H, Haldar A (2008) A novel health assessment technique with minimum information. Struct Control Health Monit 15(6):821–838
29. Katkhuda H, Martinez-Flores R, Haldar A (2005) Health assessment at local level with unknown input excitation. J Struct Eng ASCE 131(6):956–965
30. Kerschen G, Worden K, Vakakis AF, Golinval JC (2006) Past, present and future of nonlinear system identification in structural dynamics. Mech Syst Signal Process 20(3):505–592
31. Koh CG, See LM (1994) Identification and uncertainty estimation of structural parameters. J Eng Mech 120(6):1219–1236
32. Ling X, Haldar A (2004) Element level system identification with unknown input with Rayleigh damping. J Eng Mech ASCE 130(8):877–885
33. Liu X, Escamilla-Ambrosio PJ, Lieven NAJ (2009) Extended Kalman filtering for the detection of damage in linear mechanical structures. J Sound Vib 325:1023–1046
34. Martinez-Flores R, Haldar A (2007) Experimental verification of a structural health assessment method without excitation information. J Struct Eng 34(1):33–39
35. Martinez-Flores R, Katkhuda H, Haldar A (2008) A novel health assessment technique with minimum information: verification. Int J Perform Eng 4(2):121–140
36. Maybeck PS (1979) Stochastic models, estimation, and control theory. Academic, New York
37. McCaan D, Jones NP, Ellis JH (1998) Toward consideration of the value of information in structural performance assessment. Paper no. T216-6. Structural Engineering World Wide, CD-ROM
38. Montalvao M, Maia NMM, Ribeiro AMR (2006) A review of vibration-based structural health monitoring with special emphasis on composite materials. Shock Vib Dig 38(4):295–324
39. Rytter A (1993) Vibration based inspection of civil engineering structures. Ph. D. dissertation, Department of Building Technology and Structural Engineering, Aalborg University, Denmark
40. Sajjad S, Zaidi H, Zanardelli WG, Aviyente, S, Strangas EG (2007) Comparative study of time-frequency methods for the detection and categorization of intermittent fault in electrical devices. Diagnostics for electric machines, power electronics and drive, SDEMPED, IEEE symposium, 6–8 September, pp 39–45
41. Sanayei M, Imbaro GR, McClain JAS, Brown LC (1997) Structural model updating using experimental static measurements. J Struct Eng ASCE 123(6):792–798
42. Sohn H, Farrar CR, Hemez FM, Shunk DD, Stinemates DW, Nadler BR, Czarnecki JJ (2004) A review of structural health monitoring literature: 1996–2001, Los Alamos National Laboratory, LA-13976-MS
43. Spencer BF Jr, Ruiz-Sandoval ME, Kurata N (2004) Smart sensing technology: opportunities and challenges. Struct Control Health Monit 11:349–368
44. Vo PH, Haldar A (2003) Post processing of linear accelerometer data in system identification. J Struct Eng 30(2):123–130
45. Vo PH, Haldar A (2004) Health assessment of beams – theoretical and experimental investigation. J Struct Eng, Special Issue on Advances in Health Monitoring/Assessment of Structures Including Heritage and Monument Structures 31(1):23–30
46. Wang D, Haldar A (1994) An element level SI with unknown input information. J Eng Mech ASCE 120(1):159–176
47. Wang D, Haldar A (1997) System identificatin with limited observations and without input. J Eng Mech ASCE 123(5):504–511
48. Welch G, Bishop G (2006) An introduction to the Kalman filter. Technical report. TR95-041 2006, Department of Computer Science, University of North Carolina at Chapel Hill, NC
49. Yadav SK, Banerjee S, Kundu T (2011) Effective damage sensitive feature extraction methods for crack detection using flaw scattered ultrasonic wave field signal. In: Proceedings of the 8th international workshop on structural health monitoring, Stanford, USA, 13–15 September

50. Yang JN, Huang H (2007) Sequential non-linear least-square estimation for damage identification of structures with unknown inputs and unknown outputs. Int J Non-Linear Mech 42:789–801
51. Yang JN, Huang H, Lin S (2006) Sequential non-linear least-square estimation for damage identification of structures. Int J Non-Linear Mech 41:124–140
52. Yang JN, Lei Y, Lin S, Huang N (2004) Hilbert-Huang based approach for structural damage detection. J Eng Mech 130(1):85–95
53. Yang JN, Lin S (2005) Identification of parametric variations of structures based on least squares estimation and adaptive tracking technique. J Eng Mech 131(3):290–298
54. Yang JN, Lin S, Huang HW, Zhou L (2006) An adaptive extended Kalman filter for structural damage identification. J Struct Control Health Monit 13:849–867
55. Yang JN, Pan S, Lin S (2007) Least-squares estimation with unknown excitations for damage identification of structures. J Eng Mech 133(1):12–21

Characterisation of Large Fluctuations in Response Evolution of Reinforced Concrete Members

K. Balaji Rao

Abstract Large fluctuations in surface strain at the level of steel are expected in reinforced concrete flexural members at a given stage of loading due to the emergent structure (emergence of new crack patterns). Thus, there is a need to use distributions with heavy tails to model these strains. The use of alpha-stable distribution for modelling the variations in strain in reinforced concrete flexural members is proposed for the first time in the present study. The applicability of alpha-stable distribution is studied using the results of experimental investigations, carried out at CSIR-SERC and obtained from literature, on seven reinforced concrete flexural members tested under four-point bending. It is found that alpha-stable distribution performs better than normal distribution for modelling the observed surface strains in reinforced concrete flexural members at a given stage of loading.

Keywords Reinforced concrete • Surface strain • Cracking • Thermodynamics • Alpha-stable distribution

1 Introduction

Strain in steel in reinforced concrete (RC) flexural members is used in the computation of crack width. The value of strain is affected by density of cracking. It is also noted that in the context of condition assessment of existing reinforced concrete structures, measured/computed surface strains play an important role. The focus in this chapter is

More details on motivation for the proposed probabilistic model are presented in the supplementary material provided for this chapter.

K.B. Rao (✉)
Risk and Reliability of Structures, CSIR-Structural Engineering Research Centre, CSIR Campus, Taramani, Chennai 600 113, India
e-mail: balaji@serc.res.in

S. Chakraborty and G. Bhattacharya (eds.), *Proceedings of the International Symposium on Engineering under Uncertainty: Safety Assessment and Management (ISEUSAM - 2012)*,
DOI 10.1007/978-81-322-0757-3_15,

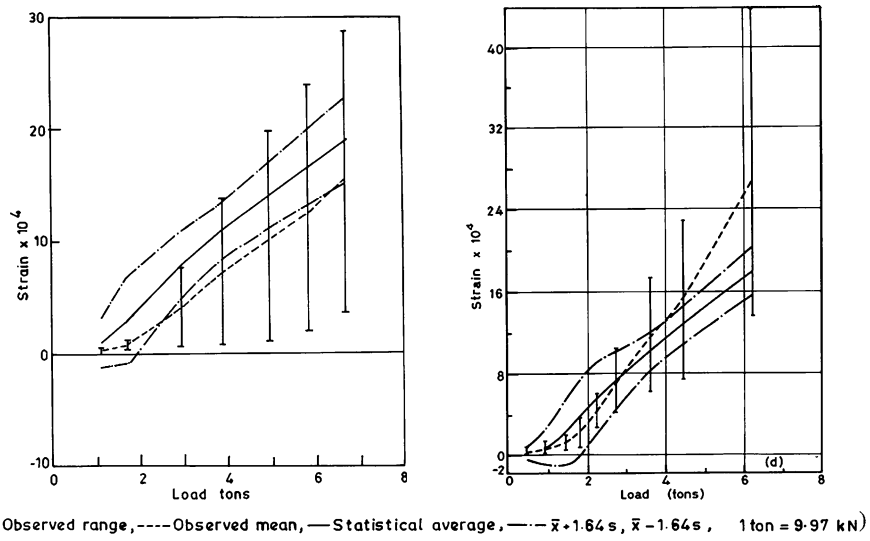

Fig. 1 Plots of load versus experimental surface strain, at the level of steel, for beams KB1 and KB2 at different stages of loading (From Desayi and Balaji Rao [17])

on identification of probabilistic models for describing the surface strain variations in reinforced concrete flexural members.

Based on an experimental investigation on RC flexural members, it has been reported that the measured strains at a given depth from extreme compression fibre, along the length of beam in pure flexure zone, exhibit large scatter [17]. Also, it has been reported that the variation of average strain across the depth is linear. Assuming linear strain variation across the depth of beam and considering various basic quantities as random variables, a probabilistic analysis of average strain, at various stages of loading, was carried out using Monte Carlo simulation. From the results of simulation (Fig. 1), it has been found that the average strain at the level of reinforcement exhibits large scatter. The probabilistic mean overestimates the experimentally observed mean strains at lower stages of loading and underestimates the same at higher stages of loading. Also, it has been found that the (mean $\pm$ 1.64 $\times$ standard deviation) limits do not enclose the observed range of strain at a given loading stage. Histogram of average strain distribution at the level of reinforcement (shown typically for the beam KB2 in Fig. 2) suggests that the distribution of average strain can be bimodal and large scatter is expected in the prediction of average strain. These observations suggest that prediction of average strain itself is beset with large uncertainty. To predict/assess the condition of a reinforced concrete member prediction of extreme (largest) value of strain is important. Hence, it is important to model the strain as a random quantity taking into account the actual mechanism of cracking and by giving due consideration to the heterogeneity of concrete. As pointed out by Bazant and Oh [7], '... This is clear even without experimental evidence, since structural analysis implies the hypothesis of smoothing of a

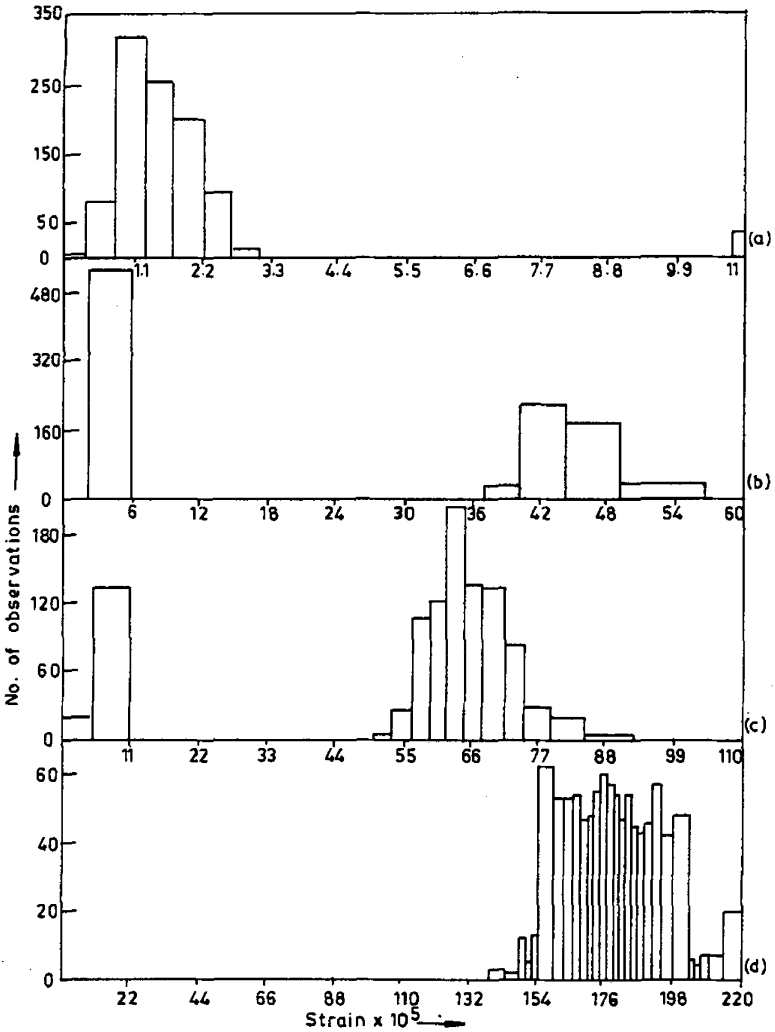

Fig. 2 Typical histograms of strains at the level of reinforcement for beam KB2 (**a**) at 1st stage of loading, (**b**) at 3rd stage of loading, (**c**) at 5th stage of loading and (**d**) at 10th stage of loading (From Desayi and Balaji Rao [17])

heterogeneous material by an equivalent homogeneous continuum in which, if one uses the language of the statistical theory of random heterogeneous materials, the stresses and strains must be understood as the averages of the actual stresses and strains in the microstructure over the so-called representative volume whose size must be taken to be at least several times the size of the heterogeneities...'. The authors also give an idea about the size of the representative volume element (RVE) as 10–20 times the aggregate size. They have presented, by considering the energy criterion of fracture mechanics and strength criterion, equations for crack spacing

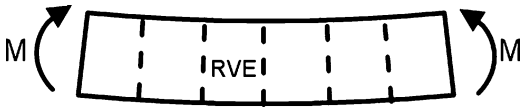

Fig. 3 The RVEs in the constant moment zone of an RC beam

and crack widths in RC members. They attribute the possible variations in cracking to the random variations in fracture energy. From this study, it is clear that when strain variation in the flexure zone is studied, the size of the RVE should be about ten times the size of aggregate.

In the present investigation, the surface strains measured over a gauge length of 200 mm are considered for further analysis satisfying the requirement of RVE. Since the RVE is statistically homogeneous and all the RVEs (Fig. 3) in the flexure zone are subjected to same moment, these elements can be considered to be identical.

As suggested by Bazant and Oh [7] and Balaji Rao and Appa Rao [2], the RC beam undergoing flexural cracking can be considered as a parallel system wherein redistribution of stresses/strains is taking place. For such a system, Bazant [5], using the fracture mechanics-based size effect theory, has recently shown that the load (or stress)-displacement (or strain) curve would exhibit jumps. However, as pointed out by Bazant [5], the size effect may not be significant in the presence of tension reinforcement. As discussed in this chapter, even the load-displacement behaviour of RC beam would exhibit multiple jumps. The points where the jumps occur are the points of bifurcation [5, 6, 15, 22]. It is known that at these points, the system which is undergoing flexural cracking would exhibit large fluctuations [33]. From the foregoing discussions, it is felt that a heavy-tailed distribution may be more appropriate to capture the large fluctuations in the concrete surface strains in reinforced concrete flexural members (at any given stage of loading, especially at the points at which an emergent crack structure forms).

Some Observations

- The RVEs located in the flexure zone of the RC member (Fig. 3) are subject to statistically similar stress/strain states. This implies that the random surface strains in the RVEs are identically distributed. While the stress/strain state in RVEs can be considered to be identical, they need not be considered to be statistically independent.
- From both the experimental and probabilistic analyses results, it is found that a random variable which exhibits large fluctuations would be preferred over those generally used (i.e. those with exponential decaying tails). Thus, it is desirable to use probability distributions that have power-law decaying tails (since they have to capture large fluctuations expected to be attendant with bifurcation phenomenon).

An experimental programme is taken up recently to check the validity of this inference. Four singly reinforced RC beams are tested under four-point bending to obtain the concrete surface strain values in the flexure zone at CSIR-SERC. Salient details of experimental investigations are presented in this chapter. An attempt is made to fit an alpha-stable distribution (which is known to have heavy tails) to the

observed strains. To study further the efficacy of alpha-stable distribution for modelling the variations in strain in concrete at the level of reinforcement in RC flexural members, experimental investigations on three singly reinforced concrete beams presented by Prakash Desayi and Balaji Rao [17, 18] are also considered. Based on the results of statistical analyses, it is inferred that the alpha-stable distribution is a good choice for modelling the surface strains in concrete, at the level of reinforcement, in RC flexural members.

2 Mechanism of Cracking: A Discussion on Emergent Structure

The strain in concrete in the tension zone of a RC flexural member depends on the level of cracking in the member. To understand the strain behaviour in the tension zone, it is important to know the mechanism of cracking in RC flexural member. The mechanism of cracking is described in several references (see for instance [10, 29, 31]). Only a brief description of the same will be presented here.

When an under-reinforced concrete beam is subjected to monotonically increasing four-point bending (Fig. 4), the following points can be noted:

1. As long as the applied load is less than the first crack load of the beam, the tension forces are shared both by concrete and steel. The load-deflection curve will be essentially linear (portion A of Fig. 5). There will be internal microcracking of concrete present in the tension zone [10].
2. When the applied load is equal to the first crack load of the beam, visible crack(s) appears on the surface of the beam and the flexure zone of the beam will be divided into number of sections as shown in Fig. 6. The formation of first set of cracks will be characterised by a sudden drop in load (point B in Fig. 5). This

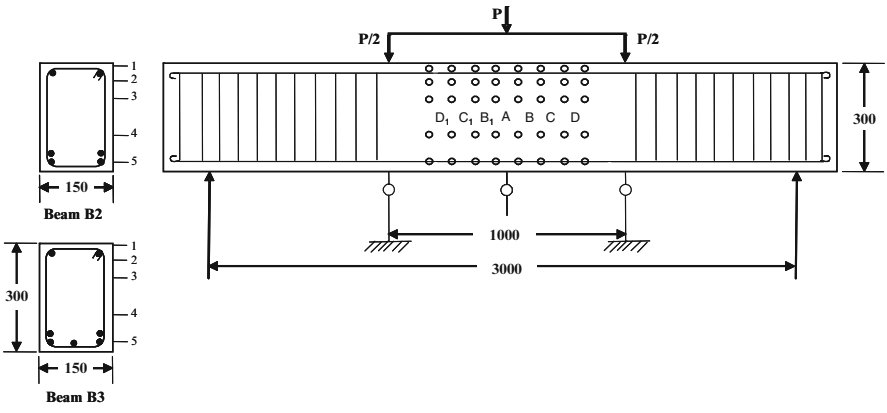

Fig. 4 Schematic representation of the test programme for beams tested at CSIR-IISc (dimensions in mm)

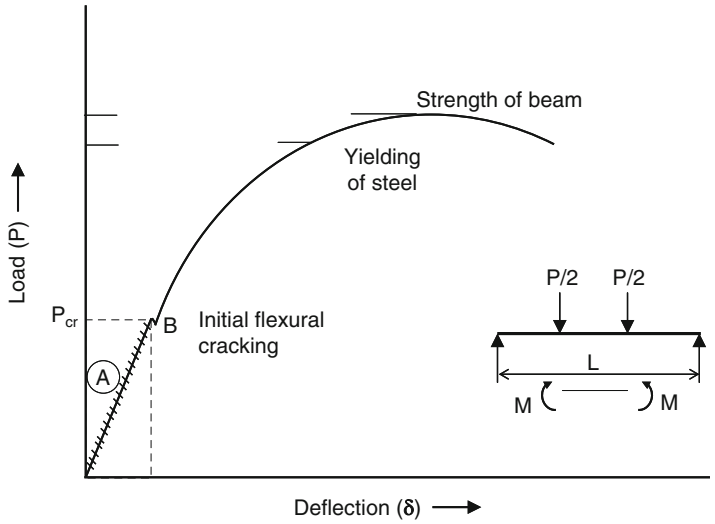

Fig. 5 Schematic load-deflection diagram of an under-reinforced concrete beam

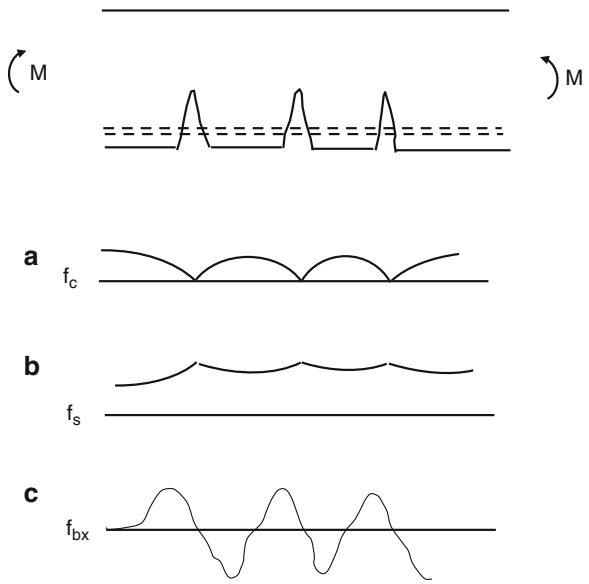

Fig. 6 Typical variation of (**a**) tensile stress in concrete, (**b**) tensile stress in steel and (**c**) bond stress in cracked beam

occurs due to sudden loss of stiffness of the beam due to cracking. Typical variations of tensile stresses in concrete and in steel and the bond stress in the flexure zone of the beam are shown in Fig. 6.

3. With the increase of load, beyond the first crack load, redistribution of stresses takes place between the cracked sections. New cracks may form in between the existing cracks, and also, the existing cracks may widen/lengthen. The formation

of new cracks results in reduction in crack spacing. The process of formation of new cracks will continue until the bottom fibre stress in concrete cannot reach a value equal to the modulus of rupture. When this condition is reached, no more new cracks form and the existing cracks will widen/lengthen with the increase of load. Thus, the spacing of cracks remains the same, and the corresponding crack spacing is called stabilised crack spacing.

2.1 *Brief Review of Relevant Models for Cracking of Concrete and Reinforced Concrete*

In this section, an attempt is made only to briefly review models that are relevant to the topic of this chapter, and it is considered that the *review is not exhaustive*.

From the above discussion, it is clear that the behaviour of RC flexural members under the external loading is quite complex. Also, it is clear that one of the outstanding features of the behaviour is the emergent structure at different stages of loading (in this chapter, emergent (dissipative) structure refers to formation of new cracks and/or widening and lengthening of the existing cracks on the surface of the flexural member, in the constant bending moment zone), as the loading is increased monotonically. At a given stage of loading, the emergent structure is characterised by the crack length, crack spacing and crack width. Efforts have already been made to approximately account for these observations in the estimation of crack spacing and crack widths [1, 11, 14, 19]. From the equations proposed in these codes (not presented here), it can be noted that cracking in RC flexural members depends on cross-sectional dimensions of the beam, the material strengths and the reinforcement details.

Recently, efforts are being made to develop numerical models within the framework of finite element simulation for prediction of load-deformation behaviour of RC members. The formulation, as can be expected, should consider the fact that the RC beams would have both distributed and localised damage in coupled form and also the bond-slip relation. Two types of models, namely, one which is based on characteristic length and the other based on damage evolution, have been proposed [7, 20, 22, 35]. The latter type of models recognises that there can be strong discontinuities in the displacement field at the points of bifurcation. These models are reviewed below to bring out the need for development of a probability distribution for strains at points of bifurcation. The information presented in Sects. 2.1.1 and 2.1.2 are directly obtained from Refs. [20] and [35]. These Sections are presented here for the sake of completeness, though no effort is made to use FEM in this chapter.

2.1.1 Reinforced Concrete Damage Modelling by Sluys and de Borst [35]

The authors reviewed the available constitutive models for concrete and also presented a bond-slip model that can be used in the FEM of concrete and reinforced concrete elements. The same are presented below.

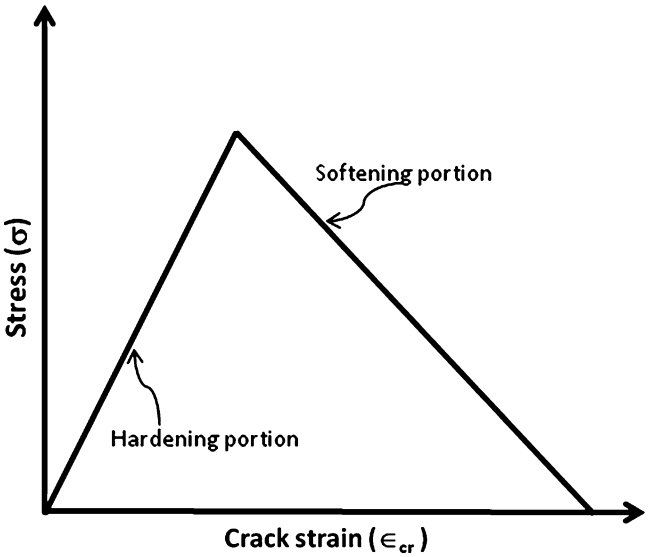

Fig. 7 Stress-strain curve for a standard crack model [35]

Concrete: The Standard Crack Model

In a standard crack model (SCM), the stress-strain curve consists of two parts, as shown in Fig. 7. The main feature of the stress-strain curve is the inclusion of the strain softening portion. The stress in softening portion is given by

$$\sigma = f_t + h\varepsilon_{cr} \tag{1}$$

where h is a constant negative softening modulus, f_t is the tensile strength and ε_{cr} is the cracking strain. The standard crack model takes into account the softening portion. However, the lack of characteristic length makes the overall response of the concrete element to be mesh sensitive, and since the problem of cracking is an ill-posed problem, the crack width is governed by the assumed size of the mesh. Also, when SCM is used for predicting the cracking in reinforced concrete members, the spacing of the cracks is more governed by the discretisation adopted. This is because by adopting finer meshes, the stress degradation occurs faster and secondary cracks form at a shorter distance (crack density increases).

Concrete: G_f -Type Crack Model

Some of the investigators have tried to overcome the lack of mesh objectivity by using higher-order terms in the displacement/strain field representation or by considering the area under the softening curve (viz. fracture energy) as a material

parameter. The fracture energy depends on the size of the process/localised zone. Since G_f is a material property, the slope of the softening portion is made function of mesh size. However, while the global load-displacement response of concrete specimen will be insensitive to meshing and hence mesh objective, no refinement takes place locally. For RC members, energy released in a single primary crack can be made mesh objective, but spacing of cracks still depends on mesh configuration. This is one of the serious limitations since the crack width in reinforced concrete members depends on the spacing of cracks.

Concrete: The Rate-Dependent Crack Model

The rate-dependent models, as the name suggest, arise in cracking of concrete/reinforced concrete due to evolution of damage/friction with time (or may be load, if it is varying). The constitutive relation in such a case is given by

$$\sigma = f_t + h\varepsilon_{cr} + m\frac{\partial \varepsilon_{cr}}{\partial t} \tag{2}$$

where m is the viscosity and all other terms are already defined. While the SCM is an ill-posed problem, rate-dependent model is well-posed initial value problem. Equation (2) caters to one experimental observation that the tensile strength increases with increase in loading rate. The length scale corresponding to this rate boundary value problem is

$$l = \frac{2m}{\sqrt{\rho E}} \tag{3}$$

Concrete: The Gradient Crack Model

One another way of solving the ill-posed problem of cracking in concrete is the use of rate of evolution of strain (i.e. rate evolution of gradients of ε_{cr}) along the spatial direction. This may be applied to static problems since the spatial variations are being dealt with. According to this model, the stress (in one dimension) is given by

$$\sigma = f_t + h\varepsilon_{cr} + \bar{c}\frac{\partial^2 \varepsilon_{cr}}{\partial x^2} \tag{4}$$

where $\bar{c}$ is the standard length parameter that takes into account interaction among the micro-defects along the length. The length scale evaluated based on solution of wave equation is given by

$$l = \sqrt{\frac{\bar{c}}{h}} \tag{5}$$

The length-scale parameter is representative of crack width in concrete and crack spacing in reinforced concrete members.

Reinforced Concrete: Bond-Slip Behaviour

It is difficult to evolve a constitutive relation for bond-slip. Recently, Dominguez et al. [20] have modelled it using the principles of thermodynamics. However, a macro-level model taking into account shear traction – slip interaction, as suggested by Dörr (in Sluys and de Borst [35]), is given by

$$\tau = \begin{cases} a\left[5\left(\frac{\delta}{\delta_0}\right) - 4.5\left(\frac{\delta}{\delta_0}\right)^2 + 1.4\left(\frac{\delta}{\delta_0}\right)^3\right] & \text{if } 0 < \delta < \delta_0 \\ 1.9a \quad \text{if } \delta > \delta_0 \end{cases} \tag{6}$$

where a is a constant which is taken equal to the tensile strength f_t and δ_0 is the deformation at which perfect slip occurs.

2.1.2 Strong Discontinuity Model by Dominguez et al. [20]

The authors formulate two-level damage model which works in coupled manner in a given element. The two levels identified, based on dissipation mechanism, are (1) continuum damage model and (2) discontinuity damage model. The first level considers, through continuous damage mechanics formulation, energy dissipation by formation of microcracks in the bulk material, while the second level considers the formation of macrocracks in localised zones resulting in surface dissipation of energy. The second level represents a strong discontinuity, and both levels are made to work in coupled manner by introduction of a displacement discontinuity. In the following, the formulation related to displacement discontinuity is presented:

Kinematics of Displacement Discontinuity Model

The authors introduce a surface of displacement discontinuity on which are concentrated all localised dissipative mechanisms due to formation and development of localisation zones. This is achieved by considering the domain Ω split into two sub-domains Ω^+ and Ω^- by surface of discontinuity, denoted as Γ_S.

The surface of discontinuity Γ_S is characterised 'at each point' by the normal and tangential vectors (m and n). The discontinuous displacement field can then be written as

$$u(X,t) = \bar{u}(X,t) + \bar{\bar{u}}(t)[H_{\Gamma_s}(X) - \phi(X)] \tag{7}$$

where $H_{\Gamma_s}(X)$ is a Heaviside step function and is equal to one if $X \in \Omega^+$ and zero if $X \in \Omega^-$. $\varphi(X)$ is 'at least' C_0 function with its 'boundary values' defined according to

$$\phi(X) = \begin{cases} 0 & if \quad X \in \partial\Omega \cap \Omega^- \\ 1 & if \quad X \in \partial\Omega \cap \Omega^+ \end{cases} \tag{8}$$

From Eq. (1), it is clear that $\bar{u}(X,t)$ has the same boundary values as the total displacement field $u(X,t)$. Now, the strain field can be written as

$$\varepsilon(X,t) = \nabla^S u(X,t) = \left[\nabla^S \bar{u}(X,t) + \bar{G}(X)\bar{\bar{u}}(t)\right] + \left\{(\bar{\bar{u}}(t) \otimes n)^S \delta_{\Gamma_s}(X)\right\} \tag{9}$$

In Eq. (9), the terms in square bracket represent the regular part of the strain field, while those in the curly brackets represent the singular part. Representation of the strain field in the form of two parts allows us to write the damage evolution equation as

$$\varepsilon = D : \sigma \tag{10}$$

The compliance D in Eq. (10) consists again of two parts, namely, the regular part and the other singular part. That is,

$$D = \bar{D} + \bar{D}\delta_{\Gamma_s}(X) \tag{11}$$

It is noted that the first term in Eq. (11) corresponds to continuous damage/dissipative mechanism in the bulk continuum containing microcracks, while the second term accounts for the discrete damage/dissipative mechanism describing the localised zones. The above equation allows stress to be finite. In order to formulate the damage evolution equation, we need to identify the internal variables that can be decomposed into regular and discrete (or singular part).

Let us define the two models and their corresponding evolutionary equations:

1. *Continuum damage model*: The microcracks in the bulk material are assumed to be quasi-homogeneously distributed, and the damage is isotropic. The damage model can be formulated in the domain/framework of plasticity of concrete. Let the damage in this model be denoted by $\bar{D}$ (in the elastic stage, the damage is denoted by D^e). The variable associated with hardening is denoted by $\bar{\xi}$. The constitutive relation is obtained optimising the dissipated energy. The Lagrange multiplier used in optimisation is denoted as $\dot{\bar{\gamma}}$. The main ingredients of continuum damage model are presented in Table 1 [20].
2. *Discrete damage model*: This damage model is constructed to account for steep strain gradients and localised damage due to formation of macrocracks. It is constructed in a similar way as it is done for the continuum damage model. As mentioned earlier, the discrete damage model has to be developed on the

Table 1 Main ingredients of continuum damage model [20]

Helmholtz free energy	$\bar{\psi}\left(\bar{\varepsilon}, \bar{\mathbf{D}}, \bar{\xi}\right) = \frac{1}{2}\bar{\varepsilon} : \bar{\mathbf{D}}^{-1} : \bar{\varepsilon} + \bar{\Xi}\left(\bar{\xi}\right)$
Damage function	$\bar{\phi}(\sigma, \bar{q}) = \underbrace{\sqrt{\sigma : \mathbf{D}^e : \sigma}}_{\|\sigma\|_{\mathbf{D}^e}} - \frac{1}{\sqrt{E}}\left(\sigma_f - \bar{q}\right)$
Constitutive equations	$\sigma = \bar{\mathbf{D}}^{-1} : \bar{\varepsilon}$ and $\bar{q} = -\frac{d}{d\bar{\xi}}\bar{\Xi}\left(\bar{\xi}\right)$
Dissipation	$\bar{\mathbf{D}}(\sigma, \bar{q}) = \frac{1}{2}\sigma : \dot{\mathbf{D}} : \sigma + \bar{q}\dot{\bar{\xi}}$
Evolution equations	$\dot{\mathbf{D}} = \dot{\bar{\gamma}}\frac{\mathbf{D}^e}{\|\sigma\|_{\mathbf{D}^e}}$ and $\dot{\bar{\xi}} = \dot{\bar{\gamma}}\frac{1}{\sqrt{E}}$

Fig. 8 Partitioning of domain Ω and the slip line Γ_S [20, 22]

Table 2 Main ingredients of discrete damage model [20]

Helmholtz free energy	$\bar{\bar{\psi}}(\bar{\bar{\mathbf{u}}}, \bar{\bar{\mathbf{Q}}}, \bar{\bar{\xi}}) = \frac{1}{2}\bar{\bar{\mathbf{u}}} : \bar{\bar{\mathbf{Q}}}^{-1} : \bar{\bar{\mathbf{u}}} + \bar{\bar{\Xi}}(\bar{\bar{\xi}})$
Damage function	$\bar{\bar{\phi}}_1(t_{\Gamma_s}, \bar{\bar{q}}) = t_{\Gamma_s}.\mathbf{n} - (\bar{\bar{\sigma}}_{\mathrm{f}} - \bar{\bar{q}})$
	$\bar{\bar{\phi}}_2(t_{\Gamma_s}, \bar{\bar{q}}) = \|t_{\Gamma_s}.\mathbf{m}\| - \left(\bar{\bar{\sigma}}_{\mathrm{s}} - \frac{\bar{\bar{\sigma}}_{\mathrm{s}}}{\bar{\bar{\sigma}}_f}\bar{\bar{q}}\right)$
Constitutive equations	$t_{\Gamma_s} = \bar{\bar{\mathbf{Q}}}^{-1} : \bar{\bar{\mathbf{u}}}$ and $\bar{\bar{q}} = -\frac{d}{d\bar{\bar{\xi}}}\bar{\bar{\Xi}}(\bar{\bar{\xi}})$
Dissipation	$\bar{\bar{\mathbf{D}}}(t_{\Gamma_s}, \bar{\bar{q}}) = \frac{1}{2}t_{\Gamma_s}.\dot{\bar{\bar{\mathbf{Q}}}}t_{\Gamma_s} + \bar{\bar{q}}\dot{\bar{\bar{\xi}}}$
Evolution equations	$\dot{\bar{\bar{\mathbf{Q}}}} = \dot{\bar{\bar{\gamma}}}_1\frac{1}{t_{\Gamma_s}.\mathbf{n}}\mathbf{n}\otimes\mathbf{n} + \dot{\bar{\bar{\gamma}}}_2\frac{1}{\|t_{\Gamma_\sigma}.\mathbf{m}\|}\mathbf{m}\otimes\mathbf{m}$ and $\dot{\bar{\bar{\xi}}} = \dot{\bar{\bar{\gamma}}} \rightarrow + \frac{\bar{\bar{\sigma}}_s}{\bar{\bar{\sigma}}_f}\dot{\bar{\bar{\gamma}}}_2$

surface of discontinuity. As shown in Fig. 8, on the surface of discontinuity, both normal and tangential components of stress exist. The evolution of this surface is governed by a multi-surface criterion where $\dot{\bar{\bar{\gamma}}}_1$ and $\dot{\bar{\bar{\gamma}}}_2$ represent the Lagrange multipliers associated, respectively, to each damage surface defining the elastic domain. Each surface is coupled to the other via a traction like variable $\bar{\bar{q}}$. The internal variables associated to softening are denoted by $\bar{\bar{\xi}}$. The main ingredients of the discrete damage model are presented in Table 2 [20].

3. *Bond-slip modelling (at the interface)*: While the continuum and discrete damage models developed help in modelling the displacement, strain, damage and stress fields in the concrete as a material, it is important to model the same in interface between the steel and concrete in the case of reinforced concrete elements. While experimentally obtained bond-slip behaviour represents the

Table 3 Main ingredients of bond-slip model [20]

Helmholtz free energy	$\rho\psi = \frac{1}{2}[\varepsilon_N E \varepsilon_N + (1-d)\varepsilon_T G \varepsilon_T + (\varepsilon_T - \varepsilon_{\mathrm{T}}^s) G d (\varepsilon_T - \varepsilon_{\mathrm{T}}^s) + \gamma\alpha^2 + H(z)$
Damage function	$\phi_s(\sigma_N, \sigma_T, X) = \left\lvert \sigma_{\mathrm{T}}^s - X \right\rvert - \frac{1}{3}\sigma_N \le 0$
	$\phi_d(Y_d, Z) = Y_d - (Y_0 + Z) \le 0$
Constitutive equations	$\sigma_N = E\varepsilon_N,$
	$\sigma_T = G(1-d)\varepsilon_T + Gd(\varepsilon_T - \varepsilon_{\mathrm{T}}^{\mathrm{s}}),$
	$\sigma_{\mathrm{T}}^{\mathrm{s}} = Gd(\varepsilon_T - \varepsilon_{\mathrm{T}}^{\mathrm{s}})$
Dissipation	$Y = Y_d + Y_{\mathrm{s}} = \frac{1}{2}\varepsilon_T G \varepsilon_T + \frac{1}{2}(\varepsilon_T - \varepsilon_{\mathrm{T}}^{\mathrm{s}}) G (\varepsilon_T - \varepsilon_{\mathrm{T}}^{\mathrm{s}}),$
	$X = \gamma\alpha,$
	$Z = H'(z) = \begin{cases} Z_1, & si\varepsilon_{\mathrm{T}}^0 < \varepsilon_{\mathrm{T}}^i \le \varepsilon_{\mathrm{T}}^2 \\ Z_1 \cdot Z_2, & si\varepsilon_{\mathrm{T}}^i \ge \varepsilon_{\mathrm{T}}^2 \end{cases}$
	$Z_1 = \left[\sqrt{Y_0} + \frac{1}{A_{d1}}\sqrt{\frac{G}{2}\ln\left((1+z)\frac{\varepsilon_T}{\varepsilon_{\mathrm{T}}^0}\right)}\right]^2$
	$Z_2 = \left[Y_2 + \frac{1}{A_{d2}}\left(\frac{-z}{1+z}\right)\right]$
Evolution equations	$\dot{d} = \dot{\lambda}_d \frac{\partial \phi_d}{\partial Y_d}, \dot{z} = -\dot{\lambda}_d \frac{\partial \phi_d}{\partial Z},$
	$\dot{\varepsilon}_{\mathrm{T}}^{\mathrm{s}} = \dot{\lambda}_s \operatorname{sign}(\sigma_{\mathrm{T}}^{\mathrm{s}}),$ and $\dot{\alpha} = -\dot{\lambda}_{\mathrm{s}} \operatorname{sign}(\sigma_{\mathrm{T}}^{\mathrm{s}}) + \frac{3}{2}\alpha X$

global behaviour, the local interface behaviour characterisation requires that the local friction and cracking to be modelled as a coupled phenomenon. This can be achieved using thermodynamics. In developing the thermodynamic model, the following aspects need to be considered: (a) cracking for an excessive tangential stress, $\sigma_{tt} = \sigma_T$; (b) inelastic strain due to sliding, $\in_T^S$; (c) coupling between tangential and normal stresses, $\sigma_{\mathrm{nn}} = \sigma_N$, in the sliding phase; and (d) hysteretic behaviour due to friction. The interface element is activated if and only if there is relative displacement between two bodies in contact. The main ingredients of the thermodynamics based bond-slip model are presented in Table 3 [20].

From the review of the above two models, it is clear that when fracture energy-based models are used in FEM of RC members, the gradient crack model proposed by Sluys and de Borst [35] with a refined bond-slip model can be used. However, it is felt that the constitutive relations proposed by Dominguez et al. [20] are best suited since they are based on strong displacement field discontinuity hypothesis. This type of model is recommended in probabilistic simulation. However, in this chapter, an attempt is made to first suggest a probabilistic model for surface strains based on phenomenological considerations and then examine its applicability based on experimental observations only. And no FE modelling and simulations are attempted. These studies are being continued at CSIR-SERC.

3 Probabilistic Model for Surface Strains in RC Members

It is known that when the principles of thermodynamics are applied to describe the cracking phenomenon of RC beams, the stage at which emergent structure forms corresponds to a transient nonequilibrium condition and subsequent formation of a metastable state(s) [3, 15]. The loading drops at the incipience of an emergent structure marking the nonequilibrium thermodynamic state. This is transient non-equilibrium thermodynamic state because further increase in load (from the load level to which it has reduced) can be achieved only with the increase in deflection of the beam. Once a particular stabilised crack pattern has formed, the beam will take further loading, which defines local equilibrium state with respect to cracking. This crack pattern will correspond to a metastable equilibrium state. The response evolution at and around the point of instability (such as the point 'B' which is in nonequilibrium state) is governed more by the fluctuations than the mean. Hence, mean field theory cannot be used to predict the behaviour around this point. However, beyond the unstable point, the response evolution can be predicted using mean field theory till another nonequilibrium point is reached (if at all possible). This behaviour is depicted in Fig. 9.

It has been pointed out in the literature [3, 15, 32] that the application of thermodynamic principles to irreversible processes (which is typically the case of cracking in reinforced concrete beams) would result in large fluctuation and

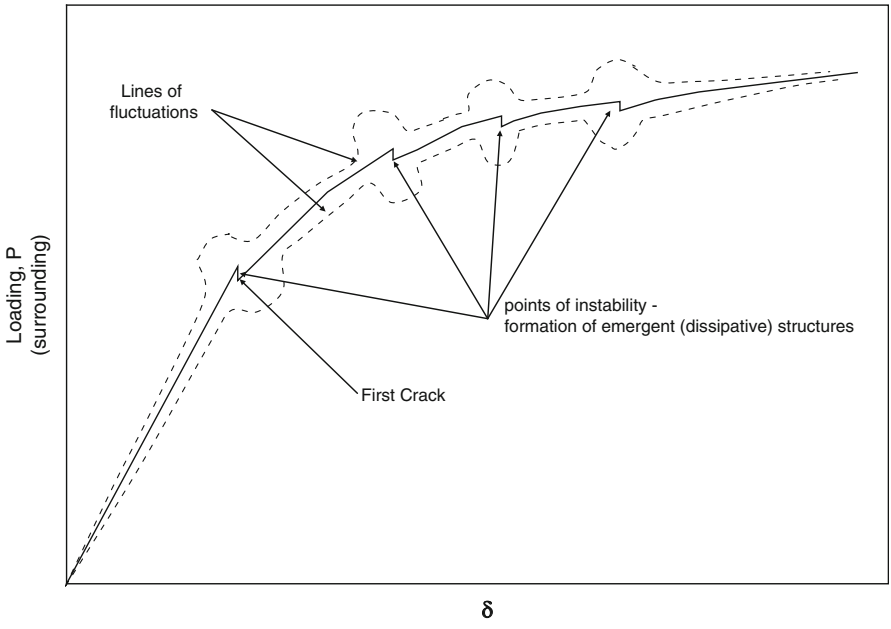

Fig. 9 Schematic of response evolution with loading showing formation of emergent (dissipative) structures

formation of a new (emergent) structure at the points of instability. This is due to the presence of wild randomness, which can simply be elucidated as follows: an environment in which a single observation or a particular number can impact the total in a disproportionate way [26]. The traditional Gaussian way of looking at the world begins by focusing on the ordinary and then deals with exceptions or so-called outliers as ancillaries. A second way, which takes the so-called exceptional as a starting point and deals with the ordinary in a subordinate manner – simply because that 'ordinary' is less consequential. These two models correspond to two mutually exclusive types of randomness: mild or Gaussian on the one hand and wild, fractal or 'scalable power laws' on the other. To characterise and quantify the fluctuations at the points of instability, a distribution with heavy tails is to be used.

3.1 Justification for Use of Alpha-Stable Distributions

One of the significant factors affecting the surface strains in concrete is the cracking in concrete. Recent developments in NDE techniques (viz. AE, GPR and other sensors) have made it possible to study the cracking process in concrete at micro-scale levels. Colombo et al. [14], with a view to identify the damage due to cracking using acoustic emission (AE) technique, conducted experimental investigations on a RC beam subjected to cyclic loading. The beam was simply supported and was subjected to two-point bending. For each loading cycle, the peak load was increased from that in the previous cycle. After the end of last (tenth) loading cycle, the RC beam was found to be severely damaged. The AE data recorded at each loading cycle was analysed to determine the *b*-value (the *b*-value is the negative gradient of the log-linear AE frequency/amplitude plot). According to Colombo et al. [14], the changes in *b*-value can be related to the different stages of crack growth in the RC beam. At initial stages of loading, microcracks are dominant and the macrocracks are starting to appear. The *b*-value corresponding to this phase is found to be greater than 1.7. In the next phase, the macrocracks are uniformly distributed along the beam and no new macrocracks are forming. The *b*-value corresponding to this phase is found to be between 1.2 and 1.7. In the final phase, the macrocracks are found to be opening up, as the beam is failing, and the *b*-value corresponding to this phase is found to be between 1.0 and 1.2. These studies thus help in locating – and assessment (qualitative) of – the damage. Carpinteri and Puzzi [12], based on both in situ field test on RC member and laboratory tests on concrete specimens, have shown that the *b*-value can be linked to the value of exponent of the power-law form for the tail portion of the probability distribution of crack size and that the value of exponent of the power law can be interpreted as the fractal dimension of the damage domain. Therefore, the random variables associated with crack size in RC flexural beams should have a form consistent with the power-law distribution (thus, may not have finite moments). By viewing the surface strains as a result of the indicated microscopic phenomena (such as bond-slip between steel and concrete, microcracking in concrete), the limiting distribution (attractor) is to be an alpha-

stable distribution, knowing that the microscopic components may have power-law distributions.

Thermodynamics Considerations: As mentioned earlier, one of the outstanding features of the behaviour of RC flexural beams under the external loading is the emergent structure at different stages of loading. The loading drops at the incipience of an emergent structure marking the nonequilibrium thermodynamic state. This is transient nonequilibrium thermodynamic state because further increase in load (from the load level to which it has reduced) can be achieved only with the increase in deflection of the beam. Once a particular stabilised crack pattern has formed, the beam will take further loading, which defines local equilibrium state with respect to cracking. This crack pattern will correspond to a metastable equilibrium state. The response evolution at and around the point of instability is governed more by the fluctuations than the mean. Hence, to characterise and quantify the fluctuations at these points, a distribution with heavy tails is to be used.

Based on Statistical Arguments: For normal distribution, 99.74% of total probability content is contained within three times standard deviation about the mean, thus giving low values of probability to the tail regions. The symmetric nature of normal distribution also restricts its applicability to phenomena exhibiting small skewness. Hence, there is a need to use distributions with heavy tails to model the strains showing large fluctuations and to estimate the extreme values. While there are different heavy-tailed alternatives to normal distribution, like alpha-stable distribution, student's t-distribution and hyperbolic distribution, the use of alpha-stable distribution is supported by the generalised central limit theorem (see Appendix A). The use of alpha-stable distribution over normal distribution has found applications in different areas (see [30, 37]). The use of alpha-stable distribution for modelling the strain in RC flexural beams at a given loading stage is explored in the present study to account for the large fluctuations.

From the above, it is clear that to predict the extreme value of strains developed in RC flexural beams, at any stage of loading, a probability distribution with power-law tails should be used.

3.2 Alpha-Stable Distribution

The alpha-stable distribution is described by its characteristic function (an explicit expression for probability density function generally does not exist) given by

$$L_{\alpha,\beta}(t) = E[\exp(itX)] = \begin{cases} \exp\left\{-c^{\alpha}|t|^{\alpha}\left[1 - i\beta\,\mathrm{sign}(t)\tan\left(\frac{\pi\alpha}{2}\right)\right] + i\delta t\right\}; & \text{for } \alpha \neq 1 \\ \exp\left\{-c|t|\left[1 + i\beta\,\mathrm{sign}(t)\,\frac{2}{\pi}\ln|t|\right] + i\delta t\right\}; & \text{for } \alpha = 1 \end{cases} \tag{12}$$

where X is the random variable, i is the imaginary unit, t is the argument of the characteristic function ($t \in \Re$), $E[\exp(itX)]$ denotes the expected value of $\exp(itX)$, α is an index of stability or characteristic exponent ($\alpha \in (0, 2]$), β is the

skewness parameter ($\beta \in [-1, 1]$), c is a scale parameter ($c > 0$), δ is a location parameter ($\delta \in \Re$), ln denotes the natural logarithm and sign(t) is a logical function which takes values -1, 0 and 1 for $t < 0$, $t = 0$ and $t > 0$, respectively. As α approaches 2, β loses its effect and the distribution approaches the normal distribution regardless of β [9]. A stable probability density function (PDF) is symmetrical when $\beta = 0$.

3.2.1 Estimation of Parameters of Alpha-Stable Distribution

Different methods have been proposed in literature for the estimations of the parameters α, β, c and δ of the alpha-stable distribution. Fama and Roll [21] suggested a quantile-based method for estimation of characteristic exponent and scale parameter of symmetric alpha-stable distributions with $\delta = 0$. However, this method is applicable only for distributions with $\alpha > 1$. This method has been modified by McCulloch [27] to include even nonsymmetric distributions with α in the range [0.6, 2.0]. Koutrouvelis [24] proposed a characteristic function-based method involving an iterative regression procedure for estimation of the parameters of the alpha-stable distribution. Kogon and Williams [22] improved this method by eliminating the iterative procedure and simplifying the regression. Ma and Nikias [25] and Tsihrintzis and Nikias [36] proposed the use of fractional lower-order moments (FLOMs) for estimating the parameters of symmetric alpha-stable distributions. Bates and McLaughlin [4] studied the performances of the methods proposed by McCulloch [27], Kogon and Williams [22], Ma and Nikias [25], and Tsihrintzis and Nikias [36] using two real data sets. They found that there are marked differences between the results obtained using the different methods. In the present study, the parameters α, β, c and δ of the alpha-stable distribution are estimated using an optimisation procedure by minimising the sum of squares of the difference between the observed cumulative distribution function (empirical distribution function) and the cumulative distribution function (CDF) of the alpha-stable distribution.

4 Applicability of Alpha-Stable Distribution

In this section, an attempt is made to examine the applicability of alpha-stable distribution to model the surface strains in RC flexural members based on experimental observations. The data on variation of strain with loading for RC beams used in this study is based on the experimental investigations carried out at CSIR-SERC, Chennai, India, and the experimental investigations reported by Prakash Desayi and Balaji Rao [17, 18]. This data is used in the present study, since strain measurements over the entire constant bending moment region along the span at different positions for different loading stages (up to ultimate) for RC flexural beams have been taken and reported, which will be useful for studying the usefulness of alpha-stable distribution for modelling the variations in measured strain. Availability of such extensive data is scanty in literature. Salient information regarding the experimental investigations is given below.

Table 4 Details of beams tested at CSIR-SERC

Set	No. of specimens	Grade of concrete	Main reinforcement[a]	Stirrups	Hanger bars	Clear cover (mm)
B2	2 (B2-1, B2-2)	M30	2, 10-mm dia 2, 12-mm dia	6-mm dia @ 140-mm c/c	2, 6-mm dia	25
B3	2 (B3-1, B3-2)	M30	5, 10-mm dia			

[a] The main reinforcement is selected so as to have approximately the same cross-sectional area of reinforcement for all the beams

4.1 Details of Experimental Investigations

4.1.1 Experimental Investigations Carried Out at CSIR-SERC

Two sets of beams (with two beams in each set) of similar cross-sectional dimensions of 150 mm × 300 mm and 3.6 m long were cast and tested in four-point bending over an effective span of 3.0 m. Stirrups of 6-mm diameter were provided in the combined bending and shear zone to avoid shear failure, and no stirrups were provided in the constant bending moment zone. Details and properties of the beams are given in Tables 4 and 5. In the constant bending moment zone of the beams (i.e. 1 m long), seven sections (denoted as D_1, C_1, B_1, A, B, C and D on the north face and D', C', B', A', B_1', C_1' and D_1' on the south face) were identified, with each section having a gauge length of 100 mm (see Fig. 1).

In each section, demec points were fixed at five different positions across the depth on both the faces of the beam (north face and south face). As can be seen from Fig. 1, position 1 corresponds almost to the extreme compression fibre for all beams, and position 5 corresponds to position of bottom layer of main reinforcing bars. The beams were tested in four-point loading. To measure the surface strains at different positions, a Pfender gauge with least count 1/1,000 mm and gauge length of 100.1 mm was used. While the strains were also monitored using electrical strain gauges embedded on the reinforcement, for health assessment and maintenance decision-making, strain readings from surface-mounted strain gauges are more useful than point estimates of strain. Hence, the present study focuses on modelling the surface strains at different stages of loading.

At each loading stage, the strain readings are taken only after the applied load is stabilised, i.e. the loading has been increased to its original value after the drop in loading due to the incipience of emergent structure. The crack pattern observed for beams B2-1 and B3-1 at different stages of loading is shown in Fig. 10. The formation of emergent structure with loading is evident from these figures.

4.1.2 Experimental Investigations Presented by Desayi and Balaji Rao [17, 18]

Three beams of similar cross-sectional dimensions of 250 mm × 350 mm and 4.8 m long were cast and tested in two-point bending over an effective span of

Table 5 Properties of beams tested at CSIR-SERC

Beam	d_1[a] (mm)	d_2[a] (mm)	Effective depth (d) (mm)	A_{st1}[b] (mm^2)	A_{st2}[b] (mm^2)	A_{st} (mm^2)	150-mm concrete cube compressive strength (MPa)[c]	Split tensile strength (MPa)[c]	Cracking load (kN)[b]	Ultimate load (kN)[c]
B2-1	227.6	263.5	249.1	139.94	208.85	348.79	45.39	1.91	21.10[d]	77.74
B2-2	227.6	263.2	249.0	144.36	217.56	361.92	50.52	1.76	21.10[d]	82.89
B3-1	229.3	264.3	250.5	144.0	219.66	363.66	50.30	1.85	21.10[d]	83.88
B3-2	229.5	264.5	250.4	146.30	217.72	364.01	43.03	1.90	21.10[d]	82.80

Note: span (l) = 3000 mm, breadth (b) =150 mm and depth (D) = 300 mm for all the beams

[a]d_1 and d_2 are the depth from top of the beam to the centre of the main reinforcing bars in the top layer and bottom layer, respectively

[b]Based on measured diameters of the reinforcing bars

[c]Obtained from experimental investigations

[d]Cracking is initiated between applied loads of 14.72 and 27.47 kN and the average of these two loads is reported here as the cracking load

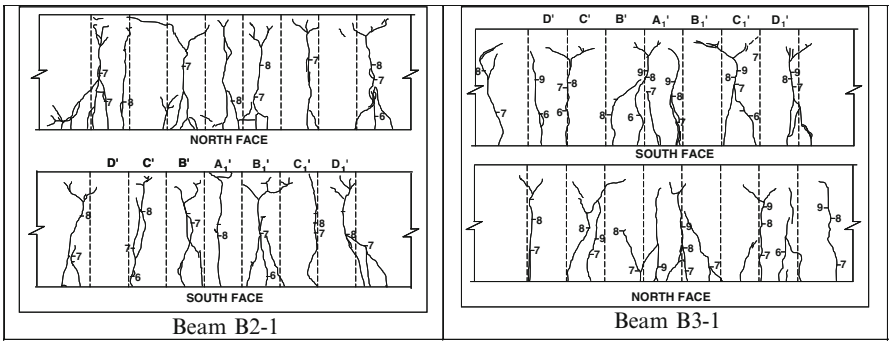

Fig. 10 Observed crack pattern for beams B2-1 and B3-1 (numbers denote the loading stage)

Table 6 Details of beams presented in Prakash Desayi and Balaji Rao [17, 18]

Beam	Effective depth (d) (mm)	A_{st} (mm^2)	150-mm concrete cube compressive strength (MPa)	Modulus of rupture (MPa)[a]	Cracking load (kN)[a]	Ultimate load (kN)[a]
KB1	311.0	402.123	33.078	4.036	23.549	95.389
KB2	305.4	437.929	40.417	3.578	14.014	104.653
KB3	303.5	529.327	22.508	2.950	8.899	84.291

Note: span (l) = 4200 mm, breadth (b) =200 mm and depth (D) = 350 mm for all three beams
[a]Obtained from experimental investigations

4.2 m. Stirrups of 6-mm diameter were provided in the combined bending and shear zone to avoid shear failure, and no stirrups were provided in the constant bending moment zone. Details of the beams are given in Table 6. The constant bending moment zone of the beams (1.4 m) was divided into eight sections (denoted as D', C', B', A', A, B, C and D on the west face and D_1, C_1, B_1, A_1, A_1', B_1', C_1' and D_1' on the east face), with each section having a gauge length of 200 mm (see Fig. 11). In each section, demec points were fixed at eight different positions on both faces of the beam (east face and west face). As can be seen from Fig. 11, position 1 corresponds almost to the extreme compression fibre for all beams, and position 7 in case of beam KB1 and positions 7 and 8 in case of beams KB2 and KB3 correspond to position of steel bars. The beams were tested in two-point loading in a 25-ton (245.25 kN) capacity testing frame. To measure the surface strains at different positions, a demec gauge with least count 1×10^{-5} and gauge length of 200.1 mm was used.

4.2 Statistical Analysis of Strain

Only the strains measured at the level of tension reinforcement are considered further in the analysis.

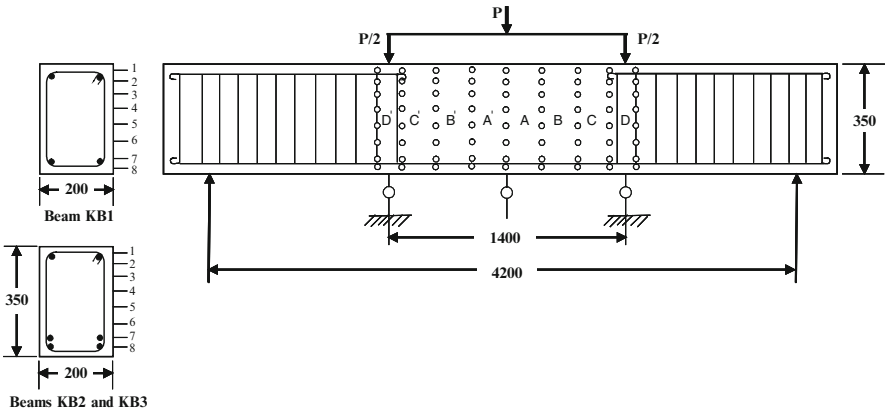

Fig. 11 Schematic representation of test programme [17, 18] (dimensions in mm)

4.2.1 Statistical Modelling of Strains for the Beams Tested at CSIR-SERC

In the present study, the aim is to model the strain in concrete at the level of bottom layer of main reinforcement (position 5 in Fig. 1) for a given loading stage. Three loading stages are considered for the sets B2 and B3, namely, those corresponding to applied loads of 27.47, 40.22 and 52.97 kN. It is known that evaluation of performance of reinforced concrete structural members under service loads is important in service life estimation. By defining the service load as approximately two-thirds of ultimate load, it is noted that the applied loads corresponding to the three loading stages considered in this study are less than the service loads, thereby helping in understanding the strain behaviour of flexural members under normal working load conditions. The typical variation of average strain across the depth for different stages of loading for the beam B2-2 is shown in Fig. 12. It is noted that the strain variation across the depth is almost linear for the loading stages considered in the present study. Similar observation is made for the other three beams also; however, the results are not presented here. This is in line with the observation regarding strain variation across the depth made by Neild et al. [28].

At any given loading stage, 14 strain readings (seven on the north face and seven on the south face) in the constant bending moment region are available for each beam in the sets B2 and B3. To enhance the sample size, the strain readings, corresponding to the same applied load, of both the beams in each set are combined together. This can be justified since the ultimate loads, cube compressive strengths and split tensile strengths for the two beams in each set are comparable with each other (see Table 5). It is also noted that the depth of neutral axis (determined using the strain gauge readings at different positions) at different loading stages for the two beams in each set is comparable, except for set B2 at an applied load of 27.47 kN. After combining the respective strain readings of beams belonging to sets B2 and B3, there are 28 strain readings at any given loading stage. These values are further processed for modelling the random variations in strain in concrete (at the level of reinforcement).

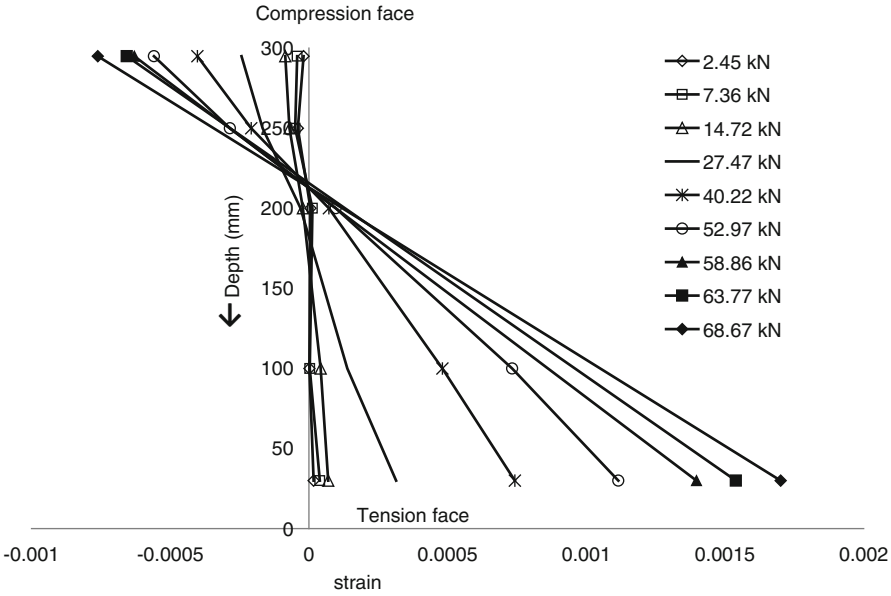

Fig. 12 Strain variation across the depth for different stages of loading for beam B2-2

4.2.2 Statistical Modelling of Strains for the Beams Presented by Desayi and Balaji Rao [17, 18]

At any given loading stage, 16 strain readings (eight on the west face and eight on the east face) in the constant bending moment region are available for the beams KB1, KB2 and KB3. These values are further processed for modelling the random variations in strain in concrete at the level of reinforcement (position 7 in case of beam KB1 and position 8 in case of beams KB2 and KB3).

4.3 Results and Discussion

The statistical properties (viz. mean, standard deviation and skewness) of the strain in concrete at the level of reinforcement have been computed based on the observed strain values. An alpha-stable distribution, $S(\alpha, \beta, c, \delta)$, is fitted to the strains in concrete at the level of reinforcement at each loading stage for the beams considered. The parameters α, β, c and δ of the alpha-stable distribution (Eq. 1) are estimated using an optimisation procedure by minimising the sum of squares of the difference between the observed cumulative distribution function (empirical distribution function) and the cumulative distribution function (CDF) of the alpha-stable distribution.

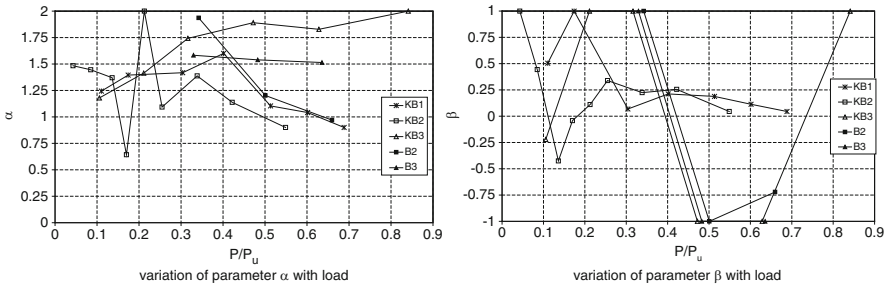

Fig. 13 Variation in parameters α and β with applied load

4.3.1 Beams Tested at CSIR-SERC

The variation in characteristic exponent, α, with applied load is shown in Fig. 13. It is noted that the values of α decrease with increase in applied load for both B2 and B3. It is known that for $\alpha = 2$, the alpha-stable distribution becomes normal distribution, and as α reduces, the tails get heavier, i.e. the tail probabilities increase [30]. This indicates that at higher stages of loading, the strain distribution deviates away from the normal distribution. This can be attributed to the formation of emergent structures and associated strain redistributions in concrete as explained in the section on mechanism of cracking. It is also noted from 13 that the reduction in α is much higher in set B2 when compared to set B3. This may be because in set B3, the cracks are more evenly distributed (lower values of crack spacing which can be attributed to the more number of smaller-diameter reinforcing bars in the beams in set B3 when compared to beams in set B2, with total area of steel in tension zone remaining approximately the same), and hence, the variability in strain is less, leading to lower values of tail probabilities.

From Fig. 13, it is noted that the value of the stability parameter (α) is almost a constant for set B3, while it shows large variation for set B2. This indicates that the strain distribution is almost stabilised for set B3. Since the strains in concrete in the tension depend on the level of cracking, a stabilised strain distribution suggests that the cracking has stabilised, i.e. no new cracks are being formed with increase in loading, rather the existing cracks are widened and extended. This is also supported by the observed crack patterns for the beams in set B3 (see Fig. 10), from which it is noted that no new major cracks are formed after the loading stage 7 (corresponding to applied load of 40.22 kN). However, from the observed crack pattern for a beam in set B2 (see Fig. 10), it is noted that a major crack has formed at the loading stage 8 (corresponding to applied load of 52.97 kN). This shows that the cracking and hence the strain distribution have not stabilised for set B2. This trend is also reflected in the values of the scale parameter (c) and the location parameter (δ). The values of c and δ increase with applied load when the strain distribution is stabilised (as is the case for set B3), indicating that the strains are increasing at an almost uniform rate in all the sections. However, when new cracks form (as is the case for set B2), there is sudden increase of strain in the section containing the crack and a decrease in strain in the adjacent sections, leading to abrupt variations in c and δ.

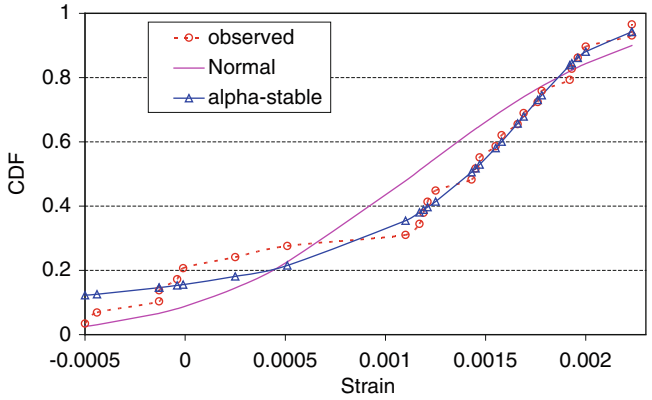

Fig. 14 Comparison of CDFs of strain for set B2 (applied load = 52.97 kN)

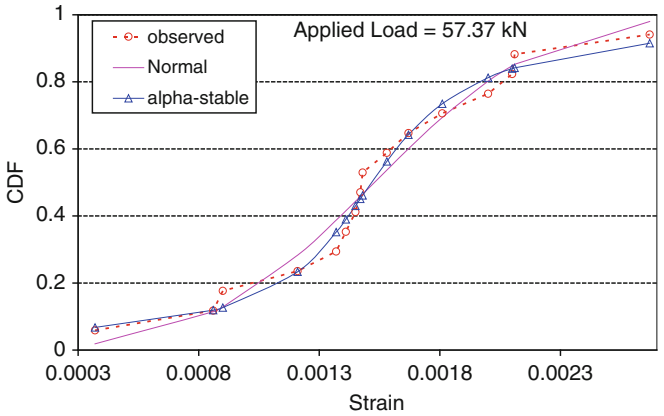

Fig. 15 Comparison of CDFs of strain for beam KB1 (applied load = 57.37 kN)

For the purpose of comparison, a normal distribution is also fitted to the observed strain data (by considering the mean and standard deviation of the normal distribution as the average and standard deviation of the observed strain data). The observed CDF, alpha-stable CDF and the normal CDF, typically for the set B2, for an applied load of 52.97 kN, are shown in Fig. 14. From this figure, it is noted that CDF corresponding to the alpha-stable distribution compares with the observed CDF better than the normal CDF (especially in the tail regions which are of interest in estimating extreme values of strains).

4.3.2 Beams Presented by Desayi and Balaji Rao [17, 18]

The observed CDF, alpha-stable CDF and the normal CDF, typically for the beam KB1, for an applied load of 57.37 kN, are shown in Fig. 15. From Fig. 15, it is noted

that CDF corresponding to the alpha-stable distribution compares with the observed CDF better than the normal CDF. This observation suggests that alpha-stable distribution is a better fit to the observed strain readings (especially in the tail regions which are of interest in estimating extreme values of strains).

4.3.3 General Observations

From the variation in α with applied load (see Fig. 13) for the beams considered, it is noted that in general, α becomes close to 1.0 at loads corresponding to approximately the working loads. It may be noted that the skewness parameter β is not the same as the classical skewness parameter [30], since for non-Gaussian stable distributions, the moments do not exist. In the case of the alpha-stable distribution, the values of β indicate whether the distribution is right-skewed ($\beta > 0$), left-skewed ($\beta < 0$) or symmetric ($\beta = 0$). It is noted that the trends of skewness of the fitted alpha-stable distribution are in agreement with the trends of skewness shown by the observed strain readings. This observation also suggests the ability of the fitted alpha-stable distribution to represent the observed variations in strain. From the variation of β with applied load (Fig. 13) for the beams considered, it is noted that in general, the strain distribution becomes symmetrical ($\beta = 0.0$) at loads corresponding to approximately the working loads.

5 Conclusions

Usefulness of alpha-stable distributions for modelling the variations in surface strain in reinforced concrete flexural members, at the level of reinforcement, is studied in this chapter, using experimentally obtained strain values from reinforced concrete flexural members tested under four-point bending. From the results obtained, it is noted that alpha-stable distribution is a better fit to the observed strain readings at a given stage of loading than the normal distribution, especially in the tail regions which are of interest in estimating extreme values of strains.

6 Supplementary Material

6.1 Why Do We Need Probability Distributions with Fat Tails to Describe the Mechanism of Cracking in Reinforced Concrete Flexural Members?

The information presented in this supplementary note is based on the concepts presented by Prof. Prigogine [33]). An attempt has been made to interpret these concepts to the phenomenon of cracking in reinforced concrete flexural members.

According to Prigogine, the concept of time in the case irreversible thermodynamic systems can be replaced by associating or suitably defining a variable associated with the phenomenon of formation of dissipative structures. Through suitable thermodynamic formulations, he has addressed the problem associated with these systems both at macroscopic and microscopic levels simultaneously. However, the use of Helmoltz free energy in the thermodynamic formulations is questioned since non-equilibrium can be source of order. Therefore, in order to formulate the problem of cracking which forms dissipative structures, the concept of open system needs to be adopted. The two components, namely, internal and external, are body of the material containing microcracks and the fictitious system containing localised macrocracks which dissipate energy through mainly surface energy. These two systems are coupled and there exists a boundary between them. In this way, the thermodynamic formulations with strong discontinuity seem to show promise (*details of formulations are reviewed in the main paper*).

The second law of thermodynamics suggests that the change in entropy is equal to or greater than zero. For a closed system, the entropy production is through the irreversible damage and sets one-sidedness of time. The positive sidedness of time is associated with increase of entropy. If entropy remains constant, time will not increase! This may be a problem with thermodynamics of closed systems. Hence, more often thermodynamics principles are applied to describe the systems near the equilibrium. To extend the thermodynamics to the nonequilibrium processes, we need an explicit expression for entropy production. Progress has been achieved along this line by supposing that even outside equilibrium, entropy depends only on the same variables as at equilibrium. This assumption leads to 'local' equilibrium. This assumption enables us to use the formulations similar to equilibrium thermodynamics. Local equilibrium requires that

$$\frac{\mathrm{d}_i S}{\mathrm{d}t} = \sum_{\rho:} J_\rho X_\rho \geq 0 \tag{13}$$

The LHS of Eq. (13) gives the rate of production of internal entropy by the system due to various irreversible processes (ρ) at a macroscopic level. J_ρ and X_ρ are rate of entropy production by individual irreversible process ρ and the driving force of the process ρ. This is the basic formula of macroscopic thermodynamics of irreversible process. At thermodynamic equilibrium, we have simultaneously for all irreversible processes

$$J_\rho = 0;\ X_\rho = 0 \tag{14}$$

It is therefore natural to assume that at least near the equilibrium linear homogeneous relations between flows and forces. The assumption of thermodynamic local equilibrium for nonequilibrium systems and application of above approach, at a macroscale, allows the use of empirical laws such as Fourier's law and Fick's second law of diffusion to various phenomenon under consideration. It may be

noted that we have not yet included the complex interaction that may takes place between the irreversible damage processes that are producing the entropy. The answer lies in the linearisation of the system at least near the 'local' equilibrium. This assumption enables the principle of superposition which is central to the local equilibrium thermodynamics and enables us to determine the rates of flow (flux) of a given irreversible process, taking into account the interactions among various irreversible processes contributing to the macroscopic equilibrium, using phenomenological coefficients ($L_{\rho\rho'}$) from the following relation,

$$J_\rho = \sum_{\rho'} L_{\rho\rho'} X_{\rho'} \tag{15}$$

Linear thermodynamics of irreversible processes is dominated by two important results, namely, Onsager reciprocity relations and the principle of minimum entropy production at or very near the local equilibrium point. The Onsager reciprocity relation is given by,

$$L_{\rho\rho'} = L_{\rho'\rho} \tag{16}$$

When the flow J_ρ, the flow corresponding to irreversible process ρ, is influenced by the force $X_{\rho'}$ of irreversible process ρ', then the flow $J_{\rho'}$ is also influenced by the force X_ρ through the same phenomenological coefficient. It may be seen that the Onsager's reciprocity relation is similar to the Betti's theorem in structural engineering.

We have established the 'local' equilibrium dynamics of the irreversible thermodynamic open system. The two central concepts have been explained above. The theorem dealing with minimum internal entropy production is very significant since it gives some kind of 'inertial' property to the nonequilibrium system near the local equilibrium point. When given boundary conditions prevent the system from reaching thermodynamic equilibrium (i.e. zero entropy production), the system settles down to the state of 'least dissipation'. It is to be noted that for far-from equilibrium points, the thermodynamic behaviour could be quite different. It has been proved now that the behaviour of the system can be opposite of minimum entropy production. In fact, the state of nonequilibrium (wherein there can be production of internal entropy) may be source of order at a macroscale.

It is interesting to note that Boltzmann's order principle as expressed by canonical distribution assign almost zero probability to the occurrence of Benard convection. Whenever new coherent states occur far from equilibrium, the very concept of probability, as implied in the counting of number of complexions, breaks down. In the case of Benard's convection, above a critical temperature small convection currents, appearing as fluctuations, get amplified and give rise to macroscopic current. A new supermolecular order appears which corresponds basically to a giant fluctuation stabilised by exchanges of energy with the outside world. This is the order characterised by the dissipative structures.

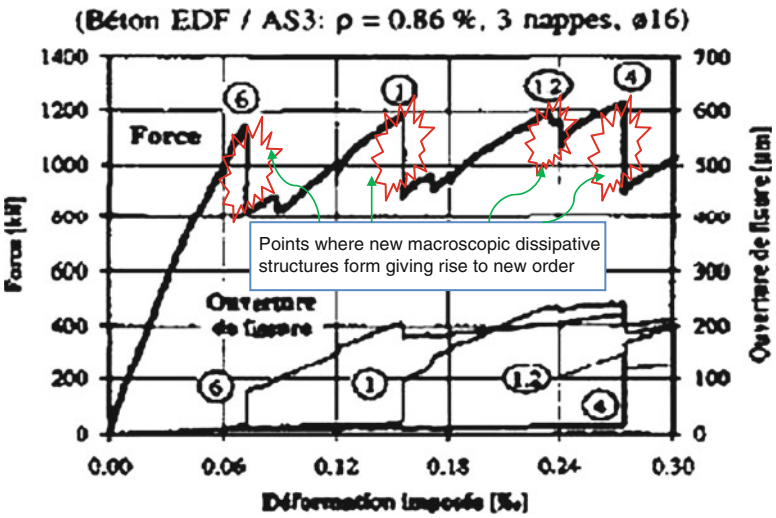

Fig. 16 Force-deformation relation of an RC member subjected to axial tension (From Ibrahimbegovic et al. [22])

Figure 16 is very important in light of the discussions presented till now. The load-deformation process in RC member under monotonically increasing loads involves irreversible damage process. But, as presented in the paper, the cracking process needs to be considered as both closed and open thermodynamic system forming dissipative structures at critical points (such as points 6, 1, 12,4 in Fig. 16). But for points at which loading drops, which are points of nonequilibrium and far from equilibrium, local equilibrium can be obtained and we can define the local stationary states of the system (this enables us to use Onsager's reciprocity relation and the minimum dissipation theorem). At the points where it has been marked as red balloons, new emergent dissipative structures form (i.e. new macrocracks form on the surface of the beam) indicating that these irreversible states correspond to the points far from equilibrium condition (something similar to Benard's convection presented by Prigogine). And, it is at these points the surface strains show large variability and the applicability of probability distribution with exponential tails is questionable. More figuratively, this is very clearly brought out in thermodynamic framework in Fig. 17.

Prigogine has shown that near critical points as well as near the coexistence curve (shown in red balloons in Fig. 16), the law of large numbers, as expressed by the expression

$$\frac{\left\langle (\delta X)^2 \right\rangle}{V} \sim \text{ finite for } V \to \infty \tag{17}$$

(where X is a random variable representing an extensive quantity of thermodynamics), breaks down, as $\left\langle (\delta X)^2 \right\rangle$ becomes proportional to a higher power of volume.

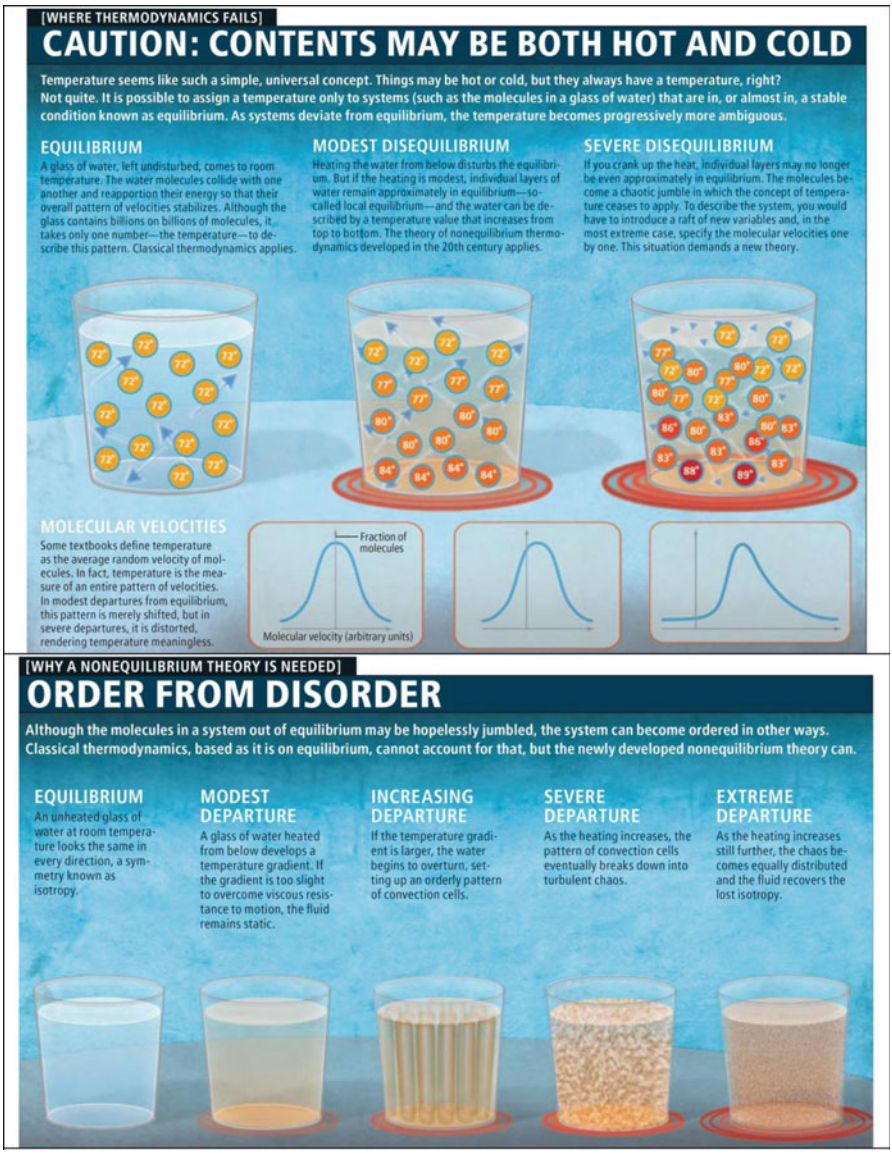

Fig. 17 Need for use of alpha-stable distribution at points of far from equilibrium due to formation of dissipative structures bringing the order (From Rubi [34])

Prigogine [33] has shown that near the critical points, probability distributions with long-range memory would be needed. It is in this context, alpha-stable distributions are proposed to describe the fluctuations in surface strains near the critical points in the flexural members.

6.1.1 Derivation of a Levy Distribution (Which Is Also Called Alpha-Stable Distribution)

The intrinsic dynamical features of the physical system need to be included in any stochastic evolution model. From the very beginning of chaotic dynamics, there were observations of intermittent character of the time/load behaviour of chaotic trajectories (as exhibited by the load-displacement curve of RC flexural member). As pointed out above, the Gaussian processes and normal diffusion are not always valid (and many situations arise when independent and weakly dependent random event models need to be abandoned).

Levy in 1937 (in Mandelbrot [25]) reconsidered law of large numbers and formulated a new approach that can also be applied to distributions with infinite second moment. The importance of approach of Levy's distributions and processes soon became clearer in many fields. Mandelbrot in [25] has presented numerous applications of the Levy's distributions and coined the notion of Levy flights.

Let $p_X(x)$ be normalised probability density function of random variable X. That is,

$$\int_{-\infty}^{\infty} p_X(x)\mathrm{d}x = 1 \tag{18}$$

with characteristic function

$$\Phi_X(t) = \int_{-\infty}^{\infty} e^{itx} p_X(x)\mathrm{d}x \tag{19}$$

Consider two random variables X_1 and X_2 and their linear combination as follows:

$$CX_3 = C_1X_1 + C_2X_2 \qquad C, C_1, C_2 > 0 \tag{20}$$

The linear combination law is stable if all $X_i s$ $(i = 1,2,3)$ are distributed according to the same $p_{X_i}(x_i), \quad (i = 1, 2, 3)$

While Gaussian distribution satisfies the stable law, another class of distributions was given by Levy (1937).

Let us write the density function of X_3 in Eq. (20).

$$p_{X_3}(x_3)\mathrm{d}x_3 = p_{X_1}(x_1).p_{X_2}(x_2).\delta\left(x_3 - \frac{C_1}{C}x_1 - \frac{C_2}{C}x_2\right).\mathrm{d}x_1\mathrm{d}x_2 \tag{21}$$

We know that the characteristic function of a random variable made up of summation of several random variables is simply multiplication of characteristic functions of individual random variables. Hence, we get

$$\Phi_{CX_3}(Ct) = \Phi_{C_1X_1}(C_1t).\Phi_{C_2X_2}(C_2t) \tag{22}$$

Taking logarithms on both the sides, we get

$$\ln \Phi_{CX_3}(Ct) = \ln \Phi_{C_1X_1}(C_1t) + \ln \Phi_{C_2X_2}(C_2t) \tag{23}$$

Equations (22) and (23) are functional ones with a solution

$$\ln \Phi_\alpha(Ct) = (Ct)^\alpha = C^\alpha e^{-\frac{i\pi\alpha}{2}(1-\text{sign}t)}|t|^\alpha \tag{24}$$

under the condition

$$\left(\frac{C_1}{C}\right)^\alpha + \left(\frac{C_2}{C}\right)^\alpha = 1 \tag{25}$$

where α is an arbitrary parameter.

Any distribution $p_X(x)$ with characteristic function

$$\Phi_\alpha(t) = e^{-C|t|^\alpha} \tag{26}$$

is known as Levy distribution with Levy index α. An important condition imposed by Levy is $0 < \alpha \leq 2$, which guarantees of positiveness of probability density function.

$$p_\alpha(x) = \int_{-\infty}^{\infty} \mathrm{d}t.e^{itx}.\Phi_\alpha(t) \tag{27}$$

The case of $\alpha = 1$ is known as Cauchy distribution

$$p_1(x) = \frac{C}{\pi}\frac{1}{\left(x^2 + C^2\right)} \tag{28}$$

An important case is the asymptotic of large $|x|$.

$$p_\alpha(x) = \frac{1}{\pi}\alpha C\,\Gamma(\alpha)\sin\frac{\pi\alpha}{2}\frac{1}{|x|^{\alpha+1}}; \quad 0 < \alpha \leq 2 \tag{29}$$

It can be shown that the moments of $p_\alpha(x)$ of order m diverge for $m \geq \alpha$.

6.2 *Implication of the Use of Alpha-Stable Distributions in Performance-Based Design of RC Structures*

The behaviour of reinforced concrete flexural members under the external loading is quite complex, as explained in the above sections. One of the outstanding features

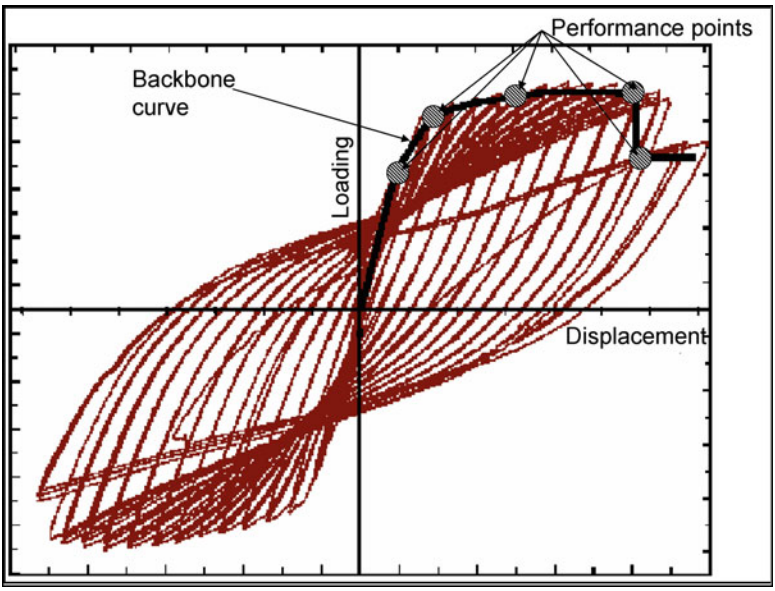

Fig. 18 Schematic of hysteretic behaviour under transient loading

of the behaviour is the emergent structures (marking the instability with respect to thermodynamic behaviour) at different stages of loading. The loading drops at the incipience of an emergent (dissipative) structure, namely, formation of new cracks and/or widening and extension of the existing cracks. Once a particular crack pattern has formed, the beam will take further loading, which defines local equilibrium state with respect to cracking. As has been explained in the earlier section on thermodynamic instability, the response evolution at and around the point of instability is governed more by the fluctuations than the mean. Hence, mean field theory fails around this point. However, beyond unstable point, the response evolution can be predicted using mean field theory.

The above discussion clearly shows that the phenomenon of cracking and deformation of reinforced concrete flexural members exhibits large scatter. To account for the inevitable large uncertainties in the behaviour, attempts have to be made to apply suitable probability distributions such as alpha-stable distributions and use convex sets to check the robustness of the system with respect to the performance limit states considered (around the points of instability shown as red balloon in Fig. 16).

While the above discussion is valid for reinforced concrete flexural members subjected to monotonic loading, this can be extended to structures/structural members subjected to transient loadings (such as earthquakes), by noting that for well designed reinforced concrete members (avoiding pinching shear failure), the load deformation response under monotonic loading forms the envelope for hysteretic behaviour (Fig. 18). The significance of this in the performance-based design is that when the reliability is sought near the point of instability, the uncertainties have to be treated properly and perhaps application of theory of convex sets is more appropriate. These suggest the need for application of hybrid reliability technique

for estimating the reliability of reinforced concrete flexural members and structures than simple reliability techniques.

The research presented in this chapter has lead to the following two important observations and perhaps sets direction for future research:

- There is a need to have a relook at the probabilistic performance-based design using the capacity curve, obtained from nonlinear static pushover analysis, since at the points of bifurcation, the behaviour is to be modelled using probability distributions that account for large uncertainties. This requires a systematic approach to be followed in two steps: (a) carrying out careful experimental investigations on RC structural components and structures for characterising their load-displacement behaviour and (b) development of backbone curves that can be used in the performance-based design.
- There is also a need to examine the approximation of envelope curve as the backbone curve for representing the hysteretic behaviour of RC structural components and structures.

Acknowledgements This chapter is being published with the kind permission of Director, CSIR-SERC, Chennai, India. The author is very thankful to his colleague Dr. M. B. Anoop, Scientist, CSIR-SERC, in the preparation of this chapter. He thanks his colleagues Dr. K. Ravisankar, Chief Scientist, Head, Structural Health Monitoring Laboratory, Shri. K. Kesavan, Dr. M. B. Anoop and Shri. S. R. Balasubramanian, Scientists, CSIR-SERC, for their involvement in the experimental work. The MATLAB programmes developed by Mark Veillette, Ph.D. Scholar, Department of Mathematics and Statistics, Boston University, Boston, USA, have been used in the present study for determining the CDFs and PDFs of the alpha-stable distributions.

Appendix A

The central limit theorem states that the sum of independent, identical random variables with a finite variance converges to a normal distribution. Let $X_1, X_2, \ldots,$ $X_n$be independent identically distributed random variables. Define

$$S_n = \underset{n \to \infty}{\text{Lim}} \sum_{i=1}^{n} X_i \tag{A.1}$$

According to central limit theorem, S_n follows a normal distribution with mean and variance given by

$$\mu = \sum_{i=1}^{n} \mu_{X_i}$$

$$\sigma^2 = \sum_{i=1}^{n} \sigma_{X_i}^2$$

where μ_{X_i} and $\sigma_{X_i}^2$ are the mean and variance of X_i.

This suggests that as long as a macroscopic phenomenon is infinitely divisible into microscopic phenomena, which exhibits finite variance with exponential tails, the random variable associated with the macroscopic phenomenon can be represented using a normal distribution. However, wide variety of microscopic phenomena exhibit statistics that needs to be characterised with algebraic-tailed distributions. An example is the random variables associated with microcracks (size as well as geometry) in concrete which exhibit a power-law distribution [13] and hence may not have a finite mean and/or variance. In such cases, the random variable associated with the macroscopic phenomenon may not have a finite mean and/or variance (see Eq. A.2), and normal distribution will not be the limiting distribution of the sum $\sum_{i=1}^{\infty} X_i$.

An Important Asymptotic Property

A probability density $L(x)$ can be a limiting distribution of the sum $\sum_{i=1}^{\infty} X_i$ of independent and randomly distributed variables only if it is stable. A random variable X is stable or stable in the broad sense if for X_1 and X_2 independent copies of X and any positive constants a and b,

$$a X_1 + b X_2 \stackrel{d}{=} c X + d \tag{A.3}$$

holds for some positive c and some $d \in \Re$ [30]. The symbol $\stackrel{d}{=}$ means equality in distribution, i.e. both expressions have the same probability law. The term stable is used because the shape is stable or unchanged under sums of the type given by Eq. (A.3).

The Gaussian – and Cauchy – distributions are potential limiting distributions, depending on the physical phenomenon that is being handled. However, there are many more distributions to which the summation series $\sum_{i=1}^{\infty} X_i$ is attracted to depending on the actual behaviour. The complete sets of stable distributions have been specified by Levy and Khinchine. A probability distribution is stable if its characteristic function is of the form as given in Eq. (12).

While Eq. (12) defines the general expression for all possible stable distributions, it does not specify the conditions which the probability density function (pdf) $p(l)$ has to satisfy so that the distribution of the normalised sum $\hat{S}_n = \sum_{i=1}^{n} p_i(l)$ converges to a particular $L_{\alpha,\beta}(x)$ in the limit $n \to \infty$. If this is the case, one can say '$p(l)$ belongs to the domain of attraction of $L_{\alpha,\beta}(x)$'. This problem has been solved completely, and the answer can be summarised by the following theorem:

Theorem: *The probability density $p(l)$ belongs to the domain of attraction of a stable density $L_{\alpha,\beta}(x)$ with characteristic exponent α ($\alpha \in (0 < \alpha < 2)$) if*

$$p(l) \sim \frac{\alpha\, a^{\alpha}\, c_{\pm}}{|l|^{1+\alpha}} \quad \text{for} \quad l \to \pm\infty \tag{A.4}$$

where $c_+ \geq 0, c_- \geq 0$ and a are constants. These constants are directly related to the scale parameter c and the skewness parameter β by

$$c = \begin{cases} \dfrac{\pi(c_+ + c_-)}{2\,\alpha\,\Gamma(\alpha)\sin(\pi\,\alpha/2)} & \text{for } \alpha \neq 1 \\ \dfrac{\pi}{2}(c_+ + c_-) & \text{for } \alpha = 1 \end{cases} \tag{A.5}$$

$$\beta = \begin{cases} \dfrac{c_- - c_+}{c_+ + c_-} & \text{for } \alpha \neq 1 \\ \dfrac{c_+ - c_-}{c_+ + c_-} & \text{for } \alpha = 1 \end{cases} \tag{A.6}$$

Furthermore, if $p(l)$ belongs to the domain of attraction of a stable distribution, its absolute moments of order λ exist for $\lambda < \alpha$:

$$\left\langle |l|^{\lambda} \right\rangle = \int_{-\infty}^{\infty} \mathrm{d}l\, |l|^{\lambda}\, p(l) = \begin{cases} <\infty & \text{for } 0 \leq \lambda \leq \alpha (\alpha \leq 2) \\ \infty & \text{for } \lambda > \alpha (\alpha < 2) \end{cases} \tag{A.7}$$

The above discussion clearly brings out that the sum of independent random variables, as $n \to \infty$, may converge to an alpha-stable distribution, $\alpha = 2$ being a specific case, with $p(l) \sim 1/|l|^3$, as a Gaussian distribution. For all other values of characteristic exponent, α, $0 < \alpha < 2$, the sum would be attracted to $L_{\alpha,\beta}(x)$, and all these classes of stable distributions show the same asymptotic behaviour for large x. Thus, the central limit theorem can be generalised as follows:

The generalised central limit theorem states that the sum of a number of random variables with power-law tail distributions decreasing as $1/|x|^{\alpha+1}$ where $0 < \alpha < 2$ (and therefore having infinite variance) will tend to a stable distribution as the number of variables grows.

The characteristic exponent α and the skewness (symmetry) parameter β have to be interpreted based on physical significance. As already mentioned, α defines the shape of the distribution and decides the order of moments available for a random variable. Longer power-law tails will lead to divergence of even lower-order moments. This should not be treated as a limitation, since, in some of the physical systems, the pdf of response quantities can have power-law tails. This may also be true of nonlinear response of engineering systems, especially at bifurcation points, where the system can exhibit longer tail behaviour. Though this can be brushed aside as a transient behaviour, for seeking performance of a system, this needs to be effectively handled. Hence, it is important to understand the pdfs and associated properties so that the systems can be modelled realistically.

References

1. ACI (2002) Control of cracking in concrete structures. ACI manual of concrete practice, ACI 224. American Concrete Institute, Detroit
2. Balaji Rao K, Appa Rao TVSR (1999) Cracking in reinforced concrete flexural members – a reliability model. Int J Struct Eng Mech 7(3):303–318
3. Balaji Rao K (2009) The applied load, configuration and fluctuation in non-linear analysis of reinforced concrete structures – some issues related to performance based design. Keynote paper. In: Proceedings of international conference on advances in concrete, structural and geotechnical engineering (ACSGE 2009), BITS Pilani, India, 25–27 Oct 2009
4. Bates S, McLaughlin S (2000) The estimation of stable distribution parameters from teletraffic data. IEEE Trans Signal Process 48(3):865–870
5. Bazant ZP (2002) Scaling of structural strength, 2nd edn., 2005. Elsevier Butterworth-Heinemann, Oxford
6. Bazant ZP, Cedolin L (2010) Stability of structures – elastic, inelastic, fracture and damage theories. World Scientific, Singapore
7. Bazant ZP, Oh B-H (1983) Spacing of cracks in reinforced concrete. J Struct Eng ASCE 109:2066–2085
8. Borak S, Härdle W, Weron R (2005) Stable distributions. SFB 649 discussion paper 2005-008, SFB 649, Humboldt-Universität zu Berlin
9. Bresler B (ed) (1974) Reinforced concrete engineering, vol 1, Materials, structural elements, safety. Wiley, New York
10. BS 8110 (1997) Structural use of concrete. Code of practice for design and construction. British Standards Institution, UK
11. Carpinteri A, Puzzi S (2009) The fractal-statistical approach to the size-scale effects on material strength and toughness. Probab Eng Mech 24:75–83
12. Carpinteri A, Cornetti P, Puzzi S (2006) Scaling laws and multiscale approach in the mechanics of heterogeneous and disordered materials. Appl Mech Rev 59:283–305
13. CEB (1990) Model code for concrete structures. Euro-International Concrete Committee, Switzerland
14. Colombo IS, Main IG, Forde Mc (2003) Assessing damage of reinforced concrete beam using "*b*-value" analysis of acoustic emission signals, J Mater Civil Eng ASCE 15:280–286
15. de Borst R (1987) Computation of post-buckling and post-failure behavior of strain-softening solids. Comput Struct 25(2):211–224
16. Desayi P, Balaji Rao K (1987) Probabilistic analysis of cracking of RC beams. Mater Struct 20 (120):408–417
17. Desayi P, Balaji Rao K (1989) Reliability of reinforced concrete beams in limit state of cracking – failure rate analysis approach. Mater Struct 22:269–279
18. Desayi P, Ganesan N (1985) An investigation on spacing of cracks and maximum crack width in reinforced concrete flexural members. Mater Struct 18(104):123–133
19. Dominguez N, Brancherie D, Davenne L, Ibrahimbegovic A (2005) Prediction of crack pattern distribution in reinforced concrete by coupling a strong discontinuity model of concrete cracking and a bond-slip of reinforcement model. Eng Comput Int J Comput Aided Eng Softw 22(5/6):558–582
20. Fama EF, Roll R (1968) Some properties of symmetric stable distributions. J Am Stat Assoc 63 (323):817–836
21. Ibrahimbegovic A, Boulkertous A, Davenne L, Brancherie D (2010) Modelling of reinforced-concrete structures providing crack-spacing based on X-FEM, ED-FEM and novel operator split solution procedure. Int J Numer Methods Eng 83:452–481
22. Kogon SM, Williams DB (1995) On the characterization of impulsive noise with alpha-stable distributions using Fourier techniques. In: Proceedings of the 29th Asilomar conference on signals, systems and computers, vol. 2, pp. 787–791, Pacific Grove, CA

23. Koutrouvelis IA (1980) Regression-type estimation of the parameters of stable laws. J Am Stat Assoc 75(372):918–928
24. Ma X, Nikias CL (1995) Parameter estimation and blind channel identification in impulsive signal environments. IEEE Trans Signal Process 43:2884–2897
25. Mandelbrot BB (1982) The fractal geometry of nature – updated and augmented, edition – 1983, W.H. Freeman and Company, New York
26. Mandelbrot B, Taleb N (2006) A focus on the exceptions that prove the rule. Financial Times (3 April)
27. McCulloch JH (1986) Simple consistent estimators of stable distribution parameter. Commun Stat Simul Comput 15(4):1109–1136
28. Neild SA, Williams MS, McFadden PD (2002) Non-linear behaviour of reinforced concrete beams under low-amplitude cyclic and vibration loads. Eng Struct 24:707–718
29. Nilson AH, Winter G (1986) Design of concrete structures, 10th edn. McGraw-Hill Book Company, New York
30. Nolan JP (2009) Stable distributions: models for heavy tailed data. BirkhÄauser, Boston. Chapter 1 online at academic2.american.edu/»jpnolan. Unfinished manuscript
31. Park R, Paulay T (1975) Reinforced concrete structures. Wiley, New York
32. Prigogine I (1967) Introduction to thermodynamics of irreversible processes, 3rd edn. Interscience Publishers, New York
33. Prigogine I (1978) Time, structure, and fluctuations. Science 201(4358):777–785
34. Rubi JM (2008) The long arm of the second law. Scientific American (November):62–67
35. Sluys LJ, de Borst R (1996) Failure in plain and reinforced concrete – an analysis of crack width and crack spacing. Int J Solids Struct 33(20–22):3257–3276
36. Tsihrintzis GA, Nikias CL (1996) Fast estimation of the parameters of alpha-stable impulsive interference. IEEE Trans Signal Process 44:1492–1503
37. Yang C-Y, Hsu K-C, Chen K-C (2009) The use of the Levy-stable distribution for geophysical data analysis. Hydrogeol J 17:1265–1273

Can Fuzzy Logic Via Computing with Words Bring Complex Environmental Issues into Focus?

Ashok Deshpande and Jyoti Yadav

Abstract Information on the status and changing trends in environmental quality is necessary to formulate sound public policy and efficient implementation of environmental pollution abatement programmes. In this quest, water/air quality indices are computed using US-EPA and US-NSF proposed methods for local and regional water/air quality management in many metro cities of the world. There are different types of uncertainties while adopting the procedure in vogue in the computation of these indices. However, it does not include expert's knowledge with a view to arrive at cause–effect relationship. We believe that the development of a method to quantify association between the pollutant and air/water-borne diseases is an important step before classifying air/water quality, either in numeric or linguistic terms. There exists aleatory uncertainty in the pollution parametric data and epistemic uncertainty in describing the pollutants by the domain experts in linguistic terms such as *poor, good, and very good*. Successes of probability theory have high visibility. But what is not widely recognised is that these successes mask a fundamental limitation—the inability to operate on what may be called perception-based information. In this chapter, we describe the case study 1 that relates to fuzzy description of river water quality in River Ganga for bathing purpose, while case study 2 presents fuzzy description of air quality in Pune City.

Keywords Bathing • River water quality • Fuzzy set theory • Linguistic terms • Fuzzy number • Degree of match • Fuzzy rule base system • Degree of certainty

A. Deshpande (✉)
Berkeley Initiative in Soft Computing (BISC)-Special Interest Group (SIG)-Environment Management Systems (EMS), University of California, Berkeley, CA, USA

College of Engineering Pune (COEP), Pune, Maharashtra, India

National Environmental Engineering Research Institute (NEERI), Nagpur, India
e-mail: ashok_deshpande@hotmail.com

J. Yadav
Department of Computer Science, University of Pune, Pune, Maharashtra, India

S. Chakraborty and G. Bhattacharya (eds.), *Proceedings of the International Symposium on Engineering under Uncertainty: Safety Assessment and Management (ISEUSAM - 2012)*,
DOI 10.1007/978-81-322-0757-3_16,

1 Introduction

You and a friend walk outside on January morning in Pune City. You announce that the weather is *mild*. Your friend declares that it is *cold*. Who is wrong? Or are you both right?

People recognise that language can be imprecise/fuzzy and that concepts such as *cold, hot, or mild do not* have well-defined boundaries. In 1965, Prof. Lotfi Zadeh introduced fuzzy sets and thereafter fuzzy logic, a means of processing data by extending classical set theory to handle partial membership. In everyday life and in fields such as environmental health, people deal with concepts that involve factors that defy classification into crisp sets—*safe, harmful*, *acceptable, unacceptable,* and so on. A classic example is a regulator carefully explaining the result of a detailed quantitative risk assessment to a community group, only to be asked over and over again, *But are we safe?* In this case, *safe* defies crisp classification because it is a multivariate state with gradations that vary among different individuals and groups.

Information on the status and changing trends in environmental quality is necessary to formulate sound public policy and efficient implementation of environmental pollution abatement programmes. One of the ways of communicating the information to the policy makers and public at large is with indices. In the computation of air/water quality index (AQI/WQI), first a numerical value is computed and then the air/water quality is described in linguistic terms. There exists aleatory uncertainty in the pollution parametric data and epistemic uncertainty in describing the pollutants by the domain experts in linguistic terms such as *poor, good, and very good*. Successes of probability theory have high visibility. But what is unrecognised is that these successes mask a fundamental limitation—the inability to operate on what may be called perception-based information. In this chapter, an attempt has been made to use fuzzy-logic-based formalism in modelling these two types of uncertainties, thereby straightway describing air/water quality in linguistic terms with a degree of certainty attached to each term.

The rest of this chapter is organised as follows: Sect. 2 is a brief account of the theoretical foundation of fuzzy-logic-based method with brief description of the other mathematical framework used. While Sect. 3 relates to a case study for describing water quality, fuzzily concluding remarks and future research efforts are covered in Sect. 4.

2 Fuzzy-Logic-Based Formalism

Will I suffer from water-borne diseases (WBD) if I take a bath in polluted river water? Realising the complexity in establishing cause–effect relationship between bathing in polluted river and water-borne diseases (WBDs), an attempt has been made to present a useful method to address the issue. Some of the important facets of our approach include interviewing student community (bather/non-bather) with a

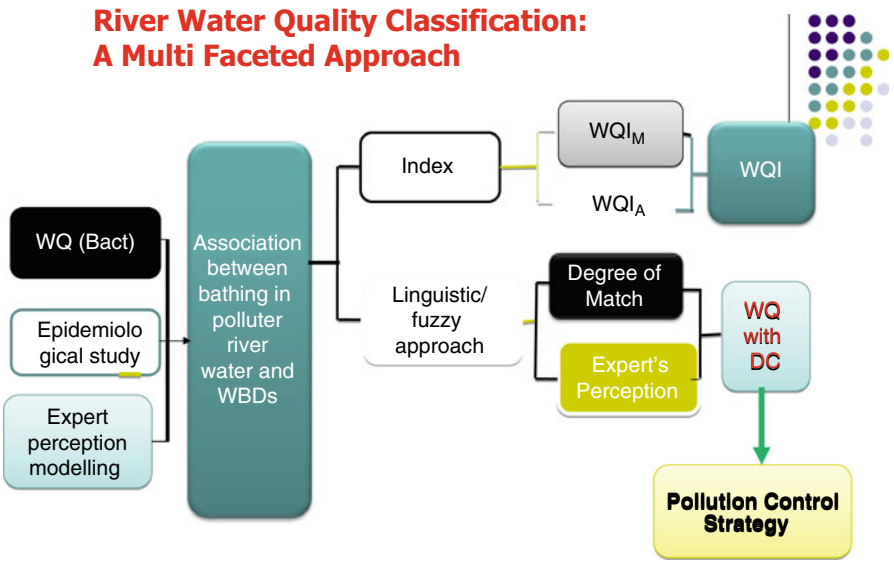

Fig. 1 Multifaceted formalism for water quality classification

structured questionnaire, collecting information on belief of the resident medical practitioners about bathing in polluted river and WBDs, and, furthermore, modelling of epistemic uncertainty in domain expert's belief in supporting their evidence for various WBDs and the like. Figure 1 presents a novel multifaceted formalism for straightway describing river water quality in linguistic terms with degree of certainty. The technique used in estimating the possible association between bathing in polluted river water and water-borne disease includes epidemiological study including case control study, river water quality analysis, perception of the resident medical professionals regarding their belief in relation to water-borne diseases, Dempster–Shafer (DS) theory of evidence, bootstrapping along with conventional statistical techniques, and the like. Some of these methods are briefly described in this section.

2.1 Fuzzy Measures and Evidence Theory

A fuzzy measure describes the vagueness or imprecision in the assignment of an element a to two or more crisp sets. In a fuzzy measure, the concern of attention is to describe the vagueness or imprecision in assigning the point to any of the crisp sets on the power set. Shafer developed Dempster's work and presented an important theory of evidence called Dempster–Shafer (DS) theory in which DS belief (Bel) and plausibility (Pl) are used to characterise uncertainty. A basic measure in DS theory is a basic belief assignment (BBA). The function (m) is a mapping function to express BBA for a given evidential event A, m (A). BBA is a representation of partial belief not only for a single possible event but also for a set of

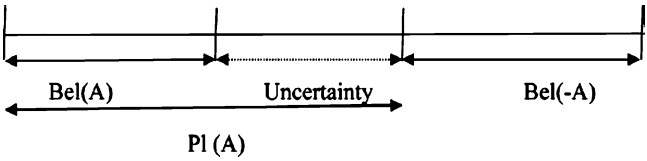

Fig. 2 Belief and uncertainty and ignorance

possible events with imprecise and incomplete knowledge and data. The main concept of evidence theory is that our knowledge of a given problem can be inherently imprecise. Hence, the bound result, which consists of both belief and plausibility, is presented (Fig. 2). BBA expresses the degree of belief in a proposition. BBA is assigned by making use of a mapping function (m) to express our belief with a number in the unit interval [0, 1]

$$m : 2x \rightarrow [0, 1]. \tag{1}$$

The number m (A) represents the portion of total belief assigned exactly to proposition A. The measure m, BBA function, must satisfy the following axioms:

$$m(A) \geq 0 \quad \text{for any } A \in 2^x \tag{2}$$

$$m(\varphi) = 0, \quad \Sigma_{\in 2x}\, mA = 1 \tag{3}$$

Though these axioms of evidence theory look similar to those of probability theory, the axioms for the BBA functions are less stringent than those for probability measure.

Dempster's Rule of Combining. The information from different sources can be aggregated by Dempster's rule of combining to make a new combined BBA structure as given in the following equation:

$$M_{12}(A) = \frac{\sum\limits_{c_i \cap c_j = A} m_1(c_i) m_2(c_j)}{1 - \sum\limits_{c_i \cap c_j = \phi} m_1(c_i) m_2(c_j)}, \quad A \neq \phi \tag{4}$$

where Ci and Cj are propositions from each sources ($m1$ and $m2$). In Eq. (4), $\sum_{c_i \cap c_i = \phi} m_1(c_i) m_2(c_j)$ can be viewed as contradiction or conflict among the information given by the independent knowledge sources (Ross 1997). Even when some conflict is found among the information, Dempster's rule disregards every contradiction by normalising with the complementary degree of contradiction to consider only consistent information. However, this normalisation can cause a counterintuitive and numerically unstable combination of information when the given information from different sources has significant contradiction or conflict. If there is a serious conflict, it is recommended to investigate the given information or to collect more information.

2.2 Belief and Plausibility Function

Owing to lack of information and various possibilities in constructing BBA structure, it is more reasonable to present a bound of the total degree of belief in a proposition, as opposed to a single value of probability given as a final result in probability theory. The total degree of belief in a proposition A is expressed within bound [bel (A), pl (A)], which lies in the unit interval [0, 1] as shown in Fig. 1, where Bel (A) and Pl (A) are given as

$$\begin{aligned} \text{Bel}(A) &= \sum_{c \subset A} m(C) : \text{ Belief function} \\ \text{Pl}(A) &= \sum_{c \subset A \neq \phi} m(c) : \text{ Plausibility function.} \end{aligned} \tag{5}$$

Bel (A) is obtained by the summation of BBAs for proposition, which is included in proposition A fully. Bel (A) is the total degree of belief. The degree of plausibility Pl (A) is calculated by adding BBAs of propositions whose intersection with proposition A is not an empty set. That is, every proposition consistent with proposition A at least partially is considered to imply proposition A because BBA in a proposition is not divided into its subsets. Briefly, Bel (A) is obtained by adding the BBAs of propositions that totally agree with the proposition A as a measure of belief, whereas Pl (A) plausibility is calculated by adding BBAs of propositions that correspond to the proposition A totally or partially. In a sense, these two measures consist of lower and upper probability bounds.

2.3 Fuzzy Inference System

Firstly, water/air quality experts are identified, and relevant field data is collected. Additional data generation is a logical step if the available data is inadequate for analysis. Perception of experts about the linguistic description of river water quality for bathing is obtained on interviewing or through a questionnaire. Modelling of uncertainty in the expert's perception by constructing fuzzy sets/fuzzy numbers and the uncertainty in the field data of water quality parameters using the concept of convex normalised fuzzy number is the next step. The parameters identified for defining bathing, say water quality by the experts, are faecal coliforms (*FC*), dissolved oxygen (DO), biochemical oxygen demand (*BOD*), *pH,* and *turbidity*. The relevant parameters could be considered while describing the overall air quality of a city/region.

Randomness in the air/water quality data can be transformed into a convex normalised fuzzy number A with membership grade function $\mu\text{A}(x)$, thereby characterising the dynamic behaviour of the water quality parameters. We refer to

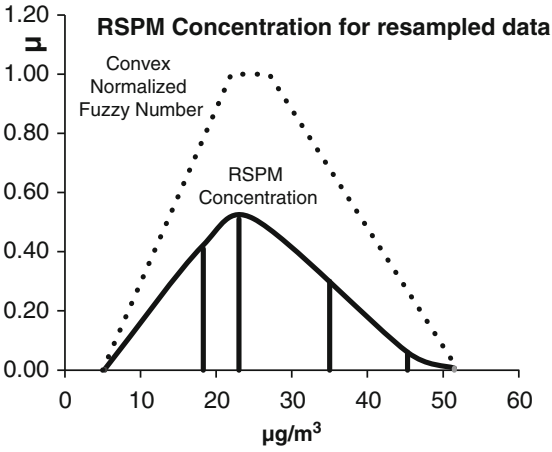

Fig. 3 Probability and possibility distribution for respirable suspended particulate matter (RSPM)

air quality parameter for illustration. If x_i is some point on the parametric domain for which $p\ (x_j)$ is maximum, then define function $\mu_A\ (x)$ (Fig. 3):

$$\mu_A(x) = p(x)/p(x_j) \tag{6}$$

Construction of fuzzy number or fuzzy sets for modelling the perception of the experts in classifying each parametric domain in linguistic terms such as *very good and good* allows for referencing all possible parametric values to be described. This transforms a random variable into a convex normalised fuzzy number A with membership grade function $\mu_A(x)$, thereby characterising the dynamic behaviour of the water quality parameter. The construction of fuzzy number or fuzzy sets for modelling the perception of the experts in classifying each parametric domain linguistically involves selection of linguistic terms such as *very good and good,* which allows for referencing all possible parametric values to be described; classification of the parametric domain and assigning linguistic terms to each class linearly by the experts reflecting the imprecision in their perception; the set of values for which all the experts assign the same linguistic term is given $\mu = 1.0$, while none of the experts assigning that term are given $\mu = 0.0$. The breakeven point membership grades 0.0 and 1.0 are connected by continuous monotonic function which presupposes that the degree of consensus among the experts goes on increasing as the parametric values approach the core of fuzzy number for the specified linguistic term.

2.4 Matching Between Two Fuzzy Values

The fuzzy number for field data (A) on parameters and the fuzzy number characterising linguistic terms (A') are matched together to arrive at a measure called degree of match (DM) defined by

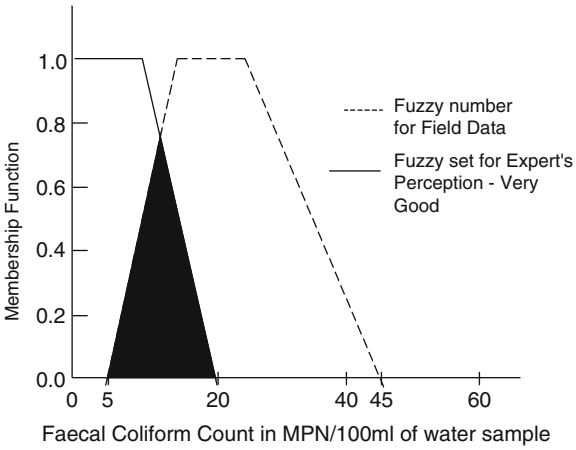

Fig. 4 Fuzzy numbers for *very good faecal coliforms*

$$\mathrm{DM_{ff}}(A, A') = \mathrm{f}\mu_{A\cap A'}(x)\ \mathrm{d}x / \mathrm{f}\mu_A(x)\ \mathrm{d}x, x \subset \mathrm{X} \tag{7}$$

in which X denotes the universe and $\mu\varsigma\cap\varsigma$, (x) is membership grade for $\varsigma\cap\varsigma$,. Furthermore, if A and A' are the discrete possibility distributions, the measure is defined as

$$\mathrm{DM_{ff}}(A, A') = \Sigma\mu_{A\cap A'}(x)/\Sigma\mu_A(x), \quad x \subset \mathrm{X} \tag{8}$$

Figure 4 shows the fuzzy number for *very good faecal coliforms* reveals that almost all the experts agree that the *faecal coliforms* count between 0 and 10 MPN/100 ml of water. The level of presumption or membership function decreases with the increasing faecal coliforms count. When the count exceeds 20, none of the experts define the parameters as *very good* for bathing purpose. This is indicated by the level of presumption $\iota` = 0$.

A set of rules is constructed for classifying air/water quality as highly acceptable, just acceptable, or not acceptable (rejected) in order to aggregate the set of attributes. Each rule has antecedent propositions connected together using AND operator, resulting in some consequences. The assertions related to its antecedent part are obtained from the users, which are imprecise or fuzzy. Thus, a fuzzy rule-based system can be developed for the knowledge representation or reasoning process. Here, the partial matching is allowed, and the analyst can estimate the extent to which the assertion satisfies the antecedent part of the rule contrary to the rule-based system which examines as to whether the antecedent part is satisfied or not [1]. A hierarchical structure for water classification resulting in a set of rules can be constructed (Fig. 5). The chemical status of water is judged in the first hierarchical level of knowledge base. The second hierarchical level characterises bacteriological, chemical, and physical status of water to arrive at the ultimate acceptable strategy of water quality for bathing purpose. If need be, a similar structure can be developed for air quality classification.

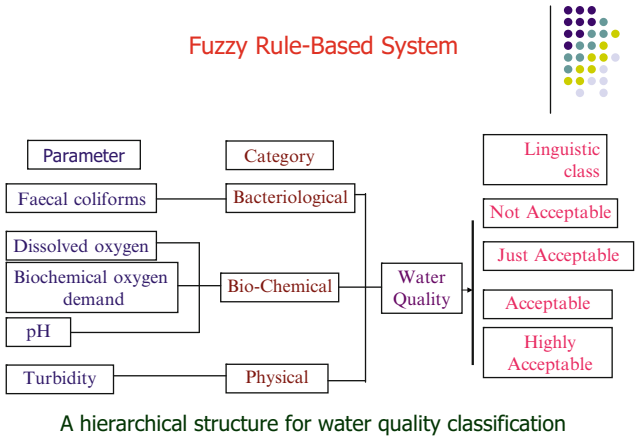

Fig. 5 Type 1 fuzzy inference system/fuzzy expert system

Following are the sample rules stored at two different hierarchical levels of the knowledge base:

Rule 1
If DO is <fair> and
BOD is <good> and
pH is <very good>,
then chemical status of water is <good>.

3 Fuzzy Description of Environment Quality

With the approach presented in this chapter, it is possible to describe any environmental quality fuzzily. We present herein water and air quality.

3.1 Case Study 1: Fuzzy Description of River Water Quality

Around 21% of communicable diseases in India are water related, and out of these, diarrheal diseases alone killed over 700,000 Indians in the year 1999. Since time immemorial, sacred bathing on the holy riverbanks (*ghats*) is practised in India and Nepal. It has been a religious belief of some of the bathers that gulping water at these holy places washes away their sins! The first study, therefore, relates to establishing the cause–effect relationship between bathing in polluted river water and water-borne diseases carried out at Alandi town near Pune situated on the

Table 1 Fuzzy description of river water quality with degree of certainty

Degree of certainty		
Water quality description	Rishikesh	Varanasi
Highly accepted	0.21	0
Accepted	**0.41**	0
Just accepted	0.36	0.01
Not accepted	0.1	**0.98**

banks of river Indrayani. We very briefly discuss the final outcome of such an investigation [2]. The analysis of the results reveals result that the combined belief of the two domain experts in identifying for the single disease *diarrhoea is 0.58*. In sum, bathing in polluted water can be a cause for the incidence of water-borne diseases in bathers [2].

Describing Ganga water quality straightway in linguistic terms, with some degree of certainty attached to each linguistic term, concludes that the Government of India should continue the efforts on the reduction of pollution levels, especially from bacteriological standpoint. Aerobic treatment is the option that should be attached great importance in future planning of GAP 2. The results depicted after Ganga Action Plan 1 infers that even at Rishikesh, the water quality of Ganga is not very good for bathing and still the pollution persists as the degree of certainty attached to fair is 0.36 while it is 0.41 for the linguistic description of water as good. Varanasi has been a serious cause of concern from the standpoint of bathing in the holy river (Table 1).

3.2 Case Study 2: Fuzzy Description of River Air Quality

The case study relates to fuzzy air quality description with the available air quality data from five monitoring stations in Pune City. These are Pimpri-Chinchwad Municipal Corporation, Karve Road, Swargate, Bhosari, and Nal Stop. In order to bring down progressive deterioration in air quality, the Government of India has enacted Air (Prevention and Control of Pollution) Act in 1981, and further stringent guidelines are promulgated in Environment (Protection) Act, 1986. The need for ambient air quality monitoring programme that is needed to determine the existing quality of air and evaluation of the effectiveness of control programme and to develop new programme was recognised. As a follow-up action, the Central Pollution Control Board (CPCB) initiated National Air Quality Monitoring (NAQM) Programme during 1984–1985 at the national level.

A well-structured air quality monitoring network involves selection of pollutants, selection of locations, frequency, duration of sampling, sampling techniques, infrastructural facilities, man power and operation, maintenance costs, and the like. The network design also depends upon the type of pollutants in the atmosphere through various common sources, called common urban air

Table 2 Comparison of conventional AQI and fuzzy description of air quality with degree of certainty

Monitoring station	Conventional AQI	AQI with degree of certainty
Karve Road	206 very poor	0.45 very poor
Bhosari	145.89 poor	0.43 very poor
Swargate	147.13 poor	0.54 poor
Nal Stop	120.2 poor	0.67 fair
PCMC	151.13 very poor	0.91 poor

pollutants, such as suspended particulate matter (SPM), respirable suspended particulate matter (RSPM), sulphur dioxide (SO_2), oxides of nitrogen (NO_x), and carbon monoxide (CO). The areas to be chosen primarily are such areas which represent high traffic density, industrial growth, human population and its distribution, emission source, public complaints if any, the land use pattern, etc. Generally, most of the times the basis of a network design is the pollution source and the pollution present.

Generation of fuzzy numbers for different linguistic hedges (*very good, good, fair, poor, very poor*) of RSPM concentration is an important issue in any FIS. According to the expert, RSPM count between 18–57 $\mu g/m^3$ is very good, 42–75 $\mu g/m^3$ is good, 67–100 $\mu g/m^3$ is fair, 90–130 $\mu g/m^3$ is poor $\mu g/m^3$, and above 120 $\mu g/m^3$ it is very poor. The level of membership function decreases with the increasing RSPM level. When it exceeds 57, the expert does not define the parameter as very good. Table 2 is the comparison between the computed AQI and the proposed fuzzy-logic-based method. It can be revealed that AQI based on the traditional method does not attach any certainty while describing the air quality. In addition, the method does not consider the aggregated effect, and the highest computed AQI is considered as the final decision on the air quality which, in our opinion, is the departure from human thinking. Alternately, using type 1 fuzzy inference system, we can describe the air quality straightway in linguistic terms with some degree of certainty attached to each term.

4 Outlook in Environmental Policy [3]

Over the past few decades, soft computing tools such as fuzzy-logic-based methods, neural networks, and genetic algorithms have had significant and growing impacts. But we have seen only limited use of these methods in environmental fields, such as risk assessment, cost-benefit analysis, and life-cycle impact assessment. Because fuzzy methods offer both new opportunities and unforeseen problems relative to current methods, it is difficult to determine how much impact such methods will have on environmental policies in the coming decades. Here, we consider some obvious advantages and limitations.

Quantitative models with explicit and crisp delineations of systems have long been the currency of discourse in engineering and the physical sciences, where basic physical laws form the foundations of analyses. These fields place high value on the causal linkages implicit in model structure and parameterization. But for problems that involve human values, language, control theory, biology, and even environmental systems, researchers have had to rely more on descriptive and empirical approaches. When the goal is to summarise the observations in an efficient and useful manner, fuzzy-logic-based methods should be further investigated as alternative—and perhaps more appropriate—methods for addressing uncertain and complex systems. For the types of complex and imprecise problems that arise in environmental policy, the ability to model complex behaviours as a collection of simple if–then rules makes fuzzy logic an appropriate modelling tool. Because fuzzy arithmetic works well for addressing linguistic variables and poorly characterised parameters, fuzzy methods offer the opportunity to evaluate and communicate assessments on the basis of linguistic terms that could possibly match those of decision makers and the public. Moreover, approximate reasoning methods such as fuzzy arithmetic do not require well-characterised statistical distributions as inputs. Another key advantage of fuzzy logic in risk assessment is the ability to merge multiple objectives with different values and meanings, for example, combining health objectives with aesthetic objectives. It also provides rules for combining qualitative and quantitative objectives [3].

But fuzzy logic has at least two limitations for expressing health risks and other environmental impacts. One problem is its strong reliance on subjective inputs. Although this is a problem in any type of assessment, fuzzy methods might provide more opportunity for the misuse of subjective inputs. Although probabilistic assessments based on tools such as Monte Carlo methods are analogous to assessments based on fuzzy logic, these two techniques differ significantly both in approach and in interpretation of results. Fuzzy logic confronts linguistic variables such as ‘safe’, ‘hazardous’, ‘acceptable’, and ‘unacceptable’, whereas Monte Carlo methods are forced to fit linguistic variables for probabilistic assessments. Fuzzy arithmetic combines outcomes from different sets in a way that is analogous to but still different from Monte Carlo methods. Possibility theory can be used as an alternative to probabilistic analysis, but this strategy creates the potential for misuse if membership functions are interpreted as probability distributions.

4.1 No More Crisp Lines?

Fuzzy logic represents a significant change in both the approach to and the outcome of environmental evaluations. Currently, risk assessment implicitly assumes that probability theory provides the necessary and sufficient tools for dealing with uncertainty and variability. The key advantage of fuzzy methods is how they reflect the human mind in its remarkable ability to store and process information that is consistently imprecise, uncertain, and resistant to classification. Our case

study illustrates the ability of fuzzy logic to integrate statistical measurements with imprecise health goals. But we submit that fuzzy logic and probability theory are complementary and not competitive. In the world of soft computing, fuzzy logic has been widely used and has often been the 'smart' behind smart machines. But more effort and further case studies will be required to establish its niche in risk assessment and other types of impact assessment. Could we adapt to a system that relaxes 'crisp lines' and sharp demarcations to fuzzy gradations? Would decision makers and the public accept expressions of water- or air-quality goals in linguistic terms with computed degrees of certainty? Resistance is likely. In many regions, such as the United States and EU, both decision makers and members of the public seem more comfortable with the current system—in which government agencies avoid confronting uncertainties by setting guidelines that are crisp and often fail to communicate uncertainty. Perhaps someday, a more comprehensive approach that includes exposure surveys, toxicological data, and epidemiological studies coupled with fuzzy modelling will go a long way towards resolving some of the conflict, divisiveness, and controversy in the current regulatory paradigm.

Acknowledgement The wholehearted assistance received from Dr. D. V. Raje and Dr. Kedar Rijal for the implementation of the concept is gratefully acknowledged. My special thanks to Professor Thomas McKone who helped the author in many fuzzy ways!

References

1. Deshpande AW, Raje DV, Khanna P (1996). Fuzzy description of river water quality. Eufit 96, 2–5 September. pp 1795–1801
2. Rijal K, Deshpande A, Ghole V (2009) Bathing in polluted rivers, water-borne diseases, and fuzzy measures: a case study in India. Int. J. Environ Waste Manage 6(3–4):255–263
3. Mckone TE, Deshpande AW (2005) Can fuzzy logic bring complex environmental problems into focus? Int J Environ Sci Technol 39(2):42A–47A

Uncertainty Evaluation in Best Estimate Accident Analysis of NPPs

S.K. Gupta, S.K. Dubey, and R.S. Rao

Abstract Recent trends in carrying out deterministic safety analysis for safety assessment are attracting more attention for the use of best estimate approach. However, conservative approaches are still used in licensing safety analysis. The best estimate approach provides more realistic information with respect to conservative approach for predictions of physical behaviour and provides information about the existing safety margins and between the results of calculation and regulatory acceptance criteria, whereas conservative approach also does not give any indication about actual plant behaviour, including time scale, for preparation of emergency operating procedures. Best estimate methodology results are affected by various sources of uncertainty like code or model uncertainty, representation uncertainty, scaling uncertainty and plant uncertainty. Therefore, uncertainty in the results due to unavoidable approximation in the modelling should be quantified. Various uncertainty analysis methodologies have been emerged after the development of code scaling, applicability and uncertainty (CSAU) by US NRC in 1989, like CIAU by Italy and GRS by Germany. This chapter deals with the sources of uncertainty and its quantifications by various methodologies in terms of confidence and probability. This chapter also deals with the application of a sampling-based uncertainty evaluation in the best estimate analysis of station blackout and small break LOCA in integral test facilities carried out under the framework of IAEA CRP. Uncertainty evaluation for TMI-II accident has been carried out using this methodology.

Keywords Uncertainty • Best estimate • Accident analysis • NPPs

S.K. Gupta (✉) • S.K. Dubey • R.S. Rao
Safety Analysis and Documentation Division, Atomic Energy Regulatory Board, Anushaktinagar, Mumbai 400094, India
e-mail: guptask@aerb.gov.in

S. Chakraborty and G. Bhattacharya (eds.), *Proceedings of the International Symposium on Engineering under Uncertainty: Safety Assessment and Management (ISEUSAM - 2012)*,
DOI 10.1007/978-81-322-0757-3_17,

1 Introduction

As per the AERB design code/standard requirement, deterministic safety analysis (frequently referred to as accident analysis) is an important tool for confirming the adequacy and efficiency of provisions within the defence in depth concept for the safety of nuclear power plants. The computer programmes, analytical methods and plant models used in the safety analysis shall be verified and validated, and adequate consideration shall be given to uncertainties [1]. Although the trends in accident analysis have continued to move to best estimate analysis rather than conservative analysis, conservative approaches are still use. The conservative approach does not give any indication of actual margins between the actual response and the conservatively estimated response. A conservative approach also does not give any indication about actual plant behaviour, including timescale, for preparation of emergency operating procedures (EOPs) or for use in accident management for abnormal operating conditions. In addition, a conservative approach often does not show margins that in reality could be utilised for greater operational flexibility. The concept of conservative methods was introduced at the early days (1970) of safety analyses to account for uncertainty due to the limited capability of modelling, the limited knowledge of physical phenomena and to simplify the phenomena. Use of a conservative methodology may lead to so large conservatism that important safety issues are masked. In the last four decades, thermal-hydraulic issues, intensive experimental research that has resulted in a considerable increase in knowledge and the development of computer codes have improved the ability of these codes to calculate results that agree with the experimental results. In order to overcome these deficiencies in conservative analysis, it may be preferable to use a best estimate approach together with an evaluation of the uncertainties to compare with acceptance criteria. A best estimate approach provides more realistic information about the physical behaviour, identifies the most relevant safety issues and provides information about the existing margins between the results of calculation and acceptance criteria. The best estimate approach is highly dependent upon an extensive experimental database to establish confidence in the best estimate codes and to define the uncertainties that have to be determined for the best estimate results.

The use of BE codes is generally recommended for deterministic safety analysis. Two options are offered to demonstrate sufficient safety margins in using BE codes: The first option is the use of the codes ‘in combination with a reasonably conservative selection of input data and a limited evaluation of the uncertainties of the results’. In this statement, evaluation of uncertainties is meant more in the deterministic sense: code to code comparisons, code to data comparisons and expert judgments in combination with sensitivity studies are considered as typical methods for the estimation of uncertainties. The second option is the use of the codes with realistic assumptions on initial and boundary conditions and taking credit in the analysis for availability of systems including time consideration for operator intervention. However, for this option, an approach should be based on statistically

combined uncertainties for plant conditions and code models to establish, with a specified high probability that the calculated results do not exceed the acceptance criteria. Both options should be complemented by sensitivity studies, which include systematic variation of the code input variables and modelling parameters with the aim of identifying the important parameters required for the analysis and to show that there is no abrupt change in the result of the analysis for a realistic variation of inputs ('cliff edge' effects). It is necessary to quantify uncertainty in best estimate accident analysis when realistic initial and boundary conditions are used because best estimate code results are affected by various sources of uncertainty like code or model uncertainty, representation uncertainty, scaling uncertainty and plant uncertainty. This chapter deals with the sources of uncertainty, evaluation of uncertainty methodologies and quantification of uncertainty in terms of confidence and probability. In this chapter, uncertainty evaluation by sampling-based methodology in the analysis of the station blackout and small break LOCA in integral test facilities carried out under the framework of IAEA coordinated research project is reported. Application of this methodology has also been demonstrated in this chapter for actual nuclear power plant TMI-II accident.

2 Sources of Uncertainty

Uncertainty in the best estimate results due to various sources of uncertainty should be quantified. Evaluation process of various sources of uncertainties including integral effect and experimental data is reported in Fig. 1. Sources of uncertainty fall within five general categories [6]:

(a) *Code or model uncertainties*: A thermal-hydraulic system code is a computational tool that typically includes three different sets of balance equations (or of equations derived from fundamental principles), closure or constitutive equations, material and state properties, special process or component models and a numerical solution method. The three sets of balance equations deal with the fluids of the system, the solid structures including the fuel rods and the neutrons. In relation to the fluids of the system, the 1-D UVUT (unequal velocities, unequal temperatures) set of partial differential equations is part of the codes under consideration. The closure (constitutive) equations deal with the interaction between the fluid and the environment as well as with the interaction of the two phases of the fluid (i.e. the gas/vapour and the liquid phase). The interfacial drag coefficient, wall to fluid friction factor and heat transfer coefficient are typically expressed by constitutive equations. Various sets of material properties are embedded into the codes, even though the user may change these properties or add new materials. Water, nitrogen, air, uranium dioxide, stainless and carbon steel and zircaloy are materials. Different levels of sophistication usually characterise the sets of properties in the different codes. This is especially true for water (Mollier diagram quantities and

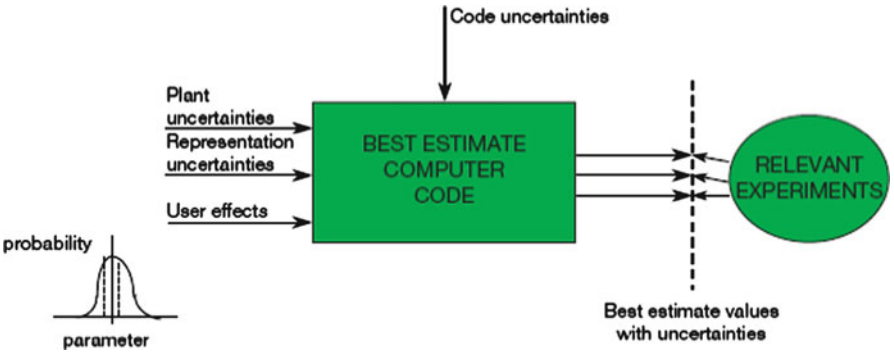

Fig. 1 Evaluation process and main sources of uncertainties [6]

related derivatives). Balance equations are not sophisticated enough for application in the modelling of special components or for the simulation of special processes. Examples of these components are the pumps and the steam separators, and examples of the special processes are the countercurrent flow limiting condition and two phase critical flow, although this is not true for all the codes. Empirical models 'substitute' the balance equations in such cases.

(b) *Representation uncertainties*: Representation uncertainty is related to the process of setting up the nodalisation (idealisation). The nodalisation constitutes the connection between the code and the 'physical reality' that is the subject of the simulation. The process for setting up the nodalisation is an activity carried out by a group of code users that aims at transferring the information from the real system (e.g. the nuclear power plant), including the related boundary and initial conditions, into a form understandable to the code. Limitation of available resources (in terms of person-months), lack of data, the target of the code application, capabilities or power of the available computational machines and expertise of the users play a role in this process. The result of the process may strongly affect the response of the code.

(c) *Scaling uncertainty*: Using data recorded in scaled experiments and the reliance on scaling laws to apply the data result to full-scale systems. Scaling is a broad term used in nuclear reactor technology as well as in basic fluid dynamics and in thermal hydraulics. In general terms, scaling indicates the need for the process of transferring information from a model to a prototype. The model and the prototype are typically characterised by different geometric dimensions, but thermal-hydraulic quantities such as pressure, temperature and velocities may be different in the model and in the prototype, as well as in the materials adopted, including working fluids. Therefore, the word 'scaling' may have different meanings in different contexts. In system thermal hydraulics, a scaling process, based upon suitable physical principles, aims at establishing a correlation between phenomena expected in a nuclear power plant transient scenario and phenomena measured in smaller scale facilities or phenomena predicted by numerical tools qualified against experiments performed in small-scale facilities.

Owing to limitations of the fundamental equations at the basis of system codes, the scaling issue may constitute an important source of uncertainties in code applications and may envelop various individual uncertainties.

(d) *Plant uncertainty*: The uncertainty bands associated with the boundary and initial conditions for the nuclear power plant condition under consideration, for example, core power, SG feed water inlet temperature. Uncertainty or limited knowledge of boundary and initial conditions and related values for a particular nuclear power plant are referred to as plant uncertainty. Typical examples are the pressuriser level at the start of the transient, the thickness of the gap of the fuel rod, the conductivity of the UO2 and the gap between the pellets and the cladding. It should be noted that quantities such as gap conductivity and thickness are relevant for the prediction of safety parameters (e.g. the PCT) and are affected by other parameters such as burn-up, knowledge about which is not as detailed as required (e.g. knowledge about each layer of a fuel element that may be part of the nodalisation). Thus, a source of error of this kind in the class of 'plant uncertainty' cannot be avoided and should be accounted for by the uncertainty method.

(e) *User effect*: The flexibility of the system codes for various volume control flags, junction control flags, solution method, etc., under consideration is a primary reason for generating a user effect. The impact of the user effect upon the final result (i.e. BE prediction plus uncertainty) may be different depending upon the selected uncertainty method. System code output results are largely affected by user's capability, qualifications and experience in the use of the code. It has been observed that results obtained by various users differ a lot for the use of same system code and same date provided for the modelling.

3 Uncertainty Methodologies

An uncertainty analysis consists of identification and characterisation of relevant input parameters (input uncertainty) as well as of the methodology to quantify the global influence of the combination of these uncertainties on selected output parameters (output uncertainty). These two main items may be treated differently by different methods. Within the uncertainty methods considered, uncertainties are evaluated using either (a) propagation of input uncertainties (Fig. 2) or (b) extrapolation of output uncertainties. For the 'propagation of input uncertainties', uncertainty is obtained following the identification of 'uncertain' input parameters with specified ranges or/and probability distributions of these parameters and performing calculations varying these parameters, schematic shown in Fig. 2. The propagation of input uncertainties can be performed by either deterministic or probabilistic methods. For the 'extrapolation of output uncertainty' approach, uncertainty is obtained from the (output) uncertainty based on comparison between calculation results and significant experimental data.

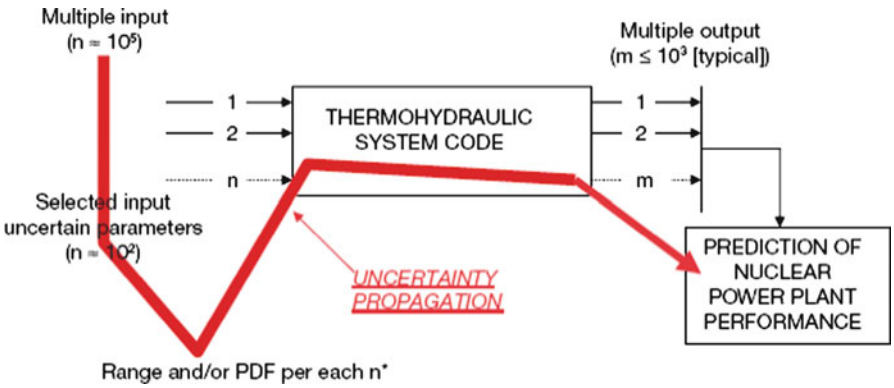

Fig. 2 Propagation of input uncertainty [6]

3.1 Propagation of Input Uncertainties

3.1.1 Probabilistic Methods

Probabilistic methods include CSAU, GRS, IPSN and the Canadian best estimate and uncertainty (BEAU) method. The probabilistic methods have the following common features:

(a) The nuclear power plant, the code and the transient to be analysed are identified.
(b) Uncertainties (plant initial and boundary conditions, fuel parameters, modelling) are identified.
(c) Some methods restrict the number of input uncertainties to be included in the calculations.

The selected input uncertainties are ranged using relevant separate effects data. The state of knowledge of each uncertain input parameter within its range is expressed by a probability distribution. Sometimes, 'state of knowledge uncertainty' is referred to as 'subjective uncertainty' to distinguish it from uncertainty due to stochastic variability. Dependency between uncertain input parameters should be identified and quantified provided that these dependencies are relevant.

3.1.2 Deterministic Methods

The deterministic methods include the Atomic Energy Authority Winfrith (AEAW) and the Electricité de France (EDF)–Framatome methods.

The deterministic methods have the following features in common with probabilistic methods:

(a) The code, nuclear power plant and transient are identified.
(b) Uncertainties (initial and boundary conditions, modelling, plant, fuel) are identified.

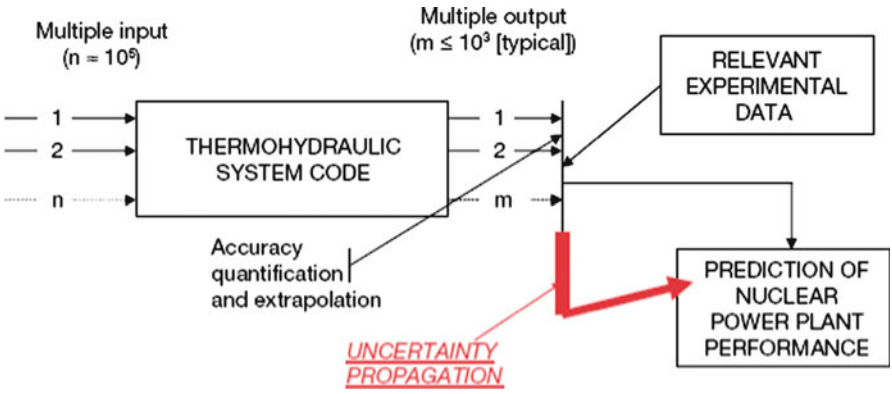

Fig. 3 Extrapolation of output uncertainty [6]

The difference with deterministic methods is in quantifying the input parameter uncertainties. No probability distributions are used; instead, reasonable uncertainty ranges or bounding values are specified that encompass, for example, available relevant experimental data. The statements of the uncertainty of code results are deterministic, not probabilistic.

3.2 Extrapolation of Output Uncertainty

The extrapolation of output uncertainty method focuses not on the evaluation of individual parameter uncertainties but on direct scaling of data from an available database, calculating the final uncertainty by extrapolating the accuracy evaluated from relevant integral experiments to full-scale nuclear power plants, known as Code with the capability to internal assessment of uncertainty (CIAU) developed by the University of Pisa, Italy. A schematic of this method is shown in Fig. 3. Considering integral test facilities (ITFs) of a reference light water reactor (LWR) and qualified computer codes based on advanced models, the method relies on code capability qualified by application to facilities of increasing scale. Direct data extrapolation from small-scale experiments to the reactor scale is difficult due to the imperfect scaling criteria adopted in the design of each scaled down facility. Only the accuracy (i.e. the difference between measured and calculated quantities) is therefore extrapolated. Experimental and calculated data in differently scaled facilities are used to demonstrate that physical phenomena, and code predictive capabilities of important phenomena do not change when increasing the dimensions of the facilities; however, available integral effect test facility scales are far from reactor scale.

4 Representation of Uncertainty

Representation of uncertainty evaluated for important parameters from the result of code output is done in many ways: confidence and probability, in terms of percentile, scatter plot and histogram, etc. The first two ways of presentation of uncertainty methodology are most commonly used in nuclear reactor technology.

4.1 Probability and Confidence

When regulatory acceptance criteria are checked for the calculated parameter obtained using best estimate system code, then it is to be ensured that what is the confidence with specified probability that the parameters will lie in the specified interval because many uncertainties are involved in the best estimate calculation. In many situations, a point estimate does not provide enough information about a parameter. Suppose if we want to estimate the mean peak clad temperature in case of LOCA, a single number may not be meaningful as an interval within which we would expect to find the value of this parameter as the calculated value of clad temperature strongly depends on many input parameters for which the exact real value is not known but the interval. This is an interval estimate called a confidence interval.

An interval estimate of an unknown parameter θ is an interval of the form $l \leq \theta \leq u$, where the end points l and u depend on the numerical value of the statistic of θ for a particular sample and on its sampling distribution, since different samples will produce the difference between l and u. These end points are values of random variables say L and U, respectively. From the sampling distribution of θ, the value of L and U can be determined such that the following probability statement is true:

$$P(L \leq \theta \leq U) = 1 - \alpha$$

where $0 < \alpha < 1$. Thus, there is a probability of $1 - \alpha$ of selecting a sample that will produce an interval containing true value of θ. The resulting interval $l \leq \theta \leq u$ is called a $100(1 - \alpha)$ percent confidence interval for the unknown parameter θ. The quantities l and u are called the lower and upper confidence limits, and $1 - \alpha$ is called the confidence coefficient. The interpretation of a confidence interval is that if an infinite number of random samples are collected and a $100(1 - \alpha)$ percent confidence interval for θ computed from each sample, then 100 $(1 - \alpha)$ percent of these intervals will contain the true value of θ.

Suppose that a population has unknown mean μ and known variance σ^2. A random sample of size n is taken from this population, say, $X_1, X_2, X_3, \ldots, X_n$. The sample mean $\bar{X}$ is a reasonable point estimator of the unknown mean μ. A 100 $(1 - \alpha)$ percent confidence interval on μ can be obtained by considering the sampling distribution of the sample mean $\bar{X}$. The sampling distribution of $\bar{X}$ is normal if the population is normal and approximately normal if the condition of the

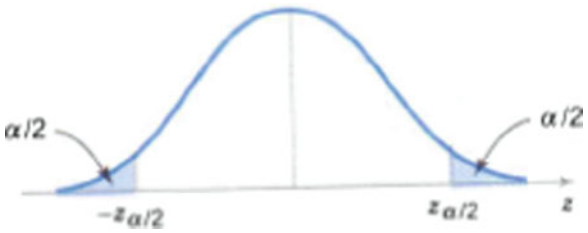

Fig. 4 The distribution of Z [7]

central limit theorem is met. The expected value or mean of $\bar{X}$ is μ, and the variance is σ^2/n. Therefore, the distribution of the statistic

$$Z = \frac{\bar{X} - \mu}{\sigma/\sqrt{n}}$$

is a standard normal distribution.

The distribution of $Z = \frac{\bar{X}-\mu}{\sigma/\sqrt{n}}$ is shown in Fig. 4. From the Fig. 4, it is found that

$$P\left\{-Z_{\alpha/2} \le Z \le Z_{\alpha/2}\right\} = 1 - \alpha$$

so that

$$P\left\{-Z_{\alpha/2} \le \frac{\bar{X} - \mu}{\sigma/\sqrt{n}} \le Z_{\alpha/2}\right\} = 1 - \alpha$$

This can be rearranged as

$$P\left\{\bar{X} - Z_{\alpha/2}\sigma/\sqrt{n} \le \mu \le \bar{X} - Z_{\alpha/2}\sigma/\sqrt{n}\right\} = 1 - \alpha$$

Therefore, it is said that if $\bar{X}$ is the sample mean of a random sample size n from a population with known variance σ^2, a $100(1 - \alpha)$ percent confidence interval on μ is given by

$$\bar{X} - Z_{\alpha/2}\sigma/\sqrt{n} \le \mu \le \bar{X} - Z_{\alpha/2}\sigma/\sqrt{n}$$

where $Z_{\alpha/2}$ is the upper $\alpha/2$ percentage point of the standard normal distribution.

Furthermore, if $\bar{X}$ is used as an estimator of μ, then with the $100(1 - \alpha)$ percent confidence that the error $|\bar{X} - \mu|$ will not exceed a specified amount E when the sample size is

$$n = \left(\frac{Z_{\alpha/2}\sigma}{E}\right)^2$$

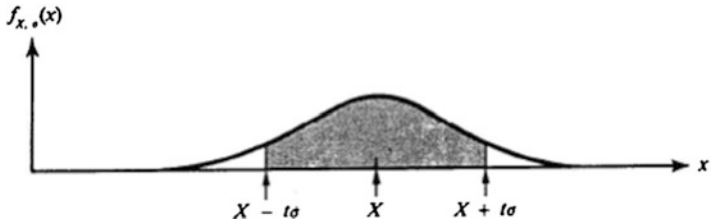

Fig. 5 Probability of a measurement with t standard deviation of X [11]

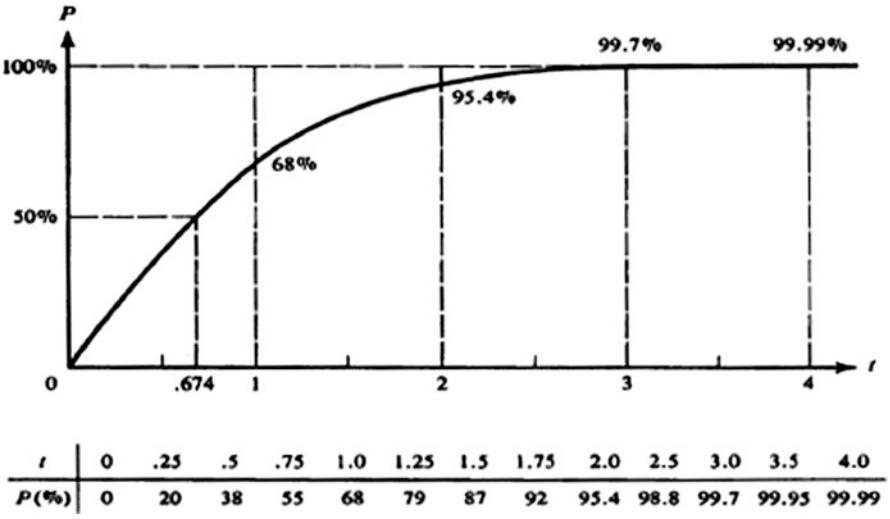

t	0	.25	.5	.75	1.0	1.25	1.5	1.75	2.0	2.5	3.0	3.5	4.0
P(%)	0	20	38	55	68	79	87	92	95.4	98.8	99.7	99.95	99.99

Fig. 6 Probability (within $t\sigma$) of a measurement that will fall within t standard deviation [11]

More generally, we could calculate P(within $t\sigma$), which means 'the probability for an answer within $t\sigma$ of X' where t is any positive number. This probability is given by the area in Fig. 5 and calculated by

$$P(\text{within } t\sigma) = \frac{1}{\sqrt{2\pi}} \int_{-t}^{t} e^{-Z^2/2} \mathrm{d}Z$$

Probability is plotted in Fig. 6 as a function of t.

In many situations, the engineer is more concerned about where individual observations or measurements may fall than about estimating parameters. In most practical situations, μ and σ are not known, and they must be estimated from a random sample. It is possible to determine a constant k such that $\bar{X} \pm ks$ will still form a tolerance interval for normal distribution. In this case, the tolerance limits are random variables because we have replaced μ and σ by $\bar{X}$ and s and the

proportion of population covered by the interval is not exact. Consequently, 100 $(1 - \alpha)$ percent confidence interval is utilised in the statement of the tolerance limit, since $\bar{X} \pm ks$ will not cover a specified proportion of the population all the time. This leads to the following conclusion.

For a normal distribution with unknown mean and variance, tolerance limits are given by $\bar{X} \pm ks$, where k is determined so that we can state with confidence 100 $(1 - \alpha)$ percent that the limit contain at least a proportion p of the population. The value of k for the required value of α and p can be obtained from Table XIV of Appendix of [7].

4.2 Percentile

For any time of a transient, if output parameters are arranged in ascending order and then rank is given to all values, from these ranks, the mean, median and the 5th and 95th percentiles are evaluated. The median value is the middle value of N ordered values (ascending order). The 5th and 95th percentiles are calculated using the following equation. The pth percentile of N ordered values is obtained by first calculating the rank (r) using the following equation and rounding to the nearest integer and taking the value which corresponds to the calculated rank:

$$r = N/100^{*}(p) + 1/2$$

And upper and lower uncertainty bands correspond to 95th and 5th value.

5 Approaches/Methodologies for Transient Analysis

The approach/methodologies to be used to qualify the nodalisation to carry out transient analysis are described here, and same nodalisation should be used for further evaluation of uncertainty. The input deck (nodalisation) is said to be qualified for particular transient when it is qualified for both 'steady-state-level' as well as 'on-transient-level' qualification. Steady-state-level qualification criteria are mainly based on D'Auria et al. [2]. These criteria consist of three parts and given in Table 1. In the first part, details of geometrical parameters from nodalisation and test facility/NPP are compared. In the second part, boundary conditions of nodalisation and test specifications/design nominal value of NPPs are compared. In the third part, some of the important thermal-hydraulic parameters for steady state which is derived from code output are compared with the experimental data/design nominal value for NPPs. In all the case, error should be less than acceptable error. In fact, first part and second part should be checked before start of code run.

On-transient-level qualification is done to demonstrate the capability of the nodalisation to reproduce the relevant thermal-hydraulic phenomena expected in

Table 1 Acceptance criteria for steady-state-level qualification [4]

Parameter	Acceptable error (%)
Geometrical parameter	
Primary circuit volume (m^3)	1.0 %
Secondary circuit volume (m^3)	2.0 %
Active structure heat transfer area (overall) (m^2)	0.1 %
Active structure heat transfer volume (overall) (m^3)	0.2 %
Volume vs. height curve (local primary and secondary circuit volume)	10.0 %
Component relative elevation (m)	0.01 m
Flow area of components like valves, pump orifices (m^2)	1.0 %
Generic flow area (m^2)	10.0 %
Boundary conditions	
Core power, PRZ heater power, core bypass heating power, decay heat curve, axial and radial power distribution, MCP velocity, pump coast down curve, SG feed water temperature, SG feed water flow rate, SG feed water pressure, ECCS water temperature, ECCS pressure, valve opening closing time, etc.	0.0 % (Zero error means error should be within the uncertainty band in the measurement)
Thermal-hydraulic parameter (from code output) initial condition	
Primary circuit power balance (MW)	2.0 %
Secondary circuit power balance (MW)	2.0 %
Absolute Pressure, (PRZ, ACC, SG) Mpa	0.1 %
Fluid temperature (K)	0.5 %
Rod surface temperature (K)	10 K
Heat losses (kW)	10.0 %
Local pressure drop (kPa) (Close-loop cumulative differential pressure vs. length curve)	10.0 %
Mass inventory in primary circuit (kg)	2.0 %
Mass inventory in primary circuit (kg)	5.0 %
Flow rates (primary and secondary circuits) (kg/s)	2.0 %
By pass mass flow rates (kg/s)	10.0 %
PRZ level (collapsed) (m)	0.05 m
Secondary side or down comer level (m)	0.1 m

the transient. This step also makes possible to verify the correctness of some systems operating only during transient events. The nodalisation is constituted by the schematisation of a facility. It is necessary to prove the capability of the code and of the nodalisation scheme during the transient analysis. The code options selected by the user, the schematisation solutions and the logic of some systems are involved during this check.

The following steps should be performed for qualitative evaluation:

(a) List of comparison between experimental and code calculation resulting time sequence of significant events (if available).

(b) Identification/verification of CSNI phenomena validation matrix applicable to the transient: A list of phenomena for LB LOCA and SB LOCA and transients are provided by CSNI phenomena validation matrix [9]. These phenomena are for code assessment. Therefore, it is to be checked that whether code calculation is able to predict all the phenomena given in the matrix or not.
(c) Phenomenological windows: Each transient scenario, that is, measured (if available) and calculated, is divided in number of phenomenological window time spans in which a unique relevant physical process mainly occurs and a limited set of parameters control the scenario for the proper interpretation.
(d) Key phenomena and relevant thermal-hydraulic aspects (RTA). In each PhW, key phenomena and RTA must be identified. RTAs are defined for a single transient and characterised by numerical values of significant parameters: single value parameters (SVP), non-dimensional parameters (NDP), time sequence of events (TSE), integral parameters (IPA), etc. The qualitative analysis is based on five subjective judgment marks (*E*, *R*, *M*, *U*, –) the list of RTAs. *E* means excellent and a good agreement exists between code and experimental results (if available, specifically applicable for transient in integral test facility); *R* is for reasonable and means that the phenomenon is reproduced by the code, but some minor discrepancies exist; *M* is for minimal and means that a relevant discrepancy is present between the code results and the experiment, but reason for the difference is identified, and it is not caused by a nodalisation deficiency; *U* is for unqualified and means that a relevant discrepancy exists, but reasons for the difference are intrinsic to the code, and nodalisation capability are not known; and '–' means not applicable to selected test. Even if one *U* result is present during the qualitative evaluation process, then nodalisation is not said to be qualified and sensitivity analysis is recommended by suitably modifying the nodalisation till route cause is not get detected and rectified.
(e) Visual comparisons between experimental and code calculated relevant parameter time trends. Major discrepancies are noticed in the process.

All the above five steps should be performed for any transient. In case of experimental data available, it would be compared otherwise it helps in proper understanding, and major discrepancies in prediction by code are identified.

6 Sampling-Based Uncertainty Methodology

Sampling-based approaches [5] to uncertainty and sensitivity analyses are demonstrated by carrying out uncertainty evaluation in the analysis of station blackout in PSB VVER integral test facility, small break LOCA in LSTF test facility and TMI-II accident. Several sampling strategies are available, including random sampling, importance sampling and Latin hypercube sampling (LHS) [8]. LHS is very popular for use with computationally demanding models because its efficient stratification properties allow for the extraction of a large amount of uncertainty and sensitivity information with relatively small sample size. In the

present study, LHS method is used. When sampling a function of N variables (input parameters), the range of each variable is divided in to M equal probable intervals. M sample points are then place to satisfy the Latin hypercube requirements; it is to be noted that it forces the number of divisions M to be equal for each variable. This sampling scheme does not require more samples for more input variables. This independence is one of the main advantages of this sampling scheme. Another advantage is that random samples can be taken one at a time, remembering which samples were taken so far. This approach involves the generation and exploration of a mapping from uncertain input parameters to uncertainty in output parameters. The underlying idea is that analysis results of output parameters (y), $y(\mathbf{x}) = [y_1(\mathbf{x}), y_2(\mathbf{x}),\ldots y_n(\mathbf{x})]$ are functions of uncertain input parameters (x), $\mathbf{x} = [x_1, x_2, \ldots x_n]$. In turn, uncertainty in input parameters (x) results in a corresponding uncertainty in output parameter (y). This leads to two questions: (1) what is the uncertainty in $\mathbf{y}$ given the uncertainty in x? and (2) how important is the individual input parameter (x) with respect to the uncertainty in output parameters (y)? The goal of uncertainty analysis is to answer the first question, and the goal of sensitivity/importance analysis is to answer the second question. In practice, the implementation of an uncertainty analysis and sensitivity analysis is very closely connected on both conceptual and computational levels. The methodology adopted for the present study consists of the following steps:

- Screening sensitivity analysis/expert judgment for the selection of uncertain input parameters
- Characterisation of uncertainty (assigning uniform distribution) to input parameters
- Calculation matrix generation using Latin hypercube sampling
- Performing best estimate thermal-hydraulic code runs
- Representation of uncertainty analysis results
- Performing importance/sensitivity analysis using linear regression (estimation of standardised rank regression coefficients, etc.)

Many authors, when referring to the degree to which an input parameter affects the model output, use words such as ‘sensitive’, ‘important’, ‘most influential’, ‘major contributor’, ‘effective’ or ‘correlated’ interchangeably. Determination of sensitivity analysis results is usually more demanding than the presentation of uncertainty analysis results due to the need to actually explore the mapping $[\mathbf{x}_i, \mathbf{y}(\mathbf{x}_i)]$, $i = 1$ to N to assess the effects of individual input parameter (x) on output parameter (y). A number of approaches to sensitivity analysis that can be used in conjunction with a sampling-based uncertainty analysis are available. The regression analysis is used to determine the importance analysis results in the present study. C_u standardised regression coefficients (SRCs) are obtained from the regression analysis. The SRCs provide a useful measure of variable importance with (1) the absolute values of the coefficients providing a comparative measure of variable importance (i.e. variable x_u is more important than variable x_v if $C_u > C_v$) and (2) the sign of C_u indicating whether x and y tend to move in the same direction or in the opposite direction as long as the x’s are independent from other input parameter considered for uncertainty analysis.

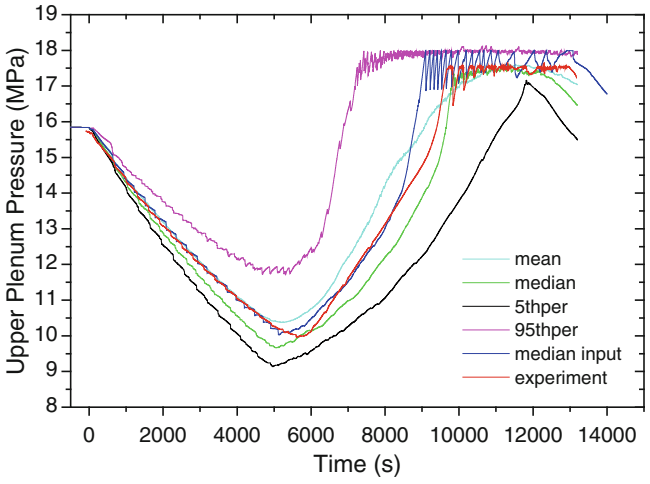

Fig. 7 Uncertainty in upper plenum pressure for SBO IN PSB VVER ITF [3]

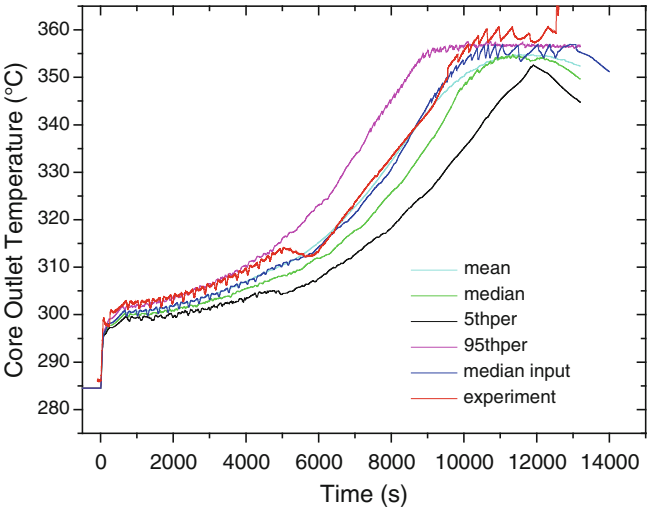

Fig. 8 Uncertainty in core outlet temperature for SBO IN PSB VVER ITF [3]

Results of uncertainty evaluation for primary pressure and core outlet temperature are shown in Fig. 7 and 8, respectively. Uncertainty in primary pressure and break discharge rate is shown in Figs. 9 and 10 for small break LOCA in LSTF. For the application of this methodology, for actual power plant uncertainty in pressuriser pressure and hot leg temperature for the analysis of TMI-II accident are shown in Figs. 11 and 12. In all the three analyses for almost all transient time experimental data and code calculated for median input are bounded by upper band (95 percentile) and lower and (5th percentile) of uncertainty.

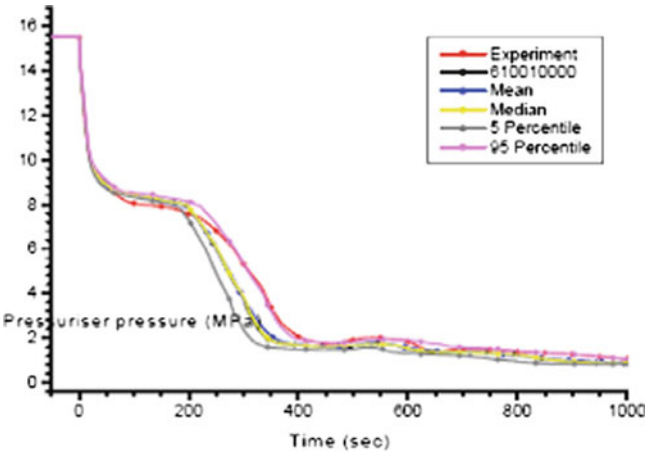

Fig. 9 Uncertainty in upper plenum pressure for small break LOCA in LSTF [10]

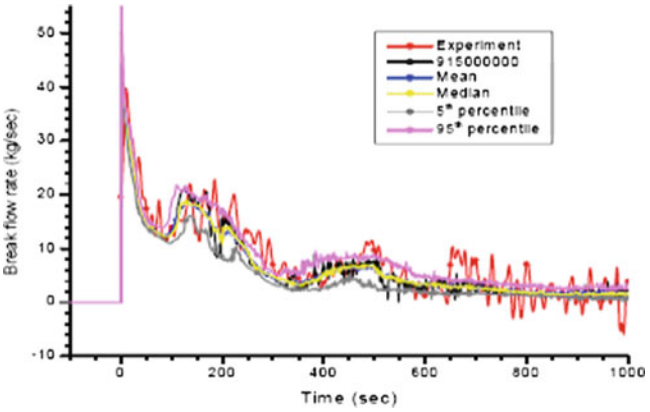

Fig. 10 Uncertainty in break flow rate for small break LOCA in LSTF [10]

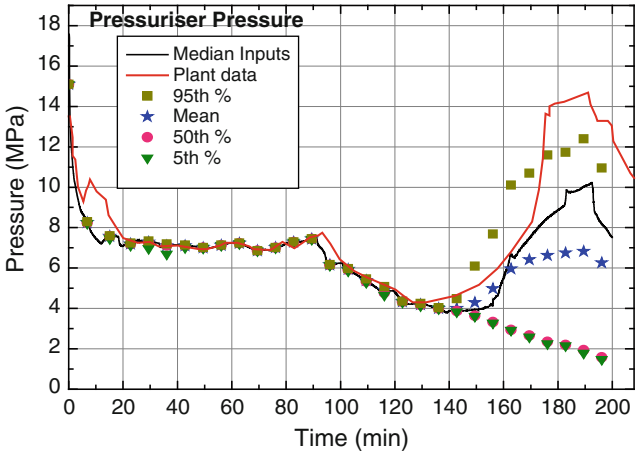

Fig. 11 Uncertainty in pressuriser pressure for TMI-II accident

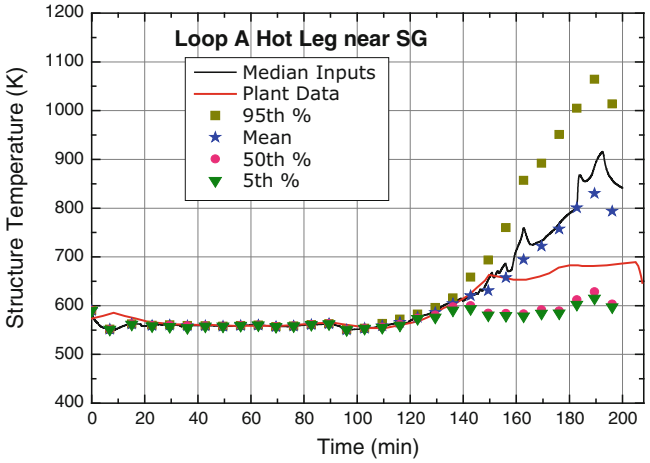

Fig. 12 Uncertainty in loop *A* hot leg temperature near SG

7 Conclusions

- Importance of conservative and best estimate accident analysis for nuclear power plants and related integral test facility are presented.
- Conservative analysis is used for licensing analysis; however, trends for deterministic safety analysis are moving towards the best estimate analysis.
- Various sources of uncertainty in carrying out best estimate accident analysis are highlighted.
- Aspects of various methodologies for uncertainty evaluation available world widely are summarised in this chapter.
- How to represent the evaluated uncertainty, that is, in terms of probability and confidence or in terms of percentile, is described in this chapter.
- Steady-state- and transient-level qualifications for the nodalisation adopted for the analysis of a transient using any system code are presented.
- Demonstration for the use of sampling-based uncertainty methodology for the evaluation of uncertainty for station blackout and small break LOCA in integral test facility is done, and application of this methodology is also extended for nuclear power plants TMI-II accident.
- This methodology is applicable to analysis of any transient using any best estimate system code.

References

1. AERB safety Code (2009) Design of pressurized heavy water reactor based nuclear power plants, no. AERB/NPP-PHWR/SC/D (Rev. 1), Mumbai
2. D'Auria F, Bousbia-Salah A, Petuzzi A, Del Nevo A (2006) State of the art in using best estimate calculation tools in nuclear technology. Nucl Eng Technol 38(1):11–32

3. Dubey SK, Rao RS, Sengupta S, Gupta SK (2011) Sampling based uncertainty analysis of station blackout in PSB VVER integral test facility. Ann Nucl Energy 38:2724–2733
4. Gupta SK (2009) Final progress report on IAEA CRP on uncertainty evaluation in best estimate accident analysis of NPPs, Mumbai
5. Helton JC (2006) Survey of sampling-based methods for uncertainty and sensitivity analysis. Reliab Eng Syst Saf 91:1175–1209
6. IAEA safety report series (2008) Best estimate safety analysis for nuclear power plants: uncertainty evaluation, IAEA, Vienna
7. Montgomery DC, Runger GC (1994) Applied statistics and probability for engineers. Wiley, New York
8. Park SR, Baek WP, Chang SH, Lee BH (1992) Development of uncertainty quantification method of the best estimate large LOCA analysis. Nucl Eng Des 135:367–378
9. Report by OECD Support Group (2001) Validation matrix for the assessment of thermal hydraulic codes for VVER LOCA and transients, NEA/CSNI/R 4
10. Sengupta S, Dubey SK, Rao RS, Gupta SK, Raina VK (2010) Sampling based uncertainty analysis of 10 % hot leg break LOCA in LSTF. Nucl Eng Technol 42(6):690–703
11. Taylor JR (1982) An introduction to error analysis-the study of uncertainty in physical measurements. Oxford University Press, Mill Valley

Failure Probability Bounds Using Multicut-High-Dimensional Model Representation

A.S. Balu and B.N. Rao

Abstract The structural reliability analysis in presence of mixed uncertain variables demands more computation as the entire configuration of fuzzy variables needs to be explored. Moreover, the existence of multiple design points plays an important role in the accuracy of results as the optimization algorithms may converge to a local design point by neglecting the main contribution from the global design point. Therefore, in this chapter, a novel uncertain analysis method for estimating the failure probability bounds of structural systems involving multiple design points in presence of mixed uncertain variables is presented. The proposed method involves weight function to identify multiple design points, multicut-high dimensional model representation technique for the limit state function approximation, transformation technique to obtain the contribution of the fuzzy variables to the convolution integral, and fast Fourier transform for solving the convolution integral. The proposed technique estimates the failure probability accurately with significantly less computational effort compared to the direct Monte Carlo simulation. The methodology developed is applicable for structural reliability analysis involving any number of fuzzy and random variables with any kind of distribution. The numerical examples presented demonstrate the accuracy and efficiency of the proposed method.

Keywords High dimensional model representation • Multiple design points • Random variables • Fuzzy variables • Convolution integral • Failure probability

A.S. Balu (✉) • B.N. Rao
Department of Civil Engineering, Indian Institute of Technology Madras, Chennai, Tamil Nadu, India
e-mail: arunsbalu@gmail.com; bnrao@iitm.ac.in

S. Chakraborty and G. Bhattacharya (eds.), *Proceedings of the International Symposium on Engineering under Uncertainty: Safety Assessment and Management (ISEUSAM - 2012)*,
DOI 10.1007/978-81-322-0757-3_18,

1 Introduction

Reliability analysis taking into account the uncertainties involved in a structural system plays an important role in the analysis and design of structures. Due to the complexity of structural systems, the information about the functioning of various structural components has different sources, and the failure of systems is usually governed by various uncertainties, all of which are to be taken into consideration for reliability estimation. Uncertainties present in a structural system can be classified as aleatory uncertainty and epistemic uncertainty. Aleatory uncertainty information can be obtained as a result of statistical experiments and has a probabilistic or random character. Epistemic uncertainty information can be obtained by the estimation of the experts and in most cases has an interval or fuzzy character. When aleatory uncertainty is only present in a structural system, then the reliability estimation involves determination of the probability that a structural response exceeds a threshold limit, defined by a limit state function influenced by several random parameters. Structural reliability can be computed by adopting probabilistic method involving the evaluation of multidimensional integral [1, 2].

In first- or second-order reliability method (FORM/SORM), the limit state functions need to be specified explicitly. Alternatively, the simulation-based methods such as Monte Carlo techniques require more computational effort for simulating the actual limit state function repeated times. The response surface concept was adopted to get separable and closed form expression of the implicit limit state function in order to use fast Fourier transform (FFT) to estimate the failure probability [3]. The high-dimensional model representation (HDMR) concepts were applied for the approximation of limit state function at the MPP and FFT techniques to evaluate the convolution integral for estimation of failure probability [4]. In this method, efforts are required in evaluating conditional responses at a selected input determined by sample points, as compared to full-scale simulation methods.

Further, the main contribution to the reliability integral comes from the neighborhood of design points. When multiple design points exist, available optimization algorithms may converge to a local design point and thus erroneously neglect the main contribution to the value of the reliability integral from the global design point(s). Moreover, even if a global design point is obtained, there are cases for which the contribution from other local or global design points may be significant [5]. In that case, multipoint FORM/SORM is required for improving the reliability analysis [6]. In the presence of only epistemic uncertainty in a structural system, possibilistic approaches to evaluate the minimum and maximum values of the response are available [7, 8].

All the reliability models discussed above are based on only one kind of uncertain information, either random variables or fuzzy input, but do not accommodate a combination of both types of variables. However, in some engineering problems with mixed uncertain parameters, using one kind of reliability model cannot obtain the best results. To determine the failure probability bounds of a structural system

involving both random and fuzzy variables, the entire configuration of the fuzzy variables needs to be explored. Hence, the computational effort involved in estimating the bounds of the failure probability increases tremendously in the presence of multiple design points and mixed uncertain variables.

This chapter explores the potential of coupled multicut-HDMR (MHDMR)-FFT technique in evaluating the reliability of a structural system with multiple design points, for which some uncertainties can be quantified using fuzzy membership functions while some are random in nature. Comparisons of numerical results have been made with direct MCS method to evaluate the accuracy and computational efficiency of the present method.

2 High Dimensional Model Representation

High dimensional model representation (HDMR) is a general set of quantitative model assessment and analysis tools for capturing the high dimensional relationships between sets of input and output model variables [4, 9]. Let the N-dimensional vector $\boldsymbol{x} = \{x_1, x_2, \ldots, x_N\}$ represent the input variables of the model under consideration and the response function as $g(\boldsymbol{x})$. Since the influence of the input variables on the response function can be independent and/or cooperative, HDMR expresses the response $g(\boldsymbol{x})$ as a hierarchical correlated function expansion in terms of the input variables as

$$g(\boldsymbol{x}) = g_0 + \sum_{i=1}^{N} g_i(x_i) + \sum_{1 \le i_1 < i_2 \le N} g_{i_1 i_2}(x_{i_1}, x_{i_2}) + \ldots + \sum_{1 \le i_1 < \ldots < i_l \le N} g_{i_1 i_2 \ldots i_l}(x_{i_1}, x_{i_2}, \ldots, x_{i_l}) + \cdots + g_{12\ldots N}(x_1, x_2, \ldots, x_N), \quad (1)$$

where g_0 is a constant term representing the zeroth-order component function or the mean response of $g(\boldsymbol{x})$. The function $g_i(x_i)$ is a first-order term expressing the effect of variable x_i acting alone, although generally nonlinearly, upon the output $g(\boldsymbol{x})$. The function $g_{i_1 i_2}(x_{i_1}, x_{i_2})$ is a second-order term which describes the cooperative effects of the variables x_{i_1} and x_{i_2} upon the output $g(\boldsymbol{x})$. The higher order terms give the cooperative effects of increasing numbers of input variables acting together to influence the output $g(\boldsymbol{x})$. The last term $g_{12,\cdots,N}(x_1, x_2, \ldots, x_N)$ contains any residual dependence of all the input variables locked together in a cooperative way to influence the output $g(\boldsymbol{x})$. The expansion functions are determined by evaluating the input–output responses of the system relative to the defined reference point $\boldsymbol{c}$ along associated lines, surfaces, subvolumes, etc., in the input variable space. This process reduces to the following relationship for the component functions in Eq. (1):

$$g_0 = g(\boldsymbol{c}), \quad (2)$$

$$g_i(x_i) = g\left(x_i, \boldsymbol{c}^i\right) - g_0, \tag{3}$$

$$g_{i_1 i_2}(x_{i_1}, x_{i_2}) = g\left(x_{i_1}, x_{i_2}, \boldsymbol{c}^{i_1 i_2}\right) - g_{i_1}(x_{i_1}) - g_{i_2}(x_{i_2}) - g_0, \tag{4}$$

where the notation $g(x_i, \boldsymbol{c}^i) = g(c_1, c_2, \ldots, c_{i-1}, x_i, c_{i+1}, \ldots, c_N)$ denotes that all the input variables are at their reference point values except x_i. The g_0 term is the output response of the system evaluated at the reference point $\boldsymbol{c}$. The higher order terms are evaluated as cuts in the input variable space through the reference point. Therefore, each first-order term $g_i(x_i)$ is evaluated along its variable axis through the reference point. Each second-order term $g_{i_1 i_2}(x_{i_1}, x_{i_2})$ is evaluated in a plane defined by the binary set of input variables x_{i_1} and x_{i_2} through the reference point, etc. The first-order approximation of $g(\boldsymbol{x})$ is as follows:

$$\begin{aligned} \tilde{g}(\boldsymbol{x}) &\equiv g(x_1, x_2, \ldots, x_N) \\ &= \sum_{i=1}^{N} g(c_1, \ldots, c_{i-1}, x_i, c_{i+1}, \ldots, c_N) - (N-1) g(\boldsymbol{c}). \end{aligned} \tag{5}$$

The notion of 0th, 1st, etc., in HDMR expansion should not be confused with the terminology used either in the Taylor series or in the conventional least-squares-based regression model. It can be shown that the first-order component function $g_i(x_i)$ is the sum of all the Taylor series terms which contain and only contain variable x_i. Hence, first-order HDMR approximations should not be viewed as first-order Taylor series expansions nor do they limit the nonlinearity of $g(\boldsymbol{x})$.

3 Multicut-HDMR

The main limitation of truncated cut-HDMR expansion is that depending on the order chosen sometimes it is unable to accurately approximate $g(\boldsymbol{x})$, when multiple design points exist on the limit state function or when the problem domain is large. In this section, a new technique based on MHDMR is presented for approximation of the original implicit limit state function, when multiple design points exist. The basic principles of cut-HDMR may be extended to more general cases. MHDMR is one extension where several cut-HDMR expansions at different reference points are constructed, and the original implicit limit state function $g(\boldsymbol{x})$ is approximately represented not by one but by all cut-HDMR expansions. In the present work, weight function is adopted for identification of multiple reference points closer to the limit surface.

Let $\boldsymbol{d}^1, \boldsymbol{d}^2, \ldots, \boldsymbol{d}^{m_d}$ be the m_d identified reference points closer to the limit state function based on the weight function. MHDMR approximation of the original implicit limit state function is based on the principles of cut-HDMR expansion,

where individual cut-HDMR expansions are constructed at different reference points $\boldsymbol{d}^1, \boldsymbol{d}^2, \ldots, \boldsymbol{d}^{m_d}$ by taking one at a time as follows:

$$\begin{aligned} g^k(\boldsymbol{x}) &= g_0^k + \sum_{i=1}^{N} g_i^k(x_i) + \sum_{1\le i_1<i_2\le N} g_{i_1 i_2}^k(x_{i_1}, x_{i_2}) + \ldots \\ &+ \sum_{1\le i_1<\ldots<i_l\le N} g_{i_1 i_2 \ldots i_l}^k(x_{i_1}, x_{i_2}, \ldots, x_{i_l}) + \ldots + g_{12\ldots N}^k(x_1, x_2, \ldots, x_N); \quad k = 1, 2, \ldots, m_d \end{aligned} \tag{6}$$

The original implicit limit state function $g(\boldsymbol{x})$ is approximately represented by blending all locally constructed m_d individual cut-HDMR expansions as follows:

$$g(\boldsymbol{x}) \cong \sum_{k=1}^{m_d} \lambda_k(\boldsymbol{x}) \left[g_0^k + \sum_{i=1}^{N} g_i^k(x_i) + \ldots + g_{12\ldots N}^k(x_1, x_2, \ldots, x_N) \right]. \tag{7}$$

The coefficients $\lambda_k(\boldsymbol{x})$ possess the properties

$$\lambda_k(\boldsymbol{x}) = \begin{cases} 1 & \text{if } \boldsymbol{x} \text{ is in any cut subvolume of the } k \text{ - th reference point expansions} \\ 0 & \text{if } \boldsymbol{x} \text{ is in any cut subvolume of other reference point expansions} \end{cases} \tag{8}$$

and

$$\sum_{k=1}^{m_d} \lambda_k(\boldsymbol{x}) = 1. \tag{9}$$

There are a variety of choices to define $\lambda_k(\boldsymbol{x})$. In the present study, the metric distance $\alpha_k(\boldsymbol{x})$ from any sample point to the reference point $\boldsymbol{d}^k; \quad k = 1, 2, \ldots, m_d$

$$\alpha_k(\boldsymbol{x}) = \left[\sum_{i=1}^{N} \left(x_i - d_i^k \right)^2 \right]^{\frac{1}{2}}; \quad d_i^k \equiv k\text{-th reference point} \tag{10}$$

is used to define

$$\lambda_k(\boldsymbol{x}) = \frac{\bar{\lambda}_k(\boldsymbol{x})}{\sum_{s=1}^{m_d} \bar{\lambda}_s(\boldsymbol{x})}, \tag{11}$$

where

$$\bar{\lambda}_k(\boldsymbol{x}) = \prod_{s=1;s\neq k}^{m_d} \alpha_s(\boldsymbol{x}). \tag{12}$$

The coefficients $\lambda_k(\boldsymbol{x})$ determine the contribution of each locally approximated function to the global function. The properties of the coefficients $\lambda_k(\boldsymbol{x})$ imply that the contribution of all other cut-HDMR expansions vanishes except one when $\boldsymbol{x}$ is located on any cut line, plane, or higher dimensional ($\leq l$) subvolumes through that reference point, and then the MHDMR expansion reduces to single point cut-HDMR expansion. As mentioned above, the l-th-order cut-HDMR approximation does not have error when $\boldsymbol{x}$ is located on these subvolumes. When m_d cut-HDMR expansions are used to construct an MHDMR expansion, the error-free region in input $\boldsymbol{x}$ space is m_d times that for a single reference point cut-HDMR expansion; hence, the accuracy will be improved. Therefore, first-order MHDMR approximations of the original implicit limit state function with m_d reference points can be expressed as

$$\tilde{g}(\boldsymbol{x}) \cong \sum_{k=1}^{m_d} \lambda_k(\boldsymbol{x}) \left[\sum_{i=1}^{N} g^k\left(d_1^k, \ldots, d_{i-1}^k, x_i, d_{i+1}^k, \ldots, d_N^k\right) - (N-1) g^k\left(\boldsymbol{d}^k\right) \right]. \tag{13}$$

4 Weight Function

The most important part of MHDMR approximation of the original implicit limit state function is identification of multiple reference points closer to the limit state function. The proposed weight function is similar to that used by Kaymaz and McMahon [10] for weighted regression analysis. Among the limit state function responses at all sample points, the most likelihood point is selected based on closeness to zero value, which indicates that particular sample point is close to the limit state function.

In this study, two types of procedures are adopted for identification of reference points closer to the limit state function, namely, (1) first-order method and (2) second-order method. The procedure for identification of reference points closer to the limit state function using first-order method proceeds as follows: (a) $n(= 3, 5, 7 \text{ or } 9)$ equally spaced sample points $\mu_i - (n-1)\sigma_i/2$, $\mu_i - (n-3)\sigma_i/2$, …, μ_i, …, $\mu_i + (n-3)\sigma_i/2$, $\mu_i + (n-1)\sigma_i/2$ are deployed along each of the random variable axis x_i with mean μ_i and standard deviation σ_i, through an initial reference point. Initial reference point is taken as mean value of the random variables. (b) The limit state function is evaluated at each sample point. (c) Using the limit state function responses at all sample points, the weight corresponding to each sample point is evaluated using the following weight function:

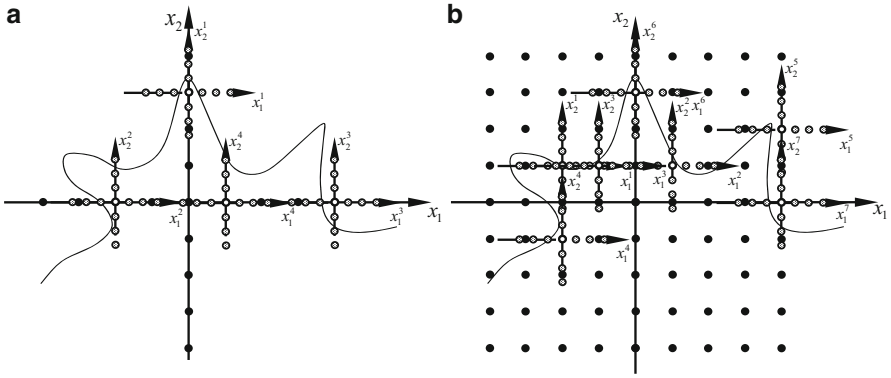

Fig. 1 MHDMR approximation of original limit state function, with (**a**) FF sampling scheme and (**b**) SF sampling scheme

$$w^I = \exp\left(-\frac{g(c_1,\ldots,c_{i-1},x_i,c_{i+1},\ldots,c_N) - g(\boldsymbol{x})|_{\min}}{|g(\boldsymbol{x})|_{\min}|}\right). \tag{14}$$

Second-order method of identification of reference points closer to the limit state function proceeds as follows: (a) A regular grid is formed by taking $n(=3,5,7 \text{ or } 9)$ equally spaced sample points $\mu_{i_1} - (n-1)\sigma_{i_1}/2$, $\mu_{i_1} - (n-3)\sigma_{i_1}/2$, …, μ_{i_1}, …, $\mu_{i_1} + (n-3)\sigma_{i_1}/2$, $\mu_{i_1} + (n-1)\sigma_{i_1}/2$ along the random variable x_{i_1} axis with mean μ_{i_1} and standard deviation σ_{i_1} and $n(=3,5,7 \text{ or } 9)$ equally spaced sample points $\mu_{i_2} - (n-1)\sigma_{i_2}/2$, $\mu_{i_2} - (n-3)\sigma_{i_2}/2$, …, μ_{i_2} , …, $\mu_{i_2} + (n-3)\sigma_{i_2}/2$, $\mu_{i_2} + (n-1)\sigma_{i_2}/2$ along the random variable x_{i_2} axis with mean μ_{i_2} and standard deviation σ_{i_2}, through an initial reference point. Initial reference point is taken as mean value of the random variables. (b) The limit state function is evaluated at each sample point. (c) Using the limit state function responses at all sample points, the weight corresponding to each sample point is evaluated using the following weight function:

$$w^{II} = \exp\left(-\frac{g(c_1,\ldots,c_{i_1-1},x_{i_1},c_{i_1+1},\ldots,c_{i_2-1},x_{i_1},c_{i_2+1},\ldots,c_N) - g(\boldsymbol{x})|_{\min}}{|g(\boldsymbol{x})|_{\min}|}\right). \tag{15}$$

Sample points $\boldsymbol{d}^1, \boldsymbol{d}^2, \ldots, \boldsymbol{d}^{m_d}$ with maximum weight are selected as reference points closer to the limit state function for construction of m_d individual cut-HDMR approximations of the original implicit limit state function locally. In this study, two types of sampling schemes, namely, FF and SF, are adopted. Figure 1a shows FF sampling scheme involving first-order method of identification of reference points and blending of locally constructed individual first-order HDMR approximations at different identified reference points using the coefficients $\lambda_k(\boldsymbol{x})$

to form MHDMR approximation $\tilde{g}(\boldsymbol{x})$. Figure 1b shows SF sampling scheme involving second-order method of identification of reference points and blending of locally constructed individual first-order HDMR approximations to form MHDMR approximation.

5 Failure Probability Bounds

Let the N-dimensional input variables vector $\boldsymbol{x} = \{x_1, x_2, \ldots, x_N\}$, which comprises of r number of random variables and f number of fuzzy variables, be divided as $\boldsymbol{x} = \{x_1, x_2, \ldots, x_r, x_{r+1}, x_{r+2}, \ldots, x_{r+f}\}$ where the subvectors $\{x_1, x_2, \ldots, x_r\}$ and $\{x_{r+1}, x_{r+2}, \ldots, x_{r+f}\}$, respectively, group the random variables and the fuzzy variables, with $N = r + f$. Then, the first-order approximation of $\tilde{g}(\boldsymbol{x})$ can be divided into three parts: the first part with only the random variables, the second part with only the fuzzy variables, and the third part is a constant which is the output response of the system evaluated at the reference point $\boldsymbol{c}$ as follows:

$$\tilde{g}(\boldsymbol{x}) = \sum_{i=1}^{r} g\left(x_i, \boldsymbol{c}^i\right) + \sum_{i=r+1}^{N} g\left(x_i, \boldsymbol{c}^i\right) - (N-1)g(\boldsymbol{c}). \tag{16}$$

The joint membership function of the fuzzy variables part is obtained using suitable transformation of the variables $\{x_{r+1}, x_{r+2}, \ldots, x_N\}$ and interval arithmetic algorithm. Using this approach, the minimum and maximum values of the fuzzy variables part are obtained at each α-cut. Using the bounds of the fuzzy variables part at each α-cut along with the constant part and the random variables part in Eq. (16), the joint density functions are obtained by performing the convolution using FFT in the rotated Gaussian space at the MPP, which upon integration yields the bounds of the failure probability.

5.1 Transformation of Fuzzy Variables

Optimization techniques are required to obtain the minimum and maximum values of a nonlinear response within the bounds of the interval variables. This procedure is computationally expensive for problems with implicit limit state functions, as optimization requires the function value and gradient information at several points in the iterative process. But, if the function is expressed as a linear combination of interval variables, then the bounds of the response can be expressed as the summation of the bounds of the individual variables. Therefore, fuzzy variables part of the nonlinear limit state function in Eq. (16) is expressed as a linear combination of intervening variables by the use of first-order HDMR approximation in order to apply an interval arithmetic algorithm as follows:

$$\sum_{i=r+1}^{N} g\left(x_i, \boldsymbol{c}^i\right) = z_1 + z_2 + \ldots + z_f, \tag{17}$$

where $z_i = (\beta_i x_i + \gamma_i)^{\kappa}$ is the relation between the intervening and the original variables with κ being order of approximation taking values $\kappa = 1$ for linear approximation, $\kappa = 2$ for quadratic approximation, $\kappa = 3$ for cubic approximation, and so on. The bounds of the intervening variables can be determined using transformations [11]. If the membership functions of the intervening variables are available, then at each α-cut, interval arithmetic techniques can be used to estimate the response bounds at that level.

5.2 Estimation of Failure Probability Using FFT

Concept of FFT can be applied to the problem if the limit state function is in the form of a linear combination of independent variables and when either the marginal density or the characteristic function of each basic random variable is known. In the present study, HDMR concepts are used to express the random variables part along with the values of the constant part and the fuzzy variables part at each α-cut as a linear combination of lower order component functions. The steps involved in the proposed method for failure probability estimation as follows:

1. If $\boldsymbol{u} = \{u_1, u_2, \ldots, u_r\}^T \in \Re^r$ is the standard Gaussian variable, let $\boldsymbol{u}^{k*} = \left\{u_1^{k*}, u_2^{k*}, \ldots, u_r^{k*}\right\}^T$ be the MPP or design point, determined by a standard nonlinear constrained optimization. The MPP has a distance β_{HL}, which is commonly referred to as the Hasofer–Lind reliability index. Construct an orthogonal matrix $\boldsymbol{R} \in \Re^{r\times r}$ whose r-th column is $\alpha^{k*} = \boldsymbol{u}^{k*}/\beta_{\mathrm{HL}}$, that is, $\boldsymbol{R} = \left[\boldsymbol{R}_1 | \alpha^{k*}\right]$, where $\mathbf{R}_1 \in \Re^{r\times r-1}$ satisfies $\alpha^{k*T}\boldsymbol{R}_1 = 0 \in \Re^{1\times r-1}$. The matrix $\boldsymbol{R}$ can be obtained, for example, by Gram–Schmidt orthogonalization. For an orthogonal transformation, $\boldsymbol{u}$=$\boldsymbol{R}\,\boldsymbol{v}$.
2. Let $\boldsymbol{v} = \{v_1, v_2, \ldots, v_r\}^T \in \Re^r$ be the rotated Gaussian space with the associated MPP $\boldsymbol{v}^{k*} = \left\{v_1^{k*}, v_2^{k*}, \ldots, v_r^{k*}\right\}^T$. Note that in the rotated Gaussian space, the MPP is $\boldsymbol{v}^* = \{0, 0, \ldots, \beta_{\mathrm{HL}}\}^T$. The transformed limit state function $g(\boldsymbol{v})$ therefore maps the random variables along with the values of the constant part and the fuzzy variables part at each α-cut into rotated Gaussian space $\boldsymbol{v}$. First-order HDMR approximation of $g(\boldsymbol{v})$ in rotated Gaussian space $\boldsymbol{v}$ with $\boldsymbol{v}^{k*} = \left\{v_1^{k*}, v_2^{k*}, \ldots, v_r^{k*}\right\}^T$ as reference point can be represented as follows:

$$\begin{aligned}\tilde{g}^k(\boldsymbol{v}) &\equiv g^k(v_1, v_2, \ldots, v_r) \\ &= \sum_{i=1}^{r} g^k\left(v_1^{k*}, \ldots, v_{i-1}^{k*}, v_i, v_{i+1}^{k*}, \ldots, v_r^{k*}\right) - (r-1)g\left(\boldsymbol{v}^{k*}\right).\end{aligned} \tag{18}$$

3. In addition to the MPP as the chosen reference point, the accuracy of first-order HDMR approximation in Eq. (18) may depend on the orientation of the first $r-1$ axes. In the present work, the orientation is defined by the matrix $\boldsymbol{R}$. In Eq. (18), the terms $g^k\left(v_1^{k*}, \ldots, v_{i-1}^{k*}, v_i, v_{i+1}^{k*}, \ldots, v_r^{k*}\right)$ are the individual component functions and are independent of each other. Equation (18) can be rewritten as

$$\tilde{g}^k(\boldsymbol{v}) = a^k + \sum_{i=1}^{r} g^k\left(v_i, \boldsymbol{v}^{k*^i}\right), \tag{19}$$

where $a^k = -(r-1)g\left(\boldsymbol{v}^{k*}\right)$.

4. New intermediate variables are defined as

$$y_i^k = g^k\left(v_i, \boldsymbol{v}^{k*^i}\right). \tag{20}$$

The purpose of these new variables is to transform the approximate function into the following form:

$$\tilde{g}^k(\boldsymbol{v}) = a^k + y_1^k + y_2^k + \cdots + y_r^k. \tag{21}$$

5. Due to rotational transformation in $\boldsymbol{v}$-space, component functions y_i^k in Eq. (21) are expected to be linear or weakly nonlinear function of random variables v_i. In this work, both linear and quadratic approximations of y_i^k are considered.
6. Let $y_i^k = b_i + c_i\, v_i$ and $y_i^k = b_i + c_i\, v_i + e_i\, v_i^2$ be the linear and quadratic approximations, where coefficients $b_i \in \Re$, $c_i \in \Re$, and $e_i \in \Re$ (nonzero) are obtained by least-squares approximation from exact or numerically simulated conditional responses $\left\{g^k\left(v_i^1, \boldsymbol{v}^{k*^i}\right), g^k\left(v_i^2, \boldsymbol{v}^{k*^i}\right), \cdots, g^k\left(v_i^n, \boldsymbol{v}^{k*^i}\right)\right\}^T$ at n sample points along the variable axis v_i. Then, Eq. (21) results in

$$\tilde{g}^k(\boldsymbol{v}) \equiv a^k + y_1^k + y_2^k + \cdots + y_r^k = a^k + \sum_{i=1}^{r} (b_i + c_i\, v_i) \tag{22}$$

and

$$\tilde{g}^k(\boldsymbol{v}) \equiv a^k + y_1^k + y_2^k + \cdots + y_r^k = a^k + \sum_{i=1}^{r} \left(b_i + c_i\, v_i + e_i\, v_i^2\right). \tag{23}$$

7. The global approximation is formed by blending of locally constructed individual first-order HDMR approximations in the rotated Gaussian space at different identified reference points using the coefficients λ_k:

$$\tilde{g}(\boldsymbol{v}) = \sum_{k=1}^{m_d} \lambda_k \tilde{g}^k(\boldsymbol{v}). \tag{24}$$

8. Since v_i follows standard Gaussian distribution, marginal density of the intermediate variables y_i can be easily obtained by simple transformation (using chain rule):

$$p_{Y_i}(y_i) = p_{V_i}(v_i)\left|\frac{dv_i}{dy_i}\right|. \tag{25}$$

9. Now, the approximation is a linear combination of the intermediate variables y_i. Therefore, the joint density of $\tilde{g}(\boldsymbol{v})$, which is the convolution of the individual marginal density of the intervening variables y_i, can be expressed as follows:

$$p_{\tilde{G}}(\tilde{g}) = p_{Y_1}(y_1) * p_{Y_2}(y_2) * \ldots * p_{Y_r}(y_r), \tag{26}$$

where $p_{\tilde{G}}(\tilde{g})$ represents joint density of the transformed limit state function $\tilde{g}(\boldsymbol{v})$.

10. Applying FFT on both sides of Eq. (26) leads to

$$FFT\left[p_{\tilde{G}}(\tilde{g})\right] = FFT\left[p_{Y_1}(y_1)\right]FFT\left[p_{Y_2}(y_2)\right]\ldots FFT\left[p_{Y_r}(y_r)\right]. \tag{27}$$

11. By applying inverse FFT on both side of Eq. (27), joint density of $\tilde{g}(\boldsymbol{v})$ is obtained.
12. The probability of failure is given by the following equation:

$$P_{\mathrm{F}} = \int_{-\infty}^{0} p_{\tilde{G}}(\tilde{g})\mathrm{d}\tilde{g}. \tag{28}$$

13. The membership function of failure probability can be obtained by repeating the above procedure at all confidence levels of the fuzzy variables part.

6 Numerical Examples

To evaluate the accuracy and the efficiency of the present method, comparisons of the estimated failure probability bounds, both by performing the convolution using FFT in conjunction with linear and quadratic approximations and MCS on the global approximation, have been made with that obtained using direct MCS. When comparing computational efforts by various methods in evaluating the failure probability, the number of original limit state function evaluations is chosen as the primary comparison tool in this chapter. This is because of the fact that number of function evaluations indirectly indicates the CPU time usage. For direct MCS, number of original function evaluations is same as the sampling size. While evaluating the failure probability through direct MCS, CPU time is more because it involves number of repeated actual finite-element analysis.

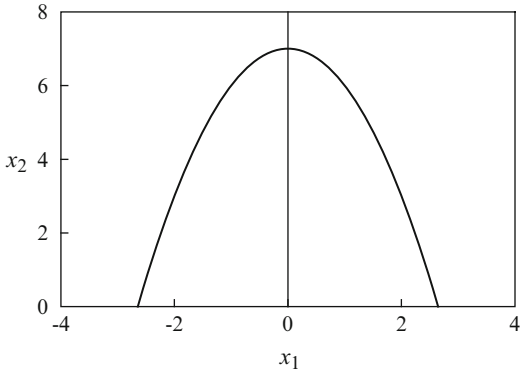

Fig. 2 Limit state function

Table 1 Identification of multiple design points with FF sampling

Sample points		$g(\boldsymbol{x})$			$g(\boldsymbol{x})\|_{\min}$			w^I		
x_1	x_2	$\alpha = 0^{(L)}$	$\alpha = 1$	$\alpha = 0^{(R)}$	$\alpha = 0^{(L)}$	$\alpha = 1$	$\alpha = 0^{(R)}$	$\alpha = 0^{(L)}$	$\alpha = 1$	$\alpha = 0^{(R)}$
−2.0	0.0	1.00	3.00	5.00	1.0	3.0	5.0	1.000	1.000	1.000
−1.0	0.0	4.00	6.00	8.00				0.050	0.368	0.549
0.0	0.0	5.00	7.00	9.00				0.018	0.264	0.449
1.0	0.0	4.00	6.00	8.00				0.050	0.368	0.549
2.0	0.0	1.00	3.00	5.00				1.000	1.000	1.000
0.0	−2.0	7.00	9.00	11.00				0.002	0.135	0.301
0.0	−1.0	6.00	8.00	10.00				0.001	0.189	0.368
0.0	0.0	5.00	7.00	9.00				0.018	0.264	0.449
0.0	1.0	4.00	6.00	8.00				0.050	0.368	0.549
0.0	2.0	3.00	5.00	7.00				0.135	0.513	0.670

6.1 Parabolic Performance Function

The limit state function considered is a parabola of the form

$$g(\boldsymbol{x}) = -x_1^2 - x_2 + x_3, \tag{29}$$

where x_1 and x_2 are assumed to be independent standard normal variables. The variable x_3 is assumed to be fuzzy with triangular membership function having the triplet [5.0, 7.0, 9.0].

The initial reference point $\boldsymbol{c}$ is taken as, respectively, the mean values and nominal values of the random and fuzzy variables. The first-order HDMR approximation, which is constructed over the initial reference point, is divided into two parts: one with only the random variables and the other with the fuzzy variables. The joint membership function of the fuzzy part of limit state function is obtained using suitable transformation of the fuzzy variables. In this example, the joint membership function is same as the membership function of the fuzzy variable x_3. As shown in Fig. 2, the limit state function given by Eq. (28) is symmetric about x_2

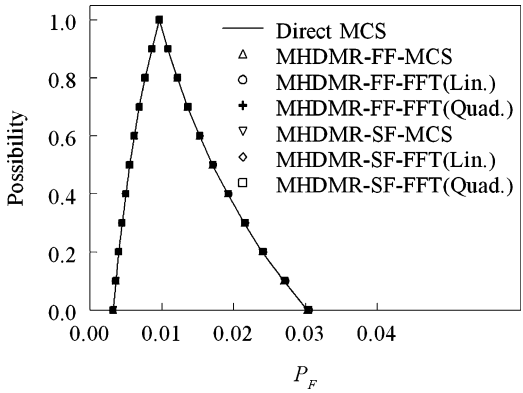

Fig. 3 Membership function of failure probability for parabolic performance function

for given value of x_3 (say the nominal value of $x_3 = 7$ at $\alpha = 1$) and has two design points. The two actual design points of the limit state function shown in Fig. 2, obtained using recursive quadratic programming (RQP) algorithm, are (2.54, 0.49) and (−2.54, 0.49) with reliability indices $\beta_1 = \beta_2 = 2.588$.

Table 1 illustrates computational details and identification of reference points $\boldsymbol{d}^1, \boldsymbol{d}^2$ using FF sampling scheme with five equally spaced sample points ($n = 5$) along each of the variable axis. In Table 1, the values corresponding to $\alpha = 0^{(L)}$ and $\alpha = 0^{(R)}$, respectively, indicate the extreme left and right values of the limit state function $g(\boldsymbol{x})$ at zero confidence level (i.e., $\alpha = 0$). Table 1 shows two reference points $\boldsymbol{d}^1 = (2, 0)$ and $\boldsymbol{d}^2 = (-2, 0)$ closer to the function. After identification of the two reference points (2, 0) and (−2, 0), local individual first-order HDMR approximations of the original limit state function are constructed at the two reference points by deploying $n = 5$ sample points along each of the variable axis. Local approximations of the original limit state function are blended together to form global approximation. The bounds of the failure probability are obtained both by performing the convolution using FFT in conjunction with linear and quadratic approximations and MCS on the global approximation.

Figure 3 shows the membership function of the failure probability P_{F} estimated both by performing the convolution using FFT and MCS on the global approximation, as well as that obtained using direct MCS.

In addition, effect of SF sampling scheme on the estimated membership function of the failure probability is studied. After identifying two reference points $\boldsymbol{d}^1 = (-2, 2)$ and $\boldsymbol{d}^2 = (2, 2)$ closer to the function producing maximum weight, the bounds of the failure probability are obtained. Figure 3 also shows the membership function of the failure probability obtained by the proposed method based on SF sampling scheme. The effect of number of sample points is studied by varying n from 3 to 9. It is observed that $n = 7$ provides the optimum number of function calls with acceptable accuracy in evaluating the failure probability with the present method.

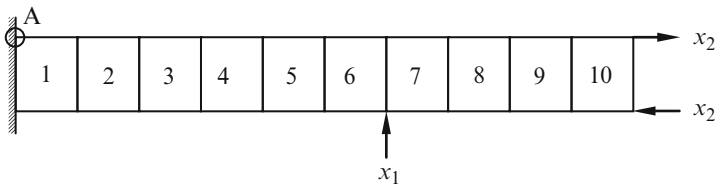

Fig. 4 Cantilever steel beam

6.2 *Cantilever Steel Beam*

A cantilever steel beam of 1.0 m with cross-sectional dimensions of (0.1 m $\times$ 0.01 m) is considered, as shown in Fig. 4, to examine the accuracy and efficiency of the proposed method for the membership function of failure probability estimation. The beam is subjected to an in-plane moment at the free end and a concentrated load at 0.4 m from the free end. The structure is assumed to have failed if the square of the von Mises stress at the support (at A in Fig. 4) exceeds specified threshold $V_{\max}$. Therefore, the limit state function is defined as

$$g(\boldsymbol{x}) = V_{\max} - V(\boldsymbol{x}), \tag{30}$$

where $V(\boldsymbol{x})$ is the square of the von Mises stress, expressed as a quadratic operator on the stress vector.

In this example, loads x_1 and x_2, modulus of elasticity of the beam E, and threshold quantity $V_{\max}$ are taken as uncertain variables. The variations of E and $V_{\max}$ are expressed as $E = E_0(1 + \varepsilon x_3)$ and $V_{\max} = V_{\max 0}(1 + \varepsilon x_4)$. Here, ε is small deterministic quantity representing the coefficient of variation of the random variables and are taken to equal to 0.05, $E_0 = 2 \times 10^5$ N/m^2 denotes the deterministic component of modulus of elasticity, and $V_{\max 0} = 6.15 \times 10^9$ N/m^2 denotes the deterministic component of threshold quantity. All variables are assumed to be independent. The mean values of random variables x_1 and x_2 are 1 and 0, respectively, with the standard deviation of 1. The variables x_3 and x_4 are triangular fuzzy numbers with [0.0 2.0 4.0] and [0.0, 0.1, 0.2], respectively.

The limit state function given in Eq. (30) is approximated using first-order HDMR by deploying $n = 5$ sample points along each of the variable axis and taking, respectively, the mean values and nominal values of the random and fuzzy variables as initial reference point (1.0, 0.0, 2.0, 0.1). The approximated limit state function is divided into two parts, one with only the random variables along with the value of the constant part and the other with the fuzzy variables. The joint membership function of the fuzzy part of approximated limit state function is obtained using suitable transformation of the fuzzy variables. Using FF sampling scheme, the sample point $\boldsymbol{d} = (1, -2)$ is identified as reference point closer to the limit state function producing maximum weight. In this case, since only one reference point is identified, local approximation is same as the global

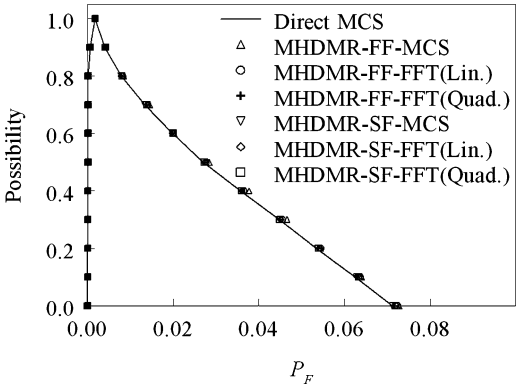

Fig. 5 Membership function of failure probability for cantilever steel beam

approximation. The bounds of the failure probability are obtained both by performing the convolution using FFT in conjunction with linear and quadratic approximations and MCS on the global approximation. Figure 5 shows the membership function of the failure probability estimated both by performing the convolution using FFT in conjunction with linear and quadratic approximations and MCS on the global approximation, as well as that obtained using direct MCS.

In addition, the membership function of the failure probability obtained by the proposed method based on SF sampling scheme is also shown in Fig. 5. The effect of number of sample points is studied by varying n from 3 to 9. It is observed that $n = 7$ provides the optimum number of function calls with acceptable accuracy in evaluating the failure probability with the present method.

6.3 80-Bar 3D Truss Structure

A 3D truss, shown in Fig. 6, is considered in this example to examine the accuracy and efficiency of the proposed method for the membership function of failure probability estimation. The loads at various levels are considered to be random, while the cross-sectional areas of the angle sections at various levels are assumed to be fuzzy as shown in Table 2.

The maximum horizontal displacement at the top of the tower is considered to be the failure criterion, as given below:

$$g(\boldsymbol{x}) = \Delta_{\text{lim}} - \Delta(\boldsymbol{x}). \tag{31}$$

The limiting deflection Δ_{lim} is assumed to be 0.15 m. The limit state function is approximated using first-order HDMR by deploying $n = 5$ sample points along each of the variable axis and taking, respectively, the mean values and nominal values of the random and fuzzy variables as initial reference point.

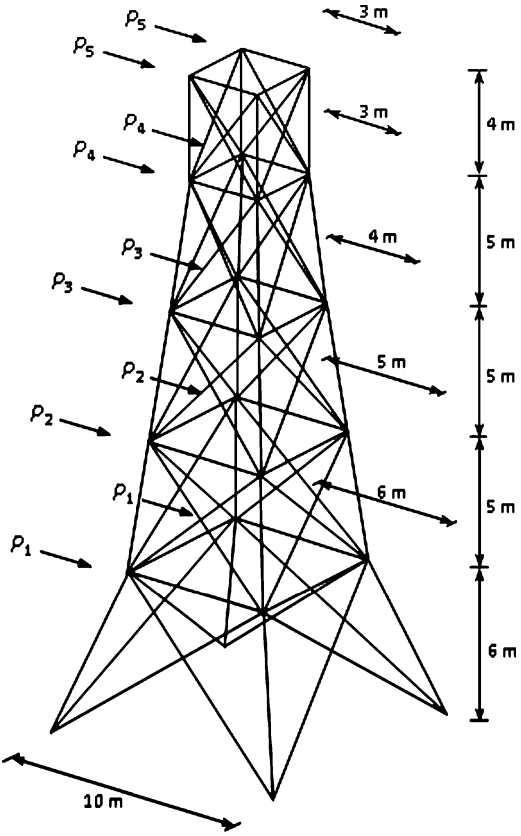

Fig. 6 3D truss structure with 80 bars

Table 2 Properties of the uncertain variables

	Random			
Uncertain variable	Mean	COV	Type	Fuzzy
P_1 (N)	1,000	0.1	Normal	
P_2 (N)	2,000	0.1	Normal	
P_3 (N)	3,000	0.1	Normal	
P_4 (N)	4,000	0.1	Normal	
P_5 (N)	5,000	0.1	Normal	
A_1 (mm^2)				[6867 7630 8393]
A_2 (mm^2)				[5571 6190 6809]
A_3 (mm^2)				[3870 4300 4730]
A_4 (mm^2)				[2088 2320 2552]
A_5 (mm^2)				[1539 1710 1881]

The approximated limit state function is divided into two parts, one with only the random variables along with the value of the constant part and the other with the fuzzy variables. The joint membership function of the fuzzy part of approximated limit state function is obtained using suitable transformation of the fuzzy variables. The two reference points closer to the function producing maximum weights,

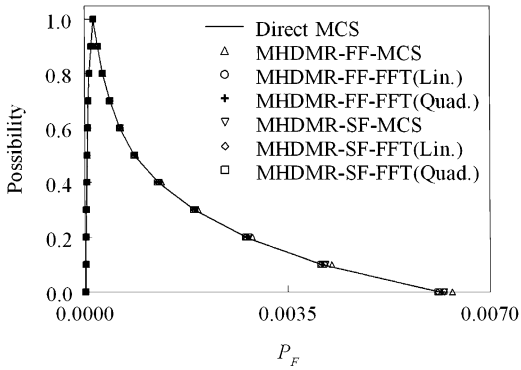

Fig. 7 Membership function of failure probability for truss structure

1.0 and 0.977, are identified. After identification of two reference points, local first-order HDMR approximations are constructed at the reference points. The bounds of the failure probability are obtained both by performing the convolution using FFT in conjunction with linear and quadratic approximations and MCS on the global approximation. Figure 7 shows the membership function of the failure probability estimated both by performing the convolution using FFT and MCS on the global approximation, as well as that obtained using direct MCS.

In addition, effects of SF sampling scheme and the number of sample points on the estimated membership function of the failure probability are studied. Figure 7 also shows the membership function of the failure probability estimate obtained by the proposed method based on SF sampling scheme.

7 Summary and Conclusions

This chapter presented a novel uncertain analysis method for estimating the membership function of the reliability of structural systems involving multiple design points in the presence of mixed uncertain variables. The method involves MHDMR technique for the limit state function approximation, transformation technique to obtain the contribution of the fuzzy variables to the convolution integral and fast Fourier transform for solving the convolution integral at all confidence levels of the fuzzy variables. Weight function is adopted for identification of multiple reference points closer to the limit surface. Using the bounds of the fuzzy variables part at each confidence level along with the constant part and the random variables part, the joint density functions are obtained by (1) identifying the reference points closer to the limit state function and (2) blending of locally constructed individual first-order HDMR approximations in the rotated Gaussian space at different identified reference points to form global approximation and (3) performing the convolution using FFT, which upon integration yields the bounds of the failure probability. As an alternative, the bounds of the failure

probability are estimated by performing MCS on the global approximation in the original space, obtained by blending of locally constructed individual first-order HDMR approximations of the original limit state function at different identified reference points.

The results of the numerical examples involving explicit hypothetical mathematical function and structural/solid-mechanics problems indicate that the proposed method provides accurate and computationally efficient estimates of the membership function of the failure probability. The results obtained from the proposed method are compared with those obtained by direct MCS. The numerical results show that the present method is efficient for structural reliability estimation involving any number of fuzzy and random variables with any kind of distribution. Two types of sampling schemes, namely, FF and SF, are adopted in this study for MHDMR approximation of the original limit state function construction. A parametric study is conducted with respect to the number of sample points n used in FF and SF sampling-based MHDMR approximation, and its effect on the estimated failure probability is investigated. An optimum number of sample points n must be chosen in approximation of the original limit state function.

References

1. Breitung K (1984) Asymptotic approximations for multinormal integrals. ASCE J Eng Mech 110(3):357–366
2. Rackwitz R (2001) Reliability analysis – a review and some perspectives. Struct Saf 23(4):365–395
3. Sakamoto J, Mori Y, Sekioka T (1997) Probability analysis method using fast Fourier transform and its application. Struct Saf 19(1):21–36
4. Rao BN, Chowdhury R (2008) Probabilistic analysis using high dimensional model representation and fast Fourier transform. Int J Comput Methods Eng Sci Mech 9(6):342–357
5. Au SK, Papadimitriou C, Beck JL (1999) Reliability of uncertain dynamical systems with multiple design points. Struct Saf 21:113–133
6. Kiureghian AD, Dakessian T (1998) Multiple design points in first and second order reliability. Struct Saf 20(1):37–49
7. Briabant V, Oudshoorn A, Boyer C, Delcroix F (1999) Nondeterministic possibilistic-approaches for structural analysis and optimal design. AIAA J 37(10):1298–1303
8. Penmetsa RC, Grandhi RV (2003) Uncertainty propagation using possibility theory and function approximations. Mech Based Des Struct Mach 81(15):1567–1582
9. Rabitz H, Alis OF, Shorter J, Shim K (1999) Efficient input-output model representations. Comput Phys Commun 117(1–2):11–20
10. Kaymaz I, McMahon CA (2005) A response surface method based on weighted regression for structural reliability analysis. Probab Eng Mech 20(1):11–17
11. Adduri PR, Penmetsa RC (2008) Confidence bounds on component reliability in the presence of mixed uncertain variables. Int J Mech Sci 50(3):481–489

Reliability Considerations in Asphalt Pavement Design

Animesh Das

Abstract This chapter presents a brief overview of the concept of reliability applied to asphalt pavement design. It discusses how reliability can be estimated for a given pavement structure and how a pavement structure can be designed for a given reliability level. Reliability-based design principles for design of new asphalt pavement, as well as rehabilitation of existing pavement, have been presented.

Keywords Pavement design • Structural failure • Reliability

1 Introduction

Asphalt pavement design process involves design input as material properties, weather conditions, traffic characteristics, design period, etc. Each input is linked with a set of design parameters. For example, material property includes elastic modulus and Poisson's ratio values of asphalt, granular, cemented, subgrade layers, etc. All these parameters show significant variability [6, 11, 18, 29, 31, 32]. It would be reasonable approach to account for such variability in the pavement design process. This is done by invoking the concepts of reliability in pavement design.

Reliability issues in pavement design have been studied as early as 1970s [5, 6, 15]. Some of the initial considerations included variation of a single parameter (e.g. the subgrade strength); [28] subsequently, variability of different parameters and different modes of failures are added to the analysis.

A. Das (✉)
Department of Civil Engineering, Indian Institute of Technology Kanpur, Kanpur 208 016, India
e-mail: adas@iitk.ac.in

S. Chakraborty and G. Bhattacharya (eds.), *Proceedings of the International Symposium on Engineering under Uncertainty: Safety Assessment and Management (ISEUSAM - 2012)*,
DOI 10.1007/978-81-322-0757-3_19,

2 Concept of Reliability

Reliability is the probability of not having a failure. Failure does not happen if the number of repetitions of expected traffic (T) does not exceed the number of repetitions that the pavement can sustain (N). Since it is assumed that there are variabilities associated with the pavement design parameters, T and N can be represented in the form of probability distributions.

Figure 1 shows a schematic diagram with hypothetical distributions of T and N for any given pavement section. These distributions are shown to be nonintersecting in the present case. In case 1, the pavement would definitely fail, because the expected traffic is always greater than the allowable traffic, indicating the reliability value as 0%. Following similar logic, it can be said that the reliability of pavement for case 2 is 100%.

Reliability values of 0 and 100% (in other scale, the reliability values of 0 and 1), are two extreme cases, and generally, the reliability value of any given pavement lies somewhere in between. Such a case is represented in Fig. 2. Thus, reliability of a pavement (R) can be defined as:

Probability (number of repetitions a pavement can sustain is greater than number of traffic repetitions expected to occur on the pavement), that is

$$R = P(N > T) \tag{1}$$

If a parameter 'safety margin' (S) is defined as $S = T - N$, reliability can be defined as $R = P(S < 0)$. If the probability density function (*pdf*) of S is given as $f_S(s)$, then R can be calculated as follows:

$$R = \int_{-\infty}^{0} f_S(s)\, ds \tag{2}$$

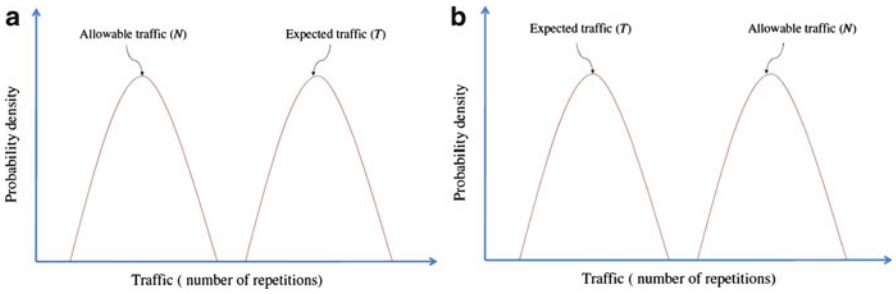

Fig. 1 Pavement reliability as 0 and 100%. (**a**) Case 1: reliability = 0%, (**b**) Case 2: reliability = 100%

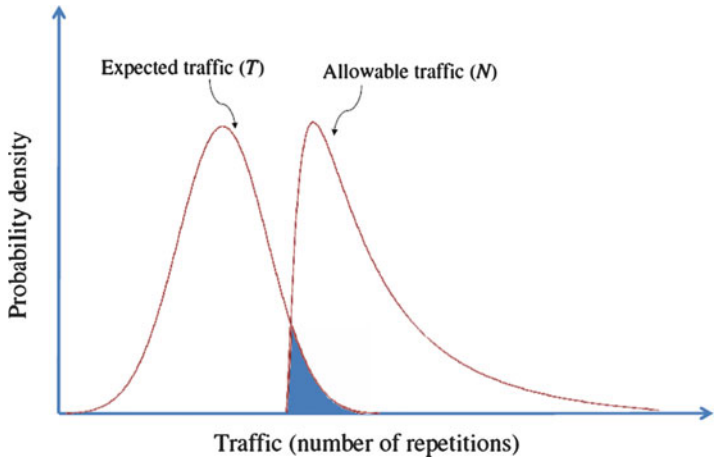

Fig. 2 Schematic diagram explaining the definition of reliability

Reliability is sometimes expressed using 'damage factor', D, defined as $D = \frac{T}{N}$. In that case, reliability can be defined as $R = P(D<1)$. If the *pdf* of D is known as $f_D(d)$, then R can be calculated as follows:

$$R = \int_0^1 f_D(d')dd' \tag{3}$$

If the distributions of T and N are known, the reliability value (R) can obtained using either Eqs. (2) or (3) [4, 14, 17, 23]. Knowing the distributions of T and N sometimes becomes a complex task.

T is dependent on traffic volume, axle load, traffic growth rate, design period, etc. The design period is generally prespecified and therefore has a fixed value. N is dependent on material properties (e.g. elastic moduli and Poisson's ratio values of the individual layers), layer thicknesses, loading configuration, performance equations, etc. The performance equation relates the critical stress/strain values to the life (in terms of traffic repetitions) of the pavement for a given mode of failure. These equations are generally developed empirically through calibration of pavement performance data. Figure 3 schematically shows various parameters that influence the distributions of T and N and, in turn, the reliability of pavement.

To estimate the pavement reliability, the distributions of these basic parameters (i.e. traffic volume, axle load, traffic growth rate, material properties, thicknesses, loading configuration, performance equation coefficients) are to be known first. Substantial literature is available which contains information on the variabilities of these parameters [4, 6, 11–13, 21, 29, 31–33]. Various analytical and numerical methods (e.g. point estimate method, first- or second-order reliability method, simulation method [3, 9, 35]) have been used [6, 14, 17] to obtain the parameter

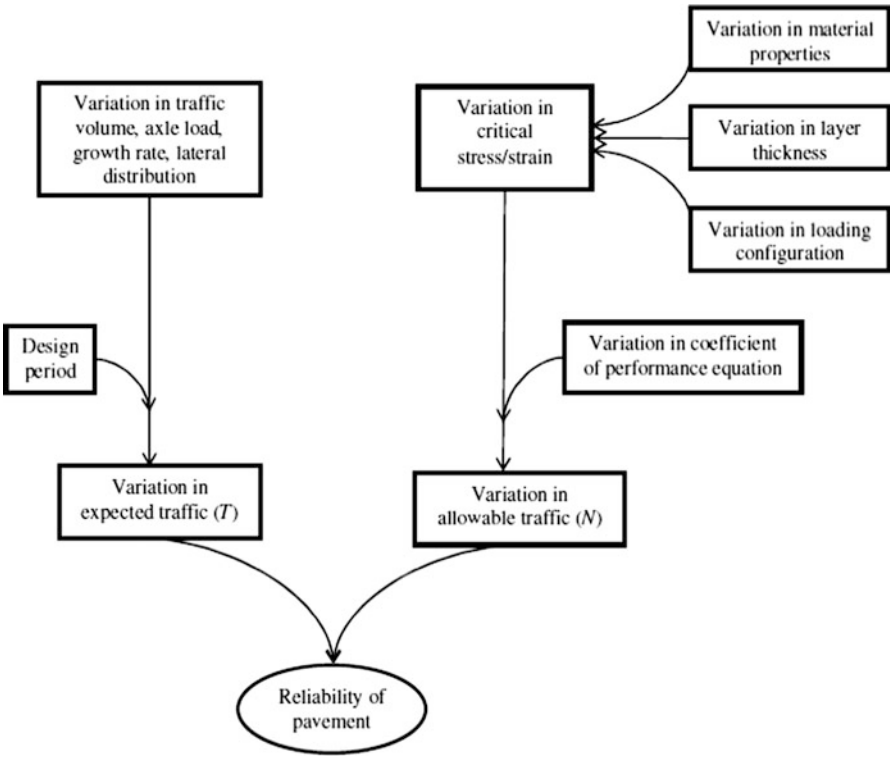

Fig. 3 Various parameters influencing reliability of pavement

related to possible distribution of T and N, when the distribution of these basic parameters are assumed to be known.

2.1 Reliability for a Single or Multiple Mode of Failure

The structural failure of asphalt pavement may occur in various modes, for example, load fatigue, thermal fatigue, rutting, thermal shrinkage and top-down cracking. The calculation of overall reliability of the pavement would depend on how the failure is defined. One may define the failure of a pavement when (1) the pavement fails due to all the failure modes or (2) the pavement fails due to any one of the failure modes [18]. These can be conceptually thought as failure modes linked in parallel (refer Fig. 4a) or failure modes linked in series (refer Fig. 4b), respectively.

If the failure probability for the ith mode is represented as F_i, then the overall reliability (R_o) can be calculated as follows:

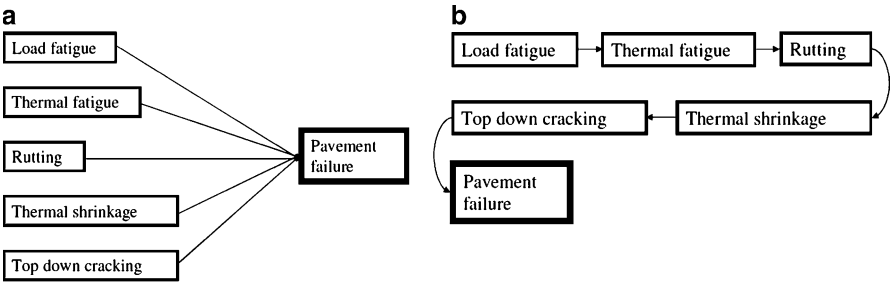

Fig. 4 Series or parallel linkage of failure modes. (**a**) Failure modes are linked in parallel, (**b**) Failure modes are linked in series

If the pavement is thought to be failed when it fails due to all the failure modes (refer Fig. 4a), then

$$R_o = 1 - \bigcap_{i=1}^{n} F_i \tag{4}$$

If the pavement is thought to be failed when it fails due to either of the failure modes (refer Fig. 4b), then

$$R_o = 1 - \bigcup_{i=1}^{n} F_i \tag{5}$$

One may even further consider the failure modes as mixed combinations of parallel and series connections, and accordingly, different expressions for the overall reliability (R_o) can be obtained. It is difficult to know the mutual dependency between the individual failure modes; the calculation of R_o, therefore, becomes quite simple when the failure modes are assumed to be mutually independent.

3 Estimation of Reliability

It is a difficult task to derive a closed-form analytical solution for estimating the critical stress/strain parameters (refer Fig. 3) of a multilayered asphalt pavement structure. Thus, Monte Carlo simulation method has been quite popularly [4, 13, 32, 33] used to estimate the reliability of a given pavement section. Simulation studies show that T generally follows a normal distribution, whereas the fatigue or rutting life of a given pavement generally follows a log-normal distribution [5, 18, 33]. Sensitivity studies have been conducted by various

researches [3, 6, 13, 18, 30, 32] to study the effect of various parameters on reliability, and it is generally observed that the thicknesses and stiffness moduli of pavement layers significantly affect the fatigue and rutting reliabilities [3, 18, 32].

4 Design of Pavement for a Given Reliability

The effect of thickness on reliability for low-temperature shrinkage cracking and reliability of thermal cracking is generally not very significant [24, 26]. The design reliability levels of these failure modes can be achieved by adjusting at the asphalt mix design stage. Thus, the asphalt pavement thickness design becomes primarily governed by the fatigue and rutting considerations. Reliability-based design of new asphalt pavement and rehabilitation of existing asphalt pavement are discussed in the following.

4.1 Design of New Pavement

Design of a pavement for a given reliability level is an iterative process. For a given traffic data, the distribution of T is fixed, and the distribution of N value changes once the trial thickness values are changed. The iteration is continued until the reliability levels (of the fatigue and rutting failure modes, since these are strongly affected by thickness) satisfy the respective design reliability levels. Similar concept is used in the AASHTO [1] guidelines, where difference between the expected traffic and allowable traffic is adjusted to achieve a reliability level. However, the recent NCHRP guidelines [20] suggest use of reliability in terms of a system of pavements (i.e. the probability that a pavement section survives out of a number of pavement sections under similar conditions) for design purpose. In this approach, empirical equations are developed from performance data (of a number of pavement sections) to predict individual pavement distresses.

Figure 5 presents a schematic pavement design chart. The asphalt pavement is assumed to be made up of three basic layers, asphalt layer, unbound granular layer and the soil subgrade. Thus, the thicknesses of the asphalt layer (h_1) and the granular layer (h_2) are the two variables to be designed. From Fig. 5, it can be seen that for a given value, h_2, the reliability level increases as h_1 increases. Similarly, for a given value of h_1, the reliability value is higher if larger h_2 is used. Different sets of curves can be obtained for various failure modes (say, fatigue and rutting). Thus, from this design chart, for given reliability levels of fatigue and rutting failure modes, one can choose suitable values of h_1 and h_2.

As seen from Fig. 5, for a given pavement design problem, a number of alternative design solutions are possible – all of them may satisfy the reliability requirements, but their costs may differ [25]. The final design solution would be the one whose cost, C (total construction cost including the cost of materials), is the

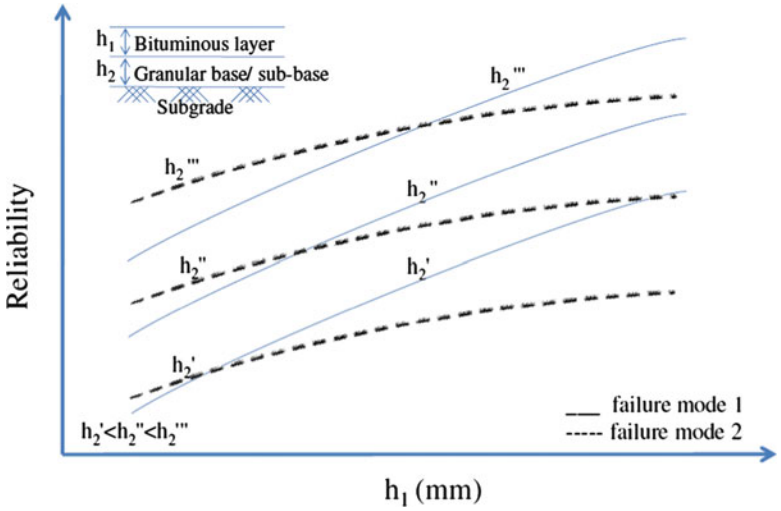

Fig. 5 Schematic diagram of a pavement design chart for two design layers and two failure modes

least. Thus, a reliability-based pavement design problem can be formulated as an optimization scheme as follows:

Minimize C

Subject to:

$$\forall_i R_i(\forall_j h_j) \geqslant R_i^{\mathrm{d}} \tag{6}$$

where j is the number of design layers, i is the number of modes for failure, $R_i(h_j)$ is the reliability of ith failure mode which is a dependent on the thickness of all the design layers (h_j) and R_i^{d} is the design reliability (i.e. target reliability) level for the ith failure mode.

4.2 Design for Rehabilitation

A newly constructed pavement undergoes deterioration with the passage of time. This deterioration is due to traffic and environmental factors. An appropriate structural design prevents a pavement to undergo premature failure, but the pavement would finally fail after the expiry of its design life. The pavement performance is however stochastic in nature [10, 16, 27, 34], and the purpose of using reliability approach is to take into account this stochasticity in the design process.

A pavement, before it undergoes complete failure, needs to be rehabilitated. Determining the optimal rehabilitation timing and the extent of rehabilitation to be applied is an optimization problem. A number of formulations for estimation of

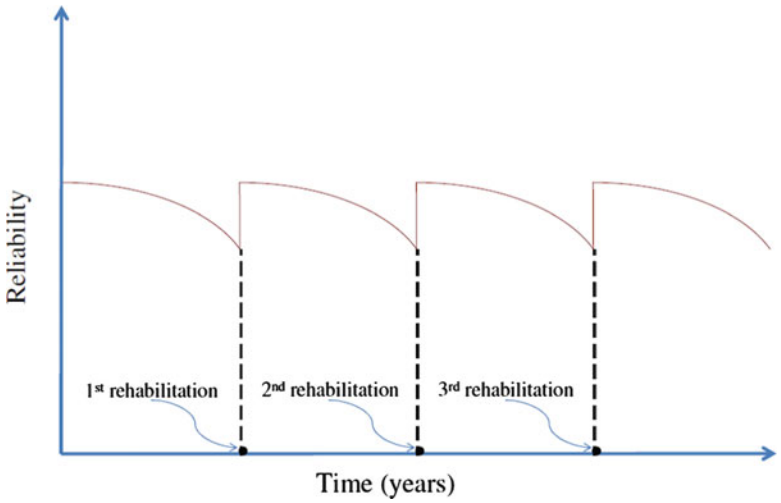

Fig. 6 Variation of reliability with time over the life cycle of the pavement

optimal rehabilitation timing are available in literature [2, 19, 22]. The scope of these formulations include minimization of total cost of construction and rehabilitation as well as the cost incurred by the road users, over the entire life cycle of the pavement.

The reliability of a pavement structure discussed above indicates the reliability value at the end of the design period, when all the expected traffic repetitions have taken place. The reliability value of a newly constructed pavement is therefore higher than the value for which it is designed, and it gradually decreases as the cumulative traffic repetitions increase [7]. Once the reliability value reaches a prespecified threshold value, a rehabilitation (say, an overlay) may be needed, which would further shift the allowable traffic (i.e. improve the pavement capacity). This is shown schematically in Fig. 6. A suitable optimization formulation would be able to estimate the optimal rehabilitation timing so that reliability value does not fall below the threshold level and at the same time the total cost is minimized [8]. This forms the basis of reliability-based rehabilitation design scheme.

5 Summary

Significant level of variabilities present in the pavement design parameters necessitates use of reliability-based approach in pavement design. This chapter has discussed the reliability principles in use for the design of asphalt pavements.

Acknowledgement The author wishes to thank Mr. Sudhir N. Varma, former master's student, Department of Civil Engineering, IIT Kanpur, for helping in drawing some of the schematic diagrams presented in this chapter.

References

1. AASHTO (1993) Guide for design of pavement structure. American Association of State Highway and Transportation Officials (AASHTO), Washington, DC
2. Abaza KA, Abu-Eisheh SA (2003) An optimum design approach for flexible pavements. Int J Pavement Eng 4(1):1–11
3. Chou YT (1990) Reliability design procedures for flexible pavements. J Trans Eng 116 (5):602–614
4. Chua KH, Kiureghian AD, Monismith CL (1992) Stochastic model for pavement design. J Trans Eng 118(6):769–786
5. Darter MI, McCullough BF, Brown JL (1972) Reliability concepts applied to the Texas flexible pavement system. Highw Res Rec HRB 407:146–161
6. Darter MI, Hudson WR, Brown JL (1973) Statistical variation of flexible pavement properties and their consideration in design. Proc Assoc Asphalt Paving Technol 42:589–615
7. Despande VP, Damnjanvic ID, Gardoni P (2010) Modeling pavement fragility. J Trans Eng 136(6):592–596
8. Despande VP, Damnjanvic ID, Gardoni P (2010b) Reliability-based optimization models for scheduling pavement rehabilitation. Comput-Aided Civ Infrastruct Eng 25:227–237
9. Harr ME (1987) Reliability based design in civil engineering. McGraw-Hill Book Company, New York
10. Hong HP, Wang SS (2003) Stochastic modeling of pavement performance. Int J Pavement Eng 4(4):235–243
11. Jiang YJ, Selezneva O, Mladenovic G, Aref S, Darter MI (2003) Estimation of pavement layer thickness variability for reliability-based design. Trans Res Rec 1849:156–165, TRB, National Research Council, Washington, DC
12. Kim HB, Lee SH (2002) Reliability-based design model applied to mechanistic empirical pavement design. KSCE J Civ Eng 6(3):263–272
13. Kim HB, Buch N (2003) Reliability-based pavement design model accounting for inherent variability of design parameters. TRB 82nd annual meeting, CD-ROM, Washington, DC
14. Kulkarni RB (1994) Rational approach in applying reliability theory to pavement structural design. Trans Res Rec 1449:13–17, TRB, National Research Council, Washington, DC
15. Lamer AC, Moavenzadeh F (1971) Reliability of highway pavements. Highw Res Rec HRB 362:1–8
16. Li N, Haas R, Xie W (1996) Reliability-based processing of Markov chains for modeling pavement network deterioration. Trans Res Board 1524:203–213
17. Lytton RL, Zollinger D (1993) Modelling reliability in pavement. TRB 72nd annual meeting, Washington, DC
18. Maji A, Das A (2008) Reliability considerations of bituminous pavement design by mechanistic-empirical approach. Int J Pavement Eng 9(1):19–31
19. Mamlouk MS, Zaniewski JP, He W (2000) Analysis and design optimization of flexible pavement. J Trans Eng 126(2):161–167
20. Mechanistic-Empirical Design of New & Rehabilitated Pavement Structures, Appendix B: Design reliability (2003) Final document, NCHRP project 1-37A, National Research Council, Washington, DC, 2003. http://www.trb.org/mepdg/guide.htm. Accessed Aug 2010
21. Noureldin SA, Sharaf E, Arafah A, Al-Sugair F (1994) Estimation of standard deviation of predicted performance of flexible pavements using AASHTO model. Trans Res Rec 1449:46–56, Transportation Research Record, TRB, National Research Council, Washington, DC
22. Ouyang Y, Madanat S (2004) Optimal scheduling of rehabilitation activities for multiple pavement facilities: exact and approximate solutions. Trans Res A Policy Pract 38:347–365

23. Rajbongshi P, Das A (2008) Estimation of structural reliability of asphalt pavement for mixed axle loading conditions. In: Proceedings of the 6th International Conference of Roads and Airfield Pavement Technology (ICPT), Sapporo, Japan, pp 35–42
24. Rajbongshi P, Das A (2008) Thermal fatigue considerations in asphalt pavement design. Int J Pavement Res Technol 1(4):129–134
25. Rajbongshi P, Das A (2008) Optimal asphalt pavement design considering cost and reliability. J Trans Eng 134(6):255–261
26. Rajbongshi P, Das A (2009) Estimation of temperature stress and low-temperature crack spacing in asphalt pavements. J Trans Eng 135(10):745–752
27. Sanchez-Silva M, Arroyo O, Junca M, Caro S, Caicedo B (2005) Reliability based design optimization of asphalt pavements. Int J Pavement Eng 6(4):281–294
28. Shell International Petroleum Company Limited (1978) Shell pavement design manual – asphalt pavements and overlays for road traffic, Shell International Petroleum Company Limited, London
29. Stubstad RN, Tayabji SD, Lukanen EO (2002) LTPP data analysis: variation in pavement design inputs. Final report, NCHRP web document 48, TRB, National Research Council, Washington, DC. http://gulliver.trb.org/publications/nchrp/nchrp_w48.pdf. Accessed Aug 2010
30. Tarefder RA, Saha N, Stormont JC (2010) Evaluation of subgrade strength and pavement designs for reliability. J Trans Eng 136(4):379–391
31. Timm DH, Briggison B, Newcomb DE (1998) Variability of mechanistic-empirical flexible pavement design parameters. In: Proceedings of the 5th international conference on the bearing capacity of roads and airfields, vol 1, pp 629–638
32. Timm DH, Newcomb DE, Briggison B, Galambos TV (1999) Incorporation of reliability into the Minnesota mechanistic-empirical pavement design method. Final report, submitted to Minnesota Department of Transportation, Department of Civil Engineering, Minnesota University, Minneapolis
33. Timm DH, Newcomb DE, Galambos TV (2000) Incorporation of reliability into mechanistic-empirical pavement design. Trans Res Rec 1730:73–80, TRB, National Research Council, Washington, DC
34. Wang KCP, Zaniewski J, Way G (1994) Probabilistic behavior of pavements. J Trans Eng 120 (3):358–375
35. Zhang Z, Damnjanović I (2006) Applying method of moments to model reliability of pavements infrastructure. J Trans Eng 132(5):416–424

Structural Reliability Analysis of Composite Wing Subjected to Gust Loads

D.K. Maiti and Anil Kumar Ammina

Abstract The design of any engineering system is a process of decision-making, under constraints of uncertainty. The uncertainty in the design process results from the lack of deterministic knowledge of different physical parameters and the uncertainty in the models with which the design is performed. In this study, the reliability analysis is conducted for composite wing subject to gust loads. For this, the probability distribution function of bending and shear stresses from random gust is calculated by power spectral analysis, and the material properties of composite skin are assumed to be normal random variables to consider uncertainty. With these distributions of random variables, the probability of failure of the wing structure is calculated by Monte Carlo simulation. The necessary modification is carried out, and it is found that the suggested modification improves the reliability of the design.

Keywords Uncertainty • Random gust load • Probability of failure • Uncertainty • Reliability analysis

1 Introduction

The response of an airplane in flight due to gust is one of the most important dynamic response problems from the structural design considerations. Gusts are the result of atmospheric turbulence. They can be categorised into two types: [1, 2] (1) vertical/lateral gusts, wherein a component of the gust velocity is at right angles

D.K. Maiti (✉)
Department of Aerospace Engineering, Indian Institute of Technology, Kharagpur, Kharagpur 721302, WB, India
e-mail: dkmaiti@aero.iitkgp.ernet.in

A.K. Ammina
Reliability Engineering Centre, Indian Institute of Technology, Kharagpur, Kharagpur 721302, India

S. Chakraborty and G. Bhattacharya (eds.), *Proceedings of the International Symposium on Engineering under Uncertainty: Safety Assessment and Management (ISEUSAM - 2012)*,
DOI 10.1007/978-81-322-0757-3_20,

to the flight path, and (2) head-on or longitudinal gusts, wherein the gust velocity is parallel to the flight path. Vertical/lateral gust causes a change in angle of attack/angle of sideslip, which is equal to the gust velocity divided by the forward speed. On the other hand, the head-on (longitudinal) gust produces only a change in the dynamic pressure. The change in lift force produced by a head-on gust is negligible compared to that of a vertical/lateral gust. Hence, a vertical/lateral gust is more critical from design considerations. There are two approaches for solving the problem of gust response. One is called as discrete gust approach which is relatively easy to handle; on the other hand, the second approach is called as turbulence gust approach. The second approach considers the nature of gust is random in nature and responses are calculated based on the statistical approach considering the uncertainty in the gust model.

The uncertainties that occur in the design process are employed for analysis of the loads and, in the geometric parameters of structure, have been dealt with for generations by experience and safety factors. The main sources of uncertainties in structural analysis and design are (a) uncertainties in the determination of the physical and mathematical model used for analysis, including uncertainties in the failure criteria (model); (b) uncertainties in the determination of the magnitudes, locations, frequency content and correlations of the external loads (either static or dynamic); and (c) uncertainties in various structural parameters such as geometries, dimensions, material properties and allowable stochastic structure. These three categories do not include other more subjective uncertainties such as human errors in the design and production.

Aerospace structures are excited by aerodynamic loads, which are usually random in nature. Flow around the wing structure creates pressure fluctuations, which have a wide range of frequency and amplitude content. The same phenomena are caused by acoustic noise created by rocket and jet outlet flows. Rotating elements such as engines and rotors create excitations with a better defined frequency content that are in many cases random in amplitudes. The use of composite materials reduced the weight and increases the payload capacity, but the flexibility and high aspect ratio become a concern particularly under gust conditions. Enough research has also been done on design and optimisation of composite structures under different loads like flutter, flight loads and natural frequency but all in connection with stability not dealt the reliability of structure.

In the past, the simple discrete gust type, for example, a one-minus-cosine pulse, was used to model the atmospheric turbulence. But, in natural, a gust profile is continuous and irregular. So the continuous gust profile, which can be idealised as a stationary Gaussian random process, is widely used for gust load analysis recently. By considering the atmospheric turbulence as a stationary random process, the power spectral methods are used for finding the root mean square (RMS) values of bending stresses. In FAR-25, two basic types of power spectral gust loads criteria are described, which are mission analysis and design envelope, respectively.

Advanced composite materials are widely used in modern aircraft structural design mainly to achieve the weight-efficient structure. Thus, the research efforts have been devoted to the optimal design of wing structures in connections of various objectives and constraints [3–7]. Penmetsa and Grandhi [8] calculated the

failure probability using interval analysis where the wing skin thickness and the loading were considered to be available as an interval. Mahadevan and Liu [9] developed the system reliability analysis procedure and applied it to the analysis of composite wing structure. In their work, material properties, ply thicknesses and orientations and pressure loads were assumed to be random variables. The aeroelastic response to time-dependent external excitation of a two-dimensional rigid/elastic-lifting surface in incompressible flow field featuring plunging–-pitching-coupled motion is addressed by Marzocca et al. [10].

In this chapter, the reliability analysis of composite wing subject to continuous random gust is conducted based on mission analysis criteria. To evaluate the probability of failure of wing structure, the wing root bending and shear stresses induced by gust loads are analysed by power spectral method, and then the probability distribution function of bending and shear stresses is calculated. The material properties of composite wing are assumed to be random normal variable to consider uncertainties. With the probability distribution functions for bending and shear stresses and material strength properties, the failure probability of wing structure can be evaluated by Monte Carlo simulation.

2 Analysis Procedure

The aeroelastic response analysis is carried out using the university version of FE package MD.NASTRAN [11]. The modal domain formulation is used for the random gust response analysis. The details of analysis procedure are given below. The basic equation in modal coordinates is

$$\left[-M_{\mathrm{hh}}\omega^2 + iB_{\mathrm{hh}}\omega + (1+ig)K_{\mathrm{hh}} - \frac{1}{2}\rho V^2 Q_{\mathrm{hh}}(m,k)\right]\{u_{\mathrm{h}}\} = \{P(\omega)\} \tag{1}$$

where M_{hh} is modal mass, B_{hh} modal damping and K_{hh} is modal stiffness. Q_{hh} is modal aerodynamic load in terms of Mach number (m) and reduced frequency (k). The external modal load, $P(\omega)$, is expressed as a function of frequency (ω) which can be aerodynamic or non-aerodynamic in nature and is a function of the frequency. The generalised load due to gust is expressed as

$$P(\omega) = qw_{\mathrm{g}}PP(\omega)\left[Q_{ij}\right]\left\{w_j(\omega)\right\} \tag{2}$$

where PP (ω) is the user supplied frequency or time variation of the gust (if the applied loading is in time domain, Fourier transform techniques are used to convert the loading into the frequency domain). q is dynamic pressure, w_{g} is gust scale factor and Q_{ij} is the aerodynamic influence coefficients. The gust downwash matrix is a function of frequency and the geometry of the aerodynamic model:

$$w_j(\omega_j) = \cos\gamma_j e^{-i\omega_j(x_j - x_0)/V} \tag{3}$$

Equation (1) is solved, and the frequency response, $H_{ja}(\omega)$, of any physical variable, u_j, due to some excitation source, $Q_a(t)$, is obtained. Then the power spectral density of the response, $\Phi_j(\omega)$, is related to the power spectral density of the gust load, $\Phi_a(\omega)$, by

$$\Phi_j(\omega) = \left|H_{ja}(\omega)\right|^2 \Phi_a(\omega) \tag{4}$$

The expected value of the number of zero crossings with positive slope per unit time, or mean frequency, is another quantity of interest from fatigue analysis and design of aircraft for gusts. This mean frequency, N_0, can be found from the spectral density:

$$N_0{}^2 = \frac{\int_0^\infty (\omega/2\pi)^2 \Phi_j(\omega) d\omega}{\int_0^\infty \Phi_j(\omega) d\omega} \tag{5}$$

3 Modelling of Gust Load

The gust velocity (V_{gust}) is small compared to forward velocity (V_∞). Otherwise, it would cause such a large change in angle of attack that the wing would stall. For a relatively small V_{gust}, the magnitude of the change in angle of attack, $\Delta\alpha$, is given by $\Delta\alpha = \tan^{-1}\left(V_{\text{gust}}/V_\infty\right) \approx V_{\text{gust}}/V_\infty$,and the change in lift coefficient is $\Delta C_{\text{L}} = C_{\text{L}_\alpha} \Delta\alpha = C_{\text{L}_\alpha}\left(V_{\text{gust}}/V_\infty\right)$. The change in lift is $\Delta L = \Delta C_{\text{L}} qS = \left(C_{\text{L}_\alpha} \rho V_{\text{gust}} V_\infty S/2\right)$, and the change in load factor is $\Delta n = (\Delta L/W) = \left(C_{\text{L}_\alpha} \rho V_{\text{gust}} V_\infty/2(W/S)\right)$. Assuming the load factor prior to encountering the gust is 1, the maximum load factor during the encounter is

$$n_{\text{gust}} = 1 + \Delta n = 1 + \frac{C_{\text{L}_\alpha} \rho V_{\text{gust}} V_\infty}{2(W/S)} \tag{6}$$

An aircraft is just as likely to encounter a *downdraft* as an updraft when flying through turbulent air. A downdraft is a vertical air current like an updraft, except that the direction of the air flow is downwards. The reaction of an aircraft to a downdraft is similar to an updraft, but since V_{gust} is negative, the second term in (6) is negative as well. The first term in (6) remains positive, so the magnitude of n_{gust} is less. However, since most aircraft have lower negative structural limits, encountering a downdraft could still be a problem.

3.1 Concepts of Random Gust

The gust profiles typically tend to be continuous and irregular in nature. Such a profile can be modelled as a "stationary Gaussian random process". A stationary Gaussian random process can be considered to be generated by the superposition of an infinite number of sinusoidal components. These components differ infinitesimally in frequency from one to the next. Each component is of prescribed infinitesimal amplitude, and each is randomly phased relative to the others. The profile or time history thus idealised is stationary in that it is considered to be of infinite duration and its statistical properties are the same whenever it may be sampled. The magnitude of a stationary random process is statistically defined by its RMS (root mean square) value and its probability distribution.

Two shapes of power spectral density (PSD), $\Phi(\omega)$, function for atmospheric turbulence have been widely used, the von Kármán and the Dryden. These are defined by mathematical expressions as follows:

$$\Phi(\omega) = \frac{2{\sigma_w}^2 (L_g/V_{gust})[1 + 2(p+1)(\bar{k}L_g\omega/V_{gust})^2]}{[1 + (\bar{k}L_g\omega/V_{gust})^2]^{p+3/2}} \tag{7}$$

where L_g is scale of turbulence and σ_w RMS gust velocity. Values of the parameters k and p are given in the following table:

	Dryden	Von Kármán
$\bar{k}$	1.0	1.339
P	0.5	0.333

The von Kármán spectrum gives a better fit to observed experimental data and is normally used for design purposes.

4 Results and Discussion

4.1 Wing Geometry and Properties

A simple wing model as shown in Fig. 1 is used for gust response analysis. The aircraft wing panel is idealised as a cantilevered composite plate made of graphite/epoxy with four-noded quadrilateral elements as shown in Fig. 2. The stacking sequence is $[90/\pm45/0]_{2s}$, and each layer has uniform thickness of 0.018 cm. An orthotropic material is a homogeneous linear elastic material having two planes of symmetry in terms of mechanical properties, and these two planes are being perpendicular to each other. Then one can show that the number of independent

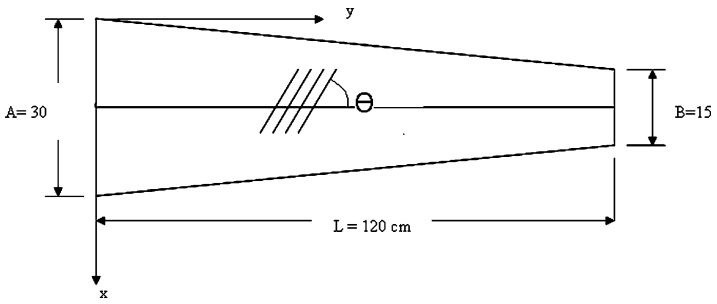

Fig. 1 Geometry and coordinate system of composite wing

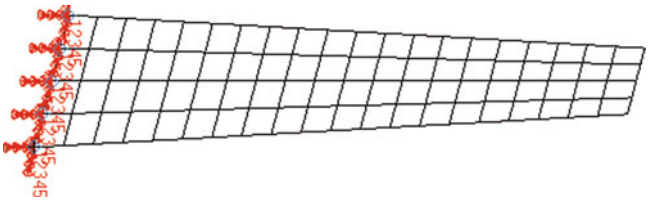

Fig. 2 Finite element model of the wing

elastic constants is nine. The constitutive relation expressed in the so-called "orthotropic" axes, defined by three axes constructed on the two orthogonal planes and their intersection line, can be written in the following form, called the engineering notation because it utilises the elastic modulus and Poisson's ratio. The material properties of the graphite/epoxy are as follows:

$E_1 = 132.16$ GPa, $E_2 = 8.65$ GPa, $\upsilon_{12} = 0.3$, $\rho = 1.59$ g/cm^3, $G_{12} = G_{13} = G_{23} = 4.12$ GPa

Thickness of the each layer = 0.018 cm.

Sequence of each stacking = $[90/\pm 45/0]_{2s}$

4.2 *Modal Analysis*

To investigate the dynamic characteristics of wing model, normal mode analysis is performed. The first four natural frequencies and mode shapes are shown in Fig. 3. It is evident from the statistical gust profile that the intensity of gust power spectral density is weak with the higher frequency ranges. In this study, first six natural modes which are less than 100 Hz are considered for gust response analysis. The summary of the first six natural frequencies and the description of the mode shapes are presented in Table 1.

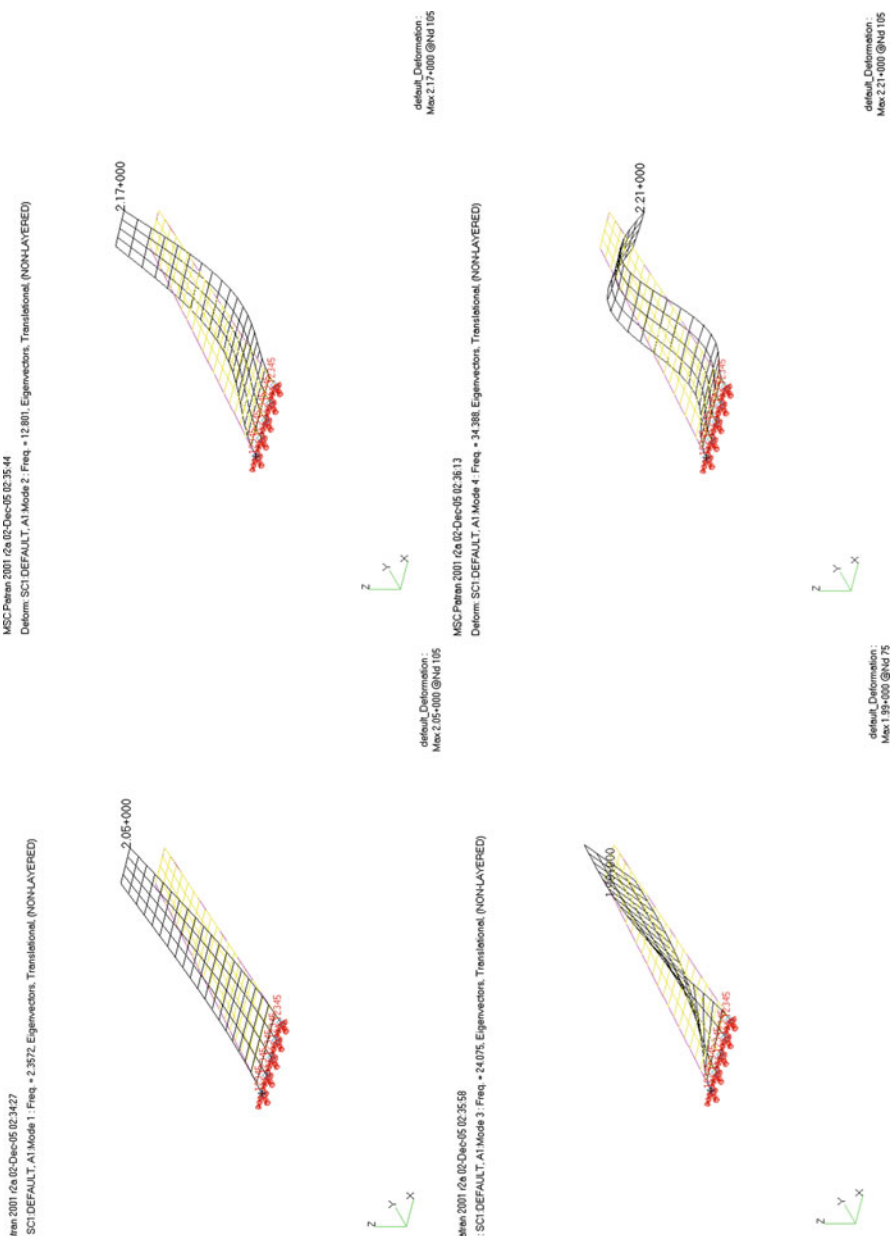

Fig. 3 Mode shape of first four natural frequencies

Table 1 Normal modes

Mode no.	Frequency (Hz)	Description of mode
1	2.45	First spanwise bending
2	13.30	Second spanwise bending
3	24.20	First chordwise bending
4	35.70	Third spanwise bending
5	61.40	Second spanwise bending and first twisting mode
6	69.20	Fourth spanwise bending

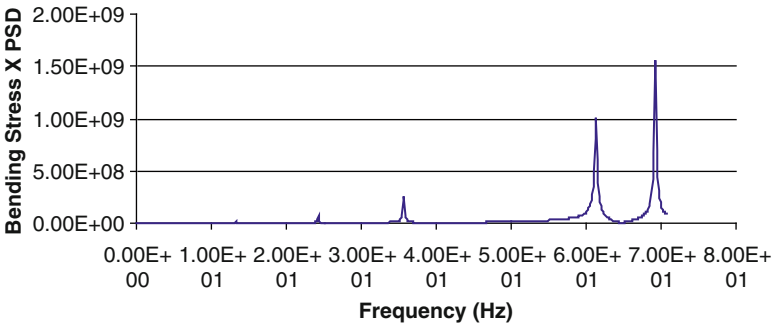

Fig. 4 PSD for wing root bending stress in *X* direction

4.3 Random Response Analysis Using MD.NASTRAN

The FEM structural model used in this work was considered as a semi-span model made of graphite/epoxy composite. The mesh divisions are as shown in Fig. 2. The aerodynamic mesh is also created to perform the unsteady aerodynamic computation in Mach (m) and reduced frequency (k) pair.

A corresponding full-span model possessing identical stiffness and mass properties was used in the two-dimensional PSD gust analysis. MD.NASTRAN is used for obtaining the bending moment PSD at the wing root. The von Karman gust PSD of the gust is considered for gust response analysis with the following input information:

$$V_{\text{gust}} = 15 \text{ m/s}, \quad \sigma_{\text{W}} = 0.3048 \text{ m/s}, \quad L_{\text{g}} = 762 \text{ m}$$

After running the random gust response analysis in MD.Nastran, it generates the required response quantities. These statistical quantities are important for failure and fatigue analyses. Here, the responses are wing root bending and shear stresses along the fibre, across the fibre and shear. The response parameters are calculated as PSD function of frequency. The required statistical quantities are calculated from these responses. The wing root bending stresses are plotted in Figs. 4, 5 and 6. It is observed from the figure that stresses are maximum at natural frequencies of the structure.

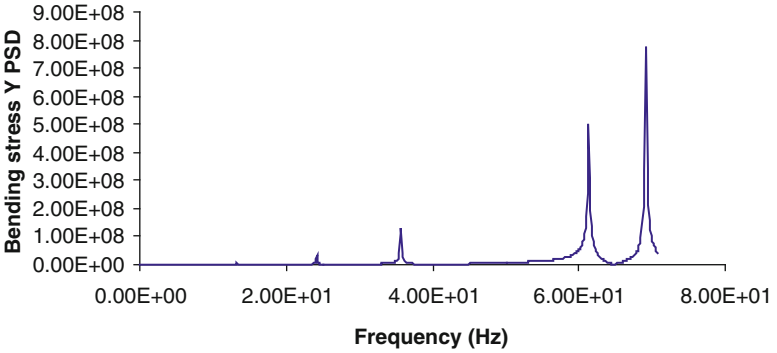

Fig. 5 PSD for wing root bending stress in *Y* direction

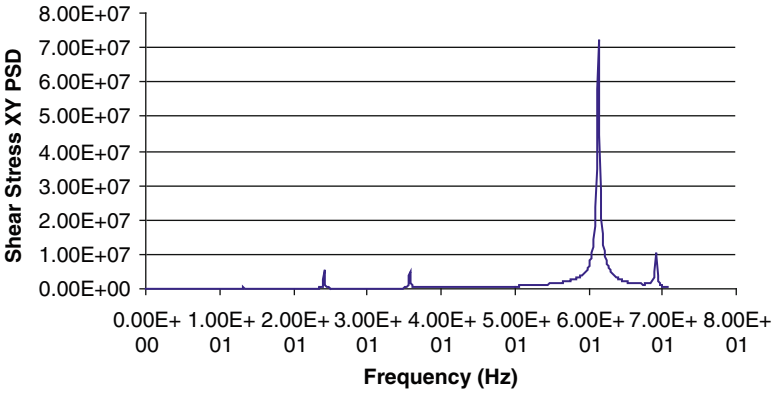

Fig. 6 PSD for wing root shear stress

4.4 Probability of Exceedance

The PSD of bending stress is calculated by power spectral analysis with gust PSD as an input. Then, the number of crossings of a given level y per unit time can be obtained by the following formula:

$$N(y) = N_0 \left[P_1 e^{-\frac{(y/\bar{A})}{b_1}} + P_2 e^{-\frac{(y/\bar{A})}{b_2}} \right] \tag{8}$$

N_0 is the number of crossing rate of level 0 as defined earlier, and $\bar{A}$ is the ratio of the RMS of output to that of the gust, which is given by

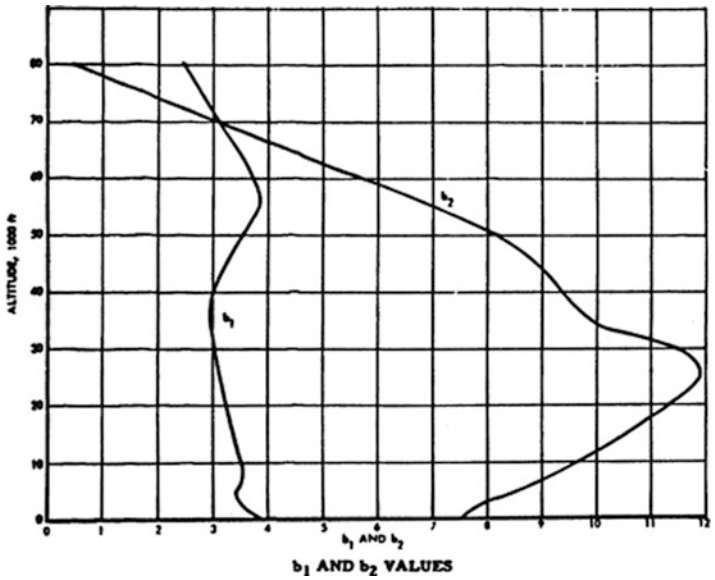

Fig. 7 Plot for b_1 and b_2 at different altitudes

$$\bar{A}^2 = \frac{\int_0^\infty \Phi_\psi(\omega)d\omega}{\int_0^\infty \Phi_w(\omega)d\omega} \tag{9}$$

In practice, the integrals defining $\bar{A}$ and N_0 are evaluated only up to a reasonable upper limit, beyond which the contribution to the integrals for computing $\bar{A}$ is negligible. According to FAR 25, P_1, P_2, b_1 and b_2 (Figs. 7 and 8 and Table 2) are constants describing the probability distribution of σ_W and depend only on altitude. P_1 and P_2 are fractions of time in non-storm and storm turbulence, respectively, and b_1 and b_2 are constants indicative of probable intensities. The statistical model of Eq. 9 is valid for an airplane flying at a constant speed and altitude. For a mission profile composed of segments that are representative of the aircraft usage, the exceedance expression given by Eq. 9 is superimposed as given below:

$$N(y) = \sum_i^{n_p} t_i N_{0i} \left[P_{1i} e^{\left(-\frac{(y/\bar{A}_i)}{b_{1i}}\right)} + P_{2i} e^{\left(-\frac{(y/\bar{A}_i)}{b_{2i}}\right)} \right] \tag{10}$$

where n_p is the number of segments in the mission profile being analysed, t_i is the fraction of time in segment i relative to the sum of all other segments, and N_{0i} and $\bar{A}_i$ are obtained by dynamic analysis for each segment. Once $N(y)$ in Eq. 10 is obtained, it is easy to calculate the probability of exceedance. However, for the frequency of

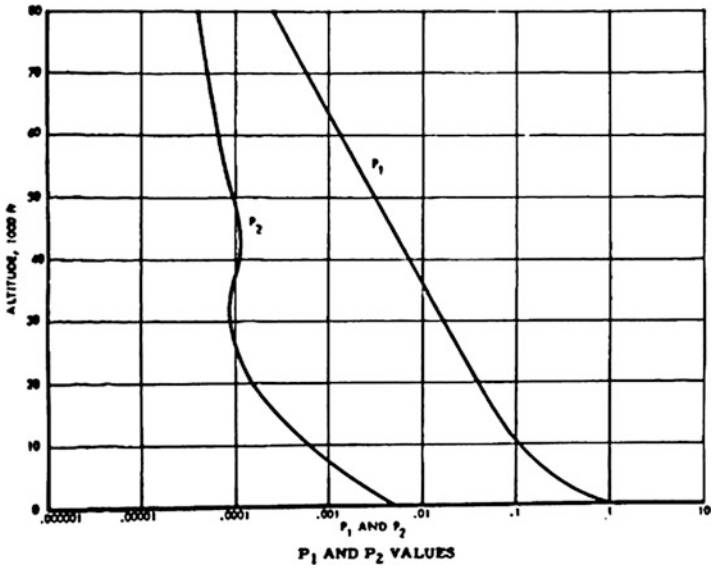

Fig. 8 Plot for P_1 and P_2 for different altitudes

Table 2 Sample values of P_1, P_2, b_1 and b_2 at different altitudes

S. No.	Altitude (ft)	P_1	P_2	b_1	b_2
1	0 (sea level)	1	0.0017	3.932	7.547
2	1,000	0.19	0.00163	3.760	7.600
3	5,000	0.1348	0.00119	3.412	8.530
4	10,000	0.112	6.5E-4	3.519	9.641
5	20,000	0.041	1.566E-4	3.25	11.354
6	30,000	0.017	8.642E-4	3.05	11.523
7	40,000	0.0008	1.265E-4	3.04	9.341
8	60,000	0.0012	8.2E-5	3.715	5.675
9	80,000	3.04E-4	6.01E-5	2.316	0.51

exceedance of very much lower value of y, the probability of exceedance obtained by multiplying frequency by flight time can give the value greater than unity. So, in this chapter, the following equation is used for relating frequency of exceedance and probability:

$$P = 1 - e^{-\lambda t} \tag{11}$$

where t is the period to which the probability applies and λ is the frequency of exceedance.

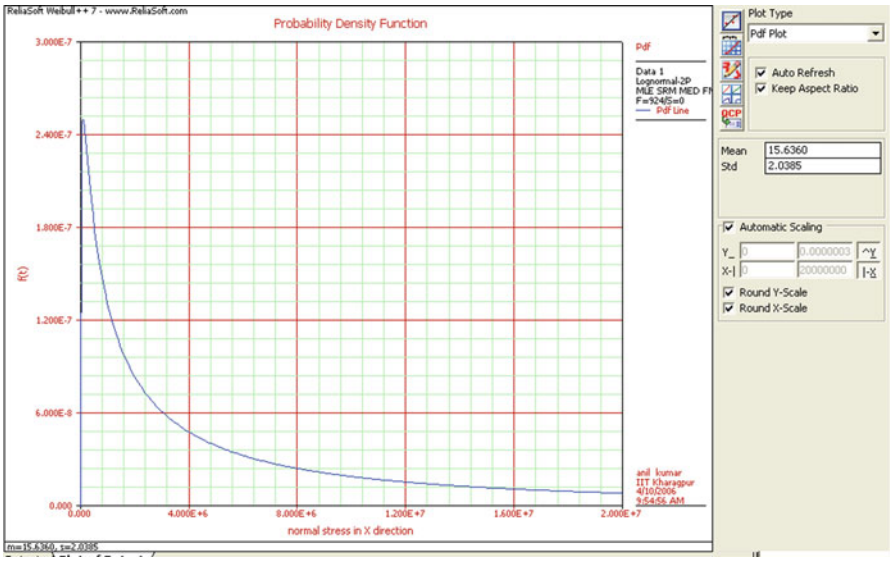

Fig. 9 PDF of normal stress (σ_x)

4.5 *Probability Distribution of Responses*

Once the frequency of exceedance is determined, it can be easily converted to probability of exceedance by Eq. 12. Namely, the probability that y is lower than y_1 is

$$F(y) = P(y<y_1) = 1 - (1 - e^{-\lambda t}) = e^{-\lambda t} \tag{12}$$

Equation 12 is the cumulative distribution function (CDF) for bending moment/stress, so probability density function (PDF) can be obtained by differentiating CDF and expressed as

$$f(y) = \frac{dF(y)}{dy} = -te^{-\lambda t}N_0\left[-\frac{P_1}{Ab_1}e^{\left(-\frac{(y/A)}{b_1}\right)} - \frac{P_2}{Ab_2}e^{\left(-\frac{(y/A)}{b_2}\right)}\right] \tag{13}$$

The PDF for wing root bending stresses, obtained by Eq. 13, are shown in Figs. 9, 10 and 11. The values for parameters P_1, P_2, b_1 and b_2 can be determined from the Table 2, while $\bar{A}$ and N_0 are obtained by power spectral analysis, and corresponding flight time t is selected as 100 h. The values of N_0 and $\bar{A}$ for different altitudes or segments in the mission profile for all responses, namely, Stress X, Stress Y and Shear XY, are calculated.

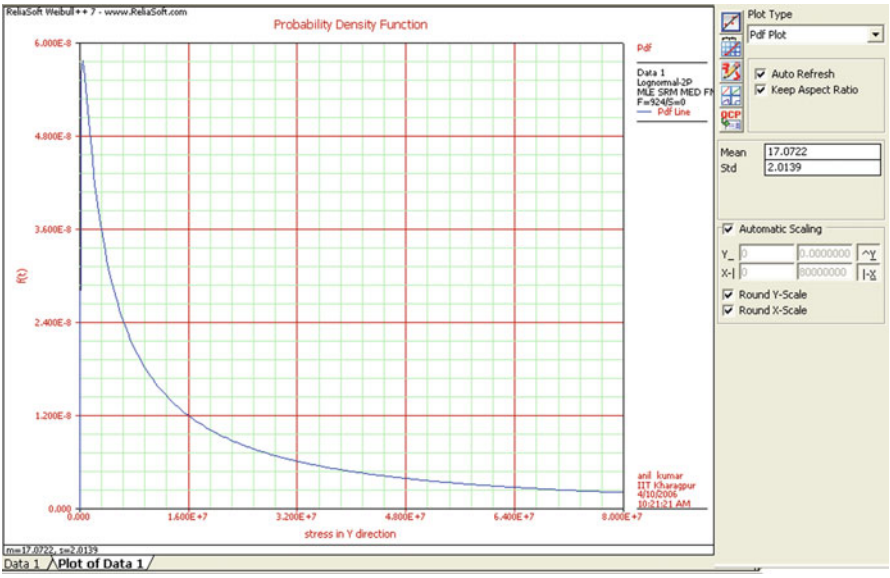

Fig. 10 PDF of normal stress (σ_y)

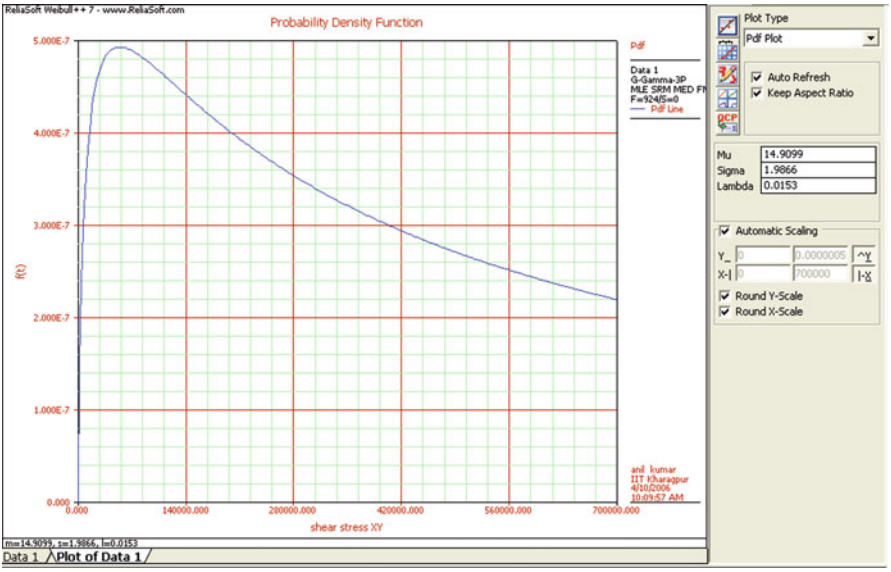

Fig. 11 PDF of shear stress (τ_{xy})

4.6 Probability of Failure

To check the failure due to wing root bending moment, failure criterion is calculated at each ply of wing root. According to Tsai–Hill criterion [12], failure occurs when

$$g(\sigma) = \frac{\sigma_1^2}{X^2} + \frac{\sigma_2^2}{Y^2} - \frac{\sigma_1 \sigma_2}{X^2} + \frac{\tau_{12}^2}{S^2} - 1 \geq 0 \tag{14}$$

where X, Y and S are lamina strengths and σ_1, σ_2 and τ_{12} are stress components in the principal material axes.

Also, material properties of the composite wing, X, Y and S, are modelled by normal random variables to consider uncertainty. Standard deviations of the distributions are assumed to be 10% of mean values. The other properties are assumed to be deterministic. With 2,000 sampling points for each random variable, an inequality of Tsai–Hill equation is examined for failure check. A sample failure table is presented in Table A.1. N_f is the number of simulation cycles; when $g(\sigma)$ is greater than zero and N is the total number of simulation cycles, the probability of failure can be expressed as

$$P_f = \frac{N_f}{N} \tag{15}$$

The above equation would give the value of failure probability, and one minus of that will give the reliability of the composite wing. This method is very efficient way to check the safety and reliability of aircraft structure subjected to gust. For $\sigma_W = 0.3048$ m/s, the failure probability, calculated using Eq. 15, was found to be 0.06. Therefore, the composite wing's success probability is 0.94 under the gust condition, but this is very low, and it is a matter of concern.

5 Modification in Wing Structure

The success probability of the previous design is very low and needed to do certain changes to improve the reliability. Methods to improve reliability are as follows:

- Optimising the mechanical properties of the wing by improving the strength in the week direction; this can be done by changing the orientation of the plies.
- Increasing the no. of laminas.
- Stiffening the structure with *stringers or longerons*.
- Going for high-strength composite.

In the present study, the modification is considered to remove two 0° and 90° layers and is replaced by two ±45° layers. The modified lamination sequence is

[90/±45/0/ ∓ 45/90/±45/90/±45/0/ ∓ 45/90]. Then the above procedure is repeated to get the failure probability. This time, the failure probability is decreased to 0.015.

N_f =30 and N = 2,000;

Therefore, success probability is 0.985.

6 Conclusion

In this study, the FE method has been established to perform the dynamic gust response analysis of a simplified aircraft wing model. First six natural frequencies are considered for the gust response study as the power spectral density diminishes with higher frequency range. Failure analysis of composite structure is performed to assess the failure probability of the base model. A reliability analysis was conducted for a composite wing subjected to continuous random gust. For this, gust load was represented by wing root bending stresses, and its probability distribution function was obtained. Monte Carlo simulation was used to handle random variables, and numerical results show that failure probability increases nonlinearly with the growth of RMS gust velocity.

It is observed that the success rate is below the acceptable range for the base model. The modification of the lamination sequence is considered, and failure probability is calculated again. It is observed that with the modification of the lamination sequence, the failure probability reduced and it is within the acceptable range.

Appendix

Table A.1 Sample failure index

1	Stress X	Stress Y	Shear X	Strength	Strength	Strength	g
2	401,151.3	86,797.84	41,013.67	1.23E + 09	90,337,605	66,178,034	−1
3	138,012.4	109,750.3	58,837.44	1.25E + 09	84,377,789	80,236,318	−1
4	112,563.3	73,538.05	103,408.7	1.04E + 09	79,070,863	73,021,476	−1
5	951,786.2	160,006.2	30,854.64	1.22E + 09	81,725,809	67,688,895	−1
6	23,128.1	49,263.65	168,206.2	1.03E + 09	84,451,323	81,083,256	−1
7	941,522.6	159,833.3	31,898.26	1.2E + 09	77,231,433	82,033,068	−1
8	1,506,422	160,806	134,387.1	1.39E + 09	87,221,197	82,911,923	−0.99999
9	2,217,938	40,466.99	144,768.8	1.14E + 09	61,389,979	68,970,014	−0.99999
10	1,105,908	45,493.47	213,074.1	1.1E + 09	87,425,271	77,149,897	−0.99999
11	1,540,061	241,163.3	38,051.89	1.2E + 09	86,792,604	54,968,889	−0.99999
12	2,356,498	29,929.41	187,735.7	1.06E + 09	91,187,309	81,251,512	−0.99999
13	2,436,160	150,225.9	74,459.79	9.73E + 08	79,874,621	72,569,404	−0.99999
14	1,775,837	205,306.9	121,056.8	1.11E + 09	80,983,458	87,974,349	−0.99999
15	3,346,433	192,095.2	42,981.48	1.12E + 09	90,144,578	72,829,447	−0.99999

(continued)

Table A.1 (continued)

1	Stress X	Stress Y	Shear X	Strength	Strength	Strength	*g*
16	1,237,790	72,521.88	223,634.9	1.18E + 09	85,450,125	62,238,419	−0.99999
17	546,138.1	86,031.75	281,387.2	1.18E + 09	91,798,601	76,211,431	−0.99999
18	3,493,641	42,323.16	171,631.3	1.18E + 09	77,783,132	68,977,825	−0.99998
19	262,642.5	75,834.34	298,013.9	1.13E + 09	83,062,112	77,773,890	−0.99998
20	2,354,829	229,962.5	24,160	1.13E + 09	64,372,400	85,230,015	−0.99998
21	3,689,102	173,391.6	127,277.1	1.01E + 09	80,294,048	73,735,580	−0.99998
22	4,978,842	123,911.8	181,979.8	1.3E + 09	77,079,460	86,167,184	−0.99998
23	80,245.52	171,473.3	339,163.3	1.09E + 09	79,240,045	82,956,734	−0.99998
24	3,921,881	163,553.1	201,569.9	1.14E + 09	84,551,745	75,967,414	−0.99998
25	1,265,606	163,452.7	363,795.4	1.21E + 09	81,435,284	85,102,869	−0.99998
26	434,054.5	96,452.5	376,276	1.28E + 09	78,872,300	80,120,513	−0.99998
27	5,081,898	9,256.32	164,585.8	1.14E + 09	88,853,717	76,372,852	−0.99998
28	1,580,984	61,176.75	389,969.7	1.07E + 09	83,822,140	80,917,604	−0.99997
29	469,398.1	39,938.21	395,661.3	1.14E + 09	74,587,737	76,865,455	−0.99997
30	613,988.5	288,373.6	316,655.4	1.01E + 09	79,824,018	82,825,087	−0.99997
31	4,745,057	59,674.38	242,368.2	1.35E + 09	87,934,583	61,958,646	−0.99997
32	4,790,091	224,434.9	134,304.5	1.11E + 09	82,586,012	71,723,634	−0.99997
33	98,208.7	272,921.3	366,708.5	1.13E + 09	81,049,631	83,968,725	−0.99997
34	5,103,056	232,005.5	222,548.9	1.22E + 09	80,178,208	95,259,879	−0.99997
35	4,384,522	246,126.8	228,573	1.19E + 09	83,412,499	68,326,241	−0.99997

References

1. Hoblit FM (1988) Gust loads on aircraft: concepts and applications, AIAA education series. AIAA, Washington, DC
2. Bisplinghoff RL, Ashley H, Halfman RL (1955) Aeroelasticity. Addison-Wesley Publishing, Cambridge, MA
3. Starnes JH, Haftka RT (1979) Preliminary design of composite wings for buckling, strength and displacement constraints. J Aircraft 16:564–570
4. Liu IW, Lin CC (1991) Optimum design of composite wing structures by a refined optimality criterion. Compos Struct 17:51–65
5. Lernet E, Markowitz J (1979) An efficient structural resizing procedure for meeting static aeroelastic design of objective. J Aircraft 16:65–71
6. Liu B, Haftka RT, Akgun MA (2000) Two-level composite wing structural optimization using response surface. Struct Multidiscip Optim 20:87–96
7. Eastep FE, Tischler VA, Venkayya VB, Knot NS (1999) Aeroelastic tailoring of composite structures. J Aircraft 36:1041–1047
8. Penmetsa RC, Grandhi RV (2002) Efficient estimation of structural reliability for problems with uncertain intervals. Comput Struct 80:1103–1112
9. Mahadevan S, Liu X (2002) Probabilistic analysis of composite structure ultimate strength. Am Inst Aeronaut Astronaut J 40:1408–1414
10. Marzocca P, Librescu L, Chiocchia G (2001) Aeroelastic response of 2-D lifting surfaces to gust and arbitrary explosive loading signatures. Int J Impact Eng 25:41–65
11. Aeroelastic Analysis User's guide, MSC.Nastran Version 68, MSC.Software Corporation, 2004.
12. Sinha PK (2006) Composite materials and structures. Department of Aerospace Engineering, IIT Kharagpur, Kharagpur (Web publication)

Seismic Fragility Analysis of a Primary Containment Structure Using IDA

Tushar K. Mandal, Siddhartha Ghosh, and Ajai S. Pisharady

Abstract The seismic fragility of a structure is the probability of exceeding certain limit state of performance given a specific level of hazard. This fragility is typically estimated for multiple hazard levels considering monotonically increasing intensity measures, such as peak ground acceleration (PGA). The seismic safety of the primary/inner containment structure, which is the most important civil engineering structure in a nuclear power plant (NPP) housing the reactor and other major safety related components, is of utmost concern for both old and new NPP. This chapter presents a novel approach of obtaining the seismic fragility curves for a primary containment structure using incremental dynamic analysis (IDA). The limit state of performance selected for these fragility estimations is based on the collapse of the structure. In order to reduce the computation involved, a simple 'stick model' of the containment structure is used for the nonlinear response-history analyses in the multi-earthquake IDA. The seismic fragility curves obtained using the proposed approaches are compared with those obtained using the conventional approach considering an elastic response spectrum and a linear elastic seismic analysis of the structure. The IDA-based fragilities are found to be more realistic than those obtained using conventional methods.

Keywords Fragility analysis • Probabilistic seismic risk analysis • Nuclear containment • Inner containment • Incremental dynamic analysis

T.K. Mandal • S. Ghosh (✉)
Department of Civil Engineering, Indian Institute of Technology Bombay, Mumbai, India
e-mail: sghosh@civil.iitb.ac.in

A.S. Pisharady
Siting & Structural Engineering Division, Atomic Energy Regulatory Board, Mumbai, India

S. Chakraborty and G. Bhattacharya (eds.), *Proceedings of the International Symposium on Engineering under Uncertainty: Safety Assessment and Management (ISEUSAM - 2012)*,
DOI 10.1007/978-81-322-0757-3_21,

1 Introduction

The objective of seismic probabilistic safety assessments (PSA) for nuclear power plants is to examine the existence of vulnerabilities against postulated earthquake hazards [7]. It involves assessing the plant's (or its components') safety numerically, in a probabilistic framework, so that appropriate measures can be taken to enhance an NPP's safety level, if needed. One of the major components in the seismic PSA of an NPP is the seismic fragility evaluation. Seismic fragility is defined as the conditional probability of failure for a given seismic intensity level. These fragilities are typically expressed using fragility plots, where these conditional probabilities are plotted against varying values of seismic intensity. Seismic fragility can be defined both at the component level and at the system level in an NPP. Fragility definitions also depend on how failure is defined while estimating the probability of failure.

India has 20 operational nuclear reactor units, 18 of which are pressurized heavy water reactor (PHWR) with the earliest dating back to 1973. All of these are located in moderate seismic zones (Zones 2 and 3 as per the current seismological intensity map of India), except for those in Narora, UP, which is in Zone 4 (IS 1893–2002). Seismic re-evaluation of these reactors, including those in moderate seismic zones, is an extremely important task, considering several factors, such as:

1. A change in the seismicity of the site based on newer information
2. Requirement of checking the safety level for greater seismic hazard than the original design basis
3. Lack of seismic design or, more commonly, poor seismic design and detailing not meeting current standards
4. Low-level analysis adopted in the original qualification (many a times owing to a lack of computational tools necessary to perform high-level analyses)

2 Conventional Seismic Fragility Analysis

Seismic fragility analyses of nuclear power plant structures and other critical components typically adopt the method proposed by Kennedy and Ravindra [8]. In their pioneering work on seismic fragility analysis, they stated that the objectives of a seismic PSA were to estimate the frequencies of occurrence of earthquake-induced accidents and to identify the key risk contributors so that necessary risk reductions could be achieved. They identified the component fragility analysis to be a major part of the seismic PSA (other parts being seismic hazard analysis, system-level analysis, accident sequence identification, etc.). Among many others, two major achievements of this work were in the identification of different levels of damage and in the treatment of system-level fragilities separately from component-level fragilities.

In this fragility analysis approach, the conditional probability of failure is computed as [1, 2]

$$P_f = \Phi\left(\frac{\ln\left(\frac{a}{A_m}\right) + \beta_U \Phi^{-1}(Q)}{\beta_R}\right) \tag{1}$$

where P_f is the conditional probability of failure for an earthquake intensity given by its peak ground acceleration (PGA) $= a$, A_m = median ground acceleration capacity of the structure/component and Q = confidence level in terms of non-exceedance probability. A_m is related to the actual ground acceleration capacity parameter, $A = A_m \varepsilon_R \varepsilon_U$, where $A_m = A_{RBGM} F_m$.

A_{RBGM} is the PGA of review basis ground motion (RBGM) or review level earthquake (RLE). ε_R is the random variable representing the aleatory uncertainties, i.e. inherent randomness associated with ground acceleration capacity. ε_U is the random variable representing epistemic uncertainty in the determination of median value, A_m, i.e. the uncertainty associated with data, modelling, methodology, etc. F_m is the median value of factor of safety, F. ε_R and ε_U are taken as lognormally distributed random variables, with logarithmic standard deviations of β_U and β_R, respectively, and both having unit median.

Once A_{RBGM} is known, determination of median factor of safety, F_m, is the key to derive A_m. Generic expression of F can be written as [10]

$$F = F_1 F_2 F_3 \tag{2}$$

F_1 is a factor representing ratio of capacity to demand and is a strength factor. F_2 corresponds to the level of conservatism in assessing the capacity; it depends primarily on the energy absorption capacity of structure, system or component (SSC) beyond elastic limit. F_3 represents the conservatism associated with calculating demand. Different methodologies for fragility analysis are all about determining the median values of F_1, F_2 and F_3 and selection of corresponding β.

There are numbers of components of an NPP which should remain functional during a seismic event, so it is very difficult to check the seismic qualification of each component individually. Components of a NPP are grouped in a number of categories, and different methods are recommended for their seismic qualification [10].

2.1 Drawbacks of Conventional Methods

The conventional methodologies for seismic fragility analysis have the following drawbacks [5,6]:

1. Though these methods are easy to implement, they require considerable engineering judgement especially in case of selecting of parameters for aleatory and epistemic uncertainties.

2. The use of a double lognormal model is mathematically feasible but doesn't have too strong theoretical basis/background.
3. The use of response spectrum-based methods introduces epistemic uncertainties:
   (a) Response contribution from different modes depends on the accuracy of different modal combination rules.
   (b) In case of nonlinear system, modal analysis is not applicable.

Thus, fragility estimated using conventional methods is not very realistic specifically for nonlinear response of structure.

3 The Proposed Method of Fragility Analysis

This chapter presents a novel approach of obtaining the seismic fragility curves for a primary containment structure using incremental dynamic analysis (IDA). The response of the IC structure, modelled as a 2-D stick, is studied for different types of ground motions.

The important assumptions made for fragility analysis are:

1. Randomness associated with the seismic forces is much more compared to that for structural parameters [3]. Hence, the randomness in seismic forces is considered only, and structural parameters are considered to be deterministic.
2. The structure will behave linearly in shear even while it behaves nonlinearly in flexure. It is done as we do not want the stick model to be failed in shear.
3. Prestressing forces are considered as uniaxial compression for the simplified stick model.
4. Reinforcement orientation in the dome portion is taken vertically for each element though it is not the case in actual, assuming that this will not affect too much in final result of the analysis as maximum strain and interstorey drift ratio usually occurs at the base of the cantilever kind of structure.
5. Openings are not considered for the stick model though it can be done by manually selecting some equivalent reduced sectional properties at the location opening. The reason behind that procedure of taking reduced section will work well during linear behaviour of structure, but it will not work beyond that as nonlinear behaviour depends largely on the actual section geometry which cannot be resembled using equivalent reduced section, and our main motive is to do nonlinear response-history analysis (NLRHA).

The basic steps of fragility analysis are:

1. Choose the ground motion data comparing its response spectrum with the design spectrum of the site and the seismological location of the site, i.e. either intraplate or at plate boundary.
2. Prepare the mathematical model appropriate for NLRHA.

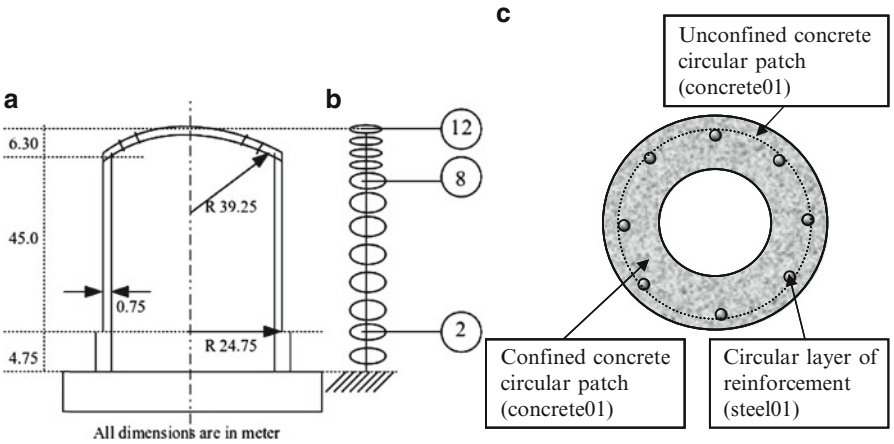

Fig. 1 (**a**) Containment structure and (**b**) its stick model, (**c**) sample fibre section (not to scale)

3. Do the incremental dynamic analysis which is basically a set of NLRHA for all ground motion data.
4. Calculate the probability of exceedance of particular limit states from the output of IDAs, and plot it to obtain fragility plot.

4 Modelling of the Structure

4.1 Description of Structure

The IC structure considered for this study consists of a prestressed concrete cylindrical wall capped by a segmental prestressed concrete dome through a massive ring beam. The containment shell is supported on a circular raft. The typical containment structure considered for the study is depicted in Fig. 1a. The containment structure responds to seismic excitation like a cantilever beam with a circular cross section. The segmental dome along with the ring beam acts to stiffen the circular cross section and also adds to the mass of the system.

4.2 Mathematical Model

The inner containment structure is idealized as a system of lumped masses at elevations of mass concentrations, connected by two-dimensional BeamColumn elements with actual section geometry other than the zone of openings. The structure is assumed to be fixed at the top of the raft foundation. The earthquake

excitation is constrained along a single horizontal direction only. The stick model of a containment structure so developed is also shown in Fig. 1b. Nonlinearity of the system is modelled in the programme *OpenSees* [9] using *NonLinearBeamColumn* element. Concrete is modelled using *Concrete01* and reinforcing steel as *steel01* in *OpenSees*. Sections at different levels are defined as *fibre* sections (Fig. 1c) with circular concrete patch and circular layer of reinforcements. As stick model made of single *fibre* section at each level cannot directly take the shear deformation, the shear-deformation behaviour is incorporated using *SectionAggregator* command. A different uniaxial elastic material is defined as the slope of stress-strain plot as GA_s, where G is the shear modulus of concrete and A_s is the shear area of the containment cross section. The *SectionAggregator* command is used to combine this material with *fibre* section previously defined with actual geometrical properties. This section is used to model the element at that level. The gravity load is calculated for each element and applied as nodal load on the upper node of each two-noded element. The average prestress is taken as 10 MPa. Total prestressing force is calculated by multiplying the prestress with the average cross section area, and it is applied as compressive force at top-most and bottom-most node.

5 Incremental Dynamic Analysis

Incremental dynamic analysis [12] is an emerging analysis method offering detailed seismic demand and capacity prediction capability through a series of NLRHA for multiple scaled ground motion. Results of IDA are presented as IDA plots. A single IDA plot is basically the variation of maximum structural response at different intensity of a scaled ground motion. Maximum structural response is known as damage measure (DM), and intensity of ground motion is known as intensity measure (IM). After analysing the structure for multiple ground motion data, the results are plotted on a single paper and the generated plot is known as multi-IDA plot.

5.1 Ground Motions Considered

The containment is assumed to be in the stable continental region of Indian peninsula. Considering this, ground motion records selected for performing a multi-IDA of this containment structure are sourced from recorded earthquakes in similar seismic regions across the world. 5% damped elastic response spectra of these records are compared with the design spectrum of the site, and those varying significantly from this design spectrum are filtered out. Details of

Table 1 Summary of ground motion data considered

Record name	No. of records	Event	Component	Epicentral distance, km	PGA-range, g
GM-1 to 2	2	Bhuj, 2001	Horizontal	Unknown	0.08–0.08
GM-3	1	Koyna, 1967	Horizontal	Unknown	0.474
GM-4 to 25	22	Saguenay, 1988	Horizontal	45–167	0.002–0.174
GM-26 to 32	7	Miramichi, 1982	Horizontal	11–23	0.125–0.575

Table 2 Limit states

Damage measure	LS-1	LS-2	LS-3	Reference
Drift	0.004	0.006	0.0075	FEMA-356 [4]
Plastic rotation (θ_P)	0.0015	0.005	0.005	FEMA-356 [4]
Curvature (obtained from θ_P)	0.00015	0.00025	0.00025	FEMA-356 [4] and Priestley [11]
Compressive strain	0.002	0.0035	0.005	IS-456 and Priestley [11]
Tensile strain	0	0.00014	0.013	OpenSees Concrete02 model

ground motions considered for study are provided in Table 1. The PGA of a ground motion data is adopted to be the intensity measure (IM) for the IDA. Based on previous literature on fragility analysis of nuclear containment structures, a maximum PGA of 5.0 g is considered. For successive NLRHA, the PGA is incremented by 0.075 g on a trial basis. For numerical convergence, this increment is modified as discussed later.

5.2 Structural Limit States Considered

The limit states of the containment structure subjected to seismic loading considered in the study are tensile cracking of concrete, crushing of concrete in compression, interstorey drift ratio (IDR) and plastic rotation of section.

1. The tensile and compressive strains developed at the innermost and the outermost fibre of each section are stored for each scale factor of ground motion and compared with limiting valued specified by FEMA-356 [4]. As FEMA-356 does not consider any tensile strength of concrete, the limiting values for tensile strain are adopted from the material model *Concrete02*.
2. The allowable total (elastic and plastic) IDR values are adopted from Table 6-19 of FEMA-356.
3. The allowable plastic rotation values are adopted from Table 6-7 of FEMA-356. Using Preistley's equation [11] limiting values in terms of curvature is calculated since *OpenSees* provides curvature as output not plastic rotation.

5.3 Numerical Convergence of IDA

As stated by Vamvatsikos and Cornell [13,14], numerical convergence is a very critical issue in performing IDA especially in the zone of higher PGA levels when the structure may reach a state of global dynamic instability. To deal with this, following steps are adopted:

1. The structure is modelled with *NonLinearBeamColumn* element which has capability to track the distributed plasticity across the member section and the length of the member.
2. Instead of single algorithm for solving nonlinear equations, a number of algorithms in sequence are tried. The following algorithms are used in sequence if one fails next one is used:

   (a) Newton-Raphson
   (b) Modified Newton-Raphson
   (c) KrylovNewton – with different combinations of tangents: initial and current
   (d) Broyden
   (e) Newton with line search (for different constants)

3. For a specific ground motion, if all algorithm fails at a particular PGA, it may be due to (1) global dynamic instability or (2) numerical failure. Here, if all the algorithm fails at any particular scale factor, it is assumed that it is global dynamic instability situation not only numerical failure, and the control is sent back to the previous scale factor with updated increment of scale factor equal to 1/10 of the regular increment of scale factor. The procedure of obtaining multi-IDA is illustrated in detail in Fig. 2.

6 Results and Discussion

Eigen value analysis is done only to get an overview of the dynamic properties of the primary containment structure (Table 3).

6.1 IDA Plots from Raw Data and Its Correction

If the raw data obtained from an IDA are plotted, it is sometimes found that there are unexpected large rebounds at high PGA level. Such a rebound is due to single data point being located far off from the other data points of the same IDA (Fig. 3c). This is inconsistent even with the previous and the next data points from structural perspective. Such problematic data points are considered to be points of numerical failure, which has not been detected by the algorithm. The IDA is replotted by

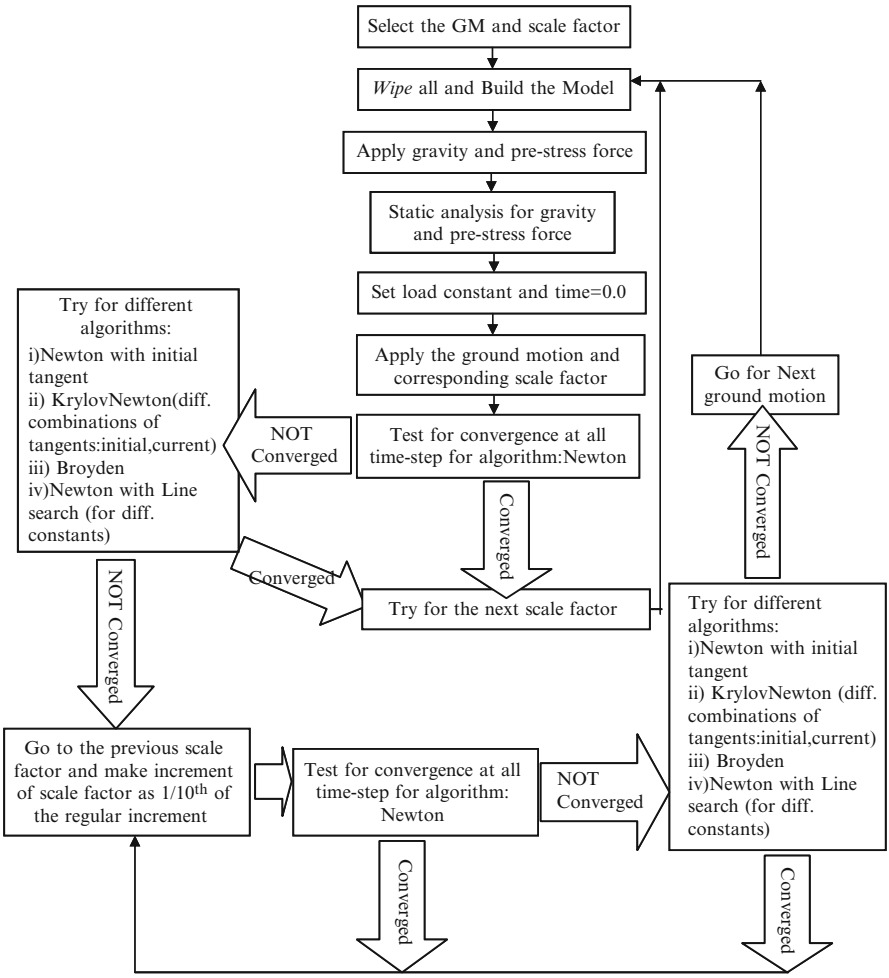

Fig. 2 IDA flow chart

Table 3 Natural period and frequencies of different modes

Mode	T, s	f, Hz
Mode-1	0.1826	5.48
Mode-2	0.0988	10.12
Mode-3	0.0595	16.82
Mode-4	0.0473	21.13
Mode-5	0.0385	25.96

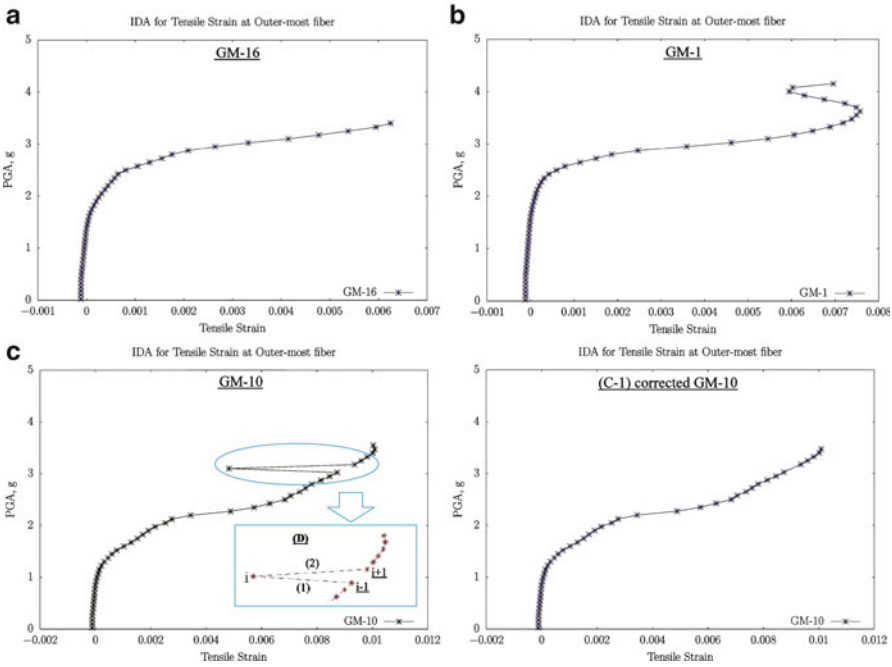

Fig. 3 Sample IDA plots: (**a**) without any rebound (**b**) with realistic rebound (**c**) with unrealistic sharp rebound (C-1) corrected IDA plot with rebound removed

removing these points causing large rebounds by placing some limiting conditions on rate of change in slope of the IDA plot (Fig. 3C-1). The other plots (Fig. 3a, b) are quiet normal as per literature review.

6.2 Fragility Plots

Seismic fragility of a structure, which is the probability of a predefined damage measure (DM) exceeding certain predefined limit states (LS) for a given intensity measure (IM), is calculated as the fraction of IDA curves exceeding the LS at the selected PGA. Fragility analysis results in a set of $P(\text{DM} > \text{LS}|\text{IM})$ vs. IM plots. All the fragility plots so obtained are stepped since a discrete number of ground motion data are used for multi-IDA. The stepped plots are smoothened using weighted cubic spline approximation by increasing the number of ground motion records and reducing the PGA increment for each IDA.

Figure 4 shows fragility plots based on various performance limit states as mentioned earlier in Table 2. Figure 4b, d also show fragility curves based on Eq. (1). Some major observations from these fragility plots are:

- Based on IDR, the fragility is zero up to PGA = 5g (Fig. 4a).
- The fragility, based on plastic rotation (or curvature) limits, is zero up to 2g for LS-1 and up to 3g for LS-2 and LS-3 (Fig. 4b).

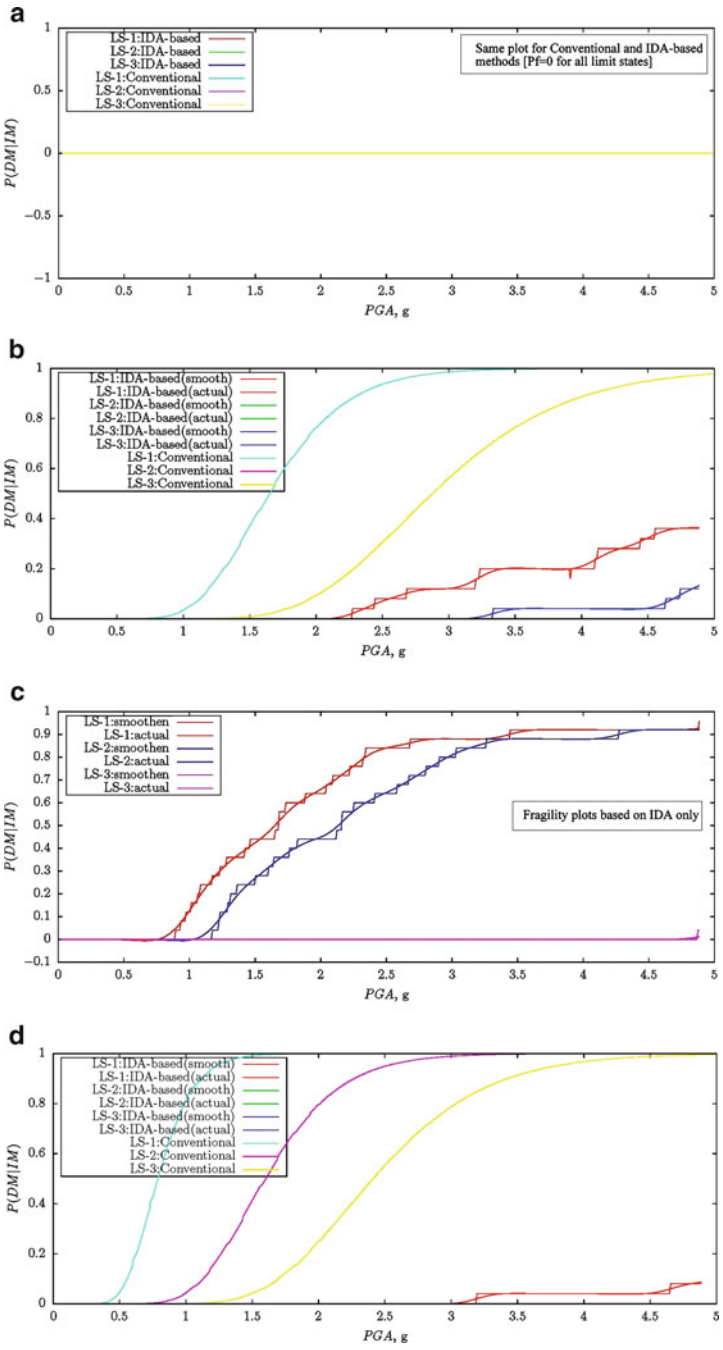

Fig. 4 Fragility plots (IDA-based and conventional methods) (**a**) Fragility for inter storey drift ratio, (**b**) Fragility for curvaturem, (**c**) Fragility for tensile strain at inner-most fiber, (**d**) Fragility for compressive strain at outer-most fiber

- The fragility based on tensile strain at the innermost fibre, which indicates a through crack along the thickness, is almost zero up to PGA = 0.5g for LS-1 (zero tensile strain) and LS-2 (cracking strain) and up to PGA = 5g for LS-3. It reaches almost 0.95 for LS-1 and LS-2 at PGA = 5g (Fig. 4c).
- Fragility curve for concrete crushing is almost zero up to PGA = 5g for all limit states.

Fragilities are also computed for the same containment using Eq. (1). A_{RBGM} is adopted as 0.214g for this PHWR. The median value of F_1 is obtained from a linear elastic analysis. The standard deviations for uncertainties and randomness are based on the recommendations of Pisharady and Basu [10]. The fragility plots obtained this way are significantly different from those obtained using multi-IDA (e.g. Fig. 4b, d). Since the linear elastic analysis shows no tensile strain at the RBGM or design PGA level, the through crack fragility based on conventional method is zero even at PGA = 5g. This shows the unrealistic nature of the fragility curves using the conventional method.

7 Conclusions

Primary containment structures are found to have almost zero fragility considering limit states based on IDR and crushing of concrete. But these structures have very high probability of failure in terms of through crack formation, which results in radiation leakage. The IDA-based fragility curves are found to be more realistic than fragility curve obtained using conventional method. This is primarily due to the fact that the effect of nonlinearities is directly incorporated in IDA-based estimation of fragility. However, it should be noted that the IDA-based fragilities shown here do not include uncertainties associated with structural modelling. Future works in this area should focus on reducing the model uncertainty by using detailed structural model, soil-structure interaction and larger number of earthquake records.

References

1. Bhargava K, Ghosh AK, Agrawal MK, Patnaik R, Ramanujam S, Kushwaha HS (2002) Evaluation of seismic fragility of structures – a case study. Nucl Eng Des 212(1–3):253–272
2. Bhargava K, Ghosh AK, Ramanujam S (2005) Seismic response and failure modes for a water storage structure – a case study. Struct Eng Mech 20(1):1–20
3. Ellingwood BR, Celik OC, Kinali K (2007) Fragility assessment of building structural systems in mid-America. Earthq Eng Struct Dyn 36(3–5):1935–1952
4. FEMA-356 (2000) Prestandard and commentary for the seismic rehabilitation of buildings. Federal Emergency Management Agency, Washington, DC
5. Gupta S, Manohar CS (2006) Reliability analysis of randomly vibrating structures with parameter uncertainties. Ph.D. thesis, Indian Institute of Science, Bangalore, pp 1–407

6. Gupta S, Manohar CS (2006) Reliability analysis of randomly vibrating structures with parameter uncertainties. J Sound Vib 297(3–5):1000–1024
7. Hari Prasad M, Dubey PN, Reddy GR, Saraf RK, Ghosh AK (2006) Seismic PSA of nuclear power plants: a case study, BARC/2006/015, BARC
8. Kennedy RP, Ravindra MK (1984) Seismic fragilities for nuclear power plant risk studies. Nucl Eng Des 79(1):47–68, 38
9. McKenna F, Fenves GL (2001) Opensees command language manual, version 1.2, Pacific Earthquake Engineering Research Center, University of California, Berkeley, USA.
10. Pisharady AS, Basu PC (2010) Methods to derive seismic fragility of npp components: a summary. Nucl Eng Des 240(11):3878–3887
11. Priestley MJN (1997) Displacement-based seismic assessment of reinforced concrete buildings. J Earthq Eng 1(1):157–192, Cited By (since 1996): 62
12. Rizkalla SH, Lau BL, Simmonds SH (1984) Air leakage characteristics in reinforced concrete. J Struct Eng 110(5):1149–1162
13. Vamvatsikos D, Cornell CA (2002) Incremental dynamic analysis. Earthq Eng Struct Dyn 31 (3):491–514
14. Vamvatsikos D, Cornell CA (2004) Applied incremental dynamic analysis. Earthq Spectra 20 (2):523–553

Nanotoxicology: A Threat to the Environment and to Human Beings

D. Dutta Majumder, Sankar Karan, A. Goswami, and N Banerjee

Abstract Nanotechnology research and development is directed towards the understanding and control of matter at dimension of roughly 1–100 nm. At this size, the physical, chemical, and biological properties of materials differ in fundamental and potentially useful ways from the properties of individual's atoms and molecules. Its applications advanced very quickly while very little has been done to measure and assess the risks of nanoparticles (NPs) to biological systems and to the ecosystems. In the year 2000, the National Nanotechnology Initiative (NNI) was formed to ensure public confidence in the field of nanotechnology research, engineering and manufacturing of nanoscale product. In this chapter, we present different kind of nanotoxicology studies to examine the environment and health risks associated with nanoparticles exposure. We also point the penetration of nanoparticles into human body via various routes and interact with the system with their toxic properties that depends on surface chemistry, particle size, surface

D. Dutta Majumder (✉)
ECSU, Indian Statistical Institute, 203, B.T. Road, Kolkata 700108, India

Institute of Cybernetics Systems and Information Technology, 155,
Ashoke Garh, Kolkata 700108, India
e-mail: duttamajumder.isi@gmail.com

S. Karan
Institute of Cybernetics Systems and Information Technology, 155,
Ashoke Garh, Kolkata 700108, India

Institute of Radiophysics and Electronics, C.U., 92, APC Road, Kolkata 700006, India
e-mail: sankar.karan@gmail.com

A. Goswami
Biological Science Division, ISI, 203, B T Road, Kolkata 700108, India
e-mail: agoswami@isical.ac.in

N. Banerjee
Department of Health and Family Welfare,
Sastha Bhawan, Kolkata 700091, India
e-mail: nupur.special.eng@gmail.com

S. Chakraborty and G. Bhattacharya (eds.), *Proceedings of the International Symposium on Engineering under Uncertainty: Safety Assessment and Management (ISEUSAM - 2012)*,
DOI 10.1007/978-81-322-0757-3_22,

charge, and surface area. Nanoparticles of oxides like Sio_2 produced and characterised in our laboratory were tested against insect's pests and pathogens. Nano silica against insect pests shows nearly 100% mortality.

Keywords Nanotechnology • Risk assessment • Capped nanoparticles • Nanotoxicology • Environmental risk and hazards • Occupational safety • Environmental risk management

1 Introduction

Nanotechnology, the science and technology of controlling matter and energy at the nanoscale (1–100 nm), promises to have far reaching impacts on the science and technology industry in areas ranging from consumer products to health care to transportation [1]. The present challenge facing nanotechnology is to manipulate matter at dimension of roughly 1–100 nm (10^{-9} m) in a controlled way to create new substances with very special properties. Industry thinks the technology holds promise to change every fact of life in some way. Substances at nanoscale, or nanoparticles, demonstrate novel physiochemical properties compared to large particles of the same substance. Their use, thus, helps to improve products. But there has not been any significant contribution as far as our knowledge goes to measure and assess the risk to human health [2] and the environment [3]. The Royal Society of London [4] appointed a committee to make a study on the subject, the report of which indicated the importance and need for extensive study on the subject. The National Nanotechnology Initiative (NNI), USA has been taken the initiative in the year 2000 for protecting human health, and the environment [5, 6] from risk and hazards generated due to nano research, engineering and manufacturing.

1.1 Background and Perspective

In the evolution of nanotechnology, manufactured nanomaterials are an important step towards a long-term vision of building objects atom-by-atom and molecule-by-molecule with processes such as self-assembly [7] or molecular assemblers [8]. Innovations in analytical and imaging technologies first paved the way for perceiving, measuring, and manipulating nanoscale objects [9, 10], typically defined as those having a characteristic dimension <100 nm. The ability to design materials at the nanoscale is now leading to the rapid development of an industry that provides nanomaterials for a range of industrial and consumer products. Overall nanotechnology has revolutionised the industry. At present, there are more than 200 nanoparticle-based products worldwide. Separate researches on the ill effects of nanoparticles are being carried out. But most are inconclusive

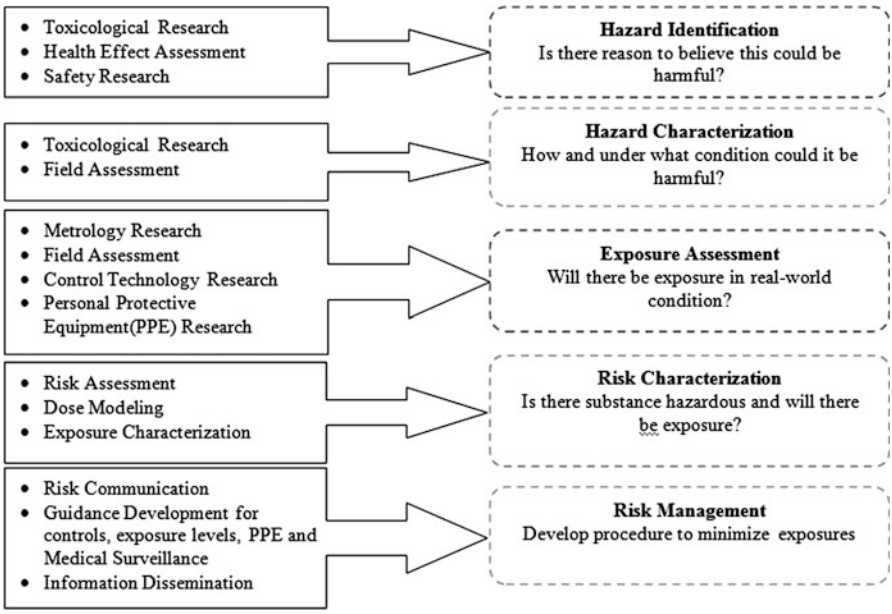

Fig. 1 Important steps to management of risk involved with nanotechnology

still. However, there is evidence that some nanoparticles are harmful [11] and regulations on their use are essential. In 2009, the Drug Controller General of India (DCGI) recalled Albupax, a nano-based medicine for breast cancer. US firm Abraxis BioScience had complained against the maker that the drug damaged the liver [12]. The generic failed the DCGI test. In medicines, nanoparticles are so tiny that they can pass through the blood-brain barrier [13]. They may be toxic, but this is little understood. Carbon as graphite used in pencils is innocuous, but carbon nanotubes show alarming similarities to asbestos [14]. Nanoparticles of zinc and titanium oxide damage DNA in cell lines [15], found IITR. The two are important constituents of sunscreen lotions. Nanosilver has antibacterial properties [16], but its unrestricted use weakens children's ability to fight infections. Nanoparticles accumulate in the environment and kill the beneficial bacteria [17]. To understand the impact of nanoparticles on human health, the U. S. Food and Drug Administration (FDA) established a nanotechnology task force in 2006 [18]. In January this year, it issued draft guidelines on safe use of nanoparticles in consumer products. The US EPA, through its Toxic Substances Control Act, keeps a tab on the manufacturing of nano-based products in the country. European Commission's REACH, a regulatory framework for chemicals, has not suggested a policy that covers nanomaterial, but it does call them substances that need to be tested (Fig. 1).

2 Materials and Methods

Silica nanoparticles were synthesised [19] and characterised in the laboratory and tested against insect's pests and pathogens. Although there are not yet international definitions of NMs and their sizes, aggregates with overall dimension in the μm range but made of primary particles of <100 nm would be regarded as nanoparticles. From the toxicological point of view, particles with diameter 10–2.5 μm are defined as coarse particles, for diameter of 2.5 μm or less are fine particles, and for less than 0.1 μm (<0.1 μm) as ultrafine particles. NPs are particles with sizes between 0.1 and 100 nm (diameter) but provide a very large surface to volume ratio [20]. The surface properties of NPs and their biocompatibility depend on the charges carried by the particle and its chemical reactivity. It has been shown that polycationic macromolecules have a strong interaction with cell membranes in vitro. Also, the interaction of NPs with the surface lining layers of biological tissues is determined by their surface chemistry and reactivity.

2.1 Mechanisms Behind Toxicity of Nanomaterial

Nano-sized particles can penetrate the human body via various routes and could persist in the system because of the incapability of the macrophages to phagocytose [21] them. Whether these persisting nanomaterial react with the body, stay inert, or interact with the system will govern their toxic properties and is primarily dependent on their surface properties.

2.1.1 Surface Chemistry

The role of surface chemistry had been underemphasized in the present research of nanotoxicity. Whether the particle remains suspended as an individual particle or as an aggregate depends upon its surface chemistry [22]. A small aggregate or single particle is presumed to be more toxic than an aggregate of nano-sized particle(NSPs) as the relative surface area could change, determining whether the material has a good wetting characteristic or has a surface characteristic that catalyses specific chemical reactions or remains passive and allows fibrous tissue to grow on its surface. It was shown that the rats, when treated to polymeric vapours of polytetrafluoroethylene (PTFE) [23] having a diameter of 18 nm, suffered severe lung injury with high mortality rate of within 4 h after a 15-min inhalation exposure to 50 $\mu g/m^3$.

2.1.2 Particle Size

Nanoparticles may be surrounded by water molecules and may or may not get agglomerated when present in fluid medium, which, in turn, will govern the

diffusion of species. The diffusion coefficient of the particles can be derived using the well-known Stokes–Einstein equation as

$$D = \frac{K_B T}{6\pi\eta R} \tag{1}$$

Equation 1, where R is the hydrodynamic radius, T is the absolute temperature, η is the viscosity, and K_B is the Boltzmann constant. The aggregation of the particles can also be quantified using the following simple formulation:

$$\frac{dn_t}{dt} = \frac{1}{2}\frac{\beta}{W} n_t^2 \tag{2}$$

If dn_t/dt is the mono disperse particle population and β is the aggregation rate constant, then Eqs. 2 and 3 can be used to derive the characteristic time of a doublet formation τ from initial particle concentration (Eq. 2), where W is the stability ratio relating the steric and electronic hindrance towards the aggregation and gives the ratio of the aggregation constant of diffusion limited cluster aggregation and the observed aggregation constant. The time for doublet formation which gives a measure of the agglomeration is given in Eq. 3:

$$\tau = \frac{2W}{\beta} = \frac{3\eta W}{4K_B T n_0} \tag{3}$$

2.1.3 Surface Charge

It can be noted that the particle size has an effect on the stability constant, and this can be altered by small changes on the particle surface, such as charge distribution. The surface potential (ΔV) of a monolayer spread at the air/water interface can be interpreted using the Helmholtz Eq. 4

$$\Delta V = \frac{\mu_0}{\varepsilon_0 A} \tag{4}$$

$$\mu_n = \mu_0 + \mu_W \tag{5}$$

where μ_n is the effective molecular dipole moment at the interface, ε is the vacuum dielectric permittivity, and A is the surface area per molecule. It is important to study, whether NPs can cross this phosphor-lipid membrane barrier and/or interact with it will decide the level of toxicity. A particle having a high affinity for phosphates may or may not react with the phospholipid membranes. Such being the case, monolayers of particles spread at the phospholipid membrane can be treated as a Vogel Mobius two capacitor model [24, 25], an effective molecular

dipole moment is given by Eq. 5, where μ_w represents the contribution of the tail group and μ_α represents the contribution from the head group of a phospholipid. These contributions can be directly influenced by the surface charge present on the molecule and the complex forming ability of the particle with the phospholipid. Zeta potential (ζ) [26] and ultraviolet-visible-spectroscopy measurements may thus provide an estimate of adsorption of proteins. The particles having mobility V_E in body fluid media which becomes an important parameter and is given by the Smoluchowski Equation

$$V_E = 4\pi\varepsilon_0\varepsilon_r \frac{\varsigma}{6\pi\eta}(1 + kr) \tag{6}$$

where ε_r and ε_0 are the relative dielectric constant and the electrical permittivity of a vacuum, respectively, η is the solution viscosity, r is the particle radius, and $\kappa = (2n_0z^2e^2/\varepsilon_r\varepsilon_0k_BT)^{1/2}$ is the Debye–Hückel parameter, n_0 is the bulk ionic concentration, z is the valence of the ion, e is the charge of an electron, k_B is the Boltzmann constant, and T is the absolute temperature.

2.1.4 Particle Shape

When developing NPs as catalysts, their shape is very important. For a certain volume of material, NPs make best catalysts when they have a large surface area. It is a challenge to find the shape that has the largest surface area for its volume. The perception of shape has been used for pattern recognition, computer vision, shape analysis [27], and image registration. Here, we used Dutta Majumder's generalised method of shape analysis and shape-based similarity measures, shape distance, and shape metric to measure the NPs shape.
The shape of an object can be defined as a subset X in R^2 if

1. X is closed and bounded.
2. Interior of X is nonempty and connected.
3. Closure property holds on interior of X.

This representation of shape remains invariant with respect to translation, rotation, and scaling. Moreover another object Y in R^2 is of same shape to object $X \in R^2$ if it preserves translation, rotation, and scaling invariance. In terms of set, these three transformations can be represented as

$$\text{Translation: } Y = \{(x + a), (y + b) : x, y \in X\} \tag{7}$$

$$\text{Rotation: } Y = \{P1(\alpha).P2(\beta)X\} \quad \text{where } P1 \,\&\, P2 \text{ are rotation around } x \text{ and } y \text{ axes} \tag{8}$$

$$\text{Scaling: } Y = \{(kx, ky) : x, y \in X\} \tag{9}$$

Distance d_1 between shape X and Y in F is defined as follows:

$$d_1(X,Y) = m_2[(X - Y) \cup (Y - X)] \tag{10}$$

where m_2 is Lebesgue measure in R^2 and d_1 satisfies following rules:

1. $d_1(X,Y) \geq 0$
2. $d_1(X,Y) = 0$ if and only if $X = Y$
3. $d_1(X,Y) = d_1(Y,X)$
4. $d_1(X,Y) + d_1(Y,Z) \geq d_1(X,Z.)$

We consider that two nanoparticles are of same shape if and only if one of the images is translation, scaling, and rotation of other.

2.2 *Exposures to Nanomaterial: Most Likely Routes*

All substances in the world are toxic at some exposure levels. Currently, very little is known about the interaction of nanoparticles in biological systems [28, 29]. Initial toxicology experiments have shown that some types of nanoparticles can enter the body, affect organ function, and possibly lead to health problems. But these experiments must be repeated many times under precisely controlled conditions using specific types and concentrations of nanoparticles to identify short-term and long-term health effects of different kinds of nanoparticles on human health. This research should study the response of living organisms to the many different kinds of nanoparticles that have different chemical compositions, sizes, shapes, and surface areas [20] (Fig. 2).

2.3 *Life Cycle Analysis (LCA) Modelling: Potential Impact Indicators*

Goal and scope definition defines the goal and intended use of the LCA (life cycle analysis) [30–33] and scopes the assessment concerning system boundaries, function and flow, required data quality, technology, and assessment parameters. We define the following parameter for analysis.

2.3.1 Life Cycle Inventory Analysis (LCI)

We define LCI as an activity for collecting data on inputs (resources and intermediate products) and outputs (emissions, wastes) for all the processes in the product system.

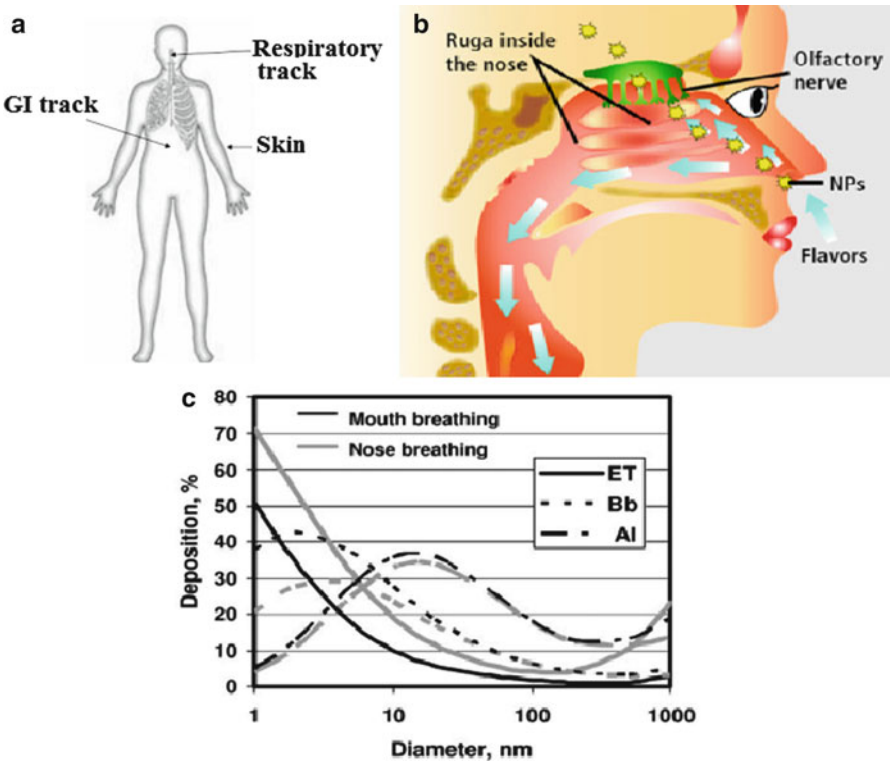

Fig. 2 (**a**) Different track of NPs expose. (**b**) The passage of nanoparticles (NPs) from the nose to the cerebral system via the cibriform plate, which separates the nasal sinus from the brain and protects the nasal nerves and nervous receptors. (**c**) Deposition of NPs in mouth and nose breathing with diameter

2.3.2 Life Cycle Impact Assessment (LCIA)

We define LCIA [34, 35] as the phase of the LCA where inventory data on inputs and outputs are translated into indicators about the product system's potential impacts on the environment, on human health, and on the availability of natural resources.

Interpretation is the phase where the results of the LCI and LCIA are interpreted according to the goal of the study and where sensitivity and uncertainty analysis are performed to qualify the results and the conclusions (Fig. 3).

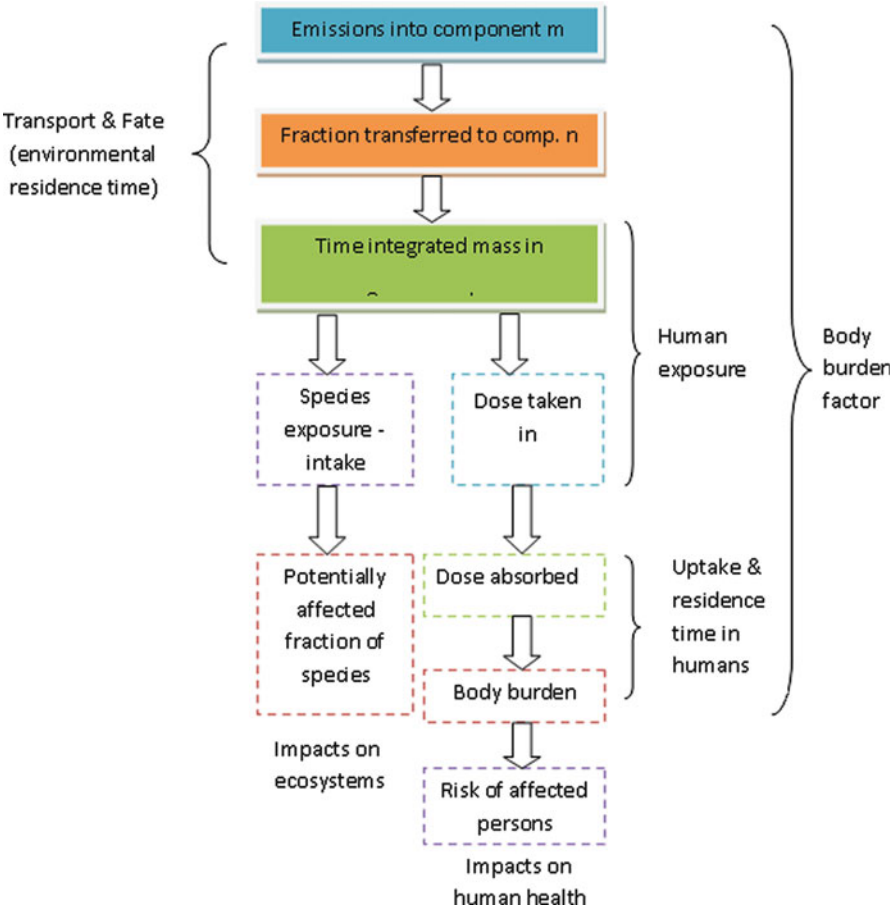

Fig. 3 Framework for assessment of toxic impacts in LCA

2.4 Damage Amount Analysis: A Case Study of SWNT (Fig. 4)

2.5 The Risk Model: Evaluation, Characterisation, and Reduction Using Genetic Algorithm (Fig. 5)

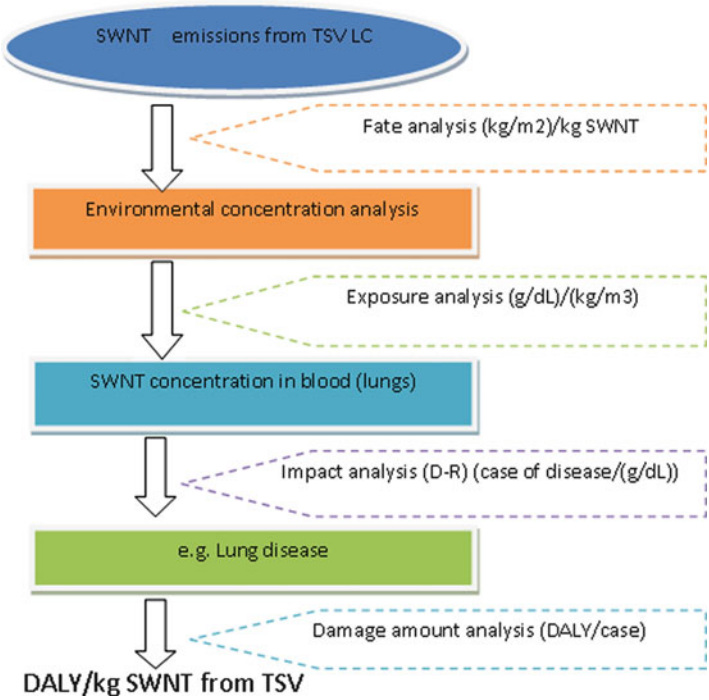

Fig. 4 Flow diagram for emitted SWNT from TSV (DALY/kg)

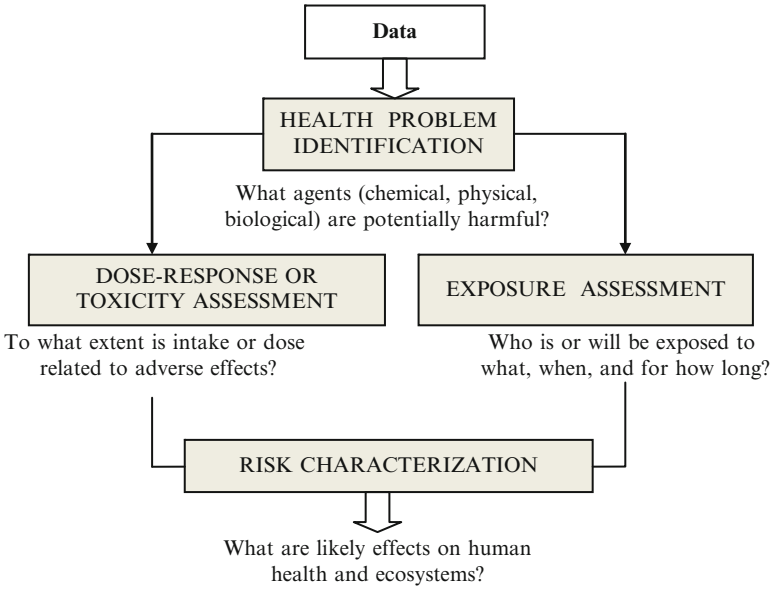

Fig. 5 Data analysis flow chart for risk evaluation for human health and ecosystem

3 Experimental Details

In this study, diatomaceous earth (DE) was used to design amorphous nano-sized hydrophilic, hydrophobic, and lipophilic silica in 15–30 nm size range. Surface-functionalized silica nanoparticles (SNP) are a viable alternative to conventional pesticides. Entomotoxicity of SNP was tested against rice weevil, *Sitophilus oryzae*, and its efficiency was compared with bulk-sized silica (individual particle larger than 1 μm). Amorphous SNP was found to be highly effective against this insect pest causing more than 90% mortality, indicating the effectiveness of SNP to control insect pests. On one hand, we studied the health and environmental hazards of NPs, and parallelly, we established the entomotoxic effect of silica NPs against *Sitophilus oryzae*. Insects *S. oryzae* were reared on whole rice grain (IR64) at 30C±1C, 75±5% r.h. in continuous darkness (insects were inbred in our laboratory by sib-mating for 20 generation). The r.h. was maintained by using saturated solution of sodium chloride. Adults less than 2 weeks old were used for the experiments.

Hydrophilic spherical SNPs of different size were synthesised in the laboratory by sol-gel method from aqueous alcohol solution of silicon alkoxide. First, aqueous ethanolic solution of silicon alkoxide was subjected to ultrasonication for 10 min. Next, a known volume of TEOS was added and the mixture was sonicated for another 10 min. At the end of the process, 24% NH_4OH was added as a catalyst to promote the condensation reaction. Sonication was continued for a further 30 min to get a white turbid suspension. The reaction was performed at room temperature. The size of the spherical monodispersed SNP could be varied by varying the concentration of the reactants. The size of the SNP obtained depends on the chain length of the alcohol used. The SNPs were lyophilized after synthesis and washed several times with double distilled water to remove all trace of ammonium hydroxide used in the process of synthesis as catalyst. Particle size of SNP synthesised in our laboratory was measured by field emission scanning electron microscope (FE-SEM, FEI Quanta 200 F, FEI, USA) in the central instrumental facility of Indian Institute of Technology (IIT), Roorkee, India (Fig. 6).

The bioassay on *S. oryzae* was performed in small plastic screw-capped jars. Twenty grams of rice (IR64) was placed in each jar. Rice in each jar was treated individually with custom-made SNPs (hydrophilic, hydrophobic, and lipophilic), laboratory-made hydrophilic modified stober SNP (average particle size 30 nm), and bulk size silica at three doses rate 0.5, 1, and 2 g kg^{-1} rice. The jars were kept for 24 h before 20 unsexed adults of *S. oryzae* were introduced into each jar. All bioassays were performed at 30°C±1°C, 75±5% r.h. Insect mortality was checked after 1, 2, 3, 7, and 14 days. Data analysis has been performed as per Table 1, 2, 3, 4, and 5 where insect mortality as the response variable and treatment, dose, and exposure interval were the main effects.

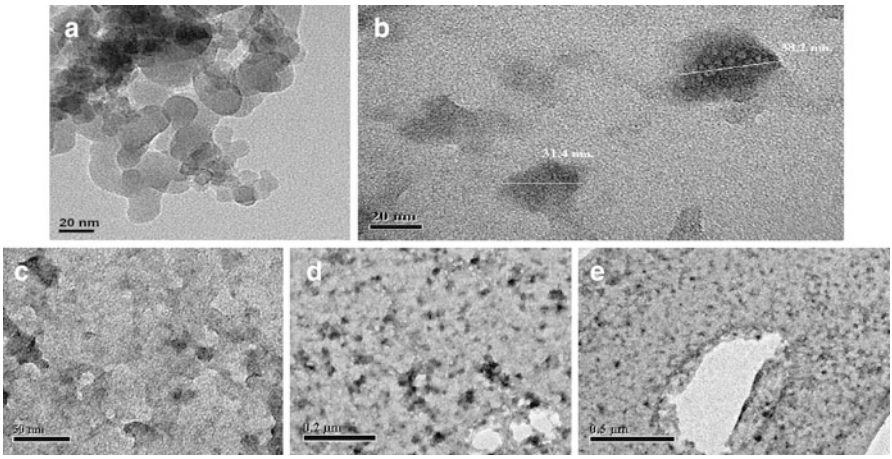

Fig. 6 Electron micrographs of custom-made silica nanoparticles. (**a**) Average diameter 20 nm. (**b**) Individual silica NPs 31.4 and 38.2 nm. (**c**) Average diameter 50 nm. (**d**) Average diameter 0.2 μm. (**e**) Average diameter 0.5 μm

Nano silica in insect pests shows nearly 100% mortality. The nanoparticle surface is proposed to be modified by coating the particle with a chemical. These surface changes can totally alter the toxicity of a specific product and have a major impact on nanoparticles' toxicity or safety.

4 Discussion

Nanotechnology is a double-edge sword [36], the same novel properties making nanoparticles attractive, which makes them potentially toxic. In the risk assessment study, our hypothesis at this point is that increase in surface area is the main reason that is associated with nanoparticle exposure hazards [20] since this increase in surface area causes nanoparticles to become more active and show toxic properties that we did not anticipate for such materials, and this surface increase also makes nanoparticles more flammable, increasing the risk of fire and explosion in workplaces. So determining the amount of size and shape [19] of nanoparticle (called critical size and critical shape) existing in a workplace is a necessary hazard prevention step. By identifying leakage sources and applying essential critical steps, we can control and reduce exposure risks associated with nanoparticles. Our occupational safety guidelines can minimise exposure, but until more is known about the potential hazards of nanomaterial, safe-handling practices may be inadequate. There has to be compromise between testing all the possible scenarios for each nanoparticle and creation of standards to unify tests.

Table 1 ANOVA parameters for main effects and their associated interaction

		Day1		Day2		Day3		Day7		Day14	
Source	df	F	P	F	P	F	P	F	P	F	P
Treatment	4	78.15	<0.001	88.07	<0.001	117.21	0.001	94.24	<0.001	121.7	<0.001
Dose	3	282.61	<0.001	593.98	<0.001	786.19	<0.001	667.39	<0.001	809.98	<0.001
Treatment × dose	12	16.87	<0.001	23.74	<0.001	25.69	<0.001	21.25	<0.001	24.04	<0.001

Table 2 Mean mortality (±SE.) of *Sitophilus oryzae* adults exposed for 1 day on rice treated with bulk and nano silica at three dose rates with control

Nanoparticle	0 g/kg	0.5 g/kg	1 g/kg	2 g/kg
SiO_2 – hydrophilic	0.0 ± 0.0 Aa	14.2 ± 6.6 Ba	67.0 ± 8.4 Ca	86.0 ± 7.4 Da
SiO_2 – hydrophobic	0.0 ± 0.0 Aa	6.0 ± 8.2 Aa	7.0 ± 7.6 Ab	42.0 ± 7.6 Bb
SiO_2 – lipophilic	0.0 ± 0.0 Aa	7.9 ± 4.2 Aa	7.0 ± 5.7 Ab	34.0 ± 8.2 Bb
SiO_2 – (modified Stober)	0.0 ± 0.0 Aa	13.2 ± 5.8 Aa	61.0 ± 8.2 Ba	81.0 ± 4.2 Ca
SiO_2 – bulk	0.0 ± 0.0 Aa	3.0 ± 4.5 Aa	7.0 ± 5.7 Ab	17.0 ± 2.7 Bc

Within each column, means followed by the same lower case letter are not significantly different, within each row means followed by the same upper case letter are not significantly different; Tukey–Kramer HSD test; $P = 0.05$

Table 3 Mean mortality (±SE) of *Sitophilus oryzae* adults exposed for 2 days on rice treated with bulk and nano silica at three dose rates with control

Nanoparticle	0 g/kg	0.5 g/kg	1 g/kg	2 g/kg
SiO_2 – hydrophilic	1.0 ± 2.3 Aa	23.3 ± 7.7 Ba	89.0 ± 4.2 Ca	95.0 ± 3.5 Da
SiO_2 – hydrophobic	1.0 ± 2.3 Aa	34.0 ± 6.5 Ba	49.0 ± 9.6 Cb	97.0 ± 2.7 Da
SiO_2 – lipophilic	1.0 ± 2.3 Aa	49.5 ± 8.4 Bb	48.0 ± 5.7 Bb	97.0 ± 4.5 Ca
SiO_2 – (modified Stober)	1.0 ± 2.3 Aa	22.3 ± 5.9 Ba	82.0 ± 5.7 Ca	92.0 ± 7.6 Ca
SiO_2 – bulk	1.0 ± 2.3 Aa	7.0 ± 4.5 Ac	11.0 ± 4.2 Ac	23.0 ± 4.5 Bb

Within each column, means followed by the same lower case letter are not significantly different, within each row means followed by the same upper case letter are not significantly different; Tukey–Kramer HSD test; $P = 0.05$

Table 4 Mean mortality (±SE) of *Sitophilus oryzae* adults exposed for 7 days on rice treated with bulk and nano silica at three dose rates with control

Nanoparticle	0 g/kg	0.5 g/kg	1 g/kg	2 g/kg
SiO_2 – hydrophilic	2.0 ± 2.7 Aa	35.4 ± 8.3 Ba	95.0 ± 5.0 Ca	97.0 ± 2.7 Ca
SiO_2 – hydrophobic	2.0 ± 2.7 Aa	62.0 ± 9.1 Bb	86.0 ± 8.2 Ca	100.0 ± 0.0 Da
SiO_2 – lipophilic	2.0 ± 2.7 Aa	62.4 ± 5.6 Bb	71.0 ± 8.9 Bb	100.0 ± 0.0 Da
SiO_2 – (modified Stober)	2.0 ± 2.7 Aa	35.4 ± 8.3 Ba	94.0 ± 4.2 Cab	97.0 ± 2.7 Ca
SiO_2 – bulk	2.0 ± 2.7 Aa	16.5 ± 5.5 Bc	21.9 ± 6.5 Bc	34.0 ± 5.5 Cb

Within each column, means followed by the same lower case letter are not significantly different, within each row means followed by the same upper case letter are not significantly different; Tukey–Kramer HSD test; $P = 0.05$

Table 5 Mean mortality (±SE) of *Sitophilus oryzae* adults exposed for 14 days on rice treated with bulk and nano silica at three dose rates with control

Nanoparticle	0 g/kg	0.5 g/kg	1 g/kg	2 g/kg
SiO_2 – hydrophilic	4.1 ± 2.3 Aa	42.5 ± 9.1 Ba	96.0 ± 4.2 Ca	100.0 ± 0.0 Ca
SiO_2 – hydrophobic	4.1 ± 2.3 Aa	69.0 ± 9.6 Bb	92.0 ± 6.7 Ca	100.0 ± 0.0 Ca
SiO_2 – lipophilic	4.1 ± 2.3 Aa	69.2 ± 5.8 Bb	89.0 ± 2.2 Ca	100.0 ± 0.0 Ca
SiO_2 – (modified Stober)	4.1 ± 2.3 Aa	41.5 ± 9.7 Ba	95.0 ± 3.5 Ca	99.0 ± 2.2 Ca
SiO_2 – bulk	4.1 ± 2.3 Aa	23.0 ± 5.7 Bc	25.0 ± 6.1 Cb	40.0 ± 6.1 Db

Within each column, means followed by the same lower case letter are not significantly different, within each row means followed by the same upper case letter are not significantly different; Tukey–Kramer HSD test; $P = 0.05$

Although progress has recently been made towards understanding the health and environmental consequences of these materials, challenges remain for future research.

Acknowledgements We are thankful particularly to all engineers and staff of Institute of Cybernetics Systems and Information Technology (ICSIT), all our colleagues at the Biological Science Division, Indian Statistical Institute, Kolkata, ECSU, Indian Statistical Institute, Kolkata, and Department of Radiophysics and Electronics, Calcutta University, Kolkata.

References

1. Wagner V, Dullaart A, Bock AK, Zweck A (2006) The emerging nanomedicine landscape. Nat Biotechnol 24(10):1211–1217
2. Mansson A, Sundberg M, Bunk R, Balaz M, Nicholls IA, Omling P, Tegenfeldt JO, Tagerud S, Montelius L (2005) Actin-based molecular motors for cargo transportation in nanotechnology – potentials and challenges. IEEE Trans Adv Packag 28(4):547–555
3. Matsui Y (2010) Cross-sectional risk assessment of various nano materials and production stages. In: Nanotechnology (IEEE-NANO), 2010 10th IEEE conference, pp 188–191
4. Royal Society, Royal Academy of Engineering (2004) Nanoscience and nanotechnologies: opportunities and uncertainties. The Royal Society and The Royal Academy of Engineering, London
5. Marra J, Den Brink W, Goossens H, Kessels S, Philips Res. Labs, Eindhoven (2009) Nanoparticle monitoring for exposure assessment. IEEE Nanotechnol Mag 3(2):6–37
6. Maynard AD, Pui DYH (2007) Nanoparticles and occupational health. Springer, Dordrecht
7. Vauthey S, Santoso S, Gong H, Watson N, Zhang S (2002) Molecular self-assembly of surfactant-like peptides to form nanotubes and nanovesicles. Proc Natl Acad Sci USA 99 (8):5355–5360
8. Drexler E, Smalley R (1993) Nanotechnology: Drexler and Smalley make the case for and against 'molecular assemblers'. Chem Eng News 81(48):37–42
9. Drexler KE (1985) Engines of creation: the coming era of nanotechnology. Forth Estate, London
10. Drexler KE (1992) Nanosystems: molecular machinery, manufacturing, and computation. Wiley, New York
11. Moore MN (2006) Do nanoparticles present ecotoxicological risks for the health of the aquatic environment? Environ Int 32(8):967–976
12. Arora S, Jain J, Rajwade JM, Paknikar KM (2009) Interactions of silver nanoparticles with primary mouse fibroblasts and liver cells. Toxicol Appl Pharmacol 236(3):310–318
13. Schroeder U, Sommerfeld P, Ulrich S, Sabel BA (1998) Nanoparticle technology for delivery of drugs across the blood–brain barrier. J Pharm Sci 87(11):1305–1307, Wiley
14. Greenemeier L (2008) Study says carbon nanotubes as dangerous as asbestos. Scientific American, 20 May 2008. http://www.sciam.com/article.cfm?id = carbon-nanotube-danger
15. Marissa D, Newman MD, Mira Stotland MD, Jeffrey I, Ellis MD (2009) The safety of nanosized particles in titanium dioxide– and zinc oxide–based sunscreens. J Am Acad Dermatol Sci Direct 61(4):685–692
16. Marambio-Jones C, Hoek EMV (2008) A review of the antibacterial effects of silver nanomaterials and potential implications for human health and the environment. J Nanopart Res 12(5):1531–1551
17. Choi O, Hu Z (2008) Size dependent and reactive oxygen species related nanosilver toxicity to nitrifying bacteria. Environ Sci Technol ACS 42(12):4583–4588

18. Wilson RF (2006) Nanotechnology: the challenge of regulating known unknowns. J Law Med Ethics 34(4):704–713, Wiley
19. Dutta Majumder D, Karan S, Goswami A (2011) Characterization of gold and silver nanoparticles using it's color image segmentation and feature extraction using fuzzy C-means clustering and generalized shape theory. In: Proceeding of the IEEE international conference on communications and signal processing 2011, pp 70–74
20. Duttamajumder D, Karan S, Goswami A (2011) Synthesis and characterization of gold nanoparticle – a fuzzy mathematical approach. In: PReMI2011, Springer, LNCS 6744, pp 324–332
21. Fadok VA, Laszlo DJ, Noble PW, Weinstein L, Riches DW, Henson PM (1993) Particle digestibility is required for induction of the phosphatidylserine recognition mechanism used by murine macrophages to phagocytose apoptotic cells. J Immunol Am Assoc Immunol 151 (8):4274–4285
22. Clift MJD, Rothen-Rutishauser B, Brown DM, Duffin R, Donaldson K, Proudfoot L, Guy K, Stone V (2008) The impact of different nanoparticle surface chemistry and size on uptake and toxicity in a murine macrophage cell line ScienceDirect. Toxicol Appl Pharm 232(3):418–427
23. Lee KP, Seidel WC (1991) Pulmonary response of rats exposed to polytetrafluoroethylene and tetrafluoroethylene hexafluoropropylene copolymer fume and isolated particles. Inhal Toxicol 3(3):237–264
24. Taylor DM, De Oliveira ON Jr, Morgan H (1990) Models for interpreting surface potential measurements and their application to phospholipid monolayers. J Colloid Interface Sci 139 (2):508–518, Elsevier
25. Karakoti S, Hench LL, Seal S (2006) The potential toxicity of nanomaterials—the role of surfaces. JOM J Miner, Met Mater Soc 58(7):77–82
26. Alice S, David E, Liqing R, Dongqing L (2003) Zeta-potential measurement using the Smoluchowski equation and the slope of the current–time relationship in electroosmotic flow. J Colloid Interface Sci 261(2):402–410, Elsevier
27. Dutta Majumder D (1995) A study on a mathematical theory of shapes in relation to pattern recognition and computer vision. Indian J Theor Phys 43(4):19–30
28. Yuliang Zhao, Hari Singh Nalwa (2006) Nanotoxicology – interactions of nanomaterials with biological systems. American Scientific Publishers, Stevenson Ranch
29. Stark WJ (2011) Nanoparticles in biological systems. Angew Chem Int Ed 50(6):1242–1258, General & Introductory Chemistry, Wiley
30. Hellweg S, Hofstetter TB, Hungerbuhler K (2005) Time-dependent life-cycle assessment of emissions from slag landfills with the help of scenario analysis. J Clean Prod 13(3):301–320
31. Hellweg S, Fischer U, Scheringer M, Hungerbuhler K (2004) Environmental assessment of chemicals: methods and application to a case study of organic solvents. Green Chem 6 (8):418–427
32. Ciambrone DF (1997) Environmental life cycle analysis. Lewis Publishers, Inc., Boca Raton
33. Keoleian GA, Menerey D (1994) Product life cycle assessment to reduce health risks and environmental impacts. Noyes Publications, Boca Raton
34. Seppala J (1997) Decision analysis as a tool for life cycle impact assessment. Finnish Environment Institute, Helsinki
35. Sonnemann G (2003) Integrated life-cycle and risk assessment for industrial processes. CRC Press, London
36. Dreher KL (2004) Health and environmental impact of nanotechnology: toxicological assessment of manufactured nanoparticles. Toxicol Sci 77:3–5

Probabilistic Assessment of Strengths of Corrosion-Affected RC Beams

Kapilesh Bhargava, Yasuhiro Mori, and A.K. Ghosh

Abstract Corrosion of reinforcement causes premature deterioration in reinforced concrete (RC) structures and reduces their intended residual service life. Damages to RC structures due to reinforcement corrosion generally manifest in the form of expansion, cracking and eventual spalling of the cover concrete, loss of steel cross-sectional area and loss of bond between corroded reinforcement and surrounding cracked concrete. These damages may sometime result in structural failure. This chapter initially presents predictive models for time-dependent damages in corrosion-affected RC beams, recognized as loss of mass and cross-sectional area of reinforcing bar and loss of concrete section owing to the peeling of cover concrete. Then these models have been used to present analytical formulations for evaluating time-dependent flexural and shear strengths for corroded RC beams based on the standard composite mechanics expressions for RC sections. Further, by considering variability in the identified basic variables that could affect the time-dependent strengths of corrosion-affected RC beams, an attempt is made in this chapter to present simple estimations for the time-dependent mean strengths and time-dependent coefficient of variation (c.o.v.) associated with the strengths for a typical simply supported RC beam. Comparison of presented simple estimations of mean strengths and c.o.v. associated with strengths has been made with those obtained using Monte Carlo simulation.

K. Bhargava (✉)
Architecture & Civil Engineering Division, Bhabha Atomic Research Center, Mumbai, India
e-mail: kapilesh_66@yahoo.co.uk; kapil_66@barc.gov.in

Y. Mori
Graduate School of Environmental Studies, Nagoya University, Nagoya, Japan
e-mail: yasu@sharaku.nuac.nagoya-u.ac.jp

A.K. Ghosh
Health Safety and Environment Group, Bhabha Atomic Research Center, Mumbai, India
e-mail: ccss@barc.gov.in

S. Chakraborty and G. Bhattacharya (eds.), *Proceedings of the International Symposium on Engineering under Uncertainty: Safety Assessment and Management (ISEUSAM - 2012)*,
DOI 10.1007/978-81-322-0757-3_23,

Keywords Reinforcement corrosion • Annual mean corrosion rate • Time-dependent flexural strength • Time-dependent shear strength • Time-dependent c.o.v. Latin hypercube sampling

1 Introduction

The basic safety requirements of a nuclear power plant (NPP) include the safe shutdown of the reactor, to remove decay heat and to limit the release of radioactivity to the environment. Safety evaluation of the structures is an important issue for any NPP, which has to be carried out to take care of number of factors including the ageing effects, if any. As NPP structures age, a number of degradation mechanisms start affecting the load carrying capacity and serviceability of these structures. Some of the degradation mechanisms for RC structures include corrosion of steel reinforcement, alkali-silica reaction, freeze-thaw damage, sulphate attack, etc. Out of these mechanisms, corrosion of steel has been identified as being the most widespread and predominant mechanism responsible for the deterioration of RC structures. Corrosion causes the reduction of reinforcement cross-sectional area which in extreme forms, can be significant enough to reduce the strength of structural members below the minimum requirements. It also results in cracking and spalling of cover concrete due to formation of expansive of corrosion products, and reduction of bond between the corroded reinforcement and concrete, thereby resulting in further structural damage. By proper control and monitoring of the reinforcement corrosion, premature failure of RC structures can be prevented. Also the assessment of performance of corrosion-damaged RC structures to withstand extreme events during their anticipated service life would help in arriving decisions pertaining to the inspection, repair, strengthening, replacement and demolition of such structures.

In this chapter initially, predictive models are presented for the quantitative assessment of time-dependent damages in RC beams, recognized as loss of concrete section owing to the peeling of cover concrete and loss of mass and cross-sectional area of reinforcing bar. Then these models have been used to present analytical formulations for evaluating time-dependent flexural and shear strengths of corroded RC beams based on the standard composite mechanics expressions for RC sections. For the corroded RC beams, loss of flexural and shear strengths would be mainly due to loss of cross section for concrete and reinforcing steel. The scope of flexural strength estimation has been limited to either by the yielding of tensile reinforcement or by the crushing of concrete in compression zone. Although the continued rebar corrosion would also affect the composite action of concrete and reinforcing steel due to bond deterioration between them, the evaluation of time-dependent flexural strength due to loss of bond has not been considered in the present study. The performance of the presented formulations has been evaluated through their ability to reproduce the available experimental trends. This chapter further presents probabilistic assessment of time-dependent strengths for a typical simply supported

corroded RC beam. The basic variables that can affect time-dependent strengths for a corroded RC beam are identified as material strengths of concrete and reinforcement, modulus of elasticity of reinforcing steel plus expansive corrosion products combine, creep coefficient for concrete, dimensions of the beams and annual mean corrosion rate. By considering variability in these variables, simple estimations of following are presented: (1) time-dependent mean strength and c.o.v. associated with the strength and (2) time-dependent mean degradation function and c.o.v. associated with the degradation function, wherein, the degradation function is defined as the ratio of strength at time, t, to the initial strength for an un-corroded RC beam. The estimation of time-dependent strengths and degradation functions are carried out for two limit states: (a) flexural failure and (b) shear failure. An attempt has also been made to present analytical models for estimating time-dependent c.o.v. associated with the degradation functions. The performance of simple estimations of mean strengths and c.o.v. associated with strengths and degradation functions has been evaluated by comparing their results with those obtained using Monte Carlo simulation.

2 Corrosion Propagation in RC Beams

A quantitative description of corrosion propagation is generally given in terms of the loss of metal per unit surface area per unit time, and this can be obtained by measuring the mass differences in the reinforcing steel with reference to its surface area exposed to corrosion. Most of the non-destructive techniques used for the corrosion monitoring are based on the electrochemical measurements, in which the annual mean corrosion rate is estimated in terms of the corrosion current density, i_{COR} [39]. This i_{COR} can be transformed into the loss of metal by using the diffusion law related to the growth of expansive corrosion products [6–8, 26]. Reduction in cross-sectional area of reinforcing bars shall result in the reduced flexural and shear strengths of the corrosion-damaged RC beams [5]. Corrosion of reinforcement causes cracking, and eventually spalling and/or peeling of the cover concrete. Reduction in concrete section owing to the peeling of cover concrete shall also result in the reduced flexural and shear strengths of the corrosion-damaged RC beams [34]. Following subsections present estimation of time-dependent loss of concrete and steel sections for the purpose of corrosion propagation in RC beams.

2.1 Loss of Concrete Section

Reduction in concrete section occurs due to peeling of bottom, top and side covers to the reinforcements. Methodology for estimating the time required for peeling of cover concrete is adopted from Bhargava [5]. Figure 1 shows the crack propagating

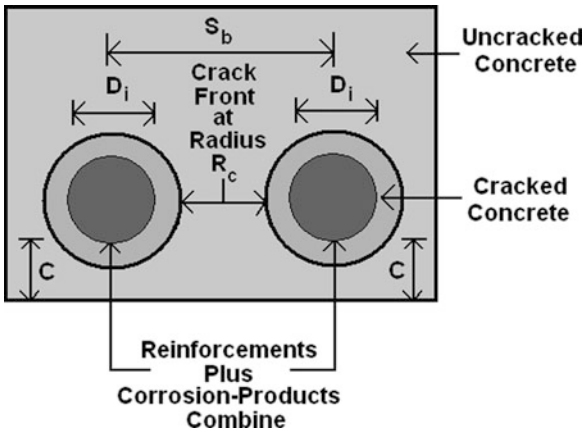

Fig. 1 Crack propagating condition for concrete block with two reinforcing bars due to reinforcement corrosion [5]

condition for the concrete block with two reinforcing bars of initial diameter D_i. The bars have clear cover, C, and the centre line spacing, S_b.

Due to the formation of corrosion products, the propagation of radial splitting cracks shall take place in all the directions to the same distance R_c, i.e. the radius of crack front. With $R_i = (D_i/2)$ and $R_o = (R_i + C)$, the cover concrete is assumed to be fully cracked when R_c becomes equal to R_o [8]. Bazant [3] reported that failure may occur in two different modes in case of R_c becoming equal to R_o: (1) when $C > (S_b - D_i)/2$, then the failure shall consist of peeling of cover concrete, and (2) when the spacing of bars, S_b, is large (sayS_b>$6 \cdot D_i$), the failure shall consist of inclined cracking. Based on the suggested failure philosophy of Bazant [3], the cover peeling time for top, bottom and side covers are evaluated using corrosion cracking model of Bhargava et al. [8].

2.2 Loss of Reinforcing Steel

Corrosion process is a dynamic process; growth of expansive corrosion products is given by Eq. (1) [6–8, 26].

$$\frac{dW_r}{dt} = \frac{k_p}{W_r} \tag{1}$$

where W_r = mass of expansive corrosion products (mg/mm), t = corrosion time (years) and k_p = function of rate of metal loss. k_p is expressed by Eq. (2) [8].

$$k_p = 2.48614 \cdot \pi \cdot D_i \cdot i_{\mathrm{COR}} \tag{2}$$

where D_i = initial diameter of reinforcement (mm) and i_{COR} = annual mean corrosion rate ($\mu A/\mathrm{cm}^2$). Various parameters associated with the loss of reinforcing steel at time, t, since initiation of corrosion are evaluated by Eqs. (3, 4, 5 and 6) [5].

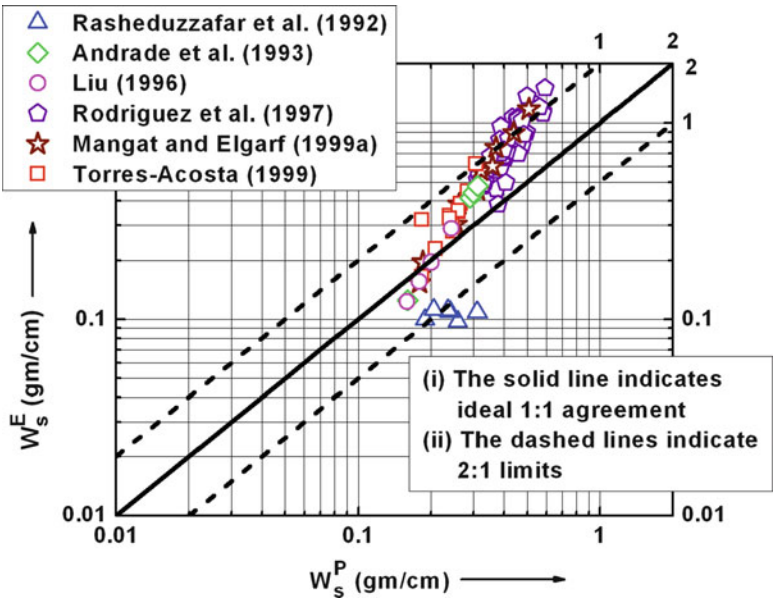

Fig. 2 Comparison between experimental W_s^E and predicted W_s^P using Eq. (3)

$$W_s(t) = 2.42362 \cdot \sqrt{D_i \cdot i_{\mathrm{COR}} \cdot t} \tag{3}$$

$$D_r(t) = \sqrt{D_i^2 - 0.39245 \cdot \sqrt{D_i \cdot i_{COR} \cdot t}} \tag{4}$$

$$A_{cor}(t) = 0.30835 \cdot \sqrt{D_i \cdot i_{\mathrm{COR}} \cdot t} \tag{5}$$

$$X(t) = \frac{1}{2} \cdot [D_i - D_r(t)] \tag{6}$$

where $W_s(t)$= mass of steel per unit length of the reinforcement (mg/mm) getting consumed by corrosion process, $D_r(t)$= reduced bar diameter (mm), $A_{\mathrm{cor}}(t)$= loss of cross-sectional area of steel (mm^2) and $X(t)$ = corrosion penetration depth (mm).

2.3 *Predictions for Loss of Reinforcing Steel: Comparison with Experimental Results*

Analytical predictions for W_s and X are made for the available experimental data by using Eqs. (3 and 6) [2, 25, 27, 33, 34, 38]. Figure 2 presents the comparison between W_s^P and W_s^E for the available experimental data. Similarly, Fig. 3 presents the comparison between X^P and X^E for the same experimental data. The superscripts

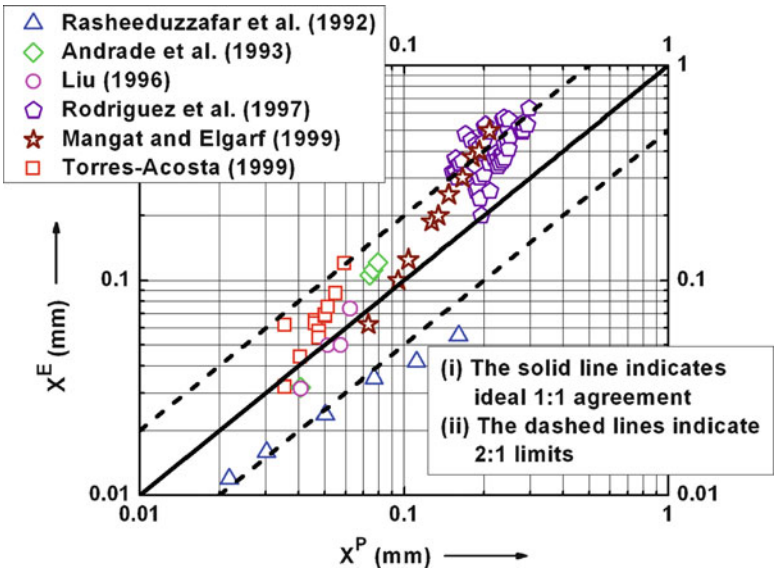

Fig. 3 Comparison between experimental X^{E} and predicted X^{P} using Eq. (6)

P and E correspond to the analytically predicted and the experimental observed values, respectively. The data in both figures are presented by different symbols to represent the analytical predictions made for different experimental data. It is clear from the same figures that the deviation between the analytically predicted and the experimentally observed values is generally less than by a factor of two, and this is a considerably good agreement in view of the large variability associated with the corrosion phenomena.

To test the goodness of Eqs. (3 and 6), the correlation between the predicted and experimental values is estimated. Assuming that $x = W_s^P$ (the independent variable), and $y = W_s^E$ (the dependent variable), the values of both r^2_{xy} and s^2_{yx} are estimated as 0.895 and 0.126 gm^2/cm, respectively, for Eq. (3), wherein r is the coefficient of correlation between x and y, and s is the root mean square error of estimate of y on x. Similarly, by assuming $x = X^P$ and $y = X^E$, the values of both r^2_{xy} and s^2_{yx} are estimated as 0.851 and 0.028 mm^2, respectively, for Eq. (6). The quite high values associated with r^2_{xy} in both the predictions suggest that Eqs. (3 and 6) can be effectively used for estimating the values of W_s and X for the reinforced concrete members exposed to the corrosive environment.

3 Time-Dependent Strengths of Corroded RC Beams

Figure 4 shows typical cross section of a simply supported un-corroded RC beam, which is subjected to flexure and shear under loads. This doubly reinforced beam has b and D as its width and depth, respectively. The beam is reinforced with

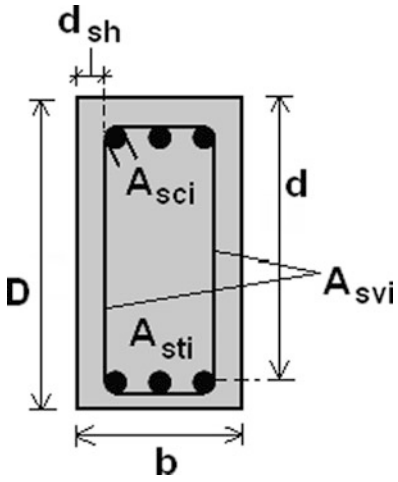

Fig. 4 Typical cross section of an un-corroded RC beam

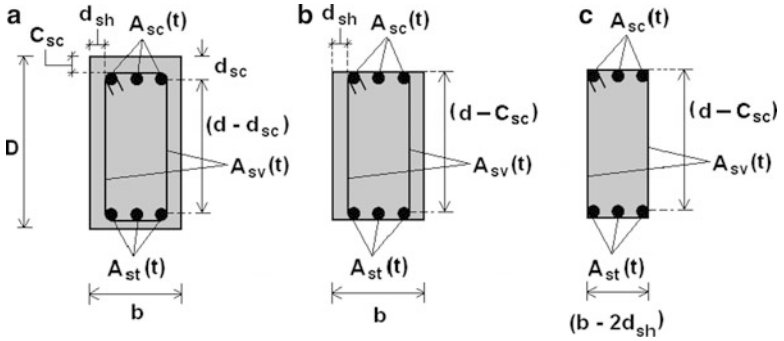

Fig. 5 Different schemes of deteriorated reinforced concrete sections for corroded RC beams (**a**) Section 1, (**b**) Section 2, (**c**) Section 3 [34]

bottom tensile reinforcing steel bars having initial area, A_{sti}, and top compressive reinforcing steel bars having initial area, A_{sci}. The distance between the centroid of tensile steel and the edge of the compression zone is d (also known as effective depth). The shear stirrups are having an initial area, A_{svi}, and are provided at spacing, S_v.

Figure 5 shows three representative schemes of deteriorated reinforced concrete sections for a corrosion affected RC beam [34]. The Section 1 indicates the intact concrete section, wherein the peeling of covers is yet to occur. The Section 2 indicates the reduced concrete section due to the peeling of top and bottom covers. In Section 2, effective depth to tensile reinforcement of the beam is reduced to $(d-C_{sc})$, wherein C_{sc} is clear cover to the compression steel. The Section 3 indicates the reduced concrete section due to the peeling of all the top, bottom and side covers. In Section 3, effective depth to tensile reinforcement and effective width of

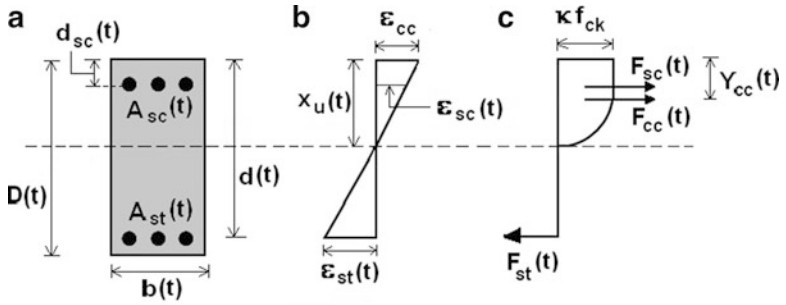

Fig. 6 Formulation of time-dependent flexural strength of corroded RC beams: (**a**) beam section, (**b**) strain distribution [9] and (**c**) stress distribution [9]

the beam are reduced to $(d - C_{sc})$ and$(b - 2 \cdot d_{sh})$, respectively, wherein d_{sh} is the clear cover to the shear stirrups. All the three sections also indicate the reduced sections of main bars and shear stirrups at time, t. It is very important to point out that the reduced concrete section for a deteriorated corroded beam at time, t, is governed by the individual cover peeling time for top, bottom and side covers, and in some cases, it may be different than those shown in Fig. 5. Formulations for time-dependent flexural and shear strengths of corroded RC beams are proposed with the considerations that the loss of strengths is mainly due to reduction in cross-sectional areas of reinforcing steel and concrete.

3.1 Time-Dependent Flexural Strength

Figure 6a shows the typical beam section for a doubly reinforced corroded beam, wherein the different notations pertaining to dimensions and reinforcing steels have their usual meanings at time, t, from the initiation of corrosion. Figure 6b and c present the strain and stress distribution across the cross section of the beam, respectively, wherein ε_{cc} is the ultimate strain in concrete and is taken as 0.0035 [9].

In the same figures, $\varepsilon_{st}(t)$ and $\varepsilon_{sc}(t)$ are the strains in tensile and compressive reinforcements, respectively; $x_u(t)$ is the height of compression zone; $F_{cc}(t)$ and $F_{sc}(t)$ are the forces of compression in concrete and compressive steel, respectively; $Y_{cc}(t)$ is the distance of point of application of $F_{cc}(t)$ from the edge of compression zone; $F_{st}(t)$ is the force of tension in tensile steel and f_{ck} is the 28-day characteristic cube compressive strength of concrete [9]. Uniform corrosion around the surface and along the length of the bar is assumed. Considering the simple bending theory, $\varepsilon_{st}(t)$ and $\varepsilon_{sc}(t)$are given by Eq. (7).

$$\varepsilon_{st}(t) = \left[\frac{d(t) - x_u(t)}{x_u(t)}\right] \cdot \varepsilon_{cc}; \varepsilon_{sc}(t) = \left[\frac{x_u(t) - d_{sc}(t)}{x_u(t)}\right] \cdot \varepsilon_{cc} \tag{7}$$

The total force of compression, $F_c(t)$, is given by Eq. (8).

$$F_c(t) = F_{cc}(t) + F_{sc}(t) \tag{8}$$

$F_{cc}(t)$ and $Y_{cc}(t)$ are given by Eq. (9).

$$\begin{aligned} F_{cc}(t) &= \kappa \cdot f_{ck} \cdot b(t) \cdot x_u(t) \cdot \left[\frac{3 \cdot \varepsilon_{cc} - 0.002}{3 \cdot \varepsilon_{cc}}\right]; \\ Y_{cc}(t) &= x_u(t) - x_u(t) \cdot \left[\frac{6 \cdot \varepsilon_{cc} - \left(\frac{0.000004}{\varepsilon_{cc}}\right)}{12 \cdot \varepsilon_{cc} - 0.008}\right] \end{aligned} \tag{9}$$

where $\kappa = a$ factor which is decided based on the design compressive strength of the concrete in the structures and the partial safety factor appropriate to the material strength of concrete [9]. The force of compression in compressive steel, $F_{sc}(t)$, is given by Eq. (10).

$$\begin{aligned} F_{sc}(t) &= \varepsilon_{sc}(t) \cdot E_{st} \cdot A_{sc}(t); \text{ for } \varepsilon_{sc}(t) \le \varepsilon_{sy}, \text{ and,} \\ F_{sc}(t) &= \eta \cdot f_y \cdot A_{sc}(t); \text{ for } \varepsilon_{sc}(t) > \varepsilon_{sy} \end{aligned} \tag{10}$$

where f_y = yield strength of reinforcing steels, η = a factor which is decided based on the partial safety factor appropriate to material strength of reinforcing steels [9], E_{st} = modulus of elasticity of reinforcing steel and ε_{sy} = yield strain for the reinforcing steels = $(\eta \cdot f_y / E_{st})$. In the present study, both κ and η are considered as 1.0. The distance, $Y_c(t)$, of point of application of total force of compression, $F_c(t)$, from the edge of compression zone is given by Eq. (11).

$$Y_c(t) = \frac{F_{cc}(t) \cdot Y_{cc}(t) + F_{sc}(t) \cdot d_{sc}(t)}{F_{cc}(t) + F_{sc}(t)} \tag{11}$$

The force of tension,$F_{st}(t)$, in tensile steel is given by Eq. (12).

$$\begin{aligned} F_{st}(t) &= \varepsilon_{st}(t) \cdot E_{st} \cdot A_{st}(t); \text{ for } \varepsilon_{st}(t) \le \varepsilon_{sy}, \text{ and,} \\ F_{st}(t) &= \eta \cdot f_y \cdot A_{st}(t); \text{ for } \varepsilon_{st}(t) > \varepsilon_{sy} \end{aligned} \tag{12}$$

By equating the force of compression given by Eq. (8) and the force of tension given by Eq. (12), the height of compression zone $x_u(t)$ is evaluated. The flexural strength, $Mu(t)$, at time, t, is then determined by Eq. (13).

$$Mu(t) = F_{st}(t) \cdot [d(t) - Y_c(t)] \tag{13}$$

3.2 Time-Dependent Shear Strength

The permissible shear stress of concrete at time, t, from the initiation of corrosion is given by Eq. (14) [9, 35].

$$\tau_c(t) = \frac{0.85 \cdot \sqrt{0.8 \cdot f_{ck}} \cdot \left(\sqrt{1 + 5 \cdot \beta(t)} - 1\right)}{6 \cdot \beta(t)}; \beta(t) = \frac{0.8 \cdot f_{ck} \cdot b(t) \cdot d(t)}{689 \cdot A_{st}(t)} \quad (14)$$

The shear strength, $Vu(t)$, at time, t, is determined by Eq. (15).

$$Vu(t) = \tau_c(t) \cdot b(t) \cdot d(t) + \frac{\eta \cdot f_y \cdot A_{sv}(t) \cdot d(t)}{S_v} \quad (15)$$

The maximum value of the shear strength of the corroded RC beam, $Vu_{max}(t)$, is given by Eq. (16) [9].

$$Vu_{max}(t) = \tau_{c\,max} \cdot b(t) \cdot d(t) \quad (16)$$

where τ_{cmax} = maximum shear stress of concrete for a given value of f_{ck} [9]. If calculated $Vu(t)$ is more than $Vu_{max}(t)$, then $Vu(t)$ is limited to $Vu_{max}(t)$ [9].

3.3 Predictions for Time-Dependent Flexural and Shear Strengths of Corroded RC Beams: Comparison with Experimental Results

Predictions have been made for the residual flexural and shear capacity of the corrosion-degraded RC beams for which the experimental results are available [34]. Rodriguez et al. [34] tested six different types of RC beams of sections 150 × 200 mm with spans ranging from 2,050 to 2,300 mm. The beams were provided with different ratios of tensile and compressive reinforcement, different spacing of shear reinforcement and different locations of curtailment of tensile reinforcing bars. The various reinforcing bars were corroded to different degree of corrosion in terms of attack penetration, i.e. reduction in bar radius. After having corroded the reinforcement, the beams were tested up to the failure.

Figures 7 and 8 present the comparison of experimentally observed and analytically predicted values for time-dependent flexural and shear strengths, respectively, for type 13 beams of Rodriguez et al. [34]. Analytical predictions are presented for all the three deteriorated schemes for RC sections (Fig. 5) for comparison purposes. However, for these beams, Section 2 deteriorated scheme (Fig. 5) is expected at the end of the corrosion period. Analytical predictions are found to agree within 17% of the experimentally observed values for flexural and shear strengths for Section 2

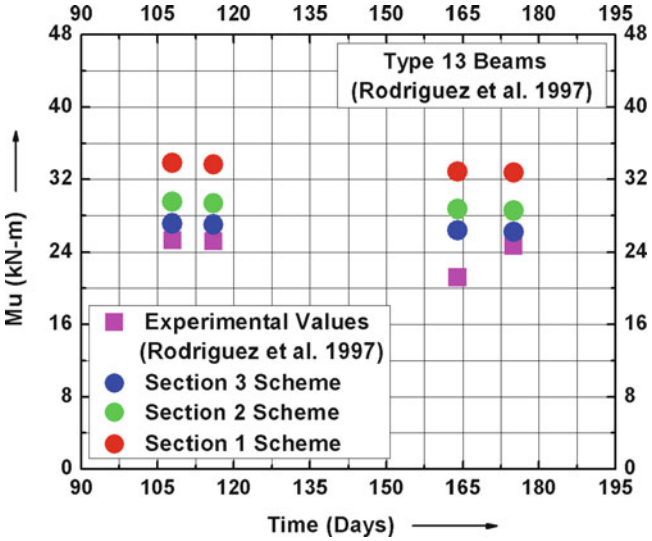

Fig. 7 Time-dependent flexural strength for type 13 corroded beams of Rodriguez et al. [34]

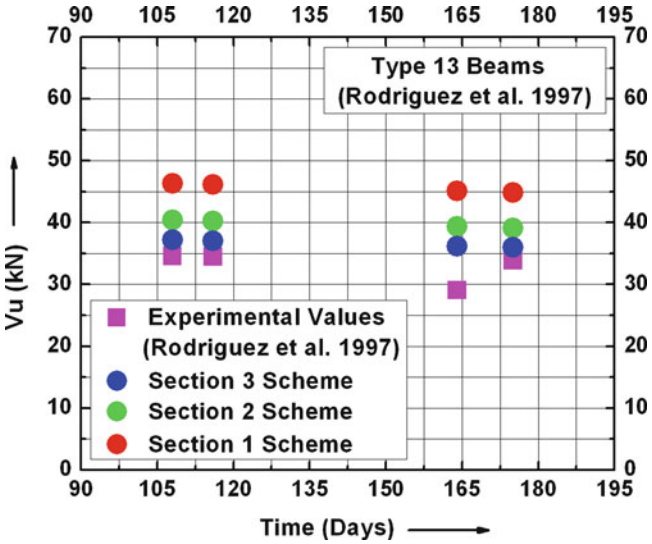

Fig. 8 Time-dependent shear strength for type 13 corroded beams of Rodriguez et al. [34]

deteriorated scheme; this is a considerably good agreement in view of the large variability associated with the corrosion phenomena. Therefore, the proposed analytical formulations for time-dependent flexural and shear strengths predict the analytical trends which are in considerably good agreement with those of the observed experimental trends.

4 Illustration of Time-Dependent Strengths of Corroded RC Beams: Probabilistic Approach

For the purpose of illustration, a simply supported RC beam with its reinforcement details as shown in Fig. 9 is considered. The span of the beam is considered as 4.0 m, and it is subjected to corrosion attack. The statistical parameters for the basic variables for material strengths, dimensions and annual mean corrosion rate appropriate for the RC beam are given in Table 1. These statistical parameters are similar to the ones suggested by many researchers [1, 9–24, 29–32, 36, 37, 39–41].

Time-dependent flexural and shear strengths are estimated using the formulations given in the preceding sections. Since the formulations are provided based on BIS [9]

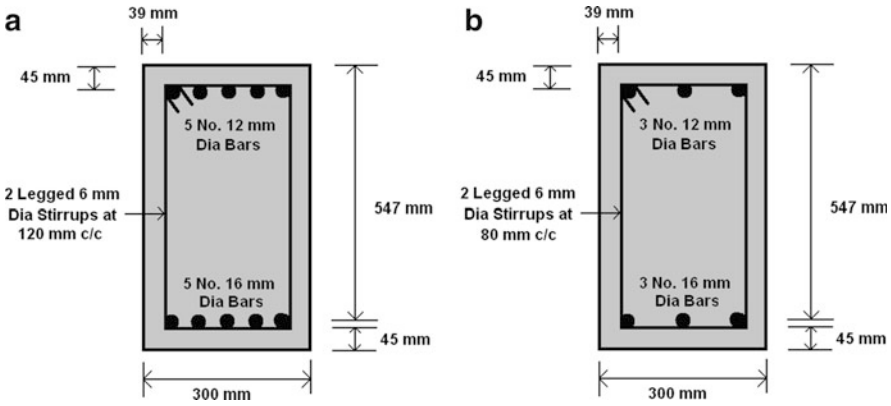

Fig. 9 Typical RC beam cross section: (**a**) at mid span and (**b**) at supports

Table 1 Statistical parameters for the basic variables for material strengths, dimensions and annual mean corrosion rate

Variables		Mean	c.o.v.	Distribution
Material strengths	f_{cm}	25.8 MPa	0.18	Normal
	τ_C	0.421 MPa	0.18	Normal
	θ	2.0	0.20	Normal
	f_y	466.88 MPa	0.11	Lognormal
	E_s	200,000 MPa	0.051	Lognormal
Dimensions	b	310.3 mm	0.033	Normal
	D	614.4 mm	0.017	Normal
	C_B	46.6 mm	0.123	Normal
	C_T	48.2 mm	0.105	Normal
	C_S	40.6 mm	0.099	Normal
Annual mean corrosion rate	i_{COR}	1, 3, 5 μA/cm^2	0.1, 0.2 and 0.3	Normal

Notations: f_{cm}: compressive strength of concrete, θ; creep coefficient, E_s; modulus of elasticity of steel plus corrosion products combine, C_B, C_T *and* C_S: clear covers to bottom, top and side reinforcements, respectively

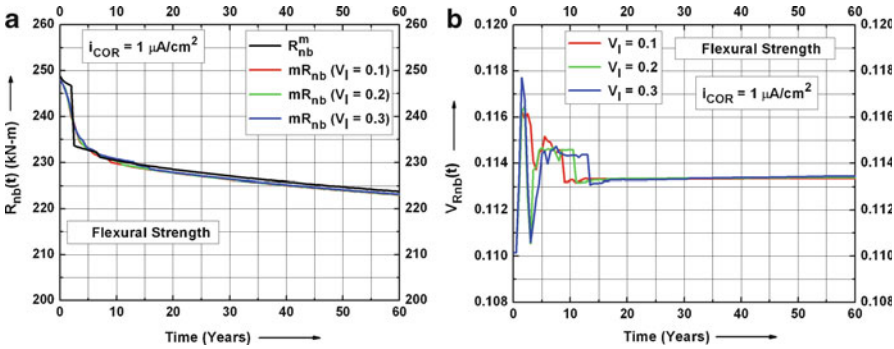

Fig. 10 (**a**): Time-dependent flexural strength (i_{COR} = 1 μA/cm^2) (**b**): Time-dependent c.o.v. for flexural strength (i_{COR} = 1 μA/cm^2)

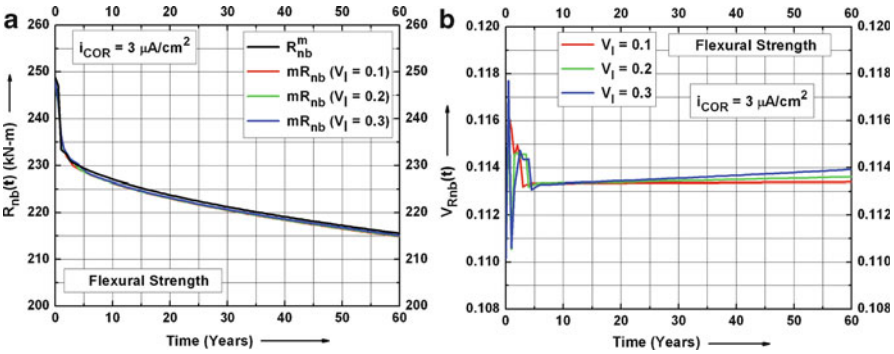

Fig. 11 (**a**): Time-dependent flexural strength (i_{COR} = 3 μA/cm^2) (**b**): Time-dependent c.o.v. for flexural strength (i_{COR} = 3 μA/cm^2)

and SP16 [35], following is adopted in the present study: (1) time-dependent flexural strength is calculated by using f_{cm} instead of $\kappa.f_{ck}$ and by using E_s instead of E_{st}, and (2) time-dependent shear strength is calculated by using f_{cm} instead of f_{ck}.

Monte Carlo simulation is used for evaluating time-dependent mean strengths and c.o.v. associated with the strengths. Here, the "Latin hypercube sampling (LHS)" technique with 40 samples [28] is used for an efficient sampling considering the variability in the variables given in Table 1. The results are presented in Figs. 10, 11, 12, 13, 14 and 15 and are discussed in the following sections. The 40 random samples of the basic variables and their random combinations obtained through LHS technique are used for evaluating the sample mean of strengths and c.o.v. associated with the strengths in Figs. 10, 11, 12, 13, 14 and 15. The approximated mean for strengths is evaluated by considering all the basic variables to be at their mean values. In all the figures, V_I stands for the c.o.v. of i_{COR}. Results are presented typically for a corrosion period of 60 years.

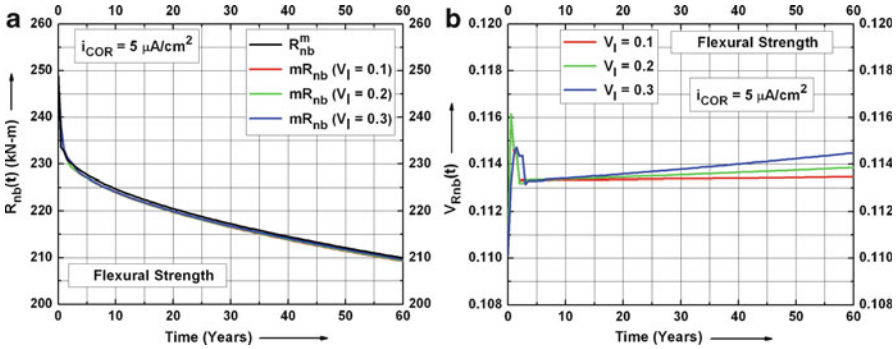

Fig. 12 (**a**): Time-dependent flexural strength (i_{COR} = 5 μA/cm^2) (**b**): Time-dependent c.o.v. for flexural strength (i_{COR} = 5 μA/cm^2)

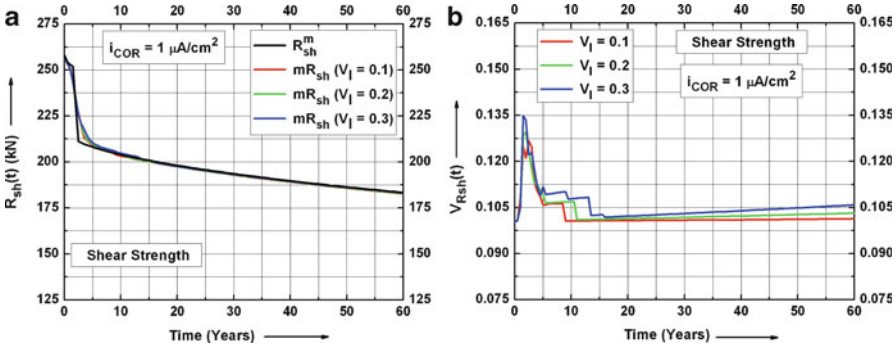

Fig. 13 (**a**): Time-dependent shear strength (i_{COR} = 1 μA/cm^2) (**b**): Time-dependent c.o.v. for shear strength (i_{COR} = 1 μA/cm^2)

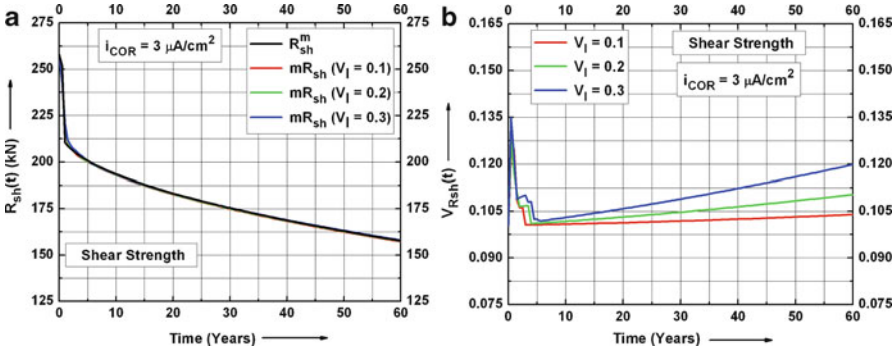

Fig. 14 (**a**): Time-dependent shear strength (i_{COR} = 3 μA/cm^2) (**b**): Time-dependent c.o.v. for shear strength (i_{COR} = 3 μA/cm^2)

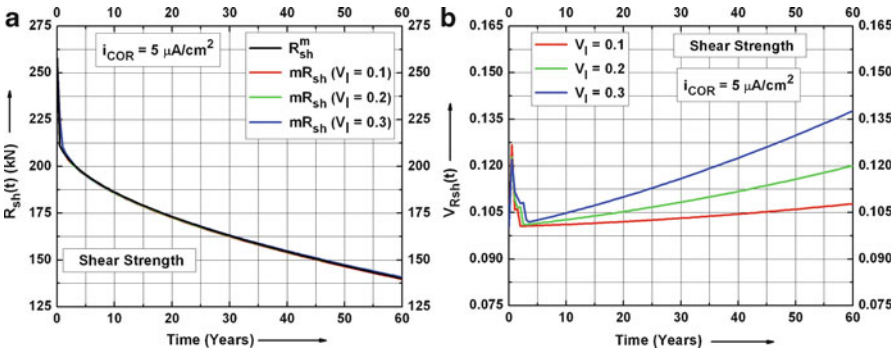

Fig. 15 (**a**): Time-dependent shear strength (i_{COR} = 5 μA/cm^2) (**b**): Time-dependent c.o.v. for shear strength (i_{COR} = 5 μA/cm^2)

4.1 Time-Dependent Flexural Strength

Figures 10a, 11a and 12a present the time-dependent flexural strength, $R_{nb}(t)$, at time t (years) from the initiation of corrosion, for different mean values of i_{COR}. In the same figures, mR_{nb} stands for the sample mean flexural strength, and R^m_{nb} stands for the approximated mean flexural strength. Figures 10b, 11b, and 12b present the time-dependent c.o.v., $V_{Rnb}(t)$, associated with $R_{nb}(t)$, at time t (years) from the initiation of corrosion, for different mean values of i_{COR}. These figures depict the following:

1. For a given i_{COR}, R^m_{nb} agrees well with mR_{nb} except in the time interval of 0–5 years, where a slight difference between them is observed. This difference is mainly attributed to the randomness associated with the time of cover peeling at bottom, top, and side resulting in the change of cross section for the concrete. Flexural strength is mainly governed by all the basic variables (except τ_C) given in Table 1 and is a non-linear function of those variables. Figure 6 also shows that, at time t, $R_{nb}(t)$ is evaluated after estimating various parameters, such as beam dimensions, cross-sectional area of steels, neutral axis depth, forces of compression in concrete and compression steel and their points of application and force of tension in tension steel and its point of application. Good agreement between the sample mean and approximated mean values of $R_{nb}(t)$ shows that the time-dependent mean flexural strength can be approximated by considering the linear terms in Taylor series expansion of performance functions (Eqs. (5, 7, 8, 9, 10, 11, 12, and 13) for the aforementioned parameters needed to evaluate $R_{nb}(t)$.
2. For a given i_{COR}, an increase in $V_{Rnb}(t)$ is observed in the time interval of 0–5 years for all V_I values. This is attributed to the randomness associated with the time of cover peeling at the bottom, top and side resulting in the change of cross section for the concrete.

3. For a given i_{COR}, V_I has negligible effect on the mean values of the $R_{nb}(t)$; however, it affects $V_{Rnb}(t)$. As V_I increases, $V_{Rnb}(t)$ also increases. This is because $R_{nb}(t)$ is a function of i_{COR}, and variation in i_{COR} values will result in the variation of corresponding $R_{nb}(t)$ values.
4. i_{COR} affects $R_{nb}(t)$ and $V_{Rnb}(t)$. As i_{COR} increases, $As_{COR}(t)$ for tension steel also increases, thus further resulting in reduced $R_{nb}(t)$ and more variability for $As_{COR}(t)$. Increase in variability for $As_{COR}(t)$ will result in the increase in $V_{Rnb}(t)$ values. Here, As_{COR} is defined as the ratio of loss of cross-sectional area to the initial un-corroded area of reinforcement.

4.2 Time-Dependent Shear Strength

Figures 13a, 14a and 15a present the time-dependent shear strength, $R_{sh}(t)$, at time t (years) from the initiation of corrosion, for different mean values of i_{COR}. In the same figures, mR_{sh} stands for the sample mean shear strength, and R_{sh}^{m} stands for the approximated mean shear strength. Figures 13b, 14b and 15b present the time-dependent c.o.v., $V_{Rsh}(t)$, associated with $R_{sh}(t)$, at time t (years) from the initiation of corrosion, for different mean values of i_{COR}. These figures depict the following:

1. For a given i_{COR}, R_{sh}^{m} agrees well with mR_{sh} except in the time interval of 0–5 years, where a slight difference between them is observed. This difference is mainly attributed to the randomness associated with the time of cover peeling at the bottom, top, and side resulting in the change of cross section for the concrete. Shear strength is governed by all the basic variables given in Table 1 and is a non-linear function of those variables. At time t, $R_{sh}(t)$ is evaluated after estimating various parameters, such as beam dimensions, cross-sectional area of steels and shear strength of concrete and stirrups. Good agreement between the sample mean and approximated mean values of $R_{sh}(t)$ shows that the time-dependent mean shear strength can be approximated by considering the linear terms in Taylor series expansion of performance functions (Eqs. 5, 14, 15 and 16) for the aforementioned parameters needed to evaluate $R_{sh}(t)$.
2. For a given i_{COR}, an increase in $V_{Rsh}(t)$ is observed in the time interval of 0–5 years. This is attributed to the randomness associated with the time of cover peeling at the bottom, top and side resulting in the change of cross section for the concrete.
3. For a given i_{COR}, V_I has negligible effect on the mean values of the $R_{sh}(t)$; however, it affects $V_{Rsh}(t)$. As V_I increases, $V_{Rsh}(t)$ also increases. This is because $R_{sh}(t)$ is a function of i_{COR}, and variation in i_{COR} values will result in the variation of corresponding $R_{sh}(t)$ values.
4. i_{COR} affects $R_{sh}(t)$ and $V_{Rsh}(t)$. As i_{COR} increases, $As_{COR}(t)$ for shear stirrups also increases, thus further resulting in reduced $R_{sh}(t)$ and more variability for $As_{COR}(t)$. Increase in variability for $As_{COR}(t)$ will result in the increase in $V_{Rsh}(t)$ values.

5. At time $t = 0$, V_{Rsh}(at $t = 0$) is slightly lower than V_{Rnb}(at $t = 0$). It is mentioned that shear strength of beam is evaluated as sum of the shear strength contributions of concrete section and stirrups. Shear strengths of concrete section is evaluated as a product of beam dimensions and permissible shear stress of concrete, while that of stirrups is evaluated as a product of effective depth of beam, yield strength and cross-sectional area of stirrups (Eq. 14, 15 and 16). Flexural strength for the given beam is mainly governed by the yielding of tensile reinforcement and is evaluated as a product of lever arm (which is a function of effective depth of beam), yield strength and cross-sectional area of tensile reinforcement (Eq. 13). Since the considered variability in beam dimensions are smaller as compared to those for material strengths of concrete and steel, it may result in V_{Rsh}(at $t = 0$) slightly lower than V_{Rnb}(at $t = 0$).

5 Time-Dependent Degradation Functions for Time-Dependent Strengths of Corroded RC Beams

Degradation function is defined as the ratio of strength at time, t, to the initial strength for an un-corroded RC beam. Time-dependent mean degradation functions for the time-dependent flexural and shear strengths, for the considered RC beam are expressed by Eq. (17).

$$g_{\mathrm{nb}}(t) = \frac{R_{\mathrm{nb}}(t)}{R_{\mathrm{nb0}}}; \quad g_{\mathrm{sh}}(t) = \frac{R_{\mathrm{sh}}(t)}{R_{\mathrm{sh0}}} \tag{17}$$

where $R_{\mathrm{nb}}(t)$and $R_{\mathrm{sh}}(t)$ = flexural strength and shear strength, respectively, at time t; R_{nb0}andR_{sh0} = flexural strength and shear strength, respectively, at time $t = 0$; and $g_{\mathrm{nb}}(t)$and$g_{\mathrm{sh}}(t)$ = mean degradation functions for flexural strength and shear strength, respectively, at time t.

Figures 16 and 17 present the time-dependent mean degradation functions, $g_{\mathrm{nb}}(t)$ and $g_{\mathrm{sh}}(t)$, for flexural strength and shear strength, respectively, for different mean values of i_{COR}. With the increase in i_{COR}, reduction in $g_{\mathrm{nb}}(t)$ and $g_{\mathrm{sh}}(t)$ is observed. This is attributed to the reduction in $R_{\mathrm{nb}}^{\mathrm{m}}$ and $R_{\mathrm{sh}}^{\mathrm{m}}$, respectively, due to increase in i_{COR}.

6 Analytical Estimation of Time-Dependent c.o.v. Associated with Degradation Function

Since time-dependent strengths and degradation functions for corroded RC beam are related to each other by Eq. (17), the time-dependent c.o.v. associated with degradation functions is evaluated by Eq. (18) [4].

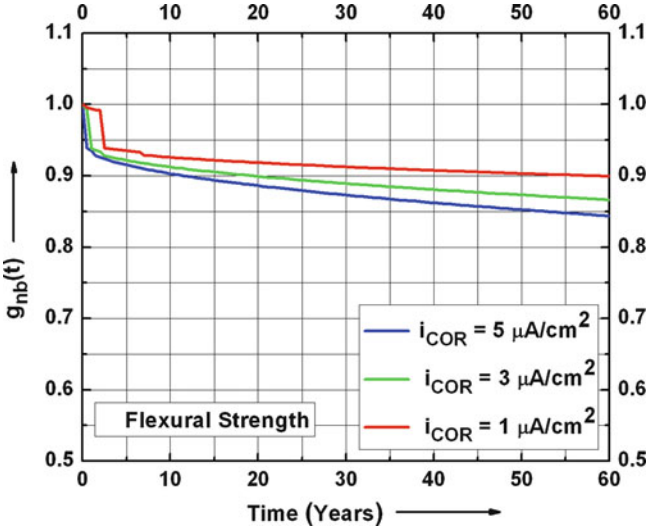

Fig. 16 Time-dependent mean degradation function for flexural strength

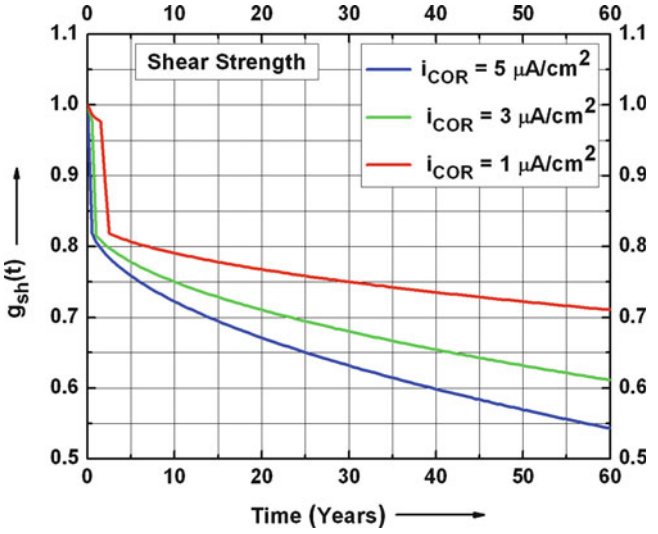

Fig. 17 Time-dependent mean degradation function for shear strength

$$V_{\mathrm{Gnb}}(t) = \sqrt{\frac{V_{\mathrm{Rnb}}^2(t) - V_{\mathrm{Rnb0}}^2}{1 + V_{\mathrm{Rnb0}}^2}}; \quad V_{\mathrm{Gsh}}(t) = \sqrt{\frac{V_{\mathrm{Rsh}}^2(t) - V_{\mathrm{Rsh0}}^2}{1 + V_{\mathrm{Rsh0}}^2}} \tag{18}$$

where $V_{\mathrm{Gnb}}(t)$ and $V_{\mathrm{Gsh}}(t)$ = c.o.v. associated with degradation functions for flexural strength and shear strength, respectively, at time t; $V_{\mathrm{Rnb}}(t)$ and

$V_{\mathrm{Rsh}}(t)$ = c.o.v. associated with flexural strength and shear strength, respectively, at time t; and V_{Rnb0} and V_{Rsh0} = c.o.v. associated with initial flexural strength and initial shear strength, respectively, at time $t = 0$. The estimation of $V_{\mathrm{Rnb}}(t)$, $V_{\mathrm{Rsh}}(t)$, $V_{\mathrm{Gnb}}(t)$ and $V_{\mathrm{Gsh}}(t)$is addressed in the following sections.

6.1 Analytical Estimation of $V_{Rnb}(t)$ and $V_{Gnb}(t)$

At time t, the flexural strength, $R_{\mathrm{nb}}(t)$, is estimated by Eq. (13) (performance functions for $R_{\mathrm{nb}}(t)$) for tension failure. $R_{\mathrm{nb}}(t)$ is a function of $F_{\mathrm{st}}(t)$, $Y_{\mathrm{c}}(t)$ and $d(t)$. At time t, if σ_{Rnbt} is the standard deviation associated with $R_{\mathrm{nb}}(t)$, then the first-order approximation of variance of $R_{\mathrm{nb}}(t)$ is given by Eq. (19) [18].

$$\sigma^2_{\mathrm{Rnbt}} = \left(\frac{\partial R_{\mathrm{nb}}(t)}{\partial F_{\mathrm{st}}(t)}\right)^2 \cdot \sigma^2_{\mathrm{Fstt}} + \left(\frac{\partial R_{\mathrm{nb}}(t)}{\partial Y_c(t)}\right)^2 \cdot \sigma^2_{\mathrm{Yct}} + \left(\frac{\partial R_{\mathrm{nb}}(t)}{\partial d(t)}\right)^2 \cdot \sigma^2_{\mathrm{dt}} \tag{19}$$

where σ_{Fstt} = standard deviation associated with $F_{\mathrm{st}}(t)$, σ_{Yct} = standard deviation associated with $Y_c(t)$ and σ_{dt} = standard deviation associated with $d(t)$. First-order approximation for σ_{Fstt}, σ_{Yct} and σ_{dt} are given by Eqs. (20a, 20b, 21, 22a and 22b).

$$\sigma^2_{\mathrm{Fstt}} = \left(\frac{\partial F_{\mathrm{st}}(t)}{\partial E_s}\right)^2 \cdot \sigma^2_{Es} + \left(\frac{\partial F_{\mathrm{st}}(t)}{\partial X_u(t)}\right)^2 \cdot \sigma^2_{\mathrm{Xut}} + \left(\frac{\partial F_{\mathrm{st}}(t)}{\partial d(t)}\right)^2 \cdot \sigma^2_{dt} + \left(\frac{\partial F_{\mathrm{st}}(t)}{\partial i_{\mathrm{COR}}}\right)^2 \cdot \sigma^2_{\mathrm{icor}} \quad \text{for } \varepsilon_{\mathrm{st}}(t) \le \varepsilon_{\mathrm{sy}} \tag{20a}$$

$$\sigma^2_{\mathrm{Fstt}} = \left(\frac{\partial F_{\mathrm{st}}(t)}{\partial f_y}\right)^2 \cdot \sigma^2_{fy} + \left(\frac{\partial F_{\mathrm{st}}(t)}{\partial i_{\mathrm{COR}}}\right)^2 \cdot \sigma^2_{\mathrm{icor}}; \text{ for } \varepsilon_{st}(t) > \varepsilon_{sy} \tag{20b}$$

$$\sigma^2_{\mathrm{Yct}} = \left(\frac{\partial Y_c(t)}{\partial F_{\mathrm{cc}}(t)}\right)^2 \cdot \sigma^2_{\mathrm{Fcct}} + \left(\frac{\partial Y_c(t)}{\partial Y_{\mathrm{cc}}(t)}\right)^2 \cdot \sigma^2_{\mathrm{Ycct}} + \left(\frac{\partial Y_c(t)}{\partial F_{\mathrm{sc}}(t)}\right)^2 \cdot \sigma^2_{\mathrm{Fsct}} + \left(\frac{\partial Y_c(t)}{\partial d_{\mathrm{sc}}(t)}\right)^2 \cdot \sigma^2_{\mathrm{dsct}} \tag{21}$$

$$\sigma_{dt} = \sqrt{\sigma^2_D + \sigma^2_{CB}}\ ; \text{(before peeling of top cover)} \tag{22a}$$

$$\sigma_{dt} = \sqrt{\sigma^2_D + \sigma^2_{CB} + \sigma^2_{CT}}\ ; \text{(after peeling of top cover)} \tag{22b}$$

where σ_{Es}, σ_{fy}, σ_{icor}, σ_D, σ_{CB} and σ_{CT} = standard deviation associated with E_s, f_y, i_{COR}, D, C_B and C_T, respectively, and are evaluated based on the statistical parameters for these variables given in Table 1. σ_{Xut} is the standard deviation

associated with $X_u(t)$, and the first-order approximation of variance of $X_u(t)$ for different strain conditions in reinforcing steels shall give its value. σ_{Fcct}, σ_{Ycct}, σ_{Fsct} and σ_{dsct} are the standard deviations associated with $F_{\text{cc}}(t)$, $Y_{\text{cc}}(t)$, $F_{\text{sc}}(t)$ and $d_{\text{sc}}(t)$, respectively, and the first-order approximation of variances of $F_{\text{cc}}(t)$, $Y_{\text{cc}}(t)$ $F_{\text{sc}}(t)$ and $d_{\text{sc}}(t)$ shall give their respective values. The time-dependent c.o.v., $V_{\text{Rnb}}(t)$, associated with $R_{\text{nb}}(t)$ is estimated from Eq. (23).

$$V_{\text{Rnb}}(t) = \frac{\sigma_{\text{Rnbt}}}{R_{\text{nb}}(t)} \tag{23}$$

At time $t = 0$, $V_{\text{Rnb}}(t = 0) = V_{\text{Rnb0}}$. Once V_{Rnb0} and $V_{\text{Rnb}}(t)$ are known, $V_{\text{Gnb}}(t)$ is evaluated from Eq. (18).

6.2 Analytical Estimation of $V_{Rsh}(t)$ and $V_{Gsh}(t)$

The shear strength, $R_{\text{sh}}(t)$, at time t, is estimated by Eq. (15) (performance functions for $R_{\text{sh}}(t)$). $R_{\text{sh}}(t)$ is a function of $\tau_{\text{C}}(t)$, $b(t)$, $d(t)$, f_y and i_{COR}. For the considered corroded RC beam (Fig. 9), $\tau_{\text{C}}(t)$ is not calculated by Eq. (14), rather τ_{C} is considered as a separate random variable with statistical parameters provided in Table 1. At time t, if σ_{Rsht} is the standard deviation associated with $R_{\text{sh}}(t)$, then the first-order approximation of variance of $R_{\text{sh}}(t)$ is given by Eq. (24) [18].

$$\begin{aligned}\sigma^2_{\text{Rsht}} = &\left(\frac{\partial R_{\text{sh}}(t)}{\partial \tau_C}\right)^2 \cdot \sigma^2_{TC} + \left(\frac{\partial R_{\text{sh}}(t)}{\partial b(t)}\right)^2 \cdot \sigma^2_{bt} + \left(\frac{\partial R_{\text{sh}}(t)}{\partial d(t)}\right)^2 \cdot \sigma^2_{dt} \\ &+ \left(\frac{\partial R_{\text{sh}}(t)}{\partial f_y}\right)^2 \cdot \sigma^2_{fy} + \left(\frac{\partial R_{\text{sh}}(t)}{\partial i_{\text{COR}}}\right)^2 \cdot \sigma^2_{\text{icor}}\end{aligned} \tag{24}$$

where $\sigma_{\tau c}$ = standard deviations associated with τ_{C} and is evaluated based on the statistical parameters for τ_{C} given in Table 1; σ_{bt} = standard deviation associated with $b(t)$ and first-order approximation of variance of $b(t)$ shall give its value. The time-dependent c.o.v., $V_{\text{Rsh}}(t)$, associated with $R_{\text{sh}}(t)$ is estimated from Eq. (25).

$$V_{\text{Rsh}}(t) = \frac{\sigma_{\text{Rsht}}}{R_{\text{sh}}(t)} \tag{25}$$

At time $t = 0$, $V_{\text{Rsh}}(t = 0) = V_{\text{Rsh0}}$. Once V_{Rsh0} and $V_{\text{Rsh}}(t)$ are known, $V_{\text{Gsh}}(t)$ is evaluated from Eq. (18).

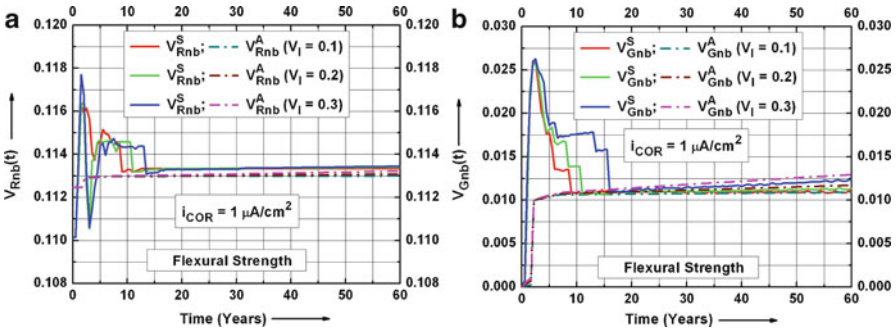

Fig. 18 (**a**): Comparison of time-dependent c.o.v. V^A_{Rnb} and V^S_{Rnb} for flexural strength (i_{COR} = 1 μA/cm^2) (**b**): Comparison of time-dependent c.o.v. V^A_{Gnb} and V^S_{Gnb} for degradation function for flexural strength (i_{COR} = 1 μA/cm^2)

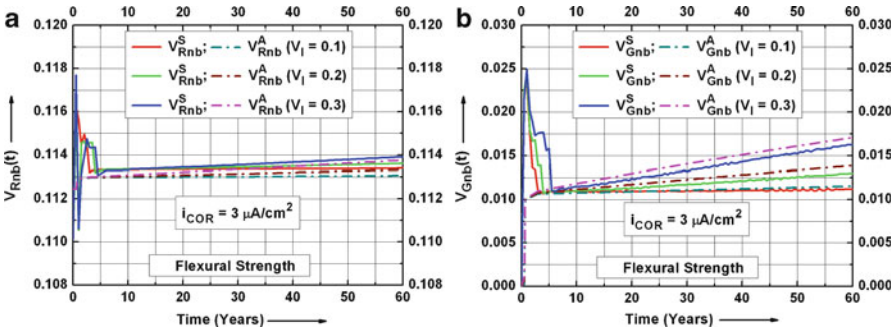

Fig. 19 (**a**): Comparison of time-dependent c.o.v. V^A_{Rnb} and V^S_{Rnb} for flexural strength (i_{COR} = 3 μA/cm^2) (**b**): Comparison of time-dependent c.o.v. V^A_{Gnb} and V^S_{Gnb} for degradation function for flexural strength (i_{COR} = 3 μA/cm^2)

6.3 Discussion of Results for Analytical Estimation of Time-Dependent c.o.v. Associated with Time-Dependent Strengths and Time-Dependent Degradation Functions

For different mean values of i_{COR}, at time t (years) from the initiation of corrosion, (1) Figures 18a, 19a and 20a present the time-dependent c.o.v., $V_{Rnb}(t)$, associated with $R_{nb}(t)$; (2) Figures 18b, 19b and 20b present the time-dependent c.o.v., $V_{Gnb}(t)$, associated with $G_{nb}(t)$; (3) Figures 21a, 22a, and 23a present the time-dependent c.o.v., $V_{Rsh}(t)$, associated with $R_{sh}(t)$; and (4) Figures 21b, 22b, and 23b present the time-dependent c.o.v., $V_{Gsh}(t)$, associated with $G_{sh}(t)$. In the same figures, V^S_{Rnb} and V^S_{Gnb} and V^S_{Rsh} and V^S_{Gsh} are evaluated using 40 random samples, V^A_{Rnb} and V^A_{Rsh} are evaluated using the analytical formulations presented in the preceding sections and

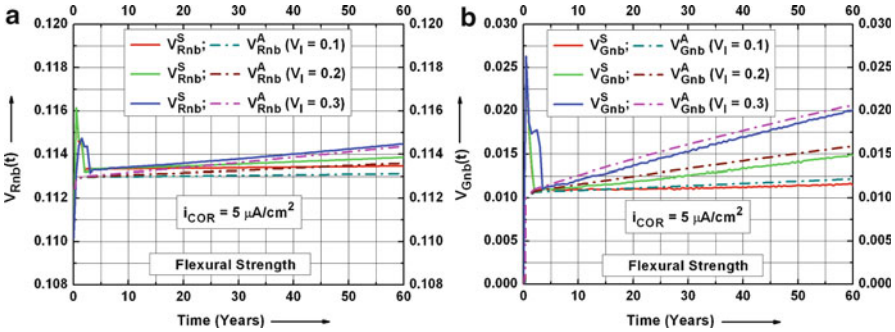

Fig. 20 (**a**): Comparison of time-dependent c.o.v. V^{A}_{Rnb} and V^{S}_{Rnb} for flexural strength ($i_{COR} = 5\ \mu A/cm^2$) (**b**): Comparison of time-dependent c.o.v. V^{A}_{Gnb} and V^{S}_{Gnb} for degradation function for flexural strength ($i_{COR} = 5\ \mu A/cm^2$)

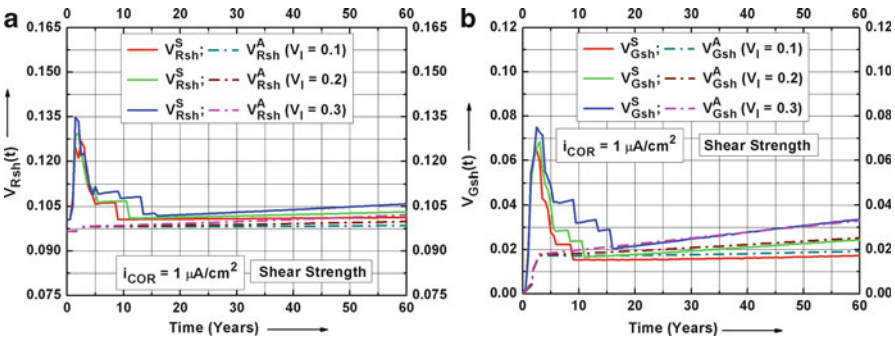

Fig. 21 (**a**): Comparison of time-dependent c.o.v. V^{A}_{Rsh} and V^{S}_{Rsh} for shear strength ($i_{COR} = 1\ \mu A/cm^2$) (**b**): Comparison of time-dependent c.o.v. V^{A}_{Gsh} and V^{S}_{Gsh} for degradation function for shear strength ($i_{COR} = 1\ \mu A/cm^2$)

V^{A}_{Gnb} and V^{A}_{Gsh} are evaluated using Eq. 18. For the purpose of comparison, (1) in Figs. 18a, 19a and 20a, V^{S}_{Rnb} are reproduced from Figs. 10b, 11b and 12b, and (2) in Figs. 21a, 22a and 23a, V^{S}_{Rsh} are reproduced from Figs. 13b, 14b and 15b. For a given i_{COR}, good agreement is observed between V^{A}_{Rnb} and V^{S}_{Rnb}, V^{A}_{Gnb} and V^{S}_{Gnb}, V^{A}_{Rsh} and V^{S}_{Rsh} and V^{A}_{Gsh} and V^{S}_{Gsh}, except in the time interval of about (a) 0–15 years, for $i_{COR} = 1\ \mu A/cm^2$, (b) 0–5 years for $i_{COR} = 3\ \mu A/cm^2$ and (c) 0–3 years for $i_{COR} = 5\ \mu A/cm^2$. The difference in the aforementioned time intervals is mainly attributed to the randomness associated with the time of cover peeling at the bottom, top and side resulting in the change of cross section for the concrete. Good agreement between the analytically estimated and simulated values for the c.o.v. in the remaining time intervals shows that the first-order approximation of mean and variance of strengths can be used for estimating c.o.v. for both strengths and degradation functions.

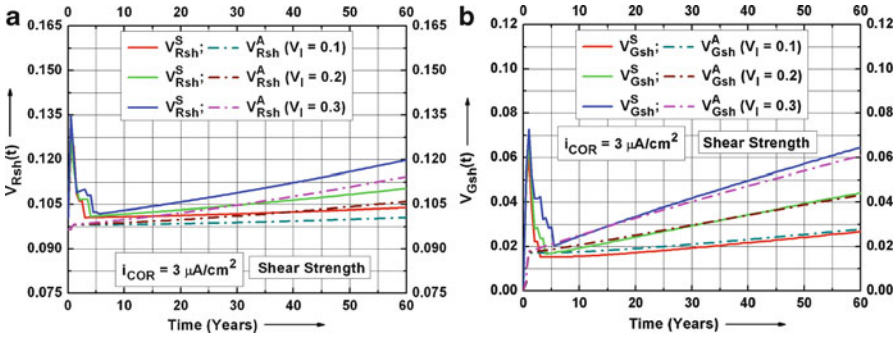

Fig. 22 (**a**): Comparison of time-dependent c.o.v. V^A_{Rsh} and V^S_{Rsh} for shear strength (i_{COR} = 3 μA/cm^2) (**b**): Comparison of time-dependent c.o.v. V^A_{Gsh} and V^S_{Gsh} for degradation function for shear strength (i_{COR} = 3 μA/cm^2)

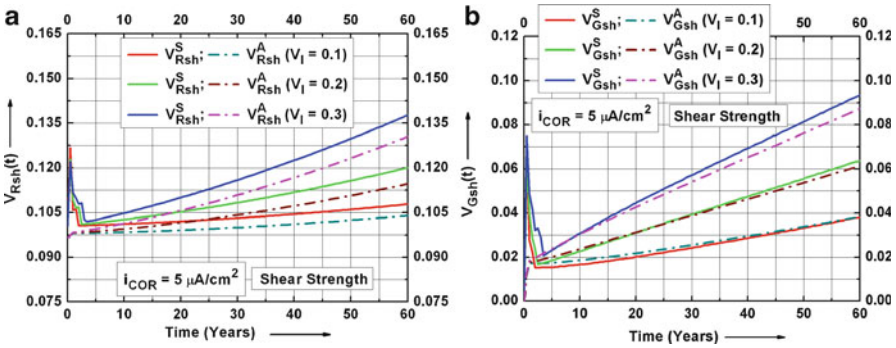

Fig. 23 (**a**): Comparison of time-dependent c.o.v. V^A_{Rsh} and V^S_{Rsh} for shear strength (i_{COR} = 5 μA/cm^2) (**b**): Comparison of time-dependent c.o.v. V^A_{Gsh} and V^S_{Gsh} for degradation function for shear strength (i_{COR} = 5 μA/cm^2)

7 Conclusions

The following conclusions are drawn from the present study:

1. Correlations with the experimental results indicate that the equations proposed for estimating the time-dependent mass loss of the reinforcement, W_s; reduced diameter of reinforcement, D_r; loss of cross-sectional area of reinforcement, A_{cor}; and corrosion penetration depth, X, are capable of providing their reasonable estimates that are in line with the available experimental trends.
2. Correlations with the experimental results indicate that good agreement is observed between analytical predictions and experimental results, for ultimate flexural and shear strengths for corrosion-affected RC beams. These findings also highlight the fair estimation of (1) time to peeling of cover concrete using

the proposed methodology to arrive at the time-dependent reduced concrete section and (2) W_s to arrive at the time-dependent reduced cross section of reinforcing steel.

3. A methodology to evaluate time-dependent strengths and c.o.v. associated with strengths is presented for corrosion-affected RC beams, by using LHS technique.
4. For corrosion-affected RC beams, it is shown that time-dependent mean flexural and shear strengths can be approximated by considering the linear terms in Taylor series expansion of their performance functions.
5. For corrosion-affected RC beams, time-dependent c.o.v. associated with the strength is influenced by the c.o.v. associated with annual mean corrosion rate, i_{COR}, at late stages of degradation (say 40–60 years).
6. Good agreement is observed between the analytical and simulated estimations for the time-dependent c.o.v. associated with flexural and shear strengths.
7. Good agreement is observed between the analytical and simulated estimations for the time-dependent c.o.v. associated with the degradation functions for the flexural and shear strengths.
8. Analytical estimation of c.o.v. associated with strengths and degradation functions substantially reduces the computational efforts involved in their estimation using LHS technique.

Acknowledgement The first author gratefully acknowledges the financial support provided by Japan Society for the Promotion of Science under JSPS RONPAKU Dissertation Ph.D. programme for pursuing Ph.D. at Nagoya University, Nagoya, Japan.

References

1. ACI (1995) Building code requirement for structural concrete (ACI 318-95) and commentary (ACI 318R-95). American Concrete Institute, Farmington Hills
2. Andrade C, Alonso C, Molina FJ (1993) Cover cracking as a function of rebar corrosion: part I – experimental test. Mater Struct 26:453–464
3. Bazant ZP (1979) Physical model for steel corrosion in sea structures – theory. J Struct Div ASCE 105(6):1137–1153
4. Benjamin JR, Cornell CA (1970) Probability, statistics, and decision for civil engineering. McGraw-Hill, New York
5. Bhargava K (2008) Time-dependent degradation and reliability assessment of RC structures subjected to reinforcement corrosion, Doctor of Engineering dissertation, Graduate School of Environmental Studies, Nagoya University, Nagoya, Japan
6. Bhargava K, Ghosh AK, Mori Y, Ramanujam S (2003) Analytical model of corrosion-induced cracking of concrete considering the stiffness of reinforcement. Struct Eng Mech Int J 16(6): 749–769
7. Bhargava K, Ghosh AK, Mori Y, Ramanujam S (2005) Modeling of time to corrosion-induced cover cracking in reinforced concrete structures. Cem Concr Res 35(11):2203–2218
8. Bhargava K, Ghosh AK, Mori Y, Ramanujam S (2006) Model for cover cracking due to rebar corrosion in RC structures. Eng Struct 28(8):1093–1109
9. BIS (2000) IS 456: 2000, Indian standard, plain and reinforced concrete – code of practice, 4th Rev, Bureau of Indian Standards, New Delhi, India

10. CEB–FIP (1990) CEB-FIP model code 1990, Comite Euro-International du Beton-Federation International de la Precontrainte. Thomas Telford, London
11. Ellingwood B (1977) Statistical analysis of RC beam-column interaction. J Struct Div ASCE 103(ST7):1377–1388
12. Ellingwood B (1982) Safety checking formats for limit states design. J Struct Div ASCE 108 (ST7):1481–1493
13. Ellingwood BR, Ang AHS (1974) Risk-based evaluation of design criteria. J Struct Div ASCE 100(ST9):1771–1788
14. Ellingwood B, Hwang H (1985) Probabilistic descriptions of resistance of safety-related structures in nuclear plants. Nucl Eng Des 88:169–178
15. Enright MP, Frangopol DM (1998) Service-life prediction of deteriorating concrete structures. J Struct Eng ASCE 124(3):309–317
16. Enright MP, Frangopol DM (1998) Probabilistic analysis of resistance degradation of reinforced concrete bridge beams under corrosion. Eng Struct 20(11):960–971
17. Frangopol DM, Lin KY, Estes AC (1997) Reliability of reinforced concrete girders under corrosion attack. J Struct Eng ASCE 123(3):286–297
18. Haldar A, Mahadevan S (2000) Reliability assessment using stochastic finite element analysis, 1st edn. Wiley, New York
19. Hong HP (2000) Assessment of reliability of aging reinforced concrete structures. J Struct Eng ASCE 126(12):1458–1465
20. Hong HP, Zhou W (1999) Reliability evaluation of RC columns. J Struct Eng ASCE 125 (7):784–790
21. Hwang H, Ellingwood B, Shinozuka M, Reich M (1987) Probability-based design criteria for nuclear plant structures. J Struct Eng ASCE 113(5):925–942
22. Israel M, Ellingwood B, Corotis R (1987) Reliability-based code formulations for reinforced concrete buildings. J Struct Eng ASCE 113(10):2235–2252
23. Li CQ (2003) Life cycle modeling of corrosion affected concrete structures – propagation. J Struct Eng ASCE 129(6):753–761
24. Li CQ, Lawanwisut W, Zheng JJ (2005) Time-dependent reliability method to assess the serviceability of corrosion-affected concrete structures. J Struct Eng ASCE 131(11):1674–1680
25. Liu Y (1996) Modeling the time to corrosion cracking of the cover concrete in chloride contaminated reinforced concrete structures, Ph.D. dissertation, Virginia Polytechnic Institute and State University, Blacksburg, Virginia, USA
26. Liu Y, Weyers RE (1998) Modelling the time-to-corrosion cracking in chloride contaminated reinforced concrete structures. ACI Mater J 95(6):675–681
27. Mangat PS, Elgarf MS (1999) Flexural strength of concrete beams with corroding reinforcement. ACI Struct J 96(1):149–158
28. Mckay MD, Bechman RJ, Conover WJ (1979) A comparison of three methods for selecting values of input variables in the analysis of output from a computer code. Technometrics 21(2):239–245
29. Mirza SA, MacGregor JG (1979) Variations in dimensions of reinforced concrete members. J Struct Div ASCE 105(ST4):751–766
30. Mirza SA, MacGregor JG (1979) Variability of mechanical properties of reinforcing bars. J Struct Div ASCE 105(ST5):921–937
31. Mirza SA, Hatzinikolas M, MacGregor JG (1979) Statistical description of strength of concrete. J Struct Div ASCE 105(ST6):1021–1037
32. Ranganathan R (2000) Structural reliability analysis and design, second Jaico impression. Jaico Publishing House, Mumbai
33. Rasheeduzzafar ASM, Al-Saadoun SS, Al-Gahtani AS (1992) Corrosion cracking in relation to bar diameter, cover and concrete quality. J Mater Civ Eng ASCE 4(4):327–343
34. Rodriguez J, Ortega LM, Casal J (1997) Load carrying capacity of concrete structures with corroded reinforcement. Constr Build Mater 11(4):239–248

35. SP16 (1980) Design aids for reinforced concrete to IS: 456-1978. Bureau of Indian Standards, New Delhi
36. Stewart MG, Rosowsky DV (1998) Time-dependent reliability of deteriorating reinforced concrete bridge decks. Struct Saf 20:91–109
37. Thoft-Christensen P (1998) Assessment of the reliability profiles for concrete bridges. Eng Struct 20(11):1004–1009
38. Torres-Acosta AA (1999) Cracking induced by localized corrosion of reinforcement in chloride contaminated concrete, Ph.D. dissertation, Department of Civil and Environmental Engineering, University of South Florida, Tampa, Florida, USA
39. Val DV, Stewart MG, Melchers RE (1998) Effect of reinforcement corrosion on reliability of highway bridges. Eng Struct 20(11):1010–1019
40. Vu KAT, Stewart MG (2000) Structural reliability of concrete bridges including improved chloride-induced corrosion models. Struct Saf 22:313–333
41. Vu KAT, Stewart MG (2005) Predicting the likelihood and extent of reinforced concrete corrosion-induced cracking. J Struct Eng ASCE 131(11):1681–1689

Refined Modeling of Crack Tortuousness to Predict Pressurized Airflow Through Concrete Cracks

L.R. Bishnoi, R.P. Vedula, and S.K. Gupta

Abstract Cracks may appear in the pressurized concrete containment of a nuclear power plant during a severe accident and provide leak paths for release of radioactive aerosols dispersed in the contained air. In this study, numerical results for air leakage through concrete cracks are reported for a range of pressure gradients and crack widths relevant to containment atmosphere during a severe accident scenario. Crack geometry in 2D is generated using statistical crack model to account for crack tortuousness. While airflow predictions through such models provide good agreement with experimental results reported in literature, the computational results generally provide over-prediction of airflow. The statistical crack models account for the gross tortuousness of the concrete cracks based on experimental studies. The local tortuousness of the order of grain size that can deflect the crack from straight path is not accounted in these models. In this study, fractal geometry-based curves are used to introduce the local tortuousness within the global crack segments represented by straight lines in the statistical models. Comparison of pressurized airflow rates obtained from such refined crack model with the experimental values reported in literature for plain concrete shows very good agreement. The effect of local tortuousness on the pressurized airflow rates was accounted indirectly in 3D crack models for reinforced concrete with modified crack morphology due to reinforcing steel. The computational results with corrections due to local tortuousness compared well with the experimental values

L.R. Bishnoi (✉)
Siting & Structural Engineering Division, Atomic Energy Regulatory Board, Mumbai, India
e-mail: lr.bishnoi@gmail.com

R.P. Vedula
Mechanical Engineering Department, Indian Institute of Technology Bombay, Mumbai, India
e-mail: rpv@iitb.ac.in

S.K. Gupta
Safety Analysis & Documentation Division, Atomic Energy Regulatory Board, Mumbai, India
e-mail: guptask@aerb.gov.in

S. Chakraborty and G. Bhattacharya (eds.), *Proceedings of the International Symposium on Engineering under Uncertainty: Safety Assessment and Management (ISEUSAM - 2012)*,
DOI 10.1007/978-81-322-0757-3_24,

for pressurized airflow through cracks in reinforced concrete panels reported in literature.

Keywords Severe accident • Containment • Concrete cracks • Tortuousness • Fractal geometry • Airflow

1 Introduction

A major fraction of the airborne radioactivity within nuclear reactor containment, consequent to a postulated severe accident involving reactor core meltdown, consists of aerosols generated by condensation of volatile fission products. The containment envelope becomes pressurized during a severe accident, and there is a possibility of cracks through concrete shell of the containment, which can provide leak paths for pressurized air and aerosol release to the outside atmosphere.

Rizkalla et al. [1] reported experimental data for leakage rate through cracks in reinforced concrete test panels and suggested correlations. Riva et al. [2] performed finite element analysis of reinforced concrete test panels to calculate equivalent average single crack width for evaluating leakage rate with different correlations and reported good match of the test leakage rate with the calculated rate using correlation of Rizkalla et al. [1]. Gelain and Vendel [3] performed experiments on plain concrete panels and computed crack geometry as an equivalent rectangular channel, which would have the same flow rate as the experimental data. Boussa et al. [4] generated cracks in a large number of test specimens of different concrete grades, modelled the crack profile in terms of statistical parameters and reported good agreement of the crack profile obtained from the statistical model with the experimental data. Bishnoi et al. [5] conducted computational studies for airflow and aerosol transport through cracks in plain concrete using statistical crack model of Boussa et al. [4] and reported good match between the computational and experimental results. Bishnoi et al. [6] studied effect of reinforcing steel on airflow through cracks in reinforced concrete using computational models incorporating modified crack morphology due to reinforcing steel derived from stress analysis of reinforced concrete panels.

In this study, numerical results for air leakage through concrete cracks are reported for a range of pressure gradients and crack widths relevant to containment atmosphere during a severe accident scenario. Crack geometry is generated using statistical crack model of Boussa et al. [4] to account for crack tortuousness. While airflow predictions using such computational model provide good agreement with experimental results reported in literature, the numerical results generally provide over-prediction of airflow. The Boussa crack model defines gross tortuousness of the concrete cracks in statistical terms derived from experimental studies. Local tortuousness of the order of grain size that can deflect the crack from straight path is not accounted in these models.

The Boussa crack model is refined in this study by using fractal geometry-based curves to introduce the local tortuousness within the global crack segments represented by straight lines. The airflow study results from such refined model are compared again with the experimental values. The comparison shows very good agreement between computational values from the refined crack model and the experimental values of Gelain and Vendel [3] for cracks in plain concrete. The computational airflow studies through cracks in reinforced concrete also shows very good agreement with experimental results of Rizkalla et al. [1] when the effect of local tortuousness is accounted along with the effect of reinforcing steel on the crack morphology.

Statistical crack model including refinement of the crack morphology to represent the local tortuousness using fractal geometry methods was implemented in MATLAB. Fluent (version 6.2.16, 2005) was used for airflow computations through the crack models.

2 Numerical Procedure

The crack model parameters were chosen to represent concrete grade in the range of M50–M60, typically used to construct containment structures. The range of pressure gradients and crack widths for the study has been reported in Bishnoi et al. [5]. These parameters were chosen to be representative of air leakage through containment leak paths, which are likely to exist under postulated severe accident conditions in water-cooled reactor-based nuclear power plants.

The 2D crack profile is defined in terms of straight segments and deviation of these segments from horizontal line by specifying mean value and standard deviation separately for these two parameters as per the approach suggested by Boussa et al. [4]. Two identical profiles placed at a constant spacing equal to the crack width represent two lips of the crack in 2D. Details of statistical crack model in 2D are reported in Bishnoi et al. [5]. Refinement of the 2D crack model was done to represent roughness due to local tortuousness, introduced by crack tip deflecting material grains using fractal geometry, for each of the straight segments. Random midpoint displacement method [7] was used to approximate local deflection of the crack due to micrometer size concrete material grains as approximate fractal Brownian motion representation.

A typical statistical crack model geometry representing global tortuousness of the crack is shown in Fig. 1. Typical global tortuousness and local tortuousness in portion 'A' of the global crack model geometry, derived using random midpoint displacement method, are depicted in Fig. 2.

To construct the fractal geometry representing local tortuousness in a straight segment of the crack, displaced y-value of the midpoint (based on x-coordinates of the end points) of the straight line is calculated as the average of the y-values

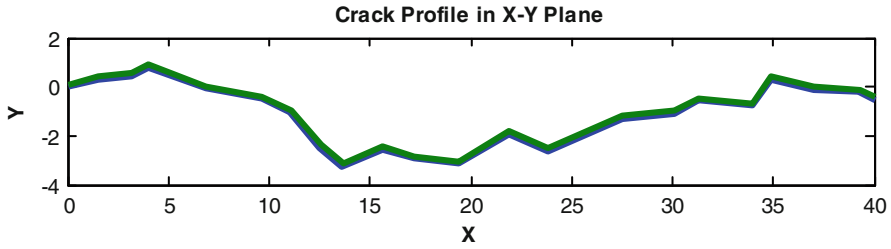

Fig. 1 Typical 2D crack model representing global tortuousness (all dimensions in mm)

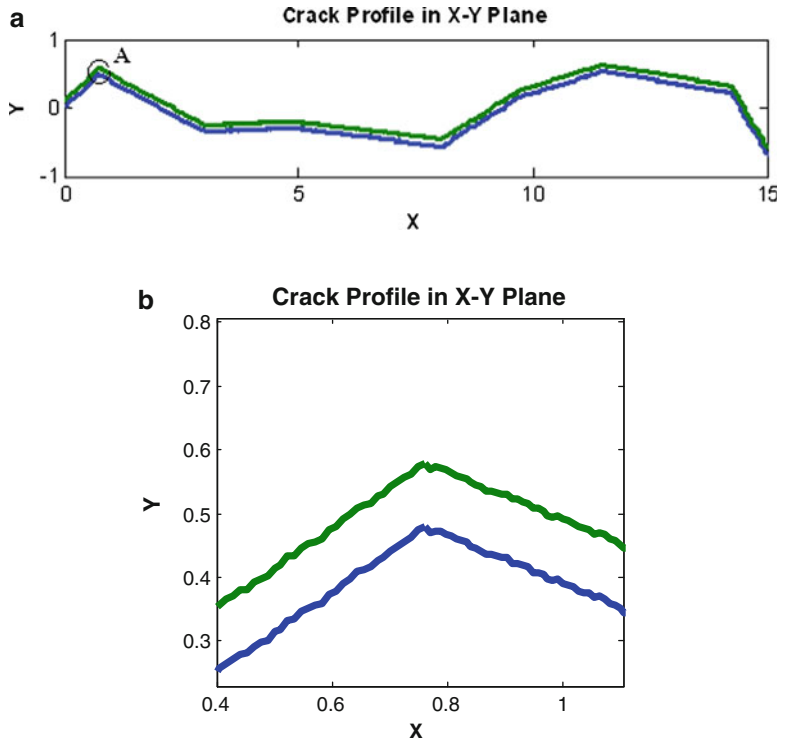

Fig. 2 Depiction of typical global and local tortuousness (all dimensions in mm). (**a**) Global tortuousness, (**b**) enlargement of portion 'A' in (**a**) to view local tortuousness

of the endpoints plus a random offset. The process is repeated by calculating a displaced y-value for the midpoint of each half of the subdivided line. The subdivision is continued until the subdivided line segments are less than a preset value, s_{lim}.

The random offset, r, is calculated as follows:

$$r = sr_g \langle L \rangle \tag{1}$$

where s is a selected 'surface roughness' factor, r_g is a Gaussian random value with mean zero and variance one and L is the length of the straight line.

Nominal diameter of the capillary pores in cement paste varies from about 0.3 to 3 μm [8]. Assuming water cement ratio of 0.45, porosity of cement paste works out to be about 11.5% [8]. Considering average size of capillary pores in the range of 1–1.5 μm, the material inhomogeneity affecting crack path (i.e. effective grain size for crack deflection) was taken in the range of 7.5–15 μm. The surface roughness (i.e. deviation from straight path) was considered to be in the range of ¼ to ½ of the grain size, and the actual variation was approximated to be 2.5–5 μm. The values adopted in the current study are 3 and 10 μm for s and s_{lim}, respectively, which were arrived at from parametric airflow computations on crack models with varying values of s and s_{lim} in the size ranges stated above.

Stress analyses were performed on finite element (FE) model of a reinforced concrete experimental test specimen (L4) from Rizkalla et al. [1] to derive morphology and extent of crack surfaces to be used for airflow calculations. Specimen L4 was selected because complete details of geometry, reinforcement, cracking and airflow results are reported for this specimen only. Uniaxial tensile load was applied to reinforcing steel bars in the stress analysis models as was done in the experimental study. Two non-linear analyses were conducted: one with reinforcing steel and another with plain concrete without reinforcement to see the effect of reinforcing steel on crack surface pattern growth compared to the plain concrete. These analyses indicated sudden spread of the concrete damage in plain concrete from exterior faces to the entire cross section, whereas the reinforcement does not allow spread of the damage over the entire cross section even at ultimate load, though the extent of damage keep increasing with load increments. Typical damage spread over the cross section of the test specimen for plain concrete and reinforced concrete are shown in Fig. 3a, b, respectively.

Linear stress analysis was conducted with a priori crack in the form of a slit of finite width to obtain the likely morphology of the crack around reinforcing steel bars under uniaxial tensile load. Typical crack surface contours due to the effect of reinforcing steel are depicted in Fig. 4. Details of these analyses and the modified 3D crack geometry are reported in Bishnoi et al. [6].

The standard Navier–Stokes and continuity equations are solved for the flow domain defined by the crack morphology using the finite volume method (FVM) with SIMPLEC algorithm for pressure–velocity coupling and second-order upwind scheme with under relaxation factor of 0.5 for discretization of momentum equations. Atmospheric pressure was assumed at outlet, and inlet pressure was calculated according to the specified pressure gradient. No-slip condition was imposed at crack wall boundaries. All case studies were conducted for a constant temperature of 300 K. Since the pressure drop across the crack is not large, the flow is assumed incompressible and confirmed by checking the flow Mach numbers, which remained much below unity for all the cases. The constant air density was assumed to be 1.225 kg/m^3. Details of optimized computational grid and validation of the crack model for 2D airflow computations are reported in Bishnoi et al. [5]. Typical grids for numerical computation of pressurized airflow in the crack model

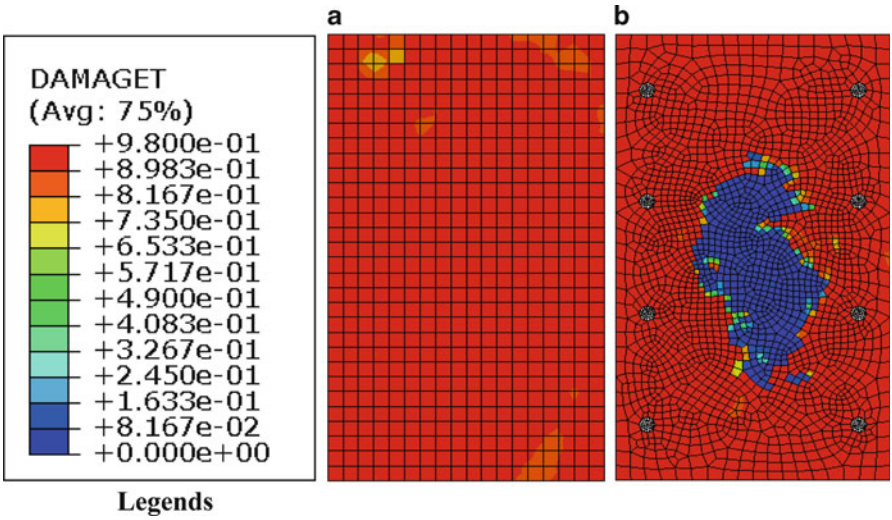

Fig. 3 Concrete damage spread over the X-sections of specimen models at ultimate load, (**a**) plain concrete, (**b**) reinforced concrete

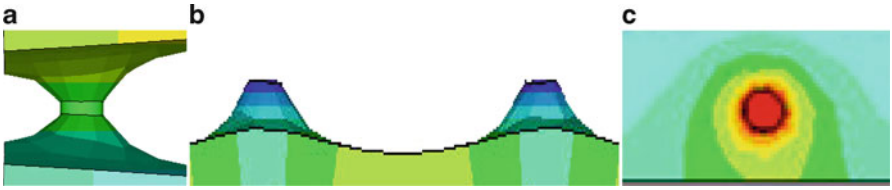

Fig. 4 Crack surface contours around rebar, (**a**) cross section along crack path through rebar, (**b**) typical crack profile across the flow path between rebar at the edge and (**c**) typical crack surface contour in plan around a rebar

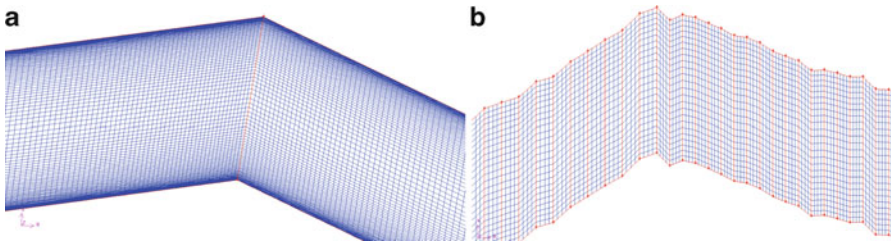

Fig. 5 Typical grids used for numerical computation of pressurized airflow using FVM, (**a**) crack model with global tortuousness alone, (**b**) refined crack model with both global and local tortuousness

with (a) the global tortuousness alone and (b) the refined crack model incorporating the local tortuousness are depicted in Fig. 5.

Numerical procedure established for airflow through 2D crack path was extended to 3D crack surfaces for airflow computations through cracks in reinforced concrete.

3 Results and Discussion

3.1 Airflow Through Cracks in Plain Concrete

Considering enormous computational resources and convergence issues associated with large-size models, a comparative study of flow rate was conducted for crack lengths of 15, 40 and 70 mm and crack widths of 0.1, 0.2 and 0.3 mm with same model parameters to explore feasibility of restricting crack length for computational model. The study confirms that a crack length as small as 15 mm could also be considered as a representative sample for airflow studies. In view of this, an intermediate crack length of 40 mm was chosen for airflow computations with the global tortuousness. The crack length was restricted to 15 mm for the refined model incorporating the local tortuousness because of computational constraints arising due to model size.

The results in terms of friction factor (f) as a function of Reynolds number (Re) for the Boussa crack model representing the global tortuousness of the crack are shown in Fig. 6a. Several different pressure gradients (0.25–1 bar/m) were used in the computations to generate the plot. The results reported by Gelain and Vendel [3] for plain concrete are superposed in the figure and the comparison is noticed to be within 25% for majority of the data points. Figure 6b depicts f versus Re along with a curve fit.

The computational study was repeated with the refined crack model incorporating the local tortuousness besides the global tortuousness. The results are shown in Fig. 7a along with the experimental results of Gelain and Vendel [3].

While most of the data points from refined model computation and experimental values are within 9%, the maximum difference in friction factor (f) values is within 16%. Figure 7b depicts f versus Re along with a curve fit for the results from the refined model.

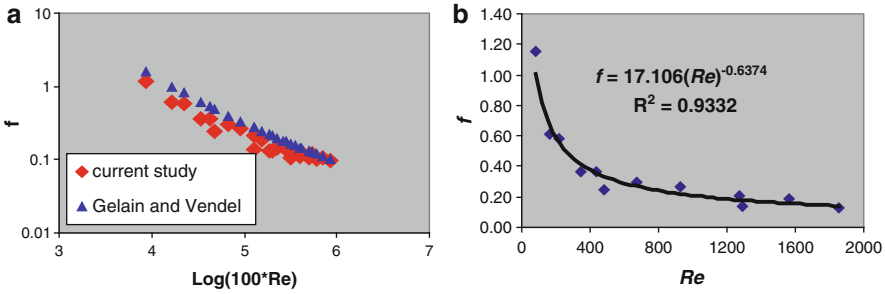

Fig. 6 Plot of f versus Re for the crack model with global tortuousness alone, (**a**) comparison of computational and experimental results, (**b**) curve-fit for computational results

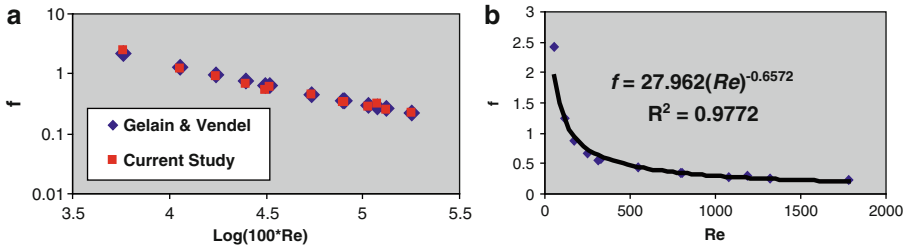

Fig. 7 Plot of f versus Re for the refined crack model incorporating local tortuousness, (**a**) comparison of computational and experimental results, (**b**) curve-fit for computational results

Table 1 Experimental and computational airflow rates through cracks in RC

Measured flow through reinforced concrete test specimen L4 [1]	Flow calculated from refined 2D crack model for plain concrete	3D crack model for plain concrete		3D crack model with modified morphology due to rebar and flow area constricted in the central region of the test specimen			
		Calculated flow	Diff. w.r.t. (2) (%)	Calculated flow	Diff. w.r.t. (1) (%)	Diff. w.r.t. (2) (%)	Diff. w.r.t. (3) (%)
(1)	(2)	(3)	(4)	(5)	(6)	(7)	(8)
5.18e-4	7.084e-4	8.288e-4	+17	5.305e-4	+2.4	−25.11	−36

3.2 *Airflow Through Cracks in Reinforced Concrete*

Airflow calculations were performed for specified pressure difference of 106 kPa across the specimen thickness of 178 mm (i.e. pressure gradient of 5.96 bar/m) and specified average crack width of 0.06 mm using the computational model generated for 3D crack morphology of the test specimen, as described earlier in numerical procedure section, as well as with refined 2D crack model. The airflow computations were repeated with 3D crack model modified by restricting the crack flow surface area in the central region of the model as observed in the non-linear stress analysis. Details of the airflow computational models are reported in Bishnoi et al. [6].

The airflow rates through the two 3D crack models were compared with the flow rate through a 3D plane crack in which two plane surfaces were separated by the average crack width value instead of the tortuous crack morphology. All the 3D crack morphology computations for flow rate were adjusted to account for the correction due to local tortuousness, which could not be accounted directly in these models. A detailed comparison of flow rates (m^3/s) from different 2D and 3D models is reported in Bishnoi et al. [6]. Results relevant to the scope of this chapter are provided in Table 1.

From the above comparison, it is seen that the 3D crack model, incorporating the crack morphology derived by considering the local effect of rebar including

the restricted flow surface area in the central region of the test specimen, a phenomenon revealed in RC members through non-linear stress analysis [6], as well as the effect of local tortuousness, provide excellent comparison with the flow obtained experimentally. The difference between the flow rate calculated from 2D crack model for plain concrete and 3D model for plain crack is attributed to the global crack tortuousness, which has been incorporated in the 2D model only and not in 3D model for plain concrete.

4 Conclusions

Results of computational studies for pressurized airflow through cracks in concrete are reported. The statistical crack model available in the literature has been refined to incorporate local tortuousness of the crack due to the smallest material inhomogeneity that can affect the airflow rates. The local tortuousness is introduced using fractal geometry-based curves. The computational results for pressurized airflow through refined crack models are compared with the experimental values reported in the literature for cracks in plain concrete and reinforced concrete. The comparison shows very good agreement between the computational results and the experimental values.

These studies have certain limitations. The parameters considered for fractal curve approximation of the crack tortuousness are the surface roughness and the limiting value of straight crack segment, which are considered to be functions of the level of material inhomogeneity affecting the crack propagation and its deflection from the straight path. These parameters have been approximated from the knowledge of cement paste properties and parametric studies for airflow were conducted to arrive at the most appropriate values. Further studies are required to establish these parameters for different grades of concrete and sensitivity of the airflow results to these parameters. In case of reinforced concrete, establishing the size of uncracked zone in the interiors of the concrete structural elements and sensitivity of the airflow results to this parameter requires further studies.

References

1. Rizkalla SH, Lau BL, Simmonds SH (1984) Air leakage characteristics in reinforced concrete. J Struct Eng (ASCE) 110(5):1149–1162
2. Riva P, Brusa L, Contri P, Imperato L (1999) Prediction of air and steam leak rate through cracked reinforced concrete panels. Nucl Eng Des 192:13–30
3. Gelain T, Vendel J (2008) Research works on contamination transfers through cracked concrete walls. Nucl Eng Des 238:1159–1165
4. Boussa H, Tognazzi-Lawrence C, La Borderie C (2001) A model for computation of leakage through damaged concrete structures. Cem Concr Compos 23:279–287

5. Bishnoi LR, Vedula RP, Gupta SK (2010) Characterization of pressurized air leakage and aerosol transport through cracks in concrete. In: Proceedings of the 37th international and 4th national conference on fluid mechanics and fluid power (FMFP2010). Paper ID: 311, Indian Institute of Technology Madras, Chennai, India, 16–18 December
6. Bishnoi LR, Vedula RP, Gupta SK (2010) Effect of reinforcing steel on pressurized air leakage through cracks in concrete, transactions, SMiRT21. Div-III: Paper ID# 496, New Delhi, India, 6–11 November 2011
7. Hearn D, Baker M (1994) Computer graphics, 2nd edn. Prentice Hall, Englewood Cliffs
8. Neville AM (2000) Properties of concrete. Pearson Education Asia Pte. Ltd., Harlow

Experiences in Subsurface Investigations Using GPR

G. Venkatachalam, N. Muniappan, and A. Hebsur

Abstract The primary source of information in a geotechnical engineering exploration programme is boreholes. However, in many projects, the investigation is inadequate, and uncertainties about the subsurface prevail and adversely affect the cost-effectiveness and reliability of the design process. Safe designs are adopted to overcome the lack of information. Since collecting additional information through boreholes may be difficult, a non-invasive technique could help. Ground-penetrating radar (GPR) is one such non-invasive technique suitable for shallow and deep subsurface mapping. It has, in recent times, emerged as a viable tool for subsurface mapping. With the choice of GPR antennae of appropriate frequencies, one can explore to depths varying from 3 to 100 m. This chapter describes the principle and practice of operation of a GPR and presents four instances where uncertainties and inadequate knowledge of subsurface were alleviated through GPR surveys and critical decisions regarding foundations could be taken confidently.

Keywords Uncertainties • GPR • Non-invasive technique • Radargram • Subsurface mapping • Foundation

1 Introduction

Geotechnical exploration is an expensive activity in any project and, not infrequently, accorded inadequate importance. Therefore, a geotechnical engineer has to frequently deal with situations involving limited in situ investigations and

G. Venkatachalam (✉)
Emeritus Fellow, Department of Civil Engineering, Indian Institute of Technology Bombay, Mumbai, India
e-mail: gveecivil@gmail.com

N. Muniappan • A. Hebsur
Research Scholar, Department of Civil Engineering, Indian Institute of Technology Bombay, Mumbai, India
e-mail: muniappan19@gmail.com; almelu84@gmail.com

S. Chakraborty and G. Bhattacharya (eds.), *Proceedings of the International Symposium on Engineering under Uncertainty: Safety Assessment and Management (ISEUSAM - 2012)*,
DOI 10.1007/978-81-322-0757-3_25,

inadequate data. Uncertainties, therefore, are not new in geotechnical engineering. The errors and uncertainties associated with the data make the decision making process difficult and of questionable reliability.

1.1 Uncertainties

There are several perceptions regarding uncertainties. An excellent idea about uncertainties can be had from Juang and Elton [11], Dodagoudar and Venkatachalam [6]. Very broadly, they are classified as aleatory and epistemic [2]. Comparative studies of different methods may be seen in Bhattacharya et al. [3] and Venkatachalam [19]. Uncertainties in geotechnical engineering arise at the exploration stage itself and propagate right up to the performance stage owing to a number of subjective factors as listed below:

1. Exploration stage:
   (a) Field description of subsurface strata in borehole logs leaves scope for interpretation, since it is not always done by a domain specialist.
   (b) Descriptions of strata even at the same location could vary when exploration is done by different agencies.
   (c) Delineating the boundaries between strata involves subjective averaging.
2. Sampling and testing stage:
   (a) Uncertainties due to spatial variability in properties.
   (b) Uncertainties due to statistically inadequate sampling.
   (c) Errors due to testing techniques, testing equipment and test conditions not simulating field conditions – (1) systematic errors and (2) random errors.
   (d) Errors due to skill of the testing personnel.
   (e) Errors due to scale of the problem – local or regional; some errors of a spatial nature get averaged out when the region is large.
3. Analysis stage:
   (a) Level of abstraction/idealization of problem – in this case, limit equilibrium method and its attendant assumptions and idealizations
   (b) Accuracy of computational models used/performance function used
   (c) Uncertainties in estimating triggering factors
   (d) Modelling support measures, e.g. reinforcement
4. Design stage:
   (a) Simplified design philosophies
   (b) Subjective judgement exercised during choice of design parameters
5. Performance stage:
   (a) Intermittent slope modification
   (b) Use of same factor of safety for short- and long-term performance

Due consideration must be given for the uncertainties arising out of these variabilities. And that is what reliability analysis does. It may be said that reliability analysis is all about the confidence that can be reposed on the deterministic analysis, and the two are to be looked upon and used as complementary techniques. Reliability engineering helps to address these uncertainties in the data. However, a way to supplement the data with more information and remove the uncertainties to an extent possible is a better alternative. Fortunately, a trend towards conducting a GPR survey as a prelude to geotechnical exploration is now evident. This is a welcome trend because it gives an opportunity to plan the geotechnical investigations economically and optimally so that no surprises are thrown up during actual foundation excavation and construction. Ground penetrating radar (GPR) is one such non-invasive technique suitable for shallow and deep subsurface mapping.

Since collecting more information through additional boreholes may be difficult, a non-invasive technique could help. GPR has, in recent times, emerged as a viable tool for subsurface mapping. With the choice of GPR antennae of appropriate frequencies, one can explore to depths varying from 3 to 100 m. This chapter describes the principle and practice of operation of a GPR and presents four instances where uncertainties and inadequate knowledge of subsurface were alleviated through GPR surveys and critical decisions regarding foundations could be taken confidently.

2 Ground Penetrating Radar

Ground penetrating radar, also referred to as georadar or GPR, is a tool for subsurface imaging, which is a form of close-range remote sensing. It is a type of radar which can be used to detect objects buried underground, in contrast with the radar used to identify features on the land or in the ocean or sky. This method uses the radio waves to probe the ‘ground’, which simply means any low-loss dielectric material (Jol [12]). It operates in the frequency range from 10 MHz to 2 GHz (microwave band), depending on the device. It has an antenna emitting electromagnetic energy and another that receives the reflected energy from the surfaces as well as from the inner layers. It works on the basis of contrasts in dielectric constant in the subsurface. The energy reflected is transformed into visual images, which provide extensive data on the subsurface materials and objects, when interpreted properly.

Ground penetrating radar (GPR) is perhaps the only geophysical technique, which detects buried objects and helps to get continuous, real-time profiles of the subsurface, through imaging in an appropriate frequency of the electromagnetic spectrum.

The degree of information obtainable about the buried objects or subsurface layers depends on the GPR antenna parameters, mainly central frequency, radial and lateral resolutions. At lower frequencies, GPR pulses can get information for higher depths but at lower resolution; similarly at higher frequencies, GPR pulses have lesser penetrability but much better resolution.

Subsurface mapping applications are reported in archaeology, foundation engineering and seepage. Conyers et al. [4] have described archaeological applications, wherein successive layers of excavation are carefully planned after ascertaining the presence of buried artefacts. Also, Nobes and Lintott [16] have successfully mapped the foundation of Victorian-age lecture hall using GPR, and Nobes and Sikma [17] tested stability of the foundations of the Cathedral of the Blessed Sacrament church. Successful identification of subsurface oil leaks by GPR is given by King [13], and accurate determination of the failing concrete floor slab which is 50 m in diameter and 8 m deep which is 7 m below the ground level was carried out by King et al. [14]. GPR has been used successfully mainly for mapping underground utilities such as pipes, conduits and cables. Underground features which have been successfully detected include buried land mines (Daniels [5]), pipes (Shihab and Al-Nuaimy [18]) and erosional voids (Anchuela et al. [1]). Gomez-Ortiz et al. [8] have reported the use of a number of frequencies, namely, 100, 200, 250 and 500 MHz for imaging the shallow substructure in coastal Spain. Whereas the 100-MHz antenna was useful in locating the water table at 5–6 m depth, the 200- to 500-MHz antennae allowed the determination of the internal structure of the coastal sand deposits helping to infer their progradation dynamics.

An interesting application of GPR is in detecting clandestine mass burial sites during criminal investigations. Fiedler et al. [7] and Koppenjan et al. [15] have reported successfully tracing buried bodies of humans, pigs and buffaloes using 200- to 900-MHz frequencies. The higher frequency gave slightly better penetration below the concrete slab covering the cadavers and the effectiveness of degradation of the body also could be judged.

3 Applications

In this chapter, four instances are illustrated, wherein GPR has been successfully used to gather useful information not available in boreholes. In these instances, the main uncertainty was regarding the lateral or vertical extension of a specific subsurface layer, which was to be the founding layer for either a shallow or a deep foundation. The details of the studies are given below.

4 Study 1

This was a site where a 16-storey residential building was being planned. Figure 1 shows the site map along with the locations of bore holes BH1, BH2, BH3 and BH4. The issue here was the uncertainty concerning the continuity of the breccia layer between the boreholes as the boreholes were far from each other, especially boreholes 2 and 4. In view of this, the usual linear interpolation did not appear reasonable. This had implications for deciding the level at which the pile foundations of the proposed building should be terminated.

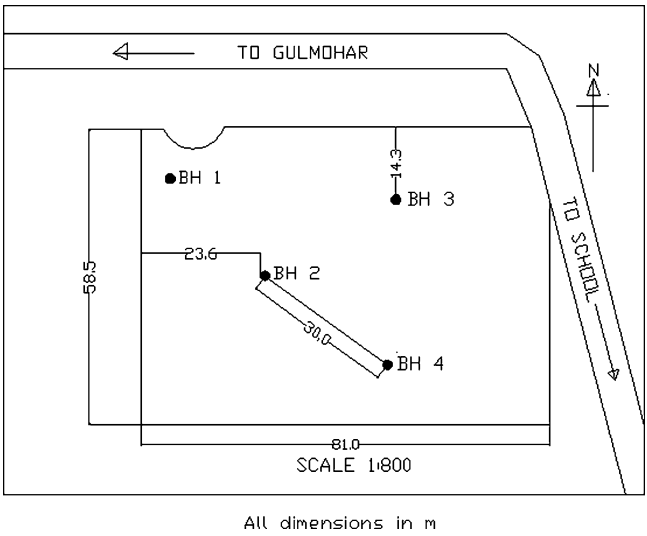

Fig. 1 Site map along with the line of traverse study area 1

Table 1 Initial settings made during data collection

Antenna used (MHz)	80
Mode of data collection	2D (point mode)
Mode of polarization	Co-polarized
Transmitter and receiver spacing (m)	1
Length or area of survey	30 m
Dielectric constant	30
Range (ns)	370
Scans/s	64
Scans/m	5
Vertical IIR filter range (MHz)	60–100
Horizontal IIR stack (no. of scans)	64

GPR data was collected along several traverses, including along the line from BH2 to BH4. Initial settings used are given in Table 1.

The borehole data BH2 and BH4 along with the core recovery values are as shown in Fig. 2. According to BH2, the location where it was driven has four layers. BH4, on the other hand, shows only 2 layers. Though the core recovery values are changing, there is no change in the layers. It is also quite possible that the layers are not captured properly as these stratifications are done manually on the basis of visual interpretation. This necessitated verification of the thicknesses of the layers, particularly, 3 and 4.

The GPR scan data is processed for position correction, data filtering using spatial FFT and stretching, (GSSI 2007) [9]. Spatial FFT is applied with low- and high-pass filters of 120 and 40 MHz, respectively, to remove the noise. For clarity, the filtered data is stretched four times using horizontal scaling. Figure 3a, b show the raw data and the corrected and stretched data.

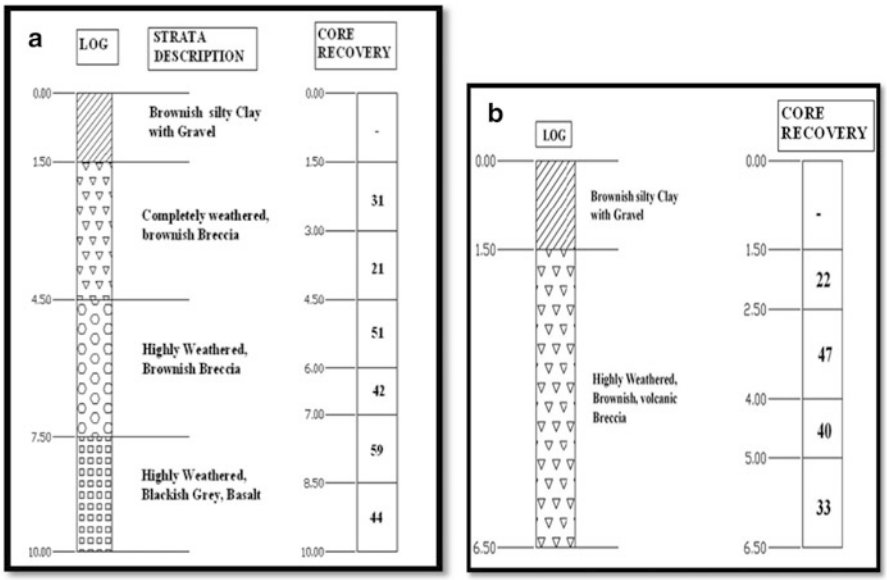

Fig. 2 Borehole data (**a**) BH2 data with core recovery values (**b**) BH4 data with core recovery values

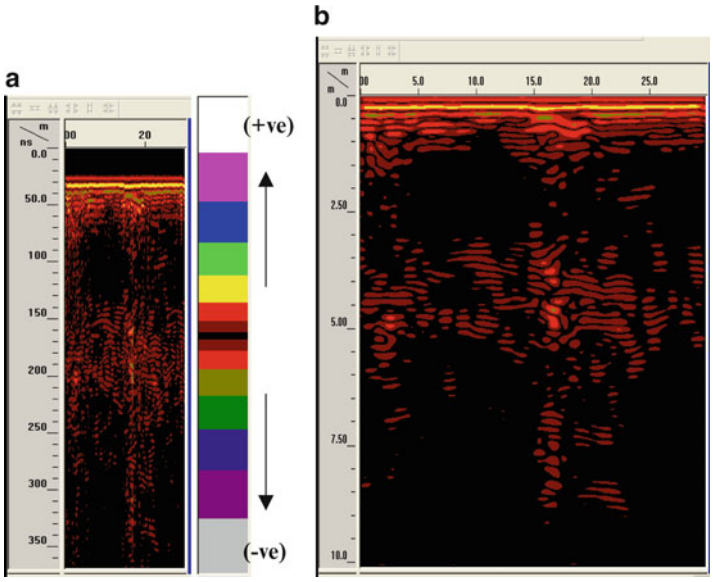

Fig. 3 Raw and post-processed data. (**a**) Raw data (**b**) corrected and stretched data

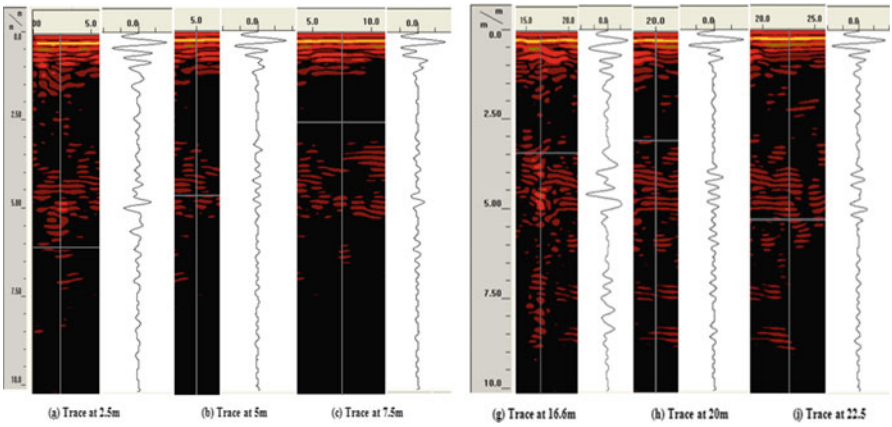

Fig. 4 Traces along the survey traverse

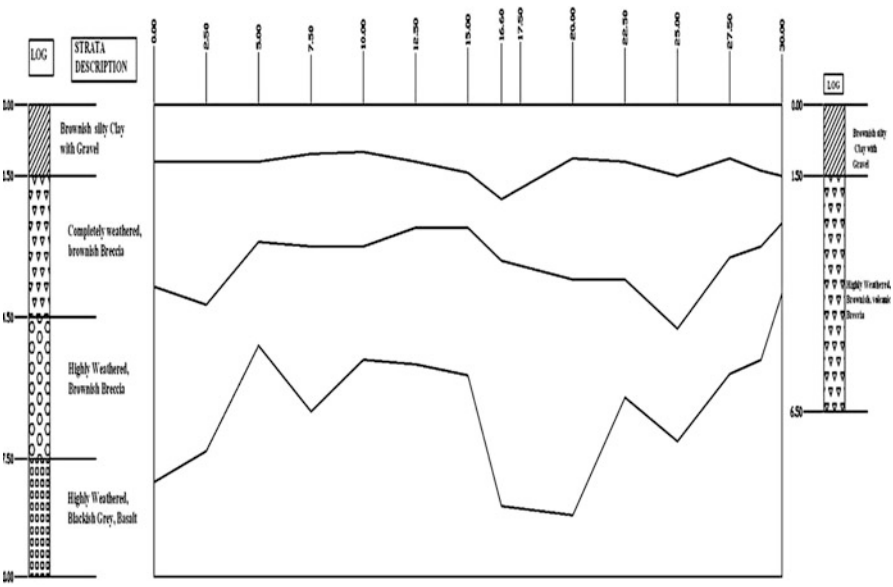

Fig. 5 Variation of subsurface layers from BH2 to BH4

From the above stretched data, at every interval of 2.5 m, wiggle traces have been taken and those up to 7.5 m from either side are presented in Fig. 4. Based on the wiggle traces and the radargram, a subsurface section is drawn as depicted in Fig. 5. The figure shows anomalies in third layer thickness at two places –2.5–7.5 m and 15–22.5 m. This was useful in deciding the founding depth of the foundations at this location. This also raised doubts about the log of BH4. A second look at the core recovery values in BH4 showed that, in fact, there are two breccia layers of different degrees of weathering.

5 Study 2

This study also relates to GPR subsurface profiling at a construction site. A four-storey building was planned at this site. The issue here was that only three boreholes were drilled almost parallel to the eastern side of the plot thus leaving the central and western sides unexplored (Fig. 6). In order to get this missing information, data was collected with 400, 200, 80 and 40 MHz antennae, with penetrabilities ranging from 3 to 15 m. GPR data was collected along 2D grids and linear traverses. A single traverse was taken from borehole location BH3 to borehole location BH1. The results of the single traverse are presented in this chapter. This was also useful to check the adequacy of the borehole investigation.

Figure 6 shows the site map along with the locations of boreholes BH1, BH2 and BH3. GPR data was collected along the line of traverse AB stretching from near BH3 to a point close to BH1.

The data acquisition settings are given below in Table 2.

The data obtained for traverse AB for 200 and 400 MHz, after post-processing are presented in Figs. 7 and 8. For 80 MHz, the results are shown in Fig. 9 in the form of wiggle traces for the first 10 m and last 10 m.

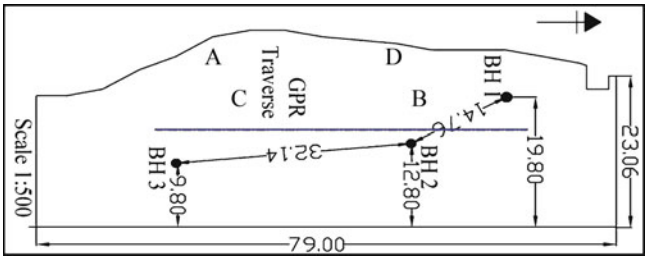

Fig. 6 Site map along with the line of traverse study area 2

Table 2 Initial settings made during data collection

Antenna used (MHz)	200, 400, 80, 40
Mode of data collection: 200, 400	Dist. mode
80, 40	Point mode
Mode of polarization	Co-polarized
Transmitter and receiver spacing (m)	1
Length or area of survey	50 m
Dielectric constant	6
Range (ns)	370
Scans/s	64
Scans/m	5
Vertical IIR filter range (MHz)	60–100
Horizontal IIR stack (no. of scans)	64

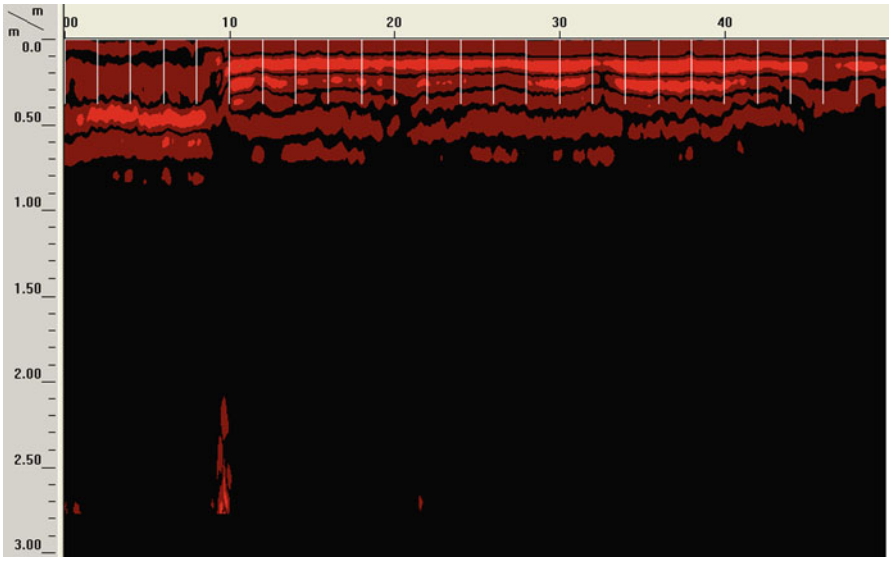

Fig. 7 Post-processed radargram for 200 MHz

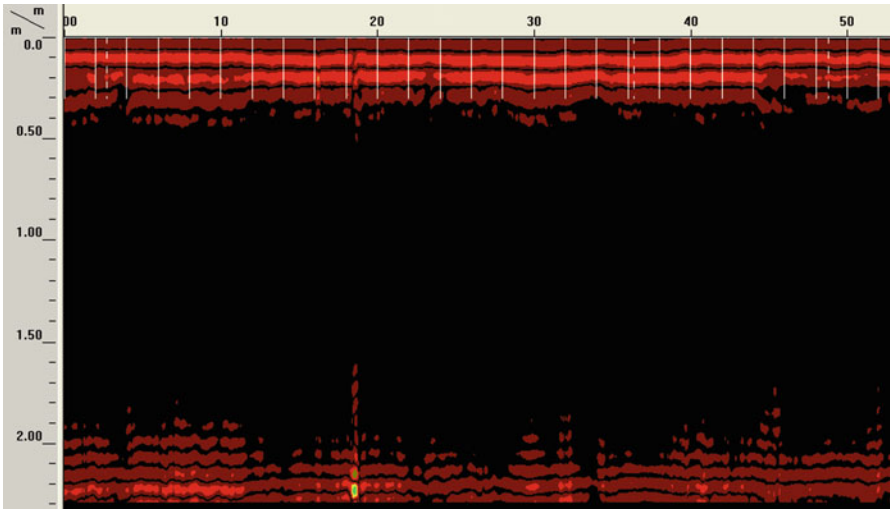

Fig. 8 Post-processed radargram for 400 MHz

Some obvious observations based on the radargrams are the following: the 200- and 400-MHz antennae show the presence of a uniform layer up to a depth of 0.5 m followed by another more reflecting material up to about 2.5 m. However, 80-MHz data shows that the second layer is extending beyond 2.5 m, possibly up to about 7 m. Beyond 7 m, 80 MHz loses the signal strength and is not sensitive enough for

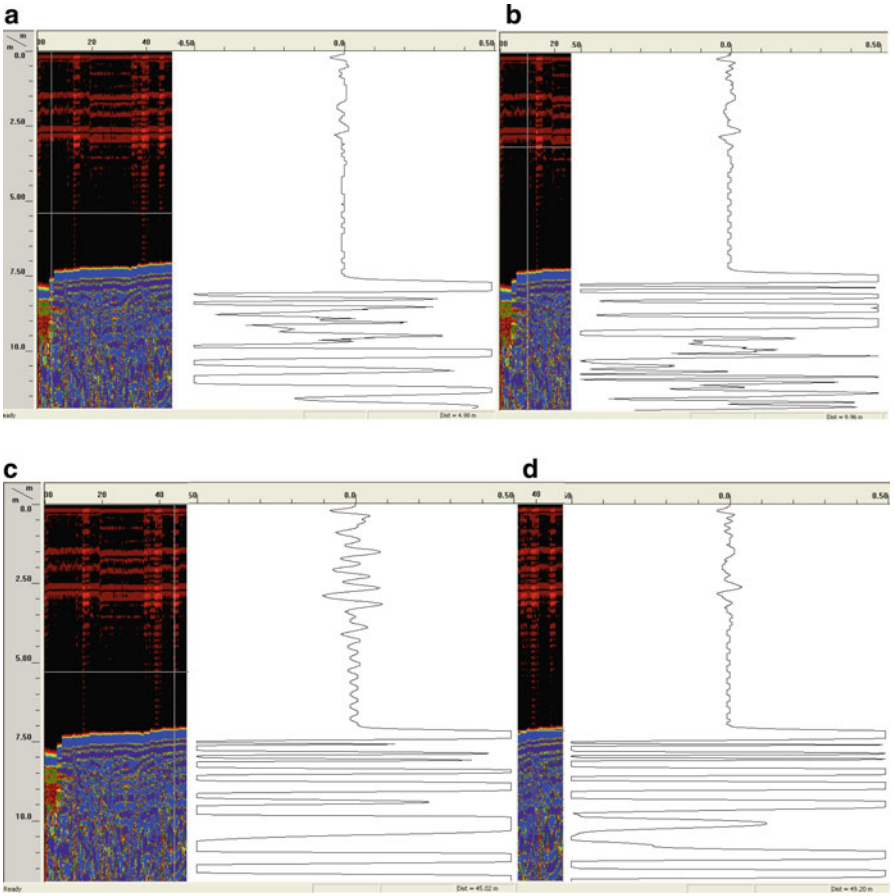

Fig. 9 Wiggle traces from 80 MHz data at 5 m interval (**a**) Trace at 5 m (**b**) trace at 10 m, (**c**) trace at 45 m (**d**) trace at 50 m

subsurface profiling. A closer study shows that there is a small zone of non-reflecting layer at around 5–7 m. This is typical of a highly weathered material in which signals are completely diffracted.

However, a more appropriate method of delineation of the layers would be through digital techniques of signal processing. In this case, the Hilbert transform is useful because it helps to separate the real and the imaginary parts and hence, the magnitude and the phase and frequency components as shown in Fig. 10. The layers of soil and rock are clearly brought out in these figures, especially in the phase components.

The GPR results are compared in Fig. 11 with the available borehole data. Several anomalies were detected at the unexplored locations of the site. One such instance at Point C (Fig. 6) is shown in Fig. 12 along with the profile as obtained

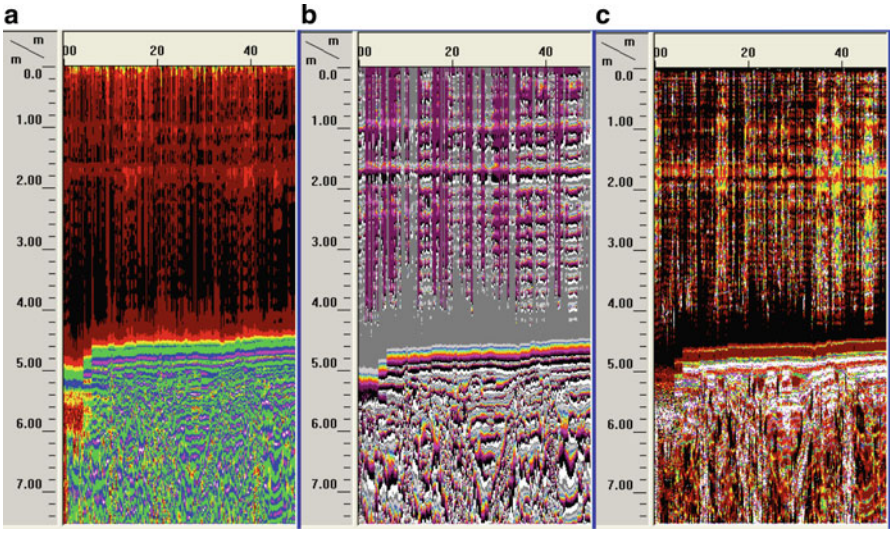

Fig. 10 HT components for 80-MHz data (**a**) Magnitude (**b**) phase (**c**) frequency

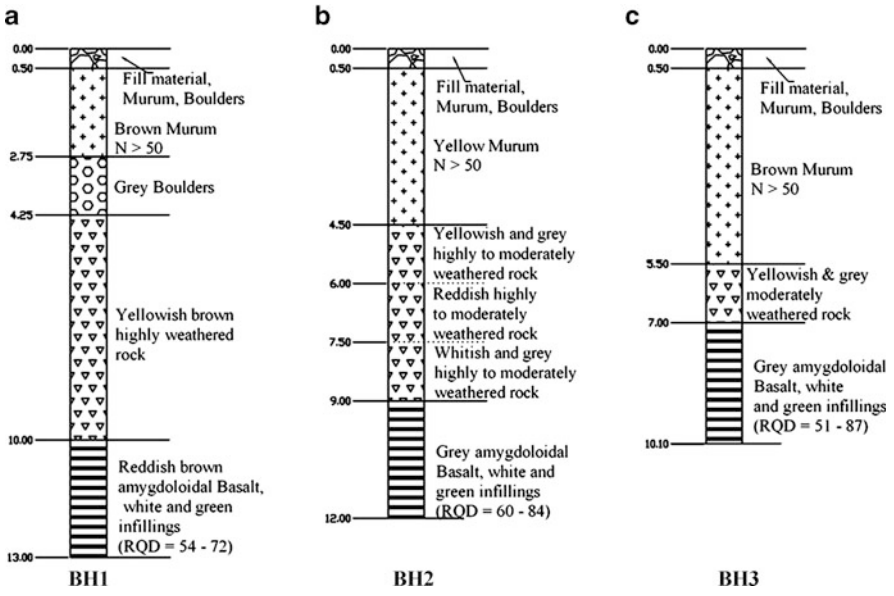

Fig. 11 Borehole logs (**a**)BH1 (**b**) BH2 (**c**) BH3

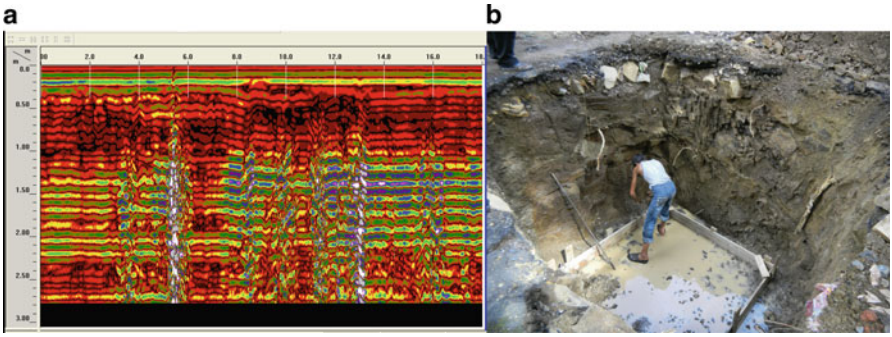

Fig. 12 Anomaly at location C (**a**) 400 MHz profile, (**b**) Photograph of rock layer

after foundation excavation was carried out. A similar situation prevailed at Point D as well. This indicated that extrapolation from borehole data to the western side of the plot would have been grossly in error. GPR studies helped detecting the anomalies in a cost-effective manner and be forewarned. However, in this case, the error was on the safer side as the rock layer was closer to the surface than predicted from boreholes.

6 Study 3

This was carried out at a construction site sandwiched between two existing buildings (Hebsur et al. [10]). A building existed at this site earlier and was subsequently demolished. The issue here was to detect buried utilities which connect the two flanking buildings and other objects, if any. This was necessary to avoid damage to buried facilities during excavation for foundation for the proposed six-storey building at the same site. The layout of the site is shown in Fig. 13.

The GPR studies included scans using 200- and 80-MHz antennae. The initial settings are shown in Table 3. The 21 m $\times$ 30 m grid used for the 200-MHz survey is shown in Fig. 13. There were 7 X traverses at 5-m interval and 8 Y traverses at 3-m interval. The data was collected in zigzag mode. The 80-MHz data was collected along three transects. Along one of the transects, both XX and YY polarizations were used.

The post-processed data is presented in 3D view (Fig. 14). One of the transects, namely, X1, is also presented as a B scan in Fig. 15.

The study yielded very valuable information about the subsurface. It was found that there were no buried utility lines to be taken care of. More importantly, it showed that there were several shallow footings which had to be taken cognizance of in order to excavate without damage to the excavating equipment. Thus, in this study, the uncertainties relating to the nature and position of buried objects were resolved without doubt.

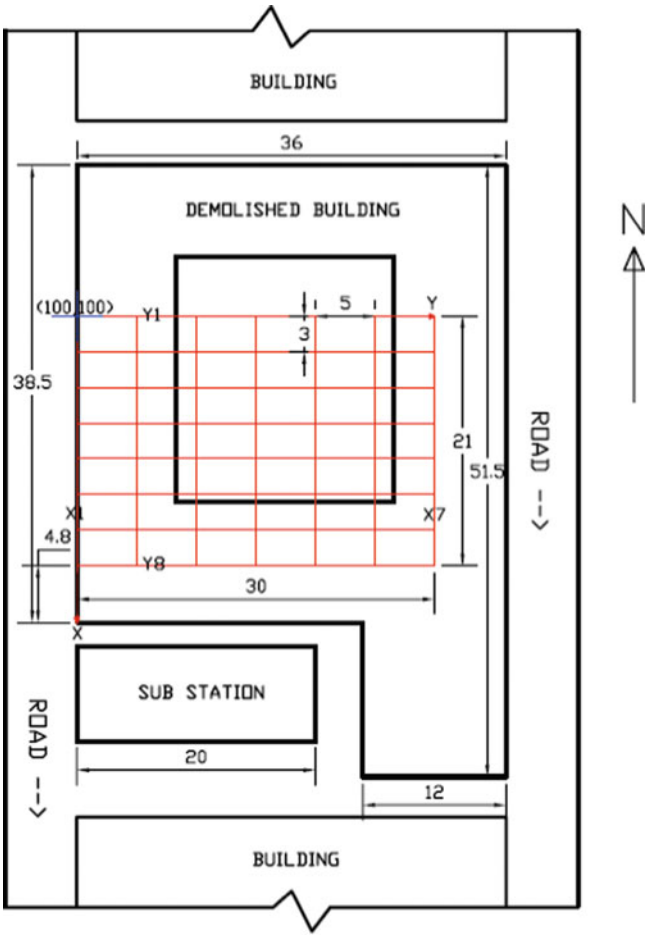

Fig. 13 Layout of study area 3

Table 3 Initial settings made during data collection

Antenna used (MHz)	200	80	
Mode of data collection	3D (time mode)	2D (point mode)	
Mode of polarization	XX & YY	XX	YY
Transmitter and receiver spacing(m)	(Fixed) 0.332	1	2
Area (m^2) or length of survey (m)	21 × 30	21	21
Dielectric constant	4.5	5	5
Range (ns)	80	200	200
Scans/s	64	64	64
Scans/m	50	5	5
Vertical IIR filter range (MHz)	180–220	60–100	60–100
Horizontal IIR stack (no. of scans)	3	64	64

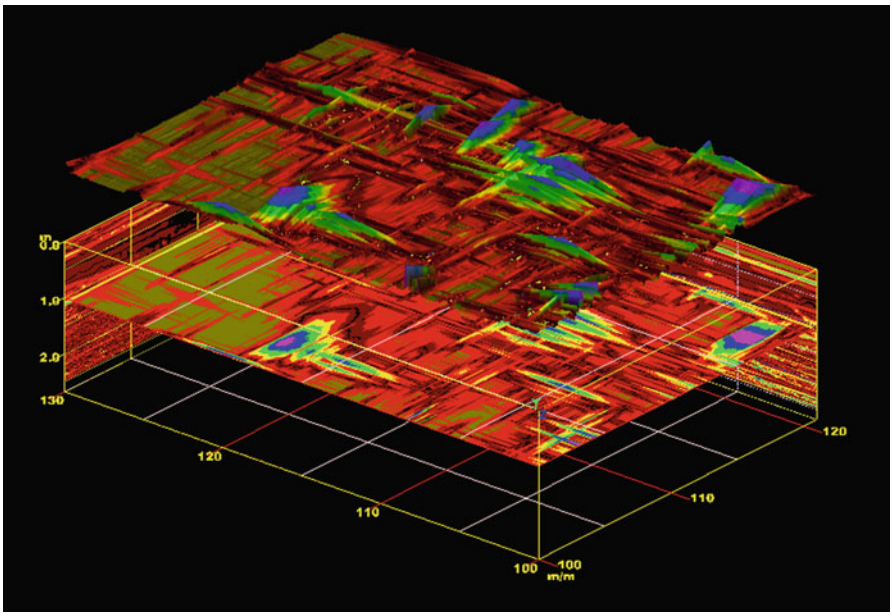

Fig. 14 200-MHz data in 3D mode at 1.4 m depth

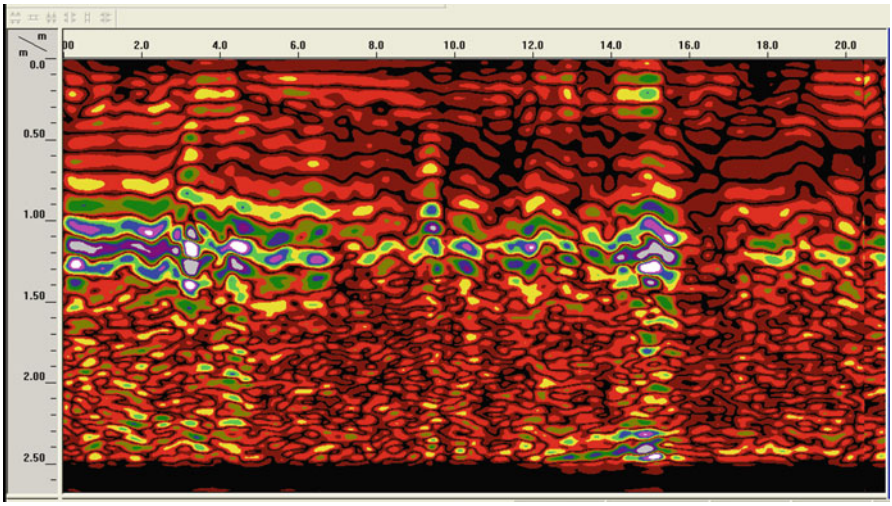

Fig. 15 Post-processed transect X1 data

7 Study 4

This study relates to the site of a tall tower of over 60 storeys planned to be erected on a slope (Fig. 16). As per prevailing construction practice, it was planned to use touch piles to stabilize the ground before excavation. The obvious choice of foundation type was piles. Thus, from considerations of slope stabilization and pile foundation, it was necessary to explore the depth and extent of suitable founding layers. The study reported here pertains to a small segment between two boreholes, 1 and 2. The issue here was that, the rock layer in one borehole was highly weathered at the top in BH2 and at the other it was not. Therefore, it was necessary to determine the depth and lateral spread of the weathered rock layer.

GPR survey using 80 and 40 MHz antennae was carried out close to the borehole which did not show weathering. The initial settings used are given in Table 4. The post-processed radargram for 40 MHz study is shown below in Fig. 17. The weathered rock layer can be seen to exist at a depth of 20 m and varying in

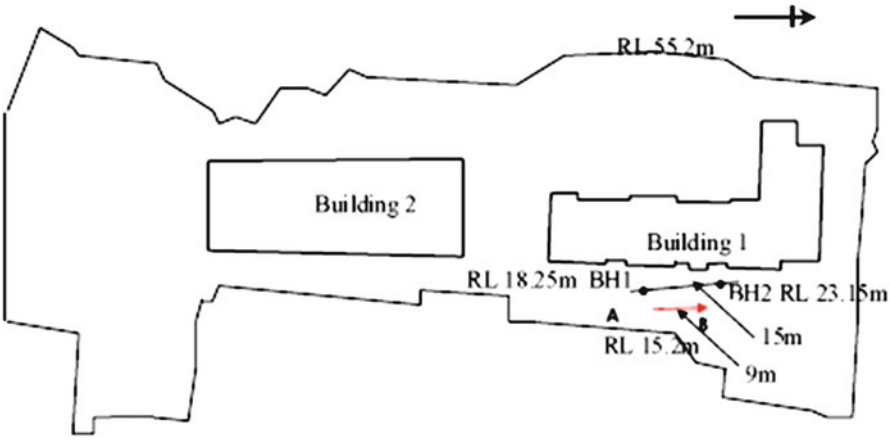

Fig. 16 Layout of study area 4

Table 4 Initial settings made during data collection

Antenna used (MHz)	80 and 40	
Mode of data collection	2D (point mode)	
Mode of polarization	XX	YY
Transmitter and receiver spacing(m)	1	2
Length of survey (m)	9	9
Dielectric constant	5,8,10	5,8,10
Range (ns)	1,000	1,000
Scans/s	64	64
Scans/m	5	5
Vertical IIR filter range (MHz)	10–90	10–90
Horizontal IIR stack (no. of scans)	4	4

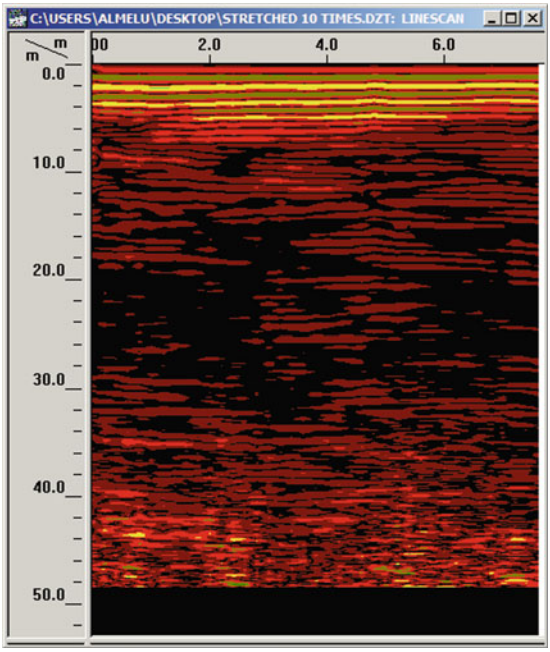

Fig. 17 Post-processed stretched radargram for 40 MHz

thickness in the lateral direction from the first borehole. The requirement at site was to embed the piles in the unweathered rock. The GPR study helped resolve the uncertainty regarding the founding stratum and depth of piles.

8 Other Uncertainties

Perhaps, the most important application of GPR is in the area of utility mapping, where determination of depth, diameter and dielectric constant of the material of the pipe are beset with uncertainties. This requires controlled basic studies on the response of buried utilities under laboratory or field conditions. But, since this is prohibitively expensive, a viable alternative is a simulation through wave propagation modelling. This is an active area of current research.

9 Conclusions

The subsurface profile obtained from GPR is in close agreement with that obtained from boreholes. Hence, GPR profiles can be used for locations within a site which are far from the boreholes and for detecting anomalies, if any. This is particularly useful when questions arise regarding the founding stratum where foundations should rest.

Acknowledgement The help, advice and critical comments and suggestions of Prof. E.P. Rao are gratefully acknowledged.

References

1. Anchuela OP, Casas-Sainz AM, Soriano MA, Pocoví-Juan A (2009) Mapping subsurface karst features with GPR: results and limitations. Environ Geol 58(2):391–399
2. Baecher GB, Christian JT (2003) Reliability and statistics in geotechnical engineering. Wiley, Hoboken
3. Bhattacharya G, Chowdhury SS, Mukherjee S, Chakraborty S (2004) Slope reliability – effect of deterministic and probabilistic methods. In: Babu GLS, Phoon KK (eds) Proceedings of the international workshop on risk assessment in site characterization and geotechnical design (GEORISK – 2004), Bangalore, pp 140–149
4. Conyers LB, Ernenwein EG, Bedal LA (2002) Ground penetrating radar (GPR) mapping as a method for planning excavation strategies. Petra, Jordan. Report of Society for American Archaeology. www.du.edu/lconyer/~petra/petra.07.html. Accessed 2 Apr 2011
5. Daniels DJ (2006) A review of GPR for landmine detection. Sens Imaging 7(3):90–123
6. Dodagoudar GR, Venkatachalam G (2000) Reliability analysis of slopes using fuzzy sets theory. Comput Geotech 27:101–115
7. Fiedler S, Illich B, Berger J, Graw M (2009) The effectiveness of ground-penetrating radar surveys in the location of unmarked burial sites in modern cemeteries. J Appl Geophys 68(3):380–385
8. Gomez-Ortiz D, Pereira M, Martin-Crespo T, Rial FI, Novo A, Lorenzo H, Vidal JR (2009) Joint use of GPR and ERI to image the subsoil structure in a sandy coastal environment. J Coast Res 56:956–960
9. GSSI (2007) RADAN 6.5 User's manual. Geophysical Survey Systems Inc., Salem, p 34
10. Hebsur A, Muniappan N, Rao EP, Venkatachalam G (2010) A methodology for detecting buried solids in second-use sites using GPR. In: Proceedings of Indian geotechnical conference – 2010, Geotrendz, IIT Bombay
11. Juang CH, Elton DJ (1996) A practical approach to uncertainty modelling in geotechnical engineering, ASCE geotechnical special publication no. 58, Uncertainty in the geologic environment: from theory to practice, ASCE, New York, pp 1269–1283
12. Jol HM (2009) Ground penetrating radar: theory and applications, 1st edn. Elsevier Sc., Killington
13. King ML (2000) Locating a subsurface oil leak using ground penetrating radar. In: GPR 2000: Proceedings of the 8th international conference on ground penetrating radar, SPIE, Gold Coast, vol 4084, pp 346–350
14. King ML, Wu DP, Nobes DC (2003) Non-invasive ground penetrating radar investigation of a failing concrete floor slab. In: International symposium (NDT-CE 2003) on non-destructive testing in civil engineering, Berlin
15. Koppenjan SK, Schultz JJ, Falsetti AB, Collins ME, Ono S, Lee H (2003) The application of GPR in Florida for detecting forensic burials. In: Proceedings of SAGEEP, San Antonio, TX, USA
16. Nobes DC, Lintott B (2000) Rutherford's "old tin shed": mapping the foundations of a victorian-age lecture hall. In: Proceedings of the 8th international conference on ground penetrating radar, SPIE, Gold Coast, vol 4084, p 887. doi:10.1117/12.383534, 22–25 May 2000
17. Nobes DC, Sikma TJ (2003) Non-invasive ground penetrating radar in the NDT of the foundations of the Cathedral of the Blessed Sacrament, Christchurch, New Zealand. In: International symposium (NDT-CE 2003) on non-destructive testing in civil engineering, Berlin.
18. Shihab S, Al-Nuaimy W (2005) Radius estimation for cylindrical objects detected by ground penetrating radar. Subsurf Sens Technol Appl 6(2):151–166
19. Venkatachalam G (2006) Reliability analysis of slopes and tunnels. Indian Geotech J 36(1):1–66

A Robust Controller with Active Tendons for Vibration Mitigation in Wind Turbine Rotor Blades

Andrea Staino and Biswajit Basu

Abstract A new robust active controller design to suppress flapwise vibrations in wind turbine rotor blades is presented in this chapter. The control is based on active tendons mounted inside the blades of a horizontal-axis wind turbine (HAWT). The multimodal model proposed includes the effects of centrifugal stiffening, gravity, and aerodynamic loading. Dynamic interaction between the blades and the tower has been included, and variable mass and stiffness per unit length of the blade have been also taken into account. A robust model predictive control (MPC) algorithm has been implemented to study the effectiveness of the proposed active control system. Due to its high complexity and to the variable nature of its operating environment, a wind turbine is subjected to changes in operating condition. As a consequence, significant variations may occur in certain parameters of the turbine. Therefore, robustness is of particular concern for control design purposes. The main advantage of the proposed method is to explicitly incorporate plant model uncertainty in designing the controller. Numerical simulations have been carried out by using data describing aerodynamic and structural properties for a 5-MW wind turbine.

Keywords Wind turbine • Active vibration control • Robust control • Model predictive control • Blade-tower interaction • Blade element momentum theory

1 Introduction

The increased flexibility of the blades (and the tower) in large multi-megawatt wind turbines entails a higher sensitivity to induce mechanical vibrations. The uncontrolled vibrations might significantly shorten components' lifetime, and large amplitude oscillations might even compromise safe operation of the power plant.

A. Staino • B. Basu (✉)
School of Engineering, Trinity College Dublin, College Green, Dublin, Ireland
e-mail: stainoa@tcd.ie; basub@tcd.ie

S. Chakraborty and G. Bhattacharya (eds.), *Proceedings of the International Symposium on Engineering under Uncertainty: Safety Assessment and Management (ISEUSAM - 2012)*,
DOI 10.1007/978-81-322-0757-3_26,

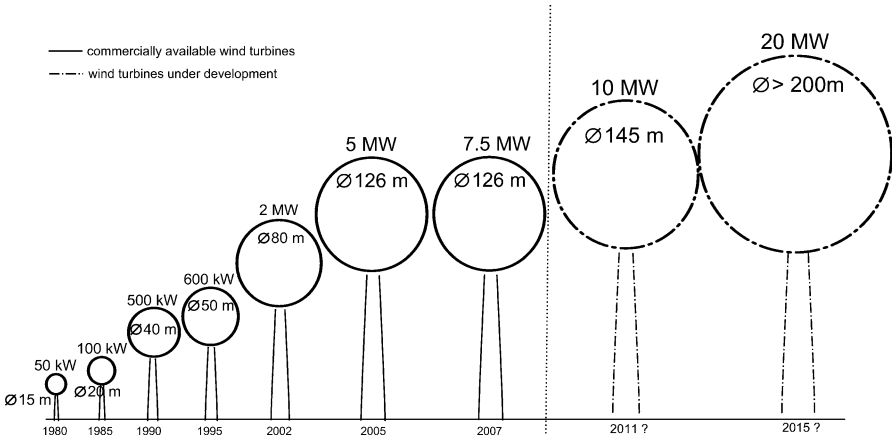

Fig. 1 Growth in size of commercial wind turbine designs

Moreover, by mitigating vibration effects, a more efficient design of the structure can be achieved, as lighter materials and components can be used (Fig. 1).

Different approaches have been investigated in the literature in order to tackle problems associated with aerodynamic loads in wind turbines. Dueñas-Osorio and Basu [3] carried out a probabilistic study on the impact of acceleration-induced damages in the wind turbine components leading to a loss of availability and reduction of power generation. Murtagh et al. [13] developed a dynamic model describing the vibration response of a wind turbine consisting of three flexible rotating blades connected to a flexible supporting tower. In Murtagh et al. [14], the authors extended their work by studying the use of a passive control device (i.e., a tuned mass damper, TMD) for reducing the wind-induced vibrations experienced by the wind turbine structure. Colwell and Basu [2] simulated the response of an offshore wind turbine subjected to wind and wave loadings and found that a considerable reduction in the peak response may be achieved by equipping the plant with a tuned liquid mass damper (TLCD). A semi-active control algorithm for the control of flapwise vibrations in wind turbine blades by means of semi-active tuned mass dampers has been proposed by Arrigan et al. [1]. Recently, significant research has also been carried out into the development of active vibration control in wind turbine blades [6, 11, 12]. An innovative structural control scheme based on active controllers has been proposed by Staino et al. [15].

In this chapter, we illustrate the use of a recently proposed active controller for suppressing the flapwise vibration in blades and mitigate their damaging effects. The effectiveness of the proposed control architecture is tested by simulating the application of a robust model predictive control (MPC) strategy [9], whose main advantage is to explicitly incorporate plant model

uncertainty in designing the controller. The MPC algorithm implemented in this study explicitly takes into account physical constraints on the evolution of the variables involved in the process to be controlled.

2 HAWT Model with Controller

A modern multimegawatt wind turbine is a highly complex mechano-electrical system consisting of several components, including structural elements like tower, rotor (consisting of nacelle and blades), and other mechanical and electrical elements such as gears, converters, and transformers as well as a high number of different sensors, actuators, and controllers. It follows that the modeling of large wind turbines is also complex and challenging, and getting accurate models entails studying the dynamics of many degrees of freedom (DOFs), leading to a high-dimensional set of equations. Because we are interested in studying the flapwise dynamics of rotor vibrations in a wind turbine, here we formulate a mathematical model that takes into account only the relevant states or degrees of freedom, representing the flapwise vibration responses and the associated coupling of the blade with the tower/nacelle motion [13]. A schematic representation of a three-bladed HAWT is shown in Fig. 2. The blades are modeled as Bernoulli-Euler cantilever beams of length "*L*," with variable bending stiffness $EI(x)$ and variable mass per unit length $\mu(x)$ along the length. The blades rotate at a constant

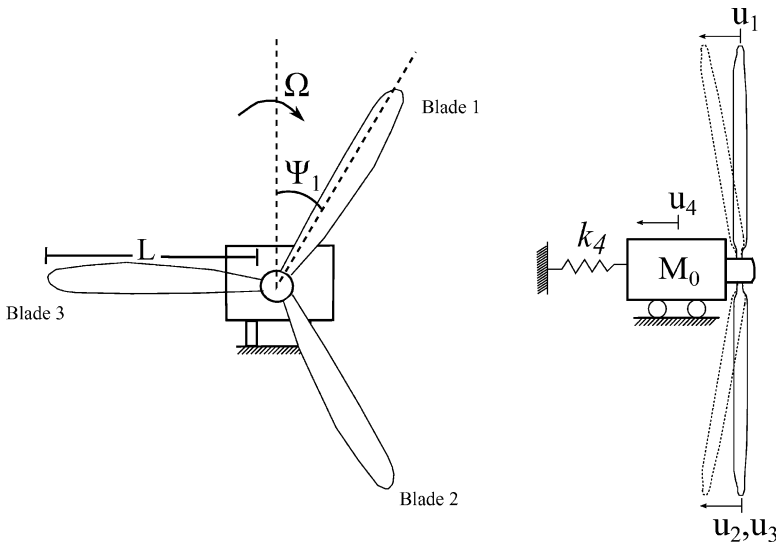

Fig. 2 Flapwise model with nacelle coupling

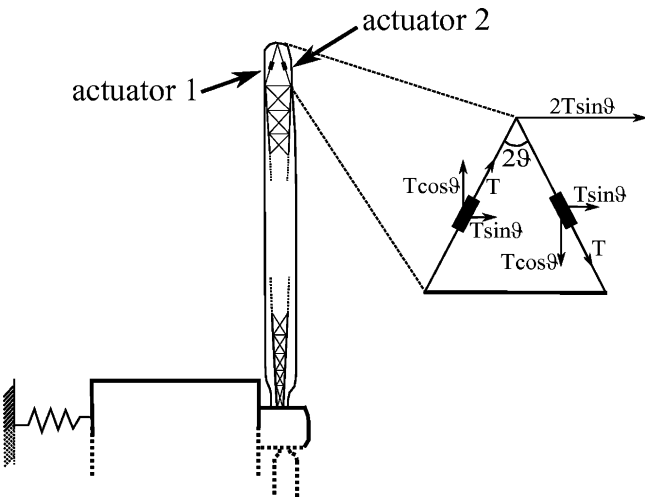

Fig. 3 Flapwise model with the controllers

rotational speed Ω rad s^{-1}, and the azimuthal angle $\Psi_j(t)$ of blade "j" at the time instant "t" is given by

$$\Psi_j(t) = \Psi_1(t) + (j-1)\frac{2\pi}{3},\ \Psi_1(t) = \Omega t;\ j = 1,2,3 \tag{1}$$

The dynamic coupling between the blade and the tower has been included through the fore-aft motion of the nacelle. The tower is modeled as a single degree of freedom system with the mass M_0, which represents the modal mass of the tower and the mass of the nacelle. The variables $u_j(x, t)$, $j = 1;2;3$, and $u_4(t)$ denote the flapwise blade and the nacelle displacements, respectively. The generalized (or modal) stiffness of the tower is represented by k_4.

The control is implemented by means of two linear actuators located inside the blade (Fig. 3). The actuators, each exerting a controlled force $T_i(t)$, are mounted on a frame supported from the nacelle. For the ith blade, the net control force acting on the blade tip in the flapwise direction is denoted by $f_{ci}(t)$. This force is proportional to $T_i(t)$ and to the sine of the angle ϑ and represents the control input to the system.

The reaction forces are transmitted along the supporting structure finally to the nacelle. The support structure for applying the control forces has to satisfy the requirement of transferring the force to the hub. This has to be accomplished ideally by avoiding the generation of a reaction force in the flapwise direction of the blade or practically by eliminating the possibility of any reaction force in the close to medium spatial proximity of the tip. This design condition can be achieved by introducing active elements in the support structure (such as active braces or active tendons) as is typically used in large engineering structures for protection against wind or earthquake loads. A Lagrangian approach has been used in order to derive the equations of motion for the system considered.

2.1 Flapwise Model Formulation

A generalized flexible model of the blade with N modes of vibration is formulated. In the generalized representation of the wind turbine, each mode of vibration is associated to the corresponding modeshape $\Phi_i(x)$, for which an appropriate function approximation can be computed from the eigenanalysis of the blade structural data. The system is therefore described by 3 N +1 generalized coordinates that provides an accurate description of the flexible blade behavior. Let $\underline{q}(t)$ be the vector of the generalized coordinates of the system defined as

$$\underline{q}(t) = \left\langle q_{11}(t) \quad q_{12}(t) \quad \ldots \quad q_{1N}(t) \quad q_{21}(t) \quad \ldots \quad q_{ji}(t) \quad \ldots \quad q_4(t) \right\rangle^{\mathrm{T}} \in R^{3N+1} \tag{2}$$

The degree of freedom $q_{ji}(t)$; $j = 1, 2, 3$, $i = 1, \ldots, N$ denotes the ith flapwise mode for the blade "j." The variable $q_4(t) = u_4(t)$ represents the motion of the nacelle. The total flapwise displacement along the blade is given by

$$u_j(x,t) = \sum_{i=1}^{N} \Phi_i(x) q_{ji}(t) \tag{3}$$

A set of differential equations, describing the dynamics of the flapwise vibrations for the system considered, has been obtained by applying the Euler-Lagrange method:

$$\frac{d}{dt}\left(\frac{\partial T}{\partial \dot{q}_i}\right) - \frac{\partial T}{\partial q_i} + \frac{\partial V}{\partial q_i} = Q_{ext,i} \tag{4}$$

where $Q_{ext,i}$ is the generalized nonconservative load for the degree of freedom i, and the terms T and V are the total kinetic energy and the total potential energy of the system, respectively, given by

$$T = \frac{1}{2}\sum_{j=1}^{3}\int_0^L \mu v_{b,j}^2 dx + \frac{1}{2} M_0 \dot{q}_4^2 \tag{5a}$$

and

$$V = \frac{1}{2}\sum_{j=1}^{3}\int_0^L EI\left(\frac{\partial^2 u_j}{\partial x^2}\right)^2 dx + \frac{1}{2} k_4 q_4^2 \tag{5b}$$

The term $v_{b,j}(x,t)$ in Eq. (5a) denotes the total velocity of the blade in the flapwise direction, i.e., it is calculated by taking into account the nacelle motion. The inclusion of the generalized coordinate $q_4(t)$ into the Lagrangian formulation has

allowed modeling of the coupling between the blade and the tower. As found by Hansen [4], the effect of centrifugal stiffening has been added to the model by considering the additional potential energy V_c which is given by:

$$V_c = \frac{1}{2}\Omega^2 \sum_{j=1}^{3} \int_0^L \left[\left(\frac{\partial u_j}{\partial x} \right)^2 \int_x^L \mu(\xi)\xi d\xi \right] dx \tag{6}$$

The contribution given from the component of the gravity acting along the blade axis has also been considered. For the *j*th blade, the component of the gravitational force at a distance "*x*" from the blade root is

$$F_{g,j}(x) = -\int_x^L \mu(\xi) g \cos(\psi_j) d\xi = -g \cos(\psi_j) \int_x^L \mu(\xi) d\xi \tag{7}$$

and the potential energy associated is

$$V_g = -\frac{g}{2} \sum_{j=1}^{3} \int_0^L \left[\left(\frac{\partial u_j}{\partial x} \right)^2 \int_x^L \mu(\xi) d\xi \right] dx \cos(\psi_j) \tag{8}$$

The final equations of motion of the HAWT flapwise model with active controllers are expressed in matrix form as

$$\mathbf{M}\ddot{\underline{q}}(t) + \mathbf{C}\dot{\underline{q}}(t) + K\underline{q}(t) = \underline{\boldsymbol{Q}}_{ext}(t), \tag{9}$$

where **M**, **C**, and **K** represent the mass, damping, and stiffness matrices of the system, $q(t)$ is the vector of generalized coordinates, and $\underline{Q}_{ext}(t)$ the generalized loading due to the aerodynamic/gravity loads and the active control forces. Wind excitation is modeled as an external modal load applied to the blade in the flapwise direction. The generalized aerodynamic load on the blade"*j*" for the *i*th mode is computed as

$$Q_{ji} = \int_0^L p_j(x,t)\Phi_i(x) dx \tag{10}$$

with $p_j(x,t)$ representing the variable wind load intensity along the blade length in the flapwise direction.

The generalized load on the nacelle corresponds to

$$Q_4 = \sum_{j=1}^{3} \int_0^L p_j(x,t) dx \tag{11}$$

Quasi-static aerodynamic wind loading time series are computed by applying the corrected blade element momentum (BEM) method.

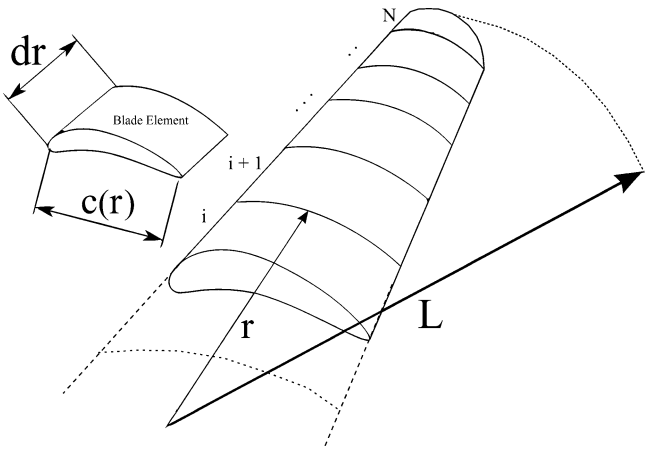

Fig. 4 Blade model according to the BEM theory approach

2.2 Wind Loading: Blade Element Momentum Theory

In this chapter, in order to have a realistic estimate of the wind loading to which the rotor is subjected to, models based on the blade element momentum (BEM) theory have been adopted [5]. These models allow to obtain a detailed quantitative description of the wind turbine rotor behavior, which is based on the aerodynamic properties of the blade section airfoils, the geometrical characteristics of the rotor, as well as the wind speed and the rotational velocity of the blades. BEM analysis is carried out by combining momentum theory and blade element theory.

The blade is assumed to be discretized into N sections (elements). Each element is located at a radial distance r from the hub (Fig. 4), and it has chord length $c = c(r)$ and width dr. Assuming no radial dependency for the annular sections, i.e., no aerodynamic interactions between different elements, and assuming that the forces on the blade elements depend only on the lift and drag characteristics of the airfoil shape of the blades, the BEM theory provides a method to estimate the axial and tangential induction factors, a and a', respectively. Once these parameters are known, local loads on each segment can be determined. The total forces acting on the blade can then be computed by performing numerical integration along the blade span. In order to describe the BEM algorithm for calculating quasi-static aerodynamic wind loads, the following quantities are defined:

$$\begin{aligned} V_{rel}(r,t) &= \sqrt{(V_0(r,t)(1-a))^2 + \Omega^2 r^2 (1+a')^2} \\ \phi(r,t) &= \tan^{-1}\left(\frac{(1-a)V_0(r,t)}{(1+a')\Omega r}\right) \\ \alpha(r,t) &= \phi(r,t) - \beta(t) - \kappa(r) \end{aligned} \tag{12}$$

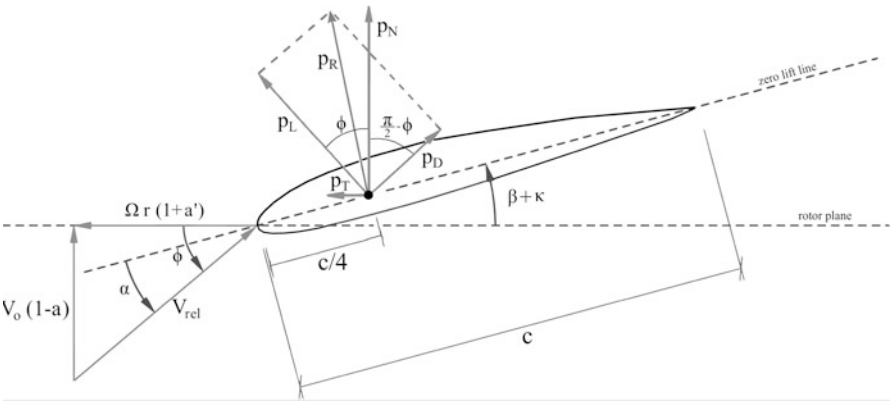

Fig. 5 Local forces and velocities in the BEM model of the blade

where V_{rel} and V_0 denote the relative and the instantaneous wind speed, respectively, ϕ is the flow angle, α the instantaneous local angle of attack, β the pitch angle, and κ the local pre-twist of the blade (Fig. 5).

The local lift and drag forces can be respectively computed as

$$p_L(r,t) = \frac{1}{2}\rho V_{rel}^2(r,t)c(r)C_l(\alpha)$$
$$p_D(r,t) = \frac{1}{2}\rho V_{rel}^2(r,t)c(r)C_d(\alpha) \tag{13}$$

where ρ is the density of air and $C_l(\alpha)$ and $C_d(\alpha)$ represent the lift and drag coefficients, respectively, whose values depend on the local angle of attack. Finally, the aerodynamic forces normal to the rotor plane (corresponding to the aerodynamic loads in the flapwise direction) can be obtained by projecting the lift and the drag along the normal plane, as shown in Fig. 5. Therefore, the local flapwise load is given by

$$p_N(r,t) = p_L(r,t)\cos(\phi) + p_D(r,t)\sin(\phi) \tag{14}$$

As suggested in Hansen [5], in order to improve the accuracy of the model, Prandtl tip loss factor and Glauert correction have been applied. The former corrects the assumption, used in the classical blade element momentum theory, of an infinite number of blades, while the latter has been applied in order to compute the induced velocities more accurately when the induction factor a is greater than a critical value a_c.

Once the local loads on the blade elements have been calculated, by integrating Eq. (14) along the blade length and considering the appropriate modeshape of the blade, the generalized flapwise load can be calculated using Eqs. (10) and (11). To account for the variation in the vertical wind shear due to the rotation of the blade, the term V_0 in Eq. (12) can be approximately assumed as a constant wind speed linearly varying with height.

2.3 Model with Polytopic Uncertainty

For the purpose of designing a controller, a number of simplifying hypothesis and approximations are assumed in the formulation of a mathematical model of the physical system. This is done in order to obtain a set of "tractable" equations, on which the design of the control law will be based. This simplified mathematical representation, in some cases, can be inaccurate or even inappropriate to adequately describe the dynamics of the phenomenon of interest. In particular, considering all parameters as constant is a highly restrictive assumption. In fact, this does not allow to take into account the change in the physical properties of the system due to fatigue and cyclic loading in time or due to change in environmental conditions. Therefore, it is reasonable to deem that the model is affected by a degree of uncertainty, which expresses the fact that many physical and geometric properties of the system are not precisely known a priori.

In this chapter, a polytopic (or multimodel) representation of the uncertainty has been adopted; [9] this accounts for errors in the identification and parametric variations in the stiffnesses of blades and nacelle/tower. Underlying the multimodel paradigm is a linear time-varying (LTV) representation of the system:

$$\begin{cases} x(k+1) = A(p(k))x(k) + B(p(k))u(k) \\ y(k) \quad\quad = Cx(k) \\ \qquad\quad [A(p(k)) \quad B(p(k))] \in \Pi \end{cases} \tag{15}$$

where $x(k) \in \mathrm{R}^{n_x}$ is the state of the system at the time instant "k," $u(k) \in R^{n_u}$ is the control input, and $y(k) \in R^{n_y}$ is the output of the plant. The system matrices A and B depend on time through the vector of time-varying parameters $p(k) \in R^p$. By assuming bounded parametric variations, i.e., $p_{\min} \leq p(k) \leq p_{\max}\ \forall k$, l linear time invariant (LTI) systems can be obtained, and the uncertainty set (polytope) Π can be expressed as

$$\Pi = C_0\{[A_1 \quad B_1], ..., [A_l \quad B_l]\} \tag{16}$$

where Co(·) denotes the convex hull of the vertices $[A_1\ B_1]$, ..., $[A_l\ B_l]$. For each parametric variation inside the given bounds, every possible dynamic realization of the system is included in the polytope Π; moreover, according to the definition, Eq. (16), every possible realization $\begin{bmatrix} \bar{A} & \bar{B} \end{bmatrix}$ of Eq. (15) can be obtained as

$$[\bar{A} \quad \bar{B}] = \sum_{i}^{L} \lambda_i [A_i \quad B_i], \quad \sum_{i=1}^{l} \lambda_i = 1 \quad 0 \leq \lambda_i \leq 1 \tag{17}$$

The uncertain dynamics of Eq. (15) can hence be described by the variation of λ_i in Eq. (16).

In this study, parametric uncertainties in the fundamental natural frequencies of the blade ω_b and the tower ω_n have been modeled. The vector of uncertain parameters corresponds to

$$p(k) = \begin{bmatrix} \omega_b(k) \\ \omega_n(k) \end{bmatrix}, \quad \omega_b(k) \in [\omega_{b_{\min}}, \omega_{b_{\max}}], \qquad \omega_n(k) \in [\omega_{n_{\min}}, \omega_{n_{\max}}] \quad \forall k \tag{18}$$

By evaluating the matrices of the multimodel representation of the system, Eq. (15) in the extreme values of the uncertain parameters, four different operating points are obtained ($l = 4$), representing the vertex of the uncertainty polytope Π for the case considered.

2.4 Robust-Constrained MPC

The purpose of the robust controller is to guarantee that the closed loop system is stable and the requirements on input and output variables are met for every possible realization of the system in the uncertainty polytope Π. The synthesis of the robust control law, based on a linear model with polytopic uncertainty, is performed by minimizing an appropriate upper bound on a robust (*worst-case*) quadratic objective function:

$$\begin{array}{lll} \min & \max & J_\infty(k) \\ u(k+i|k) & [A(k+i)B(k+i)] & \text{belongs to the polytope PI cfr. Eq. 16} \\ i = 0, \ldots, m-1 & i \geq 0 & \end{array}$$

$$J_\infty(k) = \sum_{i=0}^{\infty} \left[x^T(k+i|k) R_x x(k+i|k) + u^T(k+i|k) R_u u(k+i|k) \right] \tag{19}$$

where $R_x \in R^{n_x \times n_x}$ is the weight on the state and $R_u \in \mathrm{R}^{n_u \times n_u}$ is the weight on the input variables in the optimization process. The problem of determining the sequence of inputs that solves the given control problem, ensuring the fulfillment of constraints on input and output variables (the former referred as "*hard constraints*"), is reformulated as a convex optimization problem. Given the state $x(k) = x(k|k)$ of the uncertain system (15) at the time instant k, the robust-constrained MPC algorithm is implemented by computing the state feedback gain $F_k = YQ^{-1}$, where $Q = Q^{\mathrm{T}} \geq 0$ and Y are obtained by solving the following minimization problem with linear matrix inequalities (LMIs) constraints:

$$\min_{\gamma, Y, Q} \quad \gamma \tag{20a}$$

$$\begin{bmatrix} 1 & x^T(k|k) \\ x(k|k) & Q \end{bmatrix} \geq 0 \tag{20b}$$

$$\begin{bmatrix} Q & QA_j^T + Y^T B_j & QR_x^{\frac{1}{2}} & Y^T R_u^{\frac{1}{2}} \\ A_j Q + B_j Y & Q & 0 & 0 \\ R_x^{\frac{1}{2}} Q & 0 & \gamma I & 0 \\ R_u^{\frac{1}{2}} Y & 0 & 0 & \gamma I \end{bmatrix}_{j=1\ldots l} \geq 0 \tag{20c}$$

$$\begin{bmatrix} X & Y \\ Y^T & Q \end{bmatrix} \geq 0, \quad X_{ii} \leq u_{i,\max}^2, i = 1\ldots n_u \tag{20d}$$

$$\begin{bmatrix} Q & \left(A_j Q + B_j Y\right)^T C_i^T \\ \left(A_j Q + B_j Y\right) C_i & y_{i,\max}^2 \end{bmatrix}_{\substack{j=1\ldots l \\ i=1\ldots n_y}} \geq 0 \tag{20e}$$

where $u_{i,\max}$ and $y_{i,\max}$ denote the constraint on the ith input and output components, respectively. At the time instant "k," if a solution to Eqs. (20a, 20b, 20c, 20d, 20e) exists, the control input $u(k|k) = F_k\, x(k|k)$ is implemented. At the next sampling time, the state $x(k + 1)$ is measured, and the optimization problem is solved in order to compute F_{k+1}. The details of the control algorithm used in this study are provided in Kothare et al. [9].

3 Results

The robust MPC algorithm (20) has been simulated in Matlab® by using the LMI parser "YALMIP" and the SDP solver "SeDuMi" provided in the "Multi-Parametric Toolbox" [10]. A reduced order model has been derived for the system under consideration in order to reduce the number of states required for implementing the control and hence to decrease the computational cost associated with the calculation of the control law. In particular, for the design of the controller, each beam is assumed to be vibrating in its fundamental mode. This leads to a reduced order model with 4DOF. Also, the effect of gravity has been ignored, as it may not have a significant impact on the flapwise vibration. The proposed control scheme has been tested using data relative to the NREL 5-MW baseline offshore wind turbine, which is a three-bladed upwind turbine with a rotor diameter of about 126 m and hub height of 90 m. The blade considered (LM 61.5 P2) is 61.5 m long with an overall mass of 17,740 kg. A damping ratio of 1% in the blade flapwise mode has been specified. Full details of the NREL 5-MW baseline wind turbine are provided in Jonkman et al. [7].

Aerodynamic loads in the flapwise direction have been calculated using the blade element momentum (BEM) theory, according to the algorithm outlined by Hansen [5]. The BEM method allows to compute an estimate of the loads induced by the wind by taking into account the aerodynamic properties of the blade section

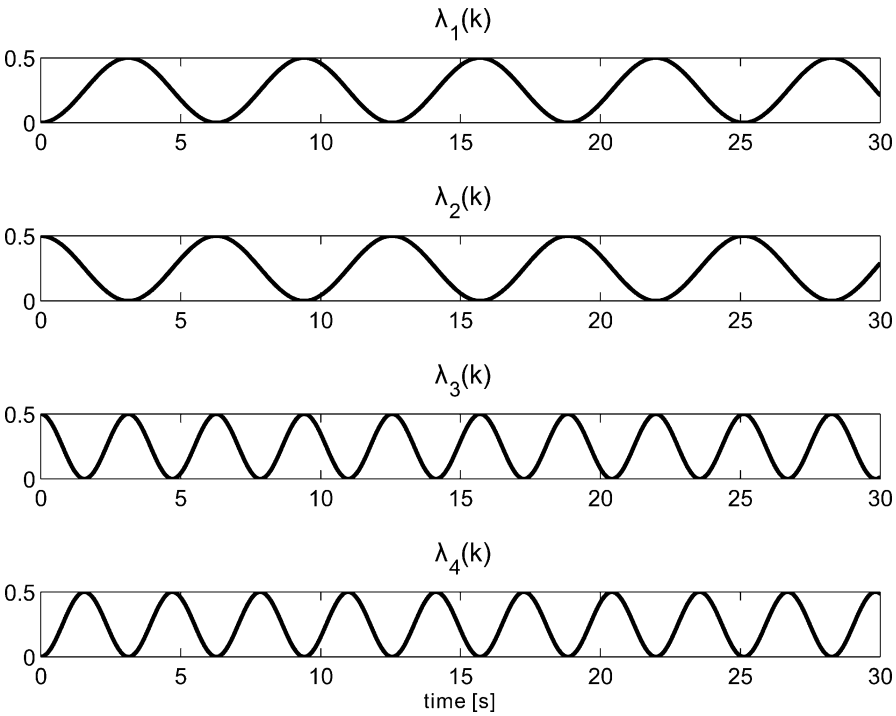

Fig. 6 Variation of the system parameters λ_i (case I)

airfoils and the structural properties of the rotor. In this chapter, a steady wind load with a mean speed value of 12 ms^{-1} has been considered, in addition to a linear wind shear in the vertical direction producing a periodic loading variation.

For studying the effect of uncertainties in the dynamic parameter variation in a wind turbine, a few different cases have been considered. Since the main aim is to analyze the robustness of the controller in presence of uncertainty, contributions from higher modes and gravity have been excluded in the numerical simulations. Instead, uncertainties in the fundamental natural frequencies of the blade and the tower as in Eq. (18) have been investigated, and different scenarios have been analyzed by setting various input and output constraints, as well as different forms of variation in the parameters of the model during the simulation.

3.1 Case I: Sinusoidal Variation

For the first numerical experiment, the bounds on the uncertain parameters assumed for the design of the robust control law are $\omega_{b_{\min}} = 2\,\text{rad/s}$, $\omega_{b_{\max}} = 15\,\text{rad/s}$, $\omega_{n_{\min}} = 1\,\text{rad/s}$, and $\omega_{n_{\max}} = 12\,\text{rad/s}$. During the simulation, the parameters λ_i in Eq. (17) are varied according to a sinusoidal pattern as shown in Fig. 6. The control

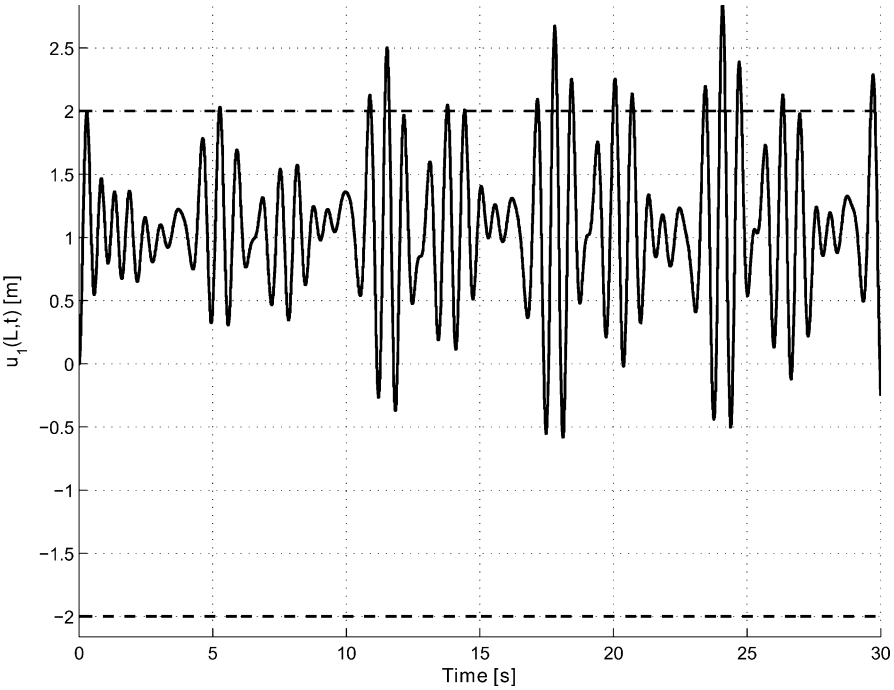

Fig. 7 Blade 1 tip displacement with sinusoidal parameter variation

law is synthesized in order to allow for each actuator a maximum control force corresponding to 15% of the total weight of the blade. Figure 7 shows the time history of the displacement response of blade 1 with the constraint limits imposed on the response.

It is observed that the constraints are violated a few times. This can be attributed to the fact that the constraints imposed are soft constraints and a penalty is imposed when violation occurs. A closer look at the response reveals that the constraints are satisfied initially (about 10 s). Subsequently, the excursion of the constraint occurs a few times. The reason for this may be because of the nature of the excitation which is persistent and decaying. The steady-state loading condition has not been accounted for in the formulation of the set of conditions for the LMI (20). In spite of this, it may be noted that the control force is limited to the constrained values once the limit on the displacement is reached. This is evident from Fig. 8 where the control force time history on the blade 1 has been plotted. It is also worth noting that the violation of the displacement limit on one blade may result in limiting the control force on another blade if the control force on that blade is close to the limit.

Figure 9 compares the controlled displacement response of blade 1 for the robust MPC algorithm with the uncontrolled response. It is observed that there is a significant reduction in the displacement response and the robust MPC is successful

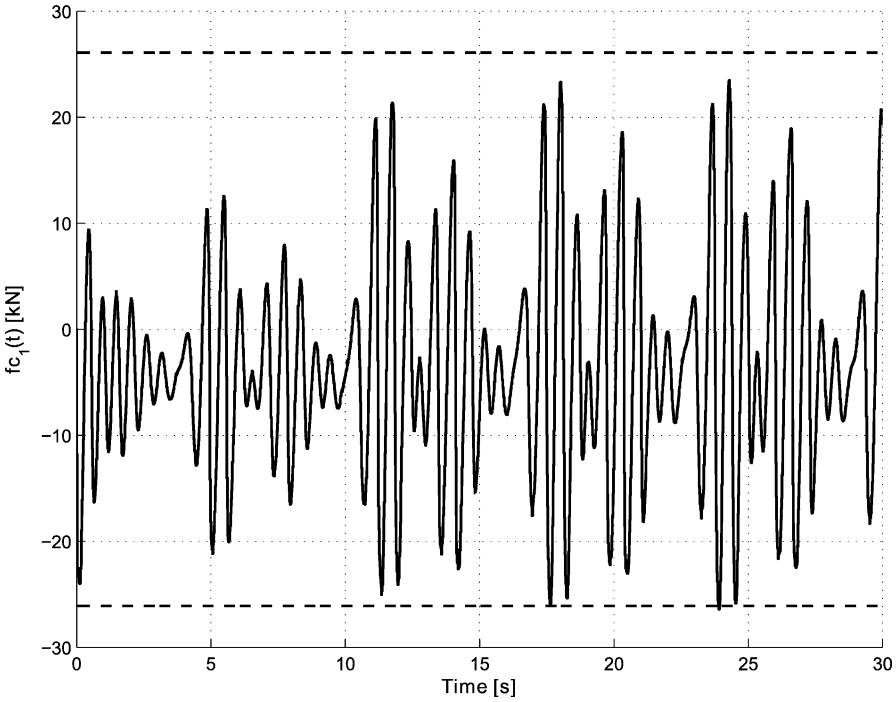

Fig. 8 Control force on blade 1 with sinusoidal parameter variation

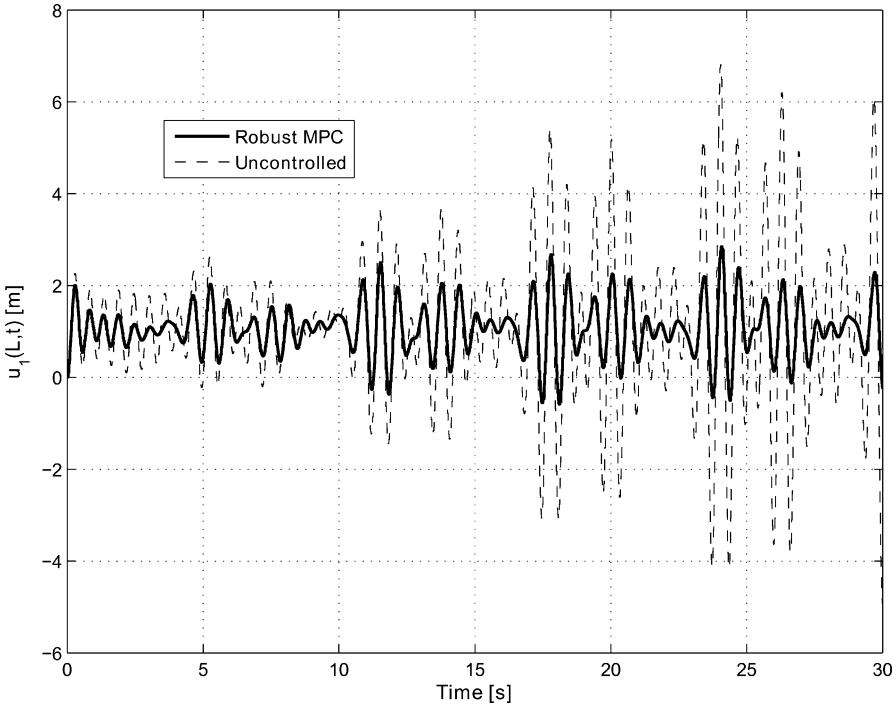

Fig. 9 Uncontrolled (*dashed*) and robust MPC-controlled (*solid*) displacement response (sinusoidal parameter variation)

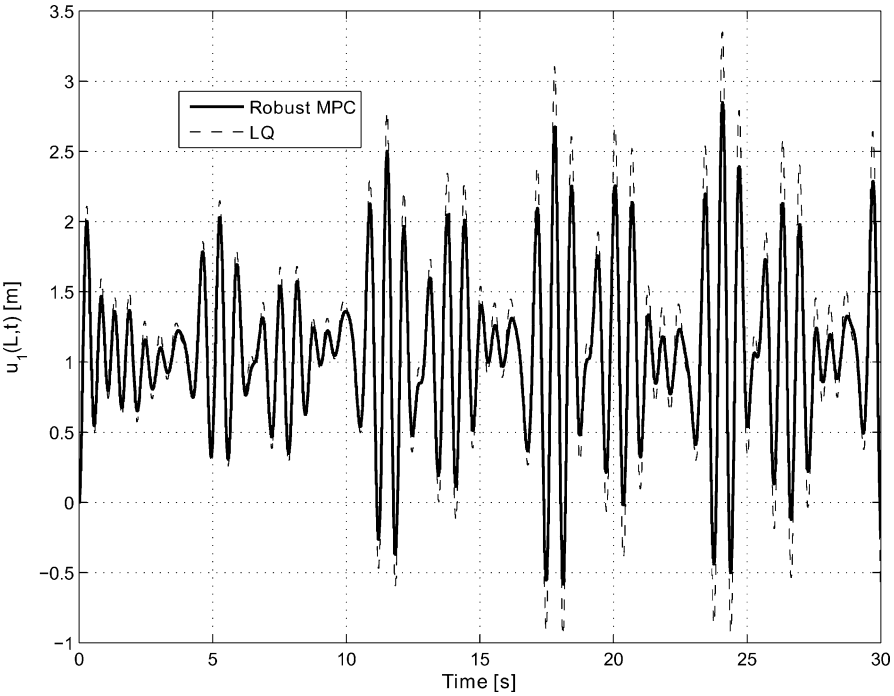

Fig. 10 LQ-controlled (*dashed*) and robust MPC-controlled (*solid*) displacement response (sinusoidal parameters variation)

in taking into account the uncertainties in the system and suppressing the vibrations while ensuring the fulfillment of hard constraints. To examine the performance of the robust MPC with the LQ regulator algorithm, the displacement response of blade 1 has been plotted in Fig. 10 for the two algorithms. It is concluded that the robust MPC is slightly better in controlling vibration response of the blade under uncertain parametric conditions.

Finally, the Fourier spectra of the controlled response (applying robust MPC) and the uncontrolled response has been plotted in Fig. 11. It is seen that the parametric uncertainties in the system have the impact of introducing a large number of high-frequency components in the response, and the robust MPC algorithm suppresses those frequency components.

3.2 Case II: Extreme Vertex

To consider the effect of an extreme variation in the parameter due to uncertainty in the system, the natural frequency variation has been assumed to be the vertex of the parameter polygon space with maximum values. Assuming that the

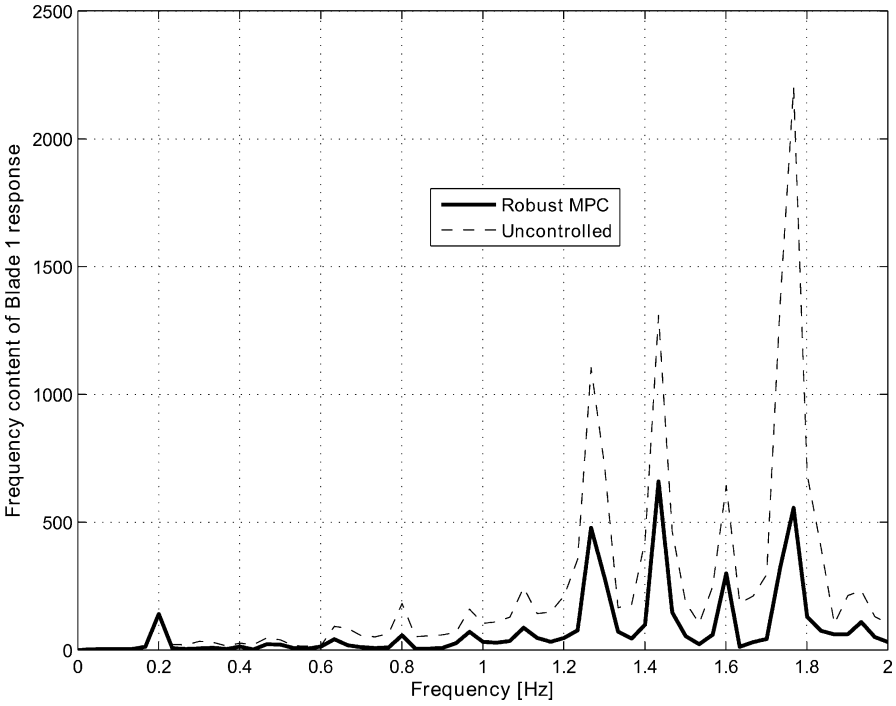

Fig. 11 Frequency content of the uncontrolled (*dashed*) and robust MPC-controlled (*solid*) displacement response (sinusoidal parameter variation)

bounds for the design of the control law $\omega_{b_{\min}}$, $\omega_{b_{\max}}$, $\omega_{n_{\min}}$, and $\omega_{n_{\max}}$ are 2, 6, 1, and 4 rad/s, respectively, the flapwise vibration model used during the simulation is instantiated with $\omega_b = \omega_{b_{\max}}$, $\omega_n = \omega_{n_{\max}} \forall k$. This corresponds to setting $\lambda_i = 0$, $i = 1, 2, 3$, $\lambda_4 = 1$. Therefore, the dynamic realization of the system used in the test is one of the vertexes of the uncertainty polytope on which the synthesis of the robust control law is based. In this respect, this corresponds to a worst-case scenario since the controller has to cope with extreme values for the modeled uncertainties. The results for this case using a maximum control force of 20% of the total blade weight and an output constraint of 5 m have been plotted in Figs. 12, 13, 14 and 15. As in the previous case, no major qualitative deviation in conclusion has been found.

Also for this case, the controlled displacement responses based on the robust MPC algorithm have been compared with the case with nominal MPC (i.e., the optimization problem in the MPC algorithm has been solved for the case with the nominal natural frequency parameters). The results indicate that the application of the nominal MPC controller with the given constraints and designed for the case considered leads to unstable displacement response while the robust MPC has again shown excellent performance (Fig. 16).

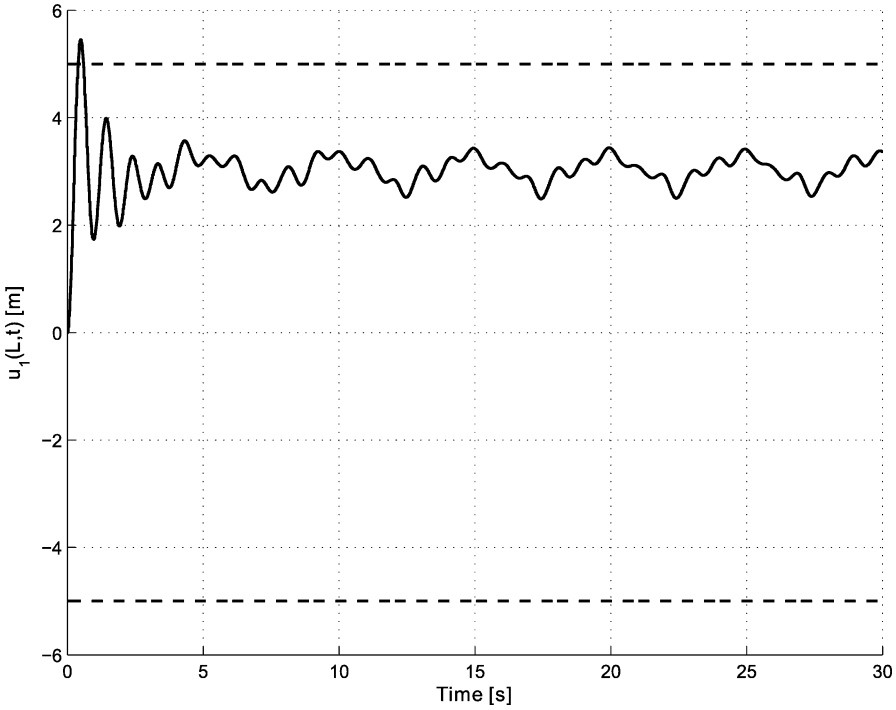

Fig. 12 Blade 1 tip displacement (extreme vertex)

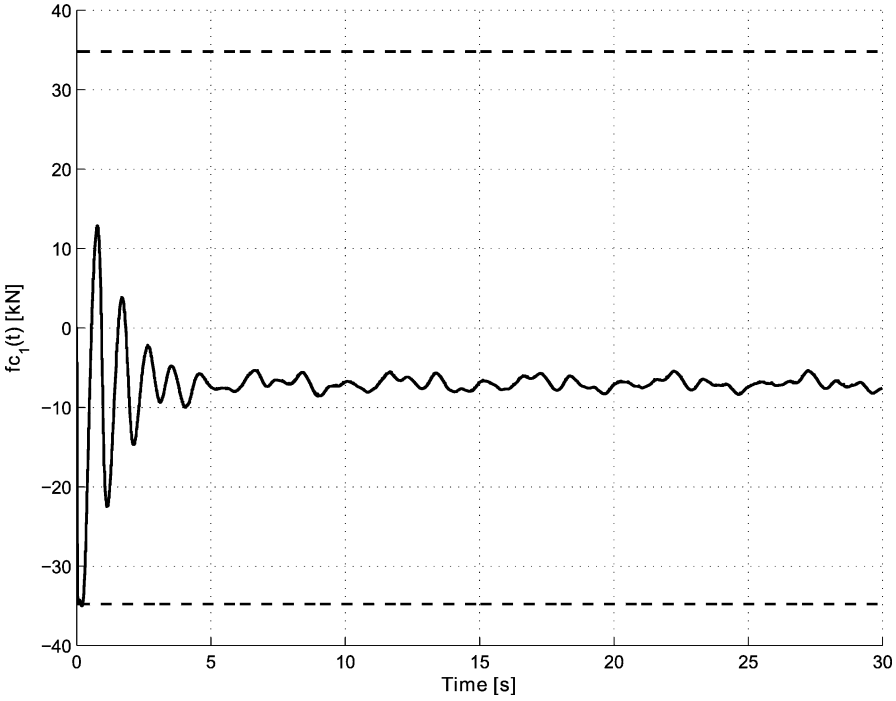

Fig. 13 Control force on blade 1 (extreme vertex)

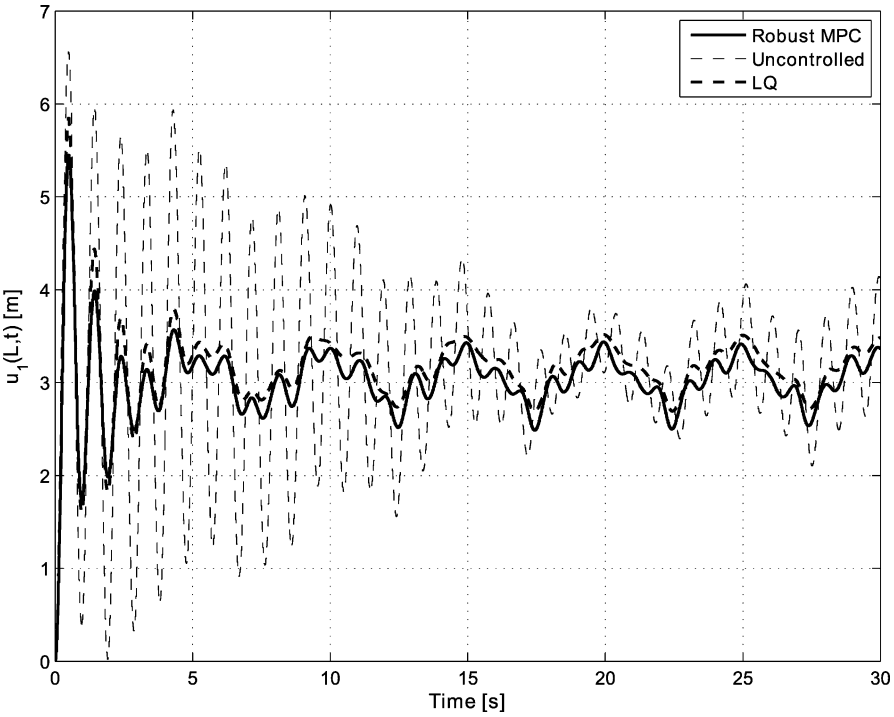

Fig. 14 Uncontrolled (*thin dashed*), LQ-controlled (*thick dashed*), and robust MPC-controlled (*solid*) displacement response (extreme vertex)

3.3 Output-Only Feedback with Robust State Observer

The robust state feedback MPC algorithm can be extended in order to implement an output-only feedback MPC controller [8]. This is obtained by designing a robust state observer, which provides an estimate $\hat{x}(k|k)$ of the state of the system based on the output measurements. By assuming that the system parameters (i.e., λ_i) are measurable at each sampling time, the state update equation for the observer is given by

$$\hat{x}(k|k) = \hat{x}(k|k-1) + GCA(k)e(k-1) \tag{21}$$

$e(k) = x(k) - \hat{x}(k|k)$ is the state estimation error. The observer gain G is designed to robustly stabilize $e(k)$ and is computed as $G = P^{-1}Y$, where $P = P^{\mathrm{T}} > 0$ and Y are obtained by solving the following set of linear matrix inequalities:

$$\begin{bmatrix} P & PA_j + YCA_j \\ A_j^T P + A_j^T C^T Y^T & P \end{bmatrix} \geq 0, \quad j = 1...l \tag{22}$$

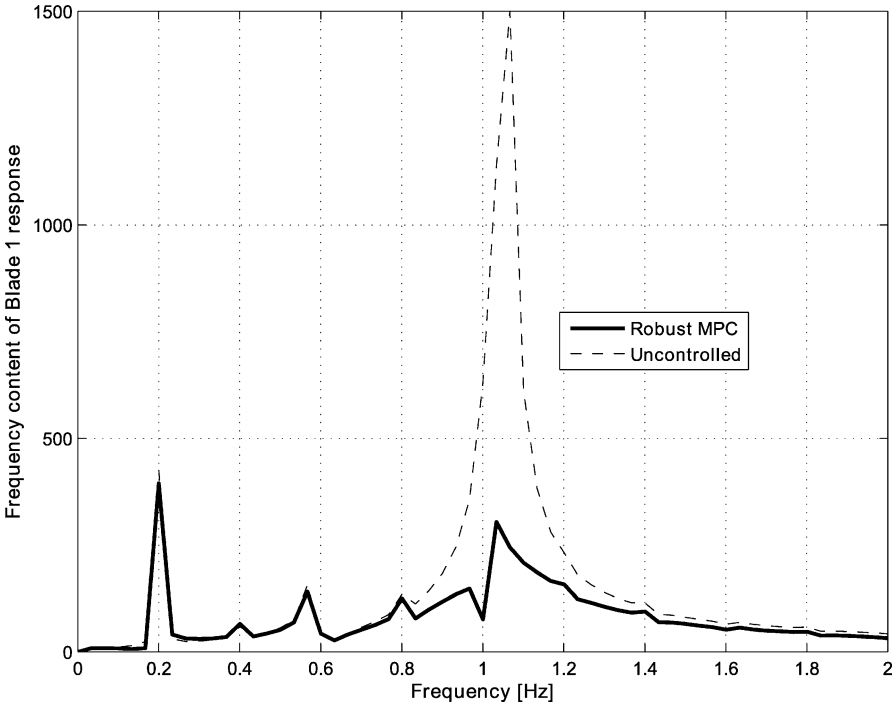

Fig. 15 Frequency content of the uncontrolled (*dashed*) and robust MPC-controlled (*solid*) displacement response (extreme vertex)

By replacing the state system $x(k|k)$ in Eq. (20a, 20b, 20c, 20d, 20e) with the estimate $\hat{x}(k|k)$ reconstructed by feeding back output variables only, the robust-constrained MPC control law is implemented as $u(k|k) = F_k\hat{x}(k|k)$. In this study, displacements have been assumed as measured outputs, and the performance of the full-state feedback controller has been compared to the output feedback case as shown in Fig. 17.

The numerical experiments have been carried out by assuming the bounds in case II and a maximum-controlled force of 15% of the total blade weight. The initial state of the observer has been set zero, while for the system state a randomly generated initial condition has been chosen:

$$x(0) = [0.1219 \quad 0.5221 \quad 0.1171 \quad 0.7699 \quad 0.3751 \quad 0.8234 \quad 0.0466 \quad 0.5979]^T \tag{23}$$

It is interesting to note that after an initial mismatch (as shown in the zoomed plot in Fig. 17) due to different initial condition, the observer converges to the system state even in the presence of persistent disturbances, as there is no appreciable difference between the output-only feedback and state feedback-controlled blade response.

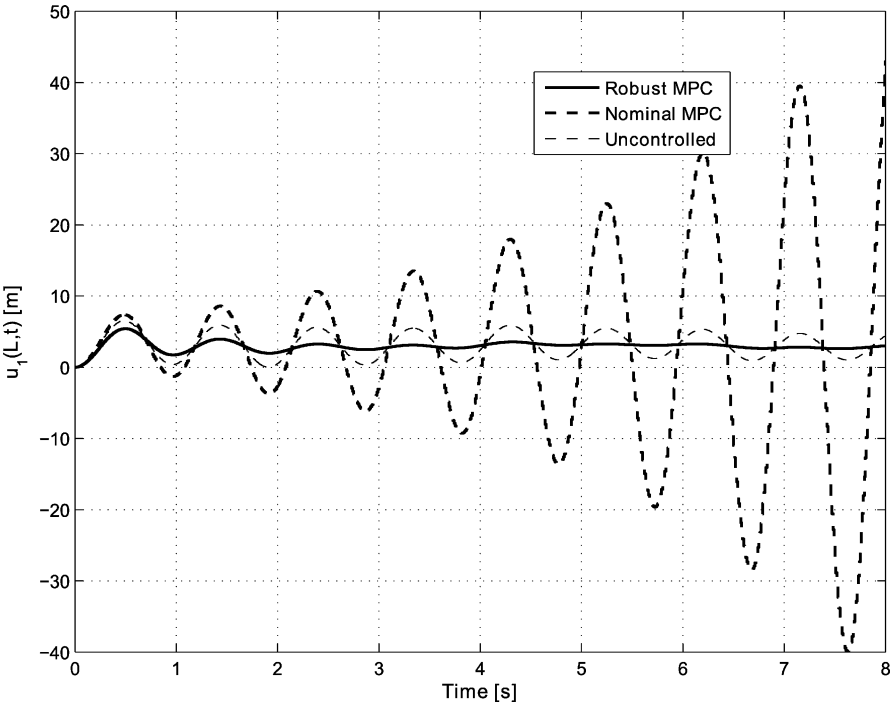

Fig. 16 Uncontrolled (*thin dashed*), nominal MPC-controlled (*thick dashed*), and robust MPC-controlled (*solid*) displacement response (extreme vertex)

4 Conclusions

In this chapter, a new control scheme for mitigating flapwise vibrations in wind turbine blades has been presented. The potential use of a new active control configuration located inside the blades has been considered. The study has been carried out by developing a mathematical model focused on the dynamics of flapwise vibrations, including the interaction between the blades and the tower and the active controllers. Steady wind loading conditions, including linear wind shear, have been considered. Uncertainties in the fundamental natural frequencies of the blade and the tower have been modeled in the framework of structured polytopic uncertainty. The robust-constrained MPC algorithm proposed by Kothare et al. [9] has been implemented in Matlab in order to ascertain the effectiveness of the proposed control strategy in presence of time-varying parametric uncertainties and hard constraints. Simulation results show that in different scenarios analyzed, the robust MPC is effective in reducing the response of the blades even when variations in the considered parameters occur and the control input is limited

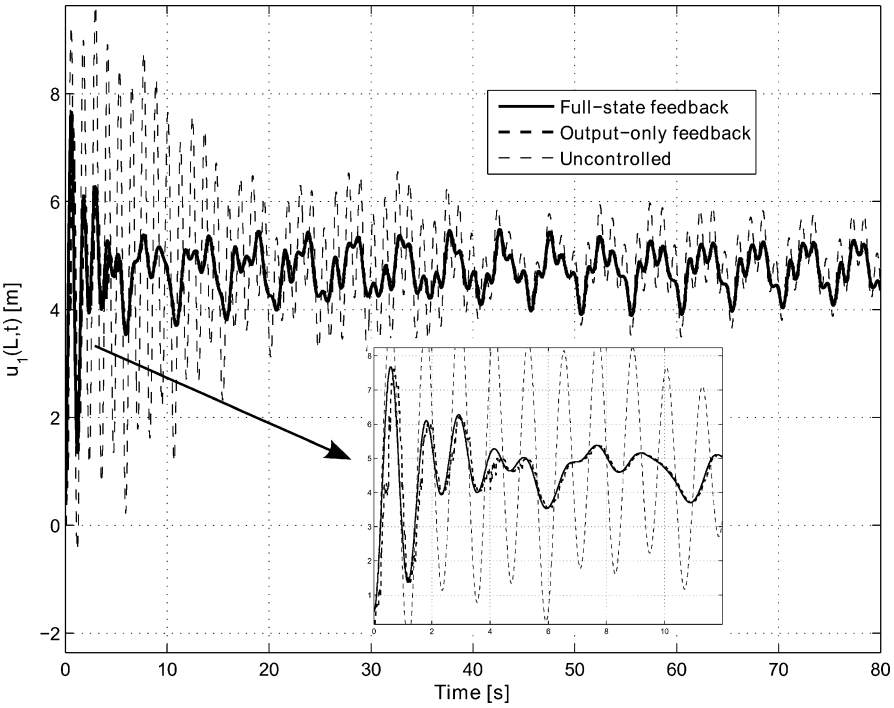

Fig. 17 Uncontrolled (*thin dashed*), robust MPC with state observer (*thick dashed*), and full-state feedback robust MPC-controlled (*solid*) displacement response (output feedback case)

to a prescribed value. The proposed active tendon controller has been also used for investigating the control of edgewise vibration of wind turbine rotor blades (which is a time-varying system), and encouraging results have been reported [15].

Acknowledgments This research is carried out under the EU FP7 funding for the Marie Curie ITN project SYSWIND (Grant No. PITN-GA- 2009-238325).

References

1. Arrigan J, Pakrashi V, Basu B, Nagarajaiah S (2010) Control of flapwise vibration in wind turbine blades using semi-active tuned mass dampers. Struct Control Health Monit 18(8): 840–851 (in press)
2. Colwell S, Basu B (2009) Tuned liquid column dampers in offshore wind turbines for structural control. Eng Struct 31(2):358–368
3. Dueñas-Osorio L, Basu B (2008) Unavailability of wind turbines from wind induced accelerations. Eng Struct 30(4):885–893
4. Hansen MH (2003) Improved modal dynamics of wind turbines to avoid stall-induced vibrations. Wind Energy 6(2):179–195
5. Hansen MOL (2008) Aerodynamics of wind turbines. Earthscan, Sterling

6. Johnson SJ, Baker JP, van Dam CP, Berg D (2010) An overview of active load control techniques for wind turbines with an emphasis on microtabs. Wind Energy 13(2–3):239–253
7. Jonkman JM, Butterfield S, Musial W, Scott G (2009) Definition of a 5-MW reference wind turbine for offshore system development. National Renewable Energy Laboratory, Technical report NREL/TP-500-38060
8. Kothare M (1997) Control of systems subject to constraints, Ph.D. thesis, California Institute of Technology
9. Kothare M, Balakrishnan V, Morari M (1996) Robust constrained model predictive control using linear matrix inequalities. Automatica 32(10):1361–1379
10. Kvasnica M, Grieder P, Baotíc M (2004) Multi-Parametric Toolbox (MPT). http://control.ee.ethz.ch/mpt/
11. Lackner MA, van Kuik G (2010) A comparison of smart rotor control approaches using trailing edge flaps and individual pitch control. Wind Energy 13(2–3):117–134
12. Maldonado V, Farnsworth J, Gressick W, Amitay M (2010) Active control of flow separation and structural vibrations of wind turbine blades. Wind Energy 13(2–3):221–237
13. Murtagh PJ, Basu B, Broderick BM (2005) Along-wind response of a wind turbine tower with blade coupling subjected to rotationally sampled wind loading. Eng Struct 27(8):1209–1219
14. Murtagh PJ, Ghosh A, Basu B, Broderick B (2008) Passive control of wind turbine vibrations including blade/tower interaction and rotationally sampled turbulence. Wind Energy 11(4):305–317
15. Staino A, Basu B, Nielsen SRK (2011) Actuator control of edgewise vibrations in wind turbine blades. J Sound Vib. doi:10.1016/j.jsv.2011.11.003

Disaster Mitigation of Large Infrastructure Systems

Baidurya Bhattacharya

Abstract Modern engineering has become a hugely complex and demanding endeavour – better and cheaper products must be produced at an ever increasing pace while they must continue to be safe and reliable. But, systems can fail and big systems fail in big ways, causing large losses. Failure, if it occurs, often happens in hitherto unknown ways. It is imperative that large infrastructure systems be designed not only to provide full functionality under normal conditions; they must also be able to absorb limited damages without tripping, be able to provide essential services after a major strike and be able to have the ability to come back up online within a reasonable time after being hit by a disaster. These requirements can be met by (1) spelling out in precise measurable terms the system performance expectations both in intact and damaged conditions, (2) clearly understanding the hazards for each performance level and (3) specifying the reliability or confidence with which these performance expectations must be met. The challenges in meeting these tasks can be grouped into three categories: (1) uncertainty quantification, (2) system level modelling and (3) risk communication.

Keywords Large infrastructure • Disaster mitigation • Uncertainty quantification • System level modelling • Risk communication

1 Introduction

Infrastructure refers to the basic framework that underlies and holds together a complex system. A country or a region depends on its civil, communication, military, financial and other infrastructure to function and serve its citizens. This chapter is

B. Bhattacharya (✉)
Department of Civil Engineering, Indian Institute of Technology Kharagpur, Kharagpur, West Bengal, India
e-mail: baidurya@civil.iitkgp.ernet.in

S. Chakraborty and G. Bhattacharya (eds.), *Proceedings of the International Symposium on Engineering under Uncertainty: Safety Assessment and Management (ISEUSAM - 2012)*,
DOI 10.1007/978-81-322-0757-3_27,

about civil infrastructure systems, i.e., the built environment which includes the transportation, power, water, etc., infrastructure systems. An infrastructure has many interconnected parts, working together to provide a desired solution to society. For example, the transportation infrastructure of a nation is composed of its port, airport, road, bridge, air, rail, etc., systems. Large-scale industrialization started in the nineteenth century, and the word infrastructure came into English less than a 100 years ago. With the harnessing of steam, electricity and explosives, together with the ability to make new and better materials, humans had the ability to span distance and reduce communication time at a scale not possible before.

2 Evolution of Engineering Design

Building complex systems does not happen by chance or in a vacuum. Up until the middle of the nineteenth century, engineering, be it making a castle, a bridge or a watch, was mostly an art – it was conceived by intuition, designed by experience, performed often by one very talented individual, expected to last long and put up by factor of safety. Testing, repeatability, collaboration or optimization was not of primary concern. The art aspect is still very much central to engineering, for one cannot build something if one cannot imagine it, but rigorous science has become the bedrock of modern engineering. The modern engineer has made society more democratic: more people have access to what once belonged only to kings – be it indoor plumbing, indoor illumination, high-speed travel or instant communication. In the process, modern engineering has also become a hugely complex and demanding endeavour – better and cheaper products must be produced at an ever increasing pace while they must continue to be safe and reliable. Such demands require constant innovation and teamwork involving hundreds or thousands of professionals often spread over a large geographical area [1, 2].

When building something, the engineer always knows that something might go wrong with it, and his/her solution might not work the way it is supposed to. Failure might mean economic/human/environmental loss to the owner and society on the one hand and, on the other, loss of business and reputation, penalty and, in ancient times, even death for the engineer. Factors of safety have been the traditional means to prevent such undesirable occurrences.

Factors of safety work well when the system is mature, pace of innovation is slow, overdesign is not a deal-breaker and knowledge of system performance – particularly under trying conditions – is limited. Traditional design is component based. The engineer designs the system component by component for ordinary demands, then makes each component safer by a comfortable factor and hopes that the system will hold good under extraordinary demands [3]. As stated above, this strategy works when the technology is mature, the cost is not much of a concern and the system is not expected to perform under extraordinary or exceptional conditions.

3 Managing Failure

But, systems do fail. And big systems fail in big ways, causing big losses. And if they fail, they often fail in hitherto unknown ways. In 2004, the worldwide loss estimate from natural disasters was USD 120 billion [4] much of which resulted from infrastructure damage. If the country's financial system is too big to fail, and it is necessary that important elements of that infrastructure be propped up to prevent collapse of the entire system, so is any one among the country's civil infrastructures – its water supply, power, transportation, building and other infrastructure systems. The difference is that important elements of the civil infrastructure system, such as a large bridge, a nuclear power plant or an airport, if they fail, cannot be propped up or replaced immediately. It can take months or even years for the system to come back up to full functionality. Remember the still unfinished levee system of New Orleans after Katrina in 2005, the unfolding of Fukushima-Daiichi nuclear meltdown of 2011, the cleanup after the Deep Horizon blow-up and oil spill in Gulf of Mexico in 2010, the aftermath of Hurricane Aila in West Bengal and Bangladesh in 2009, the destruction after the Indian Ocean tsunami of 2004, etc.

So it is imperative that large infrastructure systems be designed not only to provide full functionality under normal conditions; they must also be able to absorb limited damages without tripping, be able to provide essential services after a major strike and have the ability to come back up online within a reasonable time after being hit by a disaster. These are very demanding requirements and rather idealistic in nature. However, we must evaluate our existing as well as our upcoming infrastructure systems against these expansive desiderata in precise measurable ways, if we wish to have our engineering infrastructure serve us in normal times as well as in times of crises.

4 Performance Expectations and How to Achieve Them

The first task in designing an infrastructure system, then, is to spell out our expectations – its performance requirements – under a range of system conditions, e.g., normal, partially damaged and severely damaged [5–10]. The damage states must be defined in precise measurable terms.

Once the performance requirements are understood, the designer must make a comprehensive survey of the hazards that are likely to befall the system during its design life [11]. Different performance levels should generally be evaluated against different types and/or magnitudes of hazard [12, 13]. Man-made hazards are different from natural hazards in that the former are inflicted by an intelligent agent to cause harm and thus may cause damage disproportionate to the extent and scale of attack [14]. The engineer also has to define the so-called design envelope in order to admit that it is either too costly or technically impossible or both to meet hazard scenarios beyond this envelop.

The third task is to define the confidence or reliability with which the system must perform its intended functions subjected to the appropriate hazards [15–18]. Uncertainties abound in any engineering activity, and the uncertainties about a large infrastructural system are significant indeed. There are uncertainties about the occurrence and magnitudes of the hazards, the loads they cause on the system, the strength of each element of the system [19], the manner in which these elements influence and interact with each other, and finally in the mathematical models with which we evaluate the hazards and system performance [20]. Under such myriad uncertainties, it is clear that the system can meet its requirements not every time; the frequency or confidence with which it does so must be evaluated probabilistically and compared to a predefined target. These target reliabilities/availabilities are not in the purview of the engineer alone; they need to be set by engineers, economists and policymakers, and must take into account the consequences of failure, the cost of mitigation measures [21] and the perception of risk from the failed infrastructure by members of the public.

5 Current Challenges

Once these three tasks are in place, design of the infrastructure system can proceed in the usual iterative manner, and it is the responsibility of the designer to provide the most economical solution for the design. It can so happen that in case of severe system damage under an extreme hazard, the system can meet its performance requirements with the required reliability only if adequate post-disaster management activities are factored into the design.

At the current state of the art, the impediments to realizing the ideal solution described above relate to three major aspects: the first to do with uncertainty, the second in regard to modelling of the system and the third to do with risk communication.

1. *Uncertainty quantification*. There is lack of complete knowledge about the input, i.e., the future hazards and the future demands, to the system. For hazards that arise out of extremes of geophysical processes, how does one reconcile their spatio-temporal scales that are orders of magnitude larger than those of the engineering systems? How does uncertainty in the input propagate through a complex system? How accurately is it possible to predict the state/output of a complex system in the face of significant uncertainty in the input and the model? How are uncertainties arising from human intervention, human error and public behaviour going to affect the response of the system when disaster strikes?
2. *System level model*. It is comparatively easy to model a system in its intact form operating under normal conditions. The model of the system in severely damaged or in near failure conditions becomes inaccurate and cannot be verified against experimental data. How much is the error in the system model itself? Important system failure modes and weak progressive failure sequences may be

missed. It is relatively easy to model dependence among events if they are causally related, but associative dependence is more difficult and easy to miss which might give a false sense of safety through redundancy. If the system is instrumented, how can the sensed data under normal conditions, and those under damaged conditions, be used to estimate the extent of damage and to direct disaster response operations?

3. *Risk communication.* How much risk to life, property and the environment is society willing to accept for the benefits that it gets from the infrastructure if it fails? How much money is it willing to spend to mitigate an additional unit of risk? What failure costs are to be taken into account, and which are to be kept out? What is the value of natural beauty that is threatened by a disaster? These questions directly affect the reliability/availability to which the infrastructure system needs to be designed. There may be a large difference between the actual risk of failure of a system and the risk perceived by the public. How is the proper risk to be communicated? Society's tolerable risk to an activity may change with time: how is one to keep up with it?

References

1. Longstaff TA, Haimes YY (2002) A holistic roadmap for survivable infrastructure systems. IEEE Trans Syst Man Cybern A Syst Humans 32(2):260–268
2. Woo G (2005) Topical issues in infrastructure risk management. In: ICOSSAR 2005, Millpress, Rotterdam
3. Galambos TV (1992) Design codes. In: Blockley D (ed) Engineering safety. McGraw Hill, London/New York, pp 47–69
4. Kunreuther H (2005) Catastrophe modeling: a new approach to managing risk. In: ICOSSAR 2005. Millpress, Rotterdam
5. Augusti G, Ciampoli M (2008) Performance-based design in risk assessment and reduction. Probab Eng Mech 23:496–508
6. Collins KR et al (1996) Dual-level seismic design: a reliability-based methodology. Earthq Eng Struct Dyn 25:1433–1467
7. FEMA (1997) FEMA-273 NEHRP guidelines for the seismic rehabilitation of buildings. Federal Emergency Management Agency, Washington, DC
8. FEMA (2000) FEMA-350 Recommended seismic design criteria for new steel moment-frame buildings. Federal Emergency Management Agency, Washington, DC
9. SEAOC (1995) Vision 2000, Performance based seismic engineering of buildings. Structural Engineers Association of California
10. Wen Y-K (2001) Minimum lifecycle cost design under multiple hazards. Reliab Eng Syst Saf 73:223–231
11. Wen Y-K (1990) Structural load modeling and combination for performance and safety evaluation, Developments in civil engineering. Elsevier, Amsterdam
12. Ghobarah A (2001) Performance based design in earthquake engineering: state of development. Eng Struct 23:878–884
13. Kinali K, Ellingwood BR (2007) Performance of non-seismically designed PR frames under earthquake loading. In: International conference on applications of statistics and probability (ICASP 10), Tokyo, Japan

14. AASHTO (2002) A guide to highway vulnerability assessment for critical asset identification and protection [cited 9 Sept 2005]. Available from: http://security.transportation.org/sites/security/docs/guide-VA_FinalReport.pdf
15. Bhattacharya B et al (2001) Developing target reliability for novel structures: the case of the Mobile Offshore Base. Mar Struct 14(12):37–58
16. Ditlevsen O (2003) Decision modeling and acceptance criteria. Struct Saf 25:165–191
17. ISO (1998) ISO 2394 General principles on reliability for structures, 2nd edn. International Organization for Standardization
18. Wen Y-K (2001) Reliability and performance based design. Struct Saf 23:407–428
19. Ellingwood BR et al (1980) Development of a probability based load criterion for American National Standard A58. NBS Special Publication 577. 1980, U.S. Department of Commerce, National Bureau of Standards, Washington, DC
20. Ditlevsen O (1982) Model uncertainty in structural reliability. Struct Saf 1:73–86
21. Frangopol DM et al (1997) Life-cycle cost design of deteriorating structures. J Struct Eng ASCE 123(10):1390–1401

An Overview of Application of Nanotechnology in Construction Materials

A.K. Tiwari and Subrato Chowdhury

Abstract Nanotechnology has changed the way material and process are being today, in a used number of applications. For civil engineering applications, however, the effect is not so visible, though a couple of applications are available. One of the biggest issues of concern for civil engineers is the amount of materials being used for various developmental projects around the world. This large consumption is mostly exhausting the natural materials, which are non-reclaimable and hence the present use is unsustainable. Nanotechnology can help reduce uses of these natural materials without losing their optimum applications. Construction being the single largest industry today in the world would certainly benefit with this application. Nanotechnology has the potential to make construction faster, cheaper, safer, and more varied. Automation of nanotechnology construction can allow for the creation of structures from advanced homes to massive skyscrapers much more quickly and at much lower cost. An overview of application and opportunity of nanotechnology in construction materials is briefly introduced in the present chapter with critical insight.

Keywords Nanotechnology • Construction materials • Cement-based composites • Admixtures • Coatings • Steel • Glass

1 Introduction

Nanotechnology has changed the way material and process are being done today, in a number of applications. For civil engineering applications, however, the effect is not so visible, though a couple of applications are available. One of the biggest

A.K. Tiwari
UltraTech Cement Limited, Mumbai, India

S. Chowdhury (✉)
Research & Development, UltraTech Cement Limited, Mumbai, India
e-mail: subrato.chowdhury@adityabirla.com

S. Chakraborty and G. Bhattacharya (eds.), *Proceedings of the International Symposium on Engineering under Uncertainty: Safety Assessment and Management (ISEUSAM - 2012)*,
DOI 10.1007/978-81-322-0757-3_28,

issues of concern for civil engineers is the amount of materials being used for various developmental projects around the world. This large consumption is mostly exhausting the natural materials, which are non-reclaimable and hence the present use is unsustainable. Nanotechnology can help reduced uses of these natural materials without losing their optimum applications. Construction being the single largest industry today in the world would certainly benefit with this application. Nanotechnology has the potential to make construction faster, cheaper, safer, and more varied. Automation of nanotechnology construction can allow for the creation of structures from advanced homes to massive skyscrapers much more quickly and at much lower cost.

Nanotechnology is one of the most active research areas that encompass a number of disciplines such as electronics, biomechanics, and coatings including civil engineering and construction materials. The use of nanotechnology in construction involves the development of new concept and understanding of the hydration of cement particles and the use of nano-size ingredients such as alumina and silica and other nanoparticles. The manufacturers are also investigating the methods of manufacturing of nano-cement. If cement with nano-size particles can be manufactured and processed, it will open up a large number of opportunities in the fields of ceramics, high-strength composites, and electronic applications. At the nanoscale the properties of the material are different from that of their bulk counterparts. When materials become nano-sized, the proportion of atoms on the surface increases relative to those inside, and this leads to novel properties.

Use of nanomaterials can improve fluidity, strength, and durability of the concrete. Nanomaterials also have the potential to be used to improve the reinforcement qualities like anticorrosion. Nano-enabled coating of construction materials is going to constitute the largest application of nanotechnology in construction. Nano-products like architectural paints, water sealers, and deck treatments, treatments applied during fabrication, such as scratch-resistant coatings on vinyl or wood flooring, insulation coatings, etc., offer immense market opportunities for nanomaterials. Nanotech products and applications, among other benefits, may enhance the performance with regard to blocking of the ultraviolet rays, transparency of the structures, photo reactivity, and resistance to stain and odor. Moreover, nanotechnology-based coatings can enable creating self-cleaning surfaces. Many of these are already being embedded into window glasses and plumbing fixtures. Nanomaterials and nanotechnology-based applications will thus take the construction industry much beyond bricks and mortar.

2 Opportunities in the Fields of Cement-Based Composites

Nanotechnology is being used for the creation of new materials, devices, and systems at molecular, nano-, and microlevel [1–3]. Interest in nanotechnology concept for Portland cement composites is steadily growing. The most reported

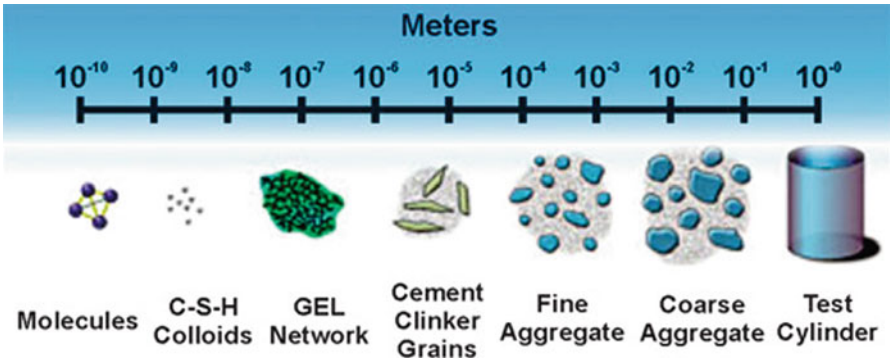

Fig. 1 Scales of various constituents of concrete [4]

research work regarding application of nanotechnology in cement-based materials is either related to coating or enhancement of mechanical and electrical properties. Some of the widely reported nanoparticles in cement concrete industries are titanium dioxide (TiO_2), nano-silica (SiO_2), alumina (Al_2O_3), carbon nanotube (CNT), etc. Currently, the most active research areas dealing with cement and concrete are the following: understanding of the hydration of cement particles and the use of nano-size ingredients such as alumina and silica particles [1–3]. A typical scale of various constituent of a normal concrete is given in Fig. 1.

Average size of Portland cement particle is about 50 μm. In applications that require thinner final products and faster setting time, micro-cement with a maximum particle size of about 5 μm is being used. Knowledge at the nanoscale of the structure and characteristics of materials will promote the development of new applications and new products to repair or improve the properties of construction materials. For example, the structure of the fundamental calcium-silicate-hydrate (C–S–H) gel which is responsible for the mechanical and physical properties of cement pastes, including shrinkage, creep, porosity, permeability, and elasticity. C–S–H gel can be modified to obtain better durability. Cement-based materials containing carbon nanotubes can be used for both strengthening and enhancing electrical and electronic properties of the concrete besides their mechanical properties. Development of smart concrete using carbon nanotubes would be easier. If nano-cement particles can be processed with nanotubes and nano-size silica particles, conductive, strong, tough, and more flexible, cement-based composites can be developed with enhanced properties, for electronic applications and coatings.

3 Nano-concrete and Nano-ingredients

Nano-concrete is defined as a concrete made with Portland cement particles with sizes ranging from a few nanometers to a maximum of about 100 μm. Nano-ingredients are ingredients with at least one dimension of nanometer size.

Therefore, the particle size has to be reduced in order to obtain nano-Portland cement. If these nano-cement particles can be processed with nanotubes and reactive nano-size silica particles, conductive, strong, tough, more flexible, and cement-based composites can be developed with enhanced properties, for electronic applications and coatings. There is also limited information dealing with the manufacture of nano-cement. If cement with nano-size particles can be manufactured and processed, it will open up a large number of opportunities in the fields of cement-based composites. Current research activity in concrete using nano-cement and nano-silica includes the following:

4 Carbon Nanotubes (CNTs)

Carbon nanotubes are among the most extensively researched nanomaterials today. CNTs are tubular structures of nanometer diameter with large aspect ratio. These tubes have attracted much attention in recent years not only for their small dimensions but also for their potential applications in various fields. A single sheet of graphite is called grapheme. A CNT can be produced by curling a graphite sheet. Carbon sheets can also curl in a number of ways. CNT can be considered as the most superior carbon fiber ever made. Addition of small amount (1% by wt) of CNT can improve the mechanical properties consisting of the main Portland cement phase and water. A CNT can be singled or multiwalled. CNTs are the strongest and most flexible molecular material with Young's modulus of over 1 TPa. The approximate diameter is 1 nm with length to micron order. CNTs have excellent flexibility. These are essentially free from defects. Nanotubes are highly resistant to chemical attack and have a high strength to weight ratio (1.8 g/cm^3 for MWNTs and 0.8 G/cm^3 for SWNTs). CNT has maximum strain of about 10% which is higher than any other material. Figure 2 shows the flexible behavior of CNTs. Electrical conductivity of CNTs are six orders of magnitude higher than copper, hence, have very high current-carrying capacity. Hence, carbon nanotubes have excellent potential for use in the cement composites (Fig. 3).

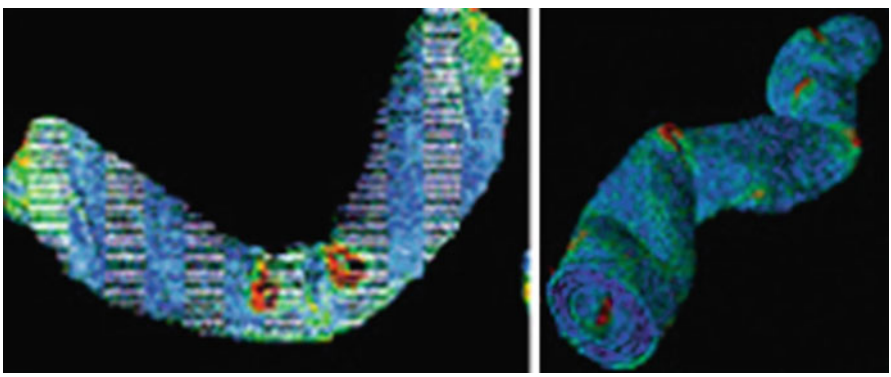

Fig. 2 Flexible behavior of CNTs [5]

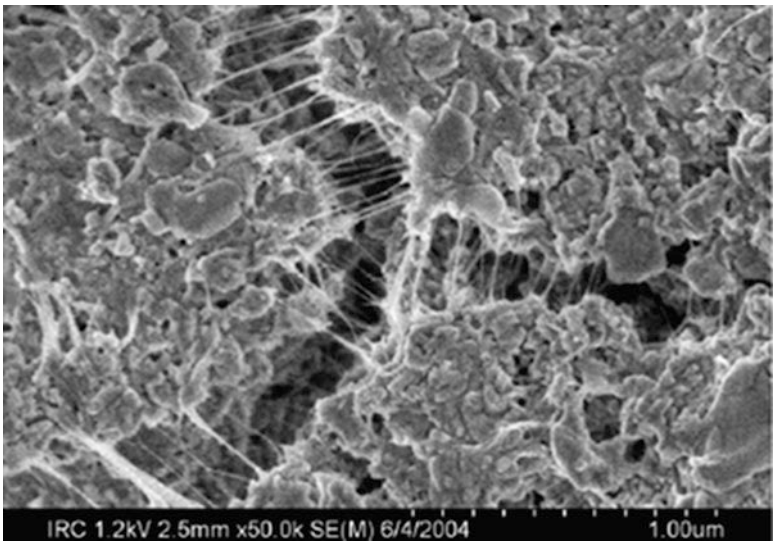

Fig. 3 Crack bridging by CNT bundles with cement matrix [5]

5 Nano-silica Fume for Improving Concrete Performance

Nano-silica is most common nano-additive to concrete. It is reported that nano-silica was found to be much effective than micron-sized silica for improving the performance such as permeability and, subsequently, durability. In addition, reduced amount of about 15–20 kg of nano-silica was found to provide same strength as 60 kg of regular or micro-silica (Fig. 4).

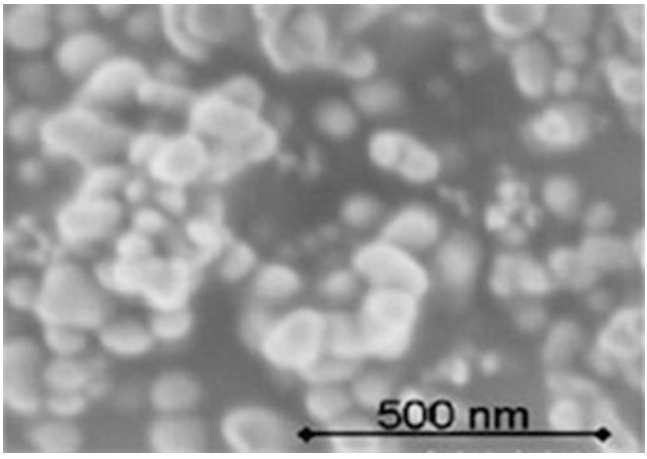

Fig. 4 A typical SEM of nano-silica particles [6]

Nano-silica is an effective additive to polymers and concrete, a development realized in high-performance and self-compacting concrete with improved workability and strength. Nano-silica addition to cement-based materials controls the degradation of the fundamental C–S–H (calcium-silicate-hydrate) reaction in water as well as blocks water penetration and leads to improvement in durability. The addition of nano-SiO_2 particles enhances the density and strength of concrete. The results indicate that nano-silica behaves not only as a filler to improve microstructure but also as an activator to promote pozzolanic reaction for fly ash concrete; as a result strength of the fly ash concrete improves particularly in the early stages.

6 Coatings for Concrete

Another major large volume application of nano-powder in cement-based materials is the area of coatings. The attractive coloring on ancient Czech glasses is found to contain nanoparticles. This shows that nanotechnology was used for coating surfaces, that is, spraying and making a product look attractive from ancient time. Nano-powders have a remarkable surface area. The surface area imparts a serious change of surface energy and surface morphology. The change in properties causes improved catalytic ability, tunable wavelength-sensing ability, and better designed pigments and paints with self-cleaning and self-healing features. One promising area of application of nanoparticle for cement-based materials is development of self-cleaning coating. Titanium oxide is commonly used for this purpose. It is incorporated, as nanoparticles to block UV light. It is added to paints, cements, and windows for its sterilizing properties as TiO_2 breaks down organic pollutants, volatile organic compounds, and bacterial membrane through powerful catalyst reactions and can reduce airborne pollutants applying to outer surfaces. Additionally, it is hydrophilic and therefore gives self-cleaning properties to surface to which it is applied.

7 Controlled Release of Admixtures

Currently, there is an extensive use of chemical admixtures mainly to control/modify the fresh and hardened properties of concrete. The most common admixtures for cement and concrete include accelerators, set retarders, air entraining agents, and superplasticizers. Their successful use requires a basic knowledge of concrete technology, standard construction procedures, and familiarity with cement-admixture interactions. A particular challenge of interest to the authors is to optimize the use of dispersing agents such as superplasticizers in high-performance concretes containing high volumes of supplementary cementing materials (SCMs). Dispersing agents such as superplasticizers are commonly used in these concretes. There are,

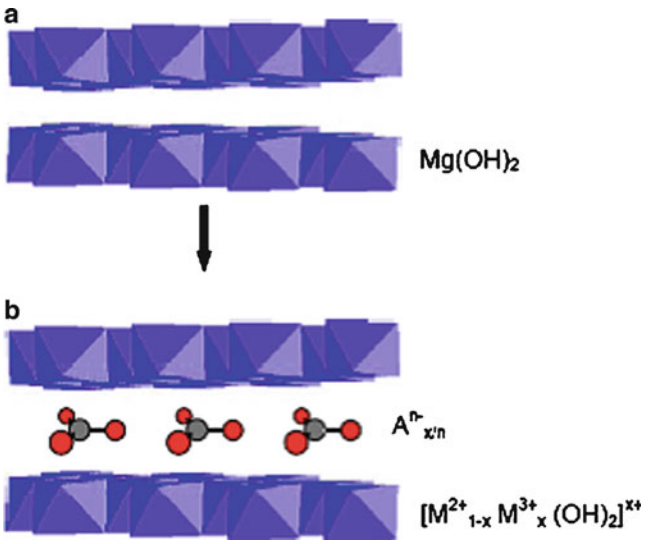

Fig. 5 Crystal structure of brucite (**a**) and LDH (**b**) [3]

however, practical problems such as loss of workability with time that are controlled by interactions with cement components. Controlling the timing of the availability of an admixture in cement systems is essential for its optimal performance. Control release technology provides a route to prolonged delivery of chemicals while maintaining their concentration over a specific time period. Here, a nanotechnology-based approach for controlled release of admixtures in cement systems using layered double hydroxides can be used.

There have been a number of applications in cement and concrete where different means of controlling the effect of admixtures via a controlled release technique were used. A number of patents and research articles describe "encapsulation" procedures for delivery of liquids and solids. A corrosion inhibitor, such as calcium nitrite, was dispersed by encapsulation in coated hollow polypropylene fibers. This anticorrosion system was activated automatically when conditions would allow corrosion to initiate in a steel-reinforced concrete. Porous aggregates were also used to encapsulate antifreezing agents. Porous solid materials (e.g., metal oxides) have also been used as absorbing matrices to encapsulate chemical additives (e.g., accelerators, retarders, and dispersants) and to release them at a slower rate when combined with oil well-treating fluids (Figs. 5 and 6).

Another method to control the release of chemicals in cement-based materials is by "intercalation/de-intercalation." A cement additive for inhibiting concrete deterioration was developed with a mixture of an inorganic cationic exchanger, a calcium zeolite capable of absorbing alkali ions (sodium, potassium, *etc.*), and an inorganic anionic exchanger, hydrocalumite capable of exchanging anions (chlorides, nitrates, sulfates, *etc.*). The results of their tests showed the potential of increasing concrete durability by exchange of alkali and chloride ions to inhibit alkali-aggregate reaction and corrosion of rebar.

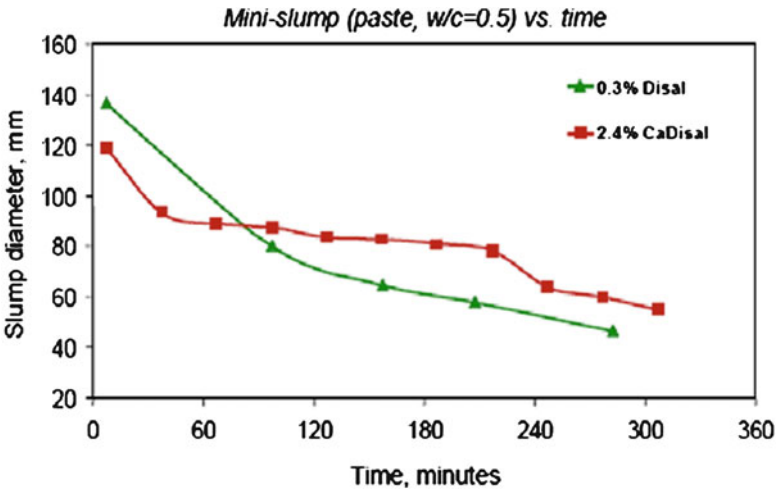

Fig. 6 Slump retention with LDH technology

More recently, work examined means to control the timing of the release of chemical admixtures through their incorporation in nanoscale composite materials. More specifically, the technique consisted of intercalating an admixture into a hydrocalumite-like material, a calcium-based LDH derivative, and adding this composite to a cement-based mix. De-intercalation of the admixture can be actively programmed through controlled chemistry involving, for example, type of layered inorganic material, charge density, concentration, and/or pH. A sulfonated naphthalene formaldehyde-based superplasticizer, called Disal™, was used to produce the controlled release formulation (CaDisal).

The effectiveness of Disal™ alone in controlling the slump-loss *versus* time characteristic was compared to that of the controlled release formulation CaDisal.

8 Nanoparticles and Steel

Steel has been a widely available material and has a major role in the construction industry. The use of nanotechnology in steel helps to improve the properties of steel. The fatigue led to the structural failure of steel due to cyclic loading, such as in bridges or towers. The current steel designs are based on the reduction in the allowable stress, service life, or regular inspection regime. This has a significant impact on the life cycle costs of structures and limits the effective use of resources. The stress risers are responsible for initiating cracks from which fatigue failure results. The addition of copper nanoparticles reduces the surface unevenness of steel which then limits the number of stress risers and hence fatigue cracking. Advancements in this technology using nanoparticles would lead to increased safety, less need for regular inspection regime, and more efficient materials free from fatigue issues for construction.

The nano-size steel produces stronger steel cables which can be in bridge construction. Also, these stronger cable materials would reduce the costs and period of construction, especially in suspension bridges as the cables are run from end to end of the span. This would require high-strength joints which lead to the need for high-strength bolts. The capacity of high-strength bolts is obtained through quenching and tempering. The microstructures of such products consist of tempered martensite. When the tensile strength of tempered martensite steel exceeds 1,200 MPa, even a very small amount of hydrogen embrittles the grain boundaries, and the steel material may fail during use. This phenomenon is known as delayed fracture, which hindered the strengthening of steel bolts, and their highest strength is limited to only around 1,000–1,200 MPa.

The use of vanadium and molybdenum nanoparticles improves the delayed fracture problems associated with high-strength bolts reducing the effects of hydrogen embrittlement and improving the steel microstructure through reducing the effects of the intergranular cementite phase.

Welds and the heat-affected zone (HAZ) adjacent to welds can be brittle and fail without warning when subjected to sudden dynamic loading. The addition of nanoparticles of magnesium and calcium makes the HAZ grains finer in plate steel, and this leads to an increase in weld toughness. The increase in toughness at would result in a smaller resource requirement because less material is required in order to keep stresses within allowable limits. The carbon nanotubes are exciting material with tremendous properties of strength and stiffness; they have found little application as compared to steel, because it is difficult to bind them with bulk material, and they pull out easily, which make them ineffective in construction materials.

9 Nanoparticles in Glass

The glass is also an important material in construction. There is a lot of research being carried out on the application of nanotechnology to glass. Titanium dioxide (TiO_2) nanoparticles are used to coat glazing since it has sterilizing and antifouling properties. The particles catalyze powerful reactions which break down organic pollutants, volatile organic compounds, and bacterial membranes.

The TiO_2 is hydrophilic (attraction to water) which can attract raindrops which then wash off the dirt particles. Thus, the introduction of nanotechnology in the glass industry incorporates the self-cleaning property of glass. Fire-protective glass is another application of nanotechnology. This is achieved by using a clear intumescent layer sandwiched between glass panels (an interlayer) formed of silica nanoparticles (SiO_2) which turns into a rigid and opaque fire shield when heated. Most of glass in construction is on the exterior surface of buildings. So the light and heat entering the building through glass has to be prevented. The nanotechnology can provide a better solution to block light and heat coming through windows.

10 Nanoparticles in Coatings

Coatings is important element in construction and are extensively used to paint the walls, doors, and windows. Coatings should provide a protective layer which is bound to the base material to produce a surface of the desired protective or functional properties. The coatings should have self-healing capabilities through a process of "self-assembly." Nanotechnology is being applied to paints to obtain the coatings having self-healing capabilities and corrosion protection under insulation. These coatings are hydrophobic and repel water from the metal pipe and can also protect metal from saltwater attack. Nanoparticle-based systems can provide better adhesion and transparency. The TiO_2 coating captures and breaks down organic and inorganic air pollutants by a photocatalytic process, which leads to putting roads to good environmental use.

11 Conclusion

Nanotechnology can change the way we construct our structure today. It can help us to utilize the natural resources to optimum level and make them sustainable. This will also allow use of resources for present development and leave the same for the use of future generations also. Though presently at research level, scope is enormous, and engineers and scientist need to increase their effort on the directions to overcome challenges.

References

1. Patel-Predd P (2007) The Nano secret to concrete, MIT Technology review
2. Ge Z (2008) Applications of nanotechnology and nano-materials in construction. In: First International Conference on Construction In Developing Countries (ICCIDC–I) 2008, Karachi, Pakistan
3. Raki L et al (2010) Cement and concrete nano-science and nanotechnology. Materials 3:918–942
4. Porro P (2005) Nano science and nanotechnology in construction Materials. In: 2nd international symposium on nanotechnology in construction 2005, Bilbao, Spain
5. Mann, S (2006) Nanotechnology and construction. Report of Nano forum
6. Ji T (2005) Preliminary study on the water permeability and microstructure of concrete incorporating nano-SiO_2. Cement Concr Res 35:1943–1947

Sensor Network Design for Monitoring a Historic Swing Bridge

Giuseppe C. Marano, Giuseppe Quaranta, Rita Greco, and Giorgio Monti

Abstract Significant advances in the development and customization of various sophisticated technologies for structural monitoring have emerged during the last decade. Technologies for instrumentation, monitoring, load testing, nondestructive evaluation and/or characterization, three-dimensional finite element modeling, and various types of analyses have now become available at a reasonable cost. Within this framework, this chapter focuses on the issues addressed in designing a sensor network for dynamic monitoring of a historic swing bridge in Taranto (Italy).

Keywords Dynamic monitoring • Movable bridge • Sensor network

1 Introduction

Bridge structures are very critical elements within a complex transportation system, and movable bridges are especially important because they allow traffic across active waterways, thus granting passage to ships that would otherwise be blocked by the structure. Therefore, reliability assessment as well as health monitoring of movable bridge structures are challenging issues that deserve significant attention

G.C. Marano (✉) • R. Greco
Department of Environmental Engineering and Sustainable Development, Technical University of Bari, Viale del Turismo, 10, 74100 Taranto, Italy
e-mail: g.marano@poliba.it

G. Quaranta
Department of Civil and Environmental Engineering, University of California, Davis, One Shields Avenue, 95616 Davis, CA, USA
e-mail: gquaranta@ucdavis.edu

G. Monti
Department of Structural and Geotechnical Engineering, Sapienza University of Rome, Via A. Gramsci 53, 00197 Rome, Italy
e-mail: giorgio.monti@uniroma1.it

S. Chakraborty and G. Bhattacharya (eds.), *Proceedings of the International Symposium on Engineering under Uncertainty: Safety Assessment and Management (ISEUSAM - 2012)*, DOI 10.1007/978-81-322-0757-3_29,

Fig. 1 Location of the "St. Francesco da Paola" bridge (*left*) and a photograph (*right*)

because a structural failure and/or a temporary lack of service may have a tremendous socioeconomic impact. Developing a reliable network for monitoring these infrastructures is, therefore, an efficient way for supporting numerical studies by making available reference experimental data to be used, for example, in finite element model elaborations.

Having this in mind, we are developing a sensor network for monitoring the "St. Francesco da Paola" bridge (Fig. 1), a historic swing bridge located in Taranto (Italy).

Taranto is a coastal city located in the southern part of Italy, in the Apulia region, in front of the Ionian Sea. The city is characterized by a hydrologic system based on two basins close to the Ionic coast. An inner, semi-enclosed basin with lagoon features – named "Mar Piccolo" – is connected with the outer basin (named "Mar Grande") through two canals, namely, the "Navigabile" canal and the "Porta Napoli" canal. The inner basin "Mar Piccolo" is divided into two inlets – named first and second inlet – which have a maximum depth of 13 and 8 m, respectively (Fig. 1). The actual swing bridge over the "Navigabile" canal – the "St. Francesco da Paola" bridge – was opened to traffic more than fifty years ago, on March 10, 1958. This swing bridge was built with two equally armed movable portions, and each of them rotates about one vertical axis. The structural health and the functionality of the opening system are crucial, because of the bridge's central role within the local transport network. The current structural reliability of the bridge is substantially unknown because it has not been investigated previously by using modern simulation-based numerical techniques. Significant experimental data are not available to date. There is no digitalized information about the bridge and only historic documents were found. Therefore, a numerical model calibrated on experimentally recorded data is an important first step for a reliable condition assessment of the bridge. For instance, records obtained from a dynamic test may be used to identify natural frequencies, mode shapes, and damping characteristics of the structure for the purpose of model updating.

In this perspective, this chapter provides an overview about our work in developing numerical models as well as experimental- and information-based technologies for monitoring the "St. Francesco da Paola" swing bridge.

2 Structural Monitoring of Bridge Structures

The evaluation of existing bridges has become an increasingly important topic in the effort to deal with deteriorating infrastructures. This is because a considerable ratio of historic bridges may be classified as deficient or in need of rehabilitation. The most critical issue for historic bridges is typically due to their seismic reliability. However, historic bridges located within relatively low-seismic regions may also have an insufficient reliability. For instance, this is due either to their decreased capacity due to decay or to an increased demand with respect to when they were built (i.e., the loads and the traffic flows are higher, fewer disturbances due to traffic-induced vibrations are accepted). Thus, performing a reliable structural assessment of a bridge becomes essential to avoid its disposal, which involves seldom-acceptable economical and safety implications, not to mention the irreparable loss of a cultural heritage artifact. The accuracy of bridge evaluation can be improved by using recent developments in the fields of bridge diagnostics, structural tests, and material tests. Advanced diagnostic procedures can be applied to the evaluation of the current capacity of the structure, monitoring of load as well as resistance histories, and evaluation of the accumulated damages. On the contrary, traditional visual-inspection-based condition assessment of bridges cost significantly while restricting operations for many months. Moreover, since visual inspections are conducted by trained and experienced bridge engineers, and/or inspectors, according to some (standardized) procedures, many have pointed out the limitations and shortcomings associated with evaluating and managing bridges primarily on the basis of essentially subjective data. As a consequence, the use of numerical models calibrated on experimental data is a more reliable and appropriate way for bridge condition assessment. The available technologies of structural monitoring tools can be classified as experimental, analytical, and information technologies. Experimental technologies are further classified as:

- Geometry monitoring (to track changes in the geometry, such as geometry changes in cable systems)
- Controlled testing (which should be static or dynamic, nondestructive, destructive or "localized" nondestructive evaluations, and continuous monitoring)

Dynamic testing of bridges, sometimes termed as "vibration analysis" by civil engineers, is an exceptionally powerful experimental technique. For instance, records obtained from a dynamic test may be used to assess the comfort on pedestrian-accessible bridges and to identify relevant modal features. Dynamic tests of bridges and civil constructions are sometimes a necessity as there is no other test technique available that provides a direct measurement of the global

dynamic properties of a structure and without the need for any external measurement reference frame.

Analytical technologies that are used for bridge health monitoring have been classified as:

- CAD and reverse CAD
- Analytical modeling based on a macroscopic, element-level, microscopic, or mixed approaches
- Linear analysis under static, moving, or dynamic loads
- Nonlinear analysis incorporating material nonlinearity, geometric nonlinearity, or both types

Information technologies cover the entire spectrum of efforts related to the acquisition, processing, and interpretation of data. This includes sensing, data acquisition, preprocessing, communication and control, transmission and synchronization, quality testing, post-processing, analysis, display and visualization, database archival and management, and interpretation for decision-making. Given the advances in experimental and analytical technologies, an extensive level of expertise is needed to take full advantage of advanced information technology tools. Teams of computer scientists and structural and electrical engineers have to be brought together so that all the necessary ingredients of know-how may be integrated into meaningful structural monitoring applications.

3 CAD and FE Model

The geometrical model of the bridge was undertaken using CAD techniques (see Figs. 2 and 3). The "St. Francesco da Paola" bridge over the "Navigabile" canal has a span equal to 89.52 m and accommodates two traffic lanes with a total 6.00 m roadway. Two pedestrian lanes are on both sides of the bridge, and the sidewalk span is equal to 1.50 m for each lane. The two movable portions of the bridge are

Fig. 2 CAD model: general view of the bridge

Fig. 3 CAD model: view on the steel truss structure

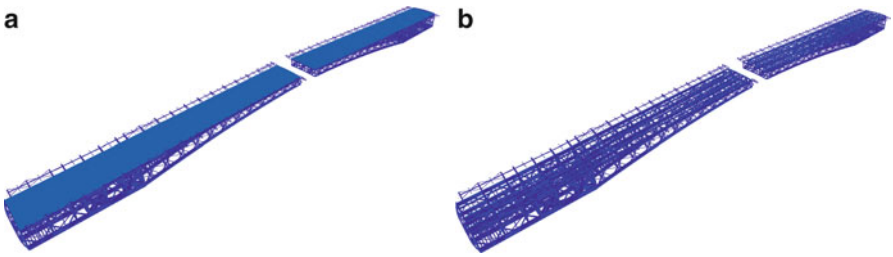

Fig. 4 FE model with (**a**) and without (**b**) steel orthotropic deck

steel truss structures. One rim bearing for each movable portion of the bridge is placed on the corresponding abutment. Each rim bearing consists of a series of conical rollers which are loaded during the bridge movement. The two movable parts of the bridge are connected to each other in four points located in the transversal section of the free ends. The steel truss structure of each movable portion of the bridge was realized as follows: 4 longitudinal truss beams, 19 transverse braces, and horizontal braces on both lower and upper chord of the truss structure.

A three-dimensional finite element (FE) model of the bridge was built by using all the available information collected into the above-illustrated CAD model. The construction of the FE model was undertaken using SAP2000© (version 12), and it is shown in Fig. 4. Only structural elements were included in the model, whereas nonstructural elements are considered as extra masses. All structural elements are made of steel with the following properties: elastic modulus 200,000 N/mm^2, Poisson's ratio 0.30, and mass density 7,850 kg/m^3. Soil-structure interaction is not considered for the purpose of the modal analysis, and the rim bearing is replaced with an appropriate set of constraints. Beam-type elements were adopted to model the element of the truss structure. Thin shell elements were used to model steel plates (including the orthotropic plate-type deck).

4 Hardware Components of the Sensor Network

Developing experimental and information technologies that meet internationally recognized guidelines and standards was one of the starting points for our project. Experimental and information technologies that conform to international standards and guidelines were the priorities in order to ensure the reliability of the final results, which the correctness of the analytical strategies depends upon. Technologies that are described in this chapter meet the requirements provided by the following standards and guidelines:

- Guideline for ANSS seismic monitoring of engineered civil systems [1]
- IEEE standards regarding hardware and software implementation

The developed system for structural dynamic monitoring was named "THOR" (Fig. 5).

THOR consists of three main components: *ThorSensors*, *ThorAgents*, and *ThorServers*. THOR is able to manage more distributed sensor networks with real-time acquisition and data processing for structural analyses. The single THOR network is able to monitor a zone with one *ThorAgent* linked to a number of *ThorSensors*. Different and also geographically distributed networks can be managed by one *ThorServer*. *ThorAgents* and *ThorSensors* cooperate with *ThorServers* to

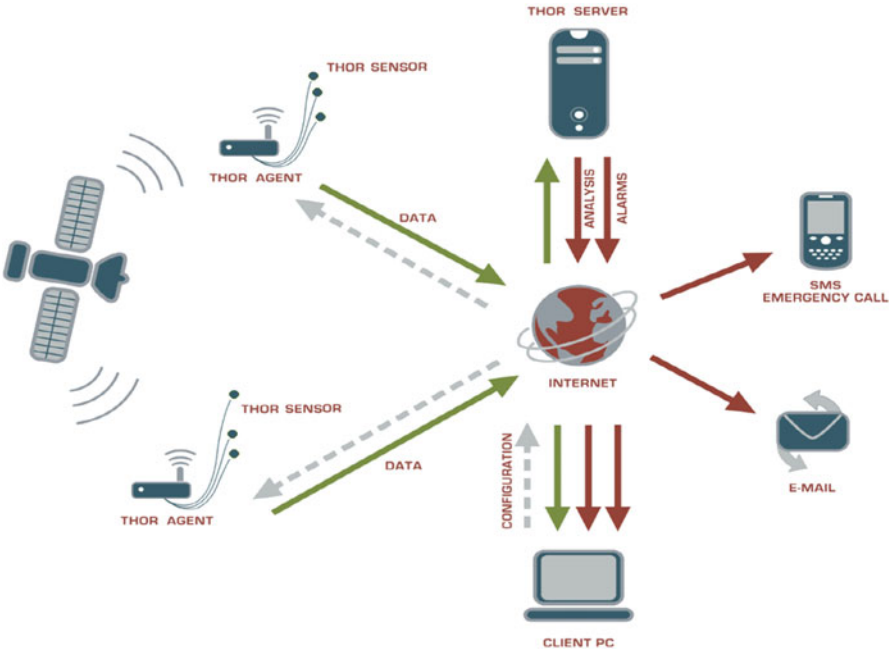

Fig. 5 "THOR" working scheme

Fig. 6 Some THOR components

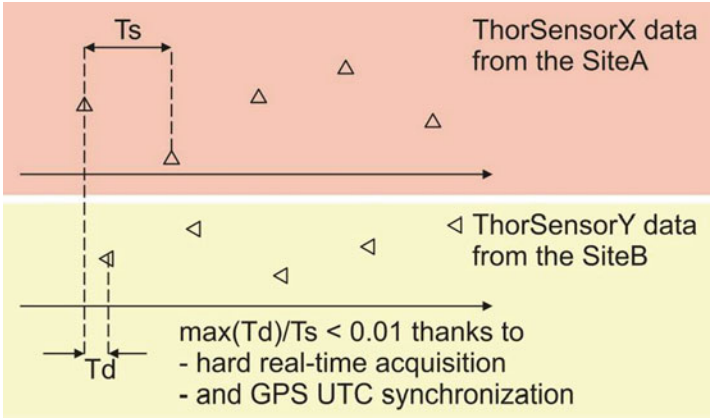

Fig. 7 GPS synchronization

monitor more sites. Some network components are shown in Fig. 6. The key point of this system is that – although each network works alone – all the data collected from different networks can be analyzed and correlated, because the system keeps hard real-time acquisition and GPS synchronization, see Fig. 7. In this way, *ThorServer* can execute intelligent algorithms for data processing and detection of critical conditions. If dangerous situations occur, *ThorServer* is able to send alarms via e-mail, GSM calls, and SMS. The entire system can be remotely accessed via web. Main features of THOR are:

- Rugged design for operation in hostile environments
- Modular design to ensure scalability of the sensor networks
- Hard real-time data acquisition with high-performance sensors
- Capability to manage more geographically distributed sensor networks

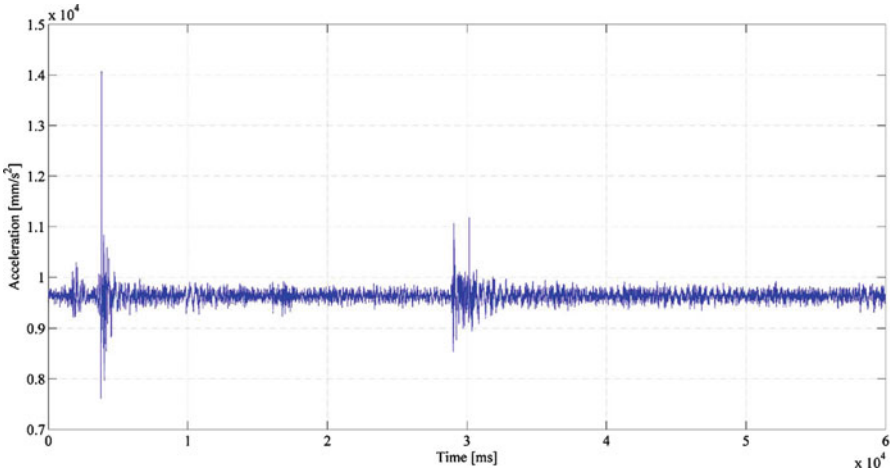

Fig. 8 Data streaming example samples analyzed online

- Capability to synchronize all the data from different networks via GPS UTC synchronization
- Capability to analyze and process real-time data from in one base time line
- Comprehensive tools for online/offline data management

These goals are typically achieved by means of expensive hardware and software technologies with lab-oriented design. On the contrary, THOR integrates the features above with reasonable costs and rugged hardware ready to use in real-world applications.

ThorSensors are force balance accelerometers that meet the following specifications: dynamic range 140 dB, bandwidth DC to 200 Hz, user selectable full-scale range up to ± 4 g, linearity $< 1{,}000$ $\mu g/g^2$, hysteresis $< 0.1\%$ of full scale, cross-axis sensitivity $< 1\%$ (including misalignment), operating temperature from -20 to 70°C, and weight 0.35 kg. *ThorAgent* specifications are real-time acquisition with GPS time stamping, data samples on all channels taken simultaneously within 1% of the sample interval, clock accuracy to UTC $\pm$ 50 ns, sample rate 1 kHz, GPRS/UMTS remote connection, Wi-Fi interface, rugged case (IP67), local storage 8 GB, and operating temperature from -20 to +60°C. An example of acquisition is reported in order to demonstrate how the developed structural monitoring network works (Fig. 8). *ThorServer* is able to show a user-defined period for each sensor acquisition via web. This allows speeding up the analysis by the user who can have a glance of a long data streaming and then can directly zoom on the interested part without any download and extra tool. Moreover, the web server implemented on *ThorServer* is also able to support the analysis with online elaboration, which results very comfortable during on-site operations where it is hard to have the office facilities.

5 Sensors Placement

Because of the existence of budgetary and practical constraints, civil engineered systems are typically monitored under natural dynamic loads (i.e., wind or traffic-induced loads) available at no cost. As historic infrastructures are concerned, output-only techniques are also preferred because of cheaper and faster test execution and minimum interference with the use and preservation of the structure. Based on these considerations, output-only measurements will be considered for this case study. This implies that the optimal sensor placement (OSP) problem is of importance for this application. It should be remarked that most of the applications regarding OSP techniques are in the field of aeronautic, aerospace, and mechanical engineering. On the contrary, few applications deal with civil engineered systems. In this field, the selection of the best DOFs to be monitored seems to be mostly based on engineering judgments only. However, numerical techniques for the OSP may provide a valuable support in order to design a sensor network for civil structural dynamic monitoring as well [2–4].

Therefore, a preliminary study was performed in order to look for the most significant DOFs to be monitored by using the available sensors and data acquisition system. To this end, the effective independence method [5] was used with the aim to look for sensor positions that maximize both the spatial independence and the signal strength of the target mode shapes by maximizing the determinant of the associated Fisher information matrix. Results for 8, 12, and 16 sensors are shown in Figs. 9, 10, and 11, respectively.

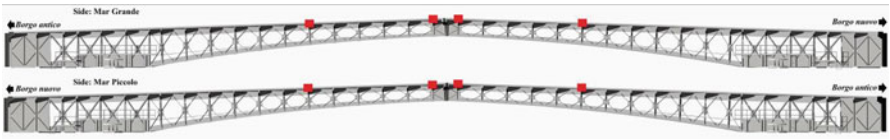

Fig. 9 Optimal sensors placement according to EFI method (8 sensors)

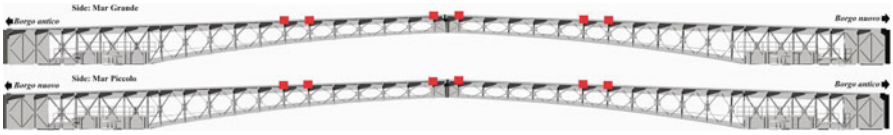

Fig. 10 Optimal sensors placement according to EFI method (12 sensors)

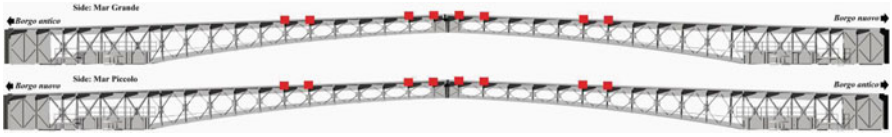

Fig. 11 Optimal sensors placement according to EFI method (16 sensors)

6 Conclusions

This chapter provided an overview about the most important steps that we are addressing for dynamic structural monitoring applications, with emphasis on the case study regarding the "St. Francesco da Paola" swing bridge in Taranto (Italy). The developed system for structural dynamic monitoring has been named as "THOR," and it fulfills the most important international standards and guidelines in this field. First, both CAD and FE model are briefly presented. Therefore, hardware specifications of the most important system components are listed. Finally, a preliminary study about the optimal sensors placement via effective independence method is presented. Results in this chapter will be useful for supporting further studies in order to design a reliable structural identification instrumentation for this bridge. Although this chapter deals with a particular bridge structure, considerations and results herein presented may provide a constructive framework for similar engineering applications.

Acknowledgements The support provided by Giuseppe Leonardo Cascella, Ph.D., and Davide Cascella, Ph.D. (Department of Electrotechnic and Electronic, Technical University of Bari) is appreciated. The assistance provided by Waveng srl (via Robert Schuman 14, 70126 Bari, Italy) is also acknowledged. Finally, we wish to thank Eng. Domenico Antonio Ricci, Eng. Erika Mastromarino, and Marco Denitto for their assistance.

References

1. ANSS (2005) Guideline for ANSS seismic monitoring of engineered civil systems. U.S. Dept. of the Interior, U.S. Geological Survey, Reston
2. Meo M, Zumpano G (2005) On the optimal sensor placement for a bridge structure. Eng Struct 27:1488–1497
3. Marano GC, Monti G, Quaranta G (2011) Comparison of different optimum criteria for sensor placement in lattice towers. Struct Des Tall Spec Build 20:1048–1056. doi:10.1002/tal.605
4. Monti G, Quaranta G, Marano GC (2010) Robustness against the noise in sensors network design for heritage structures: the case study of the Colosseum. In: 4th international workshop on Reliable Engineering Computation (REC2010), 3–5 March 2010, Singapore, pp 241–254
5. Kammer DC, Brillhart RD (1996) Optimal sensor placement for modal identification using system-realization methods. J Guid Control Dyn 19:729–731

Sensor Applications for Structural Diagnostics and Prognostics

Anindya Ghoshal

Abstract This chapter examines emerging sensor technologies in aerospace structural prognostics health management. A review of existing and emerging in situ sensor technologies for structural health monitoring for aerospace applications has been discussed in details. Details of the sensor selection criteria for the sensor technologies have been stated. For successful implementation of condition-based maintenance of aerospace vehicles, such emerging sensors are key technologies that would be required.

Keywords Condition-based structural health monitoring • In situ sensor technologies • Structural sensing • Diagnostics and prognostics

1 Introduction

Considerable advancement has been made in the sensor technology development for in situ sensor technologies for structural health diagnostics and prognostics [1]. This chapter is done with the objective of defining and selecting appropriate damage detection sensor(s) for direct monitoring of subcritical fatigue cracks in airframe primary structural elements. The sensor hardware should also provide reliable detection in representative airframe joints and/or attachments.

A. Ghoshal (✉)
ARL, Towson, MD, USA
e-mail: anindo_ghoshal@yahoo.com

S. Chakraborty and G. Bhattacharya (eds.), *Proceedings of the International Symposium on Engineering under Uncertainty: Safety Assessment and Management (ISEUSAM - 2012)*,
DOI 10.1007/978-81-322-0757-3_30,

2 Sensor Selection Criteria

The following parameters are used in sensor selection and sensor evaluation:

- Functionality of structural damage
  - Minimal detectable size of damage
  - Probability of detection (POD)
  - Sensitivity variation to size, orientation, and location of cracks
  - Boundary conditions, presence of joints, loads, and structural layers.
- Technology maturity
  - Commercial off-the-shelf with minimal customization
  - Demonstrated capability for aircraft applications or on similar products
- Sensor durability, reliability, and false alarm rate
  - Long-term stability, repeatability, and low drift (including bonding durability)
  - Sensitivity to environmental variation and normal workload
  - Temperature, vibration, and dynamic loading/static loading/structural deformation
  - Built-in smartness (through software) to reject noises or disturbance
- Structural embeddability
  - Be able to permanently mount on or bond to surface of structure for real-time monitoring or periodical scanning
  - Minimal intrusive to the structure being monitored—low profile and lightweight

3 Physical Sensor Review

This chapter further elaborates few promising damage-sensor technologies and associated vendors among a dozen of potential candidates.

Local crack monitoring sensors

- MWM-Array eddy current sensors: JENTEK Sensors, MA
- Active current potential drop sensors: Matelect Ltd, UK
- Comparative vacuum sensors: SMS Systems, Australia

Global damage sensors

- Piezoelectric acoustic sensors, Acellent, CA
- Fiber-optic sensors (fiber Bragg grating): Luna Innovations Inc, VA; Micron Optics, WA; and Insensys Inc
- Time-domain reflectometry, Material Sensing & Instrumentation, Inc., PA

- Magnetostrictive sensors: Southwest Research Institute, TX
- Carbon nanotube and graphene-based sensors

The six technologies that have high potential for the structural health monitoring application are evaluated in details as follows.

4 Eddy Current Sensors

4.1 Principle of Operation

An eddy current sensing system makes its measurement by measuring the electrical impedance change of the eddy current probe. The probe consists of coils that carry high-frequency current and generates an electromagnetic field. When the probe is placed near a metallic structure, the EM field penetrates the conductive surface and creates an eddy current within the structure. The intensity of the current or the electric impedance of the coil is a function of the material properties such as electric conductivity and permeability which is sensitive to the local structure damage or defects. This material property variation around the measurement point can then be translated into the structure defects or damage information via either a mathematic model or calibration against empirical database. The eddy current sensors can be made on thin polymer film with electric coil printed on it so they can be customizable in shapes, conformable to the surface of the structure, and cannot be easily mounted onto any complex surfaces permanently.

JENTEK Inc is today a major player in the technology of crack detection by eddy current sensing [2]. Its Meandering Winding Magnetometer Array (MWM-Array) system features high-resolution multiple-channel impedance measurement instrumentation and high-resolution imaging for crack detection. The sensing element configurations provide improved detection performance along with reduced calibration requirements and setup time.

4.2 MWM-Sensor Array

A MWM-Array system has a single period spatial mode drive with a linear array of sensing elements. The MWM-Array provides images of electrical conductivity and is suitable for crack detection with high special resolution. The MWM-Array sensors have a primary winding that is driven with a high-frequency current to produce a time-varying magnetic field with a spatial wavelength that is determined by the physical spacing between drive winding segments. The MWM-Arrays typically operate at frequencies from 10 kHz to 15 MHz. At these frequencies, the wavelength of traveling waves is long compared to the dimensions of the sensor, so the distance between the drive winding segments defines the shape of the applied

magnetic field. The magnetic field produced by the winding induces eddy currents in the material being tested. These eddy currents create their own magnetic fields that oppose the applied field. At low frequencies, these eddy currents are distributed well into the material under test; at high frequencies, these induced eddy currents are concentrated on a thin layer near the surface of the test specimen. A surface-breaking crack interferes with the flow of these eddy currents or the impedance of the winding. When MWM-Array is scanned across, an image of the impedance of the sensor array is generated which maps the structural or material abnormality of the test specimen.

Comparing with conventional eddy current sensor, MWM-Array features:

- Absolute sensing configurations (as opposed to differential sensing element designs) capable of inspecting regions likely to have cracks forming from micro-cracks into larger cracks.
- Calibration is performed on-site using either "air" or uniform reference parts without cracks, reducing calibration and training requirements.
- A crack signature is extracted off-site, only once, using either real cracks, EDM notch standards, or a simulated crack signature. This is an advantage because it eliminates dependence on crack standards and avoids potential errors encountered during calibration on such standards.

4.3 Technology and Product Maturity

JENTEK's MWM-Array sensor system has been under development and improvement since its inception in 1996 and has reached a certain level of product maturity. It currently offers a line of products typically off the shelf. The system is built around the following components: (1) a parallel architecture impedance instrument, (2) magnetic field (MWM) sensor arrays, and (3) Grid Station software environment, application modules, and tools. JENTEK is currently delivering two versions of imaging sensor array systems. The 39-channel system is a high-resolution imaging system with comprehensive imaging, decision support, and procedure development tools. The 7-channel system is designed for less image-intensive applications. These systems are supported by a wide selection of MWM-Array sensor configurations.

5 Active Current Potential Drop Sensors

5.1 Principle of Operation

Alternating current potential drop (ACPD) or direct current potential drop (DCPD) is an electrical resistance measurement technique for sizing surface-breaking

defects in metals [3]. ACPD works by inputting an alternating current into the electric conductive object. At the points (I, I′), a constant direct current is supplied. An increase in crack length produces an increase of the potential drop measured between the potential leads (V, V′). Presence of defect or crack in the material between these two points will result in a local resistance larger than that of its vicinity. By comparing potential differences with a reference value, calibrating against empirical database or FEM modeling results, crack depth and size can be estimated.

The reference measurement of potential drop is usually required to provide comparison and needs to be as close to the crack as possible. Because of the skin effect, ACPD system is more capable of measuring surface crack while DCPD can measure in-depth crack but with lower sensitivity. The crack size can be estimated as Crack Depth=$\Delta/2\ (V_c/V_r-1)$, where Δ is the probe separation and V_c is the crack voltage. V_r is the reference voltage. The techniques are available for both thick and thin structures. Custom-made ACPD sensing probe can be either hand-holding scan probe or wire spot-weld in structure. Similar to MWM-Array sensors, these sensing wires need to be permanently mounted near the cracks or where cracks would potentially develop for detection. This means it is only a local crack detection system.

5.2 Technology and Product Maturity

Among a few vendors, Matelect Ltd of UK has been selected for investigation of product availability and specification. Matelect has a line of commercial off-the-shelf ACPD or DCPD products. Their most popular crack detection is CGM-7 microprocessor-based crack growth monitor system with operating frequency ranging from 0.3 to 100 kHz and current up to 2 A. The system is able to detect cracks of 0.02–10 mil on lab specimen and 40 mil on aircraft components. For permanent crack monitoring, the potential measuring probes are usually spot-weld into structure and probe can withstand 600°C temperature. The products have been used for Rolls-Royce engine turbine disk dovetail crack inspection, and it is recently being tested on CRJ aircraft structure for crack monitoring. The vendor claimed POD is 85% on 0.004 crack, sensitive to crack orientation.

The summary of pros and cons for use of ACPD/DCPD is as follows:

- High sensitivity to incipient crack and has long history of industrial application.
- Detestability is sensitive to the orientation of crack.
- Electrode sensor needs to be spot-weld into structure for permanent monitoring and is less suitable for retrofit application.
- Need complex in field calibration.
- Vulnerable to electromagnetic interference.

6 Comparative Vacuum Sensors

6.1 Principle of Operation

Comparative vacuum monitoring (CVM) offers a novel method for in situ, real-time monitoring of structural crack initiation and propagation [4]. CVM makes use of the principle that a steady-state vacuum, maintained within a small volume, is extremely sensitive to any leakage of air. It measures the differential pressure between fine galleries containing a low vacuum alternating with galleries at atmosphere in a simple manifold. The manifold is directly mounted on structure surface being monitored for crack. If no flaw is present, the vacuum in galleries will remain at a stable level. If a crack develops and creates a passage between vacuum and atmosphere galleries, air will flow through the passage created from the atmosphere to the vacuum galleries. Sensors may either take the form of self-adhesive polymer "pads" or may form part of the component. A transducer measures the fluid flow or pressure difference between the galleries.

CVM has been developed primarily as a tool to detect crack initiation. Once a sensor has been installed, a base line reading is made. Generally, the differential pressure between the reference vacuum and the sensor will be approximately 0 Pa. However, if there is a known existing flaw or crack beneath the sensor, or the permeability of the test material is high, the fluid flow meter will measure a nonzero base value. If this nonzero value is constant, it will not affect the ability of the CVM system to detect an increase in total crack length.

When a vacuum gallery is breached by a crack, molecules of air will begin to flow through the path created by the crack. Once the system has reached an equilibrium flow rate, the volume of air passing through the crack is equal to the volume of air passing through the flowmeter, and the measured differential pressure will become constant at a higher value. Therefore, the system is very sensitive to any changes in the total crack size. The CVM method is unable to differentiate between a single large crack and several smaller flaws, but is sensitive to any increase in the total crack length. The sensitivity of the sensor is determined by the gallery wall thickness.

6.2 Technology and Product Maturity

Structural Monitoring System Inc of Australia has developed this sensor technology. A variety of sensor types have been developed. These include self-adhesive elastomer sensors for the measurement of surface crack initiation or propagation and sensors integral within structure, for example, permeable fiber within a composite. The sensors are produced from a variety of materials. The accuracy of the crack propagation sensor is governed by the accuracy of the galleries, measured optically at better than 10 mm. Once the sensor has been installed, the leading edge of the first gallery is

determined optically, and from this initial measure, all subsequent gallery positions are determined.

CVM sensors have been applied to a variety of aerospace structures for crack detection. Sandia National Lab, in conjunction with Boeing, Northwest Airlines, Delta Airlines, Structural Monitoring Systems, the University of Arizona, and the FAA, has conducted validation testing on the CVM system in an effort to adopt comparative vacuum monitoring as a standard NDI practice. The system has been tested by on Boeing 737, DC 9, C130 aircrafts, and Blackhawk helicopter by Australian air force. According to the SMS Inc., the sensor pad adhesive can hold the vacuum in the galleries for as long as 18 month. Ninety percent probability of detection with 0.020–0.025″ crack on 2024 aluminum structure has been reported.

The summary of pros and cons for use of CVM is as follows:

- High sensitivity to 0.020 mils.
- The system is lightweight, inert (safe), and less vulnerable to EMI than any electric-based system.
- Elastomeric sensor is low cost and conformable to any curved surfaces and can be easily integrated to complex structural surface.
- Easy to operate and calibrate.
- The system is capable of detecting surface break cracks only.

Overall, CVM is a good candidate technology for local crack detection

7 Networked Piezoelectric Sensor

Piezoelectric (PZT) transducer can be used to monitor structures for internal flaws when it is embedded in or surface mounted to structures. PZT transducer can act as both transmitters and sensors due to its direct and reverse piezoelectric effect. As transmitters, piezoelectric sensors generate elastic waves in the surrounding material driven by alternating electric field. As acoustic sensor, they receive elastic waves and transform them into electric signals. It is conceivable to imagine arrays of active sensors, in which each element would take, in turn, the role of transmitter and acoustic sensor and thus scan large structural areas with high-frequency acoustic waves. As global damage sensing, two PZT sensor network-based approaches are commonly used for structural health monitoring:

- Self-electromechanical (E/M) impedance method for flaw detection in local area using effect of structural damage on EM impedance spectrum
- Lamb wave propagation method for large area of detection using acoustic wave propagation and interception by presence of structural damage on the acoustic path

In the self-E/M impedance approach, pattern recognition methods are used to compare frequency domain impedance signatures and to identify damage presence and progression from the change in these signatures. In the cross impedance

approach, the acousto-ultrasonic methods identifying changes in transmission velocity, phase, and additional reflections generated from the damage site are used. Both approaches can benefit from the use of artificial intelligence neural network algorithms that can extract damage features based on a learning process.

The Acellent Technologies of Mountain View, California, offers a PZT acoustic-based structural health monitoring system commercially off-the-shelf [5]. The system comprises of SMART Layer sensors, SMART Suitcase, and ACESS Software®. This structural health monitoring solution is capable of monitoring both metallic and composite structures. The SMART Layer consists of multiple piezoelectric sensing elements with wires lithographically imprinted on the Kapton film. These sensors operate based upon the principles of piezoelectricity and its converse effects. The sensor suite uses both pulse echo and transmission mode for operability, making it capable for deployment as distributed sensor network for the global damage monitoring sensing system (GDMS). The Smart Suitcase includes the portable diagnostic hardware and customized form factor. The hardware is capable of monitoring up to 64 sensor channels simultaneously.

Under active interrogation mode, the system has the capability of generating a 50–500-kHz input excitation with a maximum of 50 V peak-to-peak amplitude in the form a single-cycle or multiple-cycle pulse through one of the transducer. The adjacent sensors are used to detect the transmitted signals generated by the traveling stress waves. This is then repeated sequentially to cover map the whole structure which is under the sensor coverage. The signals are then compared with historical data. Both the transmitted signals and the pulse echo signals are used for analysis. Through transmission, the system bandwidth is 10 kHz to 1 MHz and the pulse echo system bandwidth mode is 10 kHz to 5 MHz.

Acellent is currently flight-testing its system by deploying the sensor on an F-16 test aircraft landing gear door to monitor the edge crack growth. The system had been demonstrated to detect 0.531″ crack in 500 cycles in metallic components. For a flawed composite doubler, the Sandia National Labs tested the system's capability to monitor crack length greater than 1 in. Acellent has done considerable testing on coupons and components under laboratory conditions. This system needs calibration of crack size. Herein, it should be noted that crack size determination has not yet been proven along with its robustness. Currently under a separate program, Acellent is preparing data for flight certification (salt fog, moisture, etc.).

As this chapter is primarily on its global sensing capability, this evaluation of the Acellent SHM system focuses on its capability of crack locating and sizing. The conclusions were:

- The hardware system is basically a multiple-channel high-speed data acquisition with a set of function generating capability typically used in acoustic wave-based flaw detection.
- Passive and active mode hardware systems are separate systems as they require different DAQ boards with different sampling frequencies.
- Its standard software, "Access," comes with a diagnostic imaging plug-in that enables raw acoustic data imaging and interpreting, but not damage locating.

With a network of sensors and current version of Access software, the system is able to indicate the structural changes in between the sensors due to damage.
- To achieve the damage localization, new algorithm is to be developed and the Access software must be customized and field calibrated with sufficient number of tests on a particular specimen.
- The system is currently unable to perform detection on a 3D geometry without further customization.

8 Fiber-Optic Sensors

There are two types of FO sensors available in the market: fiber Bragg sensors and Fabry-Perot interferometry sensors (extrinsic and intrinsic) [6, 7]. The following section discusses them in some details.

8.1 Fiber Bragg Grating

Fiber-optic Bragg gratings utilize a photo- or heat-induced periodicity in the fiber core refractive index to create a sensor whose reflected or transmitted wavelength is a function of this periodicity. The biggest advantage of fiber Bragg grating sensors (FBG) is that they can be easily multiplexed to enable multiple measurements along a single fiber. One approach for multiplexing Bragg gratings is to place gratings of different wavelength in a single fiber and utilize wavelength division multiplexing (WDM). However, the limited bandwidth of the source, as well as that supported by the fiber, and the range over which the physical parameter of interest is being measured provide practical limitations on the number of gratings that can be multiplexed in a single fiber with WDM approaches. The system, based on the principle of optical frequency domain reflectometry (OFDR), enables the interrogation of hundreds or thousands of Bragg gratings in a single fiber. OFDR essentially eliminates the bandwidth limitations imposed by the WDM technique as all of the gratings are of nominally the same wavelength. Very low reflectivity gratings are utilized, which allow reflections from large numbers of gratings to be recorded and analyzed. By tracking wavelength changes in individual gratings, one is able to measure mechanical- or thermal-induced strain in the grating. United Technologies Research Center is the original developer of the fiber Bragg sensors for strain measurements. The recent developments in multi-axis FBG strain sensor technology offer a distinct advantage in creating a series of fiber sensor types that are extremely compatible with one another, allowing the usage of similar readout equipment for a variety of applications. It is possible to configure a fiber grating system so that each fiber grating is sensitive to different frequency bands. This could be done in an array that measures multi-axis strain and other key parameters. This

sensor array/neural network is nominally intended to predict and/or last the lifetime of the structure or component regarding mechanical damage tolerance. "Pre-assembly"of the fiber array could be affected in appliqué coatings. In all these potential arrangements, the simplest attachment methods will be developed capable for re-hooking the fiber array to the readout equipment. FBGs have minimal risk of electromagnetic interference and high bandwidth/sensitivity and can noninvasively inquire (passively or actively) into the health of a structure. The disadvantages of the FBG sensors are the uncertainties in the long-term durability of the sensors, sensor bonding to the airframe structure, and the fragility of the quartz elements, especially when the fiber is turned around. Several organizations, for example, NASA Langley and companies (e.g., Blue Road Research, Luna Innovations Inc., Micron Optics Inc., New Focus Inc.), are in the development of FBG demodulators for potential structural health monitoring applications, and the sensors are mainly developed. The main fiber-optic sensor manufacturers are Canadian-based companies like LXSix and FISO technologies. The normal FBG sensors are 150–250 μm in diameter and approximately 5 mm long.

8.2 Fabry-Perot Interferometry

Fiber-optic sensors can be separated into two classes for discrete strain and temperature measurement: cavity-based designs and grating-based designs. Cavity-based designs utilize an interferometric cavity in the fiber to create the sensor. Examples include the extrinsic Fabry-Perot interferometer (EFPI), the intrinsic or fiber Fabry-Perot interferometer (IFPI or FFPI), and all other etalon-type devices. Although such sensor designs have been utilized in a wide variety of applications such as in high temperature and EMI environments, they do not allow for multiplexing capability in a single fiber and thus may be limited for applications requiring large number of sensors. Originally developed by a team of scientists at Virginia Tech, this has seen widespread applications into different areas. To measure both strain and temperature, a broadband light source is transmitted to the cleaved end of a single-mode fiber. To perform the strain measurements, upon reaching the end of the fiber, the light is partially reflected while the remaining light travels past the end of the fiber and is reflected off a secondary reflector. The reflectors (also fibers) are aligned with the main fiber in a capillary tube and attached to a substrate. The two reflected light signals interfere with each other forming a fringe pattern. As the structural substrate strains, the distance between the two fiber end-faces vary, causing the fringe pattern to change. Using a spectrometer, the changing gap is measured to obtain the strain. The sensor is less prone to failure because the fiber itself is not being strained by the substrate. The temperature sensor has a small, single-crystal chip on the end of the fiber. The two faces of the chip are reflectors. Precise temperature can be obtained by measuring the temperature-dependent optical path length through the chip. Different types of fibers are used for making

the FO sensors. For temperature less than 700°C, silica fibers are used for FO sensor, and for temperature greater than 900°C, applications currently single-crystal sapphire fibers are being investigated. New fiber-optic sensor materials being developed in this area include photonic crystal fibers and wholly fibers.

8.3 Technology and Products Maturity

Several vendors of fiber-optic sensing have been evaluated for global damage and load sensing. Luna Innovations of Blacksburg, VA, has two types of commercially available solution for fiber-optic sensing—(1) Distributed Sensing System and (2) FiberPro2 (an older version is also marketed known as FiberScan). The Distributed Sensing System is able to monitor several (10,000 s) FBG sensor nodes on a single fiber, which gives the ability to measure strain at several locations on a single fiber. However, the laser scan rate is limited to 10 Hz limiting its utility for application at 8P load ranges (40 Hz). For the current rotorcraft airframe application, this system is not useful for either damage monitoring or load monitoring. FiberPro2 is the newer version of FiberScan which can monitor both FBG and Fabry-Perot Interferometer sensor. It can be connected to "MU8" which is a multiplexer, allowing the ability to individually monitor eight single sensors on eight different fibers (channels) at the same time. The demodulator can monitor both fiber Bragg sensor and Fabry-Perot Interferometry sensor. The single FPI sensors can be used to monitor strain at a higher loading frequency levels. This is suitable if we want to monitor single optic fiber sensor mounted on separate fibers at the same time at different locations. However, this is limited to eight channels (i.e., eight sensors mounted on eight fibers), which makes application of FiberPro2 also limited with regards to multisensor array on a single fiber. One of the issues that is significant is that vibration in connecting fiber can cause drifting in the sensor readings. This is significant in terms of accuracy in the measurement during flight and the airframe undergoing variable load history. The system should be able to zero out the effects of sensor drift.

Alternatives to Luna's systems are Insensys and Micron *Optics. Both of them have systems which can monitor dynamic loads over 40 Hz. Invensys did demonstrate the capability of monitoring continuous dynamic loading on a cantilever* I-beam at the AIAA SDM Conference held at Newport, April 2006. A significant innovation was the designed brackets used for mounting the fiber-optic sensors onto the airframe. Attaching the fiber-optic sensors to airframes and long-term durability of such mounts are significant challenges. Also the results from a successful observation of a bird impact strike using the FO system on a winglet spar were presented. Unlike an electric-based sensing system, FO can actually detect a lightning strike because of its electromagnetic immunity. The team is talking to Insensys, which is based in United Kingdom for a follow-up demo in Connecticut.

Micron Optics developed several optical sensing interrogators which are wavelength division multiplexing (WDM) based. The WDM interrogators work with

both FPI and fiber Bragg grating sensors. The si425-500 combines a PC with a high power, low-noise laser source. It is a stand-alone system, which can provide optical power and rapid measurement of 512 FBG sensors mounted on 4 separate optical fibers (128 sensors on a single fiber). The sensors can be placed as close as 1 cm apart. The system is expandable to 8–12 channels and customizable. The scan rate frequency is 250 Hz, and the wavelength is 1,520–1,570 nm. The sm130 can provide power and rapid measurements of several hundred sensors mounted on four separate optical fibers up to a scan rate of 1-kHz range. This unit is more applicable for rugged and harsh environment deployment.

The fiber-optic Bragg sensors that would be tested during sensor characterization part are going to be obtained from LXSix or FISO companies, which are main FO suppliers of Micron Optics. Clearly for the applications as load monitoring and damage monitoring sensors, the fiber Bragg sensors are more applicable than FPI sensors; as for FBG, we have the capability of monitoring several points for strain using a single fiber, whereas the FPI is a single discrete sensor at a single point location. Because of the limitation of the scan rate to 1 kHz, it is envisioned that the FBG sensors are more applicable for load (strain) monitoring at several locations on the component rather than using them as damage monitoring sensors.

8.4 Time-Domain Reflectometry

Time-domain reflectometry (TDR) is a method of sending a fast pulse down a controlled-impedance transmission line and detecting reflections returning from impedance and geometric discontinuities along the line. Time scales are fast, so reflections occurring at different positions in the line are separated by time-of-flight, forming a "closed-circuit radar."

TDR can potentially be used as structural global damage sensing due to its distributed nature. TDR has gained popularity in recent years in infrastructure applications. The transmission line is embedded in a bridge or highway structure, such that a flaw in the surrounding structure causes a mechanical distortion in the line, which produces an impedance discontinuity, which is located by time-of-flight.

It has been investigated for composite parts defect detection after instrumentation high spatial location resolution becomes available. TDR structural health monitoring probes the structural health of a composite part by propagating a fast electrical pulse along a distributed linear sensor which has been fabricated directly in the laminate. The sensor is formed from the native graphite fibers already used in composite manufacture and constitutes zero defects. Fibers are patterned into a microwave waveguide geometry, or transmission line, and interrogated by a rapid pulse as shown below. Structural faults along the line cause distortions in waveguide geometry, producing reflected pulses similar to radar. Cracking, delamination, disbonds, moisture penetration, marcelling, and strain can be detected by propagation delay for sensor lengths up to several meters. These features make

TDR appropriate for the permanently embedded and distributed monitoring of the structural characteristics variation.

Material Sensing & Instrumentation, Inc (MSI) of Lancaster, PA [8, 9], is one of the major players specializing in TDR concrete and composite cure monitoring. It also performs R&D in the area of composite debond or delamination detection. TDR provides a new approach to cure monitoring of advanced polymer composites fabrication process. Using a high-speed pulse and inexpensive microwave sensor, TDR cure monitoring provides an alternative between high-frequency fiber-optic methods and low-frequency dielectric methods, combining optical-style precision and miniaturization with electrode-based simplicity and robustness.

MSI is a small company which has successfully executed several government SBIRs. Its primary technical expertise lies on the composite curing monitoring. The company typically does not/is not able to provide COTS equipment to customers. The structural health monitoring using TDR, especially metallic structures, is still under preliminary development. Due to the non-dielectric nature of metallic structure, further development of this technology is currently necessary.

9 Magnetostrictive Sensors

This sensing approach is based on a novel thin-film magnetostrictive sensor material that has recently been developed by Southwest Research Institute (SwRI) for turbine engine applications [10, 11]. This thin-film is 4 μm thick and achieves high activation efficiency, as well as temperature stability, using alternate crystalline and amorphous nano-layers. Defect detection is accomplished by activating the magnetostrictive thin-film causing emission of ultrasonic guided waves into the component that are subsequently backscattered and detected by the same sensor in "pitch-catch" fashion mostly done in a pulse echo mode. Energy harvesting and radio frequency (RF) communication enable multiple, individually addressable sensors to detect and monitor damage in structural airframe components. This sensing system provides a low mass sensing system, which does not affect the dynamic response of the component and high-efficiency sensor in power density requirements for electromechanical conversion. The robustness, durability, and the accuracy level of the magnetostrictive sensors for the rotorcraft airframe component structure need to be reviewed under rotorcraft loading environment. The thin-film magnetostrictive sensor is still at R&D stage and is not commercially available yet for the time being. The currently available sensor system is handheld scanning type. The sensor-related hardware is bulky and not suited for in situ crack monitoring. However, under the DARPA SIPS program, SwRI have made considerable technological improvements in terms of the sensor hardware readiness levels for deployment. Currently, a small company located in Colorado is trying to commercialize the magnetostrictive sensor technology.

10 Conclusions

The critical conclusion drawn out of this study is that for the time being, although there are some vendors/technologies of the structural damage sensing system commercially available on the market, there are some technology gaps required to be covered to reach a sufficient maturity to be able to claim commercial off-the-shelf (COTS). Substantial customization to both the "standard hardware and software" has to be made for each particular application. The damage detection algorithms/software is still semiempirical and lacking of generality, and the sensor system will need in situ calibration if the structure being monitored is slightly different in detection ability.

References

1. Fu-Kuo Chang (ed) (2001) Structural health monitoring—the demands and challenges. In: Proceedings of the 3rd international workshop on structural health monitoring, held at Stanford University, 12–14 Sept 2001. CRC Press, Boca Raton
2. Zilberstein V, Schlicker D, Walrath K, Weiss V, Goldfine N (2001) MWM eddy current sensors for monitoring crack initiation and growth during fatigue tests and in service. Int J Fatigue 23(Suppl 1):477–485
3. Merah N (2003) Detecting and measuring flaws using electric potential techniques. J Qual Maint Eng 9(2):160–175. ISSN: 1355–2511
4. Wheatley G (2003) Comparative vacuum monitoring as an alternate means of compliance. In: Structural health monitoring 2003: from diagnostics & prognostics to structural health management: proceedings of the 4th international workshop on structural health monitoring, Stanford University, Stanford, CA, 15–17 Sept 2003, pp 1358–1365
5. Beard S, Qing PX, Hamilton M, Zhang DC (2004) Multifunctional software suite for structural health monitoring using SMART technology. In: Proceedings of the 2nd European workshop on structural health monitoring, Germany, July 2004
6. Silva JMA, Devezas TC, Silva AP, Ferreira JAM (2005) Mechanical characterization of composites with embedded optical fibres. J Compos Mater 39(14):1261–1281
7. Stewart A, Carman G, Richards L (2005) Health monitoring technique for composite materials utilizing embedded thermal fibre optic sensors. J Compos Mater 39(3):199–213
8. Kwun H, Light GM, Kim SY, Spinks RL (2002) Magnetostrictive sensor for active health monitoring in structures. In: Proceedings of SPIE, the International Society for Optical Engineering SPIE, vol 4702, pp 282–288
9. Kwun H, Kim SY, Light GM (2001) Long-range guided wave inspection of structures using the magnetostrictive sensor. J Korean Soc NDT 21:383–390
10. Hager NE III, Domszy RC (2001) Time-domain-reflectometry cure monitoring. In: SAMPE proceedings, Long Beach, CA, 6–10 May 2001, pp 2252–2264
11. Hager NE III, Domszy RC (1998) Time-domain-reflectometry cure monitoring. In: American Helicopter Society—affordable composite structures proceedings, Oct 1998

Application of Artificial Neural Network (ANN) Technique to Reduce Uncertainty on Corrosion Assessment of Rebars in Concrete by NDT Method

M. Bal and A.K. Chakraborty

Abstract The basic objective of this study is to assess corrosion behavior of steel bars in concrete members by nondestructive method of testing. Corrosion possibility is assessed by half-cell potential method (using CANIN) while resistivity meter (RESI) is used to estimate risk of corrosion of rebars in concrete members. Interestingly, higher half-cell potential indicates more possibility of corrosion, but higher value of resistivity indicates lower probability of corrosion. An extensive research program was undertaken in order to assess risk of corrosion using type 1 (Fe415:TATA-TISCON), type 2 (Fe500:TISCON-CRS), type 3 (Grade Fe415: ELEGANT steel), type 4 (Fe415:VIZAG steel), and type 5 (Fe500:SRMB steel) TMT steel bars of 16 mm diameter with M20, M40, and M60 grade concrete samples, prepared with OPC exposed both in *AIR* and *NaCl* for a period of 900 days. Taking only average values of experimental data, initially huge uncertainties were found. Secondly, after applying standard statistical method, uncertainties were slightly reduced. Third analysis was then taken up by modifying standard statistical process; satisfactory results were still not obtained. Then, fourth analysis was carried out with optimum values to minimize the uncertainties. Three-dimensional graphs for each case were plotted using MATLAB, an ANN-based software. More appropriate ANN-based software is required for better correlation.

Keywords Corrosion of rebar in concrete • Half-cell potential • Concrete resistivity • Artificial neural network

M. Bal • A.K. Chakraborty (✉)
Department of Civil Engineering, Bengal Engineering and Science University, Shibpur, Howrah 711 103, India
e-mail: manabendra_ball@yahoo.com; arunchakraborty@mailcity.com

S. Chakraborty and G. Bhattacharya (eds.), *Proceedings of the International Symposium on Engineering under Uncertainty: Safety Assessment and Management (ISEUSAM - 2012)*,
DOI 10.1007/978-81-322-0757-3_31,

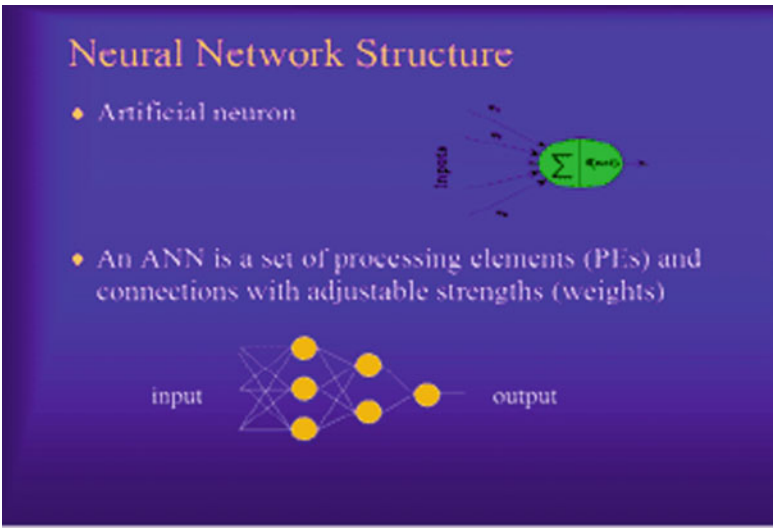

Fig. 1 Typical structure of neural network

1 Introduction

Neural network is a powerful data modeling tool, which is able to capture and represent complex input/output relationships. The motivation for the development of neural network technology stemmed from the desire to develop an artificial system that could perform "intelligent" tasks similar to those performed by our human brain. Neural networks resemble the human brain in the following two ways (Fig. 1):

1. A neural network acquires knowledge through learning.
2. A neural network's knowledge is stored within interneuron connection strengths known as synaptic weights.

True power and advantage of neural networks lies in their ability to represent both linear and nonlinear relationships and in their ability to learn these relationships directly from the data being modeled. A graphical representation of an MLP is shown below (Fig. 2).

Inputs are fed into input layer and get multiplied by interconnection weights as they are passed from the input layer to first hidden layer. Within the first hidden layer, they get summed and then processed by a nonlinear function (usually the hyperbolic tangent). As the processed data leaves the first hidden layer, again it gets multiplied by interconnection weights and then summed and processed by the second hidden layer. Finally, the data is multiplied by interconnection weights and then processed one last time within the output layer to produce the neural network output. MLP and many other neural networks learn using an algorithm called back propagation. With back propagation, the input data is repeatedly presented to the neural network. With each presentation, the output of the neural

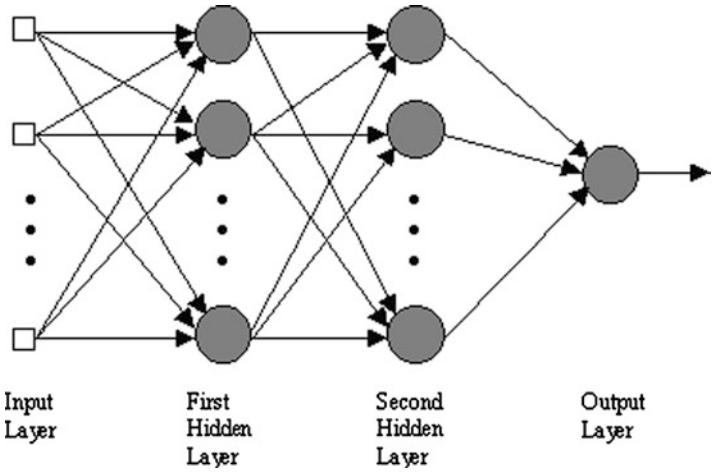

Fig. 2 Graphical representation of MLP

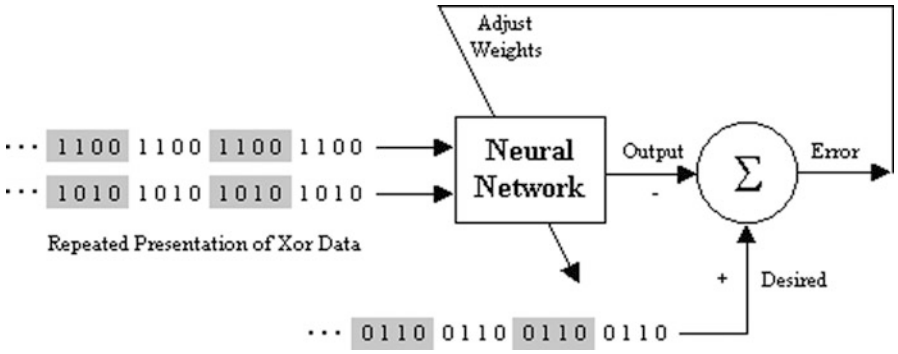

Fig. 3 Schematic diagram of "training" process

network is compared to the desired output and an error is computed. This error is then fed back (back propagated) to the neural network and used to adjust the weights such that the error decreases with each iteration and the neural model gets closer and closer to producing the desired output. This process is known as "training" (Fig. 3).

Demonstration of neural network learning is to model the exclusive-or (Xor) data. The Xor data is repeatedly presented to the neural network. With each presentation, the error between the network output and the desired output is computed and fed back to the neural network. The neural network uses this error to adjust its weights such that the error will be decreased. This sequence of events is usually repeated until an acceptable error has been reached or until the network no longer appears to be learning.

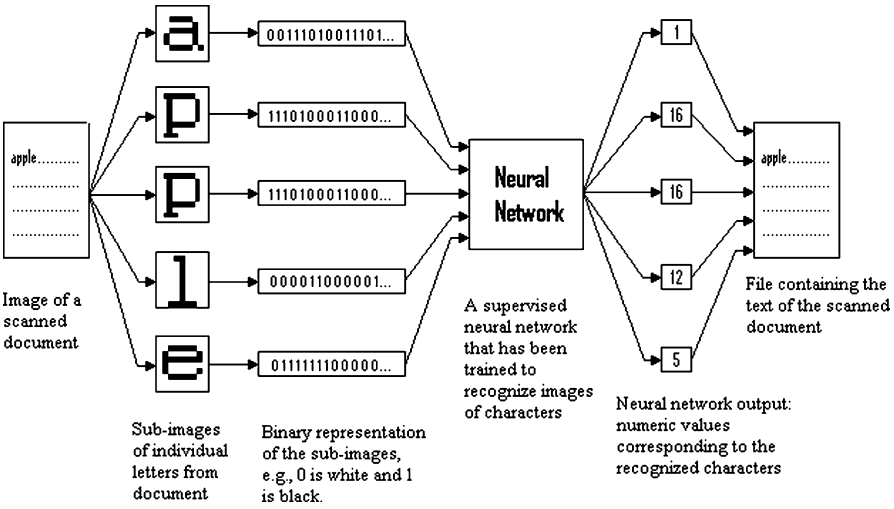

Fig. 4 Demonstration of optical character recognition (OCR)

A good way to introduce the topic is to take a look at a typical application of neural networks. Many of today's document scanners for the PC come with software that performs a task known as optical character recognition (OCR). OCR software allows you to scan a printed document and then convert the scanned image into to an electronic text format such as a Word document, enabling you to manipulate the text. In order to perform this conversion, the software must analyze each group of pixels (0 and 1s) that form a letter and produce a value that corresponds to that letter. Some of the OCR software on the market uses a neural network as the classification engine.

Demonstration of a neural network used within an optical character recognition (OCR) application is shown in Fig. 4. Original document is scanned into a computer and saved as an image. OCR software breaks image into sub-images, each containing a single character. Sub-images are then translated from an image format into a binary format, where each 0 and 1 represents an individual pixel of the sub-image. Binary data is then fed into a neural network that has been trained to make association between the character image data and a numeric value that corresponds to the character (Fig. 4).

Of course character recognition is not the only problem that neural networks can solve. Neural networks have been successfully applied to broad spectrum of data-intensive applications, such as:

- *Machine diagnostics* – Detect when a machine has failed so that the system can automatically shut down the machine when this occurs.
- *Portfolio management* – Allocate the assets in a portfolio in a way that maximizes return and minimizes risk.
- *Target recognition* – Military application which uses video and/or infrared image data to determine if an enemy target is present.

- *Medical diagnosis* – Assisting doctors with their diagnosis by analyzing the reported symptoms and/or image data such as MRIs or X-rays.
- *Engineering and technological events* – To create a network model for developing relationship among different properties of engineering materials, which creates physical or mathematical modeling between input and output data/information.
- *Credit rating* – Automatically assigning a company's or individual's credit rating based on their financial condition.
- *Targeted marketing* – Finding the set of demographics which have the highest response rate for a particular marketing campaign.
- *Voice recognition* – Transcribing spoken words into ASCII text.
- *Financial forecasting* – Using the historical data of a security to predict the future movement of that security.
- *Quality control* – Attaching a camera or sensor to the end of a production process to automatically inspect for defects.
- *Intelligent searching* – An internet search engine that provides the most relevant content and banner ads based on the users' past behavior.
- *Fraud detection* – Detect fraudulent credit card transactions and automatically decline the charge.

NeuroSolutions is one of the leading edge neural network development software that combines a modular, icon-based network design interface with an implementation of advanced learning procedures, such as Levenberg-Marquardt and back-propagation through time. Some other notable features include C++ source code generation, customized components through DLLs, neuro-fuzzy architectures, and programmatic control from Visual Basic using OLE Automation. This can be used through softwares that are conveniently available in present market. It can be tried for building and training of a neural network with available data.

2 Possibility for Application of Artificial Neural Network Technique

Like traditional use in biological events, artificial neural networks are also presently used in solving different problems of civil engineering in order to achieve particular targeted tasks by developing some mathematical models in the field of several engineering and technological events. *Artificial neural network (ANN)* provides its inbuilt properties, which facilitates to build up interconnections between artificial neurons, which may be considered as "nodal points" of a structure in civil engineering analysis. Artificial neural network (ANN) is one of the very important tools toward processing a large number of data collected from site. Practically ANN can accept both linear and nonlinear engineering, and statistical back-propagation learning algorithm is presented. For example, problem involves pattern recognition;

otherwise, it could be difficult to code in a conventional program. TMT steel bars are normally used as reinforcement in cement concrete as per design requirements. Besides various advantages, about 80% of damages occur in RCC members due to the attack of corrosion that takes place in steel bars embedded into it. RCC member as a whole loses its strength gradually and fails to survive its designed lifetime. It is similar to that of cancer infection in a body. Sometimes the effect of corrosion becomes so dangerous that a structure finally reaches to its final state of collapse quickly. It is therefore very important to understand the behavior of TMT steel bars especially in terms of susceptibility to attack of corrosion.

Factors responsible for attack of corrosion in RCC member are:

1. Thickness of cover on steel reinforcement bars in concrete
2. Type of cement used in concrete like OPC (ordinary Portland cement), blended cements like PPC (Portland pozzolana cement) and PSC (Portland slag cement), etc.
3. Grade of concrete mix like M20, M40, and M60
4. Grade of steel used like Fe415, Fe500, and CRS (corrosion resistant steel)
5. Diameter of steel bars used like 8.0, 16.0, and 25.0 mm Dia
6. Permeability of concrete
7. Electrical resistively of concrete
8. Type of exposure condition such as in NaCl and in natural air
9. Degree of carbonation.
10. Chloride ingress

Following principles of ANN, different softwares that are recently developed and available in the market can be used in computer. In this exercise, one of such computer software, *MATLAB*, having version **7.6.0.324 (R2008a),** was used as a tool to express results graphically.

Vulnerability of seismically deficient older buildings, risk parameters, significant threat to life safety, and its survivability can be assessed before by ANN [1]. Chloride-induced corrosion of steel reinforcement bars embedded in reinforced cement concrete can be enumerated before by applying neural network techniques [2]. Ductility performance of hybrid fiber reinforced concrete can be predicted by applying neural network techniques [3]. Prediction of density and compressive strength of concrete cement paste containing silica fume can be predicted using artificial neural networks [4]. Application of neural network in predicting damage of concrete structures caused by chlorides [5]. Prediction of stress-strain relationship for reinforced concrete sections by implementing neural network technique [6]. Strengthening of corrosion-damaged reinforced concrete beams can be done with glass fiber reinforced polymer laminates [7]. Corrosion mitigation in mature reinforced concrete using nanoscale pozzolan deposition [8]. The cathodic protection of reinforcing steel bars using platinized-type materials [9]. Corrosion protection of steel rebar in concrete using migrating corrosion inhibitors MCI 2021 and 2022 [10].

3 Data Processing on Experimental Results and Correlation

Data obtained from samples are at *stressed* condition in *atmospheric AIR* and *in NaCl* solution,[*NaCl at 5%* by weight of water] *for 900 days,* respectively. Readings are as follows:

1. *Readings* of *half-cell potential values* of concrete samples in *mVolt*
2. *Readings* of electrical *resistivity* of concrete samples in *kΩ–cm*
3. *Readings* of *ultrasonic pulse velocity* of concrete samples in *km/s*
4. *Readings* of *rebound hammer* with the help of *Schmidt hammer* on concrete samples in *numbers* to obtain *strength of concrete* to determine *loss of strength of concrete* in *%*
5. *Readings* of *clear cover* in *mm of concrete* samples

4 Processing of Supplied Data and Readings

A. *Initial Analysis:* Steps are as follows:

   1. Average values have been calculated for each set of observations to minimize error in taking readings indicated as *initial averages.*
   2. Three-dimensional graphs have been plotted with *initial average* values.

B. *Second Analysis:* Initial analysis is a most generalized form and does not represent true key area because average value is influenced by abnormally extreme higher and lower readings as all readings have been added altogether. To avoid this, *statistical analysis* has been done. Steps are:

   1. Extreme abnormally higher and lower values lying *above* (+) *15%* and *below* (−) *15%* of *initial average* have been omitted by *standard statistical screening process*.
   2. Again, average values have been recalculated with reasonable readings and tabulated.
   3. Three-dimensional graphs have been plotted with those *average* values.

C. *Third Analysis:* Average obtained from *standard statistical screening process* also does not represent truly because it does not obey characteristics of test parameters. Potential difference increases while resistivity decreases with the increase of degree of corrosion; hence, both extreme higher and lower values are required to preserve. Then, statistical analysis has been modified a little as per requirement. Steps are:

   1. All higher readings of potential difference and all lower values of resistivity had been preserved. Readings lying *below* (−) *15%* and *above* (+) *15%* of the *initial average*, respectively, have been omitted.
   2. Average values have been recalculated and three-dimensional graphs have been plotted.

D. *Fourth Analysis:* Analysis has been carried out with readings of optimum magnitudes for correlation with different parameters, considering the following assumptions:

1. Corrosion in concrete develops maximum at where the thickness of cover is minimum.
2. Potential difference readings exhibit maximum at where corrosion is maximum.
3. Resistivity of concrete readings shows minimum at where corrosion is maximum.
4. Ultrasonic pulse runs slower at where corrosion is maximum.
5. Percentage loss of strength of an RCC shall obviously be more at where corrosion is maximum.

On the basis of above mentioned assumptions, data have been reanalyzed. Steps are:

1. All readings of maximum potential difference have been preserved and others have been omitted.
2. All readings of minimum resistivity have been preserved and others have been omitted.
3. Average values have been recalculated with optimum readings and tabulated.
4. Three-dimensional graphs have been plotted with average values for study on correlation.

All three-dimensional graphs are shown as Graphs 1, 2, 3, 4, 5, and 6.

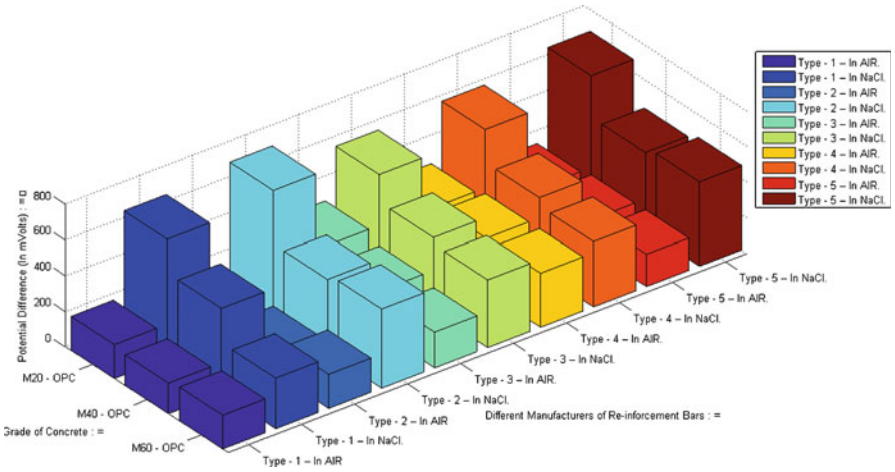

Graph 1 3D bar diagram: potential difference (initial average) vs. grade of concrete vs. different manufacturer of steel re-inforement bars with opc, using 16 mm dia bars both in "Air & Nacl" for 900 days

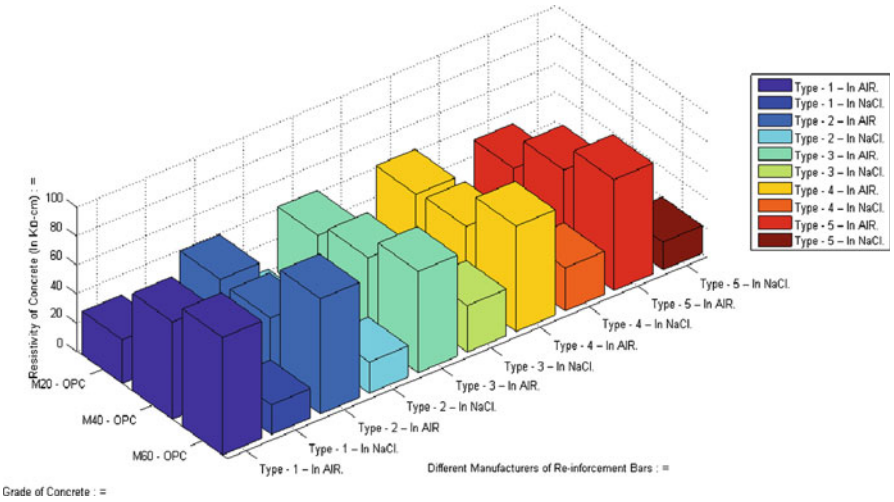

Graph 2 3D bar diagram: resistivity (initial average) vs. grade of concrete vs. different manufacturer of steel re-inforement bars with opc, using 16 mm dia bars both in "Air & Nacl" for 900 days

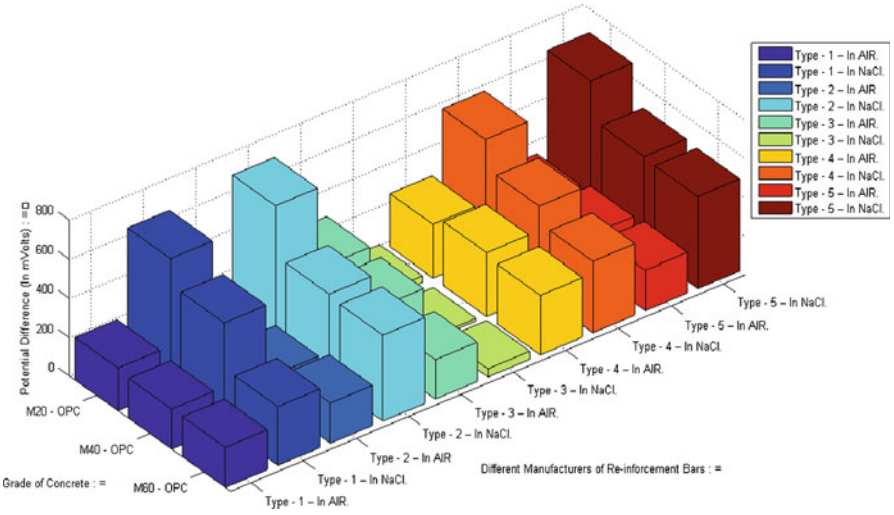

Graph 3 3D bar diagram: potential difference vs. grade of concrete vs. different types of steel re-inforement bars with opc, using 16 mm dia bars both in "Air & Nacl" for 900 days

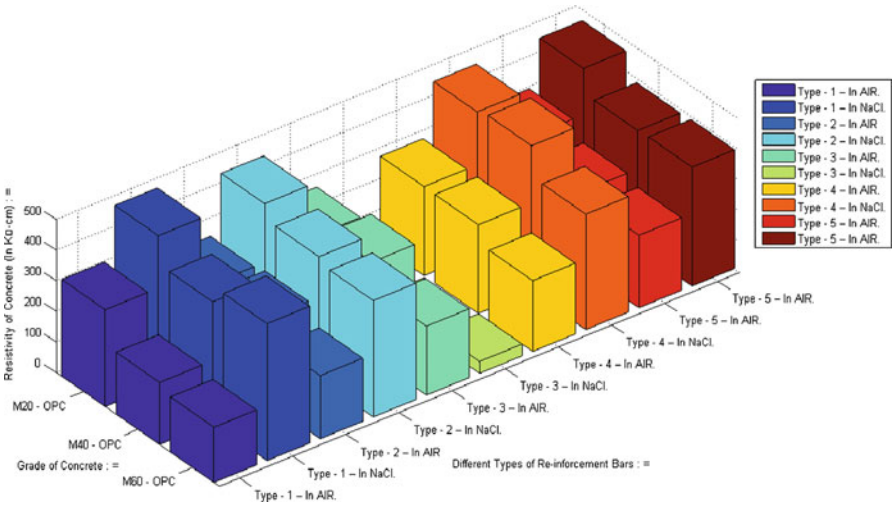

Graph 4 3D bar diagram: resistivity of concrete vs. grade of concrete vs. different types of steel re-inforement bars with opc, using 16 mm dia bars both in "Air & Nacl" for 900 days

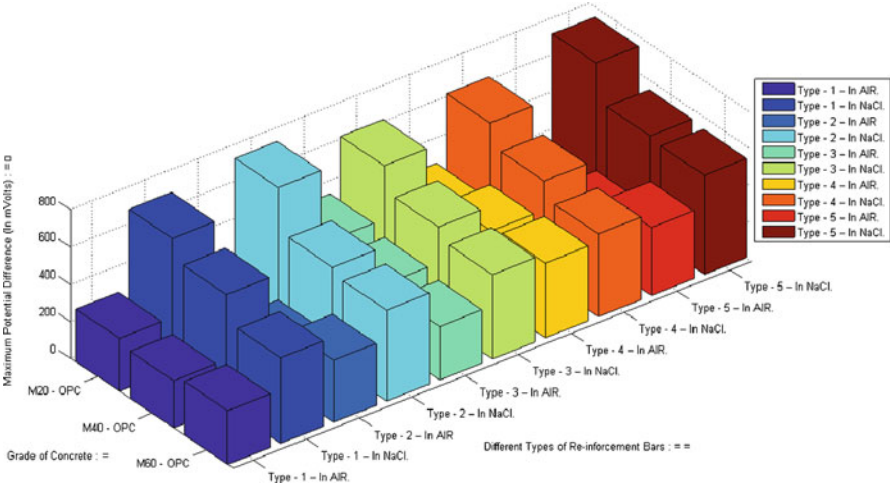

Graph 5 3D bar diagram: maximum potential difference vs. grade of concrete vs. different types of steel re-inforement bars with opc, using 16 mm dia bars both in "Air & Nacl" for 900 days

5 Conclusion

As MATLAB 7.6.0.324 (R2008a) is the most available ANN-based software, hence it is used in this exercise for the purpose of correlation of different parameters of corrosion of rebars in concrete to reduce the uncertainties. Out of all, only 3 (three) of any parameters can be plotted at a time in MATLAB against 3 (three) mutually

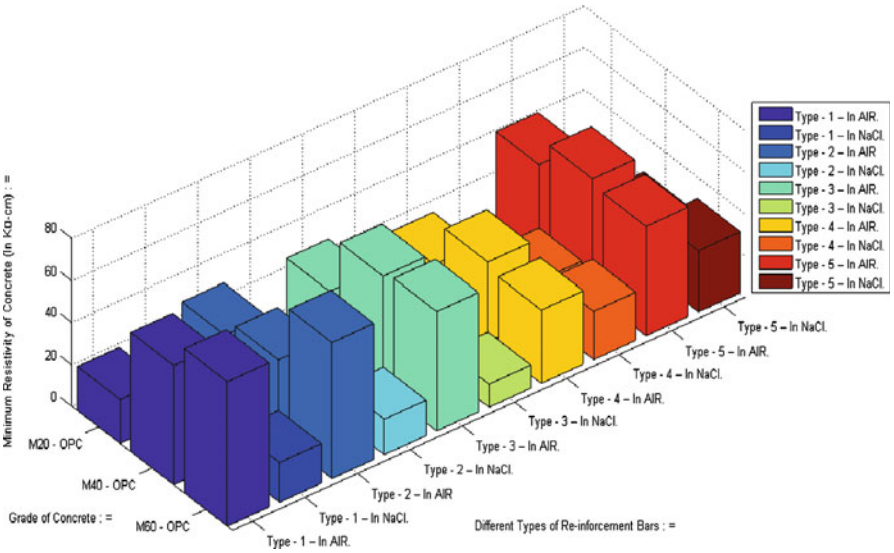

Graph 6 3D bar diagram: minimum resistivity of concrete vs. grade of concrete vs. different types of steel re-inforement bars with opc, using 16 mm dia bars both in "Air & Nacl" for 900 days

perpendicular axes. So, a number of 3- (three-) dimensional graphical representations had been obtained with different possible combinations. But more important factor was noticed at that time, 3- (three-) dimensional graphs are not clearly decipherable because normally we looked upon a 2- (two-) dimensional figure. Therefore, only 2- (two-) dimensional graphs are more convenient and easily readable. Since, corrosion is one of the most complicated phenomenon and involves so many uncertainties; hence, it was felt that a more powerful and suitable ANN-based software is necessary so that at least 10–12 parameters could be plotted simultaneously at a time in order to correlate different parameters related to corrosion of rebars in concrete assessed by nondestructive method of testing and could also be represented graphically in order to reduce uncertainties more accurately. Knowing characteristics of each parameter, mathematical expressions could be derived correspondingly. Substituting certain known values, other unknown variables/parameters could be obtained analytically for better correlations, and thus, uncertainties could also be minimized.

References

1. Solomon T, EERI M, Murat S (2008) Vulnerability of seismically deficient older buildings, risk parameters, significant threat to life safety and its survivability. Earthq Spectra 24 (3):795–821
2. Glass GK, Buenfeld NR (2001) Chloride-induced corrosion of steel reinforcement bars embedded in reinforced cement concrete by applying neural network techniques. Prog Struct Eng (Struct Control Health Monit) 2(4):448–458

3. Eswari S, Raghunath PN, Suguna K (2008) Ductility performance of hybrid fibre reinforced concrete by applying neural network techniques. Am J Appl Sci 5(9):1257–1262, ISSN 1546–9239
4. Rasa E, Ketabchi H, Afshar MH (2009) Prediction on density and compressive strength of concrete cement paste containing silica fume using artificial neural networks. Trans A Civ Eng 16(1):33–42
5. Neven U, Ivana BP Velimir U (2004) Application of neural network in predicting damage of concrete structures caused by chlorides. Published in proceedings of international symposium ASFCACT, pp 187–194
6. Mansour NJ (1996) Prediction of stress-strain relationship for reinforced concrete sections by implementing neural network technique. J King Saud Univ Eng Sci 9(2):169–189
7. Rose AL, Suguna K, Ragunath PN (2009) Strengthening of corrosion-damaged reinforced concrete beams with glass fiber reinforced polymer laminates. J Comput Sci 5(6):1549–3636, ISSN 1549–3636
8. Cardenas H, Kupwade-Patil K, Eklund S (2011) Corrosion mitigation in mature reinforced concrete using nanoscale pozzolan deposition. J Mater Civil Eng 23(6):752–760
9. Hayfield PCS (1986) The cathodic protection of reinforcing steel bars using platinised-type materials. Platin Metals Rev 30(4):158–166
10. Behzad B, Lisa R (2002) Corrosion protection of steel rebar in concrete using migrating corrosion inhibitors MCI 2021 & 2022. A report published by College of Engineering and Computer Science, California State University, Northridge, CA, pp 1–10

Effect of Very Mild Random Tremors on Saturated Sub-surface Flow

Amartya Kumar Bhattacharya and Debasish Kumar

Abstract Very mild random tremors in a saturated soil are not uncommon. Mild earthquakes, nearby piling, and the passage of underground trains all lead to vibrations in a manner that cannot be exactly predicted. High pore pressures and low effective stresses in cohesionless soil can lead to soil liquefaction and complete loss of bearing capacity of the soil. As long as the saturated sub-surface water flow is Darcian, the governing partial differential equation is elliptic in nature at all points in the flow domain. While analytical methods can be used in limited cases, numerical methods are universally available to find out the velocity components and pressure at all points in the flow domain. Tremors disrupt the steady-state flow of saturated sub-surface water. Velocity and pressure patterns vary in a random way. The possibility of saturated sub-surface water pressure mounting followed by soil liquefaction arises. In this chapter, canonical equations related to the finite element method have been considered, and the problem has been analysed.

Keywords Mild • Random • Tremors • Sub-surface • Flow

1 Introduction

Very mild random tremors in a saturated soil are not uncommon. Mild earthquakes, nearby piling, and the passage of underground trains all lead to vibrations in a manner that cannot be exactly predicted. High pore pressures and low effective stresses in cohesionless soil can lead to soil liquefaction and complete loss of bearing capacity of the soil. As long as the saturated sub-surface water flow is Darcian, the governing partial differential equation is elliptic in nature at all points

A.K. Bhattacharya • D. Kumar (✉)
Department of Applied Mechanics, Bengal Engineering and Science University, Shibpur, Howrah 711103, West Bengal, India
e-mail: dramartyakumar@gmail.com; debasishkumar0@gmail.com

S. Chakraborty and G. Bhattacharya (eds.), *Proceedings of the International Symposium on Engineering under Uncertainty: Safety Assessment and Management (ISEUSAM - 2012)*,
DOI 10.1007/978-81-322-0757-3_32,

in the flow domain. While analytical methods can be used in limited cases, numerical methods are universally available to find out the velocity components and pressure at all points in the flow domain. Tremors disrupt the steady-state flow of saturated sub-surface water. Velocity and pressure patterns vary in a random way. The possibility of saturated sub-surface water pressure mounting followed by soil liquefaction arises. In this chapter, canonical equations related to the finite element method have been considered, and the problem has been analysed.

A two-dimensional vertical slice through a soil stratum is taken. The superficial seepage velocity components in the vertical plane are v_x and v_y, where v_x and v_y are the velocity components in the horizontal and vertical directions, respectively. If the velocity potential is denoted by ϕ, then

$$v_x = \frac{\partial \phi}{\partial x} \text{ and } v_y = \frac{\partial \phi}{\partial y} \tag{1}$$

satisfies Laplace's equation,

$$\frac{\partial^2 \phi}{\partial x^2} + \frac{\partial^2 \phi}{\partial y^2} = 0 \tag{2}$$

In a static homogeneous aquifer, the hydraulic conductivity, K, is the same at all points in the flow domain. If an aquifer is subjected to very mild random tremors, the mean value of K is $\bar{K}$, and the standard deviation of K is σ_k; $\sigma_k \ll \bar{K}$.

Because it is difficult to solve for the velocity potential analytically in a vast range of situations, numerical methods like the finite element method [4, 5] have been deployed to compute the velocity potential. In the above two works, three-noded triangular finite elements with Lagrangian interpolation have been used. This has been extended to six-noded triangular finite elements with Lagrangian interpolation by Choudhury [3]. The present work follows Bhattacharya [1,2]. Whatever be the exact nature of the element being utilised, ultimately the matrix equation developed comes out to be of the form

$$\{\phi(K)\} = [G(K)]^{-1}\{P(K)\} \tag{3}$$

where $[G(K)]$ is the global constitutive matrix, $\{\phi(K)\}$ is the matrix of the nodal velocity potentials, and $\{P(K)\}$ is the equivalent of the load matrix in solid mechanics.

If the aquifer is static, a definite pattern of equipotential lines is obtained for definite flow geometry. Under the action of random tremors, the equipotential lines become stochastic. The present work addresses this situation:

$$\{\phi(K)\} = [G(K)]^{-1}\{P(K)\} \tag{3}$$

Or

$$[G(K)]\{\phi(K)\} = \{P(K)\} \tag{4}$$

Now, on differentiating Eq. (4) with respect to K, the following equation is obtained:

$$[G(K)]\frac{\partial}{\partial K}\{\phi\{K\}\} = \frac{\partial}{\partial K}\{P(K)\} - \frac{\partial}{\partial K}[G(K)]\{\phi(K)\} \tag{5}$$

or

$$\frac{\partial}{\partial K}\{\phi(K)\} = [G(K)]^{-1}\left\{\frac{\partial}{\partial K}\{P(K)\} - \{\phi(K)\}\frac{\partial}{\partial K}[G(K)]\right\} \tag{6}$$

where $\frac{\partial}{\partial K}\{\phi(K)\}$ is the sensitivity of ϕ with respect to K.

Equation (6) can be written as

$$\{\xi(K)\} = [G(K)]^{-1}\frac{\partial}{\partial K}\{P^*(K)\} \tag{7}$$

$$\{\xi(K)\} = \frac{\partial}{\partial K}\{\phi(K)\} \tag{8}$$

and

$$\{P^*(K)\} = \frac{\partial}{\partial K}\{P(K)\} - \frac{\partial}{\partial K}[G(K)]\{\phi(K)\} \tag{9}$$

Now, undertaking a Neumann expansion,

$$[G(K)] = [\bar{G}(K)] + [G'(K)] \tag{10}$$

where $[\bar{G}(K)]$ is the deterministic component of $[G(K)]$

and $[G'(K)]$ is the residual component:

$$\begin{aligned}[G(K)]^{-1} &= ([\bar{G}(K)] + [G'(K)])^{-1} = ([I] + [H])^{-1}[\bar{G}(K)]^{-1} \\ &= \left([I] - [H] + [H]^2 - [H]^3 + \ldots\right)[\bar{G}(K)]^{-1}, \text{ so,}\end{aligned} \tag{11}$$

$$[G(K)]^{-1} = \left(\sum_{n=0}^{\infty}[-H]^n\right)[\bar{G}(K)]^{-1} \tag{12}$$

$$[H] = [\bar{G}(K)]^{-1}[G'(K)] \tag{13}$$

Therefore, the velocity potential matrix can be written as

$$\{\phi(K)\} = \left(\sum_{n=0}^{\infty}[-H]^n\right)[\bar{G}(K)]^{-1}\{P(K)\}$$
$$= \left([I] - [H] + [H]^2 - [H]^3 + \ldots..\right)\{\bar{\phi}(K)\} \tag{14}$$

where $\{\bar{\phi}(K)\}$ is the mean of $\{\phi\ (K)\}$.

This can be written as

$$\{\phi(K)\} = \{\bar{\phi}(K)\} - \{\phi_1(K)\} + \{\phi_2(K)\} - \{\phi_3(K)\} + \tag{15}$$

$$\{\bar{\phi}(K)\} = [\bar{G}(K)]^{-1}\ \{P(K)\} \tag{16}$$

Now, let the random tremors be considered to be very mild.

Then,

$$\left|\bar{G}(K)\right| >> [G'(K)] \tag{17}$$

and $[H]$ is small.

It is permissible, then, to write

$$[G(K)]^{-1} \approx ([I] - [H])\ \ [\bar{G}(K)]^{-1} \tag{18}$$

and

$$\{\phi(K)\} \approx ([I] - [H])\ \ \{\bar{\phi}(K)\} \tag{19}$$

Thus,

$$\{v_x\} = \frac{\partial}{\partial x}\left[([I] - [H])\ \ \{\bar{\phi}\,(K)\}\right] \tag{20}$$

and

$$\{v_y\} = \frac{\partial}{\partial y}\left[([I] - [H])\ \ \{\bar{\phi}\,(K)\}\right] \tag{21}$$

The stochastic nature of the $\{vx\}$ and $\{vy\}$ matrices is introduced through the presence of the matrix $[H]$. However, the two velocity matrices are almost deterministic as $[H]$ is small.

2 Conclusions

It can be concluded that very mild random tremors do not appreciably alter the velocity distribution of the saturated sub-surface water. Localised changes in point velocity do occur, but these are unlikely to have a major impact on, for example, the discharge into a pumping well. The situation can change totally if the random tremors no longer remain very mild.

References

1. Bhattacharya AK (2005) Groundwater flow in a weakly-random hydraulic conductivity field. Electron J Geotech Eng 10, Bundle – E, EJGE Paper 2005–0582
2. Bhattacharya AK, Choudhury S (2001) Uncertainty analysis of groundwater flow during earthquakes. In: Proceedings, all India seminar on disaster management and civil engineering solutions, Calcutta, India, 7–8 Dec 2001
3. Choudhury S (2002) Evaluation of seepage under sheet-pile using the finite element method with six-noded triangular elements. ME thesis, Bengal Engineering College (Deemed University), Howrah, India
4. Maji S, Mondal S, Bhattacharya AK, Manna MC, Choudhury S (2002) Finite element analysis of flow under a sheet pile. In: Proceedings, international conference on water resource management in arid regions, Kuwait, 23–27 Mar 2002
5. Mondal S (2001) Finite element analysis of seepage flow under dam. ME thesis, Bengal Engineering College (Deemed University), Howrah, India

Slope Reliability Analysis Using the First-Order Reliability Method

Subhadeep Metya and Gautam Bhattacharya

Abstract This chapter pertains to a study on the reliability evaluation of earth slopes under a probabilistic framework. This study is concerned in the first phase with the determination of reliability index and the corresponding probability of failure associated with a given slip surface and then in the second phase with the determination of the critical probabilistic slip surface and the associated minimum reliability index and the corresponding probability of failure. The geomechanical parameters of the slope system have been treated as random variables for which different probability distributions have been assumed. The reliability analyses have been carried out using two methods, namely, the approximate yet simple mean-value first-order second-moment (MVFOSM) method and the rigorous first-order reliability method (FORM). Based on a benchmark illustrative example of a simple slope in homogeneous soil with uncertain strength parameters along a slip circle, an effort has been made to numerically demonstrate the nature and level of errors introduced by adopting the MVFOSM method for reliability analysis of earth slopes still widely used in the geotechnical engineering practice, vis-à-vis a more accurate method such as the FORM.

Keywords Slope stability • Slip surface • Uncertainty • Random variable • Probability distribution • Reliability analysis

S. Metya (✉)
Department of Civil Engineering, Budge Budge Institute of Technology, Kolkata 700137, India
e-mail: subhadeep.metya@gmail.com

G. Bhattacharya
Department of Civil Engineering, Bengal Engineering and Science University, Shibpur, Howrah 711103, India
e-mail: gautam@civil.becs.ac.in

S. Chakraborty and G. Bhattacharya (eds.), *Proceedings of the International Symposium on Engineering under Uncertainty: Safety Assessment and Management (ISEUSAM - 2012)*,
DOI 10.1007/978-81-322-0757-3_33,

1 Introduction

In recent years, there has been a growing appreciation among the researchers in the field of geotechnical engineering of the fact that geotechnical parameters, especially the strength parameters including pore water pressure, are highly uncertain or random. Conventional deterministic approach is, therefore, being increasingly replaced with probabilistic approach or reliability analysis within a probabilistic framework. Slope stability analysis is one of the important areas where the recent trend is to determine the probability of failure of slopes instead of, or complementary to, the conventional factor of safety.

During the last decade, quite a few studies on reliability evaluation of earth slopes have been reported in the literature. Most of these studies used the simple yet approximate reliability analysis method known as the mean-value first-order second-moment (MVFOSM) method based on a Taylor series expansion of the factor of safety. However, this method suffers from serious shortcomings such as the following: (1) The method does not use the distribution information about the variables when it is available. (2) The performance function is linearized at the mean values of the basic variables. When the performance function is nonlinear, significant errors may be introduced by neglecting higher order terms, for the reason that the corresponding ratio of mean of performance function to its standard deviation which is evaluated at the mean values may not be the distance to the nonlinear failure surface from the origin of the reduced variables. (3) Furthermore, first-order approximations evaluated at the mean values of the basic variates will give rise to the problem of invariance for mechanically equivalent limit states; that is, the result will depend on how a given limit-state event is defined.

The first-order reliability method (FORM), on the other hand, does not suffer from the above shortcomings and is, therefore, widely considered to be an accurate method. The method has been finding increasing use especially in structural engineering applications for more than a decade. More recently in the geotechnical engineering field also, there have been quite a few attempts at reliability analysis of earth slopes using the FORM method [2–4].

In this chapter, an attempt has been made to develop computational procedures for slope reliability analysis based on the first-order reliability method (FORM). Computer programs have been developed to demonstrate the application of FORM in the determination of (1) the reliability index for a given slip surface and, more importantly, in the determination of (2) the probabilistic critical slip surface and the associated minimum reliability index. Different probability distributions have been considered for the basic random variables. In determining the probabilistic critical slip surface, the basic methodology suggested by Bhattacharya et al. [1] has been adopted. The above reliability analyses have also been carried out using the approximate MVFOSM method, and the results obtained have been compared with those obtained by using the FORM to bring out the difference clearly and demonstrate numerically the shortcomings of the MVFOSM method.

2 Formulation

2.1 Deterministic Analysis

The conventional slope stability analysis follows a deterministic approach wherein out of a number of candidate potential slip surfaces, the one with the least value of factor of safety is searched out and is termed the critical slip surface. It has now been widely appreciated that the slope stability analysis is essentially a problem of optimization wherein the coordinates defining the shape and location of the slip surface are the design variables and the factor of safety functional expressed as a function of the design variables is the objective function to be minimized subject to the constraints that the obtained critical slip surface should be kinematically admissible and physically acceptable. In practice, analysis is often done based on the assumption that the slip surface is an arc of a circle, as it greatly simplifies the problem. The ordinary method of slices (OMS) [5] is the simplest and the earliest method of slices that assumes a circular slip surface geometry.

The factor of safety functional (FS) for the ordinary method of slices (OMS) is given by the following expression [Eq. (1)], where the notations have their usual meaning. Specifically, $c^{'}$ and $\phi^{'}$ denote the effective cohesion and effective angle of shearing resistance, respectively; W_i and u_i are the weight and the pore water pressure at the base of the ith slice, respectively; θ_i is the base inclination of the ith slice; and Δl_i and $\widehat{L}$ are the base length of the ith slice and the total arc length of the slip circle, respectively:

$$\mathrm{FS} = \frac{c'\,\widehat{L} + \tan\,\phi'\,\sum_{i=1}^{i=n}(W_i\,\cos\,\theta_i - u_i\Delta l_i)}{\sum_{i=1}^{i=n}(W_i\,\sin\,\theta_i)} \tag{1}$$

Substituting $W_i = \gamma b h_i$, and $u_i = r_u\,\gamma h_i$, where γ and b are the unit weight of soil and the common width of slice, respectively, h_i is the mean height of the ith slice, and r_u is the pore pressure ratio, Eq. (1) reduces to

$$\mathrm{FS} = \frac{c'\,\widehat{L} + \tan\,\phi'\,\sum_{i=1}^{i=n}(\gamma b h_i\,\cos\,\theta_i - r_u\gamma h_i\Delta l_i)}{\sum_{i=1}^{i=n}(\gamma b h_i\,\sin\,\theta_i)} \tag{2}$$

2.2 Reliability Index β Based on the MVFOSM Method

Taking the performance function as the expression for FS in a limit equilibrium method of slices such as Eq. (1) or (2) for analyzing slope stability and the corresponding limit-state equation as $\mathrm{FS}-1 = 0$, the reliability index β based on the MVFOSM method is given by

$$\beta = \frac{E[\mathrm{FS}] - 1}{\sigma\ [\mathrm{FS}]} = \frac{\mathrm{FS}\left(\mu_{x_i}\right) - 1}{\sqrt{\sum_{i=1}^{n} \left(\frac{\partial \mathrm{FS}}{\partial X_i}\right)^2 \sigma^2\,[X_i] + 2 \sum_{i,j=1}^{n} \left(\frac{\partial \mathrm{FS}}{\partial X_i}\right) \left(\frac{\partial \mathrm{FS}}{\partial X_j}\right) \rho\ \sigma[X_i]\ \sigma[X_j]}} \tag{3}$$

where n is the number of soil strength parameters (c', tan ϕ', r_u, γ, etc.) taken as random variables; E[FS], the expected value of FS; σ[FS], the standard deviation of FS; μ_{xi}, the mean value of random variable X_i; $\sigma[X_i]$, the standard deviation of X_i; and ρ, correlation coefficient between X_i and X_j.

2.2.1 Mechanically Equivalent Limit State

When using MVFOSM method, it is of interest to study how the results of reliability analysis differ when other mechanically equivalent limit states are adopted. A limit state equivalent to FS$-1 = 0$ mentioned above is given by ln (FS) $= 0$. For such a limit state, the reliability index is given by

$$\beta = \frac{E[ln\ \mathrm{FS}]}{\sigma_{ln\,\mathrm{FS}}} \tag{4a}$$

where

$$E[ln\ \mathrm{FS}] = ln(E[\mathrm{FS}]) - \frac{\sigma^2_{ln\,\mathrm{FS}}}{2} \tag{4b}$$

and

$$\sigma_{ln\,\mathrm{FS}} = \sqrt{ln\left(1 + \left(\frac{\sigma_{\mathrm{FS}}}{E[\mathrm{FS}]}\right)^2\right)} \tag{4c}$$

2.3 Reliability Index β Based on the FORM Method

In this method, the reliability index (β) is defined as the minimum distance ($D_{\min}$) from the failure surface [$g(X') = 0$] to the origin of the reduced variates, as originally proposed by Hasofer and Lind [7]. For general nonlinear limit states,

the computation of the minimum distance ($D_{\min}$) becomes an optimization problem as stated below:

Minimize $D = \sqrt{X'^t X'}$
Subject to the constraint $g(X') = 0$

where X' represents the coordinates of the checking point on the limit-state equation in the reduced coordinates system.

Two optimization algorithms are commonly used to solve the above minimization problem to obtain the design point on the failure surface and the corresponding reliability index β [6]. In the first method [10] referred to as FORM method I by Haldar and Mahadevan [6], it is required to solve the limit-state equation during the iteration. The second method [11] referred to as FORM method II by Haldar and Mahadevan [6] does not require solution of the limit-state equation. It uses a Newton-type recursive formula to find the design point. The FORM method II is particularly useful when the performance function is implicit, that is, when it cannot be written as a closed-form expression in terms of the random variables. The FORM method, however, is applicable only for normal random variables. For non-normal variables, it is necessary to transform them into equivalent normal variables. This is usually done following the well-known Rackwitz–-Fiessler method [6].

2.4 Probability of Failure

Once the value of the reliability index β is determined by any of the methods discussed above, the probability of failure p_F is then obtained as

$$p_F = \Phi(-\beta) \tag{5}$$

where $\Phi(.)$ is the standard normal cumulative probability distribution function, values of which are tabulated in standard texts.

2.5 Determination of Probabilistic Critical Slip Surface

Bhattacharya et al. [1] proposed a procedure for locating the surface of minimum reliability index, $\beta_{\min}$, for earth slopes. The procedure is based on a formulation similar to that used to search for the surface of minimum factor of safety, $FS_{\min}$, in a conventional slope stability analysis. The advantage of such a formulation lies in enabling a direct search for the critical probabilistic surface by utilizing an existing deterministic slope stability algorithm or software with the addition of a simple module for the calculation of the reliability index β. This is definitely an improvement over the indirect search procedure proposed earlier by Hassan and Wolff [8].

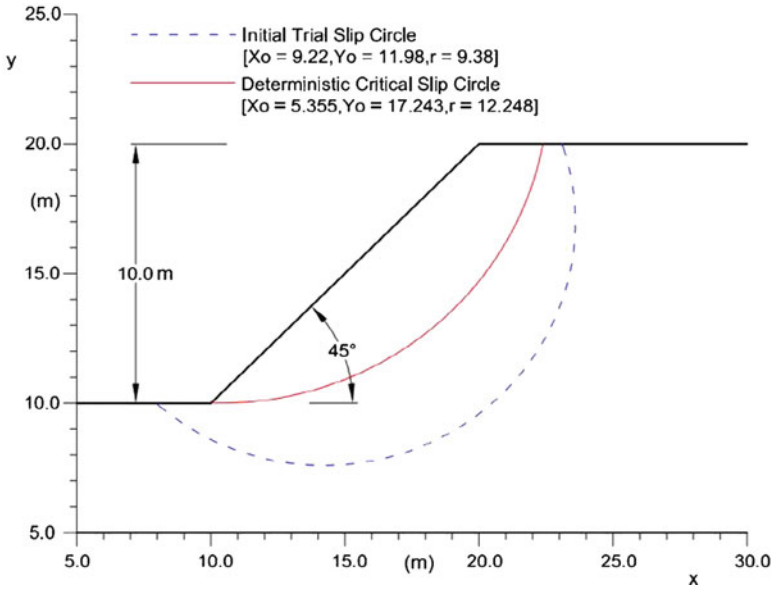

Fig. 1 Slope section and the deterministic critical slip circle in the illustrative example

Table 1 Statistical properties of soil parameters

Parameter (1)	Mean (2)	Standard deviation (3)	Coefficient of variation (4)
c'	18.0 kN/m^2	3.6 kN/m^2	0.20
tan ϕ'	tan 30°	0.0577	0.10
γ	18.0 kN/m^3	0.9 kN/m^3	0.05
r_u	0.2	0.02	0.10

3 Illustrative Example

Figure 1 shows a section of a simple slope of inclination 45° and height 10 m in a homogeneous c- ϕ soil. Previous reliability analyses of this slope under a probabilistic framework include those reported by Li and Lumb [9], Hassan and Wolff [8], and Bhattacharya et al. [1] using different methods of analysis. Thus, this example can well be regarded as a benchmark example problem. In all the previous investigations, all four geotechnical parameters, namely, the effective cohesion c', the effective angle of shearing resistance ϕ', the pore pressure ratio r_u, and the unit weight γ, were treated as random variables, and their statistical properties (mean, standard deviation, and coefficient of variation) are as in Table 1.

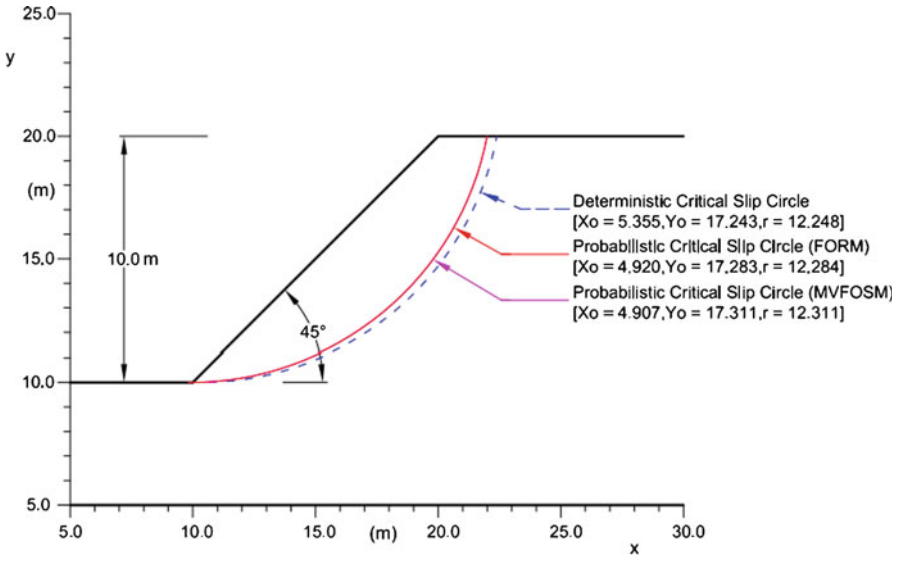

Fig. 2 Probabilistic and deterministic critical slip surfaces

4 Results and Discussion

4.1 Deterministic Analysis

For the purpose of determination of the critical slip circle, a trial slip circle ($x_o = 9.22$ m, $y_o = 11.98$ m, $r = 9.38$ m with reference to the axis system shown in Fig. 1) has been arbitrarily selected. Using Eq. (1) or (2) for the ordinary method of slices, its factor of safety (FS) is obtained as 1.70, when the parameters c', $\tan \phi'$, γ, and r_u are assumed constant at their mean values (Table 1). With this slip circle as the initial slip surface, the developed computer program based on the sequential unconstrained minimization technique (SUMT) of nonlinear optimization coupled with the ordinary method of slices (OMS) yields a critical slip circle ($x_c = 5.355$ m, $y_c = 17.243$ m, $r_c = 12.248$ m) which passes through the toe, as shown in Fig. 2. The associated minimum factor of safety (F_{min}) is obtained as 1.26.

4.2 Reliability Analysis

Reliability analysis of this slope was attempted using two methods, namely, the mean-value first-order second-moment (MVFOSM) method and the first-order reliability method (FORM), with a view to compare the two sets of results. All four parameters c', $\tan \phi'$, γ, and r_u are assumed to be normally distributed and uncorrelated. However,

reliability analyses were carried out in three phases: In phase I only two parameters, namely, the cohesion c' and the effective angle of shearing resistance in the form of tan ϕ', were treated as random variables, while the other two parameters γ and r_u were assumed as constants at their mean values. In phase II, three parameters, namely, the cohesion c', the effective angle of shearing resistance tan ϕ', and r_u, were treated as random variables, while the parameter γ was assumed as constant at its mean value, while in phase III all four parameters were assumed as random variables.

4.3 Reliability Analysis for a Given Slip Surface Using MVFOSM

For the two slip surfaces shown in Fig. 1, namely, (1) the initial slip circle ($x_o = 9.22$, $y_o = 11.98$, $r = 9.38$) and (2) the deterministic critical slip circle ($x_o = 5.355$, $y_o = 17.243$, $r = 12.248$), the reliability indices were determined by MVFOSM method by taking two mechanically equivalent limit states: FS$-1 = 0$ and ln (FS) $= 0$ using Eqs. (3) and (4a, 4b, 4c), respectively, for phase I, phase II, and phase III described above. The reliability index values for the different cases are summarized in Table 2.

4.4 Reliability Analysis for a Given Slip Surface Using FORM

Reliability index values have also been determined for the above mentioned slip surfaces using FORM. In particular, the algorithm for FORM method I [6] has been used in this case. All three phases mentioned above have been analyzed. For the sake of comparison as well as numerical demonstration, both the limit states considered in the analyses by MVFOSM have also been used here. The results are summarized in Table 2 again, alongside those obtained by using MVFOSM.

From Table 2, the following observations are made:

1. For the same slip surface and the same set of random variables (in phases I, II, and III), values of reliability index obtained for different mechanically equivalent limit states are markedly different when MVFOSM is used as the method of reliability analysis, whereas these values are identical when analyzed by the FORM method. This observation clearly demonstrates that unlike the FORM method, the MVFOSM method suffers from the "problem of invariance," that is, the result depends on how a given limit-state event is defined. In this respect, another observation from Table 2 is that when the limit state is taken as ln (FS) $= 0$, the reliability index values are higher in all three phases of analysis.
2. It may be noted from Eqs. (1) and (2) that the performance function FS is linear when only c' and tan ϕ' are treated as random variables as in phase I of reliability analysis. However, when c', tan ϕ', and r_u are treated as random variables as in

Table 2 Summary of results of reliability analyses for given slip surfaces

Method of reliability analysis	Slip surface	Values of reliability index					
		Limit state: FS − 1 = 0			Limit state: ln (FS) = 0		
		Phase I	Phase II	Phase III	Phase I	Phase II	Phase III
		(c', tan ϕ')	(c', tan ϕ', r_u)	(c', tan ϕ', r_u, γ)	(c', tan ϕ')	(c', tan ϕ', r_u)	(c', tan ϕ', r_u, γ)
MVFOSM	Initial slip circle	3.955	3.812	3.736	5.059	4.874	4.775
		(3.83×10^{-5})	(6.89×10^{-5})	(9.35×10^{-5})	(2.10×10^{-7})	(5.46×10^{-7})	(8.98×10^{-7})
	Deterministic critical slip circle	1.671	1.643	1.601	1.815	1.783	1.734
		(4.73×10^{-2})	(5.02×10^{-2})	(5.47×10^{-2})	(3.47×10^{-2})	(3.73×10^{-2})	(4.14×10^{-2})
FORM (all random variables are normally distributed)	Initial slip circle	3.955	3.862	3.851	3.955	3.862	3.851
		(3.83×10^{-5})	(5.63×10^{-5})	(5.88×10^{-5})	(3.83×10^{-5})	(5.63×10^{-5})	(5.88×10^{-5})
	Deterministic critical slip circle	1.671	1.646	1.625	1.671	1.646	1.625
		(4.73×10^{-2})	(4.99×10^{-2})	(5.21×10^{-2})	(4.73×10^{-2})	(4.99×10^{-2})	(5.21×10^{-2})

Note: Figures in the parentheses indicate the values of the probability of failure for the respective slip surface

phase II or when c', tan ϕ', r_u, and γ are treated as random variables as in phase III, the performance function FS becomes nonlinear, and the degree of nonlinearity increases from phase II to phase III. Now, from Table 2, it is seen that for phase I, the values of reliability index yielded by MVFOSM and FORM are exactly the same, whereas they are different for phases II and III. Further, this difference in case of phase III is more than in case of phase II. This observation clearly demonstrates that in those situations where the performance function is linear and all the variables are normally distributed and statistically independent, the values of reliability index by MVFOSM method agree with those given by the FORM, and the error associated with MVFOSM method increases as the degree of nonlinearity of the performance function (or limit-state equation) increases.

3. Another important observation from Table 2 is that when the number of random variables increases, the value of reliability index (β) decreases and probability of failure increases.

4.5 Reliability Analysis for Given Slip Surfaces: Effect of Probability Distributions of the Basic Variates

As already stated, the MVFOSM method does not use the information on probability distribution of the basic random variables. In the FORM method, on the other hand, this information can be incorporated in the analysis. In the present analysis, the effect of variation of probability distributions has been studied using FORM method I. Only two distributions have been considered, namely, the normal distribution and the lognormal distribution. Results have been obtained for phase I only, that is, when only two parameters c′. and tan ϕ′ are treated as random variables. Table 3 summarizes the results. It can be observed that there are substantial differences in the values of the reliability index obtained by using FORM when different combinations of probability distributions for the random variates c'. and tan ϕ' are considered. It is further observed that the β values from MVFOSM agree with those from FORM only when both the random variables are assumed to be normally distributed. Thus, it can be said that the MVFOSM method, though does not make use of any such knowledge regarding distribution of variates, implicitly assumes that all variables are normally distributed.

4.6 Probabilistic Critical Slip Surface and the Associated β_{min}

The probabilistic critical slip surface (surface of minimum β) has been determined following the same computational procedure as used for the determination of the deterministic critical slip surface, simply by replacing the objective function FS with

Table 3 Variation of reliability index with different probability distributions for the basic variates

			Values of reliability index for			
	Probability distribution		Initial trial slip circle		Deterministic critical slip circle	
Limit state surface	c'	$\tan \phi'$	MVFOSM	FORM	MVFOSM	FORM
$FS-1=0$	Lognormal	Normal	3.955	4.806	1.671	1.859
	Normal	Lognormal		4.038		1.661
	Lognormal	Lognormal		5.318		1.854
	Normal	Normal		3.955		1.671
$\ln FS=0$	Lognormal	Normal	5.059	4.806	1.815	1.859
	Normal	Lognormal		4.038		1.661
	Lognormal	Lognormal		5.318		1.854
	Normal	Normal		3.955		1.671

Note: These results correspond to the phase I analysis, that is, when only c'. and $\tan \phi'$ are treated as random variables

β [1]. A computer program was developed based on the sequential unconstrained minimization technique (SUMT) of nonlinear optimization coupled with a method of reliability analysis, MVFOSM or FORM, as the case may be.

For this search, the deterministic critical slip surface shown in Fig. 1 has been used as the initial slip surface. Several such probabilistic critical slip surfaces have been determined, and the associated minimum reliability index (β_{min}) values are summarized in Table 4. For the sake of clarity, only two of these critical surfaces are plotted in Fig. 2: the probabilistic critical slip surface for phase III analysis using MVFOSM ($x_c = 4.907$ m, $y_c = 17.311$ m, $r_c = 12.311$ m) and the probabilistic critical slip surface for phase III analysis using FORM with all four random variables normally distributed ($x_c = 4.920$ m, $y_c = 17.283$ m, $r_c = 12.284$ m). For the sake of comparison, the deterministic critical slip surface ($x_c = 5.355$ m, $y_c = 17.243$ m, $r_c = 12.248$ m) has also been plotted in Fig. 2.

From Fig. 2, as well as from the magnitudes of the coordinates of centers and radii, it is seen that the two probabilistic critical slip surfaces are located very close to each other while the deterministic critical slip circle is somewhat apart. The closeness of the deterministic and the probabilistic critical slip surfaces for the case of simple homogeneous slopes is in agreement with those reported by earlier investigators. The detailed results presented in Table 4 generally corroborate the observations made earlier from Table 2 with reference to the reliability analyses of the given slip surfaces.

5 Summary and Conclusions

In view of the growing appreciation of the uncertainty associated with the geotechnical parameters, especially, the strength parameters including the pore water pressure, the conventional deterministic approach of analysis is increasingly

Table 4 Summary of results of the minimum reliability analyses associated with the probabilistic critical slip surface

Method of reliability analysis	Values of minimum reliability index					
	Limit state: FS − 1 = 0			Limit state: ln (FS) = 0		
	Phase I (c', tan ϕ')	Phase II (c', tan ϕ', r_u)	Phase III (c', tan ϕ', r_u, γ)	Phase I (c', tan ϕ')	Phase II (c', tan ϕ', r_u)	Phase III (c', tan ϕ', r_u, γ)
MVFOSM	1.643 (1.671)	1.618 (1.643)	1.576 (1.601)	1.785 (1.815)	1.756 (1.783)	1.707 (1.734)
FORM (all random variables are normally distributed)	1.643 (1.671)	1.620 (1.646)	1.599 (1.625)	1.643 (1.671)	1.620 (1.646)	1.599 (1.625)

Note: Figures in the parentheses indicate the values of reliability index for the deterministic critical slip surface

being replaced by probabilistic approach of analysis or reliability analysis under a probabilistic framework. The mean-value first-order second-moment (MVFOSM) method based on a Taylor series expansion is rather widely used by the practitioners in the geotechnical engineering field mainly due to the simplicity and early origin of the method. However, in other fields of engineering, for example, in the structural engineering field, it is an established fact for quite some time that the MVFOSM method suffers from serious shortcomings such as the problem of invariance, as mentioned in an earlier section of this chapter.

This chapter concerns a study on the reliability analysis of earth slopes with uncertain soil strength parameters under a probabilistic framework. Reliability analyses have been carried out using a rigorous method, namely, the first-order reliability method (FORM) in conjunction with a simple slope stability model, namely, the ordinary method of slices (OMS). For the sake of comparison, results in the form of the reliability index and probability of failure have also been obtained using the MVFOSM method. Computer programs have been developed for the determination of reliability index based on both FORM and MVFOSM method for a given slip surface and then for the optimization-based determination of the probabilistic critical slip surface and the associated minimum reliability index. The developed programs have been applied to a benchmark example problem concerning a simple slope in homogeneous soil in which the geotechnical parameters are treated as random variables with given values of statistical moments. The differences between the two sets of results have been brought out for the cases of an arbitrarily selected given slip surface, the deterministic critical slip surface, and also the probabilistic critical slip surface. The study has been successfully used to demonstrate numerically all the major shortcomings of the approximate MVFOSM method and the error involved vis-à-vis the more accurate FORM method.

References

1. Bhattacharya G, Jana D, Ojha S, Chakraborty S (2003) Direct search for minimum reliability index of earth slopes. Comput Geotech 30(6):455–462
2. Cho SE (2009) Probabilistic stability analyses of slopes using the ANN-based response surface. Comput Geotech 36(5):787–97
3. Chowdhury R, Rao BN (2010) Probabilistic stability assessment of slopes using high dimensional model representation. Comput Geotech 37(7–8):876–884
4. Das SK, Das MR (2010) Discussion of "Reliability-based economic design optimization of spread foundations- by Y. Wang". J Geotech Geoenviron Eng 136(11):1587–1588
5. Fellenious W (1936) Calculation of stability of earth dams transaction. In: Second Congress on large dams, Washington, vol 4, p 445
6. Haldar A, Mahadevan S (2000) Probability, reliability, and statistical methods in engineering design. Wiley, New York
7. Hasofer AA, Lind AM (1974) Exact and invariant second moment code format. J Geotech Eng Div ASCE 100(1):111–121
8. Hassan AM, Wolff TF (1999) Search algorithm for minimum reliability index of earth slopes. J Geotech Geoenviron Eng 125(4):301–308
9. Li KS, Lumb P (1987) Probabilistic design of slopes. Can Geotech J 24(4):520–535
10. Rackwitz R, Fiessler B (1976) Note on discrete safety checking when using non-normal stochastic models for basic variables. Load project working session. MIT, Cambridge
11. Rackwitz R, Fiessler B (1978) Structural reliability under combined random load sequences. Comput Struct 9(5):484–494

Design of a Tuned Liquid Damper System for Seismic Vibration Control of Elevated Water Tanks

Anuja Roy and Aparna (Dey) Ghosh

Abstract In this paper, a Tuned Liquid Damper (TLD) system is proposed for the response mitigation of an elevated water tank structure under seismic excitation. First, a study on the performance of the TLD system attached to an elevated water tank structure modelled as a single-degree-of-freedom (SDOF) system is carried out in the frequency domain. Fluid-structure interaction is not considered in the present study. A realistic example of an elevated water tank structure is considered. The performance of the TLD system is examined on the basis of reduction in the root mean square (rms) value of the structural displacement. The sensitivity of the performance of the TLD system to change in the structural frequency due to fluctuation in the amount of water in the water tank container is examined. A time domain study is also carried out with the recorded accelerogram of the El Centro earthquake as the base input. The procedure to obtain a practical configuration of the TLD units is outlined. The performance of the designed TLD system indicates that the TLD is a promising device for the seismic vibration control of elevated water tanks.

Keywords TLD • Elevated water tank • Seismic excitation • Passive control

1 Introduction

Elevated water tanks are heavy mass structures that are vulnerable to seismic forces. Again, these are critical facilities, and it is essential that they remain serviceable even in the regions of maximum shaking intensity following a design level earthquake.

A. Roy (✉) • A.D. Ghosh
Department of Civil Engineering, Bengal Engineering and Science University, Shibpur, Howrah, India
e-mail: anuja.civil@gmail.com; aparnadeyghosh@gmail.com

S. Chakraborty and G. Bhattacharya (eds.), *Proceedings of the International Symposium on Engineering under Uncertainty: Safety Assessment and Management (ISEUSAM - 2012)*,
DOI 10.1007/978-81-322-0757-3_34,

Rai [6] in his study on the performance of elevated tanks in the Bhuj 2001 earthquake noted that the elevated water tank structure does not have much redundancy, and this is especially true for tanks with circular shaft-type stagings. Further, thin sections of shaft-type stagings also have low ductility. Thus, apart from having stringent design criteria and high-quality construction practices for these structures, it is also judicious to provide them with seismic protection devices.

Studies on the passive control of the seismic response of elevated tanks by base isolation were carried out by several researchers. Shenton and Hampton [7] evaluated the seismic response of an isolated elevated water tank structure. They compared the results with those of the corresponding fixed base tank and concluded that seismic isolation is efficient in reducing the tower drift, base shear, overturning moment and tank wall pressures for the practical range of tank capacities and height-to-diameter ratios. Shrimali and Jangid [8] examined the application of linear elastomeric bearings in the seismic response mitigation of elevated liquid storage steel tanks. Shrimali and Jangid [9] applied resilient-friction base isolator and friction pendulum system in their study of earthquake response of elevated cylindrical liquid storage tanks. Shrimali [10] investigated the earthquake response of elevated cylindrical liquid storage tanks isolated by friction pendulum system under bidirectional excitation. These studies yielded promising results in the field of seismic isolation of elevated liquid storage tanks.

In this chapter, the popular passive control device, the TLD, is studied for the seismic vibration control of elevated water tanks. The main advantages of this kind of damper over mass dampers are low installation, operational and maintenance costs, ease of installation in case of existing structures, easy adjustment of natural frequency and effectiveness even against small-amplitude vibrations.

The TLD was first proposed by Frahm in the early 1900s in which the frequency of motion of the water in two interconnected tanks was tuned to the fundamental rolling frequency of a ship so that this component of motion was successfully reduced [11]. The concept of applying TLDs in civil engineering structures as a passive vibration control device was initiated in the mid-1980s. Welt and Modi [15, 16] suggested the use of TLD in buildings to reduce structural response under wind or earthquake forces. Housner [3] took into consideration both the impulsive and convective liquid pressures in the analysis of the hydrodynamic pressures generated in a fluid container when it was subjected to horizontal acceleration. Fujino et al. [2] concluded that the fundamental sloshing frequency of TLD must be tuned to the natural frequency of the structure to obtain a higher damping value of the TLD under small-amplitude structural vibration. Koh et al. [5] reported that the liquid motion is highly sensitive to the natural frequency of the TLD as well as the amplitude and frequency content of the excitation spectrum. Yu et al. [17] presented an equivalent Tuned Mass Damper (TMD) model of the TLD and illustrated its satisfactory performance over a wide range of values of the excitation amplitude. The study by Banerji et al. [1] revealed the need for greater mass ratio of the TLD to be more efficient for larger structural damping. Kim et al. [4] performed shaking table experiments on the TLD that revealed the dependence of liquid sloshing on the amplitude of vibration and on the frequency of the damper. Tait et al. [13] studied

the performance of unidirectional and bidirectional TLD for random vibrations. Tait and Deng [12] compared the performance of TLD with different tank geometries.

In this work, a transfer function formulation for the elevated water tank structure, modelled as a SDOF system, with TLD is developed. The input excitation is characterized by a white noise power spectral density function (PSDF). A sensitivity study on the performance of the TLD is included. It is followed by an investigation on the optimum tuning ratio. A simulation study using a recorded earthquake excitation is also carried out. The design of the TLD for a realistic example elevated water tank structure is performed.

2 Modelling of the Elevated Water Tank-TLD System

The TLD is a right circular cylindrical container of radius a (Fig. 1). It is filled with water upto a height h. It has a free upper surface. The thickness of the container wall is assumed to be uniform. The water in the damper container is assumed to respond in impulsive and convective modes under horizontal base excitation. Though in theory, there are several convective modes, consideration of only a few modes is enough for practical purpose. Here, only the first mode is considered. The liquid mass associated with the first convective mode, m_d, is assumed to be attached to the SDOF system representing the elevated water tank structure (Fig. 2) by a linear spring with stiffness k_d and a linear viscous damper with damping coefficient c_d. The fluid-structure interaction in the water tank is not being taken into account. The weight of the damper container is neglected. The damping ratio of the convective mode of vibration of the damper liquid is ζ_d, while ω_d denotes the natural frequency of the fundamental sloshing mode of vibration of the liquid. The expressions for m_d and ω_d are given by Veletsos and Tang [14]. The mass, stiffness and damping of the

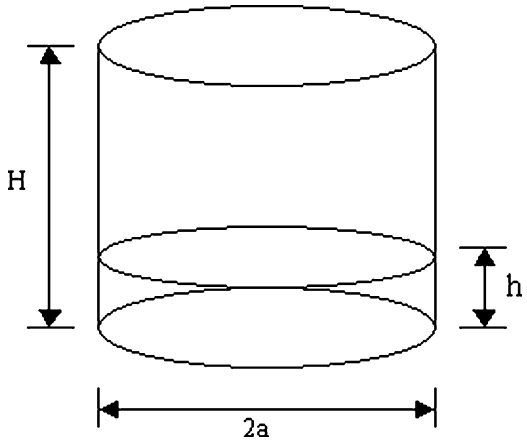

Fig. 1 Definition sketch for circular cylindrical Tuned Liquid Damper (TLD)

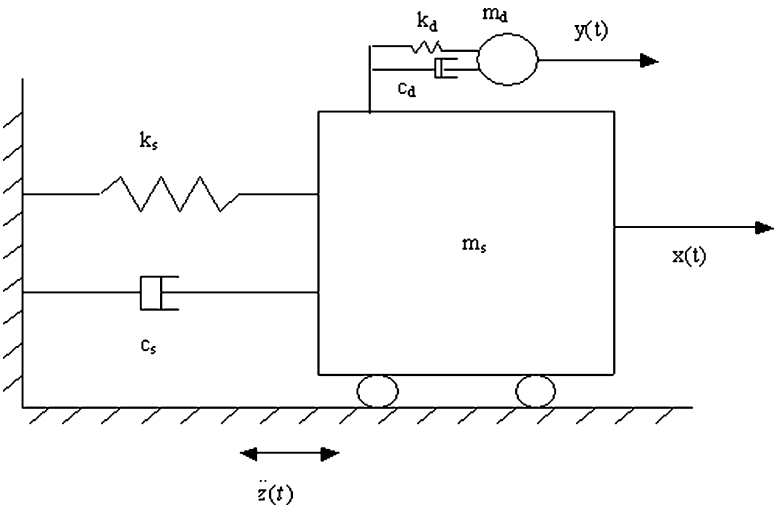

Fig. 2 Model of TLD-elevated water tank system

SDOF system representing the elevated water tank are m_s, k_s and c_s respectively. The damping ratio and the natural frequency of the same are ζ_s and ω_s.

3 Formulation of Transfer Function

3.1 Equations of Motion

Let $x(t)$ denote the horizontal displacement of the SDOF structural system relative to ground motion at a time instant t. Further, $y(t)$ represents the displacement of the convective water mass of the TLD relative to the structure at time instant t.

The equation of motion of m_d can be written as

$$\ddot{y}(t) + \ddot{x}(t) + 2\zeta_d \omega_d \dot{y}(t) + \omega_d^2 y(t) = -\ddot{z}(t). \tag{1}$$

Consideration of the dynamic equilibrium of the TLD-elevated water tank system gives

$$\ddot{x}(t) + 2\zeta_s \omega_s \dot{x}(t) + \omega_s^2 x(t) - 2\zeta_d \omega_d \mu \dot{y}(t) - \omega_d^2 \mu y(t) = -\ddot{z}(t), \tag{2}$$

where $\mu = m_d/m_s$ is the ratio of the convective liquid mass within the TLD to the mass of the structural mass.

On Fourier transforming Eqs. (1) and (2) and by appropriate substitution, the following transfer function relating the structural displacement to the input ground acceleration is obtained in frequency domain

$$X(\omega) = \frac{\{\mu[2\zeta_d\omega_d i\omega + \omega_d^2]H_1(\omega) - 1\}H_2(\omega)}{\{\mu[2\zeta_d\omega_d i\omega + \omega_d^2]\omega^2 H_1(\omega)H_2(\omega) - 1\}} \ddot{Z}(\omega),$$

where $H_1(\omega) = -\frac{1}{\omega_d^2 - \omega^2 + 2\zeta_d\omega_d i\omega}$, $H_2(\omega) = -\frac{1}{\omega_s^2 - \omega^2 + 2\zeta_s\omega_s i\omega}$ and $X(\omega)$ and $\ddot{Z}(\omega)$ are the Fourier transforms of the corresponding time-dependent variables, $x(t)$ and $\ddot{z}(t)$ respectively.

4 Numerical Study in Frequency Domain

For numerical investigation, an example elevated water tank structure is considered. To examine the performance of TLD for the passive control of elevated water reservoir, the following realistic reinforced concrete tank structure with flat top cylindrical container and shaft-type staging is taken as the example structure. The relevant data that are assumed to define the structure are listed below:

Height of shaft support = 30 m; mean diameter of shaft = 3 m; thickness of shaft wall = 0.125 m; inner height of the tank container = 4 m; mean diameter of the tank container = 10 m; thickness of the container wall = 0.2 m; thickness of the container bottom = 0.2 m; thickness of the top cover of the container = 0.1 m; height of water in the tank container = 3.8 m.

Based on the above assumed data, the three-dimensional modelling of the example tank structure is analysed using the software package Staad.Pro2004. The fundamental natural frequency of the structure is found to be 4.5432 rad/s (1.383 s) for empty condition of the water tank and 3.625 rad/s (1.733 s) for full condition of the water tank. The value of the structural damping is assumed to be 1%.

The performance criterion of the TLD is the reduction in the rms value of the displacement of the elevated water tank system. To investigate the influence of mass ratio (the ratio of the convective water mass in the damper to the mass of the structure) in the structural response reduction, the values of mass ratio considered, are 1%, 2% and 5%. The value of ζ_d is taken as 0.01 as per Veletsos and Tang [14]. The whole system is subjected to a white noise PSDF input with $S_o = 100\ \text{cm}^2/\text{s}^3$.

To investigate the effect of the TLD, the same structure with a TLD located at the top is considered. The natural frequency of the structural system varies between the values corresponding to the full condition to that for the empty condition of the tank as the water mass in the water tank is a variable quantity. Thus, if the TLD is tuned to a particular frequency of the tank, there will be some amount of detuning as the water content of the tank changes. The effect of this detuning on the performance of the damper is studied for two cases, viz., when the damper is tuned to the structural frequency corresponding to the full condition of

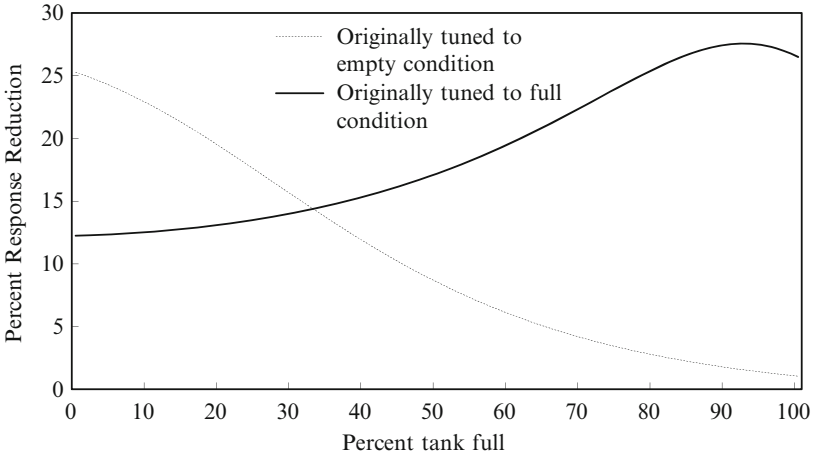

Fig. 3 Variation of percent response reduction with percent tank full

the tank and when the damper is tuned to the structural frequency corresponding to the empty condition of the tank. The response reduction varies from 12 to 26% when the damper is tuned to the structural frequency corresponding to the full condition of the tank (Fig. 3). The response reduction varies from 1 to 25% when the damper is tuned to the structural frequency corresponding to the empty condition of the tank. Thus, the results of this particular case study with mass ratio of 1% and tuning ratio (the ratio of the frequency of the TLD to the structural frequency) of unity indicated in Fig. 3 show that the performance of TLD is better if it is designed to be tuned to the frequency corresponding to the full condition of the tank. Thus, in this study, the TLD is kept tuned, with a tuning ratio of unity, to the frequency corresponding to the full condition of the tank.

Figure 4 shows the displacement transfer function curve for the structure in full condition of the tank without and with damper, subjected to ground acceleration process with white noise PSDF. Figure 4 also shows the displacement transfer function curves in full condition of the tank for different mass ratios, and it is observed that as compared to the without damper curve, now there are two peaks in each transfer function curve. Since the damper is tuned to the structural frequency, the tuning effect can be understood by the presence of the two peaks of reduced amplitude on either side of the peak of the 'without damper' curve. The nature of the curves is similar for the cases of 1%, 2% and 5% mass ratio. However, the reduction in the amplitude of the peaks due to the presence of the damper is dependent on the mass ratio. The greatest reduction for full condition of water tank is obtained for the case of 1% mass ratio. Here, the modelling of the TLD is very similar to a TMD. Generally, for a TMD, the response reduction increases with increase in mass ratio. To study the converse behaviour in the present case, a study is made on the response reduction achieved by a TMD with

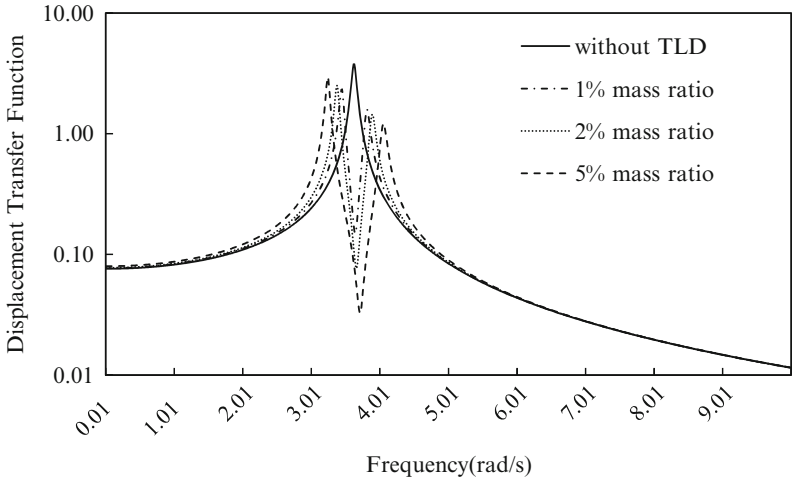

Fig. 4 Displacement transfer function of structure in full condition of the tank

Fig. 5 Variation of percent response reduction with tuning ratio and damping ratio for 1% mass ratio

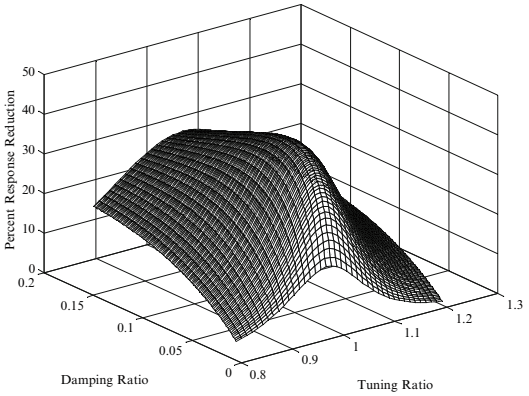

variation in tuning ratio and damping ratio for 1% and 5% mass ratio as shown in Figs. 5 and 6, respectively. A numerical illustration of the percent response reduction achieved by the damper for the full and empty conditions of the tank for the three different mass ratios is presented in Table 1.

Thus, from Table 1, it is seen that the response reduction varies in the range 6%–26% for 1% mass ratio, 10%–25% for 2% mass ratio and 19%–21% for 5% mass ratio. Hence, significant response reduction is achieved by the TLD.

Further, the sensitivity of the performance of the TLD to tuning ratio is examined. The variation in the response reduction achieved by the TLD system,

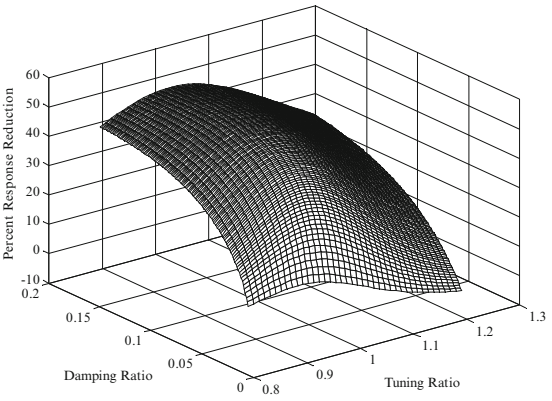

Fig. 6 Variation of percent response reduction with tuning ratio and damping ratio for 5% mass ratio

Table 1 Comparison of the percent response reduction by the TLD for different mass ratios with white noise PSDF input

Mass ratio (%)		Percentage reduction in RMS value of structural displacement	Tuning ratio
1	Empty condition	6.22	0.7979
	Full condition	26.48	1.0
2	Empty condition	10.59	0.7979
	Full condition	25.66	1.0
5	Empty condition	19.59	0.7979
	Full condition	21.73	1.0

in terms of the rms displacement of the structure, over a range of tuning ratio values, for the different values of mass ratios is observed (Fig. 7). From that study, it is found that optimal tuning ratios are 0.98, 0.97 and 0.92 for mass ratio equal to 1%, 2% and 5% respectively.

5 Simulation Study

The fourth-order Runge-Kutta method is being employed for time history analysis. The example structure is subjected to the recorded accelerogram of the El Centro earthquake. The TLD is tuned, with a tuning ratio of unity, to the frequency corresponding to the full condition of the tank, and mass ratio of 1%

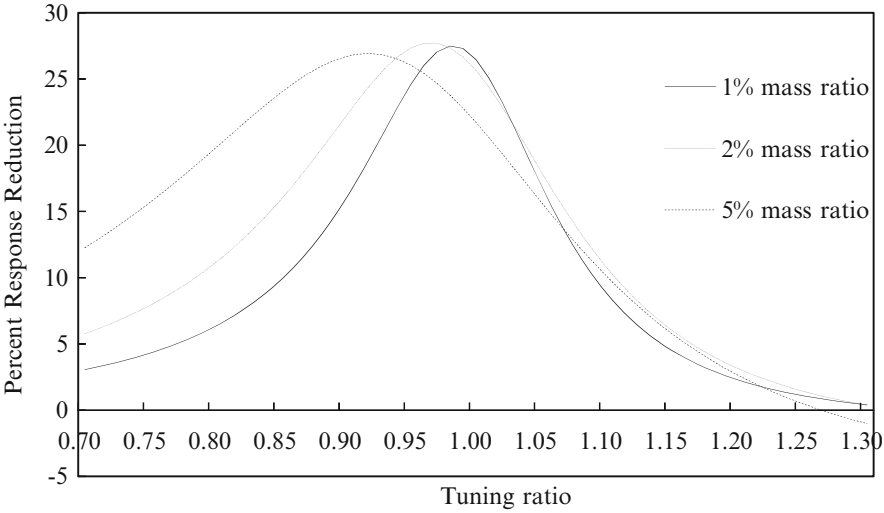

Fig. 7 Percent response reduction with tuning ratio for different mass ratios for full condition of the tank

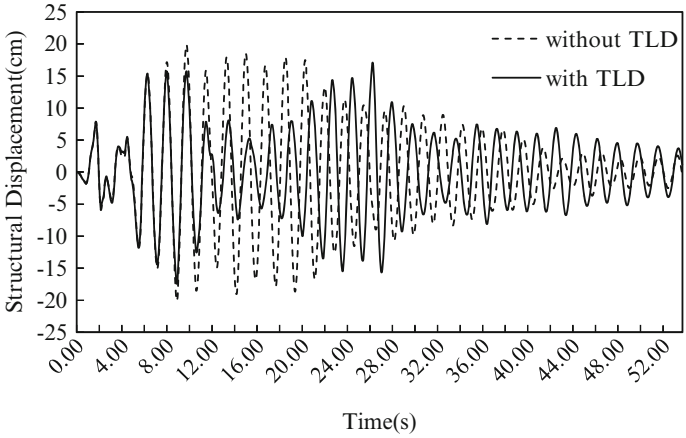

Fig. 8 Displacement Time history of SDOF structural system to E1 Centro earthquake when the tank is full

is considered. The displacement time history of the structure alone and with the TLD system for full condition of the tank is presented in Fig. 8. The response reduction achieved by the TLD system in terms of the rms displacement of the structure is 18.46% and that in terms of the peak displacement of the structure is 13.34% for full condition of the tank. The effect of detuning that occurs when

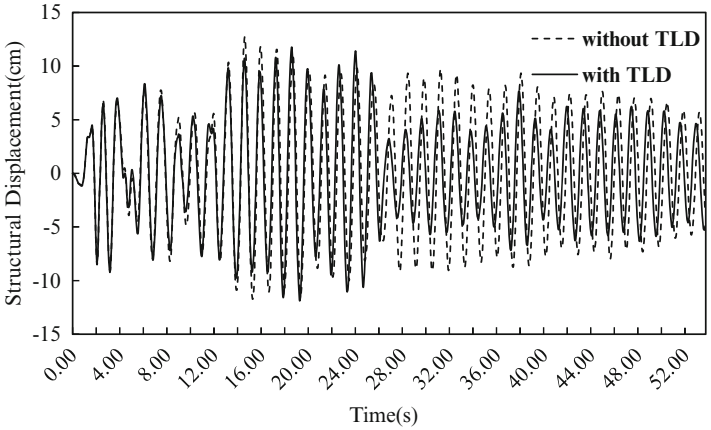

Fig. 9 Displacement Time history of SDOF structural system to E1 Centro earthquake when the tank is empty

the tank is empty is shown in Fig. 9. In this case, the response reduction achieved by the TLD system in terms of the rms displacement of the structure is 14.94% and that in terms of the peak displacement of the structure is 6.93% for empty condition.

6 Design of TLD System

The design parameters of TLD system (Fig. 1) are (1) mass ratio, (2) tuning ratio, (3) no. of TLD, (4) radius of TLD container (a), (5) height of liquid in TLD (h), (6) height of TLD container (H) and (7) h/a ratio.

The parameters should be chosen in such a way that they are compatible with the practical situation, and the TLD system should give sufficient response reduction. The studies carried out show that about 26.48% reduction in the RMS value of the displacement of the structure may be achieved by the TLD when tuned to the full condition of the tank with a tuning ratio (the ratio of the frequency of the TLD to the structural frequency) of unity for a corresponding mass ratio (convective water mass in the TLD/total mass of the structure) of about 1%. As it is not practicable to go for a very high mass ratio, 1% mass ratio is adopted. The optimum tuning ratio for 1% mass ratio is obtained as 0.98. So, a tuning ratio of 0.98 is adopted. The TLD is tuned to the frequency corresponding to the full condition of the tank. The ratio of depth of water to radius of damper container (h/a ratio) is chosen as 0.3. The radius of the TLD container (a), the height of liquid in the TLD container (h) and the height of the TLD container (H) for a single unit of damper as in Fig. 1 are designed to be 0.7 m, 0.21 m and 0.4 m,

respectively. The number of TLD required to provide the total water mass in the TLD system is 20. So 20 dampers are to be accommodated on the top of the elevated water tank container. These dampers are to be stacked. The total area required to accommodate dampers is available on the top of the elevated water tank container. The design frequency of the damper is 3.599 rad/s. The design tuning ratios are 0.993 and 0.792 for full and empty condition of the elevated water tank container respectively.

7 Performance of the Designed TLD System

The performance is observed through reduction in rms displacement of the structure in time domain and in frequency domain. In time domain, the reduction in peak displacement of the structure is also evaluated. In frequency domain study, white noise PSDF with intensity of 0.01 m^2/s^3 is chosen as the base input excitation. In case of time history analysis, the recorded accelerogram of the El Centro earthquake is taken as the input excitation.

Representative set of transfer function curve for the full condition of the water tank is given in Fig. 10 and is compared with that of the structure without damper. The variation of percent response reduction with percent content of water in the water tank is presented in Fig. 11.

The numerical value of the response reduction achieved by the TLD system varies between 11% and 27% from empty to full condition of the water tank for the designed tuned condition for white noise PSDF. The displacement time history of the TLD-structural system for full condition is presented in Fig. 12.

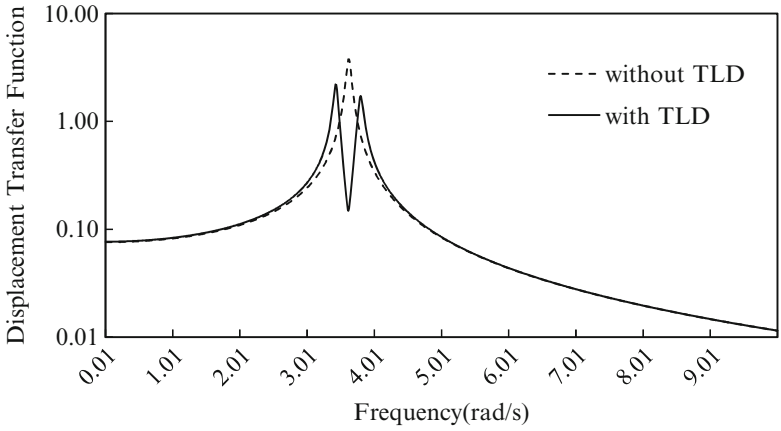

Fig. 10 Displacement transfer function of structure in full condition of the tank with designed TLD

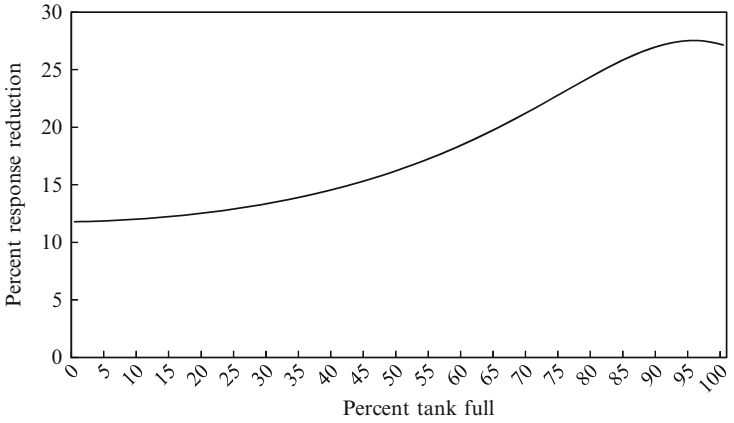

Fig. 11 Variation of percent response reduction with percent tank full

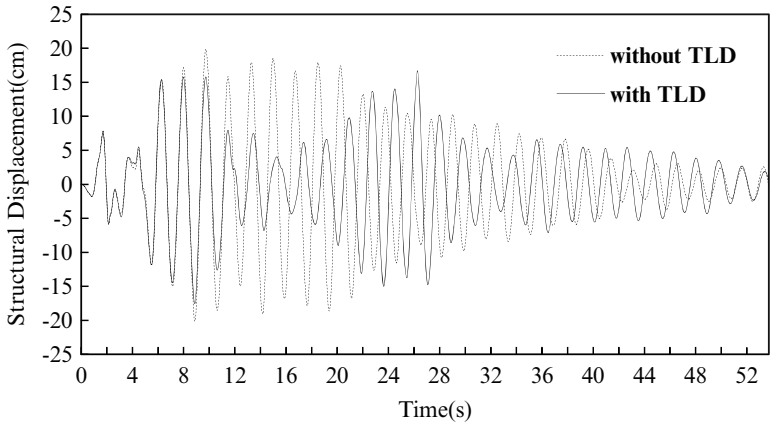

Fig. 12 Displacement Time history of SDOF structural system to E1 Centro earthquake when the tank is full

The response reduction achieved by the TLD system in terms of the RMS displacement of the structure is 22.94% and that in terms of the peak displacement of the structure is 12.89% for full condition of the tank. The effect of detuning that occurs when the tank is empty is clear from Fig. 13 where the response reduction achieved by the TLD system in the RMS displacement of the structure is 14.11%, while that in the peak displacement of the structure is 8.16%.

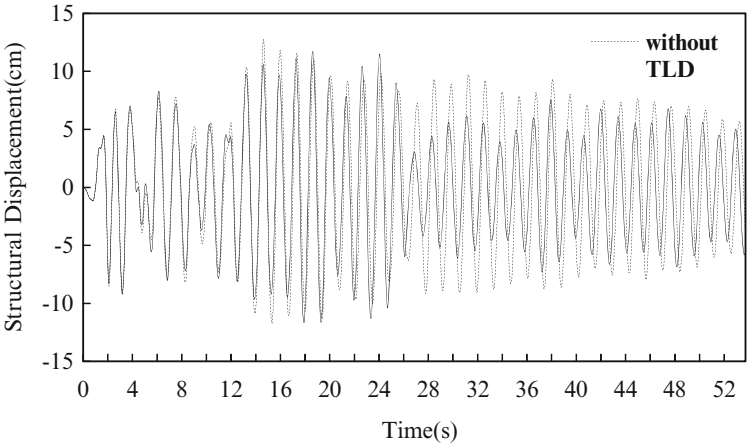

Fig. 13 Displacement Time history of SDOF structural system to E1 Centro earthquake when the tank is empty

8 Conclusions

Through this work, the applicability of TLD as a seismic vibration response reduction device for an elevated water tank is investigated. An attempt is also made to design a TLD system for a realistic elevated water tank structure. The performance of the damper system is evaluated both in frequency domain as well as in time domain. Based on the observations during the study, the following conclusions are drawn about the TLD system:

- The numerical study indicates that a TLD can be used as a promising control device for the seismic vibration suppression of elevated water tank structures. The results in frequency domain study show that substantial reduction in rms value of structural response upto 27% may be achieved by the TLD in the tuned condition, while this response reduction may be 18% as illustrated by the results of the simulation study. The reduction in case of peak displacement as obtained in time domain is 13%.
- The performance of the TLD system is better if it is tuned to the frequency corresponding to the frequency of structure in tank full condition out of the two possibilities of tuning to the frequency corresponding to the frequency of structure in empty and full condition of the tank. The reduction in the rms value of the structural response varies from 12% to 27% over the range of structural frequencies from empty condition to full condition of the tank.
- In this study, the percent response reduction is evaluated in the possible range of detuning of the damper system for the different mass ratios of the TLD system. The results indicate that the optimum tuning ratio is very close to unity for a lower mass ratio of 1%.

- The design example of the TLD system for realistic elevated water tank reveals that it will be possible to get a feasible configuration of the damper. In frequency domain, a maximum reduction of about 27% is achieved by the designed damper system even with a relatively lower mass ratio. In the extreme condition of detuning, at least 11% of response reduction is obtained. Using recorded accelerogram as input, the reduction in rms displacement of structure is 22% when the tank is full. When the tank becomes empty, it becomes 14%. The reduction in peak displacement of structure, as obtained, is 12% for the tank full condition, while that for the tank empty condition is 8%.

References

1. Banerji P, Murudi M, Shah AH, Popplewell N (2000) Tuned liquid dampers for controlling earthquake response of structures. Earthq Eng Struct Dyn 29:587–602
2. Fujino Y, Pacheco BM, Chaiseri P, Sun LM (1988) Parametric studies on tuned liquid damper (TLD) using circular containers by free-oscillation experiments. Struct Eng/Earthq Eng JSCE 5(2):381–391
3. Housner GW (1957) Dynamic pressures on accelerated fluid containers. Seismol Soc Am 47 (1):15–35
4. Kim YM, You KP, Cho JE, Hone DP (2006) The vibration performance experiment of tuned liquid damper and tuned liquid column damper. J Mech Sci Technol 20(6):795–805
5. Koh CG, Mahatma S, Wang CM (1994) Theoretical and experimental studies on rectangular liquid dampers under arbitrary excitations. Earthq Eng Struct Dyn 23:17–31
6. Rai DC (2002) Review of code design forces for shaft supports of elevated water tanks. In: Proceedings of 12th symposium on earthquake engineering, IIT Roorkee, 16–18 Dec, pp 1407–1418
7. Shenton HW III, Hampton FP (1999) Seismic response of isolated elevated water tanks. J Struct Eng ASCE 125(9):965–976
8. Shrimali MK, Jangid RS (2003) Earthquake response of isolated elevated liquid storage steel tanks. J Constr Steel Res 59:1267–1288
9. Shrimali MK, Jangid RS (2006) Seismic performance of elevated liquid tanks isolated by sliding systems. In: Proceedings of first European conference on earthquake engineering and seismology, Geneva, Switzerland, 3–8 Sept 2006
10. Shrimali MK (2008) Earthquake response of elevated liquid storage tanks isolated by FPS under bi-direction excitation. Adv Vib Eng 7(4):389–405
11. Soong TT, Dargush GF (1997) Passive energy dissipation systems in structural engineering. Wiley, UK
12. Tait MJ, Deng X (2010) The performance of structure – tuned liquid damper systems with different tank geometries. Struct Control Health Monit 17:254–277
13. Tait MJ, Isyumov N, El Damatty AA (2008) Performance of tuned liquid dampers. J Eng Mech 134(5):417–427
14. Veletsos AS, Tang Y (1990) Soil-structure interaction effects for laterally excited liquid storage tanks. Earthq Eng Struct Dyn 19:473–496
15. Welt F, Modi VJ (1989a) Vibration damping through liquid sloshing: part I – a nonlinear analysis. Proceedings of diagnostics, vehicle dynamics and special topics. ASME, Design Engineering Division (DE) 18(5):149–156.
16. Welt F, Modi VJ (1989b) Vibration damping through liquid sloshing: part II –experimental results. Proceedings of diagnostics, vehicle dynamics and special topics. ASME, Design Engineering Division (DE) 18(5):157–165
17. Yu JK, Wakahara T, Reed DA (1999) A non-linear numerical model of the tuned liquid damper. Earthq Eng Struct Dyn 28:671–686

Structural Reliability Evaluation and Optimization of a Pressure Vessel Using Nonlinear Performance Functions

P. Bhattacharjee, K. Ramesh Kumar, and T.A. Janardhan Reddy

Abstract Structural safety is one of the most important factors of any aerospace product. Until recently, a design is considered to be robust if all the variables that affect its life has been accounted for and brought under control. The meaning of robustness is changing. Designer and engineers have traditionally handled variability with safety factors. In this chapter, in the first phase, a pressure vessel made of titanium alloy is considered for safety index (structural reliability) study. The safety index is evaluated based on the data collected during manufacturing and operation. Various methods like mean value and moment methods are used for safety evaluation and same have been discussed. In the second phase of this chapter, an attempt has been made to carry out multi-objective design analysis taking into account the effect of variation of design parameters. Multiple objective of interests include structural weight, load-induced stress, deflection and structural reliability. The design problem is formulated under nonlinear constrained optimization and has been solved. Nonlinear regression relations are used for various performance functions. Nonlinear regression model is validated and found to be in good agreement with experimental results. Finally, optimum design parameters are suggested for design operating conditions.

Keywords Structural Reliability • Pressure Vessel • Safety Index and Nonlinear Constrained Optimization

P. Bhattacharjee (✉)
Reliability Engineering Division, DRDL, Hyderabad, India
e-mail: pradeep9_rqa@yahoo.com

K.R. Kumar
Production Planning Division, DRDL, Hyderabad, India
e-mail: rkkatta@rediffmail.co

T.A.J. Reddy
Mechanical Engineering, Osmania University, Hyderabad, India
e-mail: thanam.engineer@gmail.com

S. Chakraborty and G. Bhattacharya (eds.), *Proceedings of the International Symposium on Engineering under Uncertainty: Safety Assessment and Management (ISEUSAM - 2012)*,
DOI 10.1007/978-81-322-0757-3_35,

1 Introduction

Probabilistic structural design evaluation method is fast growing in aerospace engineering. In this method, all uncertainties like variability in material properties, geometry and loads are considered during design which enables a product to have better reliability compared to deterministic design. The study of reliability engineering is also developing very rapidly. The desire to develop and manufacture a product with superior performance and reliability than its predecessor is a major driving force in engineering design. The design of any engineering system requires the assurance of its reliability and quality. Traditional deterministic method has accounted for uncertainties through empirical safety factor. Such safety factors do not provide a quantitative measure of safety margin in design and are not quantitatively linked to influence different design variables and their uncertainties on overall system performance. In this chapter, a titanium air bottle (pressure vessel) is identified for structural safety index study. These air bottles are extensively used in aerospace and ground operations. The detailed safety index evaluation is discussed in this chapter.

Generally, the objective and constraint functions, load conditions, failure modes, structural parameters and design variables are treated in a deterministic manner. The problem with this approach is that, in many cases, deterministic optimization gives designs with higher failure probability than optimized structures. Therefore, since uncertainties are always present in the design for engineering structure, it is necessary to introduce reliability theory in order to achieve a balance between cost and safety for optimal design. A straightforward approach for the modelling and analysis of uncertainties is to introduce probabilistic models in which structural parameters and/or design variables are considered stochastic in nature. Then, by the combination of reliability-based design procedures and optimization technique, it is possible to devise a tool to obtain optimal designs.

The aim of this work is to establish a simple methodology, which will be useful to pressure vessel designer during design and development. This chapter deals with analysis of a typical titanium pressure vessel that is used to store high-pressure air, nitrogen or inert gas to run turbine to generate power as well as for pneumatic actuation for control system. These bottles have to be safe and reliable and shall be of lower weight. The optimum design problem formulated under nonlinear constrained optimization using nonlinear regression has been solved as 'Nonlinear Constrained Minimization' optimization. Optimum parameters of air bottle are suggested for design operating pressure.

2 Nomenclature

a, b, c: Regression coefficient
$g(x)$: Performance function
P: Pressure

p_f: Probability of failure
R: Reliability
R^2_{adj}: Adjusted R-square
R^2: Regression square
R_i: Internal radius
R_0: External radius
s, M: Material strength
t: Thickness
U, u, Z: A vector of statistically independent random variables with zero mean and unit standard deviation
V: Volume
W: Weight
β: Safety index
β_0: Design safety index requirement
γ: Poisson's ratio
δ: Deformation
μ_M: Mean material strength
μ_σ: Mean induced stress
ρ: Density
σ: Stress/standard deviation
σ_M: Standard deviation of material strength
σ_σ: Standard deviation of induced stress
Φ: Normal cdf

3 Problem Statement and Methodology Adapted

Weight optimization is one of the prime requirements of any aerospace product. Aerospace product has to be optimum in respect of weight, size, volume, cost, etc. Any weight-saving results in increase in payload capacity. Similarly, packaging density can be increased with volume optimization. But all these design optimizations should not be at the cost of safety and reliability. In this chapter, we have identified a pressure vessel which has already been designed, developed and successfully used in various grounds and space vehicles applications. These air bottles operate at very high pressure and are filled with dry air, nitrogen or inert gas. Due to its higher operating pressure, it has to be totally safe as ground personnel handle these bottles in fully charged condition.

In the first phase, safety index (structural reliability) is evaluated using mean value method (MVM) and advanced first-order second-moment (AFOSM) method using data collected during manufacturing and testing. In the second phase, an

attempt is made to optimize the weight of the air bottle to meet the target reliability. Finite element analysis (FEA) is carried out to generate maximum stress, strain and deformation for various design parameters and operating conditions. Nonlinear performance functions (regression relations) are established for stress and deflection.

4 Safety Index Evaluation

4.1 Mean Value Method

This method [1–3] is commonly referred to as the mean value first-order second-moment (MVFOSM or simply MV) method since it involves a first-order expansion about the mean to estimate the first and second moments. MV method involves developing the Taylor series expansion of $g(x)$ about the nominal or mean value of the individual random variables. The moments of the resulting approximating function are found, using which approximate statements can be made regarding the probability of failure.

$$g(x) = g(x_1, x_2, \ldots x_n); \quad \text{safety index } \beta = \frac{\mu_g}{\sigma_g}$$

where $\mu_g$and σ_g are the mean and standard deviation of performance function.

4.2 Advanced First-Order Second-Moment

Hasofer and Lind (HL) [4–6] proposed a method for evaluating the safety index (β). According to HL approach, the constraint is linearized by using Taylor series expansion retaining up to the first-order terms. The linearization point selected is that of maximum likelihood of occurrence and is known as the most probable failure point. This method is called advanced first-order second-moment (AFOSM) method. The most probable failure point is determined by transforming original random variables to normalized and independent set of reduced variables as shown in Fig. 1.

$$U = \frac{x - x_\mu}{x_\sigma} \tag{1}$$

The failure surface is mapped onto the corresponding failure surface in the reduced space. The point on this surface with minimum distance from the origin is the most probable failure point, and the geometric distance to the origin is equal

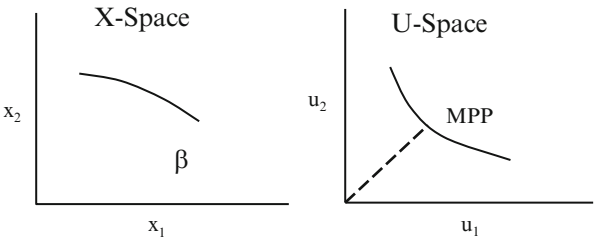

Fig. 1 Transformation of coordinate into standard space

to the safety index β. The failure surface is generally a nonlinear function, and the point with minimum distance to the origin can be evaluated by solving the following optimization problem, that is,

$$\text{Minimize } \left(U^T U\right)^{\frac{1}{2}} = \beta \tag{2}$$

$$\text{Subject to } g(U) = 0$$

where $g(U)$ is the failure function or limit state equation in reduced space. Using AFOSM, this optimization can be solved by using nonlinear optimization or iterative algorithms.

5 Optimization Formulation

This chapter deals with a practical problem of high-pressure air bottles. In the first phase of the study, we have evaluated the safety index (structural reliability) of these air bottles. After confirming that these air bottles have enough margins of safety, an attempt has been made to optimize the weight of the air bottles. These air bottles are at present under serial production and are being used in various ground and space applications. Static linear strength, deformation and safety index have been considered as design constraints. The brief optimization formulation of this problem is discussed below.

5.1 Nonlinear Performance Functions

5.1.1 Nonlinear Regression Relations

The regression relations [7] are established for induced stress and deformation due to internal load. In many engineering situations, the relationship between dependent and independent variable may not be linear but exponential, Weibull, logarithmic or inverse type. These types of equations generally fall under the category of having

Table 1 ANSYS output

		Design load 40 MPa	
Thickness (t)	Outer radius (R_0)	Hoop stress (σ) MPa	Deformation (δ) mm
2.5	152.0	1,233	1.0555
3.0	152.5	1,007	0.8819
3.5	153.0	885	0.7567
4.0	153.5	746	0.6644
4.5	154.0	665	0.5927
5.0	154.5	599	0.5353
5.5	155.0	544	0.4883
6.0	155.5	500	0.4492
6.5	156.0	461	0.4161
7.0	156.5	428	0.3877
7.5	157.0	399	0.3632
8.0	157.5	375	0.3417
8.5	158.0	358	0.3227

nonlinear parameter. In order to apply the principles of least squares, the equation should be reduced to linear form. The process of transforming the nonlinear equation into a linear form is called linear transformation. It is observed from ANSYS output data, Table 1, that the hoop stress and deflection have nonlinear relation with its wall thickness and outer radius. A logarithmic relation has been established and tested statistically for significance. The regression relations considered are as given below:

$$\log \sigma = a_1 + b_1 \log t + c_1 \log R_0 \tag{3}$$

$$\log \delta = a_2 + b_2 \log t + c_2 \log R_0 \tag{4}$$

The wall thickness of the hemispherical shell and outer radius of the air bottle are the main design geometrical parameters which account for weight. Hence, these parameters are considered for weight optimization. The nonlinear performance function relations for stress and deformation are as given below:

$$\sigma = a_1 t^{b_1} R_0^{c_1} \tag{5}$$

$$\delta = a_2 t^{b_2} R_0^{c_2} \tag{6}$$

Load-induced stress and deformation under various operating load (pressures) is evaluated using finite element analysis (ANSYS), where a_1, a_2, b_1, b_2, c_1 and c_2 are the coefficients of above regression equations. The nonlinear regressions established are given in Table 2.

Table 2 Nonlinear regression equations

Design load	$\sigma = a_1 t^{b_1} R_0^{c_1}$	$\delta = a_2 t^{b_2} R_0^{c_2}$
40 (MPa)	$\sigma = 0.0059 t^{-1.0967} R_0^{2.6386}$	$\delta = 0.00037 t^{-1.0242} R_0^{1.7701}$

5.2 Optimization Constraints

5.2.1 Static Linear Strength

The static linear strength [8] design criteria are based on load-induced stress at the critical location in the spherical shell should be less than or equal to maximum allowable stress. In other words, the maximum stress generated due to internal pressure should not exceed the material strength as defined below:

$$\frac{\sigma}{\sigma_{\max}} - 1 \leq 0 \tag{7}$$

5.2.2 Deformation

The spherical air bottle will dilate radially outward due to internal pressure. In no case the air bottle shall deform beyond maximum allowable deflection, that is,

$$\frac{\delta}{\delta_{\max}} - 1 \leq 0 \tag{8}$$

5.2.3 Safety Index (Structural Reliability)

The safety index β is defined as

$$\beta = -\frac{\mu_M - \mu_\sigma}{\left(\sigma_M^2 + \sigma_\sigma^2\right)^{\frac{1}{2}}} \tag{9}$$

$$\beta \geq \beta_0; 1 - \frac{\beta}{\beta_0} \leq 0$$

where β_0 is design safety index requirement.

'β' is achieved safety index and is evaluated using strength-stress interference model. In this chapter, both material strength and induced stress are considered normally distributed to be random variable.

5.3 Nonlinear Constrained Optimization

The main objective is to minimize the weight of the air bottle, without compromising the safety requirement. A nonlinear single objective constrained optimization method is adapted. The nonlinear regression equations as given in Table 2 are used for optimization formulation [9–11]. The optimization problem formulation is as given below:

Objective function

Minimize $W = \rho V$

Subject to

$$\frac{\sigma}{\sigma_{\max}} - 1 \leq 0; \quad \frac{\delta}{\delta_{\max}} - 1 \leq 0; \quad 1 - \frac{\beta}{\beta_0} \leq 0$$

where $\sigma = a_1 t^{b_1} R_0^{c_1}$; $\delta = a_2 t^{b_2} R_0^{c_2}$; $\beta = \frac{\mu_M - \mu_\sigma}{\left(\sigma_M^2 + \sigma_\sigma^2\right)^{\frac{1}{2}}}$; $V = \frac{4}{3}\pi\left[3R_0^2 t - 3R_0 t^2 + t^3\right]$

Bound constraints $t_l < t < t_u$ and $R_{0\,l} < R_0 < R_{0\,u}$

l and u are lower and upper design limit.

6 Nonlinear Performance Function Generation

6.1 Finite Element Analysis

To establish the performance function relations, the ANSYS output is generated for each set of design input parameters, that is, wall thickness and outer radius of spherical shell. The details of ANSYS output are given in Table 1.

6.2 Nonlinear Regression and Regression Statistics

The nonlinear regression of induced stress (σ) and deformation (δ) versus wall thickness (t) and outer radius (R_0) is established using ANSYS output as given in Table 1. These regression equations are used for optimization formulation. The nonlinear regression and regression statistics are given in Tables 2 and 3.

R^2_{adj}: Adjusted regression square; rmse: root mean square error; mse: mean square error as R^2_{adj} values are close to one, and 'rmse' value is low indicating that the regression relations are fitting well.

Table 3 Regression statistics

Design load	$\sigma = a_1 t^{b_1} R_0^{c_1}$	$\delta = a_2 t^{b_2} R_0^{c_2}$
40 (MPa)	$R^2_{\text{adj}} = 0.9999$	$R^2_{\text{adj}} = 1.0000$
	rmse $= 0.0020$	rmse $= 0.0010$
	mse $= 3.9 * 10^{-6}$	mse $= 1.0377 * 10^{-6}$

7 Design Data

To evaluate safety index, initially design data are collected from design document. The important design parameters of the air bottle are given in Table 4.

A systematic data collection is carried out during manufacturing at production centres starting from raw material to final product. Material mechanical properties are taken from test certificates provided by the suppliers which cover chemical compositions, heat treatment details, tensile strength and percentage elongation. Similarly, thickness mapping for wall thickness and internal radius is carried out before joining of each spherical shell. The statistical dispersion of various parameters is given in Table 5.

8 Design Safety Analysis

8.1 Safety Index (Structural Reliability)

The structural safety [1] of the air bottle is evaluated considering the statistical variability from the data collected during manufacturing, testing and operation. The safety index (β) evaluated using mean value method and advanced first-order second-moment method as discussed in safety index evaluation section is as follows:

8.1.1 Mean Value Method

$$g = \left(s - \frac{PRi}{2t}\right) \tag{10}$$

$$\mu_g = 484.84$$

$$\sigma_g = \left[\left(\frac{\partial g}{\partial s}\sigma_s\right)^2 + \left(\frac{\partial g}{\partial P}\sigma_P\right)^2 + \left(\frac{\partial g}{\partial R}\sigma_R\right)^2 + \left(\frac{\partial g}{\partial t}\sigma_t\right)^2\right]^{\frac{1}{2}} \quad \sigma_g = 23.2585$$

$$\beta = \frac{\mu_g}{\sigma_g}; \quad \beta = 20.8$$

Table 4 Design parameter

Internal radius (R_i)	:	149.5 mm
Wall thickness (t)	:	8.0 mm
Design pressure (P)	:	40 MPa
Material	:	Titanium alloy
Construction	:	Welded
Type of welding	:	Electron beam
Weight	:	10.5 kg

Table 5 Variability observed

Parameter	Mean (μ)	Standard deviation (σ)
Operating pressure (P)	36 (MPa)	1.98 (MPa)
Internal radius (R_i)	149.5 (mm)	0.5 (mm)
Wall thickness (t)	7.91 (mm)	0.25 (mm)
Material strength (M)	860 (MPa)	8.6 (MPa)

8.1.2 Advanced First-Order Second-Moment Method

Data from Table 5 is transformed to normal space

$$Z_1 = \frac{s - s_\mu}{\sigma_s} = \frac{s - 860}{8.6}$$

$$Z_2 = \frac{P - P_\mu}{\sigma_P} = \frac{P - 40}{1.98}$$

$$Z_3 = \frac{R_i - R_\mu}{\sigma_R} = \frac{R_i - 149.5}{0.5}$$

$$Z_4 = \frac{t - t_\mu}{\sigma_t} = \frac{t - 7.91}{0.25}$$

$$s = 8.6Z_1 + 860$$

$$P = 1.98Z_2 + 40$$

$$R_i = 0.5Z_3 + 149.5$$

$$t = 0.25Z_4 + 7.91$$

Substituting s, P, R_i and t in Eq. 10

$$g(Z) = (8.6Z_1 + 860) - \left[\frac{(1.98Z_2 + 40)\,(0.5Z_3 + 149.5)}{2(0.25Z_4 + 7.91)}\right]$$

Minimize $\beta = \sqrt{Z^T Z}$
Such that $g(Z) = 0$
Solving the above optimization problem, we get $\beta = 14.39$

9 Reliability Optimization

9.1 Nonlinear Constrained Optimization

The main objective of this chapter is to minimize the weight of the air bottle as thickness, and outer radius are the design parameters which contribute to the weight of titanium material. Hence, these parameters are optimized so as to minimize the weight of the air bottle. The nonlinear constrained optimization [10–12] is formulated as given below:

Objective function

Minimize weight (W) $= V * \rho$

Subject to

$$\frac{\sigma}{\sigma_{\max}} - 1 \leq 0, \quad \frac{\delta}{\delta_{\max}} - 1 \leq 0, \quad 1 - \frac{\beta}{\beta_0} \leq 0$$

where $V(\text{volume}) = \frac{4}{3}\pi\left[3R_0^2 t - 3R_0 t^2 + t^3\right]$

$$\rho(\text{density}) = 4.46 * 10^{-6}\ \text{kg/mm}^3; \quad \sigma_{\max} = 860\ \text{MPa}; \quad \delta_{\max} = 0.5\ \text{mm}$$

β_0 (Target safety index) ≥ 4; R (Structural reliability) ≥ 0.99996; R_i (Internal radius) $= 149.5$;

σ (Induced stress) $= a_1 t^{b_1} R_0^{c_1}$; δ (Deformation) $= a_2 t^{b_2} R_0^{c_2}$

$\beta = -\frac{\mu_M - \mu_\sigma}{\left(\sigma_M^2 + \sigma_\sigma^2\right)^{\frac{1}{2}}}$; $\sigma_\sigma = 25.91$ (experimentally observed induced stress standard deviation)

$\mu_\sigma = \sigma$, $\mu_M = \sigma_{\max}$, $\sigma_M = 8.6$ MPa and P (design load) $= 40$ MPa

Rewriting the above optimization formulation,

Objective function

Minimize weight (W) $= \left[55.67R_0^2 t - 55.67R_0 t^2 + 18.5\, t^3\right]$

Subject to

$$6.8604 * 10^{-6} t^{-1.0967} R_0^{2.6386} - 1 \leq 0 \tag{11}$$

$$7.4 * 10^{-4} t^{-1.0242} R_0^{1.7701} - 1 \leq 0 \tag{12}$$

$$5.4 * 10^{-5} t^{-1.0967} R_0^{2.6386} - 6.875 \leq 0 \tag{13}$$

Inequality constraints

$3 < t < 8$ and $152.5 < R_0 < 157.5$

Solving the above optimization problem using nonlinear programming technique, the optimized design parameters obtained are given in Table 6.

Table 6 Optimized parameters

Parameter	Design	Optimized
Inner radius 'R_i'	149.5 mm	149.5 mm
Thickness 't'	8.00 mm	5.3453 mm
Outer radius 'R_0'	157.5 mm	154.8453 mm
Weight 'W'	10.5 kg	6.8919 kg
Safety index 'β'	14.39	6.0949

10 Results and Discussion

The structural reliability (safety index) study has been carried out using moment methods; the safety index 'β' is found to be high. This indicates that titanium air bottle is over designed, and these bottles are very safe at design operating pressure. Hence, this gives scope for weight optimization.

The nonlinear regression relation of performance functions established using ANSYS output is found to be useful for prediction of stress, strain and deformation. These relations are simple and help in optimization formulation. Many complex performance functions can be written in simple linear, nonlinear or polynomial forms.

Using the above findings, the weight of the existing air bottle is optimized without compromising quality, design and safety requirements. A net weight reduction of 3.5 kg is possible which in turn helps in increasing payload capacity for aerospace mission. The optimized safety index is now $\beta = 6.09$, that is, the probability of failure of this optimized air bottle is $p_f = 0.522\text{E-}09$.

11 Conclusion

A nonlinear constraint optimization for air bottle using regression model has been developed and found to be useful in their domain validity. This method accounts for effect of design variability while providing a realistic design model where conflicting and multi-objectives, namely, structural weight, operating load, induced stress, strain, deformation and structural reliability (safety index), exist. Suggested nonlinear regressions (nonlinear performance functions) are validated. In addition to design parameters, fatigue and fracture can also be considered in safety and optimization studies.

Acknowledgment The constant encouragement and support extended by Director DRDL and help rendered by Director R&QA, DRDL are gratefully acknowledged.

References

1. Bhattacharjee P (2009) Structural reliability assessment of pressure vessel. J Aerosp Qual Reliab 5:159–163
2. Robinson DG (1998) A survey of probabilistic methods used in reliability, risk and uncertainty analysis analytical techniques −1. Sandia report SAND 98:1189–1998
3. Wong FS (1985) First order second moment methods. Comput Struct 20(4):779–791
4. Melchers RE (1987) Structural reliability analysis and prediction. Ellis Harwood Limited, Chichester, pp 104–141
5. Shu HD, Wang MO (1992) Reliability analysis in engineering applications. Van Nostrand Reinhold, New York, pp 61–132
6. Sorensen JD (2004) Notes in structural reliability theory and risk analysis. Aalborg University, Aalborg
7. Montgomery DC (2004) Design and analysis of experiments. Wiley, New York
8. El-Sayed ME (1999) Structural optimization for reliability using nonlinear goal programming. NAGI – 1837
9. Kyumchoi S, Grandhi RV, Canfield RA (2006) Reliability – based structural design. Springer, London
10. Grandhi RV, Wang L (1999) Structural reliability analysis and optimization: use of approximations. Wright State University, Ohio. NASA/CR – 209154
11. Bhattacharjee P, Ramesh Kumar K, Janardhan Reddy TA (2010) Reliability design evaluation and optimization of a nitrogen gas bottle using response surface method. Int J ReliabQual Safety Eng 17(2):119–132
12. Bhattacharjee P, Janardhan Reddy TA, Ramesh Kumar K (2009) Structural reliability evaluation using response surface method. In: Proceedings of international conference on reliability, maintainability and safety. IEEE ICRMS, pp 972–977

Dynamic Response of Rectangular Bunker Walls Considering Earthquake Force

Indrajit Chowdhury and Jitendra Pratap Singh

Abstract In prevalent design of rectangular reinforced concrete bunkers, seismic effect on the wall is usually ignored. The stored material including the container is usually considered as a rigid body whose mass is lumped to the supporting frame by a rigid link. The seismic force induced therein is considered in the frame while walls of the bunker are designed for static pressure only. In this chapter, a method is proposed to estimate the dynamic pressures induced on the wall due to earthquake force, and when in the process, the dynamic amplification to the static pressure due to vibration of the frame is also induced in it. Finally, this pressure is utilized to determine the modal response of the bunker wall and estimate its coupled (wall + frame) response considering appropriate boundary condition.

Keywords Eigenvalues • Plate element • Galerkin's method • Rankine's formula • Dynamic pressure

1 Introduction

In different industries like power, oil and gas, and steel plants, rectangular bunkers are often deployed to store materials like coal, sulfur pellets, and coke either as an input or an output product. In many cases, it becomes essential that these storage vessels remain operable after a major earthquake, for their failures could lead to severe functional problem for the plant which is expected to remain operational even after such calamities.

The present state of art does not furnish any guidelines as to how to cater to the seismic force on such bunkers (especially the walls) and are left to the structural designer's personal judgment. Common methodology that is adapted is to assume

I. Chowdhury • J.P. Singh (✉)
Petrofac International Limited, Sharjah, UAE
e-mail: Indrajit.Chowdary@petrofac.com; jitendra.singh@petrofac.com

S. Chakraborty and G. Bhattacharya (eds.), *Proceedings of the International Symposium on Engineering under Uncertainty: Safety Assessment and Management (ISEUSAM - 2012)*,
DOI 10.1007/978-81-322-0757-3_36,

the bunker and its content as a lumped mass, and the force induced in it due to seismic vibration is transferred to the frame supporting the container [3, 5]. No procedure exists to assess the dynamic pressure that is induced on the wall due to seismic force and its amplification due to primary vibration of the supporting frame.

This chapter makes an attempt to develop a procedure based on which this dynamic pressure on the wall can be estimated and be catered for – a phenomenon that has been ignored till date

2 Proposed Method

The proposed method consists of two parts – (1) analysis of the bunker frame and (2) finally the dynamic response of the bunker wall – that are elaborated hereafter.

2.1 Analysis of Bunker Frame

The mathematical model as perceived for dynamic analysis of the bunker frame is a shown in Fig. 1.

Considering stiffness matrix $[K_F]$ and lumped mass matrix $[M_F]$ of the frame are given as

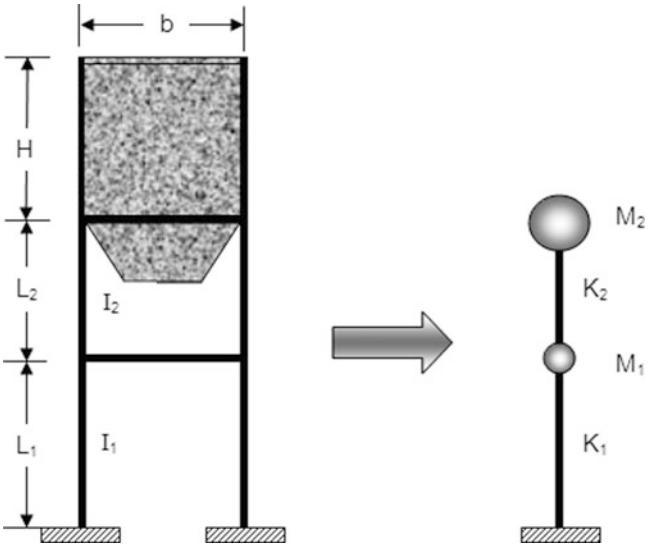

Fig. 1 Mathematical model of frame of rectangular bunker

$$[K_F] = \begin{bmatrix} K_1 + K_2 & -K_2 \\ -K_2 & K_2 \end{bmatrix} \text{ and } [M_F] = \begin{bmatrix} M_1 & 0 \\ 0 & M_2 \end{bmatrix} \tag{1}$$

where $K_1 = n\frac{12EI_1}{L_1^3}$ and $K_2 = n\frac{12EI_2}{L_2^3}$ are flexural stiffness of frame below and above tie level.

n = number of columns in the frame.
M_2 = mass of container and fill material.
M_1 = effective mass of column and beam at tie level.

The eigenvalue of the problem is given by

$$[\lambda] = \begin{bmatrix} K_1 + K_2 - M_1\lambda & -K_2 \\ -K_2 & K_2 - M_2\lambda \end{bmatrix} \tag{2}$$

Let λ_1 and λ_2 be the eigenvalues and let the corresponding eigenvectors be expressed as

$$[\phi] = \begin{bmatrix} \phi_{11} & \phi_{12} \\ \phi_{21} & \phi_{22} \end{bmatrix} \tag{3}$$

Normalized eigenvectors for first and second modes of vibration are given by

$$\begin{bmatrix} \phi_{11}^n \\ \phi_{21}^n \end{bmatrix} = \frac{1}{\sqrt{M_1\phi_{11}^2 + M_2\phi_{21}^2}} \begin{bmatrix} \phi_{11} \\ \phi_{21} \end{bmatrix} \text{ and}$$
$$\begin{bmatrix} \phi_{12}^n \\ \phi_{22}^n \end{bmatrix} = \frac{1}{\sqrt{M_1\phi_{12}^2 + M_2\phi_{22}^2}} \begin{bmatrix} \phi_{12} \\ \phi_{22} \end{bmatrix} \tag{4}$$

Modal participation factors are expressed as

$$\kappa_1 = \frac{M_1\phi_{11}^n + M_2\phi_{21}^n}{M_1\left(\phi_{11}^n\right)^2 + M_2\left(\phi_{21}^n\right)^2} \text{ and } \kappa_2 = \frac{M_1\phi_{12}^n + M_2\phi_{22}^n}{M_1\left(\phi_{12}^n\right)^2 + M_2\left(\phi_{22}^n\right)^2} \tag{5}$$

Let T_1 and T_2 be the time period of the frame corresponding to eigenvalues λ_1 and λ_2. Let $\frac{S_{a1}}{g}$ and $\frac{S_{a2}}{g}$ be the spectral acceleration coefficients from code for T_1 and T_2, respectively.

Design spectral acceleration coefficients at top of frame (node 2 of lumped mass model) for two modes of vibration are expressed as

$$\frac{D_{a1}}{g} = \kappa_1\beta\frac{S_{a1}}{g}\varphi_{21}^n \text{ and } \frac{D_{a2}}{g} = \kappa_2\beta\frac{S_{a1}}{g}\varphi_{22}^n \tag{6}$$

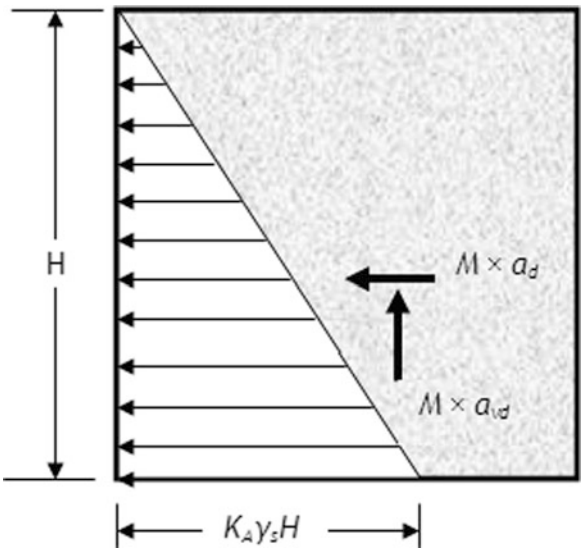

Fig. 2 Variation of pressure on vertical wall of bunker

where $\beta = \frac{ZI}{2R}$ is a code factor for seismic zone, importance, and response reduction factor [4].

The above accelerations will work on the container as shown Fig. 2.

During earthquake, pressure at any depth z from top is expressed as

$$p_h = K_A \gamma_s z + \gamma_s z \left(\frac{D_{ai}}{g}\right) + K_A \gamma_s z \left(\frac{2}{3}\frac{D_{ai}}{g}\right) \tag{7}$$

The last expression in Eq. (7) represents the effect of vertical acceleration on horizontal pressure on the bunker wall:

$$\text{or } p_h = K_A \gamma_s z \left[1 + \frac{1}{K_A}\frac{D_{ai}}{g} + \frac{2}{3}\frac{D_{ai}}{g}\right] \tag{8}$$

$$\text{or } p_h = K_A \gamma_s z \Lambda_i \tag{9}$$

$$\text{where } \Lambda_i = 1 + \frac{1}{K_A}\frac{D_{ai}}{g} + \frac{2}{3}\frac{D_{ai}}{g} \tag{10}$$

Here Λ is a dimensionless amplification factor for two modes of vibration ($i = 1, 2$) contributing to enhance the static wall pressure and shall always be $\geq$1.0.

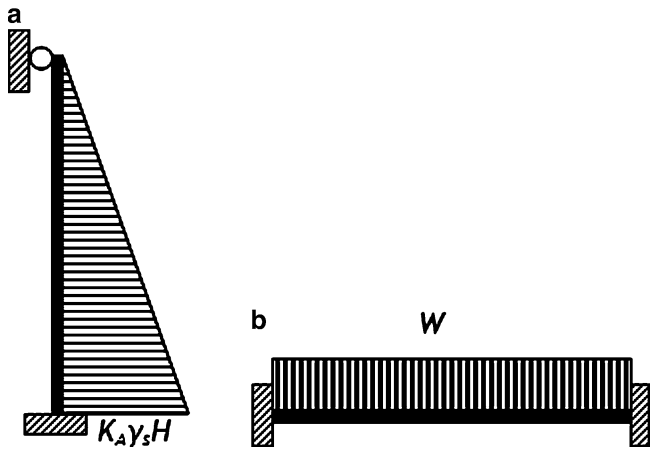

Fig. 3 (**a**) Propped cantilever and (**b**) fixed supported strips

2.2 Analysis of Bunker Wall

For analysis of the bunker wall, the wall is usually considered as three sides fixed and one side (the vertical top edge) as hinged – as in most of the cases, the roof is covered by removable precast slabs or steel checkered plates or gratings. Now considering a strip of the wall in vertical and horizontal direction, the boundary conditions and the loading on these strips are as shown in Fig. 3.

2.2.1 Shape Function of Plate

For propped cantilever strip as shown in Fig. 3a, displacement at depth z from the top is expressed as

$$\delta_z = \frac{K_A \gamma_s H^5 \Lambda_i}{30EI}\left[\frac{1}{4}\left(\frac{z}{H}\right)^5 - \frac{1}{2}\left(\frac{z}{H}\right)^3 + \frac{1}{4}\left(\frac{z}{H}\right)\right] \tag{11}$$

$$\text{or } \delta_z = \delta_{\text{static}} \times f(\xi) \tag{12}$$

where $\xi = z/H$ is a nondimensional term that varies between 0 and 1, and $f(\xi)$ is the generic shape function of propped cantilever beam given as

$$f(\xi) = \frac{\xi^5}{4} - \frac{\xi^3}{2} + \frac{\xi}{4} \tag{13}$$

Similarly, for a strip which is fixed at both ends in horizontal direction, the generic shape function of displacement can be expressed as

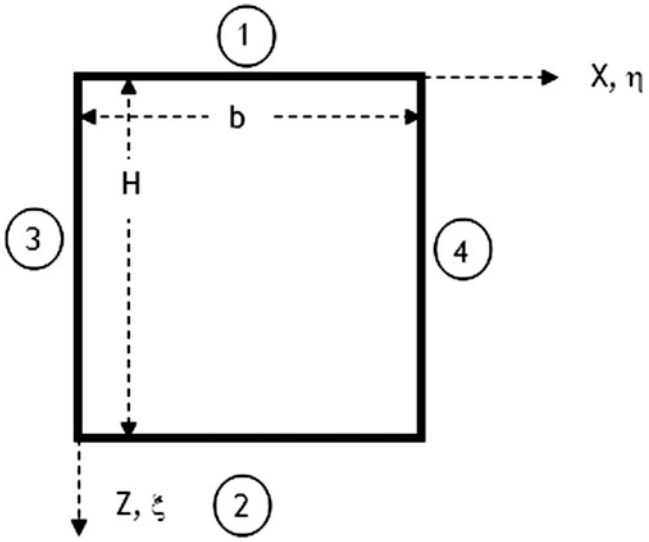

Fig. 4 Coordinate system of Bunker wall

$$f(\eta) = 16\eta^4 - 32\eta^3 + 16\eta^2 \tag{14}$$

where $\eta = x/b$ is a nondimensional term that varies between 0 and 1.

The shape functions derived in Eqs. (13) and (14) will generically satisfy plate equilibrium equation having boundary conditions of three sides fixed and one side propped but will have residual error (R_e) as they are not derived from exact analysis of the fourth order partial differential equation of an isotropic plate expressed as [6]

$$\frac{\partial^4 u}{\partial x^4} + 2\frac{\partial^4 u}{\partial x^2 \partial z^2} + \frac{\partial^4 u}{\partial z^4} = \frac{q}{D} \tag{15}$$

where u is displacement of the plate under a pressure load q. D is flexural stiffness of plate expressed as $D = Et^3/12(1 - v^2)$, and v is the Poisson ratio of bunker wall material (Fig. 4).

In natural coordinate, as expressed in Eqs. (13) and (14), Eq. (15) can be expressed as

$$\frac{1}{b^4}\frac{\partial^4 u}{\partial \eta^4} + \frac{2}{b^2 H^2}\frac{\partial^4 u}{\partial \eta^2 \partial \xi^2} + \frac{1}{H^4}\frac{\partial^4 u}{\partial \xi^4} = \frac{q}{D} \tag{16}$$

$$\text{where displacement } u \text{ is expressed as } u = \Delta . f(\xi) . f(\eta) \tag{17}$$

Substituting Eq. (17) in (16), we have

$$\frac{\Delta}{b^4}\frac{\partial^4}{\partial\eta^4}f(\xi).f(\eta)+\frac{2\Delta}{b^2H^2}\frac{\partial^4}{\partial\eta^2\partial\xi^2}f(\xi).f(\eta)+\frac{\Delta}{H^4}\frac{\partial^4}{\partial\xi^4}f(\xi).f(\eta)-\frac{q}{D}=0 \tag{18}$$

The shape functions $f(\xi)$ and $f(\eta)$ will generically satisfy Eq. (18) as they conform to boundary condition of the given plate, however will have residual error R_e which may be expressed as

$$R_e=\frac{\Delta}{b^4}\frac{\partial^4}{\partial\eta^4}f(\xi).f(\eta)+\frac{2\Delta}{b^2H^2}\frac{\partial^4}{\partial\eta^2\partial\xi^2}f(\xi).f(\eta)+\frac{\Delta}{H^4}\frac{\partial^4}{\partial\xi^4}f(\xi).f(\eta)-\frac{q}{D} \tag{19}$$

The residual error R_e is now minimized by Galerkin's [1] weighted residual method based on which

$$\int_0^1\int_0^1[R_e].f(\xi).f(\eta).d\xi.d\eta=0 \tag{20}$$

Equation (20) can thus be expressed as

$$\begin{aligned}&\frac{\Delta}{b^4}\int_0^1\int_0^1 f(\xi)^2.f'''(\eta).f(\eta).d\xi.d\eta+\frac{2\Delta}{b^2H^2}\int_0^1\int_0^1 f''(\xi)f''(\eta)f(\xi)f(\eta)d\xi.d\eta\\&+\frac{\Delta}{H^4}\int_0^1\int_0^1 f'''(\xi)f(\xi)f(\eta)^2d\xi d\eta-\frac{1}{D}\int_0^1\int_0^1 qf(\xi)f(\eta)d\xi.d\eta=0\end{aligned} \tag{21}$$

Considering $q=K_A.\gamma_s.z.\Lambda_i$, Eq. (21) can be expressed in a simplified form as

$$\Delta\left[X_1+\frac{2H^2}{b^2}X_2+\frac{H^4}{b^4}X_3\right]=\frac{K_A.\gamma_s.\Lambda_i.H^5}{D}X_4 \tag{22}$$

Considering $r=H/b$, the aspect ratio of the plate, Eq. (22) can be expressed as

$$\Delta=\frac{K_A.\gamma_s.\Lambda_i.H^5}{D(X_1+2r^2X_2+r^4X_3)}X_4 \tag{23}$$

where X_1, X_2, X_3, and X_4 are integral functions that can be solved numerically or explicitly and are as expressed in Table 1.

The maximum static displacement enhanced by the vibration of the frame for two modes of vibration of bunker wall is calculated using Eq. (23) as

$$\Delta_1=\frac{K_A.\gamma_s.\Lambda_1.H^5}{D(X_1+2r^2X_2+r^4X_3)}X_4 \tag{24}$$

and

Table 1 Values of integral functions X_1 to X_4

Integral functions	Values
$X_1 = \int_0^1 \int_0^1 f(\xi)^2 . \left[\frac{\partial^4}{\partial \eta^4} f(\eta)\right] . f(\eta) . d\xi . d\eta$	0.473
$X_2 = \int_0^1 \int_0^1 \left[\frac{\partial^2}{\partial \xi^2} f(\xi)\right] \left[\frac{\partial^2}{\partial \eta^2} f(\eta)\right] f(\xi) . f(\eta) . d\xi . d\eta$	0.124
$X_3 = \int_0^1 \int_0^1 \left[\frac{\partial^4}{\partial \xi^4} f(\xi)\right] . f(\xi) . f(\eta)^2 . d\xi . d\eta$	0.232
$X_4 = \int_0^1 \int_0^1 \xi . f(\eta) . f(\xi) . d\xi . d\eta$	0.010

$$\Delta_2 = \frac{K_A . \gamma_s . \Lambda_2 . H^5}{D(X_1 + 2r^2 X_2 + r^4 X_3)} X_4 \tag{25}$$

The displacement profile u of container wall for first two modes of vibration can thus be expressed as

$$u_1(\xi, \eta) = \Delta_1 . f(\xi) . f(\eta) \text{ and } u_2(\xi, \eta) = \Delta_2 . f(\xi) . f(\eta) \tag{26}$$

Here $f(\xi)$ and $f(\eta)$ are as expressed in Eqs. (13) and (14), respectively.

The maximum deflection will occur at $\xi = 0.447$ and $\eta = 0.5$ which gives

$$\begin{aligned} u_1(0.447, 0.5) &= \Delta_1 . f(0.447) . f(0.5) \text{ and} \\ u_2(0.447, 0.5) &= \Delta_2 . f(0.447) . f(0.5) \end{aligned} \tag{27}$$

Time period of the wall for first two modes of vibration can be expressed as

$$T_{w1} = 2\pi \sqrt{\frac{u_1(0.447, 0.5)}{g}} \text{ and } T_{w2} = 2\pi \sqrt{\frac{u_2(0.447, 0.5)}{g}} \tag{28}$$

Let S_{aw1} and S_{aw2}be the spectral acceleration coefficients from code for T_{w1} and T_{w2}, respectively.

For modal analysis, maximum amplitudes (S_{wd}) in terms of code for first two modes of vibration are expressed as [2]

$$S_{dw1} = \kappa_{w1} . \beta . \frac{S_{aw1} . g}{\omega_1^2} \text{ and } S_{dw2} = \kappa_{w2} . \beta . \frac{S_{aw2} . g}{\omega_2^2} \tag{29}$$

where $\omega_1 = 2\pi/T_{w1}$ and $\omega_2 = 2\pi/T_{w2}$ are natural frequency of the wall, β = code factor given earlier, and κ_{w1} and κ_{w2} = mode participation factors for first two modes of wall given in Eq. (30)

$$\kappa_{w1} = \kappa_{w2} = \frac{\int_0^1 \int_0^1 \xi.f(\xi).f(\eta).d\xi.d\eta}{\int_0^1 \int_0^1 \xi.(f(\xi).f(\eta))^2.d\xi.d\eta} \tag{30}$$

Equation (30) on computation gives a value of $\kappa_{w1} = 24$.

Thus, based on Eq. (29), the combined spectral displacement of the wall can be calculated using SRSS method as

$$S_{dw} = \sqrt{(S_{dw1} + \Delta_1)^2 + (S_{dw2} + \Delta_2)^2} \tag{31}$$

Finally, dynamic SRSS displacement of wall can be expressed as

$$u(\xi, \eta) = S_{dw}.f(\xi).f(\eta) \tag{32}$$

Equation (32) gives a complete dynamic displacement profile of the wall between limits 0 and 1 in both X and Z directions for first two modes.

2.2.2 Dynamic Bending Moment and Shear Force

Bending moment and shear force induced in the wall can be expressed as [6]

$$M_x = -D\left[\frac{\partial^2 u}{\partial x^2} + v\frac{\partial^2 u}{\partial z^2}\right] \tag{33}$$

$$M_z = -D\left[v\frac{\partial^2 u}{\partial x^2} + \frac{\partial^2 u}{\partial z^2}\right] \tag{34}$$

$$Q_x = -D\left[\frac{\partial^3 u}{\partial x^3} + \frac{\partial^3 u}{\partial x.\partial z^2}\right] \tag{35}$$

$$Q_z = -D\left[\frac{\partial^3 u}{\partial x^2 \partial z} + \frac{\partial^3 u}{\partial z^3}\right] \tag{36}$$

Transferring the above Eqs. (33), (34), (35), and (36) in natural coordinate and substituting in Eq. (32), dynamic moments and shears can be calculated using following equations:

$$M_x(\xi,\eta) = -\frac{D.S_{dw}}{H^2}\left[r^2.f(\xi).f''(\eta) + v.f''(\xi).f(\eta)\right] \tag{37}$$

$$M_z(\xi,\eta) = -\frac{D.S_{dw}}{H^2}\left[v.r^2.f(\xi).f''(\eta) + f''(\xi).f(\eta)\right] \tag{38}$$

$$Q_x(\xi,\eta) = -\frac{D.S_{dw}}{H^3}\left[r^3.f(\xi).f'''(\eta) + r.f''(\xi).f(\eta)\right] \tag{39}$$

$$Q_z(\xi,\eta) = -\frac{D.S_{dw}}{H^3}\left[r^2.f'(\xi).f''(\eta) + f'''(\xi).f(\eta)\right] \tag{40}$$

The successive derivatives of $f(\xi), f(\eta)$ are as shown hereafter:

$f(\xi)$	$\frac{\xi^5}{4} - \frac{\xi^3}{2} + \frac{\xi}{4}$	$f(\eta)$	$16\eta^4 - 32\eta^3 + 16\eta^2$
$f'(\xi)$	$\frac{5\xi^4}{4} - \frac{3\xi^2}{2} + \frac{1}{4}$	$f'(\eta)$	$64\eta^3 - 96\eta^2 + 32\eta$
$f''(\xi)$	$5\xi^3 - 3\xi$	$f''(\eta)$	$192\eta^2 - 192\eta + 32$
$f'''(\xi)$	$15\xi^2 - 3$	$f'''(\eta)$	$384\eta - 192$

3 Example, Results, and Discussions

As an example [5] of the application of the proposed method, we take a small square bunker. The bunker is 4.57 m^2 internally in plan and 3.66 m deep from the top of the hopper slopes. The pyramidal hopper is 2.29 m deep internally.

Data:

Size of columns = 305 mm × 305 mm
Number of columns = 4
Grade of concrete of walls, beams, and columns = M15

Fill material:

Angle of internal friction = 35 deg
Weight density of fill material = 7.85 kN/m^3
Thickness of concrete wall = 127 mm

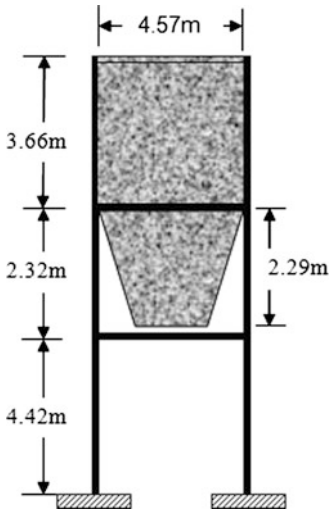

Stiffness of frame:

Stiffness of all columns below tie level $K_1 = 7.76 \times 10^3$ kN/m
Stiffness of all columns above tie level $K_2 = 5.34 \times 10^4$ kN/m

Lumped masses:

$M_1 = 6{,}808$ kg and $M_2 = 114{,}000$ kg

Hence, mass and stiffness matrix of the frame are given as

$$M = \begin{bmatrix} 6.808 \times 10^3 & 0 \\ 0 & 1.14 \times 10^5 \end{bmatrix} \text{kg and } K = \begin{bmatrix} 6.117 \times 10^4 & -5.34 \times 10^4 \\ -5.34 \times 10^4 & 5.34 \times 10^4 \end{bmatrix} \frac{kN}{m}$$

Eigensolution of the above mass and stiffness matrix:

$$T = \begin{Bmatrix} 0.833 \\ 0.065 \end{Bmatrix} \text{s.} \quad \phi = \begin{bmatrix} -0.660 & 0.999 \\ -0.751 & -0.052 \end{bmatrix}$$

Normalized eigenvectors:

$$\phi_N = \begin{bmatrix} -2.544 \times 10^{-3} & 0.012 \\ -2.896 \times 10^{-3} & -6.217 \times 10^{-4} \end{bmatrix}$$

Mode participation factors for two modes of vibrations are given as

$$\kappa_1 = -347.436 \text{ and } \kappa_2 = -249.443$$

Beta factor from IS code:

$$\beta = \frac{ZI}{2R} = 0.06$$

Spectral acceleration coefficients corresponding to two time periods from IS code for 5 % damping ratio:

$$\frac{S_{a1}}{g} = 2.004 \text{ and } \frac{S_{a2}}{g} = 1.972$$

Design acceleration coefficients at the top of frame (node 2) corresponding to two modes of vibration:

$$\frac{D_{a1}}{g} = \kappa_1 \times \beta \times \frac{S_{a1}}{g} \times \phi_{N_{21}} = 0.121 \text{ and } \frac{D_{a2}}{g} = \kappa_2 \times \beta \times \frac{S_{a2}}{g} \times \phi_{N_{22}} = 0.018$$

Amplification factors for two modes of vibration:

$$\Lambda_1 = 1.527 \text{ and } \Lambda_2 = 1.08$$

Amplitude of vibration for first and second modes of vibrations:

$$\Delta_1 = \frac{K_A.\gamma_s.\Lambda_1.H^5}{D(X_1 + 2r^2X_2 + r^4X_3)}X_4 = 5.522 \times 10^{-4} \text{ m}$$

and

$$\Delta_2 = \frac{K_A.\gamma_s.\Lambda_2.H^5}{D(X_1 + 2r^2X_2 + r^4X_3)}X_4 = 3.905 \times 10^{-4} \text{ m}$$

Deflection profile of vertical walls in two modes of vibrations:

$$u_1(\xi,\eta) = 5.522 \times 10^{-4}.f(\xi).f(\eta) \text{ and } u_2(\xi,\eta) = 3.905 \times 10^{-4}.f(\xi).f(\eta)$$

Time periods of walls in two modes of vibration:

$$T_1 = 2.\pi.\sqrt{\frac{u_1(0.447, 0.5)}{g}} = 0.047 \text{ s and } T_2 = 2.\pi.\sqrt{\frac{u_2(0.447, 0.5)}{g}} = 0.040 \text{ s}$$

Spectral acceleration coefficients corresponding to two time periods from IS code for 5% damping ratio:

$$\frac{S_{aw1}}{g} = 1.707 \text{ and } \frac{S_{aw2}}{g} = 1.595$$

Spectral displacements of walls corresponding to two modes of vibration:

$$S_{dw1} = \kappa_1 \times \beta \times \left(\frac{S_{a1}}{g}\right) \times \frac{g}{\omega_1^2} = 1.358 \times 10^{-3} \text{ and}$$
$$S_{dw2} = \kappa_2 \times \beta \times \left(\frac{S_{a2}}{g}\right) \times \frac{g}{\omega_2^2} = 8.968 \times 10^{-4}$$

Hence, spectral displacement profile over the wall is

$$S_{dw}(\xi, \eta) = \sqrt{(S_{dw1} + \Delta_1)^2 + (S_{dw2} + \Delta_2)^2} f(\xi) f(\eta) = 0.011 f(\xi) f(\eta)$$

Maximum SRSS deflection is $S_{dw}(0.447,0.5) = 0.794$ mm.
Maximum moments:

$$M_x(0.5, 0) = -4.61 \text{ kN - m/m}, M_x(0.5, 0.5)$$
$$M_x(0.5, 1) = -4.61\text{kN - m/m}.$$

$$M_y(0, 0.5) = 0.00\text{kN - m/m}, M_y(0.5, 0.5)$$
$$M_y(1, 0.5) = -6.39 \text{ kN - m/m}.$$

Maximum shear forces:

$$Q_x(0.5, 0) = 6.05 \text{ kN/m}, Q_x(0.5, 0.5)$$
$$Q_x(0.5, 1) = -6.05 \text{ kN/m}.$$

$$Q_y(0, 0.5) = 4.86 \text{ kN/m}, Q_y(0.5, 0.5)$$
$$Q_y(1, 0.5) = -10.47 \text{ kN/m}.$$

Bending moments and shear force diagram on the wall in horizontal and vertical direction vide Eqs. (37), (38), (39), and (40) are shown below.

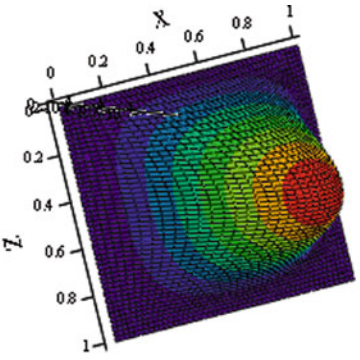

Displacement Profile

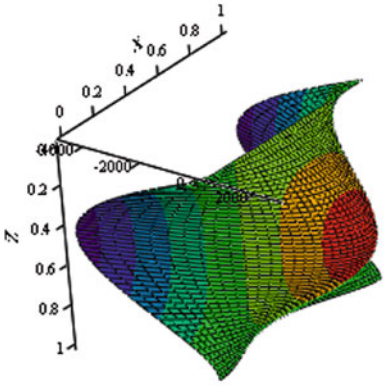

Moment M_x

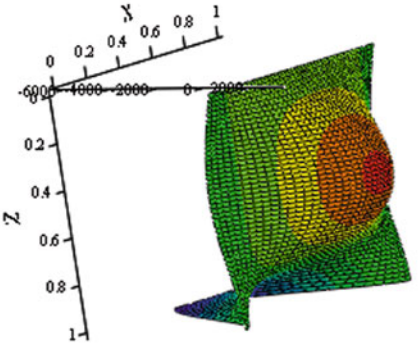

Shear Force Q_x

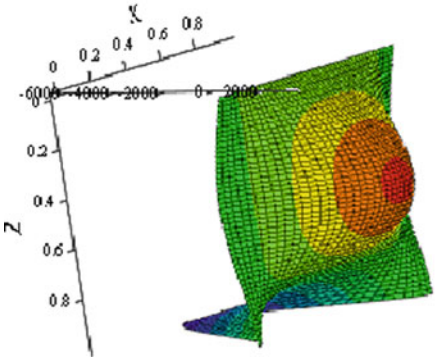

Moment M_y

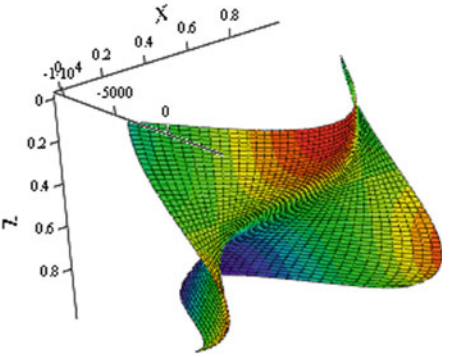

Shear Force Q_y

4 Conclusion

A comprehensive analytical solution based on Galerkin's weighted residual technique is adapted to determine the dynamic response of the bunker walls under seismic force – an important design parameter that is normally ignored in practical design office work till date. Considering the procedure that is analytic in nature does not require a sophisticated software or finite element method to be adapted and can well be carried out by a spreadsheet or using a general utility software like Mathcad with sufficient accuracy.

References

1. Chowdhury I, Dasgupta SP (2008) Dynamics of structures and foundations – a unified approach volume-1. Taylor & Francis Publication, Leiden
2. Clough RW, Penzien J (1985) Structural dynamics. MçGraw-Hill Publication, New York
3. Gray WS, Manning GP (1973) Reinforced concrete water towers bunkers and silos. Concrete Publications limited, London
4. IS 1893 (2002) Indian standard code of practice for earthquake resistant design of structures. Bureau of Indian standards, New Delhi
5. Mallick SK, Rangaswami KS (1980) Design of reinforced concrete structures. Khanna Publishers, New Delhi
6. Timoshenko S, Krieger W (1987) Theory of plates and shells. McGraw-Hill Publication, New York

Probabilistic Risk Analysis in Wind-Integrated Electric Power System Operation

Suman Thapa, Rajesh Karki, and Roy Billinton

Abstract Wind power is regarded as an environment-friendly energy source and the main alternative to the conventional energy resources. Wind power is being rapidly installed in many parts of the world and is considered to be the fastest growing energy source. The uncertain and intermittent nature of wind power, however, creates significant challenges in maintaining the reliability of wind-integrated power systems. The risk in system operation increases as the uncertainty and the amount of wind power connected to the system are increased. While operating a wind-integrated power system, the system operator requires sufficient knowledge of wind power that will be available in the near future to make decisions in committing adequate generation and allocating the reserves in appropriate generating units in order to operate the system economically and within acceptable operating risks. The wind power at a short time in future depends upon the initial condition, and it follows a diurnal pattern. This chapter presents a statistical method using the conditional probability approach to quantify the risks associated with wind power commitment. The impact of rising and falling wind trends in different seasons are considered while evaluating the operating risks.

Keywords Electric power system • Wind power • Reliability • Operating risk • Probabilistic methods

1 Introduction

Wind turbine generators (WTGs) are regarded as one of the most feasible alternatives for reducing the harmful emissions of electricity generation. Wind power is therefore growing rapidly all over the world. Wind power generation

S. Thapa • R. Karki (✉) • R. Billinton
Power System Research Group, University of Saskatchewan, Saskatoon, Canada
e-mail: rajesh.karki@usask.ca

S. Chakraborty and G. Bhattacharya (eds.), *Proceedings of the International Symposium on Engineering under Uncertainty: Safety Assessment and Management (ISEUSAM - 2012)*,
DOI 10.1007/978-81-322-0757-3_37,

depends upon the instantaneous wind speed at the wind site which is random and fluctuating. Due to the variable nature of power generation, WTGs are not considered to be dispatchable in the conventional sense. Wind power penetration is defined as the ratio of the total installed capacity of wind power to the total installed capacity of the system. In power systems with small wind penetrations, all the generated wind power can be absorbed by the system as and when available. Wind power penetration is increasing every year and is already contributing appreciable amounts of electricity supply in many electric utilities. The variable and intermittent nature of wind power generation is causing increased reliability concerns during power system operation where wind power penetration is appreciable. A power system operator has the responsibility of continuously satisfying the system demand by committing sufficient generating units. Adequate reserves should also be suitably allocated within the committed units to respond to unit failures and demand fluctuations. The inherent fluctuations in the wind power generation further increases the existing uncertainties during power system operation.

An accurate wind power forecasting is instrumental in determining the appropriate wind power contribution during system operation and to maintain reliability. Wind power forecasting is generally based upon a numeric weather prediction (NWP) [8] and/or statistical model [9]. A method based upon NWP is a very complex process that uses the information from weather stations and satellites and predicts the weather and wind by integrating a large number of equations governing weather. Statistical methods such as autoregressive moving average (ARMA) models can also be used for wind power prediction [4]. A persistence model is a statistical method which assumes that the wind power within the short term in the future will remain the same as at the present time. A persistence model despite being very simple can be very accurate for a short forecasting horizon such as 1–2 h. An ARMA model can be very effective for time horizon up to 4–6 h, while methods based upon the NWP model are more effective for a longer time horizons such as greater than 10 h [10]. A method to develop an ARMA model for a wind site is presented in [2]. An ARMA model is used to simulate the hourly wind speed from the knowledge of the hourly mean and standard deviation of the wind speed at a particular wind site for performing reliability studies of wind-integrated power system from a long-term planning perspective [1, 2, 6]. The ARMA model can also be used to simulate the wind speed data and produce a conditional probability distribution for short-term reliability evaluation in system operation [3]. This chapter utilizes the statistical method based upon the conditional probability approach to quantify the uncertainty of wind power in short future times.

2 Short-Term Wind Risk Model

The hourly wind speed data is simulated using the developed ARMA model and the actual historic mean and standard deviations of the wind speed at any hour using (1).

$$x_t = \mu_t + \sigma_t \times y_t \tag{1}$$

where x_t is the simulated wind speed at hour t, μ_t and σ_t are the mean and standard deviation of the wind speed at time t, respectively, and y_t is the time series value obtained from the ARMA model given by (2).

$$y_t = \text{Ø}_1 y_{t-1} + \text{Ø}_2 y_{t-2} + \text{Ø}_3 y_{t-1} + \cdots\cdots + \text{Ø}_n y_{t-n} + \alpha_t - \alpha_{t-1}\Theta_1 - \alpha_{t-2}\Theta_2 - \cdots\cdots - \alpha_{t-m}\Theta_m \quad (2)$$

where $\text{Ø}i(i = 1, \ldots, n)$ and $\Theta j(j = 1, \ldots, m)$ are the autoregressive and the moving average parameters of the model, respectively. $\{\alpha_t\}$ is a normal white noise process with zero mean and a variance of σ^2, i.e. $\alpha_t \in \text{NID}(0, \sigma^2)$, where NID denotes normally independently distributed. A wind site located in Toronto, Ontario, Canada, is considered in this study. The ARMA model for the wind site is published in [7] and is presented in Eq. (3).

$$\begin{aligned} y_t =& 0.4709 y_{t-1} + 0.5017 y_{t-2} - 0.0822 y_{t-3} \\ &+ \alpha_t + 0.1876 \alpha_{t-1} - 0.2274 \alpha_{t-2} \\ &\alpha_t \in \text{NID}(0, 0.5508^2) \end{aligned} \quad (3)$$

The knowledge of the initial wind speed is used to produce a conditional wind speed distribution from the hourly simulated data. The wind speed distribution is converted into wind power distribution using the conversion characteristics of a WTG. The speed-power relation of a WTG is nonlinear as given in (4) where P_t is the wind power output in per unit of the rated capacity and V_{ci}, V_r and V_{co} are the cut-in, rated and cut-out wind speeds, respectively. No power is generated when the wind speed is equal to or less than the cut-in speed V_{ci}. A WTG is shut down for safety reasons when the wind speed reaches or crosses the cut-out speed V_{co}. The A, B and C parameters of (4) are presented in [5].

$$\begin{aligned} P_t &= 0 && \text{for } V_{ci} > x_t > V_{co} \\ &= A + B x_t + C x_t^2 && \text{for } V_{ci} < x_t < V_r \\ &= 1 && \text{for } V_r < x_t < V_{co} \end{aligned} \quad (4)$$

Wind speed fluctuations generally show a diurnal variation where it starts to rise during the morning until afternoon and falls at night. Figure 1 shows the average hourly wind speed variations on the day of January 1 (day 1) and June 10 (day 161) at the wind site considered. The mean wind speed varies from 19.21 km/h at hour 2 to 26.64 at hour 13, while the hourly standard deviation varies from 8.54 km/h at hour 24 to 12.97 km/h at hour 20 on day 1. The mean wind speed over the day is 22.85 km/h while the mean standard deviation is 11.39 km/h. The hour 8 shows a rising wind trend, while the hour 20 shows a falling wind trend in the next few hours ahead. Day 161 represents a summer day where the mean wind speed varies between 9.18 and 21.89 km/h. The average

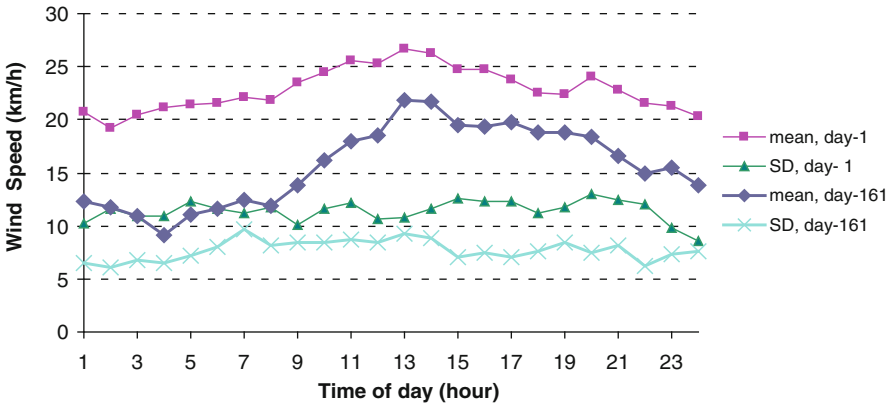

Fig. 1 Average hourly wind speed variations on day 1 and day 161 at Toronto

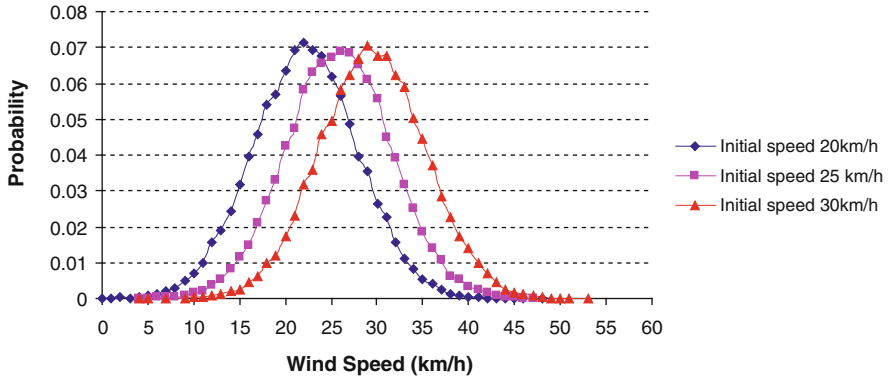

Fig. 2 Wind speed probability distributions at hour 9 conditional to wind speed at hour 8

wind speed over the day is 15.69 km/h and the standard deviation is 7.73 km/h, both of which are relatively lower compared to day 1. The diurnal wind speed variation on day 1 and day 161 is similar.

The ARMA model given in (3) is used to simulate the wind speed data for 800,000 replications to produce the conditional wind speed distributions of the wind speed in the next hour or the next few hours based upon the knowledge of initial wind speed. Figure 2 shows the wind speed probability distributions at hour 9 for three different initial wind speeds of 20, 25 and 30 km/h at hour 8 and while Fig. 3 shows the wind speed probability distribution at hour 21 for the same initial condition at hour 20. It can be seen from Figs. 2 and 3 that the probability distributions are similar to each other and they slide towards the direction of higher or lower wind speed as the initial wind speed is increased or decreased, respectively.

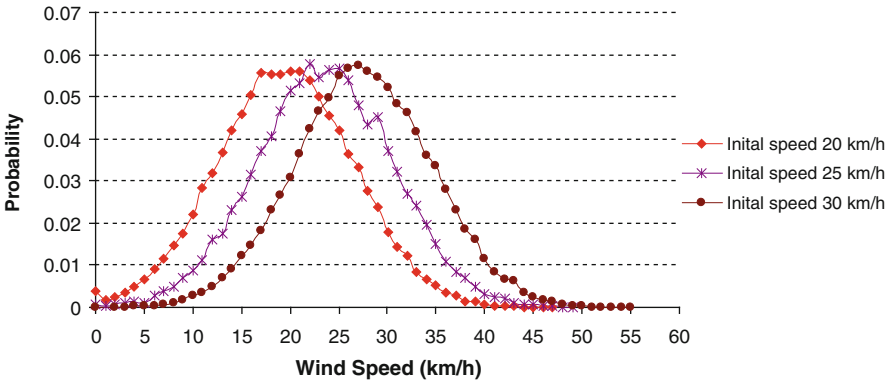

Fig. 3 Wind speed probability distributions at hour 21 conditional on the wind speed at hour 20

Table 1 Statistics of wind speed in the next hour

	Hour 9		Hour 21	
Initial wind speed at hour 8/20 (km/h)	Mean wind speed (km/h)	Standard deviation (km/h)	Mean wind speed (km/h)	Standard deviation (km/h)
20	22.18	5.70	19.51	6.99
25	25.85	5.72	23.51	7.02
30	29.51	5.74	27.53	7.04

Table 1 gives the statistics of the wind speed distributions presented in Figs. 2 and 3. The wind speed expectation in the next hour increases with increase in the initial wind speed which is an indication that the wind speed in the next hour depends upon the initial condition. The distribution moves towards a higher or lower wind speed when the initial wind speed increases or decreases, respectively. It is also evident that the mean wind speed at hour 9 is almost equal to the initial wind speed at hour 8, while the mean wind speed at hour 21 is less than the initial wind speed at hour 20. The diurnal rising and falling wind trend is therefore an important factor in the wind speed or wind power prediction.

3 Evaluation of Wind Power Commitment Risk (WPCR)

Methods based upon persistence models are generally used by the utilities to commit wind power in short future times. Figure 4 presents the wind speed distribution in hour 9 when the initial wind speed in hour 8 is 25 km/h. Figure 4 also shows a wind power curve for a typical WTG having cut-in, rated and cut-out speeds of 15, 50 and 90 km/h, respectively. The wind power cut-off is not shown in the chart as the maximum value on the abscissa is less than the cut-off speed.

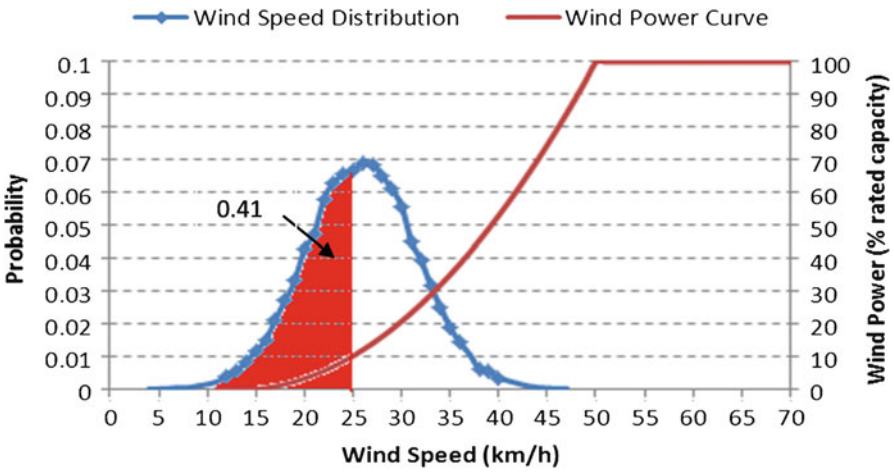

Fig. 4 Wind power commitment risk (WPCR) evaluation

The initial power is 10% of the rated capacity, and this value of wind power is committed in the considered future time according to the persistence model. The shaded area in the distribution gives the probability that the wind power at hour 9 will be less than the committed value. The probability that the actual wind power will be less than the committed value is termed the wind power commitment risk (WPCR) in this chapter and is obtained by cumulating the probabilities of the wind speeds less than the committed value. The WPCR in this case is 0.41.

3.1 Impact of Rising and Falling Wind Trend

Figure 5 presents the cumulative wind speed probability distribution at hours 9, 10 and 11 when the wind speed at hour 8 is 30 km/h. The corresponding wind power output is 20% of the rated capacity. The left ordinate on Fig. 5 gives the WPCR of committing wind power corresponding to the value given by a wind speed in the abscissa. If the wind power commitment is made on the basis of a pure persistence model, the WPCR at hour 9 will be 0.52 as shown by the 100% vertical line in Fig. 5. It can be further observed that the WPCR drops to 0.47 and 0.43 at hour 10 and hour 11, respectively, due to the rising wind trend at these hours. It may be desirable to lower the WPCR by reducing the committed value of wind power.

Table 2 shows the WPCR values by committing 100, 80 and 50% of the wind power available at hour 8 for the lead time considered. The WPCR values at the 100 and 80% commitment level decrease as the lead time is increased. The distributions crossover each other at the wind speed of 26 km/h such that the WPCR of committing wind power below the crossover show an opposite behaviour to that of the ones above it. Table 2 shows that the WPCR of 50% commitment rise as the lead time is increased.

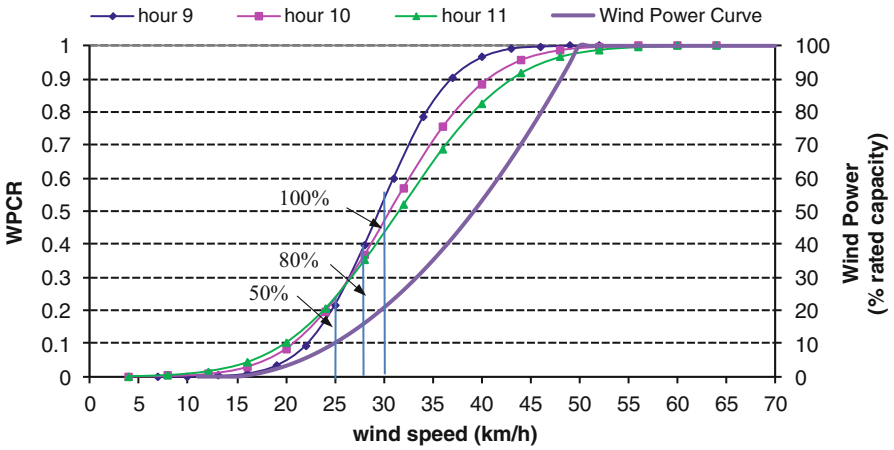

Fig. 5 WPCR analysis for a rising wind trend (initial wind speed = 30 km/h)

Table 2 WPCR for a rising wind trend (initial wind speed = 30 km/h at hour 8)

	WPCR at		
Hours	100% commitment	80% commitment	50% commitment
9	0.52	0.36	0.19
10	0.47	0.34	0.21
11	0.43	0.33	0.22

Figure 6 shows the cumulative wind speed probability distributions at hours 21, 22 and 23 when the initial wind speed at hour 20 is 30 km/h as in Fig. 5. The distributions in Fig. 6 shift to the left from hour 21 to 23, whereas the distributions in Fig. 5 shift to the right. This indicates that the WPCR of committing a certain value of wind power increases as the lead time is increased. The uncertainty increases as the lead time increases and is further augmented when the wind site is experiencing a falling wind trend. The WPCR values for the three commitments of 100, 80 and 50% of the initial power are shown in Table 3.

The impact of rising and falling wind trends can be observed from the WPCR values given in Tables 2 and 3. The WPCR after any lead time in the future will be higher in situations where the wind site is experiencing a falling wind trend than in the situations when the wind site is experiencing a rising wind trend. A higher value of wind power can be therefore committed during a diurnal rising trend as compared that to during a falling trend.

3.2 Impact of Seasonality

Figure 7 presents the WPCR analysis for a lead time of two hours on a winter day represented by day 1 and a summer day represented by day 161. The initial time is

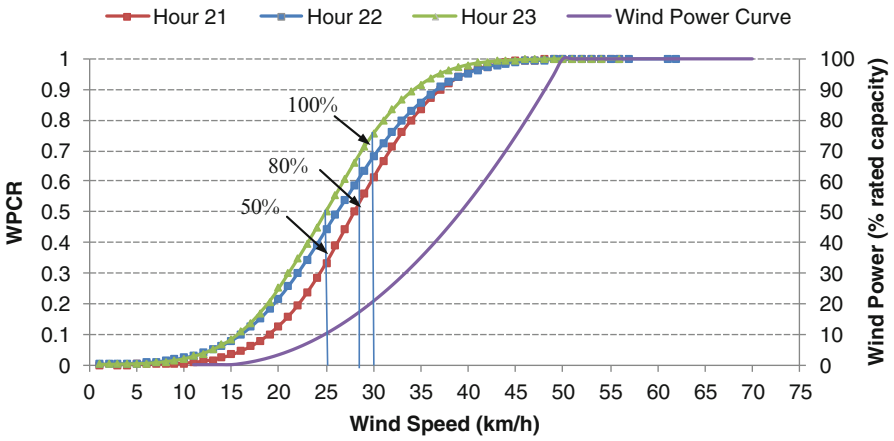

Fig. 6 WPCR analysis for a falling wind trend (initial wind speed = 30 km/h)

Table 3 WPCR for a falling wind trend (initial wind speed = 30 km/h at hour 20)

	WPCR at		
Hours	100% commitment	80% commitment	50% commitment
21	0.61	0.50	0.33
22	0.68	0.59	0.44
23	0.76	0.66	0.50

hour 8, and the initial wind speeds considered are 20 and 25 km/h. The distributions for the two days cross each other at 22 km/h (WPCR = 0.42) and 27 km/h (WPCR = 0.49) for the initial wind speed of 20 and 25 km/h, respectively. It can be seen that day 1 lies to the left of day 161 for wind speeds equal to or less than the initial value. This indicates that the WPCR of committing 100% or less of the initial power will be higher on the winter day than on the summer day. This is mainly because the summer day has lower variability as compared to the winter day, which can be seen from the hourly standard deviations on Fig. 1.

Figure 8 similarly presents the wind speed cumulative probability distribution for hour 22 conditional on the wind speeds at hour 20. The crossovers between the two respective distributions take place at 14 km/h (WPCR = 0.25) and 16 km/h (WPCR = 0.2) for initial wind speeds of 20 and 25 km/h, respectively. The WPCR values for the committed wind power below the crossovers are again lower on day 161 than on day 1.

Table 4 gives the WPCR values when committing 100, 80 and 50% of the initial power on the two days (day 1 and day 161) for the different lead times when the wind site is experiencing a rising wind trend. It can be seen from the table that the

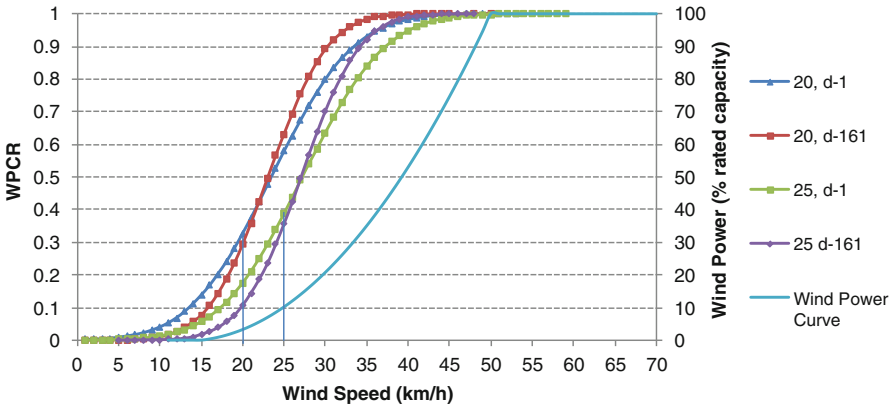

Fig. 7 WPCR analysis for hour 10 on day 1 and day 161

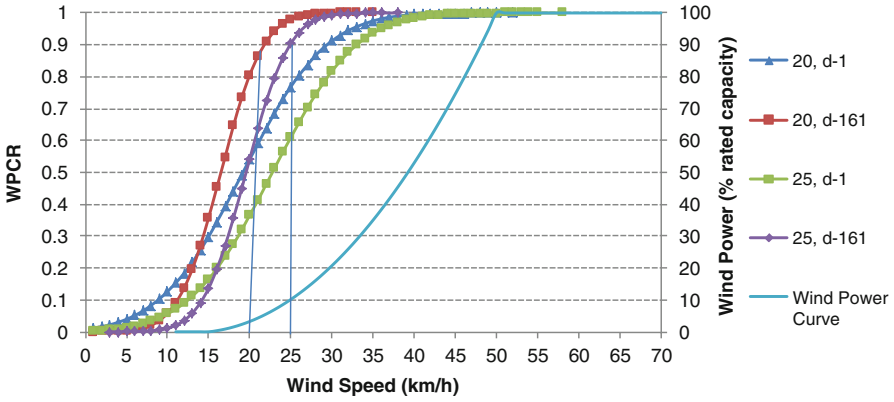

Fig. 8 WPCR analysis for hour 22 on day 1 and day 161

Table 4 WPCR for a rising wind trend (initial wind speed = 25 km/h at hour 8)

	WPCR for day 1 at			WPCR for day 161 at		
Hours	100% commitment	80% commitment	50% commitment	100% commitment	80% commitment	50% commitment
9	0.41	0.34	0.22	0.45	0.36	0.22
10	0.39	0.34	0.25	0.36	0.29	0.19
11	0.36	0.32	0.25	0.31	0.26	0.17

WPCR in hours 10 and 11 are lower in day 161 than in day 1. Table 5 shows the WPCR values on the two days (day 1 and day 161) for the different lead times when the wind site is experiencing a falling wind trend. The WPCR variations in the falling wind trend however are opposite, and the WPCR are greater in day 161 than in day 1. The WPCR during the falling wind trend are relatively high, and it may be desirable to lower the commitment to less than 50% in order to reduce the WPCR.

Table 5 WPCR for a falling wind trend (initial wind speed = 25 km/h at hour 20)

	WPCR for day 1 at			WPCR for day 161 at		
Hours	100% commitment	80% commitment	50% commitment	100% commitment	80% commitment	50% commitment
21	0.56	0.50	0.39	0.67	0.59	0.41
22	0.61	0.56	0.46	0.90	0.86	0.72
23	0.64	0.59	0.48	0.79	0.74	0.61

4 Conclusion

Short-term wind power commitments are dependent on the initial wind power and the lead time considered. A method based upon a conditional probability approach has been employed to quantify the short-term wind speed variations and evaluate the WPCR. Diurnal variations are important factors to be considered when estimating short-term wind power. The variability increases with the increase in lead time. It has been found that rising or falling wind trends can respectively offset or intensify the increase in variability. System operators may therefore need to adjust their commitment from wind farms based upon acceptable WPCR values. The seasonal impact of diurnal variations has been presented using two particular days to represent winter and summer conditions. The results show that the appropriate wind power commitment is highly dependent on the risk criterion deemed acceptable to the system.

References

1. Billinton R, Chowdhury AA (1992) Incorporation of wind energy conversion systems in conventional generating capacity adequacy assessment. IEE Proc Gener Transm Distrib 139 (1):47–56
2. Billinton R, Chen H, Ghajar R (1996) Time-series models for reliability evaluation of power systems including wind energy. Microelectron Reliab 36(9):1253–1261
3. Billinton R, Karki B, Karki R, Ramakrishna G (2009) Unit commitment risk analysis of wind integrated power systems. IEEE Trans Power Syst 24(2):930–939
4. Boone A (2005) Simulation of short-term wind speed forecast errors using a multi-variate ARMA(1,1) Time-series model. Msc thesis, Royal Institute of Technology, Sweden
5. Giorsetto P, Utsurogi KF (1983) Development of a new procedure for reliability modeling of wind turbine generators. IEEE Trans Power Appar Syst PAS-102(1):134–143
6. Karki R, Hu Po (2005) Wind power simulation model for reliability evaluation. In: Proceedings of the Canadian conference on electrical and computer engineering Saskatoon, Saskatchewan, Canada 2005, pp 541–544
7. Karki R, Hu P, Billinton R (2006) A simplified wind power generation model for reliability evaluation. IEEE Trans Energy Convers 21(2):533–540
8. Lange M (2006) Physical approach to short-term wind power prediction. Springer, Berlin
9. Milligan M, Schwartz M, Wan Y (2003) Statistical wind power forecasting models: results for U.S. wind farms. National Renewable Energy Laboratory, Washington, DC
10. Nielsen TS, Joensen A, Madsen H, Landberg L, Giebel G (1998) A new reference for wind power forecasting. Wind Energy 1:29–34. doi: 10.1002/(SICI)1099-1824(199809)1:1<29::AID-WE10>3.0.CO;2-B

A Frequency Domain Study on the Seismic Response Mitigation of Elevated Water Tanks by Multiple Tuned Liquid Dampers

Soumi Bhattacharyya and Aparna (Dey) Ghosh

Abstract In this paper, an investigation has been carried out on the passive vibration control of elevated water tank structures, subjected to earthquakes, by multiple tuned liquid dampers (MTLDs). An R.C.C. elevated water tank with shaft-type support has been considered. To account for the fluid-structure interaction, the sloshing of water in the water tank container has been modelled by the fundamental convective mode. The remaining water mass has been lumped with that of the container and supporting structure, resulting in a 2-DOF system model for the elevated water tank. The transfer function for the 2-DOF water tank model with MTLDs attached in a parallel configuration has been formulated. The input excitation has been characterized by a white noise power spectral density function (PSDF). The performance of the damper system has been examined on the basis of reduction in the root mean square (rms) value of the structural displacement. The frequencies of the TLDs have been fixed on the basis of tuning to the frequencies corresponding to the peaks of the transfer function curve of the 2-DOF system. This has been studied for three cases, namely, full, half-full and empty conditions of the water tank. The performance of the MTLD system for varying water level in the tank has been examined and has been found to be better in comparison with that for the single TLD case. The geometric parameters of the MTLDs have also been obtained and have been found to be feasible.

Keywords Elevated water tank • Passive damper • Liquid sloshing damper • Multiple tuned liquid damper

S. Bhattacharyya (✉) • A.D. Ghosh
Department of Civil Engineering, Bengal Engineering and Science University, Shibpur, Howrah, India
e-mail: soumibhttchr86@gmail.com; aparrnadeyghosh@gmail.com

S. Chakraborty and G. Bhattacharya (eds.), *Proceedings of the International Symposium on Engineering under Uncertainty: Safety Assessment and Management (ISEUSAM - 2012)*,
DOI 10.1007/978-81-322-0757-3_38,

1 Introduction

TLD is a passive energy dissipating system or passive control device, where damping is achieved by the physical properties of the system and no external forces are needed. In TLD, the mass of the damper is provided by liquid (usually water) in a container. Vibration mitigation of a structure is achieved due to the transference of the structural vibrational energy to this liquid when the natural frequency of the liquid motion is nearly equal (i.e. tuned) to the structural frequency. These passive systems impart direct damping to the structure by modifying its frequency response [6]. In 1957 Housner [4] presented an analysis of the hydrodynamic pressures generated in a fluid container when it is subjected to horizontal acceleration. Both the impulsive and convective liquid pressures were taken into consideration. After that, the TLDs have been used in marine structures. The concept of applying TLDs for reduction of vibrations in civil engineering structures began in the mid-1980s. Fujino et al. [2] have conducted an experimental study on the TLD. Since their first applications to ground structures in the 1980s [12, 17], TLDs have become a popular form of inertial damping device [1, 3, 7–9, 14–16]. Currently, both deep and shallow water configurations of TLDs are in application worldwide. The shallow water configurations dissipate energy through viscous action and wave breaking. On the other hand, deep water TLDs require baffles or screens to increase the energy dissipation of the sloshing fluid. Primarily, in case of TLDs, the circular container is suitable for shallow configurations and the rectangular ones for deep water TLDs.

The major limitation of the single damper is that its performance is not robust. In the perfectly tuned condition, the single damper can perform well, but in slightly detuned condition, its efficiency gets reduced. To overcome this situation, instead of using a single damper, *multiple dampers* can be used. In multiple dampers, a range of frequency is selected. The central damper is then tuned to the structural frequency, and other dampers are tuned within the frequency range [10]. Hence, if there is an error in calculating the structural frequency, there is a chance that at least one damper will be tuned optimally in the detuned condition. Hence, in case of detuning, multiple dampers will perform better than the single damper. Some important MTLD applications are Hobart Tower in Tasmania, Atsugi TYG Building, Narita Airport Tower, Yokohama Marine Tower [19], Gold Tower in Kagawa, Shin Yokohama Prince Hotel (SYP) in Yokohama, Nagasaki Airport Tower, Tokyo International Airport Tower at Haneda, Shanghai World Financial Center, etc.

The frequency of an elevated water tank structure will change as the water level in the tank fluctuates. Since the control device under study is a passive system, it is not possible to change the frequency of the TLD once it has been installed. In the present study, the focus is on the application of MTLD (shallow and right circular) for the seismic vibration control of elevated water tanks with shaft-type supports. The structure has been modelled as 2-DOF system in which the sloshing action of the liquid inside the water tank container has been taken into account. The

formulation for the transfer function relating the base acceleration and displacement of the MTLD-2-DOF structural system has been presented. A study has been carried out on bimodal control of the structure by MTLD system in frequency domain, and the results have been compared with those obtained for the single TLD cases. The geometric feasibility of the TLD systems has also been investigated.

2 Frequency Domain Study

2.1 Modelling of Tank with n-TLDs

The model of an *n*-TLD-2-DOF structural system has been shown in Fig. 1. The two-mass model suggested by Housner [5] for fixed-base elevated tanks has been considered here [11]. In this model, only the first convective modes of tank water and TLDs have been considered. The convective mass of tank water (m_{cs}) has been considered as an SDOF system. Secondly, the mass (m_{es}) which consists of the remaining water mass in the tank and the mass derived by the weight of container including two-thirds of the supporting structure weight (recommended in ACI 371R) has been considered as another SDOF system. The stiffness and damping of the SDOF system, represented by the mass m_{es}, are k_{es} and c_{es} respectively. The corresponding damping ratio and the natural frequency are denoted by ξ_{es} and ω_{es} respectively. The water mass associated with the fundamental convective or

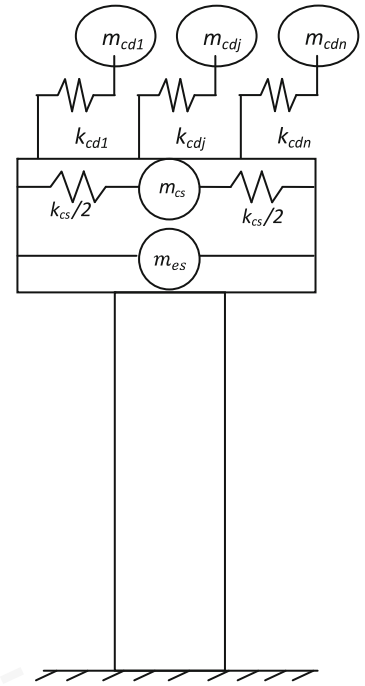

Fig. 1 Mechanical model of *n*-TLD-2-DOF structural system

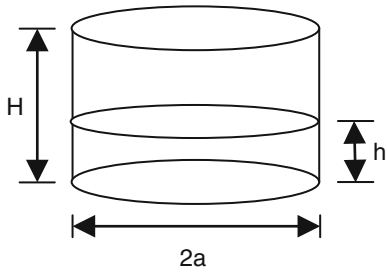

Fig. 2 Definition sketch for circular cylindrical tuned liquid damper (TLD)

sloshing mode of the tank water, m_{cs}, is assumed to be attached to the tank by a linear spring with stiffness k_{cs} and a linear viscous damper with damping coefficient c_{cs}. The damping ratio and the natural frequency of this mode are denoted by ξ_{cs} and ω_{cs} respectively.

n number of TLDs has been used in the study. A right circular cylindrical rigid TLD tank of radius a, shown in Fig. 2, is filled with an incompressible, inviscid liquid of mass density ρ_l up to a height h and has a free upper surface. The convective masses of each (j-th) TLD $(m_{cd}, j = 1 \text{ to } n)$ have been considered as an SDOF system. The liquid mass associated with this convective mode, m_{cdj}, is assumed to be attached to the tank by linear spring with stiffness k_{cdj} and linear viscous damper with damping coefficient c_{cdj}. The damping ratio and the natural frequency of this mode are denoted by ξ_{cdj} and ω_{cdj} respectively. The expressions for m_{cs}, m_{cdj}, ω_{cs} and ω_{cdj} are given by Veletsos and Tang [18].

The remaining water mass of the TLD container is assumed to be lumped with the mass $m_{es,}$ and the total mass is represented by m_{es*} in the frequency domain formulation. Although, in the numerical study, it has been assumed that $m_{es}* = m_{es}$ as the impulsive mass of the TLD liquid is small and the TLD container weight has been neglected. The stiffness and damping of the mass m_{es*} are thus k_{es} and c_{es}, respectively. As per Veletsos and Tang [18], ξ_{cs} and ξ_{cdj} have been taken as 0.01.

2.2 *Formulation of Transfer Function of Structure with n-Identical TLDs*

The mathematical model of n-TLD-2-DOF structural system has been shown in Fig. 3. Let us consider the n-TLD-2-DOF system subjected to a horizontal base acceleration, $\ddot{z}(t)$. Let $u(t)$ denote the horizontal displacement of m_{es*} relative to ground motion. $x(t)$ denotes the horizontal displacement of the convective mode of the tank liquid relative to the structure. Further, $y_j(t)$ represents the displacement of the convective liquid mass of the j-th TLD relative to the structure, where $j = 1$ to n.

The normalized equation of motion of the sloshing mass of the tank water (m_{cs}) yields the following:

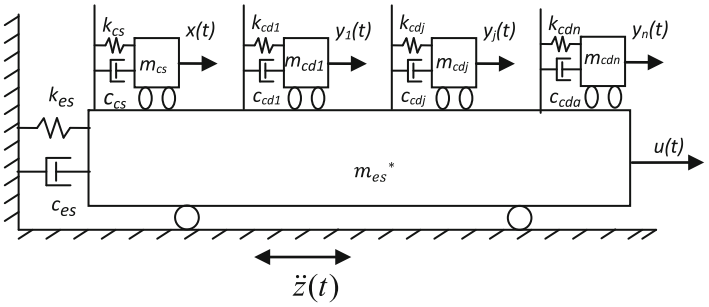

Fig. 3 Mathematical model of n-TLD-2-DOF structural system

$$\ddot{x}(t) + \ddot{u}(t) + 2\xi_{\mathrm{cs}}\omega_{\mathrm{cs}}\dot{x}(t) + {\omega_{\mathrm{cs}}}^2 x(t) = -\ddot{z}(t) \tag{1}$$

where $\frac{c_{\mathrm{cs}}}{m_{\mathrm{cs}}} = 2\xi_{\mathrm{cs}}\omega_{\mathrm{cs}}$ and $\frac{k_{\mathrm{cs}}}{m_{\mathrm{cs}}} = {\omega_{\mathrm{cs}}}^2$.

The normalized equation of motion of sloshing masses of dampers yields the following:

$$\ddot{y}_j(t) + \ddot{u}(t) + 2\xi_{\mathrm{cd}j}\omega_{\mathrm{cd}j}\dot{y}_j(t) + {\omega_{\mathrm{cd}j}}^2 y_j(t) = -\ddot{z}(t) \qquad j = 1, 2, 3 \ldots .n \tag{2}$$

where $\frac{c_{\mathrm{cd}j}}{m_{\mathrm{cd}j}} = 2\xi_{\mathrm{cd}j}\omega_{\mathrm{cd}j}$ and $\frac{k_{\mathrm{cd}j}}{m_{\mathrm{cd}j}} = {\omega_{\mathrm{cd}j}}^2$.

The normalized equation of motion of the n-TLD-2-DOF structural system yields

$$\begin{aligned} \ddot{u}(t) + 2\xi_{\mathrm{es}}\omega_{\mathrm{es}}\dot{u}(t) + {\omega_{\mathrm{es}}}^2 u(t) - 2\xi_{\mathrm{cs}}\omega_{\mathrm{cs}}\mu_{\mathrm{cses}}\dot{x}(t) - {\omega_{\mathrm{cs}}}^2\mu_{\mathrm{cses}}x(t) \\ - \sum_{j=1}^{n}\left\{2\xi_{\mathrm{cd}j}\omega_{\mathrm{cd}j}\mu_{\mathrm{cd}j\mathrm{es}}\dot{y}_j(t) + {\omega_{\mathrm{cd}j}}^2\mu_{\mathrm{cd}j\mathrm{es}}y_j(t)\right\} = -\ddot{z}(t) \end{aligned} \tag{3}$$

where $\frac{c_{\mathrm{es}}}{m_{\mathrm{es}}*} = 2\xi_{\mathrm{es}}\omega_{\mathrm{es}}$, $\frac{k_{\mathrm{es}}}{m_{\mathrm{es}}*} = {\omega_{\mathrm{es}}}^2$, $\frac{m_{\mathrm{cs}}}{m_{\mathrm{es}}*} = \mu_{\mathrm{cses}}$ and $\frac{m_{\mathrm{cd}j}}{m_{\mathrm{es}}*} = \mu_{\mathrm{cd}j\mathrm{es}}$.

The transfer function relating the displacement of an SDOF system representing mass m_{es} to the base acceleration is given by

$$H_{\mathrm{es}}(\omega) = -\frac{1}{[-\omega^2 + {\omega_{\mathrm{es}}}^2 + 2\xi_{\mathrm{es}}\omega_{\mathrm{es}}i\omega]} \tag{4}$$

The transfer function relating the displacement of an SDOF system representing the mass m_{cs} to the input acceleration is given by

$$H_{\mathrm{cs}}(\omega) = -\frac{1}{[-\omega^2 + {\omega_{\mathrm{cs}}}^2 + 2\xi_{\mathrm{cs}}\omega_{\mathrm{cs}}i\omega]} \tag{5}$$

The transfer function relating the displacement of an SDOF system representing the mass $m_{\mathrm{cd}j}$ to the input acceleration is given by

$$H_{\mathrm{cd}j}(\omega) = -\frac{1}{\left[-\omega^2 + {\omega_{\mathrm{cd}j}}^2 + 2\xi_{\mathrm{cd}j}\omega_{\mathrm{cd}j}i\omega\right]} \qquad j = 1, 2, 3 \ldots .n \tag{6}$$

On Fourier transforming Eqs. (1), (2), and (3) and by proper substituting, the input-output relation between the base acceleration and the displacement response of the structure equipped with MTLD is obtained:

$$U(\omega) = H_{\mathrm{u}}(\omega)\ddot{Z}(\omega) \tag{7}$$

where

$$H_{\mathrm{u}}(\omega) = \frac{H_{\mathrm{es}}(\omega)[\mu_{\mathrm{cses}}(\omega^2 H_{\mathrm{cs}}(\omega) - 1) + \omega^2 A - B - 1]}{[\{\omega^2 H_{\mathrm{es}}(\omega)(\mu_{\mathrm{cses}}(\omega^2 H_{\mathrm{cs}}(\omega) - 1)) + \omega^2 A - B\} - 1]} \tag{8}$$

is the transfer function relating the displacement of the structure to the input base acceleration.

$$A = \sum_{\mathrm{j}=1}^{\mathrm{n}} H_{\mathrm{cd}j}(\omega)\left(\mu_{\mathrm{cdjes}}\right) \tag{9}$$

$$B = \sum_{\mathrm{j}=1}^{\mathrm{n}} \left(\mu_{\mathrm{cdjes}}\right) \tag{10}$$

$U(\omega), X(\omega), Y_j(\omega), \ddot{Z}(\omega)$ are the Fourier transforms of the corresponding time-dependent variables $u(t)$, $x(t)$, $y_j(t)$ and $\ddot{z}(t)$, respectively. If the ground acceleration is characterized by a white noise PSDF of intensity S_0, then the PSDF of the displacement response of the structure, denoted by $S_{\mathrm{u}}(\omega)$, is expressed by Newland (1993)

$$S_{\mathrm{u}}(\omega) = |H_{\mathrm{u}}(\omega)|^2 S_0 \tag{11}$$

The rms value of the displacement response of the structure, σ_{u}, can be numerically evaluated by computing the square root of the area under the corresponding PSDF curve as given in Eq. (11).

3 Numerical Study

An R.C.C. tank structure with flat top cylindrical container and shaft support has been taken as the example structure to examine the performance of TLD for the passive control of elevated water tank. The relevant data that has been assumed to define the structure are height of shaft support = 30 m, mean diameter of shaft = 3 m, thickness of shaft wall = 0.125 m, inner height of the tank container = 4 m, mean diameter of the tank container = 10 m, thickness of the container wall = 0.2m, thickness of the container bottom = 0.2 m, thickness of the top cover of the container = 0.2 m and grade of concrete = M25. Based on these assumed data and considering the elevated water tank structure as a cantilever, the mass and stiffness of the structure have been calculated for the full, half-full and empty conditions of the tank. The structural damping has been assumed to be 1%. The fundamental natural frequencies and corresponding time period of the two different SDOF systems represented by the masses m_{cs} and m_{es} have been calculated separately for full, half-full and empty conditions of the tank which are presented in Table 1. The transfer functions have been plotted with these frequencies for full (Fig. 4), half-full (Fig. 5) and empty (Fig. 6) conditions of the tank. It is seen that in full and half-full conditions of the tank, the interaction between the structure and the first sloshing mode of water results in two different peaks in the displacement transfer function curve (Table 1). It has been also observed that the first peak is predominant when the tank is full; however, the second peak is predominant when the tank is half full, and the first peak is vanished when the tank is empty. That means, the first peak is representing the fundamental sloshing mode of the tank water, and the second peak is representing the structure along with the impulsive mass of tank liquid.

The fundamental natural frequency of the single TLD (w_{cd}) has been tuned to the frequency corresponding to the predominant mode of each case – full, half-full and empty conditions of the tank. Optimum tuning ratios with respect to minimum rms values of $u(t)$ corresponding to different mass ratios, determined through numerical optimization (Table 2) for full, half-full and empty conditions of the

Table 1 Frequencies of two different SDOF systems for full, half-full and empty conditions of tank before and after the occurrence of fluid-structure interaction

	Natural frequency of the sloshing mass of the tank		Natural frequency of the structure plus impulsive water mass of the tank		Natural frequencies of 2-DOF structural system			
					First peak		Second peak	
Condition of tank	Natural frequency (w_{cs}) (rad/s)	Time period (s)	Natural frequency (w_{es}) (rad/s)	Time period (s)	Natural frequency (rad/s)	Time period (s)	Natural frequency (rad/s)	Time period (s)
Full	1.81	3.47	3.13	2.01	1.65	3.81	3.43	1.83
Half full	1.50	4.18	3.69	1.70	1.44	4.36	3.84	1.64
Empty	–	–	4.03	1.56	–	–	4.03	1.56

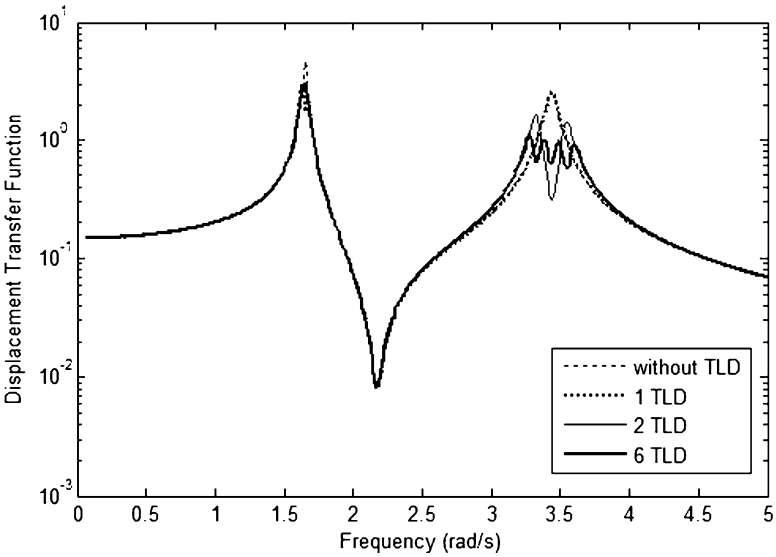

Fig. 4 Displacement transfer function of structure in full condition of the tank

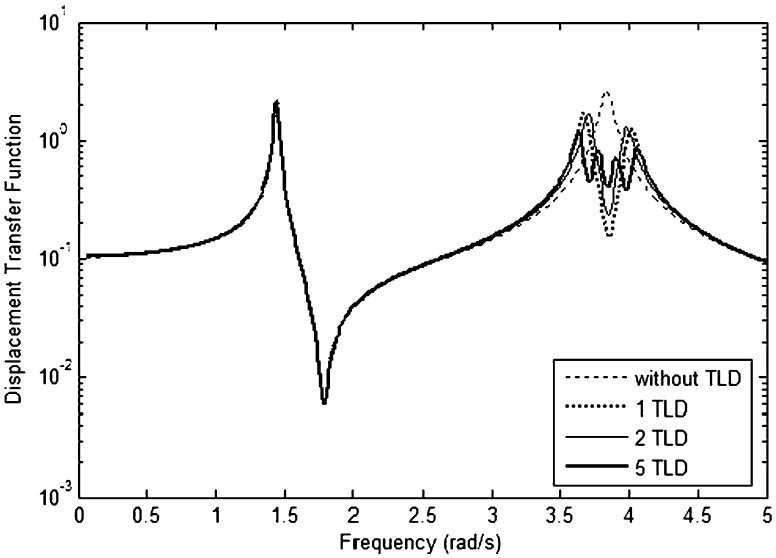

Fig. 5 Displacement transfer function of structure in half-full condition of the tank

tank, are close to unity, but in case of higher mass ratios, the optimum tuning ratio decreases slightly from unity. The influence of different mass ratios (the ratio of total mass of water in TLD to the mass which consists of the mass of the empty container including two-thirds of the supporting structure mass – namely, 1, 2, 3, 4 and 5%) on the percent response reduction of $u(t)$ has been investigated corresponding to optimum tuning ratio (Table 3).

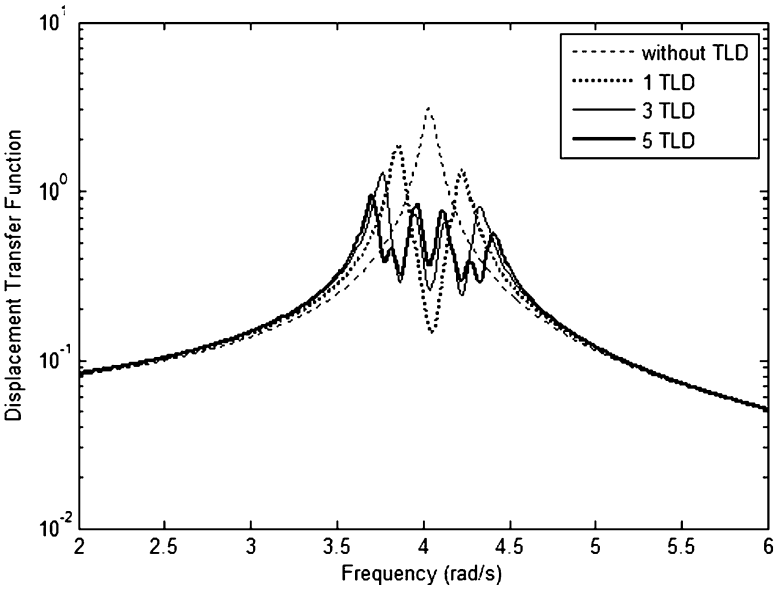

Fig. 6 Displacement transfer function of structure in empty condition of the tank

Table 2 Values of optimum tuning ratio (ν_{opt}) for single TLD for different mass ratios

Mass ratio (%)	Optimum tuning ratio (ν_{opt}) for full condition	Optimum tuning ratio (ν_{opt}) for half-full condition	Optimum tuning ratio (ν_{opt}) for empty condition
1	1.00	0.99	0.99
2	0.99	0.98	0.98
3	0.99	0.98	0.98
4	0.98	0.98	0.98
5	0.98	0.98	0.98

Table 3 Values of percent reduction in rms displacement for single TLD for different mass ratios

Mass ratio (%)	Percent reduction in rms displacement for full condition	Percent reduction in rms displacement for half-full condition	Percent reduction in rms displacement for empty condition
1	6.9058	18.7680	26.7035
2	9.5731	19.3605	27.3095
3	11.0165	19.5576	27.5030
4	11.8011	19.6048	27.5533
5	12.2492	19.6164	27.5644

Representative set of displacement transfer function curves for the cases of STLD tuned to the predominant mode of the full, half-full and empty conditions of the water tank for 2% mass ratio and tuning ratio of unity is given in Figs. 4, 5 and 6, respectively, and has been compared with that of the structure without damper. It has been observed that the magnitude of the peaks of the transfer

function curve has been reduced, thereby reducing the displacement reduction of the structure. It has been seen that when the tank is empty, the control performance of the TLD is better due to the absence of sloshing mode whereas the performance of the TLD is worse when the tank is full and the sloshing mode is most effective although the TLD is tuned to the predominant sloshing mode in full condition. It has been also observed that when the damper is tuned to frequencies corresponding to the tank half-full and empty conditions, the control performance of the TLD does not increase significantly with the increase in mass ratio.

To achieve better response reduction, two TLDs of total mass ratio 2% have been tuned to the two modes of the transfer function curve of the 2-DOF structural system for full and half-full conditions. The resulting transfer function curves (Figs. 4 and 5) have four peaks which are reduced in amplitude, and greater response reduction has been achieved (Tables 4 and 5). In the next step, an additional four TLDs of total mass ratio 2% have been tuned corresponding to the frequencies of these four modes which results in larger response reduction (Tables 4 and 5). In case of empty condition, also the same procedure has been adopted, and the results have been shown in Table 6. From Tables 4, 5 and 6, it has been observed that response reductions as high as 21, 29 and 48% for the tank full, half-full and empty conditions may be obtained by the MTLD system as described above, whereas the corresponding response reductions for the STLD were 9.22, 18.7 and 26.5% for the tank full, half-full and empty conditions, respectively. So, it can be concluded that the percent response reductions for displacement have been increased in MTLD cases with respect to the STLD cases for all the three conditions.

Since the water mass in the water tank is a variable quantity, the natural frequency of the SDOF system representing the fundamental sloshing mode of the tank water can also vary between the values corresponding to the full condition and that for the empty condition of the tank, and this will change the values of natural frequencies corresponding to the two peaks of displacement transfer function curves after fluid-structure interaction. Thus, if the TLD system is tuned to a particular frequency of the tank, there will be some amount of detuning as the water content of the tank changes. The variation in the response reduction achieved by the MTLD systems discussed above, in terms of the rms displacement of the structure, over a range of percent tank full, for different values of mass ratios has been observed for three cases (TLD system tuned to the tank full, half-full and empty conditions) and has been compared to that of the single TLD systems (Fig. 7). From Fig. 7, it can be seen that there is a significant improvement in the performance of the damper system by using MTLDs as compared to the STLD over the entire range of percent tank full. The MTLD systems tuned to empty and half-full conditions of the tank provide a very good performance when the tank is 0–50% full, but the performance of this system is very poor when the tank is 100% full. From Fig. 7, it can be observed that the MTLD system tuned to the frequencies corresponding to the full condition of the

Table 4 Frequencies, geometry and percent response reduction for MTLD system in tank full condition

Number of TLDs	Frequencies of TLD (rad/s)	Mass of water in each TLD (m_1) (kg)	Aspect ratio (h/a)	Radius of TLD (a) (m)	Water Height of TLD (m)	Total area required for TLD (%)	Percent reduction in rms value	Figure number
1	1.65	4,149.2	0.17	1.9806	0.3367	15.6906	9.2195	Fig. 4
2	1.65	2,074.6	0.14	1.6771	0.2348	16.1308	17.1251	
	3.43		0.49	1.1046	0.5412			
6	1.64	691.5	0.10	1.3008	0.1301	28.3494	21.1083	
	1.65		0.11	1.2602	0.1386			
	1.67		0.11	1.2602	0.1386			
	3.32		0.33	0.8737	0.2883			
	3.43		0.34	0.8651	0.2941			
	3.55		0.37	0.8410	0.3112			

Table 5 Frequencies, geometry and response reduction for MTLD system in tank half-full condition

Number of TLDs	Frequencies of TLD (rad/s)	Mass of water in each TLD (m_l) (kg)	Aspect ratio (h/a)	Radius of TLD (a) (m)	Water Height of TLD (m)	Total area required for TLD (%)	Percent reduction in rms value	Figure number
1	3.84	4,149.2	0.90	1.1364	1.0227	5.1655	18.7036	Fig. 5
2	1.44	2,074.6	0.11	1.8175	0.1999	17.2971	19.5483	
	3.84		0.64	1.0105	0.6467			
5	1.44	829.8	0.09	1.4318	0.1289	24.7893	28.7327	
	1.45		0.09	1.4318	0.1289			
	3.70		0.42	0.8568	0.3598			
	3.84		0.45	0.8373	0.3768			
	3.98		0.49	0.8139	0.3988			

Table 6 Frequencies, geometry and response reduction for MTLD system in tank empty condition

Number of TLDs	Frequencies of TLD (rad/s)	Mass of water in each TLD (m_l) (kg)	Aspect ratio (h/a)	Radius of TLD (a) (m)	Water Height of TLD (m)	Total area required for TLD (%)	Percent reduction in rms value	Figure number
1	4.03	4,149.2	1.08	1.0694	1.1549	4.5743	26.4926	Fig. 6
3	3.85	1,383.1	0.55	0.9285	0.5107	9.6603	41.5660	
	4.03		0.61	0.8970	0.5472			
	4.22		0.68	0.8651	0.5883			
5	3.76	829.8	0.43	0.8501	0.3655	13.0621	47.7450	
	3.85		0.46	0.8312	0.3823			
	4.03		0.50	0.8084	0.4042			
	4.22		0.55	0.7831	0.4307			
	4.33		0.59	0.7650	0.4514			

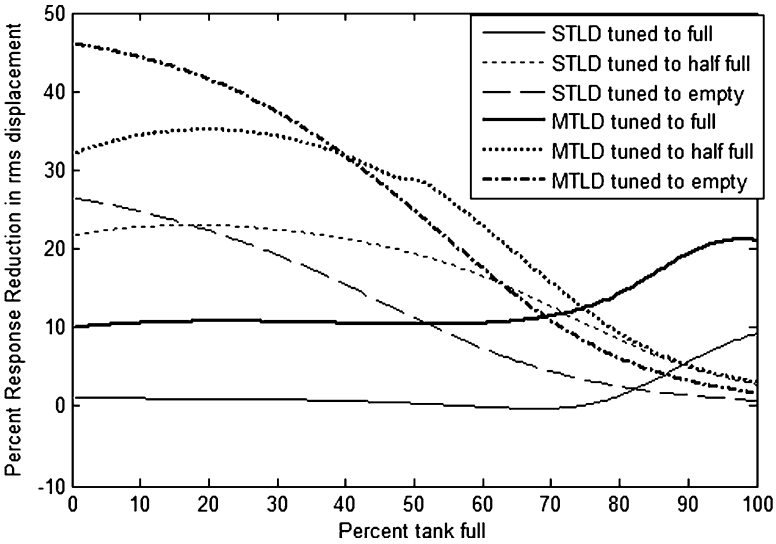

Fig. 7 Comparison of response reduction between STLD and MTLD system over a range of percent tank full for different tuning conditions

tank provides a standard response reduction (10–20%) over the entire frequency range of the structure.

3.1 Geometric Feasibility

It becomes necessary to check the geometric feasibility of the damper system. The parameters of the MTLD system, namely, the aspect ratio of each damper unit to satisfy the shallow criterion, radius and height of each TLD container and the maximum area of the water tank top surface that may be occupied by the MTLD units when tuned to the full (Table 4), half-full (Table 5) and empty (Table 6) conditions of the tank, have been evaluated from the tuning ratio, mass ratio and expression of natural frequency of the convective mass. It has been observed from Tables 4, 5 and 6 that the increase in the value of natural frequency, which is obtained as we move from the full condition to empty condition of the tank, results in an increase in the aspect ratio and decrease in the radius of the TLD. Further, in case of STLD, the aspect ratio is higher which is responsible for lowered performance of the TLD due to reduced sloshing water mass; however, STLD occupies smaller area of the water tank top surface. It has also been seen that if the number of TLD is increased maintaining the total mass ratio same, the response reduction increases although the maximum area of the water tank top surface that may be occupied by the TLD system is within 30%. In case of MTLD

system, the size of each TLD unit is smaller than that of STLD unit, which improves their constructability. From these observations, it can be concluded that the geometrical feasibility of the MTLD system is more satisfactory than that of the single TLD system.

4 Conclusion

The effectiveness of an MTLD system for the mitigation of the seismic vibrations of an elevated water tank has been investigated in frequency domain. Fluid-structure interaction has been accounted for by considering the first sloshing mass of the tank water as an SDOF system connected in parallel with the SDOF system representing the water tank structure and remaining water mass. A formulation of the displacement transfer function of a base-excited, viscously damped 2-DOF system equipped with MTLD has been developed in frequency domain. The performance of STLD has been studied first. The drawbacks of the STLD have been overcome by the MTLD systems. In case of MTLD system, bimodal control has been achieved leading to improved response reduction by clustering the TLD frequencies about the frequencies at which the peaks of the transfer function of the structural response occur. The percent response reductions have been obtained as 21% when the tank is full, 29% when the tank is half full and 48% when the tank is empty in the frequency domain, which are significantly greater than the STLD case for the same mass ratio. From the point of view of geometry, the aspect ratios and sizes of the TLD units of MTLD system are smaller than that of STLD which may improve their constructability and maintainability. The provision of more number of TLD units keeping the total mass ratio constant appears to be a more viable option. It has been observed that the MTLD system provides better response reduction over the entire range of structural frequency which varies with the fluctuating water level of the tank from empty to full condition. However, the drop in performance between the two extreme conditions (i.e. full and empty) of the tank remains. Further schemes of designing the MTLD system with the frequency designed in such a way to ensure better robustness are being studied by the authors.

References

1. Fujino Y, Sun LM (1993) Vibration control by multiple tuned liquid dampers. J Struct Eng 119 (12):3482–3502
2. Fujino Y, Pacheco BM, Chaiseri P, Sun LM (1988) Parametric studies on Tuned Liquid Damper (TLD) using circular containers by free-oscillation experiments. Struct Eng/Earthq Eng JSCE 5(2):381–391
3. Fujino Y, Sun LM, Pacheco BM, Chaiseri P (1992) Tuned Liquid Damper (TLD) for suppressing horizontal motion of structures. J Eng Mech 118(10):2017–2030

4. Housner GW (1957) Dynamic pressures on accelerated fluid containers. Seismological Soc Am 47(1):15–35
5. Housner GW (1963) The dynamic behavior of water tanks. BullSeismological Soc Am 53 (2):381–387
6. Kareem A (1983) Mitigation of wind induced motion of tall buildings. J Wind Eng Ind Aerodyn 11:273–284
7. Kareem A (1990) Reduction of wind induced motion utilizing a tuned sloshing damper. J Wind Eng Ind Aerodyn 36(2):725–737
8. Kareem A (1993) Liquid tuned mass dampers: past, present and future. In: Proceedings of the Seventh U.S. National conference on wind engineering, Los Angeles
9. Kareem A, Hsieh CC, Tognarelli MA (1994) Response analysis of offshore systems to nonlinear random waves part I: wave field characteristics. In: Proceeding of the special symposium on stochastic dynamics and reliability of nonlinear ocean systems ASME, New York, pp 39–54
10. Kareem A (1995) Performance of multiple mass dampers under random loading. J Struct Eng 121(2):348
11. Livaoglu R, Dogangun A (2006) Seismic behaviour of cylindrical elevated tanks with a frame supporting system on various subsoil. Indian J Eng Mater Sci 14(2):133–145
12. Modi VJ, Welt F (1987) On the vibration control using nutation dampers. In: King R (ed) Proceedings of the international conference on flow induced vibrations, BHRA, London, pp 369–376
13. Newland DE (1993) An introduction to random vibration, spectral and wavelet analysis. Longman, Scientific and Technical, London
14. Sakai F, Takaeda S (1989) Tuned liquid column damper – new type device for suppression of building vibrations. In: Proceedings international conference on high rise buildings, Nanjing, China, March 25–27
15. Tait MJ, Isyumov N, El Damatty AA (2008) Performance of Tuned Liquid Dampers. J Eng Mech 134(5):417–427
16. Tait MZ, Deng X (2010) The performance of structure-tuned liquid damper systems with different tank geometries. Struct Control Health Monit 17:254–277
17. Tamura Y, Fujii K, Ohtsuki T, Wakahara T, Koshaka R (1995) Effectiveness of tuned liquid dampers under wind excitations. Eng Struct 17(9):609–621
18. Veletsos AS, Tang Y (1990) Soil-structure interaction effects for laterally excited liquid storage tanks. Earthq Eng Struct Dyn 19:473–496
19. Wakahara T, Shimada K, Tamura Y (1994) Practical application of tuned liquid damper for tall buildings. ASCE Structural Congress and IASS International Symposium, Atlanta, USA, pp 851–856

Pavement Performance Modelling Using Markov Chain

S.K. Suman and S. Sinha

Abstract Pavement performance modelling is an essential element of a pavement management system (PMS). The model developed plays a critical role in several aspects of the PMS including financial analysis. In developing countries like India, PMS is the needed approach for the optimum utilisation of the available scarce resources. Pavement management system is concerned with optimal use of materials in time and space, leading to cost optimisation.

This chapter focuses on methodology involved in the prediction of pavement condition using probabilistic techniques. Since traffic loading, pavement materials, construction methods and environmental condition are not deterministic, therefore, probabilistic techniques are used. Markov chains have the property that probabilities involving the process will evolve in the future, depending only on the present state of the process and so are independent of the events in the past. The state of the transition matrix will be defined based on the overall pavement quality indices (OPQI), and element of the transition matrix will be determined by using several methods. Steady-state transition matrix will be obtained from one-step transition matrix.

The probabilistic model requires only a minimal amount of data such as pavement class, pavement condition of two consecutive years and pavement length. OPQI shall be utilised as index, and the present technique in pavement management systems will create good systems which may lead to more savings of the road maintenance funds and enhance the ability of the road network to provide better level of service at network level.

Keywords Pavement management system • Performance • Overall pavement quality index (OPQI) • Markov chain

S.K. Suman (✉) • S. Sinha
Department of Civil Engineering, National Institute of Technology Patna,
Patna, Bihar, India
e-mail: sksuman77@yahoo.co.in; sanjeev_bangkok@yahoo.com

S. Chakraborty and G. Bhattacharya (eds.), *Proceedings of the International Symposium on Engineering under Uncertainty: Safety Assessment and Management (ISEUSAM - 2012)*,
DOI 10.1007/978-81-322-0757-3_39,

1 Introduction

Pavement performance models simulate the deterioration process of pavement conditions and provide forecasting of pavement condition over time. It plays a vital role in pavement management system. The pavement performance models have several uses in pavement management system: (1) to analyse the conditions and determine the maintenance and repair requirements, (2) to decide the useful service life of the pavement on the basis of reduction in performance value to a certain terminal value, (3) to estimate long-range funding requirements to preserve the pavements, (4) to provide major inputs to perform life cycle cost analysis to compare the economics of various maintenance and repair alternatives and (5) to study the effects of various budget levels on future pavement condition.

In order to take decision of the optimum cost of maintenance and repair works of the pavement surface, there is a need to develop a comprehensive pavement performance index. A reliable pavement condition index can be achieved when all the pavement condition indicators will be incorporated simultaneously. This index includes factors related to all pavement indicators such as surface distresses, riding quality, skid resistance and deflection.

The pavement surface condition is affected by parameters like traffic axle loads, environmental conditions and moisture content that are themselves uncertain in nature; hence, the rate of pavement deterioration is uncertain. Modelling uncertainty requires the use of probabilistic operation research techniques.

In this context, the use of Markov chain in the prediction of model captures the uncertainty behaviour of pavement deterioration. The most important advantage of this technique is that it requires only 2 years or any two-threshold-justified temporal data.

The aim of this study is to highlight the approach of technique used in developing the pavement performance model.

2 Methodology

The first part of this section deals with an overview of overall pavement quality index, and the second part describes the procedures for development of pavement performance model based on Markov chain theory.

2.1 Overall Pavement Quality Index (OPQI)

OPQI is the combination of indices such as pavement quality distress-based index, pavement quality roughness-based index, pavement quality structural capacity-based index and pavement quality skid resistance-based index. This combined index is expected to give a good representation of the pavement condition and will be able to predict the performance accurately. It will also enhance the process

of optimising the life cycle costs in the selected maintenance and repair option through utilising the acceptance levels of the aforesaid four condition indicator indices. Utilising such an index in pavement management systems will create systems that lead to savings of the road maintenance funds and enhance the ability of the road network to provide better service at network level [1–6].

For more accurate estimation of pavement condition, OPQI is used which describes the pavement structural and functional capacities of the road section, taking into consideration all data collected for the surface condition. Therefore, it is envisaged that this index combines all distress types (severity and density), roughness, effective structural capacity and skid resistance value, according to the relative importance of each condition indicator. As per Shiyab [7], Eq. (1) was arrived based on theoretical concept that comprises all pavement surface conditions:

$$\mathrm{OPQI}_k = 10 \sum_{i=1}^{i=n} \left[1 - \left(1 - \frac{\mathrm{CI}_i}{10} \right) * W_{i,k} \right] \tag{1}$$

where OPQI_k = overall pavement quality index on a scale of 1–10, CI = condition indicator or distress index on a scale of 1–10, K = k-th pavement performance index, i = i-th distress or condition indicator out of the total number of the 'n' condition indicators = total number of distress types or condition indicators included in the performance index and $W_{i,k}$ = the impact or the relative weight of each distress type or condition indicator.CI incorporates index for every type of distress (e.g. RI, rutting index; ACI, alligator cracking index; BI, bleeding index; PCHI, patching index; PTI, potholes index), roughness index (RI), deflection index (ESCI) and skid resistance index (SKRI). Distress index may be obtained by using the method of Paver Systems. Deflection and roughness indices may be obtained by using Eqs. (2) and (3), respectively:

$$\text{Deflection Index} = \frac{\text{Percent (Predicted) deflection}}{\text{Maximum permissible deflection}} \tag{2}$$

$$\text{Roughness Index} = \frac{\text{Percent (Predicted) roughness}}{\text{Maximum permissible roughness}} \tag{3}$$

2.2 Markov Chain

A Markov chain is a special type of discrete-time stochastic process, when the state of a system X_{t+1} at time $t + 1$ depends on the state of the system X_t at some previous time t but does not depend on how the state of the system X_t was obtained. This can be expressed as $P(X_{t+1} = j | X_t = i)$, where P is the probability of the state at time $t + 1$ being j given that the state at time t was i, assuming that the probability is independent of time. This assumption is formally known as the stationary assumption.

This stationary assumption is used because of the limited time period of the data collected. If data were collected over a large period, the quantity and type of

materials used might change over time and influence how a typical pavement section would determine. A Markov chain can be summarised through a probability transition matrix and the initial state probabilities.

To model pavement deterioration with time, it is necessary to establish a transition probability matrix (TPM), denoted by P. The general form of P is given below:

$$P = \begin{bmatrix} p_{11} & p_{12} & p_{13} & \cdots & \cdots & \cdots & \cdots & p_{1n} \\ p_{21} & p_{22} & p_{23} & \cdots & \cdots & \cdots & \cdots & p_{2n} \\ \cdots & \cdots & \cdots & \cdots & \cdots & \cdots & \cdots & \cdots \\ \cdots & \cdots & \cdots & \cdots & \cdots & \cdots & \cdots & \cdots \\ p_{n-11} & p_{n-12} & p_{n-23} & \cdots & \cdots & \cdots & \cdots & p_{n-1n} \\ p_{n1} & p_{n2} & p_{n3} & \cdots & \cdots & \cdots & \cdots & p_{nn} \end{bmatrix}$$

The matrix contains all of the information necessary to model the movement of the process among the condition states. The transition probabilities p_{ij} indicate the probability of the portion of the network in condition i moving to condition j in one duty cycle.

Two more conditions apply to the process when it is used to simulate pavement deterioration. First, $p_{ij} = 0$ for $i > j$, signifying the belief that roads cannot improve in condition without first receiving treatment. Second, $p_{nn} = 1$, signifying a holding state whereby roads that have reached their worst condition cannot deteriorate further. Consequently, in pavement deterioration, the general form of the transition matrix P is denoted by P^1:

$$P^1 = \begin{bmatrix} p_{11} & p_{12} & p_{13} & \cdots & \cdots & \cdots & \cdots & p_{1n} \\ 0 & p_{22} & p_{23} & \cdots & \cdots & \cdots & \cdots & p_{2n} \\ 0 & 0 & p_{33} & \cdots & \cdots & \cdots & \cdots & p_{3n} \\ \cdots & \cdots & \cdots & \cdots & \cdots & \cdots & \cdots & \cdots \\ 0 & 0 & 0 & 0 & 0 & 0 & p_{(n-1)(n-1)} & p_{(n-1)n} \\ 0 & 0 & 0 & 0 & 0 & 0 & 0 & 1 \end{bmatrix}$$

A further restriction allowing the condition to deteriorate by no more than one state in one duty cycle is commonly used in pavement deterioration modelling. The transition probability matrix is then denoted by P^2:

$$P^2 = \begin{bmatrix} p_{11} & p_{12} & 0 & 0 & \cdots & \cdots & \cdots & 0 \\ 0 & p_{22} & p_{23} & 0 & \cdots & \cdots & \cdots & 0 \\ 0 & 0 & p_{33} & p_{34} & \cdots & \cdots & \cdots & 0 \\ \cdots & \cdots & \cdots & \cdots & \cdots & \cdots & \cdots & 0 \\ 0 & \cdots & \cdots & \cdots & \cdots & \cdots & p_{(n-1)(n-1)} & p_{(n-1)n} \\ 0 & 0 & 0 & \cdots & \cdots & \cdots & \cdots & 1 \end{bmatrix}$$

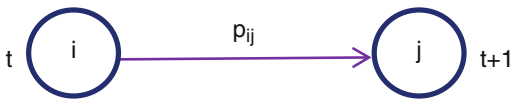

Fig. 1 The transition between two states

The entry of 1 in the last row of the transition matrix corresponding to state 10 (PCI of 0–10) indicates a holding or trapping state. The pavement condition cannot transit from this state unless repair action is performed.

The state vector for any duty cycle t is obtained by multiplying the initial state vector X (0) by the transition matrix P raised to the power of t. Thus,

$$X(1) = X(0) \cdot P$$
$$X(2) = X(1) \cdot P = X(0) \cdot P^2$$
$$\cdots\cdots\cdots\cdots\cdots\cdots\cdots\cdots$$
$$\cdots\cdots\cdots\cdots\cdots\cdots\cdots\cdots$$
$$X(t) = X(t-1) \cdot P = X(0) \cdot P^t$$

With this procedure, if the transition matrix probabilities can be estimated, the future state of the road at any duty cycle t can be predicted.

After the several cycle operations, rows of the matrix have identical entries; the reason is that probabilities in any row are the steady-state probabilities for the Markov chain, i.e. the probabilities of the state after enough time has elapsed that the initial state is no longer relevant.

2.2.1 Markov Transition Probability Matrices

These are useful in representing the change in condition of the system from one state to another over time. Change in condition is nothing but the transition from one state to another over time. So, essentially, the key elements of any Markov transition matrices are states and transitions. An interesting example of how a Markov transition matrix may be constructed is given below.

The classic example for a Markov process is a frog sitting in a pond filled with lily pads. In this example, each pad in the pond represents a state of the system. If there is a finite number of a pad in the pond, the system we are describing is a finite state system. If we were to check the pond every 5 minutes to observe the frog's location, each epoch in the model would be equivalent to 5 minutes in real time. The likelihood of the frog making a transition from pad i to j is p_{ij}. Figure 1 shows a simple schematic describing the transition from one state to the next.

There are several methods that can be used to estimate the present transition probabilities ($P_{i,i}$ and $P_{i,i+1}$). These methods are based either on the experience and adjustment of pavement experts or on sound engineering principles. Application of engineering principles requires feedback on pavement performance as obtained from field assessment of pavement distress.

Three methods are presented herewith for computing the transition probability matrix:

1. The first method is to apply the very basic definition of transition probabilities, i.e. if N_0 pavement sections are initially found in state i and N_f sections existed in state i after one transition, the transition probabilities can be estimated using

$$P_{i,i+1} = \frac{N_0 - N_f}{N_0} \tag{4}$$

and

$$P_{i,i} = 1 - P_{i,i+1} = \frac{N_f}{N_0} \tag{5}$$

2. The second method is based on estimating the service periods (D_i) in years that a pavement section is going to stay in state i. Let (t) be the length of time interval in years between successive transitions. Then, one simple equation can estimate the transition probabilities as follows:

$$P_{i,i+1} = \frac{t}{D_t} \leq 1.0 \tag{6}$$

where $\sum D_i = T$, where T is either the service life estimated from actual pavement performance records or the analysis period used in the design of pavement.

3. The standard approach is to observe, from historical data, the way in which a road network deteriorates over time and use this to estimate p_{ij} using the equation below:

$$P_{ij} = \frac{N_{ij}}{N_i} \tag{7}$$

where N_{ij} = number of road sections in the network that moved from condition i to condition j during one duty cycle and N_i = total number of road sections that started the year in condition i. The proportions are likely to vary from year to year, thereby requiring an average to be determined for each p_{ij} to ensure accuracy in the model.

2.3 Illustrative Example

A case study is conducted to demonstrate the procedure of the Markov chain-based pavement performance evaluation methodology. A bituminous-topped pavement of 12.70 km is used to generate the condition matrix by using Eq. (7). Suppose a 4.20-km length of the pavement lies between 8.1 and 10 condition ratings, i.e. in

Table 1 Condition state vector using probability distribution of pavement

Condition state	Corresponding condition rating	Length of the pavement section under consideration (km)	Probability distribution (%)
Very good	8.1–10	4.20	33.07
Good	6.1–8	3.40	26.77
Fair	4.1–6	2.80	22.05
Bad	2.1–4	1.60	12.60
Very bad	<2	0.70	5.51
Total length (km)		12.70	100.00

Table 2 Pavement condition rating distribution

Sl. no.	Condition state transition	Corresponding condition rating	Number of pavement sections
1	Very good → very good	8.1–10 → 8.1–10	665
2	Very good → good	8.1–10 → 6.1–8	29
3	Good → good	6.1–8 → 6.1–8	30
4	Good → fair	6.1–8 → 4.1–6	18
5	Fair → fair	4.1–6 → 4.1–6	110
6	Fair → bad	4.1–6 → 2.1–4	28
7	Bad → bad	2.1–4 → 2.1–4	49
8	Bad → very bad	2.1–4 → <2	15
9	Very bad → very bad	<2 → <2	56
10	Total no. of sections (100 m)		1,000

good condition state, then its probability to remain in this state is 33.07%. The pavement length of 4.20 km that comes under very good condition state is decided on the basis of Eq. (1) (Table 1).

Hence, condition matrix (1 × 5) based on overall pavement condition is given below:

$$\text{Condition matrix} = [0.3307 \quad 0.2677 \quad 0.2205 \quad 0.1260 \quad 0.0551]$$

Pavement transition matrix has been generated by using 1,000 sections of the pavement, whereas the length of the each section considered is 100 m. The process involved in arriving the transition matrix followed Tables 2 and 3. Finally, a transition probability matrix of 5 × 5 is arrived as shown in Table 4.

Pavement condition can be predicted by using condition probability matrix (1 × 5) and transition probability matrix (5 × 5). A horizon year condition matrix of 1 × 5 will come after multiplication of condition probability matrix (1 × 5) and transition probability matrix (5 × 5). Pavement condition performance graph has been plotted over the 12 years as shown in Fig. 2.

Table 3 Pre-transition probability matrix for overall pavement condition

	Future pavement condition in year (t + 1)						
		Very good	Good	Fair	Bad	Very bad	Total no. of sections
Present pavement condition in year (t)	Very good	665	29	0	0	0	694
	Good	0	30	18	0	0	48
	Fair	0	0	110	28	0	138
	Bad	0	0	0	49	15	64
	Very bad	0	0	0	0	56	56
	Total no. of sections						1,000

Table 4 Transition probability matrix for overall pavement condition

	Future pavement condition in year (t + 1)					
		Very good	Good	Fair	Bad	Very bad
Present pavement condition in year (t)	Very good	0.958	0.042	0	0	0
	Good	0	0.625	0.375	0	0
	Fair	0	0	0.797	0.203	0
	Bad	0	0	0	0.766	0.234
	Very bad	0	0	0	0	1

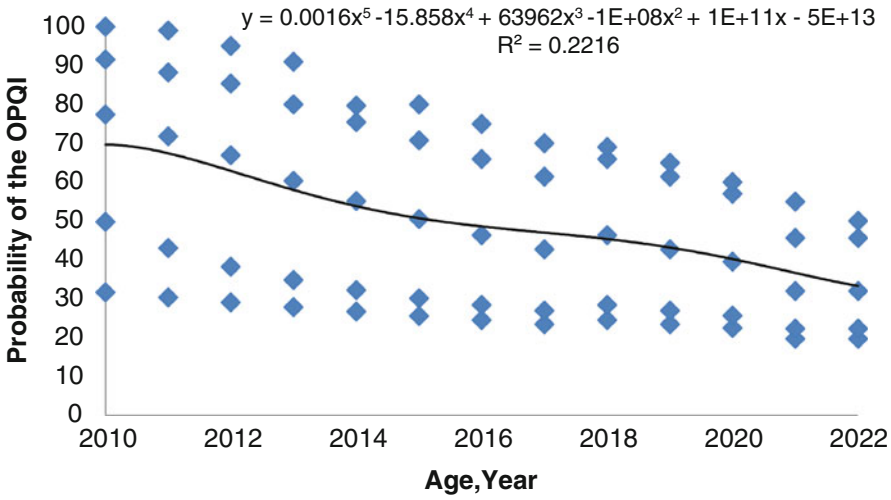

Fig. 2 Pavement condition prediction plot

2.3.1 Validation of Model

The developed model can be validated by mean absolute error (MAE), root mean squared error (RMSE), mean absolute relative error (MARE) or coefficient of

regression (R^2). In this chapter, validation is done by comparing the observed condition rating in the year 2011 with the condition rating predicted by the deterioration model developed for the same year. The reason for comparing the condition rating in year 2011 is that this is the only year for which the data is available.

In year 2011, the pavement condition rating obtained by using the model is 6.8 in 1–10 scale, whereas the observed value for the same year is 6.1. This result shows that the developed model is able to predict future condition rating with a reasonable degree of accuracy.

3 Conclusion

This chapter demonstrates the overall process for developing the pavement performance model based on Markov chain. The illustrative example gives the idea how Markov chain can be used for prediction of pavement condition. Base year pavement conditions have been identified using overall pavement quality index. Markov chain process is applied for predicting the horizon year pavement conditions. The developed model shows the satisfactory result with a reasonable degree of accuracy. Therefore, developed model can be used for prediction of pavement performance both at network and project level. Further, this model can be used by the road construction department in planning of maintenance and repair of roads.

References

1. Butt AA, Shahin MY, Feighan KJ, Carpenter SH (1987) Pavement performance prediction model using the Markov Process. Transportation Research Record, TRB, Washington, DC, 1123, pp 12–19
2. Hillear FS, Lieberman GJ (2009) Introduction to operations research, 8th edn. Tata McGraw Hill Education Private Ltd, New Delhi
3. Joseph NT, Chou YJ (2001) Pavement performance analysis applying probabilistic deterioration methods. Transportation Research Record, TRB, Washington, DC, 1769, 01–2962, pp 20–27
4. MORTH (2004) Guidelines for maintenance management of primary, secondary and urban roads. Indian Roads Congress Publications, New Delhi
5. Ortiz-Garcia JJ, Costello SB, Snaith MS (2006) Derivation of transition probability matrices for pavement deterioration modelling. J Transp Eng ASCE 132(2):141–161
6. Shahin MY (1994) Pavement management for airports roads and parking lots. Kluwer Academic Publishers, Boston/London
7. Shiyab AMSH (2007) Optimum use of the flexible pavement condition indicators in pavement management system. Ph.D. thesis, Curtin University of Technology. www.adt.curtin.edu.au/thesis/available/adt

Uncertainty of Code-Torsional Provisions to Mitigate Seismic Hazards of Buildings with Setback

Somen Mahato, Prasanta Chakraborty, and Rana Roy

Abstract Static torsional provisions in most of the seismic codes require that the earthquake-induced lateral force at each story be applied at a distance equal to design eccentricity (e_d) from the center of resistance of the corresponding story. Such code-torsional provisions, albeit not explicitly stated, are generally believed to be applicable to the regularly asymmetric buildings. Examined herein is the applicability of such code-torsional provisions to buildings with setback. A set of low-rise setback systems are analyzed using static torsional provisions and by response-spectrum-based procedure. A comparison of the response in terms of frame shear located at the perimeter and diaphragm displacements suggests the degree of reliability of code-torsional provisions for low-rise setback building.

Keywords Irregular • Torsion • Setback • Code provisions • Seismic • Low-rise building

1 Introduction

Geometry of the structure is often dictated by the architectural and functional requirements, whereas the safety of the same with optimum economy – key design aim – is ensured by structural engineers. For instance, a stepped form (setback systems) of building is often adopted by architect for adequate daylight and ventilation in the lower stories in an urban locality with closely spaced tall

S. Mahato • P. Chakraborty
Department of Civil Engineering, Bengal Engineering and Science University, Shibpur, Howrah 711103, India
e-mail: somen07@gmail.com

R. Roy (✉)
Department of Aerospace Engineering and Applied Mechanics, Bengal Engineering and Science University, Shibpur, Howrah 711103, India
e-mail: rroybec@yahoo.com

S. Chakraborty and G. Bhattacharya (eds.), *Proceedings of the International Symposium on Engineering under Uncertainty: Safety Assessment and Management (ISEUSAM - 2012)*,
DOI 10.1007/978-81-322-0757-3_40,

buildings. Such setback structures form an important subclass of irregular structures wherein irregularities are characterized by discontinuities in the distribution of mass, stiffness, and strength over the height of the building.

Seismic codes permit equivalent static procedure, usually for regular buildings, and the dynamic analysis (response-spectrum analysis or response-history analysis) for systems with significant irregularities in plan and elevation. In equivalent static analysis, the design base shear is estimated as a product of seismic weight and codified seismic coefficient associated to fundamental vibration period of the systems. Such seismic coefficient, on the one hand, accounts for the importance and ductility capacity of the structure while, on the other, represents the type of soil, seismic activity of the region, *etc*. Building codes [14] generally, for asymmetric systems, specify that the earthquake-induced lateral force at each story be statically applied with an eccentricity equal to design eccentricity (e_d) relative to the center of resistance of the corresponding story. Such design eccentricities are outlined in the form of primary design eccentricity, e_{d1j}, and secondary design eccentricity, e_{d2j}, at any typical story j, as

$$e_{d1j} = \alpha e_j + \beta D \text{ and } e_{d2j} = \delta e_j - \beta D \tag{1}$$

where D is the plan dimension of the building normal to the direction of ground motion and e_j is the static eccentricity at j-th story. α and δ are the coefficients aimed to be so calibrated that reasonable agreement in response between the equivalent static analysis specified by code and dynamic analysis is achieved. For each element, the value of e_d leading to the larger design force is to be used. The first part is a function of static eccentricity – real distance between center of mass (CM) and center of resistance. Dynamic amplification factor α in e_{d1} is intended to compensate for the dynamic effect of torsional response through static analysis. Factor δ incorporated in e_{d2} specifies the portion of the torsion-induced so-called negative shear that can be reduced for the design of stiff-side elements. The second part, referred to as accidental eccentricity, is expressed as a fraction of plan dimension, *i.e*., βD (normal to the direction of ground motion and is introduced to account for the differences between the actual and perceived eccentricities, torsional ground motion, and other imponderables).

Equivalent static procedure, recommended for regular buildings, using the concept of eccentricity and equivalent static loading "remains a basic approach" to allow for the effect of torsion. However, a lack of unanimously acceptable definition of center of resistance for multistory buildings often appears to be a major crux to implement such static procedure. A search for such resistance center defined elsewhere (e.g., [7, 11, 12, 18, 26, 27, 31, 33]) reveals a number of alternatives. Response computed on the basis of such different resistance centers, although located at variance, is often observed to be in agreement [10].

This observation indicates that the traditional notion of applicability of code-torsional provisions to regularly asymmetric systems (where center of mass and center of resistance are aligned along two vertical lines separated by a constant distance) may be over-restrictive. Thus, the applicability of code-torsional

provisions is reviewed herein in the context of buildings with setback where the center of resistance may dramatically vary story-wise. The significance of this undertaking seems obvious as the dynamic analysis, hard to perform and interpret, recommended for such systems may be bypassed subject to the adequacy of the code-static provisions – the focus of the current investigation.

2 Buildings with Setback: Research Progress

Studies (*e.g.*, [2, 13, 21]) up to mid-1980s on seismic response and relevant code provisions of systems with symmetric setback have been reviewed in the literature [34]. Research progress for systems with irregularity in elevation is scarce primarily owing to the relative difficulty to characterize such systems [20]. A simple definition to measure irregularity of such systems has been proposed and used in the recent works [19, 29]. Illustrations therein demonstrate the possibility of higher damage potential in the vicinity at and below the setback. A subsequent study [30] also corroborates such observation. Studies [4, 19] show that the participation of higher modes may be significant, and inter-story drift also magnifies in upper stories of such systems. The relative vulnerability associated to mass, strength, and stiffness irregularities has been examined elsewhere [1]. A simple method for the analysis of torsionally coupled buildings with setback has been developed recently [5, 20]. Barring very few useful attempts [35], relative paucity of experimental works in the relevant field is apparent to date.

A succinct survey [32] reveals that seismic response of structures with setback is kept unheeded in major seismic design codes (such as [3, 9, 17]) and dynamic analysis is recommended. The codes also require the base shear obtained from the dynamic analysis (and thereby, other response quantities) to be scaled up to that corresponds to the code-specified empirical formula.

In recognition of the apparent complexity of dynamic analysis in regular design and the promise of code-static approach [10], adequacy of the latter is explored in the context of low-rise setback systems. Response of such systems is computed with representative values of α and δ employing two convenient height-wise distributions of lateral load. Response so computed is compared to the same obtained due to response-spectrum-based analysis to realize the adequacy of code-static procedure.

2.1 Details of Structural Systems

Structures are idealized as rigid diaphragm (rigid in plane and flexure) model with three degrees of freedom at each floor, two translations in two mutually orthogonal directions and one in-plane rotation. Mass is assumed to be lumped at the center of mass (CM) of each floor coinciding with the geometric center of the deck.

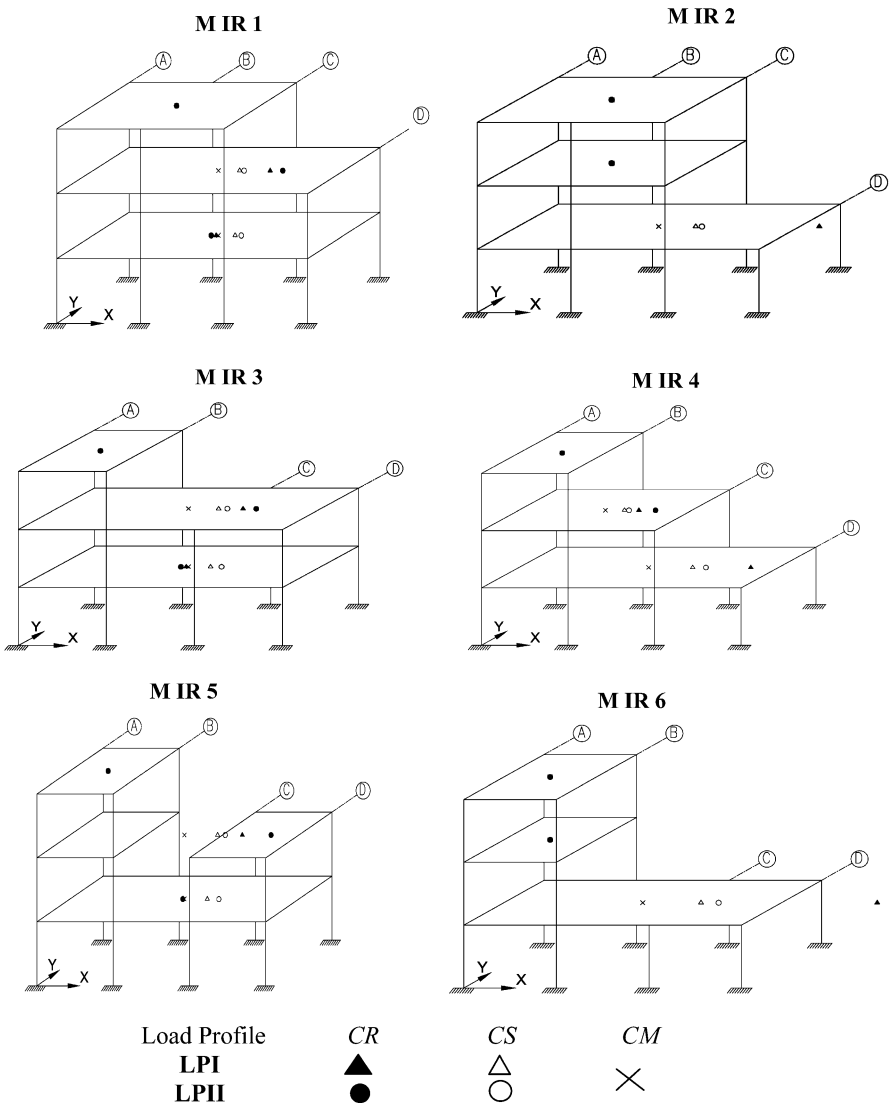

Fig. 1 Configuration of structural models showing center of mass (*CM*), center of rigidity (*CR*), and shear centre (*CS*)

Focusing on low-rise systems, three-story models with different feasible forms of setback are considered. Such systems annotated as M-IR 1 through MIR 6 are schematically presented in Fig. 1.

Irregularity indices (Φ_b, Φ_s) of the systems, proposed and utilized elsewhere [19, 29], are computed as follows and furnished in Table 1 to recognize the nature of elevation irregularity.

Table 1 System characteristics and basic seismic design parameters

Sl. no.	Category	Model identification	Irregularity index		Dynamic characteristics			Seismic weight (kN)			Design base shear (kN) [UBC 97]
			Φ_b	Φ_s	Mode 1	Mode 2	Mode 3	Story 1	Story 2	Story 3	
1	Irregular	M-IR1	1.25	1.25	0.367[a]	0.244	0.135	1,350	1,350	900	620
					0.858[b]	0.057	0.068				
2		M-IR2	2.00	1.25	0.362	0.217	0.140	1,350	900	900	540
					0.828	0.028	0.136				
3		M-IR3	1.25	2.00	0.333	0.234	0.122	1,350	1,350	450	540
					0.814	0.118	0.050				
4		M-IR4	1.75	1.75	0.326	0.183	0.121	1,350	900	450	465
					0.770	0.161	0.055				
5		M-IR5	1.75	1.75	0.303	0.218	0.120	1,350	900	450	465
					0.727	0.207	0.057				
6		M-IR6	2.00	2.00	0.306	0.158	0.134	1,350	450	450	385
					0.701	0.217	0.079				

EI for all column $= 8.54 \times 10^7 \text{Nm}^2$

[a]Values in first row represent period of vibration in each mode

[b]Values in second row represent participating mass ratio for excitation in Y-direction (Refer to Fig. 1)

$$\Phi_b = \frac{1}{n_b - 1} \sum_{i=1}^{i=n_b-1} \frac{H_i}{H_{i+1}} \text{ and } \Phi_s = \frac{1}{n_s - 1} \sum_{i=1}^{i=n_s-1} \frac{L_i}{L_{i+1}} \quad (2)$$

where n_s is the number of story, n_b is the number of bay in the first story, L is the length of bay (5m), and H (3.5m) is the height of the respective story. Length of the bay in the direction normal to setback is also kept equal to 5m.

Location of center of resistance varies as per different definitions and is also known to be dependent on the distribution of lateral load. In this context, generalized center of rigidity (denoted hereinafter as CR) and shear center (denoted hereinafter as CS) in each story are located following the procedure outlined in the literature [33]. Each of such resistance centers is located considering the height-wise distribution of lateral load as $w_i H_i^k \Big/ \sum_{i=1}^{n_s} w_i H_i^k$, where w_i and H_i are the weight and height of i story, n_s is the total number of story, and k is an exponent. Values of k are chosen as 1.0 and 2.0 in load profile LP I and LP II, respectively. Resistance centers so identified along with the center of mass (CM) are marked story-wise in respective building models (Fig. 1). Distance between CR and CM is referred to as floor eccentricity (e_R), while story eccentricity (e_S), defined as distance between CS and CM, is summarized in Table 2. In view of the lesser sensitivity of shear center and hence story eccentricity to the lateral load distribution, shear center (CS) is consistently used as reference resistance center and story eccentricity (e_S) as measure of asymmetry. In fact, the same is also reckoned to be a more reasonable measure of asymmetry [33]. Frame A and frame D (as shown in Fig. 1) are designated as flexible and stiff sides, respectively, observing the relative position of CM and CS.

2.1.1 Dynamic Properties

Dynamic properties of the systems are computed corresponding to translational (Y) and torsional degrees of freedom by standard eigenvalue solution. A review of the natural periods, corresponding mode shapes, and "participating mass ratio" (shown in percentage) in each mode (relevant to the excitation in Y-direction only), presented in Table 1, furnishes useful dynamic characteristics of the buildings.

The participating mass ratio for n-th mode is computed as $\left(f_{yn}\right)^2 / M_y$ where f_{yn} $\left(f_{yn} = {\varphi_n}^T m_y\right)$ is the participation factor in which m_y is the load corresponding to unit acceleration; M_y is the total unrestrained mass in Y-direction. The mode shapes (φ) are normalized such that $\varphi_n^T M \varphi_n = 1$ in which M is the global mass matrix [28].

Observing fundamental periods of the buildings, it seems that the same gradually increases with the reduction of irregularity (irregularity is maximum in MIR 6 and minimum in M–IR 1). Fundamental period of such systems, on the other hand, is computed as 0.43s. as per the empirical formula $T_a = 0.0731 h^{3/4}$outlined in UBC

Table 2 Eccentricities of structural systems under two different load distributions

		Load profile: LP I						Load profile: LP II					
		Floor eccentricity [e_R] (m)			Story eccentricity [e_S] (m)			Floor eccentricity [e_R] (m)			Story eccentricity [e_S] (m)		
Sl. no.	Model identification	Floor 1	Floor 2	Floor 3	Story 1	Story 2	Story 3	Floor 1	Floor 2	Floor 3	Story 1	Story 2	Story 3
1	M-IR1	0.00[a]	2.56[b]	−0.13[c]	0.00	1.28	1.00	0.00	3.87	−0.38	0.00	1.54	1.37
2	M-IR2	0.00	0.00	8.39	0.00	0.00	3.16	0.00	0.01	21.77	0.00	0.00	4.09
3	M-IR3	0.01	2.56	−0.13	0.01	1.71	1.25	0.00	3.85	−0.43	0.00	2.20	1.88
4	M-IR4	0.00	1.92	5.90	0.00	1.10	2.5	0.00	2.90	14.40	0.00	1.40	3.30
5	M-IR5	0.01	2.50	−0.05	0.01	2.20	1.50	0.00	3.80	−0.20	0.00	2.70	2.30
6	M-IR6	0.00	0.00	12.6	0.00	0.00	3.20	0.00	0.00	32.80	0.00	0.00	4.10

[a]At CM
[b]To the right of CM
[c]To the left of CM

97 where h is the overall height of the building (taken as 10.5m). This shows that the building period of this class of systems may generally be around 20% shorter than that computed by code-specified empirical formula. Thus, the code-specified empirical formula for building periods requires to be augmented since a higher estimate of period may often result in underestimation of design shear. However, it is intuitive that the effect of nonstructural elements such as infill wall may contribute to lower the period.

Vibration modes are expectedly coupled for all irregular systems. Fundamental mode of vibration appears to be primarily translational, and the second one is torsion dominated (refer to the corresponding values of participating mass ratio). Thus, the class of buildings chosen is torsionally stiff (TS) – also confirmed from the associated mode shapes. It is evident that, as irregularity of the structure decreases, contribution of torsion-dominated second mode is consistently diminishing while the participation of the translation-dominated fundamental mode increases. Thus, the simple irregularity index ($\Phi_{b,}$ Φ_s) seems consistent with the dynamic characteristics of the systems at least qualitatively implying the rationality of the irregularity index from a conceptual standpoint.

3 Method of Analysis

The response of the structures excited in Y-direction is computed utilizing equivalent static lateral load method. The base shear (V_0) is computed by multiplying the spectral ordinate relevant to period of the system, empirically determined, by seismic weight (refer to Table 1). Seismic coefficients C_a and C_v are chosen as 0.24 and 0.32, respectively. Considering zone factor Z equals to 0.2, occupancy importance factor as unity, and response reduction factor for OMRF as 3.5, design base shear is computed as per relevant guideline of UBC 97 (UBC 97). Design base shear so calculated is distributed over the building height as per LP I and LP II. α and δ (in Eq. (1)) recommended in major seismic codes generally take the value of 1.0 or 1.5 and 0.5 or 1.0, respectively. Three sets of values of α and δ are considered following international codes, viz., IS: 1893–2000, MEXICO 90, NZS 1170.5-2004, and NBCC-90. Static lateral load analysis is conducted utilizing two locations of CS and hence considering story eccentricity (e_s) associated to LP I and LP II.

The second approach employs a dynamic response-spectrum analysis (using design spectrum of UBC 97) with complete quadratic combination (CQC) for modal responses. Adequate number of modes is considered so that at least 95% of the total seismic mass is captured. Response obtained from this dynamic analysis is scaled by a factor equal to V_0/V_{dyna}, where V_{dyna} is the base shear from dynamic analysis.

4 Results and Discussions

From static analysis, maximum response in terms of frame shear, diaphragm displacement is computed employing two locations of CS relevant to LP I and LP II. Three combinations of α and δ, *viz*., $\alpha = 1.0$, $\delta = 0.5$ (NBCC-90); $\alpha = 1.5$, $\delta = 1.0$ (IS 1893–2002, Mexico-87); and $\alpha = 1.0$, $\delta = 1.0$ (NZS-92), are used.

Figure2a presents the height-wise variation of normalized frame shear in flexible side (frame A) and stiff side (frame D) located at the perimeter of the building (as the effect of torsion is maximum in the edge) relevant to the distribution of design base shear as per LP I (static analysis). Response of flexible side that is considering $\alpha = 1.0$ (NZS-92) is observed to consistently underestimate the response. However, it appears that the response of the flexible side at the base of the building can often be well predicted (with an error limit of -7 to +11) by equivalent lateral load method using $\alpha = 1.5$. However, the same may underestimate the response in the upper stories immediately above the setback in particular. This implies a higher concentration of force in the upper-story elements and in the vicinity of the setback, perhaps owing to the participation of higher modes that corroborates earlier works [8, 30]. $\delta = 0.5$ (NBCC-90) may often overestimate (around 65%), while $\delta = 1.0$ may underestimate the stiff-side response by about 20%.

Figure 2b, on the other hand, describing representative results out of comprehensive case studies, for a height-wise distribution of design base shear as per LP II (in static analysis), reflects a substantial conservatism. It may be recalled that the value of the exponent k involved in the definition of load distribution profile has been recommended [15] as unity (as in LP I) for buildings with fundamental period lesser than 0.5s. The observations of the present investigation support such recommendation.

It may be stated that, while frame shear may be used directly in design, diaphragm displacement profile may also be useful to envisage the damage potential due to pounding and may also be used to estimate inter-story drift – indicator of nonstructural damage. Maximum lateral displacements of the frames (frame A to frame D) computed for all possible combinations of codified amplification factors are normalized to the companion quantities obtained through CQC analysis.

Thus, the normalized displacement profile of the diaphragms, as presented in Fig. 3, may be regarded as the diaphragm displacement factor envelope. It is observed that such factor, in the flexible side, may be as high as 1.25 (or even more, *e.g*., 1.6 in MIR 4) at story 1 and reduces to some extent (though significant increase is noticed) in higher stories (refer to cases related to LP I). However, the same displays a propensity to decrease toward stiff side and may often underestimate in the perimeter frame. Deviation in diaphragm displacement factor envelope, although exhibits similar trend, is generally higher in case of LP II. This is in line with the earlier response scenario in terms of frame shear parameter.

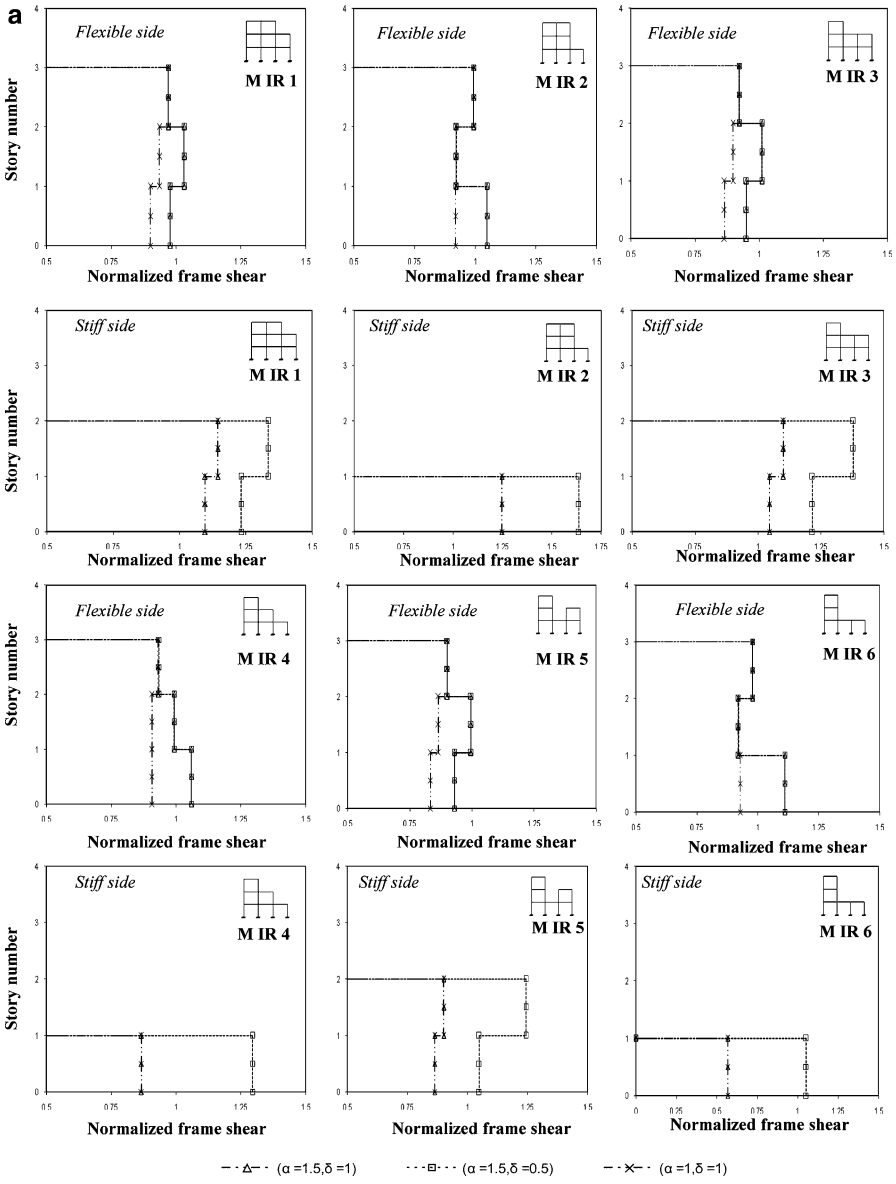

Fig. 2 (**a**) Variation of frame shear in flexible side (frame A) and stiff side (frame D) located at perimeter of code-designed systems (height-wise distribution of loads as per LP I) normalized to CQC response

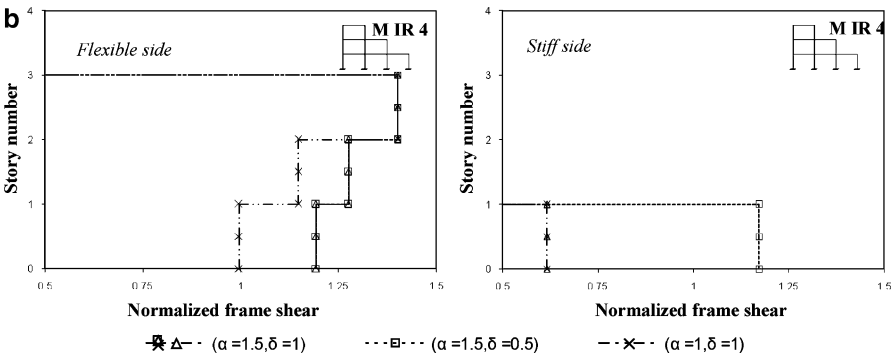

Fig. 2 (continued) (**b**) Variation of frame shear in flexible side (frame A) and stiff side (frame D) located at perimeter of code-designed systems (height-wise distribution of loads as per LP II) normalized to CQC response

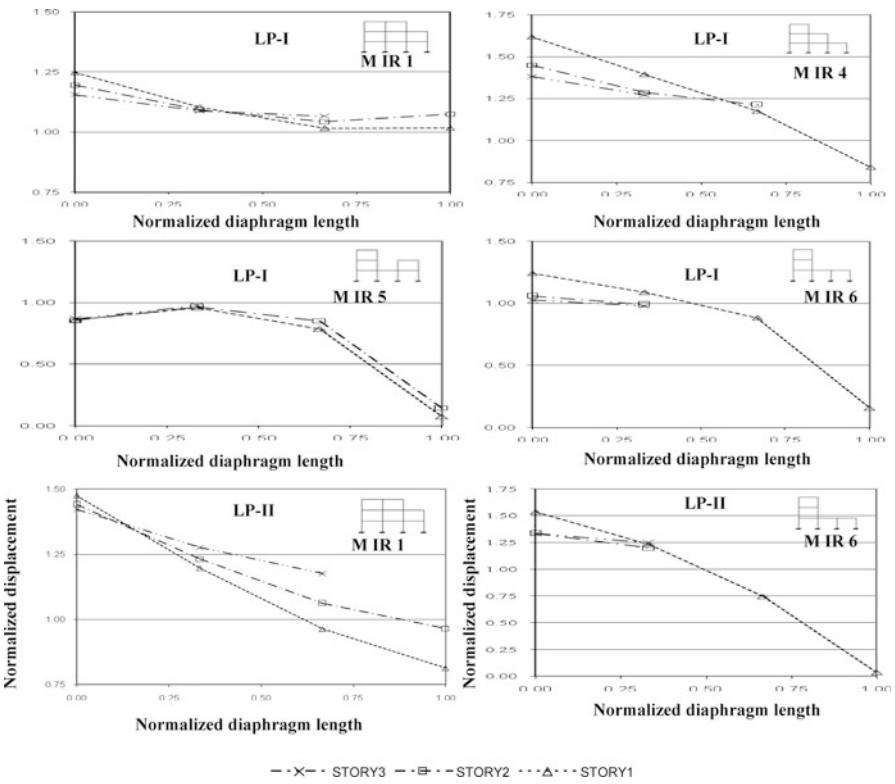

Fig. 3 Variation of diaphragm displacement envelope for code-designed systems (height-wise distribution of load as per *LP I* and *LP II*) normalized to CQC counterpart

5 Summary and Conclusions

In the context of difficulty of performing dynamic analysis in routine seismic design, codified torsional provisions, applied as adjunct to static lateral load analysis, are recognized as important tool. Such provisions, although not explicitly stated, are generally believed to be applicable to buildings with regular asymmetry. The present study examines the reliability of such codified standards for short period systems. To this end, the present investigation systematically examines the response of a number of low-rise systems covering representative forms of elevation irregularity through equivalent static lateral and response-spectrum-based methods. A comparison of the response reveals the following broad conclusions:

Direct design parameters such as frame shear may be reasonably predicted for flexible side of the buildings. Height-wise load distribution complying with LP I and relevant amplification factor $\alpha = 1.5$ should be considered for low-rise systems with setback. However, the code-static procedure does not appear promising for stiff side.

Code-torsional provisions are found to yield a substantially magnified prediction of diaphragm displacement for both the types of lateral load distribution profile adopted. Such magnification is higher toward the base of system and attains its peak at the first story level. However, since, for the purpose of design, the drift of the uppermost story is of major concern, the code-static procedure may be used to envisage the same with proper engineering judgment. Thus, the relevance of code-torsional provisions in the context of inter-story drift or floor lateral displacement – often regarded as important design consideration – is subject to be introspected further.

In view of the above observations, it is perceived that the detailed investigation is deemed essential to consolidate the applicability of code-torsional provisions for medium- to low-rise setback systems to make a final remark. Influence of nonstructural elements should also be accounted in such attempts. Further, codes generally specify to include accidental eccentricity which seems to be inconsistent in view of the relative stability of the location of center of mass in the context of other seismic design parameters [25]. Thus, the present study examines the applicability of code-torsional provisions at the exclusion of accidental eccentricity, and a rigorous study on the influence of the same is currently underway by the authors. Seismic design strategy inherently relies on ductile response, and hence, the performance of such code-designed systems in the post-elastic range of vibration also deserves to be explored in details.

References

1. Al-Ali AAK, Krawinkler H (1998) Effects of vertical irregularities on seismic behavior of building structures. Report no. 130. The John A. Blume Earthquake Engineering Center, Department of Civil and Environmental Engineering, Stanford University, Stanford, USA

2. Aranda GR (1984) Ductility demands for R/C frames irregular in elevation. In: Proceedings of the eighth world conference on earthquake engineering, San Francisco, USA, vol 4, pp 559–566
3. ASCE 7 (2005) Minimum design loads for buildings and other structures. American Society of Civil Engineers, Reston
4. Athanassiadou CJ (2008) Seismic performance of R/C plane frames irregular in elevation. Eng Struct 30:1250–1261
5. Basu D, Gopalakrishnan N (2008) Analysis for preliminary design of a class of torsionally coupled buildings with horizontal setbacks. Eng Struct 30:1272–1291
6. Chandler AM (1986) Building damage in Mexico City earthquake. Nature 320(6062):497–501
7. Cheung VWT, Tso WK (1986) Eccentricity in irregular multistory building. Can J Civil Eng 13(1):46–52
8. Cheung VWT, Tso WK (1987) Lateral load analysis for buildings with setback. J Struct Eng 113(21237):209–227
9. Eurocode 8 (2004) Design of structures for earthquake resistance, part-1: general rules, seismic actions and rules for buildings. European Committee for Standardization (CEN), Brussels
10. Harasimowicz AP, Goel RK (1998) Seismic code analysis of multi-storey asymmetric buildings. Earthq Eng Struct Dyn 27(2):173–185
11. Hejal R, Chopra AK (1987) Earthquake response of torsionally-coupled buildings. Report no. UCB/EERC-87/20. University of California, Berkeley
12. Humar JL (1984) Design for seismic torsional forces. Can J Civil Eng 12(2):150–163
13. Humar JL, Wright EW (1977) Earthquake response of steel-framed multistorey buildings with set-backs. Earthq Eng Struct Dyn 5(1):15–39
14. International Association for Earthquake Engineering (1997) Regulations for seismic design – a world list. IAEE, Tokyo
15. International Code Council (2003) International building code, 2003 edn. ICC, Falls Church
16. International Conference of Building Officials (1997) Uniform building code, 1997 edn. International Conference of Building Officials, Whittier
17. IS 1893–1984 (2002) Indian standard criteria for earthquake resistant design of structures. Bureau of Indian Standards, New Delhi
18. Jiang W, Hutchinson GL, Chandler AM (1993) Definitions of static eccentricity for design of asymmetric shear buildings. Eng Struct 15(3):167–178
19. Karavasilis TL, Bazeos N, Beskos DE (2008) Seismic response of plane steel MRF with setbacks: estimation of inelastic deformation demands. J Constr Steel Struct 64:644–654
20. Kusumastuti D, Reinhorn AM, Rutenberg A (1998) A versatile experimentation model for study of structures near collapse applied to seismic evaluation of irregular structures. Technical report MCEER-05-0002
21. Moehle JP, Alarcon LF (1986) Seismic analysis methods for irregular buildings. J Struct Eng ASCE 112(1):35–52
22. National Research Council of Canada (1990) National building code of Canada. Associate Committee on the National Building Code, Ottawa
23. National University of Mexico (1987) Design manual for earthquake engineering to the construction regulations for the Federal District of Mexico City, Mexico
24. New Zealand standard NZS 4203 (1984) Code of practice for general structural design loadings for buildings. Standards Association of New Zealand, Willington
25. Paulay T (2001) Some design principles relevant to torsional phenomena in ductile buildings. J Earthq Eng 5(3):273–308
26. Poole RA (1977) Analysis for torsion employing provisions of NZRS 4203 1974. Bull N Z Soc Earthq Eng 10(4):219–225
27. Riddell R, Vasquez J (1984) Existence of centres of resistance and torsional uncoupling of earthquake response of buildings. In Proceedings of the 8th world conference on earthquake engineering, vol 4, pp 187–194

28. SAP 2000 (2007) Integrated software for structural analysis and design. Version 11.0. Berkeley, CA. Computers and Structures, Inc.
29. Sarkar P, Prasad MA, Menon D (2010) Vertical geometric irregularity in stepped building frames. Eng Struct 32:2175–2182
30. Shahrooz BM, Moehle JP (1990) Seismic response and design of setback buildings. J Struct Eng ASCE 116(5):1423–1439
31. Smith BS, Vezina S (1985) Evaluation of centres of resistance of multistorey building structures. Proc Inst Civil Eng Part 2 Inst Civil Eng 79(4):623–635
32. Soni DP, Mistri BB (2006) Qualitative review of seismic response vertically irregular building frames. J Earthq Technol 43(4):121–132
33. Tso WK (1990) Static eccentricity concept for torsional moment estimations. J Struct Eng ASCE 116(5):1199–1212
34. Wood SL (1986) Experiments to study the earthquake response of reinforced concrete frames with setbacks. Thesis presented to the University of Illinois, Urbana, 111, in partial fulfillment of the requirements for the degree of Doctor of Philosophy
35. Wood SL (1992) Seismic response of RC frames with irregular profiles. J Struct Eng ASCE 118(2):545–566

Slope Failure Probability Under Earthquake Condition by Monte Carlo Simulation: Methodology and Example for an Infinite Slope

Jui-Pin Wang and Duruo Huang

Abstract A new approach in evaluating the slope failure probability under earthquake condition was proposed in this study. Unlike the use of a deterministic seismic coefficient in a pseudostatic analysis, the uncertainties of earthquake magnitude, location, frequency, and seismic-wave attenuation were taken into account in the new approach. The probability distributions of the earthquake parameters follow those described in probabilistic seismic hazard analysis (PSHA). Along with the considerations of the uncertainties of slope parameters, such as slope angle, slope height, and soil/rock properties, the slope failure probability can be estimated by a probabilistic analysis. In particular, the new approach used Monte Carlo simulation (MCS) in the analysis, in which random parameters were generated with prescribed probability distributions and statistics. With an n-trial MCS being performed, slope failure probability is equal to the ratio between the trial of slope failure and total trials. In this study, the approach was also demonstrated by a benchmark PSHA example integrated with a hypothetical infinite slope. For such a slope under the setup of seismicity, its failure probability increased to 8.3% in a 50-year condition, from 0.16% in a one-year condition. The increase in slope failure probability resulted from a higher earthquake frequency with respect to a longer duration of interest.

Keywords Slope failure probability • Earthquake • Monte Carlo simulation

J.-P. Wang (✉) • D. Huang
Department of Civil & Environmental Engineering, Hong Kong University of Science and Technology, Kowloon, Hong Kong
e-mail: jpwang@ust.hk; drhuang@ust.hk

S. Chakraborty and G. Bhattacharya (eds.), *Proceedings of the International Symposium on Engineering under Uncertainty: Safety Assessment and Management (ISEUSAM - 2012)*,
DOI 10.1007/978-81-322-0757-3_41,

1 Introduction

Earthquake prediction is controversial [3]. A number of research teams have spent countless efforts on earthquake prediction, but the result is not satisfactory; otherwise, the recent earthquake-induced disasters would have been prevented or mitigated. Accordingly, some researchers draw the conclusion about earthquake prediction. That is, the prediction of exact time, location, and size of coming catastrophic earthquakes seems impossible [3]. However, seismic hazard prediction is acceptable by the scientific community [3]. In brief, seismic hazard is a probability-based ground motion. In other words, the seismic hazard prediction is analogue to weather forecast, estimating the probability for a potential event. Accordingly, an earthquake-resistant design of civil engineering can be developed with the desired conservatism for a given type of structures.

A few approaches have been developed for seismic hazard assessments. One of the most popular methods is probabilistic seismic hazard analysis (PSHA), developed in the late 1960s [1]. In the past couple decades, a number of PSHA studies were performed on evaluating earthquake potentials for some regions [8, 12]. Prescribed by a few technical guidelines, PSHA has been used for developing earthquake-resistant designs for critical structures prescribed in industry [5, 15].

Slope stability under earthquake condition is commonly evaluated by the pseudostatic analysis [13], in which earthquake loading owing to excited ground accelerations becomes an extra force. In the pseudostatic analysis, the horizontal seismic coefficient, k_h ($=a_h/g$, where a_h is horizontal earthquake motion), is prescribed by a constant. As an example, in the seismic-stability analysis of a Himalayan rock slope, the horizontal seismic coefficient k_h was selected as 0.31 g based on the maximum credible earthquake around the region [10]. By design, the value ought to be adequately conservative, but the level of conservatism was unknown or unquantified by an exceedance probability or by a recurrence rate.

This study presents the methodology in evaluating the slope stability under earthquake condition, in which the uncertainty of earthquake occurrence is considered, along with those from material properties and slope characteristics. The overviews of PSHA and Monte Carlo simulation (MCS) are described in this chapter. Demonstrated by a benchmark PSHA example integrated with a hypothetical infinite slope, the slope failure probability is evaluated under earthquake condition.

2 Overviews of PSHA

PSHA considers the uncertainties of earthquake size, location, and seismic-wave attenuation and provides the annual rate for a ground motion estimate. With the use of the Poisson distribution, the exceedance probability for such a motion within the duration of interest can be estimated. As an example, the United States

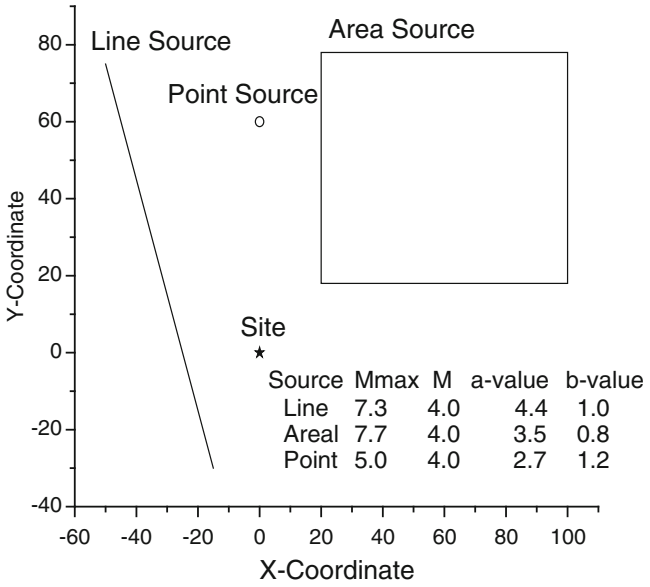

Fig. 1 Setup of the benchmark PSHA example (After Kramer [9])

Geological Survey has used PSHA to develop the national hazard maps with the update in every 6 years [14].

The assumptions and techniques for analyzing earthquake uncertainty in PSHA are described in the following. A uniform distribution is considered for earthquake recurrence in space. In other words, any location within a seismic zone shares an identical probability for the next occurrence. The uncertainty of earthquake magnitude is derived with the use of conditional probability, and accordingly the density function of earthquake magnitude can be developed [4, 11]. Seismic-wave attenuation is also uncertain and can be governed by a so-called ground motion model, which prescribes a predictive, probability-based relationship between earthquakes and ground motions.

Figure 1 shows the setup of a benchmark PSHA example [9]. Three seismic sources are present. Note that the coordinate is not in a longitude-latitude system, so that the distance (d) between two points can be calculated by $d = \sqrt{(x_1 - x_2)^2 + (y_1 - y_2)^2}$. The recurrence parameters, a-value and b-value, and maximum magnitude ($M_{\max}$) and magnitude threshold (M_0) are also summarized in Fig. 1. In addition, the ground motion model used in the example is as follows:

$$\ln Y = 6.74 + 0.859M - 1.8 \times \ln(R + 25) \tag{1}$$

where $\ln Y$ denotes the logarithm of PGA in unit of gal; M and R denote magnitude and distance, respectively.

According to the a-value, b-value, M_0, and M_{max}, the annual rates of earthquake (v) can be found as 2.52, 1.99, and 0.008 for the line, area, and point sources, respectively [11]. Note that the number of earthquakes (N) in PSHA is considered a constant, prescribed by annual rate v. However, this consideration is unrealistic, since it is very unlikely that earthquakes would recur periodically in time. Therefore, the number of earthquakes is better regarded as a random variable, and it can be modeled by the Poisson process [6] with a given annual rate. With annual rate equal to 2.52, for instance, the respective probabilities are 8 and 28% for zero earthquake and one earthquake within one year. As a result, the number of events is the additional variable, so that a total of four earthquake variables govern earthquake motion distributions at a site of evaluation.

3 Pseudostatic Analysis for an Infinite Slope in C-Φ Condition

Figure 2 shows the systematic diagram of an infinite slope without considering pore pressure. With the factor of safety (FOS) being defined as the ratio of resistant force to driving force, it was derived as follows:

$$\mathrm{FOS} = \frac{\gamma h \tan\varphi(\cos\beta - k_h \sin\beta) + \frac{c}{\cos\beta}}{\gamma h(\sin\beta + k_h \cos\beta)} \tag{2}$$

where c = cohesion, φ= angle of internal friction, k_h = horizontal seismic coefficient, β = slope angle, h = slope height, and γ = unit weight. Accordingly, the FOS for such a slope is governed by the six parameters. As an example, the FOS is equal to 1.79 in a static condition ($k_h = 0$), with those parameters summarized in Table 1. Figure 3 shows the relationship between critical FOSs and horizontal seismic coefficients. At a critical FOS equal to 1.0, the slope is subject to failure as k_h greater than 0.43.

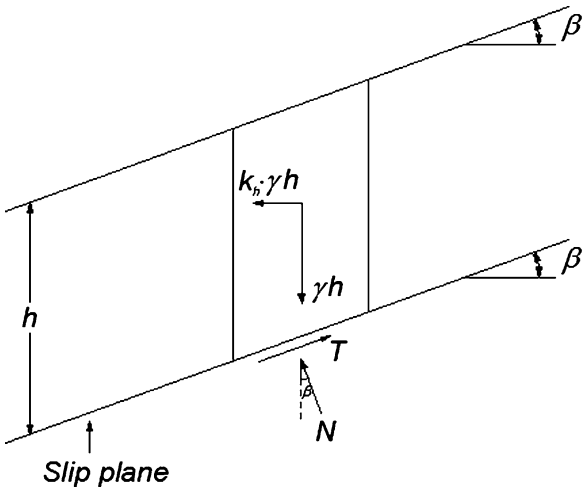

Fig. 2 Systematic diagram of an infinite slope

Table 1 Statistical characteristics of slope parameters

	c [kN/m^2]	φ [°]	h [m]	γ [kN/m^3]	β [°]
Mean value	15	35	5	27	25
COV[a] [%]	10	10	5	5	1
Probability models	Lognormal	Lognormal	Lognormal	Lognormal	Lognormal

[a]COV = coefficient of variation

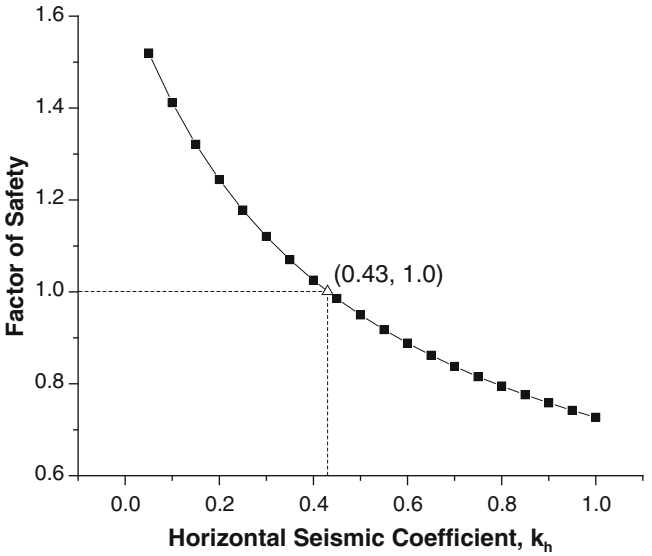

Fig. 3 Relationship between critical FOSs and horizontal seismic coefficients

4 Slope Failure Probability by Monte Carlo Simulation Under Earthquake Condition

4.1 Monte Carlo Simulation

MCS is one of the widely used probabilistic analyses. Its essential is to generate random values following prescribed statistics and probability distributions. With a number of trials being performed, the slope failure probability (P_F) is estimated as follows:

$$P_F = \frac{\sum_{i=1}^{n} F_i \leq F_C}{n} \tag{3}$$

where n is the number of trials (or sample size) in MCS and F_i and F_C denote the FOS in the ith trial and critical factor of safety, respectively. The nominator of the expression dictates the number of trials presenting a scenario of slope failure.

4.2 Randomization of Ground Motions

In this analysis, the randomization of the five slope parameters (c, φ, γ, β, h) is relatively straightforward, with their respective statistics (mean value and COV) and probability distribution being provided. However, this is not the case in the randomization of ground motion, as it is related to the four earthquake parameters as mentioned. Its randomization is described in detail in the following.

For a magnitude-distance ground motion model expressed by $f(M, R)$, such as Eq. 1, given $M = m_0$ and $R = r_0$, the mean value and SD of the logarithm of ground motion ($\ln Y$) are equal to $f(m_0, r_0)$ and σ^*, respectively. Since $\ln Y$ follows a normal distribution [9], the relationship between Z (standard normal variate), M, R, and Y can be derived as

$$\begin{aligned} Z &= \frac{\ln Y - f(M,R)}{\sigma *} \\ &\Rightarrow \ln Y = Z \times \sigma * + f(M,R) \\ &\Rightarrow Y = \exp(Z \times \sigma * + f(M,R)) \end{aligned} \tag{4}$$

Therefore, a random ground motion is governed by the three earthquake variables that are randomly generated. For a random magnitude, it can be generated with respect to the prescribed density function used in PSHA. To ensure a high precision in simulation, the magnitude density functions were developed with the use of the magnitude interval as small as 0.05. Figure 4 shows the functions for the three seismic zones. A random distance can be obtained with a random location being generated in advance. Unlike the two parameters, a random z that controls the variability in ground motion attenuation can be generated in a straightforward manner as randomly generating slope parameters, since Z follows a normal distribution with mean and SD equal to 0 and 1, respectively.

4.3 Randomization of Maximum Ground Motions

In failure assessments under earthquake condition, a deterministic criterion is usually followed. That is, catastrophic failure only occurs when the design motion is exceeded by an earthquake motion. In other words, the number of earthquake motions less than the design motion that a structure has experienced is not a matter to failure, and as long as the structure can survive under a maximum-motion condition, the failure probability is literally zero. Therefore, the distribution of the maximum motion is of interest in earthquake-resistant design.

Considering n earthquakes within a given seismic zone, the maximum ground motion ($Y_{\max}$) is as follows:

$$Y_{\max} = MAX\{Y_1, Y_2, ..., Y_n\} \tag{5}$$

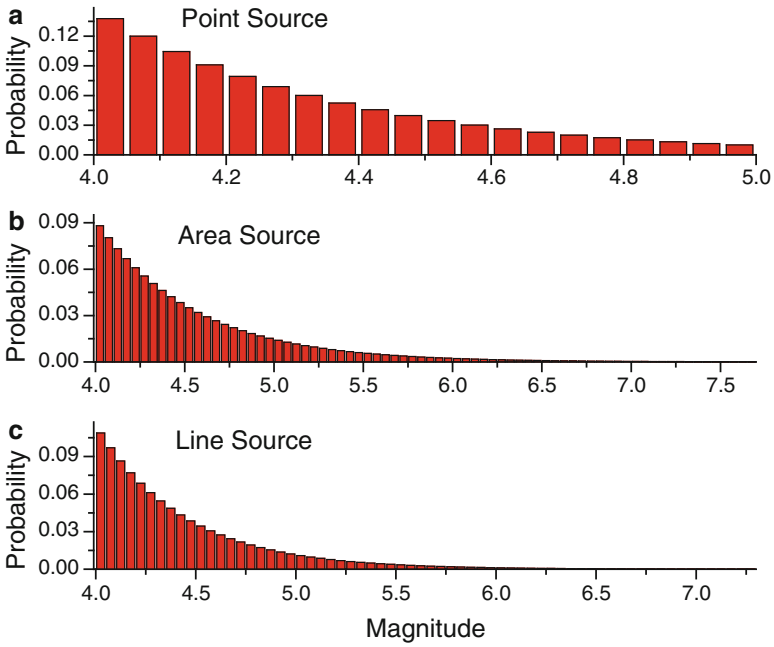

Fig. 4 Magnitude probability density functions for the three seismic sources

where Y can be obtained from Eq. 4. Normally, multiple seismic sources are present in a region as the benchmark PSHA example. Extended from Eq. 5, the ultimate maximum motion ($\tilde{Y}_{\max}$) in an m-source condition can be expressed as follows:

$$\tilde{Y}_{\max} = MAX\{Y^1_{\max}, Y^2_{\max}, ..., Y^m_{\max}\} \tag{6}$$

where $Y^i_{\max}$can be obtained from Eq. 5.

4.4 Program Tool

A program was developed in-house for the computer-aided analysis. The program was compiled with the use of the spreadsheets and "macros" (user-defined functions and subroutines) in Excel. The uniform-number generator in Excel that randomly generates values (U) between 0 and 1 was used. For those variables with given probability distributions, such as slope parameters, their respective random values (R) can be converted from U with the use of inverse probability function, $f^{-1}()$, as follows:

$$R = f^{-1}(U) \tag{7}$$

On the other hand, for earthquake magnitude with a density function back-calculated from conditional probability, random magnitudes were generated by the mapping rule as follows:

$$M = \begin{cases} m_1; & U \le \tilde{p}_1 \\ m_{i+1};\ \tilde{p}_i < U \le \tilde{p}_{i+1} \end{cases} \tag{8}$$

where m_i and $\tilde{p}_i$are the ith earthquake magnitude and cumulative probability, which can be determined from the density function shown in Fig. 4.

5 Results of the Numerical Example

5.1 Statistical Characteristics of Slope Parameters

The statistical characteristics, such as COV and probability distribution, of slope parameters (e.g., slope angle) are also summarized in Table 1. A lognormal distribution was used for simulating the distributions of material strength, such as cohesion and angle of internal friction [2, 7]. Without information available regarding probability distributions with respect to slope angle and slope height, both were assumed to follow lognormal distributions as well. The levels of variations for the slope parameters are estimated accordingly. A low variation was assigned for slope angle, since the angle in an infinite slope should keep constant.

5.2 Results and Discussions

Figure 5 shows the relationship between failure probability and critical factors of safety in four different durations. The slope failure probability increases with a longer duration being considered. With critical FOS equal to 1.0, the failure probability is increased to 8.3% in 50 years, from 0.16% in one year. A linear relationship in the $\log(P_F)-F_c$ space was found.

Figure 6 shows the relationship between slope failure probabilities and durations of evaluation. Linear relationships with a positive correlation were found between the two variables, especially when the critical factor of safety is close to 1.0. As the critical factor of safety was increased to as high as 1.5, the relationship between failure probability and duration becomes more nonlinear.

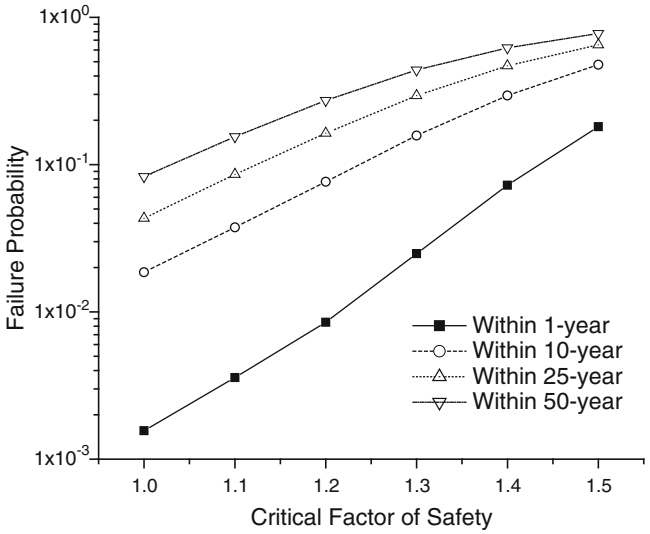

Fig. 5 Relationship between failure probability and critical factors of safety for the slope shown in Fig. 3

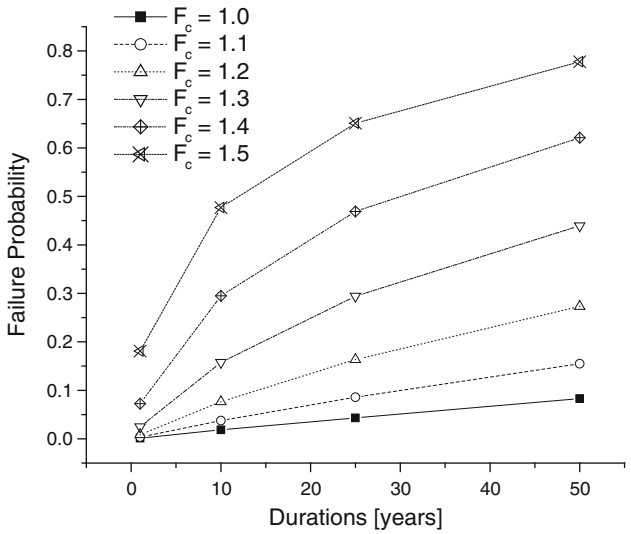

Fig. 6 Relationship between failure probability and duration for the slope shown in Fig. 3

6 Conclusions

A new approach in the assessment of slope failure probability under earthquake condition was described and proposed in this study. The new approach considers the uncertainties of earthquake parameters, such as magnitude, location, frequency,

and seismic-wave attenuation, along with the uncertainty of slope parameters. The essential of the probabilistic analysis is with the use of MCS. The slope failure probability is governed by the ratio between the trials with a slope failure scenario and total trials. The approach was demonstrated with the use of a benchmark PSHA example integrated with a hypothetical slope. The slope failure probabilities were successfully evaluated for four different durations, and a positive correlation between failure probability and duration was found.

References

1. Cornell CA (1968) Engineering seismic risk analysis. Bull Seism Soc Am 58(5):1583–1606
2. Duzgun HSB, Yucemen MS, Karpuz C (2003) Probabilistic modeling of plane failure in rock slopes. Appl Stat Probab Civ Eng 1:1255–1262
3. Geller RJ, Jackson DD, Kagan YY, Mulargia F (1997) Earthquakes cannot be predicted. Science 275(5306):1616
4. Gutenberg B, Richter CF (1944) Frequency of earthquakes in California. Bull Seism Soc Am 34(4):1985–1988
5. International Atomic Energy Agency (IAEA), Vienna (2002) Evaluation of seismic hazards for nuclear power plants safety guide, Safety standards series no. NS-G-3.3
6. Jafari MA (2010) Statistical prediction of the next great earthquake around Tehran, Iran. J Geodyn 49:14–18
7. Jimenez R, Sitar N, Chacon J (2006) System reliability approach to rock slope stability. Int J Rock Mech Min Sci 43(6):847–859
8. Kebede F, Van Eck T (1997) Probabilistic seismic hazard assessment for the Horn of Africa based on seismotectonic regionalization. Tectonophysics 270:221–237
9. Kramer AL (1996) Geotechnical earthquake engineering. Prentice-Hall, Inc., Upper Saddle River
10. Latha GM, Garaga A (2010) Seismic stability analysis of a Himalayan rock slope. Rock Mech Rock Eng 43(6):831–843
11. McGuire RK, Arabasz WJ (1990) An introduction to probabilistic seismic hazard analysis. Geotech Environ Geophys Soc Explor Geophys 1:333–353
12. Sokolov VY, Wenzel F, Mohindra R (2009) Probabilistic seismic hazard assessment for Romania and sensitivity analysis: a case of joint consideration of intermediate-depth (Vrancea) and shallow (crustal) seismicity. Soil Dyn Earthq Eng 29(2):364–381
13. Terzaghi K, (1950) Mechanics of landslides. Bull Geol Soc Am Berkeley Volume:83–123
14. United States Geological Survey (2008) United States geological survey national seismic hazard maps. http://earthquake.usgs.gov/hazards/products/conterminous/2008/maps/
15. United States Nuclear Regulatory Commission (USNRC) (2007) A performance-based approach to define the site-specific earthquake ground motion, Regulatory Guide 1.208. Washington, DC

Polynomial Chaos in Bootstrap Filtering for System Identification

P. Rangaraj, Abhijit Chaudhuri, and Sayan Gupta

Abstract The objective of this chapter is to develop a computationally efficient approach for system identification. An algorithm, the bootstrap filter in conjunction with polynomial chaos expansion, is proposed for identification of system parameters. The central idea of the proposed method is the introduction of response through polynomial chaos expansion in the filtering algorithm. Appreciable performance of the proposed algorithm is been provided by considering the problem of the identification of the properties of a single degree of freedom system.

Keywords System identification • Polynomial chaos • Spectral representation • Particle filter • Probabilistic collocation

1 Introduction

Several approaches are discussed in the literature for structural system identification. They can be broadly classified into deterministic and probabilistic approaches. Deterministic approaches to system identification have considerable limitations over probabilistic approaches. Probabilistic identification techniques can be grouped into two categories. The first includes the well-known Kalman filter and its variants [8, 7], and the second includes the Monte Carlo simulation-based algorithms, also referred to as particle filters [3, 6, 10]. The Kalman filter is an efficient method for estimating the state of the system from noisy measurement data using a simple predictor-corrector approach. It consists of a set of mathematical equations that provides a recursive means to estimate the state of the process. The filter can be used to estimate the system state only when the process model

P. Rangaraj (✉) • A. Chaudhuri • S. Gupta
Department of Applied Mechanics, Indian Institute of Technology Madras, Chennai 600036, TN, India
e-mail: rangaraj.p138@gmail.com; abhijit.chaudhuri@iitm.ac.in; sayan@iitm.ac.in

S. Chakraborty and G. Bhattacharya (eds.), *Proceedings of the International Symposium on Engineering under Uncertainty: Safety Assessment and Management (ISEUSAM - 2012)*,
DOI 10.1007/978-81-322-0757-3_42,

and measurement model equations are linear. When the process equations are non-linear, Kalman filters cannot be used directly. Instead, an adaptive strategy that enables the use of Kalman filter has to be adopted. However, in most parameter identification problems, the process model and measurement model equations are nonlinear and hence, Kalman filter-based techniques can be used only in an approximate form.

Particle filtering algorithms work on the same principle of predictor-corrector approach used in the Kalman filters. However, unlike in the case of Kalman filters, here the process of Bayesian updating is carried out using Monte Carlo simulations. Since particle filtering algorithms are based on Monte Carlo simulations, there are no restrictions on the model and/or the measurement equations being linear. As a result, particle filtering algorithms are more widely applicable.

2 System Identification

To analyze and identify system parameters of a dynamic system from measurements, the system equations are written in the form as

$$\mathbf{X}_{k+1} = f(\mathbf{X}_k, \theta_k, \mathbf{w}_k) \tag{1}$$

$$\mathbf{Z}_k = f(\mathbf{X}_k, \theta_k, \mathbf{v}_k). \tag{2}$$

Equation (1) is the process model equation that relates the states of the system at successive time instants in a recursive manner, while Eq. (2) is the measurement model equation that relates the measurements to the state of the dynamical system. Here, $\mathbf{X}_k$ is a n-dimensional vector representing the state space associated with the system at the kth time instant, θ_k denotes the vector of system parameters at time instant k, $\mathbf{Z}_k$ are measurements at time k, and $\mathbf{w}_k$ and $\mathbf{v}_k$ represent the process model noise and measurement model noise, respectively, $f(\cdot)$ denotes the functional form that relates the state vector $\mathbf{X}_k$, and $\mathbf{X}_{k+1}$ and $g(\cdot)$ represent the corresponding functional relationship between $\mathbf{X}_k$ and the measurements $\mathbf{Z}_k$. In the Bayesian approach to dynamic state estimation, one attempts to construct the posterior probability density function (pdf) of the state based on information available from measurements. Since this pdf embodies all available statistical information, it may be said to be the complete solution to the estimation problem. For many problems, an estimate is required every time that a measurement is received. In this case, a recursive filter is a convenient solution. A recursive filtering approach means that received data can be processed sequentially rather than as a batch so that it is not necessary to store the complete data set nor to reprocess existing data if a new measurement becomes available. Such a filter consists of essentially two stages: prediction and update. The prediction stage uses the system model to predict the state pdf forward from one measurement time to the next. The update operation uses the latest measurement to modify the prediction pdf. This is achieved using Bayes theorem, which is the mechanism for updating knowledge about the target

state in the light of extra information from new data. Particle filters are based on these approach of prediction-updation. It is a technique for implementing a recursive Bayesian filter by Monte Carlo simulations.

2.1 Bootstrap Particle Filtering

In this study, we use the bootstrap particle filter proposed in Gordon [6]. The objective of the bootstrap filter is to estimate the current state of the system $\mathbf{X}_k$, from the available measurements $\mathbf{D}_k$, where the set of k measurements from initial time is represented as $\mathbf{D}_k = \{\mathbf{Z}_1,\mathbf{Z}_2,\ldots,\mathbf{Z}_k\}$. We aim to explore the application of dynamic state estimation procedures to achieve parameter estimation. Since both $\mathbf{X}_k$ and $\mathbf{Z}_k$ are corrupted by noise $\mathbf{w}_k$ and $\mathbf{v}_k$, complete information of the state is possible if the pdf of $\mathbf{X}_k$ conditioned on the available measurements $\mathbf{D}_k$ and denoted as $p(\mathbf{X}_k|\mathbf{D}_k)$ is available. The key steps in the implementation of the algorithm are as follows [6]:

1. Assume $p(\mathbf{X}_k|\mathbf{D}_{k-1})$ is known. Generate the vector of random samples $\{\mathbf{X}_{k-1}\}_{i=1}^{N}$ from the pdf $\{\mathbf{X}_{k-1}\}_{i=1}^{N}$.
2. Generate samples $\{\mathbf{w}_{k-1}\}_{i=1}^{N}$ from the known distribution of $p(\mathbf{w}_{k-1})$.
3. Each sample is passed through the system model in Eq. (1) to obtain the predictions for the state at time step k. Thus,

$$\mathbf{X}_k^{*(i)} = f_{k-1}(\mathbf{X}_{k-1}^{(i)}, \mathbf{w}_{k-1}^{(i)}). \tag{3}$$

4. Once the measurements $\mathbf{Z}_k$ is available, evaluate the likelihood of each prediction $\{\mathbf{X}_k^{*(i)}\}_{i=1}^{N}$ and obtain a normalized weight for each sample, given by

$$q_i = \frac{p(\mathbf{Z}_k \mid \mathbf{X}_k^{*(i)})}{\sum_{j=1}^{N} p(\mathbf{Z}_k \mid \mathbf{X}_k^{*(j)})}. \tag{4}$$

5. Define a discrete distribution over $\{\mathbf{X}_k^{*(i)}\}_{i=1}^{N}$, with probability mass q_i associated with element i.
6. Resample N times from the discrete distribution to generate samples $\{\mathbf{X}_k^{*(i)}\}_{i=1}^{N}$ so that for any j, $P[\mathbf{X}_k^j = \mathbf{X}_k^{*(i)}] = q_i$.

The above steps of prediction and update form a single iteration of the recursive algorithm. The above algorithm was proposed to predict the state of a dynamical system [6]. However, in this study, our focus is on identifying the parameters of a dynamical system. One way to approach the problem is to augment the state vector with the vector of parameters that need to be estimated. The problem with such anapproach is that parameter identification and state estimation of the system result in an increase of the size of the vectors that need to be estimated. This results in wastage of significant computational effort in estimating the state vectors.

Instead, if the system parameters are assumed to be independent parameters and the measurement equation is expressed as a function of these parameters, then significant reduction in computational efforts could be achieved. This has been discussed by Nasrellah and Manohar [10]. Here, the model equation is written as

$$\theta_{k+1} = \theta_k + \mathbf{w}_k, \tag{5}$$

while the measurement equation is given by

$$\mathbf{Z}_k = g(\theta_k) + \mathbf{v}_k, \tag{6}$$

where the variables are as already defined earlier. It is worth commenting here on the process noise $\mathbf{w}_k$. If it is assumed that the system parameters θ_k do not change with time, then the process equation should be $\theta_{k+1} = \theta_k$. Now, if the bootstrap filter algorithm (BFA) is applied, subsequent resampling would lead to the generation of a particular sample which has the greatest weightage q_k among the N initial sampled realizations for θ_k. As the algorithm progresses, all the resampled data would converge to a particular realization and would lead to degeneracy. To overcome this problem, a small noise $\mathbf{w}_k$ is added to jitter the samples at each time step. This would enable a greater variation of resampled data at time t_{k+1} around the realization of the sample with the greatest weight at time t_k. This procedure also has the effect of increasing the least count accuracy of the algorithm in predicting the system parameters. The effect of jittering on the resampled data with artificial noise has been recommended in the literature [10]. A more exhaustive study on this has also been reported in [9].

The computational costs of the bootstrap filtering algorithm depend on

(a) The number of particles N used at each iteration
(b) The number of times the model is updated using the BFA

Here, ideally one should apply the BFA to each measurement data. This would imply that the BFA implementation rate would be equal to the measurement sampling rate. Moreover, it must be noted that application of BFA at each time step requires N calls to the process model. Thus, if there are M measurement points and N particles at each BFA step, the system would need to be solved NM times. This could be computationally very costly especially for complex structures, where the solution of a model equation could involve time in terms of hours. There is therefore a need to investigate the possibility of reducing the computational costs. This chapter focuses on the development of a polynomial chaos-based approach to reduce computational costs.

3 Polynomial Chaos Expansion

Polynomial chaos expansion (PCE) [4, 5] is a spectral uncertainty quantification tool, which is based on the homogeneous chaos theory of Wiener [11]. The stochastic input in PCE is represented spectrally by employing orthogonal

polynomial functionals from the Askey scheme as basis in the random space. In its original form, it employs Hermite polynomials as basis from the generalized Askey scheme and Gaussian random variables. It can be shown that an optimum convergence is achieved for Gaussian inputs. As per the Cameron-Martin theorem [1], a random process $X(t, \theta)$ (as function of random event θ) which is second-order stationary can be written as

$$X(t,\theta) = \hat{a}_0\psi_0 + \sum_{i_1=1}^{\infty} \hat{a}_{i_1}\psi_1(\xi_{i_1}(\theta)) + \sum_{i_1=1}^{\infty}\sum_{i_2=1}^{i_1} \hat{a}_{i_1 i_2}\psi_2(\xi_{i_1}(\theta), \xi_{i_2}(\theta)) + \ldots, \quad (7)$$

where $\psi_n(\xi_{i1}, \xi_{i2}, \ldots, \xi_{in})$ denotes the Hermite polynomial of order n in terms of n-dimensional independent standard Gaussian random variables $\xi = (\xi_{i1}, \xi_{i2}, \ldots \xi_{in})$ with zero mean and unit variance. The above equation is the discrete version of the original Wiener polynomial chaos expansion, and the continuous integrals are replaced by summations. For notational convenience, Eq. (7) can be written as

$$X(t,\theta) = \sum_{j=0}^{\infty} a_j(t)\phi_j(\xi(\theta)), \quad (8)$$

where a_j denotes the deterministic coefficients of the random process $X(t, \theta)$ and ϕ_j denotes the Hermite polynomials. ξ's are independent standard Gaussian random variables with zero mean and unit variance. The 1-D Hermite polynomials can be expressed in the recursive form as

$$\phi_n = \xi\phi_{n-1} - (n-1)\phi_{n-2}, \quad (9)$$

where the first few Hermite polynomials are

$$\phi_0 = 1, \ \ \phi_1 = \xi, \ \ \phi_2 = \xi^2 - 1, \ \ \phi_3 = \xi^3 - 3\xi, \ \ \phi_4 = \xi^4 - 6\xi^2 + 3. \quad (10)$$

An approximation of $X(t, \theta)$ can be obtained by truncating the series to p terms as

$$X(t,\theta) = \sum_{j=0}^{p} a_j(t)\phi_j(\xi(\theta)), \quad (11)$$

where

$$p = \frac{(n+n_p)!}{n!n_p!} - 1 \quad (12)$$

for n number of random variable and a polynomial order n_p. Equation (11) is referred to as p-order PCE expansion.

4 Spectral Decomposition of the Response

To illustrate how PCE can be used with BFA, we consider the single degree of freedom system excited by a harmonic excitation and governed by the equation

$$m\ddot{x} + c\dot{x} + kx = f(t) = A\cos(\omega t), \tag{13}$$

where m, c, k are the system mass, damping, and stiffness; $f(t)$ is the forcing function; and A and ω represent the amplitude and frequency of the forcing function, respectively. We assume that the response measurement at discrete time instants is available and that the objective of the study is to estimate damping parameter c. We use BFA to estimate c.

In the absence of any information, we model c as a random variable that is normally distributed with mean c_0 and standard deviation c_1. The spectral representation of c can be expressed as

$$c = c_0 + c_1\xi = \sum_{i=0}^{1} c_i\phi_i. \tag{14}$$

Substituting Eq. (14) in Eq. (13), it is possible to represent the response $x(t, \theta)$ as a PCE. Assuming the response

$$x(t,\theta) = \sum_{j=0}^{p} x_j(t)\phi_j(\xi(\theta)) \tag{15}$$

and substituting in Eq. (13), we get

$$m\left(\sum_{j=0}^{p}\ddot{x}_j(t)\phi_j(\xi)\right) + \left(\sum_{i=0}^{1} c_i\phi_i(\xi)\right)\left(\sum_{j=0}^{p}\dot{x}_j(t)\phi_j(\xi)\right) + k\left(\sum_{j=0}^{p} x_j(t)\phi_j(\xi)\right) = f(t). \tag{16}$$

Simplifying Eq. (16) leads to

$$m\sum_{j=0}^{p}\ddot{x}_j(t)\phi_j(\xi) + \sum_{i=0}^{1}\sum_{j=0}^{p} c_i\dot{x}_j\phi_i(\xi)\phi_j(\xi) + k\sum_{j=0}^{p} x_j\phi_j(\xi) = f(t). \tag{17}$$

Here, the unknowns are the deterministic coefficients, $\{x_j\}$. It must be noted that the system being linear and c being assumed Gaussian, the response $x(t)$ is also Gaussian, and hence, Eq. (15) will contain only two terms. However, in deriving the methodology, we consider a more general case where the system could be nonlinear and the response non-Gaussian. Thus, in developing the formulation,

we consider the more general case where the size of the vector $\{x_j\}$ is $p > 2$. To obtain the estimates of x_j, we decouple the Eq. (17). This can be carried out in two approaches. This is discussed in the following sections.

4.1 Classical Galerkin PCE

Using Galerkin projection on the Eq. (17), which involves multiplying by ϕ_k and taking expectations on both sides of Eq. (17), we get

$$m\sum_{j=0}^{p}\ddot{x}_j(t)<\phi_j\phi_k> + \sum_{i=0}^{1}\sum_{j=0}^{p}c_i\dot{x}_j<\phi_i\phi_j\phi_k> + k\sum_{j=0}^{p}x_j<\phi_j\phi_k> = f(t)<\phi_k>, \tag{18}$$

where the expectation operator $< \cdot >$ is defined as

$$<\phi_l, \ldots \phi_k> = \int_{-\infty}^{\infty}\phi_l \ldots \phi_k w(\xi)d\xi. \tag{19}$$

Here, $w(\xi)$ is the weighting function. For Hermite polynomials, the weighting function $w(\xi)$ is the Gaussian probability density function and is of the form

$$w(\xi) = \frac{1}{\sqrt{2\pi}}\exp^{-}\left(\frac{1}{2}\xi^T\xi\right). \tag{20}$$

The Hermite polynomials are orthogonal with respect to this weighting function in the Hilbert space. The polynomial chaos forms a complete orthogonal basis in the L_2 space of real-valued functions depending on the Gaussian random variables; hence, the inner product of two orthogonal polynomial can be replaced by the identity

$$<\phi_l\phi_k> = <\phi_l^2>\delta_{lk}, \tag{21}$$

where δ_{lk} is the Kronecker delta function, given as

$$\delta_{lk} = \begin{cases} 1 & \text{if } l = k \\ 0 & \text{otherwise.} \end{cases}$$

The inner product terms in Eq. (18) can be evaluated analytically prior to computations and substituted in the equation. The resulting system leads to a set of coupled deterministic differential equation in terms of the chaos coefficients $\{x_j\}$. The Galerkin approach is also called the intrusive approach as it modifies the system governing equations in terms of the chaos coefficients.

4.2 Nonintrusive Projection Method

A number of nonintrusive variants of PCE have been developed in the literature. In this study, we consider the stochastic projection method [2]. Here, the chaos expansions are not substituted in the governing equations; instead, samples of the solutions are used to evaluate the coefficients directly using a projection formula. As a result, this approach can utilize the existing deterministic code and hence the name nonintrusive. Here, the response is approximated by a truncated series as shown in Eq. (11). The Hermite polynomials are statistically orthogonal, i.e., they satisfy $< \phi_l \phi_k > = 0$ for $l \neq k$. Thus, the expansion coefficients can be directly evaluated as

$$x_j(t) = \frac{<x(t, \xi(\theta))\phi_j>}{<\phi_j^2>}. \tag{22}$$

The main difficulty here lies in evaluating the expectation in the numerator of the above expression. A Gauss-Hermite quadrature will be suitable for evaluating the above as the domain is ($-\infty$, ∞) and the weight is Gaussian pdf. The quadrature points are the zeros of the Hermite polynomials of chosen order. A number of deterministic runs are performed at the quadrature points. It is to be noted that the number of deterministic runs is still much lower than Monte Carlo simulations that would be necessary if we use BFA without PCE. We refer this step as a pseudo-Monte Carlo simulation approach, and it consists of the following steps:

1. The samples of the random variables in the problem are generated based on the ξ values which correspond to the Gauss-Hermite quadrature points.
2. The realizations of the system response $x(t, \theta)$ are then used to estimate the deterministic coefficients, $x_j(t)$'s, in Eq. (22) using the Gauss-Hermite quadrature rule.
3. The final response is obtained by reconstructing these determined coefficients back into the chaos expansion.

5 Polynomial Chaos Approach to Bootstrap Filtering

Using the PCE approach discussed in the preceding section, it is possible to bypass the necessity for performing computationally costly structural analysis at each step of bootstrap filtering. The basic steps involving coupling PCE with the bootstrap filter algorithm are as follows:

1. The measurements $\mathbf{X}_k$ are simulated for the known parameters. This serves as the reference for the filtering of particles.
2. The random parameter of the system, which is to be identified, is represented in a PCE for a given mean and standard deviation as shown in Eq. (14).

3. Using the available system data and excitation, response is calculated for the whole time step from the methods discussed in the previous section.
4. The normalized weights for prediction at first time step is calculated for all particles as mentioned in the filtering algorithm.
5. From the normalized weights, the resampling is done on ξ rather than the random parameter. This enables the corresponding change in both the response and the parameter.
6. The response is updated using the resampled ξ's and is used for the analysis at next time step.
7. This processing is carried out for the whole time step, enabling the random parameter updation based on ξ's.

The above method is efficient in that it avoids construction of PCE for the response at each time step, which can be computationally very costly. This is made possible by assuming that ξ to be the primary random variable rather than c. Thus, the calculated chaos coefficients for the system response at step 3 remain unchanged throughout the analysis. It is to be noted that, in BFA, the structural analysis is done for all particles at every time step, whereas in PCE approach, the structural analysis is carried out only once throughout the whole analysis. This brings about a significant reduction in the computational effort especially when dealing with large problems, where performing structural analyses many times consumes massive computational time.

If the bootstrap filtering is applied corresponding to each measurement data, then the number of structural analysis required per second of data would be NM if M is the sampling rate for data and N is the number of particles at each filtering step. Studies have shown [9, 10] that instead, if filtering is carried out every K steps of data, there is not much difference in the quality of the predictions of the parameters to be identified. However, this brings about significant reduction in the computations as the number of times the structural analyses is required is now $\frac{MN}{K}$. However, it may be argued that here, one omits some of the measurements, and in effect, one is wasting the available data from the measurements. To address this issue, we applied the BFA using the following four distinct methods and compared the quality of the predictions for the parameters.

Method 1: Bootstrap filter is carried out at all available data points. The number of times the structural analysis is carried out is NM.

Method 2: Bootstrap filter is carried out at every K available data points. The number of times the structural analysis is carried out is $\frac{MN}{K}$. However, here, we are not using the information available from the measurements and are in effect wasting available data.

Method 3: The likelihood is computed at all available data points. However, the resampling is done every K steps from the mean likelihood calculated from the preceding $\frac{M}{K}$ steps. The number of times the structural analysis is carried out is $\frac{MN}{K}$, but here, we use all the information available from the measurement data.

Method 4: Here, the mean of the measurements of preceding $\frac{M}{K}$ steps is used to calculate the likelihood at every K time step and is similar in all aspects to Method 3. Thus, it uses all the available information from the measurements. As there is a change only in calculation of likelihood, the number of structural analysis done remains same as the above method being $\frac{NM}{K}$.

6 Results

The proposed methodology was applied to a single degree of freedom system to estimate the uncertain damping parameter. The system was subjected to a harmonic loading of $A\cos(wt)$. The numerical parameters of the system considered are $m = 10$ kg, $k = 100$ N/m, $c = 20$ Ns/m, $A = 100$, $w = 1\pi$ rad/s. Sampling rate is assumed to be 100 s^{-1}. The measurements are obtained by solving the deterministic equations by adaptive fourth order Runge-Kutta algorithm. Figure 1 shows the time history of the response for 40 s. Here, the full line represents the true response and the dotted line represents the measurement which has been obtained when the response is seeded with Gaussian noise with 1 % variance. The number of measurement points for the assumed sampling rate is 4,001. We now approach the

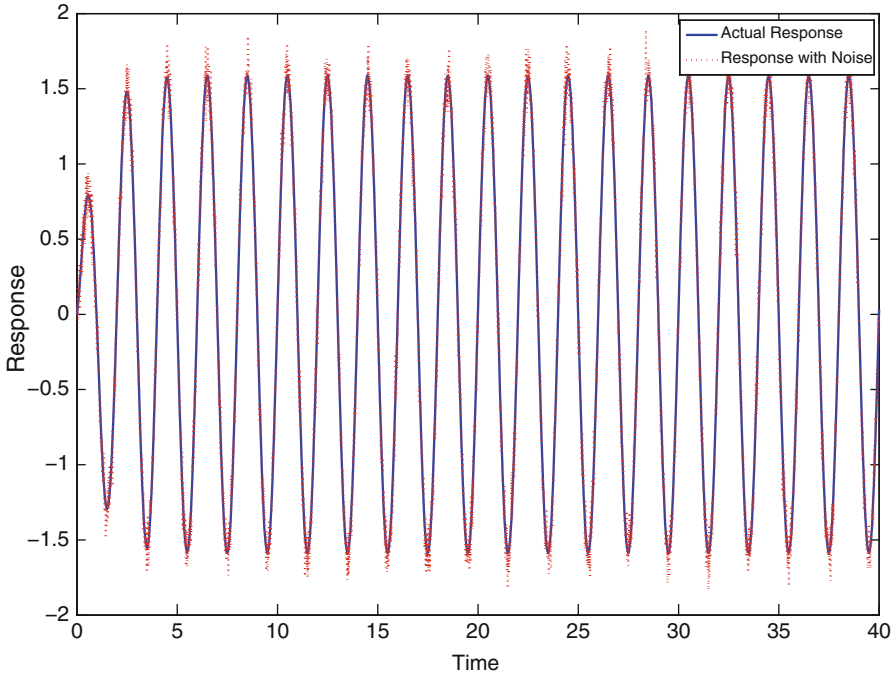

Fig. 1 Time history of the system response

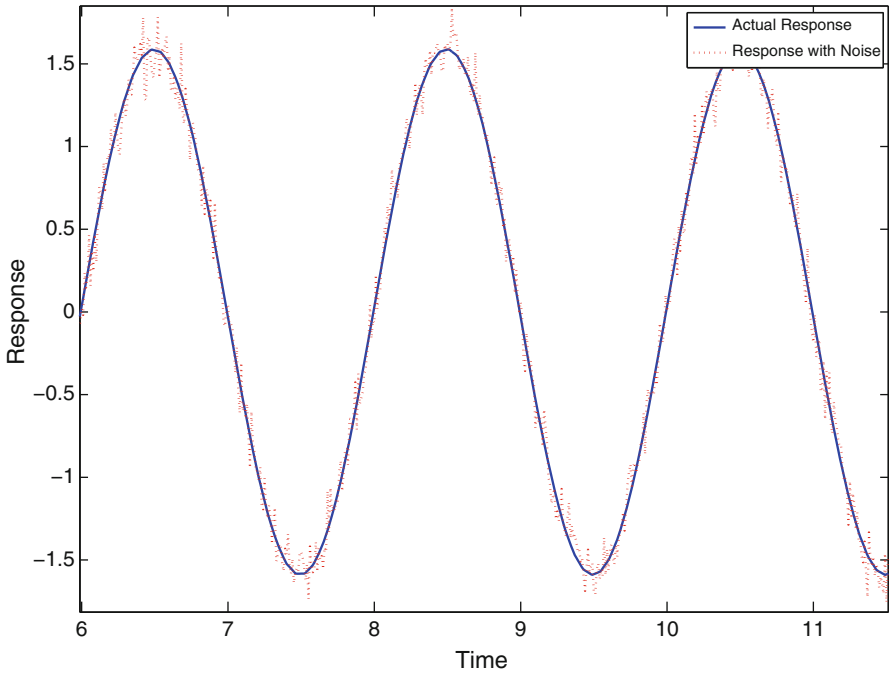

Fig. 2 Zoomed view of the time history of the response

problem assuming only the noisy measurement data is available and the parameter c is to be estimated. Initially, it was assumed c to be Gaussian distributed with mean 25 and standard deviation 5. The number of particles considered in this example is 500. The measurements and the process equations were given as input to the bootstrap filter. The analysis was carried out by using the four methods mentioned earlier (Fig. 2). Figures 3–6 show the estimated value of damping as a function of time by four methods. The horizontal line indicates the actual value of damping, and the curve with circles indicates the estimate of damping through ordinary BFA without PCE. The curve with stars and boxes indicates the analysis through PCE with Galerkin and nonintrusive approaches, respectively. We see that in all figures, initially there are little fluctuations in the estimated values of c, but as more and more measurements are incorporated, the estimates stabilize. The summary of the analysis by all the four methods is been shown in Table 1.

In method 1, filtering is carried out at all time steps; the structural analysis to calculate the system response for ordinary BFA is performed for 2,000,500 times. In the same method using Galerkin approach, the structural analysis is performed only once, whereas in nonintrusive approach, it is carried out thrice for the corresponding quadrature points. In method 1, it is seen that ordinary BFA takes almost five times the time taken when compared to its PCE counterpart. The estimated values obtained through PCE approaches are in fairly good agreement with the actual value. Thus, it is very clear that PCE-based bootstrap filtering is much quicker and efficient than ordinary filtering.

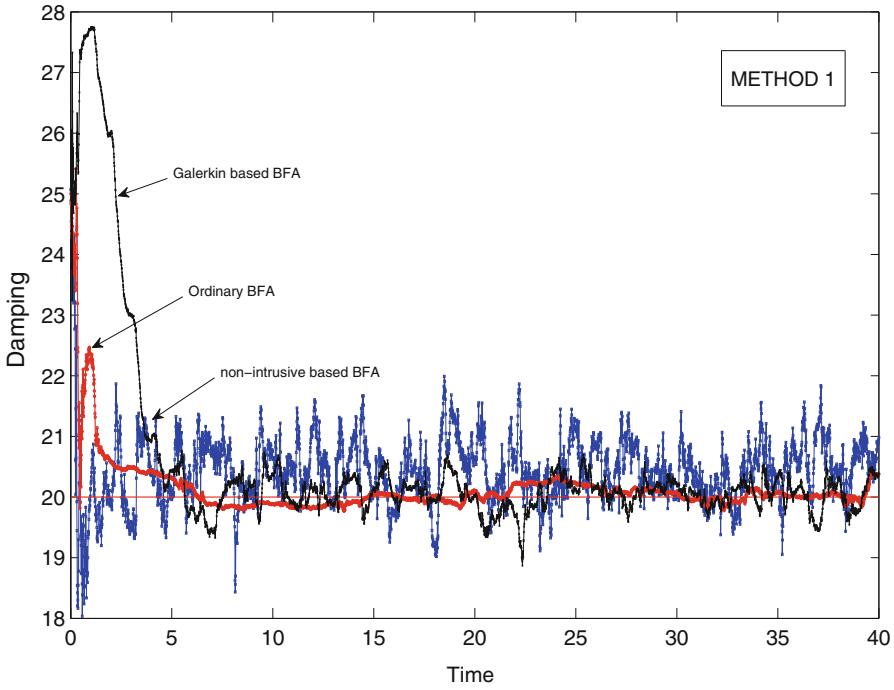

Fig. 3 Estimate of c by method 1

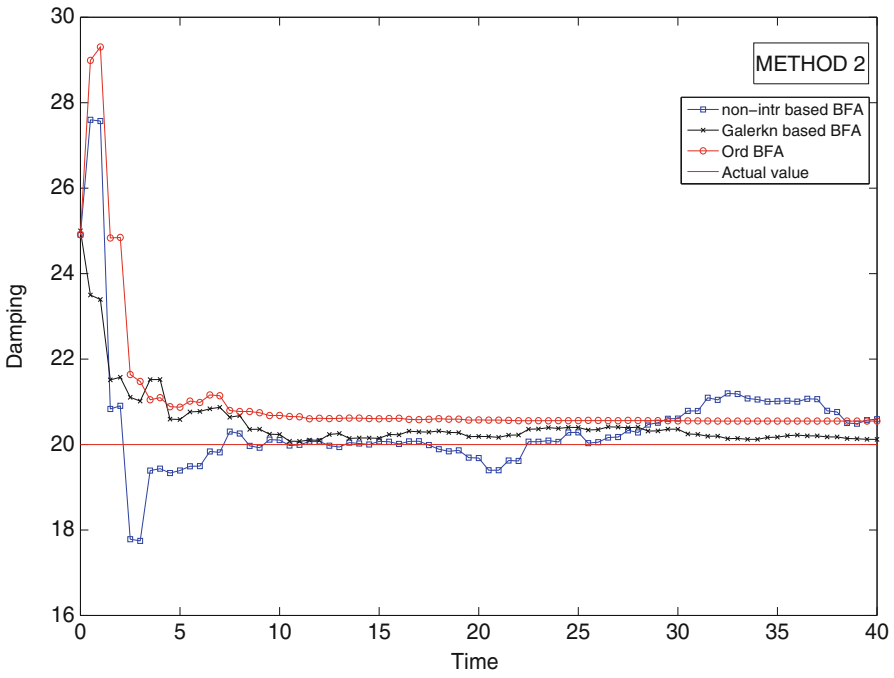

Fig. 4 Estimate of c by method 2

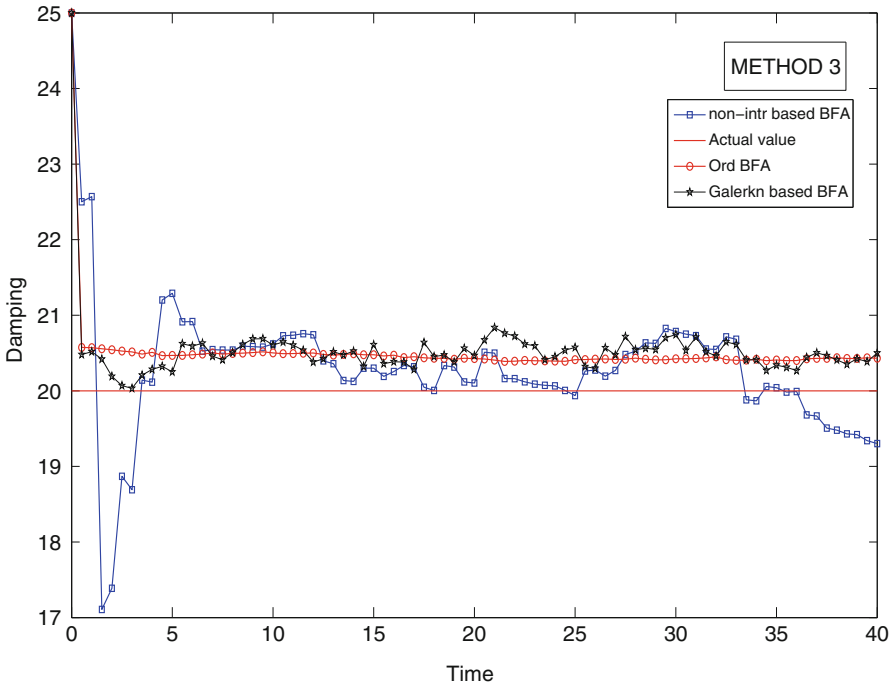

Fig. 5 Estimate of c by method 3

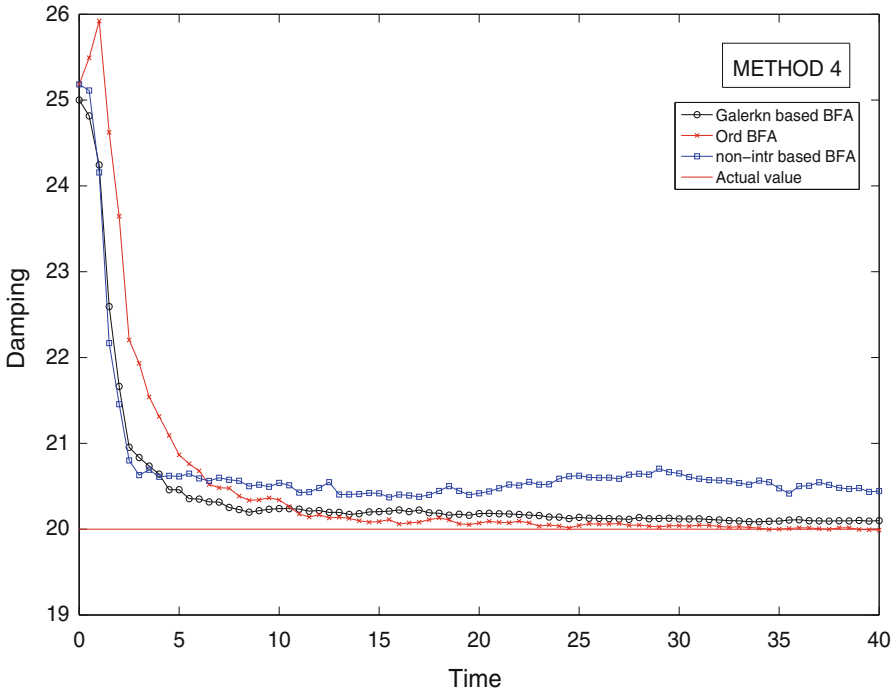

Fig. 6 Estimate of c by method 4

Table 1 Comparison of the performance of methods 1–4

Method	A	B	C	D	E	F
Method 1	Galerkin-based app.	4,001	1	19.97	− 0.15	157.26
	BFA with nonintrusive app.	4,001	3	20.59	2.95	230.3
	Ordinary BFA	4,001	2,000,500	21.94	9.7	906.77
Method 2	Galerkin-based app.	80	1	20.5	2.5	9.07
	BFA with nonintrusive app.	80	3	20.3	1.5	8.32
	Ordinary BFA	80	40,000	20.1	0.5	40.1
Method 3	Galerkin-based app.	80	1	20.5	2.5	17.42
	BFA with nonintrusive app.	80	3	20.24	1.2	14.07
	Ordinary BFA	80	40,000	20.31	1.55	116.12
Method 4	Galerkin-based app.	80	1	20.03	0.15	9.87
	BFA with nonintrusive app.	80	3	20.55	2.75	8.87
	Ordinary BFA	80	40,000	20.12	0.6	39.92

A methodology, *B* number of times BFA is implemented, *C* number of structural analyses, *D*estimated value, *E*% error, *F* CPU time in seconds

In methods (2)–(4), the BFA is carried out at every 50 time steps. As seen from the table below, these methods are quicker when compared to BFA by method 1 without compromising on accuracy. The number of filtering executed in those analyses is 80, which is much lesser than 4,001 to that used in method 1. This enables a considerable decrease in the number of structural runs computed in the algorithm. It is reflected on the time taken to execute the same process with method 1 and the other three methods. For instance, the Galerkin approach in method 2 consumes almost 15 times lesser time when compared to its similar approach using method 1. Analogous pattern is been observed in nonintrusive-based approach, indicating BFA in conjunction with PCE results in faster analysis. On dealing with problems with higher complexity, doing many structural analysis would consume a large computational effort; thus, in such cases, PCE-based BFA provides an easier way to analyze the problem.

The developed algorithm was found to be robust in yielding good results while handling uncertain parameter with larger standard deviation. Also, the algorithm still produced appreciable results on widening the gap between the two successive filtering.

7 Concluding Remarks

A computationally efficient technique for system identification using bootstrap filtering in conjunction with PCE has been successfully implemented. The used numerical example is a simple model problem to understand the mechanism of coupling PCE with bootstrap particle filtering. The PCE-based approach has been shown to be more efficient than Monte Carlo-based approaches for system identification. Various versions of the PCE approach-based bootstrap particle filtering have

been investigated to investigate the efficiency and accuracy of the proposed methods. Further work involving more complicated problems is currently in progress.

References

1. Cameron RH, Martin WT (1947) The orthogonal development of nonlinear functionals in series of Fourier–Hermite functionals. Ann Math 48:385–392
2. Desai A, Sarkar S (2010) Analysis of a nonlinear aeroelastic system with parametric uncertainties using polynomial chaos expansion. Math Probl Eng 2010:1–2. Article ID 379472
3. Doucet A, de Freitas JF, Gordon NJ (2001) An introduction to sequential Monte Carlo methods. In: Sequential Monte Carlo methods in practice. Springer, New York
4. Ghanem R, Spanos P (1991) Stochastic finite elements: a spectral approach. Springer, New York
5. Ghanem R, Spanos P (1993) A stochastic Galerkin expansion for nonlinear random vibration analysis. Probab Eng Mech 8:255–264
6. Gordon NJ, Salmond DJ, Smith AFM (1993) Novel approach to nonlinear/non-Gaussian Bayesian state estimation. IEE Proc F 140:107–113
7. Grewal MS, Andrews AP (2001) Kalman filtering: theory and practice using matlab, 2nd edn. Wiley, New York
8. Kalman RE (1960) A new approach to linear filtering and prediction problems. ASME J Basic Eng 82:34–45
9. Morla L (2011) Parameter estimation in vibrating structures using particle filtering algorithm vibration analysis. M.Tech thesis, Indian Institute of Technology, Madras
10. Nasrellah HA, Manohar CS (2010) A particle filtering approach for structural system identification in vehicle structure interaction problems. J Sound Vib 329:1289–1309
11. Wiener N (1938) The homogeneous chaos. Am J Math 60(4):897–936
12. Xiu D, Karniadakis GE (2002) The Weiner-Askey polynomial chaos for stochastic differential equations. SIAM J Sci Comput 24:619–644

Statistical Linearization of Duffing Oscillator Using Constrained Optimization Technique

Sabarethinam Kameshwar and Arunasis Chakraborty

Abstract The present work aims to evaluate the response of Duffing oscillator using equivalent linearization. The stiffness and damping forces are proportional to the cube power of the displacement and velocity, respectively. The oscillator is excited by stationary process. The method suggested in this work aims to replace the original nonlinear system with an equivalent linear system by minimizing the difference in the displacement between the nonlinear system and the equivalent linear system in a least square sense using different constraints (e.g., restoring force, potential energy, complementary energy). Numerical results are presented to show the efficiency of the proposed linearization scheme. For this purpose, instantaneous mean square values of the displacement are evaluated and compared with simulation. A close agreement between the simulations and the proposed model is observed which, in turn, shows the efficiency and applicability of the proposed model. A discussion on the use of different constraint conditions and their relative importance is also presented.

Keywords Equivalent linearization • Constrained optimization • Duffing oscillator • Stationary process

1 Introduction

Analytical solutions of stochastic nonlinear systems have remained an open area of research due to its inherent difficulties. Caughey [2] developed analytical solutions for linear and nonlinear systems excited by white noise. In this process, they used Markov process theory, and the response was evaluated by solving the corresponding

S. Kameshwar • A. Chakraborty (✉)
Department of Civil Engineering, Indian Institute of Technology Guwahati, Guwahati, Assam, India
e-mail: s.kameshwar@iitg.ernet.in; arunasis@iitg.ernet.in

S. Chakraborty and G. Bhattacharya (eds.), *Proceedings of the International Symposium on Engineering under Uncertainty: Safety Assessment and Management (ISEUSAM - 2012)*,
DOI 10.1007/978-81-322-0757-3_43,

Fokker–Planck–Kolmogorov (FPK) equation. Hammond [9] modeled the response of stochastic linear oscillator using spectral representation of the nonstationary processes. However, these closed-form solutions are limited to certain class of nonlinearities and excitations. Due to these limitations, researchers and engineers developed various approximate solutions for wide range of nonlinearity and excitations. Some of these techniques are equivalent linearization, closure approximations, and perturbation techniques. Among these approximate solutions, equivalent linearization is very popular among the engineers and the scientists for its simplicity and computational efficiency. Due to this reason, it has become a standard tool for stochastic response analysis of nonlinear dynamic systems, wherein the nonlinear system is replaced by a linear system whose parameters are optimized in stochastic least square sense.

Caughey [3] developed this technique for weakly nonlinear systems. Bulsara et al. [1] modeled the response of a cubic nonlinear system driven by Gaussian white noise. They showed that the results obtained by equivalent linearization had good agreement with the experimentally obtained responses. Iyengar [10] derived expression for the second moment of the response of Duffing oscillator excited by broad-banded signal. In this context, a comprehensive guideline on equivalent linearization for a wide range of nonlinear systems and excitations processes can be found in Roberts and Spanos [15]. Wu [17] compared equivalent linearization and Gaussian closure for different classes of nonlinearities (parametrically excited nonlinear systems and hysteretic system). In this study, the author showed that both the techniques provide same response. Similar observations were presented by Noori and Davoodi [12] while modeling stochastic response of nonlinear systems using equivalent linearization. Grigoriu [7, 8] and Proppe [13] used equivalent linearization for different classes of input processes (e.g., Levy white noise, Poisson process). Mickens [11] used this technique along with first-order averaging to solve general nonlinear systems where limit cycles exist. Ricciardi [14] used a modified Gram–Charlier series approximation of the probability density function to develop a non-Gaussian stochastic linearization method of nonlinear structural systems under white noise excitation. However, equivalent linearization used in all these studies used unconstrained stochastic least square optimization. Although the error between the nonlinear system and the equivalent linear system is minimized to obtain the parameters of the system, it does not ensure that the equivalent linear system will have same restoring force and/or other properties of the nonlinear system. In this context, Elishakoff and Zhang [4] and Elishakoff and Bert [5] suggested different criteria for stochastic least square optimization. Elishakoff [6] suggested new approach to evaluate the parameters of the equivalent linear system using force, potential energy, and complementary energy as the linearization criteria. Sobiechowski and Socha [16] developed different linearization criteria and modeled the response of Duffing oscillator under non-Gaussian excitations. However, all these criteria for stochastic linearization were used independently.

With this in view, the present work develops an equivalent linearization scheme for Duffing oscillator which minimizes the difference between the response of nonlinear and the equivalent linear system using constraints on equivalence of

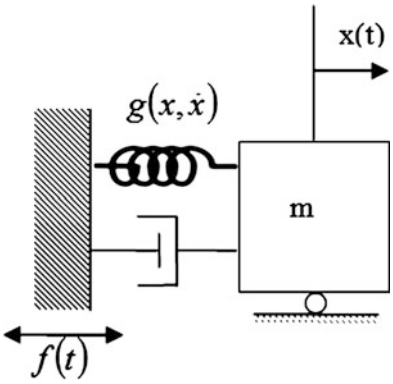

Fig. 1 Duffing oscillator

force, potential energy, and complementary energy. For this purpose, Lagrange multiplier technique is adopted to evaluate the optimized parameters of the linear system, which are driven by different stationary excitation processes. The results obtained using various constraints are compared with the simulations to prove the accuracy of the proposed linearization scheme. It also helps to identify the relative impact of different constraints on the global response.

2 Problem Formulation

Figure 1 shows the Duffing oscillator used in this study whose governing equation of motion is given by

$$\ddot{x} + g(x, \dot{x}) = f(t) \tag{1}$$

where $g(x, \dot{x})$ is the nonlinear function that describes the energy dissipation and the force associated with the spring and is given by

$$g(x, \dot{x}) = \beta \dot{x} + \omega_n^2 x + \lambda_1 \beta \dot{x}^3 + \lambda_2 \omega_n^2 x^3 \tag{2}$$

Parameters λ_1 and λ_2 control the extent of nonlinearity, while parameters β and ω_n are the damping and the natural frequency of the corresponding linear system when λ_1 and λ_2 are zero. The nonlinear single degree of freedom system shown in Fig. 1 is replaced by a linear system whose governing equation is given by

$$\ddot{x} + \beta_{\text{eq}} \dot{x} + \omega_{\text{eq}}^2 x = f(t) \tag{3}$$

In the above equation, β_{eq} and ω_{eq} are the damping and the natural frequency of the equivalent linear system, which are evaluated by minimizing the error between Eqs. 1 and 3 in stochastic least square sense.

On squaring the error and taking expectation on both sides, one gets

$$E[\varepsilon^2] = E\left[\left(g(x,\dot{x}) - \beta_{\text{eq}}\dot{x} - \omega_{\text{eq}}^2 x\right)^2\right] \tag{4}$$

Equation 4 is minimized with respect to the unknowns the parameters β_{eq} and ω_{eq} The optimum values of these parameters are evaluated by solving the two equations formed by $\frac{\partial E[\varepsilon^2]}{\partial \beta_{\text{eq}}} = 0$ and $\frac{\partial E[\varepsilon^2]}{\partial \omega_{\text{eq}}^2} = 0$. By solving these two equations, one can show that

$$\left.\begin{aligned} \beta_{\text{eq}} &= \beta\left[1 + 3\lambda_1\,\sigma_{\dot{x}}^2\right] \\ \omega_{\text{eq}}^2 &= \omega_n^2\left[1 + 3\lambda_2\,\sigma_x^2\right] \end{aligned}\right\} \tag{5}$$

where $\sigma_{\dot{x}}^2$ and σ_x^2 are the unknown variance of x and $\dot{x}$, respectively. In absence of the stochastic response of the nonlinear system, these variances are approximately evaluated using the closed-form solution of the equivalent linear system excited by the stationary input. Using this approximation, the variances of displacement and velocity of the equivalent linear system can be evaluated as

$$\left.\begin{aligned} \sigma_x^2 &= \int_{-\infty}^{\infty} |H(\omega)|^2\, S_{ff}(\omega) d\omega \\ \sigma_{\dot{x}}^2 &= \int_{-\infty}^{\infty} \omega^2 |H(\omega)|^2\, S_{ff}(\omega) d\omega \end{aligned}\right\} \tag{6}$$

In the above equation, $H(\omega)$ represents the frequency response function of the equivalent linear system which is given by

$$H(\omega) = \frac{1}{\omega_{\text{eq}}^2 - \omega^2 + i\omega\beta_{\text{eq}}} \tag{7}$$

The stationary excitation $f(t)$ is represented by its power spectral density $S_{ff}(\omega)$. In the present study, two different types of stationary excitations are considered for numerical analysis. The first one is the white noise process whose intensity is given by $S_{ff}(\omega) = S_o$ and the second one is the filtered white noise process as modeled in Kanai–Tajimi spectrum.

$$S_{ff}(\omega) = S_o \left[\frac{1 + 4\eta_g^2\left(\frac{\omega}{\omega_g}\right)^2}{\left[1 - \left(\frac{\omega}{\omega_g}\right)^2\right]^2 + 4\eta_g^2\left(\frac{\omega}{\omega_g}\right)^2}\right] \tag{8}$$

In the above equation, η_g and ω_g represent the parameters of the second-order linear filter. Using Eq. 6 in Eq. 5, one can solve the parameters of the equivalent

system for different types of excitations. For the details of this solution procedure, one may refer to Roberts and Spanos [15]. However, this linearization scheme provides the optimal values of the parameters without guaranteeing the equivalence of the spring or damping force, potential energy stored in the two systems, and/or complementary energy in the two systems. With this in view, present study aims to modify the optimization technique by incorporating different constraints. It also aims to study the relative importance of these constraints on the overall performance of the linearization technique.

3 Statistical Linearization Using Constraints

As outlined earlier, Lagrange multiplier technique is adopted to optimize the objective function F along with constraints. The total Lagrangian is given by

$$L = F + \gamma_1 G \tag{9}$$

where γ_1 is the Lagrange multiplier. For this purpose, the objective function F is modeled as

$$F = \varepsilon_1^2 + \varepsilon_2^2 \tag{10}$$

where ε_1 and ε_2 are the errors in estimating damping and natural frequency as given in Eq. 5 and are given by

$$\left.\begin{aligned} \varepsilon_1 &= \beta_{\text{eq}} - \beta\left[1 + 3\lambda_1\sigma_{\dot{x}}^2\right] \\ \varepsilon_2 &= \omega_{\text{eq}}^2 - \omega_n^2\left[1 + 3\lambda_2\sigma_x^2\right] \end{aligned}\right\} \tag{11}$$

To evaluate the optimized parameters, the total Lagrangian in Eq. 9 is differentiated with respect to the unknowns and equated to zero which leads to simultaneous equations involving β_{eq}, ω_{eq}^2 and γ_1 which are given by

$$\left.\begin{aligned} \frac{\partial L}{\partial \omega_{\text{eq}}^2} &= \frac{\partial F}{\partial \omega_{\text{eq}}^2} + \gamma_1 \frac{\partial G}{\partial \omega_{\text{eq}}^2} = 0 \\ \frac{\partial L}{\partial \beta_{\text{eq}}} &= \frac{\partial \mathrm{F}}{\partial\ \beta_{\text{eq}}} + \gamma_1 \frac{\partial G}{\partial \beta_{\text{eq}}} = 0 \\ \frac{\partial L}{\partial \gamma_1} &= G = 0 \end{aligned}\right\} \tag{12}$$

In the present study, three different constraints are chosen for optimization. These are nonlinear force, potential energy, and complementary energy.

3.1 Constraint 1: Nonlinear Force

The nonlinear forcing function in the Duffing oscillator as shown in Fig. 1 can be modeled as

$$\left.\begin{aligned}\varphi(x) &= \omega_n^2(x+\lambda_2 x^3)\\ \psi(\dot{x}) &= \beta(\dot{x}+\lambda_1\dot{x}^3)\end{aligned}\right\} \tag{13}$$

In the above equation, $\varphi(x)$ and $\psi(\dot{x})$ are nonlinear forces associated with the stiffness and the energy dissipation. Using Eq. 6, the variance of the nonlinear force can be evaluated. In the first example, the variance of the nonlinear forcing function is used as the constraint condition, which is given by

$$G_f = E[\varphi^2(x)+\psi^2(\dot{x})] - E\left[\left(\omega_{eq}^2 x\right)^2 + (\beta_{eq}\dot{x})^2\right] \tag{14}$$

In this context, it may be noticed that the constraint condition described in the above equation has the nonlinear force as a function of x and $\dot{x}$ which are the displacement and velocity of the Duffing oscillator, respectively. As these responses are unknown at the beginning, they are approximated with the displacement and velocity response of the equivalent linear system. Using Eq. 12, one can develop simultaneous equations involving three unknowns β_{eq}, ω_{eq}^2 and γ_1 which are given by

$$\begin{aligned}&2\omega_{eq}^2\left(1-3\omega_n^2\lambda_2 a+\gamma_1\sigma_x^2+\gamma_1\omega_{eq}^2 a\right)+\beta_{\mathrm{eq}}\left(-6\beta\lambda_1 c+\gamma_1\beta_{eq}c\right)-\gamma_1\left(\omega_n^4 a(1+45\left(\lambda_2\sigma_x^2\right)^2\right.\\&\left.+12\lambda_2\sigma_x^2)+\beta^2 c\left(1+45\left(\lambda_1\sigma_{\dot{x}}^2\right)^2+12\lambda_1\sigma_{\dot{x}}^2\right)\right)-2\left(\omega_n^2\left(1+3\lambda_2\sigma_x^2\right)\left(1-3\omega_n^2\lambda_2 a\right)\right.\\&\left.+\beta(1+3\lambda_1\sigma_{\dot{x}}^2)(-3\beta\lambda_1 c)\right)=0\end{aligned} \tag{15a}$$

$$\begin{aligned}&\omega_{eq}^2\left(-6\omega_n^2\lambda_2 b+\gamma_1\omega_{\mathrm{eq}}^2 b\right)+2\beta_{\mathrm{eq}}\left(1-3\beta\lambda_1 d+\gamma_1\sigma_{\dot{x}}^2+\gamma_1\beta_{\mathrm{eq}}\mathrm{d}\right)-\gamma_1\left(\omega_n^4 b\,(1+45\left(\lambda_2\sigma_x^2\right)^2\right.\\&\left.+12\lambda_2\sigma_x^2)+\beta^2 d\left(1+45\left(\lambda_1\sigma_{\dot{x}}^2\right)^2+12\lambda_1\sigma_{\dot{x}}^2\right)\right)-2\left(\omega_n^2\left(1+3\lambda_2\sigma_x^2\right)\left(-3\omega_n^2\lambda_2 b\right)\right.\\&\left.+\beta(1+3\lambda_1\sigma_{\dot{x}}^2)(1-3\beta\lambda_1 d)\right)=0\end{aligned} \tag{15b}$$

$$G_f = \omega_{\text{eq}}^4 \sigma_x^2 + \beta_{\text{eq}}^2 \sigma_{\dot{x}}^2 - \omega_n^4 \sigma_x^2 \left(1 + 15\left(\lambda_2 \sigma_x^2\right)^2 + 6\lambda_2 \sigma_x^2\right) - \beta^2 \sigma_{\dot{x}}^2 \left(1 + 15\left(\lambda_1 \sigma_{\dot{x}}^2\right)^2 + 6\lambda_1 \sigma_{\dot{x}}^2\right) = 0 \tag{15c}$$

In the above equations, a, b, c, and d are the derivatives of $\sigma_{\dot{x}}^2$ and σ_x^2 with respect to ω_{eq}^2 and $\beta_{\text{eq.}}$ Using Eqs. 15a and 15b, one can remove γ_1 and develop an equation with unknown parameters β_{eq} and ω_{eq}^2. Using this equation along with Eq. 15c, one can solve the optimized unknown parameters in the light of constraint on the nonlinear force. It can be noticed from Eqs. 15a, 15b, and 15c that the reduced equations for β_{eq}, and ω_{eq}^2 are polynomial function. In the present study, these are solved in Symbolic Math Toolbox in MATLAB.

3.2 Constraint 2: Potential Energy

The potential energy of the Duffing oscillator considered in Fig. 1 is

$$P(x) = \int_0^x \omega_n^2 (x + \lambda_2 x^3) dx \tag{16}$$

It can be shown that the energy dissipated by this system is be given by

$$D(\dot{x}) = \int_0^x \beta^2 (\dot{x} + \lambda_1 \dot{x}^3) d\dot{x} \tag{17}$$

The variance of the potential energies of the nonlinear system is used as the constraint condition, which is given by

$$G_{pe} = E[P^2(x) + D^2(\dot{x})] - E\left[\left(\omega_{\text{eq}}^2 \frac{x^2}{2}\right)^2 + \left(\beta_{\text{eq}} \frac{\dot{x}^2}{2}\right)^2\right] \tag{18}$$

Substitution of expressions of $P(x)$ and $D(\dot{x})$ in Eq. 18 and further simplification lead to a constraint equation for equivalence of potential energy. The numerical procedure outlined for evaluation of optimal parameters using Constraint 1 may be adopted here to obtain β_{eq} and ω_{eq}^2.

3.3 Constraint 3: Complementary Energy

The third constraint equation is obtained from complementary energy criterion. The complementary energy of the nonlinear spring and damper is given by

$$\left.\begin{aligned} C(x) &= x\varphi(x) - P(x) \\ M(\dot{x}) &= \dot{x}\psi(\dot{x}) - D(\dot{x}) \end{aligned}\right\} \tag{19}$$

The difference in the square of the expected values of the complementary energies of the two systems gives the following expression for the third constraint:

$$G_{ce} = E[C^2(x) + M^2(\dot{x})] - E\left[\left(\omega_{\text{eq}}^2 \frac{x^2}{2}\right)^2 + \left(\beta_{\text{eq}} \frac{\dot{x}}{2}\right)^2\right] \tag{20}$$

After obtaining the constraint condition, the optimal parameters can be obtained by following the procedure mentioned for Constraint 1.

4 Numerical Results

Using the constrained linearization model outlined in the previous section for different cases, numerical analysis is carried out to study the performance of the proposed technique. For this purpose, the parameters of the nonlinear system β, λ_1 and λ_2 are considered to be 5%, 0.1, and 0.1, respectively. As mentioned in the problem formulation, two different stationary processes are considered here. These are white noises with intensity $S_o = 50\ \text{cm}^2/s^3$ and Kanai–Tajimi spectrum with parameters S_o, η_g and ω_g equal to 50 cm^2/s^3, 0.4, and 10 rad/s, respectively. Using these parameters, numerical study is carried out to find out the optimal parameters of the equivalent linear system which are then used to evaluate the mean square value of the displacement response. Figure 2 shows the mean square value of x for different values of ω_n when the system is subjected to white noise excitations. In this context C1, C2, and C3 represent Constraints 1, 2 and 3, respectively. It may be noticed that the mean square value corresponding to C1 and C2 closely match with the simulation results (i.e., Sim). The mean square response corresponding to C3 has a constant mismatch over the entire domain of ω_n. Figure 3 shows the mean square values of nonlinear force (F), potential energy (PE), and complementary energy (CE) for the optimal solution of β_{eq} and ω_{eq} over different values of ω_n. From this figure, it can be noticed that the nonlinear forces obtained from different constraint conditions closely match with the simulation result. Also it may be noticed that the potential energy corresponding to higher ω_n closely matches with the simulation result. The mismatch in potential energy in case of higher time period may be due to the assumption of replacing the stochastic response of the nonlinear system with that of the linear system as described in Eq. 20. The complementary energy obtained from three constraint conditions again shows a mismatch with the simulation result which indicates that Lagrange multiplier technique with this constraint does not provide the best feasible solution.

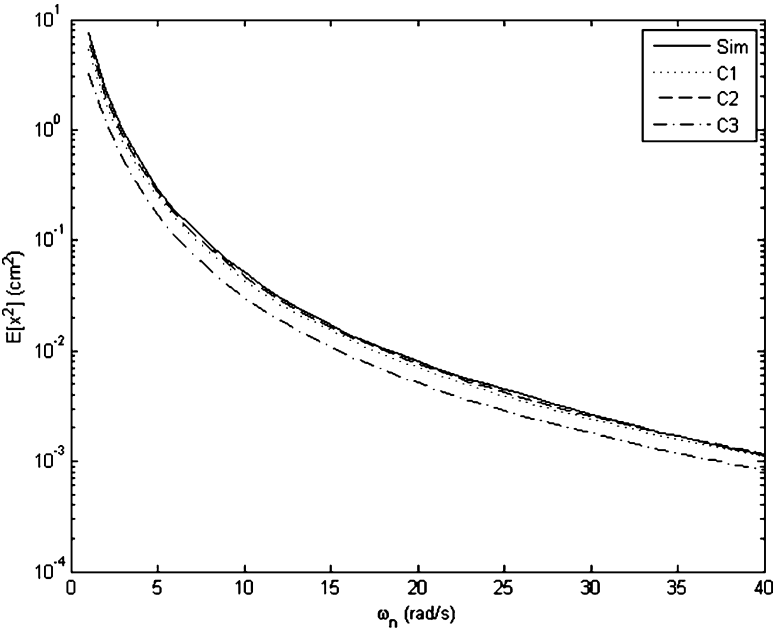

Fig. 2 Mean square value of x for different ω_n for white noise excitation

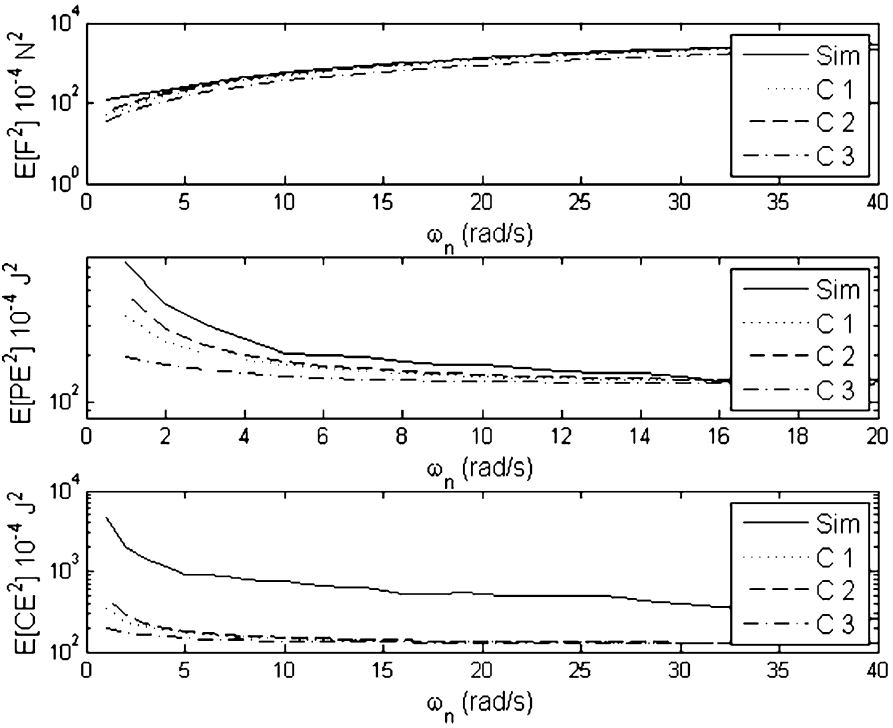

Fig. 3 Mean square value force, PE, and CE for different ω_n for white noise excitation

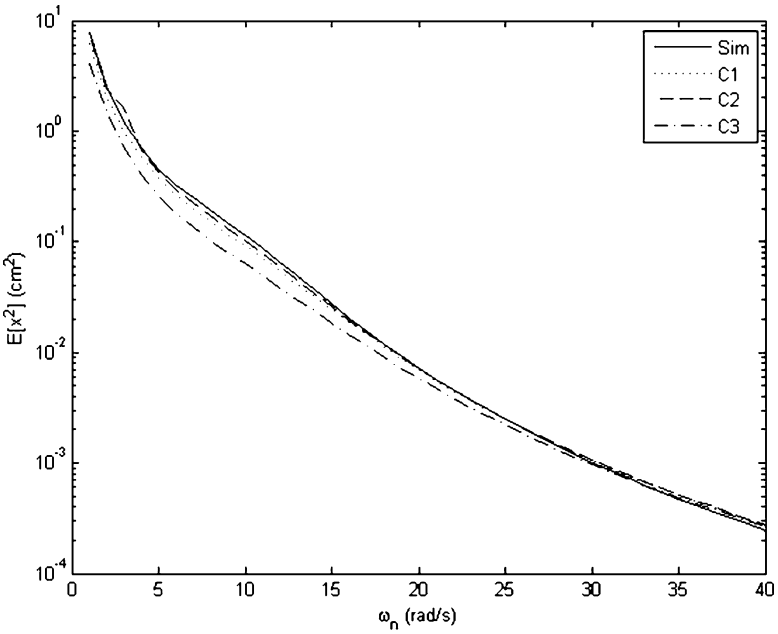

Fig. 4 Mean square value of x for different ω_n for Kanai–Tajimi excitation

The mean square value of the response for various natural frequencies ω_n for Kanai–Tajimi excitations is shown in Fig. 4. It can be observed that mean square values pertaining to constraints C1 and C2 match closely with the simulation results over the entire range. Further, for lower time period the mean square values corresponding to all the constraints match with simulation. Figure 5 shows the mean square values of force (F), potential energy (PE), and complementary energy (CE) corresponding to C1, C2, and C3. Similar to white noise excitation, for filtered white noise also the nonlinear force matches closely with the simulation over the entire range of natural frequencies. In case of filtered white noise, the mean square value of potential energy also matches closely with the simulation result. One may notice a slight deviation from the simulation results around 10 rad/s which may be attributed to resonance.

Figures 6a and 7a show the phase plots of the response of the nonlinear system, while Figs. 6b and 7b show the phase plots of the equivalent linear system for $\omega_n = 25$ rad$/s$. For brevity, phase plots are compared for Constraint 2 only. In both the figures, good similarity in results is observed between simulation and the equivalent linear system which shows that the equivalent linear system is able to emulate the random response of the nonlinear system.

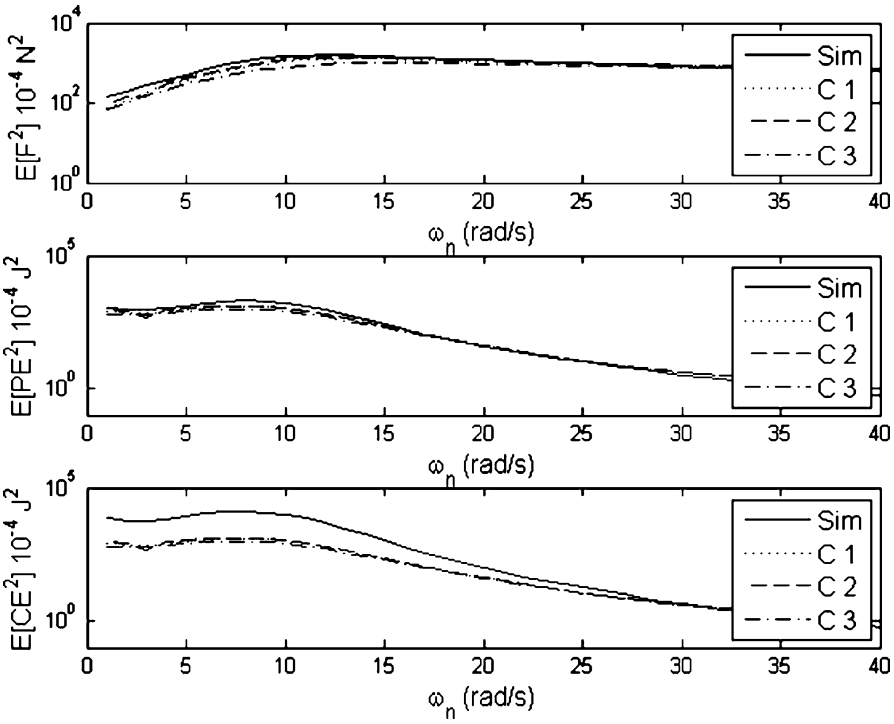

Fig. 5 Force mean square value force, PE, and CE for different ω_n for Kanai–Tajimi excitation

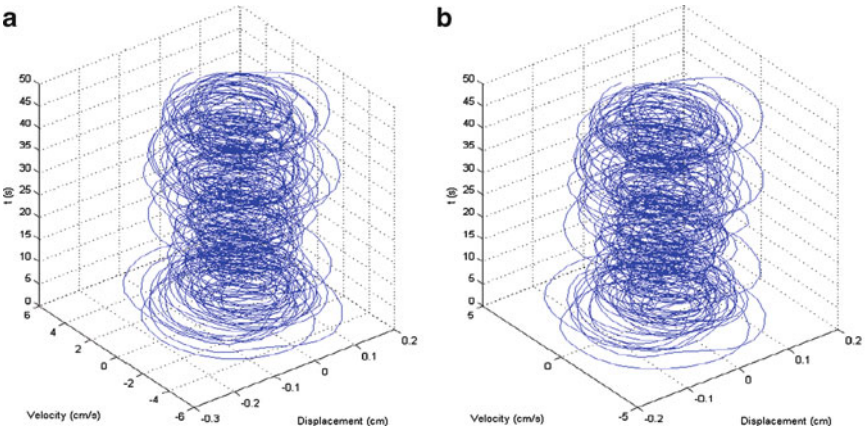

Fig. 6 Phase plot at $\omega_n = 25$ rad/s for broad-banded excitation. (**a**) The nonlinear system. (**b**) The equivalent linear system

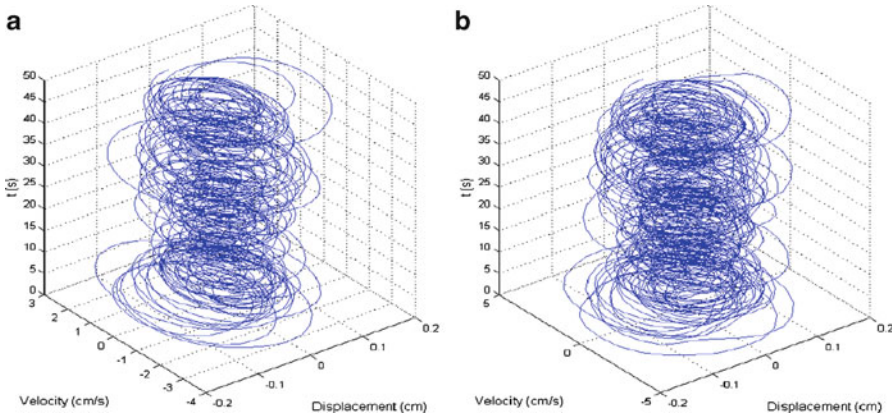

Fig. 7 Phase plot at $\omega_n = 25$ rad/s for narrow-banded excitation. (**a**) The nonlinear system. (**b**) The equivalent linear system

5 Conclusion

In this chapter, statistical linearization of Duffing oscillator is developed to study the impact of different constraint on the global response. For this purpose, three different constraints are used which are nonlinear force, potential energy, and complementary energy. The mean square value of the response for a wide range of frequencies and different stationary inputs are presented here. From these results, it may be concluded that the constraints on nonlinear force and potential energy closely match with the simulation result which prove their accuracy and efficiency. In this context, it may be mentioned that constraints associated with complementary energy do not provide satisfactory result over a wide range of frequencies. With this in view, it may be concluded that the proposed Gaussian linearization technique for stationary excitation using constraints associated with nonlinear force and potential energy may be adopted for the stochastic response analysis of Duffing oscillator.

References

1. Bulsara AR, Katja L, Shuler KE, Rod F, Cole WA (1982) Analog computer simulation of a duffing Oscillator and comparison with statistical linearization. Int J Non-Linear Mech 17 (4):237–253
2. Caughey T (1963) Derivation and application of Fokker-Planck equation to discrete dynamics system subjected to white random excitation. J Acoust Soc Am 35:1683–1692
3. Caughey T (1963) Equivalent linearization techniques. J Acoust Soc Am 35:1706–1711
4. Elishakoff I, Zhang XT (1992) An appraisal of different stochastic linearization criteria. J Sound Vib 153:370–375
5. Elishakoff I, Bert CW (1999) Complementary energy criterion in nonlinear stochastic dynamics. In: Melchers RL, Stewart MG (eds) Application of stochastic and probability. A. A. Balkema, Rotterdam, pp 821–825

6. Elishakoff I (2000) Multiple combinations of the stochastic linearization criteria by the moment approach. J Sound Vib 237(3):550–559
7. Grigoriu M (1995) Equivalent linearization for Poisson White noise input. Probab Eng Mech 10:45–51
8. Grigoriu M (2000) Equivalent linearization for systems driven by Levy White noise. Probab Eng Mech 15:185–190
9. Hammond J (1973) Evolutionary spectra in random vibrations. J R Stat Soc 35:167–188
10. Iyengar RN (1988) Stochastic response and stability of the Duffing oscillator under narrow band excitation. J Sound Vib 126(2):255–263
11. Mickens R (2003) A combined equivalent linearization and averaging perturbation method for non-linear oscillator equations. J Sound Vib 264:1195–1200
12. Noori M, DavoodI H (1990) Comparison between equivalent linearization and Gaussian closure for random vibration analysis of several nonlinear systems. Int J Eng Sci 28 (9):897–905
13. Proppe C (2003) Stochastic linearization of dynamical systems under parametric Poisson White noise excitation. Int J Non-Linear Mech 38:543–555
14. Ricciardi G (2007) A non-Gaussian stochastic linearization method. Probab Eng Mech 22:1–11
15. Roberts J, Spanos P (1990) Random vibration and statistical linearization. Wiley, New York
16. Sobiechowski C, Socha L (2000) Statistical linearization of the duffing oscillator under non-Gaussian external excitation. J Sound Vib 231:19–35
17. Wu W-F (1987) Comparison of Gaussian closure technique and equivalent linearization method. Probab Eng Mech 2(1):2–8

Parameter Identification in a Beam from Experimental Vibration Measurements Using Particle Filtering

Bharat Pokale, R. Rangaraj, and Sayan Gupta

Abstract The focus of the present study is on the development of a methodology for estimating the parameters of a cantilever beam based on experimentally measured vibration response. A aluminum cantilever beam of known dimensions is excited at a known location and the tip accelerations are measured. Subsequently, a particle-filtering-based strategy is used to estimate the system parameters from the vibration response.

Keywords System identification • Health monitoring • Dynamic state estimation • Particle filtering • Vibrations

1 Introduction

Monitoring the health of a structure or its components is very important to ensure the safe operations of important structural systems, such as components in nuclear power plants, aircrafts, automobiles, and bridges. With the passage of time, there is gradual weakening of the structure due to various degrading mechanisms such as fatigue, corrosion, and creep, to name a few. These degrading mechanisms lead to loss of structural integrity resulting in the structural system behaving in a manner that is different from its intended use. This can affect the overall safety of the structure. The structural degradation arising due to the aging mechanism results in

B. Pokale (✉)
Department of Applied Mechanics, Indian Institute of Technology Madras, Chennai 600036, India
e-mail: bhrtpkl@gmail.com

R. Rangaraj
Ashok Leyland Technical Center, Vellivoyalchavadi, Chennai 600036, India

S. Gupta
Department of Applied Mechanics, Indian Institute of Technology Madras, Chennai 600036, India
e-mail: gupta.sayan@gmail.com

S. Chakraborty and G. Bhattacharya (eds.), *Proceedings of the International Symposium on Engineering under Uncertainty: Safety Assessment and Management (ISEUSAM - 2012)*,
DOI 10.1007/978-81-322-0757-3_44,

changes in certain global parameters of the structure such as its damping and stiffness characteristics. If one can focus on monitoring how these parameters change with time, it would be possible to identify when the structure parameters have crossed the specified threshold levels and would require maintenance. Such a dynamic monitoring of the structural system would ensure that maintenance is carried out at optimal intervals, which in turn, would not only prevent unforeseen catastrophic failures but would also increase the structure lifetime. The key feature in this scheme of things is, of course, identifying the system parameters in an efficient and inexpensive manner. Vibration-based monitoring of structural components offers such an inexpensive method. The focus of studies in the literature has been to establish the system parameters and in turn the structural health from ambient vibration measurements. This chapter belongs to this genre of studies.

System identification from vibration measurements constitute an inverse problem. There is a fairly large body of work available in the literature on inverse problems and system identification. Early studies in this field focused on identification of modal parameters, such as changes in natural frequencies and, mode shapes, to estimate the health of the structure, see [2, 4]. These methods were typically ill defined and overdetermined as the number of parameters to be identified is usually much smaller than the available measurements. Moreover, these methods had no formal way of handling noise in the measurements. The past decade has focused on the use of dynamic state estimation techniques for evolving effective time-domain-based methods for parameter identification of structural systems. These methods are typically based on the Kalman Filter [7]. Here, the focus is on estimating the state parameters of a dynamical system using a Bayesian updating approach. The evolution of state parameters, as a function of time, is expressed in a recursive form through the model equation (also known as process equation) of the form

$$\mathbf{X}_{k+1} = \mathbf{f}_k(\mathbf{X}_k, \theta_k, \mathbf{w}_k), \tag{1}$$

where $\mathbf{X}_k$ is the state at time instant t_k, θ_k are system parameters, $\mathbf{f}(\cdot)$ is the functional relationship that relates $\mathbf{X}_{k+1}$ to $\mathbf{X}_k$ and depends on the system, and $\mathbf{w}_k$ is the process noise on account of the unknown errors that enter the formulation due to modeling assumptions. Typically, in the absence of any further knowledge, $\mathbf{w}_k$ is modeled as Gaussian white noise. Additionally, we have the measurement equation that relates the measurement of response at time t_k, given by $\mathbf{Y}_k$, to the system state variables and is given by:

$$\mathbf{Y}_k = \mathbf{h}_k(\mathbf{X}_k, \mathbf{v}_k). \tag{2}$$

Here, $\mathbf{h}(\cdot)$ denotes the functional relationship that relates the response measurements $\mathbf{Y}_k$ with state $\mathbf{X}_k$ and $\mathbf{v}_k$ is the measurement noise that takes into account all the uncertainties arising due to measurements and calibration errors. The focus of the filtering strategies is to estimate the states $\mathbf{X}_k$ from measurement

data $\mathbf{Y}_k$ under the conditions that $\mathbf{w}_k$ and $\mathbf{v}_k$ are unknowns. This can be achieved using a Bayesian filtering approach. The procedure involves making an assumption about the state initially and subsequently predicting the state at a future time and making appropriate corrections once the measurements at that time become available. It is obvious that as more and more measurements become available, the associated uncertainties in the problem decrease, and it is possible to arrive at the true estimates of the states. When Eqs. (1) and (2) are linear and the noise $\mathbf{w}_k$ and $\mathbf{v}_k$ are Gaussian, closed form expressions can be obtained leading to exact estimates of the states. This is the well-known Kalman filter [7]. However, Kalman filter is applicable for state estimation. One way of using the Kalman Filter for system identification would be to augment the state variable vector with the system parameters to be identified. This involves defining a new state vector $\mathbf{Z}_k = [\mathbf{X}_k, \theta_k]$. However, in such situations, the model equation becomes nonlinear and the Kalman Filter can no longer be directly applied. Several Kalman-filter-based approaches have been discussed in the literature which use different forms of linearizations and approximations; see [1, 8] for a review.

Alternative methods to dynamic state estimation involve using Monte Carlo simulations (MCS) to deal with problems of dynamic state estimation which involve nonlinear model and measurement equations. These methods rely on using MCS for approximating the integral equations in the Bayesian updating formulation where closed form solutions are not available. Such MCS-based methods are called particle filtering methods. The study presented in this chapter focuses on using the particle filtering method to identify the system parameters of a beam from the vibration response obtained from physical experiments. This study is a part of an ongoing study in the group involved in developing a particle-filter-based strategy for identifying damage in structural systems from ambient vibration measurements [9].

2 Bootstrap Particle Filtering

The objective of the filtering algorithms is to estimate the current state of the system $\mathbf{X}_k$, from the available measurements $\mathbf{D}_k = \mathbf{Y}_1, \ldots, \mathbf{Y}_k$. The bootstrap particle filter is an algorithm for propagating and updating $\{\mathbf{X}_{k-1}\}_{i=1}^{N}$ to obtain a set of values $\{\mathbf{X}_k\}_{i=1}^{N}$, which are approximately distributed as $p(\mathbf{X}_k|\mathbf{D}_k)$, where $p(\mathbf{X}_k|\mathbf{D}_k)$ is the estimate of the pdf of state $\mathbf{X}_k$, when the measurements $\mathbf{D}_k$ are available. The key steps in the implementation of the algorithm are available in [4]. However, for system identification and damage detection applications, the interest is on identifying the parameters of the system, rather than the state. One way to approach the problem is to augment the state vector with the vector of parameters that need to be estimated. However, an unfortunate consequence of such an approach is that the problem of state estimation and the problem of parameter identification of the system become coupled. This results in an increase of the size of the vectors that are being estimated

and results in significant computational effort being wasted. Following the developments in [5, 6], this problem can be averted by rewriting the model equation in terms of vector of parameters to be identified as

$$\theta_{k+1} = \theta_k + \mathbf{w}_k \tag{3}$$

and the measurement equation is expressed as in Eq. (2) but as a function of θ_k. Equation 3 basically implies that model parameters θ_k remain invariant for the duration of measurement acquisition. Here, $\mathbf{w}_k$ is model noise which is artificially included, the reason for which would be explained later. The key steps in bootstrap particle filtering algorithm are summarized below:

1. Assume $p(\theta_{k-1} \mid \mathbf{D}_{k-1})$ is known. Generate the vector of random samples $\{\theta_{k-1}\}_{i=1}^{N}$.
2. Generate samples $\{\mathbf{w}_{k-1}\}_{i=1}^{N}$ from the known distribution of $p(\mathbf{w}_{k-1})$.
3. Each sample is passed through the model equation in Eq. (3) to obtain the predictions for θ at time step k. Thus,

$$\theta_k^{*(i)} = \mathbf{f}_{k-1}(\mathbf{X}_{k-1}^{(i)}, \mathbf{w}_{k-1}^{(i)}). \tag{4}$$

4. Once the measurements $\mathbf{Y}_k$ are available, evaluate the likelihood of each prediction $\{\theta_k{}^{*(i)}\}_{i=1}{}^{N}$ and obtain a normalized weight for each sample, given by

$$q_i = \frac{p(\mathbf{Y}_k \mid \theta_k^{*(i)})}{\sum_{j=1}^{N} p(\mathbf{Y}_k \mid \theta_k^{*(j)})}. \tag{5}$$

5. Define a discrete distribution over $\{\theta_k{}^{*(i)}\}_{i=1}{}^{N}$, with probability mass q_i associated with element i.
6. Resample N times from the discrete distribution to generate samples $\{\theta_k{}^{*(i)}\}_{i=1}{}^{N}$, so that for any j, $P[\theta_k^j = \theta_k^{*(i)}] = q_i$.

The above steps of prediction and update form a single iteration of the recursive algorithm. Once this algorithm is applied for the entire length of the measurement data, the process can be repeated from time $t = 0$ with the updated estimates of θ obtained at the end of measurement time span T. This is referred to as global iterations. It has been discussed in the literature that global iterations lead to better and less noisy estimates for the parameters being identified [4, 9].

3 Problem Statement

A cantilever beam subjected to forced vibrations is considered. The equation of bending vibration of an Euler-Bernoulli beam is a fourth-order partial differential equation given by

$$m(x)\frac{\partial^2 y(x,t)}{\partial t^2} + c(x)\frac{\partial y(x,t)}{\partial t} + \frac{\partial^2}{\partial x^2}\left[EI(x)\frac{\partial^2 y(x,t)}{\partial x^2}\right] = f(x,t), \tag{6}$$

where, $m(x)$ is the mass per unit length of the beam, $c(x)$ is the damping, $y(x, t)$ denotes the transverse beam displacement as a function of the spatial coordinate x and the temporal coordinate t, and $f(x, t)$ is the general form of distributed loading having both spatial and temporal variations. Using finite elements, the partial differential equation in Eq. (6) can be discretized into a set of coupled ordinary differential equations, of the form

$$\mathbf{M}\ddot{\mathbf{X}} + \mathbf{C}\dot{\mathbf{X}} + \mathbf{K}\mathbf{X} = \mathbf{F}(\mathbf{t}), \tag{7}$$

where, **M**, **C**, and **K** are mass, damping, and stiffness matrices, respectively, and **F** (t) is the forcing function.

Here, we assume damping to be Rayleigh proportional such that

$$\mathbf{C} = \alpha\mathbf{M} + \beta\mathbf{K}, \tag{8}$$

where, α and β are mass and stiffness proportionality constants given by

$$\alpha = \frac{2\omega_1\omega_2}{{\omega_2}^2 - {\omega_1}^2}(\omega_2\eta_1 - \omega_1\eta_2), \tag{9}$$

$$\beta = \frac{2}{{\omega_2}^2 - {\omega_1}^2}(\omega_2\eta_2 - \omega_1\eta_1). \tag{10}$$

Here, ω_1 and ω_2 are the first and second natural frequencies, and η_1 and η_2 are the damping ratios corresponding to the first and second modes of vibration. In rewriting the Eq. (6) in the discretized form of Eq. (7), we assume the beam to be discretized using 1-dimensional beam elements having 2 nodes per element. Hence, each node has a one transverse and one rotational degree of freedom. This implies that if the beam is discretized into N elements, the total number of degrees of freedom in the discretized beam is $2N + 2$. Thus, after partitioning for the known and unknown degrees of freedom, **M**, **C**, and **K** are symmetric matrices of dimensions $N \times N$, and $\mathbf{X}(t)$,$\dot{\mathbf{X}}(t)$, $\ddot{\mathbf{X}}(t)$, and $\mathbf{F}(t)$ are respectively the nodal vectors of displacement, velocity, acceleration, and nodal forces of dimensions $N \times 1$.

In this study, we assume $N = 5$. A comparison of the finite element response when $N = 5$ and 15 shows that (see Fig. 1) the response when $N = 5$ leads to acceptable match. We assume that a concentrated harmonic force is applied at the fourth node corresponding to a distance 186 mm from fixed end of the 310-mm-long cantilever beam. The tip response is measured experimentally. The objective of this study is to illustrate the applicability of the proposed method in identifying

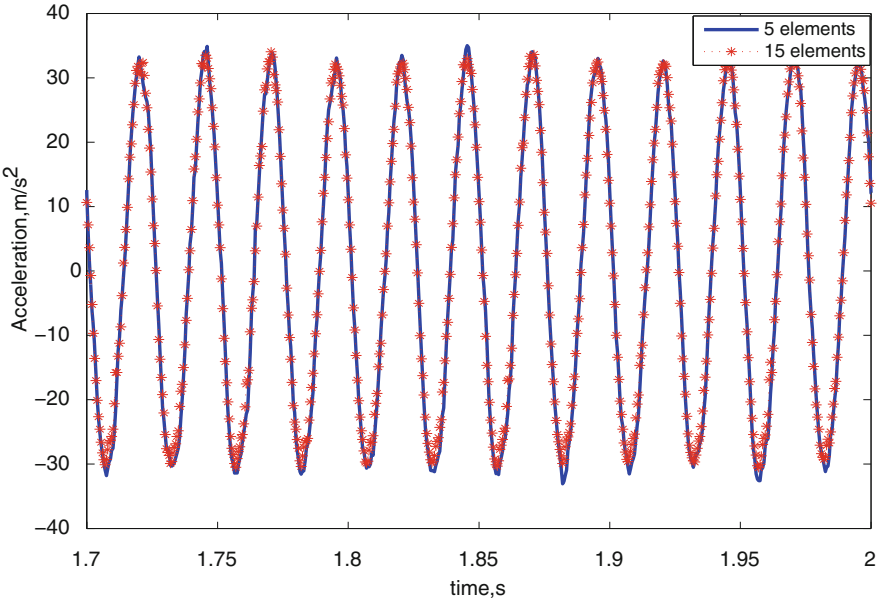

Fig. 1 Tip response of a cantilever beam

the system parameters. We consider two problems. In the first problem, we assume the damping to be the unknown parameter that is to be identified. In the second problem, we focus on identifying the flexural rigidity of the beam.

4 Experimental Setup

We consider an aluminum beam of length 310 mm and having cross-sectional dimensions of 25. 65 ×3. 25 mm. The material properties of the beam are: modulus of elasticity $E = 50$ GPa and mass density $\rho = 2,662$ kg/m^3. Figure 2 shows the actual experimental setup and Fig. 3 shows a schematic diagram of the setup. The cantilever beam is imparted a dynamic force through a V406 LDS shaker attached through a stinger to excite the beam with a vertical sinusoidal excitation force (shown in Fig. 4). A Dytran 5860B impedance head with force sensitivity of 109 mV/Lbf is placed at the point of (186 mm from fixed end) excitation, and the tip response is measured using a Dytran 3055B2 accelerometer with a sensitivity of 102.3 mv/g. Agilent U2352A, 16 channel Data Acquisition System is used to acquire the data from sensors. The measurement time history (Fig. 6) as obtained from the tip accelerometer is taken to be of duration 11 s with a sampling rate of 2,000 samples per second.

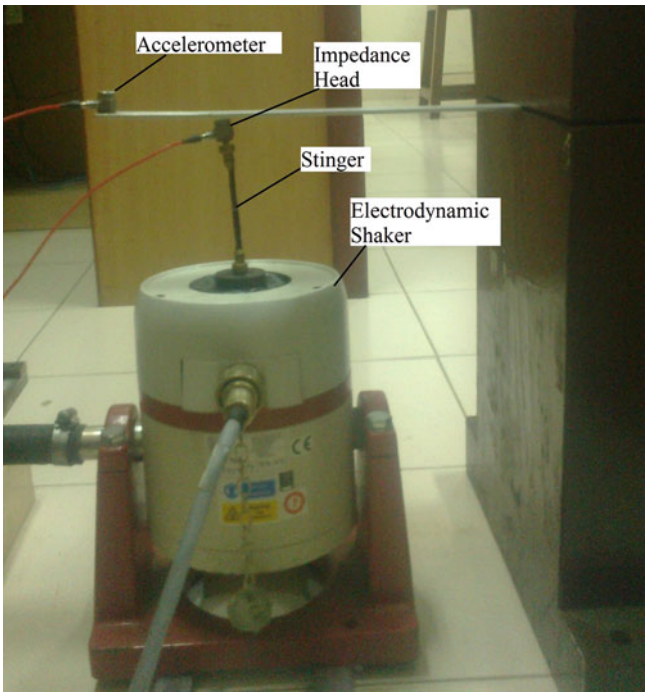

Fig. 2 Experimental setup

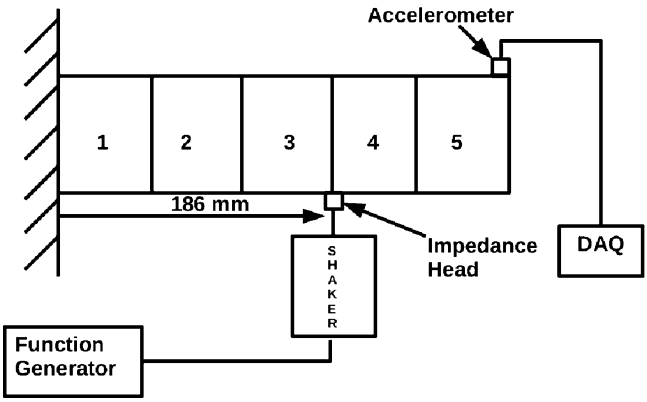

Fig. 3 Schematic of the experimental setup

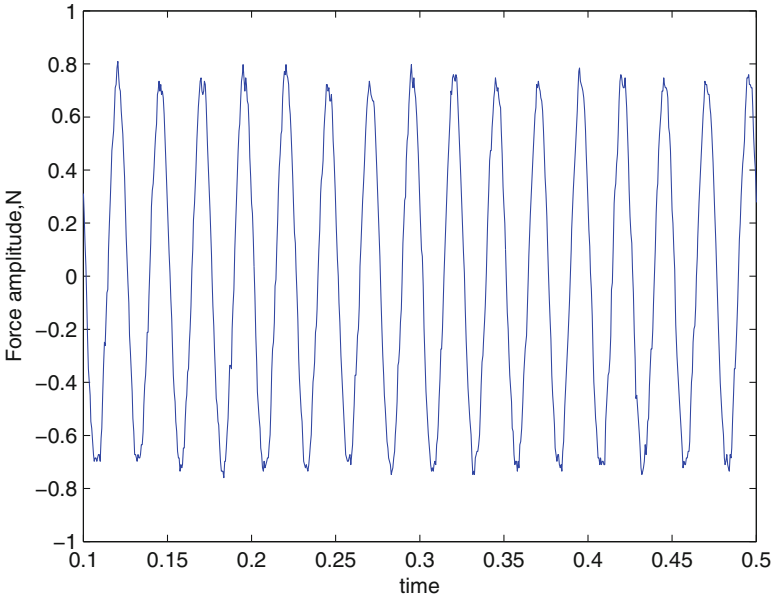

Fig. 4 Force time history

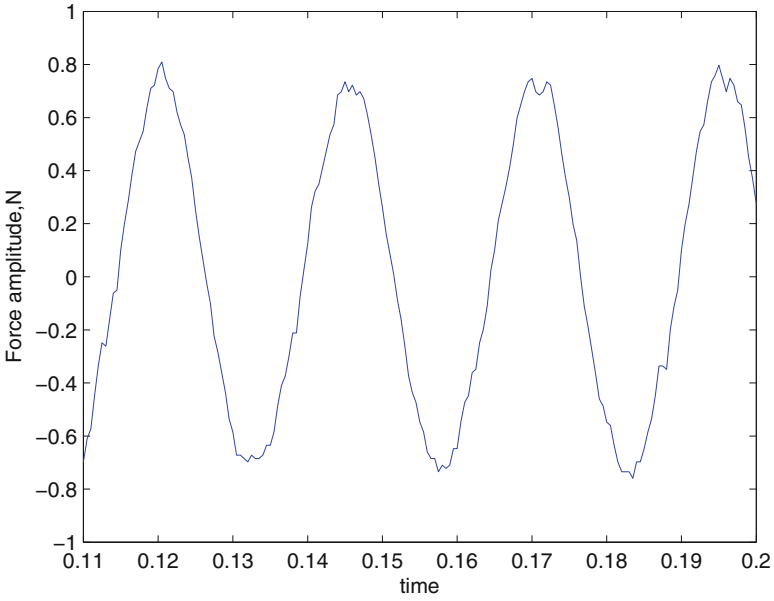

Fig. 5 Zoomed time history

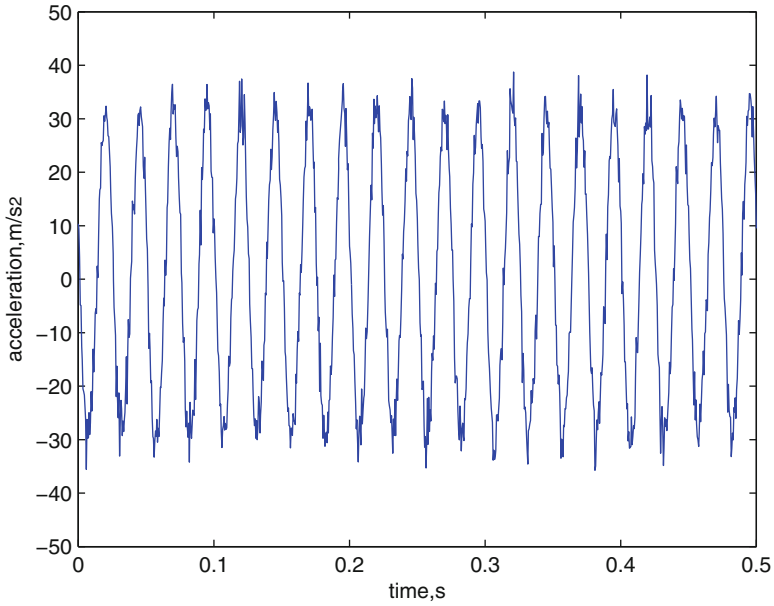

Fig. 6 Acceleration time history (measurements)

5 Numerical Results and Discussion

5.1 Example 1: Estimation of Damping in the Beam

Damping is modeled as viscous and proportional such that **C** can be expressed as in Eq. (8). The aim of this study is to estimate α and β in Eq. (8). The cantilever beam is discretized into five elements having six nodes. The sinusoidal force as shown in Fig. 4 is applied at the fourth node from the fixed end; Fig. 5 shows a zoomed portion of the forcing function measurements. The experimental measurements at the tip as shown in Figs. 6 and 7 are used as an input to the particle filtering algorithm. It can be seen from Fig. 7 that the measurements of the response are noisy. In the absence of any information, we assume α and β to be uniformly distributed in [1 10] and [0 0.01], respectively. Here, we use 100 particles, and the computation is carried out at every time step. From Figs. 8 and 9, we see that as more and more measurements become available, the estimates converge to a particular value. Taking the mean of estimates after the estimates stabilize the estimated values of α and β are found to be $2.\ 0414$ and $1.\ 39 \times 10^{-4}$, respectively.

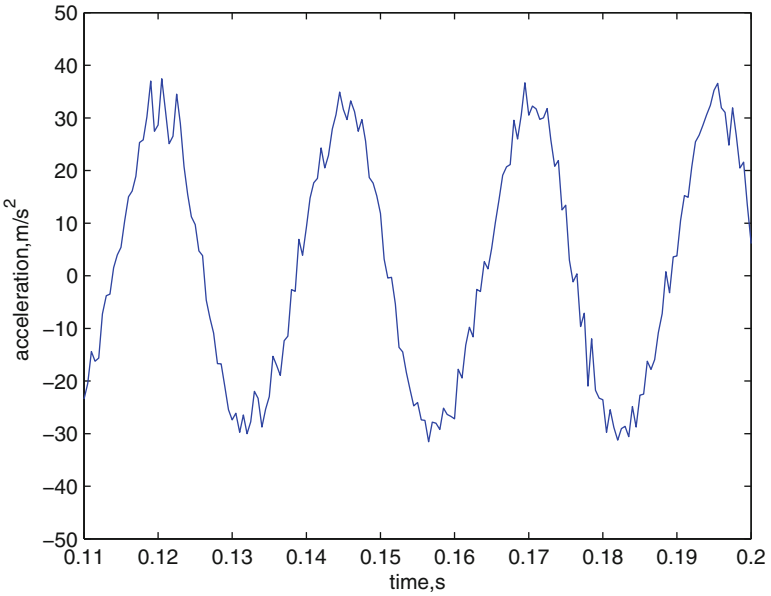

Fig. 7 Zoomed time history

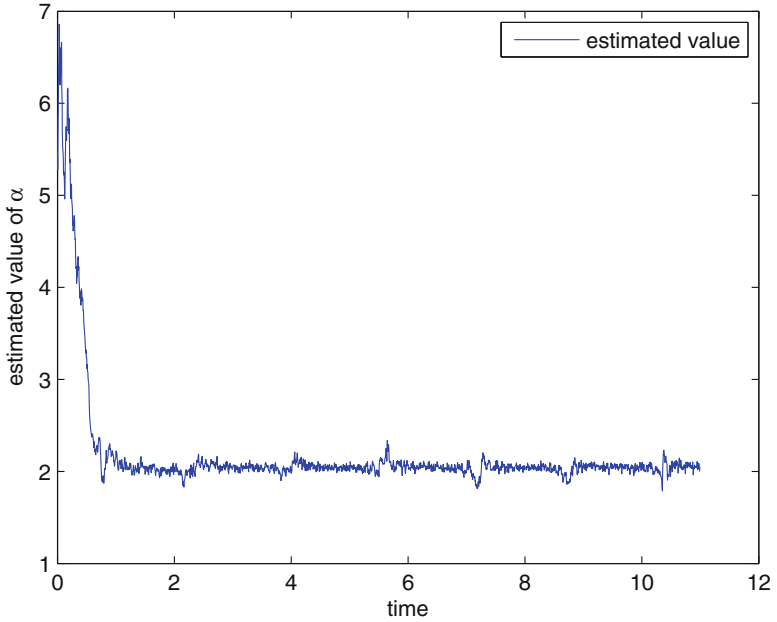

Fig. 8 Estimates of damping parameter α

Table 1 Load-deflection test

Load, P(gm)	Deflection, δ(mm)	EI(Nm^2)
50	1.33	3.66
200	5.31	3.66

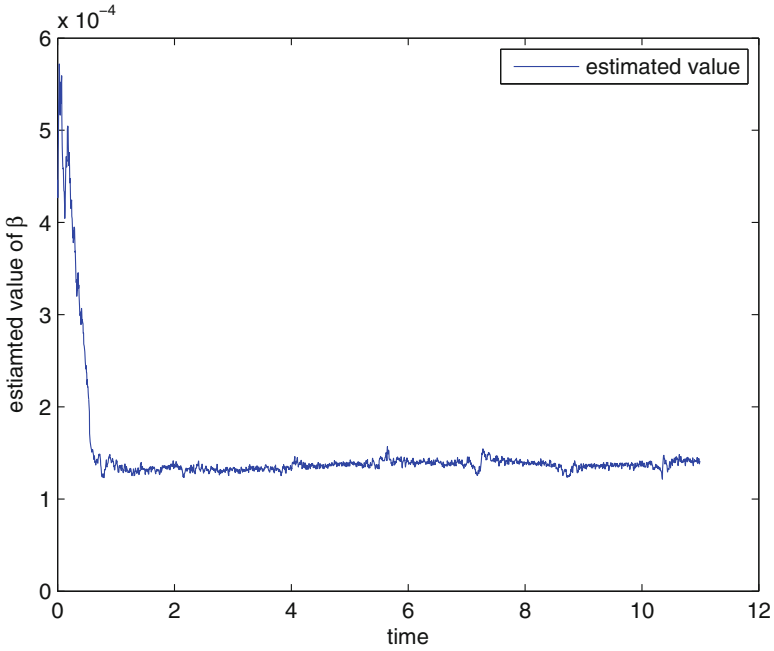

Fig. 9 Estimates of damping parameter β

5.2 *Example 2: Estimation of FlexuralRigidity(*EI*)*

The elemental stiffness matrix for a beam is given by:

$$\mathbf{K} = \frac{EIn^3}{L^3}\begin{bmatrix} 12 & 6L & -12 & 6L \\ 6L & 4L^2 & -6L & 2L^2 \\ -12 & -6L & 12 & -6L \\ 6L & 2L^2 & -6L & 4L^2 \end{bmatrix}$$

where, n is the number of discretized elements and L is the length of the beam. Clearly, the flexural rigidity, EI, is a measure of the stiffness of a system. An approximate estimate of EI value was obtained from a load-deflection test. Here, we applied known loads at the tip of the cantilever beam and measured the response; see Table 1 for data. From the available analytical expression of the tip response given by $\delta = \frac{PL^3}{3EI}$, an approximate estimate of EI was obtained to be 3.66 Nm^2. Next, we use the developed algorithm to estimate the flexural rigidity from

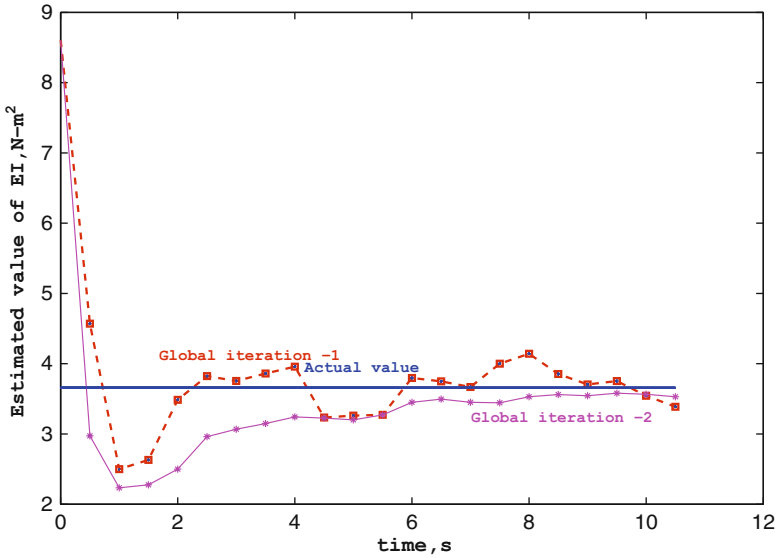

Fig. 10 Estimation of *EI* using global iteration

vibration measurement time histories. The motivation for this study is to later extend this technique for identifying local damages in the beam. The underlying assumption here is that the presence of local damage in the form of cracks, etc., would lead to a loss of flexural rigidity locally. A methodology has been already developed in the group to relate the local loss of stiffness to crack sizes [9]. The present study is a first step toward experimental demonstration of the applicability of the developed methodology [9].

We consider the beam to be discretized into five elements, and the forcing is as shown in Fig. 4 and is applied at the fourth node. Even though an estimate of *EI* is obtained as 3.66 Nm^2, for the sake of the robustness of the technique, we assume initially that *EI* is uniformly distributed in the range [10–20] Nm^2. The experimental measurements are used as an input to the particle filtering algorithm. Here, we use 50 particles at each iteration steps, and two global iterations are performed. To save computational efforts, the iterations are carried out at every 0.5 s. Hence, the total number of structural evaluations are 2,200. From Fig. 10, we observe that the algorithm leads to the correct estimates of flexural rigidity. Moreover, the fluctuations in the estimates are much less if global iterations are carried out.

6 Concluding Remarks

Application of particle filtering methodology for parameter estimation from experimental vibration data has been discussed. The numerical examples illustrate that particle filtering methodology has been successfully applied to estimate system

parameters. The further work is currently in progress to detect crack location using the particle filtering algorithm.

Acknowledgements This study has been supported by Aeronautical Development Agency, Govt. of India under the National Program on Micro and Smart Systems (NPMASS).

References

1. Brown RG, Hwang PYC (1992) Introduction to random signals and applied Kalman filtering. Wiley, New York
2. Chaudhari TD, Maiti SK (2000) Experimental verification of a method of detection of crack in taper and segmented beams based on modelling of transverse vibration. Int J Fract 102:L33–L38
3. Patil DP, Maiti SK (2005) Experimental verification of a method of detection of multiple cracks in beams based on frequency measurements. J Sound Vib 281:439–451
4. Gordon NJ, Salmond DJ, Smith AFM (1993) Novel approach to nonlinear/nonGaussian Bayesian state estimation. IEE Proc F 140(2):107–113
5. Nasrellah HA, Manohar CS (2011) Finite element method based Monte Carlo filters for structural system identification. Probab Eng Mech 26(2):294–307
6. Nasrellah HA, Manohar CS (2011) Particle filters for structural system identification using multiple test and sensor data: a combined computational and experimental study. Struct Control Health Monit 18(1):99–120
7. Kalman RE (1960) A new approach to linear filtering and prediction problems. ASME J Basic Eng 82(D):35–45
8. Myotyri E, Pulkkinen U, Simola K (2006) Application of stochastic filtering for lifetime prediction. Reliab Eng Syst Saf 91:200–208
9. Rangaraj R, Rao L, Banerjee A, Gupta S (2011) Identification of Fatigue Cracks in vibrating beams using a particle filtering algorithm. National Aerospace seminar on aircraft structures. IIT, Kanpur

Estimating Crossing Rate Statistics of Second Order Response of Structures Subjected to LMA Loadings

Jithin Jith, Sayan Gupta, and Igor Rychlik

Abstract Estimating the crossing rate statistics of response of offshore structures to wave loadings is essential for their reliability assessment. Wave loadings during heavy storms exhibit non-Gaussian properties, such as, skewed marginal distributions with heavy tails. Such processes can be modeled as Laplace driven moving average (LMA) processes. LMA processes are non-Gaussian, strictly stationary and are characterized by mean, spectrum and two other parameters which can be used to model the skewness and kurtosis of the marginal distribution. Following the Kac-Siegert representation, a second order approximation of the Volterra expansion of the system enables representing the response as a quadratic combination of vector LMA processes. The focus of this study is on estimating the crossing statistics of such a response process.

Keywords Laplace-driven moving average • Second-order response • Kac-Siegert representation • Volterra expansion • Non-Gaussian loading • Laplace motion

1 Introduction

Estimation of upcrossing frequency is of crucial importance if the risk associated with failure of structures under excitation by random loads has to be quantified. Traditionally, such systems have often been linearized, and the external loads have been considered to be Gaussian in nature. There are cases, of sufficiently weak

J. Jith (✉) • S. Gupta
Department of Applied Mechanics, Indian Institute of Technology Madras, Chennai 600036, TN, India
e-mail: jith.6631034@gmail.com; gupta.sayan@gmail.com

I. Rychlik
Mathematical Sciences, Chalmers University of Technology, SE-412 96, Göteborg, Sweden
e-mail: rychlik@chalmers.se

S. Chakraborty and G. Bhattacharya (eds.), *Proceedings of the International Symposium on Engineering under Uncertainty: Safety Assessment and Management (ISEUSAM - 2012)*,
DOI 10.1007/978-81-322-0757-3_45,

nonlinearity, where reasonable results can be obtained from such an analysis. But for the vast majority of systems, simple linearization leads to crude approximations.

In this chapter, crossing statistics of weakly nonlinear time-invariant systems under stationary non-Gaussian excitation are investigated. The response of such systems can be represented by a Volterra functional expansion, truncated after the second term. Thus, the response can be expressed as

$$Z(t) = Z_1(t) + Z_2(t), \tag{1}$$

where,

$$Z_1(t) = \int_{-\infty}^{\infty} h_1(s)X(t-s)ds, \tag{2}$$

$$Z_2(t) = \frac{1}{2}\int\int_{-\infty}^{\infty} h_2(s_1, s_2)X(t-s_1)X(t-s_2)ds_1ds_2. \tag{3}$$

Here, $Z(t)$ is the total response and is obtained as the summation of the linear response $Z_1(t)$ and the second-order response $Z_2(t)$, and $h_1(\cdot)$ and $h_2(\cdot,\ \cdot)$ are, respectively, the linear and quadratic impulse response functions of the system.

The loading $X(t)$ in Eqs. (2) and (3) is a random process with a specified power spectral density function. If $X(t)$ is Gaussian, then it can be represented as a convolution between a linear filter and Gaussian white noise

$$X(t) = \int_{-\infty}^{\infty} q(t-s)dB(s), \tag{4}$$

where $B(\cdot)$ is Brownian motion and $q(\cdot)$ is a filter dependent on the power spectral density of the loading.

A great deal of attention has been paid to modeling of physical forces in nature as Gaussian distributions primarily because they fit a wide range of data sets. This property was first articulated by P.S. Laplace in his second law (1778) which states that the frequency of the error is an exponential function of the square of the error. However, Laplace's first law (1774), which precedes the second law by 4 years, states that the frequency of an error could be expressed as an exponential function of the numerical magnitude of the error, disregarding sign [7]. This is the basis of the Laplace distribution.

However, even though Laplace distribution also fits physical observable data, the relatively more interest in Gaussian distribution has been due to its mathematical tractability in comparison to Laplace. Also, just because many physical systems exhibit Gaussian distribution does not imply that all processes should be modeled as Gaussian. In fact, it has been discussed in the literature that many processes, such as wave loadings during storms, exhibit significant non-Gaussian characteristics. Modeling such loadings as Gaussian and performing a reliability analysis severely underestimates the risk of failure [2].

The density functions for wave loadings during storms exhibit heavier tails and asymmetry. This can be attributed to the effect of sudden peaks in time histories arising due to whipping effects of the waves impinging on the structure. The asymmetric Laplace distribution, with its characteristic heavy tails, is ideally suited for modeling such loads. Hence, in this chapter we consider a Laplace-driven moving average (LMA) model to represent the wave loads.

Failures in structures can be attributed to overloading of the structure response or to fatigue damage. In either case, it can be shown that the probability of failure can be expressed in terms of the mean upcrossing frequency of the response process about a specified threshold u. Mathematically, the mean upcrossing frequency is expressed through the Rice's formula [11] and is given by

$$\nu_u^+ = \int_0^\infty \dot{z} f_{Z\dot{Z}}(u, \dot{z}) d\dot{z}. \tag{5}$$

Here, $\nu_u{}^+$ is the mean upcrossing frequency of the response process $Z(t)$ about the level u, and $f_{Z\dot{Z}}(u, \dot{z})$ is the joint probability density function of $Z(t)$ and its instantaneous time derivative $\dot{Z}(t)$. It is clear that the estimation of upcrossing frequency hinges on obtaining reasonable approximations for $f_{Z\dot{Z}}(\cdot, \cdot)$, which is not easy when $Z(t)$ is non-Gaussian.

The focus of this study is on developing a methodology for computing the mean upcrossing frequency of the structure response $Z(t)$ when the loadings are modeled as LMA processes. This chapter is divided into the following sections: First, we briefly review LMA processes and their simulation. Next, we obtain the expressions for response $Z(t)$ in terms of the LMA loading. Subsequently, the focus is on the development of a methodology for obtaining approximations for the crossing statistics. Finally, illustrative numerical examples are presented followed by a section on concluding remarks.

2 Laplace Driven Moving Average

Laplace-driven Moving Average (LMA) is a continuous time moving average of the form

$$X(t) = \int_{-\infty}^{\infty} f(t - x) d\Lambda(x), \tag{6}$$

where $f(x)$ is a kernel function and $\Lambda(x)$ is a general asymmetric Laplace motion. $\Lambda(x)$ has independent and stationary increments, and the increments follow a generalized asymmetric Laplace distribution. Since $X(t)$ is a convolution of $f(\cdot)$ with the increments of $\Lambda(x)$, it is a stationary, ergodic, and non-Gaussian process.

The characteristic function of the Laplace motion $\Lambda(x)$ is given by

$$\phi_{\Lambda(x)}(u) = E[e^{iu\Lambda(x)}] = \frac{e^{iu\zeta x}}{(1 - i\mu u + \sigma^2 v^2/2)^{x/v}}, \tag{7}$$

where σ is the space-scale parameter, ν is the timescale parameter, μ is the asymmetry parameter, and ζ is the drift of the process. The asymmetry parameter $\mu \neq 0$ ensures that the corresponding moving average process also has a nonsymmetric marginal distribution. The characteristic function of the LMA process is given by

$$\phi_{X(t)}(u) = \exp\left(\int_{-\infty}^{\infty} i\zeta u f(x) - \frac{1}{v}\log\left(1 - i\mu u f(x) + \frac{\sigma^2 f^2(x)u^2}{2}\right)dx\right). \tag{8}$$

It can be easily shown that for a LMA process, the mean and the two-sided spectral density are given by

$$E[X(t)] = (\zeta + \mu/v)\int_{-\infty}^{\infty} f(x)dx, \tag{9}$$

$$S(\omega) = \frac{1}{2\pi}\frac{\sigma^2 + \mu^2}{v} \mid \mathcal{F}f(\omega) \mid^2, \tag{10}$$

where $\mathcal{F}f(\omega)$ is the Fourier transform of the symmetric kernel $f(x)$. If the kernel is normalized such that $\int f^2(x)dx = 1$, then

$$V[X(t)] = \frac{\sigma^2 + \mu^2}{v}. \tag{11}$$

Here, $V[\cdot]$ is the variance of the process $X(t)$. There are two more free parameters left which can be used to fit the skewness s and excess kurtosis κ of the marginal distribution of X(t), and these can be shown to be

$$s = \mu v^{1/2}\frac{2\mu^2 + 3\sigma^2}{(\mu^2 + \sigma^2)^{3/2}}\int_{-\infty}^{\infty} f^3(x)dx, \tag{12}$$

$$\kappa = 3v\left(2 - \frac{\sigma^4}{(\mu^2 + \sigma^2)^2}\right)\int_{-\infty}^{\infty} f^4(x)dx. \tag{13}$$

2.1 Simulation of LMA

The asymmetric Laplace motion $\Lambda(x)$ can be represented as a subordinated Brownian motion as

$$\Lambda(x) = \zeta x + \mu\Gamma(x) + \sigma B(\Gamma(x)), \tag{14}$$

where $B(x)$ is a Brownian motion of unit scale and $\Gamma(x)$ is a gamma process of independent and homogeneous increments that follow a gamma distribution $\Gamma(\frac{dx}{\nu}, 1)$. Note that $B(x)$ and $\Gamma(x)$ are independent of each other. Differentiating Eq. (14), we get

$$d\Lambda(x) = \zeta dx + \mu d\Gamma(x) + \sigma dB(\Gamma(x)). \tag{15}$$

Now, convolving the symmetric kernel $f(x)$ with $\mathrm{d}\Lambda(x)$ yields the Laplace-driven MA as

$$X = \zeta \int f(x)dx + \mu f * G + \sigma f * (\sqrt{G} \cdot Z), \tag{16}$$

where, G is a vector of i.i.d Gamma random variables distributed as $\Gamma(\frac{dx}{\nu}, 1)$ and Z is a vector of i.i.d zero mean standard normal random variables. Here, $*$ denotes convolution, and $\sqrt{G} \cdot Z = [\sqrt{G_i} \cdot Z_i]$. More details of the simulation are available in [2].

3 Quadratic Response with LMA Forcing

In this section, we use the methodology employed in [8, 10] and the Kac-Siegert technique [6, 5] to represent the quadratic response of a weakly nonlinear system subjected to LMA loadings. From Eqs. (2) and (3), the linear and quadratic responses $Z_1(t)$ and $Z_2(t)$ may be rewritten as

$$Z_1(t) = \int_{-\infty}^{\infty} k_1(t-x)d\Lambda(x), \tag{17}$$

$$Z_2(t) = \frac{1}{2}\int\int_{-\infty}^{\infty} k_2(t-x_1, t-x_2)d\Lambda(x_1)d\Lambda(x_2), \tag{18}$$

where

$$k_1(t) = \int_{-\infty}^{\infty} h_1(x)f(t-x)dx \tag{19}$$

$$k_2(t,s) = {}^{\infty}_{-\infty}h_2(x_1,x_2)f(t-x_1)f(s-x_2)dx_1dx_2. \tag{20}$$

Under the assumption that kernels $k_1(t)$ and $k_2(t, s)$ are square integrable and hence vanish at infinity, for all practical purposes, they may be considered zero outside a bounded set. So, by choosing a large enough value of T, we can replace infinity in the limits of integration with T. Now, the Kac-Siegert technique is employed to further analyze the quadratic process $Z_2(t)$. The objective of this method is to represent the truncated kernel $k_2(t, s)$ through its eigenvalues $\{\lambda_i\}$ and eigenfunctions $\{\phi_i\}$ defined by the integral equation

$$\int_{-T}^{T} k_2(t,s)\phi(s)ds = \lambda\phi(t). \tag{21}$$

The eigenfunctions belonging to distinct eigenvalues are orthogonal since the kernel $k_2(t, s)$ is symmetric, which follows from the assumption that $h_2(t, s)$ is symmetric. For most applications, $h_2(t, s)$ is found to be symmetric. It may be assumed that $\{\phi_i\}$ form a set of orthonormal functions and that they have been ordered such that $|\lambda_i| \geq |\lambda_{i+1}| > 0$. Since the eigenvalues of a symmetric kernel are real, the corresponding eigenfunctions may also be considered real. It can also be shown [1] that $\lambda_i \to 0$ as $i \to \infty$ and that

$$k_2(t,s) = \sum_{i=1}^{\infty} \lambda_i\phi_i(t)\phi_i(s) \quad \text{in q.m.} \tag{22}$$

In other words, this implies that

$$\int_{-T}^{T} \left| k_2(t,s) - \sum_{i=1}^{n} \lambda_i\phi_i(t)\phi_i(s)\right|^2 dsdt \to 0 \quad as \quad n \to \infty.$$

Using Eqs. (18) and (22), we get

$$Z_2(t) = \sum_{i=1}^{\infty} \frac{1}{2}\lambda_i W_i(t)^2 \quad \text{in q.m,} \tag{23}$$

where, the LMA eigenprocesses $W_i(t)$, $i = 1, 2, \ldots$ are defined as

$$W_i(t) = \int_{-T}^{T} \phi_i(t-x)d\Lambda(x). \tag{24}$$

Further, in order to represent the first-order response $Z_1(t)$ in terms of the eigenprocesses $\{W_i(t)\}$, we have to make the assumption that the kernel $k_1(t)$ can be expanded in terms of $\{\lambda_i\}$ and $\{\phi_i\}$, i.e.,

$$k_1(t) = \sum_{i=1}^{\infty} c_i \phi_i(t) \quad \text{in q.m,} \tag{25}$$

$$c_i = \int_{-T}^{T} k_1(t)\phi_i(t)dt. \tag{26}$$

From Eqs. (17) and (25), we get

$$Z_1(t) = \sum_{i=1}^{\infty} c_i W_i(t) \quad \text{in q.m.} \tag{27}$$

The total response $Z(t)$ can thus be decomposed as

$$Z(t) = \sum_{i=1}^{\infty} c_i W_i(t) + \frac{1}{2}\lambda_i W_i(t)^2 \quad \text{in q.m.} \tag{28}$$

For ease of computational purposes, the sum is truncated once the eigenvalues λ_i start becoming insignificant. Assuming n eigenvalues are significantly nonzero, Eq. (28) can be rewritten as

$$Z(t) = \sum_{i=1}^{n} c_i W_i(t) + \frac{1}{2}\lambda_i W_i(t)^2, \tag{29}$$

while

$$\dot{Z}(t) = \sum_{i=1}^{n} c_i \dot{W}_i(t) + \lambda_i W_i(t)\dot{W}_i(t) \tag{30}$$

represents the instantaneous time derivative of the response.

4 Computation of Upcrossing Frequency

The mean upcrossing frequency of $Z(t)$ about the level u is given by Rice's formula in Eq. (5). The methodology developed in [8] will be followed here to evaluate Eq. (5). In [8], however, it is required that the eigenprocesses $\{W_i(t)\}$ be stationary Gaussian processes. In order to accomplish this, the LMA process, defined in Eq. (6), is conditioned on the gamma process $\Gamma(x)$. The conditioned Laplace motion can be written as

$$\Lambda[x \mid \Gamma(\cdot) = \gamma(\cdot)] = \lambda(x) = \zeta x + \mu\gamma(x) + \sigma B(\gamma(x)). \tag{31}$$

The conditioned eigenprocess

$$W_i(t) = \int_{-T}^{T} \phi_i(t-x)d\lambda(x) \tag{32}$$

follows a Gaussian distribution.

Let the conditional upcrossing frequency be

$$v_u^+(\gamma) = v_u^+(\Gamma(\cdot) = \gamma(\cdot)). \tag{33}$$

The unconditional upcrossing frequency can then be estimated by simulating a large number of gamma processes, $\{\gamma_i(\cdot)\}^N{}_{i=1}$, and averaging $\nu_u{}^+(\gamma)$:

$$v_u^+ \simeq \frac{1}{N}\sum_{i=1}^{N} v_u^+(\gamma_i). \tag{34}$$

Derivation of the joint probability density of $Z(0)$ and $\dot{Z}(0)$ will be carried out in the same way as in [8] and [3]. Under the assumption that $Z(t)$ is a function of $W_1(0)$ with all the other eigenprocesses being fixed, $f_{Z\dot{Z}}$ may be rewritten as

$$f_{Z\dot{Z}}(z,\dot{z}) = \int \cdots \int_{-\infty}^{\infty} f_{W_2\cdots W_n Z\dot{Z}}(w_2,\ldots,w_n,z,\dot{z})dw_2\cdots dw_n. \tag{35}$$

From Eq. (29), $z = g(W_1, w_2, \ldots, w_n)$, we write

$$z = c_1 W_1 + \frac{1}{2}\lambda_1 W_1^2 + \sum_{i=2}^{n} c_i w_i + \frac{1}{2}\lambda_i w_i^2. \tag{36}$$

It is clear from Eq. (36) that W_1 will have two solutions: $w_1{}^+$ and $w_1{}^-$. Transformation of variables leads to the relation

$$f_{W_2\cdots W_n Z\dot{Z}}(w_2,\ldots,w_n,z,\dot{z}) = \sum_{\epsilon=+,-} f_{W_1\cdots W_n\dot{Z}}(w_1^\epsilon,\ldots,w_n,\dot{z})\frac{\partial w_1^\epsilon}{\partial z} \tag{37}$$

The joint pdf is now rewritten as

$$f_{W_1\cdots W_n\dot{Z}}(w_1,\ldots,w_n,\dot{z}) = f_{\dot{Z}|W_1\cdots W_n}(\dot{z}|w_1,\ldots,w_n)f_{W_1\cdots W_n}(w_1,\ldots,w_n). \tag{38}$$

From Eq. (30), it can be seen that the conditioned variable $\{\dot{Z}|W_1 = w_1,\ldots,W_n = w_n\}$ is a sum of jointly Gaussian variables (when conditioned on $\Gamma(\cdot)$) and hence is itself Gaussian with parameters

$$\mu_{\dot{Z}|\mathbf{W}} = E[\dot{Z}|\mathbf{W} = \mathbf{w}]$$
$$= \partial\mathbf{g}\{E[\dot{\mathbf{W}}] + \sigma_{\dot{\mathbf{W}}\mathbf{W}}\sigma_{\mathbf{W}\mathbf{W}}^{-1}(\mathbf{w} - E[\mathbf{W}])\}, \tag{39}$$

$$\sigma_{\dot{Z}|\mathbf{W}}^2 = Var[\dot{Z}|\mathbf{W} = \mathbf{w}]$$
$$= \partial\mathbf{g}\{\sigma_{\dot{\mathbf{W}}\dot{\mathbf{W}}} - \sigma_{\dot{\mathbf{W}}\mathbf{W}}\sigma_{\mathbf{W}\mathbf{W}}^{-1}\sigma_{\mathbf{W}\dot{\mathbf{W}}}\}\partial\mathbf{g}', \tag{40}$$

where $E[\cdot]$ and σ denote the mean and covariance, respectively, the superscript $'$ denotes transposition, and

$$\partial\mathbf{g} = \left[\frac{dz}{dw_1}, \ldots, \frac{dz}{dw_n}\right]. \tag{41}$$

At time $t = 0$, from Eq. (32), the eigenprocesses $\mathbf{W}(0)$ and $\dot{\mathbf{W}}(0)$ are given by

$$W_i(0) = \zeta \int \phi_i(x)dx + \mu \int \phi_i(x)d\gamma(x) + \sigma \int \phi_i(x)dB(\gamma(x)),$$
$$\dot{W}_i(0) = \zeta \int \dot{\phi}_i(x)dx + \mu \int \dot{\phi}_i(x)d\gamma(x) + \sigma \int \dot{\phi}_i(x)dB(\gamma(x)). \tag{42}$$

The means and covariance matrices of $\mathbf{W}(0)$ and $\dot{\mathbf{W}}(0)$ are given by

$$E[W_i(0)] = \zeta \int \phi_i(x)dx + \mu \int \phi_i(x)d\gamma(x),$$
$$E[\dot{W}_i(0)] = \zeta \int \dot{\phi}_i(x)dx + \mu \int \dot{\phi}_i(x)d\gamma(x),$$
$$\sigma_{\mathbf{W}\mathbf{W}}(i,j) = \sigma^2 \int \phi_i(x)\phi_j(x)d\gamma(x),$$
$$\sigma_{\mathbf{W}\dot{\mathbf{W}}}(i,j) = \sigma^2 \int \phi_i(x)\dot{\phi}_j(x)d\gamma(x),$$
$$\sigma_{\dot{\mathbf{W}}\dot{\mathbf{W}}}(i,j) = \sigma^2 \int \dot{\phi}_i(x)\dot{\phi}_j(x)d\gamma(x). \tag{43}$$

Substituting Eqs. (35)–(43) in Eq. (5) gives the conditional mean upcrossing frequency to be

$$\nu_u^+(\gamma) = \sum_{\epsilon=+,-} \int \cdots \int_{\Omega_\epsilon} \left|\frac{\partial w_1^\epsilon}{\partial z}\right| \left\{\int_0^\infty \dot{z} f_{\dot{Z}|\mathbf{W}}(\dot{z}, \mathbf{w}^\epsilon)d\dot{z}\right\} \cdot f_{W_1\cdots W_n}(w_1^\epsilon, \ldots, w_n)dw_2 \cdots dw_n,$$
$$= \sum_{\epsilon=+,-} \int \cdots \int_{\Omega_\epsilon} \left|\frac{\partial w_1^\epsilon}{\partial z}\right| \left\{\int_0^\infty \dot{z} f_{\dot{Z}|\mathbf{W}}(\dot{z}, \mathbf{w}^\epsilon)d\dot{z}\right\} \cdot f_{W_1}(w_1^\epsilon) \prod_{i=2}^{n} f_{W_i}(w_i)dw_2 \cdots dw_n, \tag{44}$$

where, the domain of vintegration Ω_ε is such that Eq. (36) gives a real solution for ${w_1}^\varepsilon$. Since $f_{\dot{Z}|\mathbf{W}}$ is Gaussian, it can be shown that [9]

$$\int_0^\infty \dot{z} f_{\dot{Z}|\mathbf{W}}(\dot{z}, \mathbf{w}) = \sigma_{\dot{Z}|\mathbf{W}} \left\{ \phi\left(\frac{\mu_{\dot{Z}|\mathbf{W}}}{\sigma_{\dot{Z}|\mathbf{W}}}\right) + \Phi\left(\frac{\mu_{\dot{Z}|\mathbf{W}}}{\sigma_{\dot{Z}|\mathbf{W}}}\right) \right\} \\ = \sigma_{\dot{Z}|\mathbf{W}} \Psi\left(\frac{\mu_{\dot{Z}|\mathbf{W}}}{\sigma_{\dot{Z}|\mathbf{W}}}\right), \tag{45}$$

where, $\phi(\cdot)$ and $\Phi(\cdot)$ are the standard Gaussian probability density and distribution functions, respectively. Now, Eq. (44), may be rewritten as

$$v_u^+(\gamma) = \sum_{\epsilon=+,-} \int \cdots \int_{\Omega_\epsilon} \left| \frac{\partial w_1^\epsilon}{\partial z} \right| \sigma_{\dot{Z}|\mathbf{W}} \Psi\left(\frac{\mu_{\dot{Z}|\mathbf{W}}}{\sigma_{\dot{Z}|\mathbf{W}}}\right) \cdot f_{W_1}(w_1^\epsilon) \prod_{i=2}^{n} f_{W_i}(w_i) dw_2 \cdots dw_n. \tag{46}$$

Equation 46 is an $(n-1)$ dimensional integral and can be evaluated using Monte Carlo integration.

5 Numerical Examples and Discussions

5.1 *Example 5.1*

A numerical example given in [2] is considered here. The upcrossing frequency of a general quadratic response $Z(t) = Z_1(t) + Z_2(t)$ was estimated, where

$$k_1(t) = \frac{e^{-t^2/50}}{\sqrt{25\pi}}, \quad -25 \le t \le 25 \\ k_2(t,s) = 0.01 e^{-(s-t)^2/50}, \quad -25 \le t \le 25; \quad -25 \le s \le 25. \tag{47}$$

The parameters of Laplace motion $\Lambda(x)$ were chosen such that $Z_1(t)$ has mean zero, variance 1, skewness 0.5, and kurtosis 4.5. twelve eigenvalues of the kernel $k_2(t, s)$ were found to be significantly nonzero. $N = 100$ gamma processes were simulated to determine the unconditional upcrossing frequency.

The results from the proposed method were compared against Monte Carlo simulations. Since full-scale Monte Carlo simulations were too computationally expensive, the methodology used in [2] was followed here. 10^5 independent samples of $\{Z(0), \dot{Z}(0)\}$ were simulated to statistically estimate the joint probability density function $f_{Z(0)\dot{Z}(0)\}}$. Subsequently, an estimate of the upcrossing frequency was obtained by numerically integrating Eq. (5) [4].

Figure 1 illustrates the comparison of upcrossing frequencies obtained by the proposed method against the estimates obtained from Monte Carlo simulations.

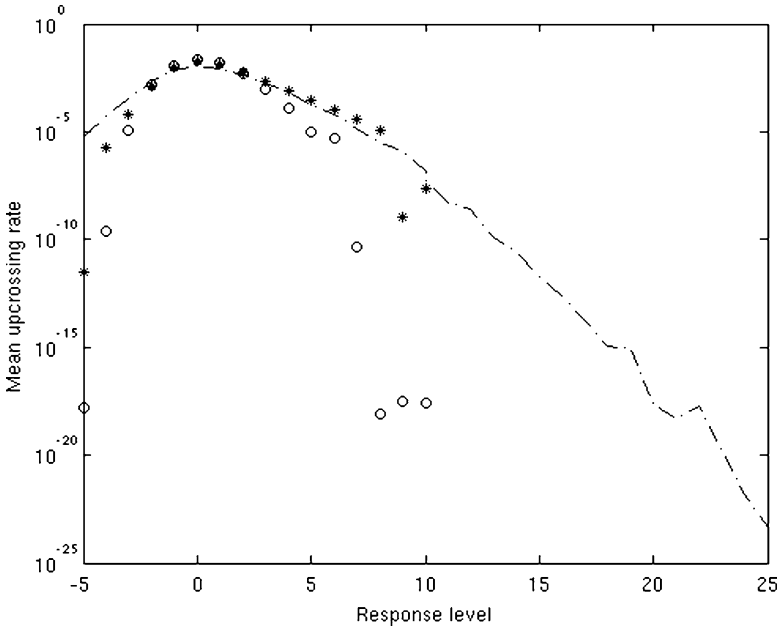

Fig. 1 Mean upcrossing frequency of $Z(0)$. *Dashed dotted line* represents the upcrossing frequency computed using the proposed method; *asterisks* represent the upcrossing frequency obtained from Monte Carlo simulations; *circles* represent the upcrossing frequency obtained from Monte Carlo simulations when $X(t)$ is represented as a Gaussian loading

It can be seen that the estimates from the proposed method match well with those obtained from MC simulations and are better at higher levels of response.

5.2 Example 5.2

The proposed method was tested on a linear SDOF system subjected to unidirectional ocean waves $X(t)$ that followed a 2-parameter Pierson-Moskowitz (PM) spectrum. The waves were assumed to have mean zero, variance 1, skewness 0.5, and kurtosis 4.5. The PM spectrum is given by

$$S(\omega) = \frac{5}{16} H_s^2 \frac{\omega_p^4}{\omega^5} \exp\left(-1.25 \frac{\omega_p^4}{\omega^4}\right), \tag{48}$$

where H_s is the significant wave height and ω_p is the peak frequency of the spectrum. In this example, H_s was assumed to be 8 m and ω_p to be 0.5 radians/s. For the SDOF system under consideration, natural frequency ω_0 was assumed to be 0.6 radians/s and damping to be 0.5%.

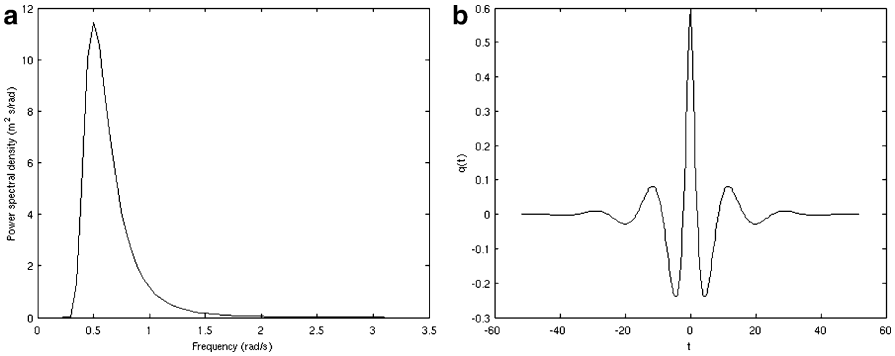

Fig. 2 (**a**) Spectral density of $X(t)$. (**b**) LMA kernel $f(x)$ of $X(t)$

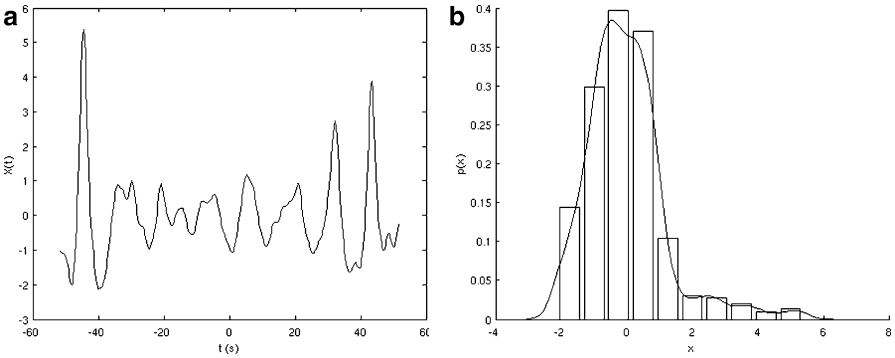

Fig. 3 (**a**) Simulated time series of $X(t)$. (**b**) Estimated probability density function of $X(t)$

The force acting on the system was assumed to be of the form $F(t) = \alpha(X(t) + \beta X(t)^2)$, where $\alpha = \omega_0{}^2$ and $\beta = 1$. The quadratic frequency response in this case becomes

$$H_2(\omega_1, \omega_2) = \alpha\beta H_1(\omega_1 + \omega_2). \tag{49}$$

Figure 2a illustrates the PM spectrum. The normalized symmetrical kernel $f(x)$, as defined in Eq. (10), is shown in Fig. 2b. Time series of $X(t)$ modeled as a LMA process can be seen in Fig. 3a. The non-Gaussian nature of the marginal distribution of $X(t)$ is illustrated in Fig. 3b.

The upcrossing frequency of the response of the SDOF system, $Z(t)$, was computed using the proposed method. First six eigenvalues of the kernel $k_2(t, s)$ were found to be significantly nonzero. A total of $N = 100$ gamma processes were simulated to determine the upcrossing frequency. It was shown in [2] that a sample size of $N = 100$ gamma processes gave reasonably accurate results.

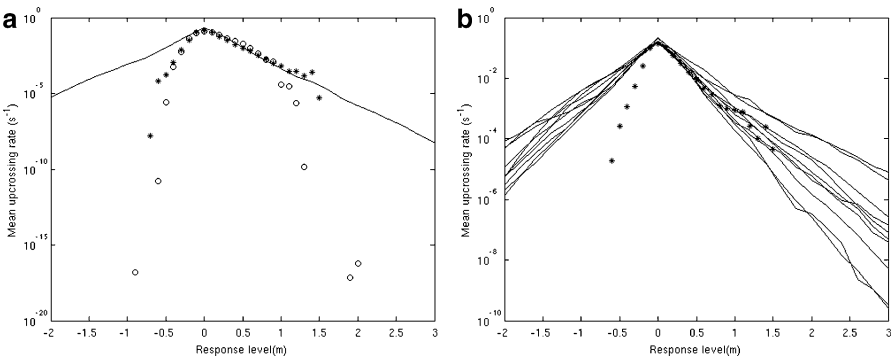

Fig. 4 Mean upcrossing frequency of $Z(0)$. (**a**) *Dashed dotted line* represents the upcrossing frequency computed using the proposed method; *asterisks* represent upcrossing frequency obtained from Monte Carlo simulations; *circles* represents upcrossing frequency obtained from MC simulations when loading $X(t)$ is assumed to be Gaussian. (**b**) *Dashed dotted lines* represent the upcrossing frequency computed using the proposed method for ten different estimate runs; *asterisks* represent the upcrossing frequency obtained from Monte Carlo simulations

Figure 4b illustrates the comparison of upcrossing frequencies obtained by the proposed method against the estimates obtained from Monte Carlo simulations. It can be seen that the results from the proposed method match well with those obtained from MC simulations. In fact, the proposed method gives better estimates for upcrossing frequencies at extreme levels of response.

6 Conclusions

The problem of estimating upcrossing frequencies of second-order response of weakly nonlinear systems was studied. The loads were modeled as stationary Laplace-driven moving average processes of non-Gaussian skewness and kurtosis. A numerical method was developed to evaluate Rice's formula with reasonable accuracy. The proposed method combines the analytical approach developed in [8], for Gaussian loads, with Monte Carlo simulations to account for non-Gaussianity. It was seen that the upcrossing frequencies were clearly underestimated when the loads were modeled as Gaussian processes. In addition, the proposed method was found to give better estimates at higher levels of response compared to ordinary Monte Carlo simulations. Currently, work is in progress on applying the developed methodology to estimate crossing statistics of offshore structures subjected to wave loads modeled as LMA processes.

References

1. Courant R, Hilbert D (1953) Methods of mathematical physics. Interscience, New York
2. Galtier T, Gupta S, Rychlik I (2010) Crossings of second-order response processes subjected to LMA loadings. J Probab Stat 2010:1–22
3. Gupta S, Rychlik I (2007) Rain-flow fatigue damage due to nonlinear combination of vector gaussian loads. Probab Eng Mech 22:231–249
4. Gupta S, van Gelder PHAJM (2007) Extreme value distributions for nonlinear transformations of vector gaussian processes. Probab Eng Mech 22:136–149
5. Kac M, Siegert AJF (1947a) On the theory of noise radio receivers with square law detectors. J Appl Phys 18:383–397
6. Kac M, Siegert AJF (1947b) An explicit representation of a stationary gaussian process. Ann Math Stat 18:438–442
7. Kotz S, Kozubowski TJ, Podgorski K (2001) Laplace distribution and Generalizations. Birkhäuser, Boston
8. Naess A (1985a) Statistical analysis of second-order response of marine structures. J Sh Res 29:270–284
9. Naess A (1985b) Prediction of extremes of stochastic processes in engineering applications with particular emphasis on analytical methods. Ph.D. thesis, Norwegian Institute of Technology
10. Naess A (1987) The response statistics of non-linear, second-order transformations to gaussian loads. J Sound Vib 115:103–129
11. Rice SO (1954) Mathematical analysis of random noise. Selected papers on noise and stochastic processes. Dover Publications, New York

Estimating the Rain-Flow Fatigue Damage in Wind Turbine Blades Using Polynomial Chaos

N. Ganesh and Sayan Gupta

Abstract Modern wind turbine blades are slender structures whose increased flexibilities have led to unforeseen aeroelastic instabilities leading to failures. In this study, the turbine blade is modeled as a two-dimensional airfoil and is subjected to random loading. The airfoil is assumed to oscillate only in the rotational degree of freedom. The loading is assumed to be stationary and Gaussian. The fatigue damage due to this loading is described through the rain-flow cycle counting method. An approach based on polynomial chaos expansion is used to obtain the response of the nonlinear oscillator.

Keywords Random fatigue • Rainflow cycles • Crossing statistics • Polynomial chaos • Wind turbine blades • Airfoils

1 Introduction

The increased pace of economic development throughout the world has led to an enormous increase in the demand for energy. Consequently, the focus in recent times has been on exploring alternative sources of clean energy. Among these, wind energy being a clean, renewable form of energy has gained popularity. The focus has been on increasing the efficiency in harnessing wind energy. This has led to the construction of wind turbines of enormous dimensions. However, the increased flexibility of the wind turbine blades, which are of enormous dimensions, has led to unforeseen failures. These failures have been attributed to aeroelastic instabilities. To develop robust designs to withstand these instabilities, a thorough understanding of the fluid-structure interaction mechanisms of these turbine blades is necessary.

N. Ganesh (✉) • S. Gupta
Department of Applied Mechanics, Indian Institute of Technology Madras, Chennai 600036, TN, India
e-mail: nganesh22@gmail.com; gupta.sayan@gmail.com

S. Chakraborty and G. Bhattacharya (eds.), *Proceedings of the International Symposium on Engineering under Uncertainty: Safety Assessment and Management (ISEUSAM - 2012)*,
DOI 10.1007/978-81-322-0757-3_46,

The modeling of the turbine blade leads to a set of highly nonlinear differential equations. It has been observed that beyond a critical value of the mean wind velocity, known as the flutter velocity, the system exhibits self-sustained oscillations. These oscillations significantly contribute to fatigue damage. From the design perspective, it is therefore desirable that the system be designed such that the operating conditions do not lead to self-sustained oscillations. The critical wind speed beyond which the system exhibits self-sustained oscillations is referred to as the bifurcation point. However, in real-life situations, the wind flow has random fluctuations about a mean value. This implies that the bifurcation point cannot be quantified in deterministic terms. Instead, the bifurcation point needs to be characterized in a probabilistic sense. To have a robust design, these random effects must be realistically represented in the modeling stage itself. However, doing so would increase the complexity in the mathematical model as these random fluctuations enter as model parameters in the governing equations of motion for the dynamical system.

Traditionally, Monte Carlo simulations (MCS) have been used in the analysis of dynamical systems with stochastic uncertainties wherein a large number of realizations of response are obtained for a given distribution of the random process. However, MCS is a computationally expensive approach, especially for problems involving significant nonlinearity and high dimensions.

2 Problem Statement

We consider a two, dimensional model for the wind turbine blade. The wind turbine blade is modeled as an airfoil with two degrees of freedom in the pitch and heave directions. The schematic diagram of the two-dimensional airfoil is shown in Fig. 2. The governing equations of motion for the airfoil can be expressed as [3]

$$\begin{aligned} m\ddot{h} + S\ddot{\alpha} + K_h h &= Q_h, \\ S\ddot{h} + I_\alpha \ddot{\alpha} + K_\alpha \alpha &= Q_\alpha. \end{aligned} \tag{1}$$

Here, h is the heave displacement, α is the pitch angle, m is the total mass per unit span, S is the mass static moment, I_α is the mass moment of inertia, K_h is the heaving stiffness coefficient, K_α is the pitching stiffness, $a_h b$ denotes the distance of the elastic axis from the mid chord, and $x_\alpha b$ is the distance of the center of mass from the elastic axis; see Fig. 1 for a schematic. The nonhomogeneous terms Q_α and Q_h represent the forcing terms and are usually represented as a set of coupled second-order differential equations which are functions of α and h [2]. Thus, these equations constitute a set of fluid-structure interaction problems. The over-dots represent differentiation with respect to time. Here, the coefficients K_α and K_h could be nonlinear functions of α and h. If pitching motion alone is considered, a simplified form for the above system, could be represented in the form of the differential equation

$$\ddot{x} + 2\eta\omega_n \dot{x} + {\omega_n}^2 x(1 + \mu x^2) = f(t, \theta). \tag{2}$$

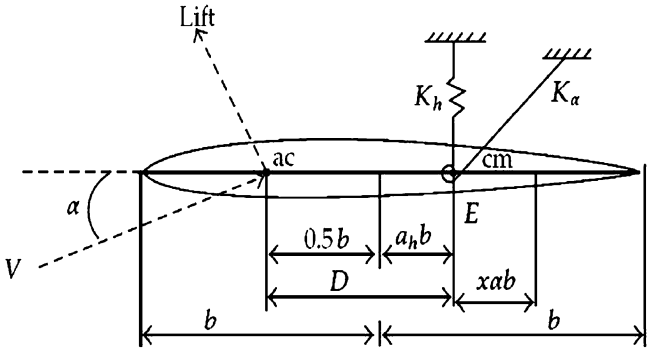

Fig. 1 Schematic diagram of the wind-turbine blade modeled as a 2-D airfoil

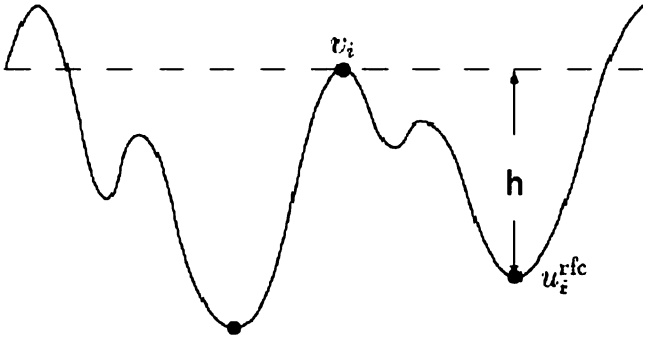

Fig. 2 Definition of rain-flow cycle

Here, η is the damping ratio, ω_n denotes the natural frequency of the system, μ represents the nonlinear stiffness coefficient, and x represents the pitching degree of freedom. Note that the nonlinearity in Eq. (2) is cubic and can be considered to be an approximation of the free play nonlinearity that typically exists in these systems. The coefficient μ determines the extent of nonlinearity. The excitation $f(t, \theta)$ is assumed to be a stationary Gaussian random process with the following autocorrelation function

$$R_{ff}(\tau) = \sigma_f^2 e^{-c_0 \tau^2}, \tag{3}$$

where, σ_f is the standard deviation of the process and c_0 denotes the inverse of the correlation length. The response of the system can be obtained by solving Eq. (2). As the excitations are random processes, the response are also random processes. However, as the equations of motion are nonlinear, even though the excitations are Gaussian, the response constitute non-Gaussian random processes. Estimating the fatigue damage due to these non-Gaussian response processes require characterization of the joint probability density of the response and its instantaneous time derivative. This is explained in the following section.

3 Rain Flow Cycle Counting Method

The rain-flow cycle counting method is a method for extracting and counting equivalent load cycles from a random time history. It is a technique which enables us to estimate the fatigue damage using Palmgren-Miner's rule [6, 7]. It leads to the best estimate of fatigue life [9]. Let $Y(t)$ be the load acting on the system and let it be a random process. The accumulated linear fatigue damage due to $Y(t)$ is denoted by D_T. Since $Y(t)$ is a random process, D_T will be a random variable. Therefore, expectation of D_T given by $\mathrm{E}[D_T]$ is to be evaluated. The process of evaluating suitable approximations for $\mathrm{E}[D_T]$ using rain-flow count is presented in the following section.

3.1 Fatigue Damage Estimation Using Rain Flow Counting

A schematic of the rain-flow cycle counting as discussed in [9, 4] is presented through Fig. 2. Here, each local maximum of the load process, say v_i, is paired with a particular local minimum, u_i, determined as follows:

- From the local maximum value (v_i), the lowest value is determined in forward and backward directions between the time point of the local maximum and the nearest points at which the load exceeds the value v_i.
- The larger of the two values determined above is the rain-flow minimum paired with v_i and is denoted by u_i^{rfc} in Fig. 2. In other words, the rain-flow minimum is the least drop before reaching the value of local maximum (v_i) again on either side. Thus, the ith rain-flow pair is (u_i^{rfc}, v_i),
- The cycle range, h, is the difference between the local maximum and the paired rain-flow minimum.

In case the local minimum, u_i^{rfc} lies outside the time interval chosen; the incomplete cycle thus formed is known as the residual and it has to be handled separately.

Using the Palmgren-Miner's rule [6, 7], the accumulated linear rain-flow damage is expressed as

$$D_T = \sum f(u_i^{rfc}, v_i) + D^{res}, \tag{4}$$

where, $f(u_i^{\mathrm{rfc}}, v_i)$ is the fatigue damage due to the rain-flow pair (u_i^{rfc}, v_i) and D^{res} is the damage due to the cycles constituting the residual. An alternative definition of rain-flow damage is as follows:

$$D_T = \int_{-\infty}^{\infty}\int_{-\infty}^{v} f_{12}(u,v)N(u,v)dudv + \int_{-\infty}^{\infty} f_2(u,u)N(u)du. \tag{5}$$

Here, $f_2(u,v) = \frac{\partial f(u,v)}{\partial v}$ and $f_{12}(u,v) = \frac{\partial^2 f(u,v)}{\partial u \partial v}$. In the above equation, for a random time history $X(t)$, the number of up-crossings of level u by $X(t)$, $t \in [0, T]$ is given by $N(u)$. $N(u, v)$ denotes the number of up-crossings of an interval $[u, v]$ by $X(t)$.

As mentioned earlier, the quantity of interest, here, is the expected fatigue damage $E[D_T]$, where $E[\cdot]$ is the expectation operator. This can be obtained by changing the order of integration in Eq. (5) as

$$E[D_T] = \int_{-\infty}^{\infty} \int_{-\infty}^{\infty} f_{12}(u,v) E[N(u,v)] du dv. \tag{6}$$

The expected damage increase in period T can be shown to be proportional to loading time duration T, and is expressed as

$$E[D_T] = T \int_{-\infty}^{\infty} \int_{-\infty}^{\infty} f_{12}(u,v) \mu(u,v) du dv, \tag{7}$$

where $\mu(u, v)$ is known as the intensity of interval up-crossings. As it is difficult to estimate $\mu(u, v)$, bounds for intensity crossings can be evaluated. It can be shown that [9]

$$\mu(u,v) \leq \min[\mu(u,u), \mu(v,v)] = \hat{\mu}(u,v), \tag{8}$$

where, $\mu(u, u) = \mu(u)$. Now, the bounds for expected damage can be given as follows:

$$E[D_T] \leq T \int_{-\infty}^{\infty} \int_{-\infty}^{v} f_{12}(u,v) \hat{\mu}(u,v) du dv. \tag{9}$$

The mean crossing rate $\mu(u)$ can be easily computed using the Rice's formula [8], which is given by

$$\mu(u) = \int_0^{\infty} \dot{x} p_{X\dot{X}}(u, \dot{x}) d\dot{x}, \tag{10}$$

where, $p_{X\dot{X}}(x, \dot{x})$ is the joint probability density function (pdf) of the process, $X(t)$, and its instantaneous time derivative, $\dot{X}(t)$. The focus of this study is on quantifying the joint pdf of the process, $X(t)$, and its instantaneous time derivative. Analytical closed form expressions for $p_{X\dot{X}}(x, \dot{x})$ are not easy to estimate, especially if the governing differential equations of motion exhibit significant nonlinearities. An alternative procedure for estimating $p_{X\dot{X}}(x, \dot{x})$ would be to obtain approximations by Monte Carlo simulations. This would necessitate generating an ensemble of realizations of the excitations $\{f(t)_i\}_{i=1}^N$, compute an ensemble of the response state $\{X(t)_i\}_{i=1}^N$ and $\{\dot{X}(t)_i\}_{i=1}^N$, and subsequently estimate $p_{X\dot{X}}(x, \dot{x})$ by statistical processing. To obtain reasonable accuracies at the tail regions of $p_{X\dot{X}}(x, \dot{x})$, N has

to be large. This would imply N numerical solutions of the governing equations of motion. For more complicated forms of differential equations such as Eq. (2), this would be computationally expensive. The focus of this study is on the development of a technique by which the computational effort could be minimized. To achieve this, we employ the polynomial chaos representation of the response. This is discussed further in the following sections.

4 Karhunen-Loeve Expansion(K-L Expansion)

A continuous random process can be represented as a series expansion involving sets of discrete random variables and deterministic basis functions. While there can be many such representations, for example, the spectral representation where the trigonometric functions are the basis functions [10], the Karhunen-Loeve expansion is the most optimal representation. The K-L expansion is based on the eigen-decomposition of the auto-covariance function. The deterministic basis functions, which are orthonormal, are the eigenfunctions of the auto-covariance function and their magnitudes are the eigenvalues. The Karhunen-Loeve expansion converges in the mean-square sense for any distribution of the stochastic process [8]. A K-L representation of a zero-mean stochastic process $f(t, \theta)$ can be represented in the form

$$f(t,\theta) = \sum_{i=0}^{\infty} \xi_i(\theta)\sqrt{\lambda_i}\phi_i(t), \tag{11}$$

where the coefficients λ_i and the functions $\phi_i(t)$, respectively, are the eigenvalues and the eigenfunctions of the covariance function and are evaluated by solving the following Fredholm integral equation of the second kind:

$$\int_0^T R_{ff}(t,s)\phi_i(s)ds = \lambda_i\phi_i(t). \tag{12}$$

The parameter "t" indicates time and θ represents the random sample. In Eq. (12), $R_{ff}(t, s)$ denotes the autocorrelation function of the process $f(t, \theta)$. In Eq. (11), $\{\xi_i(\theta)\}$ is a vector consisting of uncorrelated random variables with zero-mean and unit variance. The eigenfunctions are orthonormal and satisfy the identity

$$\int_0^T \phi_i(t)\phi_j(t)dt = \delta_{ij} \tag{13}$$

where, δ_{ij} is the Kronecker-delta function defined as

$$\delta_{ij} = \begin{cases} 1 & if\ i = j \\ 0 & otherwise \end{cases}$$

Since Eq. (11) is an infinite series, it becomes imperative to decide on the number of terms to be retained in the expansion of $f(t, \theta)$. It is seen that not all terms have a significant contribution in the expansion. The number of significant terms depends on various factors such as the form of autocorrelation function, length of the interval T, and correlation length of the stochastic process [5]. Some of these issues have been considered in this chapter to truncate the series expansion to appropriate number of terms. The K-L expansion is usually employed for a Gaussian process. For non-Gaussian process, a generalization of the K-L expansion is the polynomial chaos expansion also known as PCE. This is discussed in the following section.

5 Polynomial Chaos Expansion

Polynomial chaos expansion is a spectral representation of the random process in terms of orthonormal basis functions and deterministic coefficients. Wiener [11] introduced the homogeneous chaos theory based on Cameron and Martin theorem [1]. The homogeneous chaos theory, in its original form, employs Hermite polynomials with Gaussian random variables, from the Askey scheme, as orthonormal bases. The exponential convergence of the polynomial chaos expansion has been extended to several other types of commonly used probability distributions in the generalized polynomial chaos by Xiu and Karniadakis [12]. A random process $X(t, \theta)$ can be represented according to Cameron-Martin theorem as follows [1]:

$$X(t,\theta) = \hat{x}_0\Gamma_0 + \sum_{i_1=1}^{\infty} \hat{x}_{i_1}\Gamma_1(\xi_{i_1}(\theta)) + \sum_{i_1=1}^{\infty}\sum_{i_2=1}^{i_1} \hat{x}_{i_1 i_2}\Gamma_2(\xi_{i_1}(\theta), \xi_{i_2}(\theta)) + \ldots, \quad (14)$$

where, $\Gamma_n(\xi_{i_1}, \xi_{i_2}, \ldots, \xi_{i_n})$ denotes the Hermite polynomials of order n in terms of n-dimensional independent standard Gaussian random variables $\xi = (\xi_{i_1}, \xi_{i_2}, \ldots . \xi_{i_n})$ with zero mean and unit variance. The above equation is a discrete form representation of the Wiener polynomial chaos expansion. A generalization of Eq. (14) can be obtained by rewriting it in the form

$$X(t,\theta) = \sum_{i=0}^{\infty} x_i(t)\Psi_i(\xi(\theta)), \quad (15)$$

where, Ψ_i denotes the basis functions and $x_i(t)$ are the deterministic coefficients. The polynomials Ψ_i's are mutually orthogonal and the satisfy the following identity:

$$\langle \Psi_i \Psi_j \rangle = \langle {\Psi_i}^2 \rangle \delta_{ij}, \quad (16)$$

where, δ_{ij} is the Kronecker delta function and $\langle \cdot \rangle$ is the expectation operator of the form

$$\langle x \rangle = \int_{\Omega} x w(x) dx. \tag{17}$$

Here, $w(x)$ is an appropriate weighting function. The one-dimensional Hermite polynomials can be shown to be related in the recursive form:

$$\Gamma_{n+1} = \xi \Gamma_{n-1} - (n-1)\Gamma_{n-2}, \tag{18}$$

where the first few polynomials are of the forms

$$\Gamma_0 = 1, \ \ \Gamma_1 = \xi, \ \ \Gamma_2 = \xi^2 - 1, \ \ \Gamma_3 = \xi^3 - 3\xi, and \ \ \Gamma_4 = \xi^4 - 6\xi^2 + 3. \tag{19}$$

The two dimensional Hermite polynomials can be expressed as

$$\begin{aligned}
&\Psi_0(\xi) = \Gamma_0(\xi_1)\Gamma_0(\xi_2) = 1, \\
&\Psi_1(\xi) = \Gamma_1(\xi_1)\Gamma_0(\xi_2) = \xi_1, \\
&\Psi_2(\xi) = \Gamma_0(\xi_1)\Gamma_1(\xi_2) = \xi_2, \\
&\Psi_3(\xi) = \Gamma_2(\xi_1)\Gamma_0(\xi_2) = {\xi_1}^2 - 1, and \\
&\Psi_4(\xi) = \Gamma_1(\xi_1)\Gamma_1(\xi_2) = \xi_1\xi_2.
\end{aligned} \tag{20}$$

Truncating Eq. (15) to p terms, we approximate $X(t, \theta)$ as

$$X(t, \theta) = \sum_{i=0}^{p} x_i(t)\Psi_i(\xi(\theta)). \tag{21}$$

The number of terms up to which the series is truncated, p, is known as the order of expansion. For n number of random variables and polynomial order n_p, p is given by the following:

$$p = \frac{(n+n_p)!}{n!n_p!} - 1. \tag{22}$$

A number of methods can be used for finding the coefficients in the polynomial chaos expansion, two of which are presented.

5.1 Galerkin PCE Solution of the Equation of Motion

The solution of Eq. (2), by the Galerkin PCE approach, is presented here. In this approach, a Galerkin projection of the orthogonal polynomials is performed to modify the governing equation to a system of deterministic coupled nonlinear

equations in terms of the polynomial chaos coefficients. The governing equation is rewritten below for convenience:

$$\ddot{x} + 2\eta\omega_n\dot{x} + {\omega_n}^2 x(1 + \mu x^2) = f(t, \theta),$$
$$x(0) = \dot{x}(0) = 0. \tag{23}$$

As mentioned in the previous section, $f(t, \theta)$ is approximated as a K-L expansion, truncated up to M terms, as shown below:

$$f(t, \theta) = \sum_{i=0}^{M} \xi_i(\theta)\sqrt{\lambda_i}\phi_i(t). \tag{24}$$

The solution to the governing equation is assumed to be in the form

$$X(t, \theta) = \sum_{i=0}^{N} x_i(t)\Psi_i(\xi), \tag{25}$$

where, $x_i(t)$ are the deterministic functions to be evaluated and Ψ_i represent the polynomial chaoses. Substituting Eqs. (24) and (25) in Eq. (23), the governing equation of motion can now be written as

$$\sum_{i=0}^{N} (\ddot{x}_i(t) + 2\eta\dot{x}_i(t) + x_i(t))\Psi_i(\xi) + \mu \sum_{i=0}^{N}\sum_{j=0}^{N}\sum_{k=0}^{N} x_i(t)x_j(t)x_k(t)\Psi_i(\xi)\Psi_j(\xi)\Psi_k(\xi) = \sum_{i=0}^{M} f_i(t)\xi_i, \tag{26}$$

where,

$$f_i(t) = \sqrt{\lambda_i}\phi_i(t). \tag{27}$$

Multiplying Eq. (26) by $\Psi_m(\xi)$ and taking expectation, a set of nonlinear deterministic differential equations is obtained, which is of the form

$$\ddot{x}_m(t) + 2\eta\dot{x}_m(t) + x_m(t) + \mu \sum_{i=0}^{N}\sum_{j=0}^{N}\sum_{k=0}^{N} \frac{c_{ijkm}}{\langle \Psi_m^2 \rangle} x_i(t)x_j(t)x_k(t) = f_m(t). \tag{28}$$

Here,

$$c_{ijkm} = \langle \Psi_i\Psi_j\Psi_k\Psi_m \rangle = \int_{-\infty}^{\infty} \Psi_i\Psi_j\Psi_k\Psi_m w(\xi)d\xi. \tag{29}$$

The weight function,$w(\xi)$, in Eq. (29), is the Gaussian probability density function for Hermite polynomials and is of the form

$$w(\xi) = \frac{1}{\sqrt{2\pi}} e^{-\left(\frac{1}{2}\xi^T \xi\right)}. \tag{30}$$

It is to be noted that the orthogonality property of the Hermite polynomials given by Eq. (16) has been made use of while arriving at Eq. (28). Equation 28 is solved for various values of m and the corresponding coefficients are obtained. Once the coefficients are evaluated, the solution is reconstructed by substituting them in Eq. (26).

Although the Galerkin method minimizes the error due to truncation accurately, it has some serious drawbacks. The process of evaluating the inner products and arriving at the set of nonlinear deterministic equations is computationally expensive and can become tedious. The complexity increases with type and extent of nonlinearity, the distribution of random variables used, and the number of terms included in the expansion. In order to circumvent these difficulties, several alternative methods are available in literature. One among those, known as the nonintrusive projection method, is used in this work. This is discussed in the following section.

5.2 *Nonintrusive Projection Method*

In the nonintrusive polynomial chaos method, the polynomial chaos coefficients are evaluated by solving the governing equation at certain collocation points and then substituting them in a projection formula. In contrast to the Galerkin method, the polynomial chaos expansions are not substituted in the governing equation, and hence, it is known as nonintrusive. It is also referred to as the pseudo Monte Carlo approach as a number of runs of the deterministic equation are required, but not as large as in Monte-Carlo simulations [2]. A Galerkin projection of Eq. (15) by taking $\langle\, .\, , \Psi_j \rangle$ gives the following formula

$$x_j(t) = \frac{\langle X(t, \xi(\theta)), \Psi_j \rangle}{\langle \Psi_j^2 \rangle}, \tag{31}$$

where, x_j is the PCE coefficient and the inner product in the numerator is given by the following multidimensional integral:

$$\langle x(t, \xi(\theta)), \Psi_j \rangle = \int_{-\infty}^{\infty} \cdots \int_{-\infty}^{\infty} X(t, \xi(\theta)) \Psi_j w(\xi) d\xi. \tag{32}$$

The dimension of the integral is equal to the dimension of the vector ξ. The above multidimensional integral can be solved by suitable quadrature rules. Since the weight is a Gaussian probability density function and the domain of integration

is $(-\infty, \infty)$, Gauss-Hermite quadrature is used here. The multidimensional integral in Eq. (32) can now be approximated using the following expression:

$$\langle x(t,\xi(\theta)),\Psi_j\rangle = \sum_{k_1=1}^{N_0}\ldots\sum_{k_n=1}^{N_0} X(t,\xi_{k_1},\ldots,\xi_{k_n})(W_{k_1}\ldots W_{k_n}), \tag{33}$$

where, N_0 is the number of quadrature points and $W_{k_1}\ \ldots\ W_{k_n}$ are the weighting functions.

6 Numerical Results and Discussions

To decide the number of terms to be included in the K-L expansion, the magnitude of the eigenvalues is considered. The magnitude of the first few eigenvalues of the covariance function is given in Table 1. It is seen that the magnitude of eigenvalues quickly diminishes to zero, and only the first few eigenvalues are significant. For the sake of simplicity, the number of terms in the K-L series has been fixed at two. The resulting expansion is given by

$$f(t,\theta) = f_1(t)\xi_1(\theta) + f_2(t)\xi_2(\theta). \tag{34}$$

Now the numerator in Eq. (30) is evaluated as follows:

$$\langle X(t,\xi(\theta))\Psi_j\rangle = \sum_{k_1=1}^{N_0}\sum_{k_2=1}^{N_0} X(t,\xi_{1_{k_1}},\xi_{2_{k_1}})\Psi(\xi_{1_{k_1}},\xi_{2_{k_1}})W_{1_{k_1}}W_{2_{k_2}}. \tag{35}$$

The coefficients thus evaluated are substituted in Eq. (26) to obtain the response process. The number of quadrature points, N_0, is chosen to be 24 for each random variable making a total of 576 collocation points at which the deterministic equation is to be solved. This is much less than the number of deterministic runs performed in a Monte Carlo simulation which is generally higher than 1,000.

Table 1 Magnitude of eigenvalues

Eigenvalue	Magnitude
λ_1	7.2105
λ_2	4.5738
λ_3	2.1815
λ_4	0.8031
λ_5	0.2356
λ_6	0.0569
λ_7	0.0116
λ_8	0.0020
λ_9	0.0003
λ_{10}	0.0000

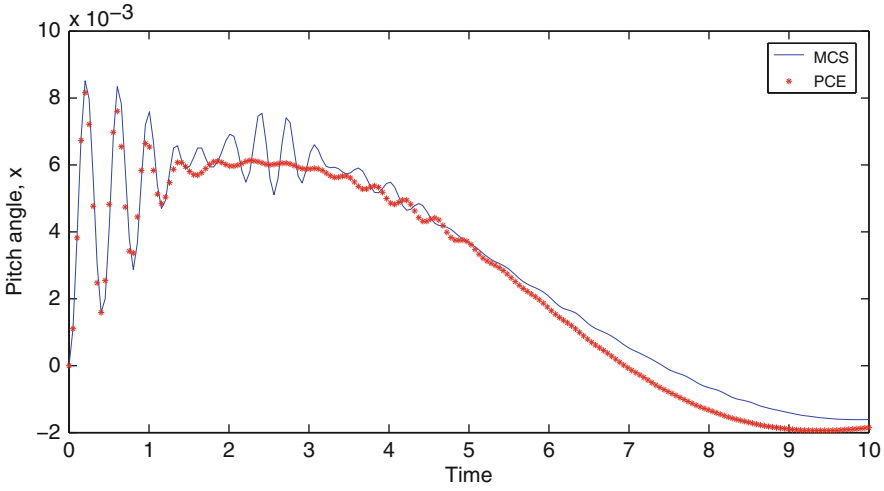

Fig. 3 Mean response; $\mu = 2$

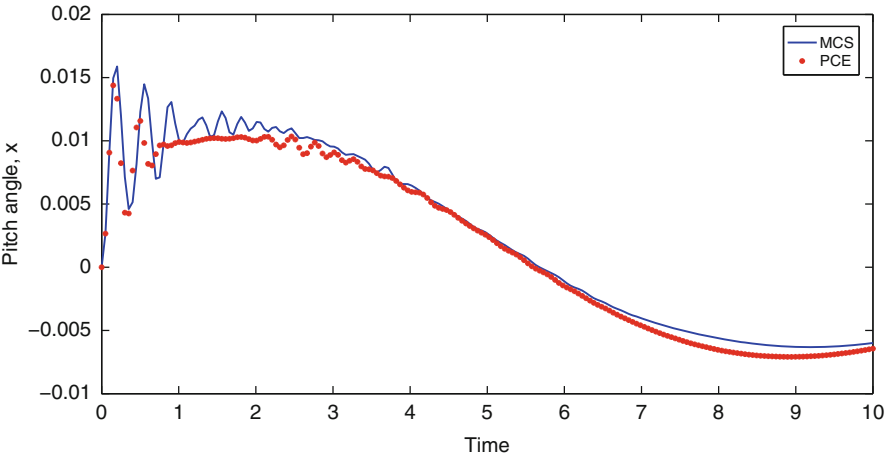

Fig. 4 Mean response; $\mu = 10$

The analysis explained in the preceding sections is performed with the autocorrelation function given by Eq. (2) and for a duration of 10 s. The excitation is represented in the form given by Eq. (24), and the response is obtained as a 12th-order polynomial chaos expansion. A damping factor of $\eta = 0.1$ has been chosen, and the inverse of correlation length, c_0, is 0.1. The natural frequency of the system, ω_n, is 200 rad/s. The deterministic differential equations are solved using an adaptive 4th-order Runge-Kutta algorithm. The polynomial chaos expansion response has been compared with the Monte Carlo simulation response. Thousand realizations of the response process are generated. Figure 3 shows the mean of the response process calculated at each time instant from 0 to 10 with $\mu = 2$, whereas Fig. 4 shows the mean response

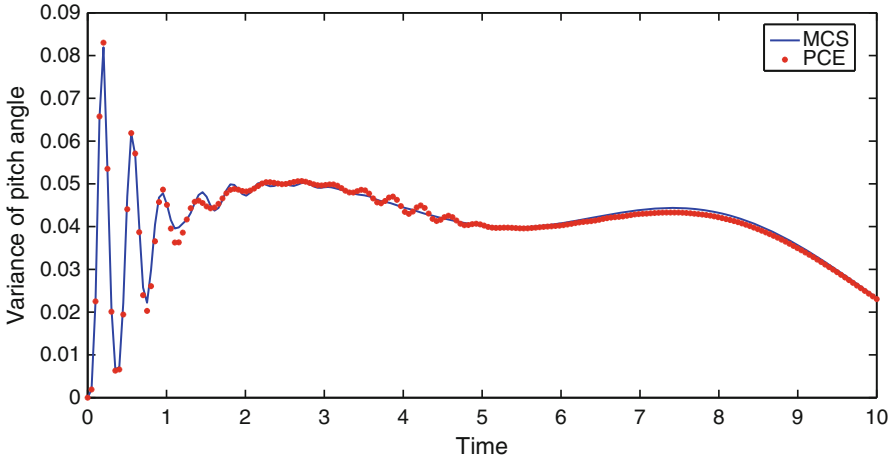

Fig. 5 Variance of response; $\mu = 2$

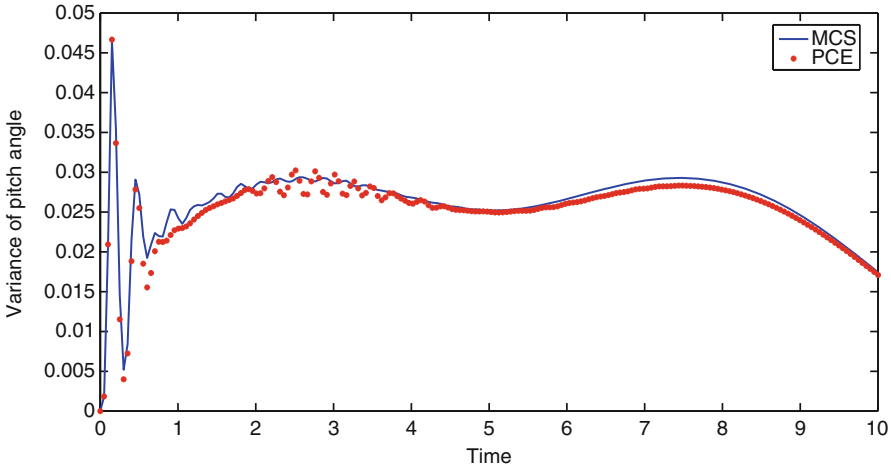

Fig. 6 Variance of response; $\mu = 10$

with $\mu = 10$. The variance of the response for the two levels of nonlinearities is shown in Figs. 5 and 6. The marginal probability density functions of response at 110th time step corresponding to the two cases are shown in Figs. 7 and 8. Figures 9–10 show the joint pdf $p_{X\dot{X}}(x, \dot{x})$ at time, $t = 5.53$ s for different values of μ, and these are compared with the corresponding joint pdfs obtained from MCS in Figs. 11–12. It is observed that a fairly good agreement between the

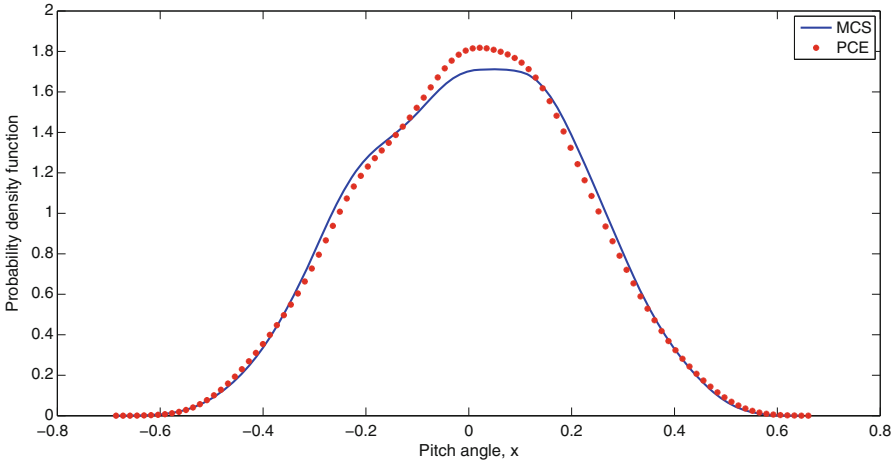

Fig. 7 Marginal pdf of response $X(t)$; $\mu = 2$

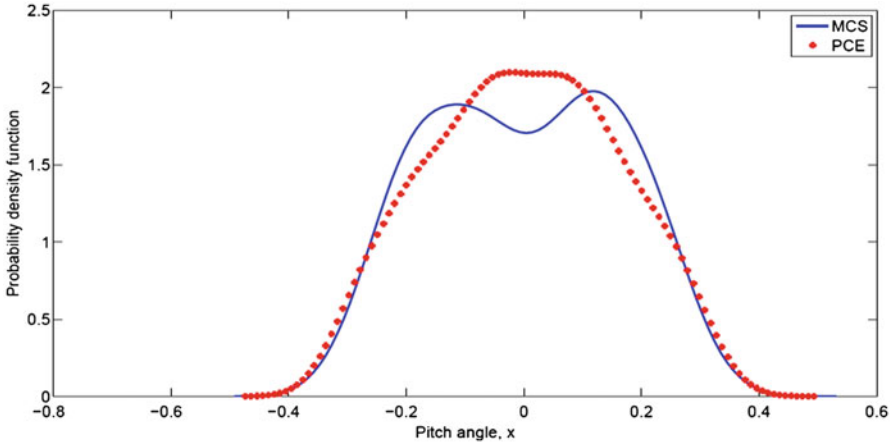

Fig. 8 Marginal pdf of response $X(t)$; $\mu = 10$

results obtained from MCS and those from PCE are obtained. This lends promise for the developed methodology for estimating the expected fatigue damage in nonlinear vibrating problems. The efficiency of the developed method in terms of computational costs would obviously increase as the complexity and the nonlinearity of the method increases. This study is currently in progress.

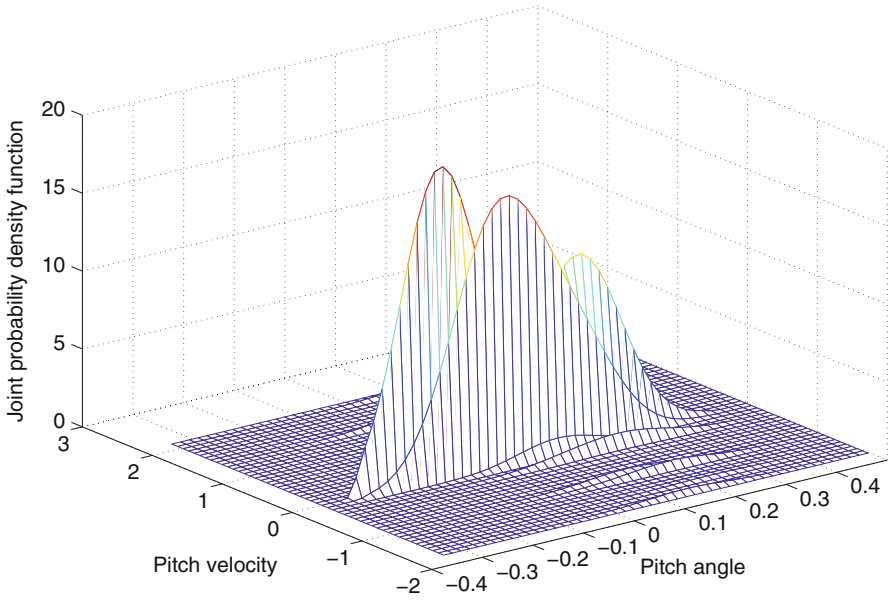

Fig. 9 Joint pdf $p_{X\dot{X}}(x, \dot{x})$; $\mu = 2$

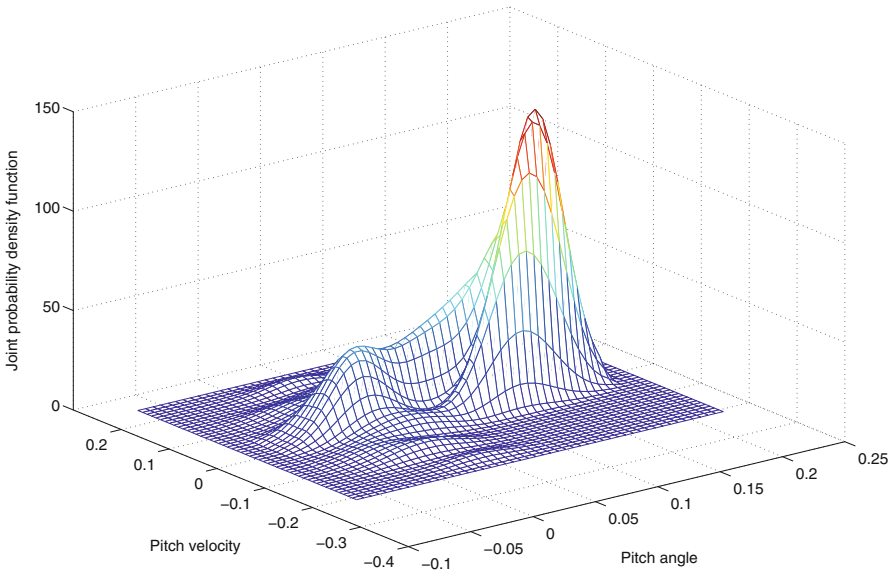

Fig. 10 Joint pdf of $p_{X\dot{X}}(x, \dot{x})$; $\mu = 10$

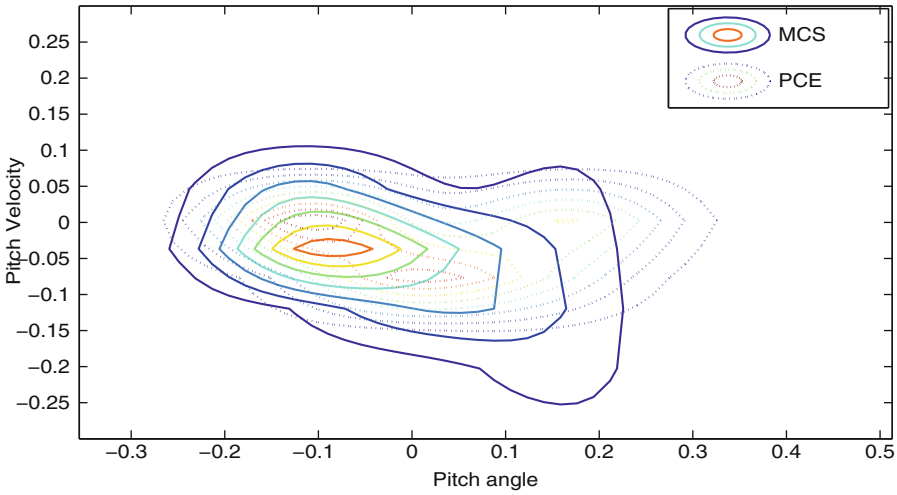

Fig. 11 Contour plots for joint pdf $p_{X\dot{X}}(x, \dot{x})$; $\mu = 2$

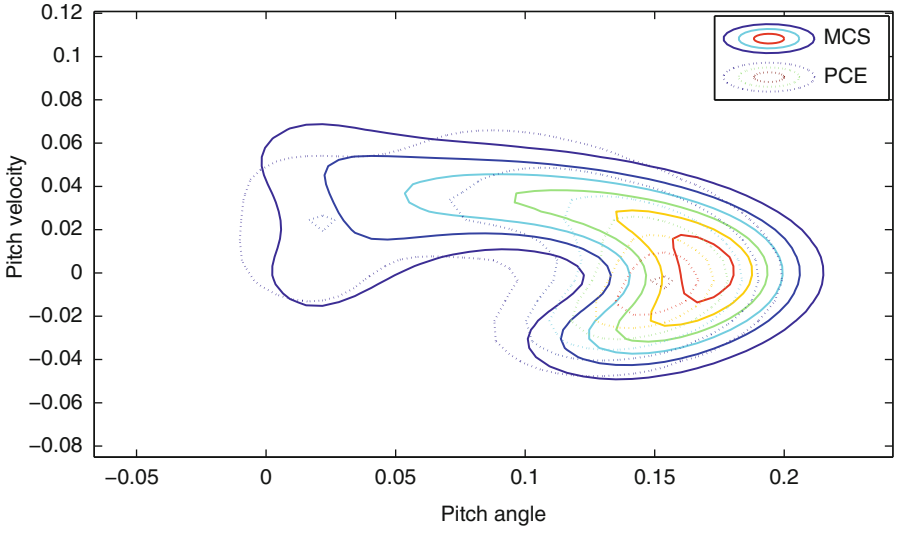

Fig. 12 Contour plots for joint pdf $p_{X\dot{X}}(x, \dot{x})$; $\mu = 10$

7 Concluding Remarks

The response of a nonlinear vibrating oscillator has been analyzed using the polynomial chaos expansion approach. The application of PCE for approximating the response of nonlinear vibrating systems has been investigated. A nonintrusive

method has been used to obtain the PCE coefficients. Numerical simulations on simple nonlinear oscillator show reasonable agreement in the mean, variance, and marginal probability distribution functions of the response obtained from the PCE approximations and full-scale MCS. The approximated probability density functions can be used to estimate mean rain-flow fatigue damage. More studies along these lines are currently in progress.

References

1. Cameron RH, Martin WT (1947) The orthogonal development of nonlinear functionals in series of Fourier–Hermite functionals. Ann Math 48:385–392
2. Desai A, Sarkar S (2010) Analysis of a nonlinear aeroelastic system with parametric uncertainties using polynomial chaos expansion. Math Probl Eng 2010:1–22. doi:10.1155/2010/379472
3. Fung YC 1955 An introduction to the theory of aeroelasticity. Wiley, New York
4. Gupta S, Rychlik I (2007) Rain-flow fatigue damage due to nonlinear combination of vector Gaussian loads. Probab Eng Mech 22:231–249
5. Li R, Ghanem R (1998) Adaptive polynomial chaos expansions applied to statistics of extremes in nonlinear random vibration. Probab Eng Mech 13:125
6. Miner MA (1945) Cumulative damage in fatigue. J Appl Mech 12:A159–A164
7. Palmgren A (1924) Die lebensdauer von kugellagern. VDI Z 68:339–341
8. Papoulis A, Pillai SU (2002) Probability, random variables and stochastic processes. Tata-McGraw-Hill, Boston
9. Rychlik I (1993) On the "narrow-band" approximation for expected fatigue damage. Probab Eng Mech 8:1–4
10. Shinozuka M, Jan CM (1972) Digital simulation of random processes and its applications. J Sound Vib 25(1):111–128
11. Wiener N (1938) The homogeneous chaos. Am J Math 60(4):897–936
12. Xiu D, Karniadakis GE (2002) The Wiener-Askey polynomial chaos for stochastic differential equations. SIAM J Sci Comput 24(2):619–644

Reconstruction of Porous Media Using Karhunen-Loève Expansion

J. Santhosh Jude, Sunetra Sarkar, and A. Sameen

Abstract A procedure to reconstruct two-phase porous media, given the porosity and the two-point correlation function of such media, is described. The random media are modelled as a discrete valued random field $Z(\mathbf{x})$, where $\mathbf{x}$ is the position vector. $Z(\mathbf{x})$ takes value 1 in regions of pores and 0 in regions of solid phase. The field $Z(\mathbf{x})$ is obtained by applying a non-linear filter—Nataf's transformation—to a correlated Gaussian random field $Y(\mathbf{x})$. The two-point correlation function R_{YY} of the Gaussian field Y is related to the two-point correlation function R_{ZZ} of the field Z and can be calculated by expanding the bivariate Gaussian probability density in terms of Hermite polynomials. This expansion results in a series representation for R_{ZZ} in terms of R_{YY}. Depending on the accuracy intended, the series could be truncated, and the appropriate root of the polynomial equation thus obtained gives R_{YY}. The correlation function of the Gaussian field is decomposed into eigenfunctions and eigenvalues required by the Karhunen-Lóeve expansion. The eigenfunctions and eigenvalues are used to generate as many samples of the Gaussian field as required, and the discrete field corresponding to each such sample can be obtained by applying the non-linear filter mentioned above. The method was tested by generating a large number of samples of two-dimensional Debye random media using different porosities and different correlation lengths, and the statistics of the ensemble was found to agree favourably with the input data. The method also has the advantage that it gives a theoretical framework for the porous media in terms of the random fields. These random fields could be used to model fluid flow through such porous media.

Keywords Porous media • Discrete valued random process • Porosity • Two-point correlation function • Nataf's transformation • Karhunen-Lóeve expansion

J.S. Jude (✉) • S. Sarkar • A. Sameen
Department of Aerospace Engineering, Indian Institute of Technology Madras, Chennai, Tamil Nadu, India
e-mail: santhoshjudeilango@gmail.com; sunetra.sarkar@gmail.com; sameen@ae.iitm.ac.in

S. Chakraborty and G. Bhattacharya (eds.), *Proceedings of the International Symposium on Engineering under Uncertainty: Safety Assessment and Management (ISEUSAM - 2012)*,
DOI 10.1007/978-81-322-0757-3_47,

1 Introduction

An understanding of the behaviour of porous media is essential in various fields of engineering. The fluid dynamics associated with porous media is of special interest in various geotechnical applications. Obtaining such knowledge about porous media through experimental investigation is difficult considering the number of samples on which the experiments have to be performed. Computational studies on porous media are mostly based on averaging the Navier-Stokes equations over a certain small volume of the porous media and solving these equations with appropriate interface conditions, most of which are empirical [2, 3, 11]. There is another direct approach in which, given the statistical properties of the porous medium such as its porosity and its various correlation functions, the porous media are reconstructed and subsequent analysis is performed on such reconstructed models.

There are a number of approaches to reconstruct random media. One of the earliest methods is based on successively passing a normalised uncorrelated random Gaussian field through a linear and then a non-linear filter to yield the discrete values representing the phases of the structure. This was started by Joshi [8] and extended by Quiblier [10] from 2-D to 3-D reconstructions. Adler et al. [1] refined the technique to accommodate periodic boundary conditions. This method provided a good computational framework for various analyses. Another different and a recent technique is the 'simulated annealing' approach developed by Yeong and Torquato [12] in which a random initial configuration of black and white pixels is chosen and the pixels are swapped systematically until a structure whose statistics match the input statistics emerges. This approach has the added advantage of incorporating as many correlation functions like the lineal path function [9] into the simulation. But both these approaches are purely computational and hence do not provide a theoretical framework for the study of porous media.

This work is a small step in this direction. The approach is similar to that developed by Joshi except that Karhunen-Lóeve expansion replaces the linear filter in former model. The advantage is that a theoretical framework for the porous media as a random process also results from this approach. Karhunen-Lóeve expansion has already been used in the study of flow through porous media in order to represent the macroscopic properties such as permeability as random processes [5]. This work presents the geometry of the porous media itself as a random process on which further analysis can be performed.

The outline of the rest of this chapter is as follows. Section 2 describes the methodology used, especially about Karhunen-Lóeve expansion, Nataf's transformation and the mathematical details. Section 3 describes the application of the procedure to simulate one-dimensional random media, and the results obtained are used as a validation of the procedure. Section 4 describes the application of the procedure to two-dimensional random media of a certain type, called the 'Debye random media'. A few samples of the porous media obtained are shown. Also the application of the method to a hypothetical correlation function is also presented. Section 5 presents the concluding remarks and possible directions for future work.

2 Formulation of the Reconstruction Procedure

The porous media considered here are all two-phase media, assumed to be homogenous and isotropic, and are modelled as a discrete valued random process $Z(\vec{x})$ defined below:

$$Z(\vec{x}) = \begin{cases} 1, & \text{if } \vec{x} \text{ is in pore space} \\ 0, & \text{if } \vec{x} \text{ is in solid space} \end{cases} \tag{1}$$

From the above definition, we can see that $1's$ have a probability equal to the porosity, which is given the symbol 'ε', and $0's$ have a probability '$1-\varepsilon$'. Hence, it is clear that both the mean '$E(Z)$' and the mean square '$E(Z^2)$' are both equal to the porosity. It follows that the variance '$E((Z-\mu_X)^2)$' is '$\varepsilon - \varepsilon^2$'. All these first-order moments are constant due to the assumption that the porous media are homogenous and isotropic. It is useful to normalise the random process Z to have zero mean and unit variance. This can be done by subtracting the mean 'ε' from Z and dividing the difference by the standard deviation '$\sqrt{\varepsilon(1-\varepsilon)}$'. Hence, we define the normalised random process $\mathbf{Z}(\vec{x})$ as

$$\mathbf{Z}(\vec{x}) = \begin{cases} \dfrac{\varepsilon - 1}{\sqrt{\varepsilon(1-\varepsilon)}}, & \text{if } \vec{x} \text{ is in pore space} \\ \dfrac{\varepsilon}{\sqrt{\varepsilon(1-\varepsilon)}}, & \text{if } \vec{x} \text{ is in solid space} \end{cases} \tag{2}$$

The two-point correlation function of the normalised random process becomes the covariance function of the original random process but normalised by dividing it with the variance. It is denoted by $R_{ZZ}(\vec{x}_1, \vec{x}_2)$:

$$R_{ZZ}(\vec{x}_1, \vec{x}_2) = \frac{E((\varepsilon - Z(\vec{x}_1)) \cdot (\varepsilon - Z(\vec{x}_2)))}{\varepsilon(1-\varepsilon)}. \tag{3}$$

Further due to the assumption of homogeneity and isotropy, the function R_{ZZ} is only a function of the distance between the two points and not the choice of origin or the direction. Thus,

$$R_{ZZ}(\vec{x}_1, \vec{x}_2) = R_{ZZ}(r) \tag{4}$$

where $r = ||\vec{x}_1 - \vec{x}_2||$ is the distance between the two points $\vec{x}_1, \vec{x}_2$.

The input statistics ε and R_{ZZ} can be obtained by an analysis of a thin slice of the porous media, and the procedure is described in considerable detail in Adler et al. [1] and Quiblier [10]. Having defined these basic ideas, the problem can be stated as follows. If the porosity ε and the correlation function R_{ZZ} are given, how can the random process $Z(\vec{x})$ be reconstructed?

The random process $Z(\vec{x})$ is constructed through an intermediate Gaussian random field $Y(\vec{x})$. To construct $Y(\vec{x})$, Karhunen-Lóeve expansion is used.

The K-L expansion requires the covariance function of a random process in order to represent it. Hence, the covariance function of Y, denoted by $R_{YY}(r)$, is calculated from the mean and the correlation function of Z. Then the Gaussian process Y is transformed to Z by Nataf's transformation. Each of these steps is described in detail below.

2.1 Karhunen-Lóeve Expansion

The Karhunen-Lóeve expansion [6] is a representation of a certain random process using the eigenvalues and eigenfunctions (normalised to have unit L_2 norm) of the covariance kernel. If $X(\vec{x})$ is a random process with mean $\mu_X(\vec{x})$ and covariance function $R_{XX}(\vec{x},\vec{y})$ then for $\vec{x} \in D$, then

$$X(\vec{x}) = \mu_X(\vec{x}) + \sum_{i=1}^{\infty} \sqrt{\lambda_i} f_i(\vec{x}) \xi_i \tag{5}$$

in which the λ_i and the $f_i(\vec{x})$ are the eigenvalues and the eigenfunctions given by the following integral equation:

$$\int_D R_{XX}(\vec{x},\vec{y}) f_i(\vec{y}) dV = \lambda_i f_i(\vec{x}), \tag{6}$$

where dV is the appropriate volume element and D is the domain of interest in the multidimensional space under consideration. The ξ_i are a set or orthonormal random variables given by

$$\xi_i = \frac{1}{\sqrt{\lambda_i}} \int_D f_i(\vec{x}) X(\vec{x}) dV, \tag{7}$$

where $X(\vec{x})$ is a realisation of the random process. The ξ_i can be shown to be normal random variables if the random process is also Gaussian. This is the primary advantage of working with the intermediate Gaussian random field $Y(\vec{x})$. Also since the covariance function is always positive definite, the eigenvalues are all real and positive and the eigenfunctions are all orthogonal (and after normalisation, orthonormal) to each other. The K-L expansion of a random process can be shown to have the least error in the mean square sense [6].

The integral equation may not yield to analytical methods in all cases. Hence, a numerical method is used to solve it. The domain is discretised by dividing it into N intervals of uniform size ΔV, and the integral is approximated by a summation of terms. Thus, Eq. (6) becomes

$$\sum_{j=0}^{N} R_{XX}(\vec{x},\vec{y_j}) f_i(\vec{y_j}) \Delta V = \lambda_i f_i(\vec{x}), \tag{8}$$

where $\vec{y}_j$ are the midpoints of the volume intervals. From Eq. (8), we can see that the problem becomes a matrix eigenvalue problem, and the λ_i and the $f_i(\vec{x})$ are the eigenvalues and the eigenvectors of the matrix $R_{ij} = R_{XX}(\vec{x}_i, \vec{y}_j) \cdot \Delta V$. The eigenvectors must be normalised in such a way so the L_2 norm is unity.

Since we are using the technique for the Gaussian process Y, the random variables ξ_i are all standard Gaussian. So once the above matrix eigenvalue problem is solved, it is easy to generate samples of the random process using the summation in Eq. (5).

2.2 Nataf's Transformation

This section explains the use of Nataf's transformation to convert the process Y into Z and also how the statistics of Z are used to compute the statistics of Y [1]. This transformation maps a certain Z value 'z' to a Y value 'y' such that both have the same value for their cumulative distribution functions (CDF). That is,

$$F_Z(z) = F_Y(y), \tag{9}$$

where $F_X(x)$ denotes the cumulative distribution function of the random variable X.

The CDF of the normalised Z looks like a step function with the height of the discontinuity at each point representing the probability of that Z. Let us denote by y^* the value of y whose Gaussian CDF is equal to the porosity ε. That is,

$$\frac{1}{\sqrt{2\pi}} \int_{-\infty}^{y^*} e^{-\frac{t^2}{2}} dt = \varepsilon. \tag{10}$$

This can be best understood from Fig. 1.

From the figure, it is clear that all values of $y < y^*$ are mapped to $\mathbf{Z} = \frac{\varepsilon - \mathbf{1}}{\sqrt{\varepsilon(\mathbf{1}-\varepsilon)}}$ (which is $Z = 1$ or 'pore space') and all $y > y^*$ are mapped to $\mathbf{Z} = \frac{\varepsilon}{\sqrt{\varepsilon(\mathbf{1}-\varepsilon)}}$ (which is $Z = 0$ or 'solid space'). Hence, the Nataf's transformation function for the current case can be summarised as

$$z = c(y) = \begin{cases} \dfrac{\varepsilon - 1}{\sqrt{\varepsilon(1-\varepsilon)}}, & \text{if } y < y^* \\ \dfrac{\varepsilon}{\sqrt{\varepsilon(1-\varepsilon)}}, & \text{if } y > y^* \end{cases}. \tag{11}$$

Now the above transformation can be used to calculate the correlation function of the intermediate Gaussian process Y given the correlation function of Z as follows. By definition,

$$R_{ZZ}(u) = \int_{-\infty}^{\infty} \int_{-\infty}^{\infty} Z_1 Z_2 P_{zz}(Z_1, Z_2) dZ_1 dZ_2, \tag{12}$$

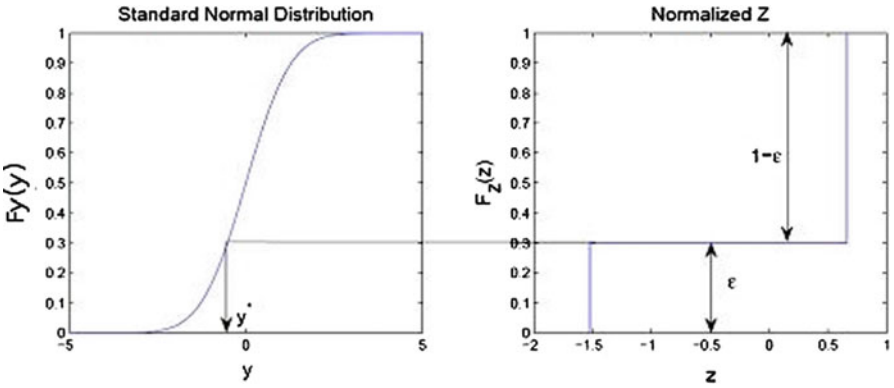

Fig. 1 Nataf's transformation

where $p_{zz}(z_1, z_2)$ represents the second order probability density function (pdf) of the process Z. Equation (12) can be transformed to the Y process as

$$R_{ZZ}(u) = \int_{-\infty}^{\infty}\int_{-\infty}^{\infty} c(y_1)c(y_2)p_{yy}(y_1, y_2)dy_1dy_2, \tag{13}$$

where p_{yy} denotes the bivariate Gaussian distribution. Substituting the complete form of the bivariate Gaussian distribution in Eq. (13) (note that Y is a zero mean unit variance process with correlation function $R_{YY}(r)$), we have

$$R_{ZZ}(r) = \int_{-\infty}^{\infty}\int_{-\infty}^{\infty} c(y_1)c(y_2)\frac{e^{-\left(\frac{y_1^2 - 2R_{YY}(r)y_1y_2 + y_2^2}{2(1-R_{YY}^2(r))}\right)}}{2\pi\sqrt{1-R_{YY}^2(r)}}dy_1dy_2. \tag{14}$$

For the sake of brevity, the argument r in $R_{ZZ}(r)$ and $R_{YY}(r)$ is dropped in the following expressions. Now we have an integral equation which relates R_{ZZ} to R_{YY}. To solve this equation for R_{YY}, we follow the approach proposed by Joshi [8]. The procedure is presented in the following subsections.

2.2.1 Expanding Bivariate Gaussian pdf Using Hermite Polynomials

Hermite polynomials are a family of polynomials defined as given below:

$$H_m(x) = (-1)^m e^{\frac{x^2}{2}}\frac{d}{dx}\left(e^{\frac{-x^2}{2}}\right). \tag{15}$$

The most important property of the Hermite polynomials is that they are orthogonal with respect to the Gaussian pdf. That is,

$$\frac{1}{\sqrt{2\pi}} \int_{-\infty}^{\infty} H_m(x) H_n(x) e^{\frac{-x^2}{2}} dx = n! \delta_{mn}. \tag{16}$$

The bivariate Gaussian distribution can be expanded in terms of Hermite polynomials as

$$p_{yy}(y_1, y_2) = \sum_{m=0}^{\infty} \sum_{n=0}^{\infty} c_{mn} H_n(y_1) H_m(y_2) \phi(y_1) \phi(y_2) \tag{17}$$

where $\phi(x) = \dfrac{e^{-\frac{x^2}{2}}}{\sqrt{2\pi}}$ is the normal Gaussian pdf. The c_{mn} in Eq. (17) are given by

$$c_{mn} = \frac{1}{m!n!} \int_{-\infty}^{\infty} \int_{-\infty}^{\infty} \frac{e^{-\left(\frac{y_1^2 - 2R_{YY} y_1 y_2 + y_2^2}{2(1 - R_{YY}^2)}\right)}}{2\pi\sqrt{1 - R_{YY}^2}} H_m(y_1) H_n(y_2) dy_1 dy_2. \tag{18}$$

This integral in Eq. (17) can be evaluated with the help of the following identity found in tables of integrals (e.g. Gradshteyn and Ryzhik [7]):

$$\int_{-\infty}^{-\infty} e^{-(x-y)^2} H_m(\alpha x) dx = \sqrt{\pi} \left(1 - \frac{\alpha^2}{2}\right)^{\frac{n}{2}} H_m\left(\frac{\alpha y}{\left(1 - \frac{\alpha^2}{2}\right)^{\frac{1}{2}}}\right). \tag{19}$$

If the exponent of the numerator in the integral given in Eq. (18) is modified in such a form to use the identity in Eq. (19), the double integral becomes a single integral, which can be evaluated using the orthogonality condition. After some algebra we get

$$c_{mn} = \frac{1}{m!} R_{YY}^m \delta_{mn}. \tag{20}$$

Thus, the bivariate Gaussian density can be expanded in terms of Hermite polynomials as follows:

$$\frac{e^{-\left(\frac{y_1^2 - 2R_{YY} y_1 y_2 + y_2^2}{2(1 - R_{YY}^2)}\right)}}{2\pi\sqrt{1 - R_{YY}^2}} = \sum_{m=0}^{\infty} \frac{R_{YY}^m}{m!} H_m(y_1) H_m(y_2) \phi(y_1) \phi(y_2). \tag{21}$$

2.2.2 Solving for R_{YY}

The expansion in Eq. (21) is substituted in the integral in Eq. (14). The summation can be taken outside the double integral. We can also see that in the integrand the

variables are separable, and thus, the integrals can be evaluated separately. The above integral can be written in a modified form as given below:

$$R_{ZZ} = \sum_{m=0}^{\infty} \frac{R_{YY}^m}{m!} \int_{-\infty}^{\infty} c(y_1) H_m(y_1) \phi(y_1) dy_1 \int_{-\infty}^{\infty} c(y_2) H_m(y_2) \phi(y_2) dy_2. \tag{22}$$

Observing that the two separate integrals are the same, and by writing

$$K_m = \frac{1}{\sqrt{m!}} \int_{-\infty}^{\infty} c(y) H_m(y) \phi(y) dy, \tag{23}$$

we have

$$R_{ZZ} = \sum_{m=0}^{\infty} K_m^2 R_{YY}^m. \tag{24}$$

This polynomial equation can be solved by truncating it to a certain number of terms to obtain R_{YY} for each R_{ZZ}. The number of terms used in the current work was limited to 32 since no significant improvement in accuracy was observed thereafter.

We conclude this section summarising the whole procedure. Given ε and R_{ZZ}, R_{YY} can be computed from Eq. (21). K-L expansion uses R_{YY} to compute $Y(\vec{x})$ using Eq. (8), and Ycan be transformed to Z using Eq. (11).

3 Tests Using 1-D Cases

The above procedure was used in one-dimensional situations in order to check the validity of the procedure. The following data were assumed:

$$\varepsilon = 0.5$$
$$R_{XX}(r) = e^{-\frac{r}{a}}$$

where a is the correlation length and was taken to be '2 units'. The porous media of the above type are called 'Debye random media' [4]. The length of the domain was taken to be '400 units', and it was divided into 1,000 intervals. The following are the results.

First, we present the variation of R_{ZZ} and R_{YY}. There were numerical problems when $R_{ZZ} \approx 1$ and the values of R_{YY} are interpolated linearly in those situations. Figure 2 shows the variation. The first 400 eigenvalues and the first four eigenvectors are shown in Fig. 3. The eigenvalues are plotted in the descending order, and hence, it can be seen that many eigenvalues are very small. When using K-L expansion, it has been observed that for a given domain length, the number of

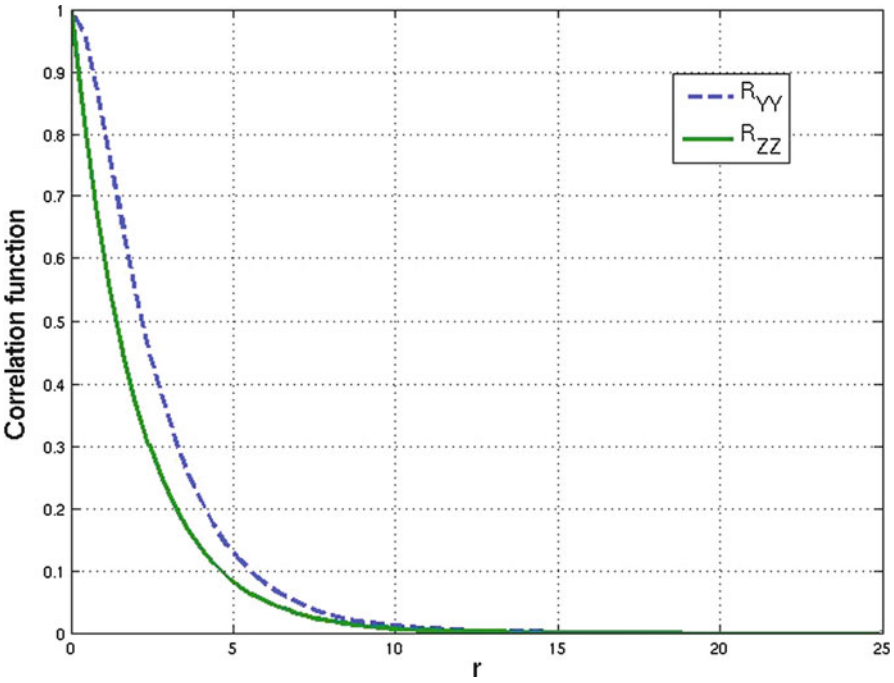

Fig. 2 Variation of R_{ZZ} and R_{YY}

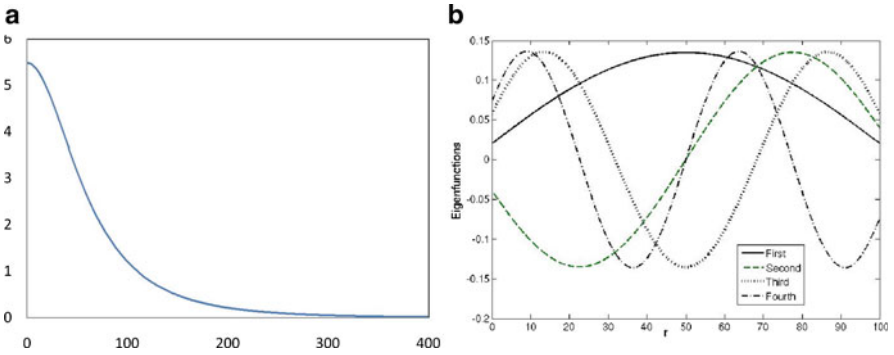

Fig. 3 (**a**) First 400 eigenvalues, (**b**) First 4 eigenfunctions

eigenvalues with considerable magnitude decreases as the correlation length increases. Thus, strongly correlated processes have fewer significant eigenvalues, and weakly correlated ones need more eigenvalues to represent them appropriately.

A large number (50,000) of samples were generated and their statistical properties—mean and correlation—were analysed. The mean was calculated in two ways. One was the ensemble mean (which is the actual mean) calculated over

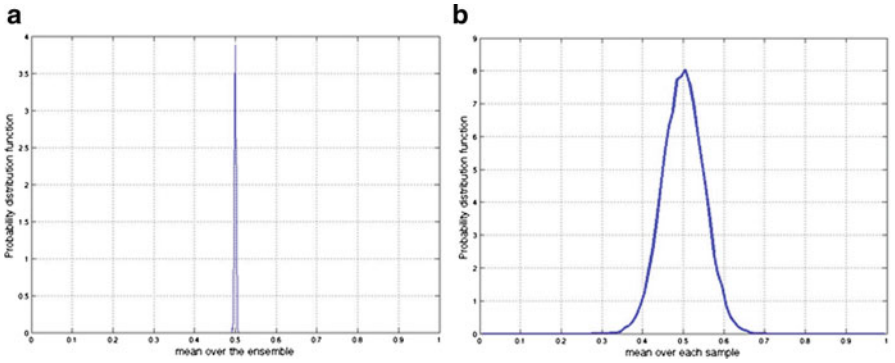

Fig. 4 pdf of the means, (**a**) Ensemble means, (**b**) Sample means

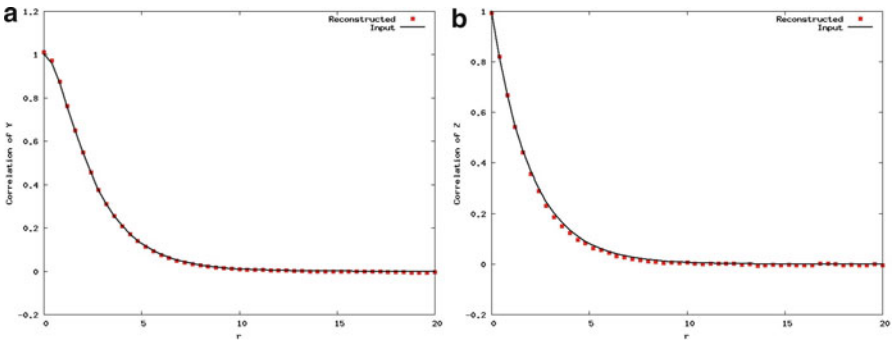

Fig. 5 Comparison of input and reconstructed correlation functions, (**a**) R_{YY}, (**b**) R_{ZZ}

the 50,000 samples. Since the domain was divided into 1,000 intervals, this gave 1,000 mean values. The distribution of these mean values was as shown in Fig. 4a. The extremely narrow distribution around 0.5 indicates that the K-L expansion works as expected. Also the mean was calculated over individual samples. This can be said to be the porosity of the samples. The pdf of the 50,000 means thus obtained is also shown in Fig. 4b.

The pdf of the sample means is not as narrow as in the case of the ensemble means. It is centred around 0.5. But it would be very desirable to obtain a pdf like in the case of ensemble means since it would mean that all the samples created have the same porosity. This is an interesting question with roots in the properties of ergodicity and its relation to K-L expansions. Still, sample mean pdf indicates that most of the samples also have the same porosity. It was also observed that the pdf of the sample means became narrower as the domain length was increased for a fixed correlation length.

The ensemble correlation function is calculated for both the Gaussian process Y and the discrete valued process Z. The plots showing the input correlation function and the ensemble correlation function are given for both the processes in Fig. 5.

The correlation functions also agree well with the input, and the statistical fluctuations at the tails are expected to diminish with an increase in the number of samples. Thus, we can see that the ensemble mean and the ensemble correlation function match the input statistics very well. We conclude this section mentioning that the above tests confirm the validity of the procedure. The 1-D porous media are not shown since they do not have any significance. In the following section, we show the results of the 2-D cases where a sample of the porous media simulated is shown.

4 Simulation of 2-D Porous Media

Having established the validity of the procedure using the 1-D case, we now move to reconstructing 2-D porous media. The following material describes the porous media thus generated using two different correlation functions. The first correlation function considered was the same as described in the 1-D case. The correlation length was '1 unit' and the domain was a square of side '10 units'. Each side was discretised into 100 intervals. Thus, there were 10,000 grid points, leading to 10,000 eigenvalues and eigenvectors. The first 200 eigenvalues are shown in Fig. 6. The first two eigenvectors (which are surfaces in this case) are shown in the Fig. 7.

Only 10,000 samples of 2-D media were created, and the statistics were computed—the pdf of the ensemble mean and the ensemble correlation function. These are shown in Fig. 8. From the figure, we can see the same results as in the 1-D case. The ensemble mean has a very narrow distribution. The sample mean distribution is not shown here. We only mention that it is more widely distributed because the domain length is just 10 times the correlation length. The correlation follows the input. A sample of the porous media thus generated is shown in Fig. 9. The white regions are pore spaces and black are solid.

Also the correlation length was reduced to 0.4 units and the calculations were performed. A sample of this porous media is given below in Fig. 9. A hypothetical correlation function described in Yeong and Torquato [12] was also used to simulate porous media. The porosity was retained at 0.5 and the correlation function had the following form:

$$R_{ZZ}(r) = e^{-\frac{r}{a}} \cos(\omega r)$$

where $a = 1$ represents the correlation length and $\omega = 10$ represents another smaller length scale of order π/ω. Thus, two distinct length scales should be visible in this case. A sample porous media is shown in Fig. 10. The sample shows the two length scales, the shorter one corresponding to the width of the walls and the longer one to the length over which such walls are similarly oriented.

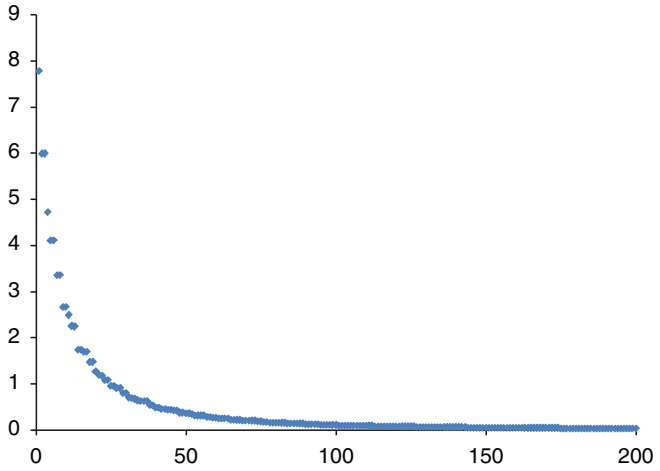

Fig. 6 First 200 eigenvalues in the 2-D case

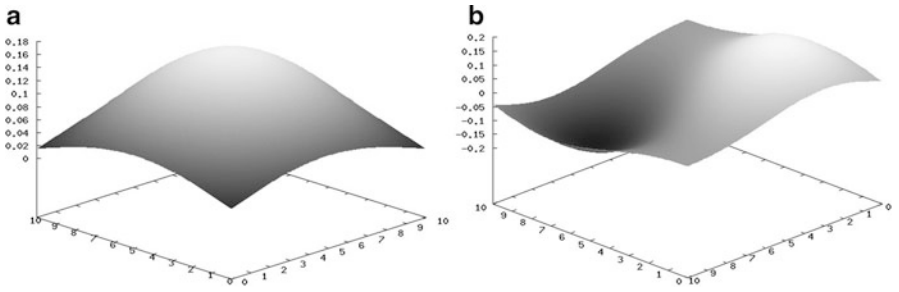

Fig. 7 Eigenfunctions in 2-D, (**a**) First, (**b**) Second

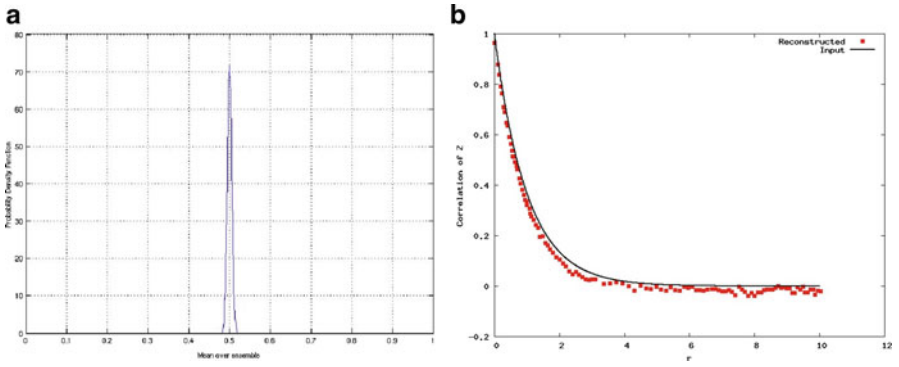

Fig. 8 (**a**) pdf of the ensemble means, (**b**) Comparison between input and output correlation

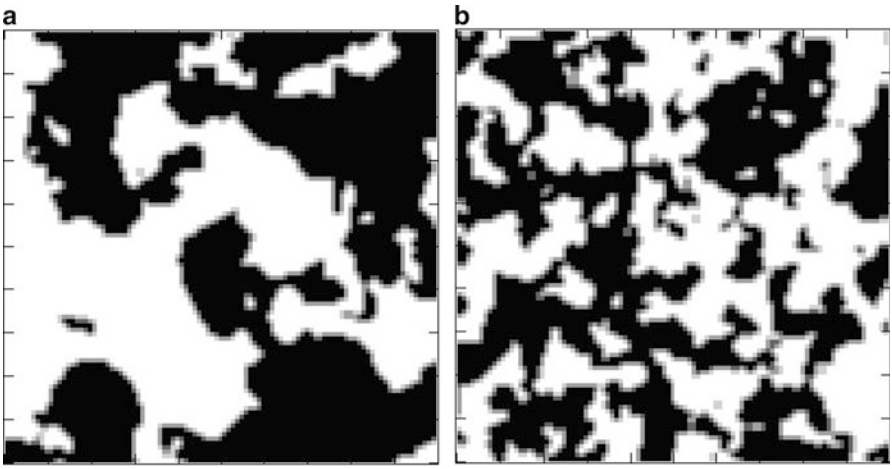

Fig. 9 A sample porous medium, (**a**) Correlation length = 2 units, (**b**) Correlation length = 0.4 units

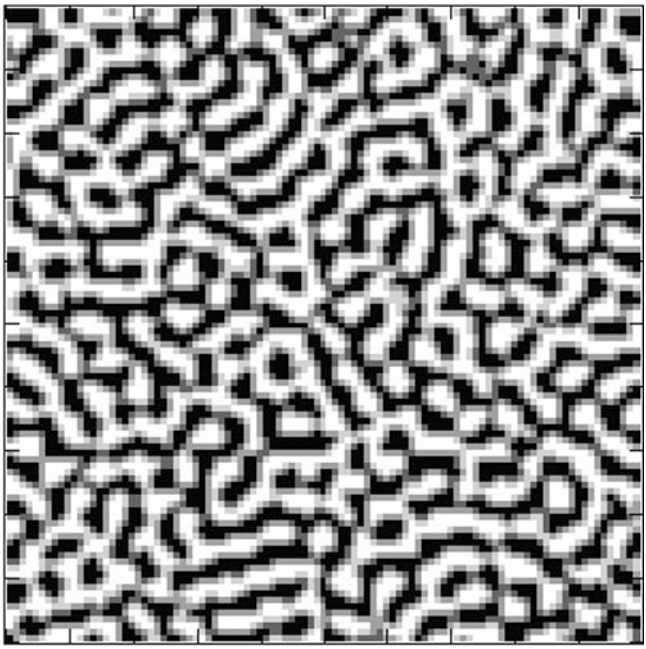

Fig. 10 A hypothetical medium

5 Conclusion

This method, which uses K-L expansion, is capable of reconstructing the porous media given its statistics. The validity of the method has been established by the fact that the statistics of the reconstructed 1-D samples agree well with the input statistics. Also the ability of the method to produce 2-D structures is also shown. The extension to three dimensions is straightforward and is limited primarily because of the computational constraints.

The method presented is also fast in the sense that for a given porosity and correlation function, the eigenfunctions and the eigenvalues have to be computed only once and then as many samples as required can be generated using them. Limitations come in the form of memory requirements when very large matrix operations are involved, for example, in the case of a finer discretisation in a 2-D or a 3-D case.

The main advantage lies in the fact that we also have an analytical framework for the structure of the porous media in terms of the random fields that are produced. These fields can be used for further analysis of the porous media. A possible direction for future work could be to include more statistical functions like the lineal path function or the pore size distribution function into the analysis so that the reconstructed samples may conform more to the original geometry they are trying to represent.

References

1. Adler PM, Jacquin CG, Quiblier JA (1990) Flow in simulated porous media. Int J Multiph Flow 16:691–712
2. Beavers GS, Joseph DD (1967) Boundary conditions at a naturally permeable wall. J Fluid Mech 30(1):197–207
3. Breugem WP, Boersma BJ (2005) Direct numerical simulations of turbulent flow over a permeable wall using a direct and a continuum approach. Phys Fluids 17:025103
4. Debye P, Bueche M (1949) J Appl Phys 20:518
5. Ghanem RG (1998) Probabilistic characterization of transport in heterogeneous media. Comput Methods Appl Mech Eng 158:199–220
6. Ghanem RG, Spanos PD (2003) Stochastic finite elements: a spectral approach. Courier Dover Publications, Minneola
7. Gradshteyn IS, Ryzhik IM (1965) Table of integrals, series and products. Academic, New York
8. Joshi M (1974) PhD thesis. University of Kansas, Lawrence
9. Lu B, Torquato S (1993) Chord-length and free-path distribution functions for many-body systems. J Chem Phys 98(8):6472–6482
10. Quiblier JA (1984) A new three-dimensional modeling technique for studying porous media. J Colloid Interface Sci 98:84–102
11. Tilton N, Cortelezzi L (2008) Linear stability analysis of pressure-driven flows in channels with porous walls. J Fluid Mech 604:411–445
12. Yeong CLY, Torquato S (1998) Reconstructing random media. Phys Rev E 57:495–506

Influence of Soil-Structure Interaction on Seismic Design of Reinforced Concrete Integral Bridges

Sreedhar Rao Gentela and Kaustubh Dasgupta

Abstract Soil-structure interaction results in a significant modification of structural behavior, which in turn affects its seismic response. Most of the current structural analysis methods, prescribed by the design guidelines of different countries, do not account for it. The necessity of incorporating soil-structure interaction in the investigation of a wide range of bridge structures has been pointed out by several post-earthquake investigations and experimental and analytical studies.

The current study is focused on the effect of soil-structure interaction on the seismic behavior of reinforced concrete (RC) piers of an integral bridge. First, a symmetric long-span RC bridge with fixed base is modeled using the computer program OpenSees. Next, the soil domain, along with the absorbing boundary conditions, is modeled in GID preprocessor program, and the bridge and soil domains are combined. Two types of scaled ground motions of different characteristics, namely, broadband and narrowband, are applied at the base of bridge, and the response of structure is studied by linear time history analysis. The forces at critical sections and displacement response are obtained.

The same bridge with fixed base is modeled in the program SAP2000, and response spectrum analysis is carried out to find the design response of structure. The design response obtained from SAP2000 model is compared with results obtained from the model using OpenSees. It is observed that the design code overestimates the possible response significantly.

Keywords Soil-structure interaction • Integral bridge • Bridge design • Absorbing boundary • OpenSees

S.R. Gentela • K. Dasgupta (✉)
Department of Civil Engineering, Indian Institute of Technology Guwahati, Guwahati 781039, Assam, India
e-mail: sreedharrao144@gmail.com; kaustubh.dasgupta@gmail.com

S. Chakraborty and G. Bhattacharya (eds.), *Proceedings of the International Symposium on Engineering under Uncertainty: Safety Assessment and Management (ISEUSAM - 2012)*,
DOI 10.1007/978-81-322-0757-3_48,

1 Introduction

Seismic soil-structure interaction is an essential part of realistic seismic analysis of structures. The soil response influences the motion of the structure, and structural response, in turn, influences the motion of the soil [10]. Ground motions that are not influenced by the presence of structures are referred to as free-field motions. When a rocky stratum at the ground surface is subjected to earthquake shaking, the extremely high stiffness of the rock constrains the rock motion to be very close to the free-field motion. Structures founded directly on rock are considered to be fixed-base structures. On the other hand, the same structure would respond differently if supported on a soft soil deposit. Firstly, the structural response will deviate from the exact free-field ground motion. Second, the dynamic response of the structure itself would induce deformation of the supporting soil. Although soil-structure interaction alters the seismic response of a structure from the fixed-base action, most of the current analyses tend to ignore this aspect due to scarce pertinent experimental data, computational intensiveness, and lack of easy application to design.

Past studies consist of nonlinear finite element modeling of IAB system with soil nonlinearity represented through nonlinear soil springs behind abutment and supporting piles [3]. It was observed that proper compaction of backfill soil behind the abutment influenced the axial force and bending moment in the superstructure bridge deck. Soil-pile interaction of these bridges was also investigated by using solid continuum elements to model soil and pile members [8]. The loads on the piles imposed by superstructure were found to affect a small volume of soil around the piles.

In the present study, a symmetric long-span integral abutment bridge is modeled with and without the underlying soil domain. The bridge and the soil are modeled using beam-column and plain strain elements, respectively, in the program OpenSees [13]. Two recorded earthquake ground motions, having broadband and narrowband characteristics, are applied at the base of the soil domain. The forces and moments in the piers of the bridge are observed with and without the presence of soil. These are compared with the design moments evaluated as per the Indian Concrete Bridge Code IRC: 6 [6]. Effect of possible liquefaction on the pier response is not considered in this study.

2 Computational Modeling

The BPS system was modeled using the graphical preprocessor user interface of GID version 10.0.4 [5]. The assigned geometric and material properties, along with the relevant boundary conditions, are discussed in the subsequent sections.

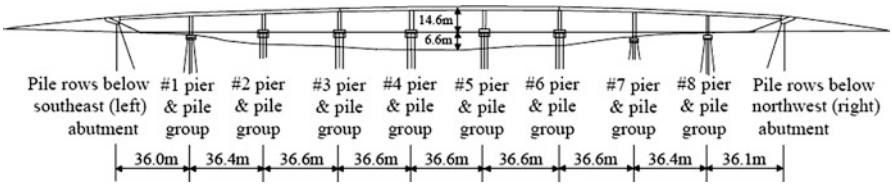

Fig. 1 Elevational view of bridge (Elgamal et al. [2])

2.1 Modeling of Bridge Structure

The present study is focused on the Humboldt Bay Middle Channel (HBMC) Bridge near Eureka in northern California, USA. The bridge is 330 m long, 10 m wide, and 12 m high (average height over the mean water level). The nine-span superstructure consists of four precast prestressed concrete I-girders and cast-in-place concrete slabs, as shown in Fig. 1. The bridge superstructure is supported by two seat-type abutments and eight bents founded on pile group foundations, each bent consisting of a single column and hammer head cap beam. The height of the piers ranges from 11 to 14 m. The deep foundations consist of driven precast prestressed concrete pile groups supporting pile caps [15]. For convenience, the piers are numbered #1 through #8 from the left to the right. The superstructure and substructure including piles were discretized using 2-noded linear beam-column elements with 3 degrees of freedom (DOF), two translational and one rotational DOF at each node. Each individual span is discretized into 5 elements, so the superstructure was discretized into 45 linear beam-column elements. The length of beam-column element varied from 7.2 to 7.32 m. The substructure was also modeled as linear beam-column element, and height was considered as 12 m (average height of pier column). Pile foundations are assumed to be extended up to 5.2-m depth from ground level. These piles also modeled as linear beam-column element as piers [4].

2.1.1 Modeling of Foundation Soil

The entire soil domain is broadly divided into two parts, namely, (1) soil above the natural ground level (backfill soil) and (2) foundation soil lying below the natural ground level. In addition to the backfill and foundation soil, there may be sometimes a small soil deposit on top of the footing level. These soil deposits have not been considered here. The interaction of backfill and possible abutment movement has not been considered in the present study.

The foundation soil was modeled up to the bedrock level which was at a depth of 16 m from the ground level, and the horizontal length of the BPS system was considered as 1,050 m [16]. The effects of pier and foundation soil on the seismic response of the system were investigated considering a ground motion which was taken from PEER strong ground motion records [14].

Entire soil domain was discretized using four-noded, bilinear, isoparametric finite elements under plane strain condition. These elements possess two translational degrees of freedom (DOF) at each node. In any FE simulation, smaller element size gives better accuracy but increases the computation time. So, a finer meshing (size: 0.4 × 0.4 m) was used throughout the domain to obtain stresses with sufficient accuracy. Kuhlemeyer and Lysmer [11] suggested that the element size in the direction of wave propagation should be restricted to 1/8th to 1/10th of the shortest wavelength considered in the analysis so that the shortest wavelength would propagate with sufficient accuracy. Based on this restriction, the element sizes were controlled throughout the soil domain. The soil domain was modeled using 1,05,000 elements and 1,07,666 nodes. The soil domain was modeled up to the bedrock level at 16-m depth from the ground surface and 6.10-m thickness [4].

2.1.2 Modeling of Soil-Structure Interfaces

Proper modeling of the soil-structure interface is very much important when permanent displacement and debonding at the interface influence the response of the structure significantly. Therefore, newly developed zero-length node-to-node contact elements were employed at the soil-pile interfaces to simulate the earthquake induced actions at the base of the piers as shown in Fig. 2 [4]. Young's modulus of these elements was taken equal to the soil for obtaining better interaction. The zero-length contact elements are connected between nodes having the same numbers of DOF. Since each soil element node has 2 DOFs and each pile node 3 DOFs, the contact element could not be connected directly between the soil and pile nodes. To facilitate this, a set of dummy nodes, with 2 DOFs at each node, were introduced at all three soil-pile interfaces. Thus, the zero-length contact elements were connected between the soil nodes and the corresponding dummy nodes, and the dummy nodes were connected to the corresponding pile nodes by equal DOF constraints along both x- and y-directions. Along the interfaces, the soil nodes, corresponding structure nodes, and the corresponding dummy nodes were created at the same physical location.

2.2 Boundary Conditions

A major difficulty in simulating the dynamic response of a semi-infinite soil domain has been the proper treatment of the boundary conditions. In a finite element (FE) model of bounded soil domain, wave energy tends to get trapped inside the computational domain without propagating away. But in reality, part of the energy propagates beyond the domain of the computational model and gets dissipated in the soil domain outside. Hence, that energy never comes back into the computational domain. Thus, the modeling of semi-infinite soil domain using a fixed or spring boundary fails to simulate the radiation damping actually observed in the

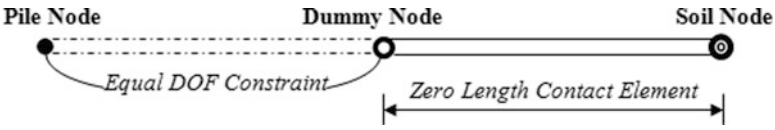

Fig. 2 Connectivity of nodes at soil-pile interface

field and results in spurious oscillations caused by the reflection of the waves along the boundaries [15].

The dimensions of the computational model should be small enough to achieve maximum computational efficiency, and thus, the need for proper treatment of the boundary conditions increases manifolds. On the contrary, the domain should be sufficiently large enough so as to reflect negligible response of the structure at the far field. The Lysmer-Kuhlemeyer's [12] boundary (generally known as L-K boundary) was applied at the boundaries to eliminate the spurious reflections. These boundaries are such that the incident wave is transmitted entirely into the computational domain without any distortion but no waves are transmitted back into the exterior domain [16]. Therefore, at each node along the base boundary of the domain, a horizontal dashpot and a vertical dashpot were attached to absorb the shear waves and the compressive waves, respectively. The coefficients for the horizontal and vertical dashpots are obtained as $C_s = \rho V_s A$ and $C_p = \rho V_p A$, respectively, where V_s and V_p are velocities of secondary and primary waves and A is the tributary area at the same location of the node. Similarly, at each node along the lateral boundary, horizontal and vertical dashpots of coefficients C_p and C_s are attached to transmit the compressive waves and shear waves, respectively [9].

To simulate this boundary condition in OpenSees, two nodes each having 2 DOFs were created at every boundary node location. In that, one was fixed in both directions, and another was constrained node which has two displacement constraints in x- and y-directions. These two nodes were connected using zero-length elements to simulate the Lysmer dashpot. Elastic material with Young's modulus of soil was used to simulate linear behavior of soil for the zero-length elements. After creating zero-length elements, constrained nodes were connected to soil nodes using equal DOF constraint as mentioned earlier [4].

2.3 Modeling of Bridge in SAP2000

The same bridge structure is also modeled without soil in the program SAP2000 V14.2 [1]. In SAP2000, the bridge elements were modeled using frame elements with all the DOFs at the bottom nodes restrained. Section properties were given as *General Section* properties. After modeling bridge, response spectrum analysis was carried out using the spectrum of Indian Earthquake Code IS 1893 (Part I): the same spectrum has also been prescribed in the draft bridge Code IRC 6 [6].

The critical shear forces and bending moments are obtained for design of bridge sections. A comparative study is carried out between the response quantities obtained using OpenSees with presence of soil and design forces obtained from the response spectrum analysis.

3 Analysis and Results

Linear dynamic analysis of the BPS was performed using ground motions taken from PEER. The responses of the BPS systems are presented in two forms of longitudinal response quantities, namely, (1) displacement at the top of pier and (2) forces at the critical sections of pier. Before performing dynamic analysis, eigenvalue analysis was carried out as part of free vibration analysis.

3.1 Free Vibration Analysis

To obtain the free vibration characteristics, i.e., natural periods and mode shapes of the BPS systems, frequency analyses were performed using conventional eigen solver in OpenSees. During these analyses, the soil material model was set as linear elastic, and the base of the model was restrained against horizontal and vertical displacements, whereas the lateral boundaries were kept free against displacements. These modifications were required to perform the frequency analyses to get the linear elastic undamped free vibration characteristics because after the application of the L-K boundary conditions, the global static stiffness matrix becomes singular. The free-field model was analyzed to get the natural frequencies and mode shapes (Table 1). The fundamental period of any soil deposit of infinite horizontal extent can be approximately obtained as [10]

$$T_1 = \frac{4H_{\text{soil}}}{v_s} \tag{1}$$

where H_{soil} is the depth of soil deposit and v_s shear wave velocity. For the free-field model ($H_{\text{soil}} = 16$ m), considering v_s as 234.41 m/s., the fundamental natural period (T_1) was calculated as 0.273s which was only 2.41% more than that obtained from the soil model. Therefore, this observation again justifies that the horizontal extent of the considered soil domain was sufficient to simulate the response of vertically propagating plane shear waves.

Table 1 Natural frequencies and periods of vibration of soil domain

Mode	Circular frequency (rad/s)	Natural frequency (Hz)	Natural period (s)
Mode 1	22.443391	3.571976	0.2799570
Mode 2	22.443404	3.571987	0.2799568
Mode 3	23.057983	3.669792	0.2724950
Mode 4	23.192339	3.691127	0.2709164
Mode 5	23.405080	3.725034	0.2684539
Mode 6	23.688007	3.770063	0.2652475

3.2 Analysis Procedure

Zhang et al. [15] outlined a staged analysis procedure to perform seismic analysis of a BPS system under similar situation. The stepwise final analysis procedure is discussed as follows:

1. The finite element mesh of the entire BPS system was created with the base nodes fixed in x- and y-directions and lateral nodes restrained in x-direction only. During this stage, soil material was set as linear elastic, and the self-weights of soil and structure were applied statically in one single step. The static equilibrium was obtained iteratively in multiple steps, and the lateral support reactions were obtained along bottom and lateral boundaries.
2. Next, the displacement restraints (in x-direction) along the lateral boundaries and in both x- and y-directions along the base boundary were removed. Reactions, obtained in step 1, were applied at the corresponding nodes (which were restrained earlier), i.e., in x- and y-directions along the base boundary and in x-direction along lateral boundary.
3. As per the L-K boundary conditions, horizontal and vertical dashpots were attached to each of the lateral and base boundary nodes. Then the model was brought into static equilibrium through iteration.
4. Finally from the static equilibrium position under gravity loads, the seismic excitation was applied as equivalent nodal shear forces along the base nodes.

3.2.1 Horizontal Displacements

Without the presence of soil, the displacement time history was carried out with ground motion. The maximum displacement was found to be 11.27 to 22.6 mm from end pier to middle pier. The ground motion data was considered up to 40s. The maximum displacement is found to be in first 5s of the motion. In presence of soil, the maximum displacement was found to vary between 16.4 and 16.5 mm. The maximum displacement is found to occur at around 5.64s of the motion. The ground motion has its PGA at around 4.16s, so maximum response is obtained at this time.

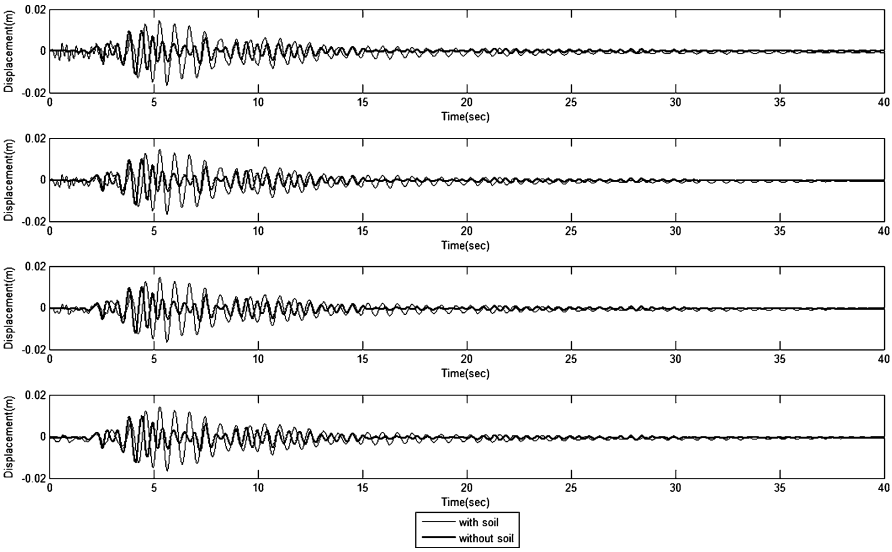

Fig. 3 Variation of displacements at the top of piers #1, #2, #3, and #4 with and without the presence of soil

Due to the presence of abutment, the displacement of pier near to that was found to be less as compared to other pier. Abutment dimensions were more than the pier so it could be able to provide resistance against displacement. The displacement of middle pier was obtained more because of superstructure lateral deformation. In some ground motions, the dominant frequencies of the motion are widely spaced with the possibility of the soil natural frequency lying in that domain. At certain time instants, these two frequencies might come closer, and this may lead to higher response in case of broadband motion. The soil domain was having natural frequency around 3.57Hz and the frequency of waves ranged from 0.12 to 40Hz [14] with the average frequency as approximately 20Hz. So there was a possibility having frequency equal to the natural frequency of soil. Thus, response of structure is also found higher than that obtained in absence of soil case.

In presence of soil, the response of the bridge structure is governed primarily by the soil response. It could be concluded that displacement at top might vary from one ground motion to the other depending on their frequency contents. It could be further concluded that the superstructure actions (i.e., inertia and vertical reaction) might change the primary mode of pier displacement as mentioned earlier. Under static condition, these displacements were almost zero, i.e., time equal to zero sec. Rigid body sliding started to occur, whereas rigid body rotation changed its direction from clockwise under static condition to counterclockwise under dynamic shaking and added to the total displacement. At the end of the motion, the displacement was tending to zero. Figure 3 shows the displacement time histories at the top of piers during earthquake motions with and without presence of soil.

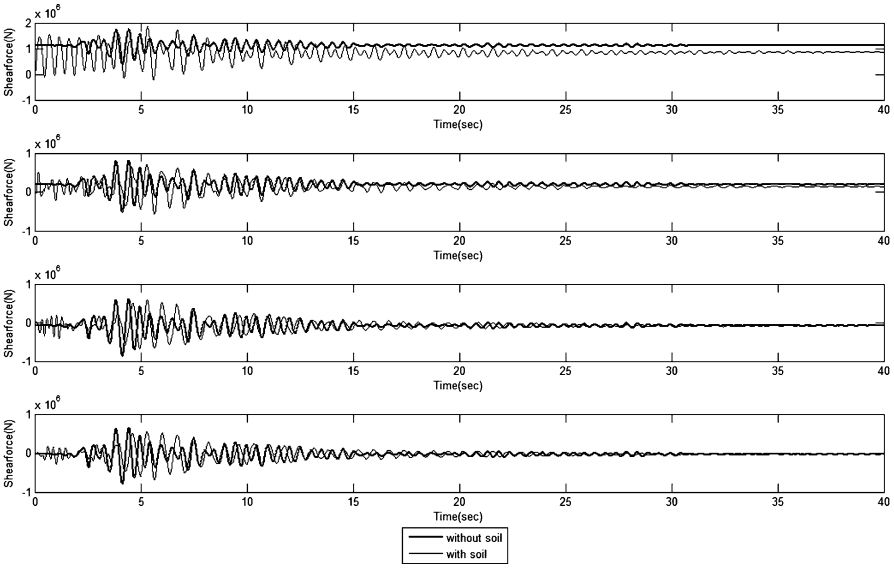

Fig. 4 Variation of shear forces for piers #1, #2, #3, and #4 with and without the presence of soil

3.2.2 Force at the Critical Section of Pier

Without presence of soil, the maximum shear force and bending moments were found to vary between 1750 to 797kN and 8,460 to 4,950kNm, respectively, from end to middle pier. The maximum shear force is found to be in first 5s of the motion for both PGAs, i.e., at 4.46s and at 4.12s respectively, as mentioned earlier. In the presence of soil, the maximum SF and BM were found to vary between 1,545 to 290.7kN and 14,850 to 2,478kNm, respectively, from end to middle pier. These peak values were observed at the time instant of 0.72s during the transient part of the response. The transient part of the response is neglected in design. At the instant of PGA, i.e., around 5.34s, these values varied from 1850 to 545.4kN and 15,950 to 4,747kNm, respectively.

In all the shear force and bending moment time histories, pier #1 showed higher shear forces (SF) and bending moments (BM) as compared to other piers. The higher difference in the case of pier #1 might be due to the presence of abutment next to it and might be due to large inertia force and vertical reaction of superstructure. Rigidity of the structure might be one of the reasons for having higher forces. Figures 4 and 5 show the variation of forces with ground motion. A few peaks in SF and BM were obtained in the transient part of the response. Due to the occurrence of the transient response over a small duration, it is expected to not affect the structural response significantly during actual shaking. Thus, it is ignored for inclusion of design guidelines.

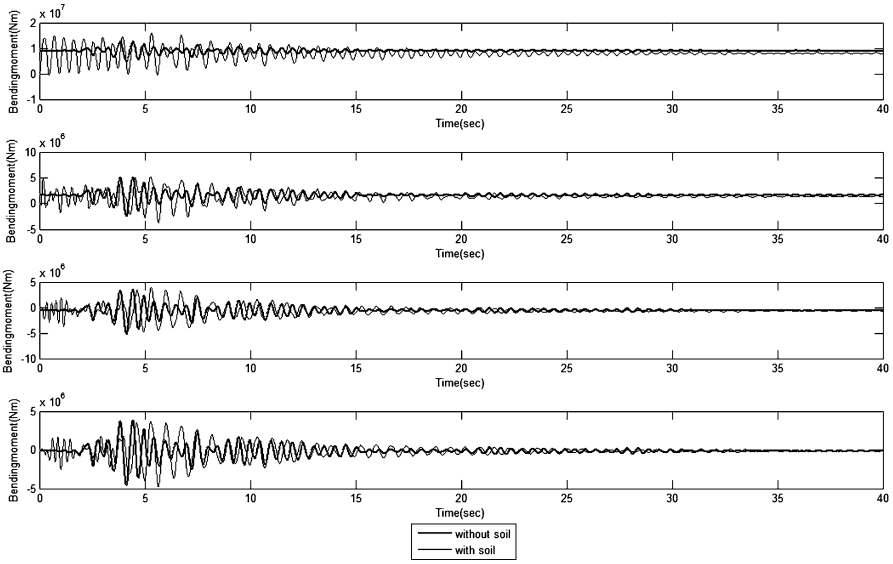

Fig. 5 Variation of bending moments for piers #1, #2, #3, and #4 with and without the presence of soil

3.3 Design Response from SAP2000

Soil-structure interaction is neglected as per the design provisions of IS 1893(Part 1): 2002; the linear structure with fixed base is considered for design. In general, it has been observed that with the presence of soil, natural period of structure increased. Correspondingly, force response also decreased compared to that without soil. So in designs, all the response of the structure will be overestimated; however, this change of response mainly depends on the soil characteristics. In case of soil, the response increased marginally than most of the responses (Table2). In some cases, it was observed slightly less than that compared to without soil case. The presence of soil plays a major role in response of structure. So soil-structure interaction is a major consideration in structural design. The structural response depends on soil, ground motion, and structural properties. But in general, the researchers had observed reduction in response in most of the situation. That could be the reason for not having proper provisions in IS 1893 (Part 1): 2002 on consideration of soil-structure interaction.

3.3.1 Design Response from SAP2000 Vs. Analytical Results with Presence of Soil

In SAP2000, the same bridge was modeled, and response spectrum analysis was carried out as per IS 1893 (Part 1): 2002. The code-prescribed response spectrum

Table 2 Comparison of BPS system and design response from SAP2000

Response	Quantitative response		SAP2000 results
	Without soil	With soil	
Disp. at pier #1	11.27mm	16.46mm	9.55mm
Disp. at pier #2	11.35mm	16.53mm	10.66mm
Disp. at pier #3	12.19mm	16.50mm	11.42mm
Disp. at pier #4	12.66mm	16.41mm	11.81mm
SF on pier #1	1,750kN	1,850kN	2,701kN
SF on pier #2	867kN	820kN	3,011kN
SF on pier #3	861kN	587kN	3,225kN
SF on pier #4	797kN	545kN	3,336kN
BM on pier #1	8,460kNm	15,950kNm	15,833kNm
BM on pier #2	4,700kNm	5,158kNm	17,640kNm
BM on pier #3	5,190kNm	4,738kNm	18,889kNm
BM on pier #4	4,950kNm	4,747kNm	19,534kNm

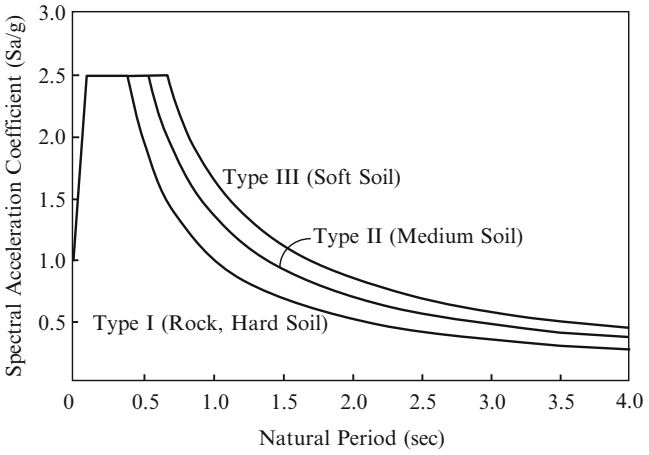

Fig. 6 Design response spectrum for soil and rocks at 5% damping [IS: 1893 (Part 1): 2002]

(Fig. 6), type III soil, and seismic zone V region were selected for the analysis input. Table 2 shows the design displacement, bending moment, and shear forces obtained from SAP2000. For all the cases, the design response was more than the analytical results except displacements in Loma Prieta with severe level of shaking. The design forces were found 10 times more than the forces obtained from analytical model; this is possibly due to the absence of soil modeling in prescribed linear analysis as per IS 1893 (Part 1): 2002. In general, the reduction in response with presence of soil has also been observed by researchers, so possibly soil-structure interaction has been excluded in some design guidelines including IS 1893 (Part 1): 2002 [7].

In the present study, the structural response is observed to get reduced as compared to the design response with using IS 1893 (Part 1): 2002 response spectrum. As the design spectrum is obtained by averaging response spectra for various ground motions for only three broad categories of soils, site-specific response spectrum analysis is required for critical structures and lifeline structures like bridges. The design spectrum of IS 1893 (Part 1):2002 may not be suitable for other types of soil also.

4 Conclusions and Recommendations

Due to soil-structure interaction, the change in structural response due to the presence of soil is likely to depend on soil properties. In the present study, the response of the bridge in the presence of soil was higher than that obtained without the soil. The following salient conclusions were drawn based on the comparison of the analytical results and the design response obtained from SAP2000:

(a) The design response of the integral bridge piers obtained from SAP2000 model was found much higher than the analytical results from the FE model of SAP2000 program.
(b) The design values of stress resultants, from response spectrum analysis, were found to be conservative. This may lead to uneconomical structural design.
(c) The current earthquake code, IS 1893 (Part 1): 2002, does not consider soil-structure interaction (SSI) for design of structures. This may be possibly due to the reduction in design response of structures while analyzing considering soil-structure interaction.
(d) The response of the structure mainly depends on the properties of structure, soil, and ground motion characteristics leading to either reduction or amplification. So detailed analysis in presence of soil needs to be carried out to obtain the design response.
(e) Current seismic design guidelines of various structures should incorporate prescribed steps of carrying out soil-structure interaction for certain types of soils.

Acknowledgement The authors would like to acknowledge the role of the Department of Civil Engineering at Indian Institute of Technology Guwahati for providing the resources to carry out the above mentioned research work. The authors are thankful to the Ministry of Human Resource and Development, Government of India, for granting financial support during the research work.

References

1. CSI (2009) SAP2000 Version 14.2 Linear and nonlinear static and dynamic analysis and design of three-dimensional structures. Computers and Structures Inc., Berkeley
2. Elgamal A, Yan L, Lu J, Yang Z, Shantz T, Conte JP (2010) Computational modeling of soil-foundation structural systems. In: Proceedings of the 9th U.S. National and 10th Canadian conference on earthquake engineering, Paper no. 1614, Toronto, ON, Canada

3. Faraji S, Ting JM, Crovo DS, Ernst H (2001) Nonlinear analysis of integral bridges: finite-element model. J Geotech Geoenviron Eng ASCE 127(5):454–461
4. Gentela SR (2011) Influence of soil-structure interaction on seismic behaviour of reinforced concrete integral bridge piers. Master of technology project report, Indian Institute of Technology Guwahati
5. GID (2010) User manual, Version 10.0.4. International Center for Numerical Methods in Engineering (CIMNE), Barcelona, Spain
6. IRC: 6 (2004) Standard specifications and code of practice for road bridges. The Indian Roads Congress, New Delhi
7. IS:1893 (Part 1): 2002 (2002) Indian standard criteria for earthquake resistant design of structures -part 1: general provisions and buildings. Bureau of Indian Standards, New Delhi
8. Khodair YA, Hassiotis S (2005) Analysis of soil-pile interaction in integral abutment. Comput Geotech 32:201–209
9. Kolay C (2009) Seismic analysis of bridge abutment-soil systems. Master of technology project report, Indian Institute of Technology Kanpur, India
10. Kramer SL (1996) Geotechnical earthquake engineering. Prentice Hall, Upper Saddle River
11. Kuhlemeyer RL, Lysmer J (1973) Finite element method accuracy for wave propagation problems. J Soil Mech Found Div ASCE 99(SM5):421–427
12. Lysmer J, Kuhlemeyer RL (1969) Finite dynamic model for infinite media. J Eng Mech Div ASCE 95:859–877
13. OpenSees (2010) Open system for earthquake engineering simulation, Version 2.2.1. Pacific Earthquake Engineering Research (PEER) Centre, Berkeley. http://opensees.berkeley.edu/index.php
14. PEER (2010) Pacific Earthquake Engineering Research Center: NGA Database. http://peer.berkeley.edu/nga/search.html. 15 Oct 2010
15. Zhang Y, Conte JP, Yang Z, Elgamal A, Bielak J, Acero G (2008) Two dimensional nonlinear earthquake response analysis of a bridge-foundation ground system. Earthq Spectra 24 (2):343–386
16. Zhang Y, Yang Z, Bielak J, Conte JP, Elgamal A (2003) Treatment of seismic input and boundary conditions in nonlinear seismic analysis of a bridge ground system. In: 16th ASCE engineering mechanics conference, University of Washington, 16–18 July 2003

Parametric Study of Lateral Load-Resisting System in Reinforced Concrete Frame Building

Sreya Dhar and Kaustubh Dasgupta

Abstract In earthquake-resistant design of reinforced concrete (RC) frame multistoreyed buildings, identification of lateral force-resisting system presents a major challenge. Certain structural elements are identified to carry the lateral forces generated during strong earthquake shaking. The stiffness and configuration of those identified elements play a major role in determining the design force levels in the elements.

A symmetric five-storied RC frame building is designed against the earthquake load combinations, specified as per Indian Earthquake Code, namely, IS:1893 (Part 1)-2002. All the frames along both the directions are expected to share the lateral forces as per the stiffness and configuration.

Next, certain frames, more specifically the outer ones, are identified to carry the lateral forces, and subsequently, the frames are made stiffer. The consequence on design is studied by obtaining the required amount of reinforcement for the two cases of varying column dimensions. Further, certain members are modelled to carry only the gravity forces by assigning release in moments along appropriate directions. Thus, the whole structure is not expected to get damaged during any strong earthquake. Consequently, the required amount of reinforcement in various frame members of different floor levels is compared for different cases.

Keywords Gravity column • Seismic design • Non-ductile column • Drift capacity • Moment release

S. Dhar
Department of Construction Engineering, Jadavpur University,
Salt Lake, Kolkata, India
e-mail: sreya.dhar@gmail.com

K. Dasgupta (✉)
Department of Civil Engineering, Indian Institute of Technology Guwahati,
Guwahati 781039, India
e-mail: kaustubh.dasgupta@gmail.com

S. Chakraborty and G. Bhattacharya (eds.), *Proceedings of the International Symposium on Engineering under Uncertainty: Safety Assessment and Management (ISEUSAM - 2012)*,
DOI 10.1007/978-81-322-0757-3_49,

1 Introduction

In many RC frame-type buildings, certain selected frame elements are assigned to participate in the lateral load-resisting mechanism during strong earthquake shaking. Other frame members primarily participate in the gravity-resisting mechanism. This leads to ductile detailing of the members contributing to the lateral resistance and non-ductile detailing of the gravity members. The gravity members are known as gravity columns. The lateral force-resisting system generally consists of moment-resisting frames and structural walls. The lateral displacements of the primary system, during strong earthquake shaking, are imposed on the gravity columns which may lead to possible collapse unless designed for adequate drift capacity. During 1994 Northridge earthquake, a number of gravity load systems collapsed due to excessive lateral deformations [5].

Past studies on gravity column systems have mostly focussed on the drift capacity of non-ductile columns as compared to the ductile columns [11] and influence of confinement in the columns on the drift capacity [1]. In the latter study, nonlinear analysis was carried out for gravity columns with actual material nonlinearities. With RC shear wall as the primary component of lateral load-resisting system, the inelastic behaviour of gravity columns were investigated with assumed plastic hinge length and moment-curvature relationships [2]. Nonlinear dynamic analyses on RC frame buildings with ductile and non-ductile frames have been carried out to assess collapse prevention during strong earthquake shaking [10].

In the present study, the influence of gravity columns on the required longitudinal and transverse reinforcement of lateral force-resisting members is investigated under design earthquake load combinations. The study is carried out for a symmetric plan building; however, the same can be carried out for an asymmetric plan building also.

2 Input Details and Modelling

A multistoreyed symmetric RC frame building of plan dimensions 15.52 m $\times$ 9.14 m and height of 16.7 m is situated in zone V as per the seismic zone map of India (IS:1893 (Part 1), 2002). A multi-storeyed building is 5-storeyed and the typical floor-to-floor height is 3.04 m. The thickness of all floor slabs is 125 mm, and the cross-sections of beams and columns are 225 mm $\times$ 300 mm and 300 mm $\times$ 300 mm, respectively. The building is assumed to be founded on rocky stratum; thus, all the degrees of freedom (DOFs) are restrained at the bottom nodes of the building. The grade of concrete is M25 and steel used is Fe 415. The sizes of the footings required under the wind and earthquake load combinations are obtained while designing other components. The modulus of elasticity, Poisson's ratio and mass density of concrete

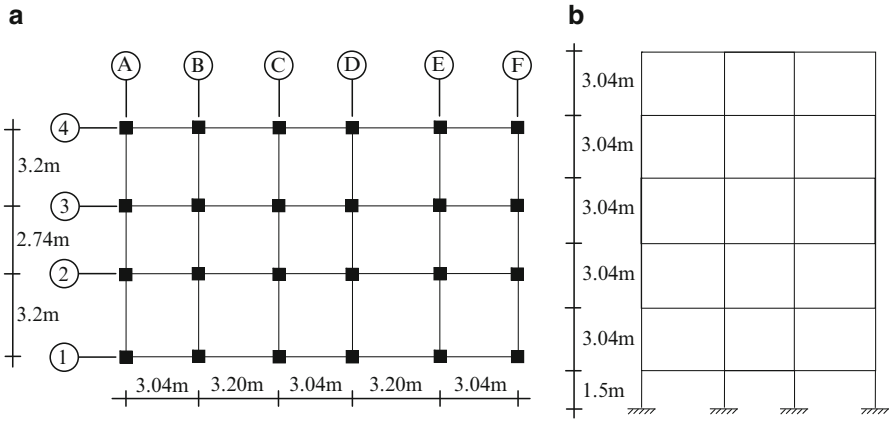

Fig. 1 (**a**) Typical floor plan and (**b**) elevation of the building along gridline A

have been considered as 25,000 MPa, 0.15 and 2,500 kg/m^3, respectively. The typical floor plan and elevation are shown in Fig. 1a, b, respectively.

The beams and columns are modelled using two-noded frame element option of the computer programme SAP2000 [3]. Each node of this frame element has six DOFs including three translational and three rotational DOFs. The slabs are modelled using four-noded thin shell elements, each having six DOFs similar to those of the frame element. To maintain compatibility of deformations along the edges of slab and the corresponding beams, each beam is discretised in six segments, along with the slab into subarea elements, at nodes common to both the beam and slab [4].

The loads on the structure are dead load (DL) (IS:875 (Part 1), [7]), live load (LL) (IS:875 (Part 2), [8]) and earthquake load along X (EL_X) and Y (EL_Y) directions (IS:1893 (Part 1), [6]), respectively. EL_X and EL_Y represent equivalent static lateral forces, due to earthquake shaking, along X- and Y-directions, respectively. The various load combinations are considered as per IS:1893 (Part 1) respectively.

3 Initial Design

The building is analysed under the specified load combinations and the reinforcement in slabs, beams and columns obtained from the limit state design principles of the Indian Concrete Code IS:456-2000 [9, 12]. Conventionally, slabs are divided into middle and edge strips, and moments are evaluated due to vertical loads only. In this study, the bending moments are evaluated from the output of the shell elements under the prescribed load combinations. Among all the floors and roof of the building, the reinforcement provided in the middle and edge strips of

the panels are Y10@250c/c and Y10@175c/c, respectively. For the beams, the design forces and moments were grouped into two categories, namely, (a) for ground, first and second floors and (b) for third and fourth floors and roof. However, the same reinforcement has been provided for both the categories with the longitudinal steel being 2 nos. Y16 bars both at supports and midspan along with transverse steel of 2-legged Y8 stirrups at 300-mm centre-to-centre distance. Similarly, for columns, the design forces and moments were grouped into two categories, namely, (a) for ground, first and second stories and (b) for third, fourth and fifth stories. However, the same reinforcement has been provided for both the categories with the longitudinal steel being 4 nos. Y16 bars throughout the height along with transverse steel of 2-legged Y8 stirrups at 250-mm centre-to-centre distance.

4 Parametric Study

4.1 Stiffening of Exterior Frames

The lateral force attracted by a particular frame of a multistoreyed building depends on its lateral stiffness. In the present study, the effect of selective frame stiffening along the two principal directions on design aspects is investigated through a parametric analysis. Two cases have been considered as follows:

(a) *Case* 1: In the first case, the depth of the columns was changed from 300 to 500 mm along global *X*-direction only at the two outer frame lines (1) and (4) (Fig. 2a). The width of column remains the same as 300 mm.
(b) *Case* 2: The depth of the columns was increased from 300 to 500 mm along global *Y*-direction only at the exterior frames (A) and (F) along *Y*-direction (Fig. 2b). The width of column remains the same as 300 mm.

With increase in depth of particular vertical members (namely, exterior columns), the columns are expected to attract more forces and moments due to enhanced stiffness. Particularly, during strong earthquake shaking, significantly increased force demand will be imposed on these columns whereas the interior columns can be designed for lesser force capacities. Thus, the interior columns are expected to be designed with less vertical reinforcement as compared to the columns with increased depth.

***Case* 1.** The bending moments on the beams are found to be less than the moment obtained for the initial design case; thus, beam reinforcement remains the same. Unlike beams, the columns with enhanced sizes (300 × 500 mm) show increased flexural demand, and the reinforcement is redesigned to 4 nos. Y20 bars. The transverse reinforcement remains the same as obtained for the initial design case. The design flexural demand corresponds to the bending moments obtained under the load combination $0.9DL + 1.5EL_X$.

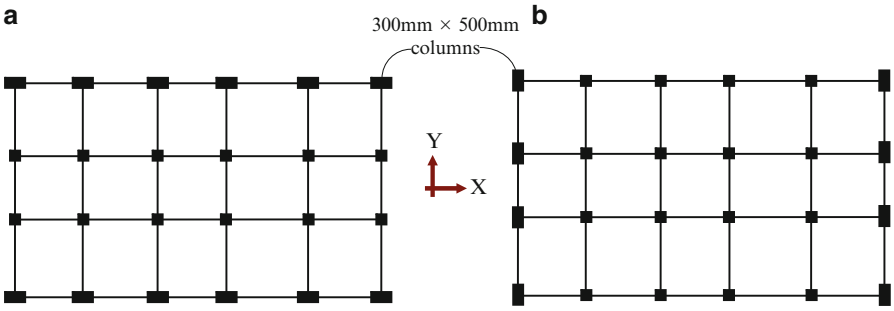

Fig. 2 Stiffening of exterior frame along global, (**a**) *X*-direction and (**b**) *Y*-direction

***Case* 2.** Due to the increased depth of 500 mm along global *Y*-direction (width of the building), both columns and beams in those two exterior frames are subjected to higher forces and moments as compared to the initial design case. In Case 1, more members (beams and columns) were available for framing action, and this did not increase flexural demand in the beams. Between the two categories, reinforcement was increased to 3 nos. Y16 bars at the support locations of the beams in ground, first and second floors; there was no change in beam reinforcement in the upper floors. The governing design moments were obtained from the load combinations $0.9DL + 1.5EL_Y$ and $1.2(DL + LL + EL_Y)$ for the midspan and support moments, respectively. However, the reinforcement in columns remains the same as obtained for initial design case.

4.2 Release of Moments

In a moment-resisting frame of a building, if the ends of a few columns are completely released against bending moments, there will not be any bending moment transfer in those columns. At the support sections, they will be subjected to only shear and axial forces depending on the loading along its height. Thus, the columns without the end releases will be subjected to higher bending moments and more predominant framing action. If the selective moment release is carried out for columns located along certain frames, the columns along other frames will form the lateral load-resisting system of that building during strong earthquake shaking. The columns for which the bending moments are released are known as gravity columns. These gravity columns are expected to have less longitudinal reinforcement as compared to the columns carrying higher bending moments.

4.2.1 Square Columns

In the second level parametric study, both ends of the all the columns of size 300 mm × 300 mm are released against transfer of bending moments for both

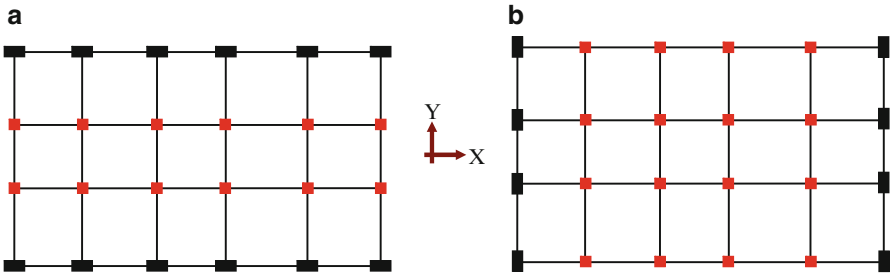

Fig. 3 Selective release of bending moments in columns for design earthquake force along global, (**a**) *X*-direction and (**b**) *Y*-direction (columns with moment release are marked *red*)

Cases 1 and 2. The predominant frame action of the exterior columns (with increased size) is investigated by applying the two design earthquake lateral loads EL_X and EL_Y for the Cases 1 and 2, respectively (Fig. 3a, b). The resulting longitudinal reinforcement is compared with the previous cases.

In Case 1, when the building is analysed against load combinations involving lateral force along global *X*-direction (EL_X), the beams along gridlines (1) and (4) tend to carry more bending moments. This results in increase of longitudinal reinforcement. As compared to the previous selective stiffening case, for ground, first and second floors, 2 nos. of bars at midspan and 3 nos. of bars at supports are provided. Also, for the upper floors, 2 nos. of bars are provided both at midspan and support sections. In the selective stiffening case, the bar diameter was 16 mm; for selective release, the required diameter of bar is 20 mm. Thus, there is an increase in reinforcement of 57% in the beam sections. However, the increased longitudinal steel in columns for selective stiffening case is sufficient to cater for the selective release case also. The design bending moments are obtained for the load combination $0.9DL + 1.5EL_X$ in second floor beams.

For Case 2, when the building is analysed against load combinations involving lateral force along global *Y*-direction (EL_Y), the beams along gridlines (A) and (F) tend to carry more bending moments. The previously assumed beam section 225 mm × 300 mm is found to be inadequate in resisting the increased flexural demand with the required beam section as 300 mm × 500 mm. Thus, the beams now tend to attract more forces and moments. For all the floors, 2 nos. of bars of 20-mm diameter are provided at midspan and at the supports. Also, for the upper floors, 2 nos. of bars are provided both at midspan and support sections. The transverse steel remains the same, i.e. 2-legged

Y8 stirrups at 300-mm centre-to-centre distance throughout the length of the beam. For the columns, the longitudinal reinforcement was increased to 4 nos. 22-mm-diameter bars. The design bending moments are obtained for the load combination $0.9DL + 1.5EL_Y$ in second floor beams.

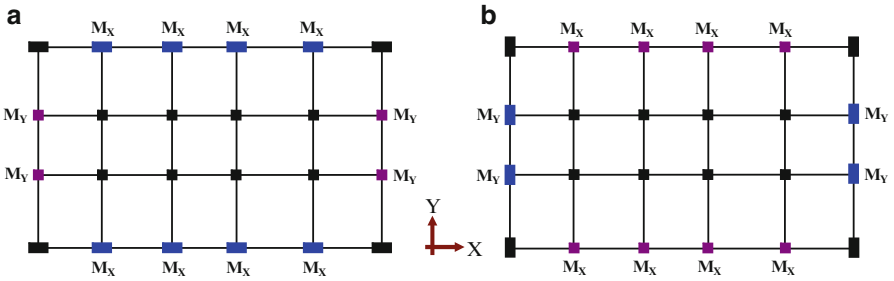

Fig. 4 Directional release of moments in peripheral columns for design earthquake force along global, (**a**) *X*-direction and (**b**) *Y*-direction

4.2.2 Directional Release of Moments

In another variation, the ends of the interior columns (size: 300 mm × 300 mm) are not released against transfer of bending moments; only the ends of the peripheral edge columns are released corresponding to particular directions (Fig. 4a, b). The directions of release of bending moments in the peripheral columns correspond to the directions of applied design earthquake lateral loads EL_X and EL_Y for the Cases 1 and 2, respectively. The ends of the interior columns are not released against transfer of bending moments along any direction.

For design earthquake loads applied along *X*-direction, there is no significant increase in bending moments for the exterior columns. Like Case 1 of the previous study, in which only the ends of the interior columns were released, 2 and 3 nos. of 20-mm-diameter bars were provided at midspan and supports in ground, first and second floors, respectively. For the upper floors, the beam reinforcement remained the same at midspan and support sections. The longitudinal and transverse steel in columns of all the stories also remains the same as in the previous case.

For design earthquake forces applied along *Y*-direction, the beams along gridlines (A) and (F) tend to carry more bending moments. Like Case 2 in the previous study, the required beam cross-section was increased to 300 mm × 500 mm. The required longitudinal and transverse reinforcement in the beams of all the floors remained the same as obtained in the previous study. However, the required longitudinal reinforcement in the columns for all the stories was 4 nos. 22-mm-diameter bars, unlike the previous study in which less reinforcement was required in the columns of upper 3 stories. The forces and bending moments are obtained for the combination $0.9DL + 1.5EL_Y$ in second floor beams.

4.2.3 Combined Study

In this analysis, the results of the previous two studies were combined and analysis carried out for design earthquake load combinations along appropriate directions. At both the ends of the columns on the peripheral edges (barring the corner

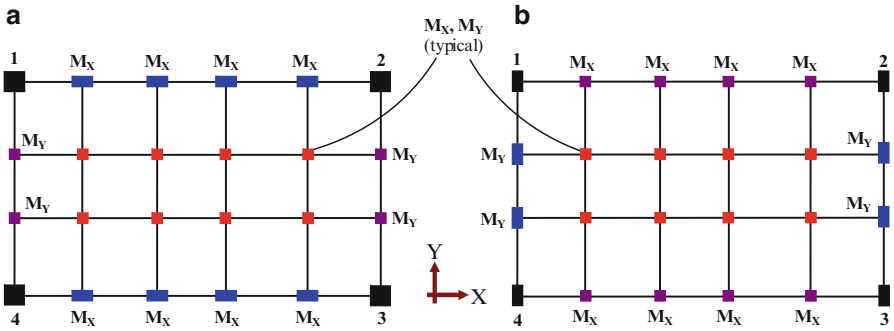

Fig. 5 Combined study of release of bending moments in columns: directional release in columns on peripheral edges along global, (**a**) *X*-direction and (**b**) *Y*-direction and release of bending moments in all the interior columns

Table 1 Comparison of maximum bending moments (kNm) in corner columns for the different analysis cases

		Selective stiffening		Moments released in interior columns		Directional release of moments	
Column labels	Initial design	Case 1	Case 2	Case 1	Case 2	Case 1	Case 2
1	21.0	50.6	60.0	80.1	128.3	91.3	128.3
2	21.0	52.1	60.0	81.8	128.3	91.3	128.3
3	19.2	52.1	58.3	81.8	126.4	88.9	126.3
4	19.2	50.6	58.3	80.1	126.4	88.9	126.3

columns), the bending moments were released along the appropriate directions of applied forces. In the interior columns, the moments were released along both the directions. The sizes of the corner columns were increased to 500 mm × 500 mm (Fig. 5).

For design earthquake loads applied along *X*- and *Y*-directions, the maximum bending moments in the corner columns are compared as obtained from the previous studies (Table 1). For the combined analysis case, the maximum bending moments among the four corner columns (1, 2, 3 and 4) are obtained as 121 and 183 kNm for Cases 1 and 2, respectively. Thus, the corner columns are attracting significantly higher forces than the previous cases due to the effect of moment release in other columns and increase in cross-section to 500 mm × 500 mm. However, due to the increased sizes of the columns, the required longitudinal reinforcement is less than the previous moment release cases; 4 nos. of 20-mm-diameter bars are required in the cross-section. The required transverse reinforcement remains the same as in the previous cases. The maximum bending moments are obtained for load combinations $0.9DL + 1.5EL_X$ and $0.9DL + 1.5EL_Y$.

In the present study, the building was subjected to linear elastic analysis under the code-specified design load combinations to obtain the influence of gravity columns on the required reinforcement of the columns. To obtain the actual seismic

behaviour, the building should be subjected to nonlinear analysis with geometric and material nonlinearities for the sections and reinforcement obtained as per the current design. The inelasticity in the beams and columns may be modelled using lumped or distributed plastic models. For lumped plasticity, shear and flexural hinges need to be modelled in the frame members of the lateral load-resisting system. Thus, the inelasticity in these members at large lateral deformations will be possibly captured after the collapse of gravity columns.

5 Conclusions

The following salient conclusions were drawn on the basis of the sequential studies as mentioned earlier:

(a) The stiffening of corner columns and columns supported along peripheral edges attracted more forces and moments on the members than release of selective columns against bending moments.
(b) As compared to the longitudinal direction, the framing members along the transverse direction attracted more forces and moments for almost the same base shear values.
(c) Moment release of the interior columns and directional moment release of the peripheral edge columns had similar influence on longitudinal reinforcement of the columns.
(d) The moment release of internal and peripheral edge columns had almost insignificant influence on the transverse reinforcement of the corner columns.
(e) The actual inelastic behaviour of the entire building needs to be investigated by modelling nonlinearities in members.

Acknowledgement The authors would like to acknowledge the role of the Department of Civil Engineering at Indian Institute of Technology Guwahati for providing the resources to carry out the above mentioned research work as part of the departmental summer internship programme.

References

1. Achary GGS (1997) Seismic drift capacity of gravity columns using nonlinear monotonic analysis. Master of Technology thesis, Indian Institute of Technology Kanpur, India
2. Agarwal V (1996) Seismic response of gravity columns in buildings with shear walls. Master of Technology thesis, Indian Institute of Technology Kanpur, India
3. CSI (2010) SAP2000 V14.0, Structural analysis program, Computers and Structures Inc. Berkeley
4. Dhar S (2011) Design of a reinforced concrete multistoried building due to wind and earthquake load combinations. Summer project report, Indian Institute of Technology Guwahati, Guwahati

5. EERI 94-01 (1994) Northridge earthquake, January 17, 1994; preliminary reconnaissance report. Earthquake Engineering Research Institute, Oakland
6. IS 1893 (Part 1):2002 (2002) Indian standard criteria for earthquake resistant design of structures-part 1: general provisions and buildings. Bureau of Indian Standards, New Delhi
7. IS 875 (Part 1):1987 (2003) Code of practice for design loads (other than earthquake) for buildings and structures part 1 dead loads – unit weights of building material and stored materials. Bureau of Indian Standards, New Delhi
8. IS 875 (Part 2):1987 (2003) Code of practice for design loads (other than earthquake) for buildings and structures: part 2 imposed loads. Bureau of Indian Standards, New Delhi
9. IS 456:2000 (2005) Plain and reinforced concrete – code of practice. Bureau of Indian Standards, New Delhi
10. Liel AB, Haselton CB, Deierlein GG (2011) Seismic collapse safety of reinforced concrete buildings II: comparative assessment of nonductile and ductile moment frames. J Struct Eng ASCE 137(4):492–502
11. Moehle JP (1994) Design of structural concrete gravity systems to resist earthquake effects. In: Proceedings of seminar on advances in earthquake engineering practice, University Extension, University of California Berkeley
12. SP:16–1980 (1999) Design aids for reinforced concrete to IS 456: 1978. Bureau of Indian Standards, New Delhi

System Identification of Structures from Limited Measured Data Based on Inverse Static Approach

Debasish Bandyopadhyay and Suprateek Roy

Abstract Structural Health Monitoring (SHM) has become significantly important in the civil and structural engineering arena particularly in the context of safety and to ensure its future usefulness. A lot of research activities particularly adopting inverse dynamic approaches have been attempted in this SHM area incorporating sophisticated instrumentations and efficient numerical techniques to solve these mathematical problems. However, it may not be feasible in practice due to some practical constraints at many occasions. System identification of structures based on limited static test data at the element level is simple and an attractive proposition. However, the accuracy of the predicted structural properties depends on the amount of data and location of measurement degrees of freedom (MDOF). A system identification technique based on inverse static approach using changes in limited data is studied with sensitivity analysis in this chapter. The structural property for each element is derived adopting a two-phase analysis processes, namely, selection of measured degrees of freedom and structural parameter identification. It is important to study the sensitivity of the limited degrees of freedom to develop an efficient system identification technique. The structural property is identified using the applied forces and measured displacement at those selected MDOF. The effect of the measurement locations is demonstrated in detail with numerical examples. The proposed method is suitable for practical problem, as it is able to identify the structural damage with limited measured data at sensitive MDOF.

Keywords Damage • Degree of freedom • Identification • Static test • System identification • Sensitivity analysis

D. Bandyopadhyay (✉) • S. Roy
Department of Construction Engineering, Jadavpur University,
Jadavpur, Kolkata, West Bengal, India
e-mail: dban65@yahoo.com; supraju1987@gmail.com

S. Chakraborty and G. Bhattacharya (eds.), *Proceedings of the International Symposium on Engineering under Uncertainty: Safety Assessment and Management (ISEUSAM - 2012)*,
DOI 10.1007/978-81-322-0757-3_50,

1 Introduction

Damage of structure during its useful life is a very common phenomenon. The geometric and material properties change in practice because of damage due to various reasons. Sometimes, it is required to identify the location and the amount of very little damage to ensure the safety and future usefulness of structure, effective, and economical restoration of the structure and to exploit better life expectancy of structure. Damage can be assessed both by static and dynamic approach. But, the static approach is not easy due to the scarcity of the information received from the static response. Besides, the effect of the damage may be concealed due to the limitation of load paths. The damaged elements which have little contribution to structural deformations under a certain load case cannot be estimated properly. In practice, these limitations can be lifted up by choosing the best lose case with the help of the proper preanalysis of the structure.

The literature on damage identification of structures adopting static response is not very rich. The first paper based on static concepts was published by Sheena et al. [8]. The elements of the stiffness matrix were adjusted for minimizing the difference between the actual and analytical stiffness matrices. The displacements were measured at certain locations, and the spline function was used to evaluate the displacements where no measurements were taken.

Sanayei and Nelson [5] and Sanayei and Scampoli [7] estimated the stiffness of the structure adopting the least square minimization of the difference between the analytical stiffness and the measured stiffness. According to their method, the displacements must be measured at the same DOF where the external forces are applied. In practical situations, it is very difficult to maintain the accuracy of the measurement at the DOF of the applied force.

Hajela and Soeiro [3] used both the measured static and modal responses to evaluate the change of stiffness on an element by element basis in a structural system. They prescribed substructuring and order reduction approach for the parameter identification of the large structures.

The static condensation technique was adopted by Sanayei and Onipede [6] to overcome the stated drawback. The difference between the force, formulated from the measured data, and the true force was minimized with the help of least square minimization technique.

The parameter estimation of complex linear structure was done by Hjelmstad et al. [4] based on an error measure. The problems of incomplete observations are managed by applying the condensation technique. A fruitful study was performed on the influence of noisy measurements using Monte Carlo simulation.

Bakhtiari-Nejad et al. [2] have expressed the change in the static displacement of certain DOF as a function of the location and magnitude of damage. The minimization of the difference between the load vectors of damaged and undamaged structures was used by them.

In the present damage assessment algorithm, the static condensation and the least square optimization techniques are adopted for predicting the parameters with limited measured data. At first, the analysis of the whole structure using forward

solution should be done for identifying the most sensitive locations for different sets of forces. The best sets of forces and the most sensitive measurement locations corresponding to those sets of forces can be pointed out with this analysis. Static loads are applied and the measurements are taken at those predefined locations. The difference between the analytical measurements based on the load cases and the true measurements is linearly optimized using the least square technique. An iterative process is very helpful for approaching the true value of the parameters.

2 Theoretical Formulation

2.1 Forward Problem

The static equation of forward problem is

$$\{f\} = [K]\{u\} \tag{1}$$

where $\{f\}$ is the force vector, $[K]$ is the stiffness matrix, and $\{u\}$ is the displacement vector.

If more than one set of force are incorporated, then the basic equation can be rewritten as

$$[F] = [K][U] \tag{2}$$

where $[F]$ is the force matrix consisting of different sets of forces and $[U]$ is the displacement matrix containing the displacements for each sets of forces.

2.2 Static Condensation

The stiffness relations of Eq. (1) are partitioned into a measured portion associated with the displacement $[U_a]$ and force $[f_a]$ and unmeasured displacement $[U_b]$ and forces $[f_b]$, i.e.,

$$\left[\frac{f_a}{f_b}\right] = \left[\frac{K_{aa}}{K_{ba}} \middle| \frac{K_{ab}}{K_{bb}}\right] \left[\frac{U_a}{U_b}\right] \tag{3}$$

$$\text{So,} \quad [f_a] = [K_{aa}][U_a] + [K_{ab}][U_b] \tag{4}$$

$$[f_b] = [K_{ba}][U_a] + [K_{bb}][U_b] \tag{5}$$

$$\Rightarrow [K_{bb}][U_b] = [f_b] - [K_{ba}][U_a]$$

$$\Rightarrow [U_b] = [K_{bb}]^{-1}([f_b] - [K_{ba}][U_a]) \tag{6}$$

Replacing the value of $[U_b]$ of Eq. (5) with the value of $[U_b]$ from Eq. (6),

$$[f_a] = [K_{aa}][U_a] + [K_{ab}]([K_{bb}]^{-1}([f_b] - [K_{ba}][U_a])$$

$$\Rightarrow [f_a] = ([K_{aa}] - [K_{ab}][K_{bb}]^{-1}[K_{ba}])[U_a] + [K_{ab}][K_{bb}]^{-1}[f_b]$$

$$\Rightarrow ([f_a] - [K_{ab}][K_{bb}]^{-1}[f_b]) = ([K_{aa}] - [K_{ab}][K_{bb}]^{-1}[K_{ba}])[U_a]$$

$$\Rightarrow [U_a] = ([K_{aa}] - [K_{ab}][K_{bb}]^{-1}[K_{ba}])^{-1}([f_a] - [K_{ab}][K_{bb}]^{-1}[f_b]) \tag{7}$$

2.3 Formation of Error Matrix and Error Vector

The difference of the predicted displacement with the true (measured) displacement is the error matrix, $[E(p)]$.

$$[E(p)] = \left([U_a]_{\text{predicted}} - [U_a]_{\text{true}}\right) \tag{8}$$

If the structure is undamaged, then the global stiffness matrix, $[K]$, remains unchanged. In that case, the error matrix should be a null matrix. Otherwise, it must not be a null matrix. The error matrix $[E(p)]$ is converted into an error vector $[E(p)]$ of size NM by 1. $\{p\}$ is a vector containing the unknown parameters' values. The size of $\{p\}$ is NUP by 1. For adjusting the parameters$\{p\}$ in $[E(p)]$, a first-order Taylor series expansion is applied. It is very necessary for the linearization of the error vector:

$$\{E(p + \Delta p)\} \approx \{E(p)\} + [S(p)]\{\Delta p\} \tag{9}$$

$$\text{where} \quad [S(p)] = \left[\frac{\partial\{E(p)\}}{\partial\{p\}}\right] \tag{10}$$

For the analytical evaluation of the sensitivity matrix $[S(p)]$, $[E(p)]$ is differentiated with respect to each parameter.

$$\begin{aligned}
[\bar{s}(p_j)] =& ([K_{aa}] - [K_{ab}][K_{bb}]^{-1}[K_{ba}])^{-1} \\
& \left(\frac{\partial[K_{ab}]}{\partial p_j}[K_{bb}]^{-1}[K_{ba}] - [K_{ab}][K_{bb}]^{-1}\frac{\partial[K_{bb}]}{\partial p_j}[K_{bb}]^{-1}[K_{ba}] + \right. \\
& \left. [K_{ab}][K_{bb}]^{-1}\frac{\partial[K_{ba}]}{\partial p_j} - \frac{\partial[Kaa]}{\partial p_j}\right) \\
& ([K_{aa}] - [K_{ab}][K_{bb}]^{-1}[K_{ba}])^{-1} \\
& ([f_a] - [K_{ab}][K_{bb}]^{-1}[f_b]) + \\
& ([K_{aa}] - [K_{ab}][K_{bb}]^{-1}[K_{ba}])^{-1}[K_{ab}][K_{bb}]^{-1}\frac{\partial[K_{bb}]}{\partial p_j}[K_{bb}]^{-1}[f_b] - \\
& ([K_{aa}] - [K_{ab}][K_{bb}]^{-1}[K_{ba}])^{-1}\frac{\partial[K_{ab}]}{\partial p_j}[K_{bb}]^{-1}[f_b]
\end{aligned}$$

The sensitivity coefficient, $[\bar{S}(p_j)]$, is evaluated for $j = 1$ to NUP. Similar to $[E(p)]$, the elements of $[\bar{S}(p_j)]$ are assembled into a vector of size NM by 1. These vectors are horizontally concatenated for $j = 1$ to NSF to form the sensitivity matrix $[S(p)]$ of size NM by NUP.

2.4 Linear Minimization

The scalar performance error function, $J\ (p + \Delta p)$, is defined as

$$J(p + \Delta p) = \{E(p + \Delta p)\}^T \{E(p + \Delta p)\} \tag{11}$$

Least square technique is applied by minimizing the scalar performance error function with respect to stiffness parameter of each element to identify the change on stiffness:

$$\frac{\partial J(p + \Delta p)}{\partial \{p\}} = \{0\} \tag{12}$$

From Eqs. (8), (11), and (12),

$$[S(p)]^T [E(p) - [S(p)]\{\Delta p\}] = \{0\} \tag{13}$$

The best sets of forces are applied, and the measurements are taken for each sets of force at selected sensitive locations (DOF). The number of independent measurements may be lesser than or equal to or greater than the number of unknown parameters.

For the first case, there is no unique solution.

For the next case,

$$\{\Delta p\} = -[S(p)]^{-1} \{E(p)\} \tag{14}$$

Here, the direct inversion method can be used.

For the last case, the sensitivity matrix $[S(p)]$ is a rectangular matrix. So, the following equation is adopted for the determination of $\{\Delta p\}$:

$$\{\Delta p\} = [[S(p)]^T [S(p)]]^{-1} [S(p)]^T \{E(p)\} \tag{15}$$

After evaluating the vector $\{\Delta p\}$, an iterative process is used for the parameter identification as

$$\{p\}^{r+1} = \{p\}^r + \{\Delta p\} \tag{16}$$

2.5 Choice of Load Cases and Measurement Degrees of Freedom

The basic problem in the static method is the selection of the load cases that can influence all the elements of structures. Under some specific load cases, the damage of some elements may not be detected due to the limitation of the load paths and slight contributions of these elements to the static response of structure.

The result of the damage detection algorithm also depends a lot on the selection of measurement locations (MDOF). These selected locations must be sensitive to any change in the structural parameters.

The analysis of the whole structure with the forward approach is very handy for identifying the best load cases and the most sensitive measurement locations.

3 Results and Discussions

3.1 Problem 1

To illustrate the proposed damage identification method, a ten-element symmetrical truss problem as shown in Fig. 1 is numerically demonstrated. The undamaged properties are given as cross-sectional area, $A = 0.0001$ M^2, and modulus of elasticity of each element, $E = 2.1 \times 10^8$ KN/M^2. A sensitivity analysis is done to predict the most sensitive MDOF.

The solution of the forward problem of the symmetrical truss is performed by applying the forces at feasible DOF to study the sensitivity of MDOF for each element. Figure 2 shows the sensitivity of various MDOF for element 1, while the force is applied at node 2 V. Similar type of information can be generated by solving the forward problem to find the sensitivity of the MDOF for different feasible FDOF in case of each element.

The static displacements are measured at those selective MDOF, and the proposed identification technique is used to evaluate the predicted stiffness of each element. Assuming element 2 marked in the circle is damaged with reduced axial rigidity, the inverse problem is solved to demonstrate the applicability of the proposed method. Initially, the element is damaged by 10% of its initial axial rigidity. The prediction of parameters in this case is almost accurate as shown in the Fig. 3a. Thereafter, it is assumed that the diagonal member, i.e., element 4 marked in the circle in Fig. 1, is damaged by 10% of its initial axial rigidity. The comparison between the predicted parameters and the true parameters is clearly shown in Fig. 3b.

Similarly, element no. 5 (vertical element) is damaged by 10% of its axial rigidity, and the proposed technique is giving satisfactory results for predicting the parameters (Fig. 4a).

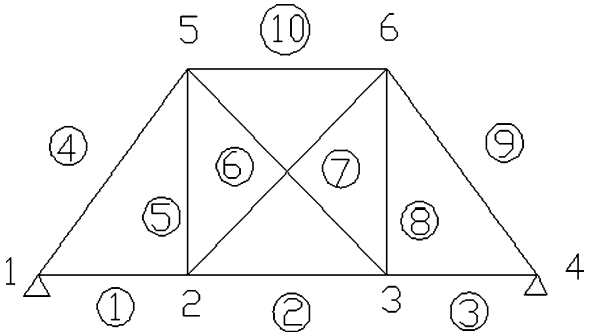

Fig. 1 A 10-element symmetric truss problem

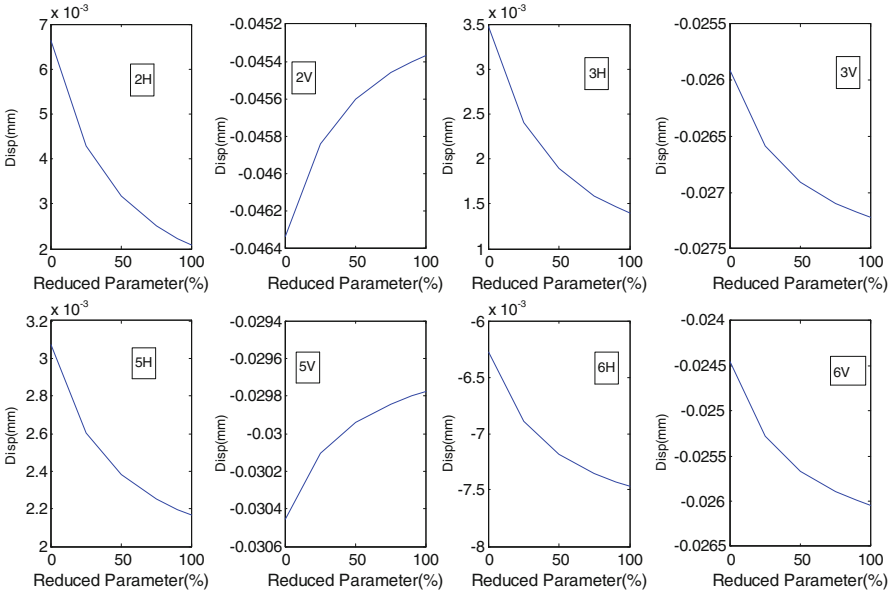

Fig. 2 Displacement vs. reduced parameter (damaged element is 1)

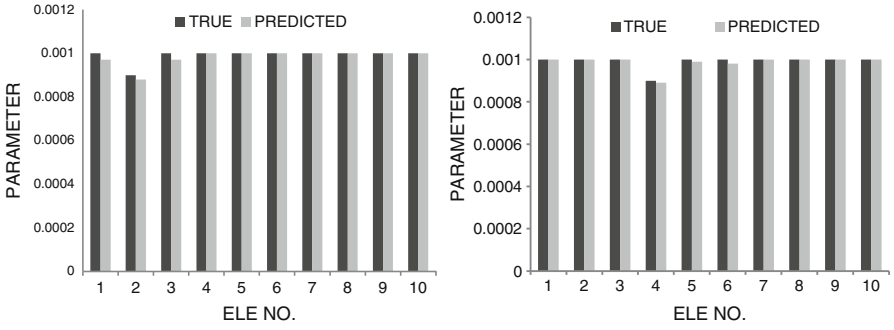

Fig. 3 Identified parameters of truss at various damaged states. (**a**) Bottom chord (element no. 2) is damaged, (**b**) diagonal (element no. 4) is damaged

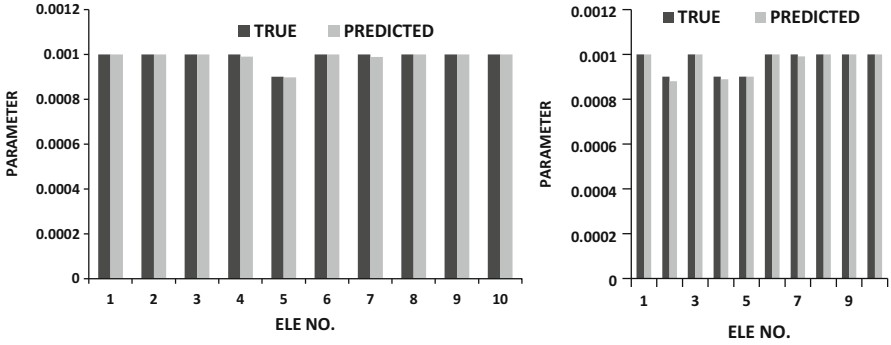

Fig. 4 Identified parameters of truss at various damaged states. (**a**) Vertical element (element no. 5) is damaged, (**b**) all types of elements are damaged

Fig. 5 Comparison of errors

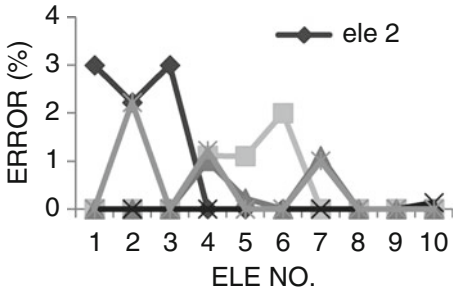

All types of element, i.e., horizontal elements (element no. 2), diagonal element (element no. 4), and vertical element (element no. 5), are damaged by 10% of its axial rigidity. The prediction of parameters with the proposed technique in this multiple damage case is also satisfactory (Fig. 4b).

The comparison of errors in different damage cases is shown in Fig. 5.

It is clearly shown in the figure that the error is within 0–3%. The errors may be decreased further with the inclusion of extra MDOF.

3.2 Problem 2

To validate the proposed methodology, another truss at different states is numerically studied as shown in Fig. 6. The undamaged properties are given as cross-sectional area, $A = 0.0001\ \mathrm{M}^2$, and modulus of elasticity of each element, $E = 2.1 \times 10^8\ \mathrm{KN/M}^2$. The most sensitive MDOF are selected with the help of forward problem (Fig. 7).

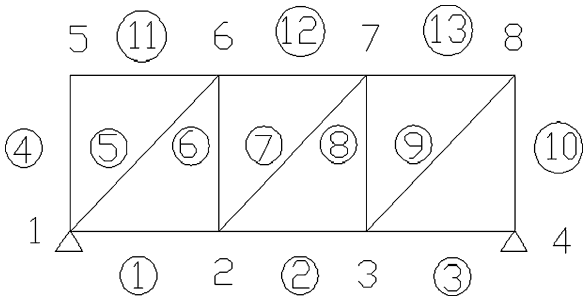

Fig. 6 A 13-element truss

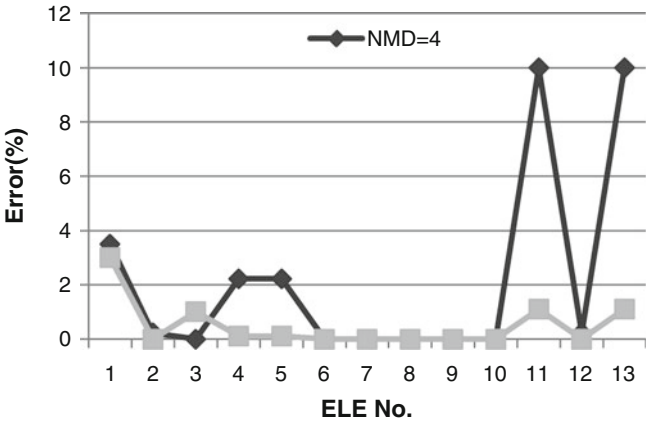

Fig. 7 Comparison of errors

4 Conclusions

System identification of truss using limited static test data is simple, and experimental data can easily be collected in real situation. Structural damage refers mainly to the stiffness reduction, so the static displacements are the primary and simple responses which may be used as the inputs to identify the present state of the structure. An identification technique based on changes in limited displacement data is studied with the sensitivity analysis in this chapter. However, the accuracy of the predicted structural properties depends on the selection of the measurement degrees of freedom (MDOF) and might lead to unreliable damage detection. The structural properties, namely, axial rigidity for each element, are derived with a two-stage analysis process, namely, MDOF selection and parameter identification. The damage is subsequently identified by comparing these structural parameters at undamaged and damaged states. Various types of damages with different locations and degrees have been considered to validate the applicability

of the proposed method. It has been observed that the selection of MDOF plays a great role to identify the damage with adequate accuracy. It is also observed that number of measurement plays a great role to identify the damage with adequate accuracy. The rank of the sensitivity matrices is important and responsible for the accuracy of the stiffness parameter identification. It may be inferred that limited static test data at selected MDOF with sensitivity analysis may able to identify structural damage with sufficient accuracy.

Acknowledgments It is acknowledged to DST-PURSE program of Jadavpur University under Department of Construction Engineering for providing necessary facility and infrastructure for this part of the research work.

References

1. Aja AM (2000) Sub-modeling techniques for static analysis. In: MSC Software first south European technology conference, Principaute de Monaco, 7–9 June 2000
2. Bakhtiari-Nejad F, Rahai A, Esfandiari A (2005) A structural damage detection method using static noisy data. Eng Struct 27:1784–1793
3. Hajela P, Soeiro FJ (1990) Structural damage detection based on static and modal analysis. AIAA J 28(6):1110–5
4. Hjelmstad KD, Wood SL, Clark SJJ (1992) Mutual residual energy method for parameter estimation in structures. J Struct Eng ASCE 118(1):223–42
5. Sanayei M, Nelson RB (1986) Identification of structural element stiffness from incomplete static test data. Society of Automotive Engineering, Technical paper ser, SAE-861793, pp 7.1237–7.1248
6. Sanayei M, Onipede O (1991) Damage assessment of structures using static test data. AIAA J 29(7):1174–1179
7. Sanayei M, Scampoli S (1991) Structures element stiffness identification from static test data. J Eng Mech Div ASCE 117(EM6), pp 1021–1036
8. Sheena Z, Unger A, Zalmanovich A (1982) Theoretical stiffness matrix correction by using static test results. Isr J Technol 20:245–53
9. Wang D, Haldar A (1997) System identification with limited observations and without input. J Eng Mech 123(5):504–511
10. Wu JR, Li QS (2006) Structural parameter identification and damage detection for a steel structure using a two stage finite element model updating method. J Construct Steel Res 62:231–239

System Identification of Cable-Stayed Bridge: A Case Study

Dutta Atanu Kumar, J.M. Caicedo, and Zarate Boris

Abstract This chapter discusses the issue of system identification as applied to a real-life cable-stayed bridge, the Bill Emerson Memorial Bridge, Missouri, USA. The bridge has been instrumented with a total of 66 accelerometers distributed in the structure and the surrounding soil (Celebi, Earthq Spectra 22:609, 2006). The identification procedure uses 66 accelerometer data and 25 channel time histories, collected from relevant locations. This chapter compares the efficacy of different procedures of identifying modal parameter of this cable-stayed bridge. The methods discussed in this chapter are SSI (subspace identification), ARMAV (auto-regressive and moving average vector) and NExT-ERA (natural excitation technique and eigenvalue realization algorithm). The SSI shows results similar to that obtained by ARMAV as reported by Song et al. (Application of ARMAV for modal identification of the Emerson Bridge. In: Third international conference on bridge maintenance, safety and management, Porto, Portugal, 2006). The high point of SSI is in using less number of parameters resulting in faster and easier implementation. SSI has also shown improvement over NExT-ERA (natural excitation technique and eigenvalue realization algorithm) with slightly higher average MAC (modal assurance criteria) values and lower MAC standard deviations (Caicedo et al., System identification and model updating of the Bill Emerson Memorial Bridge. In: 4th world conference on structural control and monitoring, San Diego, CA, 11–13 July, 2006).

Keywords System identification • ARMAV • NExT-ERA

D.A. Kumar (✉)
Department of Civil Engineering, Tezpur University, Assam, India
e-mail: atanu@tezu.ernet.in

J.M. Caicedo • Z. Boris
Civil and Environmental Engineering, University of South Carolina, Columbia, SC, USA
e-mail: caicedo@cec.sc.edu; zarate@engr.sc.edu

S. Chakraborty and G. Bhattacharya (eds.), *Proceedings of the International Symposium on Engineering under Uncertainty: Safety Assessment and Management (ISEUSAM - 2012)*,
DOI 10.1007/978-81-322-0757-3_51,

1 Introduction

Cable-stayed bridges have gained popularity in the category of long-span bridges over the last three decades due to improved structural performance and aesthetic appeal in comparison to suspension bridges. It is appreciated that development of a numerical model, which simulates natural frequencies and mode shapes of the structure, is an important step for computation of dynamic responses of any structure. However, building a numerical model to represent dynamic characteristics of a highly flexible structure, such as the cable-stayed bridge, is rather difficult as the structure exhibits complex behaviour with the flexural, lateral and torsional motions being very often coupled. As a consequence, structural characteristics and responses predicted by idealized finite element (FE) models have discrepancies and errors as compared to those obtained from the actual measurements. For example, an initial numerical model is found to be incorrect by as much as 10% in the lowest frequencies [7]. These inaccuracies are due to a combination of factors, including but not restricted to approximations in the finite element derivations, mismodelling of structural elements, differences in actual material properties and dimensions from those assumed in the model and lack of convergence of the numerical model.

A first heuristic iteration between an identification and numerical model typically reduces frequency errors to 5%, and a second iteration can further reduce them to 1–2%. Such models will be far more accurate for analysis such as flutter, dynamic loads and reflections. Sometimes, particularly in closed-loop control applications, even the refined numerical model of the plant is inadequate for the design of robust high-gain controllers. In such cases, direct use of the indentified plant model in control design is sometimes the only way to achieve desired performances.

Modal identification through full-scale testing is the most reliable method to determine the true dynamics properties (e.g. natural frequencies, damping ratios and mode shapes) of a structure. This serves as a basis for validating and/or updating an analytical model of a structure so that the model represents the actual structural properties and the boundary conditions. The grey areas of the modelling of a cable-stayed bridge, such as the damping property of the structure, idealization of bearings, appropriate representation of mass and stiffness, can be suitably incorporated in the FE model through model updating in conjunction with the system identification data.

2 System Identification: General

2.1 Definition

System identification is the process of improving a mathematical representation of a physical system using experiential data [7]. There are basically three types of identifications: modal parameter identification, structural-model parameter identification and control-model identification. Modal parameter identification and

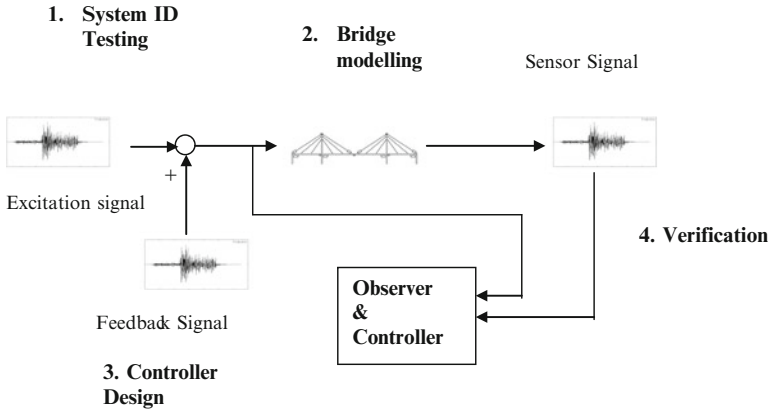

Fig. 1 Schematic diagram of control of cable-stayed bridges through System Identification

structure-model identification are used in structural engineering, whereas control-model identification is used in control of flexible structures such as aerospace structures.

2.2 Use of System Identification

A good understanding of the connection between system identification and control is essential for the success in the areas of vibration suppression in cable-stayed bridges. The procedure for control of cable-stayed bridges through system identification has been illustrated in Fig. 1

3 The Bridge

3.1 General

The cable-stayed bridge used for this study is the Bill Emerson Memorial Bridge in Missouri, USA, shown in Fig. 2. The bridge crosses the Mississippi River in Cape Girardeau, Missouri, and was designed by the HNTB Corporation. The bridge was opened to traffic on Dec 13, 2003.

Dyke et al. [4] formulated the benchmark control problem on this bridge with the design of an active controller against seismic excitation. Many researchers used the model for the benchmark control studies, structural health monitoring [1] and structural identification [8]. The structural details of the bridge have been given in detail by Dyke et al. [4] and Caicedo [1]

Fig. 2 Bill Emerson Memorial Bridge, Missouri, USA

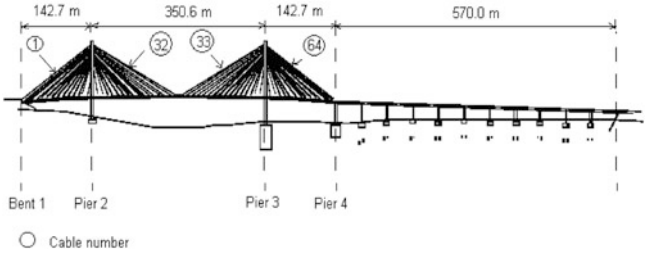

Fig. 3 Line diagram of the bridge

3.2 Structural Data

A line diagram of the bridge has been shown in Fig. 3. Structural data is given in detail elsewhere [4]. Sixteen numbers of shock transmission devices of capacity 6.67 MN each are employed in the interface between the pylon and the deck. They are oriented in the longitudinal direction of the bridge to allow for expansion of the deck due to temperature rise. These devices are found to be extremely stiff under dynamic condition and were considered as rigid links [4]. The bridge deck is restrained in the transverse direction in the deck pylon support with earthquake restrainers. Further, the deck is restrained in the vertical direction at both pylons. The bearings at bent 1 and pier 4 are designed to allow longitudinal displacement and rotation about the transverse and vertical axes.

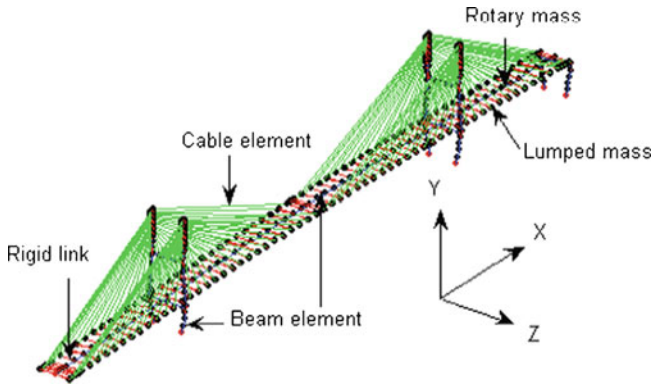

Fig. 4 Finite element model

4 Finite Element Model

A finite element model of the Emerson Bridge was previously developed for the benchmark problem for seismic response control of cable-stayed bridges by Dyke et al. [4]. The model was subsequently modified and transferred to the Matlab® environment for structural health monitoring study [1]. The finite element model has 573 nodes, 418 rigid links, 156 beam elements, 198 nodal mass elements and 128 cable elements. This has been illustrated in Fig. 4. The rigid links were modelled using constrain equations. The pylon bases were considered as fixed. The deck was idealized as a spine with half the deck masses lumped at both sides of the spine. Corrections for mass moment of inertia were applied to the spine node as the distributed masses are lumped and placed at the end of the rigid links.

4.1 Modal Characteristics

A mixed incremental-iterative method [1] was used to perform the nonlinear static analysis in order to arrive at the dead load deformed equilibrium position. The model from the dead load deformed configuration has been used to determine the dynamic characteristics of the structure through eigenvalue analysis. The first four flexural frequencies (Hz) as obtained from this study were 0.291, 0.392, 0.608 and 0.674.

5 System Identification of the Bridge

The type of system identification adopted here is modal parameter identification. Ambient vibration data has been used for identification. It is a costly proposition to capture all the mode shapes with sensors for a flexible structure such as a

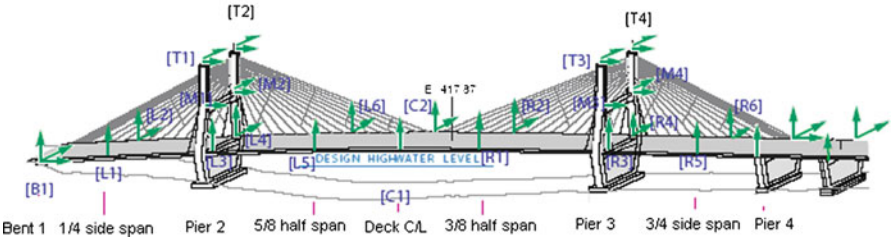

Fig. 5 Locations of sensors

cable-stayed bridge. However, first few flexural modes may be easily captured by sensing the vertical and transverse acceleration data at salient locations of the bridge.

5.1 Location of Sensors

In the present study, sensor data has been used to reconstruct first few flexural modes. Out of the total of 66 accelerometers, evenly distributed in the superstructure, substructure and surrounding soil, 23 are vertical sensors, 11 are sensors in the longitudinal direction of the bridge and remaining 22 are oriented in the transverse direction. However, for the present study, data from only 25 sensors, located at key locations of the superstructure as illustrated in Fig. 5, have been utilized.

5.2 Characteristics of Signals: PSD

In the present study, 6 h of 25 channels of acceleration data corresponding to sensors located in the deck and pylons have been used for modal identification. The sensor information of 17 accelerometers on the deck located in the vertical direction and 8 accelerometers located in the pylon oriented in the longitudinal direction have been used for the modal identification. The characteristics of the signals have been shown in Figs. 6 and 7.

5.3 Modal Identification

In a previous study, ARMAV was used by Song et al. [8] to detect the natural frequencies and mode shapes of the Bill Emerson Memorial Bridge using 16 channels of acceleration data from the sensors on the deck. The subspace identification method (SSI) has been used in the present study, and comparison of results is made with the results obtained by NExT-ERA method.

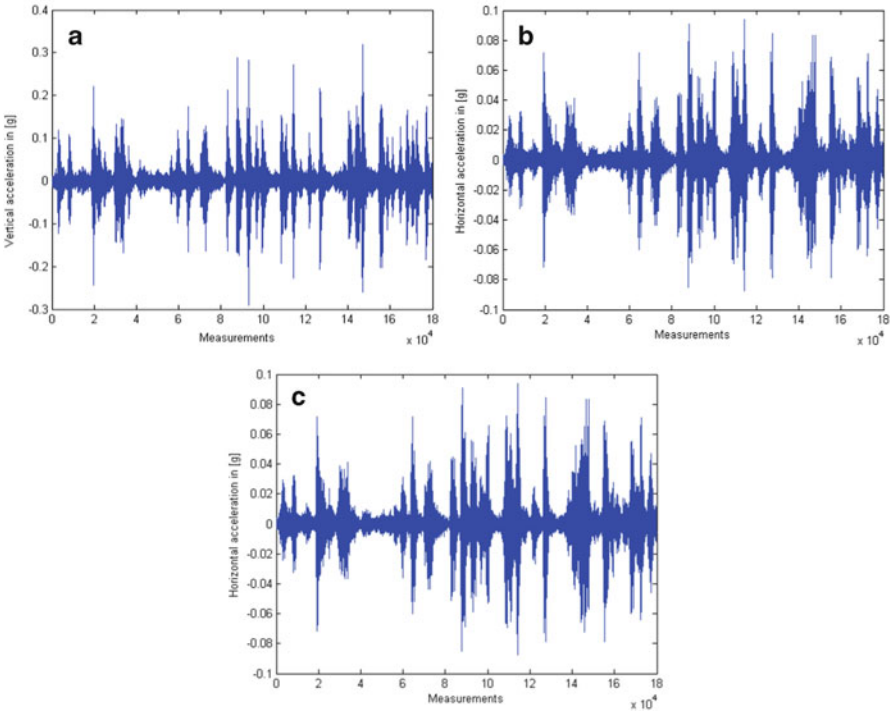

Fig. 6 Sensor signal: (**a**) mid-span, (**b**) left pylon, (**c**) right pylon

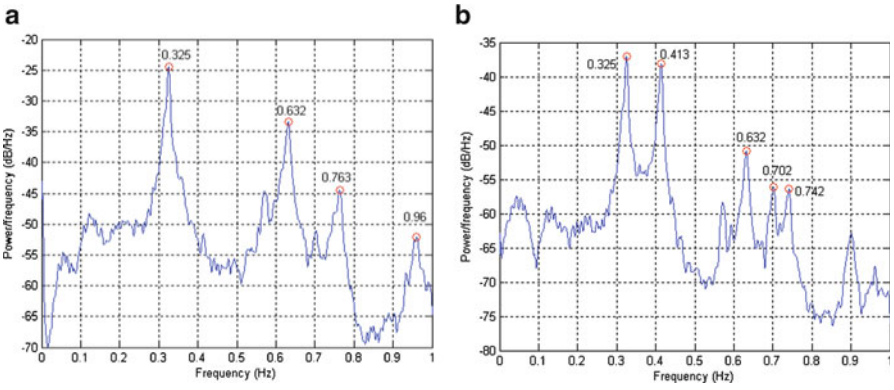

Fig. 7 PSD of signal: (**a**) top of left pylon and (**b**) signal from mid-span

5.3.1 Subspace Identification

The term 'subspace' arises from the fact that linear models can be obtained from row and column 'spaces' of certain matrices, calculated from input-output data

Table 1 Components of subspace identification

System	Geometry	Algorithm
High-order state sequence	Projection (orthogonal or oblique)	QR decomposition
Low-order state sequence	Determine finite dimension subspace	(Generalized) singular value decomposition
System matrices	Linear relations	Least squares

from dynamic testing. Typically, the columns of these matrices contain information about the model. The rows of these matrices may be used to obtain a Kalman state sequence directly from the input-output data without any knowledge of the system.

Subspace identification algorithms are based on system theory, linear algebra and statistics as illustrated in Table 1.

The main conceptual advantages of subspace method over the classical methods are given elsewhere [9]. The new features of subspace identification method could be summarized elsewhere [9]. A common mathematical background for subspace algorithms for linear systems is presented by Van et al. [9].

5.4 Identification of Modal Properties

After the modal parameters are identified with subspace identification, an automated recognition scheme [5, 6] has been used to detect the true modes from those created by noise and numerical errors. The data available is divided into 36 windows of 10 min of data. A set of natural frequencies, mode shapes and damping ratios has been obtained for each window. The true modes of vibration have been recognized by identifying parameters within some specific predefined values. The parameters used to identify real modes are the natural frequency, MAC and damping values. For a specific mode, the acceptable identified natural frequency should be within 30% of the mean of identified frequency, the damping value should be lower than 5% and the MAC values of the identified mode shapes should be higher than 0.98. Only modes with more than five hits (the same frequency identified more than five times) have been assumed to be real modes, and the others have been discarded as noise. The standard deviation of each natural frequencies and the mean MAC value of the corresponding mode shapes have been calculated. Lower standard deviation on the natural frequencies and mean MAC values closer to one are assumed to be identified with higher confidence.

5.4.1 Identified Parameters

The details of identification by SSI have been presented in Fig. 8. The hits around 0.2 Hz are scattered and considered to be from noise rather than from structural frequencies.

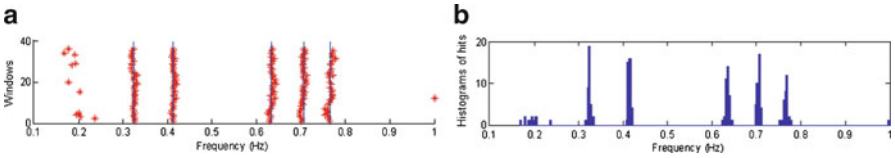

Fig. 8 Details of modal identification by SSI

Table 2 Identified parameters: SSI

Mode	Hits	Frequency (Hz)	Standard deviation of frequency (Hz)	Damping (%)	Standard deviation of damping (%)	MAC	Standard deviation of MAC
1	31	0.324	0.0036	1.05	0.37	0.9977	0.0019
2	16	0.413	0.0026	0.64	0.09	0.9967	0.0023
3	25	0.635	0.0041	0.67	0.20	0.9983	0.0009
4	21	0.706	0.0032	0.73	0.51	0.9962	0.0046

Table 3 Identified parameters: NExT-ERA

Mode	Hits	Frequency (Hz)	Standard deviation of frequency (Hz)	Damping (%)	Standard deviation of damping (%)	MAC	Standard deviation of MAC
1	39	0.324	0.0055	1.41	0.71	0.9963	0.0044
2	37	0.414	0.0045	1.09	0.55	0.9976	0.0029
3	28	0.636	0.0037	1.16	0.70	0.9952	0.0033
4	16	0.708	0.0048	0.96	0.31	0.9904	0.0048

The first four modal parameters identified with the SSI have been presented in Table 2. The number of hits corresponds to the number of times the same mode has been identified when the identification process has been repeated along all the windows. The natural frequencies and damping ratios shown have been calculated as the average of all the identified parameters for each mode.

Overall, the natural frequencies are very similar with those identified with ARMAV by Song et al. [8]. SSI is also observed to be better than NExT-ERA in terms of performance [2] as represented in Table 3. Comparing Table 2 with Table 3, it has been observed that SSI shows high average MAC values and low MAC standard deviation.

5.4.2 Limitation of the Study

It is a costly proposition to capture all the mode shapes with sensors for a flexible structure such as a cable-stayed bridge. It is due to this reason the transverse and torsional modes could not be identified with the sensors used. Moreover, the damping property of real large cable-stayed bridges is not fully understood yet

due to the complicated damping mechanism of the bridges. It is known that bridge damping in general varies with the amplitude of vibration. Therefore, the applicability of an identified damping ratio through ambient vibration tests is still an issue that needs to be evaluated further by using other identification techniques or other dynamic tests with large vibration amplitudes.

6 Conclusion

The study presented the results of system identification of a real-life cable-stayed bridge using the SSI method. The results show improvement over other established method. However, there are limitations which need to be addressed for more realistic capturing of the system. The present work can be a starting point for further realization of system identification.

Acknowledgement The first author also expresses his thanks to National Programme for Earthquake Engineering Education (NPEEE), sponsored by the MHRD, Govt. of India for providing him with financial supports during his stay in the University of South Carolina, USA, where the present work was completed.

References

1. Caicedo JM (2003) Structural health monitoring of flexible civil structures. DSc thesis, Washington University in Saint Louis, Saint Louis, MO
2. Caicedo JM, Dutta AK, Zarate B (2006) System identification and model updating of the Bill Emerson Memorial Bridge. In: 4th world conference on structural control and monitoring, 11–13 July, San Diego, CA
3. Celebi M (2006) Real-time seismic monitoring of the New Cape Girardeau Bridge and preliminary analyses of recorded data: an overview. Earthq Spectra 22:609
4. Dyke SJ, Caicedo JM, Turan G, Bergman L, Hague A, Hague S (2000) Benchmark control problem for seismic response of cable-stayed bridges. In: Proceedings of 2nd European conference on structural control, Paris, 3–6 July 2000
5. Giraldo D (2006) A structural health monitoring framework for civil structures. PhD thesis, University of St. Louis, USA
6. Giraldo D, Caicedo JM, Song W, Mogan B, Dyke SJ (2006) Identification through ambient vibration: a comparative study. In: 24th international modal analysis conference, Saint Louis, MO
7. Juang J (1994) Applied system identification. PTR Prentice Hall, Englewood Cliffs, p 7632
8. Song W, Giraldo D, Clayton EH, Dyke SJ, Caicedo JM (2006) Application of ARMAV for modal identification of the Emerson Bridge. In: Third international conference on bridge maintenance, safety and management, Porto, Portugal
9. Van VP, De Moor B (1996) Subspace identification for linear systems: theory – implementation – applications. Kluwer Academic Publishers, Boston

Dynamic Response of Steel-Sand Composite Stiffened Plates Under Blast Loading

Manmohan Dass Goel, Tanusree Chakraborty, and Vasant A. Matsagar

Abstract The present study focuses on the effectiveness of steel-sand composite stiffened plates under explosive loading for blast-resistant design. Dynamic response of steel-sand composite stiffened plates, with various stiffener layouts under blast loading, is analysed using commercially available finite element (FE) software Abaqus/Explicit. The steel plates and stiffeners are modelled using shell elements, and the effect of strain rates is incorporated through Johnson-Cook (J-C) material model. Sand is modelled as a continuum between the two steel plates. Sand response is simulated using the built-in Drucker-Prager plasticity model in Abaqus considering the strain rate effect. The contact planes between sand and the steel plates are modelled using the general contact formulation in Abaqus. Blast load is applied in the form of an equivalent rectangular uniform pressure pulse. The effect of different thicknesses of the sand layer in blast response mitigation has been investigated. The steel-sand composite stiffened plates exhibit lesser central point displacement under blast loading as compared to when no stiffeners are provided.

Keywords Blast resistant • Explosion load • Steel-sand composite • Stiffened plate • Strain rate

1 Introduction

Development of resilient civil infrastructure requires that the structures can efficiently and economically resist unanticipated loads and can be brought back to functionality with minimum repair and within reasonable time if subjected to

M.D. Goel
Advanced Materials and Processes Research Institute, CSIR-AMPRI, Bhopal 462 064, India

T. Chakraborty (✉) • V.A. Matsagar
Department of Civil Engineering, Indian Institute of Technology (IIT) Delhi, Hauz Khas, New Delhi 110 016, India
e-mail: tanusree@civil.iitd.ac.in

S. Chakraborty and G. Bhattacharya (eds.), *Proceedings of the International Symposium on Engineering under Uncertainty: Safety Assessment and Management (ISEUSAM - 2012)*,
DOI 10.1007/978-81-322-0757-3_52,

extreme events. An unanticipated load on a civil infrastructure can be caused by human activities, e.g. blast. In order to safeguard civil engineering facilities under blast-induced extreme shock wave load, it is necessary to incorporate shock-absorbing materials in civil engineering constructions through sandwich or composite structural framework. The sandwich structures are the emerging protective structures composed of stiff face-sheets made up of steel or concrete filled with metallic or non-metallic foam or sand in between the face-sheets. The strong and stiff face-sheet bears in-plane loads and transverse bending stress, whereas the core adds to the shear rigidity along the planes perpendicular to the face-sheet. The composite structures dissipate large amount of energy by plastic deformation under explosive loading.

Till the date, different materials have been explored to be used as the inner core of a composite structure for blast response mitigation such as fibre-reinforced polymer (FRP) composites, polymeric foams and metal foams to name a few [10]. Many researchers have studied the performance of composite plates with metallic or non-metallic foam cores in blast-resistant design of structures [2–4, 11]. Qiao et al. [12] have mentioned the use of sand core in composite plates and in reinforced concrete barrier structures to mitigate blast response. The easy availability and low cost of sand as compared to metallic and non-metallic foams and the energy dissipation capability of sand through friction and particle breakage make sand a suitable choice for response mitigation against blast loads. However, in the past literature, studies on sand core composite stiffened plates for blast response mitigation have not been attempted. Therefore, it is of utmost importance to study the performance of sand core composite stiffened plates for blast response mitigation.

The objectives of the present study are (1) to model steel-sand composite plates with and without stiffeners under blast loading; (2) to study the stress, deformation, strain energy and kinetic energy response of the steel-sand composite plates for different sand layer thicknesses (t_s) and stiffener configurations and (3) to compare the deformation results obtained from steel-sand composite plate analyses with the results obtained from analysis of steel plate under blast loading.

In the present study, three-dimensional (3-D) dynamic analyses of steel-sand composite structures under explosive loading have been performed using commercially available finite element (FE) software Abaqus Version 6.11 [1]. Sand response has been simulated using a strain rate-dependent Drucker-Prager plasticity constitutive model. The steel plates and stiffeners are modelled using strain rate-dependent Johnson-Cook (J-C) material model. The explicit dynamic analysis procedure in Abaqus has been used. Parametric sensitivity studies are performed by varying (1) sand layer thicknesses (t_s) and (2) stiffener configurations.

2 Steel and Sand Constitutive Models

Explosive loading on steel and sand can give rise to very high rates of strain (10^2 to 10^4 s^{-1}). In order to take the strain rate-dependent stress–strain response of steel into account, the analysis is carried out using strain rate-dependent Johnson-Cook

(J-C) model [7, 8]. The J-C model is a viscoplastic empirical model that depicts the effects of strain hardening, strain rate sensitivities and temperature softening. In the present study, the strain rate effects have been included by adjusting the dynamic yield stress, σ, according to the J-C model as follows:

$$\sigma = (A + B\varepsilon^n)(1 + C\log_e \varepsilon^*)(1 - T^{*m}) \tag{1}$$

where $\varepsilon^* = \dot{\varepsilon}/\dot{\varepsilon}_0$ is the dimensionless plastic strain rate at reference strain rate $\dot{\varepsilon}_0 = 1\ \mathrm{s}^{-1}$, $\dot{\varepsilon}$ is the equivalent plastic strain rate, T^* is the homologous temperature and m is a material constant. However, temperature dependence has not been considered in the present study.

The sand core is considered to follow the built-in Drucker-Prager material model in Abaqus with strain rate-dependent hardening. The yield surface, F, of Drucker-Prager model is given by

$$F = \frac{q}{2}\left[1 + \frac{1}{K} - \left(1 - \frac{1}{K}\right)\left(\frac{r}{q}\right)^3\right] - p' \tan\beta - d = 0 \tag{2}$$

where q is the deviatoric stress $\left[= \sqrt{3/2}\sqrt{s_{ij} : s_{ij}}\right]$, s_{ij} is the deviatoric stress tensor, p' is the mean stress $[= (\sigma'_1 + \sigma'_2 + \sigma'_3/3)]$, K is a scalar parameter that determines the shape of the yield surface and maintains the convexity of the yield surface in the deviatoric (π) plane and r is the third invariant of the deviatoric stress tensor. The parameter β is related to the angle of internal friction, ϕ, at the stage of no dilatancy (the critical state of sand) using the following correlation:

$$\tan\beta = \frac{\sqrt{3}\sin\phi}{\sqrt{1 + (1/3)\sin^2\phi}} \tag{3}$$

and d is the hardening parameter related to cohesion, c, through the following correlation:

$$\frac{d}{c} = \frac{\sqrt{3}\cos\phi}{\sqrt{1 + (1/3)\sin^2\phi}} \tag{4}$$

For sands, the cohesion (c) is considered to be zero. The plastic potential surface, G_P, of the model is given by

$$G_\mathrm{P} = \frac{q}{2}\left[1 + \frac{1}{K} - \left(1 - \frac{1}{K}\right)\left(\frac{r}{q}\right)^3\right] - p' \tan\psi_{\mathrm{tp}} \tag{5}$$

where ψ_{tp} is related to the dilatancy angle, ψ, of sand as follows:

$$\tan\psi_{\mathrm{tp}} = \frac{\sqrt{3}\sin\psi}{\sqrt{1 + (1/3)\sin^2\psi}} \tag{6}$$

A nonassociated flow rule is considered in the present analysis by considering the dilatancy angle of sand to be different from the friction angle.

3 Finite Element Model and Analysis

In the present study, 3-D explicit dynamic analyses of steel-sand composite plates under explosive loading have been performed using commercially available FE software Abaqus. Square steel-sand composite plates of size 2 m × 2 m are considered. Figure 1 shows a typical steel-sand composite plate with stiffener.

The composite plate consists of face-sheet and stiffened back-sheet with a sand core in between. The thickness of face-sheet (t_{fs}) is 10 mm, and the thickness of back-sheet (t_{bs}) is 10 mm. The explosive load is applied on the face-sheet. Three different thicknesses of sand core considered are 50, 100 and 150 mm as shown in Fig. 1.

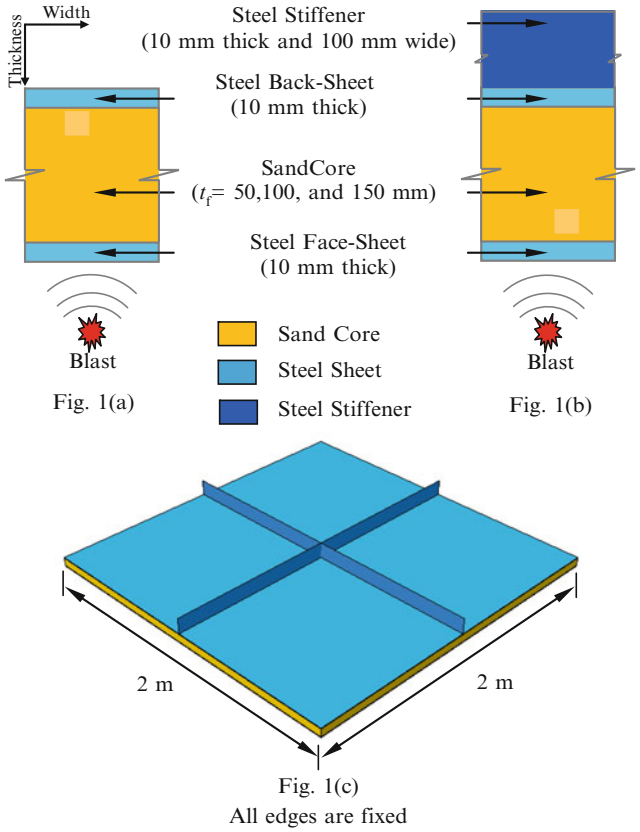

Fig. 1 (**a**) Conventional composite plate, (**b**) stiffened steel-sand composite plate and (**c**) representative 3-D model of stiffened steel-sand composite plate

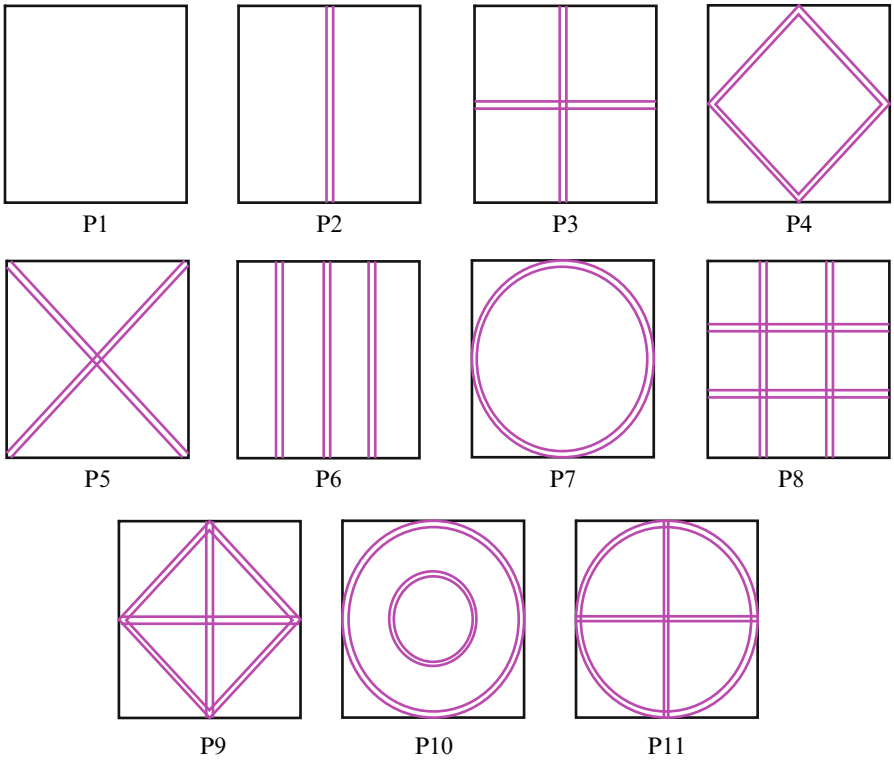

Fig. 2 Plate configurations arranged with increasing weights

Ten different stiffener configurations have been chosen for the steel back-sheet. Figure 2 shows one unstiffened steel-sand composite plate (P1) and the stiffened steel-sand composite plates with ten different stiffener configurations (P2 to P11). The composite plates P2 to P11 are arranged as per their increasing weights. The stiffeners are 100 mm in width and 10 mm in thickness for all the configurations and with the same material as that of the face- and back-sheets. The description of the model, loading, boundary and contact conditions, material properties, analysis steps and solution scheme used are described in the following sections.

3.1 Finite Element Model

The FE models of stiffened steel-sand composite plates are developed using three-dimensional part option. The extruded shell base feature available in Abaqus has been used to create geometry of the face- and back-sheets. A 3-D part with solid feature is used to define the sand core. Stiffeners are created by adding an extruded shell feature implying perfect connection without any additional constraint. Care is taken not to overlap the material of the stiffener with the

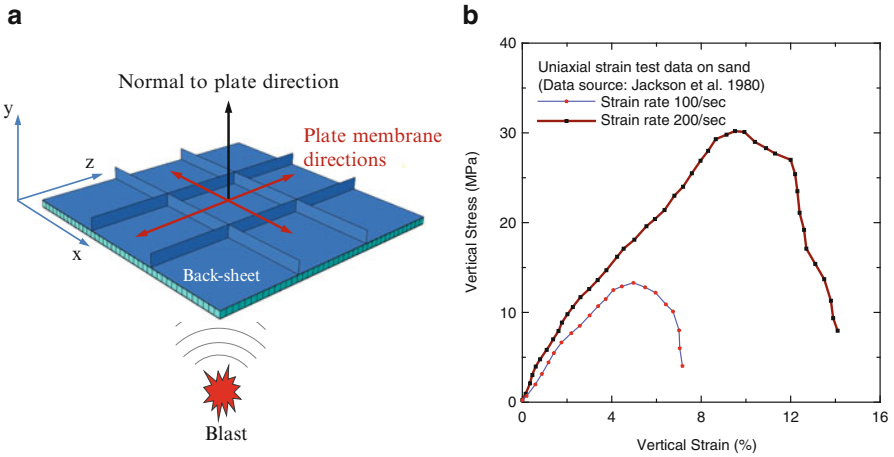

Fig. 3 (**a**) Key figure for steel-sand composite plate and (**b**) vertical stress–strain behaviour of sand

back-sheet by offsetting its reference surface from mid-surface, thus avoiding the possibility of additional stiffness at the junction. The back-sheet with stiffeners is created by removing material from a thick blank. It is a single part and meshed in one part only, thus implying a single part without any weld or joint/interface between the plate and stiffener. The steel plates along with the stiffeners have been modelled with four-node, linear shell elements with reduced integration, hourglass control and finite membrane strains (S4R). The sand core has been modelled with eight-node linear, hexagonal, reduced integration elements with hourglass control (C3D8R). First-order elements are used because of their lumped mass formulation, which are preferred to model the effect of stress waves than the consistent mass formulation used in the second-order elements [2].

A key figure of the steel-sand composite plate is presented in Fig. 3a. All four sides of the steel plates and sand core are restrained in x, y and z directions. The interface between the steel plates and sand is modelled using frictional contact and the general contact algorithm in Abaqus. A coefficient of friction of 0.5 is assumed at the steel-sand interface.

3.2 Sand and Steel Material Properties

The stress–strain response of sand is modelled using Drucker-Prager material constitutive law. The elastic- and rate-independent elastoplastic material properties assumed for sand are given in Table 1. The strain rate-dependent Drucker-Prager hardening curves for sand under uniaxial compression are obtained from Jackson et al. [6]. Figure 3b shows the vertical stress–strain plot for sand at 100 and 200 s^{-1} strain rates. The stress–strain curves are converted into true stress-logarithmic plastic strain according to Abaqus/Explicit manual.

Table 1 Material properties for sand

Parameter	Symbol	Values
Density	ρ	1,800 kg/m^3
Modulus of elasticity	E	50 MPa
Poisson's ratio	v	0.3
Friction angle	ϕ	30°
Dilatancy angle	ψ	10°
Yield surface shape parameter	K	0.8
Initial yield strength of sand	σ_y	100 kPa

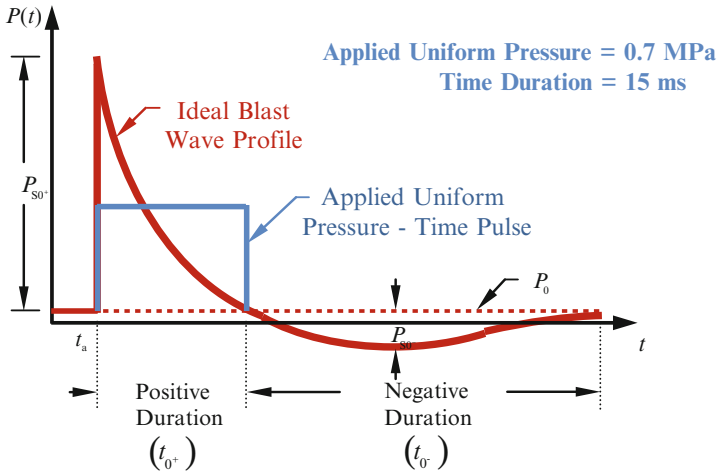

Fig. 4 Typical blast wave profile resulting from high explosives and applied loading

The face-sheet and stiffened back-sheet are made of mild steel with Young's modulus, $E = 210$ GPa, Poisson's ratio, $v = 0.3$, and density $= 7{,}800$ kg/m^3. The static yield stress of the plate material is 300 MPa. The stress–strain curves for steel obtained from mechanical testing are converted into true stress and logarithmic plastic strain according to Abaqus [1]. The material constants are obtained from mechanical testing and adopted herein for strain rates of 50 and 100 s^{-1}, respectively, as (1) $A = 375$ MPa, $B = 600$ MPa, $n = 0.07$, $C = 0.09$ and (2) $A = 360$ MPa, $B = 635$ MPa, $n = 0.114$, $C = 0.075$. These values are computed based on tensile test data of the material as per the J-C model by neglecting the temperature effects [2].

3.3 Blast Load Simulation

The blast load is considered to be caused by explosive-induced pressure, P, on the exposed surface of the face-sheet. A typical blast wave profile is presented in Fig. 4. The ideal blast wave load is described by an exponentially decaying function of time, t, as

$$P(t) = P_{S0^+}\left(1 - \frac{t}{t_{0^+}}\right)\exp\left[-\frac{b(t - t_a)}{t_{0^+}}\right] \tag{7}$$

where $P(t)$ is the time-dependent pressure (MPa), P_{S0^+} is the peak overpressure (MPa), t_{0^+} is the positive phase duration (milliseconds), b is dimensionless wave decay coefficient and t_a is the wave arrival time (milliseconds). The decay coefficient (b) is related to the ratio of peak overpressure (P_{S0^+}) and the maximum negative suction pressure (P_{S0^-})as

$$\log_e\left(b\left|\frac{P_{S0^+}}{P_{S0^+}}\right|\right) + b + 1 = 0 \tag{8}$$

Based on further simplification of this equation by Lam et al. [9], the decay coefficient is expressed with reference to scaled distance, Z $(= R/W^{1/3})$, as

$$b = Z^2 - 3.7Z + 4.2 \tag{9}$$

where W is the charge (explosive) mass in kg and R is the standoff distance in m. The correlation between the positive phase duration, t_{0^+}, and standoff distance, R, is conservatively expressed in the following form [9]:

$$\log_{10}\left(\frac{t_{0^+}}{W^{1/3}}\right) \approx -2.75 + 0.27\log_{10}\left(\frac{R}{W^{1/3}}\right) \tag{10}$$

In the present investigation, a charge mass of 100 kg with a scaled distance, $Z = 0.135$ m/kg$^{1/3}$, is considered to be detonated, and the impulse (I) is computed using the classical Held's equation [5]. The blast load is simulated in the present FE models by applying uniform pressure load with magnitude of 0.7 MPa and duration of $t_{0^+} = 15$ms on the plate area as shown in Fig. 4 having the same impulse (I).

3.4 Solution Scheme

The analyses have been performed in a single step, for total duration of 25 ms using the dynamic explicit procedure in Abaqus. Abaqus performs dynamic analysis using explicit central difference integration scheme. The method is conditionally stable for time increments (Δt) that are smaller than Courant time limit, $\Delta t \leq l/c$, where l is the smallest element dimension and c is the speed of sound wave in medium in which it travels. Also, the artificial bulk viscosity is activated to properly represent propagation of the induced compressive stress wave by employing quadratic and linear functions of volumetric strain rates with default values of 1.2 and 0.06, respectively [1].

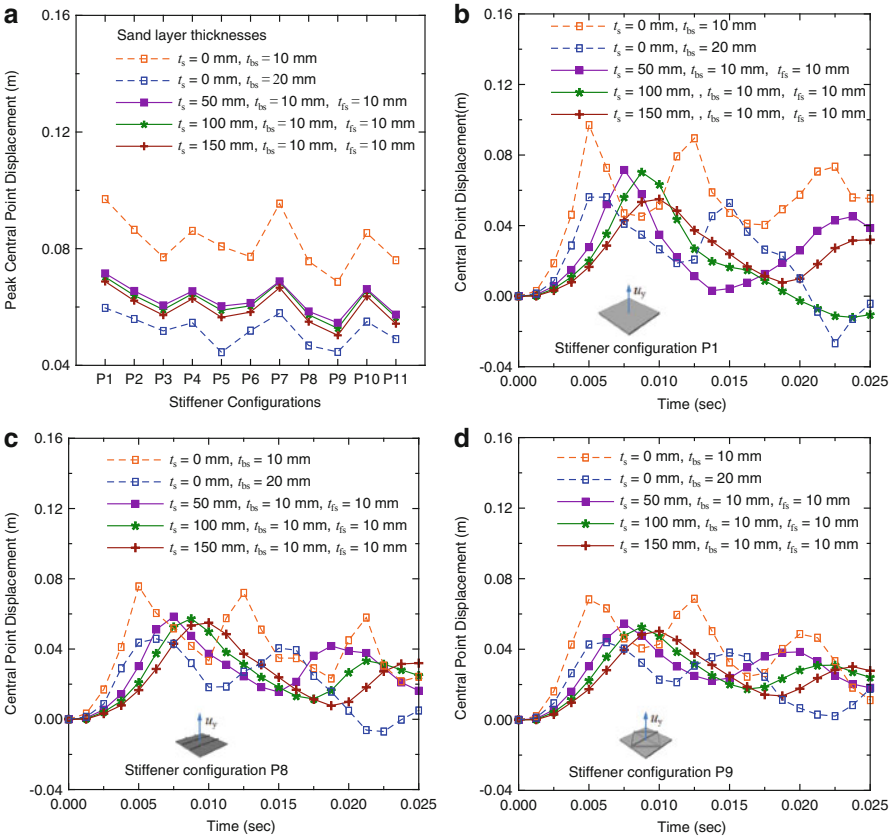

Fig. 5 (**a**) Peak displacement of back-sheet central point for different stiffener configurations and sand core thicknesses; back-sheet central point displacement time histories for stiffener configurations, (**b**) P1, (**c**) P8 and (**d**) P9

4 Results and Discussions

Figure 5a shows the peak displacement of the back-sheet central point in the direction normal to the plane of the sheet. The results have been plotted for steel-sand composite plate without stiffener (P1) with 50-, 100- and 150-mm sand layer thicknesses. Moreover, results are also presented for the stiffened steel-sand composite plates (P2 to P11) with 50-, 100- and 150-mm sand layer thicknesses. Also, the displacement response of stiffened and unstiffened steel plates without sand core with different cases of t_{bs} has been plotted for comparison purpose. Table 2 summarizes the peak central point displacement values for the composite and the non-composite plates and the percentage reduction in blast-induced displacement when $t_{bs} = 10$ mm.

It is observed that the steel-sand composite plates always show more than 20% displacement reduction as compared to the non-composite plates when $t_{bs} = 10$ mm. Displacement reduction is more for 150-mm sand layer thickness as compared

Table 2 Peak central point displacement of the back-sheet in the steel-sand composite plate perpendicular to the plane of the sheet and blast response reduction

	Peak central point displacement (mm) of back-sheet with $t_{bs} = 10$ mm				Response reduction (%) with respect to steel plate without sand layer		
	Sand layer thicknesses (mm)				Sand layer thicknesses (mm)		
Plate	0	50	100	150	50	100	150
P1	97.0	71.5	70.3	68.7	26.24	27.53	29.13
P2	86.5	65.5	64.0	62.2	24.23	26.02	28.10
P3	77.1	60.6	59.1	57.2	21.39	23.32	25.77
P4	86.1	65.4	64.5	62.8	24.01	25.05	27.04
P5	80.8	60.3	58.9	56.5	25.36	27.09	30.10
P6	77.2	61.4	60.4	58.3	20.51	21.80	24.58
P7	95.5	68.8	68.6	66.6	27.92	28.17	30.22
P8	75.7	58.5	57.3	55.0	22.68	24.23	27.35
P9	68.6	54.6	52.7	50.3	20.45	23.23	26.73
P10	85.4	66.2	65.7	63.6	22.49	22.99	25.46
P11	76.0	57.4	56.5	54.3	24.49	25.70	28.61

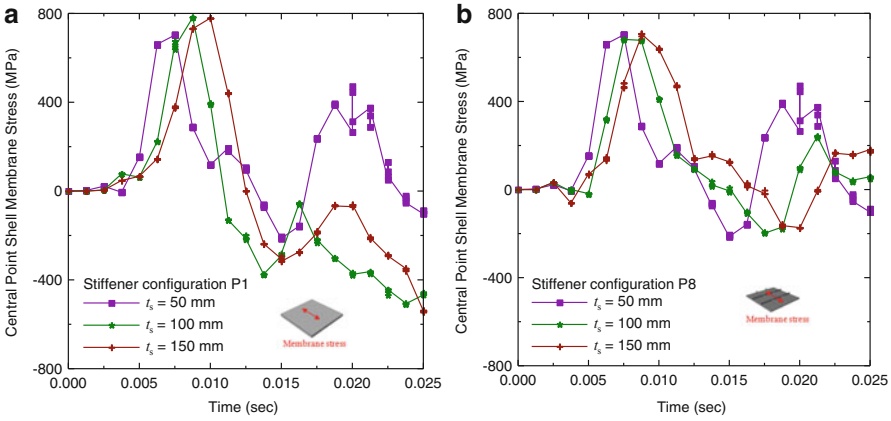

Fig. 6 Back-sheet central point membrane stress time histories for stiffener configurations P1 and P8

to the 50- and 100-mm sand layer thicknesses due to increased dissipation of energy in thicker sand layers. In all the cases, lowest displacement is observed for P9 and highest displacement is observed for P1. The plate P8 also shows considerably less displacement. Hence, in the present study, focus is on the displacement, stress and energy response of P1, P8 and P9 plates. For non-composite plates with $t_{bs} = 20$ mm, lower displacement is observed as compared to the composite plates which is attributed to their higher stiffness and lower mass.

Figure 5b, c and d show the displacement time-history plots for P1, P8 and P9 for different sand layer thicknesses and without sand layer. Also, the displacement response of stiffened and unstiffened steel plates without sand core with

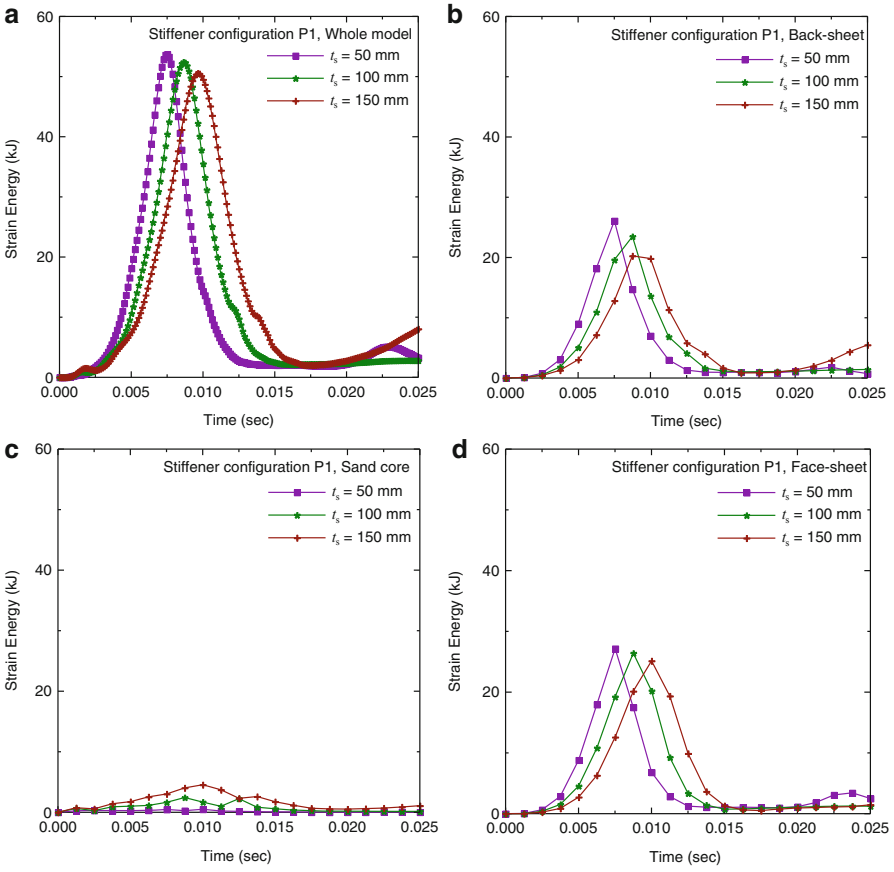

Fig. 7 Variation of strain energy in different components of steel-sand composite plate with stiffener configurations P1

different cases of t_{bs} has been plotted for comparison purpose. For the plates without sand layer, two distinct peaks are observed in the displacement time-history plots. On the contrary, the composite plates show dissipation of plate displacement after the first peak. In general, higher displacement is observed for unstiffened plates as compared to the stiffened plates owing to their lower stiffness.

Figure 6a and b show the membrane stress time history in the back-sheet for composite plates P1 and P8 with 50-, 100- and 150-mm sand layer thicknesses. In plate P1, higher stress is observed in the back-sheet in case of 150-mm-thick sand layer as compared to 50-mm-thick sand layer because, in the absence of stiffeners, higher plastic strain is observed in steel for 50-mm sand layer thickness. It is observed that the octahedral plastic strain (PEEQ) magnitudes are 0.0043, 0.0038 and 0.0033, respectively, for 50-, 100- and 150-mm sand thicknesses at the time instance when peak stress is experienced. Thus, the octahedral plastic strain reduces with increasing sand core thicknesses. In plate P8, the peak stress values are

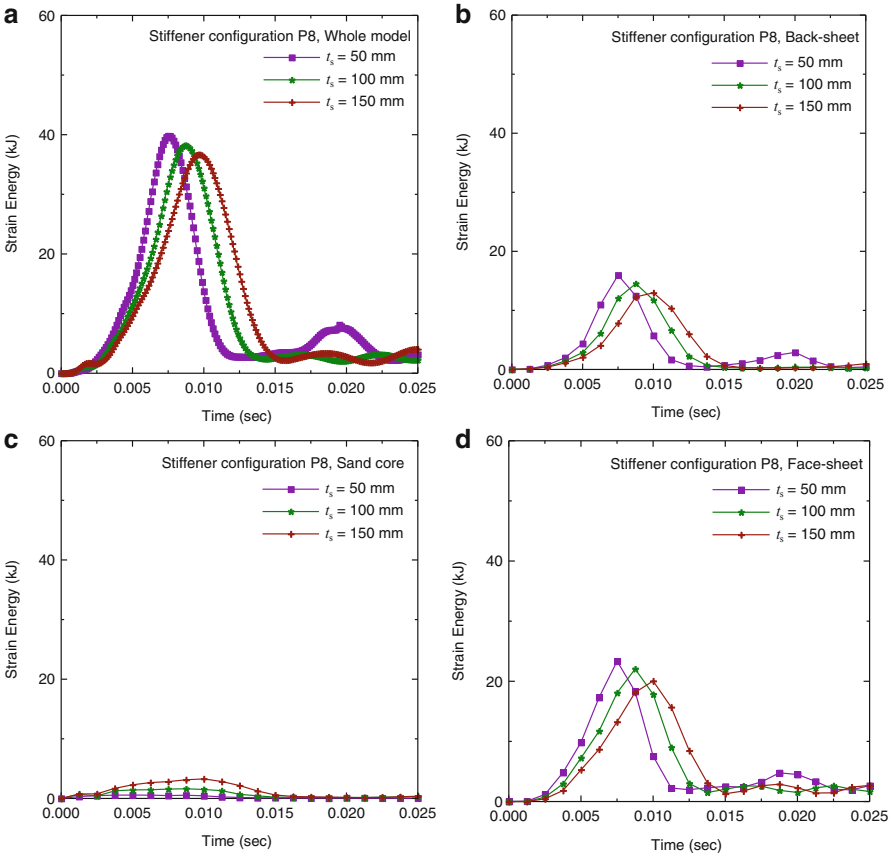

Fig. 8 Variation of strain energy in different components of steel-sand composite plate with stiffener configurations P8

observed to be nearly the same for all layer thicknesses because plastic strain generates in sand layer and the layer transfers the stress to the steel back-sheet. However, the peak stress reaches at a later time for higher sand layer thickness. The stresses dissipate faster in 150-mm-thick sand layer as compared to 50- and 100-mm-thick sand layers. Thus, the stresses in sand core dissipate faster in thicker layers as compared to thinner layers.

Figures 7, 8, and 9 present the strain energy time histories for plates P1, P8 and P9, in total, as well as each of their components, i.e. the face-sheet, the sand core and the back-sheet. Higher strain energy is experienced in the unstiffened plate as compared to the stiffened plates. In plate P1, the strain energies in the face- and the back-sheets are nearly the same, and the values are higher as compared to the strain energy in the sand core. For the stiffened plates P8 and P9, maximum strain energy is experienced in the face-sheet followed by the back-sheet. The strain energy in

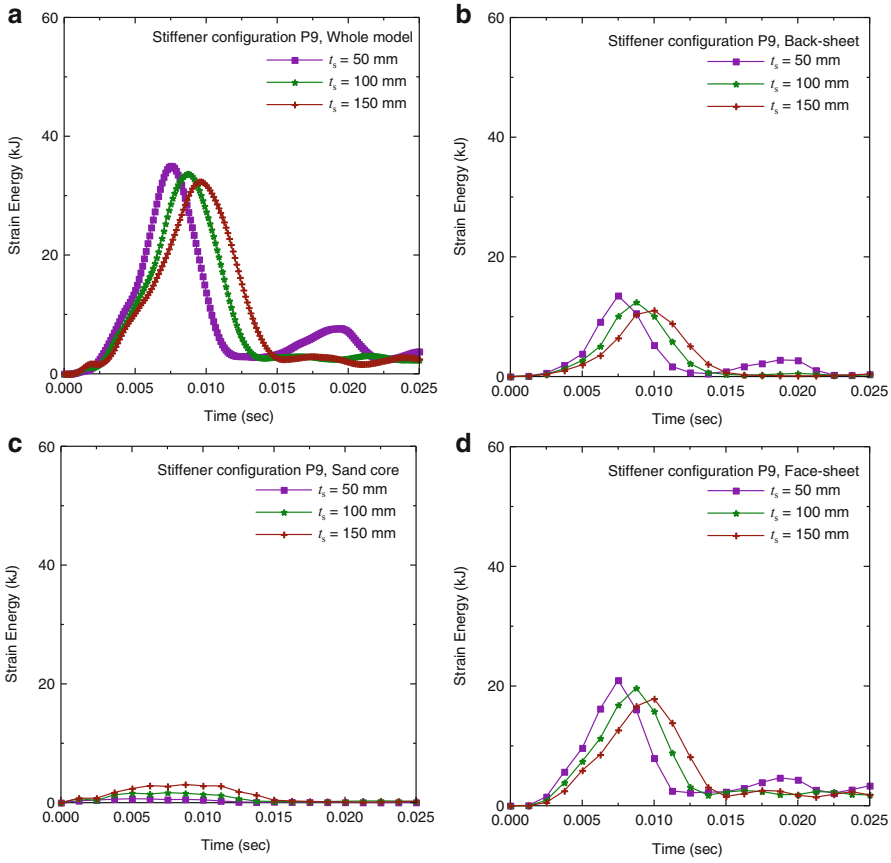

Fig. 9 Variation of strain energy in different components of steel-sand composite plate with stiffener configurations P9

sand is minimal as compared to the same in the steel face- and back-sheets. It is observed from the analysis that the stresses generated in the sand layer are almost two orders of magnitude less than the same generated in the steel plates. Thus, the lesser strain energy experienced in the sand core can be attributed to the lower stress generated in sand as compared to the steel sheets.

Figures 10, 11, and 12 present the kinetic energy time histories for plates P1, P8 and P9, in total, as well as each of their components, i.e. the face-sheet, the sand core and the back-sheet. Similar to strain energy, the kinetic energy is higher in the unstiffened plate as compared to the stiffened plate. For composite plate P1 with 100-mm-thick sand layer, the maximum velocity values perpendicular to the plane of the plate for the centre points of face-sheet, sand-core and back-sheet are 18.2, 18.8 and 17.2 m/s, respectively. For composite plate P8, the corresponding velocity values are 15.2, 14.7 and 14 m/s for the centre points of face-sheet, sand-core and back-sheet. For composite plate P9, the velocity values are 10.8, 11.2

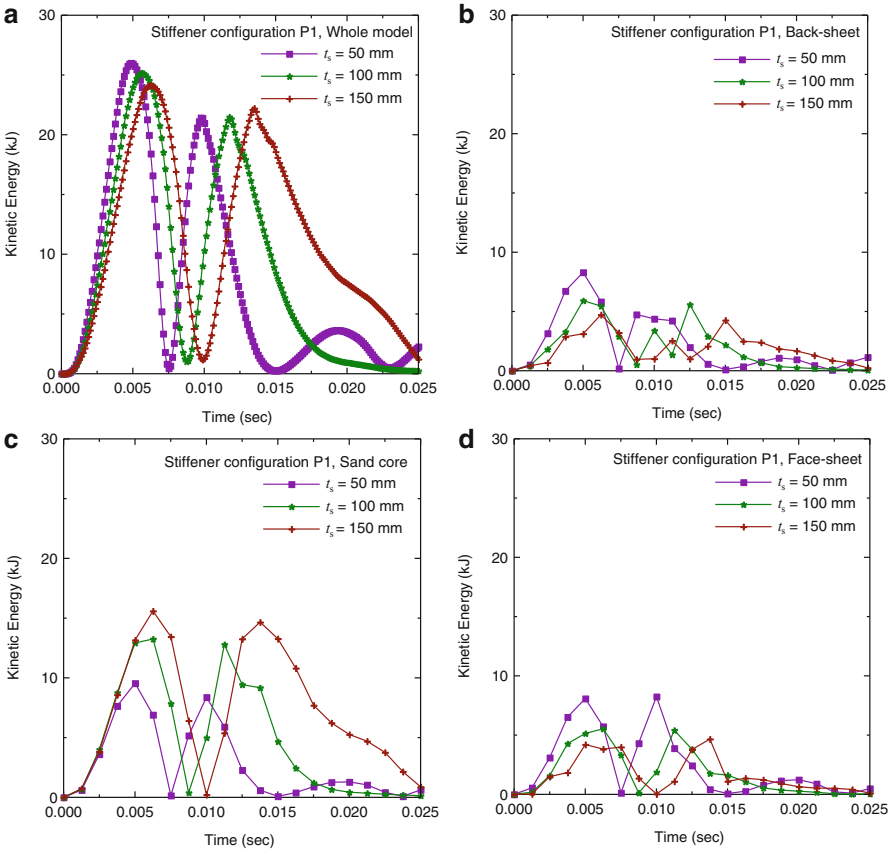

Fig. 10 Variation of kinetic energy in different components of steel-sand composite plate with stiffener configuration P1

and 11 m/s. Hence, higher kinetic energy in the unstiffened plates can be attributed to higher velocity of the unstiffened plates. Higher kinetic energy is observed in 150-mm-thick sand layer as compared to the 50- and 100-mm-thick sand layers. The kinetic energy is higher in sand core than the face- and the back-sheets because the total mass of sand is higher than the individual masses of face-sheet and back-sheet.

5 Conclusions

The present study focuses on the effectiveness of steel-sand composite stiffened plates under explosive loading for blast-resistant design. Dynamic response of steel-sand composite stiffened plates, with various stiffener layouts under blast

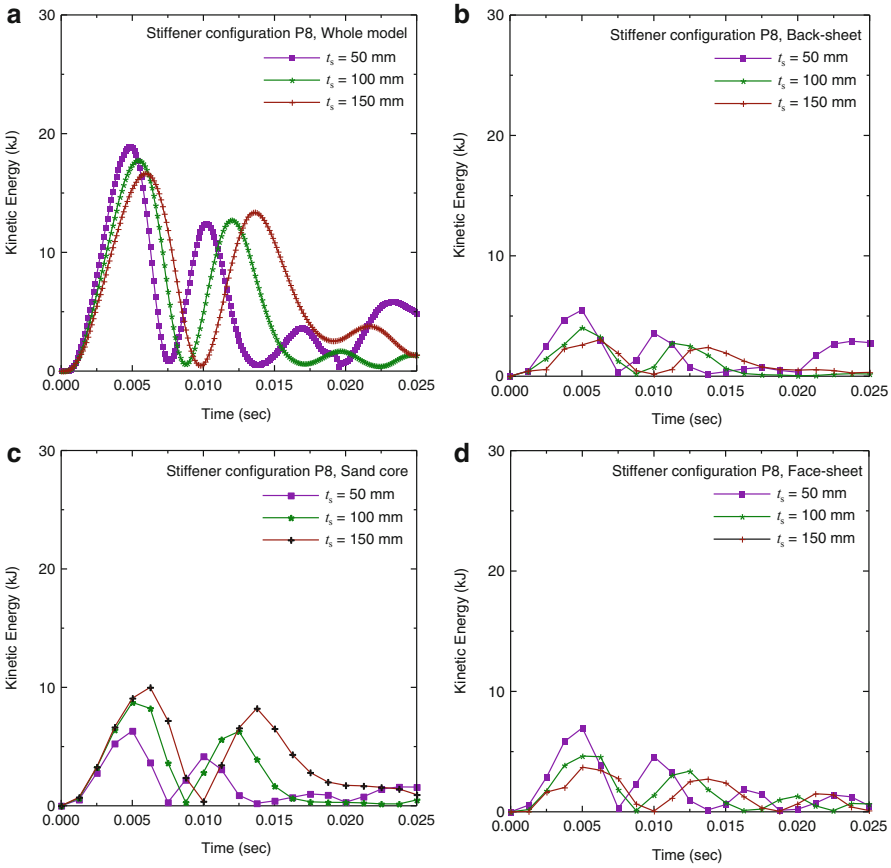

Fig. 11 Variation of kinetic energy in different components of steel-sand composite plate with stiffener configurations P8

loading, is carried out using commercially available finite element software Abaqus/Explicit. The effect of different thicknesses of the sand layer in blast response mitigation has been investigated. The following conclusions are arrived at from the study:

1. Higher displacement is observed for unstiffened plates as compared to the stiffened plates owing to their lower stiffness. The lowest central point displacement is observed for P9 (i.e. with stiffeners), and the highest central point displacement is observed for P1 (i.e. without stiffener). The steel-sand composite stiffened plates exhibit lesser central point displacement under blast loading as compared to when no stiffeners are provided.
2. The octahedral plastic strain reduces with increasing sand core thicknesses. The stresses in sand core dissipate faster in thicker layers as compared to thinner layers.

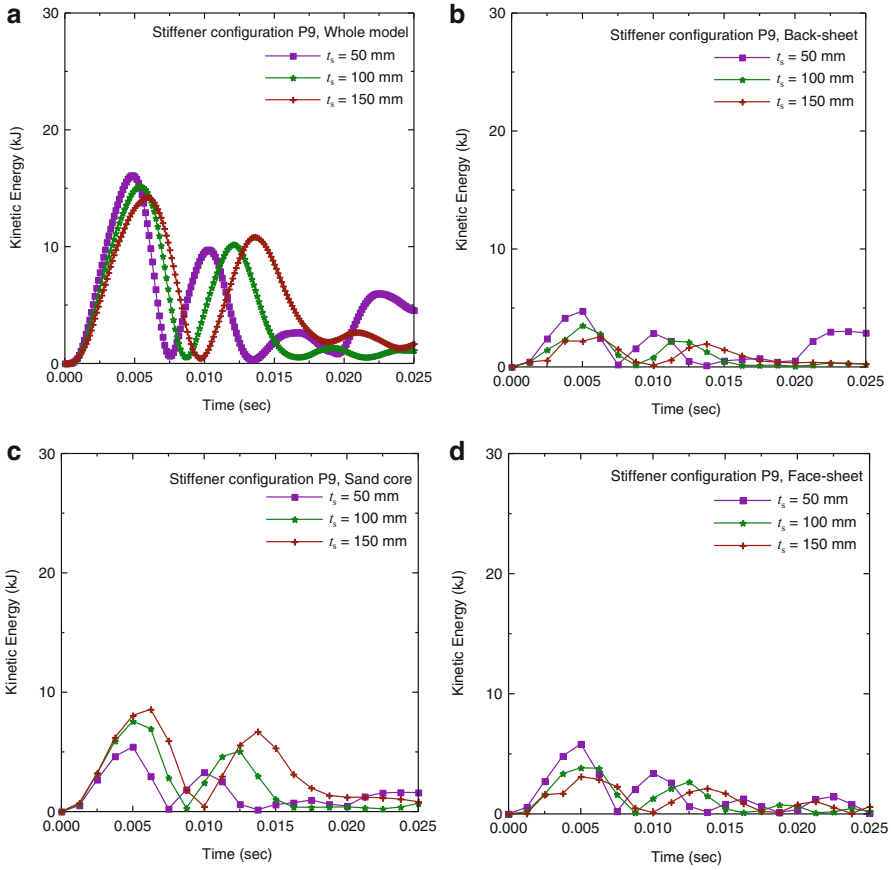

Fig. 12 Variation of kinetic energy in different components of steel-sand composite plate with stiffener configurations P9

3. Higher strain energy is experienced in the unstiffened plate as compared to the stiffened plates. The kinetic energy is higher in the unstiffened plate as compared to the stiffened plate.
4. In plate P1, the strain energies in the face- and the back-sheets are nearly the same, and the values are higher as compared to the strain energy in the sand core. For the stiffened plates P8 and P9, maximum strain energy is experienced in the face-sheet followed by the back-sheet. The strain energy in sand is minimal as compared to the same in the steel face- and back-sheets.
5. The stresses generated in the sand layer are almost two orders of magnitude less than the same generated in the steel plates. Thus, the lesser strain energy experienced in the sand core can be attributed to the lower stress generated in sand as compared to the steel sheets.

References

1. Abaqus (2011) User's manual, version 6.11. Dassault Systèmes Simulia Corporation, Providence
2. Goel MD, Matsagar VA, Marburg S, Gupta AK (2011) Blast response of stiffened sandwich foam panels. J Perform Constr Facil ASCE. doi:10.1061/(ASCE)CF.1943–5509.0000340
3. Guruprasad S, Mukherjee A (2000) Layered sacrificial claddings under blast loading. Part I: analytical studies. Int J Impact Eng 24(9):957–973
4. Guruprasad S, Mukherjee A (2000) Layered sacrificial claddings under blast loading. Part II: experimental studies. Int J Impact Eng 24(9):975–984
5. Held M (1983) Blast waves in free air. Propellants, Explosives, Pyrotechnics 8(1):1–7
6. Jackson JG, Rohani B, Ehrgott JQ (1980) Loading rate effects on compressibility of sand. J Geotech Eng Div ASCE 106(8):839–852
7. Johnson GR, Cook WH (1983) A constitutive model and data for metals subjected to large strains, high strain rates and high temperatures. In: Proceedings of 7th international symposium on ballistics, Hague, the Netherlands, pp 541–547
8. Johnson GR, Cook WH (1985) Fracture characteristics of three metals subjected to various strains, strain rates, temperatures and pressures. Int J Fract Mech 21:31–48
9. Lam N, Mendis P, Ngo T (2004) Response spectrum solutions for blast loading. Electron J Struct Eng 4(2):28–44
10. Langdon GS, Nurick GN, Yahya MY, Cantwell WJ (2010) The response of honeycomb core sandwich panels with aluminium and composite face sheets to blast loading. J Sandwich Struct Mater 12(6):733–754
11. Qiu X, Deshpande VS, Fleck NA (2003) Finite element analysis of the dynamic response of clamped sandwich beams subject to shock loading. Eur J Mech – A Solids 22(6):801–814
12. Qiao P, Yang M, Bobaru F (2008) Impact mechanics and high-energy absorbing materials: review. J Aerosp Eng ASCE 21(4):235–248

Variability and Statistical Distribution of Ocean Current Observations

Dauji Saha, M.C. Deo, and Kapilesh Bhargava

Abstract The ocean currents are created and influenced by various forces like winds, waves, Coriolis force, temperature gradients, salinity differences, tides, etc., and near the shoreline, the local bathymetry interacts and changes the patterns. The variability of ocean currents includes the ones arising in observation, the noise and gaps in data, the causal forces, due to interaction with waves, shoreline and bathymetry, among others. In this chapter, a study of the variability of the ocean currents on different temporal scales is presented. The recorded hourly mean speed and direction of the current and the meridional and zonal velocities calculated from the same exhibit different variability. The spatial resolution of hydrodynamic ocean models, at the present state of development, is large, and the evaluation of current by such models is generally underestimated. Thus, occurrence of extreme current events evaluated from these models is also underestimated. Representation of the general distribution of ocean currents by some well-known statistical distribution would enable estimation of realistic parameters of the distribution using recorded values from a relatively short period. Thus, it might be possible to evaluate the properties of the current field and occurrence of extreme events from the limited data. In this chapter, fitting some standard distribution to observed current records is also explored.

Keywords Ocean currents • Variability • Statistical distribution

D. Saha (✉)
Architecture and Civil Engineering Division, Bhabha Atomic Research Centre, Mumbai, India

Indian Institute of Technology, Bombay, India
e-mail: dauji_saha@yahoo.com

M.C. Deo
Indian Institute of Technology, Bombay, India

K. Bhargava
Architecture and Civil Engineering Division, Bhabha Atomic Research Centre, Trombay, India

S. Chakraborty and G. Bhattacharya (eds.), *Proceedings of the International Symposium on Engineering under Uncertainty: Safety Assessment and Management (ISEUSAM - 2012)*,
DOI 10.1007/978-81-322-0757-3_53,

1 Introduction

Currents in the ocean may be treated as a directed movement of seawater. The currents are created by various forces like winds, waves, temperature gradients, salinity differences and tides and are subsequently influenced by factors like Coriolis force, mesoscale phenomena, depth of water and interaction with waves, and near the shoreline, the local bathymetry interacts and changes the patterns. Hence, the current speed and direction possess inherent variability. Variability of ocean currents also includes those arising from observation, the noise and gaps in data, the models applied for analysis, among others. Variability analysis of current is sparse in literature.

The spatial resolution of hydrodynamic ocean models, at the present state of development, is large, and the evaluation of current by such models is generally underestimated [1]. As a result, occurrence of the extreme current events, which are important for applications like aquaculture, dispersion models and construction at sea, is also underestimated. Representation of the general distribution of ocean currents by some well-known statistical distribution would enable estimation of realistic parameters of the distribution using recorded values from a relatively short period. Thus, it may be possible to evaluate the properties of the current field from the limited data. Furthermore, the fitted distribution functions would be useful for addressing the variability of current in applications.

Green and Stigebrandt [1] reported that current velocities in ocean follow normal distribution, except when dominated by tidal flows. The normal probability distribution function (PDF) was fitted to current velocities measured by Acoustic Doppler Current Profilers (ADCP) at six locations. The suitability was judged with correlation coefficient as well as from the histogram and the fitted PDF, graphically. The correlation coefficients between histogram and PDF were reported to vary from 0.72 to 0.92 except for dominant tidal flow site, where it was 0.47. However, goodness of fit of the distributions was not confirmed with any standard statistical hypothesis test.

LaCasce [2] reported that the current velocities from the Atlantic Ocean and Lagrangian (as measured by floats), as well as Eulerian (as measured by metres), were statistically similar. It was also indicated that the velocity distributions deviated from Gaussian and were more like exponential distribution towards the tails. The deviations were significant, as confirmed with Kolmogorov-Smirnov (K-S) test. It was also reported that the deviation from Gaussianity was modest, with a typical kurtosis of 4.0, as compared to 3.0 for pure Gaussian distribution.

In this chapter, a study of the variability of the ocean currents on different temporal scales is presented. Generally, the observational stations record the speed and the direction of the current, averaged over some time interval, usually on hourly basis. The meridional and zonal velocities calculated from the basic variables exhibit different variability. The suitability of normal and a few common PDFs to the different components of current is also explored with graphical analysis, hypothesis tests and other statistical parameters.

Fig. 1 Location of NDBC Station No. 46081 (Source: http://www.ndbc.noaa.gov)

The outline of this chapter is as follows. In Sect 2, data sets and analysis methods are described. The results of data analysis are presented in Sect. 3, which is followed by a discussion of the results in Sect. 4. This chapter is concluded with scope of further study in Sect. 5.

2 Data and Analysis

2.1 Data

The data for analysis was obtained from National Data Buoy Centre (NDBC) website (http://www.ndbc.noaa.gov) for two locations. The deep water location, NDBC Station No. 46081, was in Gulf of Alaska (60°47′40″ N 148°17′5″ W), semi-enclosed between Pigot Bay and Cochrane Bay (Fig. 1) with 434m depth of water. The shallow water location, NDBC Station No. 41012, was on the coast of North Atlantic Ocean (30°2′29″ N 80°32′0″ W), between Georgia and Florida, facing open sea (Fig. 2), at a water depth of 37.2m. The (ADCP) records from 6-m NOMAD buoy (Station No. 46081) and 3-m discus buoy (Station No. 41012) contained hourly mean values of speed (in cm/s) and direction of current (in degrees with respect to north) for the locations, given for various depths. In both cases, records from year 2009 had minimum gaps (1 and 15%, respectively, for Station No. 46081 and Station No. 41012), and data from depth of 26.1m (Station No. 46081) and 25.1m (Station No. 41012) from still water level were taken for the study.

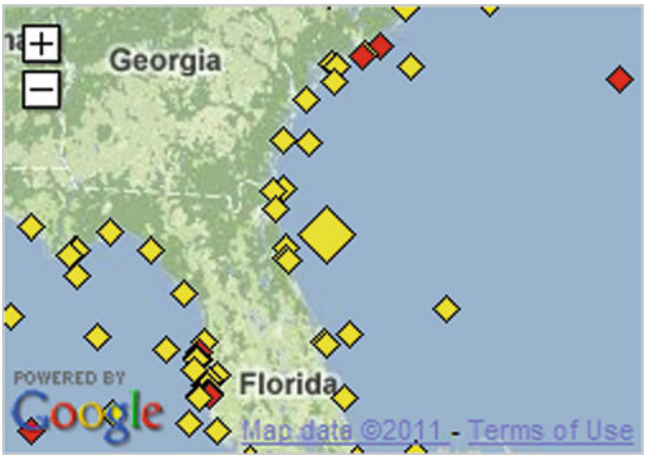

Fig. 2 Location of NDBC Station No. 41012 (Source: http://www.ndbc.noaa.gov)

2.2 *Analysis for Variability*

The data available on the website was hourly mean values of the current speed and the direction of current with respect to north, which formed the basic data. The hourly mean values for meridional or north velocity and zonal or east velocity were calculated from the same. The coefficient of variation is a normalized measure of the variability of variables. The coefficient of variation was calculated for both the locations; for current speed, current direction, meridional and zonal velocity of current, for the hourly mean values. The various temporal scales considered were annual, half-yearly, quarterly and monthly. Speed and direction of current had only positive values, while meridional and zonal velocities had both positive and negative values. For meridional velocity, positive value means northward velocity, while negative means southward velocity. Likewise, for zonal velocity, positive means eastward velocity and negative means westward velocity. The negative mean, as obtained in some cases for the velocities, signified the corresponding direction of the average velocity of current. In such cases, the modulus of the mean was used for calculation of the coefficient of variation. The analysis was repeated for the daily mean values of meridional and zonal velocities of current, calculated from the hourly mean values of the same. Subsequently, the analysis was performed for the daily mean values of speed and direction of current, which were evaluated from the corresponding daily mean meridional and zonal velocities.

2.3 *Fitting Statistical Distribution to the Data*

Histograms were constructed for the hourly mean values of speed, direction and meridional and zonal velocity components of the current for both the locations.

The temporal scales considered were annual, half-yearly, quarterly and monthly. For constructing the histograms, the data was grouped into intervals according to Eq. (1), where I is the number of intervals and N is the number of records [5]:

$$I = 1 + 3.3\log_{10}N \tag{1}$$

Some typical histograms developed for Station No. 46081 and Station No. 41012 are presented below in Figs. 3 and 4, respectively.

It was observed that the shapes obtained were not very regular and the irregularity was more in case of monthly data. Hence, distribution fitting was attempted with annual, half-yearly and quarterly data. Speed and direction of current had only positive values. In addition to the normal or Gaussian PDF, based on the histogram shapes, gamma and lognormal distributions were also fit to the data and parameters were estimated by maximum likelihood estimation (MLE) method. Standard hypothesis tests like chi-square and K-S tests [3] were applied to the fitted distributions. Akaike information criteria (AIC) and Bayesian information criteria (BIC) [4] were also evaluated to judge suitability of the fitted distribution functions. Similarly, normal and generalized extreme value (GEV) PDFs were fitted to the meridional and zonal velocities as they contained both positive and negative values. The hypothesis tests were applied, and information criteria were also evaluated. Correlation of the histogram and fitted PDF was also evaluated.

3 Results

3.1 Variability of Current

The summary of coefficient of variation for hourly mean values and daily mean values for Station No. 46081and Station No. 41012 is presented in Tables 1 and 2, respectively.

The individual coefficients of variation for Station No. 46081 and Station No. 41012 are represented in bar diagrams in Figs. 5 and 6.

3.2 Statistical Distribution for Ocean Current

The suitability of PDFs was evaluated by the AIC and BIC. The two criteria were found to be in agreement for all the data sets under consideration. For direction of current, at both locations, normal distribution was the most suitable. For the speed of current, for both locations, gamma distribution was the preferred one, except in three out of seven cases at Station No. 41012, where normal distribution appeared to be better. In two out of seven cases, at each location,

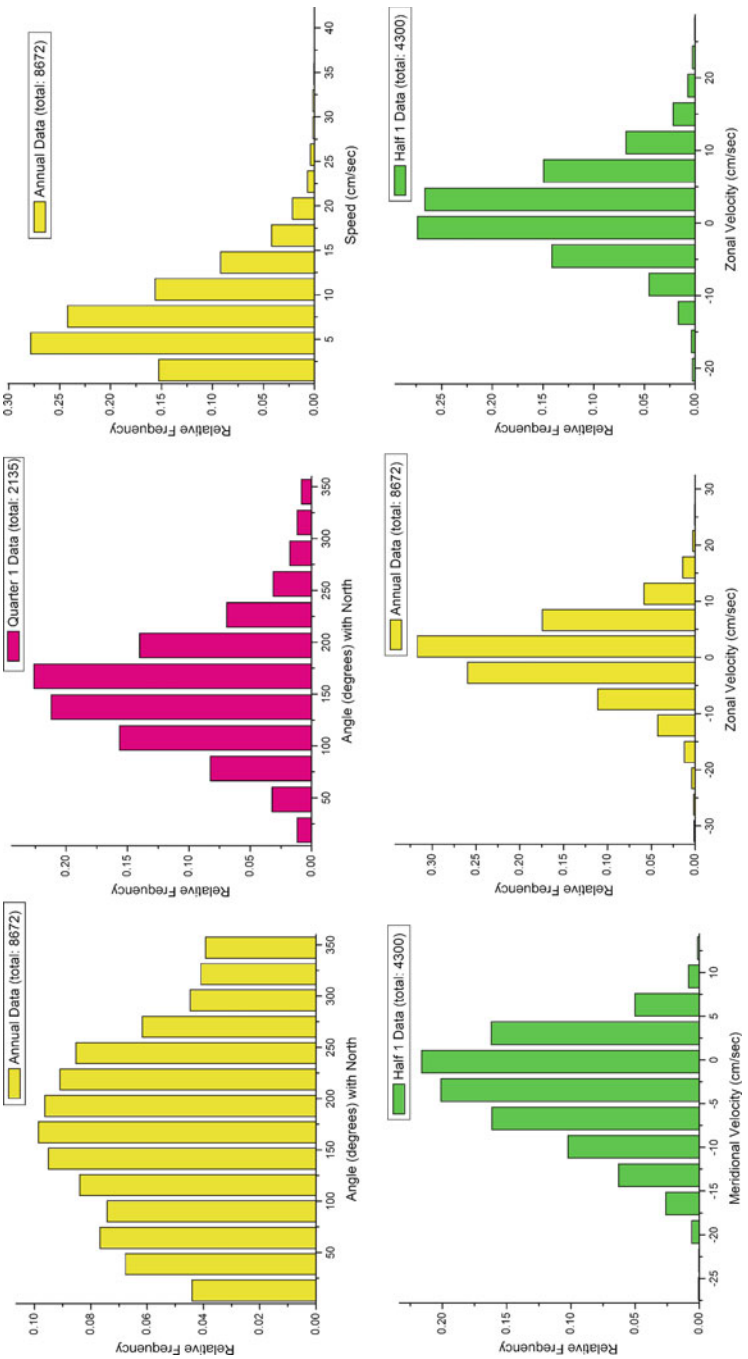

Fig. 3 Histograms from Station No. 46081, 26.1m

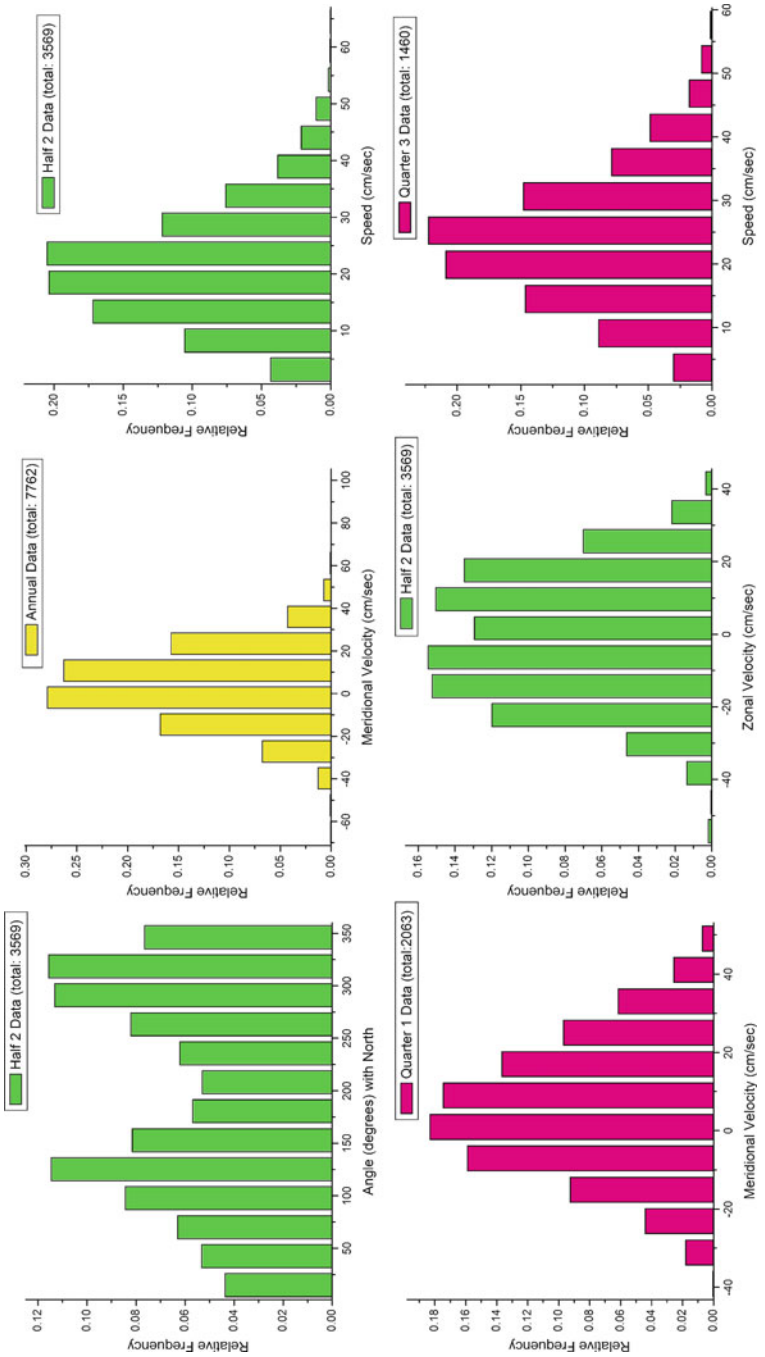

Fig. 4 Histograms from Station No. 41012, 25.1m

Table 1 Coefficient of variation for current variables at 26.1m, Station No. 46081

	Hourly mean values				Daily mean values			
Statistic	Speed	Direction	Meridional velocity	Zonal velocity	Speed	Direction	Meridional velocity	Zonal velocity
Maximum	0.74	0.64	157.21	73.86	0.81	0.74	117.24	34.08
Minimum	0.43	0.32	0.85	1.47	0.38	0.12	0.52	1.02
Mean	0.60	0.51	12.98	12.14	0.61	0.47	9.11	7.19
Standard deviation	0.08	0.09	35.39	17.58	0.14	0.18	26.38	9.08

Table 2 Coefficient of variation for current variables at 25.1m, Station No. 41012

	Hourly mean values				Daily mean values			
Statistic	Speed	Direction	Meridional velocity	Zonal velocity	Speed	Direction	Meridional velocity	Zonal velocity
Maximum	0.61	0.62	88.79	348.03	0.81	0.66	554.54	21.50
Minimum	0.38	0.42	1.34	3.54	0.44	0.28	1.01	1.09
Mean	0.49	0.54	14.39	26.73	0.61	0.46	34.86	3.79
Standard deviation	0.05	0.04	24.25	77.99	0.08	0.09	125.97	4.76

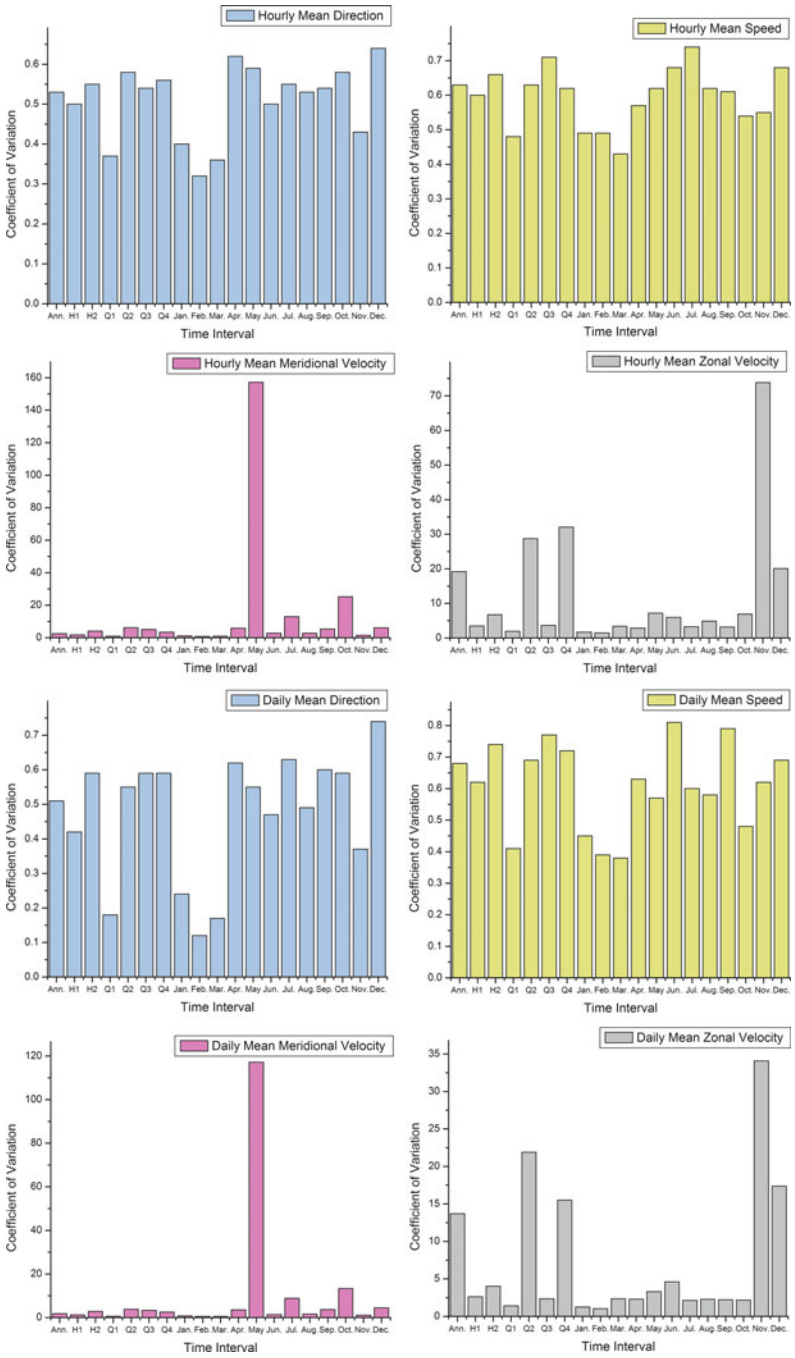

Fig. 5 Coefficient of variation for Station No. 46081 at 26.1m

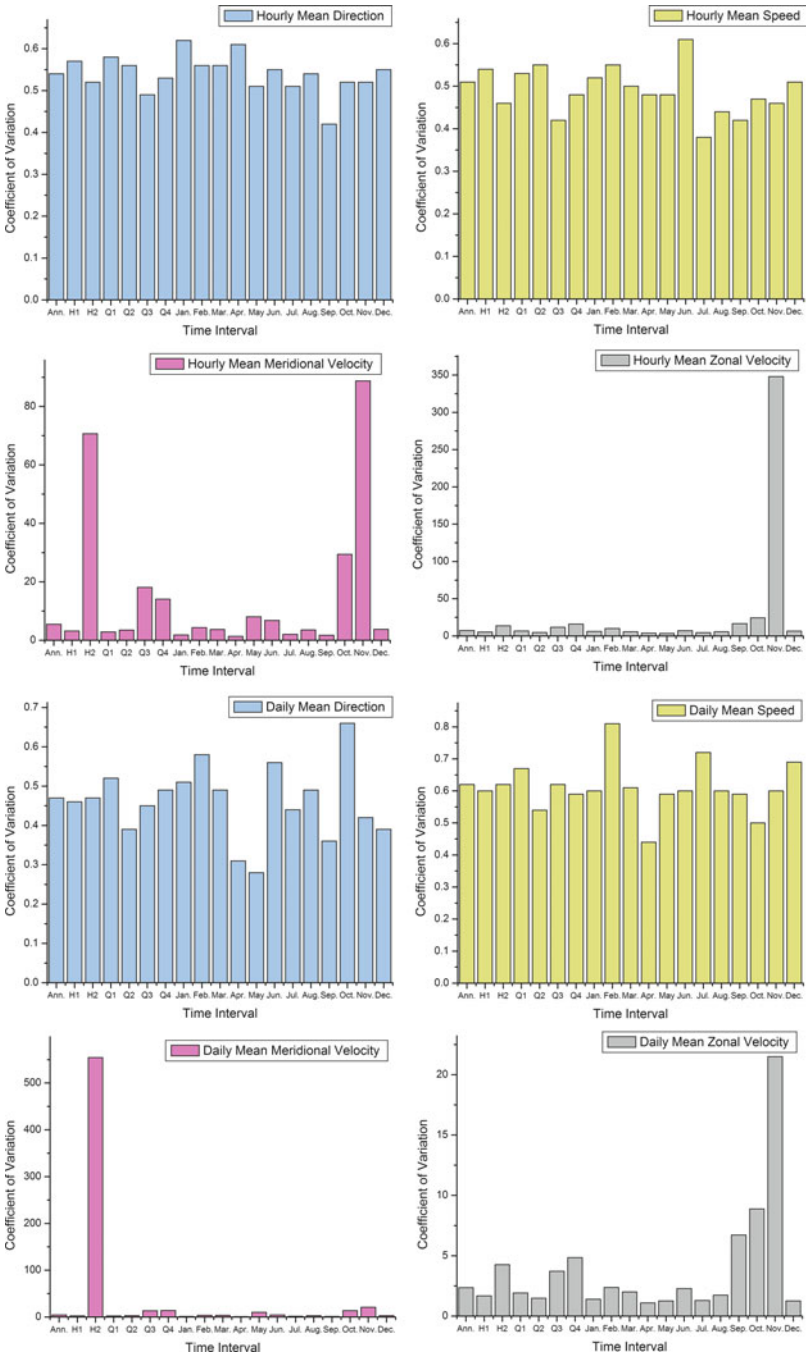

Fig. 6 Coefficient of variation for Station No. 41012 at 25.1m

generalized extreme value distribution was better suited for meridional velocity of current, compared to normal distribution. Normal distribution was suitable for other five data sets of meridional velocity at both locations. For zonal velocity, normal distribution was the preferred one for both locations, except in three out of seven cases at Station No. 41012, where generalized extreme value distribution appeared to be more suitable as per AIC and BIC.

The hypothesis tests were performed for significance levels of 10, 5 and 1%, both for chi-square test and K-S test. For both locations, the data sets of direction of current were rejected even at significance level of 1%. For other three variables, data sets passed the chi-square test for three cases at 10% and seven cases at 1% significance level. By K-S test, the numbers of set passing were 12 at 10%, 4 at 5% and 13 at 1%.

For Station No. 46081, gamma distribution was acceptable for speed data by K-S test for six cases and by chi-square test for two cases. Lognormal distribution was also acceptable in six sets of speed data by K-S test. For Station No. 41012, both gamma and lognormal distributions could be accepted only for one set of speed data by K-S test. Meridional velocity at Station No. 46081 could acceptably follow both normal and generalized extreme value distributions for a single data set according to both chi-square and K-S tests. For meridional velocity at Station No. 41012, normal distribution was accepted for three cases by chi-square test and six cases by K-S test. The corresponding numbers for generalized extreme value distribution are one and three. For zonal velocity, two cases passed both tests for normal distribution, and only one could pass K-S test for generalized extreme value distribution at Station No. 46081. For Station No. 41012, only one data set of zonal velocity passed the K-S test for generalized extreme value distribution. The histograms and fitted PDFs for a few data sets are presented in Fig. 7 for Station No. 46081 and Fig. 8 for Station No. 41012, respectively.

The correlation of the histogram and the corresponding PDF value was calculated for all the variables, at both locations. The correlation obtained ranged from 0.889 to 0.999 for speed, meridional velocity and zonal velocity of current for both the locations. For Station No. 46081, the correlation for direction of current was between −0.124 and 0.950 with two negative values. Whereas for Station No. 41012, the correlation ranged from −0.531 to 0.300 with 50% negative values.

4 Discussion

4.1 Variability of Current

It was observed that the mean variability (45–60%) of the basic variables, current speed and current direction is comparable for both hourly mean values and the daily

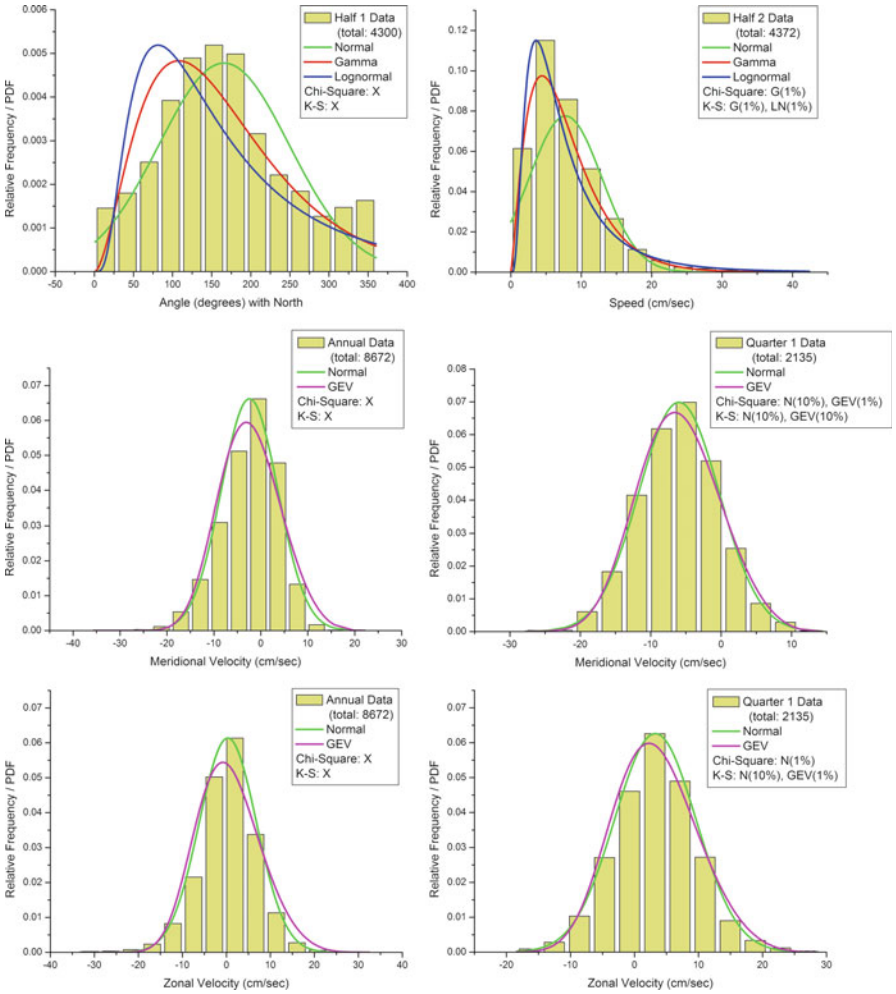

Fig. 7 Histogram and PDF for Station No. 46081

mean values, for both the locations. Furthermore, the mean variability of the derived variables, the meridional and zonal velocity, was much higher than the basic variables. This was understandable as variation in velocity could be due to variation in either speed or direction, which regularly varied, or both. It was also noted that, in a few cases, due to near-zero mean values, the coefficient of variation for the derived variables was very high (~555, ~350), without comparably high standard deviation (~12, ~16, respectively). This factor also accounted for the high average variation obtained for the meridional and zonal velocities. But, even the minimum variations (85% for hourly data and 52% for daily data for Station No. 46081 and 134% for hourly data and 101% for daily data for Station No. 41012) for the velocities were more than the average variation of the speed or direction. For the

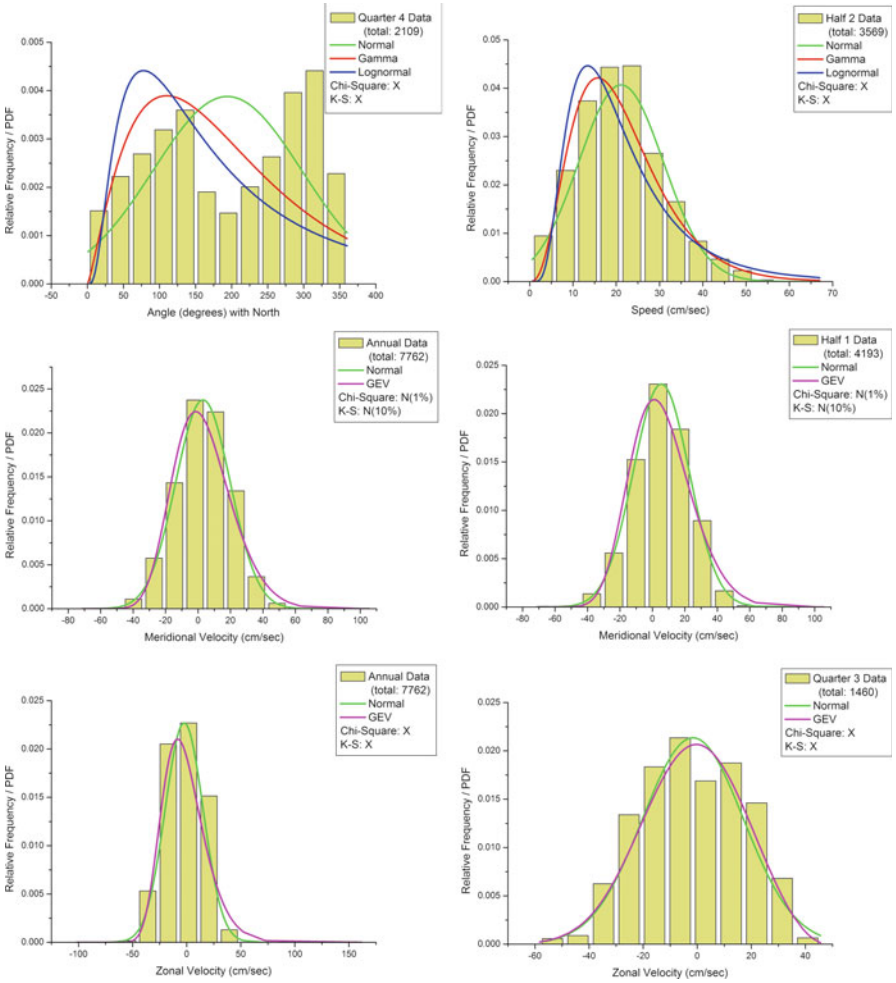

Fig. 8 Histogram and PDF for Station No. 41012

derived variables, the variability was more in shallow water location, compared to the deep water location, while for the basic variables, it was comparable. Higher variations in velocities at Station No. 41012 might be due to proximity to the shoreline, shallow depth of water or tidal flows. The importance of accounting the variability of current in various applications like dispersion models and construction at sea was brought out in the study.

4.2 Statistical Distribution for Ocean Current

The suitability of fitted distributions was evaluated with AIC and BIC. It was also observed that the suitability as judged by AIC and BIC was in agreement for all the

data sets considered. From the standard PDFs, normal or Gaussian distribution was found to be most suitable for the direction of current. For the speed of current, it was gamma distribution which was the best option. For the meridional and zonal components of current velocity, though generalized extreme value distribution was better in a few cases, generally normal distribution was the better suited alternate. This is in agreement with the findings of earlier researchers.

Out of a total of 140 distributions fitted to 56 data sets, few (29) could pass the rejection criteria at even 1% significance level by K-S test and fewer (10) by the chi-square test. The failure to pass rejection criteria by K-S test was earlier reported in literature. It appeared that as K-S test is based on only the maximum difference between fitted and empirical cumulative distribution functions (CDF), some of the distributions which could not be rejected by K-S test were rejected by chi-square test, which takes into account the deviations throughout the range. All tests which were acceptable by chi-square test were acceptable by K-S test at equal or higher significance levels. It may be inferred that the chi-square test checks for goodness of fit in a stricter manner when compared to K-S test. Furthermore, the few distributions which were acceptable by only K-S test or K-S and chi-square tests were also the most suitable as found by AIC and BIC.

The deviation from normality was more for speed of current (kurtosis ranging from ~3 to ~18) when compared to direction (kurtosis ranging from ~1.6 to ~3.8). For the velocities, as reported by investigators, the deviation from normality was moderate (kurtosis ranging from ~3 to ~5). Of the four variables considered, only speed of current exhibited predominant positive skewness.

As mentioned in literature, the fitted PDFs appeared to follow the histograms, and this was confirmed with the high correlation (~ 0.9 and above) between histograms and PDF at centre of histogram intervals, for speed and meridional and zonal velocities. Still, the probability distribution functions which were fitted to the data sets were, in general, rejected by the hypothesis tests. From the results, it appeared that the correlation of the histogram and the fitted distribution at the centre of histogram bins would not be a very reliable statistic for judging the goodness of fit.

From graphical analysis, it was inferred that representation of direction of current by some standard distribution would be difficult. As a result, though speed of current could be represented by distributions like gamma and lognormal, it might not be useful for applications without corresponding representation of the direction. A better approach would be to represent the two velocity components of current by some standard distribution function. As reported previously by investigators, there was indication that the meridional and zonal velocities of current follow the normal distribution, as can be observed in the histogram-PDF plots. By the information criteria also, it was the normal distribution which is the best suitable in most of the cases. Yet, they were rejected in many cases by hypothesis tests. This could be due to the sensitivity of the chi-square test to the number and choice of the intervals. Another possibility could be incorrect estimation of the parameters of distribution. Further exploration by varying the interval number and range is under progress. For applying K-S test, grouping of data may be attempted to take care of the irregularity in the steps of the empirical CDF.

Another approach could be to fit non-parametric distributions, like the kernel density function, to the data sets, obtain the CDF and subsequently apply for analysis. Keeping the variability of current in mind, such exercise should be based on data of sufficient length, perhaps a year or above, for being generalized enough to represent the current field appropriately.

The histograms obtained from data sets from both the locations were not very smooth, and the irregularity increased for shorter durations. It was felt that for any analysis based on such short-time series should be performed with due consideration for the additional uncertainty involved.

5 Conclusions

It was observed that there was significant variability in the current for both deep and shallow water locations, former being in semi-enclosed bay and latter facing open sea. The two locations were at latitudes 60° N and 30° N, and for both, the mean variability of speed and direction of current was around 50%, while for meridional and zonal velocities, they were comparatively more. This was observed for all temporal scales considered for analysis. For the velocities, the variability was more in shallow water location, compared to the deep water location, which might be due to proximity to the shoreline, shallow depth of water or tidal flows. It was inferred that the variability of current velocities should be appropriately addressed in applications.

Representation of the direction of current by standard distribution appeared to be difficult. Of the standard distribution functions, normal distribution was found most suitable for the meridional and zonal velocity of current, while for the speed, gamma distribution appeared to be best. In many cases, the fitted distributions had to be rejected, as they failed to pass the hypothesis tests like chi-square and K-S test at even 1% level of significance. The graphical analysis indicated the possibility of representing the velocities by normal distribution. Investigations for checking suitability of the same by variation of the interval numbers and ranges are in progress. Any analysis with short-time series, like a month or less, should be performed with adequate care for the additional uncertainty involved. Further explorations of fitting non-parametric distribution like kernel density function and identification of optimal length of data for generation of CDF for current data series are proposed to be taken up in future.

References

1. Green JAM, Stigebrandt A (2003) Statistical models and distributions of current velocities with application to the prediction of extreme events. Estuar Coast Shelf Sci 58:601–609
2. LaCasce JH (2008) Statistics from Lagrangian observations. Prog Oceanogr 77:1–29

3. Ayyub BM, McCuan RH (1997) Probability, statistics & reliability for engineers. CRC Press, Boca Raton
4. Dawson CW, Wilby RL (2001) Hydrological modeling using artificial neural networks. Prog Phys Geogr 25(1):80–108
5. Ranganathan R (1999) Structural reliability analysis and design. Jayco Publishing House, New Delhi

Risk Analysis of a Cyclic Test Rig

Pritam Poddar, Smruti Ranjan Sahoo, and Sourav Das

Abstract This chapter discusses the risk involved in the design of a cyclic test rig. The rig is used for testing the fatigue strength of an inverted "T"-shaped test specimen that is firmly secured to the foundation of the rig. The specimen is subjected to a constant vertical load applied by a hydraulic cylinder, and a horizontal hydraulic cylinder provides applies completely reversed cyclic load (Fig. 1).

Monte Carlo simulation technique is used to analyse and assess the risk. The probability distribution for analysis is obtained through Poisson distribution. The first part identifies the possible occurrence of the failures from the complicacies of the joints. The second part provides stage-wise application of the risk analysis process. The final part interprets and analyses the results of risk analysis application and includes the decisions to be made on that basis.

Keywords Poisson distribution • Failure • Probability distribution • Monte Carlo simulation • Cyclic test rig

1 Introduction

When a material is loaded too much, it may break even if the resultant stress is less than the ultimate stress. For example, if you twist a wire again and again with the same effort, it breaks after a point, though you are applying the same force. This explains cyclic loading. There are three types of mathematical models for cyclic loading – (1) fluctuating or alternating stresses, (2) repeated stresses and (3) reversed stresses. The time-stress relationships for all these models are sinusoidal with respect to time.

P. Poddar (✉) • S.R. Sahoo • S. Das
Department of Mechanical Engineering, Future Institute of Engineering and Management, Sonarpur Station Road, Kolkata 700150, India
e-mail: pritam.engg@yahoo.in; smruti.ranjan.sahoo@hotmail.com; sourav.das.1910@gmail.com

S. Chakraborty and G. Bhattacharya (eds.), *Proceedings of the International Symposium on Engineering under Uncertainty: Safety Assessment and Management (ISEUSAM - 2012)*,
DOI 10.1007/978-81-322-0757-3_54,

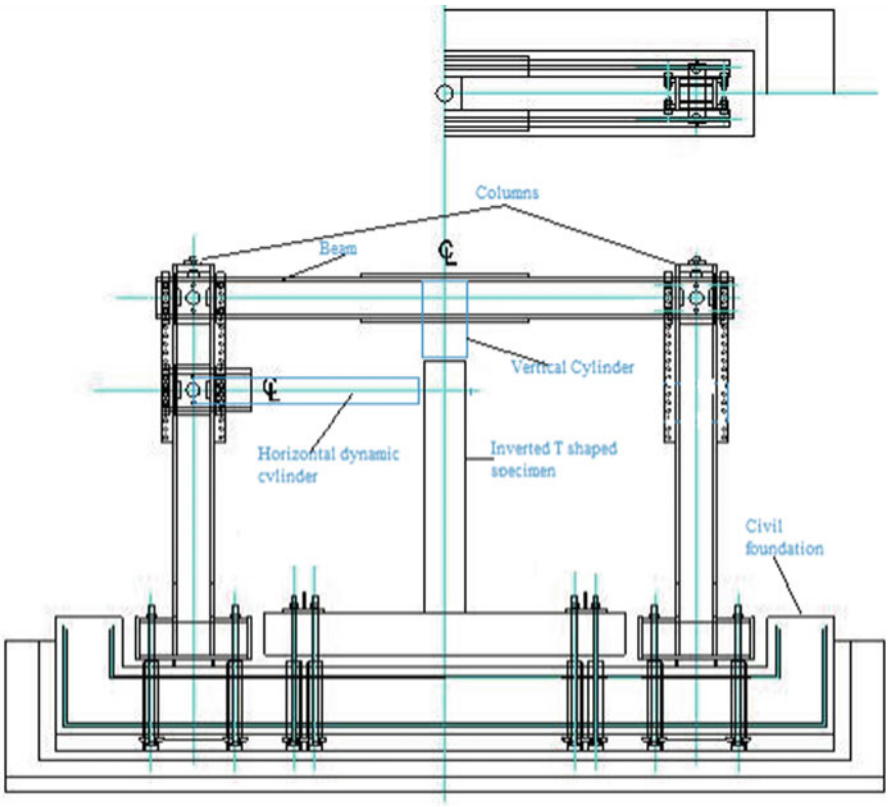

Fig. 1 Cyclic test rig general layout

The cyclic test rig [3] under study subjects an inverted T member to fluctuating or alternating stresses and calculates its life cycle. To study how a material behaves under cyclic loading [2], we make use of an S-N curve(S = stress, N = life cycle). This shows the stresses developed in a material at different cycles with a same load. This graph forms the basis of selecting a material for the required application.

There are multiple points of failure of the setup. Risk emanates from the probability of these points failing. Risk analysis therefore depends on the assessment of these failures and the measures needed to be taken to reduce the probability of their occurrence. It is also essential to understand the natures of the failures, as to which will cause the complete breakdown of the setup and which will have minor effects on the system.

2 Determination of Failure Points

For the purpose of risk analysis [4], the structure of the rig with different joints is analysed to identify the critical areas which are most likely to fail. There will be number of areas in the setup which are assumed to be vulnerable. Minor failures

have not been considered to reduce the complexity of mathematical analysis. Because the greater the number of these variables, the greater will be the number of probability distributions. Thus, greater will be the likelihood of getting inconsistent scenarios.

The areas of failure are determined on the basis of their design complexity. For example, if an area has more holes, it will be more prone to failure due to stress concentration rather than an area with a solid block.

Based on this, five critical areas are identified:

1. Bolted joints between the beam and column – The dead weight of the beams acts on these bolts directly downwards causing shear force to develop in them. Also due to completely reversed cyclic motion transferred to the specimen, the dynamic cylinder applies cyclic load on the bolts through reaction.
2. Attachment of the dynamic cylinder with the column – Dynamic cylinders will need reaction from a rigid support to apply cyclic load on the specimen. The rigid support in this case is the column to which the dynamic cylinder would be attached. Cyclic loading on the attachment between the column and the cylinder may also cause failure.
3. Failure due to leakage of the hydraulic pipes – The pipes carrying oil under pressure to dynamic cylinder may leak if the pressure exceeds the safe limit.
4. Failure of bolted joints between the column and civil foundation – This is likely to occur in the column to which the dynamic cylinder is attached, owing to high shear forces developed on the bolt due to weight of the cylinder.
5. Failure due to resonance – The dynamic cylinder would transfer completely reversed cyclic load to the specimen member under study. If the natural frequency of the cylinder becomes coherent with any member of the setup, the structure will vibrate violently. It may lead to cracking of the civil foundation.

3 Risk Analysis

There are many factors that govern our ability to forecast accurately a future event. These relate to the complexity of the system determining the outcome of a variable and the sources of uncertainty it depends on. Our ability to narrow the margins of uncertainty of a forecast therefore depends on our understanding of the nature and level of uncertainty regarding the variable in question and the quality and quantity of information available at the time of the assessment.

Monte Carlo simulation adds the dimension of dynamic analysis to project evaluation by making it possible to build up random scenarios which are consistent with the analyst's key assumptions about risk. A risk analysis application utilizes a wealth of information, be it in the form of objective data or expert opinion, to quantitatively describe the uncertainty surrounding the project. It is a technique by which a mathematical model is subjected to a number of simulation runs, usually with the aid of a computer.

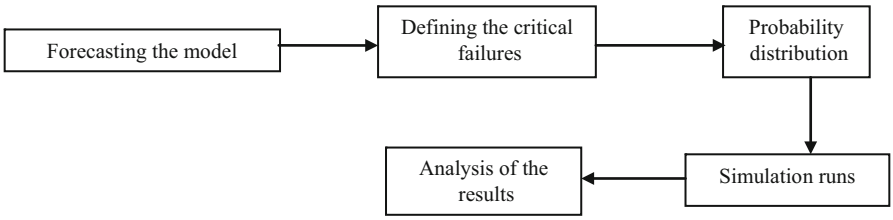

Fig. 2 Risk analysis process layout through Monte Carlo simulation

During the simulation process, successive scenarios are built up using input values for the project's key uncertain variables which are selected from multi-value probability distributions (Fig. 2).

3.1 Probability Distribution

For calculating the probability of this occurrence, an estimate of their arrival rates needs to be considered. The test rig will operate for 3 days (72 h) at a stretch for or until fatigue occurs. For convenience, a running period of 3 days is considered. It will be always desirable that no failure occurs during this period, or in other words the failures arrive after this period. If it is considered that failure occurs after 80 h, the setup will always run in the safe period. The arrival rate (λ) in this case will be 1/80.

For the probability distribution, Poisson distribution formula is used:

$$P(n,t) = \frac{(\lambda t)^n e^{-\lambda t}}{n!}$$

where
n = no. of failures (maximum 5 in this case),
t = running time in hours, and
P = probability of n failures that will occur in the length of time t.

λ is normally an arrival rate of failures which is normally obtained from past data. In absence of past data, we have assumed λ to be 1/80 as the failure rate. This is done in order to avoid any risk of failure during the duration of experiment. However, it may not be the real case for new equipment where chances of early life failure are prominent. $1/\lambda$ is the mean time between failures.

According to the Monte Carlo simulation method, random situations need to be generated to analyse the risk in a variety of situations. This is done by generating random numbers in Microsoft Office Excel.

Table 1 Random number allocations of time for $\lambda = 1/80$

	Probabilities				
Time (t)	$n = 1$	$n = 2$	$n = 3$	$n = 4$	$n = 5$
4	5.510432	0.160957	0.003134	4.58E-05	5.35E-07
10	11.60059	0.768136	0.033908	0.001123	2.97E-05
15	15.87767	1.528003	0.098033	0.004717	0.000182
17	17.90779	2.006065	0.149816	0.008391	0.000376
19	19.36771	2.403954	0.198922	0.012345	0.000613
23	22.2092	3.327947	0.332452	0.024908	0.001493
28	24.67464	4.320663	0.504381	0.04416	0.003093
34	28.08779	6.082479	0.878117	0.095079	0.008236
39	30.09717	7.410998	1.216568	0.149781	0.014753
40	30.34691	7.596147	1.267596	0.158646	0.015884
43	31.53859	8.55583	1.547358	0.209885	0.022775
45	32.06071	9.022579	1.692766	0.238191	0.026813
45	32.14437	9.100416	1.717617	0.243138	0.027534
48	32.96891	9.919416	1.989648	0.299314	0.036022
49	33.43996	10.43665	2.171526	0.338868	0.042304
58	35.13827	12.76687	3.092411	0.561787	0.081646
64	36.00286	14.51036	3.898776	0.785669	0.12666
66	36.18576	14.99416	4.142048	0.858162	0.142237
74	36.69595	17.05642	5.28526	1.228305	0.228368
75	36.72495	17.27927	5.419989	1.275066	0.23997

As the setup will run for 72 h, we take a time limit of 80 h to analyse the maximum risk that can occur. We set the range of random numbers as 1–80.

With random numbers generated for the range of time, we calculate the probability for each of random numbers. Twenty instances were taken into account.

For probability distribution, the random numbers were arranged sequentially and the probability versus time graph is plotted for $n = 1$–5 (Table 1). The graph is as follows (Fig. 3):

4 Debugging Period

Any product's chances of failure are highest during its infant operating stages, in its whole operational life. It is analysed with the aid of the bathtub curve.

The bathtub curve [1] is how reliability specialists often describe the lifetime of a population of products using a graphical representation. The bathtub curve consists of three periods: an infant mortality period with a decreasing failure rate followed by a normal life period (also known as "useful life") with a low, relatively constant failure rate and concluding with a wear-out period that exhibits an increasing failure rate (Fig. 4).

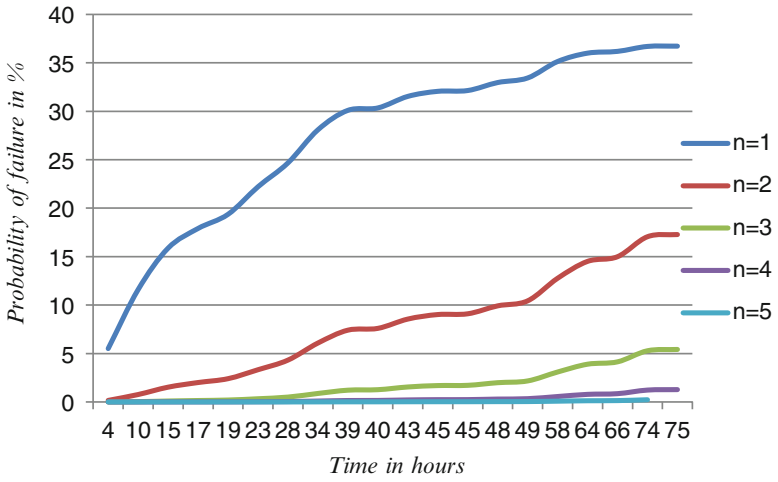

Fig. 3 Cumulative probability distribution graph for $\lambda = 1/80$

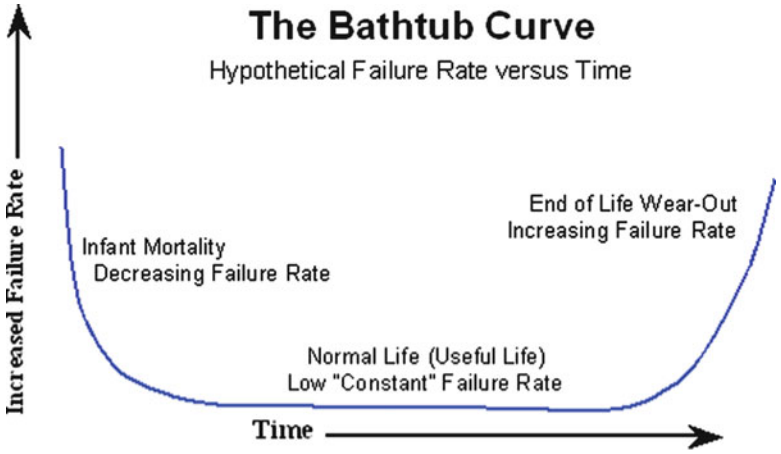

Fig. 4 The bathtub curve

Failures during infant mortality are highly undesirable and are always caused by defects and blunders: material defects, design blunders, errors in assembly, etc. Normal life failures are normally considered to be random cases of "stress exceeding strength." However, as we will see, many failures often considered normal life failures are actually infant mortality failures. Wear-out is a fact of life due to fatigue or depletion of materials (such as lubrication depletion in bearings). A product's useful life is limited by its shortest-lived component. A product manufacturer must assure that all specified materials are adequate to function through the intended product life.

Table 2 Random number allocations of time for $\lambda = 1/24$

	Probabilities				
Time (t)	$n = 1$	$n = 2$	$n = 3$	$n = 4$	$n = 5$
1	6.817054	0.250046	0.006114	0.000112	1.65E-06
5	18.42697	2.142095	0.166009	0.009649	0.000449
11	29.61553	7.067601	1.124432	0.13417	0.012808
16	34.93875	12.43949	2.952611	0.525619	0.074856
18	35.85101	14.15052	3.723504	0.73484	0.116018
21	36.59991	16.49364	4.955207	1.116525	0.201263
27	36.33424	21.19683	8.243935	2.404692	0.561144
28	36.28147	21.34609	8.372601	2.462997	0.579638
30	35.56026	22.83409	9.77488	3.138342	0.806082
33	34.64133	24.04917	11.13049	3.863578	1.07289
34	33.94096	24.73022	12.0127	4.376375	1.275494
39	31.63631	26.17254	14.43493	5.970968	1.975899
42	30.1177	26.69637	15.7758	6.991844	2.479032
45	28.42518	27.00229	17.10042	8.122207	3.086252
50	25.5169	26.98662	19.02733	10.06164	4.256467
52	24.263	26.79819	19.73218	10.89698	4.814232
55	22.68026	26.41823	20.51485	11.94797	5.566853
70	15.25251	22.64188	22.40745	16.63158	9.875629
73	14.09877	21.7573	22.384	17.27156	10.66143
74	13.63599	21.37854	22.34488	17.51618	10.98476

Therefore, for analysis of the failure probabilities during the debugging period, very high arrival rates are considered (Tables 2 and 3). We use rates of 24 and 48 h, respectively, in the subsequent calculations (Figs. 5 and 6).

5 Conclusion

We can classify the failures as:

1. Minor failure (reparable) – single or two at a time
2. Moderate failure – three at a time
3. Catastrophic failure – four or five at a time

Minor failures can be attributed to the leakage of pipes carrying fluid to the dynamic cylinders. The rig can be recovered, and normal operations can be resumed in the event of such failures.

Catastrophic failures are attributed to detachment of the beam from the columns, where the complete rig is lost and has to be set up again to resume operations.

But again, this classification will depend on the nature of the failure. If four failures occurring are minor, they cannot be defined as catastrophic failures. Again, a single major failure cannot also be classified as a minor failure.

Table 3 Random number allocations of time for $\lambda = 1/48$

	Probabilities				
Time (t)	$n = 1$	$n = 2$	$n = 3$	$n = 4$	$n = 5$
8	15.52125	1.452428	0.090609	0.004239	0.000159
12	19.87307	2.553167	0.218677	0.014047	0.000722
14	22.07889	3.280787	0.325003	0.024147	0.001435
15	23.11274	3.668924	0.388271	0.030817	0.001957
18	26.12694	5.007183	0.639745	0.061303	0.004699
20	28.19396	6.146344	0.893277	0.097368	0.008491
22	29.49484	6.984219	1.10255	0.130539	0.012364
35	35.34212	13.12386	3.248923	0.603224	0.0896
43	36.63699	16.68928	5.068322	1.154389	0.210344
44	36.69533	17.05208	5.282661	1.227409	0.228148
52	36.61607	20.16036	7.400031	2.037183	0.448659
53	36.60305	20.22292	7.448678	2.05767	0.454739
55	36.38483	21.04442	8.114512	2.346654	0.542907
58	35.9882	22.04738	9.004562	2.758224	0.675906
71	33.69706	24.93349	12.29938	4.550344	1.346776
71	33.64835	24.97229	12.35554	4.584864	1.361072
72	33.45556	25.12039	12.57457	4.720861	1.417879
74	32.90533	25.49937	13.1735	5.104279	1.582186
75	32.69723	25.62755	13.39097	5.247809	1.645258
77	32.04604	25.98201	14.04364	5.693089	1.846317

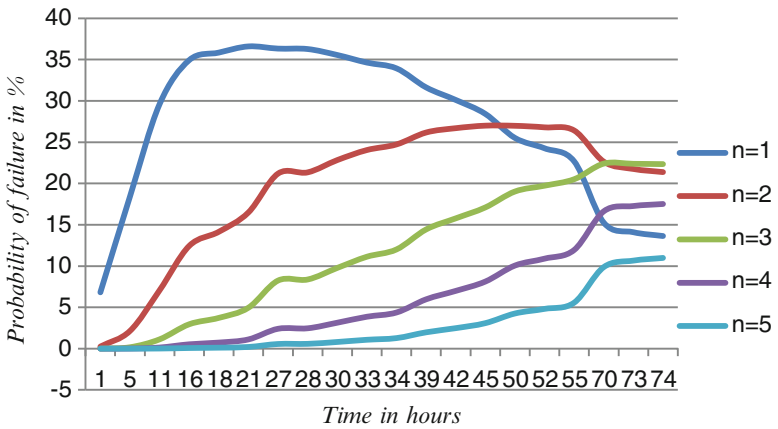

Fig. 5 Cumulative probabilty distribution graph for $\lambda = 1/24$

This tool of risk analysis only gives an idea of the probability of these failures occurring.

From the curves, it is observed:

- Minor failures have the maximum probability of occurrence (highest around 35%).

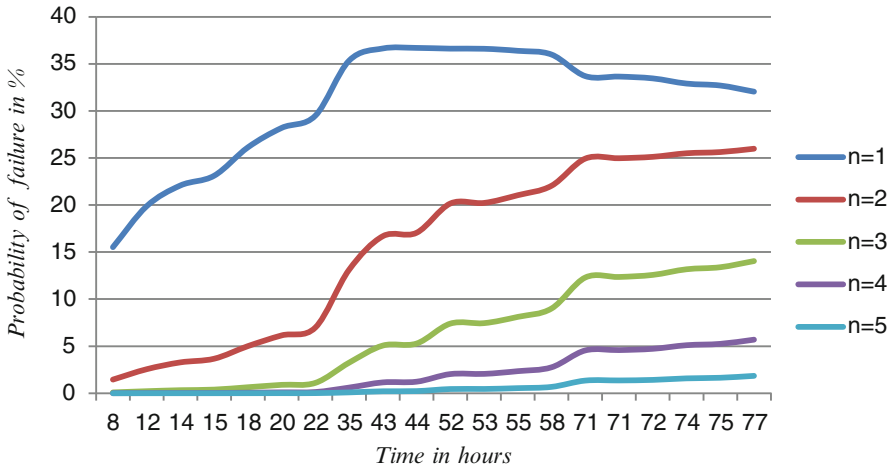

Fig. 6 Cumulative probabilty distribution graph for $\lambda = 1/48$

- Moderate failures have a probability of occurrence around 17% (highest).
- Catastrophic failures have very little chance of occurrence.

5.1 Debugging Period

From the graphs of debugging period for $\lambda = 1/24$, the probability of failures shoots up sharply and initially drops gradually, subsequently. This implies that in new machines, the probability of failure is higher during the infant operating period.

For $\lambda = 1/48$, the probability of failure increases progressively, reaches a highest value, remains constant for a certain period, then gradually decreases. Thus concluded that failure rate decreases after 1 day of working.

Results which will closely resemble the actual situation can only be obtained after exhaustive data from previous experiments have been gathered and used in the analysis. Risk analysis amplifies the predictive ability of sound models of reality. The accuracy of its predictions therefore can only be as good as the predictive capacity of the model employed.

Nonetheless, this chapter provides an approximate guidance on how the risk analysis method can be adopted in case of new machinery with no previous recorded data of its operation.

Following points may be summarized about the results:

1. It enhances decision-making on marginal projects. A project, on which experts have indigenously analysed the possible failures, may still be accepted following risk analysis on the grounds that its overall chances for yielding a satisfactory return are greater than is the probability of making an unacceptable loss.

2. Before any real expenses are incurred to gather information for a full feasibility study, it is possible to apply risk analysis, by widening the margins of uncertainty to reflect the lack of data. A substantial investment of human and financial resources is not incurred until the potential investors are satisfied that the preliminary risk/return profile of the project seems to be acceptable.
3. It highlights project areas that need further investigation and guides the collection of information.

Acknowledgements Part of the above work has been carried out in the Aerospace Engineering Department of Bengal Engineering and Science University, Shibpur, Howrah.

References

1. Wilkins DJ (2002) The Bathtub curve and product failure behavior part one – The Bathtub curve, infant mortality and burn-in. Reliability HotWire, 21. http://www.weibull.com/hotwire/issue21/index.htm
2. Kim ST, Tadjiev D, Yang HT (2000) Fatigue life prediction under random loading conditions in 7475-T7351 aluminium alloy using the RMS model. Int J Damage Mech 15:89–101
3. Preuss JL (2004) Design and analysis of a composite flywheel preload test rig. Master thesis, Texas A&M University
4. Savvides SC (1994) Risk analysis in investment appraisal. Beech Tree Publishing Surrey, 9(1):3–18

Prediction of CBR of Different Groups of Alluvial Soils for Design of Flexible Pavements

B.C. Chattopadhyay and J. Maity

Abstract In practice, determination of California bearing ratio (CBR) value in laboratory is laborious, time-consuming and costly. Furthermore, the results sometimes are not accurate due to poor quality of skill of the technicians testing the soil samples in the laboratory. In many case results, a limited number of prescribed tests may not be sufficient to map the field variation, and they may have very negative impact on the quality of the construction. Similarly enormous time is required to evaluate directly the CBR of constructed subgrade during checking for quality control. So evaluation of CBR of subgrade soils on the basis of simple, cheap and less time-consuming tests may be necessary. In the present investigation, an attempt has been made to develop a framework for prediction of CBR value of alluvial clayey soils which cover a large part of Indo-Gangetic plain and coastal area of Indian peninsula. For this purpose, a very large number of test results on soil samples collected from different sites in West Bengal have been used as the generalized parameter to characterize the clayey soil. The correlation is established in the form of an equation of CBR as a function of consistency limits by the method of regression analysis. The reliability of the proposed method has been studied for large number of tested values.

Keywords CBR • Quality control • Subgrade • Alluvial clayey soils • Consistency limits • Regression analysis

B.C. Chattopadhyay (✉) • J. Maity
CE Department, Meghnad Saha Institute of Technology, Kolkata 700 150,
West Bengal, India
e-mail: ccbikash@yahoo.com; joymaity1975@yahoo.co.in

S. Chakraborty and G. Bhattacharya (eds.), *Proceedings of the International Symposium on Engineering under Uncertainty: Safety Assessment and Management (ISEUSAM - 2012)*,
DOI 10.1007/978-81-322-0757-3_55,

1 Introduction

Prerequisite for economic upliftment of a country is proper development of right infrastructural facilities. Vast areas comprising the underdeveloped Third World countries in the world will be witnessing creation of massive transportation facilities through the length and breadth of these countries if necessary improvement in the economic conditions of those countries and their people are to be achieved. In India, as a national effort to increase such facilities, large-scale road construction is being undertaken over the last decade through different schemes like Pradhan Mantri Gram Sadak Yojona and Golden Quadrilateral projects. As a result, a large quantity of filling materials is being needed to construct the subgrades and embankments of such roads. Conventionally, materials for such fills are the available and usable soils around the alignment of the road to be constructed. Such low-volume roads are estimated to be 80% of the world's transportation infrastructure being developed, and the majority of such roads are unpaved [28]. As the riverine and coastal tracts form the most prosperous areas of any country, massive networks of roads interconnecting those areas form the primary step of development in a country. In such cases, materials for construction for road subgrade and embankments come from the local waterborne alluvial soils, which are generally most erratic in nature, both in vertical and horizontal extents.

California bearing ratio (CBR) is an empirical test, and results of such tests are widely applied in design of flexible pavement over the world. This is also used for design of rehabilitation of old pavements to determine the overlay thickness. The method was originally developed at California Division of Highways during 1928–1929 to provide assessment of the relative stability of fine-crushed rock base materials. Use of CBR test results for design of roads was introduced in the USA during the Second World War and subsequently adopted as standard method of design in other parts of the world. Flexible pavement design in India was standardized in 1970 by the Indian Road Congress (IRC) [8] which gave design curves from which the thickness of different pavement layers for a given traffic load and CBR results on subgrade soils [9, 10]. Though some reservations against the adoption of CBR method for design of flexible road pavement has been voiced in Western countries due to empiricalness of the method [4], CBR method of design of flexible pavements is most widely accepted method [19, 20].

However, to conduct a CBR test, representative soil sample has to be collected from the location selected, from which a remoulded specimen has to be prepared at predetermined optimum moisture content and γ_{dmax} with Standard Proctor Compaction, for the test to be conducted. To obtain soaked CBR value of a soil sample, it takes about a week, making CBR test expensive, time consuming and laborious. Improper handling and poor quality of testing conditions in hurriedly established field laboratories for temporary purposes in sites may have some reservations about accuracy of the results produced.

As a result, only a limited number of CBR test could be performed per kilometre length of the proposed road to be constructed, for preparation of detailed project

report, needed for sanction of fund for construction and finalizing the design of the road structure. Such limited number of CBR test results may not generally reveal the variation in the CBR values over the length of the road to enable rational, economic and safe construction. This is particularly true for road construction on alluvial soils which by nature of their development are extremely erratic in nature. In India, alluvial soil is one of the major soil type found in Indo-Gangetic plain (according to Indian Council of Agriculture Research (ICAR)). Deltaic plains along the Indian coasts are also marked by narrow to large width of alluvial soil cover. Thus, in such areas, only a limited number of CBR test values along the alignment of a road make it difficult for highway engineers to incorporate the in situ variations of soil properties of subgrade along the length of the road properly and also take rational step to identify and rectify local weakness present at any location, if any, along the length of the road.

This could be avoided only if a large number of soil sample are taken at short interval throughout the road length, and necessary CBR tests are conducted. But such a procedure will escalate the project cost and time. This problem not only arises during design before construction but also during and after construction at the time of checking the quality of construction by comparing the CBR values of the constructed portion with the designed value. In present scenario, quality control has become very important component of a road project. Such quality checking is practically becoming very difficult due to time and cost for getting CBR value at a chosen and doubtful location in a reasonable quick period of time.

In most of the modern day projects, the materials for earthwork construction come from highly variable sources, and the engineering properties of such soils after specified compaction will be varying to a large degree. In such cases, economy that might be achieved by the extensive testing to determine soil properties is out weighted by the economy due to saving in time by reasonably accurate quick prediction [30]. Thus, for cost-effective and quicker methods to evaluate the properties of subgrade soil, CBR value, on the basis of low-cost, easy-to-perform and less time-consuming tests, becomes important and necessary both during design stage and quality checking stage [22]. Development of prediction models might be useful and become a base of judgement on the validity of CBR values. In view of these factors, several attempts have been made in the recent decades to correlate with different simple properties of soils.

2 Available Correlations

Attempts have been made by several research workers to develop suitable correlation between CBR value of compacted soils at optimum moisture content (OMC) and different simple soil characteristics or results of some simple field tests. Brief reviews of these correlations are described below.

2.1 Correlations Based on Simple Field Test Results

Large numbers of researches have used the results of a simple device called Clegg Impact Tester. The Clegg Impact Value (CIV) given by the device is the resistance offered by the top soil of about 25-cm thickness against a falling hammer of standard weight.

For a variety of soils, Venkatraman et al. [29] suggested that

$$\text{CBR } (\%) = 1.3728 \text{ (CIV)} + 0.868 \tag{1}$$

In similar manner on basis of test results on soils around Tirupathi, Chandrasekhar et al. [5] suggested that

$$\text{CBR } (\%) = 1.1242 \text{ (CIV)} - 0.3466 \tag{2}$$

For general soils, Omar et al. [18] suggested that

$$\text{CBR } (\%) = 0.169 \text{ (CIV)} + 1.695 \tag{3}$$

It has been observed that different geologic origins of soils affect the correlation. With indigenously developed impact tester, Central Road Research Institute (CRRI) has developed a correlation with such test results [14].

An investigation conducted by Baghabra Al-Amoudi et al. [2] to assess the efficacy of the Clegg Impact Hammer (CIH) for estimating strength of compacted soil is conducting comparative study between tested values of CBR and predicted values for CIH tests.

Studies have been made to correlate the CBR value with dynamic cone penetration test result. Nuwaiwu et al. [16] and Karunaprema and Edirisinghe [12] had correlated CBR value with DCP and plasticity modulus (plasticity index $\times$ percentage passing 425μ test sieve) as given below:

$$\begin{gathered}\text{CBR} = 3\text{E} - 0.4\ \text{PM}^3\ 0.26\ \text{PM}^2 + 64.73\ \text{PM} - 5,306.7 \\ \text{(for laterite gravels in Nigeria)}\end{gathered} \tag{4}$$

where PM = plasticity modulus,

$$\begin{gathered}\text{Log CBR (unsoaked)} = 1.966 - 0.6671 \log \text{DCP} \\ \text{(for clayey grave; and silty gravel)}\end{gathered} \tag{5}$$

where DCP = dynamic cone penetration.

Above relations are empirical correlations and may give reliable results only for the geographical region for which such structures have been made.

2.2 Correlations Based on Simple Soil Properties

Many correlations studies for CBR have been reported over the last 50 years, taking into account different soil parameters like grain size, soil classification, index properties, compaction characteristics, bearing capacity, modulus of subgrade relation and elastic stiffness.

Black [3] developed a method to estimate the CBR value for cohesive soils in terms of the plasticity index (PI) under various liquidity indexes. Another correlation for prediction of CBR value was developed from LL, PI and grading, by using the concept of suitability index, as defined below:

$$\text{Suitability index} = \left(\frac{A}{(\text{LL})\log(\text{PI})}\right) \tag{6}$$

where A = percentage passing 2.4-mm BS sieve. Agarwal and Ghanekar [1] presented a relation between CBR and optimum moisture content (W_{opt}) and liquid limit (LL):

$$\text{CBR} = 2 - 16\log\left(W_{\text{opt}}\right) + 0.07\text{LL} \tag{7}$$

But the validity of the above relation could not be substantiated significantly [24]. Doshi et al. [7] reported that grading constant is the best parameter to discrete the influence of grain size distributions on CBR. CBR is more dependent on maximum dry density than optimum moisture content.

Central Road Research Institute [6]) developed a nomograph for prediction of soaked CBR value from sieve analysis data. The Highways Agency predicted a correlation between CBR value based on PI for British soils compacted at natural moisture content. National Cooperated Highway Research Program [15] proposed the following equation to predict CBR from index properties for soils with 12% fines and with some plasticity:

$$\text{CBR} = \left(\frac{75}{1 + 0.728(w.\text{PI})}\right) \tag{8}$$

where w = percentage passing 75μ I.S. sieve, PI = plasticity index.

Rao [19] presented correlations between CBR and group index based on tests on large number of soils. For fine-grained and coarse-grained soils, he developed the following correlation:

$$\text{CBR}\ (\%) = 22.434(\text{Group Index No})^{-0.5256} \quad \text{for fine-grained soils.} \tag{9}$$

$$\text{CBR}\ (\%) = 17.166\text{e}^{-0.444} \quad \text{for coarse-grained soils.} \tag{10}$$

For fine-grained soils, the correlations showed encouraging agreements, while the correlation developed for coarse-grained soils is less reliable.

Shukla and and Kukelyellkar [25] developed a correlation between CBR and the compaction properties for compacted fly ash. Kin [13] developed a correlation for soaked CBR from optimum moisture content and maximum dry density, as given below:

$$\text{CBR (soaked)} = \text{OMC}\left(\frac{\text{MDD}}{19.3}\right)^{20} \tag{11}$$

where MDD = max^{m} dry density in kN/m^3
OMC = optimum moisture content (%).

A study to check the validity of available correlation between CBR and other properties of soils was made by Roy and Chattopadhyay [21], and they concluded that only partial agreement between predicted and observed values of CBR was indicated.

Vinod and Cletus [30] developed a correlation for CBR on the basis of test results on lateritic soils conducted from state of Kerala at a depth of 0.5 m beneath ground surface. On the basis of regression analysis, they presented a linear relation:

$$\text{CBR} = -0.889(W_{\text{LM}}) + 45.616 \tag{12}$$

where W_{LM} is modified liquid limit and a function of liquid limit and percentage of soil coarser than 425-μm sieve and is given by

$$W_{\text{LM}}(\%) = W_{\text{L}}\left(1 - \frac{C}{100}\right) \tag{13}$$

where W_{L} = liquid limit on soil passing 425 μm (%) and C = fraction of soil coarser than 425 μm (%). Assuming that CBR (soaked) value depends both on the OMC and γ_{dmax}, Roy and Chattopadhyay [22] expressed the relation between them in nondimensional form as

$$\text{CBR(soaked)} = (\text{OMC})^{\alpha}\left(\frac{\gamma_{\text{d max}}}{\gamma_{\text{w}}}\right)^{\beta} \tag{14}$$

where α and β are nondimensional factors and γ_{w} = unit weight of water.

They evaluated the values of α and β for different groups of cohesive soils from results of a large number experimental value of CBR (soaked) for different values of γ_{dmax} and OMC of various soils of different groups like CL, CI and CH.

Taskiran [27] reported on the basis of artificial neural network study that dry unit weight is the most important parameter for prediction of CBR. Sahoo et al. [24] on the basis of results of different compaction characteristics of soils developed the following empirical relations:

$$\text{CBR} = 7.88\text{MDD} - 0.17P_{0.075} - 0.07w\text{LL} + 5.07 \quad (15)$$

where MDD = Max^{m} dry density in g/cc. and $P_{0.075}$ = percentage passing 75μ I.S. sieve.

Roy et al. [23] made a study on comparison of value of CBR by different methods and tested values of CBR for large number soils. Predicted CBR (soaked) value by presumptive design chart as specified by IRC [10] have shown significant differences from tested values. The difference grows further for nonplastic soils having the same amount of sand. Patel and Desai [17] presented some correlations for soaked and unsoaked CBR values for alluvial soils of south Gujarat from different values of LL, PI, OMC and γ_{dmax} of the soils. They concluded that as PI increases, CBR value decreases and CBR increases when PI value decreases.

3 Need for Further Study

From above brief review, it is observed that studies on the prediction of CBR value by correlating the same with easily determinable soil parameters have been made to certain extent. Such correlations being empirical in nature may give reliable results only for the geographical region from which such soil data for correlation were collected. Further majority of correlations are for CBR values in unsoaked correlation, while in design of flexible pavement in majority cases, CBR values in soaked condition are to be used.

Pointing out the urgent need for an alternate method for CBR test, Sikdar [26] indicated that possible variation in pavement thickness resulting from an error in estimation of CBR value may lead to unnecessary wastage of money. Similarly the non-identification of the weak spots along the alignment of proposed road, which is possible when only limited numbers of CBR tests are conducted in conventional manner, may lead to short life of the road itself.

Since alluvial soils exist over large part of North India and coastal plains of India, and as alluvial soils are extremely erratic in nature, it was felt that an elaborate search needs to be made to develop a correlation for CBR values in soaked condition on the basis of results of simple, less costly quick tests on such soils. The case study was made on alluvial soil deposits in different districts in West Bengal. For the study, reported test results for LL, PL, sand content, γ_{dmax} and OMC value and soaked CBR values for different sites as examined by the senior author as member of a STA for PMGSY roads, for different cases, are used.

It has been seen in the former section that correlations have been developed for CBR from different input parameters. Reliability of any prediction depends primarily on the relative importance of the factor in controlling the magnitude of the output. In search of the best correlation for CBR, the most important parameter influencing the value of CBR should be identified. This was studied by Kaur et al. [11], following innovative technique proposed. They have indicated that plasticity

index followed by the liquid limit is the most important factor influencing value of CBR. Other parameters like maximum dry density, fine fraction and sand fraction have influence but of much lesser significance. Compactive energy, no doubt, has very great influence on resulting CBR value, but as compaction effort used for most of the situations is standard proctor, so the study will not be considering the variation of compactive energy.

In view of the above discussion, a study was undertaken for finding correlation for CBR (soaked) for LL and PI of the soils from alluvial plain of the country. Validity of the correlation developed was tested by comparing the predicted value of CBR (soaked) into tested value of CBR (soaked) on alluvial soil deposits in South Gujarat as reported by Patel and Desai [17].

4 Development of Relationship Between CBR (Soaked) and Plastic Property

To develop the relationship between CBR (soaked) and plastic property, a large number of test results on soil samples collected from different sites in West Bengal like liquid limit and plastic limit have been used as the generalized parameter to characterize the clayey soil. Table 1 gives the test results of the soil sample collected from different sites in West Bengal. An index, α (alpha), is introduced to establish the relationship between CBR (soaked) and plastic property. The α (alpha) index is defined as given below:

$$\alpha \text{ (alpha) index} = \left(\frac{\text{PI}}{\text{LL}}\right)$$

where LL = liquid limit and PI = plasticity index.

For any liquid limit, the value of α is plotted against tested value of CBR (soaked) for the soils having that liquid limit but varying plastic limit. Best fit linear relationship between CBR (soaked) value and the value of α was obtained in form

$$\text{CBR} = A(\alpha) + B$$

where A and B were two constants and value of A and B for the liquid limit were obtained from the plots.

The R^2 values of the above correlation were in the range 0.78–1.

The values of the constant A and B were evaluated in similar fashion for different liquid limits. From the value of the data, A and B, for each soil group CH, CI and CL were plotted against liquid limits separately in Figs. 1, 2 and 3, respectively. The R^2 values of these correlations are in the range 0.82–0.97.

Table 1 Test results of the soil sample collected for different group soils

Test results of the soil sample collected for CH soils					Test results of the soil sample collected for CI soils				
LL	PL	PI	PI/(LL)	CBR	LL	PL	PI	PI/(LL)	CBR
69	19	50	0.725	3.9	49	21	28	0.571	4.6
69	18	51	0.739	3.6	49	22	27	0.551	4.1
69	33	36	0.522	3.4	49	23	26	0.531	4
58	22.5	35.5	0.611	3.3	49	25	24	0.49	3.3
58	26.5	31.5	0.545	3.2	49	25.4	23.6	0.48	3.3
58	26.6	31.4	0.543	3.1	44	20.4	23.6	0.538	5
58	26.7	31.3	0.541	3	44	21	23	0.523	4.3
58	28	30	0.517	2.9	44	22	22	0.5	4
58	30	28	0.483	2.9	44	23	21	0.477	3.8
57	24	33	0.579	3.3	44	24	20	0.455	3.7
57	27.2	29.8	0.52	3	44	24.8	19.2	0.439	3.2
57	27.4	29.6	0.516	2.9	44	25	19	0.432	3.2
56	18	38	0.679	4.2	43	20.4	22.6	0.524	5.2
56	22	34	0.607	4.1	43	22	21	0.488	4.3
56	26	30	0.536	3.3	43	23	20	0.465	3.9
56	28	28	0.5	3.1	43	22	21	0.488	3.9
56	27.2	28.8	0.518	2.8	43	23	20	0.465	3.7
55	20	35	0.636	5.1	43	24	19	0.442	3.6
55	20.4	34.6	0.626	4.2	43	25	18	0.419	3.4
55	26	29	0.527	4	42	20.8	21.2	0.504	5.8
55	27	28	0.509	3.3	42	22	20	0.476	4.3
54	20	34	0.63	4.5	42	23	19	0.452	4
54	22.5	31.5	0.583	4.5	42	24	18	0.429	3.8
54	23.3	30.7	0.571	4	42	25.3	16.7	0.4	3.7
54	25	29	0.537	4	42	25.4	16.6	0.393	3.6
54	26	28	0.519	3.4	41	20.2	20.8	0.507	5.3
54	27	27	0.5	3.3	41	21.2	19.8	0.482	4.6
54	28	26	0.481	3.3	41	22	19	0.463	4.4
54	29	25	0.463	3	41	22.8	18.2	0.443	4
53	20	33	0.623	5.3	41	23	18	0.439	3.9
53	21.7	31.3	0.59	4.6	41	23.6	17.4	0.425	3.7
53	24	29	0.547	3.4	Test results of the soil sample collected for CL soils				
53	26	27	0.509	3.3	LL	PL	PI	PI/(LL)	CBR
53	28	25	0.472	2.9	35	17	18	0.514	7.6
52	21	31	0.596	6	35	17.8	17.2	0.491	5.3
52	24	28	0.538	4	35	19	16	0.457	4
52	25	27	0.519	3.4	35	22	13	0.371	3.1
52	27	25	0.481	3.3	35	23	12	0.343	3
52	28	24	0.462	3.1	34	17	17	0.5	5.4
51	22	29	0.569	5.2	34	17.3	16.7	0.49	5.2
51	26	25	0.49	3.5	34	17.6	16.4	0.48	4.9
51	27	24	0.471	3	34	20	14	0.41	3.7
50	20	30	0.6	5	34	21.9	12.1	0.36	3.6
50	20.9	29.1	0.585	4.4	34	22	12	0.35	3.3
50	21	29	0.58	3.9	33	17.4	15.6	0.47	5.8

(continued)

Table 1 (continued)

Test results of the soil sample collected for CH soils					Test results of the soil sample collected for CI soils				
LL	PL	PI	PI/(LL)	CBR	LL	PL	PI	PI/(LL)	CBR
0	22	28	0.56	3.8	33	18	15	0.45	5.3
33	18.4	14.6	0.44	4.8					
33	19.8	13.2	0.4	4.1					
33	20	13	0.39	4					
33	21.4	11.6	0.36	3.9					
33	22	11	0.33	3.9					
33	22.6	10.4	0.32	3.2					
32	20	12	0.38	4					
32	21	11	0.34	3.8					
32	21.7	10.3	0.32	3.1					
30	17.2	12.8	0.43	5					
30	18	12	0.4	4.6					
30	19	11	0.37	4.1					
29	15.3	13.7	0.47	7.5					
29	17.5	11.5	0.4	5.1					
29	21	8	0.28	3.8					
28	16.9	11.1	0.39	6.8					
28	18	10	0.36	6.5					
28	22	6	0.21	4.2					
25	11	14	0.56	8					
25	13	12	0.48	7.8					
25	14	11	0.44	4.5					
24	11	13	0.54	7.5					
24	12.9	11.1	0.46	4.4					
24	14.1	9.9	0.41	3.9					
24	16.9	7.1	0.3	3.9					
23	12.2	10.8	0.47	6.4					
23	12.6	10.4	0.46	5.7					
23	13.2	9.8	0.42	4.9					
22	12	10	0.46	6.9					
22	13.1	8.9	0.41	5.4					
22	13.1	8.9	0.4	5					

5 Validation of Correlations

Validity of the correlation developed was tested by comparing the predicted value of CBR (soaked) with tested value of CBR (soaked) on alluvial soil deposits in South Gujarat as reported by Patel and Desai [17], which are reproduced in Table 2. In the same table, the values of α corresponding to the sample tested are evaluated

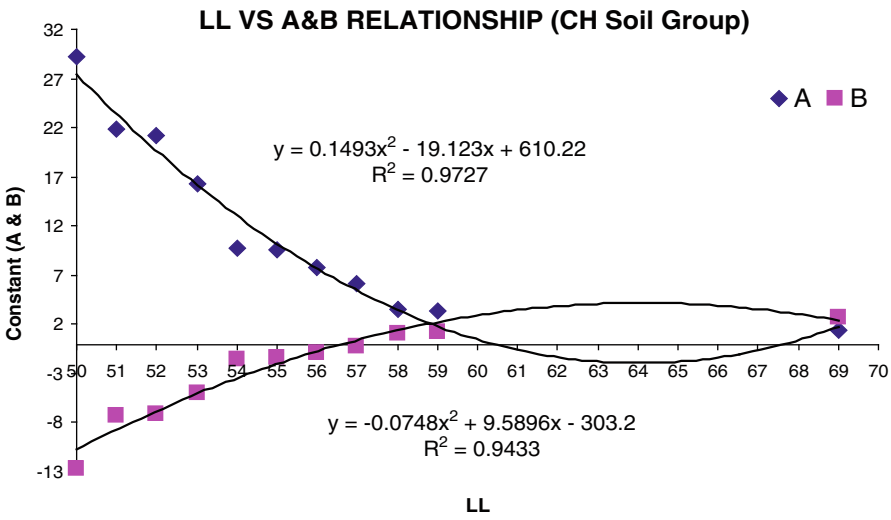

Fig. 1 Variation of constant *A* and *B* with LL for CH soils

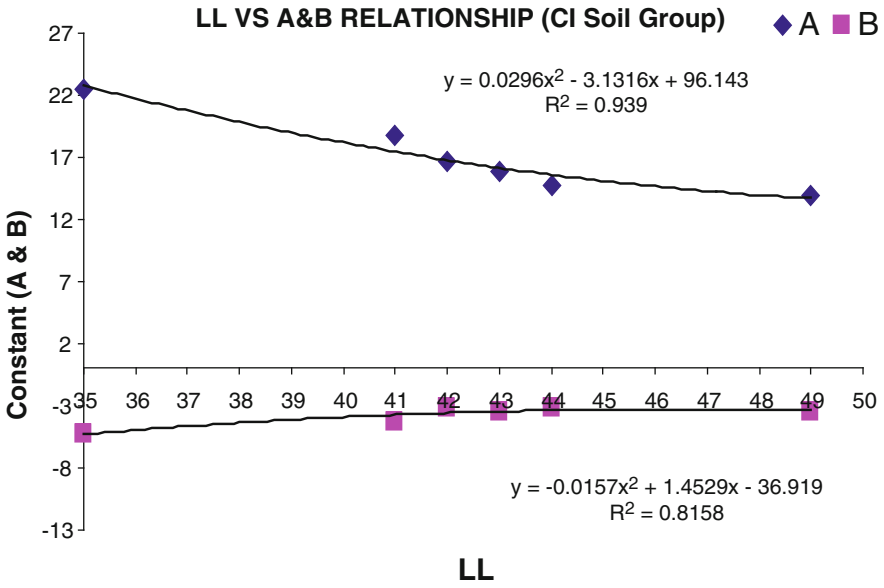

Fig. 2 Variation of constant *A* and *B* with LL for CI soils

and given. Also the constant *A* and *B* were evaluated from Figs. 1 and 2, and the values of predicted CBR (soaked) are also shown in the same table.

From Table 2, the tested value of CBR (soaked) by Patel and Desai [17] can be compared with the predicted value. Further, the measured and predicted values of

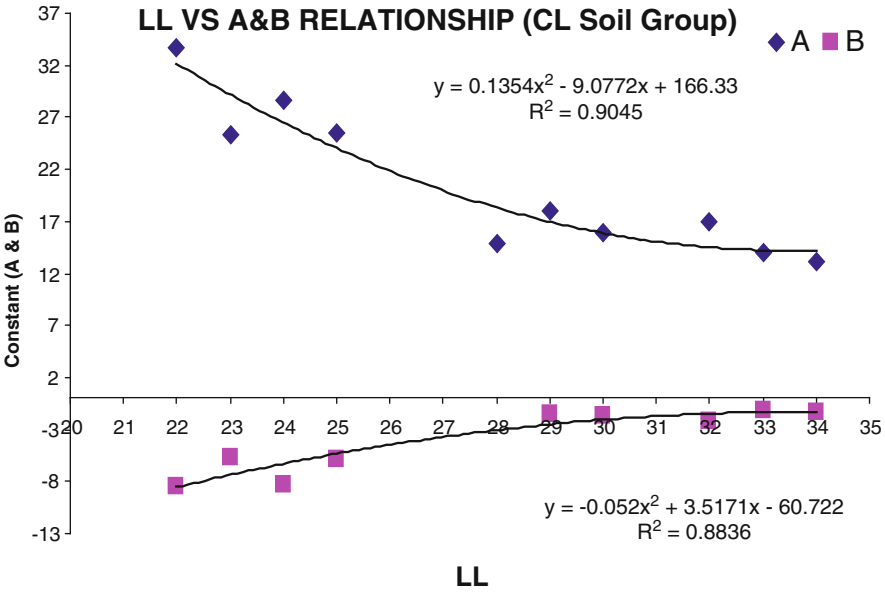

Fig. 3 Variation of constant *A* and *B* with LL for CL soils

Table 2 Tested value of CBR (soaked) on alluvial soil deposits in South Gujarat [17]

						Tested value of		
LL	PL	PI	Alpha	*A*	*B*	CBR (unsoaked)	CBR (soaked)	CBR (predicted) from present correlation
52.98	18.54	34.44	0.650	16.2	−7	5.48	1.54	3.50
63.63	26.8	36.83	0.579	−2.1	4	7.73	1.82	2.79
58.79	19.7	39.09	0.665	2.0	1.8	4.05	1.73	3.13
70.78	24.68	46.1	0.651	4.7	−0.5	3.3	2.3	2.53
59.57	20.07	39.5	0.663	0.9	2.8	5.37	3.02	3.37
50.58	18.86	31.72	0.627	24.9	−11	5.88	4.42	4.64
61.77	18.75	43.02	0.696	−1.3	4.4	5.80	3.6	3.46
64.87	17.09	47.78	0.737	−2.0	3	3.13	1.73	1.51
44.7	20.51	24.19	0.541	15.3	−4.5	2.80	2.15	3.78
53.47	19.26	34.21	0.640	14.6	−4.5	8.94	3.1	4.82
49.58	20.31	29.27	0.590	13.6	−4.7	5.47	3.35	3.35
64.39	19.81	44.58	0.692	−2.1	3	5.20	2.48	1.55

CBR (soaked) are also given in Fig. 4 for visual comparison. It may be observed from Fig. 4 that the predicted soaked CBR values are quite close to the measured values using the present correlation for majority of test results. For the samples for which large variation is observed between the listed value of CBR in soaked and unsoaked condition, it is seen that the predicted value from present correlation is much higher than the soaked tested CBR value.

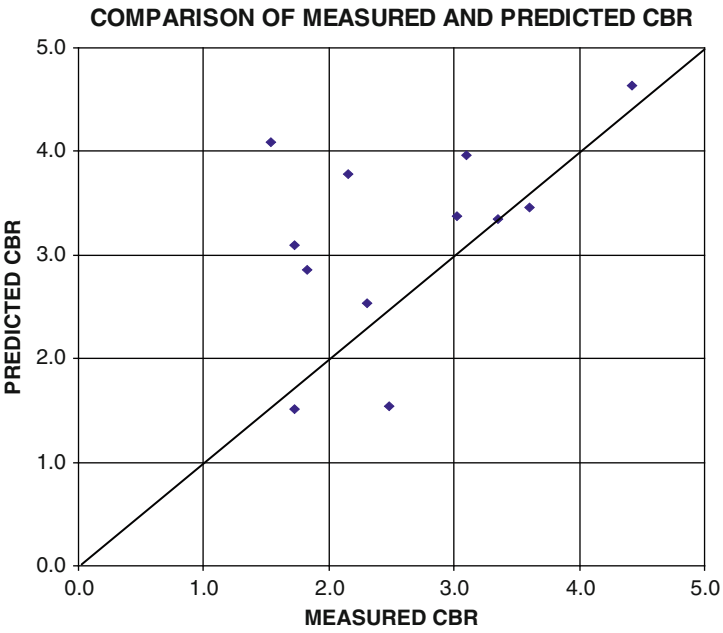

Fig. 4 Measured and predicted values of CBR (soaked) in %

6 Conclusion

On the basis of extensive test results for CBR (soaked) value of various alluvial soils having wide range of liquid limit and plastic limit, a generalized correlation between soaked CBR value and liquid limit and plastic limit of alluvial soils has been established. On the basis of comparison between tested CBR (soaked) values and predicted CBR values from the proposed correlation, encouraging agreements have been observed. The salient conclusions from this study are:

1. The CBR (soaked) values for alluvial soil can be expressed in terms of liquid limit of the soils in the form of linear relationship:

$$\text{CBR (soaked)} = A(\alpha) + B$$

where, $\alpha = (\text{PI}/\text{LL})$, and,
A and B are two nondimensional parameters depending on the value of liquid limit of the soil.
2. The design chart for A and B has been provided for all the three groups of clayey soils, namely, CH, CI and CL.
3. When compared with measured values of soaked CBR for several alluvial soils from South Gujarat, reported by Patel and Desai [17], the predicted values from present correlation indicate encouraging agreements.

References

1. Agarwal KB, Ghanekar KD (1970) Prediction of CBR from plasticity characteristics of soil. In: Proceedings of the 2nd South-East Asian conference on soil engineering, Singapore, 11–15 June 1970. Asian Institute of Technology, Bangkok, pp 571–576
2. Baghabra Al-Amoudi OS, Mohammed Asi I, AlAbdul Wahhab HL, Ziauddin A (2002) Clegg Hammer-California-bearing ratio correlations. J Mater Civil Eng ASCF 14(6):512–523
3. Black WPM (1962) A method of estimating the CBR of cohesive soils from plasticity data. Geotechnique 12:271–272
4. Brown SF (1996) Soil mechanics in pavement engineering. Geotechnique 46(3):383–426
5. Chandrasekhar BP, Vinayak RVR, Prasada RGVR (2003) A comprehensive study of soil CBR assessment through Clegg impact test, field and laboratory CBR tests. Indian Highw, IRC 31(7):39–45
6. Central Road Research Institute (1990) Document on rural road development in India, vol II. CRRI, New Delhi
7. Doshi SN, Mesdary MS, Guirguis HR (1983) Statistical study of laboratory CBR for Kuwaiti soils. In: Fourth conference of the road engineering association of Asia and Australasia, vol 2, Jakarta, 22–26 Aug 1983, pp 43–51
8. IRC: 37 (2001) Guidelines for the design of flexible pavements. Indian Roads Congress, New Delhi
9. IRC: SP: 20 (2002) Rural roads manual. Indian Roads Congress, New Delhi
10. IRC: SP: 72 (2007) Guidelines for the design of flexible pavements for low volume rural roads. Indian Roads Congress, New Delhi
11. Kaur S, Ubboveja VS, Agarwal A (2011) Artificial neural network modelling for prediction of CBR. Indian Highw 39(1):31–38
12. Karunaprema KAK, Edirisinghe AGHJ (2002) A laboratory study to establish some useful relationship for the use of dynamic cone penetrometer. Electron J Geotech Eng 7
13. Kin MW (2006) California bearing ratio correlation with soil index properties. Masters thesis, Faculty of Civil Engineering, University of Technology, Malaysia
14. Kumar P, Renu P, Saini RP, Bharadwaj AK, Chadha R, Rao PSKM (2000) An indigenous impact tester for measuring in-situ CBR of pavement materials. Highw Res Bull IRC 63:13–22
15. National Cooperative Highway Research Program (2002) Guide for mechanistic and empirical – design for new and rehabilitated pavement structures, Final document. West University Avenue Champaign, IL, USA
16. Nuwaiwu CMO, Alkali IBK, Ahmed UA (2006) Properties for iron stone lateritic gravels in relation to gravel road pavement construction. Geotech Geol Eng 24:283–298
17. Patel RS, Desai MD (2010) CBR predicted by index properties for alluvial soils of South Gujarat. In: Proceedings of the Indian Geotechnical conference, Mumbai, pp 79–82
18. Omar SBA, Ibrahim MA, Hamad IAW (2002) Clegg Hammer California bearing ratio correlation. J Mater Civil Eng 14(6):512–523
19. Rao KS (2004) Correlation between CBR and compression index. In: Proceedings of the Indian Geotechnical conference, Warangal, pp 477–480
20. Rollings MP, Rollings RS (1996) Geotechnical materials in construction. McGraw-Hill, New York
21. Roy TK, Chattopadhyay BC (2006) Prediction of compaction characteristics of subgrade materials for the road. In: Proceedings of the Indian geotechnical conference, vol 2, Chennai, pp 737–740
22. Roy TK, Chattopadhyay BC, Roy SK (2009) Prediction of CBR from compaction characteristics of cohesive soils. Highw Res J July–Dec:77–88
23. Roy TK, Chattopadhyay BC, Roy SK (2010) California bearing ratio, evaluation, and estimation: a study on comparison. In: Proceedings of the Indian Geotechnical conference, Geotrendz, Mumbai, pp 19–22

24. Sahoo UC, Kalpanrani MG, Bisht AS (2010) Effect of gradation, index properties, and compaction characteristics of subgrade strength. In: International conference on developments in road transportation, NIT, Rourkela, India, 8–10 Oct 2010
25. Shukla SK, Kukelyellkar MP (2004) Development of CBR correlations for the compacted fly ash. In: Proceedings of the Indian Geotechnical conference, Warangal, pp 53–56
26. Sikdar PK (2003) Pradhan Mantri Gram Sadak Yojana: striving for quality and economy. Indian Highw IRC 31(6):77–91
27. Taskiran T (2010) Prediction of California bearing ratio (CBR) of fine grained soils by Al methods. Adv Eng Softw 41(6):886–892
28. Tingle JS, Jersey SR (2007) Empirical design methods for geosynthetic reinforced low-volume roads. In: Transportation research record: Journal of the Transportation Research Board of the National Academics, Washington, DC, pp 91–101
29. Venkatraman TS, Samson M, Ambili TS (1995) Correlation between CBR and Clegg impact value. In: Proceedings of the national seminar on emerging trends in highway engineering, vol I, Centre for Transportation Engineering, Bangalore, pp 25.1–25.5
30. Vinode P, Cletus R (2008) Prediction of CBR value of lateritic soils using liquid limit and gradation characteristics data. Highw Res J I(1):89–98, July-Dec

Drought Risk Assessment Using GIS and Remote Sensing

Sujata Biswas, Srabasti Sinha Roy, and Suprakash Sarkar

Abstract Risk assessment is one of the key elements of a natural disaster management strategy as it allows for better mitigation and preparation. The non-structural characteristic of drought impacts has hindered the development of accurate, reliable and timely estimates of severity and planning in most of the cases. So drought risk assessment may help in the delineation of major areas facing drought, and thereby management plans can be formulated to cope with the disastrous effects of this hazard.

In recent years, geographic information system (GIS) and remote sensing (RS) have played a key role in studying different types of hazards. This study stresses upon the use of remote sensing and GIS in the field of drought risk evaluation. In the present study, an effort has been made to derive drought risk areas facing agricultural as well as meteorological drought in Bankura district of West Bengal by use of conventional data and available satellite images. The approach included creation of a spatial database and its integration in GIS environment by developing a suitable ranking and rating scheme for the generation of drought severity map. The results obtained provide information on severity of drought vulnerability, which has practical relevance to agricultural importance and for planning drought management and combating drought.

Keywords Risk assessment • Severity • Drought • Remote sensing • Geographical information system

S. Biswas (✉) • S.S. Roy • S. Sarkar
Department of Civil Engineering, Bengal Engineering and Science University, Shibpur, India
e-mail: biswas.sjb@gmail.com; sujata@civil.becs.ac.in; srabasti.besu@gmail.com

S. Chakraborty and G. Bhattacharya (eds.), *Proceedings of the International Symposium on Engineering under Uncertainty: Safety Assessment and Management (ISEUSAM - 2012)*,
DOI 10.1007/978-81-322-0757-3_56,

1 Introduction

Drought is one of the major disasters around the world leading to "severe water crisis". Risk is defined as the expected losses, including lives, personal injuries, property damages and economic disruptions, due to a particular hazard for a given area and time period (WMO [6]). Droughts are recurring climatic events bringing significant water shortages, economic losses and adverse social consequences. Drought is considered by many to be the most complex but least understood of all natural hazards, affecting more people than any other hazard.

It is true that the main cause behind drought is precipitation and its variability, but there are more other factors contributing to the rise of waterless situation. Drought is a slowly creeping natural hazard that is a normal part of climate for virtually all regions of the world which results in serious economic, social and environmental impacts. Drought onset and end are difficult to determine as its severity. It is estimated that 4 billion people of the world's population will live under conditions of water stress by 2025 with conditions severe in Africa and Asia.

Even though India has a long history of drought events in the past, it lacks proper drought management strategy at national level yet. The country needs the drought severity map for providing drought relief and management in time. There are strong links between poverty and proneness of an area to drought. Widespread crop failures leading to acute shortages of food and fodder adversely affecting human and livestock health and nutrition, scarcity of drinking water accentuated by deteriorating ground water quality and declining water tables leading to large-scale migration are the major manifestations of droughts.

Satellite data have been used frequently in the past for the study of disaster and land degradation. For qualitative assessment of drought, it is necessary to integrate and study the combined effects of terrain, meteorological and land characteristics of the area for which GIS is essentially required.

Kumar et al. [3] carried out micro-level drought vulnerability assessment utilising GIS in Addakal Mandal of Andhra Pradesh, India. The water requirement for all the 21 villages in Addakal Mandal was calculated, taking into consideration the requirements for human and livestock consumption and crop irrigation. As the groundwater condition in this region is critical, the water availability in irrigation tanks for meeting the requirements for each village was calculated for different rainfall scenarios. The percentage deficit or surplus for each village was calculated, and the drought vulnerability maps were generated. These maps were provided to the farmers along with the rainfall predictions of the season. An arrangement to monitor daily rainfall was set up and tested. This was useful in further refining the vulnerability assessment.

Chopra [1] carried out drought risk assessment using remote sensing and GIS in the State of Gujrat. Resultant risk map has been obtained by integrating agriculture, and meteorological drought risk map indicated that the area is facing a combined

hazard. The map also represented the frequency of years a particular area faced the hazard.The study shows the results that can be used in taking corrective measures timely to minimise the reduction in agricultural production in drought-prone areas.

Prakash et al. [4] prepared drought severity map in Gubbi Taluk of Karnataka, India, by integrating 17 parameters which affect the drought. The approach included creation of a spatial database and its integration in GIS by developing a suitable rating and ranking scheme for the generation of drought severity map. The drought severity map was prepared using remote sensing data and other information. It was found that moderate drought was more predominant which accounts for 85% affecting about 300 villages.

In the present study, an attempt has been made to create an overall spatial database for drought risk assessment, and a drought severity map has been prepared for Bankura district of West Bengal.

2 Study Area

Bankura district is one of the seven districts of Burdwan Division in the Indian state of West Bengal. The district has been described as the connecting link between the plains of Bengal in the east and Chota Nagpur plateau on the west. The areas to the east and northeast are low-lying alluvial plains, and to the west, the surface gradually raises comprising rocky hillocks. Bankura is situated between 22°38′ and 23°38′ north latitude and between 86°36′ and 87°46′ east longitude, having the gross area about 6,882 sq km. On the north and northeast, it is bounded by Burdwan district, from which it is separated by Damodar River. On the southeast, it is bounded by Hooghly district, on the south by Paschim Midinipur district and on the west by Purulia district. The western part of the district has poor lateritic soil with scrubs and sal woods. In the eastern part, there are wide expanses of agricultural lands. About 46% of the net cropped area is under irrigation. Rice, wheat, oil seeds and vegetables are the principal crops that occupy the majority of the gross cropped area. Intermittent gaps of in precipitation and moisture stress during the monsoon give rise to serious setback in production during the Kharif, which is the mainstay of agriculture in the district.

The climate especially to the upland tract in the west is much drier than eastern or southern Bengal. From the beginning of March to June, hot westerly winds prevail with maximum temperature around 45°C. The monsoon months (June to September) are comparatively pleasant with annual rainfall of about 1,400 mm. Winters are pleasant with temperature around 20°C.

3 Preparation of Thematic Layers

The data used for this study comprises of remotely sensed data and conventional data from different sources which includes the following:

1. Satellite image of Bankura district IRS-P6 LISS-III (acquired on Jan. 2006 from NRSA)
2. Annual rainfall and monthly rainfall data (5 years average) (acquired from National Atlas Thematic Mapping Organization (NATMO), Kolkata and IMD, Pune website)
3. Ground water yield data (NATMO, Kolkata)
4. Slope map (NATMO, Kolkata)
5. Soil map (NATMO, Kolkata)
6. Block boundary data (Bankura Zilla Parishad map)
7. Census data (Bankura govt. website)

Eight thematic layers have been generated from the above-mentioned data and used further to create a spatial database in GIS and risk assessment of drought.

3.1 Concept of Rankings and Ratings

Prior to integration of different thematic layers representing different information, individual class weights and map scores were assigned based on Saaty's Analytic Hierarchy Process. In this method, a pairwise comparison matrix was prepared for each layer using Saaty's nine-point importance scale, and this matrix was solved using eigenvector method.

Table 1 presents the details of various parameters and their relative ranking (weightage) and rating (4 having the highest and 1 having the lowest drought severity) that indicate the drought severity. The drought severity of a region depends on the cumulative effect of individual themes/classes. For this, the model is made to consider individual parameters to obtain a combined effect.

4 Development of GIS Model

The arithmetic overlay approach built into Arc View Model Builder of Spatial Analyst Module is used for the integration of the input data layers. The rating of each parameter is multiplied by its rank, and the sum of the cumulative values of all parameters is used for categorisation of drought into different classes to generate a drought severity map. Figure 1 represents the model for generation of drought severity map (Table 2).

The drought severity map generated by this model is shown in Fig. 2 which shows different drought classes which can be classified as not drought prone (0–1.6), mild

Table 1 Ranking and rating of various parameters

Sl. no.	Parameter	Ranking	Range of values	Rating
1.	Annual rainfall (mm)	0.25	>1,600	2
			1,400–1,500	3
			<1400	4
2	Monthly rainfall (mm)	0.22	240–295	2
			205–240	3
			120–205	4
3.	Soil	0.13	Gravelly soil	4
			Lateritic soil	2
			Older alluvial soil	1
			Red sandy soil	3
			Red yellow soil	3
			Younger alluvial soil	1
4.	Land use	0.11	Agriculture	1
			Dense sal	2
			Fallow land	4
			Open sal	3
			Reservoir	-
			Sand	4
			Shallow water	-
5	Ground slope	0.11	<10	1
			10–20	2
			20–80	3
			80–150	4
6	Ground water yield	0.1	>40	1
			25–40	2
			10–25	3
			1–5	4
7.	Cultivator density	0.05	116–141	1
			91–115	2
			65–90	3
			40–64	4
8.	Population density	0.03	244–358	1
			359–472	2
			473–586	3
			587–700	4

drought prone (1.6–2.4), moderate drought prone (2.4–3.2) and severe drought prone (3.2–4). The block boundary map was overlaid on drought severity map which is shown in Fig. 3. The statistics obtained from the map is presented in Table 3.

Fig. 1 Model for preparation of drought severity map

Table 2 Attributes of the drought severity map with grid code representing the severity level

Attributes of Block_droughtfin.shp						
Shape	Gridcode	Block_name	Area_Meters	Perimeter_Meters	Acres	Hectares
Polygon	4	saltora	7,505.355	399.319	1.855	0.751
Polygon	4	saltora	362.193	86.777	0.089	0.036
Polygon	4	sarenga	3,174.000	230.000	0.784	0.317
Polygon	4	saltora	17,064.740	648.244	4.217	1.706
Polygon	4	saltora	6,347.521	326.837	1.569	0.635
Polygon	4	saltora	3,833.043	288.877	0.947	0.383
Polygon	4	saltora	3,174.000	230.000	0.784	0.317
Polygon	4	sarenga	3,994.835	317.586	0.987	0.399
Polygon	4	sarenga	362.202	86.778	0.090	0.036
Polygon	4	sarenga	148,711.188	2,263.401	36.747	14.871
Polygon	4	sarenga	13,244.329	432.691	3.273	1.324
Polygon	4	sarenga	362.202	86.778	0.090	0.036
Polygon	4	sarenga	41,181.156	1,033.940	10.176	4.118
Polygon	4	saltora	3,106.744	224.529	0.768	0.311
Polygon	4	saltora	1,060.271	175.424	0.262	0.106
Polygon	4	sarenga	1,253.179	163.304	0.310	0.125
Polygon	4	sarenga	713.970	130.491	0.176	0.071
Polygon	4	sarenga	196,472.684	3,570.362	48.549	19.647
Polygon	4	saltora	362.196	86.777	0.090	0.036
Polygon	4	saltora	5,979.765	330.294	1.478	0.598
Polygon	4	saltora	714.073	130.496	0.176	0.071
Polygon	4	saltora	362.196	86.777	0.090	0.036
Polygon	4	sarenga	6,926.243	356.754	1.712	0.693
Polygon	4	sarenga	1,091.926	174.499	0.270	0.109
Polygon	4	saltora	289,477,739.309	89,991.770	71,531.221	28,947.774

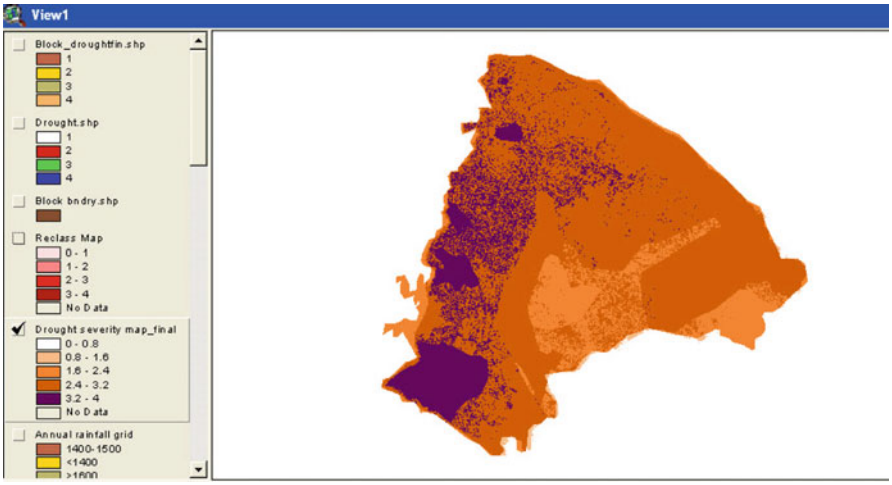

Fig. 2 Drought severity map of Bankura district

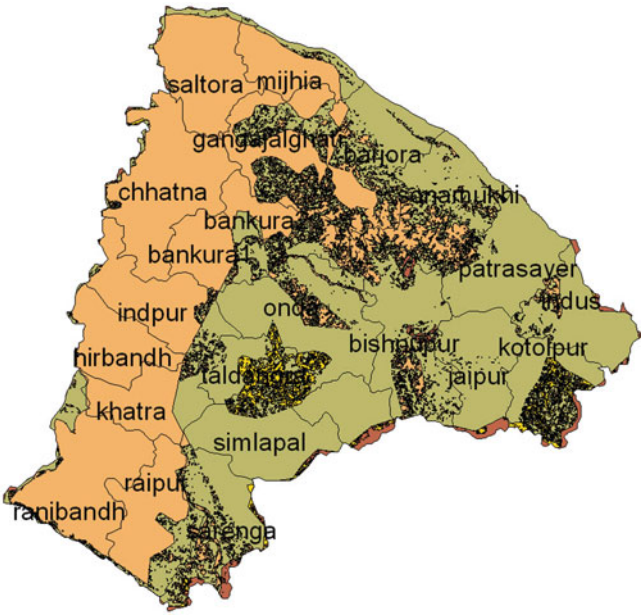

Fig. 3 Blockwise drought severity map

Table 3 Area statistics of drought severity level

SI. no.	Drought severity level	% of area
1	Not drought prone	17.5
2	Mild drought prone	2
3	Moderate drought prone	43.6
4	Severe drought prone	36.9

5 Conclusions

The main objective of the study was to prepare a drought severity map of Bankura district by integration of satellite, meteorological and other ancillary data and thus to obtain a spatial database for that.

1. It is found that about 20% area is not drought prone in Bankura, 43% of the area being moderately drought prone and 37% of area being largely susceptible to drought.
2. The drought severity map would help to point out the severity of drought vulnerability of different locations or places. This model thus provides an overall idea of drought risk associated with the district in block level.
3. This information is important for planners and administrators to take precautionary measures; moreover, the results can be used by local inhabitants to alleviate the continuation of drought phenomenon.
4. This model actually combines the meteorological data, collateral data and remote sensing data and integrates them in a GIS-based methodology to obtain the prevailing drought scenario and its management. The model thus can be used as a quick guide for identifying the extent of drought-hit locations.

References

1. Chopra P (2006) Drought risk assessment using remote sensing and GIS: a case study of Gujarat. ME thesis, Indian Institute of Remote Sensing, Dehradun & International Institute for Geo-information & Earth Observation, the Netherlands
2. Drought in India by PACS programme (2008) Issued at the national seminar on drought risk assessment. http://empowepoor.org/downloads/drought1.pdf
3. Kumar VR, Sridhar G, Nagarjan R, Balaji V (2009) Use of GIS tools to promote micro level drought preparedness: a study from Addakal Mandal, Andhra Pradesh, India. http://vasat.icrisat.org/images/New%20Folder/INCA%202008%20GIS%20Drought.pdf
4. Prakash PS, Garg PK, Ghosh SK (2006) GIS based modeling for drought assessment. In: Proceedings of ESRI conference
5. Prathumchai K (2001) Drought risk evaluation using remote sensing and GIS: a case study in Lop Buri Province. Paper presented at 22nd Asian conference on Remote Sensing, Singapore
6. World Meteorological Organization (1999), Comprehensive risk assessment for natural hazards, WMO/ TD No. 955

Mechanical Behavior of a Structural Steel at Different Rates of Loading

N.K. Singh, E. Cadoni, M.K. Singha, and N.K. Gupta

Abstract The purpose of this chapter is to investigate the mechanical properties of a structural steel under quasi-static and dynamic loads. Specimens of as-received low-carbon mild steel are tested on universal testing machine to study their stress-strain behavior under quasi-static tension (0.001 s^{-1}) and compression (-0.001 s^{-1}). Then, the specimens are tested under *split Hopkinson pressure bar* (SHPB) and *modified Hopkinson bar* (MHB) to study their material properties under dynamic compressive (-550, -800 s^{-1}) and tensile (250, 500 s^{-1}) loading, respectively. The material parameters of the existing Johnson-Cook model are determined. Finally, the applicability of the existing Johnson-Cook material model to represent the mechanical behavior of mild steel in plastic zone is examined.

Keywords Mild steel • Hopkinson pressure bar • Strain rate sensitivity • Tension • Compression • Johnson-Cook material model

1 Introduction

Low-carbon steels such as mild steels are widely used as a major structural material in several fields of engineering. It is found that the stress-strain behavior of mild steels depends on the loading rate [1, 9, 14]. Hence, the knowledge of the mechanical behavior of such steels at different strain rates is crucial in several fields of

N.K. Singh • M.K. Singha (✉) • N.K. Gupta
Department of Applied Mechanics, Indian Institute of Technology Delhi,
New Delhi 110016, India
e-mail: nilambersingh@yahoo.com; maloy@am.iitd.ac.in; nkgupta@am.iitd.ac.in

E. Cadoni
DynaMat Laboratory, University of Applied Sciences of Southern Switzerland,
6952 Canobbio, Switzerland
e-mail: ezio.cadoni@supsi.ch

S. Chakraborty and G. Bhattacharya (eds.), *Proceedings of the International Symposium on Engineering under Uncertainty: Safety Assessment and Management (ISEUSAM - 2012)*,
DOI 10.1007/978-81-322-0757-3_57,

engineering in order to improve the safety against crash, impacts, and blast loads. For example, the crashworthiness characteristics of automobile, train, and airplane are the primary concerns for the transportation industry. The penetration of body armors and sheltering structures by bullets is a challenging problem for the terrorist-hit areas. The safety of socially sensitive structures such as tunnels, bridges, and offshore platforms is of primary national importance. Therefore, several experimental studies are reported in the literature over the last few decades to understand the influence of loading rate on the yield stress and flow stress of different grades of mild steel.

The study of the mechanical properties at high strain rate needs special experimental techniques to record the stress wave propagation in the materials. The *Hopkinson pressure bar* is one of the widely used experimental techniques for measurement of the mechanical properties of materials at high strain rates [3]. Initially, Campbell and Duby [1] and Marsh and Campbell [9] studied the strain rate sensitivity of EN2A mild steel under dynamic compression; Santosham and Ramsey [14] compared the dynamic elastic behavior of mild steel (type 1020), aluminum, and copper. In general, it is observed that the flow stress of mild steel increases with the increase of strain rate. The compressive response of copper, steel, and tungsten alloy steel was studied by Couque and Walker [4] with a split Hopkinson pressure bar technique at strain rates varying from 3,000 to 7,000 s^{-1}. Lee and Liu [8] investigated the flow stresses of S15C mild steel and S50C medium alloy heat-treatable steel under different compressive strain rates and wide range of test temperatures.

Subsequently, *Hopkinson pressure bar* has been modified by several investigators to study the constitutive laws of different low-carbon steels under dynamic tensile or shear loads. Langseth et al. [7] studied the stress-strain behavior (yield stress, flow stress, and strain hardening) of St52-3 N mild steel under tension and shear at different strain rates (0.001–1,000 s^{-1}). It is observed that the lower yield stress is approximately twice as strain rate sensitive as stresses in the hardening region and that the ultimate tensile strength marginally reduces at high strain rates. Vedantam et al. [18] analyzed the tension stress-strain data for mild and DP590 steels and observed that mild steel is more strain rate sensitive compared to DP590. High strain rate tension tests have been performed on AISI 1018 CR steel specimens by Sasso et al. [15]. Rusinek et al. [11–13] studied the stress-strain behavior of ES steel at different strain rates and temperatures. Huh et al. [5] studied the mechanical behavior of different high-strength steels used in automobile industry at different strain rate (0.001–1,000 s^{-1}) and observed that strain rate hardening is strongly coupled with strain hardening. Campbell and Ferguson [2] studied the sensitivity of shear flow stress of mild steel EN3B (British standard) that was measured at temperatures from 195 to 713°K and strain rates (10^{-3} to 4×10^4 s^{-1}). Klepaczko [6] studied the behavior of low-alloy steel XC18 (French standard) under double shear at different strain rates (0.001–10,000 s^{-1}). An experimental study on the high strain rate tensile behavior of aluminum alloy 7075 T651 and IS 2062 mild steel is reported by Pothnis et al. [10].

The purpose of this chapter is to study the mechanical behavior of commercially available mild steel at Delhi under quasi-static, dynamic tensile, and dynamic compressive loads. The quasi-static experiments are conducted on a universal testing machine, while high strain rate experiments are conducted on traditional and modified *Hopkinson bar* apparatus. Further, the applicability of the existing Johnson-Cook material model to represent the strain hardening and strain rate hardening of mild steels under tensile and compressive loads is examined.

2 Experimental Setups

Three different experimental techniques are employed to study the mechanical properties of mild steel at different rates of loading. The stress-strain behavior of mild steel specimens under quasi-static tension and compression is obtained from the universal testing machine. High strain rate experiments under dynamic compressive and tensile loads are carried out in the *split Hopkinson pressure bar* and *modified Hopkinson bar* apparatus, respectively, whose working principles are described here.

The schematic diagram of the *split Hopkinson pressure bar*, available at the Impact Mechanics laboratory of IIT Delhi, is shown in Fig. 1. It consists of an incident bar (also known as input bar), one output bar, one striker, and instrumentation for recording strain data. The input and output bars (each of 20-mm diameter and 1,500-mm length) are coaxially aligned and have free axial horizontal movement. Cylindrical specimen is sandwiched between the input and output bars. The striker of 400-mm length and mass 1.0 kg strikes the input bar at a specified velocity, which creates a trapezoidal compressive stress wave at the striking end of the incident bar. The compressive stress wave (ε_i) propagates through the input bar and reaches the specimen, where one part of the incident wave is reflected back (ε_r) to the incident bar and another part (ε_t) is transmitted to the output (transmission) bar. The strain pulses are measured at the strain gauge stations on the bars (Fig. 1). The crushing of the specimen is subjected to the load equilibrium as the signals $\varepsilon_i + \varepsilon_r$ and ε_t are equal. A pulse shaper is used before the input bar, which deforms plastically as the striker strikes on it. The diameter of the pulse shaper is marginally more than the diameter of the Hopkinson bars, whereas the thickness is 1 mm. The plastic deformation of the pulse shaper increases the rise time of the compressive pulse in the input bar. This is also useful to modify the shape of the pulse and to minimize the fluctuation in the wave pulse.

Experiments under dynamic tensile loads have been performed on the *modified Hopkinson bar* (Fig. 2) available at the DynaMat laboratory of the University of Applied Sciences of Southern Switzerland. It consists of a prestressed bar, incident bar, output bar, and instrumentation for recording strain data. The specimen is connected between the input bar and the output bar. Here, tension in the prestressed bar is suddenly released to create a tensile pulse (ε_i) in the input bar. The tensile pulse propagates to the specimen with speed C_0, where one part of the pulse reflects

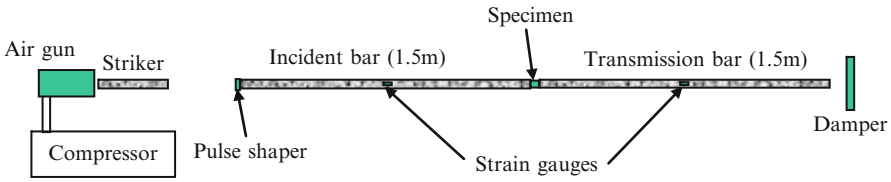

Fig. 1 Schematic diagram of the *split Hopkinson pressure bar* available at IIT Delhi

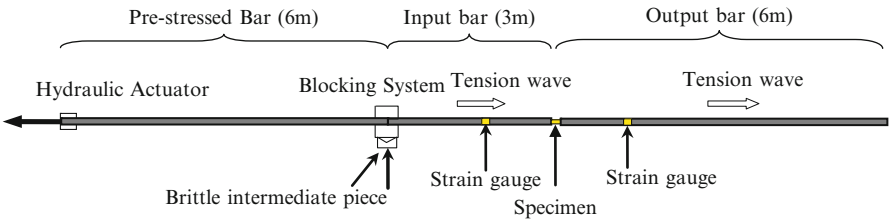

Fig. 2 Schematic diagram of the *modified Hopkinson bar* available at University of Applied Sciences of Southern Switzerland

(ε_r) back in the input bar due to the impedance mismatch and the other part gets transmitted (ε_t) through the output bar. The fracture process of the specimen is subjected to the load equilibrium as the signals $\varepsilon_i + \varepsilon_r$ and ε_t are equal. The strain rate, obtained during the experiment, depends on the prestress value (based on assumed strain rate) of the prestressed bar. The details of the working principle of modified Hopkinson bar are reported elsewhere [16, 17] and not repeated here for the sake of brevity.

3 Calculation of Stresses

The wave propagation in both the *split Hopkinson pressure bar* and *modified Hopkinson bar* is assumed to be governed with one-dimension elastic wave propagation theory by neglecting wave dispersion. Then, the engineering stress (σ_s), engineering strain (ε_s), and strain rate ($\dot{\varepsilon}_s$) on the tested specimens are expressed as [3]

$$\sigma_s = E\frac{A}{A_s}\varepsilon_t,\ \varepsilon_s = \frac{-2C_0}{L}\int_0^t \varepsilon_r dt, \text{and } \dot{\varepsilon}_s = \frac{-2C_0}{L}\varepsilon_r, \tag{1}$$

where E is the modulus of elasticity for the bar material, A is the cross-sectional area of the bar, A_s is the cross-sectional area of the specimen, L is the gauge length of the specimen, and C_0 is the speed of the stress wave in the pressure bar. ε_r and ε_t are

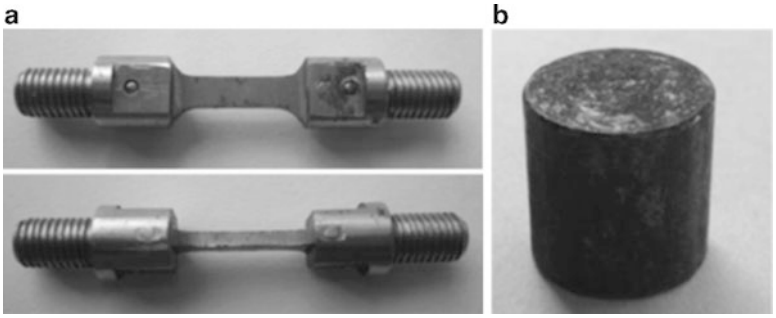

Fig. 3 Photograph of the mild steel specimens, (**a**) Tensile specimens (gauge length 10 mm, width 4 mm, and thickness 2 mm), (**b**) Compression specimens (diameter 10 mm, thickness 10 mm)

reflected and transmitted pulse strain. The corresponding true stress (σ_T) and the true strain (ε_T) on the specimen may be estimated as

$$\sigma_T = \sigma_s(1 + \varepsilon_s) \text{ and } \varepsilon_T = \ln(1 + \varepsilon_s). \tag{2}$$

4 Materials and Specimen Design

Low-carbon mild steel is obtained from a Delhi-based supplier, whose chemical composition in terms of weight % is C: 0.16%, Si: 0.27%, Mn: 0.77%, S: 0.016%, and P: 0.024%. Flat specimens (Fig. 3a) of the material having gauge length 10 mm, width 4 mm, and thickness 2 mm are prepared for tensile testing. The variation in width and thickness of the specimens is less than ± 2 and $\pm 3\%$, respectively. The specimen is inserted in the specimen holders, and a steel dowel is inserted to prevent slippage. The specimen and supports are threaded jointly for 8 mm, so that the specimen can be gripped with the bars rigidly at its both ends. Cylindrical specimens (Fig. 3b) of thickness 10 mm and diameter 10 mm are employed for compression testing.

5 Results and Discussions

Stress-strain behavior of as-received mild steel at different strain rates under tensile and compressive loads is discussed here. The engineering stress *versus* engineering strain curves are compared at various rates of loading in Fig. 4, whereas the corresponding true stress *versus* true strain curves are compared in Fig. 5. The yield stresses in these curves are measured at 0.2% offset strain. Three samples at each strain rate are tested at room temperature 25°C, and the average value of the mechanical properties is considered.

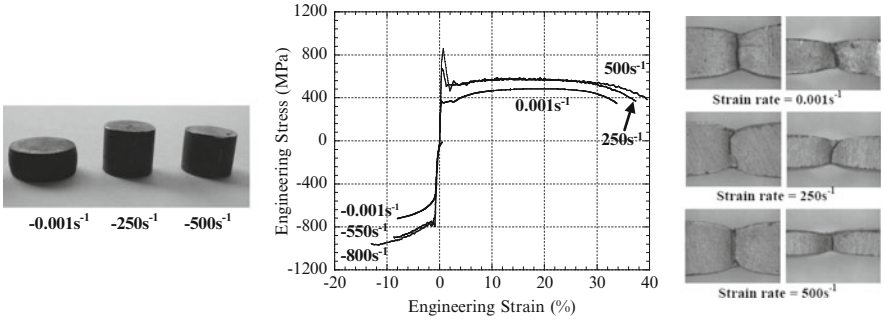

Fig. 4 Engineering stress *versus* engineering strain curves along with the photographs of the deformed and fractured specimens

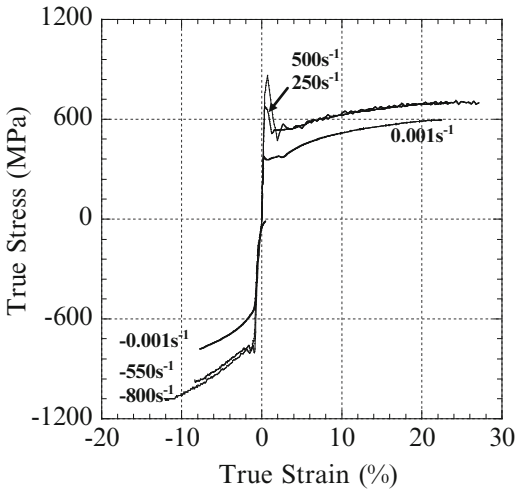

Fig. 5 True stress *versus* true strain curves of mild steel at different rates of loading

In case of tensile loading, the engineering yield stresses at strain rates 0.001, 250, and 500 s^{-1} are 361, 688, and 815 MPa, respectively, whereas the engineering ultimate tensile strengths are, respectively, 483, 574, and 576 MPa. It has been observed that yield stress of mild steel is more sensitive to strain rate than ultimate tensile strength. The ultimate tensile strength is almost maintained at high strain rates. The flow stress in the strain hardening zone increases marginally compared to the yield stress of the material as the strain rate increases. The flat and transverse sections of the fractured samples are shown in Fig. 4 at different tensile loading. The reduction in cross-sectional area at strain rates 0.001, 250, and 500 s^{-1} are 65.36, 66.72, and 68.16%, respectively. Therefore, the ductility of the material slightly increases at high strain rate compared to the quasi-static condition. The true yield stresses at strain rates 0.001, 250, and 500 s^{-1} are 363, 691, and 820 MPa,

respectively, whereas the true ultimate tensile strengths are, respectively, 596, 702, and 704 MPa. After the ultimate tensile strength, the necking in the material starts and it is very difficult to analyze the complex stresses that arise during necking. Therefore, true stress-strain curves are considered up to the point of instability at different strain rates under tensile loads. The fracture energy and toughness of the material at high strain rate is higher in comparison to the quasi-static condition because the area under the stress-strain curve at high strain rates is relatively more.

In case of compressive loading, the engineering yield stresses at strain rates 0.001, 550, and 800 s^{-1} are 541, 749, and 761 MPa, respectively, whereas the corresponding true yield stresses are, respectively, 546, 758, and 769 MPa. As the compressive load increases, the flow stress in the strain hardening zone of the material also increases in the above range of strain rate. This grade of mild steel is stronger in compression compared to tension. The yield stress increases with the strain rate under both tensile and compressive loads. The yielding instability with upper and lower peaks has been found lower in compressive loads compared to the tensile loads. The strain rate remains approximately constant during plastic deformation of the material. In case of dynamic compression, the maximum deformation is shown in Figs. 4 and 5 as the flow stress increases continuously during a particular loading after the lower yield point. It has also been observed that the rate of strain hardening is more under compression as compared to tension.

6 Material Model

The Johnson-Cook model considers three independent phenomena, which are isotropic hardening, strain rate hardening, and thermal softening, and these can be isolated from each other. Here, only two phenomena, isotropic hardening and strain rate hardening, have been considered due to the unavailability of temperature data. The model can be expressed as

$$\sigma = \left[A + B{\varepsilon_{\mathrm{p}}}^{n}\right] \times \left[1 + C \ln \dot{\varepsilon}^{*}\right], \tag{3}$$

where ε_{p} is the equivalent plastic strain, $\dot{\varepsilon}$ is the strain rate, $\dot{\varepsilon}_0$ is the reference strain rate, and $\dot{\varepsilon}^{*} = \dot{\varepsilon}/\dot{\varepsilon}_0$ is the dimensionless plastic strain rate for $\dot{\varepsilon}_0 = 0.001\ s^{-1}$. The constants A, B, C, and exponent n are the four material parameters, which are determined using experimentally obtained true stress *versus* true strain curves.

A is the true yield stress of the material corresponding to 0.2% offset true strain at the strain rate of 0.001 s^{-1}. The material parameters B and n represent the strain hardening effects of the material at the strain rate 0.001 s^{-1}, whereas C represents the strain rate sensitivity of the material. The parameters $B, C,$ and n are determined by curve-fitting method in plastic zone from the true yield stress corresponding to 0.2% offset true strain to the point of instability in case of tension. These parameters have been determined up to 8% deformation of the material under compression by

Table 1 Johnson-Cook parameters for mild steel

Mode	*A* (MPa)	*B* (MPa)	*n*	C		
Tension	363	779	0.743	0 (0.001s^{-1})	0.01744 (250s^{-1})	0.01438 (500s^{-1})
Compression	546	2692	0.928	0 (0.001s^{-1})	0.01824 (550s^{-1})	0.02067 (800s^{-1})

*The value in the bracket indicates strain rate (s-1) for the strain rate sensitivity, C

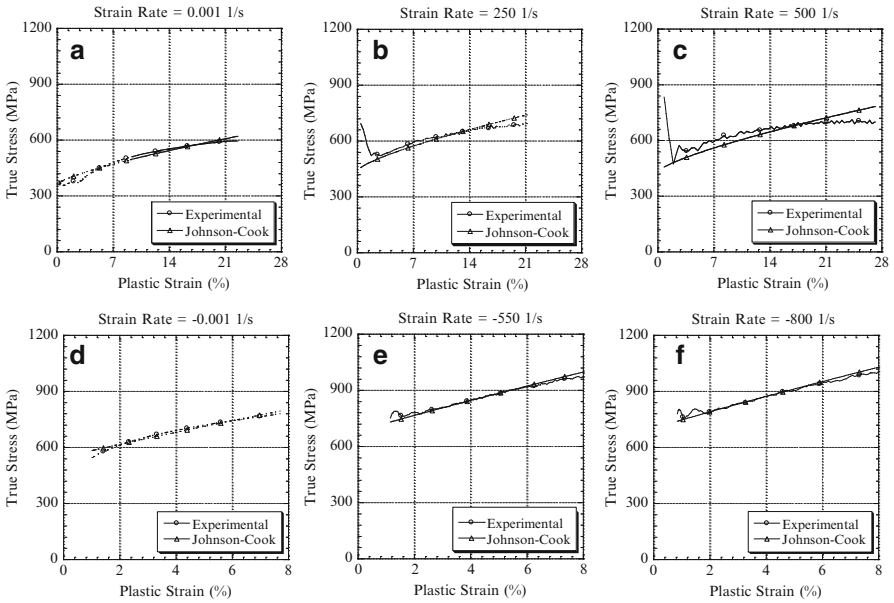

Fig. 6 Comparison between predicted and measured true plastic stress *versus* true plastic strain curves at different strain rates (**a**) 0.001 s^{-1}, (**b**) 250 s^{-1}, (**c**) 500 s^{-1}, (**d**) −0.001 s^{-1}, (**e**) −550 s^{-1}, and (**f**) −800 s^{-1}

the same procedure. The estimated material parameters (*A*, *B*, *C*, and *n*) for the Johnson-Cook model are presented in Table 1 for both tension and compression, and hence, the models may be expressed as

$$\text{Tension:} \quad \sigma = \left[363 + (779)\varepsilon_p{}^{(0.743)}\right] \times \left[1 + \text{C}.\ln \dot{\varepsilon}^*\right] \tag{4}$$

$$\text{Compression:} \ \sigma = \left[546 + (2692)\varepsilon_p{}^{(0.928)}\right] \times \left[1 + \text{C}.\ln \dot{\varepsilon}^*\right] \tag{5}$$

Here, the strain rate parameter, *C*, can be used at a particular strain rate from Table 1. The true stress *versus* plastic strain curves, obtained from the Johnson-Cook model (Eqs. 4 and 5), are compared with the experimental results in Fig. 6 at different strain rates under tensile and compressive loadings. It is observed that the Johnson-Cook model with the estimated material constants (*A*, *B*, *C*, and *n*) has good agreement with the experimental results.

7 Conclusions

The isotropic hardening and strain rate hardening of as-received mild steel under tension and compression loads are investigated here. Experiments are conducted at quasi-static, dynamic compressive and tensile strain rates (-800 to 500 s^{-1}). The parameters for the Johnson-Cook material model are determined. The present investigation reveals that:

- Mild steel is strain rate sensitive. The yield stress increases sharply with the strain rate under both dynamic tensile and compressive loads. However, flow stresses in the strain hardening zone of the material change marginally.
- Mild steel exhibits ductile fracture.
- The flow stress obtained from the Johnson-Cook material model with estimated material parameters is in good agreement with the experimental results.
- The fracture energy and toughness of the material at high strain rate is higher compared to that at quasi-static condition.

Acknowledgments Authors thank D. Forni and M. Dotta of the DynaMat Laboratory, University of Applied Sciences of Southern Switzerland for the help in some experiments. The research was financially supported by the Indo-Swiss Joint Research Program sponsored by the "*Department of Science and Technology*" of India and "*Swiss State Secretariat of Education and Research*" of Switzerland.

References

1. Campbell JD, Duby J (1956) The yield behaviour of mild steel in dynamic compression. Proc R Soc Lond A 236(1204):24–40
2. Campbell JD, Ferguson WG (1970) The temperature and strain-rate dependence of the shear strength of mild steel. Philos Mag 21(169):63–82
3. Chen W, Song B (2011) Split Hopkinson (Kolsky) bar: design testing and applications. Springer, New York
4. Couque H, Walker JD (1994) On the use of the compression split Hopkinson pressure bar to high strain rate. J De Physique IV C8(4):23–28
5. Huh H, Lim JH, Park SH (2009) High speed tensile test of steel sheets for the stress-strain curve at the intermediate strain rate. Int J Automob Technol 10(2):195–204
6. Klepaczko JR (1994) An experimental technique for shear testing at high and very high strain rates. The case of a mild steel. Int J Impact Eng 15:25–39
7. Langseth M, Lindholm US, Larsen PK, Lian B (1991) Strain-rate sensitivity of mild steel grade ST52-3 N. J Eng Mech 117(4):719–732
8. Lee W-S, Liu C-Y (2005) Comparison of dynamic compressive flow behavior of mild and medium steels over wide temperature range. Metall Mater Trans 36A:3175–3186
9. Marsh KJ, Campbell JD (1963) The effect of strain rate on the post-yield flow of mild steel. J Mech Phys Solids 11:49–63
10. Pothnis JR, Perla Y, Arya H, Naik NK (2011) High strain rate tensile behavior of aluminum alloy 7075 T651 and IS 2062 mild steel. J Eng Mater Technol 133:021026
11. Rusinek A, Zaera R, Klepaczko JR, Cheriguene R (2005) Analysis of inertia and scale effects on dynamic neck formation during tension of sheet steel. Acta Mater 53:5387–5400

12. Rusinek A, Zaera R, Klepaczko JR (2007) Constitutive relations in 3-D for a wide range of strain rates and temperatures – application to mild steels. Int J Solids Struct 44:5611–5634
13. Rodríguez-Martínez JA, Rusinek A, Klepaczko JR (2009) Constitutive relation for steels approximating quasi-static and intermediate strain rates at large deformations. Mech Res Commun 36:419–427
14. Santosham TV, Ramsey H (1969) The dynamic elastic behavior of mild steel, aluminum and copper as observed in wave propagation theory. Int J Mech Sci 11:751–765
15. Sasso M, Newaz G, Amodio D (2008) Material characterization at high strain rate by Hopkinson bar tests and finite element optimization. Mater Sci Eng A 487:289–300
16. Singh NK, Cadoni E, Singha MK, Gupta NK (2011) Dynamic tensile behavior of multi phase high yield strength steel. Mater Des 32(10):5091–5098
17. Singh NK, Cadoni E, Singha MK, Gupta NK (2011) Quasi-static and dynamic tensile behavior of CP800 steel. Mech Adv Mater Struct. doi:10.1080/15376494.2012.699594
18. Vedantam K, Bajaj D, Brar NS, Hill S (2005) Johnson-Cook strength models for mild and DP590 steels. Shock Compress Condens Matter CP845:775–778

Response Analysis of a Linear Stochastic Structural Dynamic System Using Stochastic Finite Element Method

Debraj Ghosh

Abstract This work is aimed at developing an efficient computational method for response analysis of a linear vibrating system with uncertainties in mass and stiffness properties and external force. The uncertain parameters are modeled as random quantities—random variables, vectors, and processes, to be specific. The random processes are required to be approximated by a finite set of random variables for computational purpose. In this work the spectral stochastic finite element method (SSFEM) is used for uncertainty propagation. In this method the random quantity of interest is expressed in a series expansion of random orthogonal polynomials, known as polynomial chaos expansion (PCE). The coefficients of this expansion—which are deterministic—are then estimated via a Galerkin projection. First, a random eigenvalue problem is solved—which results from the eigenvalue problem involved in finding the natural frequencies and modal vectors of a linearly vibrating system. Then, solutions of this random eigenvalue problem are used to predict the response of the system. Comparison with a Monte Carlo simulation is done for accuracy and computational speed.

Keywords Random field • Stochastic mechanics • Uncertainty quantification • Stochastic finite element

1 Introduction

A reliable prediction of the behavior of any physical system demands consideration of the uncertainties associated at various levels such as modeling, designing, manufacturing, and loading. One framework of considering these uncertainties

D. Ghosh
Indian Institute of Science, Bangalore, India
e-mail: dghosh@civil.iisc.ernet.in

S. Chakraborty and G. Bhattacharya (eds.), *Proceedings of the International Symposium on Engineering under Uncertainty: Safety Assessment and Management (ISEUSAM - 2012)*,
DOI 10.1007/978-81-322-0757-3_58,

and propagating them is the probabilistic framework. In this framework, the uncertainties are first modeled as random variables and processes, and then propagated to find the probabilistic behavior of the response. Modeling of uncertainty involves collection of data on the system ingredients such as material properties and loading, and subsequent usage of suitable statistical tools, whereas propagation of uncertainty is a pure computational task in nature, where one aims to gain computational speed and good accuracy. In this work, a new propagation method is developed based on the spectral stochastic finite element method (SSFEM).

To find the response of a dynamical system, the modal approach is widely used due to its computational advantage. When uncertainties are involved, the natural frequencies and mode shapes also become random quantities (random variables and vectors/processes, respectively)—leading to a random eigenvalue problem. These random modes can then be used to find the probabilistic behavior of the response. Several methods for solving the random eigenvalue problem and finding the response statistics have been proposed and studied so far. Historically, two widely-studied methods are perturbation methods [1, 2, 3, 4, 5, 6] and Monte Carlo simulations [7]. While the perturbation methods are computationally fast, their application is limited to systems with low variability; also, the analytical complexity of the expressions involved grows rapidly. Monte Carlo simulations, on the other hand, are the most accurate, but computationally expensive. To overcome these difficulties, new approaches have been proposed recently, for instance, dimensional decomposition method [8], analytical techniques [9]—which are applicable to a limited type of systems, and SSFEM [10, 11, 12]. In the SSFEM approach of solving the random eigenvalue problem [11], the eigenvalues and eigenvectors are first expressed in a functional space spanned by a set of orthogonal random polynomials. The representation is known as the polynomial chaos expansion (PCE). These representations are then substituted in the eigenvalue problem and a Galerkin projection performed to get a system of deterministic nonlinear equations, which is then solved using Newton-Raphson iterations. This method has been found to be much faster than the Monte Carlo method, and more accurate than the perturbation methods. Other works using polynomial approximations for response analysis includes [13, 14].

In this work, the solution of the random eigenvalue problem found using the method proposed in [11] is used to find the response of a random system. To achieve this, the response is also expressed in PCE and another Galerkin projection is performed. In a numerical study, the proposed method is found to be computationally faster than the direct Monte Carlo simulation.

This chapter is organized as follows. In the next section, the mathematical formulation is presented. Then, a numerical study is conducted to apply the proposed method and to check for accuracy and speed. The chapter ends with a few concluding remarks.

2 Mathematical Formulation

2.1 Equation of Motion and the Modal Approach

Let ξ denote a set of q-dimensional random vector characterizing the underlying uncertainty. The equation of motion of a linear vibrating system is written as

$$\mathbf{M}(\xi)\ddot{\mathbf{u}}(t,\xi) + \mathbf{C}(\xi)\dot{\mathbf{u}}(t,\xi) + \mathbf{K}(\xi)\mathbf{u}(t,\xi) = \mathbf{f}(t,\xi)\ a.s., \tag{1}$$

where the mass, damping, and stiffness matrices are denoted by $(n \times n)$ matrices $\mathbf{M}(\xi)$, $\mathbf{C}(\xi)$, and $\mathbf{K}(\xi)$, respectively; external force and response are denoted by n-dimensional vectors $\mathbf{f}(t, \xi)$ and $\mathbf{u}(t, \xi)$, respectively. The *a. s.* denotes the *almost sure* statement. The dots above u denote time derivatives. Let $\Phi(\xi)$ denote an $(n \times k_s)$ matrix constructed using k_s modes of the system. Then, using the transformation $\mathbf{u}(t, \xi) = \Phi(\xi)\mathbf{z}(t, \xi)$, the equation of motion reduces to

$$\begin{aligned}\Phi^T(\xi)\mathbf{M}(\xi)\Phi(\xi)\ddot{\mathbf{z}}(t,\xi) + \Phi^T(\xi)\mathbf{C}(\xi)\Phi(\xi)\dot{\mathbf{z}}(t,\xi) + \Phi^T(\xi)\mathbf{K}(\xi)\Phi(\xi)\mathbf{z}(t,\xi) \\ = \Phi^T(\xi)\mathbf{f}(t,\xi)\ a.s.\end{aligned} \tag{2}$$

This approach demands solving the random eigenvalue problem

$$\mathbf{K}(\xi)\phi(\xi) = \lambda(\xi)\mathbf{M}(\xi)\phi(\xi)\ a.s.; \tag{3}$$

$$\begin{aligned}&\textit{with the normalization condition} \quad \phi(\xi)^T\mathbf{M}(\xi)\phi(\xi) = 1\ a.s., \\ &\textit{where} \quad \lambda(\xi) \in \mathbf{R}, \quad \phi(\xi) \in \mathbf{R}^n.\end{aligned} \tag{4}$$

2.2 Solving the Random Eigenvalue Problem

Let $p(\xi)$ denote the joint probability density function of the random vector ξ. The expectation operator $\mathbf{E}\{\cdot\}$ is defined as

$$\mathbf{E}\{\cdot\} = \int_{\mathbf{R}^q} \cdot\, p(\xi)d\xi, \tag{5}$$

In SSFEM, the l-th eigenvalue and eigenvector of the system (3) can be represented in a truncated PCE as

$$\lambda_l = \sum_{i=0}^{P-1} \psi_i \lambda_l^{(i)}, \qquad \phi_l = \sum_{i=0}^{P-1} \psi_i \phi_l^{(i)}; \qquad \lambda_l^{(i)} \in \mathbf{R}, \quad \phi_l^{(i)} \in \mathbf{R}^n. \tag{6}$$

If ξ is Gaussian, then ψ_i are the Hermite polynomials of ξ, with properties

$$\psi_0 \equiv 1\ , \quad \mathbf{E}\{\psi_i\} = 0 \ \text{ for } \ i > 0, \tag{7}$$

$$\mathbf{E}\{\psi_i \psi_j\} = \delta_{ij} \mathbf{E}\{\psi_i^2\}. \tag{8}$$

To find the deterministic chaos coefficients $\lambda_l{}^{(i)}$ and $\phi_l{}^{(i)}$, the random matrices $\mathbf{K}(lc)$ and $\mathbf{M}(lc)$ are first represented in a finite chaos decomposition as

$$\mathbf{K} = \sum_{i=0}^{L_1-1} \psi_i \mathbf{K}^{(i)}, \quad \mathbf{M} = \sum_{i=0}^{L_2-1} \psi_i \mathbf{M}^{(i)}, \tag{9}$$

where $\mathbf{K}^{(i)}$ and $\mathbf{M}^{(i)}$ are $(n \times n)$ deterministic matrices. Then, substituting Eqs. (9) and (6) in (3) and using a Galerkin projection on the random polynomial bases, we get [11]

$$\sum_{i=0}^{L_1-1} \sum_{j=0}^{P-1} \mathbf{E}\{\psi_i \psi_j \psi_m\} \mathbf{K}^{(i)} \phi^{(j)} = \sum_{i=0}^{P-1} \sum_{k=0}^{L_2-1} \sum_{j=0}^{P-1} \mathbf{E}\{\psi_i \psi_j \psi_k \psi_m\} \lambda^{(i)} \mathbf{M}^{(k)} \phi^{(j)}, \quad m = 0, \ldots, P-1. \tag{10}$$

The subscript l is eliminated from λ_l and ϕ_l for brevity. Similarly, the normalization condition (4) becomes

$$\sum_{i=0}^{P-1} \sum_{k=0}^{L_2-1} \sum_{j=0}^{P-1} \mathbf{E}\{\psi_i \psi_j \psi_k \psi_m\} \phi^{(i)T} \mathbf{M}^{(k)} \phi^{(j)} = \delta_{m0}, \quad m = 0, \cdots, P-1. \tag{11}$$

Equations 10 and 11 are solved using Newton-Raphson method. Further details of implementations and expressions for the Jacobian can be found in [11].

2.3 *Finding the Response*

$\{\phi_{i_s}, \phi_{i_s+1}, \ldots, \phi_{i_s+k_s-1}\}$ be the set of dominant random dynamical modes for a given loading. Let introduce the matrix $\Phi = [\phi_{i_s}, \phi_{i_s+1}, \ldots, \phi_{i_s+k_s-1}]$ formed using these modes. A Rayleigh damping model is used here with the corresponding chaos coefficients denoted as $\mathbf{C}^{(i)}$. The random modal matrix Φ can be represented using Eq. (6) as

$$\Phi = \sum_{j=0}^{P-1} \psi_j \Phi^{(j)}, \qquad \Phi^{(j)} \in \mathbf{R}^{(n \times k_s)}, \tag{12}$$

where the columns of the matrices $\Phi^{(j)}$ are ${\phi_l}^{(j)}$s with $l = i_s, \ldots, i_s + k_s - 1$ in Eq. (6). The vector $\mathbf{z}(t)$ can similarly be expressed as

$$\mathbf{z}(t) = \sum_{j=0}^{P-1} \psi_j \mathbf{z}^{(j)}(t); \qquad \mathbf{z}^{(j)}(t) \in \mathbf{R}^{k_s}. \tag{13}$$

Substituting these equations into Eq. (2) and then taking another Galerkin projection on the random polynomial bases, we get,

$$\begin{aligned}
&\sum_{i=0}^{P-1} \sum_{j=0}^{L_2-1} \sum_{k=0}^{P-1} \sum_{l=0}^{P-1} \mathbf{E}\{\psi_i \psi_j \psi_k \psi_l \psi_m\} {\Phi^{(i)}}^T \mathbf{M}^{(j)} \Phi^{(k)} \ddot{\mathbf{z}}^{(l)}(t) \\
&+ \sum_{i=0}^{P-1} \sum_{j=0}^{L-1} \sum_{k=0}^{P-1} \sum_{l=0}^{P-1} \mathbf{E}\{\psi_i \psi_j \psi_k \psi_l \psi_m\} {\Phi^{(i)}}^T \mathbf{C}^{(j)} \Phi^{(k)} \dot{\mathbf{z}}^{(l)}(t) \\
&+ \sum_{i=0}^{P-1} \sum_{j=0}^{L_1-1} \sum_{k=0}^{P-1} \sum_{l=0}^{P-1} \mathbf{E}\{\psi_i \psi_j \psi_k \psi_l \psi_m\} {\Phi^{(i)}}^T \mathbf{K}^{(j)} \Phi^{(k)} \mathbf{z}^{(l)}(t) \\
&= \sum_{i=0}^{P-1} {\Phi^{(i)}}^T \mathbf{E}\{\psi_i \psi_m \mathbf{f}(t, \xi)\} \qquad m = 0, 1, \ldots, P-1.
\end{aligned} \tag{14}$$

This coupled system of $k_s P$ deterministic ordinary differential equations (ODEs) will be solved using a numerical integration scheme. Once $\{\mathbf{z}^{(i)}(t)\}_{i=0}^{i=P-1}$ are found this way, the physical response will be computed by

$$\mathbf{u}(t) = \sum_{i=0}^{P-1} \sum_{j=0}^{P-1} \psi_i \psi_j \Phi^{(i)} \mathbf{z}^{(j)}(t). \tag{15}$$

Statistical moments or probability distribution of the response can be estimated subsequently using this representation.

3 Numerical Implementation

To implement and test the proposed method, vibration of a simply supported plate of size 5 m $\times$ 4 m and of thickness 0.005 m is considered. The sources of randomness are the heterogeneity in the Young's modulus and the external loading. Heterogeneity of the Young's modulus is modeled as a random field with known

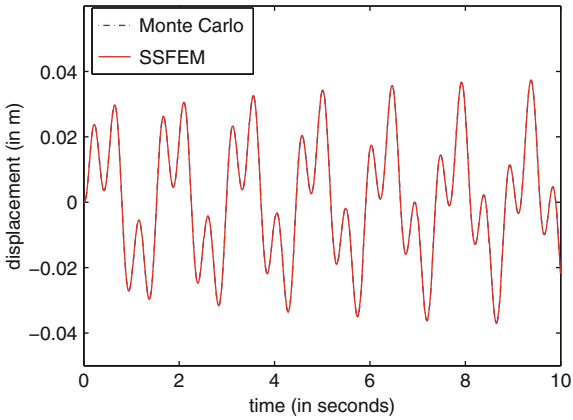

Fig. 1 Comparing the mean displacement estimated using SSFEM and Monte Carlo, an excellent agreement is observed

covariance function $C_{EE}((x_1, y_1)(x_2, y_2)) \equiv \sigma_E^2 e^{\{\frac{-|x_2-x_1|}{l_x}+\frac{-|y_2-y_1|}{l_y}\}}$. In this expression, the standard deviation of the field is denoted by σ_E and the correlation lengths along two directions are denoted by l_x and l_y. The chosen parameter values are mean Young's modulus $E_0 = 2 \times 10^5$ MPa, $\sigma_E = 0.1E_0 = 2 \times 10^4$ MPa, and $l_x = l_y = 10$ m. The Karhunen-Loève (KL) eigenvalue problem can be solved either analytically or numerically [16, 17]. Here, it is found that only two KL eigenvalues can reproduce the process with good accuracy. Accordingly, the Young's modulus is decomposed in KL expansion as

$$E(x, \xi) = E_0(x) + \sum_{i=1}^{2} \sqrt{\omega_i} \frac{(\xi_i^2 - 1)}{\sqrt{2}} \varphi_i(x), \tag{16}$$

x denoting the spatial location and ω_i and $\varphi_i(x)$ denoting the eigenvalues and eigenfunctions of the covariance kernel. ξ_2 and ξ_2 denote independent standard normal variables. The other parameters chosen are as follows: the Poisson's ratio $\mu = 0.3$ and the mass density $\rho = 7860$ Kg/m^3. Both the coefficients of the Raleigh damping are chosen as 0.05. A finite element model of the plate is build using 100 numbers of four-noded sixteen-DOF bicubic rectangular elements (conforming) [18], yielding 400 unconstrained DOF. The external force is also considered as random, represented as

$$\mathbf{f}(t, \xi) = \bar{\mathbf{f}}(t) + \xi_3 \mathbf{f}_r \sin(\omega_f t), \tag{17}$$

where $\bar{\mathbf{f}}(t)$ and $\xi_3 \mathbf{f}_r \sin(\omega_f t)$ denote the mean and random parts, respectively. ξ_3 is a standard normal variable independent of ξ_1 and ξ_2.

The proposed method is used to find the response of the uncertain system subjected to the random loading and the results are compared with Monte Carlo simulation estimates. In Figs. 1 and 2, the mean and standard deviation of the displacement at an arbitrarily chosen node are compared, and an excellent

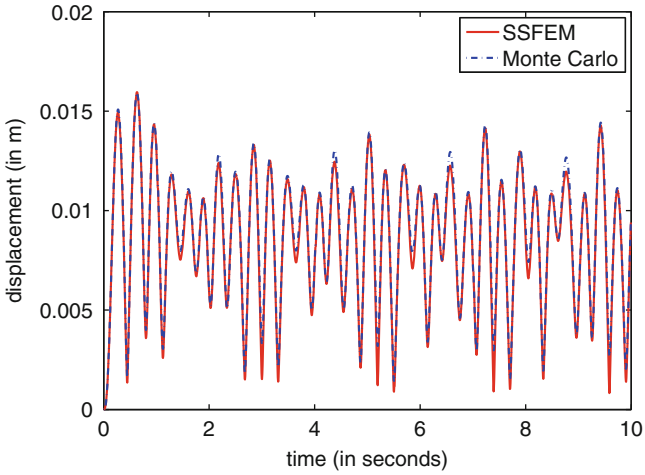

Fig. 2 Comparing the standard deviation of displacement estimated using SSFEM and Monte Carlo, an excellent agreement is observed

Fig. 3 Comparing the pdf of displacement at an arbitrarily chosen time instant

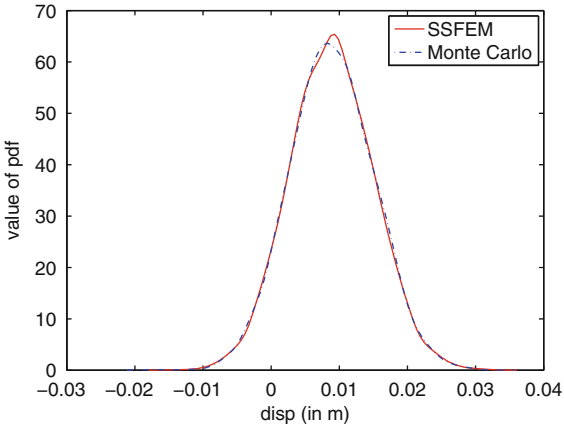

agreement is found. In Fig. 3, the probability density function (pdf) of this displacement at an arbitrary time instant is compared and again a good agreement is found. In Fig. 4, the pdf of the peak displacement is compared and a similar agreement is found. As the SSFEM-based approach was proposed with computational time saving in mind, a comparison in that aspect is necessary. In this application, the proposed method took 65 seconds to run on a desktop computer, whereas the Monte Carlo simulation (using 2,000 samples) took 768 s. Hence, the proposed method leads to a significant computational saving.

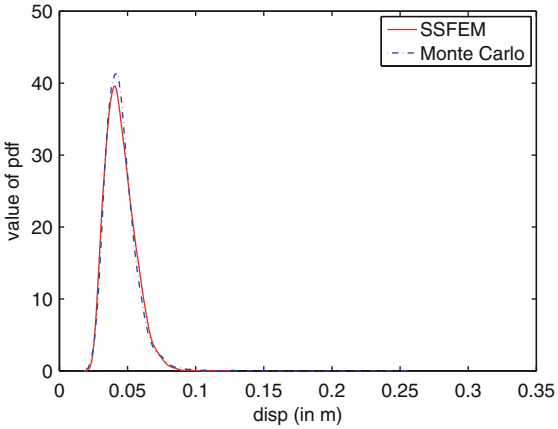

Fig. 4 Comparing the pdf of the peak displacement

4 Concluding Remarks

The proposed SSFEM-based method for finding the response of an uncertain linear system subjected to random loading is found to be computationally accurate and efficient. The computational saving comes from both the stages: solving the random eigenvalue problem, and finding the response using modal truncation. Further challenges to this proposed method will include its application to (1) larger systems and (2) systems involving much higher number of random variables.

Acknowledgements Funding from the ISRO-IISc Space Technology Cell under grant number ISTC/CCE/DG/273 is gratefully acknowledged.

References

1. Collins JD, Thomson WT (1969) The eigenvalue problem for structural systems with statistical properties. AIAA J 7(4):642–648
2. Shinozuka M, Astill CJ (1972) Random eigenvalue problems in structural analysis. AIAA J 10(4):456–462
3. Kleiber M, Hien TD (1992) The stochastic finite element method : basic perturbation technique and computer implementation. Wiley, Chichester/New York
4. Graham L, Deodatis G (2001) Response and eigenvalue analysis of stochastic finite element systems with multiple correlated material and geometric properties. Probab Eng Mech 16(1):11–29
5. Hasselman T (2001) Quantification of uncertainty in structural dynamics models. J Aerosp Eng 14(4):158–165
6. Vom Scheidt J, Purkert W (1983) Random eigenvalue problems. North Holland, New York
7. Pradlwarter HJ, Schueller GI, Szekely GS (2002) Random eigenvalue problems for large systems. Comput Struct 80:2415–2424
8. Rahman S (2007) Stochastic dynamic systems with complex-valued eigensolutions. Int J Numer Methods Eng 71:963–986

9. Adhikari S (2007) Joint statistics of natural frequencies of stochastic dynamic systems. Comput Mech 40(4):739–752
10. Ghosh D, Ghanem R, Red-Horse J (2005) Analysis of eigenvalues and modal interaction of stochastic systems. AIAA J 43(10):2196–2201
11. Ghanem R, Ghosh D (2007) Efficient characterization of the random eigenvalue problem in a polynomial chaos decomposition. Int J Numer Methods Eng 72(4):486–504
12. Verhoosel CV, Gutiérrez MA, Hulshoff SJ (2006) Iterative solution of the random eigenvalue problem with application to spectral stochastic finite element systems. Int J Numer Methods Eng 68(4):401–424
13. Jensen H, Iwan WD (1992) Response of systems with uncertain parameters to stochastic excitation. J Eng Mech 118(5):1012–1025
14. Katafygiotis LS, Papadimitriou C (1996) Dynamic response variability of structures with uncertain properties. Earthq Eng Struct Dyn 25:775–793
15. Spanos PD, Beer M, Red-Horse J (2007) Karhunen-Loéve expansion of stochastic processes with a modified exponential covariance kernel. J Eng Mech 133(7):773–779
16. Ghanem R, Spanos PD (2003) Stochastic finite elements: a spectral approach. Revised edition, Dover Publications, Mineola/New York
17. Van Trees HL (2001) Detection, estimation and modulation theory, part I. Wiley, Hoboken
18. Yang TY (1986) Finite element structural analysis. Prentice-Hall, Englewood Cliffs

Efficient Computation of Karhunen–Loéve Decomposition

Shalu Choudhary and Debraj Ghosh

Abstract In structural analysis and design, it is important to consider the effects of uncertainties in loading and material properties in a rational way. Such uncertainties can be mathematically modeled as random field. For computational purpose, it is essential to represent and discretize the random field. For a field with known second-order statistics, such a representation can be achieved by the Karhunen-Lo'eve expansion. Accordingly, the random field is represented in a truncated series expansion using a few eigenvalues and associated eigenfunctions of the covariance function and random coefficients. The eigenvalues and eigenfunctions are found by solving an integral equation with its kernel as the covariance function. Since the analytical solutions for the integral equation may not be present, therefore, it is important to find an approximate solution. It is important to consider both accuracy of the solution and the cost of computing the solution. This work is focused on exploring a few numerical methods for the numerical solution of this integral equation. A rectangular spatial domain with an uncertainty is modeled as a Gaussian random field with a known covariance function. Three different methods (1) using finite element bases, (2) approximating the covariance function by averaging locally, and (3) by the Nyström method are implemented and numerically studied.

Keywords Random field • Stochastic mechanics • Uncertainty quantification • Stochastic finite element

S. Choudhary (✉) • D. Ghosh
Indian Institute of Science, Bangalore, India
e-mail: shalu@civil.iisc.ernet.in; dghosh@civil.iisc.ernet.in

S. Chakraborty and G. Bhattacharya (eds.), *Proceedings of the International Symposium on Engineering under Uncertainty: Safety Assessment and Management (ISEUSAM - 2012)*,
DOI 10.1007/978-81-322-0757-3_59,

1 Introduction

In the modeling and analysis of mechanical behavior of structures, it is essential to incorporate various uncertainties. Uncertainties can be due to loading, boundary conditions, geometry, and material properties. For stochastic analysis, the governing equations modeling a system with uncertainties are stochastic partial differential equations. Numerically solving these stochastic partial differential equations involve, discretizing them, for example, by using finite element bases. The uncertainties in the governing equations, like material heterogeneity, can be mathematically modeled as random fields. For incorporating these uncertainties in the governing equations, it is important to represent and discretize the random fields [1]. A random field, with known second-order statistics—that is, the mean and the covariance—can be represented and discretized by the Karhunen-Loéve expansion (KLE) [2] and [3].

Consider a square-integrable random field $k(x, \theta)$ defined over a spatial domain $\mathcal{D}$, where $x \in \mathcal{D}$ is the spatial part and θ is the random part. The KLE discretizes this field via a set of orthogonal deterministic functions with corresponding random coefficients as

$$k(x,\theta) = \bar{k}(x) + \sum_{i=1}^{\infty} \sqrt{\lambda_i} f_i(x)\eta_i(\theta), \tag{1}$$

where $\bar{k}(x)$ is the mean of the field, λ_i and $f_i(x)$ are eigenvalues and corresponding eigenfunctions of the covariance function $C(x_1, x_2)$, and $\eta_i(\theta)$ are uncorrelated random coefficients. The infinite series in the above equation needs to be truncated for computational purpose. Let the required number of terms be denoted by P here. Considering a field with zero mean, the series can be written as

$$\hat{k}(x,\theta) = \sum_{i=1}^{P} \sqrt{\lambda_i}\, f_i(x)\eta_i(\theta), \tag{2}$$

where the eigenvalues are indexed in numerically descending order. It can be shown that the linear representation with P terms is the optimal representation [2]. The covariance kernel $C(x_1, x_2)$ is bounded, symmetric, and positive definite. Because of these properties of the covariance functions, the eigenfunctions are orthogonal, the eigenvalues are finite positive and decay to zero.

For two-dimensional spatial domain $\mathcal{D}$, the integral equation is written as

$$\int_{\mathcal{D}} C(\mathbf{x}_1, \mathbf{x}_2) f_i(\mathbf{x}_1) d\mathbf{x}_1 = \lambda_i\, f_i(\mathbf{x}_2), \tag{3}$$

where $\mathbf{x}_1 = [x_1, y_1]$ and $\mathbf{x}_2 = [x_2, y_2]$ are vectors denoting two spatial locations. The integral Eq. (3) is the second-order Fredholm type. Computation of the KLE

requires solving the above integral eigenvalue problem. For a few cases, an analytical solution of this integral eigenvalue problem is possible. However, for most cases it may not be available; therefore, a numerical solution is sought [4]. This chapter focuses on exploring various numerical methods to solve this integral equation and comparing for their efficiency.

Generally, this integral equation is solved by using finite element bases, and the mesh used for mechanics problem is also used for discretizing the random field [5]. Using the same meshes often makes the integral eigenvalue problem to be large and unnecessarily expensive. It is important to find a computationally efficient way to solve this integral equation. Here, efficiency is measured in terms of computational cost for a given target accuracy. There are various methods available in the literature for computing approximate solutions. This chapter explores and compares three different numerical methods to find an approximate solution for solving the integral equation. The methods are as follows:

- Using finite element bases
- By approximating the covariance function by averaging locally
- By the Nyström method

2 Methods of Solving the Integral Equation

To find the KLE, it is important to solve the integral eigenvalue problem. In this chapter, three different methods are used to find the numerical solution. Each method converts the integral equation into a matrix eigenvalue problem which can be solved with an appropriate eigensolver. In this work, three different numerical methods to solve the integral equation are studied and compared:

- Method 1: Using Finite Element Bases
- Method 2: Approximating the Covariance Function by Averaging Locally
- Method 3: By the Nyström Method

Details of the methods are given next.

2.1 Method 1: Using Finite Element Bases

In this method, eigenfunctions f_i are approximated as a linear combination of finite element bases $\{\phi_k\}^N{}_{k=1}$ and corresponding unknown nodal coefficients d_{ik} as

$$f_i(\mathbf{x}) = \sum_{k=1}^{N} d_{ik}\phi_j(\mathbf{x}). \tag{4}$$

This expression for approximate eigenfunction is substituted in the Eq. (3), and the error is minimized in Galerkin sense; the resulting equation is discretized with unknown as the values of eigenfunction at the nodes. This can be written a generalized matrix eigenvalue problem.

$$\mathbf{AD} = \Lambda \mathbf{BD}, \tag{5}$$

where the elements of these $(N \times N)$ matrices are

$$a_{kj} = \int_{\mathcal{D}} \int_{\mathcal{D}} C(\mathbf{x}_1, \mathbf{x}_2) \phi_k(\mathbf{x}_1) \phi_j(\mathbf{x}_2) d\mathbf{x}_1 d\mathbf{x}_2$$

$$b_{kj} = \int_{\mathcal{D}} \phi_k(\mathbf{x}_2) \phi_j(\mathbf{x}_2) d\mathbf{x}_2.$$

The diagonal entries of the matrix Λ are the eigenvalues and the columns of the matrix $\mathbf{D}$ are the corresponding eigenvectors. After obtaining the unknown nodal values, that is, the eigenvectors, the eigenfunctions can be computed from the Eq. (4).

2.2 *Method 2: Approximating the Covariance Function by Averaging Locally*

In this method, the spatial domain $\mathcal{D}$ of the integral equation is divided into equal subdomains. The covariance function is approximated over the whole domain by first evaluating the value of the covariance function over the midpoint of each subdomain and averaging this value over the whole subdomain by multiplying it by the area of the subdomain. This leads to approximation of the covariance function into a matrix $\mathbf{K}$. Eigenvalue problem can be solved for this matrix resulting in numerical eigensolution of the problem. In a two-dimensional domain, the elements of this matrix are

$$K_{ij} = C(\tilde{\mathbf{x}}_i, \tilde{\mathbf{x}}_j) a_i, \tag{6}$$

where $\tilde{\mathbf{x}}_i$ and $\tilde{\mathbf{x}}_j$ denote the midpoint coordinates of the ith and jth subdomains, and a_i $(= a_j)$ denotes the area of the ith subdomain.

2.3 *Method 3: Using Nyström Method*

In this method, the integral equation is approximated by the Nyström method [6]. By this, the integral equation is approximated by using a quadrature rule as a set of

linear equations, thus converting the continuous integral eigenvalue problem in to a matrix eigenvalue problem. To apply the quadrature rule, first, a set of quadrature points (or nodes) with suitable weights are selected in the domain. In one dimension the integral equation is

$$\int_a^b C(x,y)f(x)dx = \lambda f(y). \tag{7}$$

Approximating Eq. (7) with an N-point quadrature rule with quadrature point $\{x\}^N{}_{i=1}$ and with weights $\{w\}^N{}_{i=1}$ we get

$$\sum_{i=1}^{N} w_i C(x_i,y)f(x_j) = \lambda f(y). \tag{8}$$

Discretizing the above equation over N quadrature points, we will get the $(N \times N)$ matrix eigenvalue problem

$$\mathbf{Kf} = \lambda \mathbf{f}, \tag{9}$$

where

$$K_{i,j} = C(x_i,x_j)w_j.$$

Similarly, in two dimension, the terms become

$$K_{i,j} = C(\mathbf{x}_i,\mathbf{x}_j)w_i w_j.$$

These three methods are implemented, and the results are compared next.

3 Numerical Study and Results

The three methods described in the previous section are studied and compared. A two-dimensional rectangular domain with dimensions [0, 2] × [0, 2] m^2 with an uncertain property is chosen, for example, for a plate with the same rectangular domain–material inhomogeneity. The uncertain material property is modeled with Gaussian distribution as a zero mean random field with the following covariance function.

$$C(x_1,y_1,x_2,y_2) = e^{(-\alpha|x_1-x_2|)}e^{(-\alpha|y_1-y_2|)}, \tag{10}$$

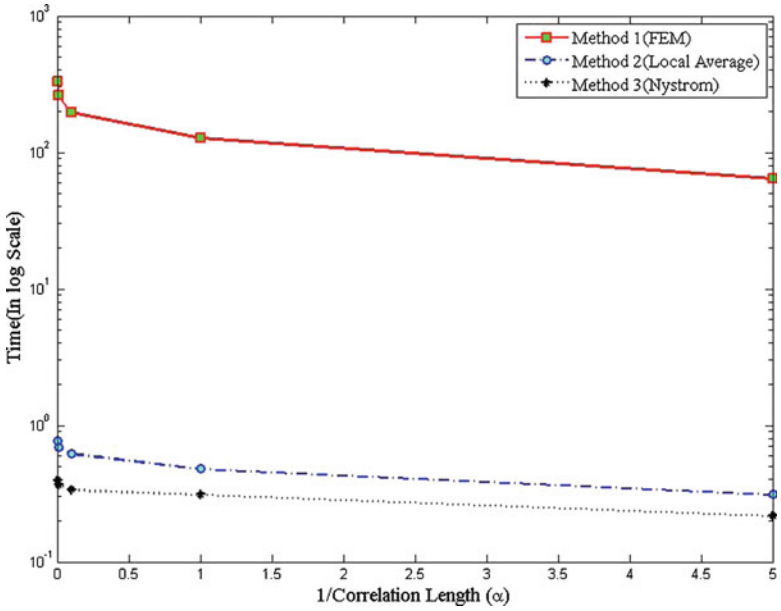

Fig. 1 Plot of time (in seconds) vs. α . Here Methods 2 and 3 are found to be faster than Method 1

where α is called correlation parameter which is the inverse of the correlation length of the random field. $[x_1, y_1]$ and $[x_2, y_2]$ are coordinates of points $\mathbf{x}_1$ and $\mathbf{x}_2$ in the spatial domain. The above covariance function is chosen because the analytical solution is available for the given domain. This analytical solution is compared with the numerical solution, and the error is computed. MATLAB® is used to code the numerical methods. To compare the numerical results, an error λ_{error} is to be defined as given in the following equation. This error is defined by using relative error in first three highest eigenvalues.

$$\lambda_{error} = \sqrt{({\lambda_{1_{error}}}^2 + {\lambda_{2_{error}}}^2 + {\lambda_{3_{error}}}^2)}, \tag{11}$$

where

$$\lambda_{i_{error}} = \frac{|\lambda_i - \hat{\lambda}_i|}{\lambda_i} \quad for \;\; i = 1, 2, 3,$$

where λ_i are analytical eigenvalues, and $\hat{\lambda}_i$ are numerical eigenvalues.

For the first set of results in Fig. 1 , the target accuracy is fixed with maximum percentage error $\lambda_{error} < .01\%$, and the computation time is noted for α equal to 5, 1, .1, .01 and .001. It is observed that Methods 2 and 3 are computationally faster than the Method 1 for a chosen accuracy and chosen correlation parameter.

For the second set of results in Fig. 2, with constant correlation parameter, $\alpha = 0.1$, computation cost in terms of time is noted by varying the error λ_{error} for

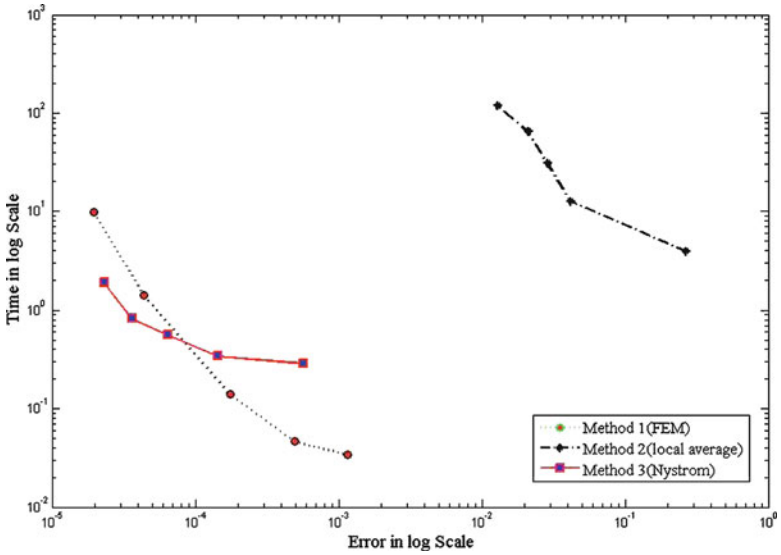

Fig. 2 Plot of time vs. error. Time required to solve the problem with given target accuracy for Method 1 is more than Methods 2 or 3

different mesh refinements for all the three methods. It is observed that the Methods 2 and 3 are computationally faster than the Method 1.

As observed from the results, it is concluded that Methods 2 and 3 are computationally faster than the Method 1 for a chosen target accuracy, thus for the given problem making these two methods computationally more efficient. Although all the three methods discretize the continuous integral eigenvalue problem into a matrix eigenvalue problem, it is done differently in each method. In Method 1, the finite element bases are used to approximate the eigenfunctions and then the error is minimized in Galerkin sense; in two dimensional case, this leads to the formulation of a matrix whose entries are found by computing a quadruple integral. This quadruple integral is computed by using an appropriate quadrature rule, whereas in Method 2, the covariance function is directly approximated by taking average values over each subdomain as explained in the previous section. And in Method 3, the integral equation is directly discretized by using a quadrature rule. This difference in implementation for all the three methods accounts for difference in observed computational time.

4 Conclusions

According to the observations from the numerical study for the chosen rectangular domain, Methods 2 and 3 are found to be computationally more efficient than the Method 1. While using Method 1 for solving a mechanics problem, the finite

element mesh used for mechanics problem is also used for discretizing the random field. This choice may be expensive. In the same mechanics problem, if Methods 2 and 3 are used to find KLE, an interpolation scheme is required to evaluate the random field at the finite element nodes. Therefore, to see the effect of this additional cost, a more complicated geometry and different covariance models should be studied. While comparing Methods 2 and 3, Method 2 can be preferred for spatial domains with simple geometry since the rule of approximation for Method 2 is simpler to implement. Other methods of solving the dense matrix eigenvalue problem, such as fast multipole method [7], and hierarchical matrices, see [8], can be explored to reduce the computational cost further.

References

1. Ghanem R, Spanos PD (2001) Spanos, stochastic finite elements: a spectral approach. Springer
2. Van Trees HL (2001) Detection, estimation, and modulation theory: part 1. Wiley Interscience, New York
3. Phoon KK, Huang SP, Quek ST (2002) Simulation of second-order processes using Karhunen-Loéve expansion. Comput Struct 80:1049–1060
4. Huang SP, Quek ST, Phoon KK (2001) Convergence study of the truncated Karhunen-Loéve expansion for simulation of stochastic processes. Int J Numer Method Eng 52:1092–1043
5. Frauenfelder P, Schwab C, Todor RA (2005) Finite elements for elliptic problems with stochastic coefficients. Comput Method Appl Mech Eng 194:205–228
6. Atkinson KE (1997) The numerical solution of integral equations of the second kind. Cambridge monographs on applied and computational mathematics (No. 4). Cambridge University Press, Cambridge/New York
7. Schwab C, Todor RA (2006) Karhunen-Loéve approximation of random fields by generalized fast multipole methods. J Comput Phys 217:100–122
8. Khoromskij B, Litvinenko A, Matthies H (2009) Application of hierarchical matrices for computing the Karhunen-Loéve expansion. Computing 84:49–67

Study of Forces Generated on the Structures Due to Tsunami Loading

Sandip B. Bhalerao, R.S. Soni, and S. Basu

Abstract Nuclear structures are generally designed for the design-basis earthquake (DBE) which is site-dependent. The DBE for nuclear structures is usually arrived at based on the stochastic approach as per the AERB guidelines/international guidelines (IAEA), and it is the probable earthquake which has the maximum damaging potential at the site and its adjoining area in a radius of 320 km around the site. Such an earthquake is called as the safe shutdown earthquakes (SSE) during which the functionality of reactor shutdown systems, the integrity of primary pressure boundary, and the reactor containment system need to be ensured. The DBE for high-hazard facilities, such as the reactors and reprocessing facilities, has a return period of 10,000 years.

It is observed and well documented in literature that earthquakes of greater magnitude ($M > 7.5$–8.0) produce destructive tsunami waves. Nuclear structures which are close to the coastal sites need to be guarded against the effects of tsunami loadings and need to have suitable emergency preparedness measures ready all the time so as to mitigate the effects of tsunami loadings, should such a situation arise in its lifetime.

The recently occurred tsunami events on December 26, 2004, (Sumatra in Indonesia) and March 11, 2011, tsunami triggered by a massive undersea earthquake of Honshu, Japan, developed lots of interest regarding design-related issues about tsunami. The main objective of this chapter is to study the various forces generated due to tsunami loading on the structure.

Keywords Tsunami • Structures • Loading • Seawall • Earthquakes • Design forces

S.B. Bhalerao (✉) • R.S. Soni • S. Basu
NRPSD & SA, Nuclear Recycle Board, Bhabha Atomic Research Center, Tarapur 401502, Maharashtra, India
e-mail: sandipbhalerao@barctara.gov.in

S. Chakraborty and G. Bhattacharya (eds.), *Proceedings of the International Symposium on Engineering under Uncertainty: Safety Assessment and Management (ISEUSAM - 2012)*,
DOI 10.1007/978-81-322-0757-3_60,

1 Introduction

Safety of nuclear structure [10] is a matter of great concern as per effects of various postulated events by the natural hazards like earthquakes, tsunamis, and cyclonic storm surges. It is important to put the Safety First motto, as nuclear accidents are low-probability high-risk events.

Strengthening nuclear safety in India is very pertinent and timely in wake of the nuclear disaster at the Fukushima nuclear power plant (NPP) site that emanated high nuclear radiation in Japan during the nuclear disaster on March 11, 2011, when a massive undersea mega-thrust earthquake of moment magnitude (Mw) 9.0 and the following tsunami hit the NPP site [1].

Several recent events, including the December 24, 2004, Indian Ocean tsunami and the April 2, 2007, South Pacific tsunami, have brought to notice the importance of studying and understanding the effects of loads induced due to tsunami and the need for improvisation of design guidelines for structures located in tsunami-prone regions.

2 Tsunamis

Tsunami is a series of large waves of extremely long period caused by violent, impulsive undersea disturbance or activity near the coast or in the ocean. The waves become extremely dangerous and damaging when they reach the shore. The word tsunami is composed of the Japanese words “tsu” (which means harbor) and “nami” (which means “wave”).

The destructive tsunamis are generated from large (dislocation of several meters), shallow earthquakes with epicenter or fault line near or on the ocean floor. Tsunamis generally occur in the oceanic subduction zones of lithospheric plates. The sudden vertical displacements over large areas disturb the ocean’s surface, displace water, and generate destructive tsunami waves. A “tsunami earthquake” is defined as an earthquake that excites much larger tsunami than expected from its seismic waves. Generally, earthquakes with Richter magnitude larger than 7.5 produce destructive tsunami waves. Table 1 shows a list of ten deadliest tsunamis in Indian Ocean. The wavelength of the tsunami waves and their periods depends on the generating mechanism and the dimensions of the source event. The period of the tsunami waves may range from 5 to 90 min. On the open ocean, the wavelength of a tsunami may be as much as 200 km.

As per the FEMA 55 Coastal Construction Manual, “Tsunamis are long-period water waves generated by undersea shallow focus earthquakes or by undersea crustal displacements (subduction of tectonic plates), landslides, or volcanic activity. Tsunamis can travel great distances, undetected in deep water, but shoaling rapidly in coastal waters and producing a series of large waves capable of destroying harbor facilities, shore protection structures, and upland buildings.”

Table 1 List of ten deadliest tsunamis in Indian Ocean

Year	Deaths	Location
Dec. 26, 2004	220,000	Sumatra
Aug. 27, 1883	36,500	Java/Sumatra
Jan. 26, 1941	5,000	Andaman Sea
Sept. 3, 1861	1,700	Sumatra
Jun. 16, 1819	1,543	Arabian Sea
Nov. 28, 1945	1,000	Arabian Sea
Feb. 16, 1861	905	Sumatra
April 2, 1762	500	Bay of Bengal
Aug. 19, 1977	500	Sunda Islands
Jan. 4, 1907	400	Sumatra

3 Tsunami Initiation

A sudden offset changes the elevation of the ocean and initiates a water wave that travels outward from the region of seafloor disruption. Tsunamis can travel all the way across the ocean, and large earthquakes have generated waves that caused damage and deaths in regions as shown in Fig. 1.

The speed of this wave depends on the ocean depth and is typically about as fast as a commercial passenger jet (about 0.2 km/s or 712 km/h). This is relatively slow compared to seismic waves, so we are often alerted to the dangers of the tsunami by the shaking before the wave arrives. The trouble is that the time to react is not very long in regions close to the earthquake that caused the tsunami as shown in Fig. 2.

Tsunamis pose no threat in the deep ocean because they are only a meter or so high in deep water. But as the wave approaches the shore and the water shallows, all the energy that was distributed throughout the ocean depth becomes concentrated in the shallow water and the wave height increases as shown in Fig. 3.

Typical heights for large tsunamis are on the order of tens of meters, and a few have approached 90 m (about 300 ft).

4 Strategies for Tsunami Events

As far back as 1480 BC, history records destruction by tsunami-huge ocean waves—with loss of life and property. Today, population pressures on coastal areas bring more and more communities and installations under this threat. Various strategies as given below need to be set for tsunami events:

1. Awareness and understanding strategy (AUS)
2. Land-use planning strategy (LUPS)
3. Proper sitting strategy for new development (PSS)
4. Protection strategy for existing development (PS)

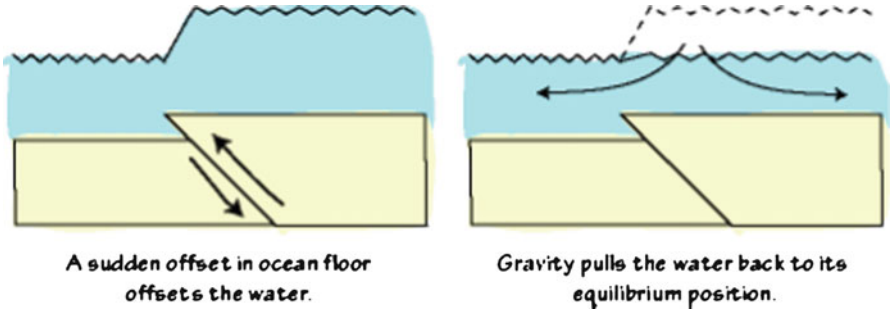

Fig. 1 Initiation of tsunamis

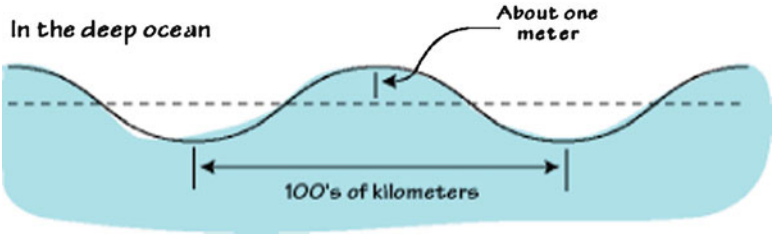

Fig. 2 Tsunami waves in deep ocean

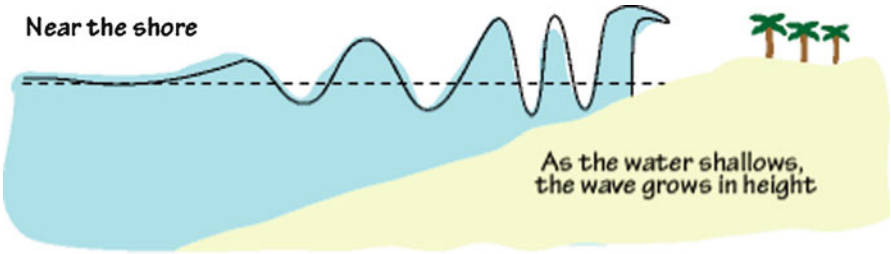

Fig. 3 Tsunami waves near the shore

5. Tsunami warning systems and vertical evacuation strategy (TWS and VES)
6. Structural design consideration strategy (SDCS)

In this chapter, focus is given on the SDCS as the design consideration of the buildings, construction practice and techniques, materials used for construction, and tsunami-specific design data and features will be able to reduce loss of life and property damage.

5 Currently Available Design Codes, Standards, and Guidelines

To date, there has been very little research undertaken on the design of structures to resist tsunamis, primarily because major tsunamis were perceived as being so rare as not to warrant attention from the point of view of public safety. However, public perceptions in this regard are changing. If suitable structural solutions are to be found, they will need to be based on a fundamental understanding of the forces imposed on structures by tsunami inundation and the response of structures to them. This will require considerable knowledge about the physical characteristics of the tsunamis as they penetrate over land [2].

Very little guidance is provided in currently available structural design codes, standards, and guidelines on loads induced by tsunami inundation. Well-established design information mainly focuses on loads due to rising water, flooding, and storm surge. While little specific guidance is provided, the presumption is that currently available flood design standards are to be used in designing for tsunami load effects.

The following are the current codes, standards, and guideline, which provide related details:

5.1 International Building Code

The International Code Council *International Building Code* (ICC [15]) Appendix G provides information on flood design and flood-resistant construction by reference to ASCE/SEI Standard 24-05, *Flood Resistant Design and Construction* (ASCE 24, [11]).

5.2 ASCE/SEI Standard 24-05

The American Society of Civil Engineers/Structural Engineering Institute (ASCE/SEI) Standard 24-05 *Flood Resistant Design and Construction* (ASCE [11]) provides minimum requirements for flood-resistant design and construction of structures located in flood-hazard areas. Topics include basic requirements for flood-hazard areas, high-risk flood-hazard areas, coastal high-hazard areas, and coastal A zones. This standard complies with FEMA National Flood Insurance Program (NFIP) floodplain management requirements.

5.3 ASCE/SEI Standard 7-05

ASCE/SEI Standard 7-05 *Minimum Design Loads for Buildings and Other Structures* (ASCE [12]) provides expressions for forces associated with flood and wave loads on specific types of structural components. This standard covers important definitions that relate to flooding and coastal high-hazard areas related to tides, storm surges, riverine flooding, seiches, or tsunamis.

5.4 FEMA (Federal Emergency Management Agency) 55 Coastal Construction Manual

The FEMA 55 *Coastal Construction Manual* (FEMA [14]) includes FEMA's most recent study of coastal seismic and tsunami loads. The *Coastal Construction Manual* addresses seismic loads for coastal structures and contains expressions for flood loads, wave loads, and load combinations for specific types of structural components.

5.5 City and County of Honolulu Building Code

The *City and County of Honolulu Building Code* (CCH [13]), Chapter 16, Article 11, provides specific guidance for "*structural design of buildings and structures subject to tsunamis*" in Section 16-11.5(f). The loading requirements in this section are based on the 1980 Dames and Moore study, but with the velocity of flow in feet per second estimated as equal in magnitude to the depth in feet of water at the structure. Estimates are also given for anticipated scour around piles and piers based on distance from the shoreline and the soil type at the building site.

5.6 Coastal Disaster Reduction Guide

After the 2004 great Indian Ocean tsunami with the endorsement of the International Association of Bridge and Structural Engineering and Engineers Australia and the support of many other organizations and engineers, *coastal disaster reduction guide* was prepared.

The guide proposes a limit state approach with three limit states being identified:

- A serviceability limit state based on the need to survive inundation without loss of life or injury and minimal physical damage to buildings and infrastructure, from events with a return period of the order of 50 years

- A normal code ultimate limit state based on the need for minimal loss of life and injury and minimal damage to essential services, while accepting significant physical damage to normal buildings and infrastructure, from events with a return period of the order of 300 years
- A postcode ultimate limit based on the need to minimize life, injury, and asset damage, as well as maintaining essential services through the incorporation of robustness in the design of buildings and infrastructure, from events with a return period of the order of 1,000 years or more

6 Tsunami-Induced Forces

It is observed that, generally three parameters are essential for defining the magnitude and application of tsunami-induced forces [3–8]: (1) inundation depth, (2) flow velocity, and (3) flow direction. These parameters mainly depend on (a) tsunami wave height and wave period, (b) coastal topography, and (c) roughness of the coastal inland.

6.1 Hydrostatic Forces

Hydrostatic forces occur when standing or slowly moving water encounters a structure or structural component. This force always acts perpendicular to the surface of the component of interest. It is caused by an imbalance of pressure due to a differential water depth on opposite sides of a structure or component. Hydrostatic forces may not be relevant to a structure with a finite (i.e., relatively short) breadth, around which the water can quickly flow and fill in on all sides. Hydrostatic forces are usually important for long structures such as seawalls and dikes or for evaluation of an individual wall panel where the water level on one side differs substantially from the water level on the other side. The horizontal hydrostatic force on a wall panel can be computed using Eq. 1:

$$F_h = p_c A_w = \frac{1}{2}\rho_s g b h_{\max}^2. \tag{1}$$

where p_c is the hydrostatic pressure, Aw is the wetted area of the panel, ρ_s is the fluid density including sediment (1,200 kg/m^3), g is the gravitational acceleration, b is the breadth (width) of the wall, and $hmax$ is the maximum water height above the base of the wall at the structure location. If the wall panel with height hw is fully submerged, then the horizontal hydrostatic force can be written as Eq. 2 and shown in Fig. 4:

$$F_h = p_c A_w = \rho_s g\left(h_{\max} - \frac{h_w}{2}\right) b h_w \tag{2}$$

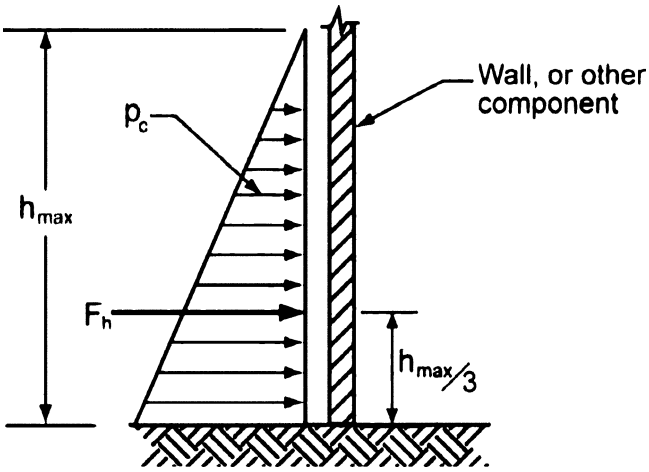

Fig. 4 Hydrostatic force distribution and location of resultant

6.2 Buoyant Forces

Buoyant or vertical hydrostatic forces will act vertically through the centroid of the displaced volume on a structure or structural component subjected to partial or total submergence. The total buoyant force equals the weight of water displaced. Buoyant forces on components must be resisted by the weight of the component and any opposing forces resisting flotation. For a watertight structure, the total buoyant force is given by Eq. 3:

$$F_b = \rho_s g V \tag{3}$$

where ρ_s is the fluid density including sediment (1,200 kg/m^3) and V is the volume of water displaced by the building. Buoyant forces on an overall building are shown in Fig. 5. If there is insufficient building weight to resist buoyant forces, tension piles may be used to increase the resistance to flotation.

6.3 Hydrodynamic Forces

When water flows around a structure, hydrodynamic forces are applied to the structure as a whole and to individual structural components. These forces are induced by the flow of water moving at moderate to high velocity and are a function

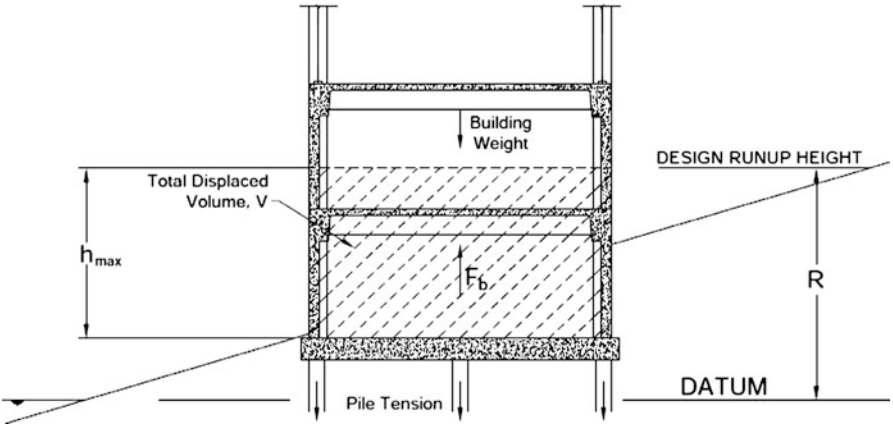

Fig. 5 Buoyant forces on an overall building with watertight lower levels

of fluid density, flow velocity, and structure geometry. Also known as drag forces, they are a combination of the lateral forces caused by the pressure forces from the moving mass of water and the friction forces generated as the water flows around the structure or component. Hydrodynamic forces can be computed using Eq. 4:

$$F_d = \frac{1}{2}\rho_s C_d B(hu^2)_{\max} \tag{4}$$

where ρ_s is the fluid density including sediment (1,200 kg/m^3), C_d is the drag coefficient, B is the breadth of the structure in the plane normal to the direction of flow (i.e., the breadth in the direction parallel to the shore), h is the flow depth, and u is the flow velocity at the location of the structure. For forces on components, B is taken as the width of the component. It is recommended that the drag coefficient be taken as $C_d = 2.0$. The resultant hydrodynamic force is applied approximately at the centroid of the wetted surface of the component, as shown in Fig. 6.

6.4 Impulsive Forces

Impulsive forces are caused by the leading edge of a surge of water impacting a structure. Ramsden [16] performed comprehensive experiments on impulsive forces. The maximum overshoot is approximately 1.5 times the subsequent hydrodynamic force, consistent with independent laboratory data obtained by Arnason [18]. The hydrodynamic force is as shown in Eq. 5:

$$F_s = 1.5F_d \tag{5}$$

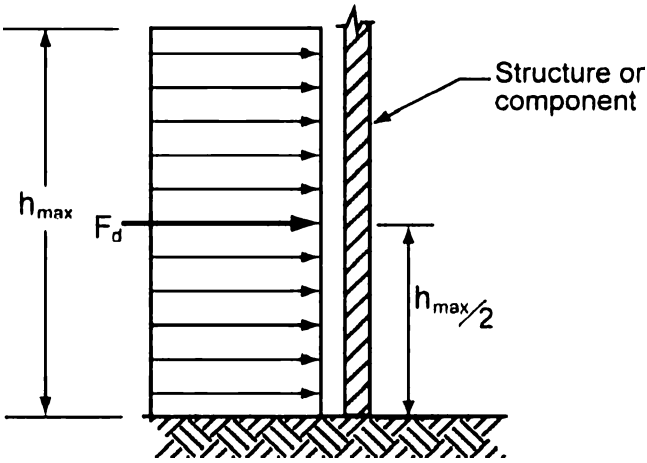

Fig. 6 Hydrodynamic force distribution and location of resultant

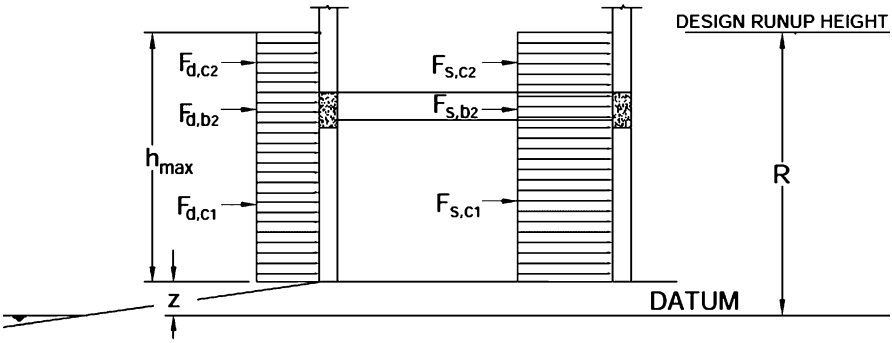

Fig. 7 Hydrodynamic impulsive and drag forces on components of a building subjected to inundation by a tsunami bore

Impulsive forces will act on members at the leading edge of the tsunami bore, while hydrodynamic forces will act on all members that have already been passed by the leading edge, as shown in Fig. 7.

6.5 Debris Impact Forces

The impact force from waterborne debris (e.g., floating driftwood, lumber, boats, shipping containers, automobiles, buildings) can be a dominant cause of building damage. Unfortunately, it is difficult to estimate this force accurately. Background

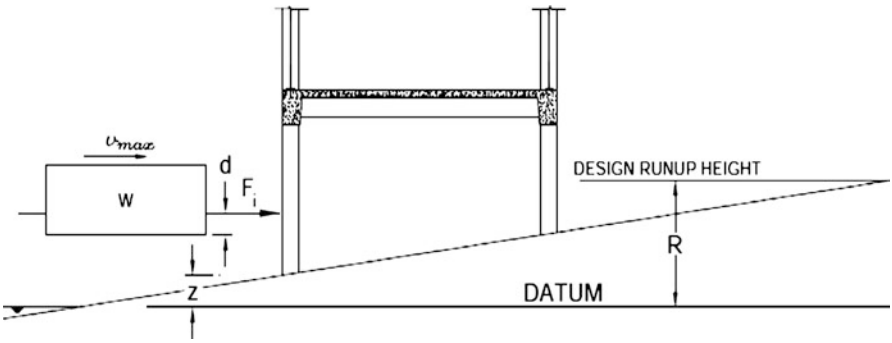

Fig. 8 Waterborne debris impact force

information on the development of the recommended impact force calculation is provided in Section 6.6 of FEMA P646 [10] and given as Eq. 6:

$$F_i = C_m u_{\max} \sqrt{\mathrm{km}} \tag{6}$$

where C_m is the added mass coefficient, $u_{\max}$ is the maximum flow velocity carrying the debris at the site, and m and k are the mass and the effective stiffness of the debris, respectively. It is recommended that the added mass coefficient be taken as $C_m = 2.0$. Unlike other forces, impact forces are assumed to act locally on a single member of the structure at the elevation of the water surface, as shown in Fig. 8.

6.6 Damming of Waterborne Debris

The damming effect caused by accumulation of waterborne debris can be treated as a hydrodynamic force enhanced by the breadth of the debris dam against the front face of the structure. Equation 7 is a modification of Eq. 4 to include the breadth of the debris dam:

$$F_{dm} = \frac{1}{2} \rho_s C_d B_d (hu^2)_{\max} \tag{7}$$

where ρ_s is the fluid density including sediment (1,200 kg/m^3), C_d is the drag coefficient, B_d is the breadth of the debris dam, h is the flow depth, and u is the flow velocity at the location of the structure. It is recommended that the drag coefficient be taken as $C_d = 2.0$.The momentum flux (h $u2$)max can be obtained by running a detailed numerical simulation model, acquiring existing simulation data.

The debris damming force, Fdm, should be assumed to act as a uniformly distributed load over the extent of the debris dam. It should be assigned to each

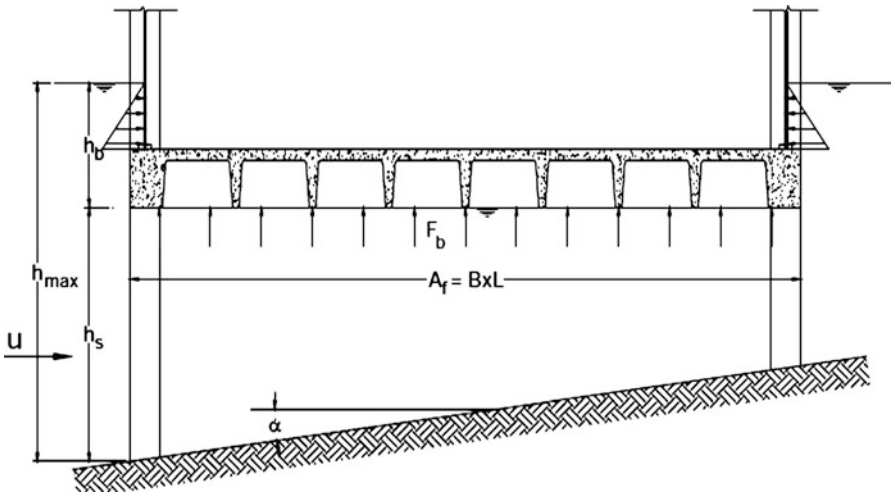

Fig. 9 A definition sketch for upward buoyant force exerted on an elevated floor

resisting structural component by an appropriate tributary width and distributed uniformly over the submerged height of each resisting component. A minimum debris dam width of $B_d = 40$ ft (or 12 m), representing a sideways shipping container or a mass of floating lumber, is recommended.

6.7 Uplift Forces on Elevated Floors

Uplift forces will be applied to floor levels of a building that are submerged by tsunami inundation. In addition to standard design for gravity loads, these floors must also be designed to resist uplift due to buoyancy and hydrodynamic forces. When computing the buoyant forces on a floor slab, consideration must be given to the potential for increased buoyancy due to the additional volume of water displaced by air trapped below the floor framing system. In addition, exterior walls at the upper floor level will exclude water until their lateral resistance is exceeded by the applied hydrostatic pressure. This can significantly increase the displaced volume of water contributing to the buoyancy, as shown in Fig. 9. The total upward buoyant force exerted on a floor system can be estimated using Eq. 8:

$$F_b = \rho_s g A_f h_b \tag{8}$$

where g is the acceleration due to gravity, A_f is the area of the floor panel or floor framing component, and h_b is the water height displaced by the floor (including potentially entrapped air).

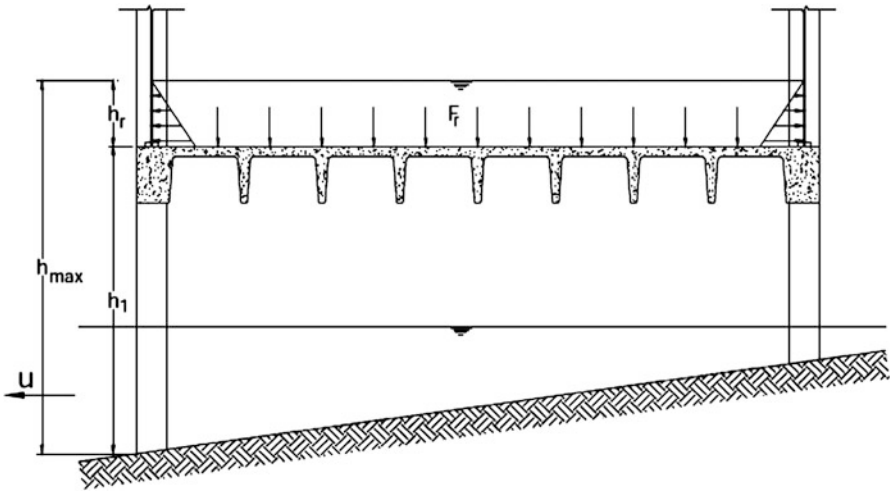

Fig. 10 Gravity loads exerted on an elevated floor with water retained by exterior walls during rapid drawdown

6.8 Additional Gravity Loads on Elevated Floors

During drawdown, water retained on the top of elevated floors, as shown in Fig. 10, will apply additional gravity loads that can exceed the loads for which the floor system was originally designed. The maximum potential downward load per unit area, f_r, can be estimated using Eq. 9:

$$f_r = \rho_s g h_r \tag{9}$$

where ρ_s is the fluid density including sediment (1,200 kg/m^3), g is the acceleration due to gravity, and h_r is the maximum potential depth of water retained on the elevated floor determined using Eq. 10:

$$h_r = h_{\max} - h_1 \leq h_{bw} \tag{10}$$

where h_{max} is the maximum inundation level predicted at the site, h_1 is the floor elevation above grade, and h_{bw} is the maximum water depth that can be retained before failure of the wall due to internal hydrostatic pressure.

7 Combination of Tsunami Forces

Not all tsunami load effects will occur simultaneously, nor will they all affect a particular structural component at the same time. Section 6.6 of FEMA P646 describes combinations of tsunami forces that should be considered for the overall

structure and for individual structural components. Other potential combinations should be considered as needed, based on the particular siting, structural system, and design of the structure under consideration.

As per FEMA P646, tsunami forces that will act on the entire structure and on individual structural components should be calculated as given in above equations. The resulting member forces (*Ts*) should then be combined with gravity load effects using the following strength design load combinations:

Load combination 1: $1.2D + 1.0Ts + 1.0LREF + 0.25\ L$
Load combination 2: $0.9D + 1.0Ts$

where *D* is the dead load effect, *Ts* is the tsunami load effect, *LREF* is the live load effect in refuge area (assembly loading), and *L* is the live load effect outside of the refuge area.

A load factor of 1.0 is used in conjunction with tsunami forces calculated in accordance with this document for the following reasons: (1) it is anticipated that the tsunami hazard level corresponding to the maximum considered tsunami will be consistent with the 2,500-year return period associated with the maximum considered earthquake used in seismic design; (2) potential variability in tsunami run-up elevations is explicitly considered by applying a 30% increase to run-up elevations used in tsunami force calculations; and (3) design for tsunami forces considers only the elastic response of components, without consideration of inelastic response and corresponding force reduction factors (as is used in seismic design).

Based on current literature, tsunami loading combination must be significantly improved and incorporated in new design codes. An example of recent improvements in loading combinations is the work of Nouri et al. [17] as shown in Fig. 10. The load combinations are separated into two scenarios: (1) initial impact and (2) post impact. The first combination occurs due to surge and debris impact forces. The second scenario considers the hydrodynamic (drag) and hydrostatic force, simultaneously with the debris impact force. The buoyant force is omitted for calculation of the global lateral force, but should be considered in the analysis and design of flooring elements.

Various forces like F_i, F_s, F_d, F_{HS}, and F_b are the debris impact, surge, drag, hydrostatic, and buoyant force components respectively and these forces are shown in Fig. 11.

8 Tsunami Effects and Design Solutions

The following table lists the possible effects of tsunamis on physical structures and suggests design solutions for each of the potential effects. It is important that design measures be based on the local hazard study so that expected forces determine the design solutions as given in the Table 2.

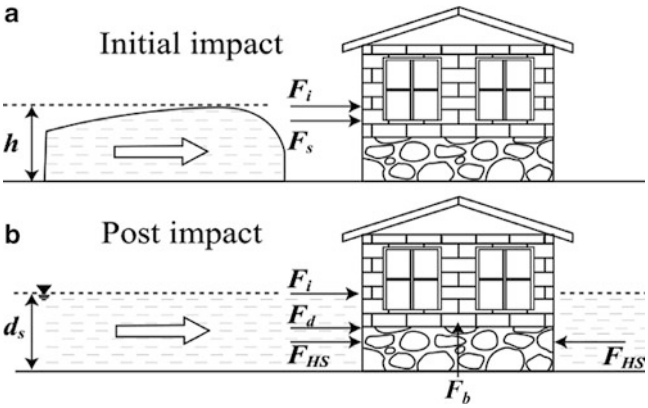

Fig. 11 Loading condition

Table 2 Tsunami effects and design solutions

Phenomenon	Effect	Design solution
Inundation	Flooded basements	Choose sites at higher elevations
	Flooding of lower floors	Raise the building above the flood elevation
	Fouling of mechanical, electrical, and communication systems and equipment	Do not store or install vital material and equipment on floors or basements lying below tsunami inundation levels
	Damage to building materials, furnishings, and contents (supplies, inventories, personal property)	Protect hazardous material storage facilities that must remain in tsunami hazard areas
	Contamination of affected area with waterborne pollutants	Locate mechanical systems and equipment at higher locations in the building
		Use concrete and steel for portions of the building subject to inundation
		Evaluate bearing capacity of soil in a saturated condition
	Hydrostatic forces (pressure on walls caused by variations in water depth on opposite sides)	Elevate buildings above flood level
		Anchor buildings to foundations
		Provide adequate openings to allow water to reach equal heights inside and outside of buildings
		Design for static water pressure on walls
	Buoyancy (flotation or uplift forces caused by buoyancy)	Elevate buildings
		Anchor buildings to foundations
	Saturation of soil causing slope instability and/or loss of bearing capacity	Evaluate bearing capacity and shear strength of soils that support building foundations and embankment slopes under conditions of saturation
		Avoid slopes or provide setback from slopes that may be destabilized when inundated

(continued)

Table 2 (continued)

Phenomenon	Effect	Design solution
Currents	Hydrodynamic forces (pushing forces caused by the leading edge of the wave on the building and the drag caused by flow around the building and overturning forces that result)	Elevate buildings Design for dynamic water forces on walls and building elements Anchor building to foundations
	Debris impact	Elevate buildings Design for impact loads
	Scour	Use deep piles or piers Protect against scour around foundations
Wave break and bore	Hydrodynamic forces	Design for breaking wave forces
	Debris impact	Elevate buildings Design for impact loads
	Scour	Design for scour and erosion of the soil around foundations and piers
Drawdown	Embankment instability	Design waterfront walls and bulkheads to resist saturated soils without water in front Provide adequate drainage
	Scour	Design for scour and erosion of the soil around foundations and piers
Fire	Waterborne flammable materials and ignition sources in buildings	Use fire-resistant materials Locate flammable material storage outside of high-hazard areas

9 Conclusion

There has been very little research undertaken on the design of structures to resist tsunamis to date. However, in past few years, various massive destructive tsunami events have been experienced worldwide. These events have caused tremendous devastation to lives, infrastructure, and properties of local communities. This required serious attention from designers, researchers, and engineers to address issues related to tsunami-resistant design.

In this chapter, study has been carried out addressing various issues related to tsunami events. Literature survey has been done regarding basics of tsunami, various strategies needed to be set for tsunami events, forces induced due to tsunami loading, and probable load combinations. Study has been also carried out to understand the probable effects of tsunami and respective design solutions. This study needs to be further extended to develop elaborate design guidelines for tsunami-resistant design.

References

1. A.K. Ghosh., (2008), Assessment Of Earthquake-Induced Tsunami Hazard At A Power Plant Site, Nuclear Engineering And Design 238 (2008) 1743–1749.
2. D. Palermo, and I. Nistor., (2008), Understanding Tsunami Risk To Structures: A Canadian Perspective, Science Of Tsunami Hazards, the International Journal of The Tsunami Society, Volume 27 Number 4 (2008).
3. Designing for Tsunamis (Seven Principles for Planning and Designing for Tsunami Hazards), March (2001), National Tsunami Hazard Mitigation Program, NOAA, USGS, FEMA, NSF, Alaska, California, Hawaii, Oregon, and Washington.
4. Harry Yeh,(2007), Design Tsunami Forces for Onshore Structures, Journal of Disaster Research Vol.2 No.6, 2007.
5. Navaratnam I. Thusyanthan, S. P. Gopal Madabhushi., (2008), Tsunami wave loading on coastal houses:a model approach, edings of ICECivil Engineering 161 May 2008, Pages 77–86 Paper 07-00037.
6. Palermo Dan, Nistor Ioan, Nouri Younes, Cornett Andrew., (2009) Tsunami loading of near-shoreline structures: a primer., Canadian Journal of Civil Engineering Publisher : NRC Research Press 36 (2009).
7. R. Silva, I.J. Losada, M.A. Losada., (2000), Reflection and transmission of tsunami waves by coastal structures, Applied Ocean Research 22 (2000) 215-223.
8. Seshu B. Nimmala, Kwok Fai Cheung., (2006), Tsunami Design Criteria for Coastal Infra-structure: A Case Study for Spencer Creek Bridge, Oregon.
9. Yong-Sik Cho, So-Beom Jin, Ho-Jun Lee., (2004), Safety analysis of Ulchin Nuclear Power Plant against Nihonkai-Chubu Earthquake Tsunami, Nuclear Engineering and Design 228 (2004) 393–400.
10. FEMA P646, (2008) Guidelines for design of structures for vertical evacuation from tsunamis. Federal Emergency Management Agency, Washington, DC, June 2008.
11. ASCE (2006a) Flood resistant design and construction, ASCE Standard 24-05. American Society of Civil Engineers, Reston
12. ASCE (2006b) Minimum design loads for buildings and other structures, ASCE/SEI Standard 7-05. American Society of Civil Engineers, Reston
13. CCH (2000) City and county of Honolulu Building Code. Department of Planning and Permitting of Honolulu Hawaii, Honolulu
14. FEMA (2005) Coastal construction manual, FEMA 55 Report, 3rd edn. Federal Emergency Management Agency, Washington, DC
15. ICC (2006) International Building Code. International Code Council, Inc., Country Club Hills
16. Ramsden JD (1993) Tsunamis: forces on a vertical wall caused by long waves, bores, and surges on a dry bed, Report no. KH-R-54, W.M. Keck Laboratory, California Institute of Technology, Pasadena
17. Palermo D, Nistor I, Cornett A, Nouri Y (2007) Tsunami-induced impact and hydrodynamic loading of near-shoreline structures, PROTECT 2007, 1st International workshop performance, protection and strengthening of structures under extreme loading, UBC, Whistler, Canada, CD-ROM, 10 p
18. Arnason H (2005) Interactions between an incident bore and a free-standing coastal structure. PhD dissertation, University of Washington, Seattle

Utility of Eccentric Bracing Frames in Seismic-Resistant, Sustainable Steel Building

Arup Saha Chaudhuri

Abstract The aim of this chapter is to show the efficacy of eccentric bracing frame (EBF) in steel structure over moment-resisting frame (MRF) and concentric bracing frame (CBF). Eccentric bracing connections in steel structures help in stability of the structural systems against horizontal forces especially in seismic condition and also economize the connection. The EBF is usually assumed to be pin-ended, but the beam–column joints may be designed for pin-ended or for full connectivity. The EBF has several desirable features as a system for resisting seismic forces. The system can be designed for appropriate stiffness and drift control, comparable to that obtained using concentric bracing. The link beam is designed to yield in shear or flexure prior to initiation of buckling or yielding of the bracing member in compression or tension. In this chapter, the behavior of a 2-D steel frame is observed under seismic loading condition. The ductility and brittleness of the frames are compared with respect to time period of vibration and ratio of static base shear vs. dynamic base shear. The superiority of the EBF system is clearly visible than MRF and CBF system comparing the time period of vibration and base shear participation. The EBF system acts as metallic damper in the building fames.

Keywords Earthquake • Steel frame • Eccentric bracing frame • Moment-resisting frame • Concentric bracing frame • Metallic damper • Yield stress

1 Introduction

Eccentric bracing connections in steel structures help in stability of the structural systems against horizontal forces especially in seismic condition and also economize the connection over MRF and CBF systems. The EBF is usually

A.S. Chaudhuri (✉)
Civil & Structural Department, L&T ECC EDRC, MIBC, Kolkata, India
e-mail: arupsc@rediffmail.com

S. Chakraborty and G. Bhattacharya (eds.), *Proceedings of the International Symposium on Engineering under Uncertainty: Safety Assessment and Management (ISEUSAM - 2012)*,
DOI 10.1007/978-81-322-0757-3_61,

assumed to be pin-ended, but the beam–column joints are usually designed for full connectivity. The EBF has several desirable features as a system for resisting seismic forces. The system can be designed for appropriate stiffness and drift control, comparable to that obtained using concentric bracing. The link beam is designed to yield in shear or flexure prior to initiation of buckling or yielding of the bracing member subjected to flexure.

EBF system can sustain plastic deformations and dissipate hysteretic energy in a stable manner through successive cycles of buckling in compression or yielding in tension. The preferred design strategy is also achieved while ensuring that plastic deformations occur due to damage takes place in the link beams leaving the columns undamaged.

Yielding of the link beam is a ductile phenomenon (as opposed to the brittle compression failure of a concentric brace) that absorbs seismic energy and reduces the dynamic structural response by increasing the damping and the natural period of vibration of the building. This system acts as metallic damper in the building frame.

In this chapter, response of MRF, EBF, and CBF under seismic excitation has been compared for different structural frames with due reference to state-of-the-art literature and code provisions. In EBF system, part of the gravity load is taken by bracing members as an intermediate support. As cost of moment connections is reduced and brittleness is avoided, EBF system is considered to be efficient than other systems for stability of the structural steel frame.

2 Earthquake and Ductility

Structural steel has many physical properties that make it a desirable building material for structures designed to resist earthquake ground motion. Among these properties, ductility of steel is important. Steel has the ability to sustain large strains, beyond the initial yield limit, without degradation of load-carrying capacity. This property allows steel structures to release energy with inelastic deformation of the members and avoids collapse for ground motion that is much more severe than that normally expected based on the code provisions. Structures having a frequency greater than 30 Hz are considered to be rigid and have an acceleration which is equal to the ground acceleration. In the frequency range between 6 and 30 Hz, there is a transition stage between the ground acceleration and the amplified acceleration region. An amplified acceleration stage is between 2 and 6 Hz. The frequency range of ground motion can be examined by transforming the motion from time domain to frequency domain through a Fourier transformation. Past earthquake histories indicate that most of the energy in the accelerogram is in the frequency range of 0.1–10 Hz and that the largest is at a frequency of approximately 1.5–2 Hz. By ductility property, the structures dissipate the energy and return back to their original position. For heavy ground motion, it undergoes inelastic deformation and stands in permanent set position. Thus, the fundamental frequency

of a structure can be reduced to less than 1 Hz by using ductile material like steel and ductile detailing.

3 MRF, EBF, and CBF Systems

Typical moment frame configurations are shown in Fig. 1. The beam–column connections are moment-carrying connections. The end moments of the beams resist the side sway of the building frame. This type of frame is flexible due to joint rotation.

Eccentric bracing configurations are described in Fig. 2. In eccentric bracing frame, the members are assumed to be pin-ended, but the beam–column joints are usually welded for full continuity capable to take care of moment and shear. The eccentric braced frame has several desirable features as a system for resisting seismic forces:

1. The system can be designed for stiffness or drift control, comparable to that obtained with concentric bracing.

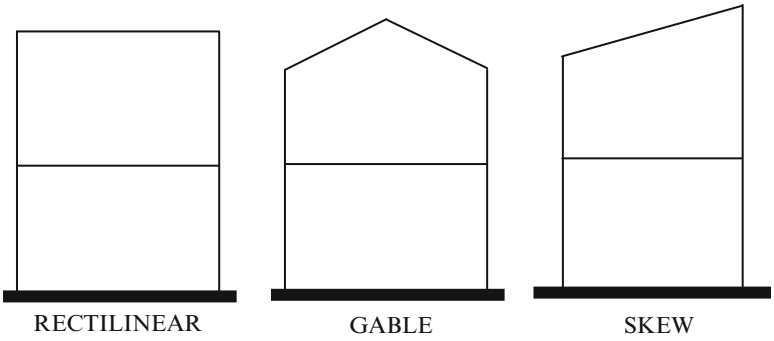

Fig. 1 Moment-resisting frames

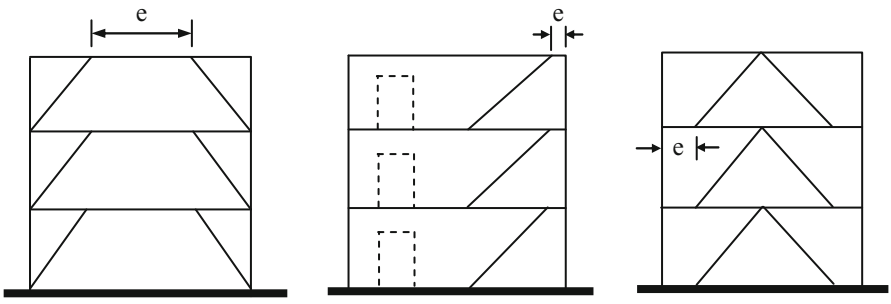

Fig. 2 Eccentrically braced frame

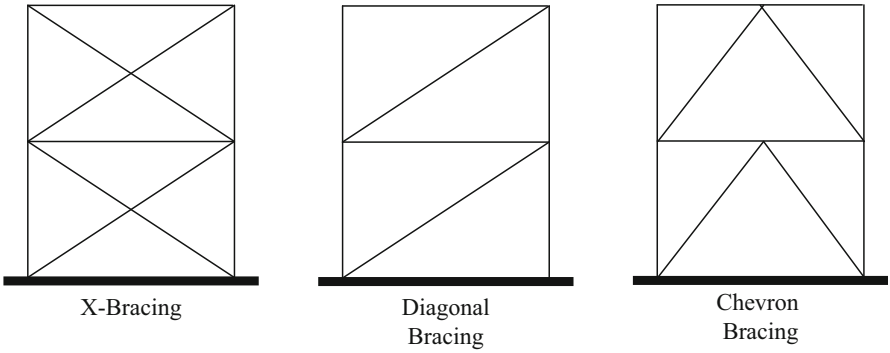

Fig. 3 Concentrically braced frame

2. The link beam is designed to yield in shear or flexure prior to initiation of buckling or yielding of the bracing member.
3. Yielding of link beam is a ductile phenomenon (as opposed to the brittle compression of a concentric brace) that absorbs seismic energy and reduces the dynamic structural response by increasing the damping and the natural period of vibration of the building.

Concentric bracing configurations are shown in Fig. 3. In the design of concentric bracing systems, it is usually assumed that the bracing members are pin-ended (i.e., they are designed only for axial tension or compression). All columns and beams in the concentric bracing system are generally pin-ended connection.

4 Present Problem

In the present problem, a (G + 4) commercial building with long-span grid frame is analyzed using STAAD. Pro, providing three types of connections, i.e., eccentric bracing connection, moment connection, and chevron bracing connection. Floor to floor height is considered 3 m (ground floor 2.5 m), and column to column spacing is considered 9 m. Columns and beams are made of steel beams, and floors are made of concrete slab. The composite behavior of steel beam and concrete slab is considered in the analysis. Live load is considered 400 kg/m^2. The beam size, column size, etc., are described for different frames as follows (Fig. 4):

4.1 EBF

The bottom two stories of column are made of UC 305 × 305 × 118 + 2 WEB PL 100 × 10 THK. Top portion of column is made of UC 305 × 305 × 97.

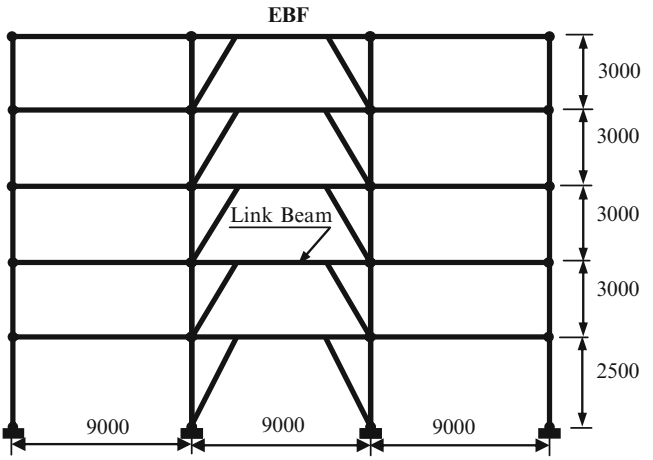

Fig. 4 Long-span steel–concrete composite EBF frame

Composite beams are made of UB 305 × 165 × 46 + 3,000 × 200 THK slab connected with shear connection at end. Link beams are made of ISMB 300 (grade Fe 540B) connected with moment connections at end. Bracing members are made of star angle 2-L 130 × 130 × 12. The frames are subjected to earthquake force of zone IV of IS: [2]. Response spectrum analysis is done for the frames.

4.2 MRF

The bottom two stories of column are made of 2-FLG PL 400 × 20 + 1 WEB PL 660 × 16. Top portion of column is made of WPB 600 × 300 × 128.8. Composite beams are made of ISMB 300 + 3,000 × 200 THK slab connected with moment connection at end. Similar response spectrum analysis is done for the frames (Fig. 5).

4.3 CBF

The bottom two stories of column are made of UC 305 × 305 × 118 + 2 WEB PL 100 × 10 THK. Top portion of column is made of UC 305 × 305 × 97. Composite beams are made of UB 305 × 165 × 46 + 3,000 × 200 THK slab connected with shear connection at end. Bracing members are made of star angle 2-L150 × 150 × 12. The frames undergo similar type of response spectrum analysis (Fig. 6).

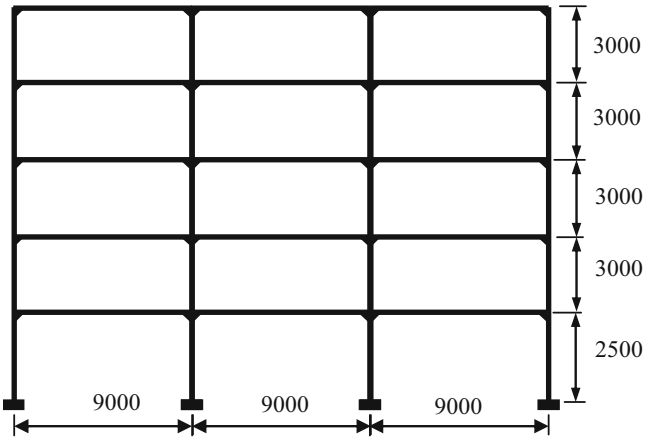

Fig. 5 Long-span steel–concrete composite MRF frame

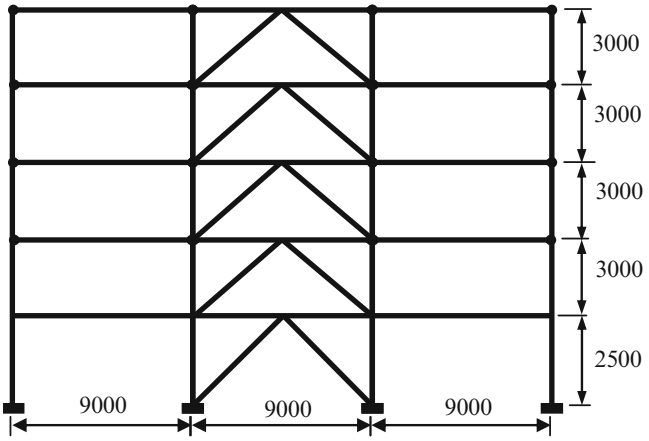

Fig. 6 Long-span steel–concrete composite CBF frame

5 Results

After analyzing the above three frames, it is observed that during seismic load, amplitude of vibration is maximum in EBF system; thus, the frequency is lesser than other two systems as shown in Table 1. Maintaining the limiting deflection criteria of code, the frequency in EBF system 0.685 Hz, i.e., the time period of fundamental mode, is 1.46 s. The reserve strength compared to CBF for base shear participation in this case is 2.1 which means the dynamic base shear is 2.1 times less than static base shear. This frequency range is not falling with the acceleration amplification zone. Results of MRF system are similar to that of EBF system. But the cost of connections is much greater than EBF system. The worst result came

Table 1 Study of flexibility of EBF, MRF, and CBF systems

	Steel frame		
	EBF	MRF	CBF
Tip deflection (mm)	64	55	13
Frequency (Hz)	0.685	0.8	1.8
Static base shear/dynamic base shear	2.1	1.9	1.0

from CBF system. The frequency is 1.8 Hz (nearer to 2 Hz) which is falling in acceleration amplification zone. As the system is rigid, the reserve strength in base shear participation is nil, i.e., the dynamic base shear is same as static base shear. So, EBF system should always be adopted because of its ductile behavior and reduced cost of connection.

6 Conclusions

Thus considering efficiency, the EBF system shall be applied in modern building systems. The IS: [2] code also says that response reduction factor (R) for EBF and MRF systems is 5 and that for CBF system is 4. For the safety against collapse, the EBF system has more reserve strength, and it will stand even experiencing a major earthquake force. The column sections in EBF system are designed for axial load only. Floor beams will have the composite action for the full length. These features give economy in steel quantity than MRF system. So, EBF system is getting more popularity over MRF system and CBF system nowadays.

References

1. AISC handbook for seismic design
2. IS: 1893 (Part 1 – 2002) Indian code of practice for seismic design
3. IS: 800 (2007) Indian code of practice for steel construction
4. Naeim F, Seismic design handbook

Performance of Connected Buildings Under Parameter Uncertainty Subjected to Random Earthquakes

Sudib K. Mishra and Sumanta Das

Abstract Interconnecting adjacent buildings by damper is established as a viable technology to avoid pounding and resulting damages observed in the past major earthquakes. Performance of such system has been investigated in the past. However, all these studies assume the system parameters as deterministic. It is well established that performance of a control system can significantly get affected by the presence of uncertainty in system parameters. In this study, the effect of parameter uncertainty is included in the stochastic response evaluation of the connected buildings under random earthquake. The buildings, modeled by two single degree of freedom systems (SDOF), are connected with nonlinear hysteretic damper. The stochastic uncertainty in the system parameters is dealt with matrix perturbation theory, using first-order Taylor series expansion. The total probability concept is used to evaluate the unconditional response of the structures under parameter uncertainty; for this, the conditional response and its sensitivities are evaluated in the random vibration framework. The efficiency of the connected building system is demonstrated in terms of substantial reduction of the seismic responses. The efficiency, however, varies drastically in the presence of uncertainty. The disparity among the displacement could be as high as 5–10% with and without considering uncertainty. Neglecting uncertainty underestimates the response for flexible structure, whereas overestimates the response for stiff structure, which might lead to unsafe design for the flexible structure provided that uncertainty is not adequately taken care of. Displacement, acceleration of the flexible building, and acceleration of stiff building show coefficient of variations around 10%, which is remarkably amplified (as high as 50%) in case of the displacement of stiff building. The findings establish the importance of parameter uncertainty on the performance of the connected buildings.

S.K. Mishra (✉) • S. Das
Department of Civil Engineering, Indian Institute of Technology, Kanpur, UP, India
e-mail: smishra@iitk.ac.in; sumantad@iitk.ac.in

S. Chakraborty and G. Bhattacharya (eds.), *Proceedings of the International Symposium on Engineering under Uncertainty: Safety Assessment and Management (ISEUSAM - 2012)*,
DOI 10.1007/978-81-322-0757-3_62,

Keywords Parameter uncertainty • Stochastic response • Connected buildings • Nonlinear hysteretic damper • Random vibration

1 Introduction

Pounding among two adjacent buildings has been observed to cause severe damage during past major earthquakes such as Mexico City (1985), Kobe (1994), and Bhuj (2001) earthquakes. Interconnecting the adjacent buildings with energy dissipating devices emerges to be a viable technology in order to avoid/control such damages. The connecting device not only reduces the probability of pounding but also causes substantial reduction of responses of both buildings. Therefore, seismic response evaluation of interconnected building using damping devices has attracted attention of the researcher community since 1989. Klein et al. [10] first proposed the concept of coupling two tall buildings, which was subsequently been expanded by usage of dissipative links [17, 19], active and semiactive [3, 10] devices for mitigation of wind, and/or earthquake-induced vibration of neighboring buildings. The connecting dampers could be of viscous [2], friction [15], hysteretic [22], visco-elastic [20], fluid [23], or magnetorheological (MR) types [7]. Among all the possible alternatives, the MR damper is one of the most appealing because it can be used in active, semiactive, or passive mode of operation.

The choice of optimal parameters for such damper has been investigated by investigators [8, 25]. The stochastic response has also been studied [12, 20–23] under random seismic motion. The uncertainty in the system parameters (dampers as well as buildings) and their implications on the system responses and optimum design has remained unexplored. The efficiency of a system may be drastically reduced if the connecting damper parameters are off tuned to the vibrating mode it is designed to suppress. Therefore, the control of structures considering uncertain parameters has attracted interests to the vibration control community [13, 14]. In this study, the stochastic response of the adjacent buildings connected with MR damper is assessed, considering the stochastic uncertainties in the system parameters along with the random earthquake itself.

2 Stochastic Response of Buildings Connected with MR Damper

The simplified mechanical model used for representing the system of connected buildings is shown in Fig. 1. The model consists of the two buildings (one is relatively stiff and the other is flexible) modeled as single degree of freedom (SDOF) system, connected with MR damper. The governing equations of motion of the building system are written as

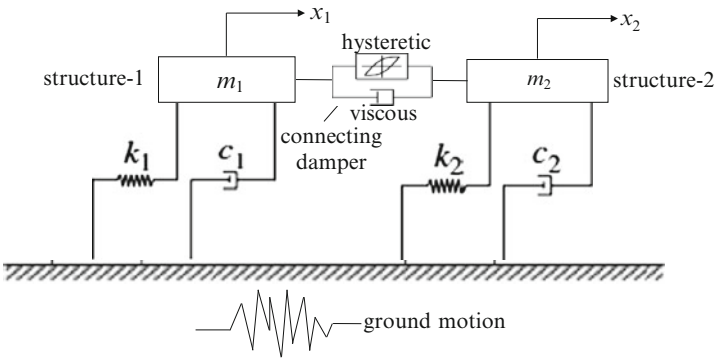

Fig. 1 Buildings modeled as single degree of freedom (SDOF) system connected with magnetorheological (MR) damper

$$\begin{bmatrix} m_1 & 0 \\ 0 & m_2 \end{bmatrix} \begin{Bmatrix} \ddot{x}_1 \\ \ddot{x}_2 \end{Bmatrix} + \begin{bmatrix} c_1 & 0 \\ 0 & c_2 \end{bmatrix} \begin{Bmatrix} \dot{x}_1 \\ \dot{x}_2 \end{Bmatrix} + \begin{bmatrix} k_1 & 0 \\ 0 & k_2 \end{bmatrix} \begin{Bmatrix} x_1 \\ x_2 \end{Bmatrix} + \begin{Bmatrix} f_d \\ -f_d \end{Bmatrix} = - \begin{bmatrix} m_1 & 0 \\ 0 & m_2 \end{bmatrix} \begin{Bmatrix} 1 \\ 1 \end{Bmatrix} \ddot{u}_g \tag{1}$$

where m_1, m_2 are the masses, k_1, k_2 are the stiffness, and c_1, c_2 are damping for the first and second building, respectively. f_d is the damping force exerted on the buildings by the damper connecting the two. $\ddot{x}_1$ and $\ddot{x}_2$, $\dot{x}_1$ and $\dot{x}_2$, and x_1 and x_2 are the acceleration, velocity, and displacement of the first and second building, respectively. $\ddot{u}_g$ is the seismic ground acceleration. The augmented equation of motion for the two buildings is written as

$$[M]\{\ddot{u}\} + [C]\{\dot{u}\} + [K]\{u\} + \{F_d\} = -[M]\{1\}\ddot{u}_g \tag{2}$$

where $\{\ddot{u}\} = [\ddot{x}_1 \quad \ddot{x}_2]^{\mathrm{T}}$, $\{\dot{u}\} = [\dot{x}_1 \quad \dot{x}_2]^{\mathrm{T}}$, and $\{u\} = [x_1 \quad x_2]^{\mathrm{T}}$. $\{F_d\}$ is a vector representing the forces from the dampers installed between the buildings, expressed as

$$\{F_d\} = \begin{Bmatrix} f_d \\ -f_d \end{Bmatrix} \tag{3}$$

The elements of the damper force vector are written as

$$f_d = -f_d = c_d(\dot{x}_1 - \dot{x}_2) + \alpha Z \tag{4}$$

where c_d is the viscous part of the damping of the connecting damper and $(\dot{x}_1 - \dot{x}_2)$ is the relative velocity of the buildings between which the damper is connected. α is

the coefficient of hysteretic damping, and Z is the hysteretic component of response of the damper. Combining Eqs. (3) and (4), the damper force vector is written as

$$\begin{Bmatrix} f_d \\ -f_d \end{Bmatrix} = \begin{bmatrix} c_d & -c_d \\ -c_d & c_d \end{bmatrix} \begin{Bmatrix} \dot{x}_1 \\ \dot{x}_2 \end{Bmatrix} + \begin{Bmatrix} -\alpha \\ \alpha \end{Bmatrix} Z \tag{5}$$

In Eq. (5), the linear viscous and nonlinear hysteretic part of the damping force can separately be denoted as $\{F_L\}$ and $\{F_H\}$, respectively, i.e.,

$$\{F_L\} = [C_L]\{u\} \tag{6}$$

$$\{F_H\} = \{C_H\}Z \tag{7}$$

Thus, Eq. (3) is rewritten as

$$\{F_d\} = [C_L]\{\dot{u}\} + \{C_H\}Z \tag{8}$$

With this, the equation of motion of the connected systems can be expressed as

$$[M]\{\ddot{u}\} + [C]\{\dot{u}\} + [K]\{u\} + [C_L]\{\dot{u}\} + \{C_H\}Z = -[M]\{1\}\ddot{u}_g \tag{9}$$

2.1 Evaluation of Hysteretic Response of the Damper

The response of the hysteretic part of the damper (Z) needs to be evaluated to solve Eq. (9). Presently, the Bouc-Wen model of hysteresis is employed to model the force-deformation characteristics of such damper [21, 22], written as

$$\dot{Z} + \gamma|\dot{x}_1 - \dot{x}_2|Z|Z|^{n-1} + \beta(\dot{x}_1 - \dot{x}_2)|Z|^n - A_d(\dot{x}_1 - \dot{x}_2) = 0 \tag{10}$$

where the parameters γ, β, and A_d are the model parameters determining the shape of the hysteresis loop and n controls the smoothness of the transition from the preyield to the postyield region. The coefficients characterizing the applied force (Eqs. 4 and 5) exerted by the MR damper are expressed in terms of the command voltage (V) as

$$\begin{aligned} \alpha &= \alpha_a + \alpha_b V \\ c_d &= c_a + c_b V \end{aligned} \tag{11}$$

The general nonlinear hysteretic form of Eq. (10) is not directly amenable for use in random vibration analysis. Stochastic linearization [1] is conventionally adopted in order to estimate stochastically equivalent linear system, expressed as

$$\dot{Z} + C_{eq}(\dot{x}_1 - \dot{x}_2) + K_{eq}Z = 0 \tag{12}$$

where C_{eq} and K_{eq} are the stochastically equivalent linear damping and stiffness. The equivalent parameters are obtained through least squares error minimization, given by

$$\begin{aligned} C_{eq} &= \sqrt{\frac{2}{\pi}}\left[\gamma \frac{E(\dot{x}_1 Z) - E(\dot{x}_2 Z)}{\sqrt{\sigma_{\dot{x}_1}^2 + \sigma_{\dot{x}_2}^2 - 2\sigma_{\dot{x}_1}\sigma_{\dot{x}_2}}} + \beta\sigma_Z\right] - A_d \\ K_{eq} &= \sqrt{\frac{2}{\pi}}\left[\gamma\sqrt{\sigma_{\dot{x}_1}^2 + \sigma_{\dot{x}_2}^2 - 2\sigma_{\dot{x}_1}\sigma_{\dot{x}_2}} + \beta\frac{E(\dot{x}_1 Z) - E(\dot{x}_2 Z)}{\sigma_Z}\right] \end{aligned} \tag{13}$$

where $\sigma_{\dot{x}_1}$ and $\sigma_{\dot{x}_2}$ are the rms of $\dot{x}_1, \dot{x}_2$, respectively, (i.e., velocities of the buildings). With the strength of Eq. (12), the equation of motion of the connecting damper is written as

$$\dot{Z} + \left[C_{eq}\right]\{\dot{u}\} + K_{eq}Z = 0 \tag{14}$$

All the terms in this equation have been defined. Equivalent stiffness and damping terms are calculated from Eq. (13). $\left[C_{eq}\right]$ is the damping matrix written as

$$\left[C_{eq}\right] = \begin{bmatrix} c_d & -c_d \end{bmatrix} \tag{15}$$

The structure of the matrix $\left[C_{eq}\right]$ is justified from Eqs. (12 and 14).

Stochastic model for earthquake loading is utilized. A widely adopted model in stationary case for $\ddot{x}_g$ is obtained by filtering a white noise process acting at a bedrock through a linear filter representing the ground, known as Kanai-Tajimi model [9]. The filter equations can be expressed as

$$\ddot{x}_g = \ddot{x}_f + \ddot{w} \tag{16a}$$

$$\ddot{x}_f + 2\xi_g\omega_g\dot{x}_f + \omega_g^2 x_f = -\ddot{w} \tag{16b}$$

Combining (16b) in Eq. (16a),

$$\ddot{x}_g = -2\xi_g\omega_g\dot{x}_f - \omega_g^2 \mathrm{x}_f \tag{17}$$

where $\ddot{w}$ is the white noise intensity at the bedrock with PSD S_0, ω_g, and ξ_g as the frequency and damping parameters representing the ground soil strata over the bedrock and underlying the building. $\ddot{x}_f$, $\dot{x}_f$, and x_f are the response of the linear Kanai-Tajimi filter.

With the system of equations obtained for the connected structure, the damper, and the stochastic model of ground motion, the system of equation for the whole system can be written as

$$[M]\{\ddot{u}\} + [C]\{\dot{u}\} + [K]\{u\} + [C_L]\{\dot{u}\} + \{C_H\}Z = [M]\{1\}\left(2\xi_f\omega_f\dot{x}_f + \omega_f^2 x_f\right) \tag{18}$$

The equations for the connecting damper are

$$\dot{Z} + \left[C_{eq}\right]\{\dot{u}\} + K_{eq}Z = \{0\} \tag{19}$$

and the equation governing the ground filter subjected to white noise motion at the bedrock is written as

$$\ddot{x}_f + 2\xi_f\omega_f\dot{x}_f + \omega_f^2 x_f = -\ddot{w} \tag{20}$$

These three sets of Eqs. [18] are collectively written in the state space form. This is done by writing the equations in terms of the state vector as

$$\{\ddot{u}\} = -[M]^{-1}[C]\{\dot{u}\} - [M]^{-1}[K]\{u\} - [M]^{-1}[C_L]\{\dot{u}\} - [M]^{-1}\{C_H\}Z + \{1\}\left(2\xi_f\omega_f\dot{x}_f + \omega_f^2 x_f\right) \tag{21}$$

$$\dot{Z} = -\left[C_{eq}\right]\{\dot{u}\} - K_{eq}Z \tag{22}$$

$$\ddot{x}_f = -2\xi_f\omega_f\dot{x}_f - \omega_f^2 x_f - \ddot{w} \tag{23}$$

The state vector for the present system is defined as $\{Y\} = [\,\{u\} \quad Z \quad x_f \quad \{\dot{u}\} \quad \dot{x}_f\,]^{\mathrm{T}}$. With this state vector, the augmented equation for the system can be written in the form

$$\frac{d}{dt}\{Y\} = [A]\{Y\} + \{W\} \tag{24}$$

where $[A]$ is the state space matrix obtained from the sets of equations. $\{W\}$ has all the terms zeros except the last row as S_0, i.e.,

$$\{W\} = [\,\{0\} \quad 0 \quad 0 \quad \{0\} \quad -S_0\,]^{\mathrm{T}}. \tag{25}$$

S_0 quantifies the intensity of the bedrock white noise.

The response of the system can be evaluated by solving Eq. (24) using numerical technique such as Runge-Kutta method. In the stochastic dynamic analysis, rather

than the response, the statistics of responses such as response covariance is evaluated. It can be shown that the covariance matrix $[C_{YY}]$ of the stochastic response state vector $\{Y\}$ (assumed as Markovian) evolves following an equation of the form [25]

$$\frac{d}{dt}[C_{YY}] = [A][C_{YY}]^T + [C_{YY}][A]^T + [S_{ww}] \tag{26}$$

$[S_{ww}]$ is matrix of the bedrock white noise intensity. The equation for response statistics of its derivative process (such as acceleration$\{u\}$) is obtained as

$$\left[C_{\dot{Y}\dot{Y}}\right] = [A][C_{YY}][A]^T + [S_{ww}] \tag{27}$$

2.2 Evaluation of Stochastic Sensitivity and the Unconditional Responses

The stochastic response of connected building system under random earthquakes is obtained by solving Eqs. (24) and (25). Such responses are conditioned on the fact that the system parameters are deterministic [6]. To include parametric uncertainties, the sensitivities of the stochastic responses with respect to uncertain parameters are essential. The random variability is reasonably assigned to the random parameters of the damper, the structures, and the load denoted as

$$\{\theta\} = \begin{bmatrix} k & c & c_d & \alpha & \xi_g & \omega_g & S_0 \end{bmatrix} \tag{28}$$

where $\{\theta\}$ is the vector of random design parameters and k is the stiffness of the second building (stiff). The stiffness of the first building (flexible) is set to be $k_1 = k/f^2$ to obtain the ratio of time periods (T_1, T_2) of the two buildings related as

$$T_1 = fT_2 \tag{29}$$

In all cases, the mass of both buildings is assumed to be identical, i.e., $m_1 = m_2 = m$. First-order sensitivity of the basic state space Eq. (24) with respect to the ith parameter θ_i is written as

$$\frac{d}{dt}\left[\frac{\partial C_{YY}}{\partial \theta_i}\right] = [A]\left[\frac{\partial C_{YY}}{\partial \theta_i}\right]^T + \left[\frac{\partial C_{YY}}{\partial \theta_i}\right][A]^T + [B] \tag{30}$$

where $\partial C_{YY}/\partial \theta_i$ is the sensitivity of the response covariance (C_{YY}) with respect to the parameter θ_i and $[B]$ is given by

$$[\mathrm{B}] = \left[\frac{\partial \mathrm{A}}{\partial \theta_i}\right][\mathrm{C_{YY}}]^{\mathrm{T}} + [\mathrm{C_{YY}}]\left[\frac{\partial \mathrm{A}}{\partial \theta_i}\right]^{\mathrm{T}} + \left[\frac{\partial \mathrm{S_{ww}}}{\partial \theta_i}\right]. \tag{31}$$

It is noted that Eq. (30) has the same form as that of (26) and can be solved similarly. The sensitivity of the time derivative process (e.g., acceleration) is obtained similarly as in Eq. (25), i.e.,

$$\left[\frac{\partial \mathrm{C_{\dot{Y}Y}}}{\partial \theta}\right] = [\mathrm{A}]\left[\frac{\partial \mathrm{C_{YY}}}{\partial \theta}\right][\mathrm{A}]^{\mathrm{T}} + [\mathrm{B_1}], \tag{32a}$$

where

$$[\mathrm{B_1}] = [\mathrm{A}][\mathrm{C_{YY}}]\left[\frac{\partial \mathrm{A}}{\partial \theta_i}\right]^{\mathrm{T}} + \left[\frac{\partial \mathrm{A}}{\partial \theta_i}\right][\mathrm{C_{YY}}][\mathrm{A}]^{\mathrm{T}} + \left[\frac{\partial \mathrm{S_{ww}}}{\partial \theta_i}\right]. \tag{32b}$$

The second-order sensitivity is obtained by further differentiating Eq. (30) with respect to the parameter θ_j and rearranging the terms. The sensitivities of the rms responses are then obtained by appropriately differentiating the rms response with respect to the ith random parameter as

$$\begin{aligned}
\frac{\partial \sigma_{\mathrm{Y_m}}}{\partial \theta_i} &= \frac{1}{2}\frac{1}{\sqrt{\mathrm{C_{Y_mY_m}}}}\frac{\partial \mathrm{C_{Y_mY_m}}}{\partial \theta_i} \\
\frac{\partial^2 \sigma_{\mathrm{Y_m}}}{\partial \theta_i \partial \theta_j} &= \frac{1}{2}\frac{1}{\sqrt{\mathrm{C_{Y_mY_m}}}}\left[\frac{\partial^2 \mathrm{C_{Y_mY_m}}}{\partial \theta_i \partial \theta_j} - \frac{1}{2}\frac{1}{\mathrm{C_{Y_mY_m}}}\left(\frac{\partial \mathrm{C_{Y_mY_m}}}{\partial \theta_i}\right)^2\right]
\end{aligned} \tag{33}$$

In the above, $\mathrm{Y_m}$ is the response and $\sigma_{\mathrm{Y_m}}$ is the rms response of the quantity$\mathrm{Y_m}$. $\partial \sigma_{\mathrm{Y_m}}/\partial \theta_i$ and $\partial^2 \sigma_{\mathrm{Y_m}}/\partial \theta_i \partial \theta_j$ are, respectively, the first- and second-order sensitivity terms with respect to the parameters θ_i and θ_j.

2.3 *Parameter Uncertainty and Unconditional Stochastic Response*

The random system parameter (θ_i) can be viewed as the superposition of the deterministic mean component $(\bar{\theta}_i)$ with a zero mean deviatoric component $(\Delta\theta_i)$. The Taylor series expansion of the rms response at the mean value of the random parameters can be written as

$$\sigma_{\mathrm{Y_m}} = \sigma_{\mathrm{Y_m}}(\bar{\theta}_i) + \sum_{i=1}^{nv}\frac{\partial \sigma_{\mathrm{Y_m}}}{\partial \theta_i}\Delta\theta_i + \frac{1}{2}\sum_{i=1}^{nv}\sum_{j=1}^{nv}\frac{\partial^2 \sigma_{\mathrm{Y_m}}}{\partial \theta_i \partial \theta_j}\Delta\theta_i \Delta\theta_j, \tag{34}$$

where nv is the total number of random variables involved in the problem and the derivative of the respective response quantities is the sensitivity terms addressed in the previous section. Assuming that the uncertain random variables are uncorrelated, the quadratic approximation provides the expected value of the unconditional rms response as

$$\sigma_{\mathrm{Y_m}} = \sigma_{\mathrm{Y_m}}\left(\bar{\theta}_i\right) + \frac{1}{2}\sum_{i=1}^{nv} \frac{\partial^2 C_{\mathrm{Y_m Y_m}}}{\partial \theta_i^2}\sigma_{\theta_i}^2 \tag{35}$$

where σ_{θ_i} is the standard deviation of the ith random parameter. The linear approximation of the Taylor series expansion furnishes the variance of the rms response:

$$\mathrm{var}[\sigma_{\mathrm{Y_m}}] = \sigma_{\sigma_{\mathrm{Y_m}}}^2 = \sum_{i=1}^{nv}\left(\frac{\partial \sigma_{\mathrm{Y_m}}}{\partial \theta_i}\right)^2 \sigma_{\theta_i}^2 \tag{36}$$

Such response quantities are referred as "unconditional" (36) because the condition that the structural parameters are deterministic has been relaxed while estimating such responses.

3 Numerical Results

The performances of the connected buildings are demonstrated with numerical illustrations. The simple model of the connected building (shown in Fig. 1) is adopted for this purpose. In spite of its simplicity, the model includes the salient features of such systems. Stiffness of 7,900 kN/m and mass of 800,000 kg are assigned to the stiff building. The factor f is set to be 2 unless specified. Therefore, the flexible building has same mass but storey stiffness ¼th of the stiff building. This is to achieve a time period ratio of two. Viscous damping of the individual building is taken as 2% of the critical. The parameters characterizing the connecting damper are adopted from [19]. The soil parameters, such as the characteristic frequency is $\omega_g = 5\pi$ rad/s and the damping is $\xi_g = 60\%$. The coefficient of variations (CoVs) in the individual random parameter is varied from 5 to 15%. These parameters are assumed to follow the normal distribution and are statistically independent.

The efficiency of the connecting damper is illustrated in terms of the reduction of response of the individual structures (flexible and stiff). The displacement reduction is more for flexible building (63%), whereas the acceleration reduction is more for stiff building (24%) for the range of parameters adopted herein. The sensitivities w.r.t the stiffness and nonlinear hysteretic damping are more (2%) comparing to that observed in flexible building (0.75%). The striking feature is the markedly enhanced sensitivity of the stiff building displacement w.r.t the intensity of earthquakes (8%), which even suppress the sensitivity w.r.t the stiffness and

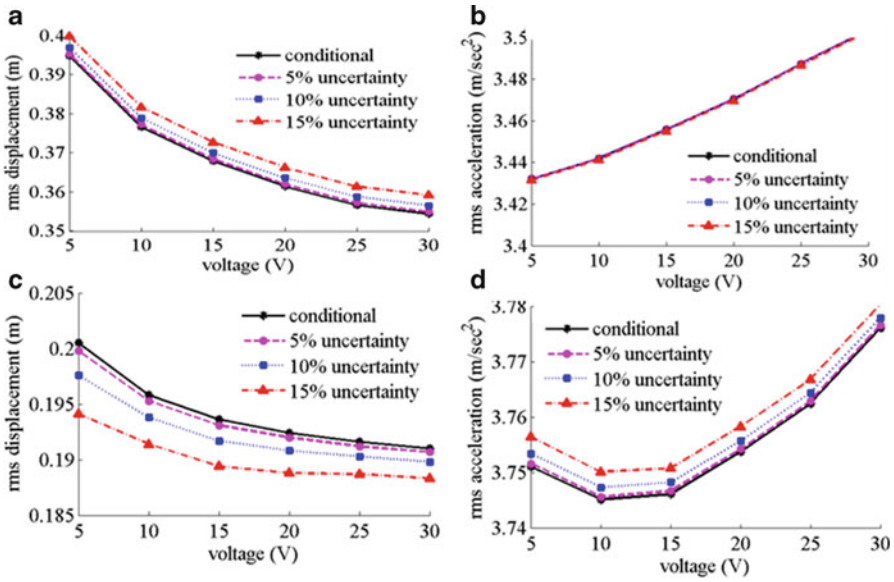

Fig. 2 Conditional and unconditional rms (**a**) displacement and (**b**) acceleration of the flexible and (**c**) displacement and (**d**) acceleration of the stiff structure with varied command voltage under parameter uncertainty

nonlinear damper mentioned earlier (around 2%). This might be due to the fact that for connected system, the stiff building is expected to share larger portion of the total inertial forces which the connected system is subjected to as a whole.

Figure 2a shows that increasing command voltage decreases the displacement monotonically, whereas increases the acceleration (Fig. 2b). The decrease in the rms displacement is larger comparing the minimal increase in acceleration. Further, the rms acceleration of the stiff building does not vary monotonically with voltage; rather there is some "optimal" value for which the rms acceleration is minimum (Fig. 2d).

The effect of parameter uncertainty is prominent for the displacement (Fig. 2a) and reduces substantially for acceleration (Fig. 2b). Further, the effects of uncertainty are more in the stiff buildings comparing the flexible one (Fig. 2a, b, c and d). The second-order sensitivity of the acceleration response w.r.t the earthquake intensity and characteristic ground frequency is of opposite sign (observed but not shown herein). Thus, the effects get nullified for both buildings.

The displacement is more sensitive to parameter uncertainty in both, though substantially larger for stiff buildings. It is noteworthy that system stochasticity increases (1%) the response in flexible structure (unconditional $>$ conditional) but decreases the responses (unconditional $<$ conditional) in stiff (3%). This conforms to the trend of second-order sensitivity of displacement w.r.t the seismic intensity, which is much higher and negative. This causes the unconditional displacement to be lesser than the conditional (Fig. 2c). For the flexible building, the second-order sensitivity of

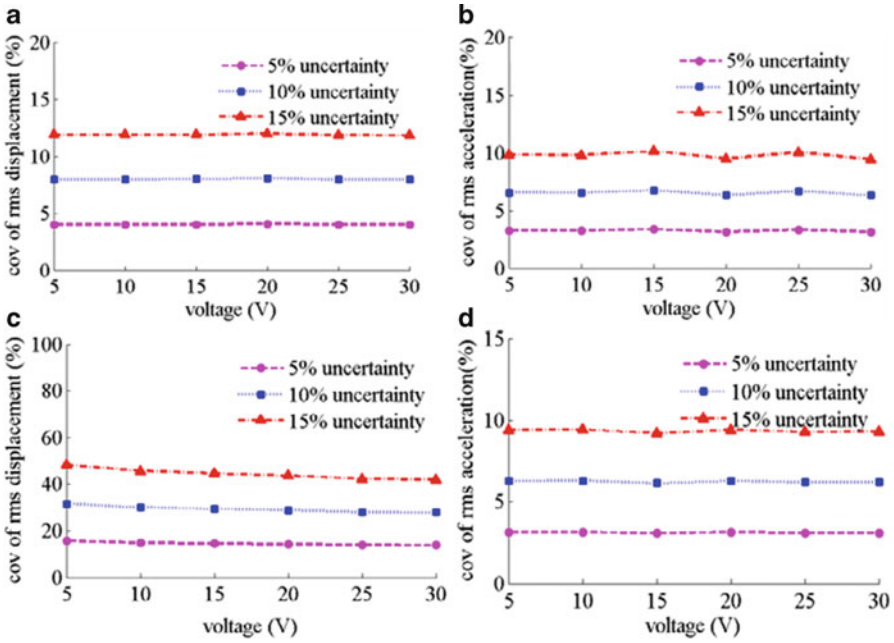

Fig. 3 CoV of the unconditional rms (**a**) displacement and (**b**) acceleration responses of the flexible structure and (**c**) displacement and (**d**) acceleration responses of the stiff structure with varied command voltage under parameter uncertainty

displacement w.r.t the dominant variables (stiffness and nonlinear damping) is positive and hence adds to the displacement response (Fig. 2a). The disparity among the conditional and unconditional response decreases with increasing command voltage in stiff building (Fig. 2c), whereas remains uniform in flexible building (Fig. 2a).

The CoVs of the unconditional responses are shown in Fig. 3a, b, c and d. Following the trend observed previously, the figure shows that, for flexible building, the CoV is slightly higher for displacement (12%) than the acceleration (10%). However, the CoV associated with the displacement of stiff building is substantially larger (50%) comparing the ranges of CoV observed in other response quantities of both stiff and flexible buildings (8–10%). This large CoV of displacement of stiff building is compatible to the sensitivity, which shows much higher sensitivity (first order) of displacement w.r.t the seismic intensity. In all cases, however, the CoV is insensitive to the variation in the command voltage.

Preceding discussion establishes the fact that the displacement and acceleration responses reasonably vary with parameter uncertainty, especially the displacement response of stiff building. Neglecting uncertainty might underestimate some response quantities of interest and thus leads to an unsafe design. More results will be discussed during presentation.

4 Conclusions

The performance of the connected building is evaluated in the presence of random seismic motion considering the stochasticity in the system parameters. It is observed that the connected building system is efficient in reducing the seismic response substantially. The efficiency, though, varies drastically in the presence of uncertainty in the system parameters. The disparity among the displacement response, considering deterministic and stochastic system parameters, could be as much as 5–10% for stiff structure especially under large intensity of earthquake. This disparity, though reduces for other response quantities depending on the type of building (stiff or flexible), cannot be ignored. Neglecting uncertainty underestimates the response for flexible structure, whereas overestimates the response for stiff structure. This might lead to unsafe design in flexible structure if uncertainty is not adequately taken care of. Both displacement and acceleration of the flexible building and acceleration of stiff building show coefficient of variations of around 10% for maximum of 15% coefficient of variation adopted in the system parameters. The stiff building, however, shows a markedly amplified effect of system uncertainty in terms of its coefficient of variations of the unconditional displacement, which is shown to be as much as 50%. These findings establish the fact that performance of the connected building system can be affected drastically in the presence of uncertainty and safety of the system can be severely violated provided system uncertainty is overruled by the conventional assumption of deterministic system.

References

1. Atalik TS, Utku S (1976) Stochastic linearization of multi-degree-of-freedom non-linear systems. Earthq Eng Struct Dyn 4(3):411–420
2. Bhaskararao AV, Jangid RS (2006) Optimum viscous damper for connecting adjacent SDOF structures for harmonic and stationary white-noise random excitations. Earthq Eng Struct Dyn 36:563–571
3. Spencer BF, Dyke SJ, Sain MK (1997) Carlson, phenomenological model of magnetorheological damper. J Eng Mech, ASCE 123(3):230–238
4. Crandall S, Mark W (1963) Random vibration in mechanical systems. Academic, New York
5. Jansen LM, Dyke SJ (2000) Semi active control strategies for MR dampers: a comparative study, ASCE J Eng Mech 126(8):795–803
6. Jensen HA (2005) Design and sensitivity analysis of dynamical systems subjected to stochastic loading. Comp Struct 83:1062–1075
7. Kageyama M, Yoshida O, Yasui Y. A study on optimum damping systems for connected double frame structures. In: Proceedings of the first world conference on structural control, Los Angeles, vol 1, pp 32–39
8. Kamagata K, Miyajima K, Seto K (1996) Optimal design of damping devices for vibration control of parallel structures. In: Proceedings of the 3rd international conference on motion and vibration control (MOVIC), vol 2, pp 334–339

9. Kanai K (1957) Semi-empirical formula for the seismic characteristics of the ground. Bull Earthq Res Inst Univ Tokyo 35:309–325
10. Klein RE, Cusano C, Stuke J (1972) Investigation of a method to stabilize wind induced oscillations in large structures. In: Proceedings of ASME winter annual meeting, paper no. 72-WA/AUT-H
11. Klein RE, Healy MD (1987) Semi-Active control of wind induced oscillations. In: Proceedings of 2nd international conference on structural control. Martinus Nijhoff Publishers, Dordrecht, pp 354–369
12. Luco JE, De Barros FCP (1998) Optimal damping between two adjacent elastic structures. Earthq Eng Struct Dyn 7(7):649–659
13. Marano GC, Greco R, Sgobba SA (2010) A comparison between different robust optimum design approaches: application to tuned mass dampers. Probab Eng Mech 25:108–118
14. Marano GC, Sgobba S, Greco R, Mezzina M (2008) Robust optimum design of tuned mass dampers device in random vibrations mitigation. J Sound Vib 313:472–492
15. Ni YQ, Ko JM, Ying ZG (2001) Random response analysis of adjacent buildings coupled with nonlinear hysteretic dampers. J Sound Vib 246(3):403–417
16. Ok Seung Yong, Junho Song, Kwan-Soon Park (2008) Optimal design of hysteretic dampers connecting adjacent structures using multi-objective genetic algorithm and stochastic linearization method. Eng Struct 30:1240–1249
17. Seto K (1994) Vibration control method for flexible structures arranged in parallel. In: Proceedings of first world conference on structural control, Los Angeles, CA, vol 3, pp 62–71
18. Taflanidis AA, Beck JL, Angelides DC (2007) Robust reliability based design of liquid column mass dampers under earthquake excitation using an analytical reliability approximation. Eng Struct 29:3525–3537
19. Westermon B (1989) The dynamics of interstructural connection to prevent pounding. Earthq Eng Struct Dyn 18:687–699
20. Xu YL, He Q, Ko JM (1999) Dynamic response of damper connected adjacent buildings under earthquake excitation. Eng Struct 21(2):135–148
21. Yang Z, Xu YL, Lu XL (2003) Experimental seismic study of adjacent buildings coupled with fluid dampers. J Struct Eng ASCE 129(2):197, 205
22. Zhang WS, Xu YL (1999) Dynamic characteristics and seismic response of adjacent buildings linked by discrete dampers. Earthq Eng Struct Dyn 28(10):1163–1185
23. Zhang WS, Xu YL (2000) Vibration analysis of two buildings linked by Maxwell model-defined fluid dampers. J Sound Vib 233(5):775–796
24. Zhang Y, Web B, Liu Q (1998) First passage of uncertain single degree of freedom nonlinear oscillations. Comput Meth Appl Mech Eng 165:223–231
25. Zhu HP, Xu YL (2005) Optimum parameters of Maxwell model-defined dampers used to link adjacent structures. J Sound Vib 279:253–574

Recent Development in Modeling, Analysis, and Design of Foundation Systems Subjected to Blast Loading Considering Uncertainties

Ranjan Kumar, Deepankar Choudhury, and Kapilesh Bhargava

Abstract Traditional design approaches simplify the problem by considering the uncertain parameters to be deterministic, and they use lumped factors of safety (empirical, based on past experience) to account for the uncertainties propagating in the design decisions. To evaluate response of foundation to blast loads, there are uncertainties involved in loading conditions, inherent spatial variability of soil properties, presence of geologic anomaly, uncertainty associated with selection of an appropriate analytical model, testing and measurements errors, and human errors. These have necessitated reliability analysis in addition to conventional analysis. As far as possible, uncertainties should be avoided, and if those are unavoidable, then those should be eliminated, and if elimination is not possible, those should be adapted in planning, design, and usage of foundation throughout its life. Unavailability of a large set of sample data and mathematical sophistication for carrying out uncertainty analysis are areas of concern.

This chapter presents sources of uncertainties in foundation design parameters, descriptors of randomness, analytical models for random variables, determination of probability distributions, randomness in response variables, and influence of spatial variation of soil mass on design. Recent development in modeling, analysis, and design of foundation systems subjected to blast loading considering uncertainties has been discussed.

Keywords Foundation • Blast loading • Uncertainties • Reliability analysis • Inherent soil variability

R. Kumar (✉) • K. Bhargava
Architecture and Civil Engineering Division, Bhabha Atomic Research Centre, Trombay, Mumbai 400 085, India
e-mail: ranjancv42@gmail.com; kapil_66@barc.gov.in

D. Choudhury
Department of Civil Engineering, Indian Institute of Technology Bombay, Mumbai, India
e-mail: dc@civil.iitb.ac.in

S. Chakraborty and G. Bhattacharya (eds.), *Proceedings of the International Symposium on Engineering under Uncertainty: Safety Assessment and Management (ISEUSAM - 2012)*,
DOI 10.1007/978-81-322-0757-3_63,

1 Introduction

Design of foundation systems subjected to blast loading basically requires evaluation of resistance of structural members which satisfies the applied load combinations. Most of the parameters related to resistance of members and applied loads are random variables. Identification and quantification of uncertainty need to be done before proceeding further for design process. The aim of design should be such that resistance should be greater than the loads. In deterministic based design, it is ensured that throughout the structure, the induced stresses are less than the allowable stresses when it is subjected to the "working" or service applied load. This approach simplifies the problem by considering the uncertain parameters to be deterministic. Uncertainties are accounted by using factor of safety which is based on past experience and empirical formulae. This method does not give idea on how the different parameters influence the safety. Reliability-based design is done considering individual sources of uncertainties. Quantitative analysis of uncertainty is carried out. Sometimes, unavailability of large set of data and mathematical sophistication demotivate engineers to carry out reliability-based design. But nowadays, various design guidelines and codes have been revised to incorporate reliability-based design.

In reliability analysis, resistance R and load S are considered as random variables that can be described by probability density functions as shown in Fig. 1. R should always be greater than S to have margin of safety.

The steps in a probabilistic study are given by Haldar and Mahadevan [8] as shown in Fig. 2.

Measures of reliability are probability of failure and reliability index.

2 Sources of Uncertainties in Foundation Design Parameters

There are two sources of uncertainties in a system, namely, noncognitive (quantitative) and cognitive (qualitative). Noncognitive (quantitative) source gives three types of variability, namely, inherent variability, statistical variability, and modeling variability. Inherent variability is involved in all physical observations. Even repeated measurements of the same physical quantity do not give the same value. This happens because of complex formation of soil/rock, test procedure, instruments, observers, etc. This type of uncertainty may be minimized by collecting large number of samples. Many a times, limited resources are available to collect large number of samples which causes statistical variability. Actual behavior in many cases is different from predictions. Many idealizations in foundation design parameters are used to simplify the problem like treating soil as homogeneous and isotropic media. Bearing capacity theories are based on the approximate representation of soil behavior. Finite element method or finite difference method for

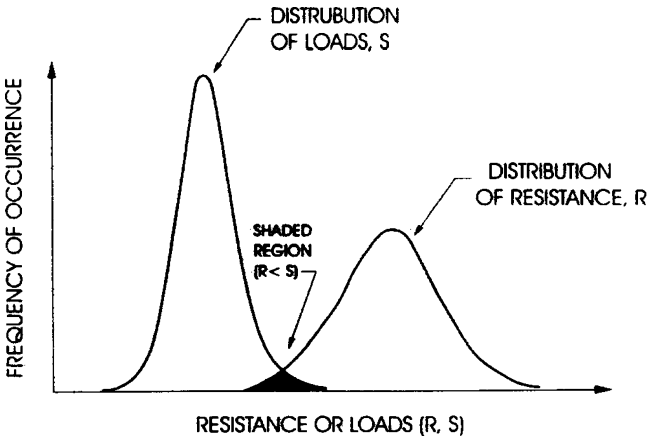

Fig. 1 Variation of load and resistance

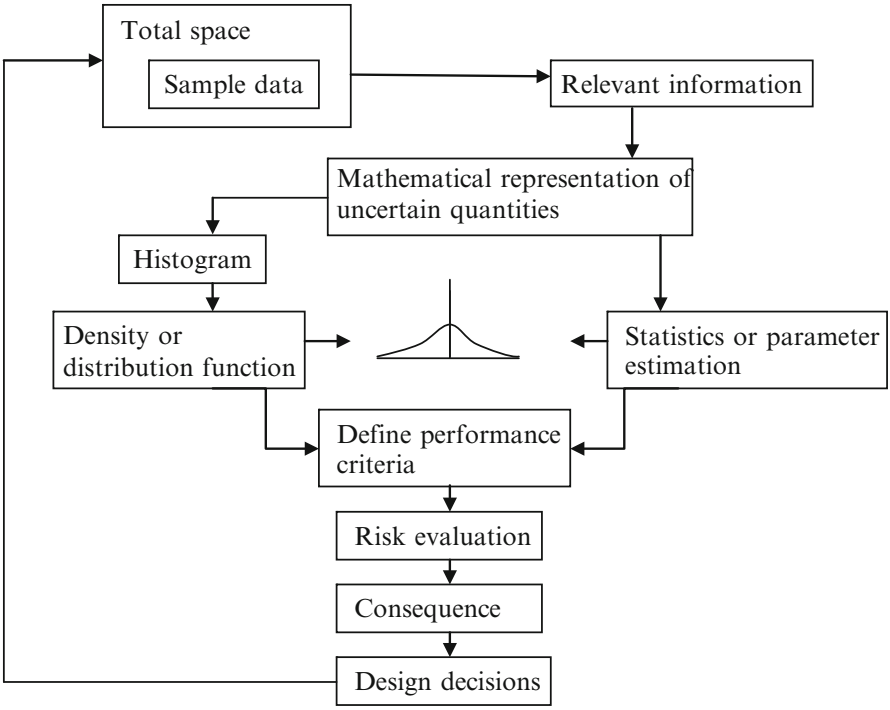

Fig. 2 Steps in a probabilistic study (Modified after Haldar and Mahadevan [8])

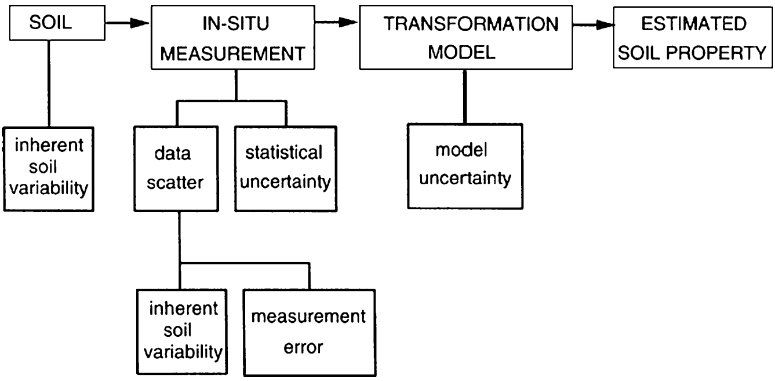

Fig. 3 Source of uncertainty in geotechnical property evaluation (Kulhawy [10])

foundation analysis is also approximate representation of system behavior in which computational prediction and actual behavior do not match exactly. All these kinds of idealizations and approximations cause modeling uncertainty. Cognitive (qualitative) sources are structural performance, quality, skill of workers, other human factors, etc.

Sources of uncertainties in foundation design parameters are loading conditions uncertainty, inherent spatial soil variability, presence of geologic anomaly, modeling uncertainty, testing and measurement errors, and human errors. The flow chart of source of uncertainty in geotechnical property evaluation is shown in Fig. 3 [10].

3 Variability of Soil Parameters

There is a natural variability of soil. Variability in soil properties is caused by errors in field/laboratory testing, statistical errors due to limited sampling. Errors in field testing may arise due to location of drilled holes, number of drilled holes, and method of testing. Errors in laboratory testing may arise due to equipment, instrumentation, collection of disturbed/undisturbed samples, simulating field conditions. Errors are also caused by using simplified transformation models, e.g., Mohr circles, bearing capacity, and settlement. Soil parameters are estimated based on data or results of in situ and laboratory tests. Duncan [6] described four methods to estimate standard deviation of soil parameters. When sufficient data is available, SD is calculated directly from data. When sufficient data is not available, published value of COV is used which when multiplied with mean value gives standard deviation. Published values are rough guide only since conditions of sampling and testing are not specified. Judgment should be used in applying values of COV from published values. Some of the published values are given in Table 1 (modified after [6]). COVs have been reported by Lee et al. [12] as well.

When limited data is available or when no data is available, three-sigma rule is used. When some parameters, e.g., preconsolidation pressure and undrained shear strength, vary with depth, graphical three-sigma rule is used. COV of inherent soil

Table 1 Values of coefficient of variation (COV) for geotechnical properties and in situ tests

Property or in situ test result	Coefficient of variation (COV) (%)	Source
Unit weight (γ)	3–7	Harr [9], Kulhawy [10]
Buoyant unit weight (γ_b)	0–10	Lacasse and Nadim [11], Duncan [6]
Effective stress friction angle (φ')	2–13	Harr [9], Kulhawy [10]
Undrained shear strength	13–40	Harr [9], Kulhawy [10], Lacasse and Nadim (1997), Duncan [6]
Compression index (C_c)	10–37	Harr [9], Kulhawy [10], Duncan [6]
Preconsolidation pressure	10–35	Harr (1984), Lacasse and Nadim [11], Duncan [6]
Coefficient of permeability of saturated clay (k)	68–90	Harr [9], Duncan [6]
Coefficient of permeability of partly saturated clay (k)	130–240	Harr [9], Benson et al. [1]
Coefficient of consolidation (c_v)	33–68	Duncan [6]
Standard penetration test blow count (N)	15–45	Harr [9], Kulhawy [10]
Electric cone penetration test (q_c)	5–15	Kulhawy [10]
Mechanical cone penetration test (q_c)	15–37	Harr [9], Kulhawy [10]

Modified after Duncan [6]

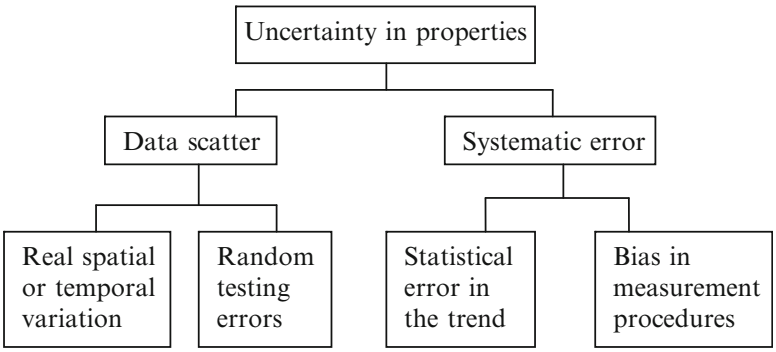

Fig. 4 Uncertainty in soil properties (Christian et al. [4])

variability, scale of fluctuation, and COV of geotechnical measurement errors have been evaluated by Phoon and Kulhawy [15].

Uncertainties in soil parameters have been attributed to data scatter and systematic error by Christian et al. [4] as shown in Fig. 4.

Data scatter consists of real spatial or temporal variation and random testing errors. Random testing errors should be removed before proceeding for further

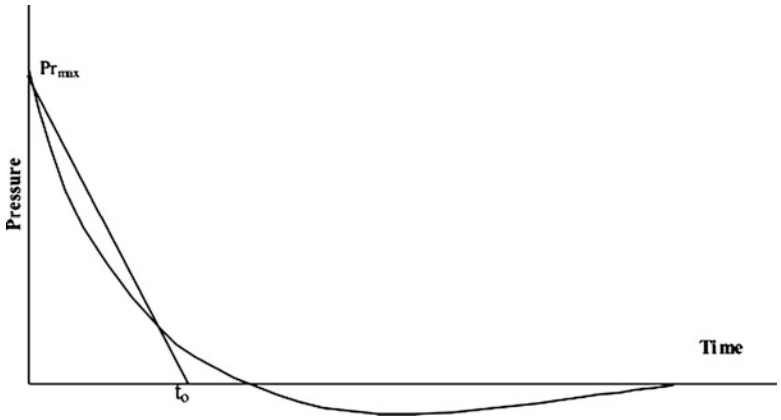

Fig. 5 Blast pressure-time history

analysis. The systematic error is divided into statistical error in the trend and bias in measurement procedures.

4 Variability of Blast Load Parameters

Normally, analysis of foundation is done in deterministic way. But there is variability in foundation dimension, material, and blast loading parameter and after due consideration of variability, probabilistic analysis is done. Reliability of a reinforced concrete slab subjected to blast loading is examined by Low and Hao [12]. Structural slab is simplified into SDOF system, and first- and second-order reliability methods have been utilized.

Blast loading pressure-time history is given in Fig. 5, and negative phase is normally neglected. Sometimes the pressure diagram is approximated into triangular shape. The ground shock at a given location due to blast loading is given by Drake and Little [5] as per the following equations:

$$P(t) = P_o e^{-\alpha t/t_a} \tag{1}$$

$$P_o = f\rho c.160\,(\frac{R}{W^{1/3}})^{-n} \tag{2}$$

$$t_a = \frac{R}{c} \tag{2a}$$

where $P(t)$ is shock stress at time t, P_o is peak stress, t_a = time of arrival of blast at a location, R is distance from the explosion, c is seismic or propagation velocity, and α is time constant.

The time constants generally vary with specific site conditions; however, it can be taken as $\alpha = 1.0$ for most applications [5]. ρc is acoustic impedance (psi fps), R is distance to the explosion (ft), W is charge weight (lb), n is attenuation coefficient, and f is ground coupling factor. Various other empirical formulae are available to predict blast pressure loading. There is large variation in prediction of shock by these formulae due to many uncertainties involved. The value of COV at each scaled distance is not same. An average COV for the entire scaled distance range under consideration is calculated from the COV values at every scaled distance in the range by Low and Hao [13].

A sensitivity analysis of blast loading parameters was performed for calculation of maximum deflection of a clamped aluminum plate subjected to a blast load, and it was concluded that response was most sensitive to loading duration time [2].

5 Descriptors of Randomness

Assume X as a random variable and n observations of X are available. If maximum and minimum value of data is used, it is difficult to obtain optimized solution. The mean or expected value of X measures central tendency of data when sample size is relatively large given by Eq. (3):

$$\text{Mean} = E(X) = \mu_x = \frac{1}{n}\sum_{i=1}^{n} x_i \tag{3}$$

The variance of X is a measure of spread in the data about the mean given by Eq. (4):

$$\text{Variance} = \text{Var}(X) = \frac{1}{n-1}\sum_{i=1}^{n} (x_i - \mu_x)^2 \tag{4}$$

Due to square of random variable, dimensional problem arises which can be avoided by using square root of variance called standard deviation given by Eq. (5):

$$\text{S.D.} = \sigma_x = \sqrt{\text{Var}(X)} = \sqrt{\frac{1}{1-n}\sum_{i=1}^{n} (x_i - \mu_x)^2} \tag{5}$$

Standard deviation alone does not clearly indicate degree of dispersion in the random variable. Ratio of standard deviation and mean is a dimensionless term called coefficient of variation (COV) expressed by Eq. (6):

$$\text{COV}(X) = \delta_x = \frac{\sigma_x}{\mu_x} \tag{6}$$

Deterministic parameter exhibits zero COV. The higher is the COV, the higher will be the dispersion of a random variable about the mean. A COV of 0.1–0.3 is common for a random variable in many engineering problems [8]. Skewness provides symmetry of the data about the mean, and it can be positive or negative. If it is positive, the dispersion is more above the mean than below the mean. Skewness is expressed by Eq. (7):

$$\text{Skewness} = \frac{1}{n}\sum_{i=1}^{n}(x_i - \mu_x)^3 \tag{7}$$

To avoid dimensional problems, skewness coefficient is used as given by Eq. (8):

$$\text{S.C.} = \theta_x = \frac{\text{Skewness}}{\sigma_x^3} \tag{8}$$

A graphical representation of a random variable in the form of a histogram gives more description about a random variable. For development of a histogram, data are arranged in increasing order. Then the data is subdivided into several equal intervals, and number of observations in each interval is counted. Finally, plot of number of observations in each interval versus the random variable is made. The probability of an event is between 0 and 1. Hence, area of the histogram is made equal to unity. The shape of the histogram and frequency diagram is same.

Multiple random variables, e.g., load and resistance effects, need to be considered to estimate the system performance. Both the variables need to be considered separately. However, if both load and resistance components are random variables, the system response will also be a random variable, and it is more meaningful to model the uncertainties jointly, using joint distributions. Also, if there is any dependency of one variable on the other, working with joint distributions is advantageous for obtaining reliable results.

Correlation coefficient (CR) is obtained by dividing covariance with product of standard deviations of individual variables as given in Eq. (9). It is also a measure of linear relationship between the two random variables:

$$\rho_{x,y} = \frac{\text{COV}(X,Y)}{\sigma_x \sigma_y} \tag{9}$$

CR varies from -1 to +1. The higher is its value, the more correlated are the random variables. Random variables are statistically independent if CR ≤ 3 and perfectly correlated if CR ≥ 0.9.

6 Analytical Models for Random Variables

There are two types of random variables, namely, continuous random variable and discreet random variable. A continuous random variable is represented in the text by an uppercase letter (e.g., X), and a particular realization of a random variable is

represented by a lowercase letter (e.g., x). Probability density function (PDF) is represented by $f_X(x)$, and it does not directly provide information on probability but only indicates the nature of randomness. To compute the probability of X having a value between x_1 and x_2, the area under the PDF between these limits needs to be calculated as in Eq. (10):

$$P(x_1 < X \leqslant x_2) = \int_{x_1}^{x_2} f_x(x)dx \tag{10}$$

Cumulative distribution function (CDF) helps to compute the probability of X having a value less than x, i.e., $P\ (X \leq x)$. To calculate this, area under the PDF needs to be integrated for all possible value of X less than or equal to x. The integration needs to be carried out from $-\infty$ to x, and the equation is given as Eq. (11):

$$P(X \leqslant x) = F_X(x) = \int_{-\infty}^{x} f_X(x)dx \tag{11}$$

Equation (10) can be expressed in terms of CDF as Eq. (12):

$$P(x_1 < X \leqslant x_2) = \int_{-\infty}^{x_2} f_X(x) - \int_{-\infty}^{x_1} f_X(x) = F_X(x_2) - F_X(x_1) \tag{12}$$

PDF is the first derivative of CDF and can be expressed by Eq. (13):

$$f_X(x) = \frac{dF_X(x)}{dx} \tag{13}$$

Discreet random variable examples are number of samples, number of earthquakes, number of strong winds, etc. A discreet random variable occurs only at certain discreet points; hence, its relative occurrence is evaluated at these discreet points. This is known as probability mass function denoted as $p_x(x)$. It is not a continuous function, and it consists of a series of spikes. CDF of a discreet random variable can be calculated as summation of PMFs as given in Eq. (14):

$$F_X(x) = P(X \leqslant x) = \sum_{x_i < x} p_X(x_i) \tag{14}$$

Mean, variance, skewness, etc., of the random variable can be calculated from the information of PDF and PMF.

Probability of events can be calculated by using mathematical models. Normal, lognormal, beta distribution, etc., are used for continuous random variables. Binomial, geometric, return period distributions, etc., are used for discreet random variables.

7 Probability Distribution and Random Number Generation

Probability distributions are determined in three ways, namely, by constructing histograms, using probability papers, and using statistical tests based on goodness of results, e.g., chi-square test and K-S test. Chi-square test is based on the error between the observed and assumed PDF of the distribution. K-S test is based on the error between the observed and assumed CDF of the distribution.

Monte Carlo simulation technique is used to estimate the probability of failure of a performance function. This is a simple and straightforward approach based on generation of random numbers. "*N*" random numbers are generated for a variable based on its probabilistic characteristics (mean, standard deviation, and distribution).

8 Recent Developments

After consideration variability in soil parameters, load parameters, and response of foundation, reliability analysis is done in terms of probability of failure or reliability index. There are various methods available in literature for computation of reliability index [8]. Guidelines have been given on target probability of failure and reliability index in geotechnical field [16] as shown in Fig. 6. Minimum reliability index value of 4 indicates good performance of the system.

The effect of model uncertainty for the bearing failure of a spread foundation has been investigated using reliability analyses for various load cases for both drained and undrained conditions [7]. The current status of geotechnical engineering reliability has been presented by Christian [3]. Effects of explosion on structures, mechanism of blast waves, methods to estimate blast loads, and structural response have been presented by Ngo et al. [14]. Organization and evaluation of geotechnical uncertainties have been presented by Whitman [17]. Reliability of shallow foundations subjected to varied inclined loads was evaluated using Monte Carlo simulation [18].

9 Conclusions

With recent increase in threats from terrorism, it is imperative to understand the behavior of foundation under blast loading. Estimation of accurate geotechnical parameters and blast load parameters, e.g., pressure-time profile, explosion size or charge weight, distance from the blast, load duration, and rise time, is needed to evaluate response of foundation. A sensitivity analysis is required to be carried out to find which of the parameter's uncertainty has the greatest effect on the response

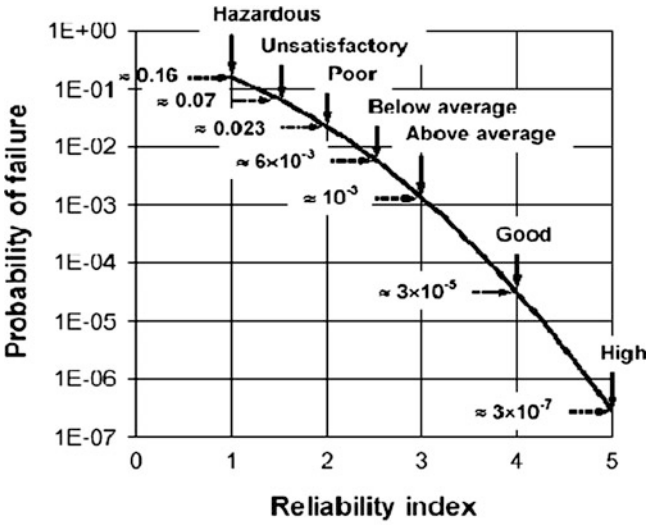

Fig. 6 Guidelines for reliability index (β) and corresponding probability of failure (p_f) (USACE [16])

of the foundation. This analysis would help in determining which parameter must be measured more precisely to get the accurate results.

Reliability analysis considers uncertainties in the parameters involved in the calculations. Standard deviations of various parameters need to be evaluated based on the data. There is degree of uncertainties in the calculation of parameters. Varying degree of uncertainties has been observed for different parameters. For some parameters, it is low, and for some, it is high which needs to be considered in reliability analysis.

References

1. Benson CH, Daniel DE, Boutwell GP (1999) Field performance of compacted clay liners. J Geotech Geoenvir Engrg, ASCE 125(5):390–403
2. Borenstein E, Benaroya H (2009) Sensitivity analysis of blast loading parameters and their trends as uncertainty increases. J Sound Vib 321:762–785
3. Christian JT (2004) Geotechnical engineering reliability: how well do we know what we are doing? J Geotech Geoenviron Eng 130(10):985–1003
4. Christian JT, Ladd CC, Baecher GB (1994) Reliability applied to slope stability analysis. J Geotech Eng 120(12):2180–2207
5. Drake LJ, Little CD Jr (1983) Ground shock from Penetrating Conventional Weapons. U.S. Army Engineer Waterways Experiment Station Vicksburg, Vicksburg, pp 1–6
6. Duncan JM (2000) Factors of safety and reliability in geotechnical engineering. J Geotech Geoenviron Eng ACSE 126(4):307–316

7. Forrest WS, Orr TLL (2011) The effect of model uncertainty on the reliability of spread foundations. In: Proceedings of 3rd International Symposium on Geotechnical Safety and Risk (ISGSR), Munich, Germany, 2–3 June 2011
8. Haldar A, Mahadevan S (2000) Probability, reliability, and statistical methods in engineering design. Wiley, New York
9. Harr ME (1984) Reliability based design in Civil Engineering. Henry M. Shaw Lecture, Dept of Civil Engineering, North Carolina State University, Raleigh, N.C.
10. Kulhawy FH (1992) On evaluation of static soil properties. In: Seed RB, Boulanger RW (eds) Stability and performance of slopes and Embankments II (GSP 31). American Society of Civil Engineers, New York, pp 95–115
11. Lacasse S, Nadim F (1997) Uncertainties in characterizing soil properties. Publ. No. 201, Norwegian Geotechnical Institute, Oslo, Norway, pp 49–75
12. Lee IK, White W, Ingles OG (1983) Geotechnical engineering. Pitman, Boston
13. Low HY, Hao H (2001) Reliability analysis of reinforced concrete slab under explosive loading. Struct Saf 23:157–178
14. Ngo T, Mendis P, Gupta A, Ramsay J (2007) Blast loadings and blast effects on structures – an overview. EJSE Special Issue 7:76–91
15. Phoon K-K, Kulhawy FH (1999) Characterization of geotechnical variability. Can Geotech J 36:612–624
16. USACE (1997) Risk-based analysis in geotechnical engineering for support of planning studies, engineering and design. US Army Corps of Engineers, Department of Army, Washington, DC, p 20314-100
17. Whitman RV (2000) Organizing and evaluating uncertainties in geotechnical engineering. J Geotech Geoenviron Eng 126(6):583–593
18. Xue J, Nag D (2011) Reliability analysis of shallow foundations subjected to varied inclined loads. In: Proceedings of 3rd International Symposium on Geotechnical Safety and Risk (ISGSR), Munich, Germany, 2–3 June 2011

Effect of Bedrock Level on Dynamic Bearing Capacity of Shallow Foundation Under Earthquake Load

Indrajit Chowdhury and Raj Tilak

Abstract Prevailing state of the art in estimating bearing capacity of a foundation under earthquake load is to multiply the static bearing capacity by a factor of 1.25. This practice is in vogue in number of international codes including the IS code for design of such foundations, though it has been shown by Richard et al. (J Geotech Div ASCE 105(GT4):662–674, 1993) that the bearing capacity factors reduce significantly when the ground is subjected to earthquake loads. The analysis is essentially pseudostatic in nature. In this chapter, Budhu and Richards' method has been modified to cater to fluctuating response of the ground due to passage of vertically propagating SV and P waves to estimate the free field time period of the site which in turn is used to estimate the design spectral acceleration (based on modal analysis) that affects the bearing capacity factors N_c, N_q, and N_γ of the foundation. It is shown that bearing capacity factors fluctuate with modes and are also affected profoundly by the bedrock level prevailing at site. Finally, a comparison with static bearing capacity is made with various dynamic parameters that affect the bearing capacity of foundation.

Keywords Dynamic bearing capacity factors • Shear wave velocity • Bedrock • Foundation • Seismic acceleration

1 Introduction

The design bearing capacity (DBC) of a foundation under general shear failure is usually obtained by deriving the ultimate bearing capacity (UBC) of the soil and then dividing the same by an appropriate factor of safety (FOS).

I. Chowdhury (✉) • R. Tilak
Petrofac International Limited, Sharjah, UAE
e-mail: Indrajit.Chowdary@petrofac.com; raj.tilak@petrofac.com

S. Chakraborty and G. Bhattacharya (eds.), *Proceedings of the International Symposium on Engineering under Uncertainty: Safety Assessment and Management (ISEUSAM - 2012)*,
DOI 10.1007/978-81-322-0757-3_64,

The UBC of soil is usually obtained from the plastic equilibrium of the triangular failure wedge that develops below the foundation under superstructure load and from whose equilibrium condition we derive the bearing capacity factors N_c, N_q, and N_γ.

A number of researchers have contributed to this development like Terzaghi [8], Meyerhoff [5], Vesic [9], Prandtl [6], and Hansen [3] to name just only the pioneering few. However, all these developments are restricted to the load on foundation being static in nature and do not provide any guidelines as to how the bearing capacity factors are affected when seismic load acts on it.

In most of the cases, DBC is increased by a factor of 1.25. The basis of this is based on probability of occurrence of a major earthquake on the life span of a structure. Considering the return period of a major earthquake as 1 in 50 years, when the structure is expected to undergo some damage but shall not collapse, an increase in the bearing capacity (vis-à-vis reduction of the FOS) for this particular instance has been an accepted norm over the years, though a number of foundations have failed with almost monotonic regularity in a number of recent major earthquakes (for instance, Bhuj 2001, Sikkim and Turkey 2011). This has rekindled interest among researchers both in academics and industry as to how much is the DBC affected by seismic forces.

Recent research by Richards et al. [7] has pointed out that the state of the art in vogue (i.e., to increase DBC by a factor 1.25) may not be a rational and correct approach, and contrary to the popular belief, the DBC actually reduces under seismic force. However, the method proposed by Richard et al. is pseudostatic in nature and only caters to the effective peak ground acceleration (PGA) that is usually obtained from empirical relationship [2], though it is a well-known fact that the PGA is dynamic in nature and is dependent of the free field time period of the site, the height of soil stratum over the bedrock level, the propagating shear wave velocity, etc.

This chapter is thus an attempt to address the effect of a number of these parameters and arrive at a more rational basis for arriving at the UBC vis-à-vis DBC of a foundation.

The discussion herein is restricted to isolated shallow foundation only. The effect of water table has also been excluded from this presentation.

2 Formulation

Shown in Fig. 1 is an isolated footing resting at a site where the soil is underlain by bedrock at a depth of H from the ground level. The failure wedge below the footing can be represented by Fig. 2, wherein additional seismic forces are introduced.

Considering the soil body in Fig. 1 in plain strain condition, the strain energy of the soil body may be expressed as

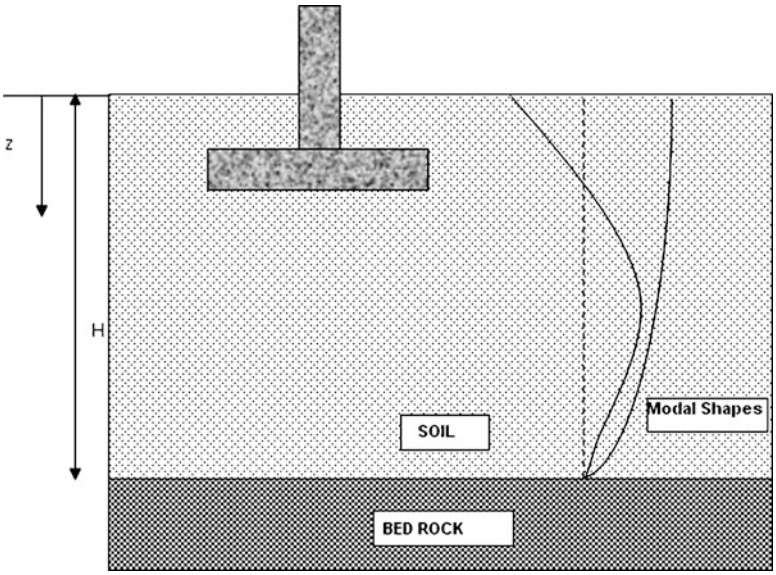

Fig. 1 Schematic diagram for soil underlain by bedrock

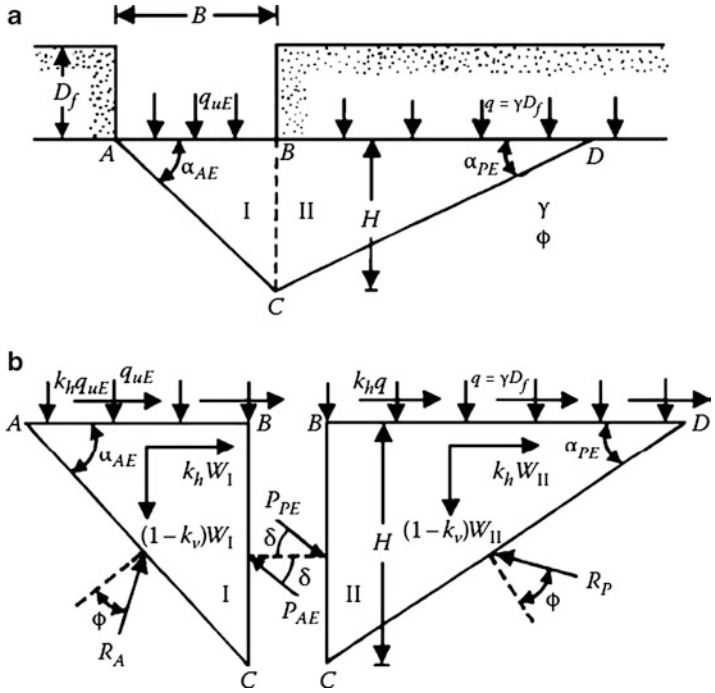

Fig. 2 Bearing capacity of a continuous foundation on sand—earthquake condition

$$U = \frac{Gv}{1-2v}(\varepsilon_x + \varepsilon_z)^2 + G\left({\varepsilon_x}^2 + {\varepsilon_z}^2\right) + \frac{G}{2}\left({\gamma_{xz}}^2\right) \tag{1}$$

Based on Eq. (1), it has been shown by Chowdhury and Dasgupta [1] that the stiffness and mass matrix of the plain strain body may be expressed as

$$[K] = \int_0^H \left[G\left(\frac{\partial \phi_i}{\partial z}\right)\left(\frac{\partial \phi_r}{\partial z}\right)\right].dz \tag{2}$$

$$[M] = \frac{\gamma_s}{g}\int_0^H (\phi_i)(\phi_r)dz \tag{3}$$

where ϕ_i and ϕ_r are shape functions expressed as

$$\phi_i = \phi_r = \cos\frac{(2n-1)\pi z}{2H} \tag{4}$$

where G = dynamic shear modulus of soil, v = Poisson's ratio, γ_s = weight density of soil, g = acceleration due to gravity, H = depth of soil over bedrock, and n = number of modes 1, 2, 3. . ..

For Gibson type of soil where the shear modulus (G_z) of soil varies with depth linearly, the stiffness matrix of the system can be represented by the following:

$$[K] = G\int_0^H \left(1 + \frac{z}{H}\right)\left[\left(\frac{\partial \phi_i}{\partial z}\right)\left(\frac{\partial \phi_r}{\partial z}\right)\right].dz \tag{5}$$

Considering three modes of vibrations, i.e., i = 1–3 and j = 1–3, and solving expression (5), we get the stiffness matrix for the given shear modulus profile (G_z) as

$$[K] = \frac{G}{H}\begin{bmatrix} \frac{3\pi^2}{16} + \frac{1}{4} & -\frac{3}{4} & \frac{5}{36} \\ -\frac{3}{4} & \frac{27\pi^2}{16} + \frac{1}{4} & -\frac{15}{4} \\ \frac{5}{36} & -\frac{15}{4} & \frac{75\pi^2}{16} + \frac{1}{4} \end{bmatrix} \tag{6}$$

Similarly, the mass matrix of the system can be represented by the following matrix, for the 3 modes of vibration:

$$[M] = \frac{\gamma_s H}{g}\begin{bmatrix} \frac{1}{2} & 0 & 0 \\ 0 & \frac{1}{2} & 0 \\ 0 & 0 & \frac{1}{2} \end{bmatrix} \tag{7}$$

Table 1 Modal participation factors for the first three modes

Mode	1	2	3
κ_i(Modal participation factor)	$\frac{8}{2+\pi}$	$\frac{8}{2-3\pi}$	$\frac{8}{2+5\pi}$

Knowing $\lambda = \omega^2$ as the eigenvalues and $T = 2\pi/\omega$ as the time period of vibration, we have

$$\lambda = \frac{V_s}{H}\begin{bmatrix} 4.125 & 0 & 0 \\ 0 & 32.998 & 0 \\ 0 & 0 & 93.965 \end{bmatrix} \tag{8}$$

The free field time period for the three modes are expressed as

$$T = \frac{H}{V_s}\begin{bmatrix} 3.092 \\ 1.094 \\ 0.648 \end{bmatrix} \tag{9}$$

From the obtained time periods, Sa/g values need to be worked out from code. For instance, based on IS 1893 [4] for soft soil, the value of Sa/g is 1 + 15 T for $T < 0.1$ s, Sa/g = 2.5 for $0.1 < t < 0.4$ s, and Sa/g = 1.67/T for $T > 0.4$ s. The factor β is considered as $\beta = ZI/2R$ where Z = zone factor, I = importance factor, and R = response reduction factor. It has been shown by Chowdhury and Dasgupta [1] that R = 2–3 gives a very reasonable value for the soil response.

For various modes, the horizontal coefficient of acceleration k_{hi} and vertical coefficient of acceleration k_{vi} may be written as follows:

$$k_{hi} = \kappa_i \beta \frac{S_{ai}}{g} \tag{10}$$

and

$$k_{vi} = \frac{2}{3} k_{hi} \tag{11}$$

where K_i is the modal mass participation factor and is represented by

$$\kappa_i = \frac{\int_0^H \cos(2n-1)\frac{\pi z}{2H}\,dz}{\int_0^H \cos^2(2n-1)\frac{\pi z}{2H}\,dz} \tag{12}$$

Here, κ_i the modal participation factor for first three modes is calculated and presented in Table 1.

The acceleration factors k_{hi} and k_{vi} change the state of equilibrium as shown in Fig. 2b.

In Fig. 2a, α_{AEi} and α_{PEi} are, respectively, the angles that the Coulomb's failure wedges would make for active and passive conditions, with the difference that suffix *i* has been added to represent various modes, while suffix "*E*" denotes seismic conditions.

Equation for α_{AEi} may be denoted as

$$\alpha_{AEi} = \alpha_i + \tan^{-1}\left[\frac{\sqrt{(1+\tan^2\alpha_i)(1+\tan(\delta+\theta_i)\cot\alpha_i)} - \tan\alpha_i}{1+\tan(\delta+\theta_i)(\tan\alpha_i+\cot\alpha_i)}\right] \tag{13}$$

where

$$\alpha_i = \phi - \theta_i \tag{14}$$

and

$$\theta_i = \frac{k_{hi}}{1-k_{vi}} \tag{15}$$

K_{AE_i}, K_{FE_i} = horizontal coefficients of active and passive earth pressures (under earthquake conditions), respectively, which can be represented as below:

$$K_{AE_i} = \frac{\cos^2(\phi-\theta_i)}{\cos\theta_i\cos(\delta+\theta_i)\left[1+\sqrt{\frac{\sin(\phi+\delta)\sin(\phi-\theta_i)}{\cos(\delta+\theta_i)}}\right]^2} \tag{16}$$

$$K_{PE_i} = \frac{\cos^2(\phi-\theta_i)}{\cos\theta_i\cos(\delta+\theta_i)\left[1-\sqrt{\frac{\sin(\phi+\delta)\sin(\phi-\theta_i)}{\cos(\delta+\theta_i)}}\right]^2} \tag{17}$$

Using $\delta = \phi/2$, variations of K_{AE_i} and K_{FE_i} for various values of θ_i can be calculated. Since θ_i is function of depth of bedrock, therefore the bearing capacity factors will vary with the variation of the depth of bedrock and shall be referred as dynamic bearing capacity factors:

$$N_{qE} = \frac{K_{PEi}}{K_{AEi}} \tag{18}$$

$$N_{cE} = (N_{qE}-1)\cot\phi \tag{19}$$

$$N_{\gamma E} = \tan\alpha_{AEi}\left[\frac{K_{PEi}}{K_{AEi}} - 1\right] \tag{20}$$

On obtaining the dynamic bearing capacity factors, bearing capacity under earthquake load shall simply be calculated from the following equation for seismic conditions:

$$q_{ultE} = c\ .N_{cE} + \ q.N_{qE} + 0.5\gamma.B.N_{\gamma E} \tag{21}$$

Later on, a comparative study has been carried to verify the difference between dynamic and static bearing capacity.

3 Case Study

The above formulation depicts that, additionally, time period would be required to assess an impact on the bearing capacity factors. We consider the linear variation of G_z as given above and depth of bedrock as H.

Following range of values of soil properties were studied:

Unit weight of soil	: 18k N/m^3
Angle of internal friction	: 10–35°
Shear modulus near surface	: 10–100 MPa
Depth of bedrock	: 10–500 m

However, sample calculations are furnished here for one set of values of soil properties, and later charts and figures are reported for the above-defined range.

Here, considering $H = 50$ m, $G = 50$ MPa, $\phi = 25°$, $\gamma = 18$ kN/m^3, and damping factor of 5%,

Vs is the shear wave velocity corresponding to given shear modulus, i.e., $G = \rho \mathrm{Vs}^2$.

The stiffness and mass matrix obtained are as follows:

$$[K] = \begin{bmatrix} 2.101 \times 10^6 & -7.5 \times 10^5 & 1.389 \times 10^5 \\ -7.5 \times 10^5 & 1.69 \times 10^7 & -3.75 \times 10^6 \\ 1.389 \times 10^5 & -3.75 \times 10^6 & 4.651 \times 10^7 \end{bmatrix} \text{N/m}$$

$$[M] = \begin{bmatrix} 4.587 \times 10^4 & 0 & 0 \\ 0 & 4.587 \times 10^4 & 0 \\ 0 & 0 & 4.587 \times 10^4 \end{bmatrix} \text{kg}$$

The salient data for first three modes are as depicted in Table 2.

4 Discussions on Results

Comparing the dynamic N_{cE}, N_{qE}, and $N_{\gamma E}$ with the static values of N_c, N_q, and N_γ which are 20.71, 10.7, and 10.9, respectively, for $\phi = 25°$, it can be observed here that while in the first mode there is instant drop of dynamic N_{cE}, N_{qE}, and $N_{\gamma E}$, the second mode gives values close to static values and then the third mode values again reduce. Refer to Figs. 3, 4, and 5 for variation of N_{cE}, N_{qE}, and $N_{\gamma E}$, with various H/Vs ratio.

Further, when the results are extrapolated to higher modes, it is observed that the dynamic bearing capacity factors tend to gradually merge to the static bearing capacity factors. This is an acceptable behavior as for all dynamic systems it has been observed that at higher frequencies the deflection converges to static

Table 2 Output for the first three modes

Design parameters	Mode-1	Mode-2	Mode-3	Remarks
λ	44.965	359.13	1024	
Time period, T	0.937	0.332	0.196	
Spectral acceleration Sa/g	1.782	2.5	2.5	
β (code factor)	0.06	0.06	0.06	$Z = 0.36$, $I = 1$, $R = 3$
Modal participation factor, κ_i	1.273	−0.424	0.255	
Horizontal acceleration k_{hi}	0.136	−0.064	0.038	
Vertical acceleration, k_{vi}	0.091	−0.042	0.025	
Acceleration ratio θ_i	0.149	−0.061	0.039	
α_i (vide Eq.14)	0.288	0.497	0.397	
Wedge angle $\alpha_{\varsigma Zi}$	0.777	0.996	0.904	
Coefficient of dynamic active earth pressure K_{AZi}	0.487	0.329	0.395	
Coefficient of dynamic passive earth pressure K_{PEi}	3.067	3.739	3.43	
N_{cEi}	11.363	22.201	16.496	Nc(static) = 20.71
N_{qEi}	6.299	11.352	8.692	Nq(static) = 10.7
$N_{\gamma gi}$	5.213	15.983	9.765	$N\gamma$(static) = 10.9

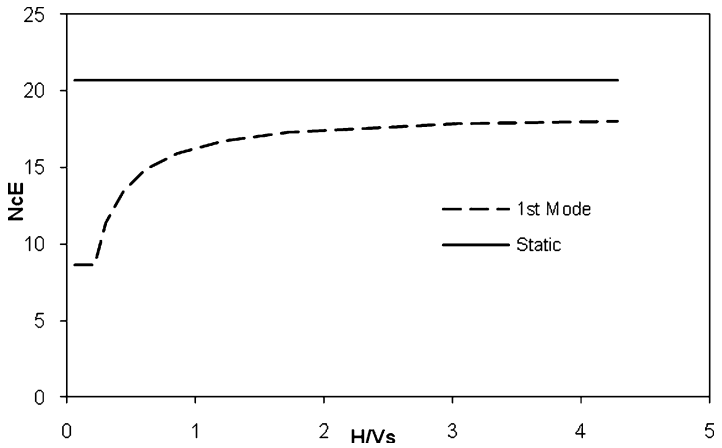

Fig. 3 Bearing capacity factor N_{cE} w.r.t. H/Vs of a continuous foundation on sand for ϕ =25°—earthquake condition

deflection. However, fundamental mode being most critical, we study the relevant engineering parameters for this mode only.

Similar obtained results for dynamic bearing capacity factors against each values of ϕ are plotted against parameter (H/Vs) to accommodate variation of depth of bedrock and shear wave velocity of the soil. Figures 6, 7, and 8 represent the

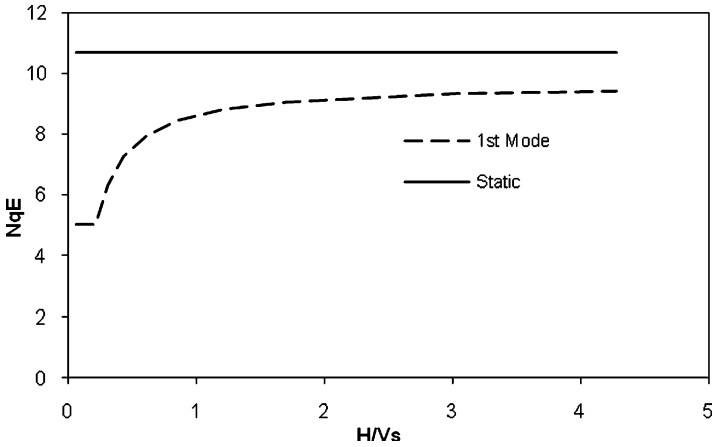

Fig. 4 Bearing capacity factor N_{qE} w.r.t. H/Vs of a continuous foundation on sand for ϕ =25°—earthquake condition

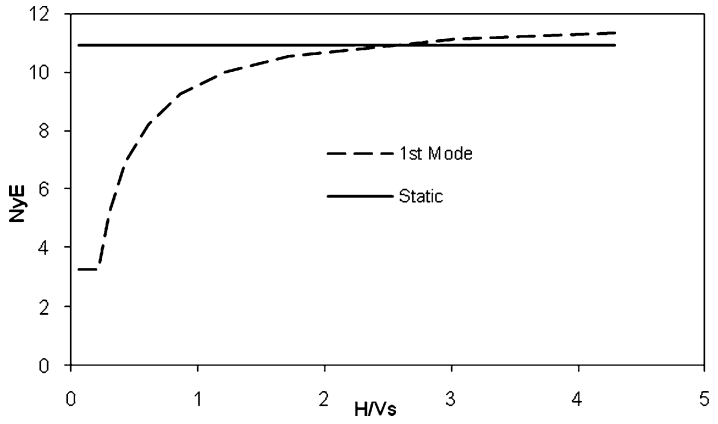

Fig. 5 Bearing capacity factor $N\gamma_E$ w.r.t. H/Vs of a continuous foundation on sand for ϕ =25°—earthquake condition

percentage reduction of dynamic bearing capacity factors as compared to static ones. It can be observed here that N_{cE} values can drop to a maximum of 25% of Nc (static), N_{qE} drops to a maximum of 45%, while $N_{\gamma E}$ drops to a maximum of 10% of its static value for low values of H/Vs. The bearing capacity factors increase slightly with the increase in shear modulus of soil or in other words with change in site classification from soft, medium, to hard soil site. Results are shown in Figs. 9, 10, and 11. This emphasizes the fact that the usual practice of increasing bearing capacity by 25–33.33% may not be correct. Instead, the bearing capacity gets reduced considerably. This is being represented in Fig. 12.

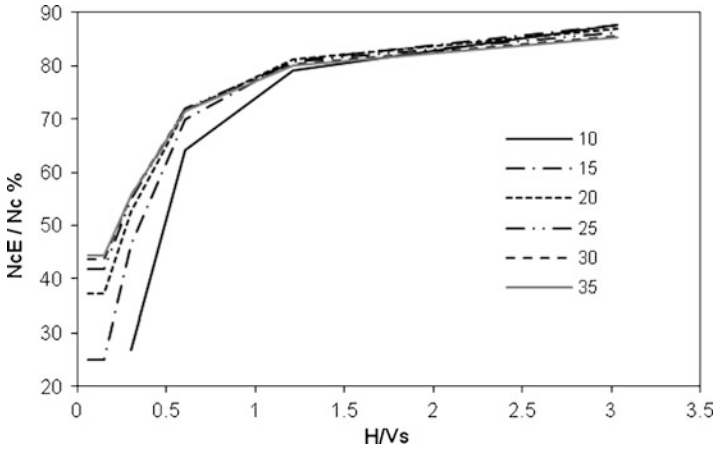

Fig. 6 Percentage reduction of dynamic bearing capacity factors *NcE* w.r.t. static bearing capacity factor *Nc*, varying with H/Vs of a continuous foundation on sand for various ϕ

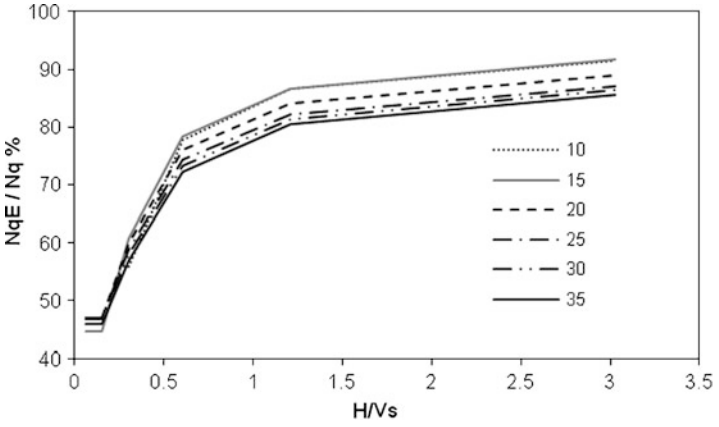

Fig. 7 Percentage of reduction of dynamic bearing capacity factors *NqE* w.r.t. static bearing capacity factor *Nq*, varying with H/Vs of a continuous foundation on sand for various ϕ

5 Effect on Bearing Capacity

In this case, a 3.0-m-wide footing placed at a depth of 1.5 m below ground in a cohesionless soil is evaluated for its UBC for various values of H/Vs.

The difference in bearing capacity with static bearing capacity factors and dynamic bearing capacity factors is plotted in Fig. 12. It may be noted here that only shear strength of soil has been considered here. The settlement calculations are not included here. As we consider that for the given foundation width, shear strength would be the governing criteria for arriving at the bearing capacity of soil. It can be observed here that the dynamic bearing capacity may get reduced to a maximum of 30% of the static bearing capacity for very low values of H/Vs.

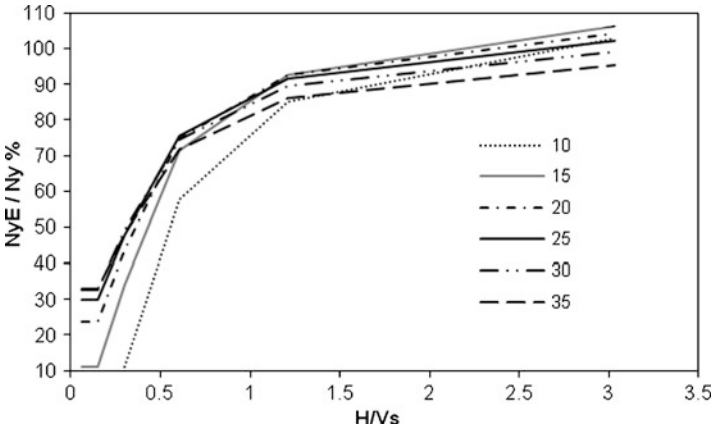

Fig. 8 Percentage of reduction of dynamic bearing capacity factors $N\gamma_E$ w.r.t. static bearing capacity factor $N\gamma$, varying with H/Vs of a continuous foundation on sand for various ϕ

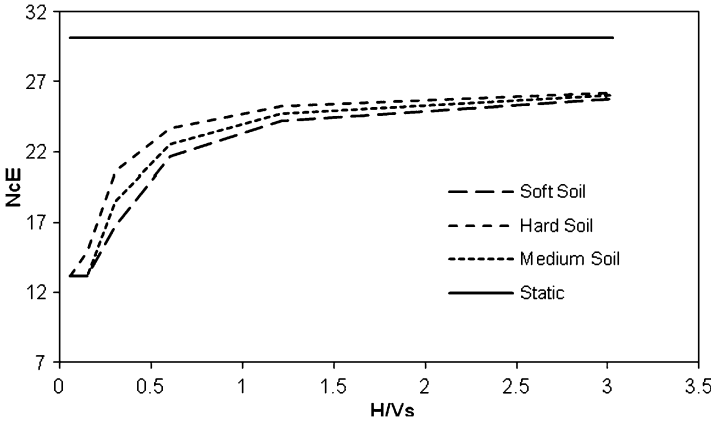

Fig. 9 Variation of Nc_E with H/Vs of a continuous foundation on sand for various site classifications ($\phi = 30°$)

6 Conclusions

This chapter gives a rational basis for estimation of bearing capacity of soil under seismic force considering modal analysis vis-à-vis the state of the art where, as per European code, the peak ground acceleration is only considered. It tries to reflect on

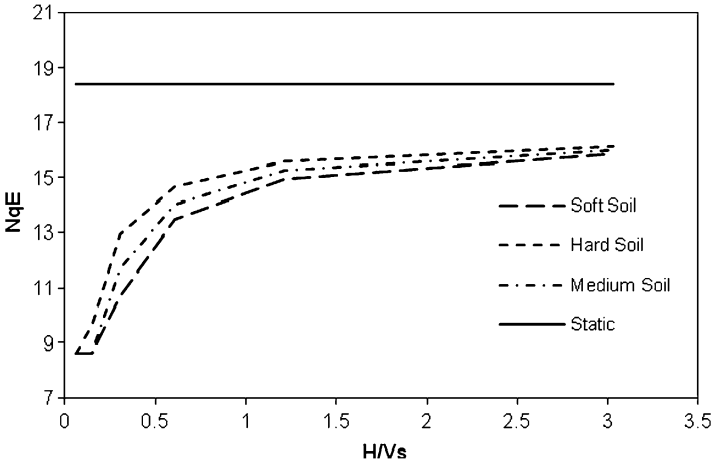

Fig. 10 Variation of Nq_E with H/Vs of a continuous foundation on sand for various site classifications ($\phi = 30°$)

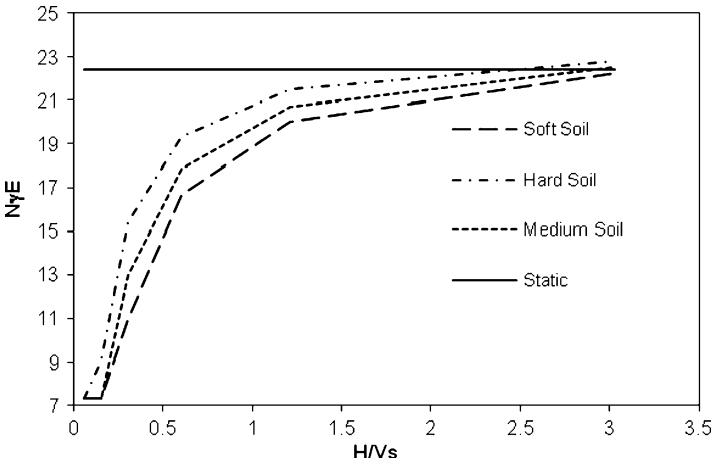

Fig. 11 Variation of $N\gamma_E$ with H/Vs of a continuous foundation on sand for various site classifications ($\phi = 30°$)

the importance of the bedrock versus shear wave velocity ratio (H/Vs) that strongly affects its behavior. It also tries to pontificate the misconception of multiplying the static bearing capacity by a factor 1.25 which is the practice in vogue in most of the design office at present. Further research in this area in terms of settlement and effect of layered soil will further enhance this study.

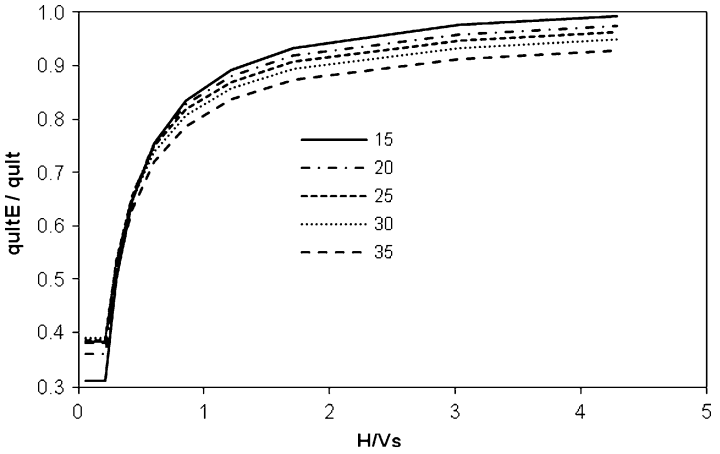

Fig. 12 Variation of qultE(dynamic)/qult (static) with H/Vs of a continuous foundation on sand for footing width of 3.0 m placed 1.5 m below ground level for various values of ϕ

References

1. Chowdhury I, Dasgupta SP (2007) Dynamic earth pressure on rigid unyielding walls under earthquake force. Indian Geotech J 37(2):81–93
2. Dowrick DJ (2003) Earthquake risk reduction. Wiley, Hoboken
3. Hansen JB (1970) A revised and extended formula for bearing capacity. Danish Geotech Inst 28:5–11
4. IS 1893 (2002) Indian standard code of practice for earthquake resistant design of structures. Bureau of Indian standards, New Delhi
5. Meyerhoff GG (1951) The ultimate bearing capacity of foundations. Geotechnique 2:301–331
6. Prandtl L (1921) Uber die eindringungsfestigkeit plastisher baustoffe und die festigkeit von schniden. Z Ang Math Mech 1(1):15–20
7. Richards R, Elms DG, Budhu M (1993) Seismic bearing capacity and settlement of shallow foundations. J Geotech Div ASCE 105(GT4):662–674
8. Terzaghi K (1943) Theoretical soil mechanics. Wiley, New York
9. Vesic AS (1973) Analysis of ultimate loads of shallow foundations. J Soil Mech Found Div ASCE 99(SM1):45–73

Reliability-Based Design of Liquid Column Vibration Absorber Under Stochastic Earthquake Load Considering System Parameter Uncertainty

Rama Debbarma, Subrata Chakraborty, and Saibal Ghosh

Abstract The reliability-based design optimization (RBDO) of tuned mass damper in vibration control considering parameter uncertainties is noteworthy. However, same is not the case for liquid dampers. The present study deals with the RBDO of liquid column vibration absorber (LCVA) parameters in seismic vibration control considering uncertainty in the properties of primary structure and ground motion parameter. The conditional second-order information of the response quantities are obtained in the random vibration framework using state space formulation. Subsequently, the total probability theorem is used to evaluate the unconditional response of the structure considering random system parameters. The unconditional root mean square displacement (rmsd) of the structure is considered as the performance index to define the failure of the system which is used as the objective function for optimum design LCVA system. Numerical study is performed to elucidate the effect of parameter uncertainty on the optimization of LCVA parameters and system performance.

Keywords Liquid column vibration absorber • Stochastic earthquake • Reliability-based design • Parameter uncertainty

R. Debbarma (✉)
Department of Civil Engineering, National Institute of Technology, Agartala, India
e-mail: ramadebbarma@gmail.com

S. Chakraborty • S. Ghosh
Department of Civil Engineering, Bengal Engineering and Science University, Shibpur, Howrah 711103, India
e-mail: schak@civil.becs.ac.in

S. Chakraborty and G. Bhattacharya (eds.), *Proceedings of the International Symposium on Engineering under Uncertainty: Safety Assessment and Management (ISEUSAM - 2012)*,
DOI 10.1007/978-81-322-0757-3_65,

1 Introduction

The liquid column damper systems have been emerged as one of the most promising passive vibration control strategies due to its easy installation procedure and flexibility in liquid frequency adjustment capability. In such system, the damper dissipates the vibration energy due to the passage of liquid mass in a U-shaped container through an orifice with inherent head loss characteristics. A more general type of such damper is called LCVA whose horizontal cross-sectional area is different than that of the vertical section. It allows better efficiency since the natural frequency of an LCVA is derived not only from the length of the liquid column but also by the area ratio of the horizontal and vertical columns. The applicability of liquid damper to mitigate the effect of wind- and seismic-induced vibration is studied extensively [1, 6, 9, 18]. In fact, the optimal design studies on passive control devices like tuned mass dampers (TMD) and tuned liquid column damper (TLCD) assuming deterministic system parameters are well established [5, 19, 20].

However, the deterministic approach as mentioned above cannot include the effects of system parameter uncertainty in the optimization process. Thus, in recent years, the studies on the effect of system parameter uncertainty have attracted a lot of interests [2, 8, 11, 13, 14, 16]. These studies are based on minimizing the unconditional expected value of the rmsd resulting in a notable different optimal TMD parameter than those obtained by considering deterministic system parameters. Though the TMD parameters optimization in seismic vibration control considering uncertain parameters is noteworthy, same is not the case for LCVA. The optimization of liquid damper system under uncertain system parameters is very limited [4, 15]. The present study deals with the RBDO of LCVA system in seismic vibration control considering uncertainty in the properties of primary structure and ground motion parameter. In doing so, the conditional second-order information of the response quantities are obtained in random vibration framework using state space formulation. Subsequently, the total probability theorem is used to evaluate the unconditional response of the primary structure considering random system parameters. The unconditional rmsd of the structures is considered as the performance index to define the failure of the primary structure which is used as the objective function to obtain the optimum LCVA parameters. Numerical study is performed to elucidate the effect of parameter uncertainty on the optimization of LCVA parameters and system performance.

2 Stochastic Response Analysis of LCVA-Structure System

A simplified model of the LCVA attached to a multi-degree-of-freedom (mdof) primary structure is shown in Fig. 1. The horizontal and vertical cross-sectional area, the length of horizontal and vertical portion and the density of liquid inside the tube are denoted by A_h, A_v, B_h, h and ρ, respectively. The mass of the liquid

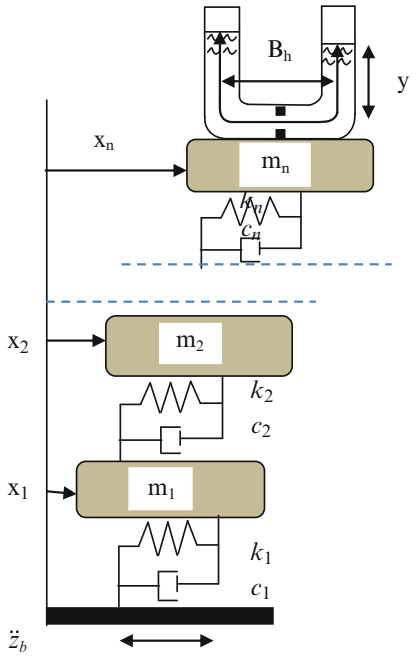

Fig. 1 The liquid column vibration absorber model

excluding the container, $m_{liq} = \rho A_v(B_h/r + 2h)$, where $r = A_v/A_h$, is the area ratio. The following notations are also introduced: the length ratio, $p = B_h/L_e$, where $L_e = (B_h r + 2h)$, is the total length of the LCVA; the liquid frequency, $\omega_l = \sqrt{2g/L_e}$; and the tuning ratio, $\gamma = \omega_l/\omega_0$. If x_n and y represent the horizontal displacement of the structure at top and the displacement of the liquid surface when the LCD structure system is subjected to a base acceleration $\ddot{z}_b$ due to earthquake, the equation of motion of the liquid can be written as

$$\rho A_h L_e \ddot{y} + \frac{1}{2}\rho A_h \xi |\dot{y}|\dot{y} + 2\rho g A_h y = -\rho A_h B_h \{\ddot{x}_n + \ddot{z}_b\} \tag{1}$$

In the above, ξ is head loss coefficient. It can be noted that Eq. (1) is nonlinear due to a drag force induced by the orifice as indicated by second term of the left-hand side of Eq. (1). Using equivalent linearization technique above can be approximated as [7]

$$\rho A_v L_e \ddot{y} + 2\rho A_v c_p \dot{y} + 2\rho g A_v y = -\rho A_v B_h \{\ddot{x}_n + \ddot{z}_b\} \tag{2}$$

Here, c_p represents the equivalent linearized damping coefficient obtained by minimizing the mean square error between Eqs. (1) and (2), assuming response as Gaussian process as [1] $c_p = \sigma_{\dot{y}} \xi r^2 / \sqrt{2\pi}$, where $\sigma_{\dot{y}}$ is the standard deviation of

liquid velocity. The equation of motion of the mdof system attached with LCVA as shown in Fig. 1 can be expressed as

$$\mathbf{M}\ddot{\mathbf{Y}} + \mathbf{C}\dot{\mathbf{Y}} + \mathbf{K}\mathbf{Y} = -\mathbf{M}\bar{\mathbf{r}}\ddot{z}_b \tag{3}$$

where $\mathbf{Y} = [y, x_n, x_{n-1}, ..., x_1]^T$ is the relative displacement vector, $\bar{\mathbf{r}} = [0 \quad \mathbf{I}]^T$, in which $\mathbf{I}$ is a unit vector of size n. $\mathbf{M}$, $\mathbf{C}$ and $\mathbf{K}$ represent the system mass, damping and stiffness matrix. Introducing the state space vector, $\mathbf{Y}_s = (y, x_n, x_{n-1}, ..x_1, \dot{y}, \dot{x}_n, \dot{x}_{n-1}, ...\dot{x}_1)^T$, Eq. (3) can be expressed as

$$\dot{\mathbf{Y}}_s = \mathrm{A}_s\mathbf{Y}_s + \tilde{\mathbf{r}}\ddot{z}_b \tag{4}$$

where $\mathrm{A}_s = \begin{bmatrix} 0 & \mathrm{I} \\ -\mathbf{M^{-1}K} & -\mathbf{M^{-1}C} \end{bmatrix}$, $\tilde{\mathbf{r}} = [0, \mathbf{I}]^T$ and $\mathbf{I}$ and 0 are the $(n + 1) \times (n + 1)$ unit and null matrices.

The well-known Kanai-Tajimi stochastic process model [17] which is able to characterize the input frequency content for a wide range of practical situations is used in the present study to represent stochastic earthquake load. The process of excitation at the base can be described as

$$\begin{aligned} \ddot{x}_f(t) + 2\xi_f\omega_f\dot{x}_f + \omega_f^2 x_f &= -W(t) \text{ and } \ddot{z}_b(t) = \ddot{x}_f(t) + W(t) \\ &= 2\xi_f\omega_f\dot{x}_f + \omega_f^2 x_f \end{aligned} \tag{5}$$

where $W(t)$ is a stationary Gaussian zero mean white noise process, ω_f is the base filter frequency and ξ_f is the filter damping. Now, defining $Z = \left(y, x_n, x_{n-1}, ...x_1, x_f\dot{y}, \dot{x}_n, \dot{x}_{n-1}, ...\dot{x}_1, \dot{x}_f\right)^T$ as the global state space vector, Eqs. (4) and (5) lead to an algebraic matrix equation of order six, i.e. the so-called Lyapunov equation [10]:

$$\mathrm{A}\mathbf{R} + \mathbf{R}\mathrm{A}^T + \mathrm{B} = 0 \tag{6}$$

where $\mathbf{A}$ and $\mathbf{B}$ are the various system parameter matrix and load matrix. The state space covariance matrix $\mathbf{R}$ can be obtained as the solution of the above equation and can be described as

$$\mathbf{R} = \begin{bmatrix} \mathbf{R}_{zz} & \mathbf{R}_{z\dot{z}} \\ \mathbf{R}_{\dot{z}z} & \mathbf{R}_{\dot{z}\dot{z}} \end{bmatrix} \tag{7}$$

in which $\mathbf{R}_{zz}, \mathbf{R}_{z\dot{z}}, \mathbf{R}_{\dot{z}z}$ and $\mathbf{R}_{\dot{z}\dot{z}}$ are the submatrices of $\mathbf{R}$. The rmsd of the liquid and that of the ith storey of the primary structure can be obtained as

$$\sigma_y = \sqrt{\mathbf{R}_{zz}(1,1)} \quad \text{and} \quad \sigma_{x_i} = \sqrt{\mathbf{R}_{zz}(p,p)} \quad \text{where,} \quad p = (n+1) - (i-1) \tag{8}$$

3 Reliability-Based Optimization

3.1 Conventional Reliability-Based Optimization of LCVA Parameters

The LCVA parameters' optimization involves determination of the tuning ratio (γ) and the coefficient of linear equivalent damping $C_p\left(\sigma_{\dot{y}}, \xi\right)$. The conventional optimization problem so defined for system subject to stochastic load can be transformed into a standard nonlinear programming problem [12]. One of the much used approaches is to minimize the mean square response of the structure. In this regard, it can be noted that minimizing the mean square response does not necessarily correspond to the optimal design in terms of reliability [13]. The exceedance of some predefined serviceability or strength limit state by the structure is more important to minimize in connection with optimum design of LCVA system. Thus, the probability of failure of the primary structure is used here as the objective function to obtain the optimum LCVA parameters. It is determined by the first crossing of any structural response x_i through a given threshold value β_i. For a system subjected to stochastic load, the first-time bilateral crossing of any response x_i to barrier level β_i can be expressed as $F_i = \{|x_i(t)| > \beta_i\}; t \in [0, T]$. The conditional failure probability $P(Fi/\mathbf{u})$ with regard to responsex_i based on the structural and excitation model specified by $\mathbf{u}$ can be estimated following classical Rice's formulation:

$$P\left(\frac{F_i}{\mathbf{u}}\right) \cong 1 - \exp\left[-\alpha_{\beta i}(\mathbf{u})T\right] \tag{9}$$

where $\alpha_{\beta_i}(\mathbf{u})$ is the conditional threshold-crossing rate for the ith failure mode and T is the duration of earthquake motion. For stationary stochastic Gaussian process with zero mean, the conditioned threshold-crossing rate can be obtained as [10]

$$\alpha_{\beta i}(\mathbf{u}) = \frac{\sigma_{\dot{x}i}}{\pi\sigma_{xi}} \exp\left(-\frac{\beta_i^2}{2\sigma_{xi}^2}\right) \tag{10}$$

where σ_{x_i} and $\sigma_{\dot{x}_i}$ are the rms of x_i and $\dot{x}_i$. For multiple failure events, $F = \sum_{i=1}^{N_q} F_i$, i.e. the system fails if any $|x_i|$ exceeds its threshold β_i. Since the mean outcrossing rate of the system can be approximated by $\alpha = \sum_{i=1}^{N_q} \alpha_{\beta_i}(\mathbf{u})$, the probability of failure $P(F/\mathbf{u})$ of the controlled structural system can be approximated by

$$P\left(\frac{F}{\mathbf{u}}\right) \approx 1 - \exp\left[-\sum_{i=1}^{N_q} \alpha_{\beta_i}(\mathbf{u})T\right] \tag{11}$$

The optimization approach involving mechanical systems subject to random load can be transformed into a standard nonlinear optimization problem as below [12]:

$$\text{Find } \overline{b} = \begin{pmatrix} \gamma \\ \xi \end{pmatrix} \text{ to minimize: } f = P_f = P(F/\mathbf{u}) \tag{12}$$

The available gradient-based techniques of optimization can be used to solve the problem. In the present study, the MATLAB routine is used for this.

3.2 The Parameter Uncertainty and Response Sensitivity Evaluation

The evaluation of stochastic response using Eq. (8) and subsequent solution of the optimization problem to obtain the optimum LCVA parameters are conditional. The uncertain system parameters are denoted by a vector **u**. To obtain the sensitivity of responses, the first-order derivative of basic Lyapunov equation can be obtained by differentiating Eq. (6) with respect to kth parameter u_k:

$$\mathrm{A}\frac{\partial \mathbf{R}}{\partial u_k} + \frac{\partial \mathrm{A}}{\partial u_k}\mathbf{R} + \frac{\partial \mathbf{R}}{\partial u_k}\mathrm{A}^T + \mathbf{R}\frac{\partial \mathrm{A}^T}{\partial u_k} + \frac{\partial}{\partial u_k}(\mathrm{B}) = 0 \text{ i.e. } \mathbf{A}\,\mathbf{R}_{,u_k} + \mathbf{R}_{,u_k}\mathrm{A}^T + \mathbf{B}_1 = 0 \tag{13}$$

where

$$\mathrm{B}_1 = \mathrm{A}_{,u_k}\mathbf{R} + \mathbf{R}\mathrm{A}^T{}_{,u_k} + \frac{\partial}{\partial u_k}(\mathbf{B}) \tag{14}$$

The sensitivity of response (rmsd as considered here) can be obtained directly by differentiating the corresponding expression of Eq. (8) with respect to kth random variable u_k as follows:

$$\frac{\partial}{\partial u_k}(\sigma_{x_i}) \text{ i.e. } \sigma_{x_i,u_k} = \frac{1}{2}\frac{\mathbf{R}_{,u_k}(j,j)}{\sqrt{\mathbf{R}(j,j)}}, \text{where } j = (n+1) - (i-1) \tag{15}$$

in which $\mathbf{R}_{,u_k}(j,j)$ is obtained by solving Eq. (13). Now, taking the second derivative with respect to lth parameter, one can further obtain the following:

$$\begin{aligned} \mathrm{A}\mathbf{R}_{,u_k u_l} + \mathbf{R}_{,u_k u_l}\mathbf{A}^T + \mathrm{B}_2 = 0\,, \\ \mathrm{B}_2 = 2\left[\mathrm{A}_{,u_k}\mathbf{R}_{,u_k} + \mathbf{R}_{,u_k}\mathrm{A}^T{}_{,u_k}\right] + \left[\mathrm{A}_{,u_k u_l}\mathbf{R} + \mathbf{R}\mathrm{A}^T{}_{,u_k u_l}\right] \end{aligned} \tag{16}$$

The second-order sensitivity of rmsd can be obtained by differentiating Eq. (15) with respect to lth random variable u_l as follows:

$$\sigma_{x_i,u_k u_l} = \frac{1}{2\sqrt{\mathbf{R}(2,2)}}\left\{\mathbf{R}_{,u_k u_l}(j,j) - \frac{1}{2}\frac{[\mathbf{R}_{,u_k}(j,j)]^2}{\mathbf{R}(j,j)}\right\} \tag{17}$$

It can be noted that the equations need to be solved for each random variable involved in the problem to obtain the first- and second-order sensitivities of the covariance matrix.

3.3 *Parameter Uncertainty and Unconditional Optimization*

Any response quantity x is a function of the system parameters $\mathbf{u}$. Now the Taylor series expansion of rmsd about its mean value is

$$\sigma_{x_i} = \sigma_{x_i(\bar{u}_k)} + \sum_{i=1}^{nv}\frac{\partial\sigma_{x_i}}{\partial u_k}\Delta u_k + \frac{1}{2}\sum_{k=1}^{nv}\sum_{l=1}^{nv}\frac{\partial^2\sigma_{x_i}}{\partial u_k \partial u_l}\Delta u_k \Delta u_l + \ldots \tag{18}$$

In the above, nv is the total number of random variables involve in the problem. Assuming uncertain variables $\mathbf{u}$ are uncorrelated, the quadratic approximation provides the expected value as

$$\sigma_{x_i} = \sigma_{x_i(\bar{u}_k)} + \frac{1}{2}\sum_{i=1}^{nv}\frac{\partial^2\sigma_{x_i}}{\partial u_k^2}\sigma_{u_k}^2 \tag{19}$$

where σ_{u_k} is the standard deviation of ith Gaussian random parameter. This unconditional response can be now used to evaluate the unconditional crossing rate using Eq. (10) and subsequently the unconditional probability of failure using Eq. (11). Thus, the final optimization is performed by the unconditional probability of failure as the performance function in Eq. (12).

4 Numerical Study

A three-degree-of-freedom primary structure with an attached LCVA subjected to stochastic earthquake excitation is undertaken to study the performance of the proposed LCVA parameters optimization procedure considering random system

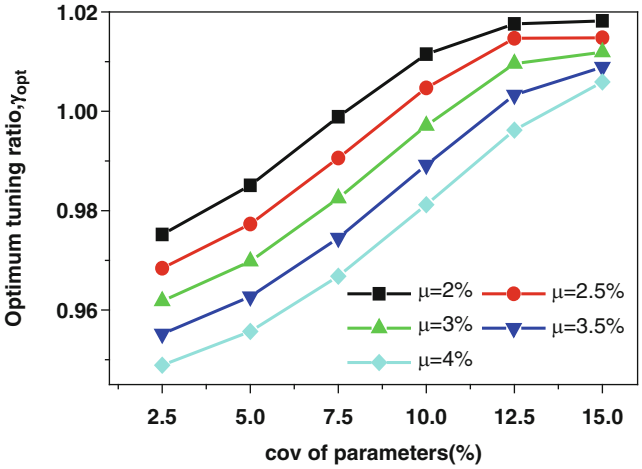

Fig. 2 The optimum tuning ratio with increasing level of uncertainty for different mass ratios

parameters. The primary structure has the following mass and stiffness values: $m_{s1} = 5.0 \times 10^5$ kg, $m_{s2} = 5.0 \times 10^5$ kg, $m_{s3} = 4.0 \times 10^5$ kg and $k_1 = k_2 = k_3 = ks = 11.0 \times 10^7$ N/m. The associated natural frequencies of the system are 6.9861, 19.2581 and 27.1168 rad/s. Unless mentioned otherwise, the following nominal values are assumed for various parameters: $\xi_s = 3\,\%$, $\mu = 3\,\%$, $p = 0.7$ and $r = 1.5$. The PSD of the white noise process at bed rock S_0 is related to the standard deviation $\sigma_{\ddot{z}_b}$ of ground acceleration [3] by $S_0 = 2\xi_f \sigma^2_{\ddot{z}_b} \Big/ \pi\left(1 + 4\xi_f^2\right)\omega_f$. For numerical study, the peak ground acceleration is taken as $PGA = 0.2\ g$, where 'g' is the acceleration due to gravity. It is assumed that $PGA = 3\sigma_{\ddot{z}_b}$. The mean value of ω_f and ξ_f is taken as 9π rad /s and 0.6, respectively. The uncertainties are considered in $k_s, \xi_s, \omega_f, \xi_f$ and S_0 which are assumed to be statistically independent Gaussian random variables.

The variations of the optimum tuning ratio and head loss coefficient with increasing level of randomness of the system parameters represented by respective coefficient of variation (cov) are shown in Figs. 2 and 3 for different mass ratios. The associated change in the reduction of probability of failure of the primary structure is shown in Fig. 4 with increasing level of randomness.

The variations of optimum tuning ratio and head loss coefficient with increasing level of damping ratio of the primary structure and different levels of randomness are shown in Figs. 5 and 6. The associated change in the probability of failure is shown in Fig. 7.

It can be observed from these plots that there is a definite and noticeable change in the damper parameters considering random system parameters with respect to that of a deterministic system. The probability of failure increases as the cov increases which indicates that the efficiency of LCVA reduced. The optimum damping parameters obtained by assuming deterministic system parameters

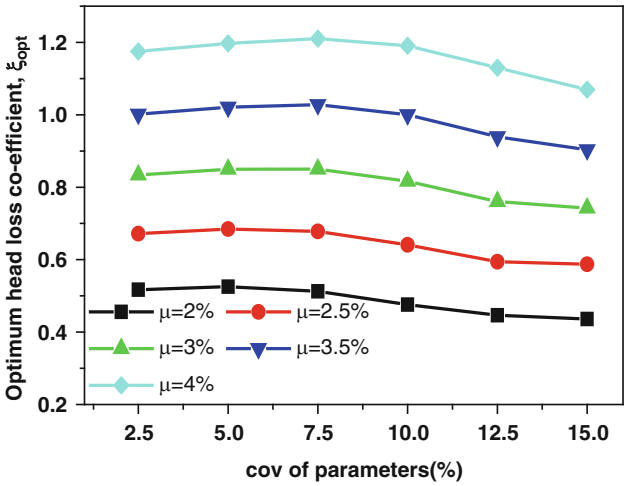

Fig. 3 The optimum head loss coefficient with increasing cov for different mass ratios

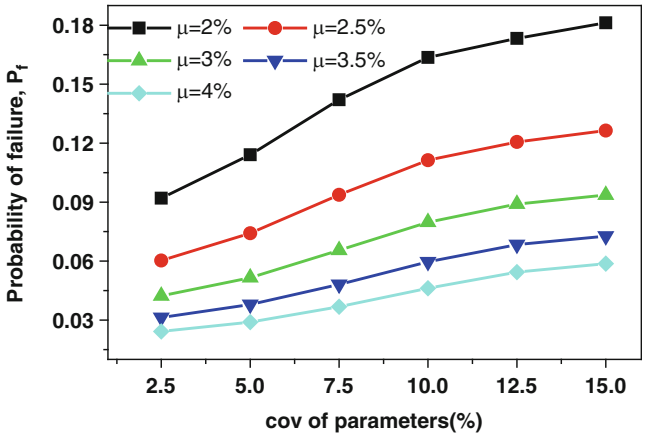

Fig. 4 The probability of failure of the primary structure increasing cov and different mass ratios

indicate that the damper performance is overestimated. This can be a potential problem in the optimization and warns the application of LCVA without proper consideration of uncertainty. It may be observed from the plots that the effect of uncertainty on damper performance is more for comparatively lower structural damping. In this regard, it may be pointed out here that the control devices are applied typically to reduce the vibration level of flexible structure having smaller structural damping. Thus, the effect of uncertainty will be a critical issue in such cases. The effect of uncertainty, i.e. the visible differences of optimum results, can

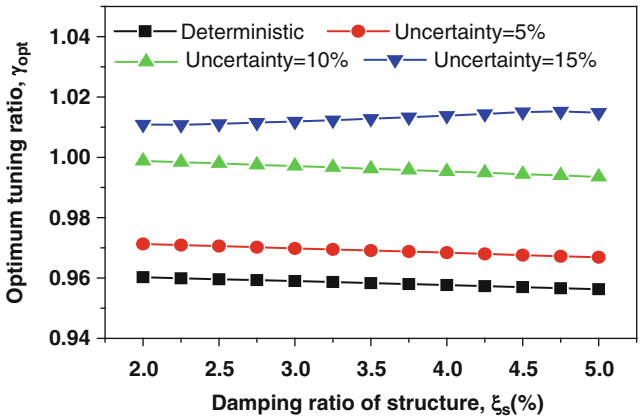

Fig. 5 The optimum tuning ratio with increasing damping ratio and different uncertainty levels

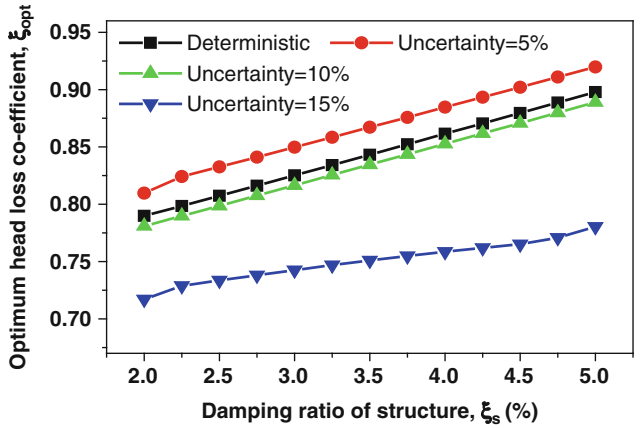

Fig. 6 The optimum head loss coefficient with increasing damping ratio and different uncertainty levels

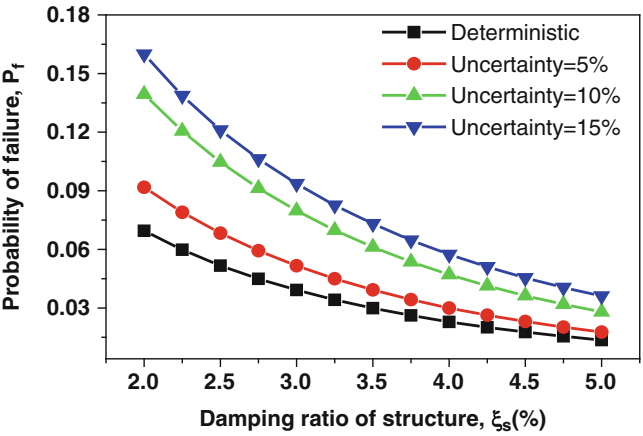

Fig. 7 The probability of failure of the primary structure with increasing damping ratio of the structure and different uncertainty levels

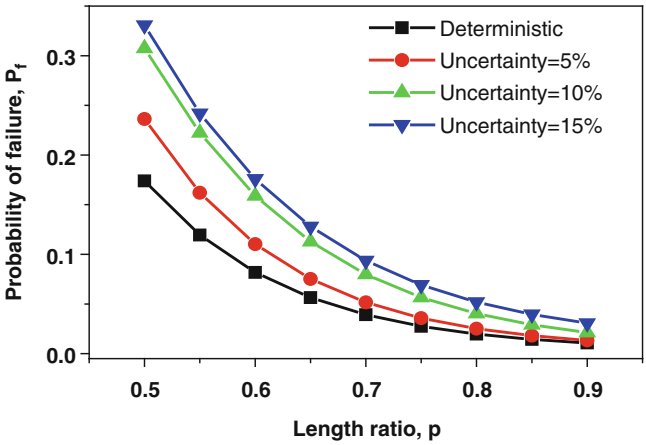

Fig. 8 The variation of probability of failure of the structure with increasing length ratio and different uncertainty levels

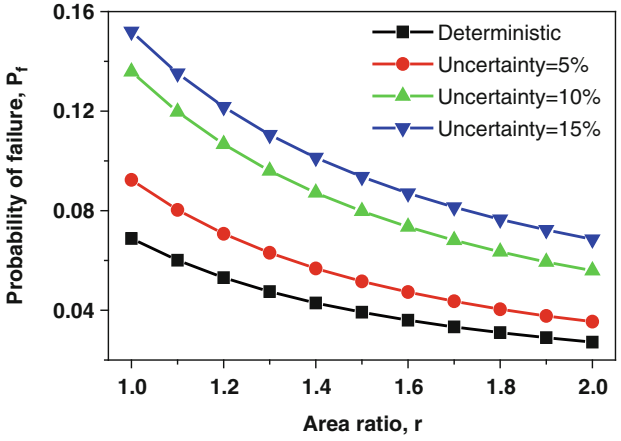

Fig. 9 The probability of failure of the structure with increasing area ratio and different uncertainty levels

be noted when the response of the structure is comparatively higher. For such higher response level, the optimization results are so sensitive that a small change in the system parameters affects the optimization results.

The variation of optimum probability of failure of the structure for changing length ratio is shown in Fig. 8. Similar results are shown in Fig. 9 for changing area ratio. It can be observed from these figures that the effect of uncertainty is less for higher area ratio and the efficiency of damper is better as well. Thus, apart from

better efficiency of LCVA with respect to TLCD, it is expected that the variance of the performance will be less in case of LCVA with respect to that of TLCD due to parameter uncertainty.

5 Conclusions

The effect of parametric uncertainty in the RBDO of LCVA system for control of vibration level of building frame structure subjected to stochastic earthquake load is presented. The random variability in the design process is incorporated in the stochastic optimization framework through the total probability theorem. As expected, the rmsd of the structure is quite significantly reduced, resulting less probability of failure with increasing mass ratio and damping ratio of the structure. However, when the system parameter uncertainties are considered, there is a definite change in the optimal tuning ratio and head loss coefficient of the LCVA, yielding a reduced efficiency of the system. It is clearly demonstrated that though the randomness in the seismic events dominates, the random variations of the system parameters have a definite and important role to play in affecting the design. In general, the advantage of the LCVA system tends to reduce with increasing level of uncertainties. However, the efficiency is not completely eliminated as it is seen that the probability of failure of the structure still remains much lower than that of the unprotected system. In general, the advantage of the LCVA tends to reduce with increasing level of uncertainties. However, the efficiency is not completely eliminated.

Acknowledgment The first author gratefully acknowledges the financial support from the QIP Programme, Govt. of India.

References

1. Chang CC, Hsu CT (1998) Control performance of liquid column vibration absorbers. Eng Struct 20(7):580–586
2. Chakraborty S, Roy BK (2010) Reliability based optimum design of tuned mass damper in seismic vibration control of structures with bounded uncertain parameters. Probab Eng Mech 26(2):215–221
3. Crandall SH, Mark WD (1963) Random vibration in mechanical systems. Academic, New York
4. Chakraborty S, Debbarma R (2011) Stochastic earthquake response control of structures by liquid column vibration absorber with uncertain bounded system parameters. Struct Saf 33:136–144
5. Gao H, Kwok KCS, Samali B (1997) Optimization of tuned liquid column dampers. Eng Struct 19(6):476–486
6. Hitchcock PA, Kwok KCS, Watkins RD (1997) Characteristics of liquid column vibration absorbers (LCVA)-I. Eng Struct 19:126–134

7. Iwan WD, Yang IM (1972) Application of statistical linearization techniques to non-linear multi-degree of freedom systems. J Appl Mech 39:545–550
8. Jensen H, Setareh M, Peek R (1992) TMDs for vibration control of system with uncertain properties. J Struct Eng 18(2):3285–3296
9. Lee HH, Wong S-H, Lee R-S (2006) Response mitigation on the offshore floating platform system with tuned liquid column damper. Ocean Eng 33:1118–1142
10. Lutes LD, Sarkani S (1997) Stochastic analysis of structural and mechanical vibrations. Prentice Hall, Upper Saddle River
11. Marano GC, Sgobba S, Greco R, Mezzina M (2008) Robust optimum design of tuned mass dampers devices in random vibrations mitigation. J Sound Vib 313:472–492
12. Nigam NC (1972) Structural optimization in random vibration environment. AIAA J 10 (4):551–553
13. Papadimitriou C, Katafygiotis LS, Au SK (1997a) Effects of structural uncertainties on TMD design: a reliability based approach. J Struct Control 4(1):65–88
14. Son YK, Savage GJ (2007) Optimal probabilistic design of the dynamic performance of a vibration absorber. J Sound Vib 307:20–37
15. Taflanidis AA, Beck JL, Angelides DC (2007) Robust reliability-based design of liquid column mass dampers under earthquake excitation using an analytical reliability approximation. Eng Struct 29:3525–3537
16. Taflanidis AA, Scruggs JT, Beck JL (2008) Reliability-based performance objectives and probabilistic robustness in structural control applications. J Eng Mech 134(4):291–301
17. Tajimi H (1960) A statistical method of determining the maximum response of a building during earthquake. In: Proceedings of the 2nd world conference on earthquake engineering, Tokyo
18. Won AYJ, Piers JA, Haroun MA (1996) Stochastic seismic performance evaluation of tuned liquid column dampers. Earthq Eng Struct Dyn 25:1259–1274
19. Yalla SK, Kareem A (2000) Optimum absorber parameters for tuned liquid column dampers. J Struct Eng 126(8):906–915
20. Zou L, Nayfeh SA (2004) Minimax optimization of multi-degree-of-freedom tuned-mass dampers. J Sound Vib 272:893–908

Robust Optimum Design of Tuned Mass Damper in Seismic Vibration Control of Structures Under Uncertain Bounded System Parameters

Bijan Kumar Roy and Subrata Chakraborty

Abstract The optimum design of tuned mass damper (TMD) system considering model parameter uncertainty is usually performed by minimising the performance measure obtained by the total probability theory concept without any consideration to the variation of the performance of TMD due to uncertainty. However, such a design method does not necessarily correspond to an optimum design in terms of maximum response reduction as well as its minimum dispersion. The present study is focused on robust optimum design of TMD system of protection to mitigate the seismic vibration effect of structures considering uncertain but bounded (UBB)-type system parameters. The root mean square displacement (rmsd) of the primary structures is considered as the performance index. The robust optimisation is obtained by using a two-criterion equivalent deterministic optimisation problem where the weighted sum of the nominal value of the performance function and its dispersion is minimised. The conventional interval analysis-based bounded optimum solution is also obtained to demonstrate the effectiveness of the robust optimum solution. A numerical study is performed to elucidate the effect of parameter uncertainty on the robust optimum design of TMD parameters by comparing the robust optimisation results with the optimisation results obtained by solving usually adopted interval optimisation procedure.

Keywords Seismic vibration control • Tuned mass damper • Uncertain bounded parameters • Bounded optimisation • Robust optimisation

B. Kumar Roy (✉) • S. Chakraborty
Department of Civil Engineering, Bengal Engineering and Science University, Shibpur, Howrah 711103, India
e-mail: bijan.roy@rediffmail.com; schak@civil.becs.ac.in

S. Chakraborty and G. Bhattacharya (eds.), *Proceedings of the International Symposium on Engineering under Uncertainty: Safety Assessment and Management (ISEUSAM - 2012)*,
DOI 10.1007/978-81-322-0757-3_66,

1 Introduction

In the field of passive vibration control, the TMDs are amongst the oldest control devices effectively used to suppress undesirable vibration induced due to wind and earthquake. One of the most important design issues is the parameter optimisation. The optimal design of TMD assuming deterministic system parameters are well developed [13, 17, 18]. A major limitation of the deterministic approach is that the uncertainties in the performance-related decision variables cannot be included in the optimisation process. But the efficiency of dampers may be drastically reduced if the parameters are off tuned to the vibrating mode it is designed to suppress due to unavoidable presence of uncertainty in the system parameters. Thus, the probabilistic vibration control considering uncertain parameters is gaining more importance in recent past. The reliability-based design optimisation (RBDO) in passive vibration control applications was originally proposed by Papadimitriou et al. [11]. The control problems for a wide class of mechanical systems with uncertainty were presented in [5]. The concept of robust reliability against failure has been introduced by Papadimitriou and Katafygiotis [10], and it serves as an important metric by which the quality of controlled systems may be judged. Taflanidis et al. [15] presented theoretical analysis of RBDO for passive or active structural control applications that optimises a control system explicitly to minimise an upper-bound first-passage failure probability.

The studies on optimisation of damper parameters allowing model parameter uncertainty as discussed above primarily use the total probability theory concept to obtain the unconditional response or the failure probability of the system which is subsequently used as the performance measure. Such design approach does not consider the possible dispersion of the performance and the damper parameters, so design may be sensitive to the variations of the input parameter due to uncertainty. However, it is desirable to achieve a balance where an optimum design will also assure less sensitivity with respect to the variations of the parameters due to uncertainty. For this, an additional ‘dimension’ is required to be introduced in the analysis by using information about the uncertain system parameters. The robustness is generally measured in terms of the dispersion of a performance function from its nominal value which is usually expressed in terms of the variance and percentile difference. In this regard, it is worth mentioning here that in many real situations, the maximum possible ranges of variations expressed in terms of percentage of the corresponding nominal values of the parameters are only known and can be modelled as UBB-type parameters. In such cases, the interval analysis method in the framework of set theoretical description is usually employed [2–4]. However, the bounded solutions thus obtained are the worst case measures and have little importance for practical design. The robust design optimisation (RDO) in which the bounds on the magnitude of uncertain parameters are only required will be a viable alternative in such cases. The concepts of RDO have been developed independently in different scientific disciplines, and the developments in recent past are noteworthy [1, 12, 19]. However, there have been a few applications of RDO

with respect to the reduction of vibration levels of structures. Hwang et al. [6] have minimised the mean and variance of displacement at the first resonance frequency of an automobile mirror system with both stiffness and mass variation. Son and Savage [14] proposed a probabilistic approach of designing vibration-absorber parameters to reduce both the mean and variance of the dynamic performance measure over the excitation frequency range. Marano et al. [7, 8] studied the RDO criterion in seismic vibration control of structure considering random system parameters.

The primary objective of the present study is to propose an RDO procedure to obtain the optimum TMD parameters to mitigate seismic vibration effect of structures characterised by UBB-type uncertain parameters. This involves optimisation of TMD parameters that include the frequency and damping properties of TMD considering uncertainty in the properties of the primary structure and ground motion parameters as well. The RDO is obtained by using a two-criterion equivalent deterministic optimisation problem, where the weighted sum of the nominal value of the performance function and its dispersion is optimised. The maximum root mean square displacement (rmsd) of the primary structures is considered as the performance index. The conventional interval analysis-based bounded design optimisation (BDO) is also performed to demonstrate the effectiveness of the proposed RDO approach. A numerical study elucidates the effect of parameter uncertainty on RDO of TMD system of protection by comparing the present RDO results with those obtained by the usually adopted interval optimisation procedure.

2 Stochastic Dynamic Response of TMD-Structure System

The TMD in its simplest form consists of an additional mass connected to a main system by a spring and a damper. The mechanical model of a TMD-structure system is represented in Fig. 1 which is described by a single mass m_s, linked with the base by a linear spring k_s and a dash pot c_s. It is excited by a base acceleration $\ddot{y}_b(t)$, and it is connected with a secondary mass m_T by a spring k_T and a dash pot c_T. The dynamic equilibrium of the equation of the system can be expressed as

$$\mathbf{M}\ddot{\mathbf{Y}}(\mathbf{t}) + \mathbf{C}\dot{\mathbf{Y}}(\mathbf{t}) + \mathbf{K}\mathbf{Y}(\mathbf{t}) = \mathbf{r}\ddot{y}_b(t) \tag{1}$$

where $\mathbf{Y}(\mathbf{t})$, $\dot{\mathbf{Y}}(t)$ and $\ddot{\mathbf{Y}}(t)$ denote the relative displacement, velocity and acceleration vectors; $\boldsymbol{r}$ is the influence coefficient vector; and **M, C** and **K** are, respectively, the mass, damping and stiffness matrices of the combined system. The well-known Kanai-Tajimi stochastic process [16] which is able to characterise input frequency content for a wide range of practical situations is used in the present study, and $\ddot{y}_b(t)$ is represented as

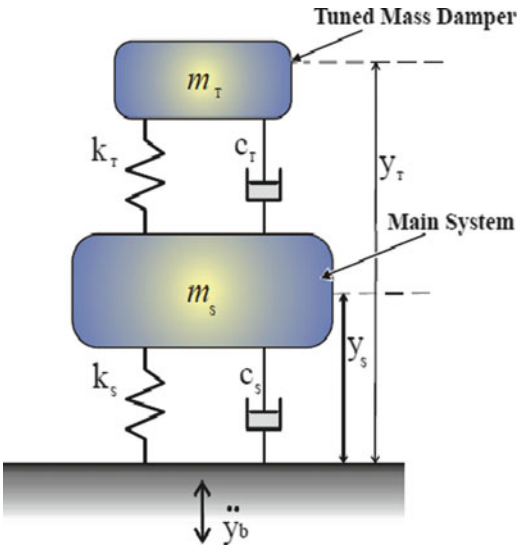

Fig. 1 Linear model of TMD system

$$\begin{aligned} &\ddot{y}_b(t) = \ddot{x}_f(t) + w(t) = -\left(2\xi_g\omega_g\dot{x}_f(t) + {\omega_g}^2 x_f(t)\right) \text{ and} \\ &\ddot{x}_f(t) + 2\xi_g\omega_g\dot{x}_f(t) + {\omega_g}^2 x_f(t) = -w(t) \end{aligned} \tag{2}$$

In the above, $x_f(t)$ is the response of the filter representing the ground and ξ_g and ω_g are, respectively, the damping ratio and the frequency of this filter, $w(t)$ being the white noise process, representing the excitation at the bedrock.

Introducing the space state vector $Z = (y_T,\ y_S,\ x_f,\ \dot{y}_T,\ \dot{y}_S,\ \dot{x}_f)^T$, the stochastic response of the system can be obtained by using the covariance matrix $\mathbf{R}_{ZZ}$ obtained by solving the following Lyapunov equation:

$$AR_{ZZ} + R_{ZZ}A^T + B = 0 \tag{3}$$

where the state **A** is

$$A = \begin{bmatrix} 0 & 0 & 0 & 1 & 0 & 0 \\ 0 & 0 & 0 & 0 & 1 & 0 \\ 0 & 0 & 0 & 0 & 0 & 1 \\ -\omega^2{}_T & \omega^2{}_T & \omega^2{}_f & -2\xi_T\omega_T & 2\xi_T\omega_T & 2\xi_f\omega_f \\ \omega^2{}_T & -(\mu\omega^2{}_T + \omega^2{}_T) & \omega^2{}_f & \mu 2\xi_T\omega_T & -(\mu 2\xi_T\omega_T + 2\xi_S\omega_S) & 2\xi_f\omega_f \\ 0 & 0 & -\omega^2{}_f & 0 & 0 & -2\xi_f\omega_f \end{bmatrix} \tag{4}$$

and where the matrix **B** has all null elements, except the last on the main diagonal: $[\mathbf{B}]_{6,6} = 2\pi S_0$, where S_0 is the intensity of the white noise. The System mechanical

parameters in matrix are as follows, where ω is natural frequency and ξ is damping ratio of concerned system:

$\omega_T = \sqrt{k_T/m_T}$, $\omega_S = \sqrt{k_S/m_S}$; $\xi_T = c_T/2\sqrt{m_T k_T}$, $\xi_S = c_S/2\sqrt{m_S k_S}$; and $\mu = m_T/m_S$.

The space state covariance matrix $\mathbf{R}_{zz}$ (of size 6×6) is obtained by solution in Eq. (3). The rmsd of TMD and the primary system can be then obtained as

$$\sigma_{y_T} = \sqrt{R_{zz}(1,1)}, \quad \sigma_{y_S} = \sqrt{R_{zz}(2,2)} \tag{5}$$

3 Optimization of TMD Parameters

The optimum TMD parameters are generally obtained by minimising the vibration effect of a structure under dynamic load. The problem of optimisation of the TMD system of protection consists of determining optimum frequency (ω_T) and damping ratio (ξ_T) of the damper system. The design vector (DV) can be thus defined as $\bar{b} = (\omega_T, \xi_T)$. The stochastic structural optimisation (SSO) problem under random earthquake load can be formulated as the search of a suitable set of DVs, over a possible admissible domain Ω to minimise a desired objective. For stochastically excited structures, a tractable measure of performance can be given in terms of mean square responses (displacement, acceleration, stress, etc.). The failure probability of the structure or the total life-cycle cost of the structure can be also used as the performance index. In the present study, the rmsd of the primary structure is considered as the objective function. The SSO problem so defined leads to a standard nonlinear programming problem [9] as follows:

$$\text{Find } \bar{b} \in \Omega \text{ to minimize, } f = \sigma_{y_s} \tag{6}$$

3.1 The Parameter Uncertainty and Optimisation of TMD system

The response statistic evaluated under stochastic earthquake load to solve the SSO problem as described by Eq. (6) intuitively assumes that these parameters characterising the structure and stochastic earthquake load model are completely known. But the uncertainty in these parameters may lead to an unexpected excursion of responses affecting the desired safety of the structure. Thus, in the design of optimum TMD system of protection, apart from the stochastic nature of the earthquake load**,** the uncertainty with regard to these parameters should be taken into account. This will involve sensitivity analysis of stochastic dynamic system. In the present section, the related formulations are briefly discussed for UBB-type

system parameter. If $\bar{x}_i$ is the nominal value of the ith UBB parameter viewed as the mean value and $\pm\Delta x_i$ represents the maximum deviation from the nominal value, then the UBB parameter value deviating from the nominal value can be expressed as $x_i^I = \left[x_i^l, x_i^u\right] = \bar{x}_i + \Delta x_i[-1,1] = \bar{x}_i + \Delta x_i e_\Delta, \bar{x}_i = \frac{x_i^l + x_i^u}{2} e_\Delta[-1,1]$. Thus, the ith interval variable can be written as $x_i = \bar{x}_i + \delta x_i$, where $|\delta x_i| \leq \Delta x_i$, $i = 1, 2, .., m$. The system matrix $\mathbf{A}$ and $\mathbf{B}$ and response covariance matrix $\mathbf{R}$ can be expanded with respect to 'm' numbers of such UBB parameters in Taylor series about the nominal values in first-order terms of δx_i as

$$\mathbf{A} = \bar{\mathbf{A}} + \sum_{i=1}^{m} \frac{\partial \mathbf{A}}{\partial x_i} \delta x_i + ..., \mathbf{B} = \bar{\mathbf{B}} + \sum_{i=1}^{m} \frac{\partial \mathbf{B}}{\partial x_i} \delta x_i + ... \text{ and } \mathbf{R} = \bar{\mathbf{R}} + \sum_{i=1}^{m} \frac{\partial \mathbf{R}}{\partial x_i} \delta x_i + ... \tag{7}$$

In the above, the bar over the parameter represents the matrices corresponding to the nominal values of the UBB parameters. The derivatives are evaluated at $x_i = \bar{x}_i$. Substituting Eq. (7) in Eq. (3) for ith UBB parameters and equating the equal-order term after neglecting the higher-order term, the following equation can be readily obtained:

$$\bar{\mathbf{A}}\bar{\mathbf{R}} + \bar{\mathbf{R}}\bar{\mathbf{A}}^T + \bar{\mathbf{B}} = \mathbf{0} \tag{8}$$

$$\bar{\mathbf{A}} \frac{\partial \mathbf{R}}{\partial x_i} + \frac{\partial \mathbf{R}}{\partial x_i} \bar{\mathbf{A}}^T + \mathbf{B}^I = \mathbf{0} \text{ where } \mathbf{B}^I = \frac{\partial \mathbf{A}}{\partial x} \bar{\mathbf{R}} + \bar{\mathbf{R}} \frac{\partial \mathbf{A}^T}{\partial x} \tag{9}$$

The mean covariance matrix $\mathbf{R}$ is obtained by solving Eq. (8) considering the mean values of system parameter matrices $\mathbf{A}$, i.e. the system matrices correspond to the mean value of the system parameters. The first-order sensitivity of the covariance matrix $\partial \mathbf{R}/\partial x_i$ can be obtained by solving Eq. (8). It may be noted that the equation needs to be solved for each uncertain parameter involved in the problem.

The performance function, i.e. the rmsd as defined by Eq. (5), is also a function of the uncertain parameters and can be expanded in first-order Taylor series as the mean and fluctuating part as follows:

$$\sigma_x = \bar{\sigma}_x + \sum_{i=1}^{m} \frac{\partial \sigma}{\partial x_i} \delta x_i + ... \tag{10}$$

In the above, $\bar{\sigma}_x$ is obtained by using the solution of Eq. (8) in Eq. (5). The sensitivity of the rmsd can be obtained by differentiating the appropriate expression of Eq. (5) with respect to the ith UBB parameters as follows:

$$\frac{\partial \sigma_x}{\partial x_i} = \frac{1}{2} \left[\frac{\partial \mathbf{R}(2,2)}{\partial x} \Big/ \sqrt{\mathbf{R}(2,2)} \right] \tag{11}$$

in which $\partial \mathbf{R}/\partial x_i$ is obtained by solving Eq. (9). Now, by making use of interval extension in interval mathematics assuming monotonic responses, the interval extension of the above expression can be obtained. The interval region of the function involving the UBB variables can be then separated out to the upper and lower bound as below:

$$\sigma_x^u = \bar{\sigma}_x + \sum_{i=1}^{m} \frac{\partial \sigma_x}{\partial x_i} \Delta x_i + \ldots \quad \text{and} \quad \sigma_{xl} = \bar{\sigma}_x - \sum_{i=1}^{m} \frac{\partial \sigma_x}{\partial x_i} \Delta x_i + \ldots \tag{12}$$

The optimisation now involves two objective functions yielding the upper and lower-bound solutions.

3.2 Robust Optimisation of TMD Parameters

The BDO procedure as presented above does not consider the possible dispersion of the design performance with respect to variation of parameters due to uncertainty. Thus, it may be sensitive due to the variations of the input system parameters. As already mentioned, the RDO solution aims to improve the design by minimising the variability of the structural response, meeting the requirements of the performance. The robustness of performance function (σ_x) is generally expressed in terms of its dispersion, $\Delta\sigma$, from the nominal value, $\bar{\sigma}_x$, defined as follows:

$$\Delta\sigma = \sum_{i=1}^{m} \left| \frac{\partial \sigma}{\partial x_i} \right| \Delta x_i \tag{13}$$

The objective of an ideal design is to achieve the optimal performance as well as less sensitivity of the performance with respect to the variation of system parameters. The two criteria often conflict with each other. The problem is dealt as a multi-objective optimisation, where the conventional objective function and its dispersion are two objectives that need to be optimised, i.e. find x, to minimize $\{\bar{\sigma}_x, \Delta\sigma\}$. The two-criterion optimisation problem is transformed to minimisation of an equivalent single objective as

$$\phi = \alpha * \bar{\sigma}_x + (1 - \alpha) * \Delta\sigma \tag{14}$$

where α is a weight factor in the bi-objective optimisation problem. The maximum robustness will be achieved for $\alpha = 0.0$, and for $\alpha = 1.0$ indicates optimisation without any robustness. The optimisation can be performed based on the standard unconstrained nonlinear optimisation routine available with MATLAB Optimization Toolbox. Once the optimal design point is obtained by solving Eq. (14), the dispersion of performance can be estimated at the optimal point using Eq. (13).

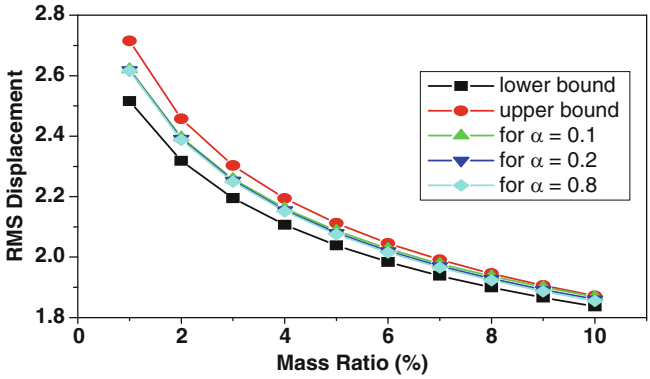

Fig. 2 The variation of rmsd of the TMD with varying mass ratio

4 Numerical Study

The primary system with an attached TMD as shown in Fig. 1 is undertaken to elucidate the proposed RDO of TMD system in seismic vibration control of structure characterised by UBB-type system parameters. The uncertainties considered in $m_S, k_S, m_T, k_T, \xi_g, \omega_g$, S_0 are represented by the maximum possible dispersion (Δx_i) expressed in terms of the percentage of corresponding nominal value $(\bar{x}_i)$. Unless mentioned otherwise, the following nominal values are assumed in the present numerical study: $\xi_s = 3\%$, $\mu = 4\%$, $\omega_s = 4.5\pi$ rad/s, $\omega_f = 7\pi$ rad/s, $\xi_f = 0.4$, $S_0 = 300$ cm^2/s^3 and $\Delta x_i = 10\%$. Based on this, the rmsd of the unprotected system, i.e. without TMD, is computed to be 3.36 cm. The rmsd of the primary structure is optimised by the proposed RDO procedure. The optimum mean value of the rmsd of the structure versus the mass ratio is plotted in Fig. 2 for different settings of weight factor α. The associated dispersion of the rmsd of the primary structure is shown in Fig. 3. The corresponding optimum tuning ratio and damping ratio of the TMD are shown in Figs. 4 and 5, respectively.

The BDO procedure considering the upper and lower-bound performance functions as described by Eq. (12) are also performed. The results are shown in the same plot for ease in comparison with the RDO results. The uncertainty level of 10% and 3% damping ratio is considered to develop these plots. It can be readily observed from the plots that the bounded solutions are too far apart which is obvious as interval method gives a conservative estimate of the upper and lower-bound solutions. In such situation, an upper-bound solution is usually suggested to be used as the performance function for optimum design is merely a conservative deterministic solution of the problem without any consideration on the possible dispersion of the suggested design. Though the lower-bound solution is efficient in terms of response reduction, the associated dispersion of the design is more. The efficiency of the RDO solution is marginally less compared to that of the lower-bound solution and lies in between the bounded solutions. However, the dispersion

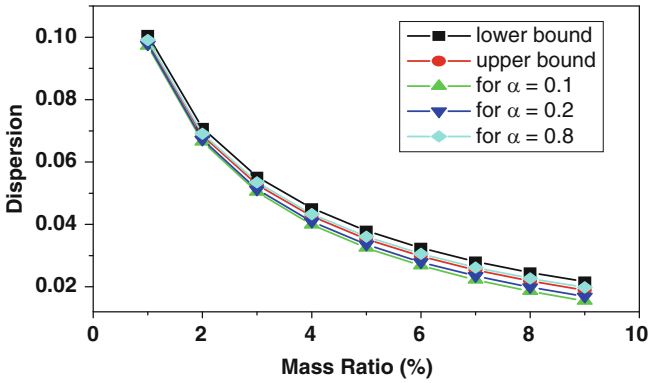

Fig. 3 The variation of dispersion with varying mass ratio

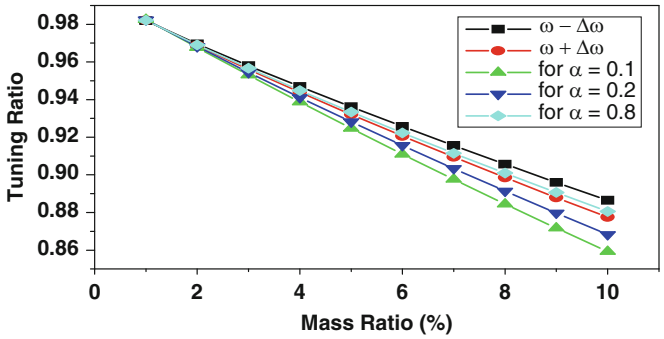

Fig. 4 The variation of tuning ratio of the TMD with varying mass ratio

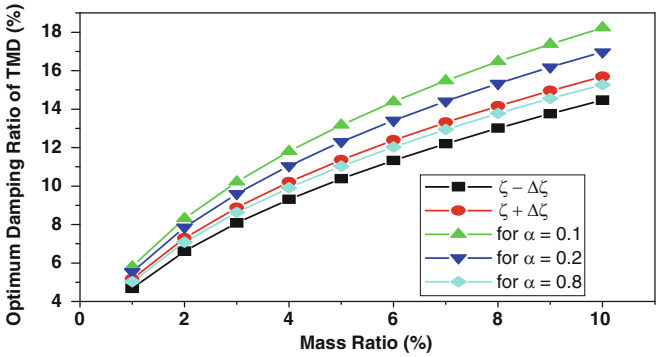

Fig. 5 The variation of damping of the TMD with varying mass ratio

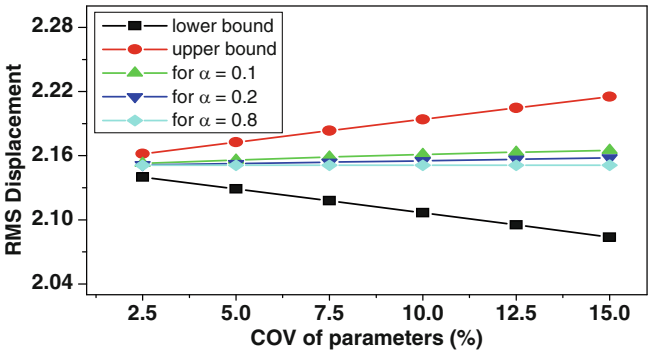

Fig. 6 The variation of rmsd with varying level uncertainty

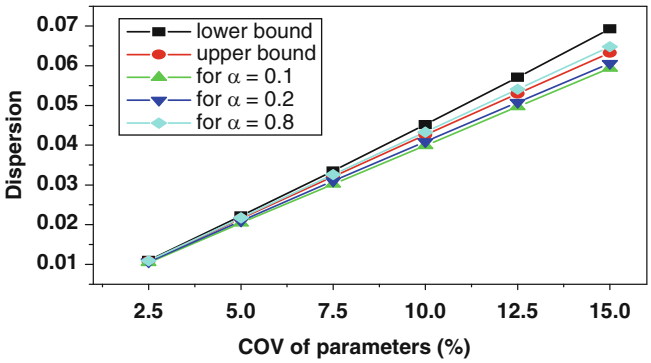

Fig. 7 The variation of dispersion of rmsd with varying level uncertainty

of the design is much lower than the dispersion of the lower-bound case solution, and the designer has the necessary flexibility to control the design through suitable choice of the weight factor α to achieve the desired level of performance efficiency (i.e. the reduction of vibration level) and its dispersion under parameter uncertainty.

The mean value of the rmsd of the primary structure versus uncertainty range is plotted in Fig. 6 for different values of weight factor α. The associated dispersion of the rmsd is shown in Fig. 7. The corresponding optimum tuning ratio and damping ratio are shown in Figs. 8 and 9, respectively. The results of the BDO procedure are also shown in the same plot. The width of the bounded solution increases sharply with increasing level of uncertainty. However, the change in the optimum rmsd is nominal by the proposed RDO case. As expected, the dispersion of the rmsd value increases with increasing level of uncertainty for all RDO cases, i.e. for all settings of α. However, the dispersion of the design is much smaller than the dispersion of the lower-bound case irrespective of uncertainty level. The change in tuning ratio and damping ratio as shown in Figs. 8 and 9 with increasing level of uncertainty is notable. The mass ratio and damping ratio of the primary structure are considered as 4 and 3%, respectively.

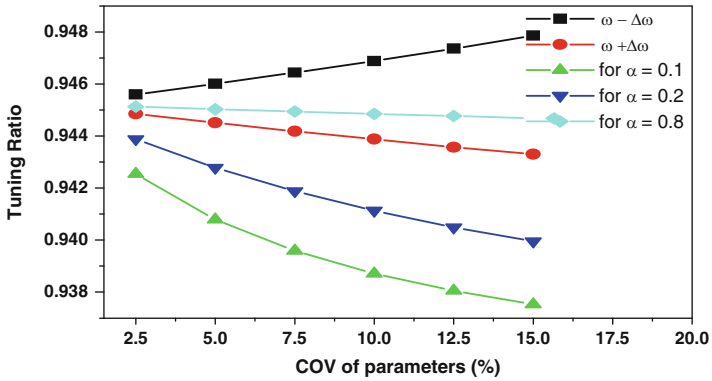

Fig. 8 The variation of tuning ration of the TMD with varying uncertainty level

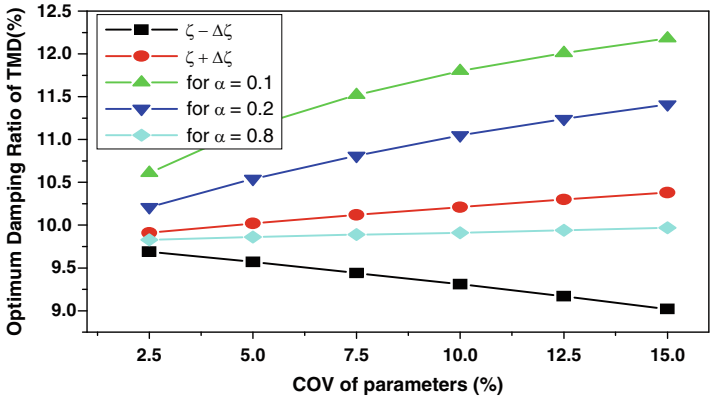

Fig. 9 The variation of damping of the TMD with varying uncertainty level

It is generally observed that there is a trade-off between the objective values of a design and its robustness. The situation can be studied further in terms of Pareto front. The Pareto front is generated by solving the RDO by varying the weight factor α, and the results are plotted in Fig. 10 for different mass ratios. The uncertainty ranges for all parameters are taken as 10%, and damping is considered to be 3%. It can be observed from the plot that the dispersion of the optimum weight decreases, and the rmsd increases as α value decreases. Thus, more robustness is achieved at the cost of sacrificing the performance of TMD. This is one of the important characteristics obtained from multi-objective optimisation procedure.

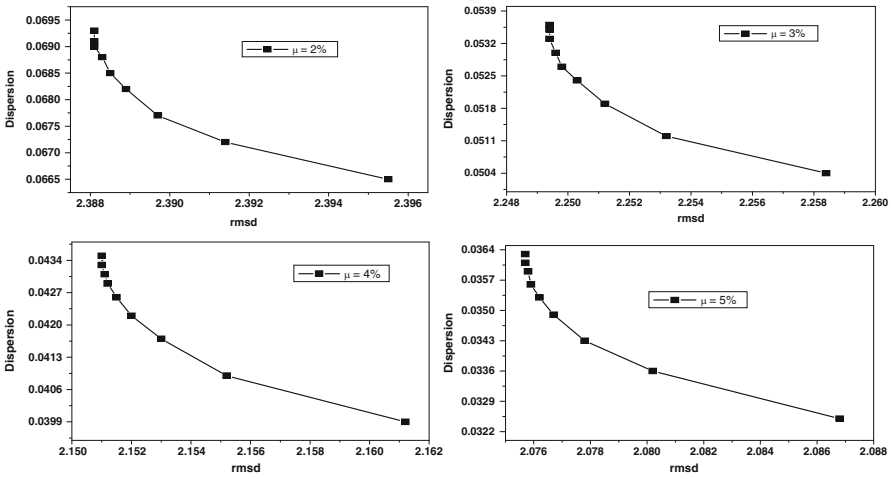

Fig. 10 The variation of dispersion with varying rmsd for different mass ratios

5 Conclusions

The RDO of TMD system of protection in mitigating seismic vibration effect of structures characterised by UBB-type system parameters is studied in the present work. The advantage of RDO approach in absence of complete probabilistic information to describe the system parameters is demonstrated. The BDO solutions conventionally obtained in such situation are too far apart. The conservative upper-bound solution usually suggested in such cases is of little use for practical design application. Moreover, such approach fails to provide information about the possible dispersion of the design performance. But, the RDO approach provides the necessary flexibility to the designer to achieve the desired level of performance efficiency (i.e. the reduction of vibration level) and its dispersion under uncertain environment through suitable choice of parameter α. Thus, one can make more effective use of the resources available in a given structural control situation and provide for more realistic and cost-effective trade-offs between the control performance and its robustness with due importance to the unavoidable presence of system parameter uncertainty. It is generally observed that more robustness is achieved at the cost of sacrificing the optimum weight, an obvious characteristic of results obtained from any multi-objective optimisation problem. Though the efficiency of RDO solution is comparatively less compared to that of the lower-bound solution, the dispersion of the design is much lower than the dispersion of the lower-bound case solution. The formulation presented here involves linear perturbation-based approximation of the responses around the mean values of the UBB parameters.

For larger level of uncertainty, alternative approach to linear perturbation analysis is needed which required further study. It may be noted that the approach being generic in nature can be applied for RDO of TMD for vibration control of MDOF system.

References

1. Beyer H, Sendhoff B (2007) Robust optimization – a comprehensive survey. Comput Methods Appl Mech Eng 196:3190–3218
2. Chakraborty S, Roy BK (2011) Reliability based optimum design of tuned mass damper in seismic vibration control of structures with bounded uncertain parameters. Probab Eng Mech 26(2):215–221
3. Chen SH, Zhang XM (2006) Dynamic response of closed-loop system with uncertain parameters using interval finite-element method. ASCE J Eng Mech 132(8):830–840
4. Chen SH, Song M, Chen YD (2007) Robustness analysis of vibration control structures with uncertain parameters using interval algorithm. Struct Saf 29:94–111
5. Ferrara A, Giacomini L (2000) Control of a class of mechanical systems with uncertainties via a constructive adaptive/second order VSC approach. J Dyn Syst Meas Control 122(1):33–39
6. Hwang KH, Lee KW, Park GJ (2001) Robust optimization of an automobile rear view mirror for vibration reduction. Struct Multidiscip Optim 21:300–308
7. Marano GC, Greco R, Sgobba S (2010) A comparison between different robust optimum design approaches: application to tuned mass dampers. Probab Eng Mech 25:108–118
8. Marano GC, Sgobba S, Greco R, Mezzina M (2008) Robust optimum design of tuned mass dampers devices in random vibrations mitigation. J Sound Vib 313:472–492
9. Nigam NC (1972) Structural optimization in random vibration environment. AIAA J 10 (4):551–553
10. Papadimitriou C, Katafygiotis LS (2001) Updating robust reliability using structural test data. Probab Eng Mech 16:103–113
11. Papadimitriou C, Katafygiotis LS, Au SK (1997) Effects of structural uncertainties on TMD design: a reliability-based approach. J Struct Control 4(1):65–88
12. Park GJ, Lee TH, Lee K, Hwang KH (2006) Robust design: an overview. AIAA J 44 (1):181–191
13. Rana R, Soong TT (1998) Parametric study and simplified design of tuned mass dampers. Eng Struct 20:193–204
14. Son YK, Savage GJ (2007) Optimal probabilistic design of the dynamic performance of a vibration absorber. J Sound Vib 307:20–37
15. Taflanidis AA, Scruggs JT, Beck JL (2008) Reliability-based performance objectives and probabilistic robustness in structural control applications. ASCE J Eng Mech 34(4):291–301
16. Tajimi H (1960) A statistical method of determining the maximum response of a building during earthquake. In: Proceedings of the 2nd world conference on earthquake engineering, Tokyo
17. Thomson AG (1980) Optimizing the tuned viscous dynamic vibration absorber with primary system damping; a frequency locus method. J Sound Vib 73:469–472
18. Warburton GB, Ayorinde EO (1980) Optimum absorber parameters for simple system. Earth Eng Struct Dyn 8:197–217
19. Zang C, Friswell MI, Mottershead JE (2005) A review of robust optimal design and its application in dynamics. Comput Struct 83:315–326

Fuzzy Rule-Based Approach for Diagnostics in Nuclear Plant Diesel Generators

Aniruddh Nain and P.V. Varde

Abstract This chapter presents a comprehensive method of fault diagnosis that will enhance the condition-based maintenance capability of engineering system and reduce the dependence on human experts for fault diagnosis using system modelling and fuzzy rule-based integrated approach. This method can be used in a complex system where failure data is either unavailable or scarcely available, which does not allow us to use extensive data-driven techniques. This methodology uses the integrated approach wherein reliability-based techniques like failure mode and effect analysis (FMEA) and the fault tree analysis (FTA) is utilised. The FMMEA is used for finding various failure modes and mechanism and identification of appropriate parameters which can be used to assess impending failure. The fault tree analysis (FTA) is utilised for the qualitative analysis of various failure modes and mechanism and finding various relations between them. This knowledge is then utilised for making fuzzy rules in fuzzy rule-based diagnostics system. Further, mathematical model has been developed using laws of physics, which relates various parameters of the system. This mathematical model gives the healthy baseline and failure definition of various failures, this information will be used in fuzzy rule-based system for making membership function. Finally, a case study is carried out on diesel generator used in nuclear plant.

Keywords Diagnostics • Reliability • Fuzzy rule-based system

1 Introduction

Diagnosis is treated as a process of fault detection and isolation in a system due to the collection, conversion, analysis and evaluation of diagnostic signals. At first is the detection stage, where values of diagnostic signals are measured and compared

A. Nain • P.V. Varde (✉)
BARC, Mumbai, India
e-mail: varde@barc.gov.in

S. Chakraborty and G. Bhattacharya (eds.), *Proceedings of the International Symposium on Engineering under Uncertainty: Safety Assessment and Management (ISEUSAM - 2012)*,
DOI 10.1007/978-81-322-0757-3_67,

with the prior knowledge of faults. The comparison reveals the existence of the faults. The next step is fault isolation where the type of the fault, its location and time of appearance are defined. And finally is fault identification which consists in more precise definition of the fault, e.g. its size and location of a leak from the installation [1]. Current maintenance strategies have progressed from breakdown maintenance to preventive maintenance, then to condition-based maintenance (CBM) managed by experts, and lately towards a futuristic view of intelligent predictive maintenance systems. Prognostics and health monitoring (PHM) is a step towards this direction [2]. CBM attempts to monitor machinery health based on condition measurements that do not interrupt normal machine operation. CBM is a decision-making strategy where the decision to perform maintenance is reached by observing the "condition" of the system and/or its components. The condition of a system is quantified by parameters that are continuously monitored and are system or application specific. In CBM the diagnosis is performed based on the input from the sensors and comparing it with healthy baseline. Some of the advantages of CBM are prior warning of impending failure and increased precision in failure prediction. The disadvantage, of course, is the necessity to install and use monitoring equipment and to develop some level of modelling or decision-making strategy [3]. The CBM also depends upon the capability of an individual who is monitoring the system to predict the health of the system.

Piotr Gmytrasiewicz et al. [4] described the use of fuzzy set theory as a tool for diagnostics of a system described by the means of fault tree. The fault tree is used by system analyst to depict logical relationships between components of the system and system availability or response. This chapter proposes the use of the wealth of information available in fault tees as a diagnostics knowledge base. Zhao Peng et al. [5] proposed an approach of fault diagnosis for communication control system based on fuzzy fault tree. It performs the fuzzy analysis for the fault tree to determine the confidence interval of probability of top event and achieve fuzzy reasoning diagnosis result.

2 An Integrated Approach to Diagnostics Using Fuzzy Logic

The two most widely used methods in diagnostics are rule-based system and model-based system. *Rule-based expert systems* have a wide range of applications for diagnostic tasks where expertise and experience are available but deep understanding of the physical properties of the system is either unavailable or too costly to obtain. In the rule-based systems, knowledge is represented in the form of production rules. A rule describes the action that should be taken if a symptom is observed. The empirical association between premises and conclusions in the knowledge base is their main characteristic. These associations describe cause-effect relationships to determine logical event chains that were used to represent the propagation of

complex phenomena. The rule-based approach has a number of weaknesses such as lack of generality and poor handling of novel situations.

In *model-based diagnostic expert systems* a model (mathematical) is employed to describe the nominal behaviour of the monitored system. The generated residual signals that indicate differences between the model's output and measured process output are interpreted and evaluated to isolate faults. Fault detection is realised after checking some measurable variables of a system in regard to a certain tolerance of the normal values and taking an appropriate action when a limit value is exceeded. Residuals are generated by comparing the sensed measurements to the predicted output of a model. The residuals are expected to be close to zero in fault tree cases but are distinguishably different from zero in the case of a fault in the system. Model-based diagnostic expert systems offer more robustness in diagnosis because they can deal with unexpected cases that are not covered by rule-based system. Difficulties with model-based fault detection methods arise from the fact that the accuracy of the measurements needed to calculate the evolution of faults should be of high quality. It requires high quality of sensors. The reliability of sensor itself induces certain kind of uncertainty.

From the above it is felt that there is a need for an integrated approach for diagnostics which can combine the advantages of the two diagnostic methods and CBM to provide a comprehensive diagnostic tool. This chapter presents an integrated approach for fault diagnosis and the architecture for such an integrated system is shown in Fig. 1.

3 Integrated Model-Based and Fuzzy Rule-Based Expert Diagnostic System with a Case Study on Diesel Generator Used in Nuclear Plant

The case study is conducted on 500-kVA diesel generator supplied by M/s GRSE Ltd., Calcutta and used in providing standby power supply to nuclear plant. The diagnostic tool will be developed for the lubricating oil system of the DG.

3.1 Expert Knowledge and System Characterisation

The first step is to assimilate as much knowledge about the system as possible. This can be achieved from system maintenance manual, historical data and expert opinion. This knowledge will be used in system characterisation, which is the process of physical and/or functional decomposition of system that identifies component level operating characteristics or parameters in product hierarchy essential to accomplish desired system level functional performance. The main

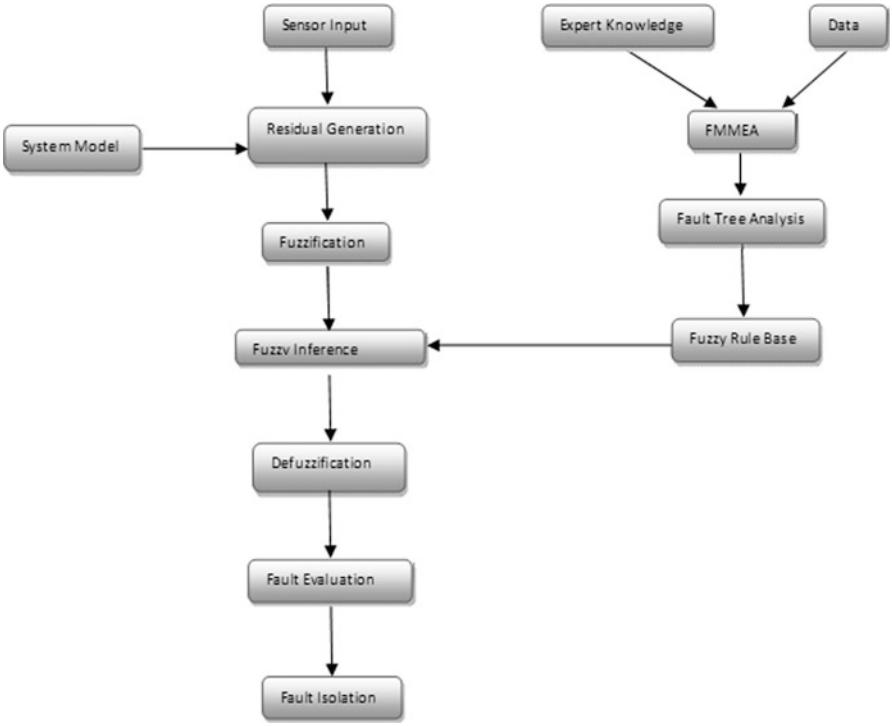

Fig. 1 Integrated model-based and fuzzy rule-based expert diagnostic system

purpose of this exercise is to develop a comprehensive understanding of the complex system function and working principle and to identify component level operating characteristics or design parameters. The basic aim is to develop a system knowledge based upon which the diagnostic tools will be made. Since the lubricating oil system of DG sets is used as case study, all the relevant information was collected from maintenance manual, historical data and expert opinion.

3.2 FMMEA and FTA

The next step is to carry out failure mode mechanism and effect analysis (FMMEA) and fault tree analysis (FTA) using the knowledge gained in step 3.1. The FMMEA is the procedure to recognise and evaluate the potential failure of the product and its effects and also to prioritise failure mechanism. The FMMEA provides information on *critical parameters* that when monitored will provide appropriate diagnostic information [6]. These critical parameters after identification need to be *modelled* to find out their effect on the system and to find out the fault baseline value. The FMMEA of lubricating oil system of DG set is shown in Fig. 2.

Failure Mode, Mechanism and Effect Analysis of Lubricating Oil System of Diesel Generator

Number	Description	Function	Potential Failure Modes	Failure Mechanism	Effect			Controlling Parameter
					Local Effect	Next higher Effect	End Effect	
1.1.0.1.1	Lubricating oil system	Provide lubricating oil to the bearings of diesel generator	Low Pressure	Lack of lubricating Oil in the oil sump				
1.1.0.1.2				Low Viscosity of Lubricating oil in the system low				Pressure, Temperature
1.1.0.1.3				Leakage from the system			Engine will fail to start	Pressure
1.1.0.1.4				Air inside the system				Pressure
1.1.0.1.5				Filter Fouling				Pressure
1.1.0.1.6				Failure of pressure regulating mechanism				Pressure
1.1.1.1.1	Oil Pump	Supplies oil to all bearing	Does not supply oil to bearing	Oil Pump break down	Low Pressure	Failure of pressure regulating mechanism	Low pressure	Pressure
1.1.2.1.1	Relief valve	Releases pressure if pressure in oil pump is >114psi	Unable to release pressure in oil pump	Component struck in closed position	Component breakdown	Damage to oil pump	Low pressure	Pressure
1.1.2.2.1			Unable to maintain pressure	Component struck in open position	Component breakdown	Low oil pressure	Low pressure	Pressure

Fig. 2 The FMMEA analysis of lubricating oil system of DG set

The next step is to carry out FTA, which is a reliability-based technique which illustrates the failure logic of the system and shows combination and sequence of failure which can lead to failure condition under condition (top event)[7]. The FTA helps in formulating the logical relationship between various systems and subsystems, which can be depicted using cut-sets.

These cut-sets will help in for formulation of fuzzy rules for fuzzy rule-based system. Figure 3 shows the fault tree for the problem of low oil viscosity in diesel generator.

Gates

B_1 = Low Oil viscosity B_2 = Heat Exchanger Not Working Properly

Basic Event

A_1 = Ageing of Oil A_2 = Leakage from Heat Exchanger

A_3 = Fouling in Heat Exchanger A_4 = Bye pass valve not working properly

Using FTA the Cut-sets obtained are:

$\boldsymbol{B_2 = A2\ U\ A3}$

$\boldsymbol{B_1 = A_1\ U\ A_2\ U\ A_3\ U\ A_4}$ or we have $\boldsymbol{B_1 = A_1\ U\ B_2\ U\ A_4}$

From the above cut-sets, we get the following rules:

If A_1 is high or A_2 is high or A_3 is high or A_4 is high, then viscosity is low
If A_1 is low or A_2 is low or A_3 is low or A_4 is low, then viscosity is normal

Similarly other rules can also be obtained from similar cut-sets.

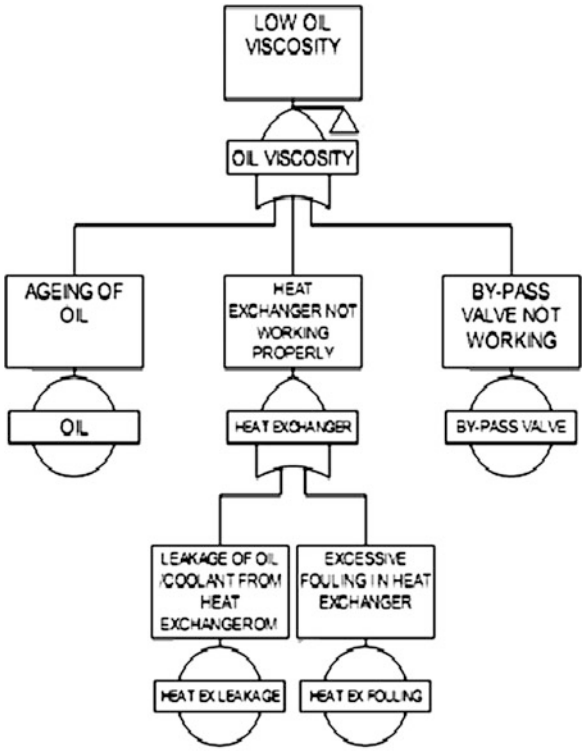

Fig. 3 Fault tree depicting the causes for low viscosity in lubricating oil in diesel generator

3.3 System Model

The FMMEA analyses have helped us in identifying the critical parameters with help of which we can get appropriate diagnostic information. Now the next step is to develop a transfer function, which is the representation of the mathematical relationship between component level operating characteristics (or design parameters) and system level functional outputs. A generic transfer function model for the functional output Y and the component level operating characteristics of parameter (inputs), X_i, is given as

$$Y = f(X_i), \quad i = 1, 2, 3 \ \ldots.$$

This mathematical model could either be linear or nonlinear depending upon the complexity of the system, working principle and laws of physics, which essentially define the system behaviour and functionality. The system model created then needs to be simulated, which will give us the healthy baseline of the parameter for each component. This healthy baseline when compared with the input from the sensors will give us the residual value, and the magnitude of this residual value will

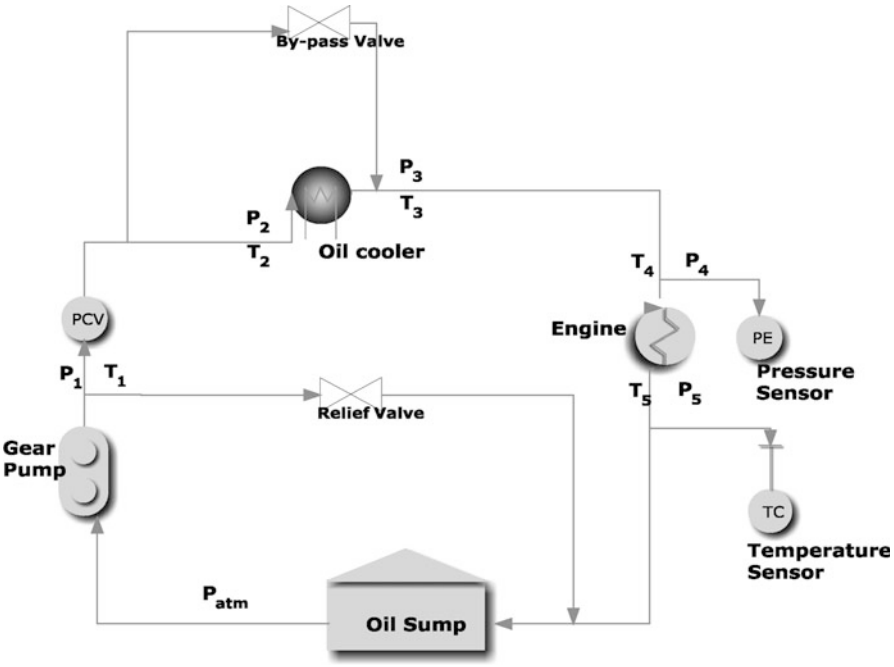

Fig. 4 Block diagram of lubricating oil System depicting the controlling parameters

indicate the malfunction in the component. The mathematical relations reflecting the state of various components of lubrication system are given below.

3.3.1 Mathematical Model of Flow Conditions and Heat Transfer Within the Lubrication System

When modelling the lubrication system of an engine (Fig. 4), the pressure losses and the resulting oil flow rate in one section had an effect on the pressures and flow rates in the other sections [12]. The mathematical model of flow condition within the lubricating system will help in finding the pressure and flow rate value at each component of the system. The full thermo fluid simulation of an engine lubrication system was achieved by an interaction between an analysis of the flow conditions and an analysis of the heat transfer within the system. *In diesel generator engine lubrication system, we will be considering heat conduction and internal forced convection only*. The heat loss due to radiation was small and thus neglected. The heat transfer within the lubrication system consists of two parts: heat transfer within the pressurised side of the system and heat transfer to the oil splashed onto the engine bearing. The mathematical model of lubrication system was made using the following assumptions:

1. It was assumed that there was negligible change in the oil temperature as it passed through non-heat-generating components, such as oil pump, oil filter and valves.
2. It was assumed that the heat generation in components like pipes and heat exchanger due to friction was considered as negligible and does not contribute to temperature rise. Only heat loss from these components was taken into account.
3. The flow of fluid is in single phase.
4. There is perfect contact at *interface* so that there is no temperature jump at the interface.
5. The heat transfer is in steady state, i.e. it does not vary with time at a point.
6. The fluid is Newtonian and incompressible.

3.3.2 Oil Pump

The relationship between flow rate and pressure difference can be expressed by

$$\text{Power} = (P_{\text{in}} - P_{\text{out}})Q/\eta$$

where P_{in} = pressure at inlet
P_{out} = pressure at outlet
η = efficiency of gear pump

3.3.3 Pipes

The friction losses through the pipe were represented by an adaption of the Darcy-Weisbach formula [8]

$$\Delta P = \frac{fL}{D}\,\rho\,\frac{V^2}{2}$$

The mean fluid temperature at the exit of pipe T_{e} as

$$T_{\text{e}} = T_{\text{s}} - (T_{\text{s}} - T_{\text{i}})\exp\left(\frac{hA_{\text{s}}}{\dot{m}C_{\text{p}}}\right)$$

Assuming constant surface temperature we get for fully developed laminar flow in a circular tube subjected to constant surface heat flux, the Nusselt number is given by

$$N_u = \frac{hD}{k} = 4.36$$

3.3.4 Oil Cooler

The pressure loss in oil cooler is calculated from equation given below [9]:

$$\Delta p = n_{\mathrm{p}}\left(4f\frac{L}{D}\frac{\rho u^2}{2} + K\frac{\rho u^2}{2}\right)$$

where n_{p} is the number of tubes and K is the number of velocity heads lost per pass due to entry, exits and turnarounds.

The method of number of transfer units (NTU) based on the concept of heat exchanger effectiveness is used for thermal analysis of heat exchanger. The overall heat transfer coefficient(U) for a heat exchanger depends upon the convective heat transfer coefficient between the hot fluid and the heat transfer surface, the thermal conductivity and thickness of the heat transfer surface, and the convective heat transfer coefficient between the heat transfer surface and the cold fluid. For the unfinned, clean tubular heat exchanger, the U is given by [10]

$$\frac{1}{UA} = \frac{1}{h_{\mathrm{o}}A_{\mathrm{o}}} + \frac{\ln\left(\frac{r_{\mathrm{o}}}{r_{\mathrm{i}}}\right)}{2\pi kl} + \frac{1}{h_{\mathrm{i}}A_{\mathrm{i}}}$$

Heat exchanger effectiveness is written as [9, pp. 57–60]

$$\varepsilon = \frac{C_h(T_{h1} - T_{h2})}{C_{\min}(T_{h1} - T_{c1})} = \frac{C_c(T_{c2} - T_{c1})}{C_{\min}(T_{h1} - T_{c1})}$$

Now number of transferable units (NTU) is given by

$$\mathrm{NTU} = \frac{AU}{C_{\min}}$$

where A = surface area, U = overall heat transfer coefficient and $C_{\min}$ = minimum heat capacity rate among the two fluids.

$$C* = \frac{C_{\min}}{C_{\max}}$$

where $C_{\min}$ and $C_{\max}$ are the minimum and maximum of the two heat capacities C_h and C_c. From the above relations we get for counter flow heat exchanger [10]

$$\varepsilon = \frac{1 - \exp\left[-\mathrm{NTU}\left(1 - \frac{C_{\min}}{C_{\max}}\right)\right]}{1 - \left(\frac{C_{\min}}{C_{\max}}\right)\exp\left[-\mathrm{NTU}\left(1 - \frac{C_{\min}}{C_{\max}}\right)\right]}$$

The above relations can be used to find out the inlet and outlet temperature of the lubricant in heat exchanger.

3.3.5 Main Bearing

Diesel engines contain partially grooved main bearings. Commonly, all the main bearings apart from the central main bearing were partially grooved. The groove extended for 180° around the circumference of the bearing, on the non-loaded side . The coefficient of fiction is given by [11]

$$f = 2\pi^2 \left(\frac{\mu n}{p}\right) \left(\frac{r}{c}\right)$$

The above equation is called *Petroff's* equation where

n = angular speed of shaft r.p.m

p = pressure or the radial load per unit of bearing projected area, which is given by $p = W/2rl$ where $W = wt$ of crank shaft on bearing

r = radius of shaft

l = length of bearing

r/c = clearance ratio which is obtained from charts

From the above equation we get the frictional torque as

$$T_{\mathrm{f}} = fFr$$

The frictional loss is given by

$$\Delta P = T_{\mathrm{f}}\omega$$

where ω is given by

$$\omega = \frac{2\pi n}{60}$$

The frictional heat generated can be found out from [11]

$$H_{\mathrm{g}} = Wf\omega$$

Now we get bearing characteristic number from

$$S = \left(\frac{r}{c}\right) 2\frac{\mu n}{p}$$

From the *Raimondi and Boyd,* we get the friction factor f

The oil temperature rise can be estimated from heat balance equations.

Heat dissipated: $H_{\mathrm{d}} = CA(T_{\mathrm{H}^-} T_{\mathrm{A}})$

A similar expression as above can be drawn for the temperature difference $T_{\mathrm{o}} - T_{\mathrm{H}}$ between the lubricating film and the housing. Here we have a new relation which depends upon the lubrication system and quality of lubricant circulation.

$$T_o - T_H = b(T_{H^-} T_A)$$

The value of b gives us the ratio of heat dissipated to lubricating oil to heat dissipated to surroundings. Combining above equations, we get

$$H_d = CA\left(\frac{1}{b+1}\right)\ (T_o - T_A)$$

$$H_d = CAB\ (T_o - T_A)$$

where $B = \left(\frac{1}{b+1}\right)$ and its value for self-contained bearing is $B = 0.954$

3.3.6 Valves and Bends

The pressure loss through valves and bends is called *minor loss* and is given by the equation [8]

$$\Delta P = K_{\mathrm{L}}\left(\frac{V^2}{2g}\right)$$

where K_{L} = *head loss coefficient having various values for various s components like elbow bend, T- bend and ball valve*.

3.3.7 Simulation

The simulation of mathematical model developed for the lubrication system of the diesel generator was performed using MATLAB/Simulink. The Simulink model was developed to have a rigorous evaluation of the mathematical model. The Simulink model is shown in Fig. 5.

3.3.8 Results of Simulation

The same are displayed in Table 1.

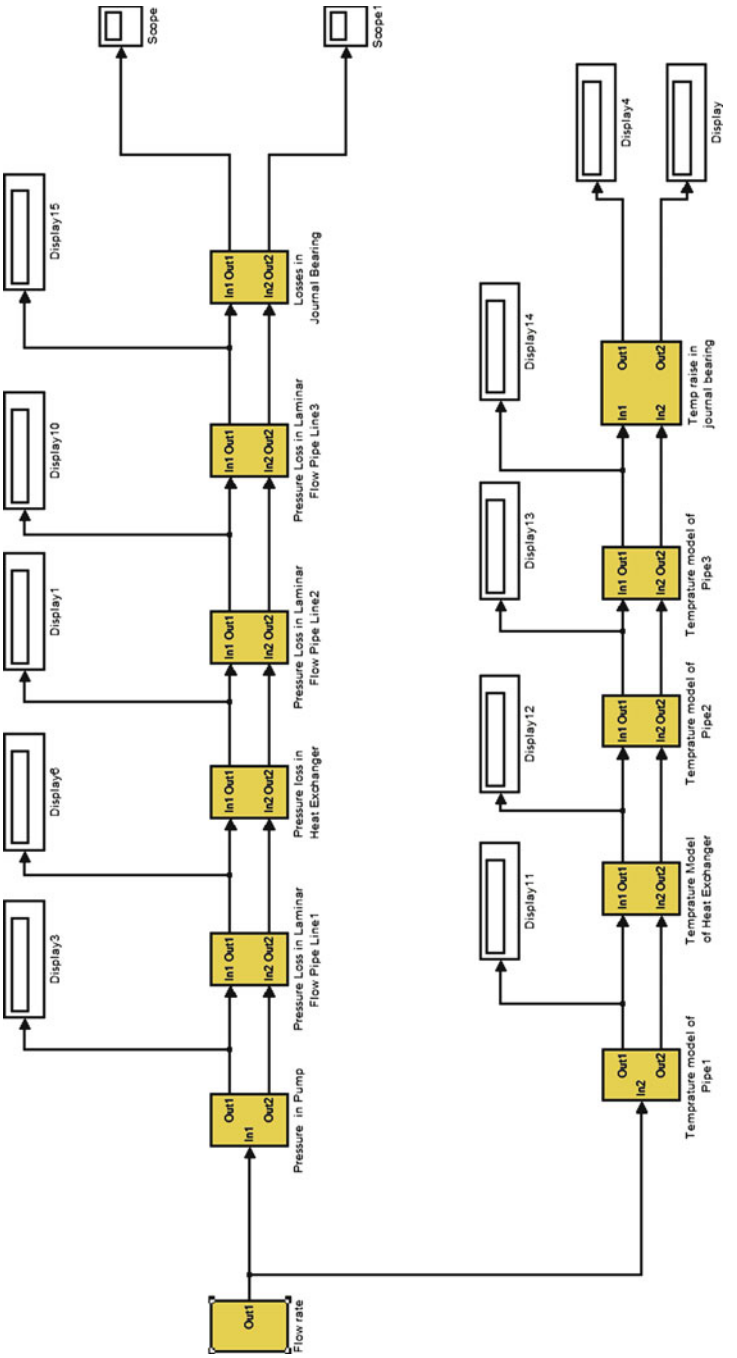

Fig. 5 Simulink model of DG lubricating system

Table 1 Results of simulation

Sl. no.	Nodal point	Variable	Value
1.	Outlet of pump	Pressure	7.9 kg/cm^2
2.	Outlet of pipe 1/inlet of oil cooler	Pressure	7.6 kg/cm^2
3.	Outlet of oil cooler/inlet of pipe 2	Pressure	5.8 kg/cm^2
4.	Outlet of pipe 2	Pressure	5.5 kg/cm^2
5.	Outlet of pipe 3	Pressure	5.3 kg/cm^2
6.	Outlet of journal bearing	Pressure	5.2 kg/cm^2
7.	Outlet of pipe 1/inlet of oil cooler	Temperature	308.7 K
8.	Outlet of oil cooler/inlet of pipe 2	Temperature	304.6 K
9.	Outlet of pipe 2	Temperature	304.0 K
10.	Outlet of pipe 3	Temperature	303.5 K
11	Outlet of journal bearing	Temperature	309.8 K

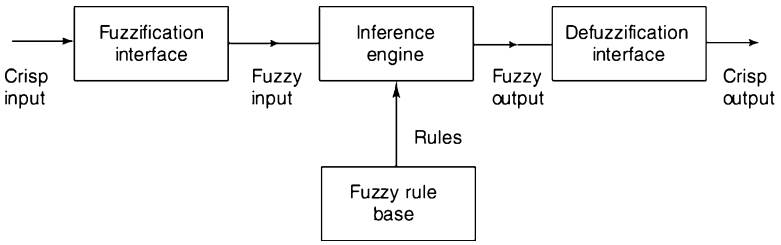

Fig. 6 Architecture of fuzzy inference system

3.4 Fuzzy Inference System

A fuzzy expert system is simply an expert system that uses a collection of fuzzy membership functions and rules, instead of Boolean logic, to reason about data. A fuzzy set A in X is defined as a set of ordered pairs.

$$A = \{(x, \mu_A(x)) \,|x \in X\}$$

where $\mu_A(x)$ is called the membership function (MF) for the fuzzy set A [13].

Figure 6 illustrates the basic architecture of a fuzzy expert system. The main components are a fuzzification interface, a fuzzy rule base (knowledge base), an inference engine (decision-making logic) and a defuzzification interface. Table 2 shows the linguistic variable for DG lubricant oil system for the event B. The input variables (which are the input from the sensors) are fuzzified whereby the membership functions defined on the input variables are applied to their actual values, to determine the degree of truth for each rule antecedent. Fuzzy if-then rules and fuzzy reasoning are the backbone of fuzzy expert systems, which are the most important modelling tools based on fuzzy set theory. The fuzzy rule base is characterised in the form of *if-then* rules in which the antecedents and consequents involve linguistic

Table 2 Linguistic variables and their states for an event

Event	Linguistic variable	State
A_1	Ageing of oil	Low/medium/high
A_2	Leakage	Low/medium/high
A_3	Fouling in heat exchanger	Low/medium/high
A_4	Bypass valve not working properly	Low/medium/high
B_1	Oil viscosity	Normal/low/very low

variables. This chapter presents the use of cut-sets from FTA in making fuzzy rules. From 5.2 we know that there are four events that lead to low oil viscosity: A_1, A_2, A_3 *and* A_4.

Now using the cut-set $B_1 = A_1\, U\, A_2\, U\, A_3\, U\, A_4$, we have 4 events and each event linguistic variable has been given 3 states. Therefore, the total number of combination is $4^3 = 64$. Thus, we will have 64 fuzzy rules from these cut-sets. It is important to note here that although there is only one Boolean relation, there are 64 fuzzy rules. Thus the biggest advantage of using fault tree for making the fuzzy rule bases system is that the rule base is more comprehensive and the chances of human error are minimised. Similarly if a cut-set has 5 events, then the number of fuzzy rules is $5^3 = 125$. Now consider the rules

R_1 = *if* A_1 *is high or* A_2 *is medium or* A_3 *low or* A_4 *is medium, then viscosity is very low.*

R_2 = *if* A_1 *is medium or* A_2 *is medium or* A_3 *low or* A_4 *is medium, then viscosity is low.*

The collection of these fuzzy rules forms the rule base for the fuzzy logic system. Using suitable inference procedure, the truth value for the antecedent of each rule is computed and applied to the consequent part of each rule. This results in one fuzzy subset to be assigned to each output variable for each rule. Again, by using suitable composition procedure, all the fuzzy subsets assigned to each output variable are combined together to form a single fuzzy subset for each output variable. Finally, defuzzification is applied to convert the fuzzy output set to a crisp output. The basic fuzzy inference system can take either fuzzy inputs or crisp inputs, but the outputs it produces are always fuzzy sets. The defuzzification task extracts the crisp output that best represents the fuzzy set. With crisp inputs and outputs, a fuzzy inference system implements a nonlinear mapping from its input space to output space through a number of fuzzy if-then rules. There are several defuzzification techniques. The most widely used defuzzification technique uses the centroid of area method as follows:

$$\text{Centroid of area } Z = \frac{\int \mu_A(z) z dz}{\int \mu_A(z) dz}$$

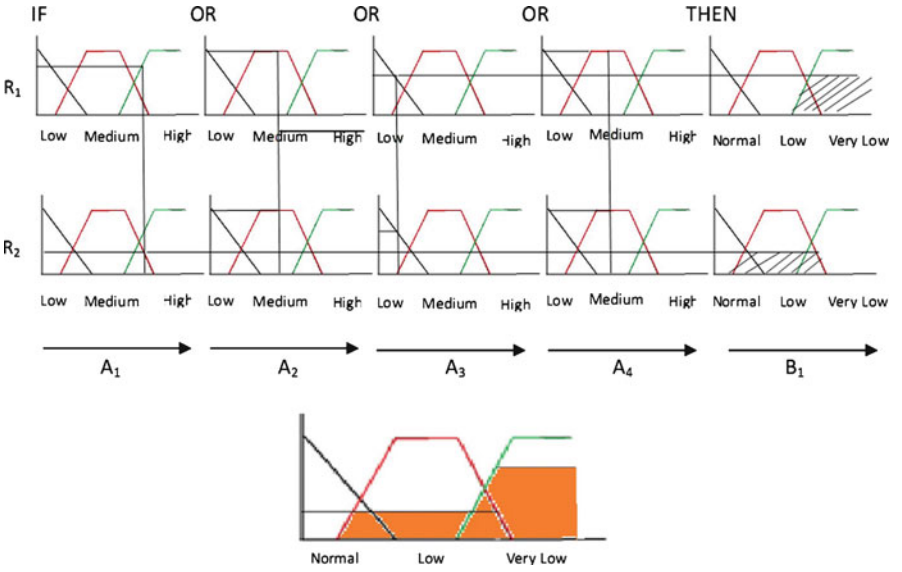

Fig. 7 Process of fuzzification and defuzzification

Figure 7 shows the fuzzification and defuzzification process using the rules R_1 and R_2 for the low-viscosity fault of lubricating oil system of diesel generator.

4 Conclusion

The health monitoring and diagnostics of a modern machine is a complex phenomenon. Often the health monitoring tools provided by the manufacturer are inadequate. Therefore, the user needs to develop its own diagnostic and health monitoring tools. But the biggest challenge in such cases is the lack of data or scarcity of data. This chapter proposes an integrated methodology wherein the system characterisation is done with the help of reliability-based methods like FMMEA and FTA, which help in qualitative analysis of the system. They depict the logical relationship between the component of the system and system response, which will help in formulation of rule-based system. The methodology further proposed the use of fuzzy rule-based system which utilises the capability of human expert in predicting system health, thus eliminating the dependencies on human expert and can be used by nonexpert. The proposed methodology uses modelling of system and its simulation for getting the healthy baseline and failure definition of various failures parameters. This information will be used in fuzzy rule-based system for making membership function.

Acknowledgement The authors would like to thank Shri V.K. Raina, director, reactor group, BARC, and Shri R.C. Sharma, head RRSD, BARC, for giving us opportunity to work on diesel generator used in nuclear plant.

References

1. Korbicz J (2010) Modeling, diagnostics and process control. Springer, Berlin/Heidelberg
2. Jardine AKS et al (2006) A review on machinery diagnostics and prognostics implementing condition based maintenance. Mech Syst Signal Process 20(7):1483–1510
3. Kothamasu R et al (2006) System health monitoring and prognostics-are view of current paradigms and practices. Int J Adv Manuf Technol 28:1012–1024
4. Gmytrasiewicz P et al (1990) Fault tree based diagnostics using fuzzy logic. IEEE Trans Pattern Anal Mach Intell 12(11):1115–1119
5. Peng Z et al (2008) An approach of fault diagnosis for system based on fuzzy fault tree. In: International conference on multimedia and information technology, Chiang Mai, Thailand 3–5 July, pp 697–700
6. Analysis techniques for system reliability – Procedure for failure mode and effects analysis (FMEA) International Standard IEC 60812
7. Fault Tree Handbook NUREG-0492
8. DOE Fundamentals Handbook (1992, June) Thermodynamics, heat transfer, and fluid flow vol.3. U.S. Department of Energy
9. Butterworth D (2002) Design of shell-and-tube heat exchangers when the fouling depends on local temperature and velocity. Appl Therm Eng 22:789–801. www.elsevier.com/locate/apthermeng
10. Kakac S (2002) Heat exchangers selection rating and thermal design. CRC Press, Boca Raton
11. NPTEL-Machine Design II-Module5 http://nptel. iitm .ac.in/courses/IIT- MADRAS/Machine Design II/
12. Munson (2009) Fundamentals of fluid mechanics. Wiley, New York
13. Sivanandam SN et al (2007) Introduction to fuzzy logic using MATLAB. Springer, Berlin/Heidelberg

Structural Reliability and Integrity Assessment of a Thin Maraging Steel Cylindrical Pressure Vessel

P. Bhattacharjee, K. Ramesh Kumar, and T.A. Janardhan Reddy

Abstract High reliability and operational safety are most important requirements of an aerospace product. Traditionally, structural safety in the design is ensured by implementing appropriate safety factors to account for shortcomings stemming from lack of knowledge, insufficient data or inherent variability. The factor of safety concept does not provide a quantitative measure of the structural reliability. Even with the implementation of the safety factor, there exists a finite probability of failure of a structure. In this chapter, a thin maraging steel cylindrical pressure vessel is identified for structural reliability and safety analysis. Thin maraging cylindrical pressure vessels are used extensively in aerospace vehicles. Reliability (safety index) analysis is carried out using actual data collected during design, manufacturing and testing. Two distinct failure modes, i.e. fracture failure and plastic yielding, are considered for safety evaluation. The structural integrity is evaluated using an empirical model to predict the burst pressure. Moment methods are used for reliability analysis. This chapter will help pressure vessel designer to assess the structural safety and integrity during preliminary design.

Keywords Structural reliability • Cylindrical pressure vessel • Moment methods • Burst pressure and safety index

P. Bhattacharjee (✉)
Reliability Engineering Division, DRDL, Hyderabad, India
e-mail: pradeep9_rqa@yahoo.com

K.R. Kumar
Production Planning Division, DRDL, Hyderabad, India
e-mail: rkkatta@rediffmail.com

T.A. Janardhan Reddy
Mechanical Engineering, OU, Hyderabad, India
e-mail: thanam.engineer@gmail.com

S. Chakraborty and G. Bhattacharya (eds.), *Proceedings of the International Symposium on Engineering under Uncertainty: Safety Assessment and Management (ISEUSAM - 2012)*,
DOI 10.1007/978-81-322-0757-3_68,

1 Introduction

Traditionally, structural safety is defined in terms of safety factors, which are used to compensate for uncertainties in loading, material properties and inaccuracies in geometry. Probabilistic approaches in design result in more accurate measures of safety. Structural safety is measured in terms of probability of failure to satisfy some performance criterion. The probability of failure is often expressed in terms of a reliability index. This reliability index is evaluated using various statistical methods such as moment, response surface and simulation. The moment method is discussed in detail in this chapter.

To achieve high reliability, the quality has to be built into the design. It starts from selection of raw material, manufacturing and testing to final product realization. In case of pressure vessels, the product designer will not be confident until the product is tested to its ultimate limit. In many cases, the product is tested till its destruction.

In this chapter, the structural reliability (reliability index) evaluation is carried out for a thin maraging steel cylindrical pressure vessel. The plastic and elastic failure modes are considered as important failure modes. Few pressure vessels are identified and their data collected during manufacturing and testing. Finally, three identical vessels are subjected to ultimate hydraulic load till they burst. Burst pressure results are compared with suggested empirical model. The structural reliability evaluation methodology is discussed in detail and will be useful to pressure vessel designer during initial design phase.

2 Nomenclature

D	:	Diameter
$g(\mathbf{x})$, $G(\mathbf{x})$, M	:	Limit state function
K_{IC}	:	Plane strain fracture toughness
P	:	Pressure
P_f	:	Probability of failure
R	:	Resistance
R_i	:	Internal radius
S	:	Strength
t	:	Thickness
Z	:	Stress
α	:	Direction cosine
α'	:	Crack length in transverse direction
β	:	Reliability/safety index
β'	:	Crack shape factor
μ_m	:	Mean of limit state

σ_m : Standard deviation of limit state
σ_{ys} : Yield strength
σ_{ult} : Ultimate strength

3 Structural Reliability

Uncertainties and randomness associated with both loads and structural characteristics introduce variability in structural response. The predicted response of structure based on mathematical and statistical models with imperfect knowledge tends to depart from reality. Recent developments in the area of probabilistic methods and statistical inference offer a mathematical basis that will enable designer to incorporate the influence of variability and uncertainties arising from a variety of sources more effectively into design process. Some of these developments are discussed in this chapter from the standpoint of reliability of thin maraging steel cylindrical pressure vessel structure.

The structural analysis is accomplished by examining the limit state, which describes the conditions that render a structure unsatisfactory for one of the intended roles under one load effect or a combination of load effects. From the ultimate strength standpoint, the limit state equations are generally expressed in terms of structural resistance and load effects, whereas, for serviceability, the limit state equations represent the evaluation of a performance criterion.

The two basic variables representing action and resistance are function of a number of other variables. An increase in number of variables in the limit state equation and the departure of their distributions from the normal together with a nonlinear failure function introduces complexity to the problem. In such case, the limit state, $(G = R - S = 0)$, is a hypersurface of n-dimensional space and separates the failure and safe regions. The probability of failure is equal to the volume integral over the failure region [1]:

$$p_f = \int_{G(X)<0} f_x(X)dx \tag{1}$$

in which $f_x(X)$ is the joint probability density function of the n-dimensional vector X. The preceding integral may be evaluated by means of one of the following techniques or combination of either, viz.,

(a) numerical integration, (b) approximation methods and (c) simulation.

In this chapter, we discuss on approximation methods.

The reliability index β is defined as

$$\beta = -\Phi^{-1}(p_f) \text{ i.e. } p_f = \Phi(-\beta) \tag{2}$$

where Φ is the standard normal cumulative distribution function.

3.1 Approximate Methods

The advantages of the analytical methods are mainly that they are simple, have apparent physical interpretations and do not usually require excessive computation time. Analytical methods are first-order reliability method (FORM) and second-order reliability method (SORM) [2, 3], respectively, also known as moment methods discussed as under

3.1.1 Mean-Value First-Order Second Moment Method (MVFOSM)

The limit state function can be presented as follows:

$$M = g(x_1, x_2, \ldots x_n) \tag{3}$$

where x_i are the load and strength parameters considered as variables and the limit state function $g(.)$ is a function that relates their variables for the limit states of interest (serviceability or ultimate state). The limit state is reached when

$M = g\ (x_1, x_2, \ldots x_n) \leq 0$

The probability of failure can be calculated by integrating Eq. (1). This reliability analysis can be very difficult to apply in practice. The two main reasons for it are lack of information to determine the joint probability density function of the design variables and the difficulty associated with evaluation of the resulting multiple integrals because of the complexity of the limit state function.

The limit state function can be expanded using Taylor's series; if only the first-order terms are retained, we get

$$g(x_1, x_2, ..., x_n) \approx g\left(x_1^*, x_2^*, ..., x_n^*\right) + \sum_{i=1}^{n} \left(x_i - x_i^*\right) \left(\frac{\partial g}{\partial x_i}\right)_{x^*} \tag{4}$$

where x_i^* is the linearization point and the partial derivatives are evaluated at that point. In the MVFOSM method, the linearization point is set at the mean value $(E(x_1), E(x_2), ..., E(x_n))$.

The mean and variance of M are then approximated by

$$\mu_m \approx g(\mu_1, \mu_2, ...\mu_n) \tag{5}$$

$$\sigma_m^2 \approx \sum_i \sum_j \left(x_i - x_i^*\right) \left(\frac{\partial g}{\partial x_i}\right)_{\bar{x}_j} \left(\frac{\partial g}{\partial x_j}\right)_{\bar{x}_j} \rho_{x_i x_j} \sigma_{x_i} \sigma_{x_j} \tag{6}$$

where $\rho_{x_i x_j}$ is the correlation coefficient and the $\left(\frac{\partial g}{\partial x_i}\right)_{\bar{x}_j} \left(\frac{\partial g}{\partial x_j}\right)_{\bar{x}_j}$ denote evaluation of the partial derivatives at the mean point $\mu_i = E(x_i) = \bar{x}_i$,

$$\sigma_m^2 \approx \sum_i \left(\frac{\partial g}{\partial x_j}\right)^2_{\bar{x}_j} \sigma_{x_i}^2 \tag{7}$$

The standardized margin G_M, which has a zero mean and a unit standard deviation, can be written as

$$G_M = \frac{M - \mu_m}{\sigma_m} \tag{8}$$

Failure occurs when $M \leq 0$ so that the probability of failure can be written as $p_\mathrm{f} = p[M \leqslant 0]$:

$$p_\mathrm{f} = p[M \leq 0] = F_M(0) = F_{GM}\left(\frac{-\mu_m}{\sigma_m}\right) = F_{GM}(-\beta) \tag{9}$$

where $\beta = \frac{\mu_m}{\sigma_m}$ is safety index, which is the inverse of the coefficient of variation of the safety margin and the probability of failure is thus $p_\mathrm{f} = \Phi(-\beta)$.

3.1.2 Hasofer–Lind Method (HL)

Hasofer and Lind (HL) [4] attributed instead of expanding Taylor's series about the mean-value point, which cause the invariance problem; the linearization point is taken at some point on the failure surface. On the failure surface, the limit state function $g(.)$ and its derivatives are independent of how the problem is performed. In the Hasofer–Lind procedure, the load and resistance variables, x_i, are transformed to standardized variables with zero mean and unit variance by

$$Y_i = \frac{x_i - \mu_i}{\sigma_{x_i}} \tag{10}$$

The HL reliability index is defined as the shortest distance from the origin to the failure surface in the reduced (standardize) space. This point is found by solving the following set of equations:

$$G\left(y_1^*, y_2^* \ldots . y_n^*\right) = 0 \tag{11}$$

$$y_i^* = -\alpha_i^* \beta \tag{12}$$

$$\alpha_i^* = \frac{\left(\frac{\partial g}{\partial y_i}\right)_{y_i^*}}{\sqrt{\sum_i \left(\frac{\partial G}{\partial y_i}\right)^2_{y_i^*}}} \tag{13}$$

G (.) is the failure surface in the reduced space, and μ_i^* are coordinates of point closest to the origin in the reduced space.

All the partial derivatives are evaluated at the design point. In effect, this procedure is equivalent to linearizing the limit state function in the reduced variable space at the checking point and computing β associated with that point.

In the original space, the checking point is obtained as below:

$$x_i^* = \bar{x}_i + \sigma_{x_i} x_i^* = \bar{x}_i - \sigma_{x_i} \alpha_i \beta \tag{14}$$

In general, for a linear limit state function, the Hasofer–Lind method will yield the same result for 'β' as the MVFOSM method.

4 Structural Integrity

4.1 Burst Pressure Evaluation

The structural integrity of an aerospace pressure vessel is very important; the designer will be confident if burst pressure (structural integrity) can be predicted. There are many empirical methods that have been suggested by various authors [5, 6]; in this chapter, a series of pressure vessel of different types have been subjected to burst pressure. The details of these vessels, their dimensions and burst pressure are given in Table 1. In case of thin maraging cylindrical pressure vessel, the burst occurs without yielding as there is no considerable difference between the yield strength (σ_y) and ultimate tensile strength (σ_{ult}). The burst pressure data have been used for regression modelling. The regression relation Eq. (15) is the empirical model for thin maraging steel cylindrical pressure vessel. This model is statistically verified for significance test, and regression coefficients are shown below:

$$P_{burst} = 50 + 2710\left(\frac{t}{R_i}\right) - 62\left(\frac{\sigma_{ys}}{\sigma_{ult}}\right) \tag{15}$$

$R^2 = 0.9977$ (R-square) and $R_{adj}{}^2 = 0.9969$ (R-square adjusted)

Table 1 Burst pressure

Vessel type	(t/R_i)	$(\sigma_{ys}/\sigma_{ult})$	Burst pressure (MPa)
1	0.0254	0.9656	60
2	0.0400	0.9874	94
3	0.0377	0.9874	92
4	0.0119	0.9497	22
			24.3
5	0.0125	0.9806	23.34
			23.25
			22.07
6	0.0355	0.9874	87

Table 2 Design parameter (type 5)

Internal Diameter	:	222.5 mm
Working P_r	:	10.30 MPa
Design P_r	:	13.24 MPa
Proof P_r	:	19.86 MPa
Thickness	:	1.4 mm
Design code	:	ASME Pressure Vessel

Table 3 Parameter variability

Sl. no.	Parameter	Mean (μ)	Standard deviation (σ)
1	Pressure (P)	13.24 MPa	0.5297
2	Internal diameter (D)	222.5	0.15
3	Thickness (t)	1.4	0.025
4	Fracture toughness (K_{IC})	94.44	3.84
5	UTS	1750 Mpa	50
6	α'	1	0.15
7	β'	1.12	0.112

5 Design Data

The design data of the present thin maraging cylindrical pressure vessel (type 5) obtained from the design document are given in Table 2.

6 Manufacturing Data

Pressure vessel (type 5) data collected time to time from manufacturing centre, viz., internal diameter, thickness and ovality. Other material properties like ultimate tensile strength, yield strength and fracture toughness have been generated in material testing lab. The details of various parameters and their variability are placed in Table 3.

7 Analysis

In this chapter, the failure modes considered are plastic failure and elastic fracture [7, 8]. All the physical quantities are considered realistically as statistical variables, including the fracture toughness, yield stress, radius, thickness, crack size, crack geometry and maximum operating load. The elastic fracture occurs when

$$\frac{PD\beta'\sqrt{\pi\alpha'}}{4tK_{IC}} \geq 1.0 \tag{16}$$

Similarly plastic collapse takes place when

$$\frac{PD}{2tS} \geq 1.0 \tag{17}$$

All the physical quantities appearing in above equations are considered realistically as statistical variables. The limit state function is written as

$$g_1 = \left(S - \frac{0.5PD}{t}\right) \tag{18}$$

$$g_2 = \left(K_{IC} - 0.4431\frac{PD\beta'\sqrt{\alpha'}}{t}\right) \tag{19}$$

7.1 Reliability Index

The reliability index (β) is evaluated [9, 10] for both the failure modes, using Hasofer–Lind method, and the β values are found as below:

$$\beta_{\text{Plastic}} = 9.97$$
$$\beta_{\text{Elastic}} = 11.69$$

7.2 Structural Integrity

The structural integrity of pressure vessel (type 5) that is collapse load (burst pressure) is predicted using Eq. (15) as shown below:

$$P_{burst} = 50 + 2710\left(\frac{t}{R_i}\right) - 62\left(\frac{\sigma_y}{\sigma_{ult}}\right)$$

where $t = 1.4$, $R_i = 111.25$, $\sigma_y = 1{,}720$, $\sigma_{\text{ult}} = 1{,}750$ and $P_{\text{burst}} = 23.16$ Mpa (236 Kg/cm^2).

Table 4 Burst pressure MPa

Sl. no.	Predicted	Observed	% error
1	23.16	23.33	0.73
2	23.16	23.24	0.34
3	23.16	22.06	4.7

7.3 Model Validation

The structural integrity empirical model Eq. (15) is used to evaluate burst pressure prediction. The predicted and observed burst pressure data are placed in Table 4.

8 Results and Discussion

The structural reliability for flawless thin maraging steel cylindrical pressure vessel is evaluated for plastic and elastic failure mode. $\beta > 9$ indicates that the reliability of the vessel is of very high order, and these vessels are safe for aerospace applications. The structural integrity of the vessels (burst pressure) is also found high as the ratio of burst pressure to design pressure is 1.75.

9 Conclusion

The structural reliability of maraging steel cylindrical pressure vessel is evaluated using Hasofer–Lind method. This methodology will be very useful to pressure vessel designer during design phase as this analysis adds to confidence. The maraging steel cylindrical pressure vessels are extensively used in aerospace vehicle, and hence their safety and integrity are the most important requirements. The empirical models to predict burst pressure are validated and found in good agreement with experimental results. This model will be useful to designer during preliminary design stage.

Acknowledgement The constant encouragement and support extended by Director DRDL and help rendered by Director R&QA DRDL are gratefully acknowledged. We also like to extend our sincere thanks to Mr K Ramesh Scientist DRDL for providing excellent technical support.

References

1. Robinson DG (1998) A survey of probabilistic methods used in reliability, risk and uncertainty analysis analytical techniques-I SANDIA REPORT SAND 1998
2. Melchers RE (1987) Structural reliability analysis and prediction. Ellis Harwood Limited, Chichester, pp 104–141

3. Dai S-H, Wang M-O (1992) Reliability analysis in engineering applications. Van Nostrand Reinhold, New York, pp 61–132
4. Wong FS (1985) First –order second –moment method. Comput Struct 20(4):779–791
5. Christopher T, Rama Sarma BSV et al (2002) A comparative study on failure pressure estimations of unflawed cylindrical pressure vessels. Int J Press Vessel Pip 79:53–66
6. Bhattacharjee P, Ramesh Kumar K, Janardhan Reddy TA (2010) Structural reliability and an empirical approach to burst pressure prediction of thin maraging steel cylindrical pressure vessel. In: 3rd international conference on advance in mechanical engineering, pp 428–432
7. Yang JN, Chen HY, Chang CM, Shee HK (1993) Reliability analysis and quality assurance of rocket motor case considering proof testing. In: AIAA/ASME/ASCE/AHS/ASC structures, structural dynamics, and materials conference, 34th and AIAA/ASME adaptive structures forum, La Jolla, CA, 19–22 April, pp 714–733
8. Zheng W (1993) Structural reliability design on solid rocket motor case. In: AIAA/SAE/ASME/ASEE 29th joint propulsion conference and exhibit, Monterey, CA, 28–30 June, pp 1–5
9. Bhattacharjee P (2009) Structural reliability assessment of pressure vessel. J Aerosp Qual Reliab 5(1):159–163
10. Bhattacharjee P, Ramesh Kumar K, Janardhan Reddy TA (2010) A comparative study of probabilistic structural safety analysis of a titanium pressure vessel. J Aerosp Sci Technol 62 (4):1–8

Performance of N-Z Base Isolation System for Structures Subject to Underground Blast

Papiya D. Mondal, Aparna (D.) Ghosh, and Subrata Chakraborty

Abstract Blast-induced ground vibration due to construction and mine blasting can cause substantial damage to nearby structures. It is thereby important to study the effectiveness of established vibration control technologies to the blast-resistant design of structures. In the present work, an attempt is made to study the effectiveness of the New Zealand (N-Z)-type base isolator devices in mitigating structural vibration effects due to underground blast. For the purpose, the blast load is modelled by an exponentially decaying function representative of a typical rock blast. The superstructure is idealised as a linear, viscously damped, single-degree-of-freedom (SDOF) system. The nonlinear force-deformation of the N-Z system is represented by Bouc-Wen's bilinear model, and the dynamic response analysis is performed in the time domain. The influence of various parameters of the base-isolated system on the performance of the N-Z-type base isolator is investigated. Results indicate that the base isolation technology is highly effective in reducing both the structural acceleration and displacement. However, when the blast load intensity is high, the peak displacement of the base isolator and its permanent deformation may be of concern. These can be restricted by adopting a proper combination of the parameters of the N-Z system, without significantly compromising the response reductions obtained by it.

Keywords Base isolation • N-Z system • Bilinear model and Underground blast-induced ground motion

P.D. Mondal (✉) • A.(D.) Ghosh • S. Chakraborty
Department of Civil Engineering, Bengal Engineering and Science University, Shibpur, Howrah, India
e-mail: papiya.mondal@gmail.com; aparna@civil.becs.ac.in; schak@civil.becs.ac.in

S. Chakraborty and G. Bhattacharya (eds.), *Proceedings of the International Symposium on Engineering under Uncertainty: Safety Assessment and Management (ISEUSAM - 2012)*,
DOI 10.1007/978-81-322-0757-3_69,

1 Introduction

Ground vibration generated from construction activities and mine blasting can cause major damage to adjacent structures. The accidental blasting of underground ammunition storage is another source of significant damage to nearby structures. Constraints on space, cost and safety issues have limited the number of experimental investigations on structural response and damage due to blasting, though there are several simulation studies on the same by various researchers (Dowding [3], Wu and Hao [17], Hao and Wu [6], Carvalho and Battista [2], etc.). To mitigate the blast vibration effect on structures, various codes and regulations (NATO [12], GSO [4], etc.) recommend different criteria that were predominantly established from empirical correlations between observed damage and recorded peak velocities during field blast tests. These criteria have many lacunae as they do not consider the inherent structural condition, site condition and ground motion features. Hence, the protection of structures subjected to blast-induced ground motion (BIGM) needs careful attention.

Over the last few decades, there have been extensive efforts by researchers in the development of structural vibration control technologies such as those of base isolation, viscous fluid dampers, tuned mass and liquid dampers for earthquake and wind loading. It may be noted that even though earthquakes and underground blast both cause ground vibrations, blast pulses are extremely dissimilar from seismic motions as they are characterised by large-amplitude, high-frequency waves and are of extremely short duration. Hence, specific studies are needed on the applicability of established vibration control technologies to structures subjected to underground blast, which is hitherto a largely unexplored area.

Some limited studies on vibration control methodology for blast loading in the open literature include those by Miyamoto and Taylor [11] and Wu et al. [18]. Miyamoto and Taylor [11] evaluated the effectiveness of fluid viscous dampers in the reduction of responses of steel buildings subjected to air blast. Wu et al. [18] proposed the mitigation of ground shock effects on structures by the provision of a sand layer in the foundation of the structure. The sand base was found to be effective in reducing the structural response and damage. This particular study was a motivating factor for the present paper.

One of the most established and widely implemented base isolator devices is the lead-plug or N-Z bearing which was first introduced in New Zealand and is basically the laminated rubber bearing with a central lead core. A large number of experimental as well as analytical studies were made by various researchers in controlling the structural vibration due to seismic excitation. Interestingly, there are also some studies on base-isolated structures subjected to near-fault earthquakes which are characterised by large, high-energy pulse-like signals, similar to blast motions. Though earlier studies by Heaton et al. [7], Hall et al. [5], etc. were discouraging due to excessive bearing displacements, Jangid and Kelly [10] and Alhan and Gavin [1] reported that lead rubber bearings with appropriate properties are quite effective for seismic isolation of structures subjected to near-fault

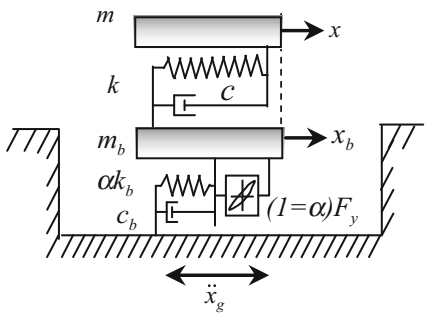

Fig. 1 2-DOF system with N-Z bearing

motions. Jangid and Kelly [10] showed that there exists an optimum damping of the isolation system for which the superstructure acceleration attains a minimum value. Further, the optimum yield strength of the N-Z system under different system parameters was derived by Jangid [9]. Supplemental viscous dampers to mitigate the large isolator displacements under near-fault ground motion were studied by Providakis [13]. It is thus felt that it would be meaningful to undertake a study on the performance of base isolation system for ground motion caused by an underground explosion.

In this paper, to study the effectiveness of base isolation technology against underground BIGM, the superstructure is modelled as a linear, viscously damped SDOF system. It must be noted that ground shocks can involve vertical components which may also induce significant amount of vibration effects on structures. However, for the current investigation, only horizontal excitation is considered. Parametric studies are carried out on the base-isolated system, and the influence of the various important BI parameters observed here is the isolation period, yield strength, rigidity ratio and damping ratio. The intensity of the blast input is another parameter studied here. The focus of the parametric study is to find the existence of optimum parameters, if any, by considering the optimality criteria as the minimisation of both the peak absolute acceleration and peak base displacement. The vibrational characteristics of the BI are also studied in detail.

2 Modelling of the Structure-Base Isolator System

For a single-storied building on N-Z-type BI as shown in Fig. 1, the equation of motion of the mass, m, may be written as

$$m\ddot{x} + c\dot{x} + kx = -m\left(\ddot{x}_g + \ddot{x}_b\right) \tag{1}$$

where m, c and k are the mass, damping and stiffness of the superstructure modelled as a SDOF system; x is the displacement of the superstructure measured with respect to the base mass; and overdot represents differentiation with respect to time. $\ddot{x}_g$ is the

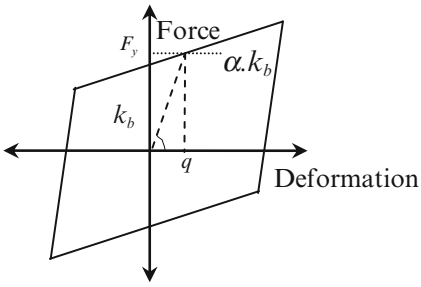

Fig. 2 Force-deformation of N-Z system

blast-induced horizontal ground acceleration, and $\ddot{x}_b$ is the acceleration of the base mass measured with respect to ground. The SDOF system model as described above is considered to be linearly elastic in the present study. The equation of motion for the base mass can be written as

$$m_b\ddot{x}_b + F_b - c\dot{x} - kx = -m_b\ddot{x}_g \tag{2}$$

where m_b is the mass of the base isolator and F_b is the restoring force exerted by the N-Z system. The ratio of the base mass to the mass of the superstructure is given by $\mu = (m_b/m)$.

2.1 Mathematical Model of the N-Z system

In the N-Z-type base isolation system, the lead core provides an additional damping to reduce the bearing displacement, and energy dissipation occurs due to yielding of the lead core. Here, the force-deformation behaviour is nonlinear and is generally expressed by the bilinear model shown in Fig. 2. This behaviour can be approximated by Bouc-Wen's equation ([16]). The horizontal force (F_b) induced in the N-Z system in the post-yield phase can be expressed as the sum of three forces acting in parallel as follows:

$$F_b = c_b\dot{x}_b + \alpha k_b x_b + (1-\alpha)F_y Z \tag{3}$$

where c_b represents the viscous damping; k_b is the initial stiffness of the N-Z bearing; x_b and $\dot{x}_b$, respectively, represent the displacement and velocity of the bearing measured relative to ground; α is the rigidity ratio, i.e. ratio of the post- to pre-yield stiffness; F_y is the yield force of the lead plug; and Z is the nondimensional hysteretic component and is expressed by the following nondimensional first-order differential equation:

$$q\dot{Z} = A\dot{x}_b - \gamma|\dot{x}_b|Z|^{\eta-1} - \beta\dot{x}_b|Z|^{\eta} \tag{4}$$

where q is the yield displacement of the bearing and is given by F_y/k_b. β, γ and A are the nondimensional parameters of the hysteresis loop. η is an integer which

controls the transition from elastic to plastic response. The parameters α, β, γ, η and A control the shape of the loop and are selected such that the predicted response from the model closely matches with the experimental results. It may be noted from Eq. (3) that the value of α is within the range of $0 \leq \alpha \leq 1$, and lower value of α is associated with greater elasto-plastic behaviour, i.e. greater degradation of stiffness beyond yield. For the same initial stiffness (k_b), yield displacement is proportional to the normalised yield strength. The parameters adopted for the present study are $\beta = \gamma = 0.5, A = 1$ and $\eta = 1$ as considered by Jangid [9]. α is selected in such a way that the design value of the post-yield stiffness provides the specific value of the isolation period, T_b, of the N-Z bearing. The isolation period, T_b , and the damping ratio of the bearing (ξ_b) can be expressed as

$$T_b = 2\pi\sqrt{\frac{M_0}{\alpha k_b}} \tag{5}$$

$$\xi_b = \frac{c_b}{2M_0\omega_b} \tag{6}$$

where $M_0 = (m_b + m) =$ total mass of the building and $\omega_b = 2\pi/T_b$ is the base isolation frequency. Thus, the N-Z bearing is characterised by the isolation period (T_b), damping ratio (ξ_b) and normalised yield strength $\left(F_0 = F_y/W\right)$, in which $W = M_0 g$ is the total weight of the isolated building and g is the acceleration due to gravity. Now Eq. (2) can be restructured by substituting the expression of F_b (as given by Eq. (3)) and expressed as follows:

$$\ddot{x}_b = \frac{c}{m_b}\dot{x} + \frac{k}{m_b}x - \frac{c_b}{m_b}\dot{x}_b - \alpha\frac{k_b}{m_b}x_b - (1-\alpha)\frac{F_0(m_b+m)g}{m_b}Z - \ddot{x}_g \tag{7}$$

Equations (1) and (7) lead to the following:

$$\begin{aligned}\{\ddot{x}\} = {} & [m]^{-1}[c]\{\dot{x}\} - [m]^{-1}[k]\{x\} \\ & - \left(\frac{c}{m_b}\dot{x} + \frac{k}{m_b}x - \frac{c_b}{m_b}\dot{x}_b - \alpha\frac{k_b}{m_b}x_b - (1-\alpha)\frac{F_0(m_b+m)g}{m_b}Z\right)\end{aligned} \tag{8}$$

The fourth-order Runge–Kutta method is applied for the solution of the differential equations of motion of the base-isolated system for a given blast input.

3 Modelling of Blast-Induced Ground Motion

In the present study, the BIGM generated typically from an underground explosion is modelled by an exponentially decaying function by following Carvalho and Battista [2]. The blast loading on the structure, $F(t) = m\ddot{x}_g(t)$, is obtained from the blast-induced ground acceleration, $\ddot{x}_g(t)$, as expressed by

$$\ddot{x}_g(t) = -(1/t_d)\bar{\dot{x}}_g e^{(-t/t_d)} \tag{9}$$

In the above equation, $\bar{\dot{x}}_g$ is the peak particle velocity (PPV) and $t_d = R/C_p$ is the arrival time. R and $C_p = \sqrt{E/\rho}$ denote the distance to the charge centre and propagation velocity of wave in soil or rock, respectively. E is the Young's modulus, and ρ is the average mass density of the rock or soil mass. The value of PPV is computed from the empirical attenuation relation given by Wu and Hao [17]. The relation, considering a granite site, is reproduced below in Eqs. (10) and (11):

$$\text{PPV} = 2.981 f_1 \left(R/Q^{(1/3)}\right)^{-1.3375} \tag{10}$$

with

$$f_1 = 0.121(Q/V)^{0.2872} \tag{11}$$

Here, f_1 is the decoupling factor for PPV, Q is the TNT charge weight in kilogram, V is the volume of the charge chamber in cubic metre and R is measured in metres.

For the blast input model, typical values of the volume of charge chamber (V), charge centre distance (R) and propagation velocity of wave (C_p) are taken as 1,000 m^3, 50 m and 5,280 m/s (for granite rock), respectively. Three different blast input acceleration time histories are considered for the present numerical study (named as cases A, B and C) corresponding to three values of TNT charge weight (Q), namely, 10, 50 and 100 t. The PPVs of the three types of input motions are calculated as 22.66, 73.74 and 122.56 cm/s, respectively. The resulting ground accelerations are shown in Fig. 3.

4 Numerical Study

In this section, the performance of the base isolation system in mitigating the underground blast-induced ground vibrations of the superstructure modelled by a SDOF system is illustrated through some numerical examples. Next, the variations in the design parameters of the BI as well as the blast input properties are considered to analyse their influences on the peak response reductions of the SDOF model of the superstructure. For the blast loading, BIGM as shown in Fig. 3 is considered.

The model of the isolated structural system under consideration is characterised by the parameters, namely, the fundamental time period of the superstructure (T_s), the damping ratio of the superstructure (ξ_s), the fundamental period of the base-isolated system (T_b), the damping ratio of the BI (ξ_b), the mass ratio (μ) which is the

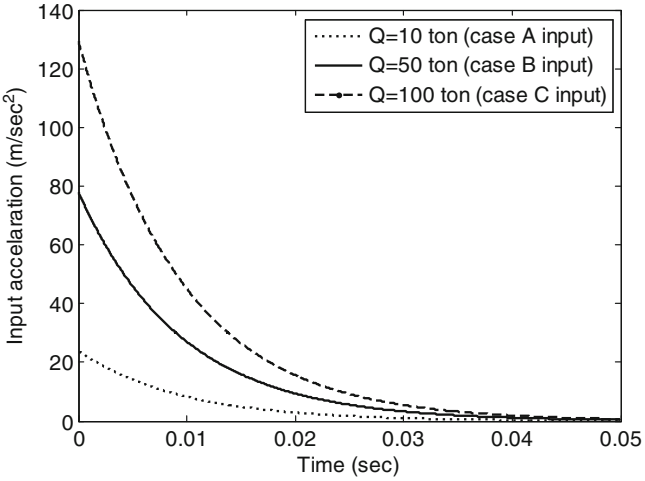

Fig. 3 Input acceleration time history

ratio of mass of the BI to the total mass of the structure, the normalised yield strength of the bearing (F_0) and the rigidity ratio (α). Unless mentioned otherwise, the system parameters are taken as $T_s = 0.5$ s, $\xi_s = 2\%$, $T_b = 2.5$ s, $\xi_b = 5\%$, $\mu = 0.2$, $F_0 = 0.05$ and $\alpha = 0.05$. Figure 4a, b represent the displacement and acceleration time histories of the fixed base and isolated system with the aforesaid parameters subjected to type C blast input (ref. Fig. 3), which has the highest intensity of the blast input acceleration. These two plots indicate that the peak acceleration and the peak displacement are very effectively reduced by the base isolation system. Similar observations are obtained for the response time histories of the other two cases of BIGM (not shown here). The quantitative estimate of the response reductions for all the three cases of blast input is presented in Table 1. It is clear from Table 1 that the BI is able to reduce the peak acceleration as well as the peak displacement of the structure subjected to BIGM. It may also be noted that the percent reduction of peak displacement and that of absolute acceleration are almost the same. Although very high response reductions of the superstructure are achieved by using BI, it is necessary to examine the peak bearing displacement because, as discussed earlier, base-isolated buildings are vulnerable to large pulse-like ground motions (similar to the impulsive BIGM) generated at near-fault location due to large isolator displacements (Heaton et al. [7], Hall et al. [5], etc.). Base displacement time histories for all three cases of blast input are shown in Fig. 4c, and the values of the peak base displacements are also given in Table 1. The peak base displacement of N-Z-type BI under seismic vibration can be noted here to compare with that due to underground blast. For example, for the three earthquake records of Loma Prieta, Northridge and Kobe with peak ground accelerations (PGAs) of 0.57, 0.6 and 0.86 g, respectively, peak base displacements of a N-Z-type base-isolated system ($T_s = 0.5$ s, $T_b = 2.5$ s, $q = 2.5$ cm) have been reported as 69.34, 57.06 and 35.48 cm, respectively [15]. Hence,

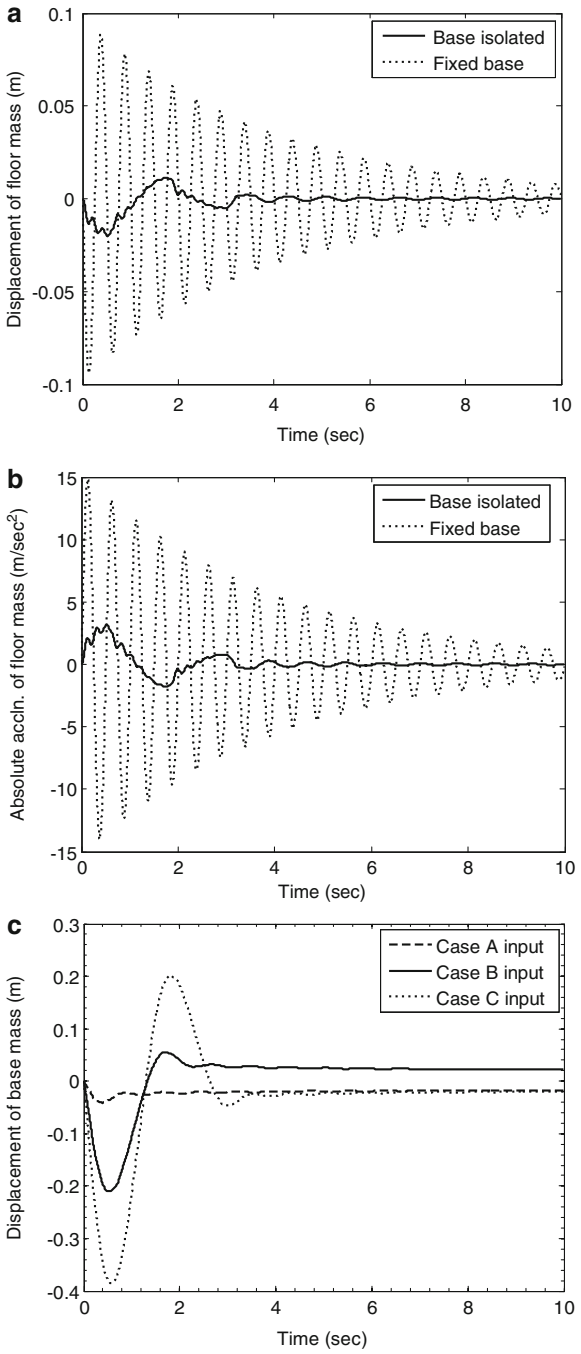

Fig. 4 (**a**) Displacement time history for $T_b = 2.5$ s (case C input), (**b**) acceleration time history for $T_b = 2.5$ s (case C input), (**c**) base displacement time history for $T_b = 2.5$ s (case A-, B- and C-type blast input)

Table 1 Peak responses reduction and peak base displacement of 2-DOF base-isolated system for three cases of blast input

Type of blast input	Reduction in peak displacement of floor mass w.r.t. base (%)	Reduction in absolute peak acceleration of floor mass (%)	Peak base displacement (cm)
Case A	64.46	64.43	4.10
Case B	77.43	77.44	20.95
Case C	78.63	78.64	38.50

unless the blast loading intensity is very high (i.e. higher than case C), peak base displacements are within the moderate to low ranges as compared to those from earthquake loading. Base displacement time histories in Fig. 4c also show that there is a permanent deformation of the BI, the magnitude of which is not necessarily proportional to the corresponding blast intensity. Thus, parametric studies are necessary to evaluate the optimum combination of BI parameters that would minimise the peak acceleration while restricting the peak base drift as well as the permanent deformation of the BI for a particular blast input.

Now, the influence of various parameters on the performance of the base isolation system is studied. In order to understand the influence of the shape of the bilinear hysteresis loop of the BI, the normalised yield strength (F_0) and the rigidity ratio (α) are next considered in the parametric study. First, the variation of peak acceleration reduction with F_0 is presented in Fig. 5a for three values of $T_b = 1.5$, 2 and 2.5 s. The results for both case A and case C blast inputs are presented. The other parameters remain same as earlier. It is observed in Fig. 5a that with the increase of F_0, the peak acceleration reduction decreases. For example, for case C input and $T_b = 1.5$ s, the peak acceleration reduction achieved by the BI is brought down from 66 to 43% with the increase in the value of F_0 from 0.01 to 0.4. The effect of F_0 is greater for case A blast input as compared to case C. For case B input, this reduction trend is similar to that of case C. The influence of F_0 on the peak base displacement is shown in Fig. 5b for case C blast input. Here, the increase in F_0 proves beneficial as it reduces the bearing displacement. Similar trends are followed for the other two cases of blast input. The nature of these two figures can be explained by the fact that for higher value of F_0 (i.e. for higher yield strength F_y), the isolation system remains more in the elastic state (see Fig. 2) which results in lower flexibility in the structural system and lesser amount of energy dissipation. Consequently, the absolute acceleration of the superstructure increases, while the bearing displacement decreases with increase of isolator characteristic strength. Thus, the lower value of F_0 is more advantageous from peak acceleration reduction point of view. But the resulting higher base drift at such lower F_0 value needs to be checked against the peak base displacement limit of that particular base isolator. Seismic codes (UBC [14] and IBC [8]) recommend the permissible limit of peak bearing displacement. Though no such code has been developed so far for design of base isolation system for blast vibration control, one can readily recognise that the peak base displacement has to be controlled. Thus, a constrained optimisation problem needs to be solved for the final selection of the value of F_0.

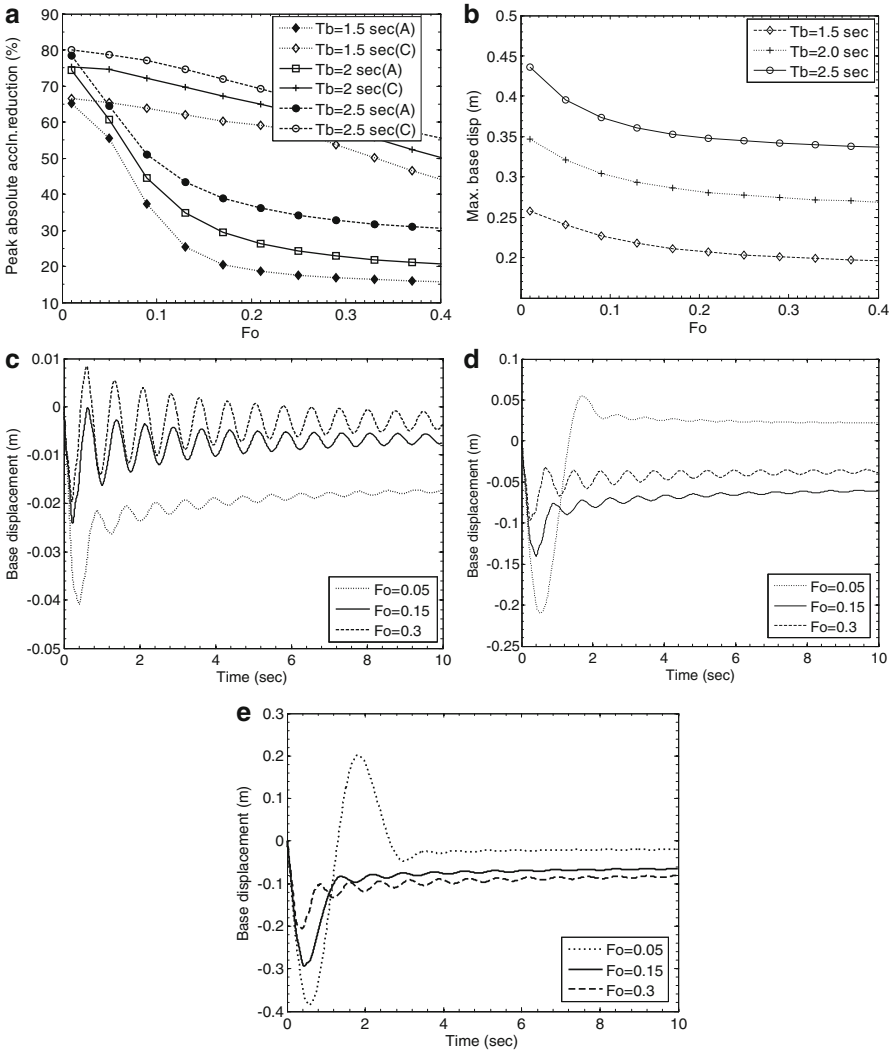

Fig. 5 (**a**) Variation of peak acceleration reduction with F_0 for different T_b (case A and C input), (**b**) variation of peak base displacement with F_0 for different T_b (case C input), (**c**) base displacement time histories for three values of F_0 ($T_b = 2.5$ s and case A input), (**d**) base displacement time histories for three values of F_0 ($T_b = 2.5$ s and case B input), (**e**) base displacement time histories for three values of F_0 ($T_b = 2.5$ s and case C input)

As discussed earlier in Fig. 4c, the permanent set of the isolator is another parameter of concern for designing the base-isolated system under BIGM. The base displacement time histories for the three cases of blast input are thereby plotted for three values of F_0 (= 0.05, 0.15 and 0.3) in Fig. 5c–e, respectively. For this, only one value of T_b (= 2.5 s) is taken and other system parameters are as in

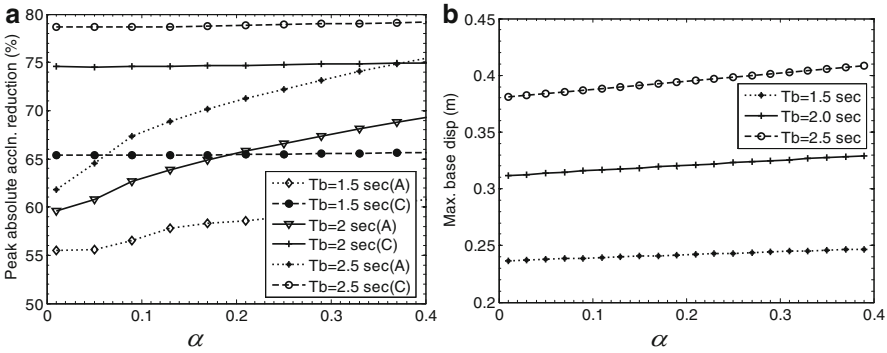

Fig. 6 (**a**) Variation of peak acceleration reduction with α for different T_b ($T_b = 2.5$ s and case A input), (**b**) variation of peak base displacement with α for different T_b (case A input)

Fig. 5b. When the blast intensity is low (i.e. for case A in Fig. 5c), then lower value of F_0 leads to greater amount of permanent set. But as the blast intensity increases (see Fig. 5d, e), the vibration response of the BI is such that the permanent set of the BI having lower value of F_0 is decreased, and for case C input, the permanent set of the BI with the smallest F_0 ($= 0.05$) becomes the lowest, but it is not possible to predict the trend in which the permanent set will be varying with F_0. Hence, in addition to the reduction of peak acceleration and peak base drift, the permanent set of the BI should also be considered while solving for F_0 in the constrained optimisation problem for a particular case of blast input.

The rigidity ratio (α) is another factor that guides the shape of the hysteresis loop of the BI. The effects of α on the peak absolute acceleration reduction as well as on the base displacement are depicted in Fig. 6a, b, respectively, for the three sets of T_b considered earlier. In Fig. 6a, results for both case A- and C-type blast input are presented (as in Fig. 5a), while in Fig. 6b, results for case C-type blast input are shown. It can be noted from Fig. 6a that the peak absolute acceleration reductions for higher intensity of blast input remain almost unchanged for different values of α corresponding to a fixed isolation period. But for the lower intensity of blast input as in case A, these reductions increase significantly with α. The trend for case B-type input (not shown) is same as that of case C. From Fig. 6b, it is observed that the peak bearing displacement increases only slightly with α and the same is true for the other two cases of blast input as well. It thus appears from Fig. 6a, b that for higher intensities of blast input, the peak responses are almost independent of the rigidity ratio, though for lower intensity of input, higherα is more effective in reducing the peak acceleration of the superstructure. However, for higher values of F_0, the effect of rigidity ratio is more pronounced (though not shown here) both for the peak acceleration reduction and for the peak base drift, irrespective of the blast input intensity.

Finally, the effect of the damping ratio of the BI, ξ_b, on the reduction of peak acceleration as well as on the resulting maximum base displacement is illustrated in Fig. 7a, b, respectively. The responses are plotted for three sets of T_b as earlier. From

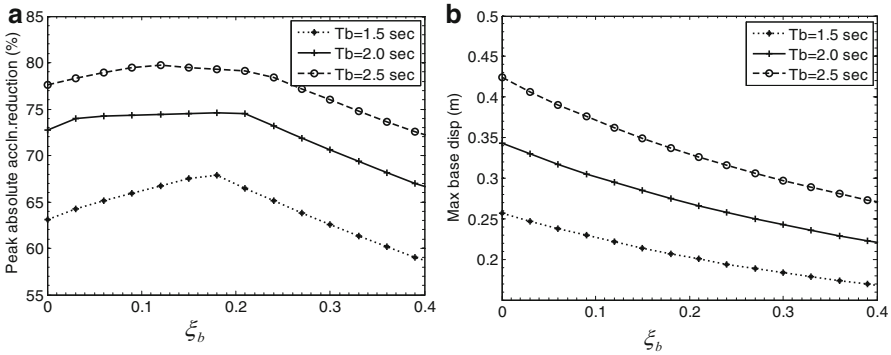

Fig. 7 (**a**) Variation of peak acceleration reduction with ξ_b for different T_b (case C input), (**b**) variation of peak base displacement with ξ_b for different T_b (case C input)

Fig. 7a, it is noted that an optimum value of ξ_b exists so far as minimisation of peak absolute acceleration response is concerned. However, the peak bearing displacement decreases monotonically with increase of ξ_b. Thus, the increase of ξ_b beyond the optimum value indicated in Fig. 7a may decrease the bearing displacement but will transmit higher acceleration into the superstructure. It is also observed in Fig. 7a that the optimum value of ξ_b is dependent on the value of T_b. The results for the other two cases of blast input are similar to those made above.

5 Conclusions

The study on the performance of the N-Z-type base isolation system for structures subject to underground BIGM reveals that it can provide substantial reduction in the peak absolute acceleration, which is extremely significant for structures subjected to blast, as well as mitigate the peak displacement of the superstructure. The peak bearing displacements, which are often critical in base isolation design, are also computed, and it is seen that unless the blast loading intensity is very high, these values are within the moderate to low range as compared to those typically obtained in case of earthquake excitation.

A sensitivity study on the peak acceleration reduction and peak base displacement to the various important BI parameters, e.g. the yield strength, rigidity ratio and damping ratio, is performed. Parametric studies are also carried out for different intensities of blast input by varying the TNT charge weight. It is observed that there is an optimum value of the damping ratio (ξ_b) for which the reduction in peak acceleration of the superstructure is maximised. The bearing displacement, however, decreases with the increase in the damping. Thus, increasing the damping beyond a certain value may decrease the base drift but may cause higher acceleration transmission into the superstructure. The normalised yield strength and the rigidity ratio are the other two important guiding factors for designing the BI. Though the reduction in peak structural acceleration is greater at lower value of

the normalised yield strength of the BI (F_0), it is noted that the peak base displacement also becomes high then. Again, depending upon the blast input characteristics, the nature of the permanent set of the BI is different for different values of F_0. For the smaller blast intensity, lower value of F_0 leads to greater amount of permanent set. But when the blast intensity is very high, lower values of F_0 result in lower amount of permanent set in the system. The effect of the rigidity ratio is more pronounced both for the peak acceleration reduction as well as for the peak base drift for higher values of F_0. But when F_0 is small, for higher intensity of blast input, the peak responses are almost independent of the rigidity ratio, though for lower intensity of input, higher α is more effective in reducing the peak acceleration of the superstructure. Thus, depending upon the constraint on the peak displacement and permanent set of the BI, coupled with the response reduction requirement, a judicious combination of F_0, ξ_b and α should be selected for designing the BI.

References

1. Alhan C, Gavin H (2003) A parametric study of linear and non-linear passively damped seismic isolation systems for buildings. J Eng Struct 26:485–497
2. Carvalho EML, Battista RC (2003) Blast induced vibration in urban residential buildings. Int J Struct Build 156:243–253
3. Dowding CH (1996) Construction vibrations. Prentice-Hall, Upper Saddle River
4. German standard organization (GSO) (1984) Vibration in building construction. DIN 4150, Berlin
5. Hall JF, Heaton TH, Halling MW, Wald DJ (1995) Near-source ground motion and its effect on flexible buildings. Earthq Spectra 11(4):569–605
6. Hao H, Wu C (2005) Numerical study of characteristics of underground blast induced surface ground motion and their effect on above-ground structures. Part II. Effects on structural responses. Int J Soil Dyn Earthq Eng 25:39–53
7. Heaton TH, Hall JF, Wald DJ, Halling MW (1995) Response of high-rise and base-isolated buildings to a hypothetical Mw 7.0 blind thrust earthquake. Sci 267:206–211
8. International Building Code (2000) International code council
9. Jangid RS (2010) Stochastic response of building frames isolated by lead-rubber bearing. J Struct Control Health Monit 17:1–22
10. Jangid RS, Kelly JM (2001) Base isolation for near fault motions. J Earthq Eng Struct Dyn 30:691–707
11. Miyamoto HK, Taylor D (1999) Structural control of dynamic blast loading using passive energy dissipaters. SEAOC 1999 Convention, pp 299–317
12. NATO (1993) Manual on NATO safety principles for the storage of NATO ammunition and explosives. In document: AC/258-D/258, Bonn
13. Providakis CP (2009) Effect of supplemental damping on LRB and FPS seismic isolators under near-fault ground motions. Int J Soil Dyn Earthq Eng 29:80–90
14. Uniform Building Code (1997) International conference of building officials, Whitter, CA
15. Matsagar VA, Jangid RS (2004) Influence of isolator characteristics on the response of base-isolated structures. J Eng Struct 26:1735–1749
16. Wen YK (1976) Method of random vibration of hysteretic systems. J Eng Mech 102:249–263

17. Wu C, Hao H (2005) Numerical study of characteristics of underground blast induced surface ground motion and their effect on above-ground structures. Part I. Ground motion characteristics. Int J Soil Dyn Earthq Eng 25:27–38
18. Wu C, Ha H, Lu Y, Sun S (2004) Numerical simulation of structural responses on a sand layer to blast induced ground excitations. Int J Comput Struct 82:799–814

Geotechnical Uncertainty and Its Influence on Groundwater Level and Seawater Interface in a Land Reclamation Project

Amit Srivastava

Abstract Land reclamation in coastal areas has significant influence on local groundwater systems. Steady-state analytical solutions based on Dupuit and Ghyben–Herzberg assumptions are available (Guo and Jiao, Ground Water 45(3):362–367, 2007) to evaluate the rise in GWT (groundwater table) and saltwater–freshwater interface. It is established that the amount of these changes depends on the extent of reclamation (geometric extent) and the hydraulic conductivity of the fill material. The closed-form analytical solutions provide a single value of parameters such as rise in GWT and distance of saltwater–freshwater interface. Considering the fact that the soil is a natural material which is used as fill material for reclamation purpose, it is difficult to assure a unique value of hydraulic conductivity of the fill material. Uncertainties in the estimation of hydraulic conductivity of the fill material will always lead to the uncertainty in the estimation of output parameters. Conventional approach defines factor of safety to handle uncertainty in geotechnical design and applications which is solely based on past experiences, good engineering judgment, and confidence level of the designer. Alternatively, probabilistic approach, which is gaining importance in recent years, can handle uncertainty in a mathematical framework. In the present study, the role of uncertain parameter, i.e., "hydraulic conductivity of the fill material" and its influence on probabilistic assessment of groundwater level and seawater interface in a coastal land reclamation projects, is highlighted. Two situations are considered, both with groundwater flow resulting from precipitation recharge: (1) the coastal aquifer of an extensive landmass and (2) an island.

Keywords Coastal land reclamation • Probabilistic • Hydraulic conductivity • Groundwater • Uncertainty

A. Srivastava (✉)
Department of Civil Engineering, JUET, Guna, India
e-mail: 2002.lala@gmail.com

S. Chakraborty and G. Bhattacharya (eds.), *Proceedings of the International Symposium on Engineering under Uncertainty: Safety Assessment and Management (ISEUSAM - 2012)*,
DOI 10.1007/978-81-322-0757-3_70,

1 Introduction

Most large urban centers lie in coastal regions, which are home to about 25% of the world's population. Rapid industrial and commercial expansion in recent years has created the need for more land. It is estimated that the current coastal urban population of 200 million is projected to almost double in the next 20–30 years. To meet the growing demand for more housing and other land uses, land has been reclaimed from the sea in coastal areas in many countries, including China, Britain, Korea, Japan, Malaysia, Saudi Arabia, Italy, the Netherlands, and the United States. As well known to everyone, one of the most famous case histories is Palm Jumeirah [7] in Dubai, which is an artificial archipelago created using coastal land reclamation.

The direct impact of land reclamation on coastal engineering, environment, and marine ecology is well recognized and widely studied [6, 8, 10, 11]. It is also recognized that reclamation changes the regional groundwater regime, including groundwater table (GWT) as well as interface between seawater and fresh groundwater. Extensive studies on impact of coastal land reclamation on groundwater level and the seawater interface have been carried out in the recent past [2, 4, 5, 9]. Guo and Jiao [3] provided analytical solutions for the alternation of the saltwater interface in response to land reclamation with the assumption that flow satisfies the Ghyben–Herzberg relationship and the Dupuit assumption. The study is useful in assessing long-term impact of the land reclamation on both the GWT and the saltwater interface in a coastal landmass and an island with unconfined groundwater condition. The following section provides a brief review of work carried out by Guo and Jiao [3].

1.1 Impact of Reclamation in an Extensive Landmass

Figure 1a shows a coastal unconfined groundwater system receiving uniform vertical recharge w. The hydraulic conductivity of the aquifer is K_1. The distances from the water divide to the coastline and the tip of the saltwater tongue are denoted as L_1 and X_t, respectively. The head in the freshwater, h, is measured in relation to the horizontal impermeable bottom of the aquifer, which is H_o below sea level. Figure 1b shows the influence of reclamation when steady-state condition is reached. It is indicated that coastline moves seaward by a distance L_2 and the hydraulic conductivity of the fill material is K_2 (the boundary between K_1 and K_2 is approximated as vertical). The distance of the tip of saltwater tongue from the water divide after reclamation is assumed to be X_{tr}. The following closed-form analytical solutions were derived to obtain the depth of GWT (h) and distance X_{tr} for the reclaimed land:

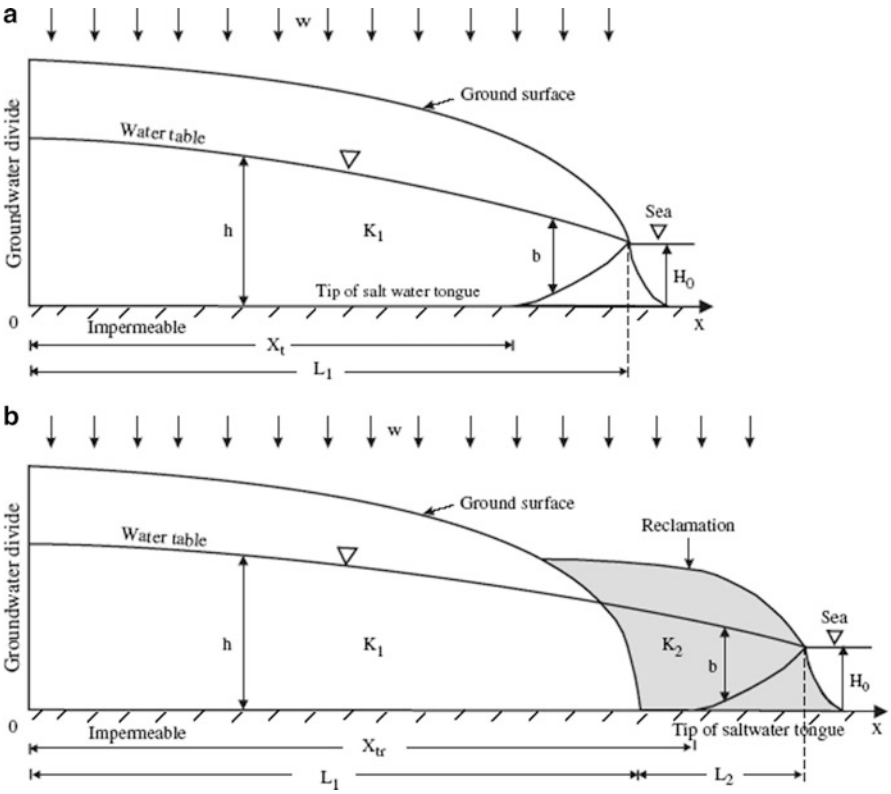

Fig. 1 Sketch of an unconfined aquifer system and the saltwater interface in a coastal extensive landmass (**a**) before reclamation and (**b**) after reclamation [3]

$$h = \sqrt{w\left[\frac{1}{K_1}\left(L_1^2 - X^2\right) + \frac{1}{K_2}(2L_1 + L_2)L_2\right] + \frac{\rho_s}{\rho_f}H_o^2}, \quad 0 \le X \le L_1 \tag{1}$$

$$h = \sqrt{\frac{w}{K_2}\left[(L_1 + L_2)^2 - X^2\right] + \frac{\rho_s}{\rho_f}H_o^2}, \quad L_1 \le X \le X_{\text{tr}} \tag{2}$$

$$h = \sqrt{\frac{w\left(\rho_s - \rho_f\right)}{K_2\rho_s}\left[(L_1 + L_2)^2 - X^2\right]} + H_o, \quad X_{\text{tr}} \le X \le L_1 + L_2 \tag{3}$$

The location of the tip of the saltwater tongue (X_{tr}) can be obtained from the following expression:

$$X_{\mathrm{tr}} = \sqrt{(L_1 + L_2)^2 - \frac{K_2\left(\rho_s^2 - \rho_s\rho_f\right)}{w\rho_f^2} H_o^2} \tag{4}$$

For more detailed study on the topic, it is suggested that this chapter should be read in the light of Guo and Jiao [3]. The proposed analytical solutions can be used in estimating the increase in GWT (Δh) as well as location of the tip of the saltwater tongue (X_{tr}) for the reclaimed land.

1.2 Impact of Reclamation in an Island

Jiao [4] indicated that in an island, the water divide will be moved when reclamation is significant compared to the size of the original groundwater catchments. The reclamation on one side changes the groundwater flow in the whole island, including the water level and position of the saltwater interface on the other side. The analytical solutions derived for h (with reference to Fig. 2) is as follows:

$$h = \sqrt{\frac{w\left(\rho_s - \rho_f\right)}{K_1\rho_s}(L_1X - X^2) + H_o}, \quad 0 \le X \le X_{\mathrm{t1}} \text{ or } X_{\mathrm{t2}} \le X \le L_1 \tag{5}$$

$$h = \sqrt{\frac{w}{K_1}(L_1X - X^2) + \frac{\rho_s}{\rho_f}H_o^2}, \quad X_{t1} \le X \le X_{t2} \tag{6}$$

The locations of the tips of the saltwater tongues can be readily obtained by setting h equal to $\rho_s H_o/\rho_f$ in either Eq. (5) or Eq. (6) and then solving for X_{t1} and X_{t2}. The reclamation length and hydraulic conductivity of the reclamation material are taken as L_2 and K_2, respectively. The current distances from the coastline on the unreclaimed side to the tips of saltwater tongues are X_{tr1} and X_{tr2}, and the groundwater divide after reclamation is assumed to be at $X = X_d$.

The solution for X_d is obtained as below:

$$X_d = \frac{K_1L^2 + (K_2 - K_1)L_1^2}{2(L_1K_2 + L_2K_1)} \tag{7}$$

The final solutions of the head distributions (h) are as follows:

$$h = \sqrt{\frac{w\left(\rho_s - \rho_f\right)}{K_1\rho_s}(\beta X - X^2) + H_o}, \quad 0 \le X \le X_{\mathrm{tr1}} \tag{8}$$

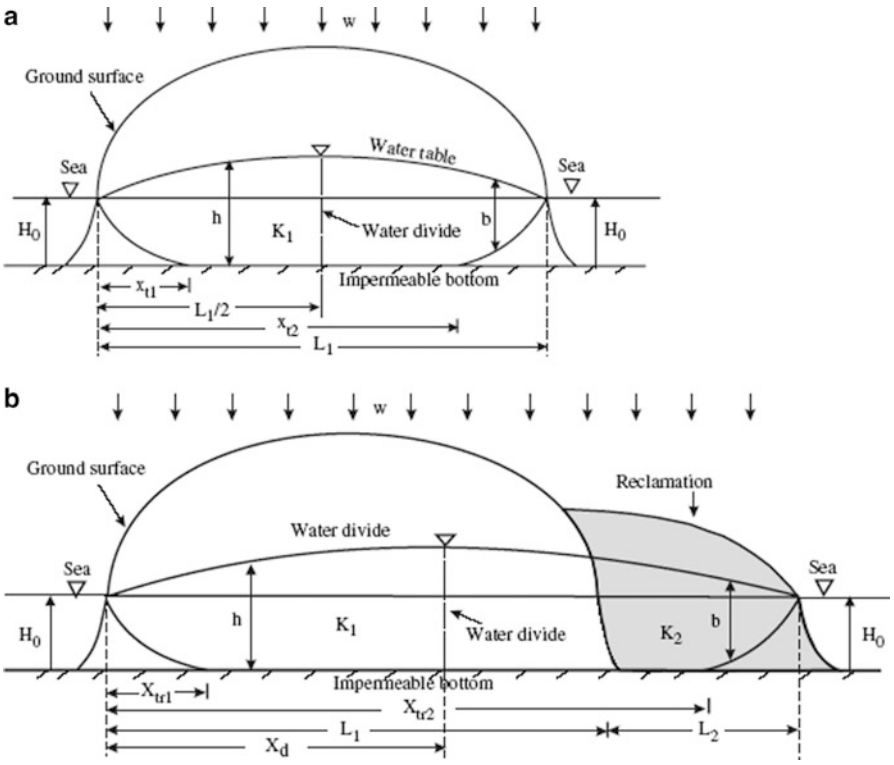

Fig. 2 A schematic sketch of the groundwater flow system in an oceanic island receiving uniform vertical recharge (**a**) before reclamation and (**b**) after reclamation [3]

$$h = \sqrt{\frac{w}{K_1}(\beta X - X^2) + \frac{\rho_s}{\rho_f}H_o^2}, \quad X_{t1} \le X \le L_1 \tag{9}$$

$$h = \sqrt{\frac{w}{K_2}(\beta X - X^2 + 2\gamma/w) + \frac{\rho_s}{\rho_f}H_o^2}, \quad L_1 \le X \le X_{tr2} \tag{10}$$

$$h = \sqrt{\frac{w\left(\rho_s - \rho_f\right)}{K_2\rho_s}(\beta X^2 - X^2 + 2\gamma/w) + H_o}, \quad X_{t2} \le X \le L \tag{11}$$

where $\beta = \left[K_1L^2 + (K_2 - K_1)L_1^2\right]/(L_1K_2 + L_2K_1)$ and $\gamma = wL_1L_2L(K_2 - K_1)/2 \times (L_1K_2 + L_2K_1)$.

After reclamation, the locations of the tips of the saltwater tongues can be obtained by setting h equal to ρ_sH_o/ρ_f in either Eq. (9) or Eq. (10) and then solving for X_{tr1} and X_{tr2}. The displacement of the water divide, Δd, can be calculated as:

$$\Delta d = X_d - \frac{L_1}{2} = \frac{K_1L_2(L_1 + L_2)}{2(L_1K_2 + L_2K_1)} \tag{12}$$

Equation (12) shows that the water divide will move toward the new coastline after reclamation, indicating that groundwater discharge to the sea on the non-reclamation side will be increased by an amount of $w\Delta d$ per unit width of flow.

In the development of analytical solutions, it is assumed that the Dupuit assumptions and the Ghyben–Herzberg relationships are valid. Guo and Jiao [3] indicated that although the results obtained using these expressions are accurate in many cases, one of the major shortcomings of the Ghyben–Herzberg relationships is that there is no seepage face at the coastline. Further, the model does not include the more complicated cases like (1) heterogeneity of the aquifer system, (2) complicated topography at the coast, and (3) the transient process immediately after the reclamation.

It can be noted that in the proposed analytical solutions, the permeability of the in situ soil (K_1) and also reclamation material (K_2) are the governing parameters in deciding the waterheads of GWT and location of the tip of the saltwater tongue (X_{tr}). Being soil a natural material and heterogeneous in nature, deterministic estimate of K_1 and K_2 (i.e., single value) is virtually impossible. The uncertainty in estimation on these parameters brings uncertainty in determination of waterheads of GWT and location of the tip of the saltwater tongue. Hence, probabilistic assessment of these parameters becomes imperative in which the input parameters are treated as random variables, and the influence of these input variables on the output responses, i.e., waterheads of GWT and location of the tip of the saltwater tongue, are studied.

2 Objectives of the Present Study

In the present study, the work proposed by Guo and Jiao [3] is studied in the light of probabilistic analysis. The heterogeneity of the aquifer system is taken into consideration to study the impact of coastal land reclamation on GWT (h) and seawater interface (X_{tr}). Monte Carlo simulations are done to obtain the statistical information on mean and variance of output parameters h and X_{tr}. Using FORM, the reliability of getting a particular value of h and X_{tr} are evaluated.

3 Geotechnical Uncertainties and Its Quantification

Quantitative assessment of soil uncertainty modeling requires use of statistics, as well as probabilistic modeling to process data from laboratory or in situ measurements. In the probabilistic analysis, the input parameters are modeled as either discrete or continuous random variables defined by their probability density functions (*pdf*) or the parameters of distributions [1].

Normally, in geotechnical practice, the soil parameters are either modeled as normally distributed or lognormally distributed continuous random variables. The

Table 1 CoV% for the selected geotechnical parameters

Property	CoV% range
Dry unit weight (γ_d)	2–13
Undrained shear strength (c_u)	6–80
Effective friction angle (ϕ')	7–20
Elastic modulus (E_s)	15–70
Coefficient of permeability (k)	68–90

parameters of the normal and lognormal probability distribution function (*pdf*) are directly related to the unbiased estimates of statistical moments, i.e., sample mean (μ) and variance (σ^2) of the measured data set. The coefficient of variation (CoV%), which is obtained by dividing the sample standard deviation (σ) by the sample mean (μ), is commonly used in quantifying the geotechnical uncertainty analysis because of the advantages of being dimensionless as well as providing a meaningful measure of relative dispersion of data around the sample mean.

Where site-specific data are not available to estimate parameters of random variables, uncertainty can be characterized by assuming that the coefficient of variation (CoV%) of a parameter is similar in magnitude to that observed at other sites. Typical values of coefficients of variation for soil properties have been compiled and reported by Uzielli et al. [13]. Typical values of range of coefficient of variation (CoV%) for selected geotechnical parameters are provided in Table 1.

Consideration of these uncertainties in the input soil parameters and its impact on the performance of a geotechnical system are studied using the reliability-based design procedures. Reliability analysis focuses on the most important aspect of performance, i.e., probability of failure (p_f).

4 Methods of Reliability Analysis

In FORM, if the demand is defined as D and capacity is defined as C, the margin of safety or the performance function $G(x)$ or M is defined as below:

$$G(x) = M = C - D. \tag{13}$$

If both C and D are uncorrelated continuous random variables defined by their probability distribution and parameters of distribution means (μ_C, μ_D) and standard deviations (σ_C, σ_D), in the case of lognormally distributed C and D, the expression of β is defined as below [1]:

$$\beta = \frac{\ln\left[\left(\frac{\mu_C}{\mu_D}\right)\sqrt{\left(1+\delta_C^2\right)\left(1+\delta_D^2\right)}\right]}{\sqrt{\ln\left[\frac{\left(1+\delta_C^2\right)}{\left(1+\delta_D^2\right)}\right]}} \tag{14}$$

where δ_C, δ_D is coefficient of variation in C and D, respectively.

USACE [12] made specific recommendation on target probability of failure (p_f) and reliability indices (β) in geotechnical and infrastructure projects. The suggested guidelines say that a reliability index (β) value of at least 5.0 is considered to indicate high performance of the system and 3.0 for the above average performance.

5 Results of Analysis and Discussion

5.1 Deterministic Solutions

A typical case of reclamation site of an extensive landmass in Hong Kong [5] with the numerical values of the following parameters $K_1 = 0.1$ m/day, $L_1 = 1{,}000$ m, $\rho_s = 1.025$ g/cm^3, $\rho_f = 1.000$ g.cm^3, $w = 0.0005$ m/day, and $H_o = 20$ m is considered. The land reclamation will increase the GWT and change the freshwater and seawater interface. From the available analytical solutions, it can be seen that the highest GWT increase is at the original coastline. For $L_2 = 500$ m and $K_2 = 0.5$ m/day, the increase is 20.74 m.

Figure 3 shows the displacement of the tip of the saltwater tongue with hydraulic conductivity of the reclamation material and for different reclamation length (given values of $K_1 = 0.1$ m/day, $L_1 = 1{,}000$ m, $\rho_s = 1.025$ g/cm^3, $\rho_f = 1.000$ g/cm^3, $w = 0.0005$ m/day, and $H_o = 20$ m). It can be noted that permeability of reclamation material has high impact on displacement of the tip of the saltwater tongue. As the permeability value reduces, the tip of the seawater tongue moves seaside. Hence, it is always beneficial to keep the permeability of the reclamation material as low as possible.

Considering the case of an island, assuming $L_1 = 2{,}000$ m and other parameters same as $K_1 = 0.1$ m/day, $L_1 = 1{,}000$ m, $\rho_s = 1.025$ g/cm^3, $\rho_f = 1.000$ g.cm^3, $w = 0.0005$ m/day, and $H_o = 20$ m, the calculations show that the displacement of the tip of the saltwater tongue near the coastline on the reclamation side is similar to the results obtained in Fig. 3.

It is observed that after reclamation, the saltwater interface on the reclamation side is pushed toward the post-reclamation coastline. The saltwater interface on the unreclaimed side will similarly be pushed seaward. This is because the water divide moves toward the reclaimed side, increasing the recharge to the aquifer and the groundwater discharge to the sea on both sides of the island. The water table increases throughout the island as a result of the reclamation. The results are similar to those obtained for reclamation of extensive landmass.

5.2 Probabilistic Solutions

It can be noted that the deterministic values obtained for increase in GWT (Δh) and distance of seawater–freshwater interface (X_{tr}) are reliable to the extent the

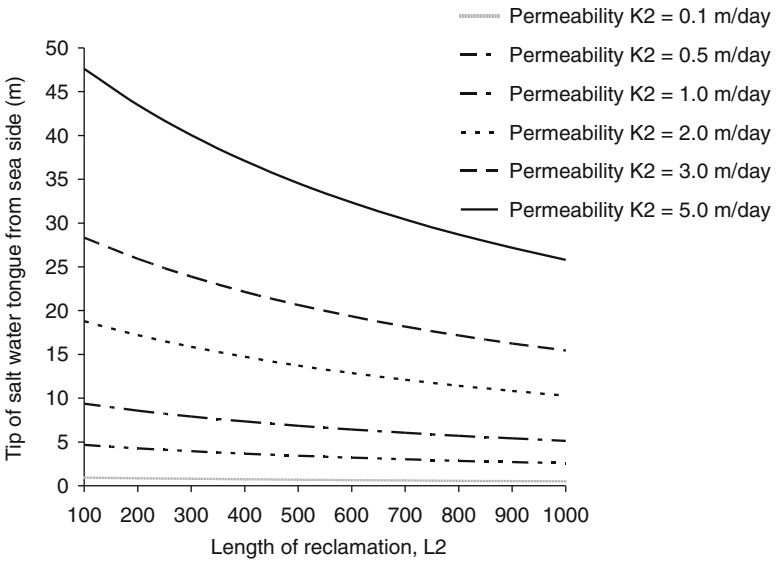

Fig. 3 Displacement of the tip of the saltwater tongue with hydraulic conductivity of the reclamation material and for different reclamation length

accuracy with which the permeability parameters of the soil are obtained from field or laboratory test results. As indicated earlier, it is almost impossible to attain a single (deterministic) value of K_1 and K_2 parameters for the in situ soil and reclamation material, respectively.

From Table 1, it is evident that the coefficient of variation (CoV%) in the permeability parameter can be expected in the range of 68–90%. Hence, assessment of groundwater level and seawater interface in a reclamation project is extremely difficult in an uncertain environment. Through reliability analysis, the uncertainty in permeability parameters can be handled in a mathematical framework, and the best way to answer to the following questions is probabilistically:

1. What is the reliability of getting tip of the saltwater tongue at a particular distance (X_{tr})?
2. What is the reliability of getting increased value of GWT (Δh) of some numerical value?

For the reliability index calculations, the mean capacity (μ_C) is taken as the calculated value of Δh or X_{tr}, and the demand (μ_D) is taken as deterministic (predefined numerical) values of Δh and X_{tr}. The results of the reliability analysis of reclamation of extensive landmass are presented. Similar calculations can be performed for the reclamation of an island.

For the reliability analysis of the given problem in hand, the permeability parameter (K_2) is considered as lognormally distributed continuous random variable. The coefficient of variation in demand is taken as zero, i.e., $\delta_D = 0$. The

information on mean (μ_C) and coefficient of variation (δ_C) in capacity are obtained through Monte Carlo simulation results. For the parametric study, different values of mean (K_2 parameter = 0.1, 0.5, and 1.0 m/day) and the coefficients of variation (as 60, 70, 80, and 90%) of permeability parameter (K_2) are assumed that constitutes the following cases:

Case A: Mean K_2 = 0.1 m/day and CoV = 60, 70, 80, and 90%
Case B: Mean K_2 = 0.5 m/day and CoV = 60, 70, 80, and 90%
Case C: Mean K_2 = 1.0 m/day and CoV = 60, 70, 80, and 90%

For each case, 30,000 random numbers for K_2 parameter are generated to perform Monte Carlo simulations and to estimate the statistical information on mean and variance of Δh and X_{tr}. For that purpose corresponding to each value of K_2, proposed analytical solutions [3] are utilized to obtain the corresponding values Δh and X_{tr}. The simulation provides 30,000 numerical values of Δh and X_{tr}, which can be utilized in calculating mean (μ_C) and coefficient of variation (δ_C) in the capacity, as the case may be. It is further assumed that output values are random variables following lognormal distribution so that Eq. (14) can be utilized to calculate reliability index (β).

Table 2 shows typical results of the reliability analysis obtained for X_{tr} for case A. It can be noted that the deterministic value of X_{tr} from analytical solution is 1499.317 m. From the results of the reliability analysis, it can be noted that as X_{tr} is increased from 1,495 to 1,498 m, the reliability index value decreases for the range of CoV% values assumed for K_2. For 60% CoV in K_2 parameter, an acceptable value of $\beta \geq 5.0$ is achieved when the value of $X_{tr} \leq 1496.71$ m. If the CoV in K_2 parameter is 90%, $\beta \geq 5.0$ is achieved when $X_{tr} \leq 1495.0$ m. Since the permeability of the reclamation material is very low (0.1 m/day in case A), a very low value of coefficient of variation is obtained in X_{tr} through Monte Carlo simulations. Hence, not much variation in X_{tr} is observed for which reliability index (β) ≥ 5.0.

In other two cases B and C, in which mean value of K_2 parameter is relatively high, the influence of variation in K_2 parameter is remarkably observed. The results of the reliability analysis for case B and case C are presented in Tables 3 and 4, respectively. For case B, it can be noted that the deterministic value of X_{tr} from analytical solution is 1496.579 m. The results of the reliability analysis indicate that a reliability index (β) ≥ 5.0 is achieved when X_{tr} is assumed at 1484.8 and 1475.6 m for 60 and 90% CoV in K_2 parameter, respectively. Similarly for case C, it can be noted that the deterministic value of X_{tr} from analytical solution is 1493.152 m. The results of the reliability analysis indicate that a reliability index (β) ≥ 5.0 is achieved when X_{tr} is assumed at 1473.2 and 1465.6 m for 60 and 90% CoV in K_2 parameter, respectively. Similar calculations were performed for the reliability index (β) evaluation of Δh value, and results are presented in Tables 5, 6, and 7 for all the three cases. It can be noted that as CoV% in K_2 parameter increases, the reliability index (β) values decreases for the given value of Δh. The β value also decreases with increase in Δh values.

The results of the reliability analysis can be interpreted as follows: If the mean and CoV% in K_2 parameter are 0.1 m/day and 60%, respectively, the reliability of

Table 2 Results of the reliability analysis of X_{tr} for case A

Mean X_{tr} (μ_C)	1499.203	1499.168	1499.123	1499.086
	0.033	0.039	0.049	0.055
	Reliability index (β) values			
CoV% in X_{tr} (δ_C)	←(CoV% in K_2 parameter)→			
X_{tr}(m)	60%	70%	80%	90%
1,495	8.46	7.11	5.58	4.94
1,496	6.44	5.40	4.22	3.73
1,497	4.43	3.70	2.87	2.52
1,498	2.42	1.99	1.52	1.31

Table 3 Results of the reliability analysis of X_{tr} for case B

Mean X_{tr} (μ_C)	1496.187	1496.078	1495.948	1495.826
	0.152	0.185	0.215	0.272
	Reliability index (β) values			
CoV% in X_{tr} (δ_C)	←(CoV% in K_2 parameter)→			
X_{tr}(m)	60%	70%	80%	90%
1,480	7.14	5.84	4.99	3.91
1,485	4.92	4.02	3.42	2.67
1,490	2.72	2.20	1.85	1.44
1,495	0.52	0.39	0.30	0.20

Table 4 Results of the reliability analysis of X_{tr} for case C

Mean X_{tr} (μ_C)	1493.291	1493.479	1493.579	1493.855
	0.270	0.299	0.360	0.382
	Reliability index (β) values			
CoV% in X_{tr} (δ_C)	←(CoV% in K_2 parameter)→			
X_{tr} (m)	60%	70%	80%	90%
1,470	5.82	5.29	4.42	4.22
1,475	4.56	4.16	3.48	3.33
1,480	3.31	3.03	2.54	2.44
1,485	2.06	1.90	1.60	1.56

getting $\Delta h \leq 12.6$ m is very high($\beta \geq 5.0$). The reliability decreases as Δh increases. It can be noted that for the same case, analytical solution provides a deterministic value of $\Delta h = 61.61$ m. With due consideration of variability in estimating K_2 parameters, the reliability of getting $\Delta h = 61.61$ m is extremely low. From these observations, it can be stated that probabilistic assessment of groundwater level and seawater interface in coastal land reclamation projects is essential in view of heterogeneity of the material and uncertainties associated with the estimation of permeability properties governing the flow characteristics of reclaimed site.

Table 5 Results of the reliability analysis of Δh for case A

Mean Δh (μ_C)	64.971	65.893	66.765	68.494
CoV% in Δh (δ_C)	34.91	41.95	44.27	55.26
	Reliability index (β) values			
	←(CoV% in K_2 parameter)→			
Δh (m)	60%	70%	80%	90%
10	5.69	4.88	4.70	3.99
12	5.15	4.43	4.27	3.63
14	4.70	4.05	3.90	3.33
16	4.30	3.72	3.59	3.07
18	3.95	3.42	3.31	2.85
20	3.64	3.16	3.06	2.64

Table 6 Results of the reliability analysis of Δh for case B

Mean Δh (μ_C)	22.994	23.831	24.499	25.367
CoV% in Δh (δ_C)	42.65	54.99	57.00	64.87
	Reliability index (β) values			
	←(CoV% in K_2 parameter)→			
Δh (m)	60%	70%	80%	90%
1	7.87	6.43	6.30	5.75
2	6.18	5.08	4.99	4.58
3	5.19	4.29	4.22	3.90
4	4.48	3.73	3.68	3.41
5	3.94	3.30	3.26	3.04
6	3.49	2.94	2.92	2.73

Table 7 Results of the reliability analysis of Δh for case C

Mean Δh (μ_C)	15.135	16.296	17.574	19.334
CoV% in Δh (δ_C)	45.56	52.67	60.56	69.234
	Reliability index (β) values			
	←(CoV% in K_2 parameter)→			
Δh (m)	60%	70%	80%	90%
1	6.47	5.89	5.41	5.05
2	4.88	4.49	4.17	3.94
3	3.94	3.67	3.44	3.29
4	3.28	3.09	2.93	2.83
5	2.77	2.64	2.53	2.47
6	2.35	2.27	2.20	2.18

6 Conclusions

The study highlights the influence of extent of variation in the permeability parameter in the increase in groundwater level and seawater interface in coastal land reclamation projects. The probabilistic analysis approach gives an opportunity to handle variability in a mathematical framework, and it is a useful tool in decision-making process. The results of the reliability analysis provide more rational information on selection of appropriate value of X_{tr} and Δh that can be based upon the extent of variation in input K_2 parameter and desired value of reliability index (β) acceptable to decision makers. It is noted that low mean value and low coefficient of variation in permeability of reclamation material is always beneficial and insures higher chances of getting increased X_{tr} and Δh values. These observations are essentially useful in quality control purposes in land reclamation projects.

References

1. Baecher GB, Christian JT (2003) Reliability and statistics in geotechnical engineering. Wiley, Chichester
2. Bear J, Dagan G (1964) Some exact solutions of interface problems by means of the holograph method. J Geophys Res 69(8):1563–1572
3. Guo H, Jiao J (2007) Impact of coastal land reclamation on ground water level and the sea water interface. Ground Water 45(3):362–367
4. Jiao JJ (2000) Modification of regional groundwater regimes by land reclamation. Hong Kong Geol 6:29–36
5. Jiao JJ, Nandy S, Li H (2001) Analytical studies on the impact of reclamation on groundwater flow. Ground Water 39(6):912–920
6. Lumb P (1976) Land reclamation in Hong Kong. In: Proceedings of residential workshop on materials and methods for Low coast road, rail and reclamation works, Leura, Australia, pp 299–314
7. Nakheel (2007) The Palm Jumeirah. http://www.nakheel.com/Developments/The_Palm/The_Palm_Jumeirah. Retrieved 19 June 2007
8. Seasholes NS (2003) Gaining ground: a history of landmaking in Boston. MIT Press, Cambridge, MA
9. Strack ODL (1976) A single-potential solution for regional interface problems in coastal aquifers. Water Resour Res 12(6):1165–1174
10. Stuyfzand PJ (1995) The impact of land reclamation on groundwater quality and future drinking water supply in the Netherlands. Water Sci Tech 31(8):47–57
11. Suzuki T (2003) Economic and geographic backgrounds of land reclamation in Japanese ports. Mar Pollut Bull 47:226–229
12. USACE (1997) Risk-based analysis in geotechnical engineering for support of planning studies, engineering and design. US Army Corps of Engineers, Department of Army, Washington, DC, 20314-100
13. Uzielli M, Lacasse S, Nadim F, Phoon KK (2007) Soil variability analysis for geotechnical practice. In: Phoon KK, Hight DW, Leroueil S, Tan TS (eds) Characterization and engineering properties of natural soils. Taylor & Francis group, London. ISBN 978-0-415-42691-6

A Simulation-Based Approach for Design of Rural Feeder Service with Fixed-Route Fixed-Schedule Form of Operation

Bhargab Maitra, Rahul Padwal, Manfred Boltze, and Sudhanshu Sekhar Das

Abstract In rural India, people are predominantly from low-income group with negligible private vehicle ownership. Therefore, it has become necessary to design suitable feeder service, as an alternative to walking or bicycling, for providing transportation linkage between village settlements and bus stops. Design of feeder service needs consideration of several aspects such as type of vehicle, selection of route, service frequency, and fare. As feeder service is designed for bus-stop catchments, a key issue is the starting point of the routes to bus stop. Travel behavior analysis is another important consideration as the selection of route, vehicle type, fare, etc., will influence the user cost. For rational estimation of user cost, it is necessary to understand trip maker's willingness to pay (WTP) with respect to various attributes of rural feeder service. The operational viability is another key aspect required to be considered in the process of designing the feeder service. This chapter considers all the above-mentioned aspects while demonstrating a simulation-based approach for the design of rural feeder service to bus stop with fixed-route fixed-schedule form of operation. A rational approach for design of rural feeder service with due consideration to various aspects and its application to a study area are the two major components of the work.

B. Maitra (✉) • R. Padwal
Civil Engineering Department, IIT Kharagpur, Kharagpur, India
e-mail: bhargab@civil.iitkgp.ernet.in; raul7775@gmail.com

M. Boltze
Transport Planning and Traffic Engineering, Darmstadt University of Technology, Darmstadt, Germany
e-mail: boltze@verkehr.tu-darmstadt.de

S.S. Das
Department of Civil Engineering, RSR Rungta College of Engineering and Technology, Bhilai, Chattisgarh, India
e-mail: ssdas8@gmail.com

S. Chakraborty and G. Bhattacharya (eds.), *Proceedings of the International Symposium on Engineering under Uncertainty: Safety Assessment and Management (ISEUSAM - 2012)*,
DOI 10.1007/978-81-322-0757-3_71,

Keywords Rural feeder service • Measure of effectiveness • Feeder vehicles • Feeder routes • Simulation

1 Introduction

All major roads in rural India are largely served by bus system, but the road connectivity was generally poor between villages and bus stops. As a result, walking and bicycle have been used by rural commuters for accessing bus stops. In the recent years, road connectivity in rural India has improved significantly with the construction of roads under a rural road development program [7]. With the development of rural roads, it is now possible to operate feeder service for transfer of passengers between villages and bus stops. Accordingly, design of rural feeder service has become a necessary task. Several studies have been reported in literature on routing, scheduling, and design of feeder service in urban areas [3, 5, 6, 8–10, 11]. However, there is little information available regarding the design of rural feeder service in developing countries. This chapter demonstrates a simulation-based approach for design of fixed-route fixed-schedule feeder service in rural India. Design of a feeder service is carried out considering both user cost and operational viability which are dependent on several factors such as type of vehicle, fare, route, and headway. Generalized cost (GC) is used as a comprehensive measure of user costs which includes disutilities associated with walking distance, waiting time, and discomfort during traveling. GC is expressed using trip maker's willingness to pay (WTP) with respect to various attributes of rural feeder service. To limit the scope of research work, the major network of bus routes is considered as fixed and not discussed here.

Das et al. [2] investigated road user's WTP with respect to various attributes of rural feeder service. About 200-square-km area in the state of West Bengal, India was selected as the case study. The study area is bounded by national highway (NH) in the eastern side, major district roads (MDRs) in northern and western sides, and river Subarnarekha in the southern side. The NH and MDRs are served by bus. However, the roads within the study area are not served by any feeder system so far. In this chapter, the design of rural feeder service is demonstrated with reference to the same study area. The study area is presently served by 12 bus stops which are located on the study area boundary. The user costs associated with feeder service are also obtained using the database and model developed by Das [1] and Das et al. [2].

2 Methodology

The purpose of the feeder service is to provide a beneficial and efficient service to the rural commuters. Thus, the aim is to maximize the user benefits through optimal selection of route, type of vehicle, and fare, keeping in mind the operational viability of the feeder service. A feeder route is aimed to serve rural population who are located in the catchments of a bus stop. Therefore, one end (i.e., the bus stop) of the route is fixed, but the other end could be any of the villages located in

the catchments of the bus stop. A key issue influencing both user costs and operational viability is the starting point of the route in the village end. The selection of route affects the waiting time, walking distance, distance traveled, and hence the generalized cost to the user. Thus, route with minimum generalized cost is selected after simulation of vehicular movements on all possible routes of a particular bus-stop catchment for the given span of operation. The selected optimal route should yield a viable solution for the efficient operation of the feeder service. The headway, the fare, and thus the operational viability also depend on the vehicle type. The methodology followed for maximizing user benefits through optimal selection of route, type of vehicle, and headway of service is summarized in the Fig. 1.

Step 0: Inputs

The inputs include present daily travel demand for each village in the catchments of a bus stop, span of operation of feeder service, directional variation of demand over the span of operation, village settlements, and their distance from bus stop as per the spanning tree road network, journey speed, and cutoff revenue model for two types of vehicle, i.e., tempo and trekker, vehicle capacity under normal condition and vehicle capacity under congested seating for each type of vehicle, minimum layover time of feeder vehicles at each end, and fares for tempo and trekker.

Step 1: Select a Bus Stop

The given study area is divided into various bus stops, and thus, a single bus stop and the villages in its influence need to be considered at a time.

Step 2: Calculate Directional Hourly Demands

Calculate directional hourly demands with respect to each village using the present daily travel demand for each village in the catchments of a bus stop, span of operation of feeder service, and directional temporal variation of demand over the span of operation.

Step 3: Generate Arrival Time of Passengers

For each stop, once the directional hourly demands are known, arrival times of passengers at each hour for each village are generated for both direction of travel assuming a uniform random distribution.

Step 4: Arrange the Arrival Times in Ascending Order

These generated arrival times are then sorted in ascending order to represent the arrival of commuters at various villages for a particular bus-stop catchment.

Step 5: Calculate Maximum Directional Peak Hourly Link Loads

Using hourly demands (step 2) and village settlements and their distance from bus stop as per the spanning tree road network (an input in step 0), the maximum directional peak hourly link loads are calculated.

Step 6: Select a Feeder Vehicle

Two types of feeder vehicle are considered. Consider a feeder vehicle.

Step 7: Define a Feeder Route

Several villages are located in the influence area of a bus stop. A feeder route will have one of these villages at one end, and the bus stop at the other end. There are different possible feeder routes. Take a possible feeder route.

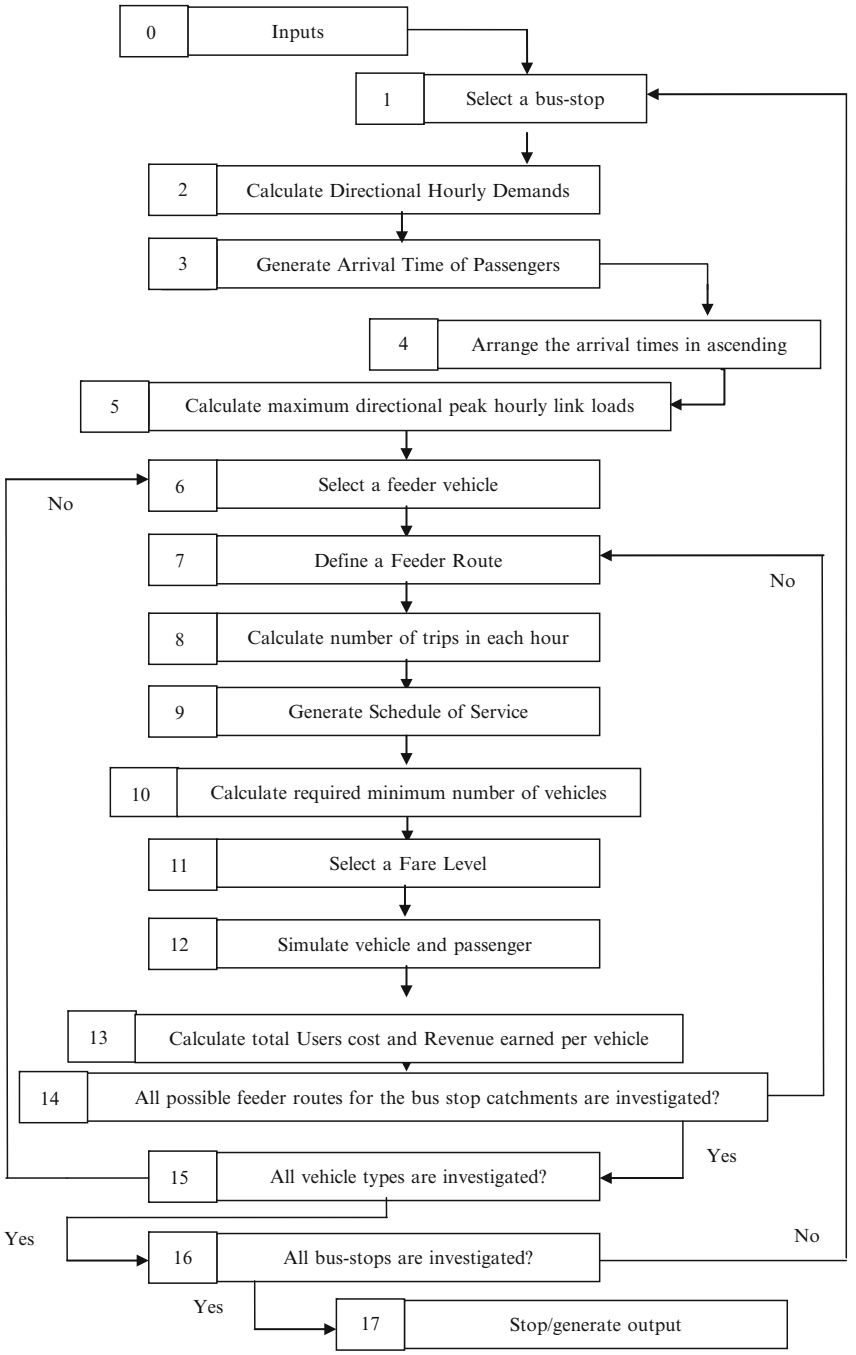

Fig. 1 Selection of optimal feeder route, vehicle type, and fare

Step 8: Calculate Number of Trips in Each Hour of Service

Using the maximum directional peak hourly link loads (step 5) and vehicle capacity under normal condition (step 0), calculate the number of trips required in each hour of operation for the assumed feeder route (step 7) of the considered bus stop.

Step 9: Generate Schedule of Service

With the knowledge of number of trips required in each hour of operation (step 8), generate the schedule of these trips. Schedule means starting time of trips at both ends of the route. Schedule depends upon the headway which depends on the number of trips in each hour of operation.

Step 10: Calculate Required Minimum Number of Vehicles

First, calculate the round-trip time using average journey speed, route length, and minimum layover time at each end. Using the number of trips in the busiest hour of operation and round-trip time, calculate the minimum required number of vehicles to sustain the operation during the busiest hour.

Step 11: Select a Fare Level

Consider the fare model.

Step 12: Simulate Vehicle and Passenger Movements

The details of simulation of vehicle and passenger movements are given in Fig. 2 and explained through steps 12.a, 12.b, 12.c.1, and 12.c.2.

Step 12.a: Start the First Trip

From the schedule generated (step 9) for every hour, the trip starting time for a particular route for the selected bus stop is noted, and the trip is started accordingly.

Step 12.b: Identify the Direction in Which the Passengers Are More, i.e., Outward or Inward

If outward (i.e., village to bus stop) is more, then follow step 12.c.1 and then step 12.c.2, i.e., start the trips at the non-bus-stop end of the selected route for the selected bus stop.

If inward (i.e., bus stop to village) is more, then follow step 12.c.2 first and then step 12.c.1, i.e., start the trip at the bus-stop end of the selected route for the selected bus stop.

Step 12.c.1: Pick Up Villagers Traveling in the Outward Direction

This step includes the following sub-steps:

A. *Storing travel attributes*. For the passenger who gets picked up, the following attributes need to be stored:

- Total distance traveled by the passenger (input to the fare model, i.e., in computing the direct fare).
- Waiting time, i.e., difference in the arrival of passenger (randomly generated) and arrival of vehicle to that node (depends on speed and schedule).
- Walking distance, i.e., for a particular route, some villages may not be directly covered and so the passengers from these villages have to travel to

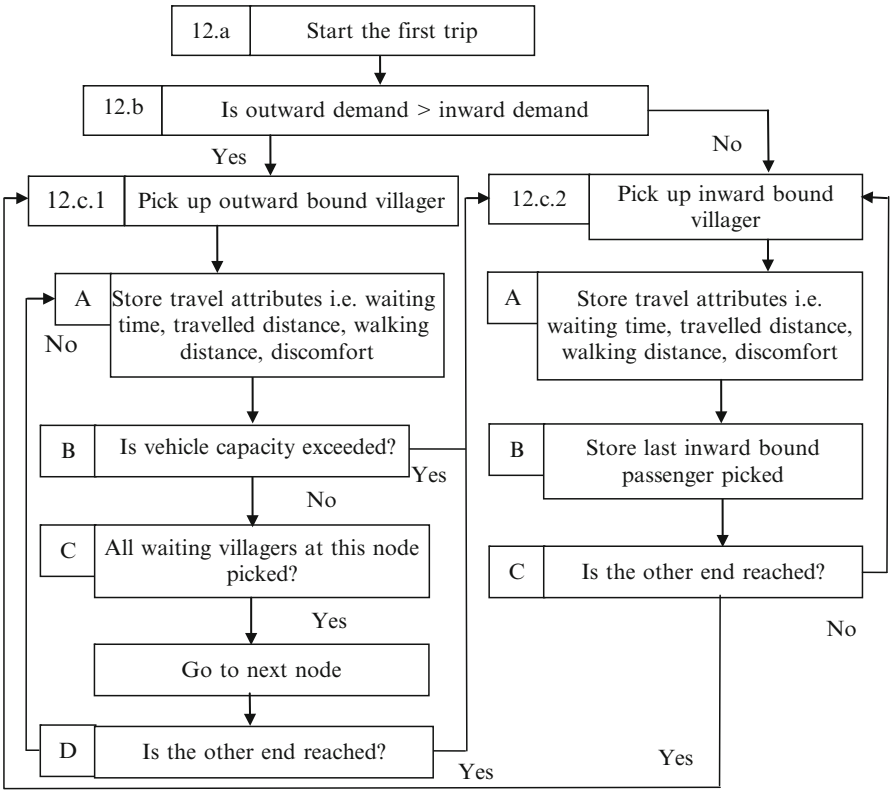

Fig. 2 Simulation of vehicle and passenger movements

the "nearest village" (i.e., nearest node on route), and this walking distance is considered as cost to the user.

- Discomfort, i.e., the distance traveled under "congested seating" (explained in detail later). Note that this discomfort is stored for all passengers traveling under congested seating.

B. *Is the capacity for the selected vehicle exceeded?*

- If yes, then store the last picked-up villager for the node and end the trip.
- If no, then go to step C.

C. *All waiting villagers at this node picked?*

- If yes, then store the location of last picked-up villager, go to next node on the route, and repeat step A for that node.
- If no, then repeat step A for the remaining passengers of the same node.

D. *Is the other end reached?*

- If yes, stop for the minimum layover time before starting the inward journey.
- If no, continue with the simulation of the outward journey.

Step 12.c.2: Pick Up Villagers Traveling in the Inward Direction
This step includes the following sub-steps:

A. *Storing travel attributes*. For the passenger who gets picked up at bus stop, the following attributes need to be stored:

- Total distance traveled by the passenger (input to the fare model, i.e., in computing the direct fare).
- Waiting time, i.e., difference in the arrival of passenger (randomly generated) and arrival of vehicle to that node (depends on speed and schedule).
- Walking distance, i.e., for a particular route, some villages may not be directly covered and so the passengers from these villages have to travel to the "nearest village" (i.e., nearest node on route), and this walking distance is considered as cost to the user.
- Discomfort, i.e., the distance traveled under "congested seating" (explained in detail later). Note that this discomfort is stored for all passengers traveling under congested seating.

B. *Store the last picked-up passenger*. Here, the villagers are all waiting at the same node for their inward journey, i.e., the bus stop. If the number of villagers waiting is less than the capacity, then all the waiting villagers are picked up and the location of last picked-up villager is stored. If, however, the number of villagers waiting at the bus stop is more than the capacity of vehicle, then the excess waiting passengers have to wait for the next vehicle to arrive and only the passengers up to the capacity of the vehicle are picked up in this trip. The location of the last picked-up villager is stored so that for the next inward trip, the starting point in known. Note that the passenger arrival times are sorted, and so the location alone is sufficient to know where to start the next inward trip.

C. *Is the other end reached?*

- If yes, stop for the minimum layover time before starting the outward journey again.
- If no, continue with the simulation for the inward journey.

Step 13: Calculate Total User Cost and Revenue Earned per Vehicle
Calculate the total user cost during the span of operation and revenue earned per vehicle.

Step 14: All Possible Feeder Routes for the Bus-Stop Catchments Are Investigated?
If yes, then identify the optimal solution based on comparison of all possible feeder routes and fare models. But, this is an optimal solution for a specific vehicle type. Now, go to step 15.

If no, then go to step 7 (basically investigating another feeder route).
Step 15: All Vehicle Types Are Investigated?
If yes, then identify the optimal solution based on comparison of all possible feeder routes, fare models, and vehicle types. Now, go to step 16.
If no, then go to step 6 (basically investigating another vehicle type).
Step 16: All Bus Stops Investigated?
If yes, then identify the optimal solution based on comparison of all possible feeder routes, fare models, and vehicle types for all the bus stops considered.
If no, then go to step 1 (basically investigating another bus stop).
Step 17: Stop/Generate Necessary Outputs
Optimal paths for different vehicle types and for all the bus stops are thus identified for the given study area by using a simulation-based approach and under the fixed-route fixed-schedule rule of operation.

3 Input Database

The input database includes road network, i.e., the various bus stops and the villages in their influence; vehicle characteristics such as the capacity under normal and congested seating, cutoff revenue for both types of vehicles, journey speed, and minimum layover time; generalized cost to the user; and travel demand and measure of effectiveness (MOE) which being the generalized cost (GC) to the users. Various inputs used to develop the database are described below.

3.1 Road Network

The road network considered for design of rural feeder service is same as that developed under the rural road development program, which aims at providing all weather roads to connect the villages in India. The database included length of each link and connecting nodes (i.e., village or bus stop). The road network considered in the present work is shown in Fig. 2. Some salient features of the bus stops surrounding the study area are given in Table 1. In a developing country like India, walking is the most common form of travel for a distance of up to 1–2 km [4]. Therefore, the villages within 2 km of the bus stops are excluded for the purpose of design of the feeder service.

3.2 Vehicle Characteristics and Cutoff Revenue

The two types of vehicles considered are tempo and trekker with capacities of six and ten, respectively. These types of vehicles are commonly used for transit in rural

Table 1 Generalized costs for different feeder routes and vehicles for Salajpur bus stop

Vehicle type: tempo										
Node no.	2	3	4	5	6	7	8	9	10	11
Village name	Kutki	Sarisa	Chandpur	Rasra	Karat	Murabani	Alikosa	Maljamuna	Srikrisnapur	Manikora
Run 1	5861.2	5833.8	5881.3	6277.5	6307.4	6472.5	6570.2	4365.2	6087.6	7436.2
Run 2	5900.3	5878.4	5917.5	6342.0	6314.2	6461.7	6633.0	4373.3	6138.0	7472.0
Run 3	5900.2	5884.6	5922.8	6318.9	6320.6	6482.6	6597.2	4381.8	6170.2	7483.2
Run 4	5901.1	5875.4	5923.4	6323.2	6270.0	6440.3	6571.6	4344.7	6114.4	7469.1
Run 5	5911.3	5879.7	5912.1	6339.9	6300.7	6461.4	6580.7	4330.7	6110.0	7448.1
Average	5894.8	5870.4	5911.4	6320.3	6302.6	6463.7	6590.6	4359.1	6124.0	7461.7
Vehicle type: tempo										
Run 1	5949.0	5966.9	5339.2	6517.7	5168.6	5265.1	4882.9	4681.9	4759.9	5305.0
Run 2	5986.4	6000.6	5304.0	6478.7	5206.9	5294.0	4946.8	4745.4	4787.0	5457.6
Run 3	5968.7	6016.1	5341.0	6513.6	5182.8	5306.5	4886.2	4745.6	4813.2	5442.6
Run 4	5989.5	6010.0	5336.4	6520.5	5176.9	5321.4	4910.2	4737.6	4763.8	5452.6
Run 5	5997.0	6006.1	5363.1	6511.3	5172.0	5278.2	4875.1	4675.1	4710.1	5393.4
Average	5978.1	6000.0	5336.7	6508.3	5181.4	5293.1	4900.2	4717.1	4766.8	5410.2

India. The cutoff revenue, i.e., the minimum earning required covering the fixed cost, running cost of a vehicle, and profit to the operator, is another important input from the point of view of operational viability of the service. The estimated cutoff revenues (CR) for the two types of vehicles are given below:

$$\mathrm{CR}_{(\mathrm{Trekker})} = 247 + 2.8 * d + P \tag{1}$$

$$\mathrm{CR}_{(\mathrm{Tempo})} = 199 + 1.5 * d + P \tag{2}$$

where CR_i is the required cutoff revenue per day in INR for vehicle type "i," d is the distance traveled per vehicle per day in km, and P is the minimum profit for operator per day in INR.

3.3 Journey Speed and Minimum Layover Time

For calculation of total journey time and total vehicles required to maintain a headway, two inputs are required, namely, the journey speed and the minimum layover time. In the present work, journey speed is taken as 40 km per hour, and minimum layover time is taken as 5 min at each end.

3.4 Travel Behavior Analysis

For design of rural feeder service, it is necessary to estimate the demand likely to be shifted to feeder service and the resulting benefits to users. Travel behavior analysis was required to fulfill these two requirements. Das et al. [2] reported willingness to pay (WTP) of rural commuters with respect to different attributes of rural feeder service. The analysis included only the stated preference (SP) alternatives which were presented to respondents and their choice responses. Although respondents were also asked to state their choices including the present mode used for travel to bus stop, the analysis of data including the present mode of travel was not included in Das et al. [2]. Using the WTP values reported by Das et al. [2] for different attributes of feeder service, analysis was carried out for the other database (which included the present mode), and the results are used for demand modeling (i.e., for estimating the share of demand likely to be shifted to feeder service) and estimation of user costs or benefits (with due consideration to the present mode of travel) in the present work. The details of model estimation and WTP calculation [1] are omitted here as the focus of this chapter is on design of rural feeder service. The generalized cost (GC) used in the present work is given below:

$$\mathrm{GC} = 0.832 * \mathrm{WD} + 0.121 * \mathrm{TD} + K * D + \text{Direct Fare} \tag{3}$$

It may be mentioned that 0.832 is the value of walking distance (in Rupees per km walking distance), and 0.121 (in Rupees per minute) is the value of waiting time. In rural India, small vehicles (tempo or trekker) are found to carry more passengers than the seat capacity specified by manufacturer. Accommodating more passengers causes discomfort to passengers, and the travel condition is described as "congested seating." When vehicles carry passenger only up to the seat capacity as specified by the manufacturer, the travel condition is described as "comfortable seating." K is to account for such discomfort due to congested seating, and the value of K is 0.437 (in Rupees per km) under congested seating. The value of K is 0 when it is comfortable seating.

3.5 Fare Model

The fare model considered in the present work is given below:

$$\text{Fare} = X * R2 \tag{4}$$

In this case, X is the distance and $R2$ is the fare per km. $R2$ is varied from 2.5 to 3.5 in 20 intervals.

3.6 Travel Demand

Travel demand between each village and nearest bus stop is a key input for the work. It was necessary to model bus stop bound travel demand generated from various villages in the study area and capture the temporal variation of demand. Accordingly, trip rates for different categories of household are analyzed. Households are classified into three categories, namely, cultivator, daily labor, and service/business on the basis of the occupation of the head of household. Trip rates are also estimated separately for revenue-generating and non-revenue-generating trips. Non-revenue-generating trips are further classified in two categories, namely, educational trips (i.e., trips made for educational purpose only) and household trips (i.e., trips made for social, recreational, and household purposes).

3.7 Measure of Effectiveness

It is necessary to consider an appropriate measure of effectiveness (MOE) while selecting feeder routes and vehicles. An attempt is made to optimize the MOE in the process of identifying operationally viable feeder routes. The MOE primarily represents the objective of providing feeder service in a quantitative manner. The

Table 2 Summary of recommended feeder routes and vehicles in the study area

Bus Stop	Optimum GC with feeder service	Type of feeder vehicle	% of road length served by feeder service	GC without feeder service	% savings in GC by feeder service
Bhasra	9309.5	Trekker	61.4	11443.7	18.6
Daihara	2045.2	Trekker	85.3	2764.1	26.0
Dantan	5399.9	Trekker	71.7	7267.3	25.7
Kalbani	3479.1	Tempo	74.7	4859.0	28.4
Khokra 1	3615.8	Tempo	65.2	4943.3	26.9
Khokra 2	2445.6	Tempo	57.4	2716.0	10.0
Kukai	1951.5	Trekker	74.5	2495.4	21.8
Monaharpur	3976.3	Tempo	61.7	5083.8	21.8
Nachipur	1494.4	Tempo	41.2	1804.4	17.2
Panchiyar	1725.6	Tempo	37.5	1829.9	5.7
Salajpur	4359.1	Tempo	74.0	5208.0	16.3
Sarisa	1381.6	Tempo	31.4	2146.8	35.6
Syamalpur	1395.4	Tempo	47.8	1669.2	16.4

selection of MOE is, therefore, a policy matter. In the present work, selection of feeder routes and vehicles are demonstrated GC as the MOE. A reduction in GC is a rational measure of user benefits. Therefore, with GC as MOE, the routes and vehicle types are selected in order to minimize the GC.

4 Results and Discussion

The results for alternative feeder routes and feeder vehicles for the bus stop called Salajpur are given in Table 1. The road network connects 11 nodes. Node 1 represents the bus stop, while node 2 to node 11 represents different village settlements. The average of five simulation runs is taken for comparison of various routes and feeder vehicles. It may be observed that when tempo is considered as a feeder vehicle, the GC is optimum with node 9 (i.e., Maljamuna village) as the starting point of the feeder route in the village end. When trekker is considered as a feeder vehicle, the same feeder route produces the optimal GC. However, it is found that using tempo as a feeder vehicle is beneficial as it brings down the GC further as compared to trekker. Therefore, for the Salajpur bus stop as feeder route, connecting Maljamuna to the bus stop with tempo as a feeder vehicle is recommended. Similarly, the optimal feeder route and type of vehicle for all other bus stops are also obtained, and the results are summarized in Table 2. Table 2 also indicates the percentage savings in GC due to the feeder service.

It may be observed from Table 2 that selection of feeder route and vehicle is a function of catchment characteristics such as location of villages and travel demands. It is also observed that feeder service may be instrumental in bringing benefits to the rural community. Of course, the benefit is also a function of catchment characteristics. In the present case study, feeder service is expected to bring benefits in the range of 5.6–35.6% with an average value of about 20.8%.

5 Conclusions

Public transport system is an important consideration in rural India. Although buses generally serve majority of higher-order roads, access to bus stops from villages using appropriate feeder service is largely a missing component. A simulation-based approach is demonstrated for the design of feeder service in rural India with fixed-route fixed-schedule form of operation. In the present work, due consideration is given to user costs and operational viability of the service. User costs are expressed in terms of a comprehensive measure called as generalized cost (GC). User costs include not only the direct cost of travel but also other costs associated with qualitative and quantitative attributes of the feeder service. Some of the key outcomes are vehicle types, routes, fare, and headway. The work demonstrates the influence of catchment characteristics (i.e., number of villages, size of villages, and spatial separation represented by road network connecting villages to bus stop) on feeder service attributes (i.e., type of vehicle, route, headway of service, and fare). It is also shown that feeder service could be instrumental in bringing benefits to rural community. In the present work, the benefit resulting from feeder service is expressed in terms of a reduction in the GC. The results presented in this chapter are case specific, but the methodology can be applied for design of feeder services in other rural regions.

Acknowledgments The work presented in this chapter is carried out with support from Deutscher Akademischer Austausch Dienst (DAAD) and Alexander von Humboldt-Stiftung. Authors express their sincere thanks to Deutscher Akademischer Austausch Dienst (DAAD) and Alexander von Humboldt-Stiftung for their support toward international exchange and research.

References

1. Das SS (2008) Planning of rural feeder service to bus stop. Unpublished Doctoral thesis, IIT Kharagpur
2. Das SS, Maitra B, Boltze M (2009) Valuing travel attributes of rural feeder service to bus stop: a comparison of different logit model specifications. J Transp Eng ASCE 135(6):330–337
3. Geok K, Perl J (1988) Optimization of feeder bus routes and bus stop spacing. J Transp Eng 114(3):341–354
4. Iles R (2005) Public transport in developing countries. Elsevier, Amsterdam
5. Li X, Quadrifoglio L (2010) Feeder transit services: choosing between fixed and demand responsive policy. Transp Res Part C Emerg Technol 18(5):770–780
6. Martins CL, Pato MV (1998) Search strategies for the feeder bus network design problem. Eur J Oper Res 106:425–440
7. Sikdar PK (2002) Pradhan Mantri Gram Sadak Yojana, for the people, by the people. Indian Highw 30(6):59–68
8. Shrivastava P, Dhingra SL (2001) Development of feeder routes for suburban railway stations using heuristic approach. J Transp Eng ASCE 127(4):334–341

9. Shrivastava P, O'Mahony M (2006) A model for development of optimized feeder routes and coordinated schedules—a genetic algorithms approach. Transp Policy 13:413–425
10. Shrivastava P, O'Mahony M (2009) Modeling an integrated public transportation system—a case study in Dublin, Ireland. European Transport\Trasporti Europei no. 41:28–46
11. Wirasinghe SC (1980) Nearly optimal parameters for a rail feeder bus system on a rectangular grid. Transp Sci 14A(1):33–40

Probabilistic Assessment of Container Crane Under Wind Loading

Sourav Gur and Samit Ray-Chaudhuri

Abstract Container cranes are highly susceptible to damage or even failure during severe windstorms. Damage of container crane causes significant amount of economic loss both in terms of repair/replacement and downtime. This chapter focuses on the effect of uncertainty of different parameters of wind field on the performance of container cranes. A representative crane of tower height 72.60 m and total boom length of 131.00 m is chosen and modeled in a commercial software considering both material and geometric nonlinearities. Stochastic fluctuating wind fields have been simulated by means of spectral representation method using the Kaimal and Simiu power spectra in conjunction with along and across wind coherence functions. Nonlinear time history analyses are carried out using simulated wind fields, and the performance of the crane is assessed in terms of fragility curves. Further, a sensitivity analysis is conducted by means of a tornado diagram and first-order second-moment analysis to rank different uncertain parameters of wind field. Based on these results, a few considerations for design have been provided.

Keywords Container crane • Parametric uncertainty • Stochastic wind field • Nonlinear dynamic analysis • Fragility curve • Sensitivity analysis

1 Introduction

Seaports are essential nodes of national and international transport system of a country. It is thus essential to minimize the damage of ports under natural disasters such as earthquakes and severe windstorms. In a port facility, container cranes are one of the most important types of structures that facilitate the movement of cargos between a ship and storage yards. Thus, damage or collapse incidents of cranes can

S. Gur (✉) • S. Ray-Chaudhuri
Department of Civil Engineering, Indian Institute of Technology Kanpur, Kanpur, India
e-mail: sourav.gur.1987@gmail.com; samitrc@iitk.ac.in

S. Chakraborty and G. Bhattacharya (eds.), *Proceedings of the International Symposium on Engineering under Uncertainty: Safety Assessment and Management (ISEUSAM - 2012)*,
DOI 10.1007/978-81-322-0757-3_72,

hinder smooth port operation, causing significant amount of economic loss in terms of repair or replacement, downtime, and enduring loss of business due to permanent traffic rerouting. Although significant advancements have been achieved in terms of design and construction of modern-day huge cranes, recent failure incidents such as (a) in 2003, at Pusan port of *S*. Korea, and (b) in 1996, the Zhanjiang port of Guangdong, indicate that these cranes are highly vulnerable to windstorm-induced loadings. Several researchers such as McCarthy and Vazifdar [5], McCarthy et al. [6, 7] carried out a few studies to identify different components of container cranes that are highly susceptible to failure during severe windstorm (tie-down wharf bracket and stowage-pin system, link plates, and turnbuckles) and different retrofitting schemes. In addition, several numerical and experimental studies are conducted (viz., Eden et al. [1], Huang et al. [2], Lee et al. [4], and Lee and Kang [3]) to determine values of different governing parameters for design of container crane due to wind load. Important conclusions of all those studies are the following: (a) effect of Reynolds number (*Re*) and Strouhal number (*S*) on different aerodynamic coefficients is negligible, (b) maximum value of uplifting force at any support occurs either for yaw angles between 20° and 40° or between 130° and 150°, and minimum value occurs at the yaw angle 90°.

It can be observed from previous research that no systematic studies have been carried out to investigate the effect of different parameters on failure of container crane as well as all those previous studies did not explicitly consider the influence of spatial variation of wind field on failure vulnerability of container crane. The primary purpose of this study is twofold: (a) identification of different parameters that have significant influence on failure vulnerability of container cranes and (b) estimate the influence of these parameters on failure of container cranes.

2 Stochastic Wind Field Simulation

Wind speed at any point and any instant of time [$V(x,y,z;t)$] consists of two parts: (a) mean wind speed [$\bar{V}(z)$], which is independent of space and time but only varies along the height and (b) fluctuating wind speed [$v(x, y, z; t)$], which varies both in space and time [8], as given by:

$$V(x, y, z; t) = \bar{V}(z) + v(x, y, z; t) \tag{1}$$

In this study, wind fields are simulated by means of spectral representation method (viz., Shinozuka and Deodatis [9]; Shinozuka and Deodatis [10] and Shinozuka and Jan[14]).

2.1 Mean Wind Field Simulation

For the simulation of mean wind speed, at first, the original coordinate system (x, y, y) is transformed to the coordinate system of the wind flow direction (x_1, y_1, z_1)

considering wind flow as horizontal and varying the yaw angle (θ, in degree). It is considered that the value of mean wind speed is zero at ground level and varying only with height according to the well-known power law, which is given as:

$$\bar{V}(z) = V_g \left(\frac{Z}{Z_g}\right)^{\alpha} \tag{2}$$

where $\bar{V}(Z)$ is the mean wind speed at height Z, V_g is the gradient wind velocity at gradient height Z_g (the height at which wind velocity become constant), and α is a power law exponent that depends on terrain conditions.

2.2 Fluctuating Wind Field Simulation

Fluctuating part of wind speed is simulated as a zero mean, one-dimensional, multivariate (1D-mV) stationary Gaussian stochastic wind field and can be rewritten as:

$$\begin{aligned} v_j^{(i)}(p\Delta t) &= Re\left\{\sum_{q=1}^{j}\sum_{l=0}^{M-1} B_{jql} \exp\left[i\, l p \frac{2\pi}{M}\right]\right\} \\ j &= 1, 2, \ldots\ldots, m; p = 0, 1, \ldots\ldots, M-1; \\ l &= 0, 1, \ldots\ldots, N-1 \end{aligned} \tag{3}$$

where

$$B_{jql} = 2|H_{jk}(l\Delta\omega)|\sqrt{\Delta\omega}\, \exp\left[-i\theta_{jq}(l\Delta\omega)\right]\, \exp\left[i\Phi_{ql}\right] \tag{3a}$$

$$\Delta\omega = \frac{\omega_u}{N};\ \Delta t = \frac{2\pi}{M\Delta w};\ \text{ and } M = 2N \tag{3b}$$

$$S^0(\omega) = H(\omega)H^{-T}(\omega) \tag{3c}$$

$$\theta_{jq}(l\Delta\omega) = \tan^{-1}\left(\frac{Im\left[H_{jq}(l\Delta\omega)\right]}{Re\left[H_{jq}(l\Delta\omega)\right]}\right) \tag{3d}$$

$H_{jk}(l\Delta\omega)$ is the lower triangular matrix, obtained from decomposing the spectral density matrix $[S^0(\omega)]$, using Cholesky's method. Elements of the spectral density matrix $[S^0(\omega)]$ can be expressed as:

$$S_{jj}^0(\omega) = S_j(\omega)\ j = 1, 2, \ldots, m \tag{4a}$$

$$S_{jk}^{0}(\omega) = \sqrt{S_j(\omega)S_k(\omega)} * \eta_{jk} * \gamma_{jk} \qquad j,k = 1,2,\ldots,m,\ j \neq k \tag{4b}$$

where

$$S_j(\omega) = \frac{1}{2}\frac{1}{2\pi}200\,u_{\bullet}^{z}\frac{Z}{V(Z)}\frac{1}{\left[1+50\frac{|\omega|Z}{2\pi V(Z)}\right]^{5/3}}\text{(Kaimal and Simiu power spectra)} \tag{4c}$$

$$\eta_{jk}(\omega, dX) = exp\left[-\frac{|\omega|C_X\,dX}{2\pi\ V_{m_{jk}}(Z)}\right]\text{(Along wind coherence function)} \tag{4d}$$

$$\gamma_{jk}(\omega, dY, dZ) = exp\left[-\frac{|\omega|\sqrt{(C_Y\,dY)^2+(C_Z\,dZ)^2}}{2\pi\ V_{m_{jk}}(Z)}\right]\text{(Across wind coherence function)} \tag{4e}$$

Therefore, the total wind speed at any point of the structure and at any instant of time is given by:

$$V(x,y,z;t) = V_g\left(\frac{Z}{Z_g}\right)^{\alpha} + Re\left\{\sum_{q=1}^{j}\sum_{l=0}^{M-1}B_{jql}\ \exp\left[i\,l\,p\frac{2\pi}{M}\right]\right\} \tag{5}$$

For simulation, the values of different parameters are assumed as $N = 2048$, $M = 4096$, and $\omega_u = 4\pi$. Realizations of the wind speed time histories are simulated for 1023.75 s with an interval of 0.25 s. Figure 1a shows a realization of simulated wind speed data for Z_g of 30.0 m and V_g of 60.0 m/s at different nodes for a time window of 400–500 s. To check the accuracy of simulated wind speed, cross power spectral density function (CPSDF) between these two nodes (node 55 and 40) are calculated from the simulated wind field data and then considering 20 samples, the average is calculated. Figure 1b shows the comparison of generated CPSDFs (a sample, the average CPSDF computed from 20 realizations obtained using a moving average method with a window size of 16 and the assumed one) for a frequency range of 0.1–1.0 Hz. It shows that in mean sense, the CPSDFs generated from the wind speed data are in very good agreement with the assumed CPSDF.

2.3 Wind Force Computation

Only the drag and lift forces at each node are considered in the direction of wind and perpendicular to the plane of wind flow, i.e., in the vertical direction. The drag force F_{D} and lift force F_{L} at any point can be expressed as [13]:

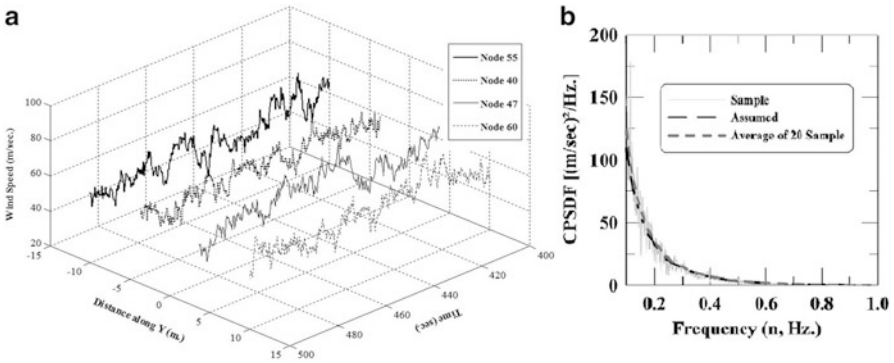

Fig. 1 (**a**) Total wind speed along "*X*" at different points plotted with respect to time and distance and (**b**) comparison of CPSDFs of wind speed between nodes 40 and 55

$$F_{\mathrm{D}}(x,y,z;\ t) = \frac{1}{2}\rho[V(x,y,z;t)]^2\, C_{\mathrm{D}}\, A \text{ and } F_{\mathrm{L}}(x,y,z;\ t) = \frac{1}{2}\rho[V(x,y,z;\ t)]^2\, C_{\mathrm{L}}\, A \tag{6}$$

where F_{D} and F_{L} are the drag and lift forces, respectively; ρ is the density of air (1.225 Kg/m^3), C_{D} and C_{L} are the drag and lift coefficients, respectively; and A is the effective area of any node in the direction of wind flow. Drag (C_{D}) and lift (C_{L}) coefficient values are taken from Lee and Kang [3].

3 Numerical Modeling and Analysis

For this study, a container crane of tower height 72.60 m and total boom length of 131.0 m (back reach length 32.0 m, rail span 29.0 m, and outreach length 70.0 m) has been considered (Fig. 2). The lifting capacity of the container crane model is 65.0 t. The proposed container crane at different boom positions is modeled in SAP 2000 V14 using frame element (67 nodes, connected by 109 elements). For modeling, isotropic tendon-type steel [unit weight (γ): 76972.86 N/m^3, modulus of elasticity (E): 1.999×10^{11} N/m^2, Poisson's ratio (v): 0.30, shear modulus (G): 7.690×10^{10} N/m^2, minimum yield stress (F_{y}): 1.493×10^9 N/m^2] with 3% kinematic hardening is considered.

3.1 Modal Properties

Analysis is performed to estimate natural frequencies and mode shapes of the models. Ritz vector method is employed to extract only the first six modes of the

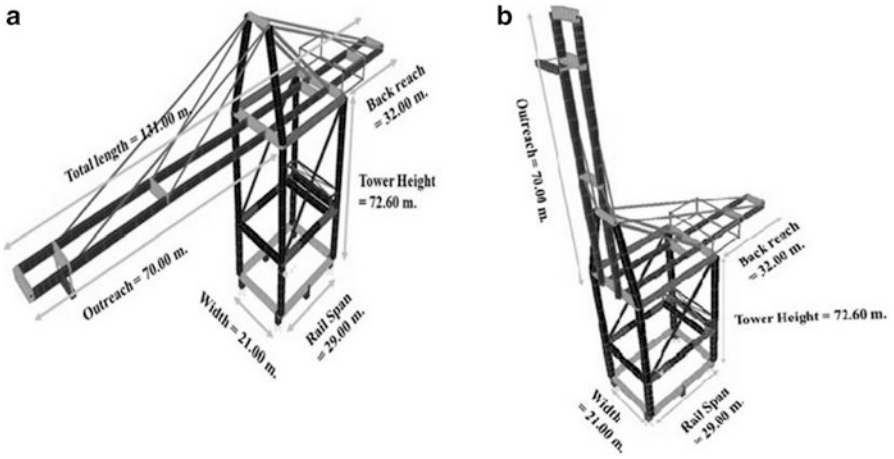

Fig. 2 Representative container crane model at two different boom positions, (**a**) boom down and (**b**) boom up

Table 1 Natural periods and mode shape of the first six modes

	Time periods (in s)		Mode shape type	
Mode number	Boom down	Boom up	Boom down	Boom up
1st	3.14162	3.66817	LOB	LOB
2nd	2.38287	2.58208	LBB	TOB1
3rd	1.30613	2.11273	LTV	L
4th	1.06751	1.50134	T	LT
5th	0.80840	0.99998	VB	T
6th	0.71979	0.73545	LT	TOB2

LOB lateral motion of outreach of boom girder; *LBB* lateral motions of back reach of boom girder; *LTV* lateral torsion with vertical motion; *T* transverse motion; *VB* vertical motion of boom girder; *LT* lateral torsion motion; *TOB*1 transverse motion of outreach of boom girder; *L* lateral motion; *TOB*2 torsional motion of outreach of boom girder

model. Table 1 provides the natural periods of the first six modes of container crane models. It can be observed from these results that the periods in all modes of boom-up model is higher than the corresponding boom-down position, thereby implying that the boom-up position is more flexible, as one can expect.

3.2 Static and Wind Load Analysis

For a container crane, static load comes from different sources. These loads are applied at each nodes of the crane model, and analysis is performed to obtain the state of stress and deformation of the model. For static analysis, geometric

nonlinearity (P-Δ effect and large deformation) is considered. At first, the static load analysis is performed. Then holding the states of deformation and stress due to the applied static loads, the wind load analysis is performed. The wind load time history is applied at each node in both the directions (horizontal and vertical). Nonlinear time history analysis is carried out using Newmark's direct integration technique.

4 Convergence Test and Sensitivity Analysis

Since wind fields are stochastic in nature, a convergence test of response parameters (normalized base moment) has been performed for Z_g of 30.0 m and V_g of 60.0 m/s to determine the approximate sample size of random wind field required for simulation convergence. Sensitivity analysis is then carried out to identify parameters that may have significant influence on failure of container cranes. Tornado diagram method and FOSM analysis is used for the purpose of sensitivity study. In tornado diagram method, all the uncertain parameters are considered as random variables, and their two extreme values are chosen as mean − standard deviation and mean + standard deviation. The mean values and coefficients of variation of different uncertain parameters considered for the sensitivity analysis are given in Table 2. Swings have been plotted for all random variables from top to bottom in a decreasing size. These swings demonstrate relative contribution of each variable on the desired response parameter. Here, larger swing implies higher influence of a random variable on the response parameter than the shorter one. FOSM analysis is performed to determine relative variance contribution by neglecting correlation terms.

Table 2 Input parameter uncertainties

Parameter	Unit	Mean	COV (in %)
Yaw angle [θ]	In degree	90.0	33.33
Gradient height [Z_g]	In m	25.0	10.0
Gradient wind speed [V_g]	In m/s	50.0	10.0
Power law exponent [α]	—	1/7	20.0
Roughness height [z_0]	In m	0.01	20.0
Coherence function constant [C_X, C_Y, C_Z]	—	6.0, 10.0, 16.0	15.0
Boom position	—	Boom down	Boom articulated and boom up
Yield strength [F_y]	In N/m^2	1.493×10^9	20.0
Elastic modulus [E]	In N/m^2	200×10^9	20.0
Kinematic hardening ratio [n]	In %	3.00	15.0
Damping ratio [ξ]	In %	2.00	15.0

5 Vulnerability Assessment

Windstorm can sustain for a long duration, which can cause high magnitude of stress concentration along with frequent stress reversals. This may lead to low-cycle fatigue failure of the members connected to the supports. Now, the ratio R of the absolute value of the developed moment (M) in a member connected to any support to the plastic moment capacity (M_{P}) of the section can be used to determine the failure probability of the member. In mathematical form, this can be expressed as:

$$M_{\mathrm{p}} = F_y Z_{\mathrm{p}} \text{ and } R = \frac{|M|}{M_{\mathrm{p}}} \tag{7}$$

where Z_{P} is the plastic section modulus and F_{Y} is the yield stress. For any loading case, if the value of this ratio (R) becomes more than or equal to unity, the section, and thus the structure, can be considered to have been failed. After defining the damage state, fragility analysis is performed to determine failure probability of the container crane. In this method of fragility analysis, the median and log-standard deviation of fragility curve for different damage states are estimated simultaneously with the aid of maximum likelihood method (viz., [11, 12]). Due to use of a single log-standard deviation for different damage states, fragility curves for different damage states do not cross each other in this method. If failure of the structure is assessed with respect to the parameter a, then the failure probability of the structure at a particular damage state of E_k is expressed as:

$$P_{ik} = P(a_i; E_k) \tag{8a}$$

$$F_k(a_i; c_k, \zeta) = \Phi\left[\frac{ln\left(\frac{a_i}{c_k}\right)}{\zeta}\right] \tag{8b}$$

where $P_{i1} = P(a_i; E_1) = 1 - F_1(a_i; c_1, \zeta)$, $P_{ik} = P(a_i; E_k) = F_{k-1}(a_i; c_{k-1}, \zeta) - F_k(a_i; c_k, \zeta)$, and $P_{in} = P(a_i; E_n) = F_{n-1}(a_i; c_{n-1}, \zeta)$.

To calculate different medians for different damage states $(c_1, c_2, \ldots\ldots c_n)$ and a common log-standard deviation (ζ) for all the damage states, the method of maximum likelihood method is used here.

6 Results and Discussions

Important results of this study are listed as follows:

1. Figure 3 shows that the normalized base moment value converges for a sample size of approximately 60.

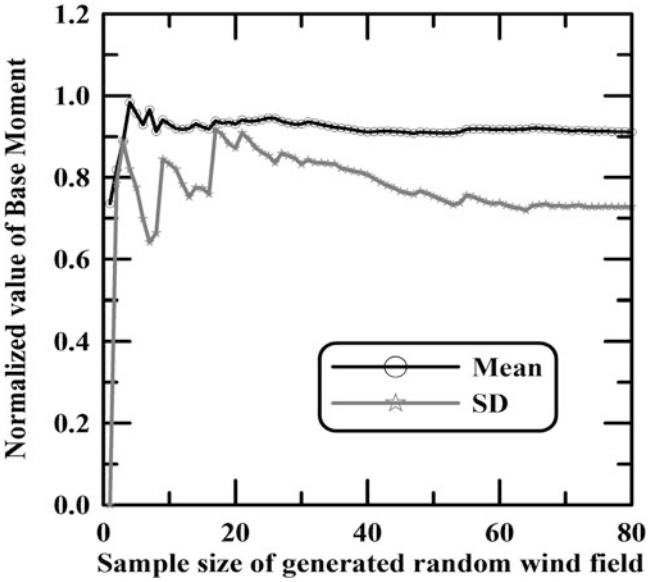

Fig. 3 Median and standard deviation (SD) of the normalized base moment for different sample sizes of generated random wind field

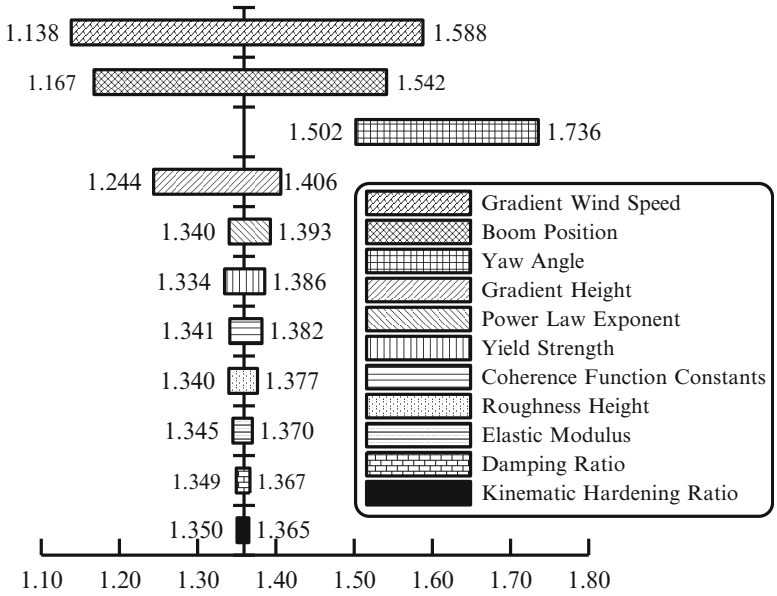

Fig. 4 Tornado diagram considering uncertainty in different parameters

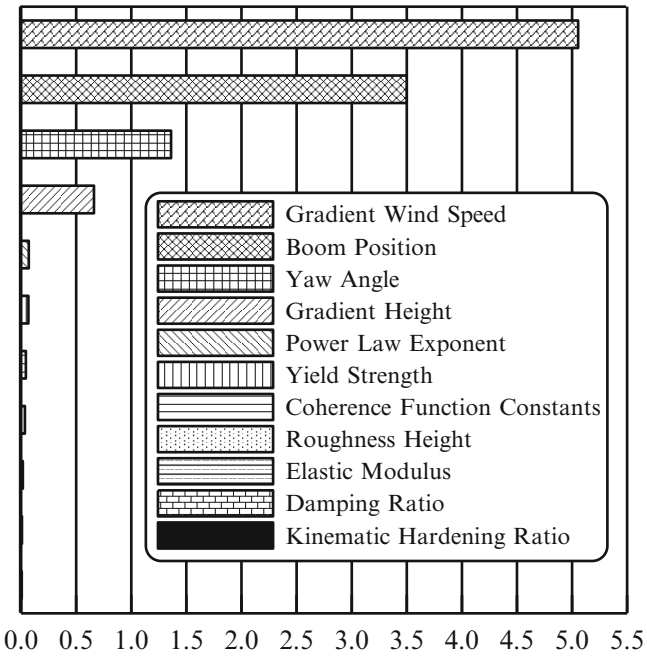

Fig. 5 Relative variance contribution (neglecting correlation terms) from FOSM analysis

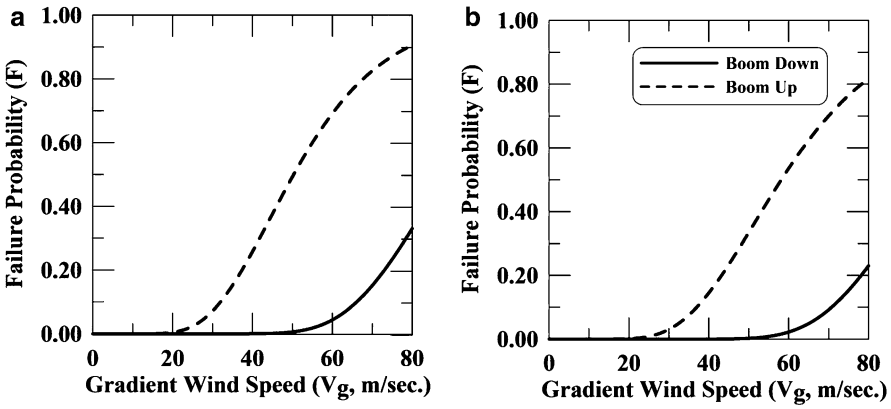

Fig. 6 Fragility curve at boom-down and boom-up condition for a particular yaw angle [(**a**) 60°, (**b**) 120°] and gradient height

2. Figures 4 and 5 show the sensitivity analysis results. From both of the figures, it can be observed that the gradient wind speed, boom position, yaw angle, and gradient height are the most important wind field parameters (in decreasing sequence of importance) to control the failure vulnerability of the container crane.

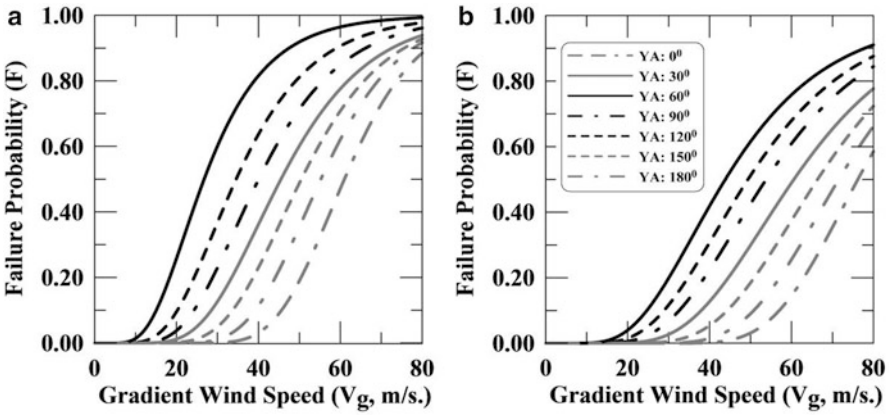

Fig. 7 Fragility curve at boom-down condition for a particular gradient height [**(a)** 10.0 m, **(b)** 15.0 m] and different yaw angle

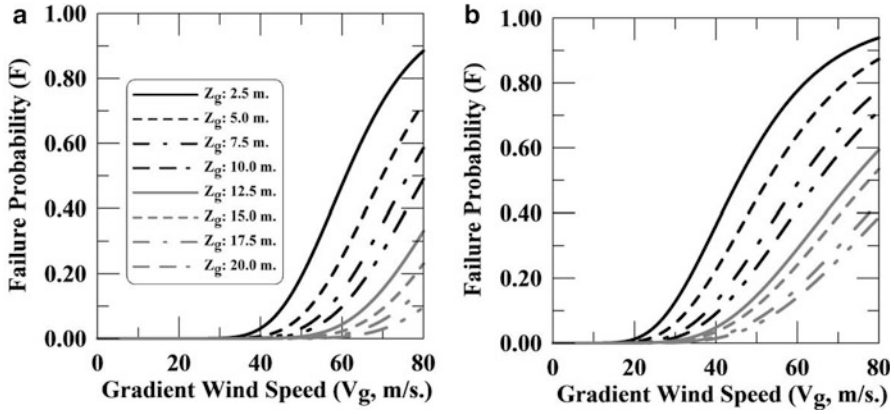

Fig. 8 Fragility curve at boom-down condition for a particular yaw angle [**(a)** 60°, **(b)** 120°] and different gradient height

3. From Fig. 6, it can be observed that considerable amount of variation in the failure probability occurs due to a change in boom position. Since the boom-up position is more flexible than the boom-down position, the failure probability at boom-up position is much more that of the boom-down position.
4. Figure 7 depicts that the failure probability of container crane also changes significantly with the change in yaw angle. At boom-down position, the failure probability decreases with the yaw angle in the sequence of 60°, 120°, 90°, 30°, 150°, 180°, and 0°. However, at boom-up condition, this sequence of the yaw angle becomes 60°, 120°, 0°, 180°, 90°, 30°, and 150°.
5. From Fig. 8, it can be observed that at a particular yaw angle and boom position, failure probability reduces with an increase in gradient height. A probable reason behind this is that at lower value of gradient height, the mean wind field becomes very stiff, which causes higher application of wind load on the structure and thus increases the failure probability.

7 Conclusions

A parametric study is conducted to identify different wind field parameters that significantly influence the failure of container crane. Influence of these significant parameters on failure vulnerability of the container crane is then assessed in terms of fragility curves. It is observed from the results that the gradient wind speed, boom position, yaw angle, and gradient height are the most important parameters that significantly influence the failure of container crane. It is also observed that the boom-up position is much more vulnerable than the boom-down position. Considerable amount of variation in the failure probability can occur with the change in yaw angle. It is also found that the failure probability of container crane increases with an increase in gradient wind speed and decreases with an increase in gradient height.

References

1. Eden JF, Iny A, Butler AJ (1980) Cranes in storm winds. Engineering structure, 1981, vol 3. Engineering and science, EPMESC X, 21–23 Aug 2006, Sanya, Hainan, China
2. Huang P, Wang JY, Gu M (2006) Wind tunnel test and numerical simulation of mean wind loads on a container crane. In: The fourth international symposium on Computational Wind Engineering (CWE2006), Yokohama, 2006
3. Lee JS, Kang HJ (2007) Wind load on a container crane located in atmospheric boundary layers. J Wind Eng Ind Aerodyn 96:193–208
4. Lee SW, Kim Y, Han DS, Han GJ (2'007) Wind tunnel study on the structural stability of a container crane according to the boom shape. In: Proceedings of the 4th WSEAS international conference on fluid mechanics, Gold Coast, QLD
5. McCarthy P, Vazifdar F (2004) Securing cranes for storm wind: uncertainties and recommendations. In: ASCE Ports 2004 conference, Houston, TX
6. McCarthy P, Jordan M, Lee K, Werner S (2007) Increasing hurricane winds dockside crane retrofit recommendations. In: ASCE Ports 2007 conference, San Diego
7. McCarthy P, Soderberg E, Dix A (2009) Wind damage to dockside cranes: recent failures and recommendations. In: TCLEE 2009 conference, Oakland
8. Paola MD (1998) Digital simulation of wind field velocity. J Wind Eng Ind Aerodyn 74–76 (1998):91–109
9. Shinozuka M, Deodatis G (1991) Simulation of stochastic processes by spectral representation. Appl Mech Rev 44(4):191–204, ASME Book No AMR094
10. Shinozuka M, Deodatis G (1996) Simulation of multi-dimensional Gaussian stochastic field by spectral representation. Appl Mech Rev 49(1):29–53, ASME Book No AMR183
11. Shinozuka M, Feng MQ, Kim HK, Kim SH (2000a) Statistical analysis of fragility curves. J Eng Mech 126(12):1224–1231
12. Shinozuka M, Feng MQ, Lee J, Naganuma T (2000b) Statistical analysis of fragility curves. J Eng Mech 126(12):1224–1231
13. Simiu E, Scanlan HR (1986) Wind effects on structure, 2nd edn. Wiley, New York
14. Shinozuka M Jan CM (1991) Digital simulation of random process and its applications. J Sound Vib 25(1)111–128

Autogressive Model for Structural Condition Assessment in Presence of Parametric Uncertainty

Koushik Roy and Samit Ray-Chaudhuri

Abstract Long-term and often short-term vibration-based structural health monitoring data show variations in response even though there is no visible change in structural properties. Although these variations are attributed to environmental factors causing change in structural parameters, such uncertainties in structural parameters make the condition assessment of a structure difficult. In this study, the autoregressive (AR) model, where the coefficients of the model are related to structural model parameters and are considered as one of the efficient tools often used in modal identification and damage detection, is used to investigate its efficiency in damage detection and localization when parametric uncertainties are present. A numerical study conducted with an eight-story shear building, where uncertainties in stiffness are assumed in terms of known probability density functions, shows that the AR model is highly efficient in damage detection and localization even when significant parametric uncertainties are present. For this purpose, damage is being induced in a particular story, and the response is analyzed with the autoregressive model to gauge the efficiency of the model. To broaden the practical applicability of the method when noise is present in the measurement data, the Kalman filter approach has been adopted and successfully shown to handle the noisy data.

Keywords Autoregressive model • Uncertainty • Damage detection • Sensitivity analysis

K. Roy • S. Ray-Chaudhuri (✉)
Indian Institute of Technology Kanpur, Kanpur, India
e-mail: koushik@iitk.ac.in; samitrc@iitk.ac.in

S. Chakraborty and G. Bhattacharya (eds.), *Proceedings of the International Symposium on Engineering under Uncertainty: Safety Assessment and Management (ISEUSAM - 2012)*,
DOI 10.1007/978-81-322-0757-3_73,

1 Introduction

Vibration-based structural damage detection has drawn considerable attention in recent years due to its nondestructive nature. Since the last few decades, several methodologies have been developed for this purpose. Brincker et al. [1] proposed a frequency domain method for structural modal identification of output-only systems. Sohn et al. [15] applied statistical pattern recognition paradigm in structural health monitoring. Kiremidjian et al. [9] adopted an enhanced statistical damage detection algorithm using time series analysis. Caicedo et al. [2] demonstrated the efficacy of natural excitation technique (NExT) and eigensystem realization algorithm (ERA) by applying on simulated data generated from the popular IASC-ASCE benchmark problem. Lu and Gao [12] proposed an efficient time-domain technique based on autoregressive prediction model for structural damage localization. Later they extended their study to quantify damage with noisy signal with the help of Kalman filter-based algorithm. Samuel da Silva et al. [14] applied autoregressive AR-ARX models and statistical pattern recognition on damage detection of a structure. Xiaodong et al. [16] took a practical model excited with simulated ambient signal to identify the modal parameters using NExT-ERA. Cheung et al. [4] validated experimentally the statistical pattern recognition methods for damage detection to field data. Gao and Lu [8] set up a proposition with acceleration residual generation for structural damage identification. Le and Tamura [10] used two frequency domain techniques—frequency domain decomposition and wavelet transform for modal identification from ambient vibration data. Liu et al. [11] explained the usage of extended Kalman filter in health monitoring of linear mechanical structures. Chiang et al. [5] put forward ERA with its modified form to identify modal parameters from ambient vibration data. Chiang and Lin [6] stated NExT-ERA in complete time domain with correlation technique. Caicedo [3] provided some practical guidelines for the NExT-ERA approach of modal identification using ambient vibration data. There are many other prediction models for structural damage detection [13] based on neural network, fuzzy logic, genetic algorithm, etc. These models have been used successfully with mostly simulated data.

In addition to deterministic methodologies in damage detection, stochastic damage detection procedures attract equal attention due to their capability in dealing with structural parametric uncertainties and noise in measured data. Structural parametric uncertainty can be classified in two categories: epistemic and aleatory. Epistemic uncertainty deals with the errors associated with measurement noise, whereas aleatory uncertainty deals with inherent modeling errors, i.e., the error due to parametric variation. From a different perspective, uncertainties in structural response in terms of errors can be categorized as biased errors and random errors. Random errors are evidently with zero mean and usually expected to follow Gaussian distribution. Measurement noise is also assumed as a zero mean random process. For uncertainty in structural parameters such as mass and stiffness, the response of a structure is of biased uncertain nature, which can be dealt with

probability density functions by applying the reverse procedures as proposed by Xu et al. [17]. Zhang et al. [20] developed a probabilistic damage detection approach for output-only structures with parametric uncertainties.

In this chapter, the behavior of an autoregressive model is investigated in presence of structural parametric uncertainties. An autoregressive model is one of the most popular models for safety assessment of a structure. The model is used to predict future possible data of a signal based on its previous data. The coefficient of this model is directly related to the modal properties of the structure. The following section describes the details of the autoregressive model.

2 Model Description

For a system with n degrees-of-freedom (DOF) having mass, stiffness, and damping matrices M_0, K_0, and C_0, respectively, the equations of motion can be expressed as follows:

$$M_0\ddot{\xi}(t) + C_0\dot{\xi}(t) + K_0\xi(t) = L_0u(t)$$
$$\ddot{\xi}(t) + J\dot{\xi}(t) + K\xi(t) = Lu(t)$$

Where $J = M_0^{-1}C_0, K = M_0^{-1}K_0 = \Phi\Lambda\Phi^T$, and $L = M_0^{-1}L_0$ with L_0 being the input coefficient or influence matrix with dimensions n *by* m. The defining equation of the autoregressive model thus takes the following form:

$$y(t) = \sum_{i=1}^{p} \phi_i y(t-i) + e(t) \tag{2}$$

where $\phi_i = i$th coefficient of the model, $y(t) =$ signal at time step t to be predicted, $e(t) =$ model residual error, and $p =$ order of the model.

A modified form of this prediction model, called autoregressive model with exogenous (ARX) input, is employed here mainly for the purpose of damage localization. The model expression relating among input data $u(t)$, output data $y(t)$, and residual error $e(t)$ in the time domain can be written as

$$A(q)y(t) = B(q)u(t) + C(q)e(t) \tag{3}$$

where A, B, and C are polynomials in the delay operation q^{-1} and can be expressed as follows:

$$A(q) = 1 + a_1 q^{-1} + a_2 q^{-2} + \cdots + a_{1na} q^{-na}$$
$$B(q) = 1 + b_1 q^{-1} + b_2 q^{-2} + \cdots + b_{nb} q^{-nb+1}$$
$$C(q) = 1 + c_1 q^{-1} + c_2 q^{-2} + \cdots + a_{nc} q^{-nc}$$

In Eq. (4), the numbers *na*, *nb,* and *nc* are the order of the respective polynomials. Based on these orders, the autoregressive model can be categorized as AR model, ARMA model, ARX model, and ARMAX model.

3 Theory

Due to lack of space, a detailed mathematical derivation is not presented here. Rather, a very brief theoretical background of the new approach in time domain to find out modal properties is discussed here. An autoregressive model with order [2, 3, 0] is expressed as follows:

$$y(k) = \sum_{i=1}^{2} A_i y(k-i) + \sum_{i=1}^{3} B_i u(k-i) \tag{5}$$

According to the proposed method, only the first AR coefficient A_1 is the only parameter of interest, and A_1 is given by

$$\mathrm{A}_1 = 2\phi \cos\left(\Lambda^{\frac{1}{2}}\Delta \mathrm{t}\right)\phi^T \tag{6}$$

where

$$\Lambda = \begin{bmatrix} \omega_1^2 & \cdots & \\ \vdots & \ddots & \vdots \\ & \cdots & \omega_n^2 \end{bmatrix}; \quad \cos\left(\Lambda^{\frac{1}{2}}\Delta \mathrm{t}\right) = \begin{bmatrix} \cos(\omega_1 \Delta \mathrm{t}) & \cdots & \\ \vdots & \ddots & \vdots \\ & \cdots & \cos(\omega_n \Delta \mathrm{t}) \end{bmatrix} \tag{7}$$

Thus, A_1 can be expressed as

$$A_1 = 2\phi \begin{bmatrix} \cos(\omega_1 \Delta \mathrm{t}) & \cdots & \\ \vdots & \ddots & \vdots \\ & \cdots & \cos(\omega_n \Delta \mathrm{t}) \end{bmatrix} \phi^T \tag{8}$$

4 Parametric Uncertainty

Due to variation in different environmental factors, model error, measurement error etc., uncertainty is indispensible resulting in variation in structural responses. To deal with uncertainty in structural parameters, various approaches are commonly utilized. These are probability theory, fuzzy set theory, stochastic finite element

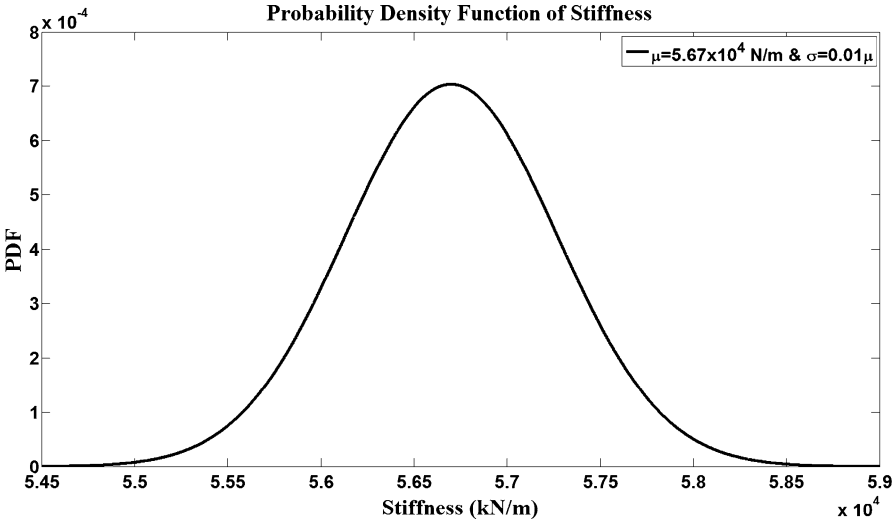

Fig. 1 Probability density function of story stiffness

method (FEM), interval analysis, control methodology, and meta-modeling. Among them, the probability theory is the most popular and thus used in this work to deal with parametric uncertainty. According to Xu et al. [17] and Zhang et al. [20], uncertainty in structural parameters can be expressed in the form of a certain distribution function. For the convenience of the numerical execution, in this study, only normal distribution has been considered to model uncertainty in structure parameters. It is also assumed that the structure is undamped or slightly damped and of the linear time invariant (LTI) nature. Among various structural parameters, only stiffness is taken as uncertain. The stiffness properties are modeled using a truncated normal distribution (no negative side) with mean μ as deterministic stiffness value and a reasonable value of standard deviation σ as suggested in previous studies.

In this work, 1% of the mean value is taken as the standard deviation in the numerical calculation (coefficient of variation is assumed as 0.01). The reason behind choosing such a small standard deviation to represent uncertainty is the assumption that the level of environmental perturbation is much less compared to the intensity of damage. Figure 1 provides the probability density function of particular story stiffness.

5 Detailed Procedure

Lu and Gao [12] made a new proposition to localize and quantify damage with the help of Kalman filter using AR model. In their study, the major goal was to study the influence of uncertainty in stiffness in detecting damage. In addition, a new

absolutely time-domain method [19] has also been proposed by them to determine the modal properties from the response signal of an output-only system with the help of autoregressive model coefficients. Further, the performance of AR model under different damping level was also studied by them.

In this work, to localize damage, all the structural response is collected from structure's undamaged (reference) and damaged (unknown) states. Further, any one of the output (structural response) is considered as an input as the ARX (autoregressive model with exogenous input) model is employed to investigate the position of damage. The residual error σ of the damaged state with respect to the reference state estimated from the model represents the deviation of the system from its original condition. Hence, the standard deviation of this residual error $\sigma(e)$ works as a damage-sensitive feature (DSF), i.e., $\sigma(e)$ is more at a damaged spot in this feature-based technique. Now, once uncertainty is present in an output signal due to uncertainty in stiffness, the DSF varies and shows its competence to undertake such circumstances.

Now, to quantify damage, an algorithm with Kalman filter as proposed by Gao and Lu [7] is followed, where another DSF is assigned to be the ratio of the aforementioned DSF for damage localization to the standard deviation of the output response. That is,

$$DSF = \frac{\sigma(e)}{\sigma(y)} \times 100\% \tag{9}$$

The step-by-step algorithm to determine the modal properties of an MDOF undamped system using the proposed time-domain technique is given as follows:

1. Collect the ambient vibration acceleration response data from each DOF.
2. Pick any one of these responses and consider it as base excitation of the structure.
3. Then the base excitation and all the output acceleration responses are used for the autoregressive-exogenous-input (ARX) model to calculate the model coefficients for prediction.
4. All the coefficients contain the modal properties of the structure. The first coefficient is taken to calculate the modal properties.
5. A singular value decomposition (SVD) is applied to calculate the matrix with singular values as well as vectors.
6. The singular values are directly associated with the modal frequencies, and the associated vectors are nothing but the mode shapes.

6 Numerical Results

Representative models of a six-story (Fig. 2) and two-story shear buildings are considered for numerical investigation. The two-story model is employed only when the Kalman filter [18] is used to denoise data and quantify damage.

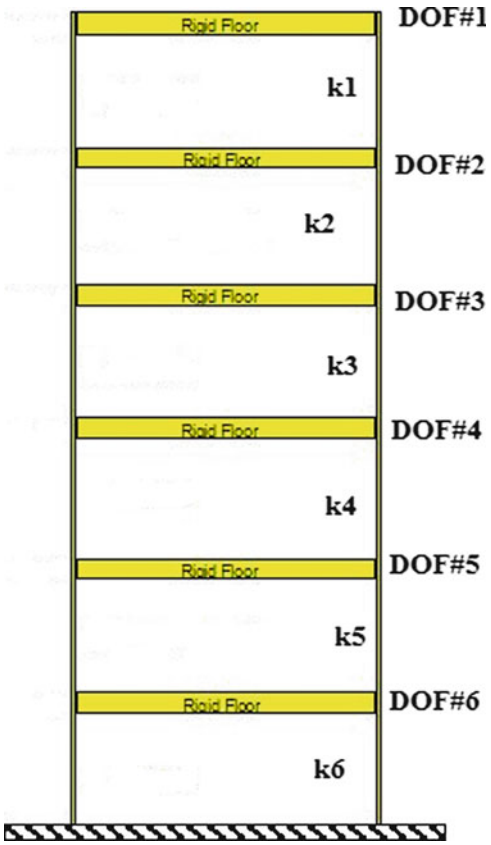

Fig. 2 Shear building

The six-story model is however used to show the efficacy of the autoregressive model in damage localization in the presence of parametric uncertainty. For both the buildings, the story stiffness is taken as 56.7 kN/m, and the mass of each floor is taken as 400 kg (lumped mass).

For the two-story building, to show the proficiency as well as the performance of ARMAX model (Kalman filter) in data denoising [7], several levels of noise scenarios (10 and 20% in the input and output signals of models as well as state conditions) are explored. Before considering the moving average part with autoregressive model, the DSF for no damage condition of the structure is evaluated and presented in Table 1a. Table 1b provides the DSF values after applying Kalman filter. It can be observed from this table that the DSF values are significant and increase with an increase in intensity of noise even though there is no damage. However, after applying the Kalman filter, the DSF values become less than unity highlighting the importance of Kalman filter in tackling noisy data.

For localization of damage, the six-story shear building is considered. Damage is induced by reducing the stiffness of spring k_3 by 20%. Here, DSF is chosen to be the ratio of standard deviation of AR model residual error of damage state (ε_d) to the

Table 1 Comparison between the DSF before and after applying Kalman filter

(a) *DSF before applying Kalman filter*

	Noise at reference model		
Noise at state model	0%	10%	20%
0%	0.0030	2.7354	10.8861
10%	35.4070	34.3964	35.6530
20%	70.8712	69.8263	68.6789

(b) *DSF after applying Kalman filter*

	Noise at reference model		
Noise at state model	0%	10%	20%
0%	0.2132	0.1852	0.7252
10%	0.3236	0.2516	0.8720
20%	0.1295	0.3625	0.2404

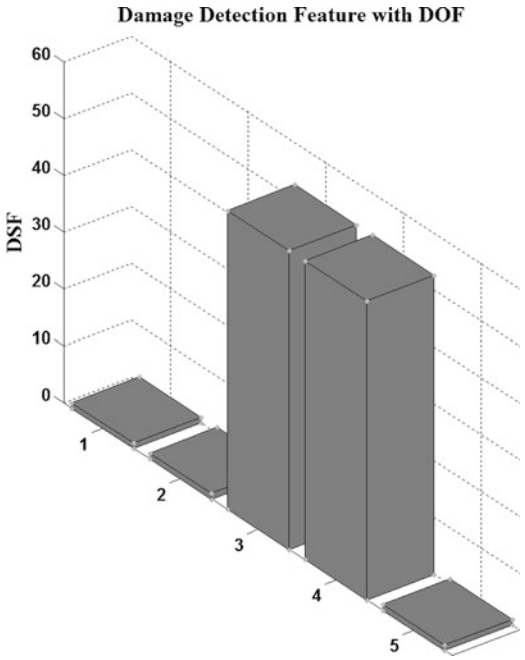

Fig. 3 Localization with DSF

reference state (ε_u) for every DOF. Now, plot of DSF with DOF in Fig. 3 shows the plot of DSF versus DOF, which can be used for the localization of damage in this deterministic model.

Now a confidence interval of 95% for the probability density function of the story stiffness of any floor k is considered, i.e., $\mu - 1.96\sigma \leq k \leq \mu + 1.96\sigma$, where $\sigma = 0.01\ \mu$ and $\mu = 56.7$ kN/m (see Fig. 1). Following the same procedure as explained in case of the deterministic model, DSF versus DOF plot is generated and presented in Fig. 4. It can be observed from this figure that the damage can be localized even when there is uncertainty in stiffness parameters.

To see if the ARX model can localize damage in presence of damping in a structure, the same approach is applied. Figure 5 presents the DSF for different

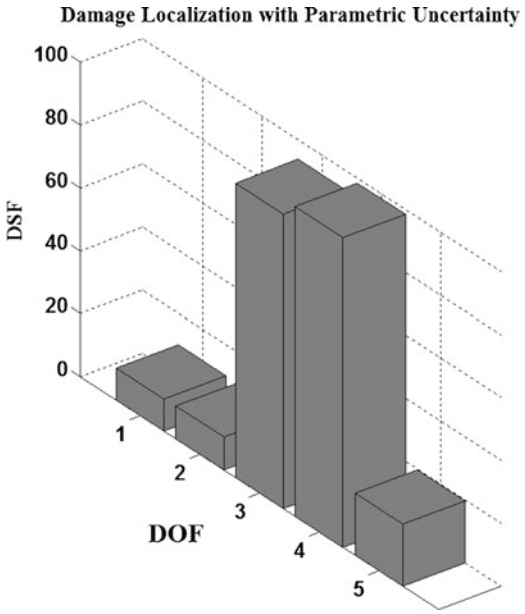

Fig. 4 Localization in presence of uncertainty

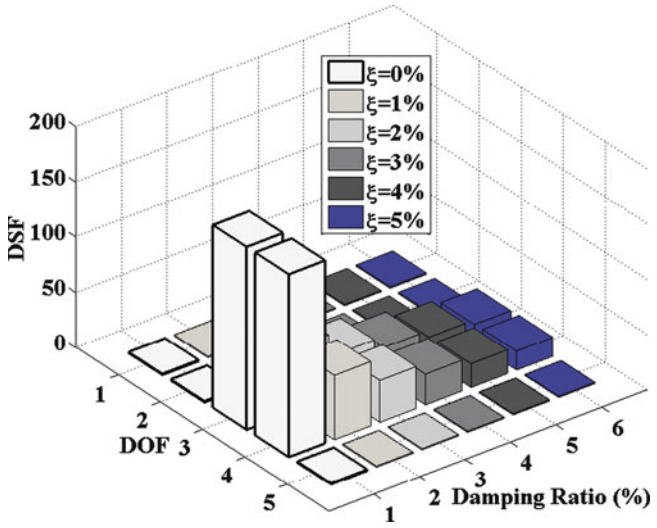

Fig. 5 Performance of the model with increase damping

values of critical damping. Note that the damping is assumed to be same for all modes. It can be observed from Fig. 5 that the DSF drops down reducing the difference of DSF of DOFs adjacent to the damaged spring in comparison to that of the undamaged one.

Now, applying the time-domain approach described previously, the results of the numerical study are presented in Table 2, which shows the calculated frequencies

Table 2 Actual and calculated frequencies using the proposed algorithm

Actual (Hz)	Calculated (Hz)	Error (%)	Calculated (Hz)	Error (%)
	Undamped		Damping = 1%	
0.4570	0.4614	0.9456	0.6807	0.3285
1.3445	1.3443	−0.019	1.5008	0.1041
2.1539	2.1538	−0.005	2.3054	0.0657
2.8381	2.8381	0.00	2.9912	0.0512
3.3573	3.3575	0.0024	3.5124	0.0441
3.6815	3.6816	0.003	3.8351	0.0400

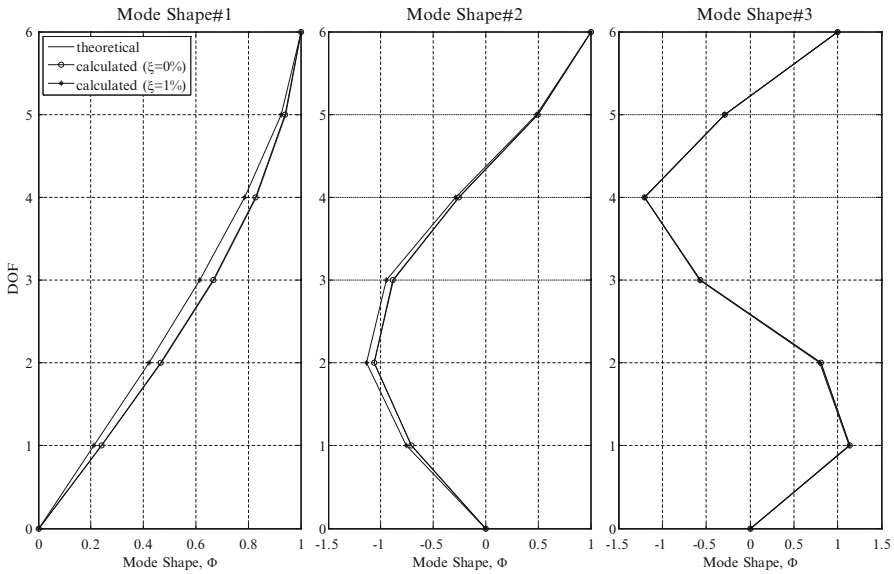

Fig. 6 Comparison of estimated and actual mode shapes

along with the error. It can be observed from Table 2 that, in general, this error is negligibly small for all damping values. However, for the fundamental mode, this error is not that insignificant, especially in case of undamped system. Figure 6 provides a comparison of the actual mode shapes and the mode shapes estimated using the proposed algorithm for the first three modes. It can be observed from this figure that the mode shapes are very close to the actual values.

7 Conclusion

Uncertainty in structural parameters may result in variability of structural response. In this study, the autoregressive (AR) model, where the coefficients of the model are related to structural model parameters, is used to investigate its efficiency in

damage detection and localization when parametric uncertainties are present. A numerical study is conducted with a two-story and eight-story shear buildings. Uncertainties in stiffness are assumed in terms of known probability density functions. It is found that the proposed ARX model can localize damage, especially, if the structure has negligible damping. It is also found that the ARMAX model with Kalman filter can tackle noisy data, which is demonstrated through a two-story shear building.

References

1. Brincker R et al (2001) Modal identification of output-only systems using frequency domain decomposition. Smart Mater Struct 10:441–445
2. Caicedo JM et al (2004) Natural excitation technique and Eigen system realization algorithm for phase I of the IASC-ASCE benchmark problem: simulated data. J Eng Mech 130(1):49
3. Caicedo JM (2010) Practical guidelines for the natural excitation technique (NExT) and the Eigen system realization algorithm (ERA) for modal identification using ambient vibration. Exp Tech 35(4):52–58
4. Cheung A et al (2008) The application of statistical pattern recognition methods for damage detection to field data. Smart Mater Struct 17(6):065023
5. Chiang D-Y et al (2010) Identification of modal parameters from ambient vibration data by modified Eigen system realization algorithm. J Aeronaut Astronaut Aviat 42(2):79–85
6. Chiang D-Y, Lin C-S (2010) Identification of modal parameters from ambient vibration data using Eigen system realization algorithm with correlation technique. J Mech Sci Technol 24 (12):2377–2382
7. Gao F, Lu Y (2006) A Kalman-filter based time-domain analysis for structural damage diagnosis with noisy signals. J Sound Vibr 297(3–5):916–930
8. Gao F, Lu Y (2009) An acceleration residual generation approach for structural damage identification. J Sound Vibr 319(1–2):163–181
9. Kiremidjian AS et al (2003) An enhanced statistical damage detection algorithm using time series analysis. In: Proceedings of the 4th international workshop on structural health monitoring, Stanford, CA, 15–17 Sept 2003
10. Le TH, Tamura Y (2009) Modal Identification of ambient vibration structure using frequency domain decomposition and wavelet transform. In: The seventh Asia-Pacific conference on wind engineering, Taipei, Taiwan
11. Liu X et al (2009) Extended Kalman filtering for the detection of damage in linear mechanical structures. J Sound Vibr 325(4–5):1023–1046
12. Lu Y, Gao F (2005) A novel time-domain autoregressive model for structural damage diagnosis. J Sound Vibr 283(3–5):1031–1049
13. Nair KK et al (2006) Time series-based damage detection and localization algorithm with application to the ASCE benchmark structure. J Sound Vibr 291:349–368
14. da Silva S et al (2007) Damage detection in a benchmark structure using AR-ARX models and statistical pattern recognition. J Braz Soc Mech Sci Eng 29:174–184
15. Sohn H et al (2001, December) Structural health monitoring using statistical pattern recognition techniques. J Dyn Syst Meas Control 123(4):706–711
16. Xiaodong J et al (2007) Experimental study of modal parameter identification in a simulated ambient-excited structure. Front Archit Civ Eng China 1:281–285
17. Xu YL et al (2011) Stochastic damage detection method for building structures with parametric uncertainties. J Sound Vibr 330:4725–4737

18. Yang JN et al (2006) An adaptive extended Kalman filter for structural damage identification. Struct Control Health Monit 13(4):849–867
19. Zhou W, Chelidze D (2006) Generalized Eigen value decomposition in time domain modal parameter identification. J Vibr Acoust 130(1):011001 (1–6)
20. Zhang K et al (2011) A probabilistic damage identification approach for structures with uncertainties under unknown input. Mech Syst Signal Process 25:1126–1145

A Sensitivity Analysis for Modal Frequencies of Vincent Thomas Suspension Bridge

Debasis Karmakar, Samit Ray-Chaudhuri, and Masanobu Shinozuka

Abstract To develop a better numerical model, often model updating is performed by measuring ambient/forced vibration response of the structure involved and then identifying modal frequencies and mode shapes. For a complex structure, model updating becomes a tedious job as in an ideal case, all parameters related to elastic, inertial properties, and boundary conditions should be considered. In addition, if too many parameters are considered for model updating, then the probability of obtaining unreliable model increases. Therefore, a comprehensive eigenvalue sensitivity study is usually performed to identify the most sensitive parameters to be considered. Focusing on Vincent Thomas suspension bridge, which connects the city of San Pedro and Terminal Island of Los Angeles Port, USA, this study presents a sensitivity analysis of various parameters on calculated modal frequencies of the bridge. For this purpose, a detailed three-dimensional finite element (FE) model of the bridge is developed using a widely used commercial software, and uncertainty in 19 parameters including elastic modulus and mass density of different set of structural members, and stiffness of the soil springs, is considered. It has been found from this study that up to the fifth mode, the mass density of deck slab and elastic modulus of bottom chord are the two most significant parameters. It is also found that the same amount of a positive and a negative change in some of the uncertain parameters considered may not produce the same amount of variation in the modal frequencies.

D. Karmakar (✉)
M&H Enterprises, Inc., Houston, TX, USA
e-mail: dkarmakar@gmail.com

S. Ray-Chaudhuri
Department of Civil Engineering, IIT Kanpur, India
e-mail: samitrc@iitk.ac.in

M. Shinozuka
Department of Civil and Environmental Engineering, University of California Irvine, CA, USA
e-mail: shino@uci.edu

S. Chakraborty and G. Bhattacharya (eds.), *Proceedings of the International Symposium on Engineering under Uncertainty: Safety Assessment and Management (ISEUSAM - 2012)*,
DOI 10.1007/978-81-322-0757-3_74,

Keywords Suspension bridge • Uncertainty • Sensitivity analysis • Modal parameters • System identification

1 Introduction

Throughout the history of suspension bridges, their tendency to vibrate under different dynamic loadings such as wind, earthquake, and traffic loads has been a matter of concern. For performance prediction of a long-span suspension bridge under such loading scenarios, development of a sufficiently accurate model of the bridge is very important. To develop a better model, often model updating is performed by measuring ambient/force vibration response of the structure involved and then identifying modal frequencies and mode shapes. For a complex structure, model updating becomes a tedious job as in an ideal case, all parameters related to elastic, inertial properties, and boundary conditions should be considered. In addition, if too many parameters are considered for model updating, then the probability of obtaining unreliable model increases. For this reason, parameter selection is a very important task in model updating process. Practically, if the parameters considered do not have much effect on the modal frequencies and mode shapes, then they should be excluded from the list of parameters to be updated. Therefore, a comprehensive eigenvalue sensitivity study is usually performed to identify the most sensitive parameters to be considered.

This study focuses on Vincent Thomas suspension bridge. This is a long suspension bridge connecting the city of San Pedro and Terminal Island of Los Angeles Port and carries an overwhelming number of port traffic. Concerns regarding the seismic safety of the bridge have gained significant attention after the finding that the main span of the bridge lies directly over the Palos Verdes fault, which has the capacity to produce an earthquake of magnitude Mw 7.25 (Mw) with a return period of 1,000 years. The bridge was thus retrofitted in spring 2000. Considering the importance of this bridge, seismic performance prediction of this bridge under future earthquakes using a realistic model continues to be one of the important agenda of California Department of Transportation (Caltrans).

This study presents a sensitivity analysis of various parameters on calculated modal frequencies of the Vincent Thomas suspension bridge. For this purpose, a detailed 3-dimensional model of the bridge is developed using a widely used commercial software, and uncertainty in 19 parameters including elastic modulus and mass density of different set of structural members, and stiffness of the soil springs, is considered. Although there are several methods to perform a sensitivity analysis, in this study, the tornado diagram analysis and the first-order second-moment (FOSM) analysis have been used due to their simplicity and efficiency to identify sensitivity of uncertain parameters.

2 Numerical Modeling

A detailed three-dimensional finite element model used in calculating the response of the bridge is developed using SAP 2000 V10 [2], a widely used commercial computer program. For modeling of any suspension bridge, determination of initial shapes of cables of a suspension bridge is one of the important steps. Initial shapes of the cables of Vincent Thomas Bridge have been determined using a nonlinear shape-finding analysis. The shape-finding analysis determines the coordinates of the main cables and their initial tension as well as initial tension in hangers, which satisfy the design parameters at the initial equilibrium state under full dead loads. Details of the analysis methodology are described in Kim et al. [5].

Finite element modeling of the member-based detailed structure is developed [6] using SAP 2000. For three-dimensional FE modeling, the cables and suspenders are modeled as 3-D elastic tension-only truss elements. The chords, vertical members, and diagonal members in the stiffening girder are modeled as 3-D truss elements. Also, members in the diaphragm are modeled as truss elements. The tower, the cable bent leg, and the strut members are modeled as frame elements. The reinforced-concrete deck is modeled as shell element, and the supporting stringers are modeled as beam elements. Hydraulic, viscous dampers between the tower and the suspended structure are also modeled according to their properties mentioned in the design drawing. To consider the mass of nonstructural components, equivalent point mass and mass moment of inertia are distributed at joints in the diaphragm. Note that in previous studies as that carried out by Niazy et al. [8], uniform mass distribution over the center span and the side spans was considered, whereas in present study, actual mass distribution over the length of the bridge is considered.

To consider the effect of soil structure interaction, kinematic three translational and three rotational soil springs with their coupling effects are considered at the foundations of east tower, west tower, east cable bent, west cable bent, east anchorage, and west anchorage. The stiffness of the soil springs is calculated from the equivalent pile group stiffness at the foundations discussed earlier. Table 1 gives the number of piles at different foundations considered for the FE model of the bridge. Figure 1 shows the finite element model of the bridge with foundation springs.

Table 1 Location and number of piles considered

Location	Number of piles
East tower	167
West tower	167
East cable bent	48
West cable bent	48
East anchorage	188
West anchorage	188

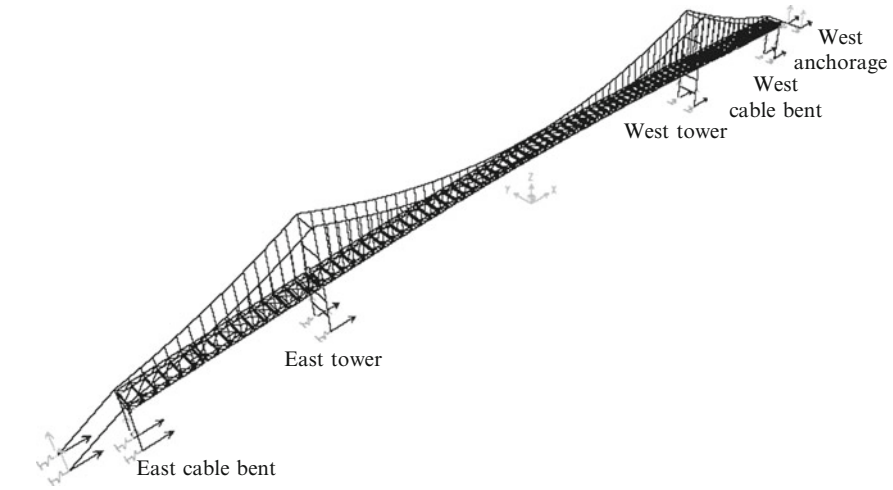

Fig. 1 Detailed model in SAP 2000 with foundation springs

Table 2 Comparison of modal frequencies (in Hz) of the Vincent Thomas Bridge

		Identified (system ID)		Computed		
Mode number	Dominant motion	Ambient vibration	Chino Hills earthquake	SAP 2000 (present study)	Ref. [4]	Ref. [3]
1	L*-S*1	0.162	0.168	0.160	0.135	0.130
2	V*-AS*1	0.219	–	0.220	0.171	0.182
3	V-S1	0.229	0.228	0.222	0.229	0.226
4	V-S2	0.369	0.362	0.362	–	–
5	V-AS2	–	0.467	0.372	–	–
6	T*-S1	0.471	0.491	0.478	0.510	0.511
7	V-S3	–	–	0.483	–	–
8	L-AS1	0.534	–	0.491	0.420	0.409

*L lateral, S symmetric, V vertical, AS antisymmetric, T torsional

3 Modal Parameter Identification

Modal parameters of the Vincent Thomas Bridge are obtained using ambient vibration data and Chino Hills earthquake (July 29, 2008, M_w 5.4) data recorded at the bridge site. Frequency domain decomposition method [1] is used for system identification. Table 2 compares the modal frequencies of the bridge obtained from ambient vibration and Chino Hills earthquake data. One can notice from Table 2 that these two sets of identified frequencies match very well. Note also that the two other previous studies [3, 4] involving detailed models under predicted modal frequencies (also shown in Table 2) significantly for the first two modes.

3.1 Uncertain Parameters Considered

For model updating purpose, in ideal case, all parameters related to elastic, inertial properties, and boundary conditions should be considered. However, if too many parameters are considered for model updating, then chances of obtaining unreliable model increase [10]. For this reason, parameter selection is a very important task in model updating process. Practically, if the parameters considered do not have much effect on the modal frequencies and mode shapes, then they should be excluded from the list. Therefore, a comprehensive eigenvalue sensitivity study is performed to figure out the most sensitive parameters to be considered for suspension bridge finite element model calibration.

A total of 19 parameters are considered for the sensitivity analysis. The selection of these parameters is based on the outcome of previous research [10] and engineering judgments. Elastic modulus and mass density of different set of structural members, boundary conditions (deck and tower connection, and deck and cable bent connection), and stiffness of the soil springs are considered as variable parameters. However, the cable and the concrete deck have homogeneous properties, but due to corrosion, the structural strength may get decreased over the service life of the bridge. To capture the effect of strength degradation, elastic modulus and mass density of cable and concrete deck are considered as variable parameters in the analysis. Also, for the generality of the analysis, kinematic spring stiffness (soil spring stiffness) is also considered as variable parameter in the analysis. Since there was no tower dominant mode in the considered first 8 mode shapes, therefore, the stiffness and inertial properties of the tower are not considered as variable parameters in the present study.

For evaluating the effect of uncertainty in the modal parameters of Vincent Thomas Bridge, uncertainty associated with elastic and inertial property of different members is represented by assigning a mean and standard deviation in terms of coefficient of variation for each parameter. The mean values considered here are calculated based on the design drawing of the bridge. Table 3 lists these parameters with their mean values. To assess the sensitivity, coefficients of variation (COV) of all the parameters are considered as 10%. In the analysis, all the 36 values of the spring stiffness matrices are varied by 10 % for the case of east tower, west tower, east cable bent, and west cable bent. For the FOSM analysis, only lateral translational stiffness of each foundation spring is considered.

(continued)

3.2 Analysis Methods

Reduction of the number of uncertain parameters cuts down the computational effort and cost. One way of doing this is to identify those parameters with associated ranges of uncertainty that lead to relatively insignificant variability in response and then treating these as deterministic parameters by fixing their values at their best estimate, such as the mean. For ranking uncertain parameters according to their sensitivity to desired response parameters, there are various methods such as tornado diagram analysis, FOSM analysis, and Monte Carlo simulation [7, 9]. Monte Carlo simulation, which is computationally demanding due to the requirement of a large number of simulations, especially for a model consisting of a large number of degrees of freedom as in the case here, is not used in this study because of these practical considerations. Instead, the tornado diagram analysis and the FOSM analysis have been used here due to their simplicity and efficiency to identify sensitivity of uncertain parameters.

For the tornado diagram analysis, all uncertain parameters are assumed as random variables, and for each of these random variables, two extreme values the 84th percentile and 16th percentile corresponding to assumed upper and lower bounds, respectively, of its probability distribution have been selected. One can observe that these extreme values come from the normal distribution assumption, mean + standard deviation and mean − standard deviation, respectively, representing their upper and lower bounds. Using these two extreme values for a certain selected random variable, the modal frequencies of the model have been evaluated for both cases, while all other random variables have been assumed to be deterministic parameter with values equal to their mean value. The absolute difference of these two modal frequency values corresponding to the two extreme values of that random variable, which is termed as swing of the modal frequency corresponding to the selected random variable, is calculated.

This calculation procedure has then been repeated for all random variables in question. Finally, these swings have been plotted in a figure from the top to the bottom in a descending order according to their size to demonstrate the relative contribution of each variable to the specific mode under question. It is noteworthy that longer swing implies that the corresponding variable has larger effect on the modal frequency than those with shorter swing.

For the FOSM analysis, the modal frequency has been considered as a random variable Y, which has been expressed as the function of random variables, X_i (for $i = 1$ to N), denoting uncertain parameters, and Y is given by

$$Y = g(X_1, X_2, ..., X_N) \tag{1}$$

Let X_i be characterized by mean μ_X and variance ${\sigma_X}^2$. Now, the derivatives of $g(X)$ with respect to X_i, one can express Y by expanding Eq. (1) in Taylor series as

$$Y = g\left(\mu_{X_1}, \mu_{X_2}, \ldots, \mu_{X_N}\right) + \frac{1}{1!}\sum_{i=1}^{N}\left(X_i - \mu_{X_i}\right)\frac{\delta g}{\delta X_i} + \frac{1}{2!}\sum_{i=1}^{N}\sum_{j=1}^{N}\left(X_i - \mu_{X_i}\right)\left(X_j - \mu_{X_j}\right)\frac{\delta^2 g}{\delta X_i \delta X_j} + \cdots \tag{2}$$

Considering only the first-order terms of Eq. (2) and ignoring higher-order terms, Y can be approximated as

$$Y \approx g\left(\mu_{X_1}, \mu_{X_2}, \ldots, \mu_{X_N}\right) + \frac{1}{1!}\sum_{i=1}^{N}\left(X_i - \mu_{X_i}\right)\frac{\delta g}{\delta X_i} \tag{3}$$

Taking expectation of both sides, the mean of Y, μ_Y can be expressed as

$$\mu_Y \approx g\left(\mu_{X_1}, \mu_{X_2}, \ \ldots\ , \mu_{X_N}\right) \tag{4}$$

Utilizing the second moment of Y as expressed in Eq. (3) and simplifying the variance of Y, ${\sigma_Y}^2$ can be derived as

$$\sigma_Y^2 \approx \sum_{i=1}^{N}\sum_{j=1}^{N}\operatorname{cov}\left(X_i, X_j\right)\frac{\delta g(X_1, X_2, \ldots, X_N)}{\delta X_i}\frac{\delta g(X_1, X_2, \ldots, X_N)}{\delta X_j}$$

$$\approx \sum_{i=1}^{N}\sigma_{X_i}^2\left(\frac{\delta g(X_1, X_2, \ldots, X_N)}{\delta X_i}\right)^2 + \sum_{i=1}^{N}\sum_{j\neq i}^{N}\rho_{X_i X_j}\frac{\delta g(X_1, X_2, \ldots, X_N)}{\delta X_i} \times \frac{\delta g(X_1, X_2, \ldots, X_N)}{\delta X_j} \tag{5}$$

where $\rho_{X_i X_j}$ denotes correlation coefficient for random values X_i and X_j (i.e., coefficient defining the degree to which one variable is related to another). The partial derivative of $g(X_1, X_2, \ldots, X_N)$ with respect to X_i has been calculated numerically using the finite difference equation given below:

$$\frac{\delta g(X_1, X_2, \ldots, X_N)}{\delta X_i} = \frac{g(x_1, x_2, \ldots, \mu_i + \Delta x_i, x_N) - g(x_1, x_2, \ldots, \mu_i - \Delta x_i, x_N)}{2\Delta x_i} \tag{6}$$

(continued)

Table 3 Parameters considered for sensitivity analysis

Serial number	Parameters	Mean value
1	Side link elastic modulus	2.00×10^8 kPa
2	Cable bent and girder connection elastic modulus	2.00×10^8 kPa
3	Top chord elastic modulus	2.00×10^8 kPa
4	Top chord mass density	7.85 kg/m^3
5	Bottom chord elastic modulus	2.00×10^8 kPa
6	Bottom chord mass density	7.85 kg/m^3
7	Stringer elastic modulus	2.00×10^8 kPa
8	Stringer mass density	7.85 kg/m^3
9	Deck slab elastic modulus	2.48×10^7 kPa
10	Deck slab mass density	1.48 kg/m^3
11	Main cable elastic modulus	1.66×10^8 kPa
12	Main cable mass density	8.37 kg/m^3
13	Suspender elastic modulus	1.38×10^8 kPa
14	Suspender mass density	7.85 kg/m^3
15	Wind shoe elastic modulus	2.00×10^8 kPa
16	East tower spring	1.30×10^6 kPa
17	East cable bent spring	7.35×10^6 kPa
18	West tower spring	1.19×10^6 kPa
19	West cable bent spring	4.65×10^6 kPa

In this case, a large number of simulations were performed, varying each input parameter individually to approximate the partial derivatives as given in Eq. (6). For these calculations, the mean and the standard deviation values given in Table 3 are used.

For these sensitivity analyses, at first, the reference model with mean parameters of each 19 random variable considered in this study is analyzed. Then the analyses have been carried out using their lower and then upper bounds. Altogether 39 cases of modal analysis are performed for each set of parameters; modal frequencies expressed as $Y = g(X_1, X_2, ..., X_N)$ are observed.

4 Results and Discussion

For tornado diagram analysis, all the 19 parameters shown in Table 3 are used for total 8 mode shapes. Figure 2 shows tornado diagrams for 8 modes developed according to the procedure described earlier. The vertical line in the middle of tornado diagrams indicates modal frequency value calculated for a certain mode considering only the mean values of all random variables, and the length of each swing (horizontal bar) represents the variation in the modal frequency due to the variation in the respective random variable.

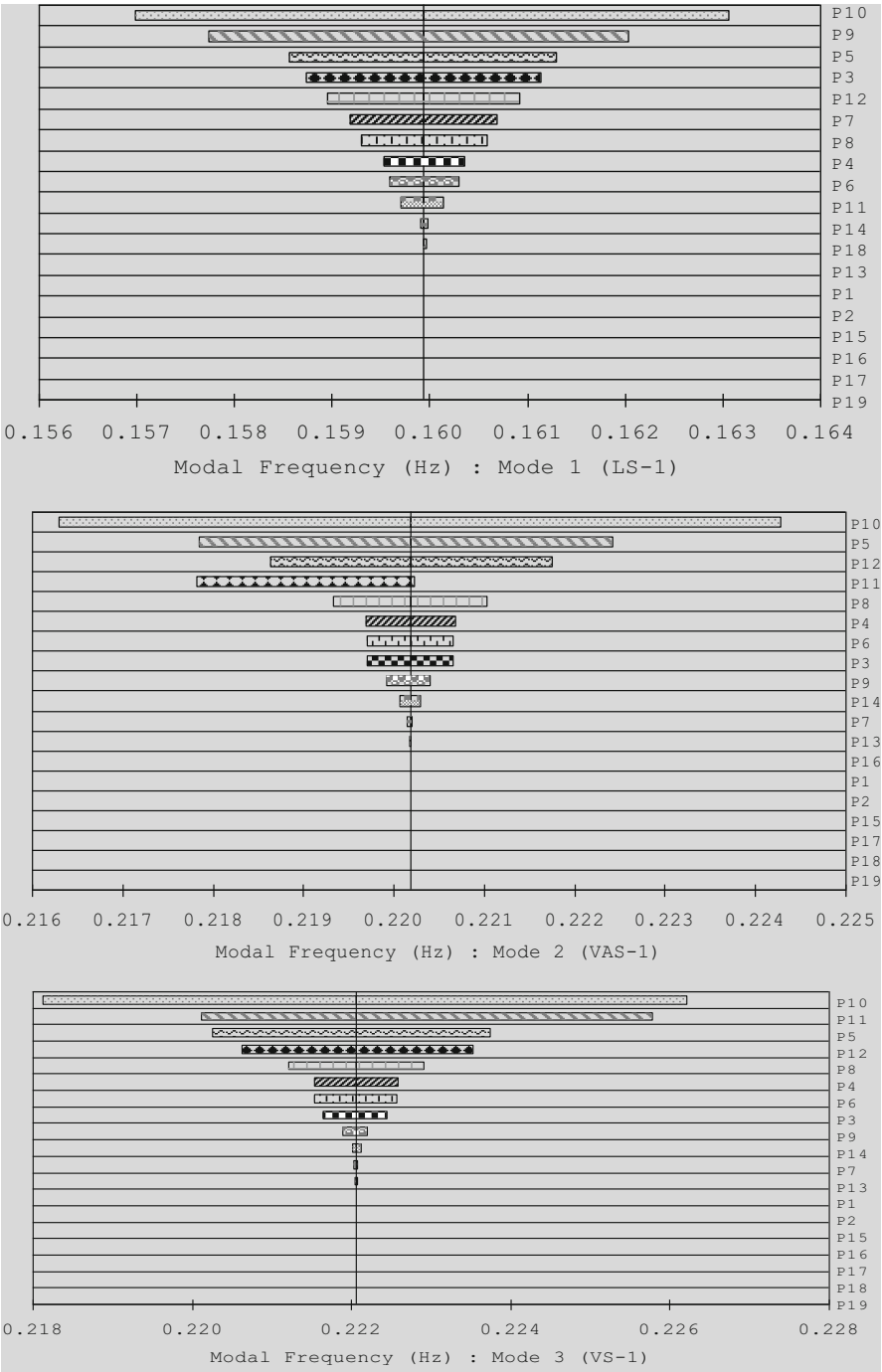

Fig. 2 Tornado diagram considering 19 parameters

(continued)

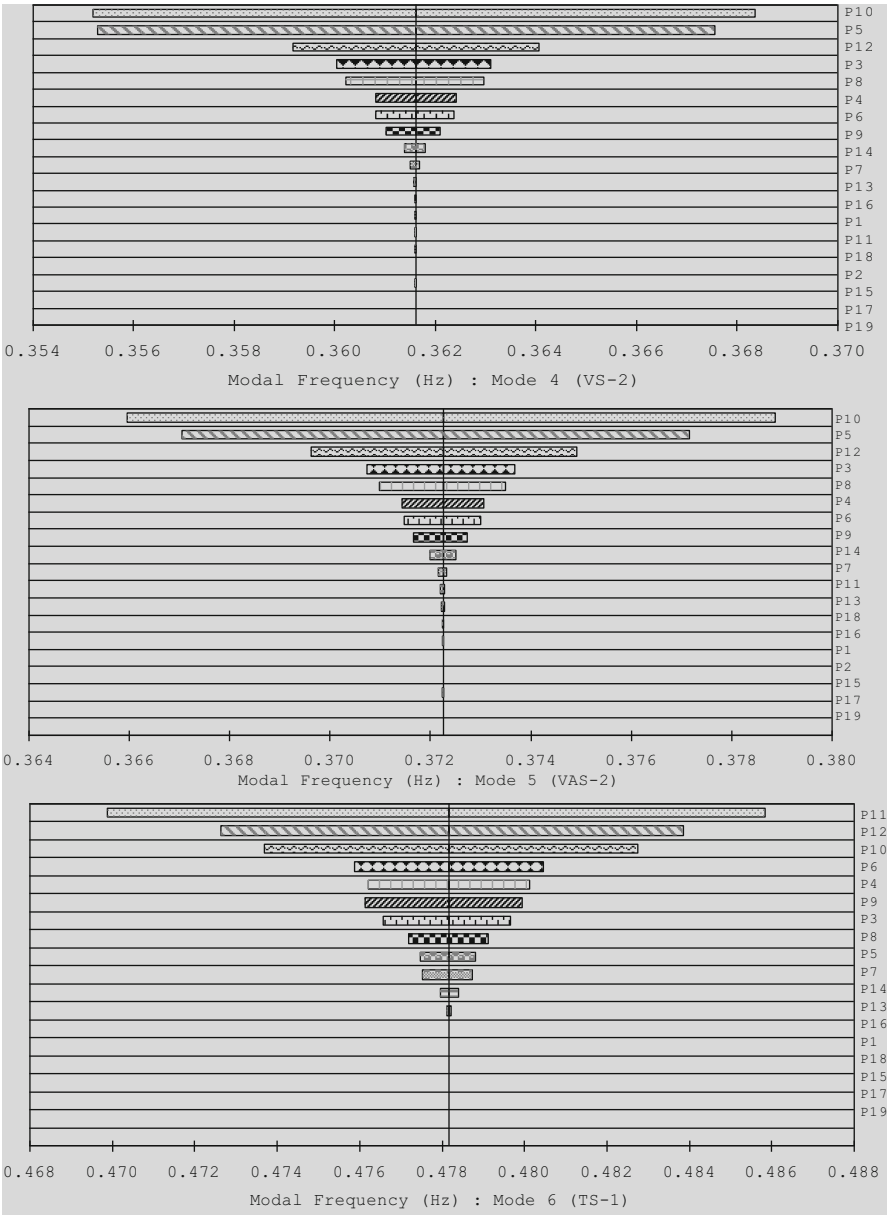

Fig. 2 (continued)

It is clear from Fig. 2 that, up to mode #5, deck slab mass density and bottom chord elastic modulus have almost the largest contributions in response variability. In mode numbers 2, 3, 6, and 7, mostly vertical and torsional modes, main cable elastic modulus is significant contributor of the

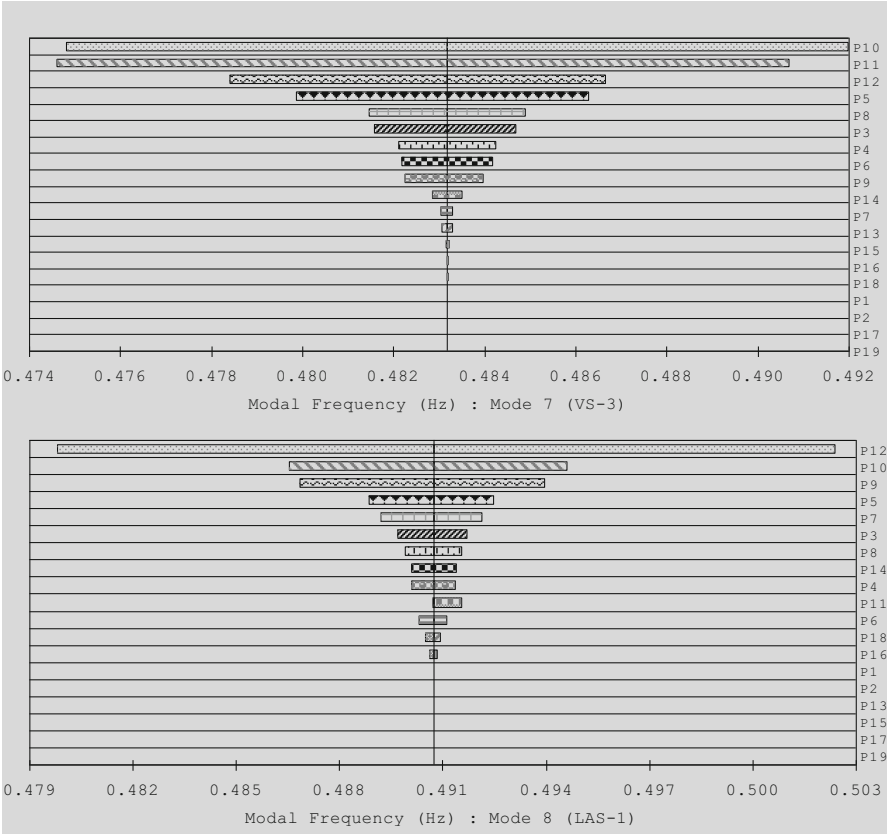

Fig. 2 (continued)

response variability. One can also notice from Fig. 2 that a couple of swings are asymmetric about the vertical line. This skew of the modal frequency distributions implies that the problem is highly nonlinear. In other words, the same amount of a positive and a negative change in these parameters does not produce the same amount of variation in modal frequency. This skewness is very clear for 2nd mode in case of main cable elastic modulus variation. Since the 2nd mode is vertically antisymmetric, increase in main cable elastic modulus does not have much effect on increase in frequency, but decrease in the stiffness of main cable decreases the frequency by 8 % from the base model frequency. Interestingly, deck slab stiffness has most contribution in the 1st mode, but it does not have any contribution in rest of the modes except the 8th mode. Most of the boundary condition (P1, P2, and P15)- and soil spring (P16, P17, P18, and P19)-related parameters have very insignificant effect on response variability.

(continued)

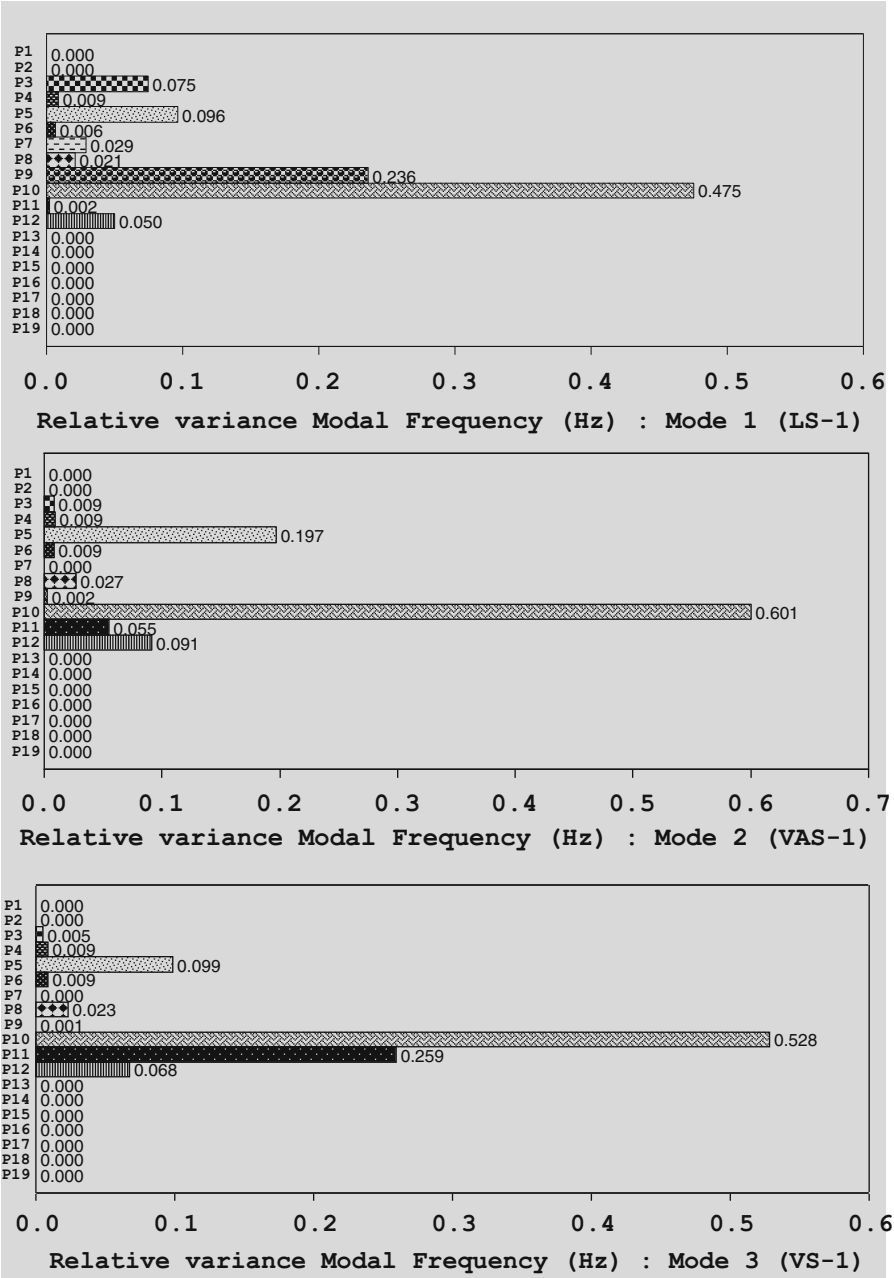

Fig. 3 Relative variance contribution (neglecting correlation terms) from FOSM analysis

For FOSM method, analyses have been carried out to determine the sensitivity of modal frequencies to the uncertainty in each random variable. Focus has been placed on the variance of modal frequency when considering

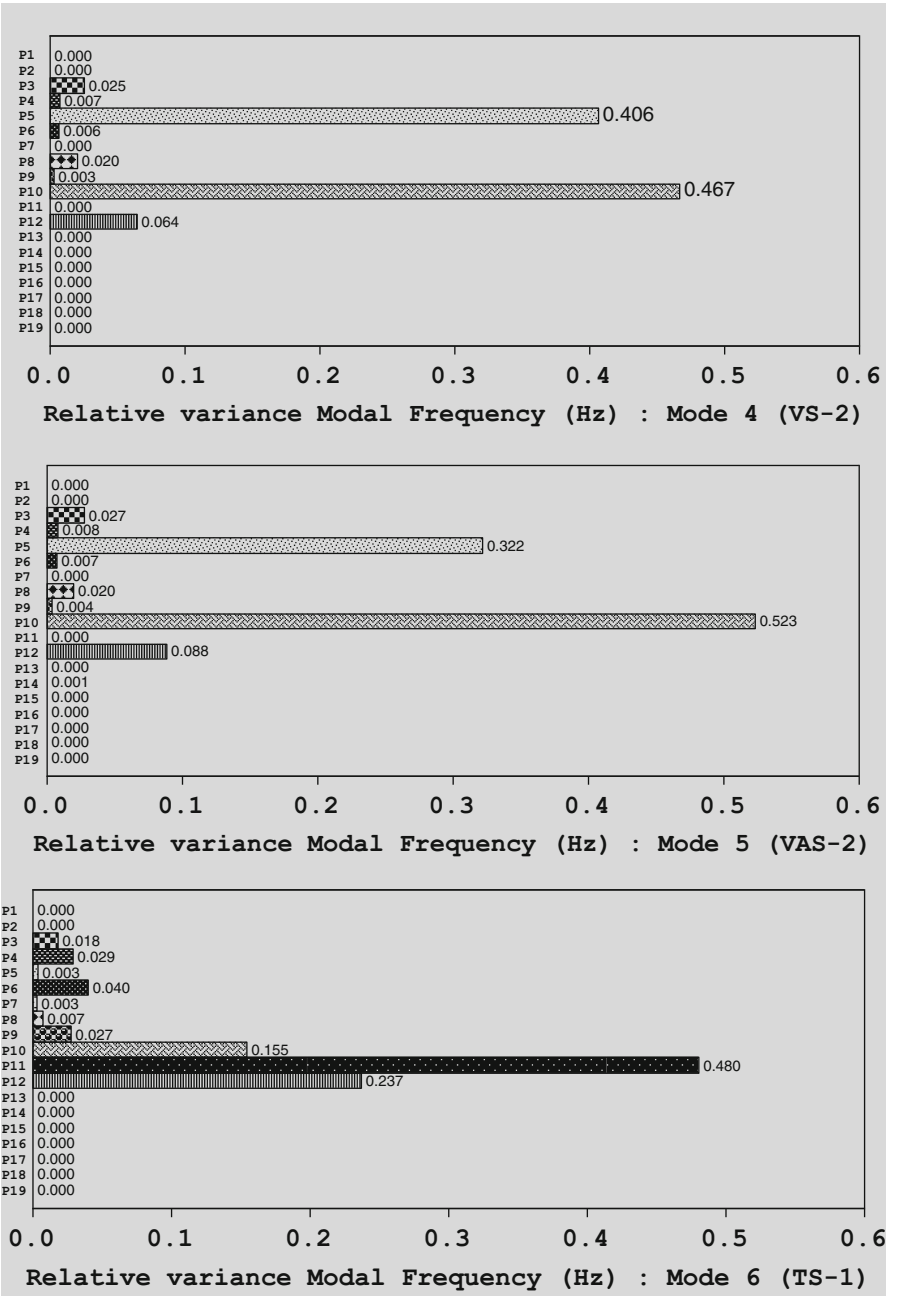

Fig. 3 (continued)

(continued)

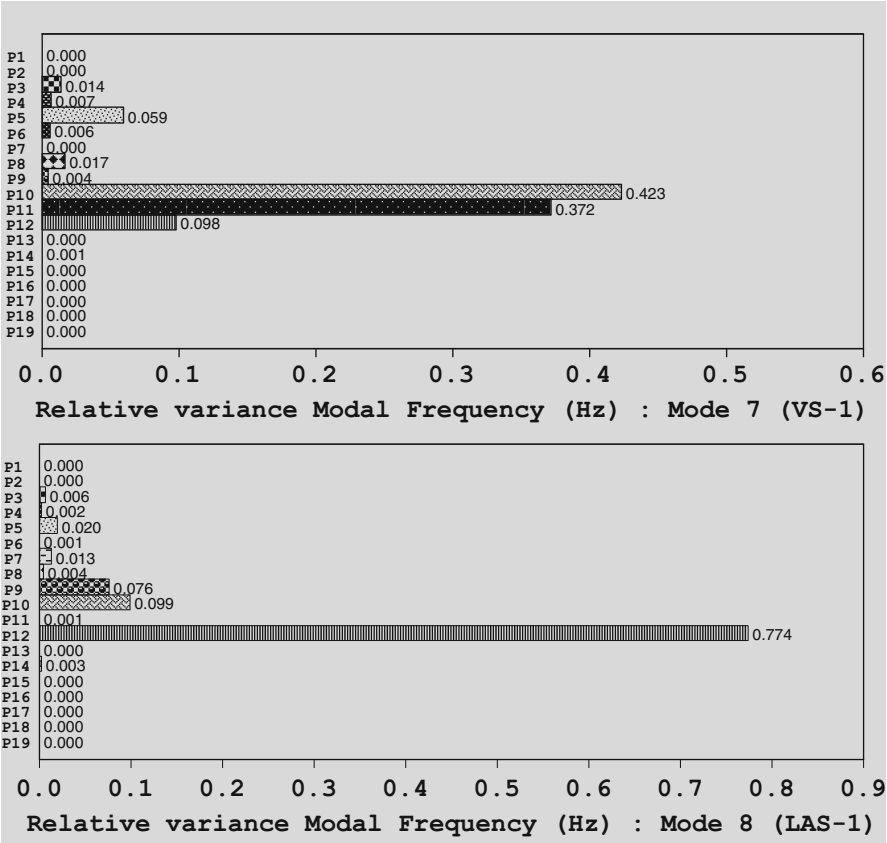

Fig. 3 (continued)

uncertainties of 19 input parameters. Figure 3 shows relative variance contributions of each parameter to the modal frequency when the correlation, as given in the second term of Eq. (6), is neglected. From this figure, it can be observed that the uncertainties in the deck slab mass density and bottom chord elastic modulus contribute mostly to the variance of modal frequencies. This is the same trend as observed from the tornado diagram analysis for all the 8 modes considered.

5 Conclusions

To develop a better numerical model, often model updating is performed by measuring ambient/force vibration response of the structure involved and then identifying modal frequencies and mode shapes. For a complex structure, model updating becomes a tedious job as in an ideal case, all parameters related to elastic,

inertial properties, and boundary conditions should be considered. In addition, if too many parameters are considered for model updating, then the probability of obtaining unreliable model increases. To this end, focusing on Vincent Thomas suspension bridge, at first to demonstrate the appropriateness of the bridge model developed, eigen properties of the model are evaluated in this chapter and compared with those of the system identification results obtained using frequency domain decomposition technique on ambient vibration and recorded earthquake response data. After that, a comprehensive sensitivity analysis is performed considering 19 different structural and soil spring parameters. First eight modal frequencies are considered for the sensitivity study. Tornado diagram and FOSM methods are applied for the sensitivity study. It is observed that the mass density of deck slab and elastic modulus of bottom chord contribute most to the modal frequencies of the bridge. This kind of study will be very helpful in selecting parameters, and their variability ranges for FE model updating of suspension bridges.

Acknowledgments Support of this work was provided by Caltrans under Contract No. 59A0496, Project Manager Dr. Li-Hong Sheng. Helpful comments and suggestions by Mr. Ho Li and Dr. Li-hong Sheng are greatly appreciated.

References

1. Brincker R, Zhang L, Andersen P (2001) Modal identification of output-only systems using frequency domain decomposition. Smart Mater Struct 10(3):441–445
2. Computer and Structures, Inc (2002) SAP 2000 nonlinear user's manual, V. 10, Berkeley. www.csiberkeley.com
3. Fraser M (2003) Exploration of sensor network field deployment on a large highway bridge and condition assessment. ITR report. http://healthmonitoring.ucsd.edu/publiction_materials.jps
4. Ingham TJ, Rodriguez S, Nader M (1997) Nonlinear analysis of the Vincent Thomas Bridge for seismic retrofit. Comput Struct 64(5/6):1221–1238
5. Kim H-K, Lee MJ, Chang SP (2002) Non-linear shape-finding analysis of a self-anchored suspension bridge. Eng Struct 24:1547–1559
6. Karmakar D (2009) Probabilistic performance evaluation of Vincent Thomas Bridge under seismic, wind, and traffic loads. PhD thesis, University of California, Irvine, CA, USA
7. Lee TH, Mosalam KM (2006) Probabilistic seismic evaluation of reinforced concrete structural components and systems. Report 2006/04, Pacific Earthquake Engineering Research Center, University of California, Berkeley, USA
8. Niazy A-SM, Abdel-Ghaffer AM, Masri SF (1991) Performance of the Vincent-Thomas suspension on bridge during the Whittier, California Earthquake of October 1, 1987. Report no. CRECE 91-05. Department of Civil Engineering, University of Southern California, Los Angeles, CA, USA
9. Porter KA, Beck JL, Shaikhutdinov RV (2002) Sensitivity of building loss estimates to major uncertain variables. Earthq Spectra 18(4):719–743
10. Zhang QW, Chang YP, Chang CC (2001) Finite-element model updating for the Kap Shui Mun cable-stayed bridge. J Bridge Eng 6(4):285–293

A Systematic Study and Statistical Inferences on Electrocoagulation Design Parameters with Reference to Arsenic Removal

Chanchal Majumder

Abstract Effects of three electrocoagulation design factors such as current density ($i = I/A$), electrode area to volume ratio ($r = A/V$), and charge density ($q = I*t/V$) are investigated for arsenic removal from synthetic groundwater by electrocoagulation. Two-level four-factor full-factorial-designed experiment is used to arrive at the conclusion of the factors' effect. Statistical inferences are drawn on the three factors and found that current density is not a significant factor if the factor is studied by varying the electrode area keeping current strength constant. Similarly, electrode area to volume ratio ($r = A/V$) is not significant if the factor is studied by varying the electrode area. The study showed that charge density ($q = I*t/V$) is the significant factor in arsenic removal. Effects of current density (i) and area to volume ratio (r) should be studied in such a way that during the study, charge density (q) is not varied.

Keywords Arsenic • Groundwater • Electrocoagulation • Factor • Charge density • Current density

1 Introduction

Throughout the world, arsenic is creating potentially serious environmental problems on human health and on other living organisms. Several studies have reported that carcinogenic effect is primarily due to consumption of arsenic-contaminated drinking water at concentrations around 0.10 mg/L [10]. In countries like Bangladesh, India, Taiwan, Argentina, and Chile, the arsenic concentration has been reported to reach levels up to 1 mg/L [9]. Both geochemical and anthropogenic

C. Majumder (✉)
Civil Engineering Department, Bengal Engineering and Science University, Shibpur, Howrah 711103, West Bengal, India
e-mail: chanchalmajumder@yahoo.co.in

S. Chakraborty and G. Bhattacharya (eds.), *Proceedings of the International Symposium on Engineering under Uncertainty: Safety Assessment and Management (ISEUSAM - 2012)*,
DOI 10.1007/978-81-322-0757-3_75,

activities are responsible for this contamination. Arsenic is usually found in the form of inorganic oxyanions. Arsenate (i.e., $HAsO_4^{2-}$, $H_2AsO_4^{-}$) is likely to predominate in aerobic surface water, whereas arsenite (i.e., $HAsO_3^{2-}$ or $H_2AsO_3^{-}$) in groundwater [12]. The U.S. EPA [13] has classified arsenic as a carcinogen and recommends that the maximum contaminant level (MCL) for arsenic in drinking water be reduced to below 0.01 mg/L. Traditional treatment processes, such as aeration, prechlorination, coagulation, sedimentation, and filtration, do not always comply with the proposed MCL for arsenic in drinking water. Therefore, it is an emerging issue to develop new treatment technology, which can meet this MCL for arsenic in drinking water.

Electrocoagulation (EC) is a process by which sacrificial electrode (anode) is used to deliver coagulant for both water and wastewater treatment. For arsenic removal, usually iron/aluminum electrodes are used to generate Fe^{2+}/Al^{3+} ions, which subsequently form ferric/aluminum hydroxide to remove the dissolved arsenic by adsorption, coprecipitation, and surface complexation. It also helps in arsenite oxidation during coagulant dosing thereby showing higher removal compared to chemical coagulation [7]. During EC, charge density (Coulomb/L) has been found to be the most appropriate design parameter than current density [7]. It is reported that current density changes the characteristics of electrochemically generated sludge and removal will be more if EC operating time is more for a particular charge density [1]. Balasubramanian et al. [3] modeled arsenic removal by Box and Behnken Design (BBD). BBD is a cuboctahedron in Euclidean 3-space, E3 [5]. The effect of current density on arsenic removal was studied by varying the current strength and found that arsenic removal increases with increasing current density. But, if current density is varied by varying the current strength, keeping electrode area constant, the charge delivered in a particular time will be different. Thus, it is not clear whether current density or charge density is responsible for arsenic removal. Energy optimization during arsenic removal by Taguchi method, Martinez-Villafane and Montero-Ocampo [8] considered four EC operating factors, such as interelectrode distance (d), current density (i), electrode area to volume ratio (r), and liquid motion driving mode (D). It is found that electrode area to volume ratio (r) and current density (i) are the least effective process parameters, whereas electrode distance and liquid motion driving mode are the most significant factors for energy consumption. They kept solution volume (V) constant, and current density (i) was varied by varying the current strength (I). Electrode area to volume ratio (r) was maintained by varying the electrode area (A). As a result, the variables "i" and "r" are not independent, because $i = I/A$ and $r = A/V$. Hence, there were no controls over the preselected levels of the studied parameters. They did not separate out the factors as independent. Their attempt was very good with real groundwater but requires further study by separating the variables as independent.

Electrocoagulation is a low-cost, effective, and versatile water and wastewater treatment technology, but systematic study on electrocoagulation design parameters is not reported. Some reported positive effect of current density (Balasubramanian [3]; [11]), while others reported no or low effect on arsenic removal or wastewater treatment [1, 4, 8]. Thus, in such situation, a systematic

statistical investigation seems to be deemed fit to investigate why different researchers are reporting different effects on the same parameter for arsenic removal during electrocoagulation. In this study, two-level full-factorial-designed experiment has been carried out to arrive at the decision of factor effects on arsenic removal by EC.

1.1 Objectives

The objectives of the present study can be outlined as follows. Systematic study on EC design parameters such as:

1. Effect of current density (i) on arsenic removal
2. Effect of electrode area to volume ratio (r) on arsenic removal (r)
3. Effect of charge density (q) on arsenic removal

2 Materials and Methods

Stock arsenite solution of 1,000 mg/L was prepared by dissolving desired amount of sodium arsenite (Merck) in 100 ml deionized water and was preserved with acidification by HNO_3. Laboratory tap water (underground water, Table 1) was spiked with aliquots of this stock solution to obtain desired arsenic concentration of 0.23 mg/L and was kept constant in all the experiments. The EC experiments were conducted in two glass jars (borosilicate) of 1.2 and 3.2-L capacity to maintain the levels of the volume studied. All the experiments were conducted in batch mode with two mild steel plates ($12.8 \times 7.6 \times 0.3$ cm^3) as electrodes. The interelectrode distance was maintained at 1.5 cm apart. A DC 32 voltage source (Model No. 104 3005 32V/5A, PSD series DC Power Supplies, Scientific, India) was used to supply desired operating current. Effective electrode area was varied by changing the

Table 1 Characteristics of laboratory tap water

Parameter	Range
Alkalinity	320–350 mg/Las $CaCO_3$
pH	7.3–7.55
Hardness	690–720 mg/L as $CaCO_3$
Conductivity	3.35 ms/cm
Chlorides	650–700 mg/L
Iron	0.6–1.0 mg/L
Arsenic	NIL
Phosphate	1.24 mg/L
Silica	16.71 mg/L as Si
Sulphate	1.39 mg/L
Nitrate	1.082 mg/L

Table 2 Levels of the factors studied

Factor	Symbol	Low	High	Unit
Volume	V	1.00(−1)	30.00(+1)	L
EC area	A	57.00(−1)	91.20(+1)	cm^2
Current	I	0.60(−1)	3.00(+1)	amp
Time	t	30.00(−1)	120.00(+1)	s

Table 3 Experimental result of the factorial experiment

Run no	*V*	*A*	*I*	*t*	Influent As(III)	Removal (%)
1	−1	−1	−1	−1	0.23	48.70
2	−1	−1	−1	1	0.23	86.52
3	−1	−1	1	−1	0.23	89.13
4	−1	−1	1	1	0.23	96.96
5	−1	1	−1	−1	0.23	58.26
6	−1	1	−1	1	0.23	84.78
7	−1	1	1	−1	0.23	90.87
8	−1	1	1	1	0.23	95.22
9	1	−1	−1	−1	0.23	42.50
10	1	−1	−1	1	0.23	59.57
11	1	−1	1	−1	0.23	69.13
12	1	−1	1	1	0.23	89.13
13	1	1	−1	−1	0.23	42.61
14	1	1	−1	1	0.23	64.78
15	1	1	1	−1	0.23	71.74
16	1	1	1	1	0.23	90.43

depth of the immersed portion of the electrode. After passing desired amount of current for stipulated time, the contents were briefly stirred by a glass rod and allowed to settle for 30 min. A small portion (100 mL approx.) of the content was then withdrawn and filtered through 0.45-μm cellulose nitrate filter paper, and the filtrate was preserved with HNO_3 for arsenic analysis. Arsenic was analyzed with the help of an atomic absorption spectrometer with attachment of continuous hydride vapor generation (AA-202, Chemito, India) as per standard methods [2] with a minimum detection limit of 1 μg/L. The variance analysis (ANOVA) of the test result was carried out by MATLAB 7.0 software. The different levels of the factors studied are presented in Table 2. The values in parenthesis are the coded value of the factors. The full-factorial-designed experiment with factor combinations and the test result are presented in Table 3.

3 Results and Discussion

3.1 Effect of Current Density

Current density is expressed by the ratio of current strength (*I*) and active electrode area (*A*). So we can vary current density either by varying the current strength or by

varying the electrode area. Thus, the effect of current density was studied at constant current mode and at constant area mode in four "blocks." The test result is presented in Tables 4 and 5, respectively. The variance analysis is presented in Tables 6 and 7, respectively.

It is seen from Tables 6 and 7 that the current density is not significant (P values for blocks >0.05) at 0.05 significance level. This is due to the fact that when current is kept constant at a particular value (here 0.6 or 3 amp), EC does not significantly change the iron dosing, thus showing no significant change in arsenic removal. Electrochemical principle suggests that after attaining the limiting current density, iron dissolution from anode will not increase notably [6]. So, for a particular charge density, indiscriminate increase of the current density will not improve removal. It is not the current density, but charge density is responsible for arsenic removal [7]. Similar result was reported by other researchers [8].

The effect of current density on arsenic removal at constant area mode (varying current) is presented in Tables 8 and 9. It is clear from variance analysis that the effect of current density is now significant as $P < 0.05$ (Tables 10 and 11). Thus, increasing the current density, by increasing the current strength, more and more charges are delivered thereby showing higher removal. Thus, variance analysis (Tables 10 and 11) is showing significant effect of current density on arsenic removal. In this case, the higher removal is due to high charge loading not the higher current density.

3.2 *Effect of Electrode Area to Volume Ratio*

Similarly, the effect of electrode area to volume ratio (r) was studied at constant area and constant volume mode in four "blocks." The experimental results for two different volumes are presented in Tables 12 and 13, respectively. The variance analysis of the result is presented in Tables 14 and 15, respectively. It is clear that the area to volume ratio is not significant ($P > 0.05$) at 0.05 significance level.

The effect of area to volume ratio at constant area mode (varying volume) is presented in Table 16 and in Table 17, respectively. The variance analysis of the result is presented in Tables 18 and 19. It is clear from variance analysis that the area to volume ratio is now significant ($P < 0.05$). This is because, by varying the volume, we are indirectly varying the charge density which is a significant factor in arsenic removal. So effect of A/V ratio should be studied by varying the area, and thus, it is not a significant factor in arsenic removal [8].

3.3 *Effect of Charge Density*

Charge density is the amount of charge delivered in per unit volume of water. The effect of charge density was studied by varying all the three factors, namely, "I,"

Table 4 Percent arsenic removal at different current densities at constant current[a]

		Block-I current density 6.58 mA/cm^2	Block-II current density 10.53 mA/cm^2
V	t	% removal	% removal
−1	−1	58.26	48.70
−1	1	84.78	86.52
1	−1	42.61	38.70
1	1	64.78	59.57

[a]The factor combinations and result of SET-I data at constant current = 0.6 amp. The effect of current density is studied by varying the electrode area

Table 5 Percent arsenic removal at different current densities at constant current[a]

		Block-I current density 32.89 mA/cm^2	Block-II current density 52.63 mA/cm^2
V	t	% removal	% removal
−1	−1	90.87	89.13
−1	1	95.22	96.96
1	−1	71.74	69.13
1	1	90.43	89.13

[a]The factor combinations and result of SET-II data at constant current = 3.0 amp. The effect of current density is studied by varying the electrode area

Table 6 Analysis of variance showing the effect of current density at varying area mode[a]

Source	Sum sq.	d.f	Mean sq.	F	Prob > F
Block	24.9925	1	24.9925	0.7893	0.4245
V	609.0050	1	609.0050	19.2331	0.0118
t	1315.3320	1	1315.3320	41.5398	0.0030
Error	126.6575	4	31.6644		
Total	2075.9870	7			

[a]Variance analysis of SET-I data (Table 4) at constant current = 0.6 amp. The effect of current density (Block) is not significant ($P = 0.424 \gg 0.05$) at 5 % significance level

Table 7 Analysis of variance showing the effect of current density at varying area mode[a]

Source	Sum sq.	d.f.	Mean sq.	F	Prob > F
Block	1.9110	1	1.9110	0.0820	0.7888
V	334.7578	1	334.7578	14.3650	0.0193
t	323.4696	1	323.4696	13.8806	0.0204
Error	93.2151	4	23.3038		
Total	753.3536	7			

[a]Variance analysis of SET-II data (Table 5) at constant current = 3 amp. The effect of current density (Block) is not significant ($P = 0.7888 \gg 0.05$) at 5 % significance level

"t," and "V" in eight blocks. The factor combination and the experimental result are presented in Table 20. Table 21 shows the variance analysis of the test result. It is clear from variance analysis that the effect of charge density is significant. This is

Table 8 Percent arsenic removal at different current densities at constant area[a]

		Block-I current density 10.53 mA/cm^2	Block-II current density 52.63 mA/cm^2
V	t	% removal	% removal
−1	−1	48.70	89.13
−1	1	86.52	96.96
1	−1	38.70	69.13
1	1	59.57	89.13

[a]The factor combinations and result of SET-III at constant electrode area = 57 cm^2. Effect of current density is studied by varying the current strength

Table 9 Percent arsenic removal at different current densities at constant area[a]

		Block-I Current density 6.58 mA/cm^2	Block-II Current density 32.89 mA/cm^2
V	t	% removal	% removal
−1	−1	58.26	90.87
−1	1	84.78	95.22
1	−1	42.61	71.74
1	1	64.78	90.43

[a]The factor combinations and result of SET-IV data at constant area = 91.2 cm^2. Effect of current density is studied by varying the current strength

Table 10 Analysis of variance showing the effect of current density at varying current mode[a]

Source	Sum sq.	d.f.	Mean sq.	F	Prob > F
Block	1432.7304	1	1432.7304	23.9051	0.0081
V	464.8200	1	464.8200	7.7555	0.0496
t	855.3248	1	855.3248	14.2711	0.0195
Error	239.7361	4	59.9340		
Total	2992.6114	7			

[a]Variance analysis of SET-III data (Table 8) at constant area = 57 cm^2. The effect of current density (Block) is significant ($P = 0.0081 \ll 0.05$) at 5 % significance level

Table 11 Analysis of variance showing the effect of current density at varying current made[a]

Source	Sum sq.	d.f.	Mean sq.	F	Prob > F
Block	1196.3386	1	1196.3386	30.7584	0.0052
V	443.5731	1	443.5731	11.4045	0.0279
t	643.1491	1	643.1491	16.5356	0.0153
Error	155.5790	4	38.8947		
Total	2438.6398	7			

[a]Variance analysis of SET-IV data (Table 9) at constant area = 91.2 cm^2. The effect of current density (Block) is significant ($P = 0.0052 < 0.05$) at 5 % significance level

due to the fact that whatever the ways the charge density is varied, the removal is also varied. Again, this variation in removal is dependent on coagulant dose which is proportional to the charge delivered into the volume [7].

Table 12 Percent arsenic removal at different area to volume ratio (A/V) at constant volume[a]

		Block-I $r = A/V = 0.057$ cm^{-1}	Block-II $R = A/V = 0.0912$ cm^{-1}
I	t	% removal	% removal
−1	−1	48.70	58.26
−1	1	86.52	84.78
1	−1	89.13	90.87
1	1	96.96	95.22

[a]The factor combinations and result of SET-V data at constant volume = 1 L. Effect of A/V ratio is studied by varying the electrode area

Table 13 Percent removal at different area to volume ratio (A/V) at constant volume[a]

		Block-I $r = A/V = 0.019$ cm^{-1}	Block-II $R = A/V = 0.0304$ cm^{-1}
I	t	% removal	% removal
−1	−1	38.70	42.61
−1	1	59.57	64.78
1	−1	69.13	71.74
1	1	89.13	90.43

[a]The factor combinations and result of SET-VI data at constant volume = 3 L. Effect of A/V ratio is studied by varying the electrode area

Table 14 Variance analysis on the effect of A/V ratio on arsenic removal at constant volume[a]

Source	Sum sq.	d.f.	Mean sq.	F	Prob > F
Block	7.8013	1	7.8013	0.0816	0.7893
I	1102.1512	1	1102.1512	11.5329	0.0274
t	731.5313	1	731.5313	7.6547	0.0505
Error	382.2650	4	95.5663		
Total	2223.7487	7			

[a]Variance analysis of SET-V data (Table 12) at constant volume = 1 L. The effect of A/V ratio (Block) is not significant ($P = 0.7893 \gg 0.05$) at 5 % significance level

Table 15 Variance analysis on the effect of A/V ratio on arsenic removal at constant volume[a]

Source	Sum sq.	d.f.	Mean sq.	F	Prob > F
Block	10.7185	1	10.7185	6.0257	0.0710
I	1536.7968	1	1536.7968	863.9636	0.0000
t	759.7202	1	759.7202	427.1030	0.0000
Error	7.1151	4	1.7788		
Total	2314.3506	7			

[a]Variance analysis of SET-VI data (Table 13) at constant volume = 3 L. The effect of A/V ratio (Block) is not significant ($P = 0.0701 > 0.05$) at 5 % significance level

Table 16 Percent arsenic removal at different area to volume ratio (A/V) at constant area[a]

		Block-I $r = A/V = 0.0192$ cm^{-1}	Block-II $r = A/V = 0.057$ cm^{-1}
I	t	% removal	% removal
−1	−1	38.70	48.70
−1	1	59.57	86.52
1	−1	69.13	89.13
1	1	89.13	96.96

[a]The factor combinations and result of SET-VII data at constant area = 57 cm^2. Effect of A/V ratio is studied by varying the solution volume

Table 17 Percent arsenic removal at different area to volume ratio (A/V) at constant area[a]

		Block-I $r = A/V = 0.0304$ cm^{-1}	Block-II $r = A/V = 0.0912$ cm^{-1}
I	t	% removal	% removal
−1	−1	42.61	58.26
−1	1	64.78	84.78
1	−1	71.74	90.87
1	1	90.73	95.22

[a]The factor combinations and result of SET-VII data at constant area = 91.2 cm^2. Effect of A/V ratio is studied by varying the solution volume

Table 18 Variance analysis on the effect of A/V ratio on arsenic removal at constant electrode area[a]

Source	Sum sq.	d.f.	Mean sq.	F	Prob > F
Block	464.8201	1	464.8201	7.7555	0.0496
I	1432.7304	1	1432.7304	23.9051	0.0081
t	855.3248	1	855.3248	14.2711	0.0195
Error	239.7361	4	59.9340		
Total	2992.6114	7			

[a]Variance analysis of SET-VII data (Table 16) at constant electrode area = 57 cm^2. The effect of A/V ratio (Block) is significant ($P = 0.0496 \ll 0.05$) at 5 % significance level

Table 19 Variance analysis on the effect of A/V ratio on arsenic removal at constant electrode area[a]

Source	Sum sq.	d.f.	Mean sq.	F	Prob > F
Block	443.5731	1	443.5731	11.4045	0.0279
I	1196.3386	1	1196.3386	30.7584	0.0052
t	643.1491	1	643.1491	16.5356	0.0153
Error	155.5790	4	38.8947	16.5356	0.0153
Total	2438.6398	7			

[a]Note: Variance analysis of SET-VII data (Table 17) at constant electrode area = 91.2 cm^2. The effect of A/V ratio (Block) is significant ($P = 0.0279 < 0.05$) at 5 % significance level

Table 20 Percent arsenic removal at different charge density[a]

	V (−1), 1 L				V (+1), 3 L			
	I(−1), 0.6 amp		I(+1), 3.0 amp		I(−1), 0.6 amp		I(+1), 3.0 amp	
	T(−1), 30 s	t(+1), 120 s	t(−1), 30 s	t(+1), 120 s	t(−1), 30 s	t(+1), 120 s	t(−1), 30 s	t(+1), 120 s
A	Block II (18C/L)	Block V (72C/L)	Block VI (90C/L)	Block VIII (360C/L)	Block I (6C/L)	Block III (24C/L)	Block IV (30C/L)	Block VII (120C/L)
−1	48.70	86.52	89.13	96.96	38.70	59.57	69.13	89.13
+1	58.26	84.78	90.87	95.22	42.61	64.78	71.74	90.43

[a]Note: Blocks are numbered according to increasing order of charge density (C/L), (−1) and (+1) are the coded values of factors at low and high levels respectively (SET-IX)

Table 21 Variance analysis showing the effect of charge density on arsenic removal

Source	Sum sq.	d.f.	Mean sq.	F	Prob > F
Block	5381.3527	7	768.7647	107.8461	1.36E-06
A	18.1689	1	18.1689	2.5488	0.15441
Error	49.8984	7	7.1283		
Total	5449.4201	15			

4 Conclusion

In this study, full-factorial-designed experiment followed by statistical analysis is used to conclude on the electrocoagulation design parameters for arsenic removal. Based on the study, the following conclusions can be made:

1. Current density ($i = I/A$) is not a significant parameter in EC design for arsenic removal. Current density is found significant if it is studied by varying the current strength and found to be insignificant when it is studied by varying the electrode area. Effect of current density should be studied by varying the electrode area because if current strength (I) is varied, charge density will vary.
2. Effect of electrode area to volume ratio ($r = A/V$) is not a significant factor when it is studied by varying the electrode area but found to be significant when the factor is studied by varying the solution volume. Effect of this parameter should be studied in such ways that (varying the electrode area) charge density is not varied, i.e., keeping volume constant.
3. Charge density is found to be the most important design factor.

References

1. Addy SA (2008) Electrochemical arsenic remediation for rural Bangladesh. PhD dissertation, University of California, Berkeley
2. APHA (1995) Standard methods for the examination of water and wastewater, 19th edn. American Public Health Association, APHA, AWWA, WEF, Washington, DC
3. Balasubramanian N, Kojima T, Srinivasakannan C (2009) Arsenic removal through electrocoagulation: kinetic and statistical modeling. Chem Eng J 530(1–2):76–82

4. Chen X, Chen G, Po LY (2000) Separation of pollutants from restaurant wastewater by electrocoagulation. Sep Purif Technol 19(1):65–76
5. Doehlert DH, Klee VL (1972) Experimental designs through level reduction of the d-dimensional cuboctahedron. Discrete Math 2(4):309–334
6. Glasstone S (2002) An introduction to electrochemistry, 10th printing. Affiliated East-west Press Pvt. Ltd., New Delhi
7. Kumar PR, Chaudhari S, Khilar KC, Mahajan SP (2004) Removal of arsenic from water by electrocoagulation. Chemosphere 55(9):1245–1252
8. Martinez-Villafane JF, Montero-Ocampo C (2010) Optimization of energy consumption in arsenic electro-removal from groundwater by the Taguchi method. Sep Purif Technol 70 (3):302–305
9. Nordstrom DK (2002) Worldwide occurrences of arsenic in groundwater. Science 296 (5576):2143–2145
10. Pontius FW, Brown KG, Chen CJ (1994) Health implications of arsenic in drinking water. J Am Water Works Assoc 86(9):52–63
11. Pouet MF, Grasmick A (1995) Urban wastewater treatment by electrocoagulation and flotation. Water Sci Technol 31(3–4):275–283
12. Tallman DE, Shaikh AU (1980) Redox stability of inorganic arsenic (III) and arsenic (V) in aqueous solution. Anal Chem 52(1):196–199
13. USEPA (2002) Implementation guidance for the arsenic rule, EPA report-816-D-02–561 005. Office of Groundwater and Drinking Water, Cincinnati

Simulation of Renewable Hybrid System to Study the Uncertainty of the System

D. Bhattacharyya, Prokash C. Roy, and N. Chakraborty

Abstract A model of the hybrid system has been developed to study the uncertainty of renewable stand-alone solar PV and wind hybrid system for distributed power generation based on the resources available at Sagar Island, a remote area distant to grid operation. Study has been made based on the real-life data to analyze the feasibility of the system and per unit generation cost of electricity. Optimization of the system has been made to reduce the uncertainty of the system.

Keywords Hybrid system • Renewable energy • Uncertainty analysis

1 Introduction

Currently, complex power generation scheduling, correlated uncertainties, environmental issues, and hybrid energy system modeling have become very important research topics due to rapid growth of large-scale distributed renewable energy system, deregulated electric power markets, and responsive demand. The intermittent nature of the primal energy sources (i.e., wind, sun, water) increases uncertainty as well as the complexity of the hybrid renewable energy systems.

D. Bhattacharyya
Bengal College of Engineering and Technology, Durgapur, India

P.C. Roy (✉)
Department of Mechanical Engineering, Jadavpur University,
Kolkata 700032, West Bengal, India
e-mail: prokash.roy@gmail.com

N. Chakraborty
Department of Power Engineering, Jadavpur University Salt Lake Campus,
Kolkata 700098, West Bengal, India

S. Chakraborty and G. Bhattacharya (eds.), *Proceedings of the International Symposium on Engineering under Uncertainty: Safety Assessment and Management (ISEUSAM - 2012)*,
DOI 10.1007/978-81-322-0757-3_76,

Simulation and optimization of hybrid renewable energy systems having different combination of energy sources have been carried out by several researchers such as diesel generator (DG) operating time optimization and cost minimization of PV-DG hybrid system model [1], optimization of a hybrid system consisting of PV-WTG using genetic algorithm [2], and simulation of optimized design for a stand-alone solar-wind hybrid system based on process integration principles and design space approach [3]. A deterministic mixed integer linear mathematical programming model (time series) is developed by Gupta et al. for performance and cost optimization based on demand and potential constraints of a hybrid energy generation system consisting of a photovoltaic array, biomass (fuel wood), biogas, small/micro-hydro, battery bank, and fossil fuel generator [4]. The simulation of a stand-alone hybrid renewable energy system by Prodromidis et al. confirmed the feasibility of an off-grid hybrid RE system with zero emissions and reduced total costs (initial and operational) [5]. A stand-alone hybrid energy system consisting of fuel cells, wind turbines, some electrolyzers, a reformer, an anaerobic reactor, and some hydrogen tanks has been modeled considering the uncertainty in the wind power availability using a particle swarm optimization (PSO) subroutine embedded in a multivariate Monte Carlo simulation by Valizadeh Haghi et al. [6]. A robust dispatch algorithm called generation control application (GCA) is developed by Cheung et al. for increasing the reliability of a grid integrated with the uncertain renewable sources which has adequate system ramping capability to cope with the uncertainty in intermittent sources while maintaining system reliability in large grid operations [7]. A renewable energy-based hybrid power generation system is designed and optimized by Giannakoudis et al. considering the uncertainties in weather (solar radiation and wind speed) and operating conditions of the system components [8].

As a further significant extension of the hybrid energy modeling with correlated uncertainty research aspects, we have analytically studied the feasibility and uncertainty of the designed hybrid energy system based on the resources available at Sagar Island, a remote area distant to grid operation.

2 Problem Definition

A model of hybrid renewable energy system having solar and wind as alternative energy sources is designed as well as operation of the model optimally simulated. Wind turbine generator, photovoltaic generator, diesel generator, rectifier, inverter, charge controller, and battery are the components of the hybrid energy system of study. The objective of this model is to analyze the feasibility of the system for providing load demand by the renewable sources optimally, to evaluate per unit cost of electricity generation, and most significantly to review critically the uncertainty of the model hybrid renewable energy system performance. The developed data-driven model is based on the resources available at Sagar Island, a remote area distant to grid operation. Hybrid renewable energy system is very useful as well as cost-effective option for

remote area power applications where extension of grid supply is difficult and expensive like in Sagar Island. Uncertainty of the hybrid renewable energy system performance, fluctuation in power output, and presence of some conflicting objectives such as cost and steady provision of meeting load demand are important aspects of concern with respect to reliability of hybrid renewable energy system model. In this study, uncertainty and feasibility of the designed hybrid energy system are critically analyzed after optimally simulating the model, and cost factor is also taken into account.

3 Configuration of the Hybrid Power System

A stand-alone hybrid energy system consisting of renewable energy sources (wind turbine generator source and photovoltaic generator source), battery and diesel generator, and based on AC load is represented by a block diagram in Fig. 1.

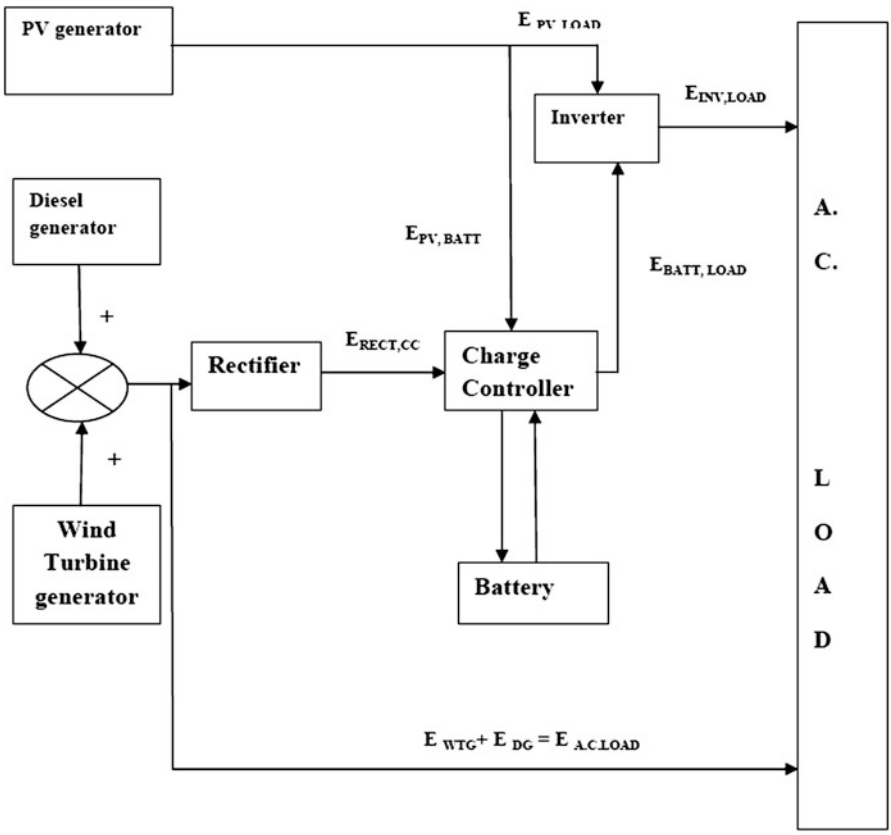

Fig. 1 The configuration of the hybrid energy system

For providing load, electric energy can be obtained from renewable energy sources, diesel generator, and battery as per our designed model. When the load demand is greater than the total output from renewable energy sources and battery bank storage sources, diesel generator is started to provide the unmet load. Diesel generator would be turned on or run till maximum permissible operating time limit:

$$E_{\mathrm{WTG}}(t) = E_{\mathrm{WTG,LOAD}}(t) + E_{\mathrm{WTG,BATT}}(t) \tag{1}$$

$$E_{\mathrm{PV}}(t) = E_{\mathrm{PV,LOAD}}(t) + E_{\mathrm{PV,BATT}}(t) \tag{2}$$

$$E_{\mathrm{DG}}(t) = E_{\mathrm{DG,LOAD}}(t) + E_{\mathrm{DG,BATT}}(t) \tag{3}$$

$$E_{\mathrm{Batt,in}}(t) = \eta_{\mathrm{CHG}} * \eta_{\mathrm{CC}} * \left[E_{\mathrm{PV,BATT}}(t) + \eta_{\mathrm{RECT}} * \left(E_{\mathrm{WTG,BATT}}(t) + E_{\mathrm{DG,BATT}}(t)\right)\right] \tag{4}$$

$$E_{\mathrm{BATT,LOAD}}(t) = \eta_{\mathrm{DCHG}} * [E_{\mathrm{Batt,in}}(t)] \tag{5}$$

$$E_{\mathrm{Load}}(t) = [E_{\mathrm{WTG,LOAD}}(t) + E_{\mathrm{DG,LOAD}}(t) + \eta_{\mathrm{inv}} * (E_{\mathrm{PV,LOAD}}(t) + E_{\mathrm{BATT,LOAD}}(t))] \tag{6}$$

Equation (4) gives the total obtained energy for charging the battery, and Eq. (5) gives the obtained energy from the battery to provide the load demand at any instant t. Equation (6) gives the total energy providing the load demand.

4 Model Description of System Components

4.1 Mathematical Model of Wind Turbine Generator

The wind velocity in m/s. is measured at each instant. The power output from wind turbine generator at each instant is then calculated by using the following equation:

$$P_w(t) = 0.000 * (v(t))^5 - 0.002 * (v(t))^4 + 0.025 * (v(t))^3 - 0.050 * (v(t))^2 + 0.071 * v(t) \tag{7}$$

The hourly energy output from wind turbine generator is calculated using the following equation:

$$E_{\mathrm{TG}}(t) = T * N_{\mathrm{TG}} * P_w(t) \tag{8}$$

where, T is the time interval in hours covered by each instant and N_{TG} is the number of wind turbines used in the system.

4.2 Mathematical Model of Photovoltaic (PV) Generator

The PV generator converts the sunlight into electricity using PV arrays. The hourly energy output (DC) from the PV generator is calculated using the following equation:

$$E_{\mathrm{PV}}(t) = \eta_{\mathrm{pv}} * N_{\mathrm{PV}} * S_{\mathrm{PV}} * T * G(t) \tag{9}$$

where η_{pv} is the efficiency of PV generator, N_{PV} is the number of PV modules, S_{PV} is the surface area of each PV module in m^2, T is the time interval in hours covered by each instant, and $G(t)$ is the hourly solar radiation in $\mathrm{KWh/m}^2$.

4.3 Mathematical Model of Diesel Generator *(DG)*

$$P_{\mathrm{DG}}(t) = S_{\mathrm{DG}}(t) * \cos\Phi \tag{10}$$

$$E_{\mathrm{DG}}(t) = T * P_{\mathrm{DG}}(t) \tag{11}$$

where $P_{\mathrm{DG}}(t)$ is the rated power in KW, $S_{\mathrm{DG}}(t)$ is the rated apparent power in KVA, $\cos\Phi$ is the rated power factor, T is the time interval in hours covered by each instant, and $E_{\mathrm{DG}}\ (t)$ is the hourly energy output of diesel generator.

4.4 Mathematical Model of Rectifier

The rectifier converts the additional AC power (AC energy left after meeting load demand) from WTG and DG into DC power:

$$E_{\mathrm{RECT,OUT}}(t) = \eta_{\mathrm{RECT}} * (E_{\mathrm{RECT,WTG}}(t) + E_{\mathrm{RECTDIN}}(t)) \tag{12}$$

where $E_{\mathrm{RECT,\ OUT}}\ (t)$ is the hourly energy output from rectifier, $E_{\mathrm{RECT,WTG}}(t)$ and $E_{\mathrm{RECTDIN}}(t)$ are the additional energy at any time t from WTG and DG sources, respectively, and η_{RECT} is the efficiency of the rectifier.

4.5 Mathematical Model of Charge Controller

The hourly energy from the charge controller is calculated as follows:

$$E_{\mathrm{CC,OUT}}(t) = \eta_{\mathrm{CC}} * E_{\mathrm{CCIN}}(t) \tag{13}$$

$$E_{\mathrm{CCIN}}(t) = E_{\mathrm{RECT,OUT}}(t) + E_{\mathrm{PVBATT}}(t) \tag{14}$$

where $E_{\mathrm{PVBATT}}(t)$ is the additional DC output from PV source (DC energy left after meeting load demand by PV source), η_{CC} is the efficiency of charge controller, $E_{\mathrm{CC,OUT}}(t)$ and $E_{\mathrm{CCIN}}(t)$ are the hourly output and input energy from charge controller, respectively.

4.6 Mathematical Model of Inverter

The inverter converts the DC power output from PV source and battery into AC power to provide the AC load demand:

$$E_{\mathrm{PV,INV}}(t) = \eta_{\mathrm{inv}} * E_{\mathrm{PV}}(t) \tag{15}$$

$$E_{\mathrm{Batt,ACL}}(t) = \eta_{\mathrm{inv}} * \eta_{\mathrm{DCHG}} * E_{\mathrm{Batt}}(t) \tag{16}$$

where $E_{\mathrm{Batt,ACL}}(t)$ is the hourly energy output from inverter when input to inverter is the DC energy in the battery available to provide the load, $E_{\mathrm{PV,INV}}(t)$ is the hourly energy output from inverter when input to inverter is the DC energy output from PV source, $E_{\mathrm{Batt}}(t)$ is the energy stored in battery at an instant t, η_{inv} is the efficiency of inverter, and η_{DCHG} is the discharging efficiency of battery, respectively.

4.7 Mathematical Model of Battery

The additional output energy from all generator sources after providing load at an instant t which is stored in the battery is given by the following equation:

$$E_{\mathrm{Batt}}(t) = E_{\mathrm{Batt}}(t-1) + \eta_{\mathrm{CHG}} * E_{,\mathrm{out}}(t) \tag{17}$$

When the output energy from the renewable energy sources is less than the load demand, the battery discharges its stored energy to provide the load:

$$E_{\mathrm{Batt,After}}(t) = E_{\mathrm{Batt}}(t) - E_{\mathrm{Batt,L}}(t) \tag{18}$$

$$E_{\mathrm{Batt},L}(t) = (E_{\mathrm{URE}}(t))/(\eta_{\mathrm{DCHG}} * \eta_{\mathrm{inv}}) \tag{19}$$

where $E_{\mathrm{Batt,\,L}}(t)$ is the hourly stored energy in battery available to provide the load and $E_{\mathrm{URE}}(t)$ is the hourly energy of the load demand that is unmet by the renewable energy sources (WTG and PV sources). $E_{\mathrm{Batt}}(t)$, $E_{\mathrm{Batt}}(t-1)$ is the hourly energy

stored in battery at instant t and instant $(t-1)$, respectively. $E_{\text{Batt,After}}(t)$ is the hourly energy stored in battery after providing load at instant t and η_{CHG} is the charging efficiency of the battery, respectively. The constraints for the charge stored in the battery are:

$$\text{SOC}_{\min} \leqslant \text{SOC}(t) \leqslant \text{SOC}_{\max}$$

where $\text{SOC}_{\min}$ and $\text{SOC}_{\max}$ are the minimum and maximum state of charge of the battery and SOC (t) is the state of charge of the battery at instant t.

$$\text{SOC}_{\max} = 1$$
$$\text{SOC}_{\min} = 1 - \text{DOD}$$

DOD is the maximum depth of discharge of the battery.

5 Methodology

5.1 Assumptions

- The hybrid system is in steady state.
- The system operates round the clock due to perpetual process of electrification.
- Only AC load connected to the load bus is in this system.
- Each time instant is of 1-h duration in the entire hybrid model simulation.
- Temperature effect, connection losses, wiring, and other losses in the PV generator are neglected; PV generator uses a maximum power point tracker (efficiency 100%) [9].
- The WTG source is assumed to operate when the power generated by the wind turbines is greater than zero.
- The output from renewable sources and the electrical load demand are constant for each time instant.
- First time instant starts at 12 midnight and ends at 1 a.m.

As per unit of concern for this proposed model, power and energy are measured in KW and KWh, respectively.

5.2 Specifications

- The photovoltaic generator has an efficiency of 11.54%, and area of photovoltaic (PV) array is 202 m^2. The hourly irradiance in kWh/m^2 varies according to sunshine variation and is zero after sunset and before sunrise. The rectifier and charge controller efficiencies are 95 and 90%, respectively [10].

- The rated power output from diesel generator is 5.2 KW and 6.5 KVA. The maximum permissible daily operating time is assumed to be 10 h, and efficiency is 100% [10].
- The modeling is done using hourly data for a particular day (14th of June 2001).
- Each instant in the day is of 1-h duration with the first instant starting from 12 o' clock at midnight and ends at 1 a.m.
- Load data in KW for 24 instants has been considered. Hence, load data for total 24 time samples has been taken into account.
- The air density is 1.23 kg/m^2, number of wind turbines used is three, and input wind velocity in m/s. is assumed to vary at each instant of the day [11, 12].
- Hourly solar radiation data in KW/m^2 for the particular day has been considered.
- Hourly wind velocity in m/s. for the particular day has been considered.
- The charging and discharging efficiency of battery are taken 85% [13].
- The inverter efficiency is 90% [14].

5.3 Constraints

5.3.1 Integer Variable Constraints

The integer variables characterize the working status of the renewable sources, diesel generator, and battery. X_{PVG}, X_{TG}, X_{BAT}, and X_{DG} are the variables that indicate whether PV, WTG, battery, and DG source of the hybrid system should work at a particular time instant:

$X_k = 1$, if unit k serves the load
$X_k = 0$, otherwise

5.3.2 Basic Constraints

1. Generator Capacity Constraint. The supplied power of each generator must be equal to or less than the unit capacity:

$$P_k(t) \leqslant \mathrm{Cp}_k \quad \text{for all } t$$

   Cp_k is the capacity for unit k, and $P_k(t)$ is the supplied power of each generator for unit k.
2. Unit Generation Constraint. The hourly generation of each unit must be within its maximum and minimum generation limits for successful operation of the unit:

$$P_{\mathrm{jmin}} \leqslant P_j(t) \leqslant P_{\mathrm{jmax}} \quad \text{for all } t$$

where P_{jmin} and P_{jmax} are the minimum and maximum generation limits and $P_j(t)$ is the hourly generation of the unit j.

3. Battery Storage Constraint. The stored energy in the battery must lie within the minimum and maximum energy that can be stored in the battery to avoid overcharging or over discharging at any instant of time:

$$E_{\mathrm{BAT,min}} \leqslant E_{\mathrm{Batt}}(\mathrm{t}) \leqslant E_{\mathrm{BAT,max}} \text{for all } t$$
$$E_{\mathrm{BAT,min}} = (1 - \mathrm{DOD}) * E_{\mathrm{BAT,max}}$$

where $E_{\mathrm{BAT,\ min}}$ and $E_{\mathrm{BAT,\ max}}$ are the minimum and maximum energy that can be stored in the battery.

4. Nonnegative Constraints: Electrical energy and power flow values are always positive or zero, so the decision variables must be nonnegative.

5.3.3 Decision Variables, Constraints for WTG Source

X_{TG} is the integer decision variable for WTG source which indicates whether WTG is working or not at an hour t, $E_{\mathrm{gen},\ k\ =\ \mathrm{TG}}\ (t)$ is the power generation from WTG source at an instant t, and $E_{k,\ \mathrm{load}}(t)$ is the amount of load that should be provided by unit k at any instant t. The generation characteristics of WTG are given by the following equations:

$$\begin{aligned} & E_{gen,k}(t) = E_{k,load}(t) < [T * N_{TG} * P_w(t)] * X_{TG} \\ \Rightarrow \quad & E_{gen,k}(t) = E_{k,load}(t) + E_{k,BATT}(t) \\ & \qquad = T * N_{TG} * P_w(t) \end{aligned}$$

$$\begin{aligned} & E_{\mathrm{gen},k}(t) = E_{k,\mathrm{load}}(t) \geqslant [T * N_{\mathrm{TG}} * P_w(t)] * X_{\mathrm{TG}} \\ \Rightarrow \quad & E_{\mathrm{gen},k}(t) = E_{k,\mathrm{load}}(t) = T * N_{\mathrm{TG}} * P_w(t) \end{aligned}$$

5.3.4 Decision Variables, Constraints for PVG Source

X_{PVG} is the integer decision variable for PVG source which indicates whether PVG is working or not at an hour t, $E_{\mathrm{gen},\ k\ =\ \mathrm{PVG}}\ (t)$ is the power generation from PVG source at an instant t, and $E_{k,\ \mathrm{load}}\ (t)$ is the amount of load that should be provided by unit k at any instant t. The generation characteristics of PVG are given by the following equations:

$$\begin{aligned} & E_{\mathrm{gen},k}(t) = E_{k,\mathrm{load}}(t) < \left[\eta_{\mathrm{pv}} * N_{\mathrm{PV}} * S_{\mathrm{PV}} * T * G(t)\right] * X_{\mathrm{PVG}} \\ \Rightarrow \quad & E_{\mathrm{gen},k}(t) = E_{k,\mathrm{load}}(t) + E_{k,\mathrm{BATT}}(t) \\ & \qquad = \eta_{\mathrm{pv}} * N_{\mathrm{PV}} * S_{\mathrm{PV}} * T * G(t) \end{aligned}$$

$$E_{gen,k}(t) = E_{k,load}(t) \geqslant \left[\eta_{pv} * N_{PV} * S_{PV} * T * G(t)\right] * X_{PVG}$$
$$\Rightarrow \quad E_{gen,k}(t) = E_{k,load}(t) = \eta_{pv} * N_{PV} * S_{PV} * T * G(t)$$

5.3.5 Decision Variables, Constraints for DG Source

When DG source is selected, the value of power generated by DG source at any instant t should be within its minimum generation (considered as 80% of rated power) and maximum generation (rated power) limits or should be zero. The generation characteristics for DG are given by the following equations:

$$E_{\text{gen},k}(t) = E_{k,\text{load}}(t) < [T * P_{\text{DG}}(t)] * X_{\text{DG}}$$
$$\Rightarrow \quad E_{\text{gen},k}(t) = E_{k,\text{load}}(t) + E_{k,\text{BATT}}(t)$$
$$= [0.8 * P_{\text{DG}}(t), 1.0 * P_{\text{DG}}(t)] * T$$

$$E_{\text{gen},k}(t) = E_{k,\text{load}}(t) \geqslant [T * P_{\text{DG}}(t)] * X_{\text{DG}}$$
$$\Rightarrow \quad E_{\text{gen},k}(t) = E_{k,\text{load}}(t) = [1.0 * P_{\text{DG}}(t)] * T$$

The total time of operation of DG source in a day (T_{DG}) must be less than or equal to the maximum permissible operating time for the generator in a day (K):

$$\sum_{t=1}^{24} X_{\text{DG}} \leqslant T_{\text{DG}}$$

$$0 \leqslant T_{\text{DG}} \leqslant K$$

5.3.6 Decision Variables, Constraints for Battery

When battery is selected, the value of energy discharged by the battery at any instant t should be within its minimum discharge capacity (considered as 20% of rated capacity of the battery) and maximum discharge capacity (rated capacity of the battery) limits or should be zero. The generation characteristics for battery are given by the following equations:

$$E_{\text{gen},k}(t) = E_{k,\text{load}}(t) < [T * \eta_{\text{DCHG}} * P_{\text{Batt}}(t)] * X_{\text{BAT}}$$
$$\Rightarrow \quad E_{\text{gen},k}(t) = E_{k,\text{load}}(t) / (\eta_{\text{inv}} * \eta_{\text{DCHG}})$$
$$= [0.2 * P_{\text{Batt}}(t), 1.0 * P_{\text{Batt}}(t)] * T * \eta_{\text{DCHG}}$$

$$E_{\text{gen},k}(t) = E_{k,\text{load}}(t) \geqslant [T * \eta_{\text{DCHG}} * P_{\text{Batt}}(t)] * X_{\text{BAT}}$$
$$\Rightarrow \quad E_{\text{gen},k}(t) = 0$$

In this system, it is considered that the battery state of charge at the end of the day must be greater than or equal to 80% of the maximum state of charge:

$$\text{SOC}_{t=24} \geqslant 0.8 * \text{SOC}_{\max}$$

6 Results and Discussion

Since the objectives of the work are cost optimization of hybrid power system and correlated uncertainty study, the trend of output energy from renewable sources (PV and WTG) in different instances throughout the year 2001 and fluctuation of output depending upon the weather conditions are explained critically based on data obtained from the simulation work. For more precise analysis of two extreme situations with respect to cost, output energy of all instances for two particular days having highest solar radiation (14th June 2001) and lowest solar radiation (10th January 2001) is rigorously studied.

Analyzing the total energy generation from PV and WTG sources vs. time instant for 14th June 2001, the peaks of energy output curve from PV generator are found at 11th instant and 13th instant with the values of 29.224284 and 29.288155 KWh, respectively, as shown in Fig. 2. The peaks of energy output curve from PV generator for 10th January 2001 are also found at 11th instant and

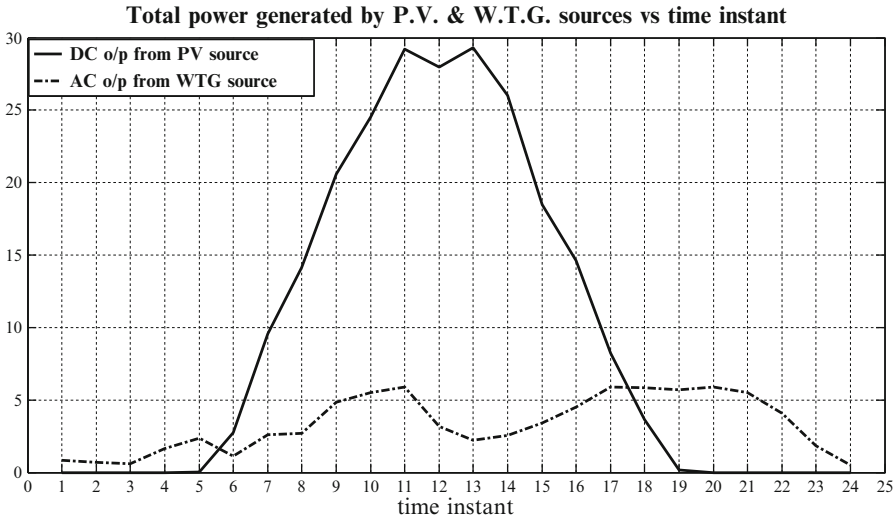

Fig. 2 The total energy generation (kWh) from PV and WTG sources vs. time instant (1 h) for a particular day (14th June 2001)

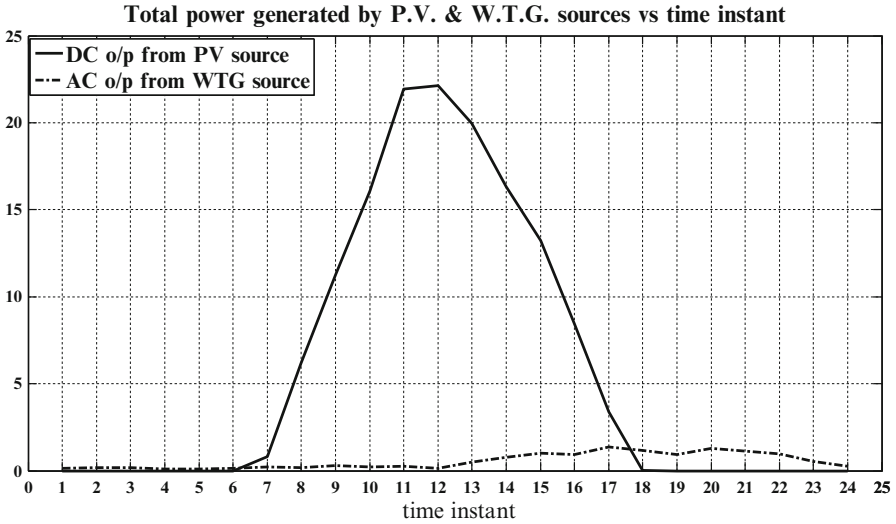

Fig. 3 The total energy generation (kWh) from PV and WTG sources vs. time instant (1 h) for a particular day (10th January 2001)

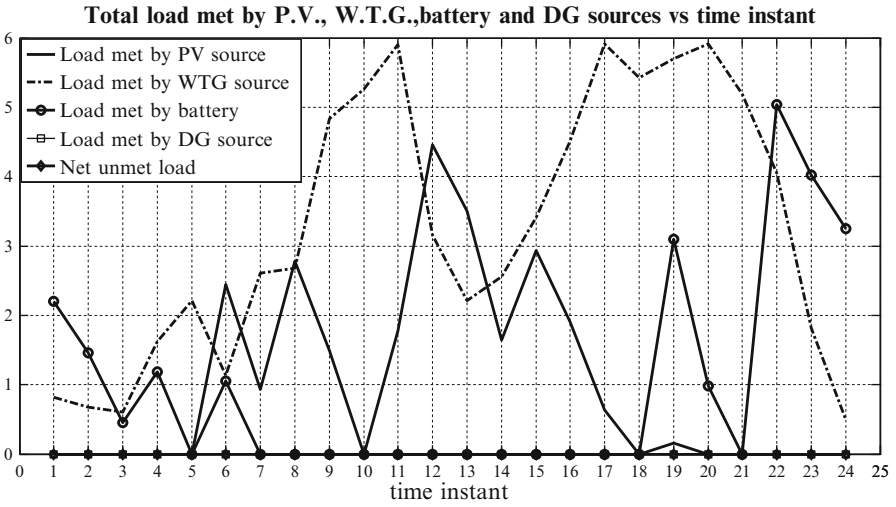

Fig. 4 Load met by PV, WTG, DG, and battery vs. time instant (1 h) for a particular day (14th June 2001)

13th instant with less in values compared to 14th June, i.e., 21.945020 and 19.961970 KWh, respectively (refer Fig. 3). Analyzing the total energy generation from PV and WTG sources vs. time instant for 14th June 2001, the peaks of energy output curve from WTG are found at 11th instant and 17th instant with the values of 5.908184 and 5.913463 KWh, respectively, as shown in Fig. 2.

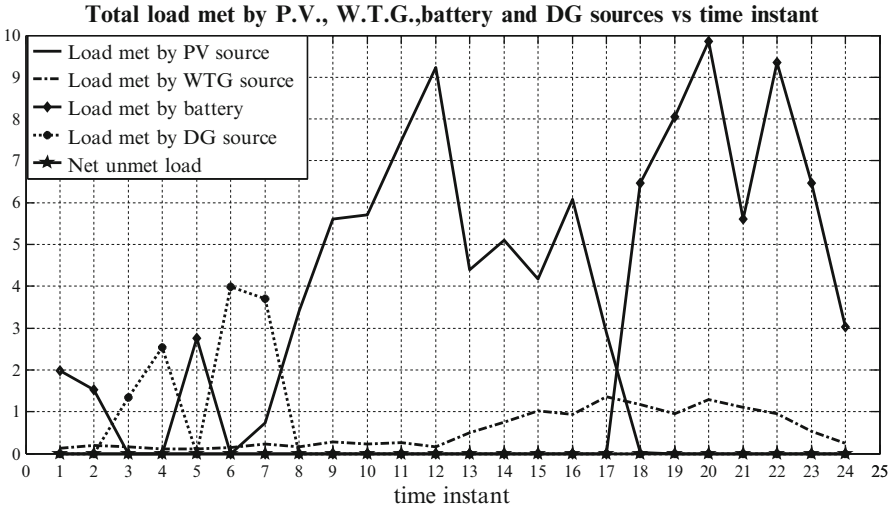

Fig. 5 Load met by PV, WTG, DG, and battery vs. time instant (1 h) for a particular day (10th January 2001)

Whereas the peaks of energy output curve from WTG generator for 10th January 2001 are found at 17th instant and 20th instant with less in values compared to 14th June, i.e., 1.364592 and 1.285518 KWh, respectively (refer Fig. 3).

Analyzing the total load demand provided by the renewable energy sources (PV and WTG sources), battery bank, and diesel generator (DG) vs. time instant for 14th June 2001, as per Fig. 4, higher (>5.5 KWh) outputs from WTG source are used to meet load demand of 5.908184 KWh at 11th instant, 5.913463 KWh at 17th instant, and 5.914009 KWh at 20th instant. Similarly referring the total load demand provided by the renewable energy sources (PV and WTG sources), battery bank, and diesel generator (DG) vs. time instant for 10th January 2001 in Fig. 5, the higher-output energies from WTG source are used to meet load demand of 1.364592 KWh at 17th instant and 1.285518 KWh at 20th instant.

As a sample month, we study January month of the year 2001 and obtained following details. The total energy generated by WTG source in the month of January is 386.639 KWh or 386.639 billing units (in India). The PV source operates when the hourly solar radiation in kWh/m^2 is greater than zero. The total energy generated by PV source in the month of January is 3719.441 KWh or 3719.441 billing units (in India). The average optimized unit cost for the month of January is 10.2361 Rs./KWh. The average of the monthly optimized unit cost for all the 12 months gives the average optimized annual unit cost. The average optimized annual unit cost is 7.596 Rs./KWh for the year 2001.

According to Fig. 6 and Table 1, the maximum and minimum per unit cost for the whole year (2001) is 12.173404 Rs./KWh on 1st January and 3.2615 Rs./KWh on 5th June, respectively. It is evident from Fig. 7 and Table 1 that the maximum

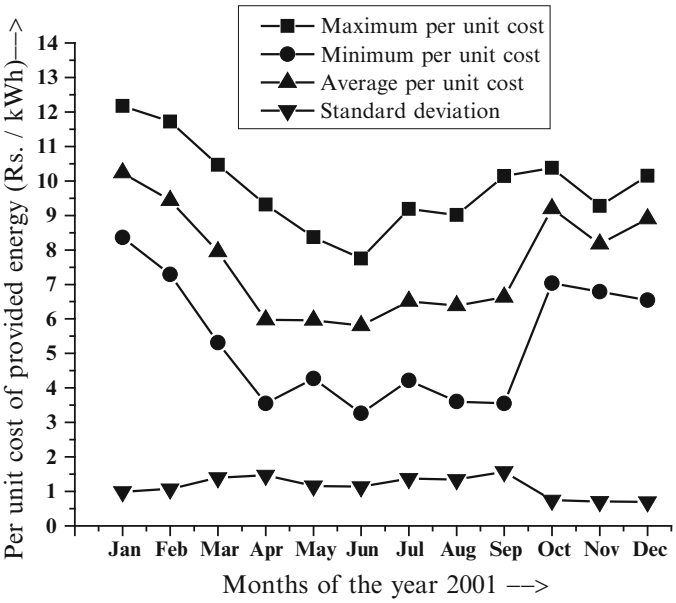

Fig. 6 Monthly average, maximum, and minimum per unit cost and standard deviation vs. months of the year 2001

Table 1 Monthly per unit cost details of the year 2001

Months of 2001	Date of max p. u. cost	Max p.u. cost	Date of min p. u. cost	Min p.u. cost	Std. deviation	Avg. monthly p.u. cost
Jan	01-Jan	12.173404	02-Jan	8.363316	0.993347331	10.236084
Feb	08-Feb	11.722876	28-Feb	7.290801	1.071347031	9.435516
Mar	28-Mar	10.463032	18-Mar	5.313473	1.399120359	7.945184
Apr	11-Apr	9.314134	26-Apr	3.550415	1.465889561	5.972452
May	11-May	8.371845	26-May	4.270128	1.155424331	5.967078
Jun	30-Jun	7.752802	05-Jun	3.2615	1.135942642	5.80387
Jul	08-Jul	9.191100	22-Jul	4.22046	1.372266507	6.514899
Aug	11-Aug	9.015912	29-Aug	3.609085	1.343795357	6.383503
Sep	22-Sep	10.14047	07-Sep	3.550165	1.575533507	6.629771
Oct	20-Oct	10.382071	11-Oct	7.032918	0.743912464	9.194708
Nov	13-Nov	9.276022	20-Nov	6.791329	0.70813149	8.169053
Dec	09-Dec	10.144813	22-Dec	6.542435	0.697100828	8.899727

and minimum monthly average per unit cost is 10.236084 Rs./KWh in the month of January and 5.80387 Rs./KWh in the month of June, respectively. The standard deviation is highest in September and equal to 1.575533507. Fluctuating nature of weather leads to uncertainty in the output energy trend from the renewable sources, i.e., PV and WTG. Higher standard deviation depicts more uncertain nature of the system for that particular month. Therefore, it can be inferred that maximum fluctuations of per unit cost have occurred during the month of September.

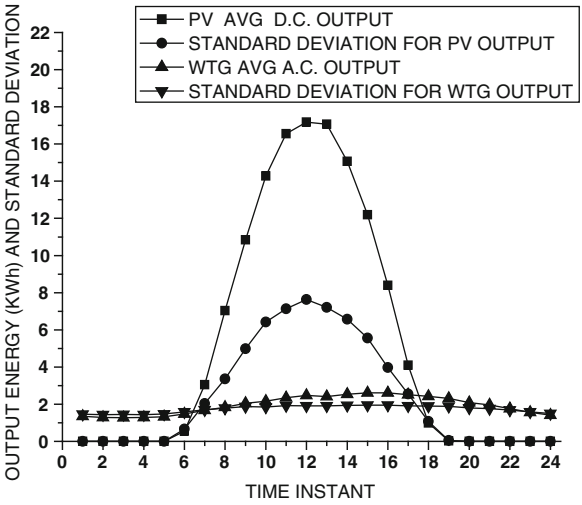

Fig. 7 Plots of yearly average output energies for time instant from PV, WTG, and corresponding standard deviations vs. time instant

It is found from Fig. 7 that the yearly average output from PV source is maximum around 12th instant, also the standard deviation for output from PV source is maximum around 12th instant. The maximum standard deviation reveals that the uncertainty in PV source output is maximum at that particular instant, i.e., 12th instant. It is also evident from Fig. 7 that the yearly average output from WTG source is maximum around 15th instant and the standard deviation for output from WTG source is maximum around 15th instant. It is seen that the maximum standard deviation for PV source output is more compared to the maximum standard deviation for WTG source output. Hence, the PV source output is more uncertain compared to the WTG source output in the studied hybrid system model.

7 Conclusion

The hybrid system simulation work and correlated uncertainty study can help substantially toward efficient hybrid renewable source-based energy system configuration and operation plan. The performance of weather-dependent renewable energy sources is very prone to fluctuations. So uncertainty in load demand met by PV and WTG and uncertainty in cost estimation of per energy unit are common. In this aspect, the present optimized hybrid system modeling and uncertainty study will be very helpful. This work is a significant step toward future complex hybrid renewable energy modeling of a remote area with rigorous study of correlated uncertainty.

References

1. Singh SN, Tigga VN, Mishra S (2010) Rural home energy management by soft computing fuzzy control models for a photovoltaic system in India. IJRRAS 35:262–268
2. Zeng J, Li MJ, Liu F, Wu J, Ngan HW (2010) Operational optimization of a stand-alone hybrid renewable energy generation system based on an improved genetic algorithm. In: Power and Energy Society general meeting, Minneapolis, MN, 25–29 July, pp 1–6
3. Sreeraj ES, Chatterjee K, Bandyopadhyay S (2010) Design of isolated renewable hybrid power systems. Solar Energy 84:1124–1136
4. Gupta A, Saini RP, Sharma MP (2011) Modelling of hybrid energy system-Part I: problem formulation and model development. Renew Energy 36:459–465
5. Prodromidis GN, Coutelieris FA (2010) Simulation and optimization of a stand-alone power plant based on renewable energy sources. Int J Hydrog Energy 35:10599–10603
6. Haghi HV, Hakimi SM, Tafreshi SMM (2010) Optimal sizing of a hybrid power system considering wind power uncertainty using PSO-embedded stochastic simulation. In: 11th international conference on Probabilistic Methods Applied to Power Systems (PMAPS), IEEE, Singapore, 14–17 June 2010, pp 722–727
7. Cheung KW, Rios-Zalapa R (2011) Smart dispatch for large grid operations with integrated renewable resources. In: Innovative Smart Grid Technologies (ISGT), IEEE PES, Hilton Anaheim, CA, 17–19 Jan 2011
8. Giannakoudis G, Papadopoulos A, Seferlis IP, Voutetakis S (2010) Optimum design and operation under uncertainty of power systems using renewable energy sources and hydrogen storage. Int J Hydrog Energy 35:872–891
9. Enrique JM, Dura´n E, Sidrach-de-Cardona M, Andu´ jar JM (2007) Theoretical assessment of the maximum power point tracking efficiency of photovoltaic facilities with different converter topologies. Solar Energy 81:31–38
10. Gupta A, Saini RP, Sharma MP (2010) Steady-state modelling of hybrid energy system for off grid electrification of cluster of villages. Renew Energy 35:520–535
11. Ai B, Yang H, Shen H, Liao X (2003) Computer-aided design of PV/wind hybrid system. Renew Energy 28:1491–1512
12. Lagunas JC, Patricia CO, Gonzalez R (2004) Model design of wind/PV/fossil-fuel hybrid systems. In: 1st international conference on electrical and electronics engineering, ICEEE, 403–408. DOI:10.1109/ICEEE.2004.1433916 (Print ISBN: 0-7803-8531-4)
13. Muselli M, Notton G, Louche A (1999) Design of hybrid-photovoltaic power generator, with optimization of energy management. Solar Energy 65:143–157
14. Dufo-López R, Bernal-Agustín JL (2005) Design and control strategies of PV-diesel systems using genetic algorithms. Solar Energy 79(1):33–46

Shallow Foundation Response Variability due to Parameter Uncertainty

Prishati Raychowdhury and Sumit Jindal

Abstract Uncertainty in soil parameters may play a crucial role in response variation of foundations and the supporting structures and, consequently, may control several design decisions. It is, therefore, extremely important to identify and characterize the relevant parameters. Furthermore, it is also important to identify the sources and extent of uncertainty of soil and model input parameters, along with the effect of their uncertainty on the shallow foundation response. This chapter intends to investigate the effect of soil and model parameter uncertainty on the response of shallow foundation-structure systems resting on dry dense sand. In this study, the soil-foundation interface is modeled using Winkler-based concept, where the soil-foundation interface is assumed to be an assembly of discrete, nonlinear elements composed of springs, dashpots, and gap elements. The sensitivity of both soil and model input parameters on various force and displacement demands of the foundation-structure system is investigated using first-order second-moment analysis and Latin hypercube technique. It has been observed that the force and displacement demands of the foundation-structure system are highly sensitive to the soil and model parameters.

Keywords Soil-structure interaction • Winkler modeling • Parametric uncertainty • Nonlinear analysis • Sensitivity analysis

1 Introduction

Most soils are naturally formed in many different depositional environments; therefore, it shows variation in their physical properties from point to point. The soil properties exhibit variations even within an apparently homogeneous soil

P. Raychowdhury (✉) • S. Jindal
Indian Institute of Technology, Kanpur, India
e-mail: prishati@iitk.ac.in; jndlsmt@gmail.com

S. Chakraborty and G. Bhattacharya (eds.), *Proceedings of the International Symposium on Engineering under Uncertainty: Safety Assessment and Management (ISEUSAM - 2012)*,
DOI 10.1007/978-81-322-0757-3_77,

profile. Basic soil parameters that control the strength and stiffness of the soil-foundation system are cohesion, friction angle, unit weight, shear modulus, and Poisson's ratio of soil. These soil parameters can be delineated using deterministic or probabilistic models. Deterministic models use a single discrete descriptor for the parameter of interest, whereas probabilistic models define parameters by using discrete statistical descriptor or probability distribution (density) function. Uncertainty in soil properties can be formally grouped into aleatory and epistemic uncertainty [9]. Aleatory uncertainty represents the natural randomness of a property and is a function of spatial variability of the soil property. This type of uncertainty is inherent to the variable and cannot be reduced or eliminated by additional information. Epistemic uncertainty results from lack of information and shortcomings in measurements and calculations [9]. Epistemic uncertainty can usually be reduced by acquisition of more information or improvements in measuring methods.

In last few decades, significant research has been carried out for proper understanding of the behavior of structure due to uncertainty in soil parameters. In an early work, Lumb [10] showed that the soil parameters can be modeled as random variables confirming to the Gaussian distribution within the framework of probability theory. Ronold and Bjerager [11] observed that the model uncertainties are important in reliability analysis for prediction of stresses, capacities, deformation, etc., in structure and foundation systems. Chakraborty and Dey [2] studied the stochastic structural responses considering uncertainty in structural properties, soil properties, and loadings using Monte Carlo simulation technique. Lutes et al. [21] evaluated the response of a seismically excited structural system with uncertain soil and structural properties. Ray Chaudhuri and Gupta [16] investigated the variability in seismic response of secondary systems due to uncertain soil properties through a mode acceleration method. Foye et al. [4] described a thorough study for assessment of variable uncertainties by defining the probability density functions for uncertain design variables in load resistance factor design (LRFD). Na et al. [14] investigated the effect of uncertainties of geotechnical parameters on gravity-type quay wall in liquefiable condition using tornado diagram and first-order second-moment (FOSM) analysis. Raychowdhury [17] studied the effect of soil parameter uncertainty on seismic demand of low-rise steel building supported by shallow foundations on dense silty sand with considering a set of 20 ground motions. Raychowdhury and Hutchinson [18] carried out the sensitivity analysis of shallow foundation response to uncertain input parameters using simplified FOSM and tornado diagram methods.

This chapter focuses on studying the effect of uncertainty in soil and model parameters on the response of shallow foundation-supported [8] shear wall building. To incorporate the nonlinearity at the soil foundation interface, a beam-on-nonlinear-Winkler-foundation (BNWF) approach is adopted. The uncertainty analysis is carried out using simplified first-order second-moment method and Latin hypercube sampling technique.

2 Numerical Modeling

In this chapter, a beam-on-nonlinear-Winkler-foundation (BNWF) approach is used to model the nonlinear soil-structure interaction of shallow foundations subjected to lateral loads. The BNWF model includes a system of closely spaced independent, mechanistic, vertical, and lateral elements consisting of nonlinear springs, dashpots, and gap elements (Fig. 1). The vertical springs ($q - z$ elements) are intended to capture the axial and rotational behavior of the footing, whereas the lateral springs, $t - x$ element and $p - x$ element, are intended to capture the sliding and passive resistance, respectively. The material models were originally developed by Boulanger et al. [1] and modified by Raychowdhury and Hutchinson [15]. This model is capable of reasonably capturing the experimentally observed behavior for various shallow foundation conditions. For more details regarding the BNWF modeling, one can look into Raychowdhury and Hutchinson [15].

The backbone curves are thus characterized by a linear elastic region, then an increasingly growing nonlinear region (Fig. 2). For $q - z$ material, ultimate vertical capacity q_{ult} is calculated based on general bearing capacity equation given by Terzaghi [20]:

$$q_{ult} = cN_cF_{cs}F_{cd}F_{ci} + \gamma D_fN_qF_{qs}F_{qd}F_{qi} + 0.5\gamma BN\gamma F_{\gamma s}F_{\gamma d}F_{\gamma i} \quad (1)$$

where q_{ult} is the ultimate vertical bearing capacity per unit area of footing, c the cohesion, γ the unit weight of soil, D_f is the depth of embedment, B the width of

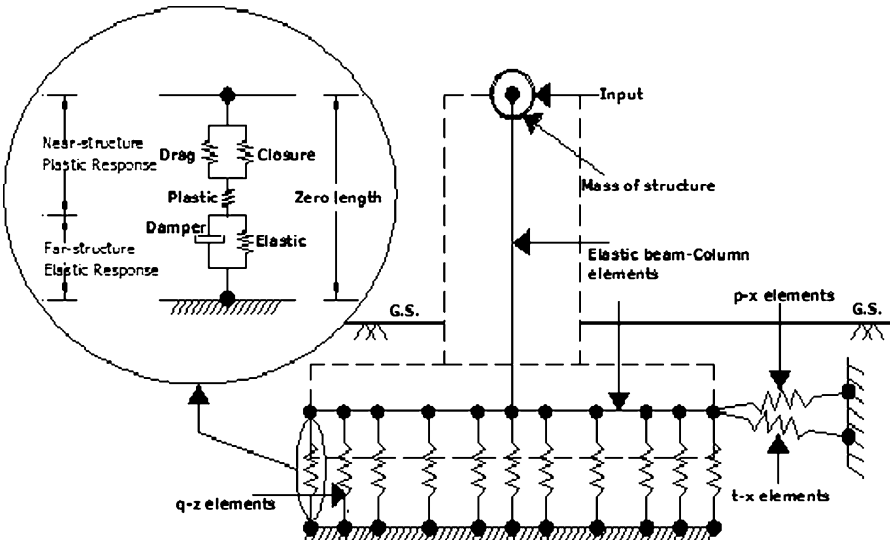

Fig. 1 Schematic diagram of structure with BNWF model for shallow foundations

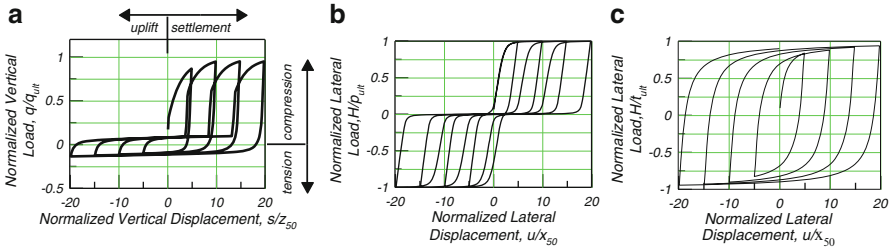

Fig. 2 Behavior of material models: (**a**) $q - z$ element, (**b**) $p - x$ element, and (**c**) $t - x$ element

footing, and N_c, N_q, N_γ are bearing capacity factors calculated after Mayerhof [13]. For the $p - x$ material, the passive resistance p_{ult} is calculated as

$$p_{\text{ult}} = 0.5\gamma K_p {D_f}^2 \tag{2}$$

where p_{ult} is the passive earth pressure per unit length of footing and K_p the passive earth pressure coefficient. For the $t - x$ material, the sliding resistance t_{ult} is determined using classical Mohr-Coulomb failure criteria

$$t_{\text{ult}} = W_g \tan\delta + cA_f \tag{3}$$

where t_{ult} is the frictional resistance per unit area of foundation, W_g the weight on the foundation from the structure, δ the angle of friction between foundation and soil, which typically varies from 1/3 to 2/3 ϕ, and A_f the surface area of the foundation.

The vertical and lateral stiffness, K_v and K_h, are calculated using expressions given by Gazetas [5] as follows:

$$k_v = \frac{GL}{1-v}\left[0.73 + 1.54\left(\frac{B}{L}\right)^{0.75}\right] \tag{4}$$

$$k_h = \frac{GL}{2-v}\left[2 + 2.5\left(\frac{B}{L}\right)^{0.85}\right] \tag{5}$$

In order to investigate the effect of uncertain input parameters on the shallow foundation response, a single shear wall structure supported by strip footing resting on dense dry sand of relative density 80% is considered for this study. The dimensions of footing are 1.0 m wide and 0.25 m in height, and depth of embedment is 0.5 m. Shear wall dimensions are 0.5 m in length and 0.2 m in width, and the height of wall is 5.0 m. A monotonic loading is applied at the top of the structure, and responses are evaluated in terms of maximum absolute values of moment, shear, rotation, and settlement demands.

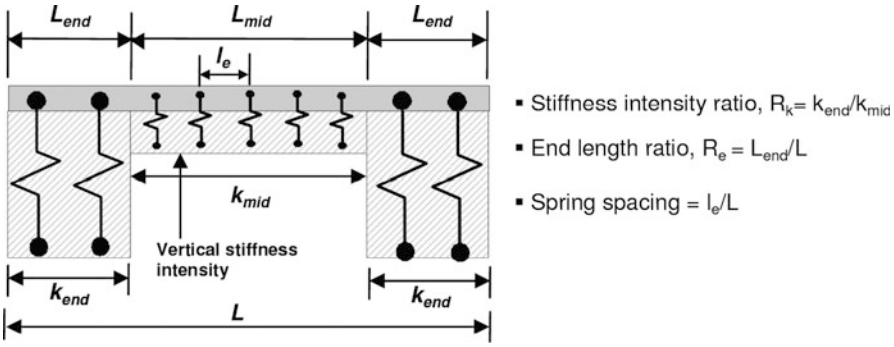

Fig. 3 Vertical spring distribution along the footing length

It is evident from the above discussion that the strength and stiffness of the spring elements of a particular size of footing are functions of basic soil properties such as friction angle, shear modulus, Poisson's ratio, and unit weight. Therefore, these soil properties are expected to influence the response of the footing-structure system. However, in addition to these soil properties, few model parameters such as spring spacing and ratio of spring stiffness along the length (as shown in Fig. 3) may also alter the foundation responses.

3 Selection of Uncertain Parameters

Based on the discussion provided in the previous section, the parameters shown in Table 1 are chosen for the uncertainty analysis. The parameters are selected for dense dry sand of relative density 80%. These values are based on EPRI [3] and Harden et al. [6]. It is assumed that all uncertain input parameters are random variables with a Gaussian distribution, having no negative values. The upper and lower limits of the random variables are assumed to be in 95th and 5th percentile of its probability distribution. The corresponding mean (μ) and standard deviation (σ) can be calculated as

$$\mu = \frac{L_L + L_U}{2} \text{ and } \sigma = \frac{L_L + L_U}{2k}$$

where L_L and L_U are the lower and upper limits, respectively, and k depends on the probability level (e.g., $k = 1.645$ for a probability of exceedance = 5%). The assumed correlations among the uncertain parameters are provided in Table 2.

Table 1 Uncertain parameters considered in this study

Parameters	Symbol	Range	Mean(μ)	Coeff. of. variation (C_v) (%)
Friction angle (deg)	ϕ'	38–42	40	3
Poisson's ratio	v	0.3–0.5	0.4	16
Shear modulus (MPa)	G_s	12–20	16	15
End length ratio	R_e	1–17	9	54
Stiffness intensity ratio	R_k	1–9	5	48
Spring spacing (%)	S_s	1.0–3.0	2	30

Table 2 Correlation matrix of the parameters

	ϕ'	v	G_s	R_e	R_k	S_s
ϕ'	1	0.1	0.6	0	0	0
v		1	0.2	0	0	0
G_s			1	0	0	0
R_e				1	0.3	0.1
R_k					1	−0.1
S_s						1

4 Uncertainty Analysis

In order to perform uncertainty analysis, two different techniques are adopted: first-order second-moment (FOSM) method and Latin hypercube method. Below is a brief description of both methods.

4.1 First-Order Second-Moment (FOSM) Method

The FOSM method is used to perform simplified sensitivity analysis to evaluate the effect of variability of input variables on each response variable. This method uses a Taylor series expansion of the function to be evaluated, and expansion is truncated after the linear first-order term. It is assumed that the relationship between the response variables and the uncertain input parameters is assumed to be linear or low-to-moderately nonlinear.

The response of the foundation is considered as a random variable Q, which has been expressed as a function of the input random variables, P_i (for $i = 1,\ldots,N$) denoting uncertain parameters and Q given by

$$Q = h(P_1, P_2, \ldots, P_N) \tag{6}$$

P_i has been characterized by its mean μ_p and variance ${\sigma_p}^2$. Now, Q can be expanded using a Taylor series as follows:

$$Q = h(\mu P_1, \mu P_2, ..., \mu P_N) + \frac{1}{1!}\sum_{i=1}^{N}(P_i - \mu_{Pi})\frac{\delta h}{\delta P_i} + \frac{1}{2!} \times \sum_{j=1}^{N}\sum_{i=1}^{N}(P_i - \mu_{Pi})(P_j - \mu_{P_j})\frac{\delta^2 h}{\delta P_i \delta P_j} + ... \tag{7}$$

Considering only the first-order terms of Eq. (7) and ignoring higher-order terms, Q can be approximated as taking expectation of both sides of Eq. (6), the mean of Q can be expressed as

$$Q \approx h(\mu_{p1}, \mu_{p2}, ..., \mu_{2,N}) + \sum_{i=1}^{N}(Pi - \mu)\frac{\delta h}{\delta P_i} \tag{8}$$

$$\mu_Q = h(\mu_{P_1}, \mu_{P_2}, \mu_{P_N}) \tag{9}$$

Utilizing the second-order moment of Q as expressed in Eq. (7), the variance of Q can be derived as

$$\begin{aligned}\sigma_Q^2 &\approx \sum_{i=1}^{N}\sum_{j=1}^{N} covariance(P_i, P_j)\ \ \underset{\partial P_i}{\delta h(P_1, P_2, \ldots, P_N)}\ \ \underset{\partial P_j}{\delta h(P_1, P_2, \ldots, P_N)} \\ &\approx \sum_{i=1}^{N}\sigma_{P_i}^2\left(\frac{\delta h(P_1, P_2, \ldots, P_N)}{\delta P_i}\right)^2 \\ &+ \sum_{i-1}^{N}\sum_{j+1}^{N}\rho_{P_i,P_j}\frac{\delta h(P_1, P_2, \ldots, P_N)}{\delta P_i}\frac{\delta h(P_1, P_2, \ldots, P_N)}{\delta P_j}\end{aligned} \tag{10}$$

where $\rho_{Pi,Pj}$ denotes correlation coefficient for random variables P_i and P_j. The partial derivative of $h(P_1, P_2,..,P_N)$ with respect to P_i has been calculated numerically using the finite difference method (central) as follows:

$$\frac{\delta h(P_1, P_2, \ldots, P_N)}{\delta P_i} = \frac{h(p_1, p_2, \ldots, \mu_i + \Delta_{p_i}, p_N) - h(p_1, p_2, \ldots, \mu_i - \Delta_{p_i}, p_N)}{2\Delta_{P_i}} \tag{11}$$

4.2 Latin Hypercube Method

For probabilistic analysis of engineering structures having uncertain input variables, Monte Carlo simulation (MCS) technique is considered as a reliable

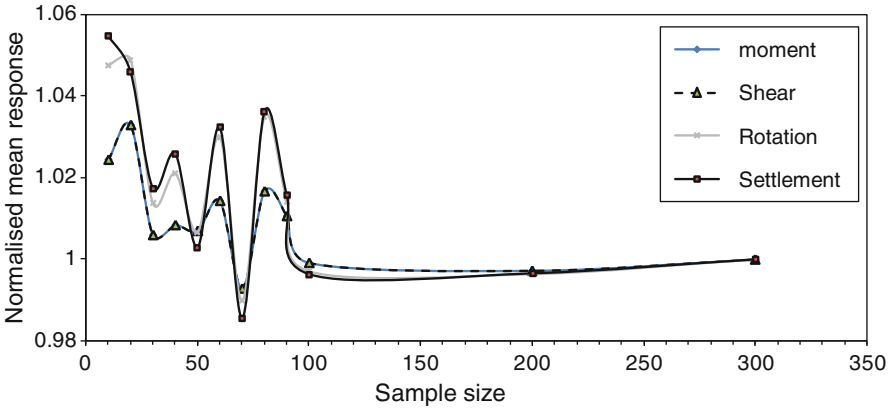

Fig. 4 Convergence test for Latin hypercube sampling method

and accurate method. However, this method requires a large number of equally likely random realizations and consequent computational effort. In order to decrease the number of realizations required to provide reliable results in MCS, Latin hypercube sampling (LHS) approach [12] is widely used in uncertainty analysis. LHS is a type of stratified MCS which provides a very efficient way of sampling variables from their multivariate distributions for estimating mean and standard deviations of response variables [7]. It follows a general idea of a Latin square, in which there is only one sample in each row and each column. In Latin hypercube sampling, to generate a sample of size K from N variables, the probability distribution of each variable is divided into segments with equal probability. The samples are then chosen randomly in such a way that each interval contains one sample. During the iteration process, the value of each parameter is combined with the other parameter in such a way that all possible combinations of the segments are sampled. Finally, there are M samples, where the samples cover N intervals for all variables. In this study, to evaluate the response variability due to the uncertainty in the input parameters, samples are generated using Stein's approach [19]. This method is based on the rank correlations among the input variables defined by Iman and Conove [7], which follows Cholesky decomposition of the covariance matrix.

In this study, the covariance matrix is calculated by using standard deviation (Table 1) and correlation coefficient (Table 2) between any two input parameters. The previously mentioned shear wall structure is considered for this analysis. The response of this soil-foundation structure system is dependent on the six independent input and normally distributed variables defined in Tables 1 and 2. In order to find out the correct sample size, pushover analysis is carried out using 10, 20,. . ., 100, 200, and 300 number of samples. Figure 4 shows the plot sample size versus the mean responses normalized by value corresponding to a sample size of 300. From Fig. 4, it can be observed that the mean of the responses tends to converge as the sample size increases. At the sample size of 100, the response of the system has almost converged. Therefore, for six independent and normally distributed variables, a sample size of 100 is used.

5 Results and Discussion

In order to evaluate the effect of soil and model parameter uncertainty on the response of the shallow foundation, four response parameters are chosen: absolute maximum moment $|M_{max}|$, absolute maximum shear $|V_{max}|$, absolute maximum rotation $|\theta_{max}|$, and absolute maximum settlement $|S_{max}|$. A monotonic loading is applied at the top of the structure, and responses and forces and displacements are obtained. The analysis is done using finite element software OpenSees (Open System for Earthquake Engineering Simulation). Figure 5 shows the comparison results for the centrifuge experiment conducted in the University of California, Davis. The results are for two extreme values of friction angle. The results include moment-rotation, settlement-rotation, and shear-rotation behaviors with the BNWF simulation shown in black and experimental results shown in gray scale. These comparisons indicate that the BNWF model is able to capture the hysteretic features such as shape of the loop, peaks, and unloading and reloading stiffness reasonably well. It can also be observed from Fig. 5 that with increasing the friction angle from 38° to 42°, peak moment and peak shear demands increase, whereas peak settlement demand decreases. It can also be noted that the variation of friction angle from 38° to 42° has the most significant effect on settlement prediction (more than 100%). However, the moment, shear, and rotation demands are moderately affected by this parameter. This indicates that the uncertainty in one parameter may have significantly different influence on the prediction of different responses, pointing out toward the importance of proper characterization of each parameter and conducting the sensitivity analysis.

Similarly, the analysis is carried out for varying each parameter at a time while keeping other parameters fixed at their mean values, and FOSM analysis is carried out to find out the sensitivity of each parameter on the responses. Figures 6, 7, 8, and 9 show the results of FOSM analysis for moment, shear, rotation, and settlement, respectively. It can be observed that for moment and shear, friction angle is the most important parameter (60% relative variance). Poisson's ratio and shear modulus are moderately important (about 23 and 16%, respectively), and model parameters have negligible effect (less than 5%). However, model parameter stiffness intensity ratio, R_k, seems to have great effect on the rotational demand (~67%). Settlement is observed to be affected by all three soil parameters (friction angle, shear modulus, and Poisson's ratio), almost equally (~30%) for each parameter. Model parameters do not affect this response much.

Table 3 shows the result obtained from Latin hypercube method. The response is presented in terms of the mean and coefficient of variation (C_v) of each demand parameters. It can be observed from this table that with 3, 16, 15, 54, 48, and 30% C_v of friction angle, Poisson's ratio, shear modulus, end length ratio, stiffness intensity ratio, and spring spacing input parameters, respectively, can result in moderate variation in demand parameters with C_v as 16, 16, 22, and 24% for the

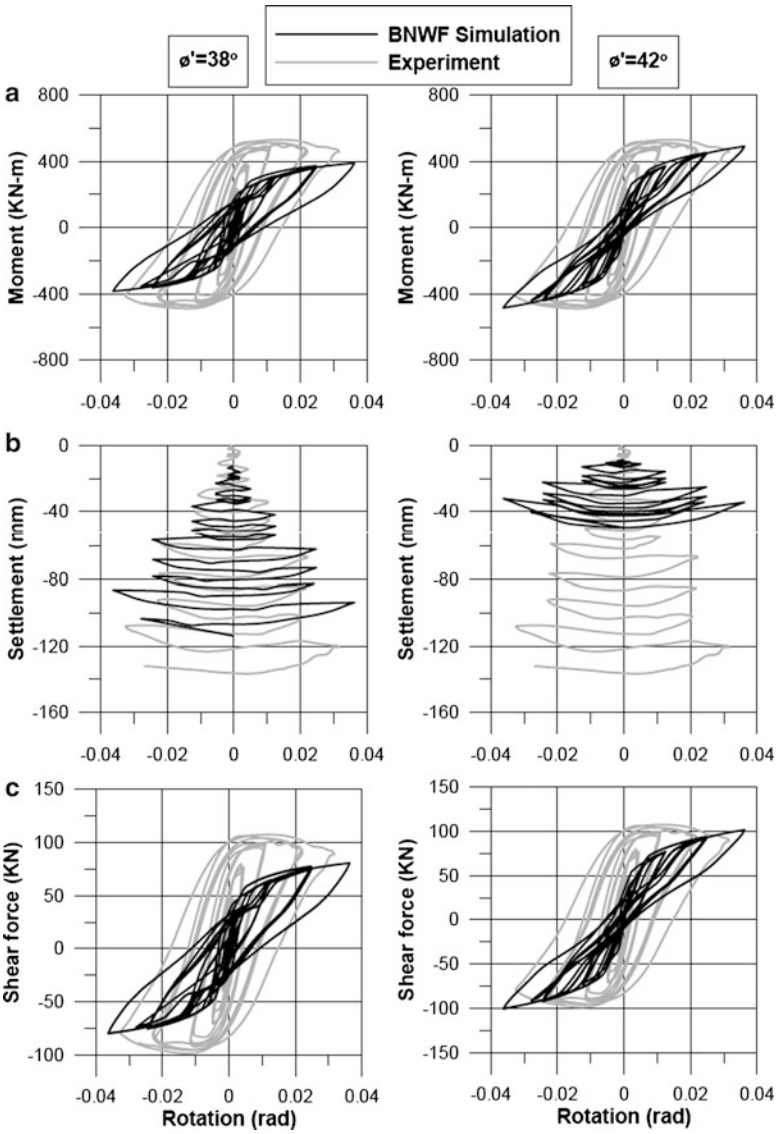

Fig. 5 Response of shear wall-footing system

absolute maximum moment, shear, rotation, and settlement demands, respectively. Note that all responses are more sensitive to the soil parameters than the model parameters. Friction angle is the most sensitive among all input parameter, as with a 3% C_v results in significant variation in the response variables.

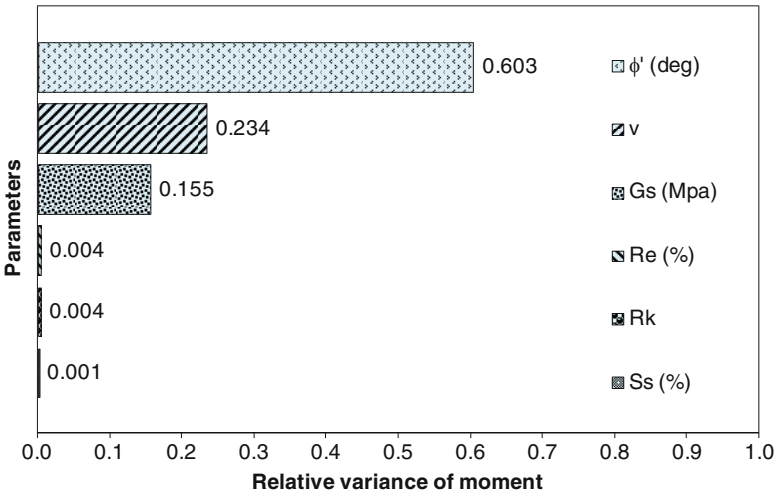

Fig. 6 Results of FOSM analysis: relative variance for moment

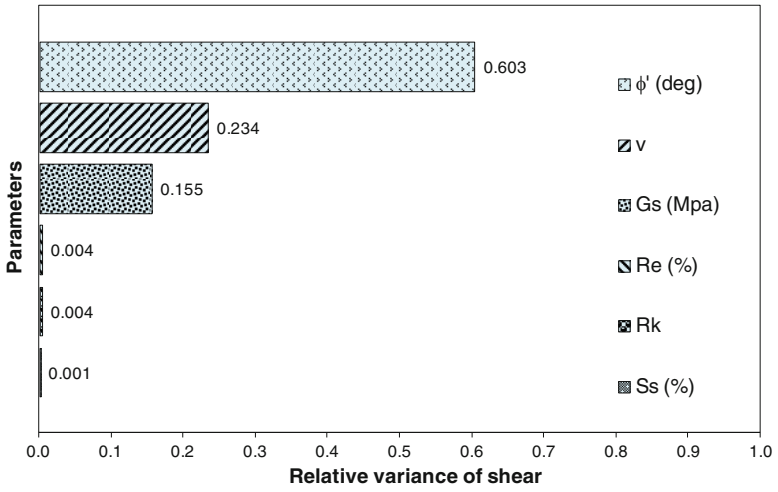

Fig. 7 Results of FOSM analysis: relative variance for shear

Table 3 Variability of response parameters using Latin hypercube method

	Moment $\lvert M_{max}\rvert$	Shear $\lvert V_{max}\rvert$	Rotation $\lvert \theta_{max}\rvert$	Settlement $\lvert S_{max}\rvert$
Mean (μ)	78.09 kN-m	15.62 kN	0.14 rad	39.11 mm
Coeff. of variation (C_v)	16%	16%	22%	24%

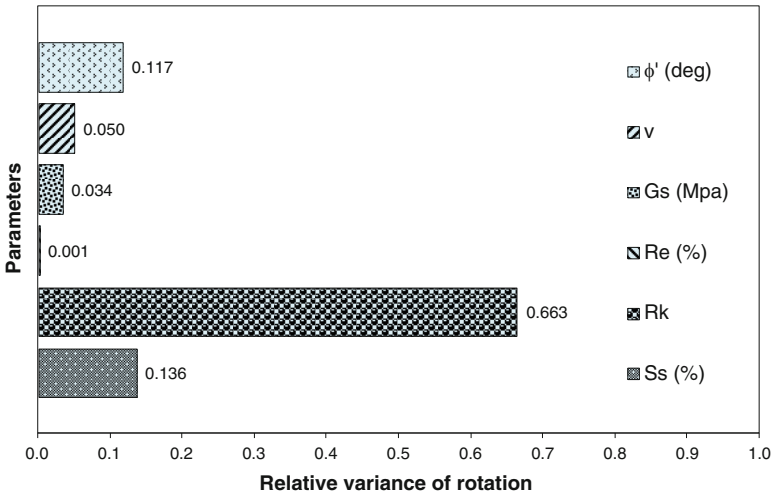

Fig. 8 Results of FOSM analysis: relative variance for rotation

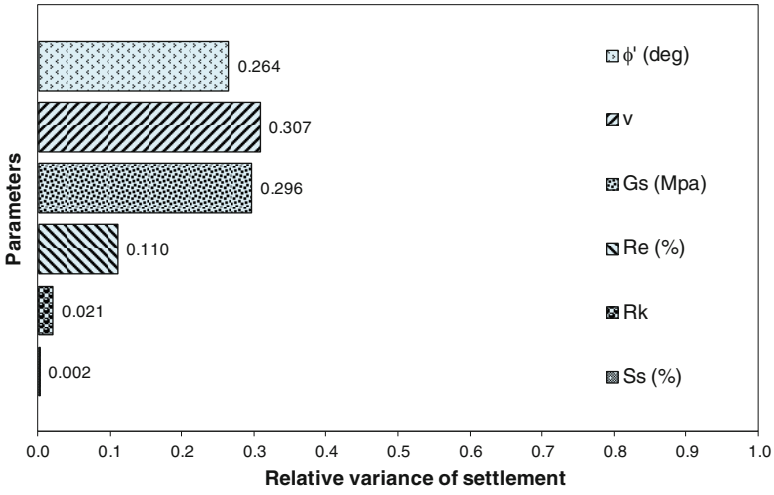

Fig. 9 Results of FOSM analysis: relative variance for settlement

6 Conclusions

The effect of uncertainty in soil and model parameters on the soil-foundation system response has been studied in this chapter. The soil-foundation system has been modeled using BNWF concept, and the uncertainty analyses are carried out using FOSM and Latin hypercube method. It has been observed that for moment and shear, friction angle is the most important parameter (60% relative variance),

Poisson's ratio and shear modulus are moderately important (about 23 and 16%, respectively), and model parameters have negligible effect (less than 5%). The rotational demand (~67%) is largely dependent on stiffness intensity ratio. The settlement demand is almost equally sensitive to friction angle, shear modulus, and Poisson's ratio (~30% variance for each parameter). The results from Latin hypercube method indicate that a coefficient of variation of 3% in friction angle results in 16, 16, 22, and 24% for the absolute maximum moment, shear, rotation, and settlement demands, respectively, indicating that these parameters have great effect on each response variables. It can finally be concluded that soil parameters such as friction angle, shear modulus, and Poisson's ratio may have significant effect on the response of foundation. Therefore, selection of these parameters should be considered critically when designing a structure with significant soil-structure interaction effect.

References

1. Boulanger RW, Curras CJ, Kutter BL, Wilson DW, Abghari A (1999) Seismic soil-pile-structure interaction experiments and analyses. J Geotech Geoenviron Eng 125(9): 750–759
2. Chakraborty S, Dey SS (1996) Stochastic finite-element simulation of random structure on uncertain foundation under random loading. Int J Mech Sci 38(11):1209–1218
3. EPRI (1990) Manual on estimating soil properties for foundation design. Electric Power Research Institute, Palo Alto
4. Foye KC, Salgado R, Scott B (2006) Assessment of variable uncertainties for reliability based design of foundations. J Geotech Geoenviron Eng 132(9):1197–1207
5. Gazetas G (1991) In: Fang HY (ed) Foundation engineering handbook. Van Nostrand Rienhold, New York
6. Harden CW, Hutchinson TC, Martin GR, Kutter BL (2005) Numerical modeling of the nonlinear cyclic response of shallow foundations, Technical report 2005/04. Pacific Earthquake Engineering Research Center, Berkeley
7. Iman RL, Conover WJ (1982) A distribution free approach to including rank correlation among input variables. Bull Seism Soc Am 11(3):311–334
8. Jindal S (2011) Shallow foundation response analysis: a parametric study. Master's thesis, Indian Institute of Technology Kanpur, India
9. Lacasse S, Nadim F (1996) Uncertainties in characterizing soil properties. In: Uncertainty in the geologic environment: from theory to practice, proceedings of uncertainty 96, Madison, Wisconsin, July 31–August 3 1996, New York, USA, ASCE Geotechnical Special Publication No. 58, pp 49–75
10. Lumb P (1966) The variability of natural soils. Eng Struct 3:74–97
11. Ronold KO, Bjerager P (1992) Model uncertainty representation in geotechnical reliability analyses. J Geotech Eng 118(3):363–376
12. McKay MD, Beckman RJ, Conover WJ (1969) A comparison of three methods for selecting values of input variables in the analysis of output from a computer code. Technometrics 21 (2):239–245
13. Meyerhof GG (1963) Some recent research on the bearing capacity of foundations. Can Geotechn J 1(1):16–26
14. Na UJ, Ray Chaudhuri S, Shinozuka M (2008) Probabilistic assessment for seismic performance of port structures. Soil Dyn Earthq Eng 28:147–158

15. Raychowdhury P, Hutchinson TC (2008) Nonlinear material models for winkler-based shallow foundation response evaluation. In: GeoCongress 2008, characterization, monitoring, and modeling of geosystems, New Orleans, LA, 9–12 March, ASCE Geotechnical Special Publication No. 179, pp 686–693
16. Ray Chaudhuri S, Gupta VK (2002) Variability in seismic response of secondary systems due to uncertain soil properties. Eng Struct 24(12):1601–1613
17. Raychowdhury P (2009) Effect of soil parameter uncertainty on seismic demand of low-rise steel buildings on dense sand. Soil Dyn Earthq Eng 29:1367–1378
18. Raychowdhury P, Hutchinson TC (2010) Sensitivity of shallow foundation response to model input parameters. J Geotechn Geoenviron Eng 136(3):538–541
19. Stein M (1987) Large sample properties of simulations using Latin hypercube sampling. Technometrics 29(2):143–151
20. Terzaghi K (1943) Theoretical soil mechanics. Wiley, New York
21. Lutes et al (2000) Response variability for a structure with soil–structure interactions and uncertain soil properties. Probab Eng Mechan 15(2):175–183

Effect of Nonlinear SSI on Seismic Response of Low-Rise SMRF Buildings

Prishati Raychowdhury and Poonam Singh

Abstract Nonlinear behavior of soil-foundation system may alter the seismic response of a structure by providing additional flexibility to the system and dissipating hysteretic energy at the soil-foundation interface. However, the current design practice is still reluctant to consider the nonlinearity of the soil-foundation system, primarily due to lack of reliable modeling techniques. This study is motivated toward evaluating the effect of nonlinear soil-structure interaction (SSI) on the seismic responses of low-rise steel moment-resisting frame (SMRF) structures. In order to achieve this, a Winkler-based approach is adopted, where the soil beneath the foundation is assumed to be a system of closely spaced, independent, nonlinear spring elements. Static pushover analysis and nonlinear dynamic analyses are performed on a 3-story SMRF building, and the performance of the structure is evaluated through a variety of force and displacement demand parameters. It is observed that incorporation of nonlinear SSI leads to increase in story displacement demand and reduction in base moment, base shear, and interstory drift demands significantly, indicating the importance of its consideration toward achieving an economic yet safe seismic design procedure.

Keywords Soil-structure interaction • Winkler modeling • Nonlinear analysis • Seismic response

1 Introduction

Nonlinear behavior of a soil-foundation interface due to mobilization of the ultimate capacity and the consequent energy dissipation during an intense seismic event may alter the response of a structure in several ways. Foundation movement can increase

P. Raychowdhury (✉) • P. Singh
Indian Institute of Technology Kanpur, Kanpur, Uttar Pradesh, India
e-mail: prishati@iitk.ac.in; poonamsingh.222@gmail.com

S. Chakraborty and G. Bhattacharya (eds.), *Proceedings of the International Symposium on Engineering under Uncertainty: Safety Assessment and Management (ISEUSAM - 2012)*,
DOI 10.1007/978-81-322-0757-3_78,

the period of a system by introducing flexibility, nonlinear behavior and hysteretic energy dissipation at the soil-foundation interface may reduce the force demand to the structure, and foundation deformations may alter the input ground motion. However, till date, current design practice is reluctant to account for the nonlinear soil-structure interaction (SSI), primarily due to the absence of reliable nonlinear modeling techniques and also in anticipation that consideration of SSI generally leads to more conservative design.

In the past few decades, a number of analytical and experimental studies have been conducted to understand the effect of SSI on the seismic behavior of structures [1, 6, 7, 9, 12, 13, 16–18, 21, 23]. These studies indicated that the nonlinear soil-foundation behavior under significant loading has considerable effect on the response of structure-foundation system. Design and rehabilitation provisions (e.g., [2, 3, 8, 14]) have traditionally focused on simplified pseudo-static force-based or pushover-typeprocedures, where the oil-foundation interface is characterized in terms of modified stiffness and damping characteristics. However, the above-mentioned approaches cannot capture the complex behavior of nonlinear soil-foundation-structure systems, such as hysteretic and radiation damping, gap formation in the soil-foundation interface and estimation of transient and permanent settlement, and sliding and rotation of the foundation.

In this chapter, the seismic response of a ductile steel moment-resisting frame (SMRF) building [adopted from Gupta and Krawinkler [11]] has been evaluated considering nonlinear SSI through a beam-on-nonlinear-Winkler-foundation (BNWF) approach, where the soil-foundation interface is assumed to be a system of closely spaced, independent, inelastic spring elements [12, 15]. The details of the modeling technique, soil and structural properties considered, and analysis procedures adopted are discussed below.

2 Numerical Modeling of Nonlinear SSI

The BNWF model is an assembly of closely spaced, independent, nonlinear spring elements (Fig. 1). Vertical springs (q-z elements) distributed along the length of the footing are intended to capture the rocking, uplift, and settlement, while horizontal springs (t-x and p-x elements) are intended to capture the sliding and passive resistance of the footing, respectively. The constitutive relations used for the q-z, p-x, and t-x mechanistic springs are represented by nonlinear backbone curves that were originally developed by Boulanger [4], based on an earlier work of Boulanger et al. [5], and later on calibrated and validated by Raychowdhury [15] for more appropriate utilization toward shallow foundation behavior modeling. Details of the BNWF modeling technique along with its predictive capabilities to achieve experimentally observed soil-foundation behavior can be found in Raychowdhury [15], Raychowdhury and Hutchinson [16, 17], and Gajan et al. [9]. The initial elastic stiffness and vertical capacity of the soil springs are calculated based on Gazetas [10] and Terzaghi [22], respectively. Springs are distributed at a spacing of 1%

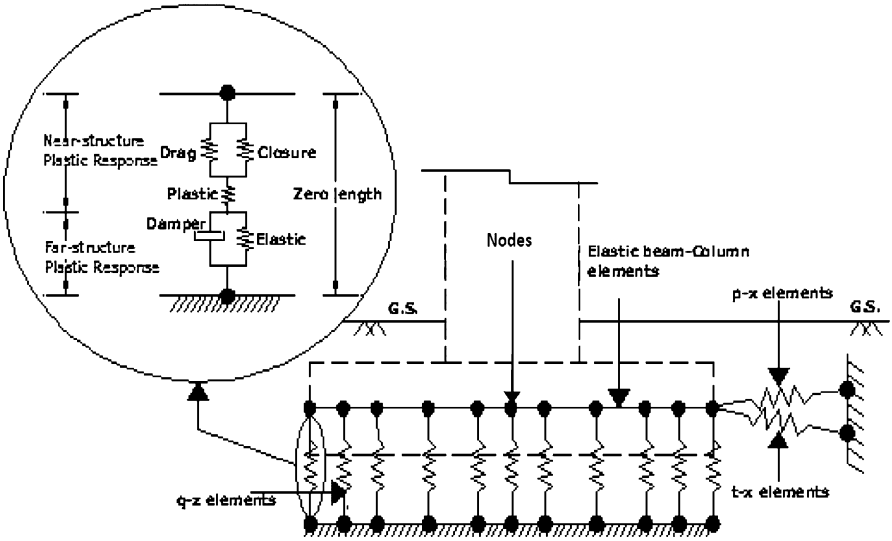

Fig. 1 Idealized BNWF model

of the footing length at the end region and of 2% of the footing length at the mid-region. The end region is defined as high stiffness region extending 10% of footing length from each end of the footing, while the mid-region is the less stiffer middle portion. This variation in the stiffness distribution is provided based on the recommendations of ATC-40 [3] and Harden and Hutchinson [12] in order to achieve desirable rocking stiffness of the foundation.

3 Selection of Structure, Soil Properties, and Ground Motions

A 3-story, 4-bay steel moment resisting frame (SMRF) building adopted from Gupta and Krawinkler [11] is considered for the present study. The building is designed based on the weak-beam strong-column mechanism, with floor area of 36:6 $\times$ 36:6 m and four bays at an interval of 9.15 m in each direction (Fig. 2). The section properties and geometric details of the structure have been taken from Gupta and Krawinkler [11]. The columns of the building are assumed to be supported on mat foundation resting on dense silty sand of Los Angeles area (site class-D, NEHRP), with the following soil properties: cohesion 70 kPa, unit weight 20 kN $=$ m3, shear modulus 5.83 MPa, and Poisson's ratio 0.4. The effective shear modulus is obtained by reducing the maximum shear modulus (corresponding to small strain values) by 50% to represent the high-strain modulus during significant earthquake loadings. The foundation is designed in such a way that it has a bearing capacity three times of the vertical load coming to it (i.e., a static vertical factor of safety of 3). More details can be found in Singh [19]. Nonlinear dynamic analysis

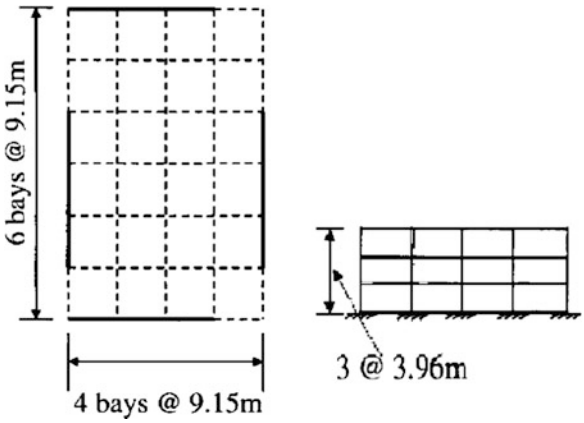

Fig. 2 SMRF structure considered in the study (Adapted from Gupta and Krawinkler [11])

is carried out using SAC ground motions [20] representing the probabilities of exceedance of 50, 10, and 2% in 50 years, with return periods of 72 years, 475 years, and 2,475 years, respectively. In this chapter, these three sets of ground motions are denoted as 50/50, 10/50, and 2/50, respectively, for brevity. A 2% Rayleigh damping is used in the dynamic analysis.

4 Results and Discussion

Before performing the dynamic analysis, eigenvalue analysis and static pushover analysis were carried out and compared with that obtained by Gupta and Krawinkler [11]. It has been observed that when the building is considered fixed at its base (i.e., ignoring the SSI effects), the fundamental period is obtained as 1.03 s, which is in accordance with the period obtained by Gupta and Krawinkler [11]. However, when the base flexibility is introduced, the fundamental period is observed to be 1.37 s, indicating significant period elongation (~33%) due to SSI effects.

The static pushover analysis shows the effect of SSI on the force and displacement demands of the structure in an effective way (Fig. 3). It can be observed that when the soil-foundation interface is modeled as linear, the global response of the system is altered only slightly from that of a fixed-base case. However, when the soil springs are modeled as nonlinear, the curve becomes softer, resulting in lower yield force and higher yield displacement demands (Table 1), which may be associated with yielding of the soil beneath the foundation.

Figures 4, 5, 6, and 7 provide the statistical results of the various force and displacement demands obtained from the nonlinear dynamic analysis using 60 ground motions mentioned earlier. The maximum absolute value of each response parameter (such as story displacement, moment, and shear) is considered as the respective demand value. Before incorporating the nonlinear SSI effects, the

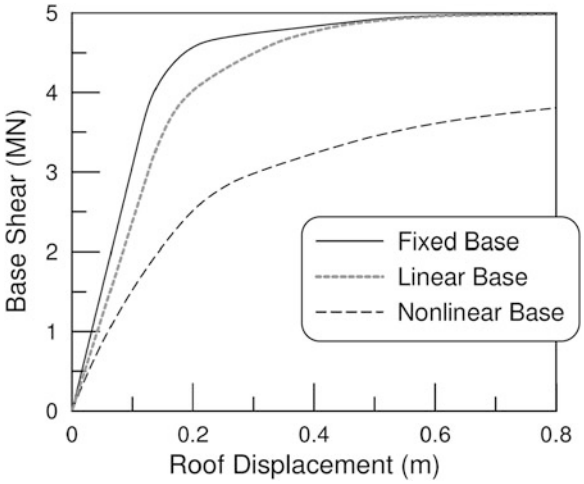

Fig. 3 Global pushover curves for different base conditions

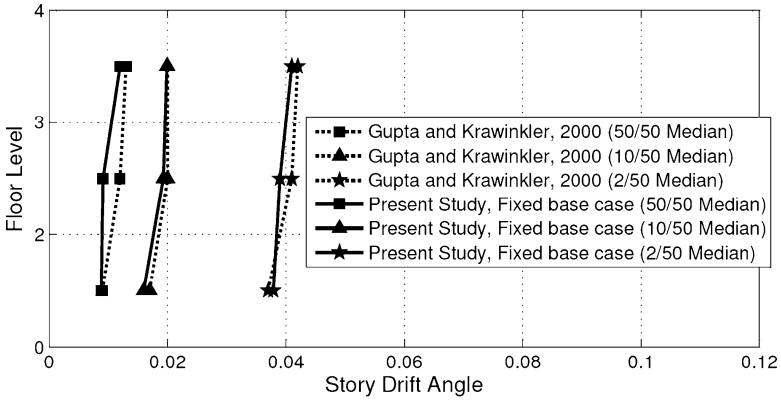

Fig. 4 Median values of inter-story drift demands: comparison of fixed-base case with Gupta and Krawinkler [11]

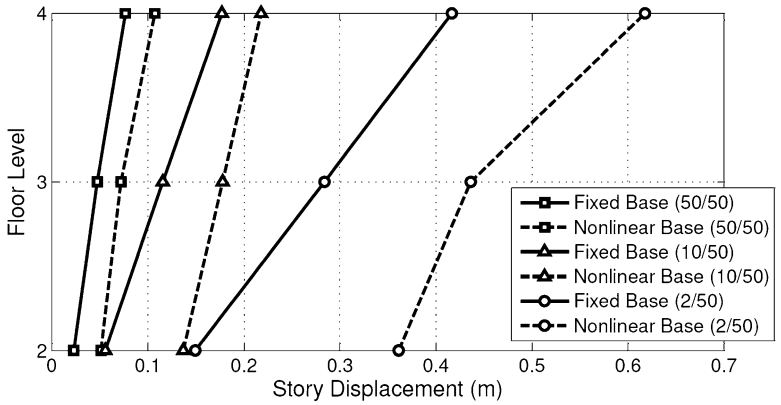

Fig. 5 Median values for story displacement demands

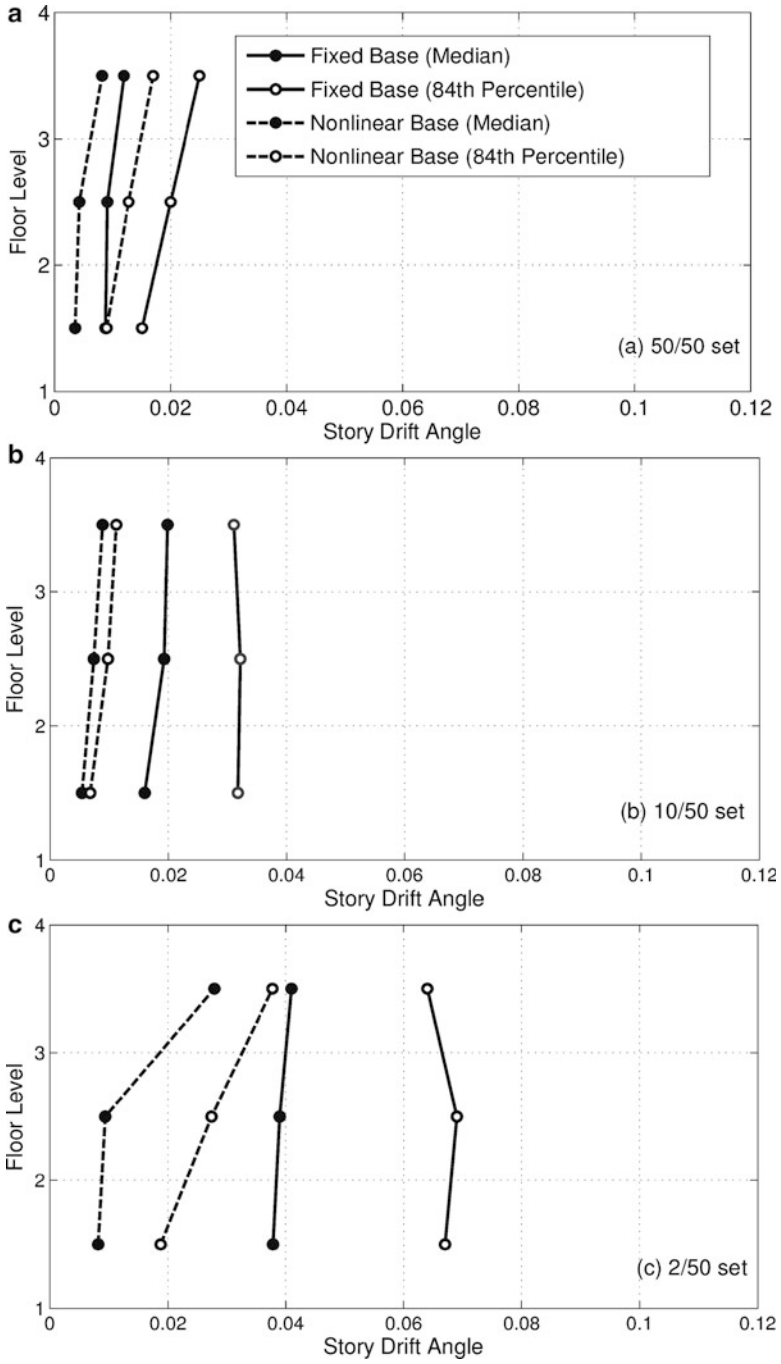

Fig. 6 Statistical values of inter-story drift demands for ground motions: (**a**) 50% in 50 years, (**b**) 10% in 50 years, and (**c**) 2% in 50 years hazard levels

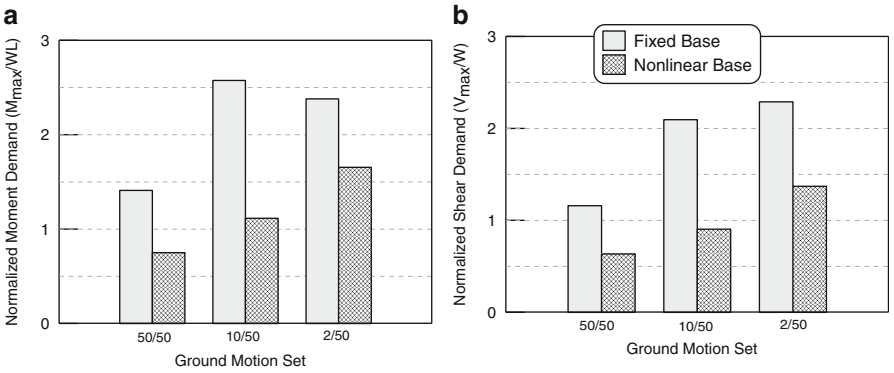

Fig. 7 Median values for (**a**) normalized base moment demand and (**b**) normalized base shear demand (*W* weight of the building, *L* length of the footing)

Table 1 Pushover analysis results

Base condition	Yield displacement(m)	Yield force (MN)
Fixed Base	0.19	4.53
Linear Base	0.25	4.28
Nonlinear Base	0.28	2.86

response of the fixed-base structure is compared with that obtained by Gupta and Krawinkler [11]. It has been observed that response of the fixed-base case is in accordance with that of Gupta and Krawinkler [11] with minor deviation in second story for 50/50 set of motion (Fig. 4). Figure 5 shows the median values of the story displacements considering fixed-base condition and nonlinear SSI. It can be observed that consideration of nonlinear SSI increases the story displacement demand significantly (more than 100%) for each set of ground motion and at each floor level. This indicates that neglecting the nonlinear SSI effects during the structural design may lead to an unconservative estimation of story displacement demands. However, when the inter-story drift demands are compared, it is observed that the inclusion of base nonlinearity reduces the same (see Fig. 6). Moreover, this reduction is significant and consistent for each floor level and each set of ground motion. Since inter-story drift demand is an important parameter for designing individual structural members, it is very likely that the members will be designed over-conservatively if the SSI effects are neglected. Similar observations are also made from comparison of force demands, where median values of both base moment and base shear are observed to decrease 25–50% when nonlinear SSI is introduced at the foundation level (Fig. 7). Note that since the pushover analysis indicated that linear assumption of SSI does not have significant effect on the response of a structure, the dynamic analysis results are provided for the fixed and nonlinear base conditions only.

5 Conclusions

The present study focuses on the effect of foundation nonlinearity on various force and displacement demands of a structure. A medium-height SMRF building adopted from Gupta and Krawinkler [11] has been used for this purpose. The nonlinear behavior of soil-foundation interface is modeled using a Winkler-based model concept. Static pushover analyses and nonlinear dynamic are carried out using SAC ground motions of three different hazard levels provided by Somerville et al. [20]. The following specific conclusions are made from the present study:

- Pushover analysis results indicate that the global force demand of a structure reduces with incorporation of SSI, whereas the roof displacement demand decreases with the same. Further, this alteration is much significant when inelastic behavior of soil-foundation interface is accounted for.
- It is observed from the dynamic analysis that the story displacement demands increase significantly when base nonlinearity is accounted for. However, the inter-story drift angle is observed to decrease, indicating lower design requirement for the structural members.
- The global force demands such as base moment and base shear of the columns are also observed to get reduced as much as 50% with incorporation of nonlinear SSI, indicating the fact that neglecting nonlinear SSI effects may lead to an inaccurate estimation of these demands.

Finally, it may be concluded from this study that the soil-structure interaction effects may play a crucial role in altering the seismic demands of a structure, indicating the necessity for incorporation of inelastic foundation behavior in the modern design codes to accomplish more economic yet safe structural design.

References

1. Allotey N, Naggar MHE (2007) An investigation into the Winkler modeling of the cyclic response of rigid footings. Soil Dyn Earthq Eng 28:44–57
2. ASCE-7 (2005) Seismic evaluation and retrofit of concrete buildings. Structural Engineering Institute (SEI) and American Society of Civil Engineers (ASCE), Reston
3. ATC-40 (1996) Seismic evaluation and retrofit of concrete buildings. Applied Technology Council (ATC), Redwood City
4. Boulanger RW (2000) The PySimple1, TzSimple1, and QzSimple1 material models, documentation for the OpenSees platform. URL: http://opensees.berkeley.edu
5. Boulanger RW, Curras CJ, Kutter BL, Wilson DW, Abghari A (1999) Seismic soil-pile-structure interaction experiments and analyses. ASCE J Geotech Geoenviron Eng 125 (9):750–759
6. Chopra A, Yim SC (1985) Simplified earthquake analysis of structures with foundation uplift. ASCE J Struct Eng 111(4):906–930
7. Dutta SC, Bhattacharya K, Roy R (2004) Response of low-rise buildings under seismic ground excitation incorporating soil-structure interaction. Soil Dyn Earthq Eng 24:893–914

8. FEMA 356 (2000) Prestandard and commentary for the seismic rehabilitation of buildings. American Society of Engineers, Reston
9. Gajan S, Raychowdhury P, Hutchinson TC, Kutter B, Stewart JP (2010) Application and validation of practical tools for nonlinear soil-foundation interaction analysis. Earthq Spectra 26(1):111–129
10. Gazetas G (1991) Formulas and charts for impedances of surface and embedded foundations. J Geotech Eng 117(9):1363–1381
11. Gupta A, Krawinkler H (2000) Behavior of ductile SMRFs at various seismic hazard levels. ASCE J Struct Eng 126(1):98–107
12. Harden CW, Hutchinson TC (2009) Beam-on-nonlinear-Winkler-foundation modeling of shallow, rocking-dominated footings. Earthq Spectra 25(2):277–300
13. Nakaki DK, Hart GC (1987) Uplifting response of structures subjected to earthquake motions. U.S.-Japan Coordinated Program for Masonry Building Research. Report no. 21–3. Ewing, Kariotis, Englekirk and Hart
14. NEHRP (2003) Recommended provisions for seismic regulations for new buildings. Building Seismic Safety Council, Washington, DC
15. Raychowdhury P (2008) Nonlinear winkler-based shallow foundation model for performance assessment of seismically loaded structures. PhD thesis, University of California, San Diego
16. Raychowdhury P, Hutchinson TC (2009) Performance evaluation of a nonlinear winkler-based shallow foundation model using centrifuge test results. Earthq Eng Struct Dyn 38:679–698
17. Raychowdhury P, Hutchinson TC (2010) Sensitivity of shallow foundation response to model input parameters. ASCE J Geotech Geoenviron Eng 136(3):538–541
18. Raychowdhury P, Hutchinson TC (2011) Performance of seismically loaded shearwalls on nonlinear shallow foundations. Int J Numer Anal Methods Geomech 35:846–858
19. Singh P (2011) Performance evaluation of steel-moment-resisting-frame building incorporating nonlinear SSI. Master's thesis, Indian Institute of Technology Kanpur, India
20. Somerville P, Smith N, Punyamurthula S, Sun J (1997) Development of ground motion time histories for phase 2 of the FEMA/SAC steel project. http://www.sacsteel.org/project/
21. Stewart JP, Kim S, Bielak J, Dobry R, Power MS (2003) Revisions to soil-structure interaction procedures in NEHRP design provisions. Earthq Spectra 19(3):677–696
22. Terzaghi K (1943) Theoretical soil mechanics. Wiley, New York
23. Yim SC, Chopra A (1985) Simplified earthquake analysis of multistory structures with foundation uplift. ASCE J Struct Eng 111(12):2708–2731

On Reliability Evaluation of Structures Using Hermite Polynomial Chaos

Sabarethinam Kameshwar and Arunasis Chakraborty

Abstract Reliability assessment using first- or second-order methods (FORM or SORM) demands evaluation of first derivative (i.e., slope) of the limit, which is often difficult to evaluate for real-life structures due to limited information about the performance function. To avoid this, present study aims to use stochastic response surface methodology (SRSM) to evaluate the reliability of the structure. In this method, uncertainty is modeled using series expansion of standard normal random variables (i.e., polynomial chaos expansion). The coefficients of the polynomial chaos expansion are obtained by stochastic collocation which demands limited number of evaluation of the performance function. Once the order of the polynomial and the coefficients is evaluated, reliability index is obtained by FORM. Numerical examples are presented to show the applicability of the proposed SRSM-based reliability analysis.

Keywords Reliability index • Stochastic process • Limit Surface • Polynomial chaos

1 Introduction

First-order reliability methods have been extensively used for reliability analysis of structural systems [11, 14] due to its simplicity. For this purpose, Rackwitz–Fiessler algorithm is often used to find out the optimal distance (i.e., reliability index) of the limit surface from the origin in standard normal space. This method needs to evaluate the slopes (i.e., first derivative of the limit surface) to locate the most probable design point and subsequently the reliability index. However, limit surfaces are often unknown in the close form (i.e., implicit), and hence, their

S. Kameshwar • A. Chakraborty (✉)
Department of Civil Engineering, Indian Institute of Technology, Guwahati, India
e-mail: s.kameshwar@iitg.ernet.in; arunasis@iitg.ernet.in

S. Chakraborty and G. Bhattacharya (eds.), *Proceedings of the International Symposium on Engineering under Uncertainty: Safety Assessment and Management (ISEUSAM - 2012)*,
DOI 10.1007/978-81-322-0757-3_79,

derivatives are difficult to evaluate. In this context, Bucher and Bourgand [2] developed response surface method (RSM) for reliability analysis. In RSM, the unknown limit surface is approximated by a multidimensional quadratic polynomial near the failure region. In the recent past, engineers and researchers have extensively used this method for various applications like performance evaluation, crash simulation, and reliability-based design optimization [1, 3, 6, 9, 10]. However, as this polynomial approximation of the original limit state is valid near the failure region, it often faces difficulty to find out the optimal distance for limit states with multiple design points. Moreover, as this is a deterministic representation, it fails to capture the stochastic characteristics of the original limit state.

To avoid this problem, stochastic response surface method (SRSM) was proposed by Isukapalli [7]. In this method, the stochastic signature of the original limit state is mapped in the standard normal space using polynomial chaos expansion (PCE). Wiener [16] first introduced PCE to model the turbulence where infinite orthonormal functions in standard normal space are used to model the stochastic phenomenon. Ghanem and Spanos [5] showed that Hermite polynomials form an orthogonal basis for PCE and is convergent in the mean-square sense. However, this representation needs to evaluate the coefficients of the Hermite polynomials to model the original performance function. Tatang [15] developed probabilistic collocation technique where Gauss quadrature points were used to evaluate the coefficients of the PCE. Isukapalli [7] used the roots of one order higher than polynomial as the reference points and evaluated the coefficients by regression analysis. Gavin [4] showed that SRSM works better for complex structures with low failure probability where Monte Carlo simulation (MCS) and approximate methods are either computationally intensive or inaccurate. It models the global stochastic nature of the limit surface as opposed to model the local nature near the failure region in RSM. This property may be used to identify the local minima where multiple design points exist. Due to these advantages, SRSM has gained momentum for reliability analysis of civil engineering structures in the recent past. Li et al. [9] performed reliability analysis of rock slopes using SRSM with higher order polynomials. Mollon [12] used collocation-based SRSM to analyze the stability of a circular tunnel driven by a pressurized shield.

With these in view, present study aims also apply SRSM to analyze the reliability of a retaining wall against overturning. The results obtained from this method will be compared with Monte Carlo simulations to check the efficiency and accuracy of the SRSM.

2 Stochastic Response Surface Methodology

The limit surface divides the probability space into safe and failure zones, which is symbolically represented as

$$g(X) = 0 \tag{1}$$

where $X = [x_1, x_2, \ldots x_n]$ and $_{xi}$ are the random variables that describe the failure plane. In the above equation, $g(x) < 0$ represents the failure region. The probability of failure for a limit state described in Eq. (1) can be represented as

$$p_f = \int \ldots\ldots\ldots \int_{g(x)<0} f_{X_1,X_2\ldots\ldots,X_n}(x_1, x_2, \ldots\ldots, x_n) dx_1 dx_2 \ldots\ldots\ldots dx_n = P[g(X) \leq 0] \quad (2)$$

However, probability evaluation using above equation demands the complete description of the joint probability distribution function f which are often unknown. The problem is more complex where the performance function described in Eq. (1) is not available in explicit form. To evaluate the reliability for these cases, either RSM or SRSM is used. However, RSM often faces difficulties for nonsmooth failure planes with multiple local minima as the polynomial approximation near the MPP is carried out for this case. Under these situations, SRSM can be a better alternative as the stochastic nature of the failure plane, irrespective of the presence of local minima, is modeled using PCE. Reliability evaluation using SRSM involves the following four major steps:

(a) Functional/polynomial chaos representation of output
(b) Evaluation of unknown coefficients
(c) Representation of input random variables in terms of standard normal variables
(d) Evaluation of reliability using FORM/SORM

2.1 Functional/Polynomial Chaos Representation of Output

Polynomial chaos is defined by an orthonormal set of standard normal variables $\{Z_i\}_{i=1}^{\infty}$. Therefore, PC of order p (i.e., Γ_p) is defined by the set of polynomials of order p which is orthogonal to all of polynomials of order $p - 1$. Using these orthonormal set of standard normal variables, any function f can be represented as

$$f = \sum_{p \geqslant 0} \sum_{n_1+n_2+\cdots+n_r=p} \sum_{\rho_1,\ldots,\rho_r} a^{n_1,\ldots,n_r}_{\rho_1,\ldots,\rho_r} \Gamma_p(z_{\rho_1,\ldots\ldots,z_{\rho r}}) \quad (3)$$

In the above equation, p and r represent the order and the dimension, respectively, and $a^{n_1,\ldots,n_r}_{\rho_1,\ldots,\rho_r}$ represent the coefficients. In this context, Hermite polynomials are used to represent f which is given by Ghanem and Spanos [5] and Issukapalli[7]:

$$\Gamma_p(z_{i_1}, \ldots z_{i_r}) = e^{\frac{1}{2}z^t z}(-1)^p \frac{\partial p}{\partial z_{i_1}, \ldots, z_{i_r}} e^{-\frac{1}{2}z^t z} \quad (4)$$

where Z is the standard normal random variable. Using the expressions for PCE given in Eqs. (3) and (4), the limit state given in Eq. (1) can be represented in standard normal space as

$$g_p(Z) = 0 \tag{5}$$

The above expression of performance function is the linear combination of n-dimensional polynomials involving unknown coefficients $a^{n_1,\ldots,n_r}_{\rho_1,\ldots,\rho_r}$ which are evaluated using collocation points.

2.2 Evaluation of Unknown Coefficients

Once the functional representation of the output is known, the next step is to evaluate the unknown coefficients. For this purpose, regression analysis is performed using collocation points which are the roots of one dimensional Hermite polynomial that are one order higher than the order of the polynomials used to represent the limit surface. Therefore, the number of collocation points available for n dimensional pth order PCE is $(p + 1)^n$ [8]. In this format, it can be shown that the numbers of collocation points are more than the number of unknowns. Using the values of the limit state function at these points, the unknown coefficients are evaluated by stochastic regression analysis.

2.3 Representation of Stochastic Inputs

The regression analysis mentioned in the previous section demands the evaluation of the performance function represented by Eq. (1) at $(p + 1)^n$ collocation points. However, as the collocation points are in standard normal space, the equivalent points in the original space are found by one-to-one mapping of cumulative distribution function (CDF) of the two random variables. For the details of this transformation, one may refer to Isukapalli [8].

2.4 Evaluation of Reliability

Once the coefficients are evaluated using stochastic least square technique described in previous section, the performance function in Eq. (1) is transformed into standard normal space which may be further used for first-order reliability analysis. For this purpose, the optimal distance from the origin in the standard

normal space (i.e., reliability index β) can be evaluated using Rackwitz–Fiessler algorithm [13]. In this iterative procedure, β is obtained as

$$\beta = \left. \frac{\Sigma z_i \nabla_i g_p(Z)}{\left\| \nabla_g(Z) \right\|} \right|_{z^*} \tag{6}$$

In the above equation, Z^* represents MPP in standard normal space and $\|.\|$ represents the Euclidean norm. It can be shown that the probability of failure is related to β through the following relation:

$$p_f = \Phi(-\beta) \tag{7}$$

3 Example Problems

The SRSM method described in the previous section is used to evaluate the reliability of two different limit states.

Example 1: Nonlinear and Nonsmooth Limit State In the first problem, the following performance function is considered:

$$g(X) = \frac{-1}{25}(X_1 - 1)^2 - \frac{X_2}{3} + 3 + \frac{\sin(5X_1)}{5} \tag{8}$$

where $X_1$and X_2 are the two random variables.

Example 2: Retaining Wall Against Overturning In the second problem, the reliability of a retaining wall as shown in Fig. 1 against overturning is considered.

The parameters in Fig. 1 and the details of the stabilizing and overturning moments are given in Appendix A. The limit state describes the failure in this case is given by

$$g(X) = M_r - M_o \tag{9}$$

In the above equation, M_r represents the stabilizing moment and M_o represents the overturning moment. The random variables associated with the limit states are surcharge load (q), unit weight of concrete (W_c), unit weight of soil Ws, soil friction angle (φ), and wall friction angle (δ).

4 Numerical Results and Discussion

SRSM discussed in the previous sections is used to solve example cases and evaluate the reliability. In Example 1, X_1 and X_2 are the two uncorrelated random variables with the values of mean and standard deviation are 3.5 and 1, respectively.

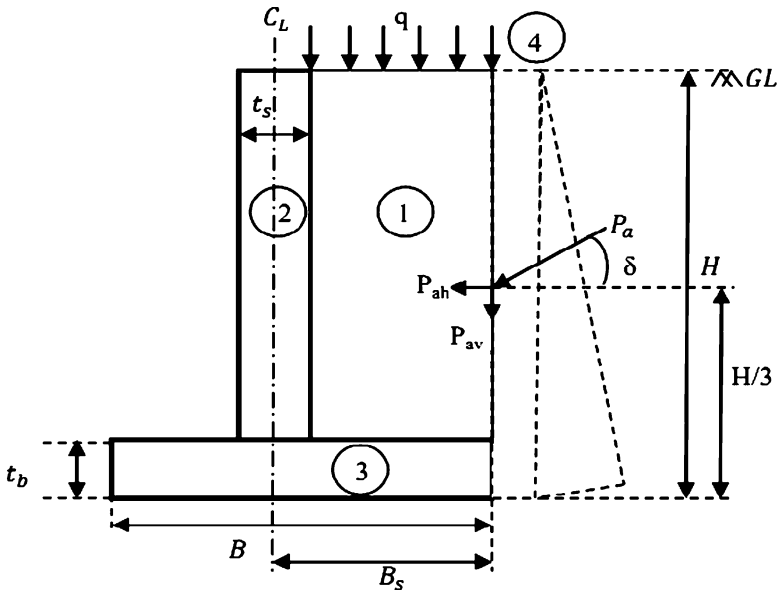

Fig. 1 Retaining wall

In this case, different combinations of normal and lognormal variables are considered and the results are compared with Monte Carlo simulations. The unknown coefficients of the PCE are evaluated using collocation points. For this purpose, 4th-order polynomials are used. The total number of unknowns in Eq. (5) is 15. To generate the collocation points, roots of the 5th order (i.e., 4 + 1) are used. As the dimension of the problem is 2, the possible combinations using these roots are 2^5 (i.e., 32.) Although 32 collocation points are available for the regression analysis, only 23 (i.e., 1.5 × 15) points are used. It has been observed that the convergence can be achieved with 1.5*n* collocation points. In this context, the points that are close to the origin were given the priority. Figure 2 shows the CDF of the limit state using PCE and Monte Carlo simulations. It can be observed from this figure that the 4th-order polynomial estimates CDF satisfactorily. Using this 4th-order PCE, Hasofer–Lind reliability index is evaluated as described in Eq. (6). Table 1 shows the reliability index and probability of failure for different combinations of random variables X_1 and X_2. From this table, it can be concluded that SRSM results match closely with simulations. In this context, six million samples were used for simulations.

The SRSM-based technique is further used to evaluate the reliability of the retaining wall. Table 2 shows the distributions and the parameters of the random variables used in this model. It can be observed that the dimension of this problem is 5. In this case also, a 4th-order PCE is used to model the limit state in the standard normal space. Total number of unknowns for this 5th dimensional and 4th-order PCE representation is 126. To evaluate these unknown coefficients, roots of the

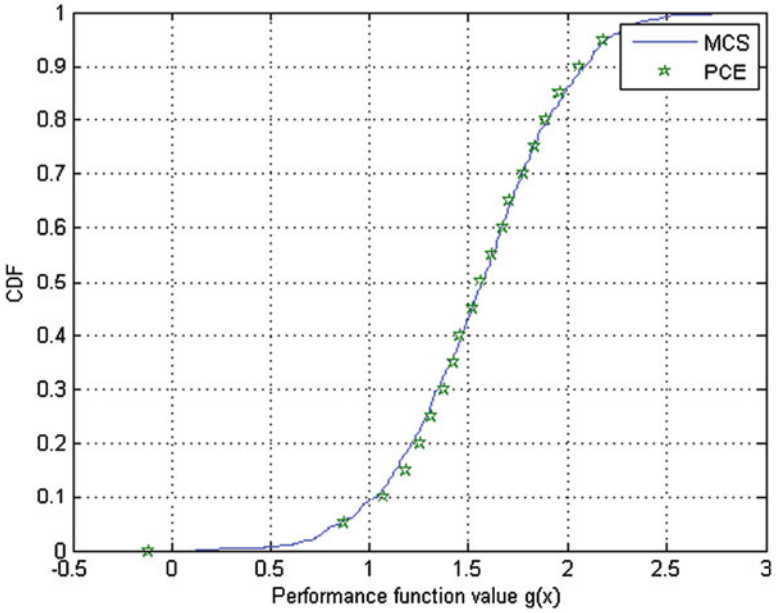

Fig. 2 CDF of the limit state in Example 1

Table 1 Reliability index and probability of failure in Example 1

		β		pf	
X_1	X_2	Monte Carlo	SRSM	Monte Carlo	SRSM
N	*N*	3.3692	3.4325	0.00037	0.00029
N	LN	2.8977	2.8094	0.00187	0.00248
LN	*N*	2.7879	2.8019	0.00265	0.00254
LN	LN	2.6461	2.8058	0.00407	0.00250

N normal, *LN* lognormal

Table 2 Variables of retaining wall problem

		Statistics	
Variable	Distribution	μ	Cov(%)
q	LN	20	10
w_c	*N*	24	7
w_s	*N*	18	7
φ	LN	30	7
δ	LN	10	7

5th-order polynomial are again used as the collocation points. As described in previous section, total numbers of collocation points available in this case are 3,125 (i.e., 5^{4+1}). However, 183 collocation points (i.e., 1.5×126) which are closer to the origin are used for regression analysis. Using these collocation points, CDF of the limit state is obtained and is shown in Fig. 3. In this case also, one can

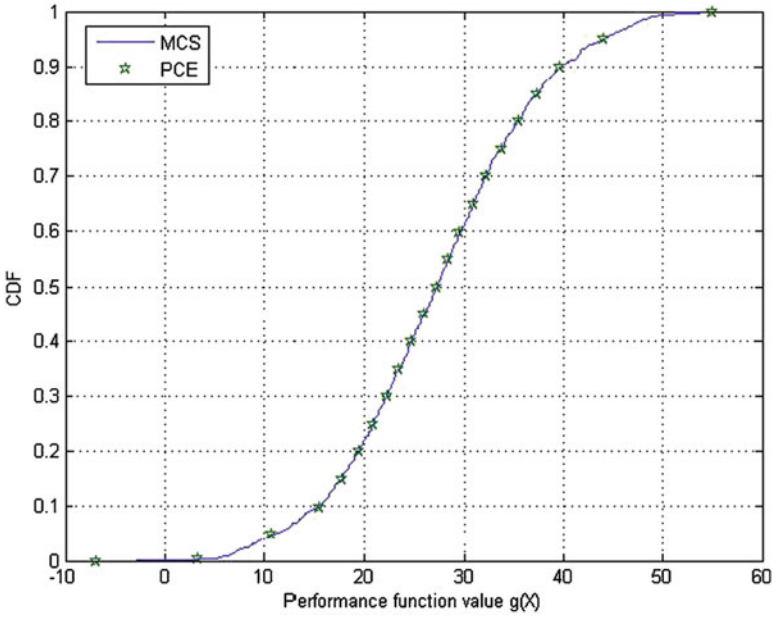

Fig. 3 CDF of the limit state in Example 2

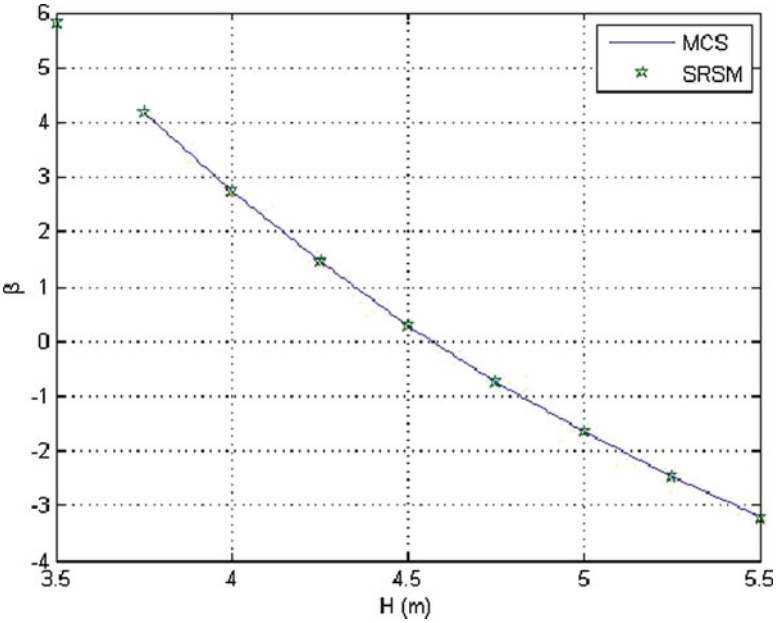

Fig. 4 Change of β with height of the wall

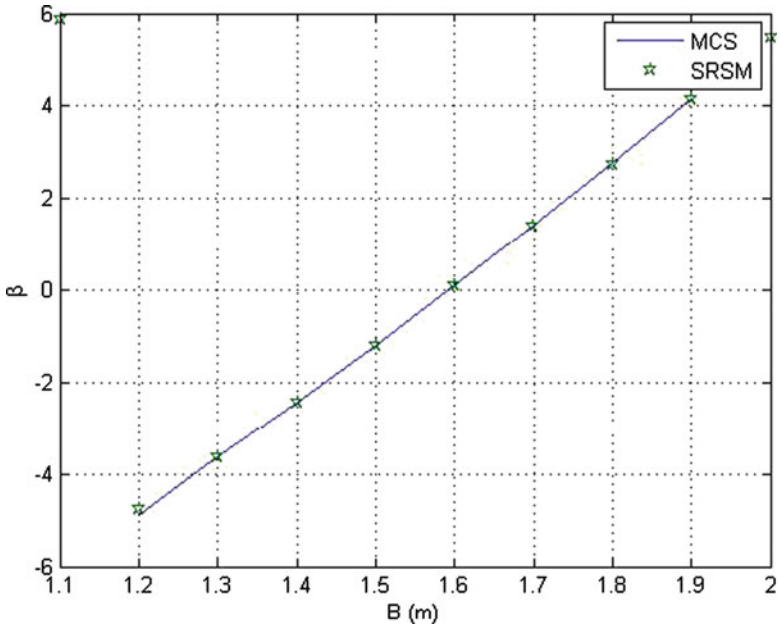

Fig. 5 Change of β with base width

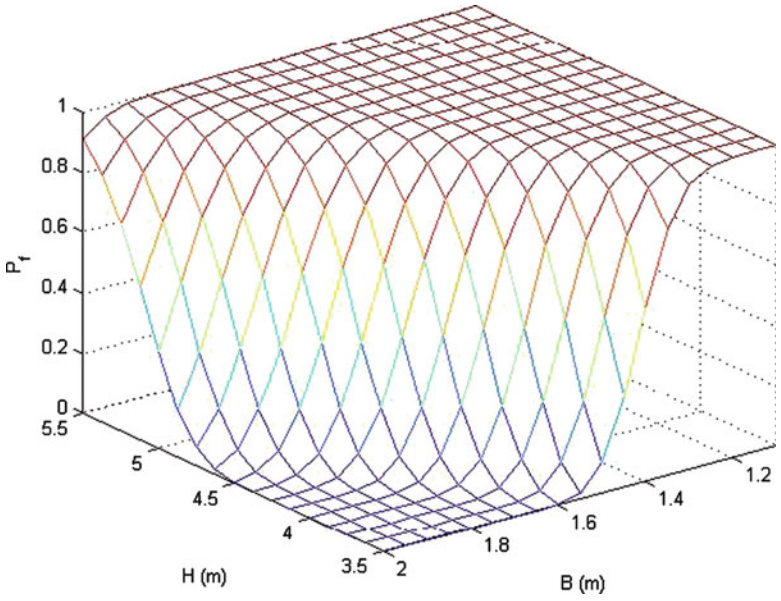

Fig. 6 Variation of P_f for different height and base width

notice a close match between the PCE and simulations. Figures 4 and 5 show the reliability index for different values of height and base width of the retaining wall. From these figures, one can conclude that the reliability index obtained by SRSM closely matches with the simulations. Figure 6 shows the probability of failure for different values of height and base width. From this figure, one can easily evaluate the reliability ($1 - p_f$) for a given combination of height and base width.

5 Conclusions

In this chapter, stochastic response surface method is used to evaluate the reliability for different limit state functions. In this method, the random nature of the limit state is modeled by multidimensional polynomial chaos expansion whose coefficients are evaluated by regression analysis. For this purpose, the roots of the polynomial of dimension one order higher than the original one are used to generate the collocation points. Once the coefficients are evaluated, the optimal distance in standard normal space (i.e., reliability index) is evaluated using Rackwitz–Fiessler algorithm. The example cases shown in this chapter prove the accuracy and efficiency of the SRSM-based reliability analysis.

Appendix A

Figure 1 shows the retaining wall used in Example 2. In this figure, H, B, B_s, t_s, and t_b are the height of wall, length of base, distance of centerline of stem to heel, thickness of stem, and thickness of base slab, respectively. The thickness of the stem and the base is taken to be 0.45 m. Further, q and δ represent the surcharge and the wall friction angle, while p_a represents the active earth pressure which has horizontal and vertical components as p_{ah} and p_{av}, respectively. M_1, M_2, M_3, and M_4 are the moments due to self weights of different components of the wall–soil combination marked 1, 2, 3, and 4, respectively, which are given by

$$M_1 = w_s \frac{\left(B_s - \frac{t_s}{2}\right)^2}{2}(H - t_b) \tag{A1.a}$$

$$M_2 = w_c t_s (H - t_b) B_s \tag{A1.b}$$

$$M_3 = w_c t_b \frac{B^2}{2} \tag{A1.c}$$

$$M_4 = \frac{q}{2}\left(B_s - \frac{t_s}{2}\right)^2 \tag{A1.d}$$

The total downward force due to the weights of different components (i.e., soil mass, stem of the wall, base of the wall, and surcharge) is given by

$$W = w_s\left(B_s - \frac{t_s}{2}\right)(H - t_b) + w_c t_s(H - t_b) + w_c t_b B + q\left(B_s - \frac{t_s}{2}\right) \tag{A2}$$

The point of action of the total weight W can be obtained as

$$x_w = \frac{M_w}{W} \tag{A3}$$

Using Eqs. (A2) and (A3), the total resisting moment about the toe of the wall can be expressed as

$$M_r = W(B - x_w) \tag{A4}$$

Thus, the active earth pressure acting on the wall due to the soil mass is given by

$$P_a = \frac{1}{2}K_a w_s H^2 + K_a\, qH \tag{A5}$$

where the active earth pressure coefficient k_a is defined as

$$K_a = \frac{\cos^2(\varphi - \alpha)}{\cos^2(\alpha)\cos(\alpha + \delta)\left[1 + \sqrt{\frac{\sin(\varphi+\delta)\sin(\varphi+\gamma)}{\cos(\alpha+\delta)\cos(\gamma-\alpha)}}\right]^2} \tag{A6}$$

In the above equation, φ, α, and γ are the soil friction angle, the angle of the wall, and the inclination of the backfill, respectively. Using Eqs. (A5) and (A6), one can estimate the total overturning moment acting on the wall as

$$M_o = \left(\frac{1}{2}K_a w_s \frac{H^3}{3} + K_a q \frac{H^2}{2}\right)\cos(\delta) \tag{A7}$$

References

1. Babu G, Sivakumar L, Amit S (2010) Reliability analysis of earth dams. J Geo-Tech Geo Environ Eng 136(7):995–998
2. Bucher CG, Bourgund U (1990) A fast and efficient response surface approach for structural reliability problems. Struct Saf 7:57–66
3. Deb K, Gupta S, Daum D, Branke J, Mall AK, Padmanabhan D (2009) Reliability- based optimization using evolutionary algorithms. IEEE Trans Evol Comput 13(5):1054–1074

4. Gavin Henri P, Chung YS (2008) High-order limit state functions in the response surface method for structural reliability analysis. Struct Saf 30:162–179
5. Ghanem R, Spanos P (1991) Stochastic finite elements: a spectral approach. Springer, New York
6. Gupta S, Manohar CS (2004) Improved response surface method for structural reliability analysis. Struct Saf 26:123–139
7. Isukapalli SS (1999) Uncertainty analysis of transport –transformation models. PhD thesis, State University of New Jersey, New Brunswick
8. Isukapalli SS, Roy A, Georgopoulos PG (1998) Stochastic response surface methods (SRSMs) for uncertainty propagation: application to environmental and biological systems. Risk Anal 18(3):351–363
9. Li Dianqing, Chen Yifeng, Lu Wenbo, Zhou Chuangbing (2011) Stochastic response surface method for reliability analysis of rock slopes involving correlated non-normal variables. Comput Geotech 38:58–68
10. Li Minghao, Frank Lam, Foschi RO (2009) Seismic reliability analysis of diagonal-braced and structural-panel-sheathed wood shear walls. J Struct Eng 135(5):587–596
11. Lu Renjian, Luo Yuanhui, Conte Joel P (1994) Reliability evaluation of reinforced concrete beams. Struct Saf 14:277–298
12. Mollon G, Daniel D, Abdul-Hamid S (2011) Probabilistic analysis of pressurized tunnels against face stability using collocation-based stochastic response surface method. J Geotech Geo Environ Eng 137(4):385–397
13. Melcher RE (1999) Structural reliability and prediction. Wiley, Chichester
14. Rodriguez RJ, Sitar N, Chacon J (2006) System reliability approach to rock slope stability. Int J Rock Mech Min Sci 43:847–859
15. Tatang MA (1995) Direct incorporation of uncertainty in chemical and environmental engineering systems. PhD thesis, Massachusetts Institute of Technology
16. Wiener N (1938) The homogeneous chaos. Am J Math 60:897–936

Probability-Based Method for Assessing Liquefaction Potential of Soil Using Genetic Programming

S.K. Das and P.K. Muduli

Abstract Liquefaction of soil due to earthquake is one of the major causes for the significant damages to the buildings, lifeline systems, and harbor facilities. Probabilistic method is now being preferred over deterministic method due to uncertainty in soil and seismic parameter. At present, artificial intelligence techniques such as artificial neural network (ANN) and support vector machine (SVM) based models are found to be more efficient compared to statistical methods. In the present study, an attempt has been made to develop a limit state function for assessing the cyclic resistance ratio (CRR) of soil based on cone penetration test (CPT) data obtained after Chi-Chi earthquake, Taiwan, 1999, using evolutionary artificial intelligence technique, genetic programming (GP), and to evaluate the liquefaction potential of soil in a probabilistic approach through a Bayesian mapping function. A comparative evaluation of the present study is made with three existing CPT-based statistical methods for prediction of liquefied and non-liquefied cases in terms of percentage success rate with respect to the field manifestations.

Keywords Liquefaction • Probabilistic method • Cyclic resistance ratio • Cyclic stress ratio • Liquefaction index • Factor of safety

1 Introduction

Liquefaction of soil is one of the most disastrous seismic hazards, and in the last century, seismic hazard accounts around 30% of total casualties and 60% of the total property loss due to different natural hazards [1]. Soil liquefaction phenomena have been noticed in many historical earthquakes after first large-scale observations

S.K. Das (✉) • P.K. Muduli
Civil Engineering Department, NIT, Rourkela, India
e-mail: saratdas@nitrkl.ac.in; pradyut.muduli@gmail.com

S. Chakraborty and G. Bhattacharya (eds.), *Proceedings of the International Symposium on Engineering under Uncertainty: Safety Assessment and Management (ISEUSAM - 2012)*,
DOI 10.1007/978-81-322-0757-3_80,

of damage in the 1964 Niigata, Japan, and 1964 Alaska, USA, earthquakes. Since 1964, a lot of work has been done to explain and evaluate the liquefaction hazard [5, 13, 14].

Empirical methods based on standard penetration test (SPT), cone penetration test (CPT), and shear wave velocity measurement test are most commonly used for the assessment of liquefaction potential of soils, due to difficulty in obtaining high-quality undisturbed samples and cost involved therein. Simplified methods pioneered by Seed and Idris [14] mostly depend on a boundary curve which presents a limit sate and separates liquefaction cases from the non-liquefaction cases basing on field observations of soil in earthquakes. Though SPT is the most widely used soil exploration method, CPT is becoming more acceptable due to consistent, repeatable identification of continuous soil profile. Hence, CPT is being widely used for liquefaction susceptibility analysis of soil using various statistical and regression analysis techniques [9, 12, 15]. Artificial intelligence techniques such as artificial neural network (ANN) [2, 6] and support vector machine (SVM) [3, 10] are found to be more efficient compared to statistical methods. However, the ANN has poor generalization, attributed to attainment of local minima during training and needs iterative learning steps to obtain better learning performances. The SVM has better generalization compared to ANN, but the parameters "C" and insensitive loss function (ε) need to be fine-tuned by the user. Moreover, these techniques will not produce an explicit relationship between the variables, and thus, the model obtained provides very little insight into the basic mechanism of the problem.

The evolutionary artificial intelligence techniques based on the Darwinian theory of natural selection provide strong alternatives to the mentioned techniques. Genetic programming (GP) is one of such techniques which can automatically select the system inputs to develop a model which fits well the input-output relationship of the system. In the present study, an attempt has been made to develop a limit state function for assessing the cyclic resistance ratio (CRR) of soil based on CPT data obtained after Chi-Chi earthquake, Taiwan, 1999 [8], using GP and to evaluate the liquefaction potential of soil in a probabilistic approach through a Bayesian mapping function. A comparative evaluation of the present study is made with three existing CPT-based statistical methods for prediction of liquefied and non-liquefied cases in terms of percentage success rate with respect to the field manifestations.

2 Methodology

The development of limit state function for assessing the CRR of soil and the corresponding mapping function for determination of probability of liquefaction from the calculated factor of safety is presented as follows:

3 CPT-Based Method for Prediction of Liquefaction Potential

The common deterministic methods used for the liquefaction potential evaluation of a site based on CPT data base follow the general stress-based approach pioneered by Seed and Idriss [14]. These methods are based on determination of factor of safety (F_s) against the liquefaction occurrence and are defined as $F_s = \text{CRR}/\text{CSR}_{7.5}$, where $\text{CSR}_{7.5}$ = cyclic stress ratio adjusted to the benchmark earthquake (moment magnitude, $M_w = 7.5$) as presented by Youd and Idriss [16]. In deterministic approach, liquefaction and non-liquefaction cases are predicted on the basis of corresponding F_s, with $F_s \leq 1$ for liquefied and $F_s > 1$ non-liquefied case, respectively. Due to model and parameter uncertainties, there is always some probability that liquefaction can occur even if $F_s > 1$ [5]. In order to understand the meaning of calculated F_s within the framework of probability, it is expressed in terms of probability of liquefaction (P_L) through Bayesian mapping function [6].

3.1 Genetic Programming for Evaluation of Liquefaction Potential

Genetic programming (GP) is a pattern recognition tool where the model is developed on the basis of adaptive learning over a number of cases of provided data, developed by Koza [7]. It mimics biological evolution of living organisms and makes use of principle of genetic algorithm (GA). In traditional regression analysis, the user has to specify the structure of the model, whereas in GP, both the structure and the parameters of the mathematical model are evolved automatically. It provides a descriptive solution in the form of tree structure or in the form of compact equation based on the provided data set. GP has been successfully implemented in various engineering problems, but its use in solving geotechnical engineering problems is limited [4, 11]. A brief description about GP is presented for the completeness, but the details can be found in Koza [7].

GP models are composed of nodes and resemble to a tree structure, and thus well known as GP tree. Nodes are the elements either from a functional set or terminal set. A functional set may include arithmetic operators (+, ×, ÷, or −), mathematical functions (sin(.), cos(.), or ln(.)), Boolean operators (AND or OR), logical expressions (IF or THEN), or any other user-defined functions. The terminal set includes variables (like x_1, x_2, x_3, etc.) or constants (like 2, 5, 9, etc.) or both. The functions and terminals are randomly chosen to form a computer model with a root node and the branches extending from each function nodes to end in terminal nodes as shown in Fig. 1.

The fitness criteria are calculated by the objective function, and it determines quality of the individual in competing with the rest of the population. At each generation, a new population is generated by selecting individuals according to

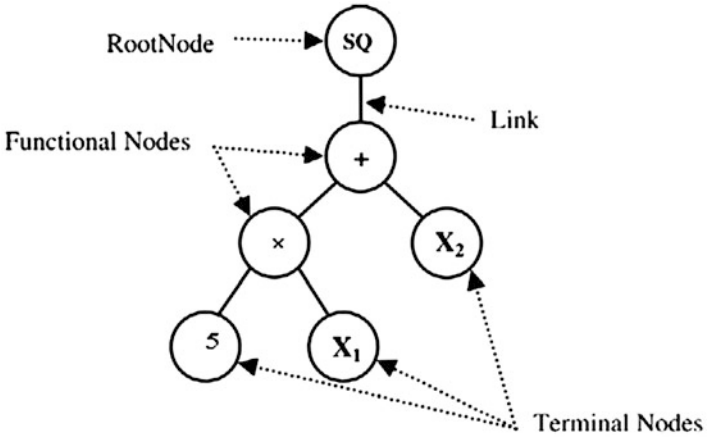

Fig. 1 Typical GP tree representing function $(5X_1 + X_2)^2$

their fitness and implementing various evolutionary mechanisms like reproduction, crossover, and mutation to the functions and terminals. The new population then replaces the existing population. This process is iterated until the termination criterion, which can be either a threshold fitness value or maximum number of generations, is satisfied. The GP model is developed using MATLAB [17].

4 Results and Discussions

A devastating earthquake of moment magnitude (M_w) 7.6 struck Taiwan on 21 September 1999. The epicenter was at 23.87° N, 120.75° E which is near Chi-Chi of Taiwan. In this earthquake, liquefaction of soil was the major cause of heavy damages [5]. In the present study, post-earthquake field observations and the CPT data collected, from Wufeng, Nantou, Yuanlin, and Lunwei areas of Taiwan as per Ku et al. [8], are used. The database consists of total 134 cases, 46 out of them are liquefied cases and other 88 are non-liquefied cases. The depth at which the soil strata are considered ranges from 2.5 to 19.5 m. The various soil and earthquake parameters considered herein are as follows: q_c = measured cone tip resistance values range from 0.18 to 20.05 Mpa, f_s = sleeve resistance values are in the range of 0.2–358.56 kPa, σ_v = vertical total stress of soil at the depth studied values is within 46.25–364.5, σ'_v = vertical effective stress of soil at the depth studied values is in the range of 31.3–180.8 kPa, and (a_{max}/g) = peak horizontal ground surface acceleration in terms of g (acceleration due to gravity) values ranges from 0.123 to 0.789.

4.1 GP Model for Liquefaction Index

In the present study, a model is developed using GP for predicting liquefaction index (LI) using CPT-based liquefaction field performance dataset; LI = 1 for liquefaction and LI = 0 for non-liquefaction [6].

The general form of proposed GP model can be presented as:

$$\mathrm{LI} = \sum_{i=1}^{n} F[X, f(X), b_i] + b_0 \tag{1}$$

where F = the function created by the GP process referred herein as liquefaction index function, X = vector of input variables { q_{c1N}, I_c, σ_v', CSR}, q_{c1N} = normalized cone tip resistance, I_c = soil-type index as per Juang et al. [6], σ'_v = vertical effective stress of soil at the depth studied, b_i is constant, f is a function defined by the user and n is the number of terms of target expression, and b_0 = bias.

In the present study, a multigene GP is adopted where each individual consists of more than one gene, each of which is a traditional GP tree. Here, function set used includes +, ×, ÷, −, sin(.), cos(.), and exp(.). Out of the mentioned 134 cases of data, 94 cases are randomly selected for training and remaining 40 data are used for testing the developed model. The data was normalized in the range 0–1 to avoid the dimensional effect of input parameters.

In the GP procedure, a number of potential models are evolved at random, and each model is trained and tested using the training and testing cases, respectively. The fitness of each model is determined by minimizing the root-mean-square error (RMSE) between the predicted and actual value of the output variable (LI) as the objective function,

$$f(\delta) = \sqrt{\frac{\sum_{i=1}^{n} (\delta)^2}{n}} \tag{2}$$

where n is the number of cases in the fitness group and δ is the difference between the predicted and actual value of LI as per the field data set. If the errors calculated by using Eq. 2 for all the models in the existing population do not satisfy the termination criteria, the evolution of new generation of population continues till the best model is developed.

The best LI model was obtained as described below with population size of 2,000 individuals and 150 generations with reproduction probability of 0.05,

crossover probability of 0.85, mutation probability of 0.1, maximum number of genes as 2, maximum depth of GP tree as 4 and tournament selection procedure.

$$\mathrm{LI} = \begin{pmatrix} 0.9873\tanh\left(71.61(I_c - 1.352)\Big/\left(\sigma_v' - 31.3\right) - \exp(0.005827 q_{c1N} - 0.0157)\right) \\ -0.4182\tanh\left(71.61(I_c - 1.352)\Big/\left(\sigma_v' - 31.3\right) - \exp(1.346\,CSR - 0.148)\right) \\ -(0.0004024\,CSR - 0.0007193)\Big/\left(\left(0.479 I_c - 0.008415\sigma_v' - 0.384\right)(1.346\,CSR - 0.651)\right) + 0.495 \end{pmatrix} \tag{3}$$

It was observed that the performances of GP for training and testing data are comparable, and for LI within ±15% error limit, the successful prediction values are 95% for both training and testing data set. This GP model (Eq. 3) is further used for the development of proposed CRR model.

4.1.1 Searching for Artificial Points on the Limit State Boundary Curves

The developed GP model for LI as given by the Eq. 3 is used to search for points on the unknown boundary curve separating liquefied cases from the non-liquefied ones following the search technique developed by Juang et al. [6]. In the present study, 112 searched or generated data points are obtained using optimization technique. These artificial data points are generated for the development of limit state or the boundary curve.

4.1.2 GP Model for CRR

Similarly as mentioned earlier here, a multigene GP is adopted for development of CRR model using artificially generated 112 data points, out of which 78 data points are selected randomly for training and the rest 34 numbers for testing. The data was normalized in the range 0–1 to avoid the dimensional effect of input parameters. The several CRR models were obtained with population varying from 1,000 to 3,000 individuals at 100–300 generations with reproduction probability = 0.05, crossover probability = 0.85, mutation probability = 0.1, maximum number of genes = 2–4, maximum depth of GP tree = 4, and tournament selection. Then, developed models were analyzed with respect to engineering understanding of CRR of soil, and after careful consideration of various alternatives, the following expression was found to be most suitable for the prediction of CRR:

$$\begin{aligned} \mathrm{CRR} = {} & 0.022 + 0.18\left(0.005827 q_{c1N} + 0.006689\sigma_v' - \exp(0.005822(q_{c1N} - 2.7)) - 0.225\right)^2 \\ & + 7.075 \times 10^{-5}(q_{c1N} - 2.7)^2 \cos\left(0.006689\sigma_v' - 0.209\right) \\ & \times \left(0.006689\sigma_v' - 0.479 I_c + 3.898 \times 10^{-5}(q_{c1N} - 2.7)\left(\sigma_v' - 31.3\right) + 0.439\right) \end{aligned} \tag{4}$$

Table 1 Statistical performances GP model for CRR

	Statistical performances			
Data set	Correlation coefficient	Coefficient of determination	Coefficient of efficiency (R^2)	RMSE
Training	0.958	0.977	0.916	0.313
Testing	0.942	0.978	0.885	0.172

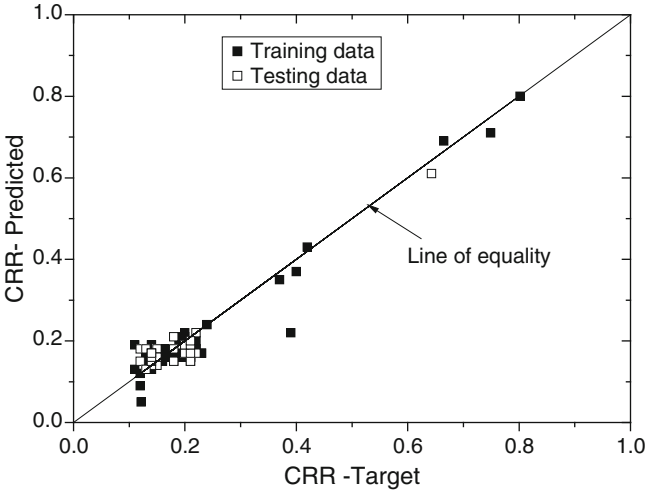

Fig. 2 Performance of the proposed GP model

Based on the statistical performances as presented in Table 1, the proposed GP model (Eq. 4) was able to learn the complex relationship between the CRR and its main contributing factors with a high accuracy. It can be noted that the performances of GP model for training and testing data are comparable showing good generalization of the developed model. Figure 2 shows the plot between the predicted CRR and the target CRR. The goodness of fit is evident from the coefficient of efficiency, R^2 as mentioned in Table 1. Figure 3 shows the developed GP limit state curve, separating the liquefied and non-liquefied cases of the data base. Thus, CRR can be calculated by this model using three input parameters, q_{c1N}, $I_{c,}$, and σ_v'.

In deterministic method, F_s is then calculated and a prediction is considered to be successful if it agrees with the field manifestations. Though high-statistical performances were observed for predicted and target CRR values, the overall success rate in the deterministic approach is found to be 80%. Due to both parameter and model uncertainty, there is some probability of occurrence of liquefaction in a particular case even if $F_s > 1$. Keeping this in view, proposed GP model for CRR and CSR equation as presented by Youd et al. (2001) needs to be calibrated with the field observations to develop a relationship between F_s and the probability of occurrence liquefaction.

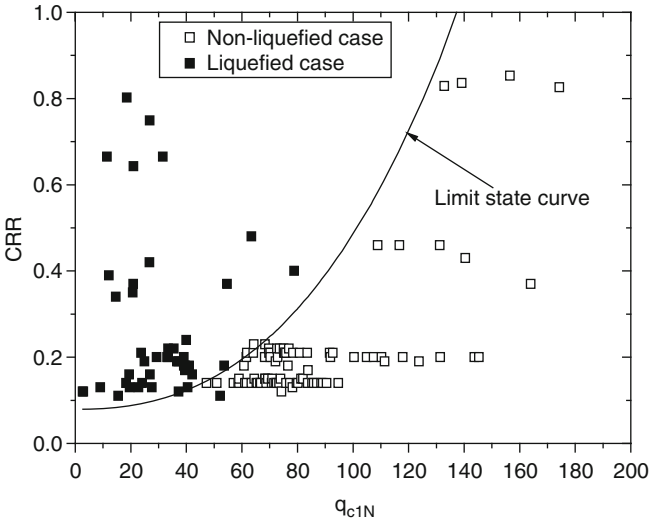

Fig. 3 Showing developed GP limit state curve separating liquefied cases from non-liquefied cases

4.1.3 Development of the Bayesian Mapping Function

The calculated F_s values for different cases of the database are grouped according to whether liquefaction actually occurred at the site or not (Fig. 4).

After considering several different distribution functions, it is found that both the liquefied (L) and non-liquefied (NL) groups are best fitted by a Rayleigh distribution with the parameter 0.6528 and 1.5087, respectively. The probability that the liquefaction will occur for a case in which the F_s has already been calculated by the deterministic approach can be obtained based on Bayesian theory [6]. Probabilistic analyses of the present 134 cases in the database are made, and a mapping function between factor of safety and P_L is obtained as presented in Eq. 5 with $R^2 = 0.99$:

$$P_L = \frac{0.832}{1 + (F_s/A)^B} - 0.027 \tag{5}$$

where the coefficients A and B are 1.472 and 4.6, respectively. Therefore, the probability of liquefaction of a soil with similar site conditions as that of the present database can be obtained from the Eq. 5 in a future seismic hazard. The probability of liquefaction helps in taking more rational design decisions, that is, the selection of a proper factor of safety depending on the importance of the structure to be constructed.

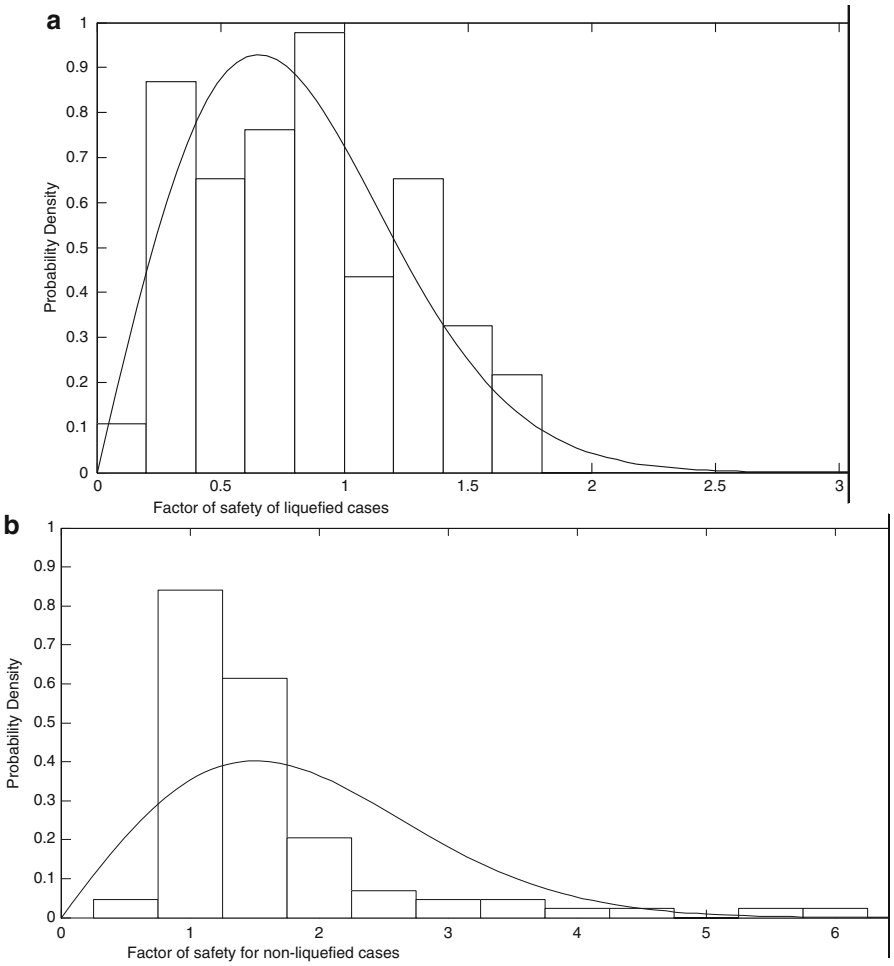

Fig. 4 Histogram showing the probability distribution of F_s: (**a**) liquefied (L) cases and (**b**) non-liquefied (NL) cases

The probability of liquefaction of the total 134 cases as obtained using the statistical CPT-based methods (Robertson, Olson and Juang) as presented in Juang et al. [5] and the proposed GP model are evaluated and compared in Table 2. The assessed probability is used to judge whether the prediction of occurrence of liquefaction/non-liquefaction by a particular method is correct or not on the basis of the field manifestation. In this study, the success rate is measured based on three criteria from stringent to liberal (*A*–*C*); that is, $P_L = 0.85$–1.0 is the most stringent consideration and in the range 0.5–1.0 is the least stringent consideration for liquefied cases, and similarly for non-liquefied cases, a prediction is considered to be successful and most stringent if P_L is in the range 0–0.15; if P_L is within the

Table 2 Comparison of developed GP model results with other statistical methods

Criterion for P_L	Juang method		Olsen method		Robertson method		Present GP model	
	No. of successful prediction	Rate (%)	No. of successful prediction	Rate (%)	No. of successful prediction	Rate (%)	No. of successful prediction	Rate (%)
$A(P_L > 0.85)$	39	85	19	42	33	72	0	0
$B(P_L > 0.65)$	42	92	30	66	36	79	31	68
$C(P_L > 0.5)$	45	98	39	85	40	87	40	87
$A(P_L < 0.15)$	6	7	0	0	2	3	18	21
$B(P_L < 0.35)$	35	40	20	23	10	12	32	37
$C(P_L < 0.5)$	52	59	32	37	28	32	44	50
A	45	34	19	15	35	27	18	14
B	77	58	50	38	46	35	63	47
C	97	73	71	53	68	51	84	63

range 0–0.5, then it is considered to be least stringent criterion. Based on the comparison presented in Table 2, all the three statistical methods and the proposed GP-based method are quite comparable in accuracy, whereas the Juang method is more accurate than other methods. But the GP approach of prediction of occurrence of liquefaction/non-liquefaction is better than all the statistical methods considering the simplicity and compactness of the CRR model. The Eqs. 4 and 5 can be used by professionals using a spreadsheet to evaluate the liquefaction potential of soil without going into complexities of model development using GP.

5 Conclusion

Case histories of soil liquefaction due to 1999 Chi-Chi earthquake is analyzed using evolutionary artificial intelligence technique, the genetic programming, to predict the liquefaction potential of soil within probabilistic framework. It can be noted that the performances of proposed GP model for training and testing data are comparable, showing good generalization of the generalization capabilities of GP approach. The results are compared with the currently used statistical methods in terms of probability of liquefaction. The developed GP model is found to be as good as the existing statistical methods in separating liquefaction and non-liquefaction cases. However, it needs more study with new data sets of different liquefaction case histories to confirm or disprove the present findings. The probability of liquefaction in a future seismic event of a soil with similar site conditions as that of the present database can be obtained from the developed Bayesian mapping function. The probability of liquefaction helps in taking better design decisions for the selection of a proper factor of safety.

References

1. Das SK, Muduli PK (2011) Evaluation of liquefaction potential of soil using extreme learning machine. In: Proceedings of the 13th international conference of the IACMAG, Melbourne, Australia, 9–11 May 2011, vol 1, pp 548–552
2. Goh ATC (1994) Seismic liquefaction potential assessed by neural networks. J Geotechn Eng 120(9):1467–1480
3. Goh TC, Goh SH (2007) Support vector machines: their use in geotechnical engineering as illustrated using seismic liquefaction data. J Comput Geomech 34:410–421
4. Javadi AA, Rezania M, Nezhad MM (2006) Evaluation of liquefaction induced lateral displacements using genetic programming. J Comput Geotech 33:222–233
5. Juang CH, Yuan H, Lee DH, Ku CS (2002) Assessing CPT-based methods for liquefaction evaluation with emphasis on the cases from the Chi-Chi, Taiwan, earthquake. J Soil Dyn Earthq Eng 22:241–258
6. Juang CH, Yuan H, Lee DH, Lin PS (2003) Simplified cone penetration test- based method for evaluating liquefaction resistance of soils. J Geotech Geoenviron Eng 129(1):66–80
7. Koza JR (1992) Genetic programming: on the programming of computers by natural selection. The MIT Press, Cambridge
8. Ku CS, Lee DH, Wu JH (2004) Evaluation of soil liquefaction in the Chi-Chi, Twain earthquake using CPT. J Soil Dyn Earthq Eng 24:659–673
9. Olsen RS (1997) Cyclic liquefaction based on the cone penetration test. In: Proceedings of NCEER workshop on evaluation of liquefaction resistance of soils. Technical report no. NCEER-97-0022. National Center for Earthquake Engineering Research, State University of New York at Buffalo, Buffalo, NY, pp 225–276
10. Pal M (2006) Support vector machines-based modeling of seismic liquefaction potential. J Numer Anal Methods Geomech 30:983–996
11. Rezania M, Javadi AA (2007) A new genetic programming model for predicting settlement of shallow foundations. J Can Geotech 44:1462–1473
12. Robertson PK, Campanella RG (1985) Liquefaction potential of sands using the CPT. J Geotech Eng 111(3):384–403
13. Robertson PK, Wride CE (1998) Evaluating cyclic liquefaction potential using cone penetration test. J Can Geotech 35(3):442–459
14. Seed HB, Idriss IM (1971) Simplified procedure for evaluating soil liquefaction potential. J Soil Mech Found Div ASCE 97(9):1249–1273
15. Stark TD, Olson SM (1995) Liquefaction resistance using CPT and field case histories. J Geotechn Eng 121(12):856–869
16. Youd TL, Idriss IM (eds) (2001) Liquefaction resistance of soils: summary report from the 1996 NCEER and 1998 NCEER/NSF workshops on evaluation of liquefaction resistance of soils. J Geotech and Geoenviron Eng 127(10) : 817–833
17. MathWork Inc (2005) Matlab User's Manual, version 6.5. The Math Works Inc, Natick

Performability Analysis of Reinforced Concrete Bridge Girders in Corrosive Environments Using Markov Chains with Fuzzy States

M.B. Anoop and K. Balaji Rao

Abstract A methodology for performance evaluation of reinforced concrete bridge girders in corrosive environments is proposed. The methodology uses the concept of performability and considers both serviceability - and ultimate - limit states. A non-homogeneous Markov chain is used for modelling the condition state evolution of the bridge girder with time. The condition states of the bridge girder are represented by fuzzy sets to consider the ambiguities arising due to the linguistic classification of condition states. The methodology is illustrated through the performance evaluation of a reinforced concrete T-beam bridge girder.

Keywords Reinforced concrete • Bridge girder • Chloride-induced corrosion • Performability • Markov chain • Fuzzy sets

1 Introduction

Development of rational methodologies for the evaluation of performance of civil infrastructure systems against different degradation mechanisms is an area of active research [2, 14, 17]. Chloride-induced corrosion of reinforcement is identified as one of the major degradation mechanisms for reinforced concrete (RC) members of infrastructural systems, especially for those located in the marine environment [15]. In this chapter, a methodology for performance evaluation of reinforced concrete structural members against chloride-induced corrosion of reinforcement, using the concept of performability, is proposed. Performability, defined as a measure combining reliability and performance measure, gives a more detailed and more accurate evaluation of the performance. In the proposed methodology, the condition of the bridge girder is described by assignment of a condition state. The stochastic

M.B. Anoop (✉) • K.B. Rao
CSIR-Structural Engineering Research Centre, Chennai, India
e-mail: anoop@serc.res.in

S. Chakraborty and G. Bhattacharya (eds.), *Proceedings of the International Symposium on Engineering under Uncertainty: Safety Assessment and Management (ISEUSAM - 2012)*,
DOI 10.1007/978-81-322-0757-3_81,

evolution of condition of the RC bridge girder with time is modelled using Markov chain model. Use of homogeneous Markov chain models for modelling evolution of damage with time in bridge girders/bridges has been proposed by various researchers [6, 10, 11]. However, from the results of experimental investigations reported in literature [25], it is noted that the loss of area of reinforcement due to corrosion with time is nonlinear, and hence, the state transition probabilities need to be considered as a function of time. Thus, the use of a non-homogeneous Markov chain model would be more rational. Also, since the classification of states is based on linguistic description, the states can better be represented by fuzzy sets rather than crisp sets. Use of fuzzy set theory provides a rational method to broaden the probability-based uncertainty handling framework to incorporate uncertainties arising due to linguistic description [4, 12]. Hence, in this study, a non-homogeneous Markov chain model with fuzzy states is proposed for modelling condition evolution with time. The transition probability matrix (TPM) obtained for the crisp states is operated upon to obtain the TPM for the fuzzified states. The performance of the bridge girder is described using performability measure. The usefulness of the methodology is illustrated through the performance evaluation of an RC T-beam bridge girder. It may be noted that the computation of performability will be useful for making engineering decisions for answering questions like 'How serviceable is the structure'.

2 Proposed Methodology

The development of the methodology for performability analysis of RC bridge girders using Markov chains with fuzzy states involves the following steps:

Step 1: *Development of an analytical procedure for estimating the state of the RC bridge girder at different times:* The current methods of bridge condition assessment are generally based on results from visual inspections and are subjective in nature [2]. The need for developing an objective method for condition assessment has been pointed out by Aktan et al. [2]. The chloride-induced corrosion of reinforcement affects the safety against both the serviceability limit state (SLS) due to cracking of cover concrete of the RC bridge girder and the ultimate limit state (ULS) due to the reduction in load-carrying capacity. These two aspects should be considered while carrying out condition assessment of corrosion-affected RC bridge girders. The first step is the development of an analytical procedure for determining the condition of the RC bridge girder, taking into consideration the effect of chloride-induced corrosion on the safety against both the SLS and ULS of the member.

Step 2: *Modelling the condition evolution of the bridge girder with time using Markov chain:* In a corrosion-affected RC bridge girder, the area of reinforcement reduces with time which affects the condition of the girder.

Therefore, the condition evolution of the bridge girder with time should be treated as a stochastic process. Markov chains (MC) are found to be a useful tool for stochastic modelling of condition evolution of RC bridge girders with time [6, 10, 11, 18, 19], and hence, the same is used in the present study.

Step 3: *Representation of states using fuzzy sets:* The states of the RC girder are defined using linguistic terms (such as excellent condition, poor condition, critical condition). The uncertainties arising out of the use of linguistic terms can be modelled more rationally in the framework of fuzzy set theory. Hence, it is more appropriate to represent the states by fuzzy sets. In the present study, the TPM for Markov chain with fuzzy states is determined from the TPM for Markov chain with discrete states using approach proposed by Bhattacharyya [7] and Symeonaki and Stamou [29].

Step 4: *Computation of performability of the RC bridge girder:* For assessment of the performance, the condition of the RC bridge girder at any time should be related to the performance requirements. Performability analysis is found to be useful for evaluating the performance of degrading systems [23], and hence, the same is used in this study.

The details related to each of these steps are given below.

2.1 Determination of Condition State of the Girder

The condition of the bridge girder is specified by the assignment of a condition state. The guidelines given by FHWA Bridge Inspector's Reference Manual [26] is used in the present study for defining the condition state for the girder. It may be noted that these guidelines are applicable for the condition rating of the superstructure system; however, the same is used in this study for condition rating of the individual girder. This is justifiable since 'the primary member rating represents the condition and functional capacity of the main members of the bridge span as a system NYDoT [21]'. As specified in NYDoT [21], if the condition of a primary member is the controlling condition in a load path non-redundant system, the rating would be used for the primary member system. The condition states and their description are given in Table 1.

2.1.1 Safety Against SLS (SSLS)

In the present study, the SSLS is defined based on the level of cracking (characterised by crack width) in the girder due to chloride-induced corrosion of reinforcement. Models have been proposed by various researchers relating the level

Table 1 Definition of condition states for RC bridge girder (Based on [26])

Condition state	Description
CS9	Excellent condition
CS8	Very good condition: no problems noted
CS7	Good condition: some minor problems
CS6	Satisfactory condition: structural elements show some minor deterioration
CS5	Fair condition: all primary structural elements are sound but may have minor section loss, cracking or spalling
CS4	Poor condition: advanced section loss, deterioration, spalling or scour
CS3	Serious condition: loss of section, deterioration or spalling has seriously affected primary structural components. Local failures are possible. Shear cracks in concrete may be present
CS2	Critical condition: advanced deterioration of primary structural elements. Shear cracks in concrete may be present. Unless closely monitored, it may be necessary to close the bridge until corrective action is taken
CS1	'Imminent' failure condition: major deterioration or section loss present in critical structural components. Bridge is closed to traffic, but corrective action may put back in light service
CS0	Failed condition: out of service. Beyond corrective action

of corrosion to the formation of cracks. Based on the review of these models [3], the following models are chosen for the crack initiation and crack width propagation due to corrosion of reinforcement in concrete.

Loss in area of steel cross section corresponding to crack initiation (ΔA_{so} in mm^2) and evolution of maximum crack width (w_{max}, in mm) are given by (from Ref. [30])

$$\Delta A_{so} = A_s \left[1 - \left[1 - \frac{\alpha}{\phi_{(0)}} \left(7.53 + 9.32 \frac{d}{\phi_{(0)}} \right) \times 10^{-3} \right]^2 \right] \tag{1}$$

$$w_{\max} = 0.101 \left(\Delta A_s - \Delta A_{so} \right) \tag{2}$$

where A_s is the initial area of steel cross section in mm^2, α is a factor for including the effect of highly localised pitting normally associated with chloride-induced corrosion, (d) is the clear cover in mm and ϕ_0 is the initial bar diameter in mm. Using Eqs. (1) and (2), the level of cracking (characterised by the crack width) due chloride-induced corrosion of reinforcement at any time can be determined based on the loss in area of reinforcement at that time. The SSLS for the bridge girder is determined based on the level of cracking using the guidelines given in Table 2.

2.1.2 Safety Against ULS (SULS)

In this study, it is assumed that the safety against ULS of the bridge girder at any time depends on the capacity of the girder to sustain the applied loads. While assessment of load-carrying capacity is usually carried out using

Table 2 SSLS for the bridge girder

SSLS	Description
1	Corrosion is yet to initiate
2	Corrosion initiated, but no cracking
3	Cracking initiated, but crack width less than the allowable value of 0.3 mm specified in code of practice [8]
4	Crack width greater than 0.3 mm but less than 1.0 mm (no spalling)
5	Crack width $\geq$1.0 mm, spalling of concrete [31]

deterministic- or semi-probabilistic (partial safety factor) approaches (which are sometimes considered to be conservative), reliability-based approaches explicitly taking into account the uncertainties in variables are emerging [17]. The load and resistance factor rating (LRFR) method proposed by AASHTO [1] is reliability-based and provides a more realistic assessment of the safe load capacity of existing bridges [20]. Hence, this method is adopted in the present study for defining the SULS. According to LRFR, the load rating is generally expressed as a rating factor (RF), given by AASHTO [1],

$$\mathrm{RF} = \frac{C - \gamma_{\mathrm{DC}}\mathrm{DC} - \gamma_{\mathrm{DW}}\mathrm{DW} \pm \gamma_P P}{\gamma_L \mathrm{LL}(1 + \mathrm{IM})}; \quad C = \phi_c \phi_s \phi \, R_n \text{ with } \phi_c \phi_s \geq 0.85 \tag{3}$$

where C is the capacity, R_n is the nominal member resistance, DC is the dead-load effect due to structural components and attachments, DW is the dead-load effect due to wearing surface and utilities, P is the permanent loads other than dead loads, LL is the live-load effect, IM is the dynamic load allowance, γ_{DC} is the LRFD load factor for structural components and attachments, γ_{DW} is the LRFD load factor for wearing surface and utilities, γ_P is the LRFD load factor for permanent loads other than dead loads and γ_L is the evaluation live-load factor. ϕ_c is the condition factor for taking into account the increased uncertainty in the resistance of deteriorated members and varies from 0.85 for members in poor condition to 1.0 for members in good or satisfactory condition; ϕ_{s} is the system factor for taking into consideration the level of redundancy of the entire super structure and varies from 1.0 for redundant multi-girder bridges to 0.85 for non-redundant systems such as two-girder, welded girder and truss bridges. ϕ is the LRFD resistance factor.

The methodology for LRFR comprises of three distinct procedures: (1) design load rating, (2) legal load rating and (3) permit load rating. The permit load rating is required for the issuance of overweight permits based on request and applies only to bridges that satisfy the legal load rating. Therefore, this level of rating is not considered in the present study for determining the SULS of the girder.

2.1.3 Modelling of Time Varying Resistance

For a bridge girder subjected to chloride-induced corrosion of reinforcement, the nominal resistance will reduce with time after corrosion initiation, due to the reduction in area of reinforcement (the effect of other factors like creep and shrinkage of concrete, and loss of bond between steel and concrete are not considered in the present study). The reduction in area of reinforcement due to corrosion is determined as follows:

Assuming ingress of chlorides into cover concrete as a diffusion process, time-to-corrosion initiation (t_i) can be determined from Fick's second law of diffusion as [13]

$$t_i = \frac{d^2}{4D}\left[\text{erf}^{-1}\left(\frac{c_s - c_{\text{cr}}}{c_s}\right)\right]^{-2} \tag{4}$$

where d is the clear cover to reinforcement, D is the diffusion coefficient for chlorides in concrete, c_s is the surface chloride concentration and c_{cr} is the critical chloride concentration.

Researchers have proposed different models for determining the remaining area of reinforcing bar subjected to corrosion [24]. From a brief review of these models, it is found that the model proposed by Rodriguez et al. [25] is generally used. Using this model, the remaining reinforcing bar diameter, $\phi(t)$ (in mm), at any time t (in years), can be estimated as

$$\phi(\text{t}) = \phi(0) - 0.0116\ \alpha\ I_{\text{corr}}(t - t_i) \tag{5}$$

where $\phi(0)$ and $\phi(t)$ are diameters of bar before corrosion initiation and at time 't', respectively, I_{corr} is the corrosion current density (in μA/cm^2), 0.0116 is a factor which converts μA/cm^2 to mm/year, t_i is the time for initiation of corrosion (in years) and α is a factor for including the effect of highly localised pitting normally associated with chloride-induced corrosion.

To account for variations in workmanship and exposure conditions, d, D, c_s, c_{cr}, I_{corr} and α are treated as random variables. Once the reduced diameter of the reinforcing bars is determined, the rating factors for the girder can be computed. The SULS for the bridge girder at any time is determined based on the value of rating factor at that time using the conditions given in Table 3.

2.1.4 Determination of Condition States

After determining the safety against the serviceability limit state (SSLS) and the safety against ultimate limit state (SULS) at any time, the condition state (CS) at that time of the girder is determined. For this purpose, a rule base is formulated

Table 3 SULS for the bridge girder

SULS	Definition	Description
1	$RF_{OL} \geq 1.0$	Bridge girder satisfies the design load rating at operating level
2	$RF_{OL} < 1.0$ and $RF_{LL} \geq 1.0$	Bridge girder does not satisfy the design load rating but satisfies the legal load rating
3	$0.60 \leq RF_{LL} < 1.0$	Bridge girder does not satisfy the legal load rating; reduced loads can be permitted
4	$0.30 \leq RF_{LL} < 0.60$	Bridge girder does not satisfy the legal load rating; highly reduced loads can be permitted
5	$RF_{LL} < 0.30$	Bridge to be closed to traffic

Note: RF_{OL} rating factor for design load rating at operating level, RF_{LL} rating factor for legal load rating

relating the SULS and SSLS to the condition state of the girder (see Table 4). More details regarding the formulation of rule base are given in Anoop [3].

To estimate the elements of the transition probability matrix to describe the stochastic evolution, the procedure presented in the next section is used.

2.2 Modelling the Condition State Evolution

Markov chains are found to be a useful tool for stochastic modelling of condition evolution with time [5, 10, 11, 16, 18, 19]. Using data on bridge superstructure condition rating from the United States and Hungary, Chase and Gáspár [11] have shown that predictions on condition state using MC are in good agreement with the observed condition states. Therefore, in the present study, MC modelling is used for the condition evolution of the bridge girder with time. The index space of this stochastic process is the time, which can be considered as discrete, $\{T_1, T_2, \ldots\}$. The state space of the stochastic process represents the condition state of the girder, which is also discrete, $S = \{\text{CS9}, \text{CS8}, \ldots, \text{CS0}\}$. Hereafter, the condition states are represented as $S = \{CS_9, CS_8, \ldots, CS_0\}$. The probabilistic evolution of the bridge girder is given by the transition probability matrix (TPM). Since, due to chloride-induced corrosion, the cross-sectional area of reinforcement reduces with time, there is transition only from higher condition states to the lower condition states. Therefore, the TPM will be an upper triangular matrix.

Balaji Rao et al. [6] used a homogeneous MC for corrosion damage evolution with time. From the results of experimental investigations reported in literature [25], it is noted that the loss of area of reinforcement with time is nonlinear, and hence, the condition state transition probabilities need to be considered as a function of time. Thus, the use of a non-homogeneous Markov chain (NHMC) model would be more rational [5]. Hence, in this study, a NHMC model is proposed for modelling the condition evolution with time. Monte Carlo simulation (MCS) approach is used for determining the elements of the TPM. The step-by-step

Table 4 Rule base for determining the condition state

Safety against ULS →		SULS				
		1	2	3	4	5
Safety against SLS ↓		($RF_{OL} \geq 1.0$)	($RF_{OL} < 1.0$& RFEL ≥ 1.0)	($0.6 \leq RF_{EL} < 1.0$)	($0.3 \leq RF_{EL} < 0.6$)	$RF_{EL} < 0.3$)
SSLS	1 (No corrosion)	CS9	CS7	CS5	CS3	CS1
	2 (Corrosion initiated; no cracking)	CS8	CS6	CS5	CS2	CS1
	3 (Crackwidth $\leq$ 0.3 mm)	CS7	CS6	CS4	CS2	CS1
	4 (Crackwidth $\leq$ 1.0 mm)	CS5	CS4	CS4	CS2	CS0
	5 (Crackwidth $>$ 1.0 mm)	CS3	CS3	CS3	CS2	CS0

procedure for determining the elements of the transition probability matrix (**P**) for the condition state evolution between two successive time instants, T_k and T_{k+1}, is given below:

1. Select values of mean and COV for D, c_s, c_{cr}, cover thickness (d), I_{corr} and α.
2. Determine mean and standard deviation of time-to-corrosion initiation (Eq. 4) using first-order approximation. Assume t_i follows a lognormal distribution.
3. Carry out MCS at two successive time instants, T_k and T_{k+1}, considering t_i, I_{corr} and α as random variables.
   For each time instant and for each simulation:
   (i) Determine the remaining diameter of the reinforcing bar (Eq. 5) and the loss in area of reinforcement.
   (ii) Compute the width of the crack formed due to corrosion (using Eq. 2) and identify the safety against SLS (SSLS) using Table 2.
   (iii) Carry out LRFR and identify the safety against ULS (SULS) using Table 3.
   (iv) Determine the condition state (CS) for the girder using the rule base given in Table 6.
4. Compute the elements of the TPM as

$$\mathrm{P}(i,j) = p_{ij} = \frac{\Pr(\mathrm{CS} = \mathrm{CS}_m | T = T_{k+1} \cap \mathrm{CS} = \mathrm{CS}_l | T = T_k)}{\Pr(\mathrm{CS} = \mathrm{CS}_l | T = T_k)};$$

$$1 \le i \le 10; i \le j \le 10; l = 10 - i; m = 10 - j$$

$$= \frac{\begin{array}{c}\text{number of simulation cycles for which CS} = \mathrm{CS}_m \text{ at time } T_{k+1} \\ \text{and CS} = \mathrm{CS}_l \text{ at time } T = T_k\end{array}}{\text{number of simulation cycles for which CS} = \mathrm{CS}_l \text{ at time } T = T_k} \tag{6}$$

2.3 Markov Chain with Fuzzy States

From Table 1, it is noted that the condition states are defined using linguistic terms (such as excellent condition, poor condition, critical condition). The uncertainties arising out of the use of linguistic terms can be modelled more rationally in the framework of fuzzy set theory. Hence, it is more appropriate to represent the condition states by fuzzy sets. Also, the number of states are large (ten states), and there is a need to aggregate the states of the system to make decisions regarding the maintenance. Fuzzufying the state space provides a rational framework for aggregating the states for decision making [7]. The TPM for Markov chain with fuzzy states (P_F) can be determined from the TPM for Markov chain with discrete states using the following formulations taken from by Bhattacharya [7] and Symeonaki and Stamou [29].

Table 5 Membership functions of fuzzy condition states

	CS9	CS8	CS7	CS6	CS5	CS4	CS3	CS2	CS1	CS0
Good	1	1	1	0.6	0	0	0	0	0	0
Average	0	0	0	0.4	1	1	0.5	0	0	0
Poor	0	0	0	0	0	0	0.5	1	1	1

Let $S = \{1, 2,\ldots, k\}$ be the discrete state space and $F = \{F_1, F_2,\ldots, F_N\}$ be the fuzzy state space, i.e. the set of fuzzy states. F_r is a fuzzy set on S and $\mu_{F_r}(\cdot): S \rightarrow [0, 1]$ denotes the membership function of F_r for $r = 1, 2,\ldots, N$, which satisfies the orthogonality conditions $\sum_{r=1}^{N} \mu_{F_r}(i) = 1$ for all $i \in S$. Then the elements of TPM for the Markov chain with fuzzy states are given by

$$p_{F_rF_s} = (m_{F_r})^{-1} \sum_{i=1}^{k} \sum_{j=1}^{k} p_{ij} \mu_{F_r}(i) \mu_{F_s}(j); m_{F_r} = \sum_{i=1}^{k} \mu_{F_r}(i) \tag{7}$$

In the present study, three fuzzy states are considered, $F = \{$GOOD, AVERAGE, POOR$\}$. The grades of membership of the original non-fuzzy states $\{CS_9, CS_8,\ldots, CS_0\}$ in the fuzzy states are given in Table 5. While the TPM for the Markov chain with discrete condition states will be an upper triangular matrix (as explained earlier), the same cannot be expected for the TPM for the Markov chain with fuzzy condition states, due to the interaction between the fuzzy sets.

After modelling the condition evolution of the girder with Markov chain, the next step is to determine the performability of the girder, and the same is explained in the next section.

2.4 *Performability*

Performability models, also called stochastic reward models [27], consist of a stochastic process and a reward structure. The stochastic process describes the evolution of the system. Markov chains are most commonly used in performability analysis for describing the stochastic evolution of the system [8]. In such a case, the process is often referred to as a structure-state process since it describes the state of the system structure. The set of rewards associated with the states of a structure-state process are referred to as the reward structure.

The reward structure relates possible behaviours of the process to a specified performance variable. Typically, this is done by associating a 'reward rate' with each state, the interpretation being that this rate is the rate at which reward accumulates while the process is in the state. The reward structure is typically a set of one or more functions defined over the states or on transitions between the states in the process [27]. Thus, two kinds of reward can be distinguished, namely,

(1) rate reward, reward obtained when the system is in a certain discrete state, and (2) impulse reward, reward obtained with some 'event' of the process, i.e. for instance, transition from one state to another.

Once the reward structure is specified, the performance variable can be defined in terms of the reward structure. The performance variables can be [27]:

- Instant-of-time variable: The variable typically represents the states of the modelled system at some time 't' (instantaneous reward).
- Interval-of-time variable: The variable typically represents the accumulated benefit derived from operating the system for some interval of time (accumulated reward).
- Time-averaged interval-of-time variable: The variable represents the (time-averaged) rate at which reward is accumulated during an interval of time, obtained by dividing the reward accumulated during some time interval by the length of the interval (time-averaged accumulated reward).

The accumulated reward and the time-averaged accumulated reward are relatively insensitive to the state of the system at a particular instance as compared to the instantaneous reward, especially at large times [28]. Hence, the instantaneous reward will be more useful for making decisions on inspection, repair or replacement which should be based upon the state of the system at a given time. The accumulated reward and time-averaged accumulated reward will be useful for comparing the performances of different alternatives (for instance, for comparing the performances of different design alternatives over a period of time for selecting the best alternative).

2.4.1 Computation of Performability

Let the vector r represent the reward structure (i.e. r_i is the reward rate assigned to the bridge girder if the bridge girder is in condition state CS_i). Let $CS(T_k)$ be the vector representing the condition state of the girder at time T_k. Then $Z(T_k) = r_{CS(T_k)}$ refers to the instantaneous reward rate of the girder at time T_k [8]. The expected instantaneous reward rate and the variance of the instantaneous reward rate are given by [8, 22]

$$E[Z(T_k)] = \sum_{i \in S} r_i P_i^U(T_K);$$
$$\mathrm{Var}[Z(T_k)] = \sum_{i \in S} {r_i}^2 P_i^U(T_K) - \left(\sum_{i \in S} r_i P_i^U(T_K) \right)^2 \tag{8}$$

where $P^U(T_k)$ unconditional probability vector of the condition states at time T_k.

The probability that the instantaneous reward rate does not exceed to a certain performance level at time T_k is given by [9]

$$p_z(T_k) = \Pr ob[Z(T_k) \leq z] = \sum_{i \in S, r_i \leq z} P_i^U(T_K) \tag{9}$$

The accumulated reward, $W(T_k)$, the expected accumulated reward, $E[W(T_k)]$, and the expected time-averaged accumulated reward, $E[Y(T_k)]$, over the period (T_1, T_k) are given by [22, 23]

$$\begin{aligned} W(T_k) &= \sum_{j=2}^{k} Z(T_j); E[W(T_k)] = \sum_{j=2}^{k} \sum_{i \in S} r_i P_i^U(T_j); \\ E[Y(T_k)] &= \frac{1}{(T_k - T_1)} \sum_{j=2}^{k} \sum_{i \in S} r_i P_i^U(T_j) \end{aligned} \tag{10}$$

2.4.2 Specification of Reward Rates: Proposed Structure

The set of rewards associated with the different states of the system is called the reward structure. It relates possible behaviours of the process to a specified performance variable. For instance, consider a binary reward structure r defined such that a value of $r = 1$ is assigned to the 'up' states of the system and $r = 0$ is assigned to the 'down' states of the system. In this case, $E[Z(T_k)]$ gives the reliability of the system at time T_k, while $E[W(T_k)]$ gives the expected 'uptime' for the system over the period (T_1, T_k). If the reward structure r is considered such that r_i represents the capacity of the system in state 'i', then $E[Z(T_k)]$ gives the expected instantaneous capacity of the system at time T_k and $p_z(T_k)$ gives the probability that the capacity of the system does not exceed 'z' at time T_k. If r_i represents the loss occurring due to the system being in state 'i', then $E[Z(T_k)]$ gives the expected instantaneous loss at time T_k and $E[W(T_k)]$ gives the expected cumulative loss over the period (T_1, T_k). Some of the commonly used reward structures are presented in Bolch et al. [9].

The reward rates can be stationary (reward rate do not change with time) or dynamic (reward rate changes with time). Since the service life of bridge girders is long (typically 75 years), it is more rational to consider a dynamic reward rate. It makes more sense to assign a higher reward rate for the bridge girders if it is at a given condition state at the final stages of its service life than when it is the same condition state at the initial stages. In the present study, the reward rates are assigned based on the urgency of maintenance when the girder is in different condition states (Table 6). The maintenance urgency guidelines given in Ryan et al. [26] are used for this purpose. Since the reward rate changes from 0 for no immediacy of maintenance action to 1.0 for immediate maintenance action, it is more appropriate to term it as a penalty rate rather than reward rate. This reward

Table 6 Reward structure

Condition state	Reward structure: penalty rate
Good	0
	(No immediacy of maintenance action)
Average	0.5
	(Maintenance within current season)
Poor	1.0
	(Immediate maintenance)

structure will be useful for comparing the maintenance urgency for different bridge girders for planning of maintenance and allocation of resources. In this case, $E[Z(T_k)]$ gives the expected value of immediacy of maintenance at time T_k, while $p_z(T_k)$ gives the probability that the immediacy of maintenance of the girder does not exceed a specified value of immediacy of maintenance at time T_k.

The use of the proposed methodology for performability analysis is illustrated through an application in the next section.

3 Application

The reinforced concrete T-beam bridge girder, given as an illustrative example in the LRFR Manual [1], is considered in the present study. It is assumed that the superstructure system is a load path non-redundant system, and hence, the condition rating of the girder would be used for the superstructure system. The cross-sectional details of the girder are shown in Fig. 1. The girder has a span of 7.9 m. The compressive strength of concrete (f'_c) is 20.7 MPa and the yield strength of steel (f_y) is 227.6 MPa. The values of mean and coefficient of variation (COV) of the random variables considered are given in Table 7. It has been noted that both I_{corr} and α show large variations [19], and hence, in this study, a large value of COV of 0.30 is assumed for these variables. All the random variables are assumed to be statistically uncorrelated with each other. The mean and standard deviation of time-to-corrosion

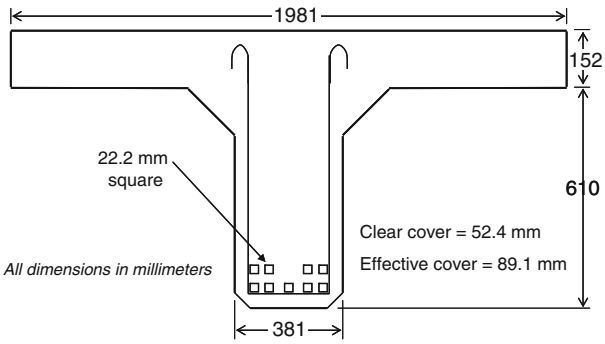

Fig. 1 Cross-sectional details of the T-beam bridge girder [1]

Table 7 Statistical properties of the random variables considered

Variable	Mean	COV*
d (mm)	52.4	0.05
D (cm^2/s)	5×10^{-8}	0.20
c_s (% by weight of concrete)	0.25	0.20
c_{cr} (% by weight of concrete)	0.125	0.20
i_{corr}	3.5	0.30
α	5.25	0.30

Note: * - assumed

Table 8 Values of load effects and load factors to be used in load rating (From [1])

Parameter		Moment (KN-m)	Load factor
DC		114.88	1.25
DW		37.84	1.25
LL	Design load	400.4	1.35
	Legal load type 3	238.98	1.65
	Legal load type 3S2	224.43	1.65
	Legal load type 3-3	192.33	1.65

initiation is determined using first-order approximation, and it is assumed that t_i, d, I_{corr} and α follows lognormal distribution.

It may be noted that the beam considered is reinforced with square rebars of size 22.2 $\times$ 22.2 mm (see Fig. 1). But the models used for determining the remaining diameter of reinforcing bar (Eq. 5) and for determining the loss of reinforcement area corresponding to crack initiation (Eq. 1) require the diameter of the rebar. The diameter of a circular rebar with the same cross-sectional area as that of the square rebar (of size 22.2 $\times$ 22.2 mm) is 25 mm, and this value is used as the initial diameter of the rebar in the present study.

For determination of SULS, the ultimate limit state of flexure is only considered in this study. The results of the dead-load analysis and live-load analysis for the bridge girder considered are taken from the LRFR Manual [1] and are given in Table 8. Monte Carlo simulation method with ten million cycles is used for determining the elements of TPM at different time-steps.

4 Results and Discussion

The TPMs at different times are determined using Eq. (6), and the TPMs for Markov chain with fuzzy states are computed using Eq. (7). The evolution of fuzzy condition states with time is shown in Fig. 2. The expected instantaneous reward rate, $E[Z(t)]$, at different times is computed using Eq. (8). The variation of expected instantaneous reward rate with time is shown in Fig. 3.

The value of $E[Z(t)]$ is a measure of the expected performance of the girder at time t. While $E[Z(t)]$ is useful for comparing the performance of different bridge girders over time, this measure does not address the likelihood of completing a given amount of work (or satisfying a given level of performance) over time

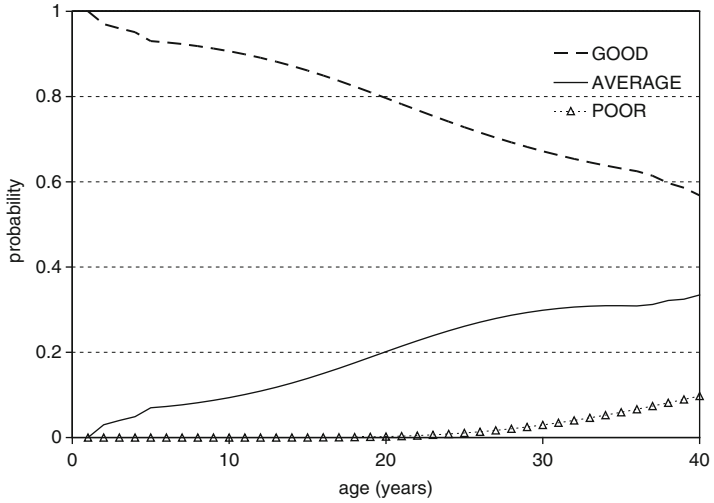

Fig. 2 Evolution of condition state of the bridge girder with time

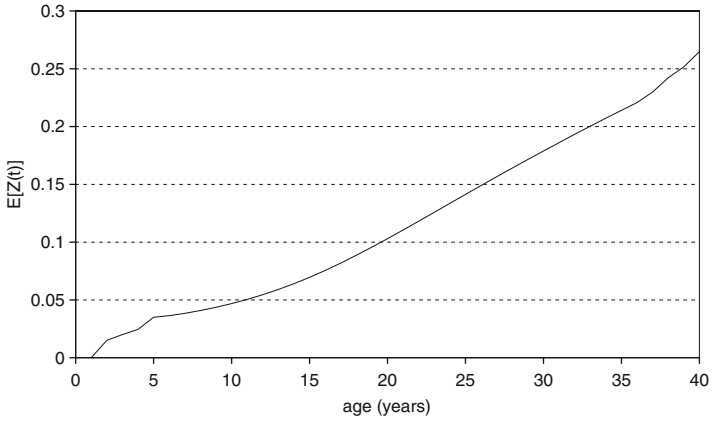

Fig. 3 Variation of expected instantaneous penalty rate with time for the bridge girder

[28]. This aspect is more important for remaining life assessment for the planning of maintenance, and probability distribution of $Z(t)$ will be more useful for this purpose.

5 Summary

A methodology for performance evaluation of corrosion-affected reinforced concrete bridge girders is proposed. The methodology integrates the following: (1) non-homogeneous Markov chain for modelling the stochastic evolution of

condition of the bridge girder with time, (2) fuzzy states to take into account the ambiguities arising due to the linguistic description of states and (3) performability measure for describing the performance of the bridge girder. The usefulness of the methodology is illustrated through the performability assessment of a reinforced concrete T-beam bridge girder.

Acknowledgements This chapter is being published with the kind permission of the Director, CSIR-SERC, Chennai.

References

1. AASHTO (2003) Manual for condition evaluation and load and resistance factor rating (LRFR) of highway bridges. American Association of State Highway Officials, Washington, DC
2. Aktan AE, Farhey DN, Brown DL, Dalal V, Helmicki AJ, Hunt V, Shelley SJ (1996) Condition assessment for bridge management. J Infrastruct Sys ASCE 2(3):108–117
3. Anoop MB (2009) Remaining life assessment of reinforced concrete structural elements subjected to chloride-induced corrosion of reinforcement. PhD thesis, Department of Civil Engineering, Indian Institute of Science, Bangalore
4. Anoop MB, Balaji Rao K, Lakshmanan N (2008) Safety assessment of austenitic steel nuclear power plant pipelines against stress corrosion cracking in the presence of hybrid uncertainties. Int J Press Vessels Pip 85(4):238–247
5. Balaji Rao K, Anoop MB, Lakshmanan N (2004a) Modelling the evolutionary non-guassian processes using NHGMC. In: Proceedings of the International Congress on Computational Mechanics and Simulation (ICCMS-2004), Indian Institute of Technology, Kanpur, India, 9–12 Dec 2004, vol I, pp 182–189
6. Balaji Rao K, Anoop MB, Lakshmanan N, Gopalakrishnan S, Appa Rao TVSR (2004) Risk-based remaining life assessment of corrosion affected reinforced concrete structural members. J Struct Eng 31(1):51–64
7. Bhattacharyya M (1998) Fuzzy Markovian decision process. Fuzzy Sets Syst 99:273–282
8. BIS (2000) Indian standard code of practice for plain and reinforced concrete: IS 456-2000. Bureau of Indian Standards, New Delhi
9. Bolch G, Greiner S, de Meer H, Trivedi KS (1998) Queuing networks and Markov chains: modeling and performance evaluation with computer science applications. Wiley, New York
10. Cesare MA, Santamarina C, Turkstra C, Vanmarcke EH (1992) Modeling bridge deterioration with Markov chains. J Transp Eng ASCE 118(6):820–833
11. Chase SB, Gáspár L (2000) Modeling the reduction in load capacity of highway bridges with age. J Bridge Eng ASCE 5(4):331–336
12. Corotis RB (2009) Risk communication with generalized uncertainty and linguistics. Struct Saf 31:113–117
13. Crank J (1975) Mathematics of diffusion. Oxford University Press, Oxford
14. Durango-Cohen PL, Madanat SM (2008) Optimization of inspection and maintenance decisions for infrastructure facilities under performance model uncertainty: a quasi-Bayes approach. Transp Res Part A 42:1074–1085
15. fib (2006) Model code for service life design. fib Bulletin 34. International Federation for Structural Concrete, Lausanne
16. Frangopol DM, Kallen M-J, van Noortwijk JM (2004) Probabilistic models for life-cycle performance of deteriorating structures: review and future directions. Prog Struct Eng Mater 6(4):197–212

17. Godart B, Vassie PR (2001) Bridge management systems: extended review of existing systems and outline framework for a European system. BRIME Deliv D13:PL97–PL2220
18. Jiang M, Corotis RB, Ellis JH (2000) Optimal life-cycle costing with partial observability. J Infrastruct Syst ASCE 6(2):56–66
19. Lay S, Schießl P (2003) LIFECON deliverable 3.2: service life models. cbm-Technische Universität München
20. Minervino C, Svakumar B, Moses F, Mertz D, Edberg W (2004) New AASHTO guide manual for load and resistance factor rating of highway bridges. J Bridge Eng ASCE 9(1):43–454
21. NYDoT (1997) Bridge inspection manual. New York State Department of Transportation, New York
22. Platis A (2006) A generalized formulation for the performability indicator. Comput Math Appl 51:239–246
23. Platis A, Limnios N, Du ML (1998) Dependability analysis of systems modeled by non-homogeneous Markov chains. Reliab Eng Syst Saf 61:235–249
24. Raupach M, Warkus J, Gulikers J (2006) Damage process due to corrosion of reinforcement bars – current and future activities. Mater Corros 57(8):648–653
25. Rodriguez J, Ortega LM, Casal J, Diez JM (1996) Assessing structural conditions of concrete structures with corroded reinforcement. In: Dhir RK, Jones MR (eds) Concrete repair, rehabilitation and protection. E&FN Spon, London, pp 65–78
26. Ryan TW, Hartle RA, MannJE, Danovich LJ (2006) Bridge inspector's reference manual. Report No. FHWA NHI 03-001. Federal Highway Administration National Highway Institute, Virginia
27. Sanders WH, Meyer JF (1991) A unified approach for specifying measures of performance, dependability ad performability. In: Avizicuis A, Lapric J (eds) Dependable computing for critical applications. Springer, New York, pp 515–537
28. Smith RM, Trivedi KS, Ramesh AV (1988) Performability analysis: measures, an algorithm and a case study. IEEE Trans Comput 37(4):406–417
29. Symeonaki MA, Stamou GB (2004) Theory of Markov systems with fuzzy states. Fuzzy Sets Syst 143(3):427–445
30. Vidal T, Castel A, Francois R (2004) Analyzing crack width to predict corrosion in reinforced concrete. Cement Concr Res 34(1):165–174
31. Vu KAT, Stewart MG (2005) Predicting the likelihood and extent of reinforced concrete corrosion-induced cracking. J Struct Eng ASCE 131(11):1681–1689

Seismic Evaluation of RC Stepped Building Frames

Pradip Sarkar, Devdas Menon, and A. Meher Prasad

Abstract 'Stepped building' frames, with vertical geometric irregularity, are now increasingly encountered in modern urban construction. This chapter proposes a new method of quantifying irregularity in such building frames, accounting for dynamic characteristics (mass and stiffness). The proposed 'regularity index' provides a basis for assessing the degree of irregularities in a stepped building frame. This chapter also proposes a modification of the code-specified empirical formula for estimating fundamental period for regular frames, to estimate the fundamental time period of the stepped building frame. The proposed equation for fundamental time periods is expressed as a function of the regularity index. It has been validated for various types of stepped irregular frames. A new approach to determine the lateral load pattern, considering the contributions from the higher modes, is proposed that is suitable for pushover analysis of stepped buildings. Also, a modification to the displacement coefficient method is proposed, based on time history analysis of 78 stepped frames. When the newly proposed load pattern is combined with the modification of the displacement coefficient method of FEMA 356, the target displacement for the stepped building frame is found to match consistently the displacement demand given by the time history analysis.

Keywords Stepped building • Pushover analysis • Target displacement • Plastic hinge • Time history • Life safety • Design basis earthquake

P. Sarkar (✉)
Department of Civil Engineering, National Institute of Technology Rourkela, Orissa 769 008, India
e-mail: sarkarp@nitrkl.ac.in

D. Menon • A.M. Prasad
Indian Institute of Technology Madras, Chennai 600 032, India
e-mail: dmenon@iitm.ac.in; prasadam@iitm.ac.in

S. Chakraborty and G. Bhattacharya (eds.), *Proceedings of the International Symposium on Engineering under Uncertainty: Safety Assessment and Management (ISEUSAM - 2012)*,
DOI 10.1007/978-81-322-0757-3_82,

1 Introduction

A common form of vertical discontinuity arises from reduction of the lateral dimension of the building along its height. This building category is known as 'stepped' building [8]. Figure 1 shows a typical example of a stepped building located in urban India (New Delhi). Stepped buildings are characterised by staggered abrupt reductions in floor area along the height of the building, with consequent drops in mass, strength and stiffness (not necessarily at the same rate). Height-wise changes in stiffness and mass render the dynamic characteristics of these buildings different from the 'regular' building. Design codes have not given particular attention to the stepped building form. This is perhaps due to the paucity of research on stepped buildings reported in literature. This chapter discusses some of the key issues regarding analysis and design of stepped buildings. In the present study, a new approach for quantifying the irregularity in stepped building is proposed. It accounts for properties associated with mass and stiffness distribution in the frame. This approach is found to perform better than the existing measures to quantify the irregularity. The empirical equations of fundamental period given in the design codes are function of building height, which is ambiguous for a stepped building. Based on free vibration analysis of 78 stepped frames with varying irregularity and height, this study proposes a correction factor to the empirical code formula for fundamental period, to render it applicable for stepped buildings.

Fig. 1 A typical stepped building located in New Delhi, India

A new approach to determine the lateral load pattern, considering the contributions from the higher modes, is proposed that is suitable for pushover analysis of stepped buildings. Also, a modification to the displacement coefficient method is proposed, based on time history analysis of 78 stepped frames. When the newly proposed load pattern is combined with the modification of the displacement coefficient method of [3], the target displacement for the stepped building frame is found to match consistently the displacement demand given by the time history analysis.

2 Quantifying Irregularity

The purpose of the present study is to address the specific stepped irregularity of the framed building. 78 building frames representing varying degree of stepped irregularity are considered for the study. All the building models considered here have four bays (in the direction of earthquake) with a uniform bay width of 6 m. However, the results were checked for frames with different number of bays, and it has been observed that number of bays does not affect the building response significantly. Seven different height categories were considered for the study, ranging from 6 to 18 storeys, with a uniform storey height of 3 m. These building frames include different (equal and unequal) step heights and widths.

The results presented here are limited to 23 building frames having three different building geometries with different stepped irregularities due to the successive reduction of one bay and one step height of one storey (S1), two storeys (S2) and three storeys (S3), at the top of the building, as shown in Fig. 2. The regular frame (R), without any step, is also included. Additional studies carried out on 55 building frames are available elsewhere [7]. Although all of these stepped building frames have identical geometric irregularity as per the definition of IS 1893 and ASCE 7, these frames show significantly different responses. That means the design code procedure of considering geometry alone to define irregularity is not appropriate.

Ideally, the stiffness and mass distributions in the frame have to be considered in quantifying the irregularity of a stepped building. Studying the dynamic properties of regular building, it is found that the participation of the first mode is dominant. However, when the vertical irregularities (steps in the building frame) are introduced, it is observed that as the irregularity increases, the first-mode participation decreases with increased participation on some higher modes. This is reflected in the histogram shown in Fig. 3, which presents the normalised modal participation factors in 8-storey frames for the four categories, R, S1, S2 and S3, considering as many as 50 modes, of which the first 10 modes are shown.

It can be seen that irregularity in the stepped frame can be captured by the relative first-mode participation factor. Accordingly, a regularity index (η) is proposed to quantify the irregularity of a stepped frame, as follows:

$$\eta = \frac{\Gamma_1}{\Gamma_{1,\text{ref}}} \tag{1}$$

twhere Γ_1 is the first-mode participation factor for the stepped frame under consideration and $\Gamma_{1,\text{ref}}$ is the first-mode participation factor for the similar regular

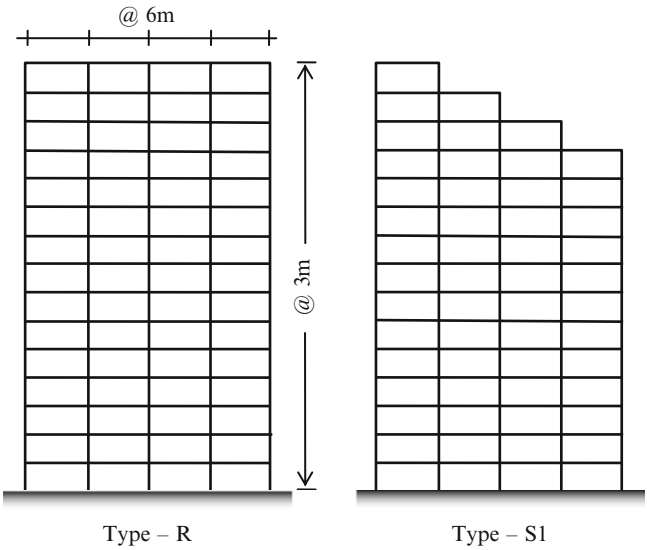

Fig. 2 Typical building models considered for the present study

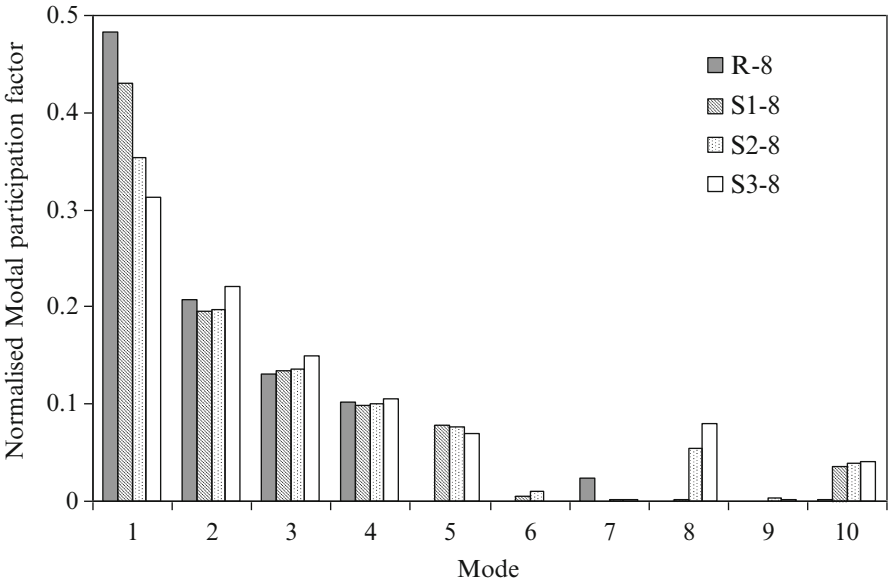

Fig. 3 Modal participation factor in 8-storey building frames

building frame without steps (R). Approximate values of these two factors can be obtained from simple static analyses, using the concept of Rayleigh (1945). For any stepped building, the value of the regularity index (η) will be less than unity as the first-mode participation factor will always be less than that of a regular building. This index accounts for properties associated with mass and stiffness distributions in the frame.

3 Estimation of Fundamental Time Period for Stepped Building

Design codes [1, 2, 4] recommend dynamic analysis for irregular buildings including stepped buildings, with the base shear scaled up to the value corresponding to the fundamental period as per the code-specified empirical formulas. These formulas, however, have been developed for regular buildings and are a function of building height only.

For a stepped building, the height is not constant. It varies from one side to the other side of the frame. The building height at the lower side is likely to underestimate the actual time period and, consequently, overestimates the base shear. Conversely, if we consider the overall building height, we will get an unconservative estimate of the base shear. It is found that, generally, the fundamental period decreases with the increased irregularity when the overall building height is the same. Most of the stepped buildings are high-rise and multi-storeyed, and their period falls in the constant velocity region of the response spectrum, where the spectral acceleration value is very sensitive to the fundamental period. A slight reduction in the fundamental period in this region results in a considerable increase in the design base shear. In this study, an attempt has been made to improve the code-based empirical equation for estimating the fundamental period to make it useful for the stepped building.

In a stepped building, both mass and stiffness decrease with decreasing regularity index (η). Reduction of mass reduces the building fundamental period, whereas reduction of stiffness increases the fundamental period. So, the fundamental period does not have a monotonic relation with the regularity index. Ratio of the fundamental period of stepped frame (T) to that of similar regular frame without step (T_{ref}) obtained from the modal analysis of 78 stepped frames with varying regularity indices and building height are plotted and shown in Fig. 4. Based on a polynomial fit for these data, the following correction to the code empirical formula for building fundamental period is proposed for stepped buildings where h = overall building height (in m) and η = regularity index:

$$T = 0.075h^{0.75} \times \kappa \tag{2a}$$

$$\kappa = \frac{T}{T_{\text{ref}}} = [1 - 2(1-\eta)(2\eta - 1)] \quad \text{for} \quad 0.6 \leq \eta \leq 1.0 \tag{2b}$$

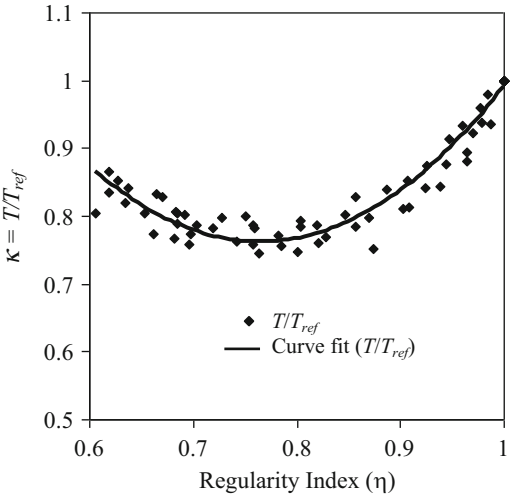

Fig. 4 Variation of time period ratio with regularity index

Figure 4 shows that the correction factor (κ) initially decreases with decreasing regularity index (i.e. increasing irregularity), and it shows minimum value of correction factor when the regularity index (η) reaches 0.75, and then it increases with decreasing regularity index. It is to be noted that this correction factor is based on the stepped building frames with regularity index ranging from 0.6 to 1.0, which generally covers the stepped buildings encountered in practice. The correction factor calculated using Eq. (2b) matches closely with the exact value obtained from the free vibration analysis results.

4 Pushover Analysis of Stepped Building

An earthquake load profiles for the nonlinear pushover analysis of stepped buildings were developed, based on SRSS combination. The basic concept is taken from the upper-bound load profile proposed by Jan et al. (2004). A study was performed to investigate the effect of higher dynamic modes in elastic time history responses of stepped building frames, and it is found that [7] the contribution of the first three modes needs to be accounted for in the elastic response of the stepped buildings. Therefore, considering the first three modes, the proposed lateral load distribution for pushover analysis of stepped building is established as

$$F_j = \sqrt{\left(\frac{m_j \phi_{1,j}}{T_1^2}\right)^2 + \left(\frac{m_j \phi_{2,j}}{T_2^2}\frac{q_2}{q_1}\right)^2 + \left(\frac{m_j \phi_{2,j}}{T_3^2}\frac{q_3}{q_1}\right)^2} \tag{3}$$

Here, F_j is the force at jth storey; m_j is the mass at jth storey; and ϕ_n, q_n and T_n are the modal coordinate, mode shape and period for nth mode, respectively.

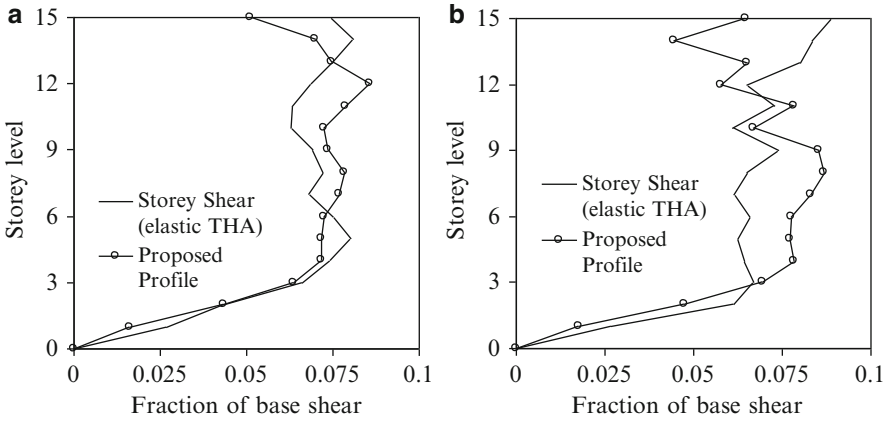

Fig. 5 Comparison of the proposed load profile with the mean storey shear profile (**a**) S1-15 (**b**) S2-15

Linear time history analyses were carried out for all the 23 designed stepped frames subjected to 20 earthquake ground motions, and the distribution of mean of the storey shear was calculated. Figure 5 presents the comparison of the proposed load profile with the mean storey shear profile obtained from linear time history analysis for a typical 15-storeyed stepped frame (S1-15 and S2-15). The figure shows that the proposed lateral load profile fairly matches closely with the storey shear profile. Figure 6 presents the comparison of the proposed lateral load profiles with some of the existing load profiles available for pushover analysis for a typical 15-storeyed stepped frame (S1-15). FEMA 356 recommends the adoption of two load profiles: (1) uniform distribution or adaptive distribution and (2) fundamental mode shape or design code-specified load distribution for equivalent static analysis.

Figure 6 shows that compared to the existing lateral load profiles, the proposed profile adds more loads in the lower storeys and reduces load in the upper storeys. The mass and stiffness of the stepped buildings get reduced at the upper floors compared to the lower floors. The reduced mass and reduced stiffness are both responsible for attracting less seismic forces at the upper floors compared to similar regular buildings without steps. This is reflecting in proposed lateral load profile. Studies carried out on other frames with different heights and bays shown similar trends.

The present study also attempts to develop an improvement to the displacement coefficient method of FEMA 356 for its application to the stepped buildings as this method is the most popular in practice. Change in building geometry will affect C_0 factor of displacement coefficient method significantly, whereas it is likely to have very little influence on the other factors. As per FEMA 356, the values of C_0 factor for shear buildings depend only on the number of storeys and the lateral load pattern used in the pushover analysis. To assess the validity of the values of C_0 factor given in FEMA 356, linear time history analysis of 78 stepped frames has been carried out for 20 earthquake ground motions, scaled for peak ground acceleration = 0.36 g.

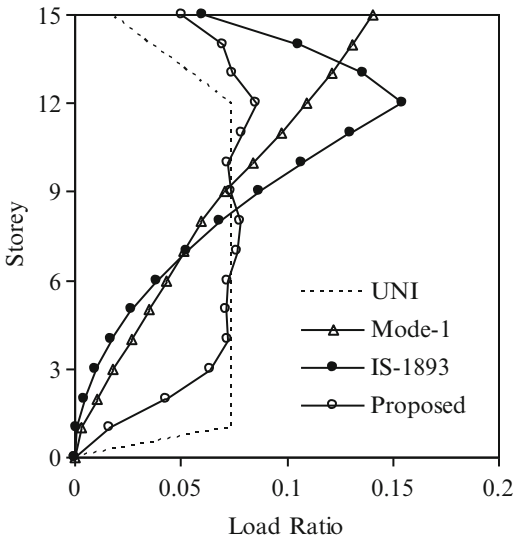

Fig. 6 Comparison of the lateral load profile

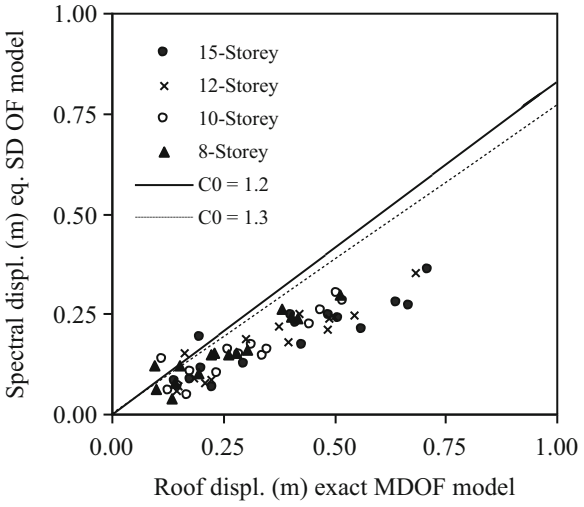

Fig. 7 Correlation of time history response for S3 frames ($0.61 < \eta < 0.76$)

The mean value of the maximum roof displacement of each frame and the mean value of spectral displacement of corresponding equivalent SDOF system for all the 20 earthquakes are calculated. The equivalent period (T_{eq}) can be generated from the base shear versus roof displacement curve (pushover curve) obtained using the proposed load profile (Eq. 3). The elastic spectral displacement corresponding to this period is calculated directly from the response spectrum representing the seismic ground motion under consideration for a specified damping ratio (5%). Figure 7 shows the results obtained for S3-type stepped frames ($0.61 < \eta < 0.76$).

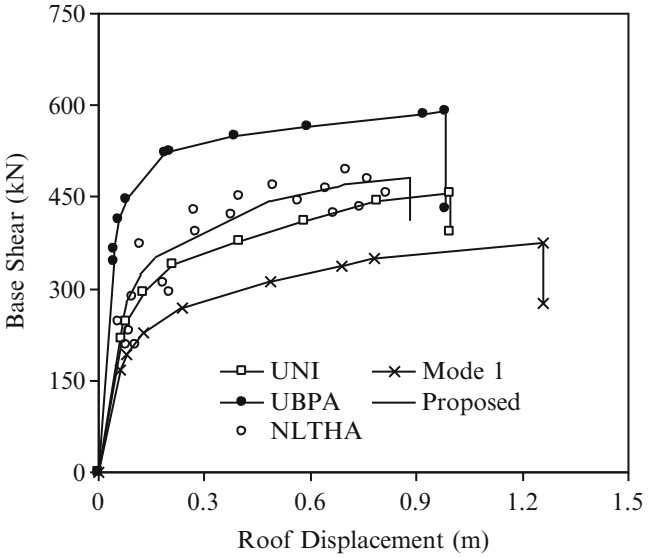

Fig. 8 Pushover curve for 15-storey stepped frame (S3-15, $\eta = 0.78$)

Results for five height categories in each of these four types of frames are shown here. This figure also shows two lines representing the C_0 values given by FEMA 356 for triangular load pattern ($C_0 = 1.3$) and uniform load pattern ($C_0 = 1.2$). It is clear from this figure that, for most of the cases, C_0 does not match with the FEMA-prescribed values.

It is found that the deviation is less for regular frames (R), but as the irregularity increases, the deviation tends to increase. Also, for the lower storey frames, the deviation from the FEMA values is less compared to the higher storey frames. This indicates that the ratio of elastic roof displacement for an exact MDOF frame to the elastic spectral displacement for equivalent SDOF system increases with the increase in the number of storeys (building height) and with decrease in regularity index (i.e. increase of irregularity). Based on the time history analysis results for 78 stepped frames, a nonlinear regression analysis has been carried out and the following empirical equation has been arrived at for calculating the value of C_0 factor:

$$C_0 = 1.5 + 0.5\eta(1-\eta)\left(\frac{h}{10} - 0.4\right) \tag{4}$$

where η = regularity index and h = building height (in m). Selected 23 designed frames with varying irregularity and height were analysed using the proposed pushover analysis procedure and other alternative procedures available in literature. The pushover analysis results are then compared with the nonlinear time history (NLTHA) analysis results for 20 selected earthquake ground motions. Figure 8

presents the comparison of typical pushover curves using the proposed lateral load profile and some of the existing load profiles available for pushover analysis. The results shown in Fig. 8 reveal that the two load patterns recommended by FEMA 356 cannot bound the solution for the stepped building with less regularity index ($\eta < 0.8$).

5 Conclusions

Stepped building frames constitute a category of vertical irregularity, whose seismic evaluation has not received adequate attention in existing research and code formulation. In this chapter, a detailed study has been carried out to address this shortcoming. The salient conclusions from the present study are:

1. A measure of vertical irregularity, suitable for stepped buildings, called 'regularity index', is proposed, accounting for the changes in mass and stiffness along the height of the building. This is simple in concept and is shown to perform better than existing measures.
2. An empirical formula (modification of the existing code formula for regular RC framed building) is proposed to calculate the fundamental time period of stepped building, as a function of regularity index. This has been validated by eigenvalue analysis performed on 78 stepped frames.
3. A lateral load profile, appropriate for stepped building frames, is proposed for use in pushover analysis. This has been validated by nonlinear time history analysis on 23 stepped frames for 20 earthquake ground motions.
4. An empirical formula (modification of existing FEMA 356 displacement coefficient method for regular RC framed building) is proposed to estimate the 'target displacement' in stepped building frames. This has similarly been validated by nonlinear time history analysis.
5. The proposed pushover analysis of RC stepped frames, incorporating the proposed load profile and 'target displacement' estimation procedure, shows consistently good performance in comparison with the existing methods of pushover analysis.

References

1. ASCE 7 (2005) Minimum design loads for buildings and other structures. American Society of Civil Engineers, Reston
2. Eurocode 8 (2004) Design of structures for earthquake resistance, part-1: general rules, seismic actions and rules for buildings. European Committee for Standardization (CEN), London
3. FEMA 356 (2000) Prestandard and commentary for the seismic rehabilitation of buildings. American Society of Civil Engineers, Reston

4. IS 1893 Part 1 (2002) Indian standard criteria for earthquake resistant design of structures. Bureau of Indian Standards, New Delhi
5. Jan TS, Liu MW, Kao YC (2004) An upper-bond pushover analysis procedure for estimating the seismic demands of high-rise buildings. Eng Struct 26:117–128
6. Rayleigh JWSB (1945) The theory of sound. Dover, New York
7. Sarkar P (2009) Seismic evaluation of reinforced concrete stepped building frames. PhD thesis, Indian Institute of Technology Madras, Chennai.
8. Sarkar P, Meher Prasad A, Menon D (2010) Vertical geometric irregularity in stepped building frames. Eng Struct 32(8):2175–2182, Elsevier

Prediction of Soaked CBR for Subgrade Layer by Using Artificial Neutral Network Model

Tapas Kumar Roy, Ambika Kuity, and Sudip Kumar Roy

Abstract Among the different layers of the pavement, subgrade is the bottom most layer, and this layer plays a very important role in the design of pavements. However proper characterization of the said layer involves different types of test data like maximum dry density (MDD), optimum moisture content (OMC), plasticity index, and California bearing ratio (CBR). Among which, CBR is the most important parameter used effectively for assessment of the strength parameter of the subgrade soil. For proper characterization of the subgrade, a large number of CBR tests are required. The CBR tests are elaborative, costly and also time consuming which may delay the progress of constructional activity of the road. In such situation, the value of soaked CBR may be predicted with the help of artificial neural network (ANN), which may help to run the project smoothly. The word "network" in ANN refers to the interconnections between the neurons in the different layers of each system. Those preliminary testing data i.e. percent fines, MDD, OMC, LL, PL, PI etc., are required to find out the regression value and mean square error of the training, validation, and test data to create a model by using neural network algorithm. The tested data are taken during testing the model. The method is based on ANN is found to be reliable, cost-effective, and a quick tool for reasonably accurate estimation of CBR from the basic soil properties.

Keywords Subgrade • Soaked CBR • Artificial neural network • Backpropagation algorithm

T.K. Roy (✉) • A. Kuity • S.K. Roy
Bengal Engineering and Science University, Shibpur, Howrah, West Bengal, India
e-mail: tapash2000@hotmail.com; sudip@civil.becs.ac.in; ambika.kuity86@gmail.com

S. Chakraborty and G. Bhattacharya (eds.), *Proceedings of the International Symposium on Engineering under Uncertainty: Safety Assessment and Management (ISEUSAM - 2012)*,
DOI 10.1007/978-81-322-0757-3_83,

1 Introduction

A major portion of the road networks in India are reported to be composed of flexible pavement as per highway statistics (http://en.wikipedia.org/wiki/West_bengal), and such pavements are multilayered, heterogeneous structures that are designed to "flex" under repeated traffic loading. The service life and performance of pavements depend to a large extent on the strength and stiffness characteristics of subgrade [8]. Also, the characteristics of subgrade assist road engineers in the selection of materials for subbase and base courses of pavement [4]. Hence, the evaluation of subgrade strength assumes great importance in pavement design. In determination of the strength of soil subgrade, the California bearing ratio (CBR) test that estimates the bearing capacity of pavement subgrades with respect to the strength of well-graded high-quality crushed stone aggregate was used for a long time. Most of the current flexible pavement design methods are generally empirical and based on the CBR of subgrade [5]. Among this, CBR method is the most influential early work on pavement design, and associated soil testing was carried out by the California Division of Highways. This CBR method was gradually adopted in the UK and elsewhere. The Indian Roads Congress (IRC) first brought out guidelines in 1970 for the design of flexible pavement in India based on California bearing ratio and recommended the design charts from which the thickness of pavements was estimated for design traffic load and CBR value of subgrade. These design curves were later revised by IRC in the year 1984 in order to accommodate heavy volume of traffic. IRC had further revised these guidelines in 2001 with the adoption of empirical-mechanistic approved in design. But the design method is still based on CBR subgrade. The tests are conducted as per IS: 2720 (per XVI) 1979, and for achieving the results in soaked condition, 96 hrs soaking of the sample are essential. So, this method is time consuming and laborious [18]. Over the last few years or so, the use of ANNs has increased in many areas of engineering. In particular, ANNs have been applied to many geotechnical engineering problems and have demonstrated some degree of success [16]. But in pavement engineering, ANN is mostly used to find out surface deflections resulting from applied impulsive load [11]. A study has been made for accurate estimation of the stiffness of cement-bound base courses using deflection measurements [13]. ANN's applications have been used in the development of estimating several soil properties such as soil strength [10], soil classification [6], and preconsolidation pressure [7]. Literature is also available to predict CBR of soil by ANN [12]. The method based on ANN requires two sets of data – training data, and tested data and in this paper, the data collected by the West Bengal State Rural Development Authority (WBSRDA) for the design of Pradhan Mantri Gram Sadak Yojana (PMGSY) projects are used as training data. The data are grain size, liquid limit, plastic limit, plasticity index, maximum dry density, optimum moisture content, and subgrade soaked CBR value of alluvial soil.

2 Artificial Neutral Network

A neural network is an interconnected assembly of simple processing elements, units, or nodes whose functionalities are loosely based on the animal neurons. The processing ability of the network is stored in the interunit connection strengths, or weights, obtained by a process of adaption to, or learning from, a set of training patterns by Kevin Gurney [20]. One type of network sees the nodes as "artificial neurons." These are called artificial neural networks. An artificial neuron is a computational model inspired in the natural neurons. Neural networks are composed of simple elements operating in parallel [3]. These elements are inspired by biological nervous systems. It is a network with interactions, in attempt to mimicking the brain [17]. The part of mimicking the brain is achieved technically by arranging the neuron in three different parts:

Units: artificial neuron (linear or nonlinear input-output unit), small numbers, a few hundreds
Interactions: simply by weights, how strong a neuron affects others [4]
Structure: could be feed forward, feedback, or recurrent

3 Utilization of Collected Sample Data for ANN

Total instance is 80 and among of which, are considered as training data and used to the network during training, and the network is adjusted according to its error; balance 15%, i.e., 12, are considered as validation data and used to measure network generalization and to halt training when generalization stops improving, and another balance 15%, i.e., 12, are considered as testing data, and the same have no effect on training and so provide an independent measure of network performance during and after training [1]. Statistical parameters of the data used for training, validation, and testing are given in Table 1. Mean value, maximum value, minimum value, and standard deviation have been calculated for training data, validation data, and testing data separately.

Table 1 Regression value and mean square error for training, validation, and testing data

	Training data		Validation data		Testing data	
Network	*R*-value	MSE value	*R*-value	MSE value	*R*-value	MSE value
7-2-1	9.869e-1	6.915e-3	9.892e-1	4.376e-3	8.093e-1	1.639e-2
7-3-1	9.831e-1	8.677e-3	9.111e-1	4.720e-3	9.875e-1	6.485e-3
7-4-1	9.885e-1	4.697e-3	8.724e-1	8.868e-3	9.917e-1	9.402e-3
7-5-1	9.854e-1	7.041e-3	9.869e-1	8.870e-3	9.719e-1	2.095e-2
7-6-1	9.941e-1	3.309e-3	9.809e-1	2.064e-2	8.902e-1	1.117e-2
7-7-1	9.553e-1	2.141e-2	6.145e-1	7.470e-3	9.897e-1	2.982e-2
7-8-1	9.969e-1	2.096e-3	8.575e-1	1.113e-2	6.541e-1	2.436e-2
7-9-1	9.933e-1	5.137e-3	7.451e-1	1.559e-2	9.728e-1	1.241e-2

4 Input and Output Layer

In input layer, seven kinds of characteristics are considered as input, and they are given below:

1. Sieve analysis and percentage of passing
   (a) 4.25 mm
   (b) 2 mm
   (c) 0.425 mm
   (d) 0.075 mm
2. Plasticity index (%)
3. Standard proctor test
   (a) Maximum dry density(g/cc)
   (b) Optimum moisture content (%)

The output layer consists only measured soaked CBR value.

5 Structure of ANNS

Neural networks are typically arranged in layers. Each layer in a layered network is an array of processing elements or neurons. Information flows through each element in an input-output manner. In other words, each element receives an input signal, manipulates it, and forwards an output signal to the other connected elements in the adjacent layer. The units in the output layer receive the weighted sum of incoming signals and process it using an activation function [14]. Information is propagated forward until the network produces an output. For smoothly running the ANN structure, one of the most popular multilayer perceptron learning rules is the error backpropagation algorithm. The backpropagation learning is a kind of supervised learning introduced by Werbos [19] and later developed by Rumelhart and McClelland [15]. At the beginning of the learning stage, all weights in the network are initialized to small random values [2]. The algorithm uses a learning set, which consists of input pattern–desired output pattern pairs and the flow diagram of the same is shown in Fig. 1.

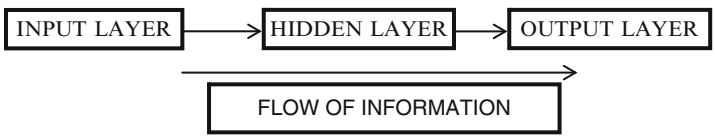

Fig. 1 Structure of artificial neutral network

6 Running the ANN Model

Neural network training follows the Levenberg-Marquardt backpropagation algorithm under supervised learning method. Each input–output pair is obtained by the offline processing of historical data. These pairs are used to adjust the weights in the network to minimize the mean squared error (MSE) which measures the difference between the real and the desired values of overall output neurons and all learning patterns. In this paper, seven inputs and one output are taken into consideration. The number of hidden neuron has been taken as 2, 3, 4, 5, 6, 7, 8, and 9. But in the case of training, the regression value and mean square error value are maximum and minimum in the case of the four numbers of hidden neurons.

7 Data of Neutral Network

From the above Tables 2, 3, and 4, the soaked CBR's measured data and predicted data are used to layout the graphical representation of sample number for training set, validation set, and testing set, respectively, in Figs. 2, 3, and 4.

8 Result and Discussion

In the training data set, validation data set, and testing data set, the error lies within the range of +0.1551 to −0.1312%, +0.1332 to −0.0746%, and +0.1904 to −0.0767%, respectively. These errors are less than 0.20%. After adjusting the hidden neurons in hidden layer, the more efficient result is coming out for the four numbers of hidden neurons. In this artificial neural network, the regression (R) values are 9.885e-1, 8.724e-1, and 8.917e-1, respectively, for training data, validation data, and testing data, respectively. Mean square errors are 4.697e-3, 8.868e-3, and 9.402e-3 for training, validation, and testing data individually.

9 Weight Analysis

The higher a weight of an artificial neuron is, the stronger the input which is multiplied by it will be [9]. Weights can also be negative, so it can say that the signal is inhibited by the negative weight. Depending on the weights, the computation of the neuron will be different and the weight of input parameters as computed in this study are shown in Table 5.

Table 2 Training data used for training the ANN model

	Sieve analysis % passing					Standard proctor test		Soaked CBR value (%)		
Sl no	4.25 mm	2.00 mm	0.425 mm	0.075 mm	Plasticity index (%)	MDD (g/cc)	OMC (%)	Measured	Predicted	Error (%)
1	99.06	97.01	92.28	73.03	15.76	1.85	10.23	5.4	5.3726	0.0274
2	99.53	97.3	94.45	74.91	16.07	1.82	11.85	5.2	5.1443	0.0557
3	99.32	97.3	93.27	75.86	15.99	1.81	11.98	5.1	5.1317	−0.0317
4	99.4	97.35	94	75.86	15.07	1.79	12.62	5.1	5.0877	0.0123
5	99.45	97.36	94.11	75.53	15.18	1.81	12.37	5.1	5.1033	−0.0033
6	99.93	97.55	93.53	74.28	16.08	1.84	11.3	5.3	5.28866	0.0134
7	99.53	97.66	93.86	73.57	16.06	1.85	10.55	5.4	5.3126	0.0874
8	99.47	98.28	94.54	75.17	14.95	1.81	12.09	5.2	5.1426	0.0574
9	99.32	97.71	94.54	73.87	16.08	1.83	11.59	5.3	5.1721	0.1279
10	99.27	97.28	93.21	74.68	14.96	1.82	11.92	5.2	5.814	0.0186
11	99.35	98.22	95.45	75.72	14.75	1.8	12.79	5.1	5.0431	0.0569
12	99.65	98.07	94.56	76.52	14.87	1.79	12.93	5.1	5.0603	0.0397
13	99.32	97.86	94.47	74.86	15.23	1.81	11.85	5.2	5.1564	0.0436
14	99.26	97.27	92.38	73.98	15.18	1.84	11.46	5.3	5.2700	0.0300
15	99.31	97.83	94.1	74.46	15.66	1.82	11.21	5.2	5.2330	−0.0330
16	99.25	97.24	92.75	74.38	15.64	1.82	11.09	5.2	5.2784	−0.0784
17	99.32	97.68	93.64	75.24	12.62	1.89	12.34	5.2	5.2060	−0.0060
18	99.67	98.84	94.97	77.55	15.53	1.84	14.87	4.9	4.9226	−0.0226
19	99.45	98.11	95.24	76.66	14.38	1.85	14.46	4.9	5.0029	−0.1029
20	99.65	98.51	95.24	78.21	15.93	1.82	15.39	4.8	4.7831	0.0169
21	99.53	97.66	94	75.29	12.46	1.89	12.13	5.2	5.2165	−0.0165
22	99.47	98.28	95.41	76.28	11.87	1.86	13.82	5	5.0104	−0.0104
23	99.27	97.28	92.81	74.48	10.41	1.91	11.73	5.4	5.3048	0.0952
24	99.38	97.33	95.86	75.46	11.33	1.88	13.38	5.1	5.0961	0.0039
25	99.2	97.47	94.22	74.57	12.6	1.9	11.94	5.3	5.2236	0.0764
26	99.35	97.49	95.44	75.77	11.55	1.87	13.81	5	5.0705	−0.0705
27	99.38	98.15	94.89	75.09	12.7	1.93	11.13	5.3	5.2536	0.0464
28	99.27	97.6	94.35	73.94	10.78	1.93	10.29	5.5	5.3699	0.1301
29	99.65	98.91	95.68	76.49	14.41	1.72	13.55	5.2	5.2055	−0.0055

30	99.25	97.42	93.81	74.52	14.86	1.73	12.74	5.1	5.2021	−0.1021
31	99.45	98.91	97.28	76.32	14.16	1.72	13.69	5.3	5.2074	0.0926
32	99.59	98.62	95.05	75.67	15.41	1.72	13.32	5.1	5.1622	−0.0622
33	99.61	97.84	94.33	75	14.9	1.73	12.62	5.4	5.2449	0.1551
34	99.41	98.63	95.68	76.71	14.47	1.71	13.92	5.2	5.1703	0.0297
35	99.58	98.63	96.6	77.65	14.18	1.72	13.87	5.2	5.1981	0.0019
36	99.32	97.68	93.64	75.24	12.62	1.75	12.34	5.2	5.3312	−0.1312
37	99.67	98.84	95.97	77.55	15.53	1.73	14.87	4.9	4.8721	0.0279
38	99.45	98.11	95.24	76.66	14.38	1.72	14.46	4.9	4.9877	−0.0877
39	99.65	98.51	95.24	78.21	15.93	1.71	15.39	4.8	4.7945	0.0055
40	100	99.1	97.1	74.69	13.52	1.74	13.41	5.1	5.1421	−0.0421
41	99.65	99.25	95.82	73.27	13.22	1.76	12.07	5.3	5.3247	−0.0247
42	100	99.03	97.03	74.63	14.71	1.74	13.67	5.1	5.0329	0.0608
43	99.39	98.12	95.1	72.86	14.11	1.75	12.82	5.2	5.1506	0.0494
44	98.97	97.36	95.49	73.32	13.39	1.74	13.25	5.1	5.0977	0.0023
45	100	99.66	98.19	72.69	13.14	1.76	12.2	5.3	5.2892	0.0108
46	99.93	98.26	97.65	74.33	13.7	1.74	13.31	5.1	5.1116	−0.0116
47	100	99.53	96.86	75.52	14.98	1.73	14.23	5	4.9912	0.0088
48	99.06	97.01	92.28	73.03	11.88	1.78	9.49	5.5	5.5306	−0.0306
49	99.53	97.3	94.45	74.91	10.21	1.77	10.78	5.4	5.4337	−0.0337
50	99.48	98.07	94.38	73.12	14.12	1.75	13.89	5	5.0859	−0.0859
51	99.36	97.93	95.03	72.13	14.29	1.77	12.81	5.2	5.1461	0.0539
52	99.59	98.45	95	73.03	14.12	1.75	13.59	5.1	5.0848	0.0152
53	99.25	97.71	94.59	71.12	14.72	1.78	11.57	5.3	5.2837	0.0163
54	99.67	98.08	95.14	72.21	14.09	1.77	12.71	5.2	5.1809	0.0191
55	99.86	99.05	96.38	73.35	14	1.76	13.79	5.1	5.0427	0.0573
56	99.58	97.97	94.24	70.99	14.64	1.78	11.28	5.3	5.3693	−0.0693

Table 3 Validation data used to check the validity of ANN model

	Sieve analysis % passing					Standard proctor test		Soaked CBR value (%)		
Sl no	4.25 mm	2.00 mm	0.425 mm	0.075 mm	Plasticity index (%)	MDD (g/cc)	OMC (%)	Measured	Predicted	Error (%)
1	99.68	99.12	96.29	73.02	15.47	1.75	13.29	5	5.0535	−0.0535
2	97.97	96.34	93.35	70.78	14.96	1.77	12.64	5.1	5.1304	−0.0304
3	99.95	99.65	98.58	90.55	16.59	1.67	16.59	3.6	3.6299	−0.0299
4	99.95	99.31	97.48	91.43	16.55	1.66	18.26	3.4	3.4624	−0.0624
5	99.85	99.47	98.25	92.69	18.86	1.65	19.19	3.3	3.3074	−0.0074
6	99.71	99.22	98.16	90.26	16.4	1.67	16.34	3.6	3.6576	−0.0576
7	99.53	98.51	96.6	74.62	12.54	1.88	11.47	5.1	5.1746	−0.0746
8	99.22	97.78	95.49	74	12.26	1.89	11.23	5.2	5.2134	−0.0134
9	99.63	98.5	96.16	73.54	10.62	1.92	9.79	5.5	5.4719	0.0281
10	99.25	97.6	95.32	73.27	12.39	1.9	10.98	5.4	5.2668	0.1332
11	99.8	99.13	96.66	74.97	13.3	1.86	11.95	5.1	5.1395	−0.0395
12	99.51	98.27	96.69	77.14	14.26	1.85	12.33	5	5.0378	−0.0378

Table 4 Testing data used to test the ANN model

	Sieve analysis % passing					Standard proctor test		Soaked CBR value (%)		
Sl no	4.25 mm	2.00 mm	0.425 mm	0.075 mm	Plasticity index (%)	MDD (g/cc)	OMC (%)	Measured	Predicted	Error (%)
1	100	99.82	98.78	75.31	24.69	27.74	12.56	5.5	5.5348	−0.0348
2	99.27	97.67	93.92	78.13	21.14	32.19	14.81	4.9	4.8527	0.0473
3	98.48	95.02	90.18	72.91	25.57	24.87	10.85	5.6	5.4096	0.1904
4	99.23	97.49	94.84	75.57	23.66	29.61	13.24	5.2	5.1126	0.0874
5	99.4	97.34	92.87	75.42	23.98	27.97	12.83	5.3	5.2533	0.0467
6	99.62	98.08	95.04	77.64	21.98	31.26	14.07	5	4.9590	0.0410
7	98.13	94.06	86.87	73.4	24.73	24.52	10.58	5.4	5.4335	−0.0335
8	98.95	96.9	95.17	74.8	24.15	29.89	13.32	5.2	5.1813	0.0187
9	99.99	99.75	97.9	74.89	25.1	22.25	10.03	5.5	5.5203	−0.0203
10	99.92	97.25	95.43	74.12	25.8	25.47	11.27	5.4	5.3192	0.0808
11	100	100	100	97	3	29.54	16.45	3.5	3.5767	−0.0767
12	100	100	97	92	8	28.47	15.2	3.75	3.6652	0.0848

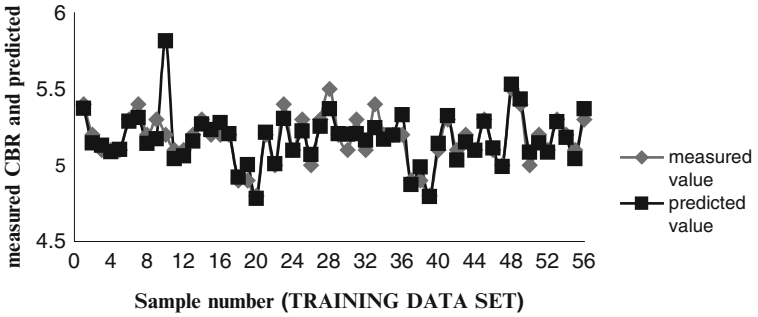

Fig. 2 Comparison of measured (lab) CBR vs. the BPNN-predicted CBR training data

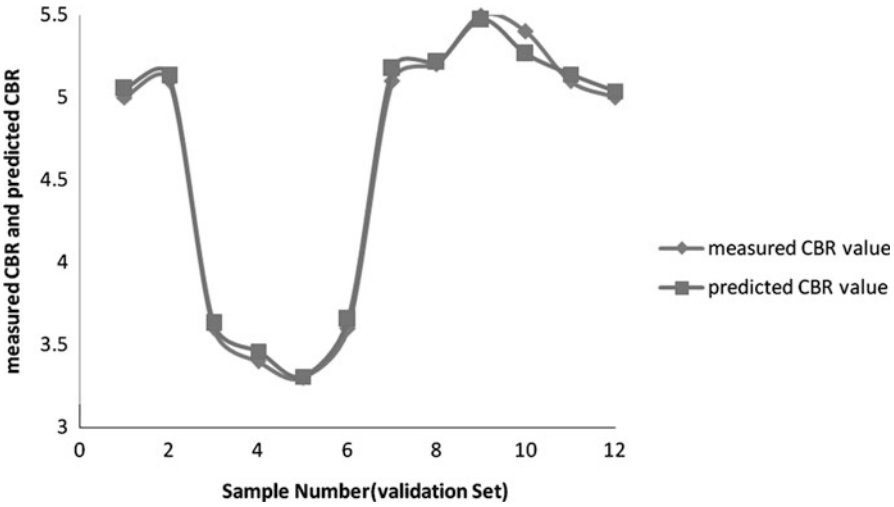

Fig. 3 Comparison of measured (lab) CBR vs. the BPNN-predicted CBR validation data

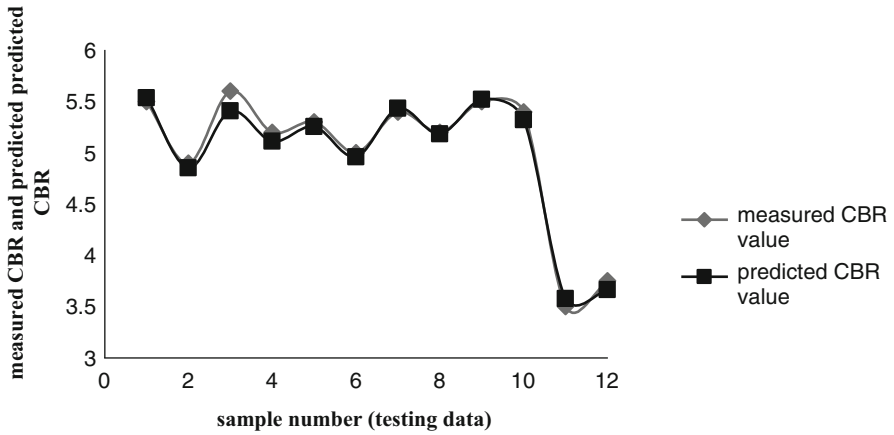

Fig. 4 Comparison of measured (lab) CBR vs. the BPNN-predicted CBR testing data

Table 5 Weight of input parameter

Input parameters	Weight from ANN model	Relative importance (%)
I. Sieve analysis and percentage of passing		
(a) 4.25 mm	0.44279	11.08
(b) 2 mm	0.28274	7.08
(c) 0.425 mm	0.61339	15.35
(d) 0.075 mm	0.64440	16.13
II. Plasticity index (%)	0.85194	21.32
III. Standard proctor test		
(a) Maximum dry density(g/cc)	0.54888	13.74
(b) Optimum moisture content (%)	0.61143	15.30

10 Conclusion

The number of hidden neurons has great influence to establish a better artificial neural network. But in this investigation, priority has been given on four numbers of hidden neurons for achieving the design regression value with minimum error. To find out the precious value of error, the weight on input parameters has the great influence in the ANN model. Plasticity index has the major priority of 21.32% weight among the other input parameters, and the percentage of passing through 2-mm sieve has the less effect of 7.08%. Otherwise, all other parameters appear to be almost equal impact on the result within the range of 11.08–16.13%.

In this network model, results of comparison made by determining error indicated that the variation between the measured value and predicted value of CBR is less than 0.20%. So this model may help the designer, contractors, and managers to develop a better understanding about the soil types and their strength characteristics which is very much essential for designing, bidding, and construction of a roadway pavement.

Acknowledgment Authors are thankful to the University Grant Commission (UGC) for their financial support during the entire period of study. The assistance of the West Bengal State Rural Development Authority (WBSRDA) in the collection of test data is gratefully acknowledged.

References

1. Arulmozhi V (2011) Classification task by using Matlab Neural Network Tool Box-A beginner's view. Int J Wishdom Based Comput 1(2):59–60
2. Azadeh A, Maghsoudi A, SohrabKhani S (2009) Using an integrated artificial neural networks model for predicting global radiation: the case study of Iran. Elsevier 50(6):1497–1505
3. Ball R, Tissot P (2006) Demonstration of artificial neural network in Matlab, Division of Nearhsore Research, Texas A&M University – Corpus Christi, pp 1–5

4. Berrymam CW et al (2010) Computer aided modelling of soil mix designs to predict characteristics and properties of stabilized road bases. Nebraska department of roads, final report. p 319
5. Brown SF (1996) Soil mechanics in pavement engineering. Geotechnical 46(3):383–426
6. Cal Y (1995) Soil classification by neural -network. Adv Eng Softw 22(2):95–97
7. Celik S, Tan O (2005) Determination of pre consolidation pressure with artificial neural network. Civil Eng Environ Syst 22(4):217–231
8. Geroge V, Rao CN, Shivasankar R (2009). Investigation on unsoaked blended laterite using PFWD, PBT, DCP and CBR tests. Paper no556, pp 224–233
9. Gershenson C (2003) Artificial neural networks for beginners, computer science, neural and evolutionary computing, tutorial, pp 1–8
10. Goh ATC (1995) Modelling soil correlations using neural networks. J Comput Civ Eng ASCE 9(4):275–278
11. Gopalkrishnan K (2010) Effect of training algorithms on neural networks aided pavement diagnosis. Int J Eng Sci Technol 2(2):83–92
12. Kaur S, Ubboveja VS, Agarwal A (2011) Artificial neural network modelling for prediction of CBR. Indian Highw 39(1):31–37
13. Miradi M, Molenaar AAA, Van de Van MFC (2009) Back calculation procedure for the stiffness modulus of cement treated base layers using computational intelligence based models. TRB, annual meeting CD-ROM
14. Rajasekaran S, Vijayalakshmi Pai GA (2010) Neural networks, fuzzy logic, and genetic algorithms synthesis and applications, 14th edn. PHI Learning Private Limited, Prentice Hall Connaught circus, New Delhi-110001
15. Rumelhart DE, McClelland JL (1986) Parallel distributed processing: explorations in the microstructure of cognition, vol I. MIT Press, Cambridge, MA, pp 318–362
16. Shahin MA et al. (2001) Artificial neural network applications in geotechnical engineering. Australian Geomechanics 36:49–62
17. Sivanandam SN, Sumathi S, Deepa SN (2006) Introduction to neural networks using Matlab 6.0. Tata McGraw Hill Publishing Company Limited, New Delhi
18. Swamy GN, Kumar GV (2006) Neural networks. Scitech Publications (India) Pvt. Ltd., Chennai-600017:1.3
19. Werbos PJ (1974) Beyond regression: new tools for prediction and analysis in the behavioral sciences. PhD thesis, Harvard University
20. Wu S, Sargand S (2007) Use of dynamic cone penetrometer in subgrade and base acceptance. Ohio University, Ohio research Institute for Transportation and Environment Stocker Center,141 Athens, Ohio, pp 45701–2979

Prediction of the Stiffness of Nanoclay-Polypropylene Composites Using a Monte Carlo Finite Element Analysis Approach

G.S. Venkatesh, A. Deb, A. Karmarkar, and N.D. Shivakumar

Abstract The present work deals with the prediction of stiffness of an Indian nanoclay-reinforced polypropylene composite (that can be termed as a nanocomposite) using a Monte Carlo finite element analysis (FEA) technique. Nanocomposite samples are at first prepared in the laboratory using a torque rheometer for achieving desirable dispersion of nanoclay during master batch preparation followed up with extrusion for the fabrication of tensile test dog-bone specimens. It has been observed through SEM (scanning electron microscopy) images of the prepared nanocomposite containing a given percentage (3–9% by weight) of the considered nanoclay that nanoclay platelets tend to remain in clusters. By ascertaining the average size of these nanoclay clusters from the images mentioned, a planar finite element model is created in which nanoclay groups and polymer matrix are modeled as separate entities assuming a given homogeneous distribution of the nanoclay clusters. Using a Monte Carlo simulation procedure, the distribution of nanoclay is varied randomly in an automated manner in a commercial FEA code, and virtual tensile tests are performed for computing the linear stiffness for each case. Values of computed stiffness modulus of highest frequency for nanocomposites with different nanoclay contents correspond well with the experimentally obtained measures of stiffness establishing the effectiveness of the present approach for further applications.

Keywords Polypropylene • Nanoclay • Nanocomposite • Stiffness • Monte Carlo simulation • Randomness

G.S. Venkatesh (✉) • A. Deb • N.D. Shivakumar
Centre for Product Design and Manufacturing, Indian Institute of Science, Bangalore, India
e-mail: venkatesh@cpdm.iisc.ernet.in; adeb@cpdm.iisc.ernet.in

A. Karmarkar
Institute of Wood Science and Technology, Malleswaram, Bangalore, India
e-mail: ajay@icfre.org

S. Chakraborty and G. Bhattacharya (eds.), *Proceedings of the International Symposium on Engineering under Uncertainty: Safety Assessment and Management (ISEUSAM - 2012)*,
DOI 10.1007/978-81-322-0757-3_84,

1 Introduction

It has been well known in the recent times that the addition of small amounts of nanoparticles to a polymer matrix can have a strong influence on its mechanical response. Nanocomposites are composite materials in which the matrix material is reinforced with one or more separate nanomaterials in order to improve mechanical and physical properties [1–5]. A higher weight of filler loading (up to 50%) is usually required in order to impart the desired mechanical or thermal properties to the virgin polymer, but organically modified layered silicates (organoclay) can achieve the same properties with typically 2–5% by weight of filler, thereby producing materials of lower density and better processing ability [6]. The properties of the composites depend on the properties of respective constituent materials and on the filler microstructures such as size, shape, orientation, and spatial arrangement embedded in the matrix. Nanoparticles in the matrix can exist separately or as clusters. The arrangement of these clusters or individual particle during manufacturing can give different stiffness to the composites.

Standardized and statistically determined material properties along with experimental results are important in efficient design and development of products. Based on the requirements from the design and manufacturing community, statistically determined material properties can give the guidelines for design and manufacturing engineers. However, among the challenges encountered in simulation are the selection of appropriate input distributions to characterize the stochastic behavior of the modeled system [7, 8]. Failure to select appropriate input distributions can result in misleading simulation output and therefore to inappropriate material design decisions.

Monte Carlo methods are a class of computational algorithms that rely on repeated random sampling to compute their results. These methods are most suited to calculation by a computer and tend to be used when it is infeasible to compute an exact result with a deterministic algorithm and to model phenomena with significant uncertainty in inputs. It uses random numbers to do statistical experiment, and then statistical Eigen value is the approximate solution of the problem. Lu et al. [9] carried out a Monte Carlo simulation based on elastic-plastic finite element analysis for estimating effect of matrix property on composite strength and reliability. They showed that if yield stress or work hardening of the matrix decreased, composite strength decreased and the strength scatter increased. The mechanical response, predominantly in the small deformation regime, has been studied by Jorgen and Boyce [10] using the finite element method, and the latter authors have shown that it is possible to get quantitative agreement between experimental data and FE (finite element) simulations, particularly, the correlation between volume fraction of filler particles and the initial Young's modulus of the material. They also claimed that stochastic simulations of three-dimensional representative volume elements containing many filler particles could be accurately modeled to get better correlation.

In the current work, stiffness of polypropylene (PP) reinforced nanoclay composites is determined through experiments. FEA in conjunction with Monte

Carlo simulation was carried out to know the effects of position and orientation of nanoclay clusters in the polymer matrix leading to the development of PP-nanocomposites with different volume fractions of nanoclay. Atomic force microscopy was used to confirm that the clusters comprised of nanoclay platelets are indeed present in parallel orientations as this configuration only yields closest correlation of predicted stiffness of nanocomposite with experimental result.

2 Experimental Procedure

2.1 Formulation of Nanocomposites

Natural montmorillonite modified with quaternary ammonium salt (Crysnano 1010P), procured from Crystal Nanoclay Pvt. Ltd., Pune, India, was chosen as the reinforcing material. Isotactic PP with the trade name Repol H110MA and supplied by Reliance Polymers India was used as the matrix in the formulation of the nanocomposite.

PP granules (30 g) were added to the mixing chamber of a torque rheometer preheated to 150°C. Thirty grams of oven-dried nanoclay was then added to the mixing chamber. After thorough mixing for sufficient time, the blend was removed and cooled to room temperature. The resulting lumps of nanoclay-PP mixture, referred to here as "master batch," were later palletized into approximately 3-mm-sized pallets which were now ready for formulating the nanoclay-PP composite specimens with varying percentages (in the range of 3–9% by weight) of nanoclay. An appropriate amount of nanoclay-PP taken from the master batch and a required amount of pure PP were dry blended in a blender, and the dry mixture was then fed into the inlet hopper of a corotating twin-screw extruder and heated through several stages ranging from 165 to 180 °C. The usage of the twin-screw extruder ensured a homogeneous compounding of PP and nanoclay in an efficient manner resulting into a nanocomposite, which has been subsequently labeled as PPN_x (x being the concentration of nanoclay by weight varying from 3 to 9%) in the present study. The nanocomposite was recovered from the twin-screw extruder in the form of a molten extrudate, which was guided into a standard cold water stranding bath. The cooled strands were chopped into pellets, dried, and stored in sealed plastic bags. Finally, the compounded pallets of nanoclay-PP composites were molded into standard ASTM-type specimens using a microprocessor-controlled closed-loop injection molding machine.

2.2 Tensile Coupon Tests

Tensile tests were conducted in accordance with ASTM D638 [11] standard using type I specimens. Cross-head speed was set at 50 mm/min for the tensile tests. Deflection was recorded using a strain gauge-type extensometer with a span of 50 mm.

3 Micromechanical Modeling

Micromechanical modeling is a tool that can be employed to estimate the mechanical properties of a composite material on the basis of the properties of its constituents and their microstructural ordering. In order to analyze a microstructure by a micromechanical finite element simulation, there are basically two requirements: (1) the definition of a representative volume element (RVE) that accounts for the microstructural arrangement of the components and (2) the choice of appropriate constitutive laws that are able to describe the different features of the deformation behavior realistically.

SEM images of PP-nanocomposites were obtained from Quanta LV/ESEM scanning electron microscope. SEM micrographs were analyzed using SigmaScan Pro image analyzer software. Figure 1 shows an SEM image of PPN_3. It is observed from this figure that nanoclay clusters are randomly distributed in the polymer matrix. Information such as number of nanoparticle clusters and area occupied by the clusters in a total area of composite of 300 μm × 300 μm is obtained by SigmaScan Pro image analysis software and is used to construct an RVE in the analysis carried out here. It is noted that construction of an RVE that can realistically reflect the underlying multiscale hierarchical structure of a nanocomposite is critical for reliable property prediction. A good RVE should have all major geometric and material characteristics. The geometric features include attributes of nanoparticle clusters, in particular, their average shape, size, dispersion, and orientation. To estimate the effective properties of the nanocomposite based on the SEM image of Fig. 1 and material properties of the constituent phases, FEM (finite element modeling)-based micromechanics has been used.

The overall stress and strain of a composite with N distinct phases can be represented [12] as follows:

$$\overline{\sigma} = \sum_{r=1}^{N} \phi_r \overline{\sigma}_r \tag{1}$$

$$\overline{\varepsilon} = \sum_{r=1}^{N} \phi_r \overline{\varepsilon}_r \tag{2}$$

$$\overline{\sigma}_r = \left[\sigma_x \quad \sigma_y \quad \sigma_z \quad \sigma_{xy} \quad \sigma_{yz} \quad \sigma_{xz} \right]_r^T \tag{3}$$

$$\overline{\varepsilon}_r = \left[\varepsilon_x \quad \varepsilon_y \quad \varepsilon_z \quad \varepsilon_{xy} \quad \varepsilon_{yz} \quad \varepsilon_{xz} \right]_r^T \tag{4}$$

where $\overline{\sigma}_r$ represents stress components and $\overline{\varepsilon}_r$ strain components of phase r, $\phi_r$is the volume fraction of phase r, and the overbar denotes a volume-averaged quantity.

In the case of a linear static structural analysis, the assembled finite element equations are of the form

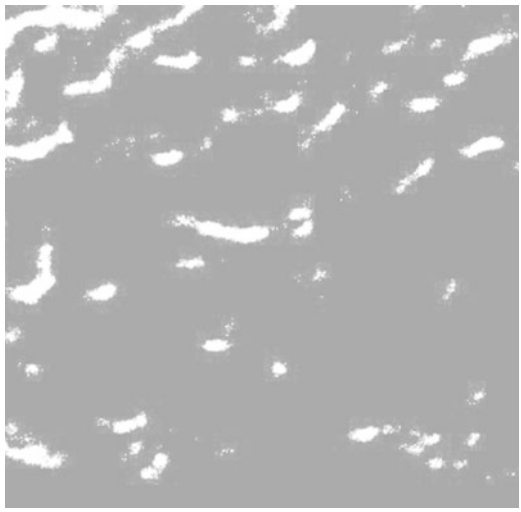

Fig. 1 SEM image of PPN_3 analyzed through SigmaScan Pro software

$$K\overline{d} = \overline{R} \tag{5}$$

where K is the system stiffness matrix, $\overline{d}$ is the nodal degrees of freedom displacement vector, and $\overline{R}$ is the applied load vector. Composite materials can be envisaged as a periodical array of the RVEs. Therefore, the periodic boundary conditions must be applied to the RVE models. This implies that each RVE in the composite has the same deformation mode and there is no separation or overlap between the neighboring RVEs [13]. This periodicity condition on the boundary is given as

$$u_i = \overline{\varepsilon}_{ik} x_k + u_i^* \tag{6}$$

where $\overline{\varepsilon}_{ik}$ are the average strains, x_k is a position vector from a reference point to a point on the boundary, and u_i^* is the periodic part of the displacement components on the boundary surfaces which is generally unknown and is dependent on the applied global loads.

In current finite element modeling, the following material and geometric properties are used for the constituent phases:

Polypropylene (matrix)

E_m = 1,755 MPa (Young's modulus – average experimental result)

v_m = 0.3 (Poisson ratio)

V_m = Volume fraction of matrix

W_m = Weight fraction of matrix

Table 1 Weight and volume fraction of nanoclay composites

Material	Weight fraction of nanoclay (%)	Volume fraction of nanoclay (%)
PPN_3	3	1.44
PPN_6	6	2.88
PPN_9	9	4.32

$\gamma_m = 8{,}829\ \text{N/m}^3$ (specific weight of matrix)

Nanoclay (particle reinforcement)

$E_p =$ 2E05 MPa (Young's modulus)
$\nu_p = 0.3$ (Poisson ratio)
$V_p =$ Volume fraction of nanoclay
$W_p =$ Weight fraction of nanoclay
$\gamma_p = 18{,}639\ \text{N/m}^3$ (specific weight of nanoclay)

Volume fractions of nanoclay particulate reinforcement corresponding to different weight fractions of nanoclay, and densities of matrix and nanoclay can be obtained from the following relation and are given in Table 1:

$$V_p = (W_p/\gamma_p)/(W_p/\gamma_p + (1 - W_p)/\gamma_m) \tag{7}$$

In the FEM-based prediction of mechanical properties of nanoclay-PP composite to be described later, plane stress analysis has been resorted to. This approach has been followed due to reasons such as (1) the thin plate profile of the nanocomposite specimens tested, (2) feasibility of obtaining an SEM image for ascertaining spatial distribution of nanoclay platelets and area occupied relative to matrix area, and (3) computational efficiency of a planar model especially when a large number of simulations are involved. It may be noted that planar idealizations of three-dimensional distribution of discontinuous reinforcements for the convenience of numerical study have been adopted in the past [14].

4 Monte Carlo Simulation

A Monte Carlo simulation can be regarded as a probabilistic technique that makes use of random numbers to analyze a problem [15]. In a typical Monte Carlo approach, values of input parameters are generated in a random manner and the problem is solved deterministically for every set of input data; an inference is then drawn by statistically analyzing the output results for all cases solved.

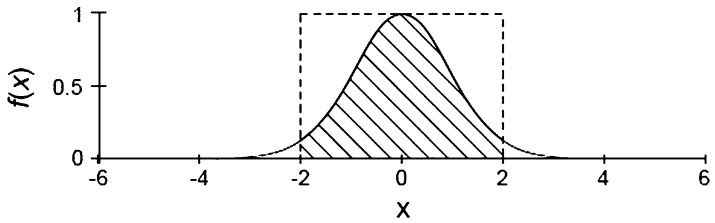

Fig. 2 Illustration of Monte Carlo integration

The Monte Carlo method of estimating integrals is probably the best-known Monte Carlo technique. The method estimates an integral by firing random points at the function [16]. The law of large numbers predicts that as more random points are chosen, the ratio of points below to points above the function will approximate the ratio of the area beneath the function to total area of the sample space from which the random points are drawn. Evaluation of the integral I given by identity (8) for the unit normal distribution as integrand is considered using the Monte Carlo approach as an illustration.

$$I = \int_{-2}^{2} e^{-(x^2/2)} dx = \int_{-2}^{2} f(x) dx \tag{8}$$

where,

$$f(x) = e^{-(x^2/2)} \tag{9}$$

Random points (x, y) are chosen between the ranges $-2 \leq x \leq 2$ and $0 \leq y \leq 1$. As can be seen from Fig. 2, darts thrown randomly at that range can be expected to fall below the function (given by Eq. 2) proportional to the area that lies beneath this function. Since the Monte Carlo method does not attempt to solve the integral analytically, the function need not be known explicitly and, in fact, can be in the form of tabular data since the method only needs to be informed of whether a given point falls above or below the function.

5 Results and Discussion

5.1 Tensile Testing

The mean tensile modulus obtained from a set of five tests is presented in Fig. 3 for pure PP and nanocomposites of varying nanoclay concentrations. It is seen from Fig. 3 that the tensile modulus rises appreciably from about 1.75 GPa for pure PP to 2.75 GPa for PPN_9 (implying an increase of 53%).

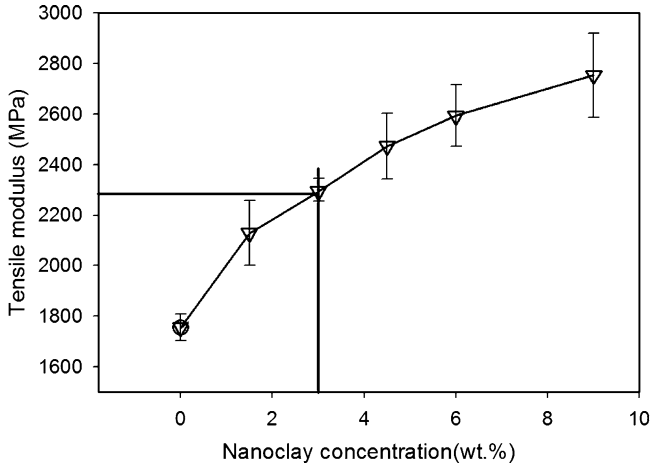

Fig. 3 Variation of tensile modulus with respect to nanoclay content

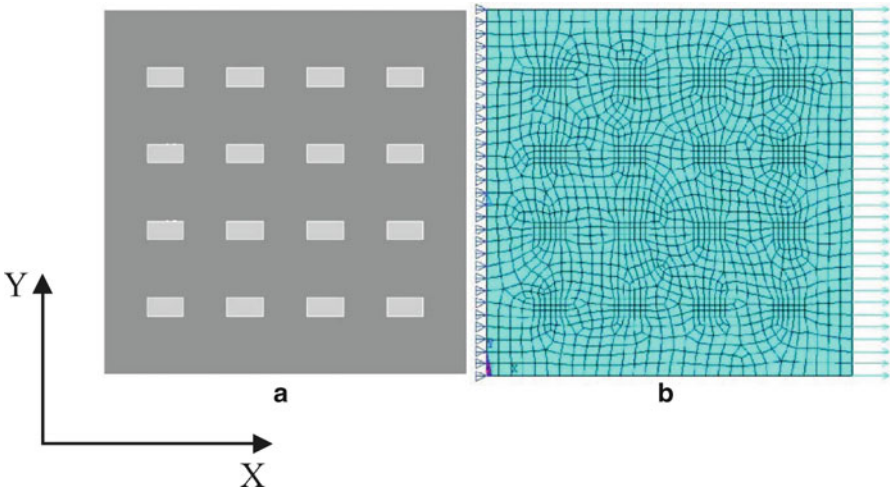

Fig. 4 (**a**) CAD model of unidirectional nanoclay clusters (shown as *whitish*) in a PP matrix; (**b**) corresponding FE model with boundary conditions and applied nodal loads

5.2 Micromechanical Finite Element Modeling (FEM)

Micromechanical FEM is used to predict the stiffness of a given nanocomposite by knowing the stiffness and volume/area fractions of the reinforcement and the matrix. The planar geometric model of 16 unidirectional rectangular nanoclay clusters (in light shade) of uniform size dispersed in PP matrix is shown in Fig. 4a. The corresponding finite element model with boundary supports and

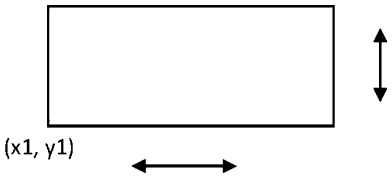

Fig. 5 Single nanoclay cluster movement without any change in orientation

loading configuration for plane stress analysis is shown in Fig. 4b. The total area occupied by the nanoclay clusters is based on the 300 μm × 300 μm SEM image, shown in Fig. 1, of a thin nanocomposite plate with 3% nanoclay by weight and analyzed with SigmaScan Pro image analysis software. The mesh in Fig. 4b is comprised of 4-node plane stress elements (PLANE 42) available in the commercial FEA code, ANSYS. The model represents a small fragment of a coupon specimen subjected to uniaxial tensile test in a standard UTM. A bilinear (elastoplastic) material model is used for the matrix by defining yield strength (28 MPa) and tangent modulus (600 MPa) in addition to Young's modulus (1.755 GPa) as reported in published literature. The reinforcement is assumed to behave elastically with a Young's modulus of 200 GPa. "Mac" file, a macro containing a sequence of ANSYS commands stored in a file, was created and used as an input for probabilistic analysis in ANSYS. An output of interest from each analysis is the effective Young's modulus of the nanocomposite obtained as the ratio of stress to strain in the linear elastic region.

5.3 Monte Carlo Simulation

A principal objective of the present numerical study is to be able to predict the experimental elastic modulus of a nanocomposite of a given clay content by taking into account the randomness in the distribution and orientation of nanoclay clusters. To this end, two types of Monte Carlo simulations are performed: (1) with unidirectional nanoclay clusters as shown in Fig. 4b with the positions of these clusters changed in a random manner by keeping their orientation as fixed as indicated for a single cluster in Fig. 5 and (2) with arbitrarily oriented nanoclay clusters as shown in the finite element model in Fig. 6a with one corner of each cluster remaining at a fixed location and its inclination with respect to the x-direction being randomly varied as implied in Fig. 6b. It is noted that for case (i), the initial lower left vertex ($x1$, $y1$) for a given platelet cluster changes position for every Monte Carlo simulation run, while for case (ii), the same remains anchored at the initial position. It is noted that Monte Carlo simulations are performed with 4 (i.e., 2 × 2), 9 (i.e., 3 × 3), 16 (i.e., 4 × 4), and 25 (i.e., 5 × 5) clusters for case (i) in order to ascertain the effect of number of clusters on the prediction of effective Young's modulus of a nanocomposite with a given weight fraction of nanoclay.

Once the parameters for Monte Carlo simulations are defined, ANSYS automatically performs a large number of analyses after carrying out automatic remeshing

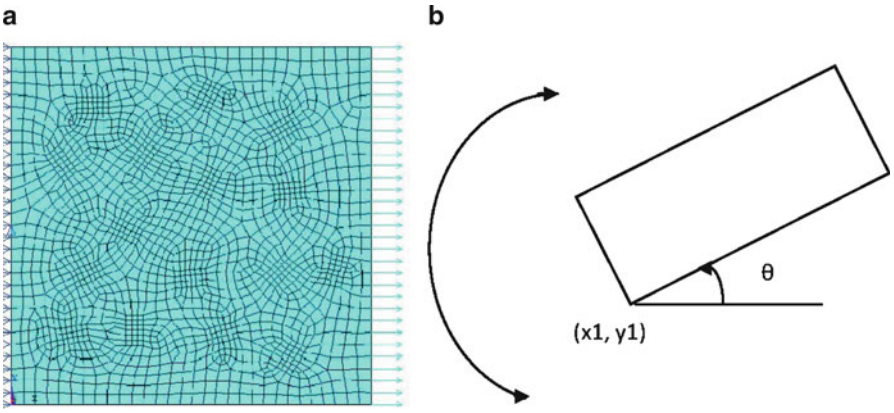

Fig. 6 (**a**) FE model of randomly oriented nanoclay clusters; (**b**) an oriented nanoclay cluster with angular movement about a vertex point ($x1$, $y1$)

Table 2 Predicted Young's modulus for different numbers of nanoclay clusters

Number of nanoclay clusters in FE model	Highest frequency Young's modulus (GPa)	% change with respect to the previous value of Young's modulus
2 × 2	2.22	N/A
3 × 3	2.26	1.89
4 × 4	2.27	0.66
5 × 5	2.27	0.0

for every changed configuration of nanoclay clusters belonging to case (i) or (ii) already defined. For each of these cases, Monte Carlo simulation is performed for 3,000 cycles with 3,000 different positions/orientations of nanoclay clusters to predict the range of values of Young's modulus of a given nanocomposite. It is noted that in the Monte Carlo simulations for case (ii), the distribution parameter, i.e., the mean value of orientation for each of the clusters, is taken as 0°; another parameter, namely, standard deviation for each of the clusters, is assumed as 30°.

Histogram plots for the output parameter considered here, namely, Young's modulus, are shown in Fig. 6a through d for unidirectional clusters with different numbers of clusters in Monte Carlo simulation models. The results from these plots are summarized in Table 2 by noting the values of Young's modulus of highest frequency for a given number of clusters. As mentioned earlier, the area fraction of nanoclay clusters is the same in models with varying numbers of clusters, i.e., 4, 9, 16, and 25; in other words, the sizes of individual clusters reduce as the number of clusters increases. It can be seen from Table 2 that the highest frequency elastic modulus converges to a practically constant value as the number of clusters becomes 16 (i.e., 4 × 4). Hence, a cluster number of 16 for the area of nanocomposite considered in the SEM image of Fig. 1 can be considered as optimum for simulation. The highest frequency Young's modulus for the 16-cluster nanoclay simulation from Table 2 is 2.27 GPa. This compares extremely well with

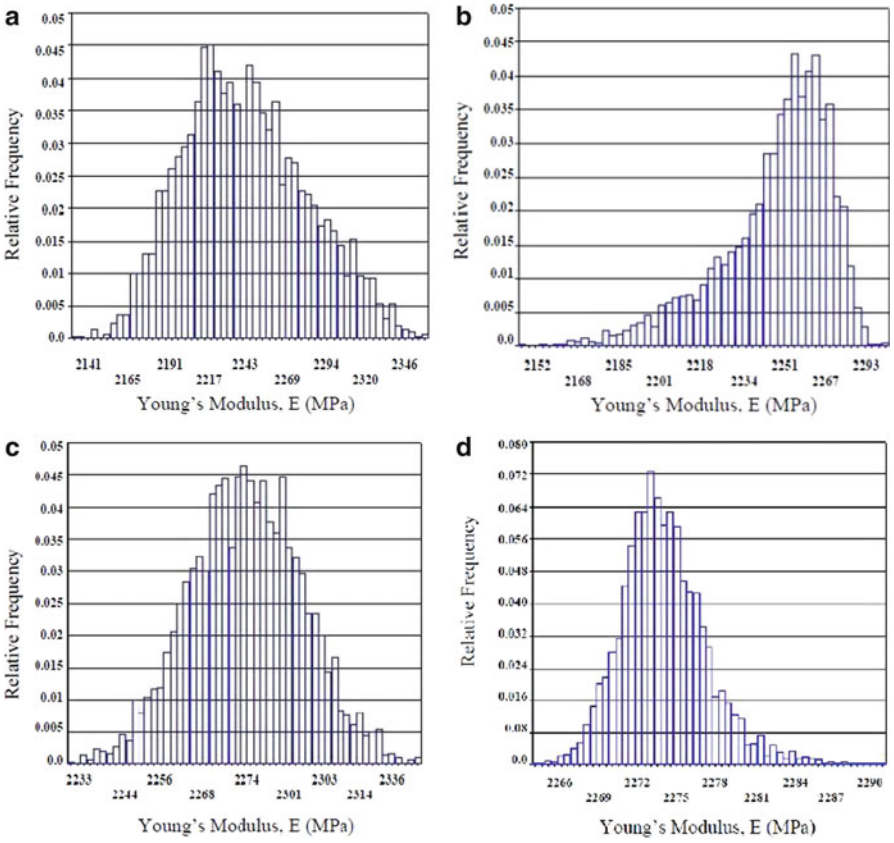

Fig. 7 Histograms of relative frequency versus Young's modulus for (**a**) 4-cluster, (**b**) 9-cluster, (**c**) 16-cluster, and (**d**) 25-cluster models of PPN_3 belonging to case (i), i.e., unidirectional cluster type

the experimentally obtained Young's modulus of 2.29 GPa for the nanocomposite labeled as PPN_3 with an underestimation of only 0.9%. In a similar manner, Monte Carlo simulations carried out for PPN_6 and PPN_9 nanocomposites also yielded close correlation of Young's modulus with experimental values (Fig. 7).

The histogram plot of Fig. 8 for randomly oriented nanoclay clusters points out to a highest frequency Young's modulus of 2.14 GPa, approximately, which is 6.6% lower than the experimental value of 2.29 GPa mentioned above. Based on this outcome of lower prediction and the previous closer prediction of Young's modulus obtained for unidirectional clusters, it can be said that the nanoclay clusters in the current nanocomposites are likely to be predominantly unidirectional rather than being randomly oriented. This possibility of nanoclay cluster orientation arising out of Monte Carlo simulation is supported also by the SEM image given in Fig. 1 in which a majority of the nanoclay clusters in white shade are either oriented in one direction (parallel to the horizontal edge of the image) or are inclined at a relatively small angle (i.e., much less than 90°) to this direction.

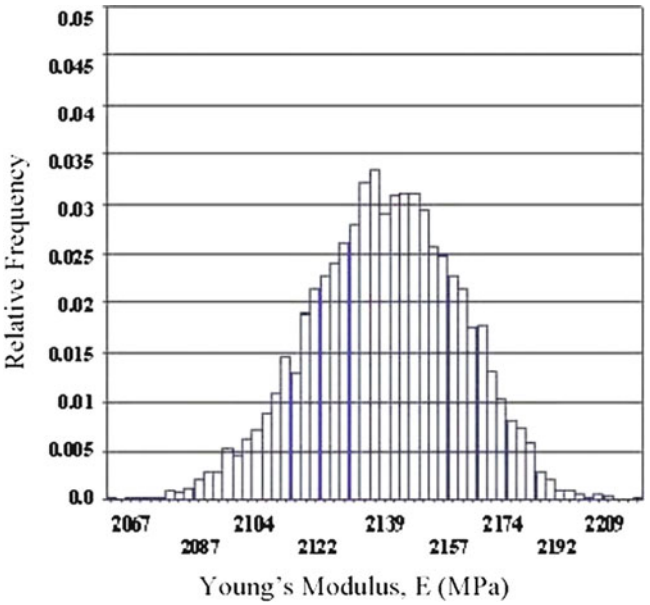

Fig. 8 Histogram of relative frequency versus Young's modulus for 16-cluster models belonging to case (ii), i.e., randomly oriented nanoclay cluster type

6 Conclusions

The present study has shown that it is possible to capture the effect of random variations in distribution and orientation of particulate reinforcements in a composite on its resultant stiffness modulus with the aid of Monte Carlo finite element simulations. In particular, it has been shown that the highest frequency Young's modulus of a nanocomposite of a given nanoclay concentration (with unidirectional nanoclay clusters) can match extremely well with the experimentally obtained mean Young's modulus of nanocomposite samples fabricated by the authors using a torque rheometer for mixing an Indian nanoclay with polypropylene followed up with twin-screw extrusion and injection molding. The planar finite element model adopted here is based on an SEM image of the considered nanocomposite. The consistency of the model has been established by varying the number of nanoclay clusters while keeping the area fraction of nanoclay as constant and establishing the convergence of the predicted highest frequency Young's modulus. With the help of an optimum 16-cluster nanocomposite finite element model, the effect of random orientations of nanoclay clusters on lowering of the Young's modulus is shown thereby corroborating that the nanoclay clusters are predominantly unidirectional as revealed in the SEM image of the nanocomposite. The current approach has the potential for further development and can be useful in the design as well as prediction of uncertainties in mechanical behavior of a host of composites including cement concrete and geomaterials.

References

1. Shao-Yun Fu, Xi-Qiao Feng, Bernd Lauke, Yiu-Wing Mai (2008) Effects of particle size, particle/matrix interface adhesion and particle loading on mechanical properties of particulate–polymer composites. Compos Part B Eng 39:933–961
2. Yuan Q, Chen YJ, Yang, Misra RDK (2010) Nanoparticle interface driven microstructural evolution and crystalline phases of polypropylene: the effect of nanoclay content on structure and physical properties. Mater Sci Eng A 527:6002–6011
3. Rohlmann CO, Horst MF, Quinzani LM, Failla MD (2008) Comparative analysis of nanocomposites based on polypropylene and different montmorillonites. Eur Polym J 44:2749–2760
4. Lai SM, Chen WC, Zhu XS (2009) Melt mixed compatibilized polypropylene/clay nanocomposites: Part 1 – the effect of compatibilizers on optical transmittance and mechanical properties. Compos Part A Eng 40:754–765
5. Sheng Zhang A, Horrocks R, Hull R, Kandola BK (2006) Flammability, degradation and structural characterization of fibre-forming polypropylene containing nanoclayeflame retardant combinations. Polym Degrad Stab 91:719–725
6. Deenadayalan E, Vidhate S, Lele A (2006) Nanocomposites of polypropylene impact copolymer and organoclays: role of compatibilizers. Polym Int 55:1270–1276
7. Chick SE (2001) Input distribution selection for simulation experiments: accounting for input uncertainty. Oper Res 49:744–58
8. Wagner MAF (1995) Graphical interactive simulation input modeling with Bivariate Bezier distributions. ACM Trans Model Comput Simul 5:163–189
9. Yun Lu, Jin Pan, Koichi Goda, Hideharu Fukunaga (1999) Effect of the matrix properties on the strength and reliability of fiber reinforced metals composite ICCM – 12 Europe
10. Bergstrom JS, Boyce MC (1999) Mechanical behavior of particle filled elastomers. Rubber Chem Technol 72:633–56
11. ASTM, D638 (1995) Standard test method for tensile properties of plastics. ASTM, Philadelphia
12. Valavala PK, Odegard GM (2005) Modeling techniques for determination of mechanical properties of polymer nanocomposites. Adv Mater Sci 9:34–44
13. Zihui Xia, Yunfa Zhang, Ellyin F (2003) A unified periodical boundary conditions for representative volume elements of composites and applications. Int J Solids Struct 40 (8):1907–21
14. Ramakrishnan N, Kumar AM, Radhakrishna Bhat BV (1996) A generalized plane strain technique for estimating effective properties of particulate metal matrix composites using FEM. J Mater Sci 31:3507–3512
15. Halton JH (1970) A retrospective and prospective survey of the Monte Carlo method. SIAM Rev 12:1–63
16. Brian Korver (1994) The Monte Carlo method and software reliability theory, TR 94:1–27

Investigations of Shaking Table Test of Randomly Base-Excited Building Structures with MR Dampers

Jie Li, Zhen Mei, and Yong-Bo Peng

Abstract Structural vibration control has demonstrated its value for mitigating earthquake hazards and enhancing the safety and serviceability of structural systems in recent years. However, in most existing investigations of numerical simulations and experimental verifications on seismic control of structures, only several ground motions at different levels are considered. The experimental investigations of seismic performance of controlled structures accounting for the randomness inherent in the earthquake ground motions did not receive sufficient attentions. In this chapter, a complete shaking table test on a multistory shear frame structure with MR dampers is carried out. The representative time histories of ground accelerations, as the base excitation, are generated employing the stochastic ground motion model. The stochastic response analyses of the experimental structures with and without control are conducted, respectively. Experimental and analytical results indicate that the seismic performance of the test structure is significantly improved compared with that of the uncontrolled structure.

Keywords Shaking table test • Stochastic ground motions • Structural control • Probability density evolution method • MR dampers

J. Li (✉) • Z. Mei
School of Civil Engineering, Tongji University, 1239 Siping Road, Shanghai 200092, China

State Key Laboratory of Disaster Reduction in Civil Engineering, Tongji University, Shanghai, China
e-mail: lijie@tongji.edu.cn

Y.-B. Peng
State Key Laboratory of Disaster Reduction in Civil Engineering, Tongji University, Shanghai, China

Shanghai Institute of Disaster Prevention and Relief, Tongji University, Shanghai, China

S. Chakraborty and G. Bhattacharya (eds.), *Proceedings of the International Symposium on Engineering under Uncertainty: Safety Assessment and Management (ISEUSAM - 2012)*,
DOI 10.1007/978-81-322-0757-3_85,

1 Introduction

In the last four decades or so, the application of modern control techniques to mitigate the effects of seismic loads on civil engineering structures offers an appealing alternative to the traditional earthquake resistant design method, and considerable researches have been conducted to advance structural control as a direct means of vibration attenuation [4, 11].

It is noted, however, that in the experimental research and numerical simulation on structural vibration control under earthquake actions, only several ground motions at different levels, like El Centro earthquake and so on, are considered as excitations [3, 8]. The experimental investigations of seismic performance of controlled structures accounting for the randomness inherent in the earthquake ground motions did not receive sufficient attentions. Moreover, the efficacy of vibration mitigation is usually given by the reduction of dynamic responses (particularly peak displacements or peak accelerations) under control compared to those without control [9, 10]. The statistical values, such as the standard deviation, as well as the probability distributions of responses of the controlled and uncontrolled structures cannot be obtained in most cases. The guaranty of requirement of safety or serviceability of controlled structures is still a challenging task. Therefore, stochastic vibration control of structures subjected to the random earthquake ground motion should be studied [6, 7].

The focus of this chapter is to experimentally investigate the efficacy of seismic response control considering the randomness involved in earthquake excitations. A complete shaking table test on a multistory shear frame structure with MR dampers is carried out. The representative time histories of ground acceleration, using for the base excitation of the shaking table test, are generated based on a physical stochastic ground motion model [5]. Following that, the experimental setup and experimental program are both described in detail. Some experimental and analytical results of stochastic vibration control tests are included.

2 Simulation of Earthquake Ground Motions

2.1 Brief Introduction of Physical Stochastic Ground Motion Model

Based on a physical background, seismic ground motions are mainly affected by the properties of the sources, propagation paths, and the properties of the site soil. The uncertainty of the three factors is the cause of the randomness of seismic ground motions. For a certain engineering site, the ground motion parameters at the bedrock could be provided by the seismic hazard assessment considering the properties of the sources and the propagation process [2]. Therefore, taking into

Table 1 Statistical values of peak accelerations of the sampled ground motions

Statistic quantity	Min	Max	Mean	Std.d
Value (m/s^2)	0.78	4.61	2.18	0.56

Annotation: *Min* minimum, *Max* maximum, *Std.d* standard deviation

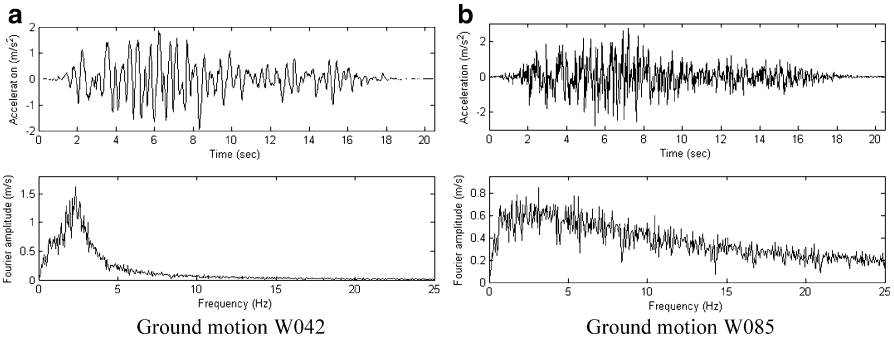

Fig. 1 Two typical time histories and Fourier amplitude spectra of ground accelerations. (**a**) Ground motion W042, (**b**) Ground motion W085

account the properties of the site soil and combining with the ground motion at the bedrock will lead to the so-called physical stochastic ground motion model [5].

The effects of engineering site could be regarded as a multilayer filtering operator. For the sake of clarity, it is modeled as a single-degree-of-freedom (SDOF) system. Using the ground motion at the bedrock as the input process, the absolute response of the SDOF system is, namely, the process of the ground motion at the surface of the engineering site. More details on the physical stochastic ground motion model proposed by Li and Ai could be found in the two references just mentioned.

2.2 Simulation of Representative Time Histories of Ground Acceleration

In conjunction with the strategy of tangent spheres for selecting representative points [1], time histories of ground acceleration at the engineering site considered can be generated employing the physical stochastic ground motion model outlined in the preceding section. In this investigation, 120 representative ground accelerations are generated. Meanwhile, the ground acceleration valued by mean of parameters of the model is obtained, and its peak acceleration is 2.00 m/s^2.

It should be noted that the peak accelerations as well as the frequency spectrum characteristics of the representative ground accelerations differ from each other. The statistical properties of peak accelerations of these ground motions are given in Table 1. In Fig. 1, two typical ground accelerations, labeled W042 and W085, and

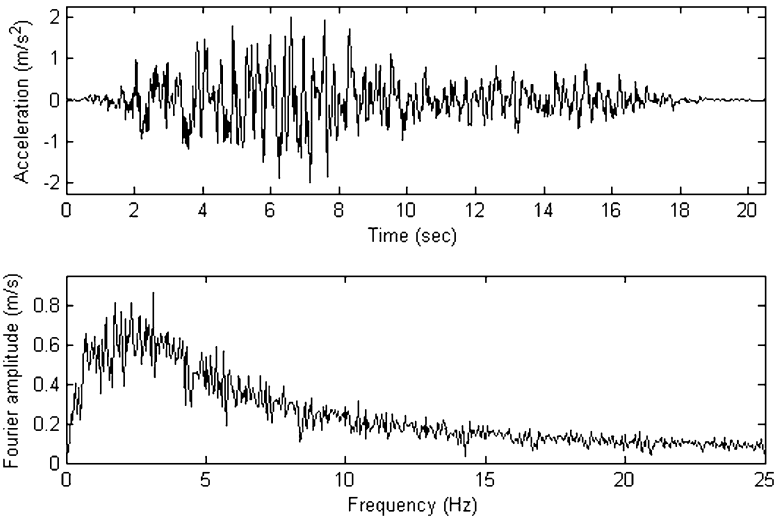

Fig. 2 Ground acceleration valued by mean of parameters and its Fourier amplitude spectrum

the corresponding Fourier amplitude spectra are illustrated, respectively. Additionally, the ground acceleration generated using the mean parameters, labeled W000, and its Fourier amplitude spectrum are presented in Fig. 2.

3 Design of Experiments

3.1 Experimental Setup

Experimental investigations were performed in the State Key Laboratory of Disaster Reduction in Civil Engineering in Tongji University, China. The test structure used in this experiment is a six-story, single-bay, model steel structure (Fig. 3). It is designed to be a scale model of a part of a prototype building. This steel model structure is of 5 m high. The total mass of the model is about 2.8 ton, excluding additional artificial quality (total of 7.2 ton, distributed evenly among the six floors). The ratio of model quantities to those corresponding to the prototype structure is employed as follows: time = 0.4472, force = 0.04, mass = 0.04, displacement = 0.2, and acceleration = 1.

The MR dampers (marked as MRD-A and MRD-B, respectively) employed in the experiment are shown in Fig. 4. The two dampers have the same design parameters. Forces of up to 10 kN can be generated by the damper. It is of 72.5 cm long in its extended position, and the main cylinder is of 10.0 cm in diameter. The damper has a ±5.5-cm stroke, and its input current is in the range

Fig. 3 Photograph of the test structure with MR dampers

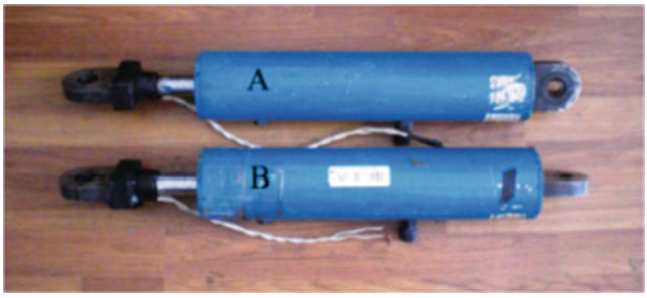

Fig. 4 MRD-100-10-type MR dampers

of 0–2 A. The force generated by this device is stable in the range of –40 to 60 °C. Additionally, the total weight of the damper is approximately 20 kg.

In the shaking table test, the data are recorded by an automatic data acquisition system. An accelerometer as well as a displacement transducer is used to measure the shaking table's actual motion. Simultaneously, six accelerometers and six displacement transducers are installed to measure the dynamic responses of each floor. The setup of transducers is given in Fig. 5.

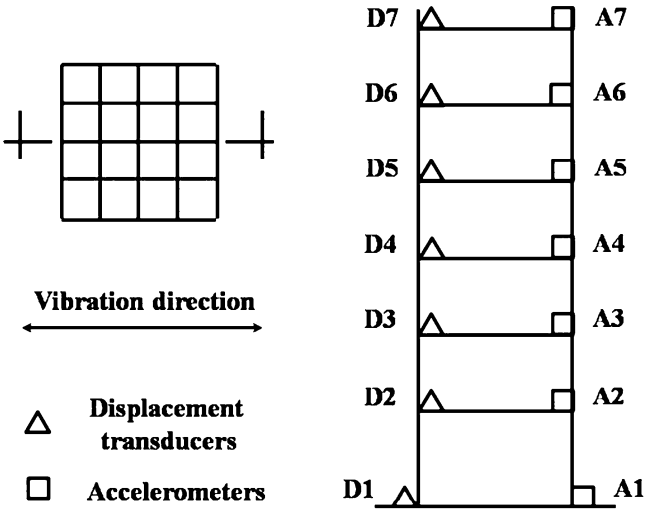

Fig. 5 Setup of transducers

Table 2 Experimental program

Case number	Seismic input	Amplitude (m/s^2)	Remark
1	W000	1.00	Without control
2–121	W001–W120	Statistical values as shown in Table 1	Passive-on control (two MR dampers installed)
122–241	W001–W120	Half of the amplitudes in cases 2–121, respectively	Without control
242	W000	1.00	Without control

3.2 Experimental Program

In the stochastic control tests, the time histories of ground acceleration generated in Section "Simulation of Earthquake Ground Motions" are used as the one-dimensional inputs. There are total 242 cases as shown in Table 2. In the uncontrolled cases (case nos. 1, 242), the ground acceleration W000 is considered as the seismic inputs, and experimentally measured frequency response functions (FRFs) are used in the identification of the test structure. In the passive-on control cases (case nos. 2–121), the two MR dampers pictured in Fig. 4 are installed as the control devices. The MRD-A is placed between the ground and first floor, and the MRD-B is placed between the second and third floors of the model structure, as shown in Fig. 3. Additionally, the currents applied to the two dampers are held fixed at 1.5 A in the controlled cases.

4 Results of Stochastic Control Experiments

4.1 Identification of Dynamic Characteristics of Test Structure Without Control

In the experiments, dynamic characteristics of the test structure without control can be obtained from the experimentally measured FRFs. The first six natural frequencies of the test structure without control are identified, and the results are listed in Table 3. According to the results, it is seen that the first six natural frequencies of the model structure is only slightly changed through the whole experiment. For instance, the first natural frequency is changed from 1.460 to 1.453 Hz, only decreases by about 0.48%. Moreover, the first three identified mode shapes of the test structure without control are presented in Fig. 6. It is clear that the first three modes remain almost unchanged.

In view of the identification results, it can be assumed that the test structure itself still remains within the range of linear state in the whole tests. It is noted that the amplitudes of seismic inputs in cases nos. 122–241 are only half of those in case nos. 2–121, respectively. As such, the experimentally measured data of the test structure without control should be doubled based on the assumption that the model remains in the linear state.

Table 3 The first six natural frequencies of the test structure without control.

	First six natural frequencies (Hz)					
Case number	1	2	3	4	5	6
1	1.460	4.624	8.365	12.452	16.803	20.277
242	1.453	4.605	8.338	12.385	16.745	20.184

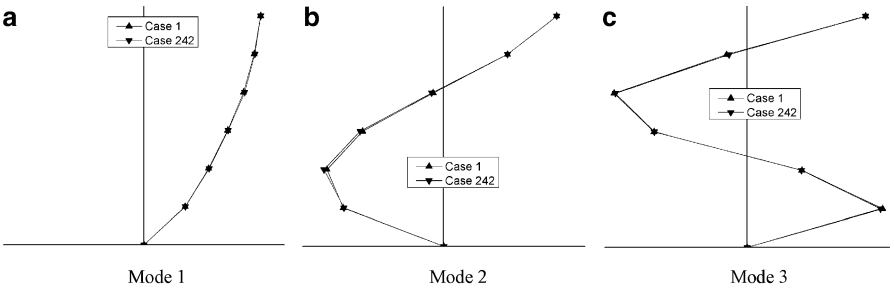

Fig. 6 The first three mode shapes of the test structure without control. (**a**) Mode 1, (**b**) Mode 2, (**c**) Mode 3

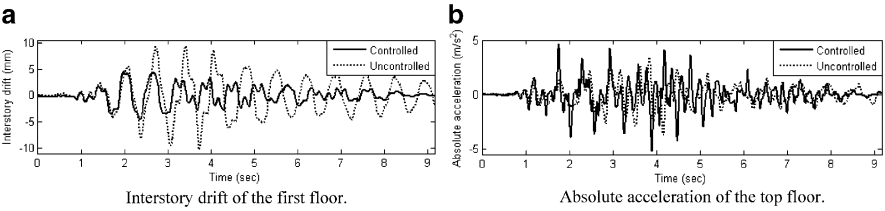

Fig. 7 Comparison of structural responses subject to ground acceleration W042. (**a**) Interstory drift of the first floor. (**b**) Absolute acceleration of the top floor

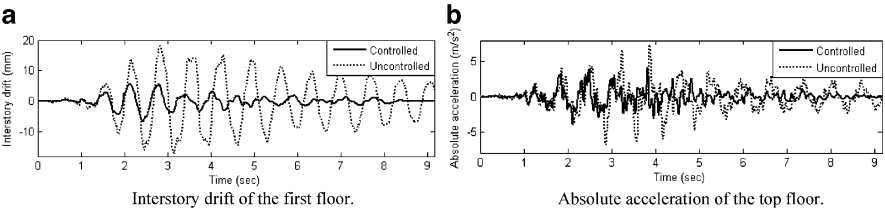

Fig. 8 Comparison of structural responses subject to ground acceleration W085. (**a**) Interstory drift of the first floor, (**b**) Absolute acceleration of the top floor

4.2 Structural Responses Subject to Representative Ground Motions

The comparative studies of structural responses with and without control subject to the two representative ground motions pictured in Fig. 1 are carried out. The time histories of responses of the controlled (Con.) and uncontrolled (Unc.) structures are shown, respectively, in Figs. 7 and 8. It is easily seen that the control effectiveness is of difference in case that the test structure is subject to various ground motions. The passive-on control is relatively more capable in mitigating both interstory drifts and absolute accelerations when the ground motion time history, labeled W085, is used as the seismic input. In Fig. 7b, the absolute acceleration with control, however, is even amplified compared to that without control during the time interval from 1.5 to 5.0 s. Therefore, the randomness involved in earthquake excitations should not be ignored.

4.3 RMS Responses of Test Structure

The root mean square (RMS) responses of the test structure along with the structural height with and without control are shown in Fig. 9. It is quite evident that RMS responses in the controlled cases are evidently smaller than those in the uncontrolled cases. As shown in Fig. 9a, the values of mean and standard deviation

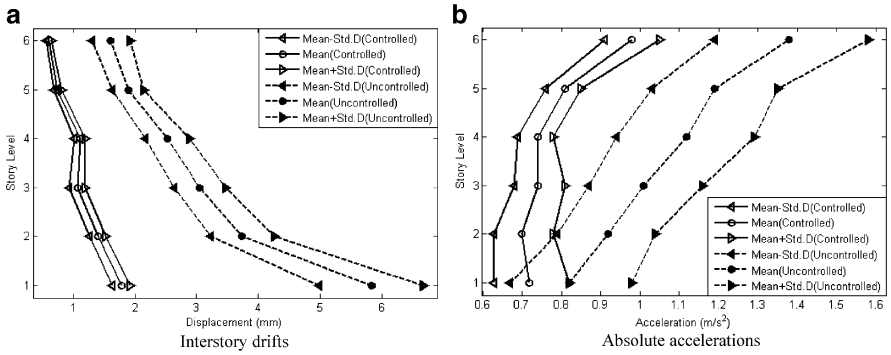

Fig. 9 RMS responses of test structure with and without control. (**a**) Interstory drifts, (**b**) Absolute accelerations

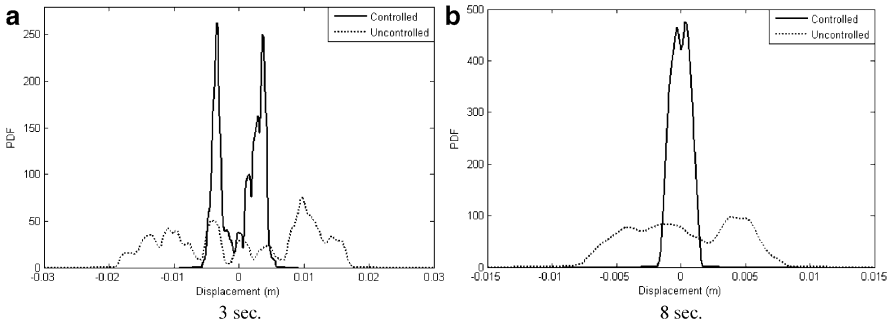

Fig. 10 Typical PDFs of interstory drifts of the first floor at different instants of time. (**a**) 3 s, (**b**) 8 s

of RMS interstory drifts are averagely reduced by 62.7 and 77.5%, respectively. As pictured in Fig. 9b, similar capacity toward the mitigation of RMS absolute accelerations is clearly exposed. The passive-on control system is able to reduce the mean values of RMS absolute accelerations of each story by 12.6–34.0% and the standard deviations by 38.7–75.1%.

4.4 PDFs of Responses of Test Structure

In this section, stochastic response analysis of the controlled and uncontrolled structures is carried out employing the probability density evolution method [6]. Typical PDFs of structural responses with and without control at instants of time (3 and 8 s) are shown in Figs. 10 and 11. One can readily see that the PDFs are mostly irregular, quite different from widely used regular probability distributions.

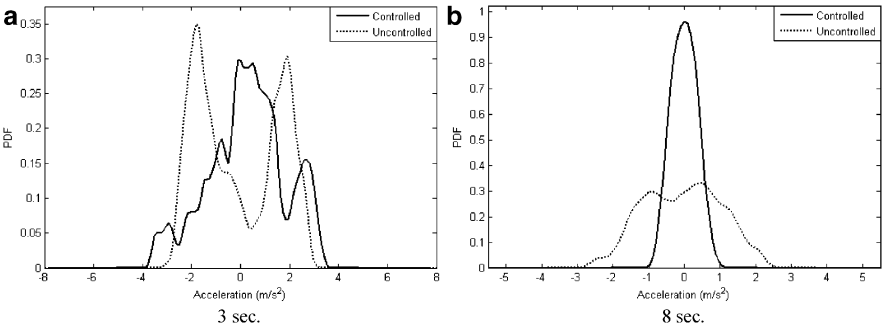

Fig. 11 Typical PDFs of story acceleration of the top floor at different instants of time. (**a**) 3 s, (**b**) 8 s

Moreover, the PDFs vary greatly against time. One might realize, for instance, from Fig. 10 that the distribution width of PDFs of the first interstory drifts at 3 s is larger than that at 8 s in the controlled cases. It is also seen that the fluctuation (characterized by the distribution width of the PDF) is significantly reduced with control. That is to say, the variation of interstory drifts of the first floor is obviously decreased. Similarly, the distribution ranges of the PDFs of the top story acceleration become narrower with the control. Moreover, the shape of the PDFs of responses arises to be more regular in the controlled cases, compared with that in the uncontrolled cases. In brief, the seismic performance of the primary structure has been greatly enhanced after the passive-on control applied.

5 Concluding Remarks

In this chapter, stochastic control of structures subject to random earthquake ground motions is experimentally investigated. Experimental results indicate that the seismic performance of the test structure with MR dampers is significantly improved compared with that in the uncontrolled cases. It is seen that control effectiveness of the test structure is different in case of different ground motions. The RMS responses of the controlled structure are obviously smaller than those in the uncontrolled cases. In the controlled cases, the distribution range of PDFs of typical responses becomes narrower, and the shape of the PDFs arises to be more regular. Therefore, more attentions should be paid to the randomness involved in seismic excitations.

Acknowledgements The supports of the National Natural Science Foundation of China (Grant Nos. 50621062, 10872148, 51108344), the Hi-tech Development Plan ("863" Plan) of the Ministry of Science and Technology (Grant No. 2008AA05Z413), and the Ministry of Education for New Century Excellent Talents are highly appreciated.

References

1. Chen JB, Li J (2008) Strategy for selecting representative points via tangent spheres in the probability density evolution method. Int J Numer Methods Eng 74(13):1988–2014
2. Dowrick DJ (2003) Earthquake risk reduction. Wiley, Chichester
3. Dyke SJ, Spencer BF Jr, Sain MK, Carlson JD (1996) Modeling and control of magnetorheological dampers for seismic response reduction. Smart Mater Struct 5(5):565–575
4. Housner GW, Bergman LA, Caughey TK et al (1997) Structural control: past, present, and future. J Eng Mech ASCE 123(9):897–971
5. Li J, Ai XQ (2006) Study on random model of earthquake ground motion based on physical process. Earthq Eng Eng Vib 26(5):21–26 (in Chinese)
6. Li J, Peng YB, Chen JB (2010) A physical approach to structural stochastic optimal controls. Probab Eng Mech 25(1):127–141
7. Li J, Peng YB, Chen JB (2011) Probabilistic criteria of structural stochastic optimal controls. Probab Eng Mech 26(2):240–253
8. Nagarajaiah S, Sahasrabudhe S, Iyer R (2000) Seismic response of sliding isolated bridges with MR dampers. Proc 2000 Am Control Conf 6:4437–4441
9. Ohtori Y, Christenson RE, Spencer BF Jr, Dyke SJ (2004) Benchmark control problems for seismically excited nonlinear buildings. J Eng Mech 130(4):366–385
10. Spencer BF Jr, Dyke SJ, Deoskar HS (1998) Benchmark problems in structural control: part I-active mass driver system. Earthq Eng Struct Dyn 27(11):1127–1139
11. Yao JTP (1972) Concept of structural control. J Struct Div ASCE 98(ST7):1567–1574

Comparative Study of Equivalent Single Degree of Freedom Systems Based on Pushover Analysis

Debarati Datta

Abstract Nonlinear static pushover analysis is a method to evaluate MDOF system response for a specified level of earthquake where the MDOF system is replaced by equivalent single degree of freedom (ESDOF) system. In recent past, various damage indicators have been proposed as the system response. Among them, Park-Ang damage index is most widely recognized and used. In the present work Park-Ang damage index (D_{PA}) is considered as the seismic damage indicator for nonlinear elastic perfectly plastic SDOF oscillator. Three ESDOF systems are developed by pushover analysis, and these equivalent systems are validated by estimating D_{PA} demands. Two steel moment-resisting frame buildings are considered for study. A bias factor is used to measure the accuracy of an ESDOF system. So Park-Ang damage index (D_{PA}) for these structures is obtained for several real ground motions. Bias factors and bias statistics of D_{PA} for certain ESDOF systems are shown. The bias statistics shows the suitability of an equivalent system for designing real MDOF buildings.

Keywords Nonlinear static pushover analysis • Equivalent single degree of freedom system Park-Ang damage index • Steel moment resisting frame

1 Introduction

For the rational earthquake resistant design of new buildings, as well as for the seismic evaluation of existing buildings, a procedure is needed which would, firstly, yield an adequate estimate of demand in terms of structural stiffness, strength, ductility, and energy dissipation, and which would, secondly, not be more complicated than necessary. The methods applied in building codes are based on

D. Datta (✉)
Visvesvaraya National Institute of Technology, Nagpur 440010, India
e-mail: d_debarati@yahoo.co.in; debaratidatta@apm.vnit.ac.in

S. Chakraborty and G. Bhattacharya (eds.), *Proceedings of the International Symposium on Engineering under Uncertainty: Safety Assessment and Management (ISEUSAM - 2012)*,
DOI 10.1007/978-81-322-0757-3_86,

the assumption of linear elastic structural behavior and fail to meet the first requirement. On the other hand, the nonlinear dynamic time-history analysis of multi-degree-of-freedom (MDOF) mathematical models is not practical for everyday design use.

In the above context, equivalent single degree of freedom (ESDOF) system obtained from pushover analysis provides a convenient solution for prediction of seismic response of a structure. Based on several properties of the real MDOF structure, the corresponding ESDOF system is developed, and the MDOF response for a ground motion is obtained from ESDOF response using suitable correlation. Several researchers [3, 6] authenticated the usefulness of ESDOF systems. It is now well established that ESDOF methodology gives quite good estimate of displacement demand or some other inelastic response of a real structure.

This chapter discusses the different equivalent system approaches for obtaining Park-Ang damage index for real MDOF system. In this connection, a brief description of the real MDOF structures used for the validation of the proposed approaches is presented. Finally the steps and methods used for developing ESDOF systems and the comparison of D_{PA} values from MDOF and ESDOF systems are provided.

2 Park-Ang Damage Index

The damage index [9] can be considered for the structure as a whole using the following equation:

$$D_{\mathrm{PA}}=\frac{d_M-d_y}{d_u-d_y}+\frac{\beta}{V_y d_u}\sum_{i=1}^{n}\int_0^t \mathrm{d}E_i. \tag{1}$$

where d_M = peak roof displacement obtained from nonlinear response history analysis for a specific record, d_u = monotonic roof displacement capacity based on ductility capacity assumed, d_y = yield displacement obtained from nonlinear static pushover analysis, V_y = yield base shear based on pushover analysis, E_i = hysteretic energy at i-th plastic hinge, and n = number of plastic hinges.

3 Estimation of Park-Ang Damage Index for MDOF Structures

The equivalent system schemes are validated for the real MDOF systems through bias factors. The D_{PA} values for a certain equivalent system corresponding to particular building is obtained for five real ground motions. These values are compared with MDOF D_{PA} for same ground motions.

As the first step for developing a seismic design checking methodology based on Park-Ang damage index, the D_{PA} values are obtained for two steel moment-resisting frame buildings under real strong ground motion scenarios. The buildings considered for this study are the 3- and 9-story "pre-Northridge" design steel moment frames considered for SAC joint venture. These frames were considered for various recent research works, and details of these building frames are available in published literature [7]. The north-south frames of each building are considered for this study. Gravity load effects, P-Δ effects, flexibility of joint panel zones, and stiffness contribution from gravity-frame members are not considered for analyses. Members of the moment frame are considered to be elastic perfectly plastic (i.e., no strain hardening). Rayleigh damping is assumed for dynamic analysis. The mass proportional and the stiffness proportional damping coefficients (α_m and β_k, respectively) are obtained by adopting a modal damping factor (ξ) of 0.05 in the first two modes. Three different ductility capacity (μ) values (4.0, 6.0, and 7.5) are considered for defining d_u of D_{PA}. β is considered to be 0.025.

To obtain yield displacement and yield base shear of the structure, nonlinear static pushover analysis is performed up to 7.5% drift in DRAIN-2DX. This drift limit is chosen arbitrarily considering the fact that this limit represents the nonlinear response quite well beyond the yield point. The static load distribution vector for pushover analysis is obtained following the International Building Code [8] based on lateral load distribution. Detail of load vector is discussed in later section. The base shear vs. roof displacement is plotted to obtain the pushover curve, and it is idealized as an approximate elastic perfectly plastic curve satisfying the following criteria:

- The initial or the elastic stiffness for the approximate curve is adopted to be the same as in the original plot.
- The area under the original pushover curve and approximate curve are equal.
- The performance limit (i.e., roof displacement) is same for both the curves.

Yield drift and yield strength for the equivalent system is obtained from this approximating curve. Figure 1 shows the idealization of pushover curve and location of yield point. This yield displacement (d_y) is multiplied by the ductility capacity value, μ to obtain d_u, i.e., roof displacement capacity stated in D_{PA} (Table 1).

The total hysteretic energy value is also obtained from dynamic analysis by DRAIN-2DX. The bending moment and plastic rotation value for the structure members are noted from the output files of DRAIN-2DX. The hysteretic energy for each element is calculated, and summing up hysteretic energy value for all members, the total hysteretic energy is obtained. Fortran programming and spreadsheets are used to obtain the hysteretic energy values. From all the required databases, finally the D_{PA} values are obtained for all the ground motions for all the buildings and for all ductility capacity (μ) values. Tables 2 and 3 show the D_{PA} values for 3- and 9-story buildings, respectively.

The D_{PA} values obtained from this methodology are used to obtain the bias factor required for further work, described in later sections. In the next section, the

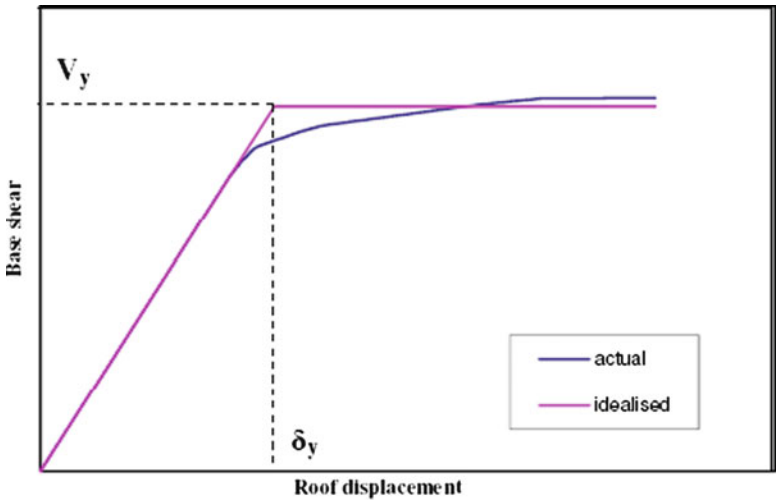

Fig. 1 Idealization of pushover plot to obtain δ_y and V_y

description of the building frames used to obtain the MDOF response and their various behavioral properties is stated.

4 Description of Steel Moment-Resisting Frame Buildings

Two pre-Northridge SAC steel moment frame buildings (3- and 9-story) in Los Angeles, USA, are considered for the present work. Earlier these buildings were considered for SAC joint venture. These model buildings are built following UBC 1994. These designs have the standard beam-to-column welded connection. The perimeter moment-resisting frames are considered as the structural system.

The building frames are subjected to the following floor load distribution (steel weight is assumed as 13 psf (0.622 kN/m^2) for all designs):

Floor dead load for weight calculations: 96 psf (4.596 kN/m^2)
Floor dead load for mass calculations: 86 psf (4.118 kN/m^2)
Roof dead load excluding penthouse: 83 psf (3.974 kN/m^2)
Penthouse dead load: 116 psf (5.554 kN/m^2)
Reduced live load per floor and for roof: 20 psf (0.958 kN/m^2)

Cladding and parapet loads are based on the surface area of the structures. Based on these loading definitions, the seismic mass for the structures is as follows (the values are for the entire structure):

Table 1 Information on the ground motion records used for validation of the equivalent systems

Sr. no	Record name	Earthquake	Recording station	Date	Direction[a]
1	ll	Landers	Lucerne	06.08.1992	280
2	nn	Northridge	Newhall Fire Station	01.17.1994	090
3	nr	Northridge	Rinaldi Receiving Stn.	01.17.1994	228
4	ns	Northridge	Sylmar Converter Stn.	01.17.1994	142
5	arlet90	Northridge	Arleta-Nordhoff Fire Stn.	01.17.1994	090
6	newh360	Northridge	Newhall Fire Station	01.17.1994	360
7	newh90	Northridge	Newhall Fire Station	01.17.1994	090
8	parkcsp1	Parkfield	Parkfield	06.28.1966	
9	syl360	Northridge	Sylmar – Olive View Med. FF	01.17.1994	360
10	syl90	Northridge	Sylmar – Olive View Med. FF	01.17.1994	090
11	kobe	Kobe	Takatori	01.16.1995	090
12	chy08036	Chi-Chi	Yunlin – Tsaoling	09.21.1999	360
13	chy0809	Chi-Chi	Yunlin – Tsaoling	09.21.1999	090
14	tcu06536	Chi-Chi	Taichung – Wufeng School	09.21.1999	360
15	tcu0659	Chi-Chi	Taichung – Wufeng School	09.21.1999	090
16	tcu0789	Chi-Chi	Taichung – Wufeng School	09.21.1999	090
17	cpm000	Cape Mendocino	Cape Mendocino	04.25.1992	000
18	gaz000	Gazli	Karakyr	05.17.1976	000
19	gaz090	Gazli	Karakyr	05.17.1976	090
20	kjm000	Kobe	Kobe	01.16.1995	000
21	kjm090	Kobe	Kobe	01.16.1995	090
22	lgp000	Loma Prieta	UCSC Station 16	10.18.1989	000
23	pcd164	San Fernando	Pacoima Dam	02.09.1971	164
24	pcd254	San Fernando	Pacoima Dam	02.09.1971	254
25	tabtr	Tabas, Iran	Tabas	09.16.1978	
26	tar090	Northridge	Tarzana – Cedar Hill Nursery A	01.17.1994	090
27	tar360	Northridge	Tarzana – Cedar Hill Nursery A	01.17.1994	360
28	s1010	Nahanni, Canada	Nahanni	12.23.1985	010

[a]Direction is measured in degrees clockwise from North

3-story structures

Roof: 70.90 kips-sec^2/ft (1037.05 kN-sec^2/m)
Floor 3 and floor 2: 65.53 kips-sec^2/ft (958.51 kN-sec^2/m)

9-story structures

Roof: 73.10 kips-sec^2/ft (1069.23 kN-sec^2/m)
Floor 9 to floor 3: 67.86 kips-sec^2/ft (992.59 kN-sec^2/m)
Floor 2: 69.04 kips-sec^2/ft (1009.85 kN-sec^2/m)

Table 2 Comparison of Park-Ang damage index (D_{PA}) for the MDOF and different ESDOF systems for the 3-story frame

	D_{PA}											
	MDOF			ESS1			ESS2			ESS3		
Ground motion record	$\mu = 4$	$\mu = 6$	$\mu = 7.5$	$\mu = 4.0$	$\mu = 6.0$	$\mu = 7.5$	$\mu = 4.0$	$\mu = 6.0$	$\mu = 7.5$	$\mu = 4.0$	$\mu = 6.0$	$\mu = 7.5$
nn	0.1906	0.1151	0.0888	0.3269	0.1970	0.1518	0.3256	0.1961	0.1511	0.3301	0.1988	0.1532
nr	1.0000	0.6889	0.5307	1.0000	0.7668	0.5908	1.0000	0.7675	0.5913	1.0000	0.7720	0.5948
ns	1.0000	0.6544	0.5044	1.0000	0.6587	0.5081	1.0000	0.6475	0.4993	1.0000	0.6716	0.5178
arlet90	0.1536	0.0924	0.0712	0.1558	0.0938	0.0722	0.1549	0.0932	0.0717	0.1637	0.0984	0.0758
newh360	0.5724	0.3451	0.2660	0.5738	0.3463	0.2670	0.5636	0.3399	0.2620	0.5969	0.3600	0.2775
newh90	0.1889	0.1140	0.0879	0.3227	0.1945	0.1499	0.3212	0.1935	0.1491	0.3256	0.1962	0.1511
syl360	0.4152	0.2504	0.1930	0.4248	0.2560	0.1973	0.4208	0.2535	0.1953	0.4394	0.2648	0.2040
syl90	0.2916	0.1754	0.1351	0.1723	0.1038	0.0800	0.1640	0.0987	0.0761	0.1854	0.1116	0.0860
kobe	1.0000	0.6318	0.4877	1.0000	0.6903	0.5331	1.0000	0.6911	0.5336	1.0000	0.6947	0.5364
parkcsp1	0.1292	0.0779	0.0600	0.1169	0.0704	0.0543	0.1181	0.0711	0.0548	0.1263	0.0761	0.0586
cpm000	0.3288	0.1979	0.1524	0.3516	0.2115	0.1629	0.3504	0.2108	0.1623	0.3636	0.2187	0.1683
gaz000	0.1823	0.1104	0.0853	0.2642	0.1598	0.1234	0.2643	0.1598	0.1234	0.2620	0.1585	0.1223
kjm000	0.3310	0.2009	0.1552	0.4019	0.2435	0.1880	0.4017	0.2434	0.1879	0.4030	0.2442	0.1885
kjm090	0.3524	0.2131	0.1644	0.3492	0.2114	0.1632	0.3490	0.2110	0.1628	0.3643	0.2202	0.1699
lgp000	0.3866	0.2338	0.1804	0.4743	0.2867	0.2212	0.4752	0.2871	0.2215	0.4819	0.2913	0.2247
pcd164	0.4873	0.2941	0.2268	0.5641	0.3406	0.2627	0.5639	0.3404	0.2625	0.5632	0.3400	0.2622
pcd254	0.3085	0.1859	0.1432	0.4064	0.2447	0.1885	0.4056	0.2441	0.1880	0.4090	0.2462	0.1896
tabtr	0.2479	0.1498	0.1155	0.2810	0.1697	0.1309	0.2805	0.1692	0.1305	0.2871	0.1733	0.1336
tar090	0.4090	0.2472	0.1908	0.3491	0.2105	0.1622	0.3440	0.2073	0.1597	0.3538	0.2131	0.1642
tar360	0.1012	0.0616	0.0476	0.1663	0.1000	0.0770	0.1683	0.1011	0.0778	0.1717	0.1032	0.0794
s1010	0.0633	0.0381	0.0294	0.0662	0.0398	0.0307	0.0679	0.0408	0.0314	0.0734	0.0441	0.0340
ll	0.2061	0.1239	0.0954	0.2090	0.1256	0.0967	0.2075	0.1247	0.0960	0.2286	0.1375	0.1058
gaz090	0.0548	0.0331	0.0255	0.0951	0.0572	0.0440	0.0997	0.0600	0.0462	0.1043	0.0627	0.0483
chy0809	1.0000	0.9061	0.6985	1.0000	1.0000	1.0000	1.0000	0.8025	0.6190	1.0000	0.8256	0.6369
chy08036	0.9224	0.5566	0.4291	1.0000	0.8776	0.6757	0.8724	0.5272	0.4067	0.8908	0.5383	0.4153

tcu0659	0.8763	0.5308	0.4099	0.5962	0.3626	0.2804	1.0000	0.6282	0.4851	1.0000	0.6371	0.4920
tcu0789	0.1905	0.1147	0.0883	0.3071	0.1847	0.1422	0.2871	0.1726	0.1329	0.2990	0.1797	0.1384
tcu06536	0.7402	0.4480	0.3458	1.0000	0.8981	0.6918	1.0000	0.6261	0.4829	1.0000	0.6451	0.4976

Table 3 Comparison of Park-Ang damage index (D_{PA}) for the MDOF and different ESDOF systems for the 9-story frame

	D_{PA}											
	MDOF			ESS1			ESS2			ESS3		
Ground motion record	$\mu = 4.0$	$\mu = 6.0$	$\mu = 7.5$	$\mu = 4.0$	$\mu = 6.0$	$\mu = 7.5$	$\mu = 4.0$	$\mu = 6.0$	$\mu = 7.5$	$\mu = 4.0$	$\mu = 6.0$	$\mu = 7.5$
nr	0.2576	0.1554	0.1198	0.3371	0.2030	0.1564	0.3436	0.2069	0.1594	0.3632	0.2188	0.1685
ns	0.1985	0.1202	0.0928	0.3552	0.2138	0.1647	0.3674	0.2212	0.1704	0.3668	0.2208	0.1701
newh360	0.1434	0.0865	0.0666	0.1373	0.0827	0.0637	0.1428	0.0859	0.0662	0.1550	0.0933	0.0718
syl360	0.1260	0.0766	0.0592	0.4893	0.2948	0.2272	0.4836	0.2913	0.2244	0.5042	0.3038	0.2340
syl90	0.1262	0.0763	0.0589	0.2010	0.1213	0.0935	0.1857	0.1121	0.0864	0.2335	0.1408	0.1085
kobe	0.4312	0.2606	0.2010	0.4589	0.2775	0.2142	0.4718	0.2852	0.2201	0.4926	0.2978	0.2297
parkcsp1	0.1033	0.0622	0.0479	0.1555	0.0935	0.0720	0.1610	0.0968	0.0745	0.1753	0.1054	0.0812
kjm000	0.1550	0.0935	0.0721	0.0554	0.0334	0.0258	0.0633	0.0382	0.0294	0.0563	0.0339	0.0262
lgp000	0.4592	0.2769	0.2135	0.6001	0.3614	0.2785	0.6009	0.3619	0.2788	0.6501	0.3915	0.3016
pcd164	0.2046	0.1233	0.0950	0.2096	0.1261	0.0971	0.2156	0.1297	0.0999	0.2315	0.1393	0.1073
tabtr	0.1614	0.0978	0.0755	0.4346	0.2616	0.2015	0.4145	0.2495	0.1922	0.4777	0.2875	0.2214
tar090	0.1664	0.1002	0.0771	0.1983	0.1192	0.0918	0.2160	0.1299	0.1000	0.2187	0.1315	0.1012
tar360	0.0506	0.0308	0.0238	0.1990	0.1197	0.0921	0.1765	0.1062	0.0818	0.2017	0.1213	0.0934
ll	0.3309	0.1542	0.1187	0.3260	0.1960	0.1509	0.3241	0.1949	0.1500	0.3611	0.2171	0.1671
gaz090	0.0792	0.0476	0.0367	0.0601	0.0361	0.0278	0.0643	0.0387	0.0298	0.0758	0.0456	0.0351
chy0809	0.0843	0.0515	0.0399	0.3696	0.2222	0.1710	0.3812	0.2292	0.1764	0.3749	0.2254	0.1735
chy08036	0.1253	0.0759	0.0587	0.1914	0.1151	0.0886	0.2062	0.1240	0.0954	0.2126	0.1278	0.0984
tcu0659	0.4148	0.2510	0.1937	0.7521	0.4213	0.3247	0.6396	0.3860	0.2977	0.7797	0.4702	0.3624
tcu06536	0.1882	0.1144	0.0885	0.4412	0.1398	0.1080	0.1650	0.1006	0.0778	0.2462	0.1494	0.1154

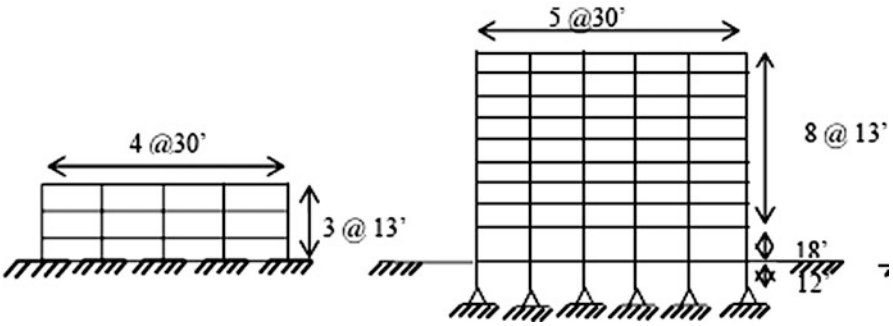

Fig. 2 Elevation of SAC buildings: 3- and 9-story (from *left* to *right*)

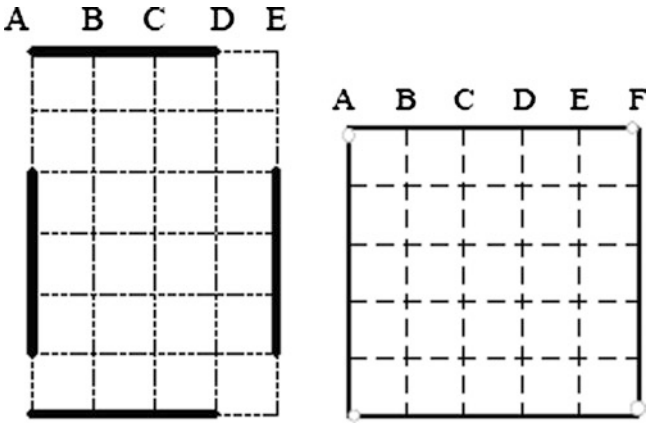

Fig. 3 Floor plans of SAC buildings: 3- and 9-story showing location of moment-resisting frames (from *left* to *right*) (not to scale)

In the 9-story building, one of the exterior bays has only one moment-resisting connection to avoid biaxial bending in the corner column. The design yield strength of the beams and girders is 36 ksi ($24.94 \times 10^4 \text{kN/m}^2$) and of the columns is 50 ksi ($34.64 \times 10^4 \text{kN/m}^2$) (Figs. 2 and 3).

5 Proposed Equivalent System Methodology

The formulation of the equivalent system starts from the dynamic response of an MDOF cantilever-type structure subjected to horizontal base motion:

$$[M]\{\ddot{u}\} + [C]\{\dot{u}\} + \{R\} = -[M]\{1\}\ddot{u}_g, \tag{2}$$

where $[M]$ = mass matrix (assumed to be diagonal), $\{u\} = \{u(t)\}$ = lateral displacement vector (one displacement for each floor), $[C]$ = damping matrix, $\{R\} = \{R(t)\}$ = restoring force vector, $\{1\}$ = unit vector, and $u_g = u_g(t)$ = ground displacement.

The lateral displacement vector $u(t)$ is represented as the product of roof-displacement $D(t)$ and a time invariant displacement profile or shape vector $\{\Phi_1\}$. Thus, $u(t)$ is replaced by $\{\Phi_1\}D(t)$. $\{\Phi_1\}$ is obtained from static pushover analysis of the MDOF system. The pushover load $\{f\}$ is chosen in such a way that $\{1\}^T\{f\} = 1$. It signifies that $\{f\}$ corresponds to a base shear of unity. To obtain actual lateral force vector corresponding to $\{f\}$, it has to be multiplied by V, thus representing the force vector by $V\{f\}$ where V is the actual base shear for the structure. The restoring force vector $\{R\}$ can be replaced by this same set of forces, i.e., $V\{f\}$. Thus, substituting $\{R\}$ and $\{u\}$ by $V\{f\}$ and $\{\Phi_1\}D$, respectively, Eq. 3 becomes

$$[M]\{\Phi_1\}\ddot{D} + [C]\{\Phi_1\}\dot{D} + V\{f\} = -[M]\{1\}\ddot{u}_g. \tag{3}$$

The mathematical relationship between V and D can be shown by $V = KG(D)$. K is the initial slope of the pushover curve and $G(D)$ a scalar mathematical function which describes the shape of the curve. So Eq. 3 can be written as

$$[M]\{\Phi_1\}\ddot{D} + [C]\{\Phi_1\}\dot{D} + KG(D)\{f\} = -[M]\{1\}\ddot{u}_g. \tag{4}$$

Premultiplying both sides by a second vector $\{\Phi_2\}^T$, this vector equation is reduced to a single equation:

$$\begin{aligned}\{\Phi_2\}^T[M]\{\Phi_1\}\ddot{D} + \{\Phi_2\}^T[C]\{\Phi_1\}\dot{D} + \mathrm{KG}(D)\{\Phi_2\}^T\{f\} \\ = -\{\Phi_2\}^T[M]\{1\}\ddot{u}_g.\end{aligned} \tag{5}$$

Equation 5 is simplified by defining the following terms: $M^*=\{\Phi_2\}^T[M]\{\Phi_1\}$, $C^* = \{\Phi_2\}^T[C]\{\Phi_1\}$, $K^* = K\{\Phi_2\}^T\{f\}$, $L^* = \{\Phi_2\}^T[M]\{1\}$, $P^* = L^*/M^*$, $(\omega^*)^2 = K^*/M^*$, and $C^*/M^* = 2\xi\omega^*$, and the equation becomes

$$M*\ddot{D}+C*\dot{D}+K*G(D) = -L*\ddot{u}_g. \tag{6}$$

After dividing by M^*, Eq. 6 becomes

$$\ddot{D}+2\xi(\omega*)\dot{D}+(\omega*)^2G(D) = -P*\ddot{u}_g. \tag{7}$$

Equation 7 can be interpreted as the equation of motion of a SDOF oscillator with linear elastic frequency ω^* and damping ratio ξ.

The vector $\{\Phi_2\}$ is chosen as $\{\Phi_2\} = \{\Phi_1\}$. So Eq. 7 is consistent with the equivalent SDOF equation derived using the principle of virtual work. This

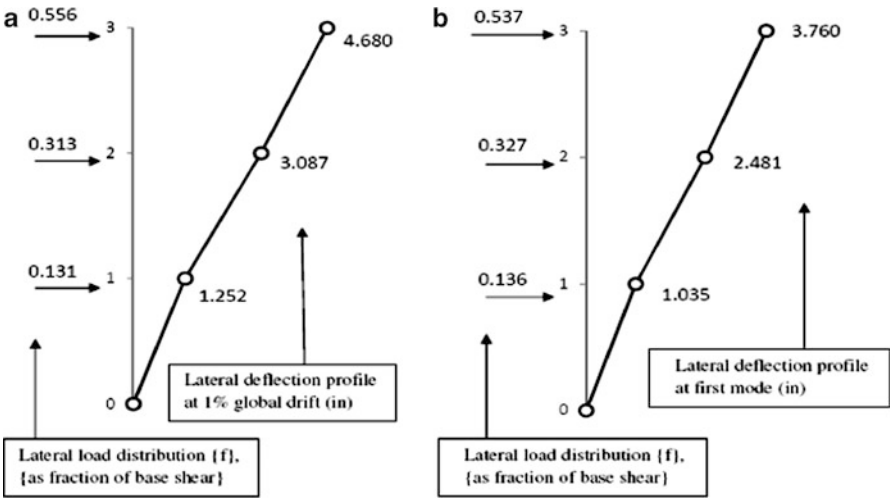

Fig. 4 Lateral load distribution $\{f\}$ and lateral deflection profile related to the pushover analysis for ESS1 (**a**) and ESS3 (**b**) for 3-story building

formulation of ESDOF system is referred as the "virtual work" formulation in this study. However, the term $K^*G(D)$ does not represent the base shear V, since K^* is not equal to K.

In the present work, equivalent system parameters are calibrated from the results of nonlinear pushover analysis. The MDOF structure is subjected to pushover analysis for 2.5% target roof drift – which shows the nonlinear behavior fairly well beyond yield point for all the buildings. The pushover plot is idealized as elastic perfectly plastic curve satisfying the same three criteria stated in Sect. 3. The yield displacement and yield base shear for MDOF structure is obtained from the idealized curve.

The following three different equivalent system schemes (ESS) are adopted for the virtual work formulation based on the bilinear approximation procedure and the choice of shape vector $\{\Phi_1\}$.

ESS 1: The pushover analysis is done considering IBC 2006 [8] load distribution. $\{\Phi_1\}$ is the displacement profile at 1% global drift.

ESS 2: The pushover analysis is done considering IBC 2006 [8] load distribution. $\{\Phi_1\}$ is the displacement profile at elastic region.

ESS 3: Pushover analysis is carried out for a load distribution corresponding to first mode. This is a simplified form of the modal pushover analysis (MPA) [2]. Instead of using multiple modes (specified in MPA), only the first mode is considered. $\{\Phi_1\}$ is the displacement profile at first mode.

The IBC 2006 and first mode load distribution are illustrated through figures. The load distribution and displacement profile corresponding to ESS 1 and ESS 3 for 3- and 9-story buildings are shown in Figs. 4 and 5, respectively.

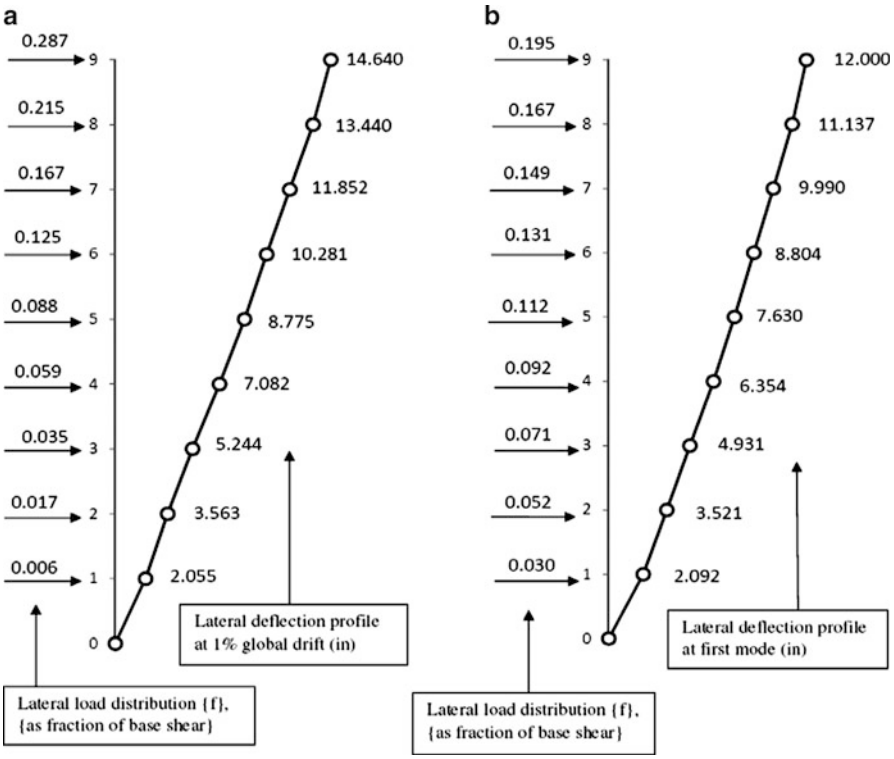

Fig. 5 Lateral load distribution $\{f\}$ and lateral deflection profile related to the pushover analysis for ESS1 (**a**) and ESS3 (**b**) for 9-story building

6 Validation of Equivalent System Methodology

The proposed ESDOF methodologies are validated for the steel moment-resisting frame buildings. Park-Ang damage indices under different ground motion scenarios are obtained for these ESDOF systems (by Fortran Program). These ground motions are same as those used for the case of MDOF systems. The D_{PA} values obtained for the ESDOF schemes are compared with damage indices of the actual MDOF structures for each of the selected records. Tables 2 and 3 present comparison of D_{PA} for the MDOF and different ESDOF systems for the moment-resisting frames. Information on the comparison between the MDOF response and the response of ESDOF system is illustrated using scatterplots. In scatterplots for each of the buildings, D_{PA} for all ductility capacity (μ) values (i.e., 4.0, 6.0, and 7.5) are considered together since it has been observed that D_{PA} values do not differ much for different μ values.

In each plot, a data point represents a comparison of the MDOF and the ESDOF responses for a single earthquake and a specific ductility capacity. The diagonal line across scatterplots represents the ideal ESDOF response, which is exactly the same as the MDOF response in terms of Park-Ang damage index. A data point above that line signifies that the ESDOF model overpredicts the MDOF response, and vice versa. The

Table 4 Equivalent system bias statistics for Park-Ang damage index (D_{PA}) for 3-story frame

	N								
	ESS1			ESS2			ESS3		
Ground motion record	$\mu = 4.0$	$\mu = 6.0$	$\mu = 7.5$	$\mu = 4.0$	$\mu = 6.0$	$\mu = 7.5$	$\mu = 4.0$	$\mu = 6.0$	$\mu = 7.5$
nn	0.5831	0.5843	0.5848	0.5855	0.5870	0.5876	0.5776	0.5790	0.5795
nr	1.000	0.8983	0.8983	1.000	0.8975	0.8975	1.000	0.8923	0.8922
ns	1.000	0.9935	0.9927	1.000	1.011	1.010	1.000	0.9743	0.9740
arlet90	0.9859	0.9860	0.9860	0.9915	0.9920	0.9922	0.9386	0.9390	0.9391
newh360	0.9975	0.9967	0.9963	1.016	1.015	1.015	0.9589	0.9586	0.9585
newh90	0.5852	0.5864	0.5869	0.5880	0.5895	0.5901	0.5800	0.5814	0.5820
syl360	0.9773	0.9779	0.9782	0.9867	0.9876	0.9880	0.9447	0.9454	0.9457
syl90	1.692	1.689	1.688	1.779	1.777	1.776	1.573	1.572	1.571
kobe	1.000	0.9152	0.9147	1.000	0.9142	0.9139	1.000	0.9095	0.9091
parkcsp1	1.105	1.106	1.106	1.094	1.095	1.095	1.023	1.024	1.024
cpm000	0.9352	0.9354	0.9355	0.9384	0.9388	0.9390	0.9045	0.9049	0.9051
gaz000	0.6901	0.6909	0.6912	0.6899	0.6909	0.6913	0.6959	0.6967	0.6971
kjm000	0.8236	0.8250	0.8255	0.8240	0.8254	0.8259	0.8214	0.8227	0.8232
kjm090	1.009	1.008	1.007	1.010	1.010	1.010	0.9675	0.9675	0.9675
lgp000	0.8150	0.8155	0.8157	0.8135	0.8142	0.8145	0.8022	0.8026	0.8028
pcd164	0.8638	0.8636	0.8635	0.8640	0.8640	0.8640	0.8652	0.8650	0.8649
pcd254	0.7590	0.7596	0.7598	0.7607	0.7615	0.7618	0.7543	0.7550	0.7553
tabtr	0.8823	0.8825	0.8827	0.8838	0.8850	0.8854	0.8635	0.8644	0.8648
tar090	1.172	1.175	1.176	1.189	1.193	1.195	1.156	1.160	1.162
tar360	0.6089	0.6157	0.6184	0.6015	0.6087	0.6115	0.5897	0.5965	0.5993
s1010	0.9555	0.9573	0.9581	0.9320	0.9339	0.9346	0.8621	0.8640	0.8647
ll	0.9864	0.9867	0.9868	0.9933	0.9936	0.9938	0.9015	0.9014	0.9014
gaz090	0.5760	0.5788	0.5799	0.5489	0.5517	0.5528	0.5248	0.5274	0.5284
chy0809	1.000	0.9061	0.6985	1.000	1.129	1.128	1.000	1.098	1.097
chy08036	0.9224	0.6342	0.6351	1.057	1.056	1.055	1.036	1.034	1.033

(continued)

Table 4 (continued)

	N								
	ESS1			ESS2			ESS3		
Ground motion record	$\mu = 4.0$	$\mu = 6.0$	$\mu = 7.5$	$\mu = 4.0$	$\mu = 6.0$	$\mu = 7.5$	$\mu = 4.0$	$\mu = 6.0$	$\mu = 7.5$
tcu0659	1.470	1.464	1.462	0.8763	0.8450	0.8449	0.8763	0.8332	0.8331
tcu0789	0.6203	0.6210	0.6213	0.6636	0.6645	0.6649	0.6373	0.6381	0.6384
tcu06536	0.7402	0.4988	0.4999	0.7402	0.7155	0.7161	0.7402	0.6944	0.6949
Mean	0.9198	0.8911	0.8839	0.9081	0.9052	0.9055	0.8783	0.8714	0.8717
SD	0.2521	0.2640	0.2658	0.2417	0.2437	0.2433	0.2118	0.2124	0.2121
COV	0.2741	0.2962	0.3008	0.2662	0.2692	0.2687	0.2412	0.2437	0.2433
Max	1.692	1.689	1.688	1.779	1.777	1.776	1.573	1.572	1.571
Min	0.5760	0.4988	0.4999	0.5489	0.5517	0.5528	0.5248	0.5274	0.5284

Table 5 Equivalent system bias statistics for Park-Ang damage index (D_{PA}) for 9-story frame

	N								
	ESS1			ESS2			ESS3		
Ground motion record	$\mu = 4.0$	$\mu = 6.0$	$\mu = 7.5$	$\mu = 4.0$	$\mu = 6.0$	$\mu = 7.5$	$\mu = 4.0$	$\mu = 6.0$	$\mu = 7.5$
nr	0.7644	0.7655	0.7660	0.7499	0.7511	0.7516	0.7093	0.7105	0.7109
ns	0.5589	0.5620	0.5632	0.5404	0.5433	0.5445	0.5413	0.5442	0.5454
newh360	1.044	1.046	1.046	1.004	1.006	1.007	0.9251	0.9270	0.9277
syl360	0.2576	0.2597	0.2605	0.2606	0.2628	0.2637	0.2499	0.2520	0.2529
syl90	0.6278	0.6291	0.6297	0.6794	0.6808	0.6814	0.5404	0.5421	0.5428
kobe	0.9397	0.9389	0.9385	0.9141	0.9135	0.9133	0.8754	0.8751	0.8749
parkcsp1	0.6640	0.6653	0.6658	0.6414	0.6426	0.6430	0.5891	0.5902	0.5906
kjm000	2.795	2.796	2.796	2.448	2.450	2.451	2.752	2.753	2.754
lgp000	0.7652	0.7662	0.7667	0.7642	0.7653	0.7658	0.7063	0.7074	0.7078
pcd164	0.9764	0.9774	0.9778	0.9493	0.9502	0.9505	0.8841	0.8852	0.8856
tabtr	0.3713	0.3737	0.3747	0.3893	0.3918	0.3928	0.3378	0.3401	0.3410
tar090	0.8390	0.8401	0.8405	0.7700	0.7711	0.7716	0.7607	0.7617	0.7621
tar360	0.2542	0.2570	0.2581	0.2865	0.2896	0.2908	0.2507	0.2535	0.2546
ll	1.015	0.7867	0.7868	1.021	0.7912	0.7913	0.9165	0.7103	0.7103
gaz090	1.319	1.319	1.319	1.232	1.232	1.233	1.046	1.046	1.046
chy0809	0.2281	0.2320	0.2335	0.2212	0.2249	0.2264	0.2249	0.2287	0.2301
chy08036	0.6547	0.6601	0.6622	0.6076	0.6126	0.6146	0.5894	0.5942	0.5961
tcu0659	0.5515	0.5958	0.5966	0.6485	0.6502	0.6508	0.5320	0.5338	0.5345
tcu06536	0.4266	0.8185	0.8193	1.141	1.138	1.137	0.7646	0.7661	0.7667
Mean	0.7923	0.8047	0.8054	0.8036	0.7930	0.7936	0.7471	0.7380	0.7386
SD	0.5697	0.5590	0.5588	0.4929	0.4895	0.4893	0.5437	0.5419	0.5417
COV	0.7190	0.6947	0.6938	0.6134	0.6173	0.6166	0.7278	0.7343	0.7334
Max	2.795	2.796	2.796	2.448	2.450	2.451	2.752	2.753	2.754
Min	0.2281	0.2320	0.2335	0.2212	0.2249	0.2264	0.2249	0.2287	0.2301

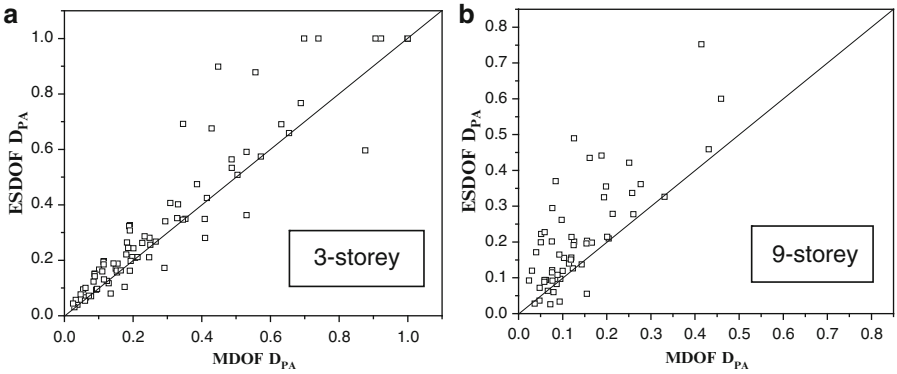

Fig. 6 Scatterplot comparing D_{PA} values of MDOF and ESDOF system for ESS1

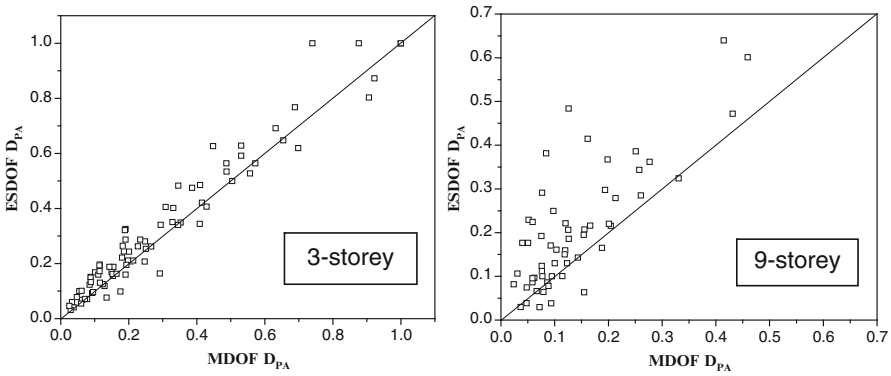

Fig. 7 Scatterplot comparing D_{PA} values of MDOF and ESDOF system for ESS2

trend of overestimation or underestimation by the ESDOF model is analyzed through bias factor (N) statistics, where the bias factor is defined as the ratio of the D_{PA} for the MDOF system to the D_{PA} for the ESDOF system response for a particular earthquake. The bias statistics for all the frames are discussed below.

Tables 4 and 5 present the bias statistics for the frames. As stated earlier, three different ductility capacity values are considered for each frame, and the statistics for each frame include the results for different ductility capacities. When $D_{PA} < 0.05$ (for all μ values), they are not considered, since lower values will amount to negligible inelasticity. This reduces the number of records for the 9-story frames to 19. Figures 6, 7, and 8 present the scatterplots comparing D_{PA} values of MDOF and various ESDOF systems for 3- and 9-story buildings.

The bias statistics results show that all three equivalent system schemes (ESSs) work very well for the 3-story building. For the 9-story building, the adopted ESS

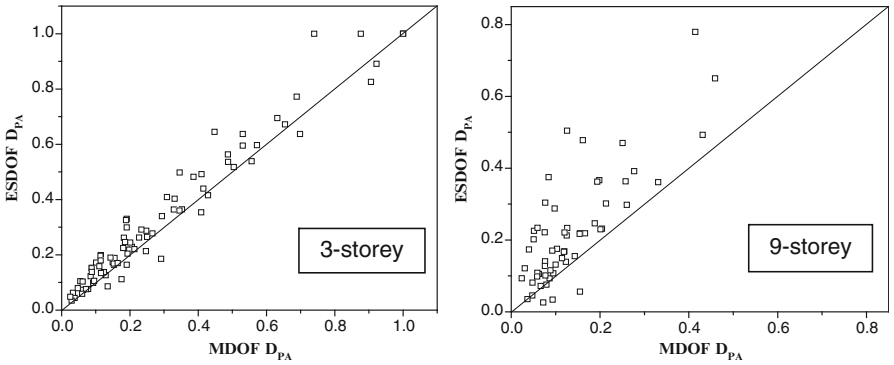

Fig. 8 Scatterplot comparing D_{PA} values of MDOF and ESDOF system for ESS3

schemes predict the responses fairly well. For both cases (3-story and 9-story), ESS1 and ESS2 give better result than ESS3.

The scatterplots for 3-story building shows good results with slight overprediction. ESS2 gives best result for 3-story building. For 9-story building, the scatter is very high for all the adopted ESS schemes, and the ESDOFs overestimate the results.

The results indicate that the equivalent schemes adopted in this work are most suitable for 3-story building, but for 9-story building they are not very ideal. This is because the higher mode effects are not considered to develop the ESDOF system.

From the observation of the scatterplots, it can be said that higher number of bias factor data points will lead to better understanding about suitability of a certain ESS. But the aim of present work is to portray the effective use of the information (given by ESS) in design. So such computation heavy analysis is avoided. To optimize the ESDOF methodology, further research work is needed. Various other ESDOF schemes (e.g., ESS schemes considering higher mode effects) should be tried for large number of ground motion records.

References

1. Bureau of Indian Standards (2002) *IS 1893* – Criteria for earthquake resistant design of structures, Part −1, India
2. Chopra AK, Goel RK (2002) A modal pushover analysis procedure for estimating seismic demands for buildings. Earthq Eng Struct Dyn 31:561–582
3. Collins KR, Wen YK, Foutch DA (1996) Dual-level seismic design: a reliability based methodology. Earthq Eng Struct Dyn 25:1433–1467

4. Datta D (2009) Reliability based design of steel moment frames using Park-Ang damage index. PhD thesis, Department of Civil Engineering, IIT, Bombay
5. Ghosh S (2003) Two alternatives for implementing performance based seismic design of buildings- life cycle cost and seismic energy demand. PhD thesis, Department of Civil Engineering, University of Michigan, Ann Arbor
6. Ghosh S, Collins KR (2006) Merging energy-based design criteria and reliability-based methods: exploring a new concept. Earthq Eng Struct Dyn 35(13):1677–1698
7. Gupta A, Krawinkler H (1999) Seismic demands for performance evaluation of steel moment resisting frame structures (SAC Task 5.4.3), Report no. 132, John A Blume Earthquake Engineering Center, Department of Civil and Environmental Engineering, Stanford University, Stanford, CA
8. International Code Council (ICC) (2006) International Building Code
9. Park YJ, Ang AH-S (1985) Mechanistic seismic damage model for reinforced concrete. ASCE J Struct Eng 111(4):722–739

Seismic Reliability Analysis of Base-Isolated Buildings

M.C. Jacob, G.R. Dodagoudar, and V.A. Matsagar

Abstract Seismic base isolation is achieved via inserting flexible isolator element between the foundation and superstructure which lengthens the vibration period and increases the energy dissipation. Values adopted for uncertain parameters in earthquake engineering deviate from their nominal values. The stochastic response analysis of the base-isolated building is studied considering uncertainties in the characteristics of the earthquakes. Artificial acceleration time histories developed using probabilistic ground motion model are used in the study. The uncertainties in peak ground acceleration, frequency content, and time duration are considered to develop 5,000 artificial acceleration time histories. A bilinear model of the isolator described by its characteristic strength, post-yield stiffness, and yield displacement is used, and the stochastic response is calculated by using an ensemble of generated earthquakes. The study also presents the results of seismic reliability analysis of the five-storey base-isolated building. The first-order reliability method (FORM) and Monte Carlo simulation (MCS) method are used to evaluate the probability of failure associated with the top floor acceleration response of the building. The top floor acceleration response statistics are used in the performance function considering 0.3 g as a maximum allowable acceleration, and the probability of failure is evaluated. The probability of failure evaluated using the FORM is fairly in good agreement with the value obtained by the MCS.

Keywords Base isolation • Artificial earthquakes • Stochastic response • Reliability • FORM • MCS

M.C. Jacob (✉)
JACOB Engineers, Selaiyur, Chennai 600 073, India
e-mail: cibijacob@jacobengineers.in

G.R. Dodagoudar
Department of Civil Engineering, Indian Institute of Technology Madras, Chennai 600 036, India
e-mail: goudar@iitm.ac.in

V.A. Matsagar
Department of Civil Engineering, Indian Institute of Technology Delhi, New Delhi 110 016, India
e-mail: matsagar@civil.iitd.ac.in

S. Chakraborty and G. Bhattacharya (eds.), *Proceedings of the International Symposium on Engineering under Uncertainty: Safety Assessment and Management (ISEUSAM - 2012)*,
DOI 10.1007/978-81-322-0757-3_87,

1 Introduction

Ground motion at a particular site due to earthquakes is influenced by source, travel path and local site conditions. The first relates to the size and source of the source mechanism of the earthquake. The second describes the path effects of the earth as the wave travels from the source to the site. The third describes the effects of the upper hundreds of metres of rocks and soil and the surface topography at the site. It is well known that earthquake ground motions are nonstationary in time and frequency domains. Temporal nonstationarity refers to the variation in the intensity of the ground motion in time. Spectral nonstationarity refers to the variation in the frequency content of the motion in time.

One of the emerging tools for protecting structures from the damaging effects of earthquake ground motion is the use of isolation systems. Base isolation or base isolation system is a collection of structural elements which substantially decouple a superstructure from its substructure which is resting on a shaking ground, thus protecting a building or nonbuilding structure's integrity. The base isolation minimizes the inter-storey deformations and the floor accelerations by interposing elements of high axial and low horizontal stiffness between the structure and the foundation. It is meant to enable a building or nonbuilding structure to survive a potentially devastating seismic impact through a proper initial design or subsequent modifications. In some cases, application of base isolation can raise both a structure's seismic performance and its seismic sustainability considerably. Various theories of seismic isolation, testing programmes and isolation systems have been used in structures [3, 4]. Previous studies have demonstrated that the Monte Carlo simulation is an effective method in obtaining stochastic response statistics. The objective of this study is to carry out the stochastic response evaluation and reliability analysis of the isolated building structure under earthquake excitations with emphasis on the uncertainty in the earthquake loading. The seismic reliability analysis of the five-storey base-isolated building is analysed using the first-order reliability method (FORM) and Monte Carlo simulation (MCS) method. Thestructural characteristics are considered as deterministic, and the top floor acceleration response is evaluated using 5,000 artificial acceleration time histories. Using these response values, probabilistic characteristics of the top floor acceleration response are obtained. These characteristics are used in the performance function considering 0.3 g as a maximum allowable acceleration, and the probability of failure is evaluated. All the 5,000 acceleration response values of the top floor are used in the MCS to obtain the probability of failure associated with the five-storey base-isolated building. The probability of failure evaluated using the FORM is fairly in good agreement with the value obtained by the MCS.

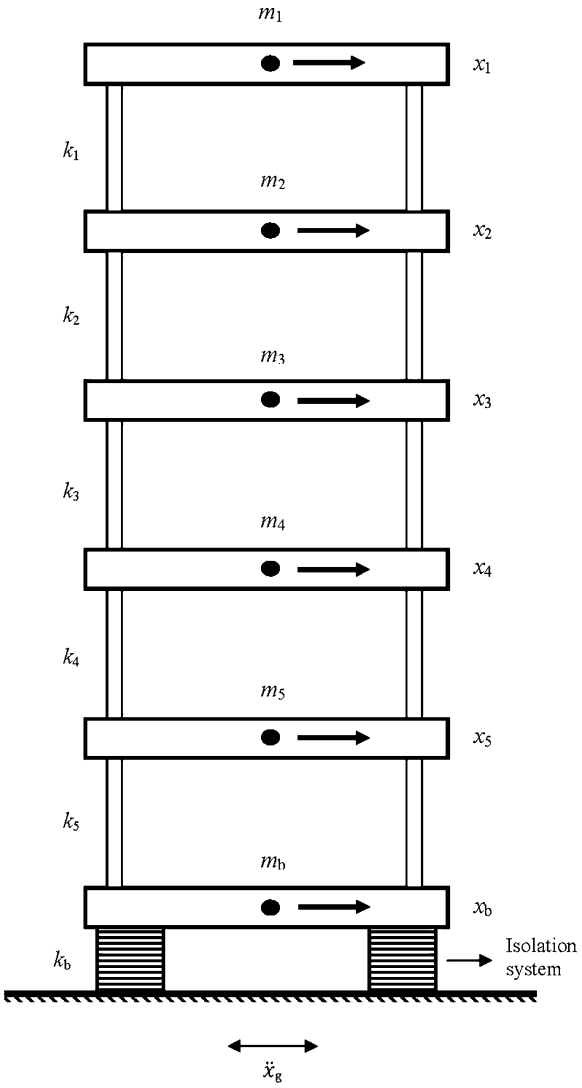

Fig. 1 Mathematical model of a five-storey base-isolated building

2 Deterministic Response of an Isolated Building

In this study, the lumped mass modelling is adopted for the superstructure and the isolator. The effect of rotation in the structure and isolator is not taken into consideration. The base-isolated building is modelled as a shear-type structure mounted on isolation system with one lateral degree of freedom at each floor. Figure 1 shows the idealized mathematical model of the five-storey base-isolated building considered in the study. The following assumptions are made: (1) The superstructure is considered to remain within the elastic limit during the earthquake

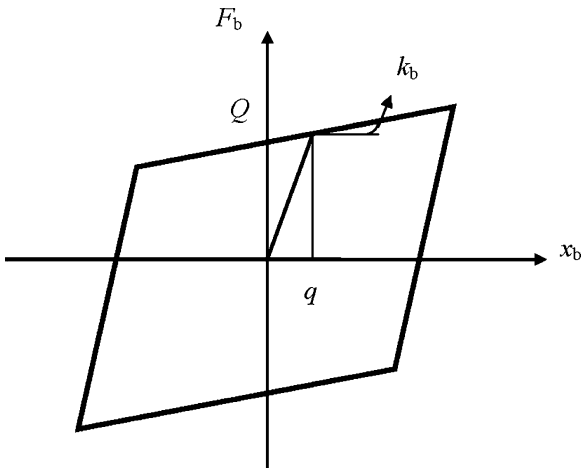

Fig. 2 Mathematical model of the isolator

excitation; (2) the floors are assumed as rigid in its own plane, and the mass is supposed to be lumped at each floor level; (3) the columns are inextensible and weightless providing the lateral stiffness; (4) the system is subjected to single horizontal component of the earthquake ground motion; and (5) the effect of soil-structure interaction is neglected. The x_j is the relative floor displacement at the jth floor, m_j is the floor mass at the jth floor, k_j is the stiffness of the jth floor, x_b is the displacement of the isolator and m_b is the mass of the isolator.

The force-deformation behaviour of the isolator is modelled as nonlinear hysteretic represented by the bilinear model. This model is depicted in Fig. 2. The nonlinear force-deformation behaviour of the isolation system is modelled through the bilinear hysteresis loop characterized by three parameters: (1) characteristic strength, Q; (2) post-yield stiffness, k_b; and (3) yield displacement, q. The characteristic strength, Q, is related to the yield strength of the lead core in the elastomeric bearings and friction coefficient of the sliding type isolation systems. The post-yield stiffness of the isolation system, k_b, is generally designed in such a way to provide the specific value of the isolation period, T_b, expressed as

$$T_b = 2\pi\sqrt{\frac{M}{k_b}} \tag{1}$$

where $M = m_b + \sum_{j=1}^{5} m_j$ is the total mass of the base-isolated structure. The characteristic strength, Q, is mathematically related to the damping ratio, ζ_b, by the following equation [5]:

$$\zeta_b = \frac{4Q(D-q)}{2\pi k_b D^2} \tag{2}$$

where D is the design displacement. Thus, the bilinear hysteretic model of the base isolation system can be characterized by specifying the three parameters, namely, T_b, Q and q.

2.1 Equations of Motion and Solution Procedure

The general equations of motion for the superstructure-isolator model illustrated in Fig. 1 can be expressed as

$$M\ddot{X}^{\mathrm{Tot}}(t) + C\dot{X}(t) + KX(t) = 0 \tag{3}$$

where $X = \{x_j\}^T$ is the column vector of relative structural displacements with respect to the isolator, $X^{\mathrm{Tot}} = \left\{x_j^{\mathrm{Tot}}\right\}^T$ is the column vector of total structural displacements, M is the mass matrix of the structure, C is the viscous damping matrix of the structure and K is the stiffness matrix of the structure. The x_j^{Tot} is expressed as

$$x_j^{\mathrm{Tot}} = x_j + x_b + x_g \tag{4}$$

where x_g is the displacement of the ground due to the earthquake and x_b is the displacement of the isolator. The equations of motion for a five-storey base-isolated building is written as

$$M\ddot{X} + C\dot{X} + KX = -M\ddot{X}g \tag{5}$$

where

$$X = \{x_1, x_2, x_3, x_4, x_5, x_b\}^T \tag{6}$$

$$M = \begin{bmatrix} m_1 & 0 & 0 & 0 & 0 & m_1 \\ 0 & m_2 & 0 & 0 & 0 & m_2 \\ 0 & 0 & m_3 & 0 & 0 & m_3 \\ 0 & 0 & 0 & m_4 & 0 & m_4 \\ 0 & 0 & 0 & 0 & m_5 & m_5 \\ 0 & 0 & 0 & 0 & 0 & m_b \end{bmatrix} \tag{7}$$

$$K = \begin{bmatrix} k_1 & -k_1 & 0 & 0 & 0 & 0 \\ -k_1 & k_1 + k_2 & -k_2 & 0 & 0 & 0 \\ 0 & -k_2 & k_2 + k_3 & -k_3 & 0 & 0 \\ 0 & 0 & -k_3 & k_3 + k_4 & -k_4 & 0 \\ 0 & 0 & 0 & -k_4 & k_4 + k_5 & -k_5 \\ 0 & 0 & 0 & 0 & -k_5 & k_5 + k_b \end{bmatrix} \tag{8}$$

$$\overline{M} = \{m_1, m_2, m_3, m_4, m_5, m_b\}^T \tag{9}$$

The damping matrix of the superstructure, C, is not known explicitly. It is constructed by assuming the modal damping ratio in each mode of vibration of the superstructure.

Classical modal superposition technique cannot be employed in the solution of equations of motion here, because (1) the system is nonclassically damped because of the difference in the damping in isolation system compared to the damping in the superstructure and (2) the force-deformation behaviour of the isolation systems considered is nonlinear. Therefore, the equations of motion are solved numerically using Newmark's method of step-by-step integration, adopting linear variation of acceleration over a small time interval of Δt. The response quantities of interest such as acceleration, velocity and displacement at any degree of freedom and force in the isolator are calculated at each time interval [8].

2.2 Numerical Example

In order to find the deterministic response of the isolated structure, a recorded earthquake accelerogram is considered. The earthquake motion selected for the study is N00E component of 1989 Loma Prieta earthquake recorded at Los Gatos Presentation Center. The peak ground acceleration (PGA) of the Loma Prieta earthquake is 0.57 g. The acceleration response of the structure and the isolator response are calculated. The response quantities of interest are the top floor absolute acceleration and relative isolator displacement. The above response quantities are chosen because the floor accelerations developed in the superstructure are proportional to the forces exerted by the earthquake ground motion. The bearing displacements are crucial in the design of isolation systems. The various parameters of the superstructure and the isolator considered for the example problem are given. The ratio of mass of each floor is 1:1:1:1:1, and ratio of stiffness of each floor is 2:3:4:5:6. The floor mass of each floor of the superstructure is considered as equal. The stiffness is considered in such a way that the top floors are less stiff than the bottom floors. The stiffness increases proportionally from top to bottom. The appropriate time period of the five-storey building is taken as 0.5 s. The damping ratio of the superstructure is taken as 0.02 and kept constant for all modes of vibration. The inter-storey stiffness of the superstructure is adjusted such that a specified fundamental time period of the superstructure, T_s, is achieved. The mass of the isolator is considered to be equal to that of a floor. The damping ratio of the isolator, ζ_b, is 0.1. The time period of the isolator, T_b, is taken as 2 s. The design displacement, D, is 53.61 cm, and yield displacement, q, is taken as 2.5 cm. The peak top floor acceleration of the fixed base structure is 2.92 g and that of the base-isolated structure is 0.66 g. The peak isolator displacement is 42.57 cm.

3 Stochastic Simulation of Ground Motions

A method to generate an ensemble of artificial earthquake ground motions is described in this section. The method is based on the *probabilistic ground motion model* developed by Jacob et al. [2]. The probabilistic model is based on the fully nonstationary stochastic ground motion model proposed by Rezaeian and Kiureghian [6] which uses filtering of a discretized white-noise process. The nonstationarity is achieved by modulating the intensity and varying the filter properties in time. The stochastic ground motion model considers both the temporal and spectral nonstationarities. A database to be used in the *probabilistic ground motion model* is created by choosing the recorded earthquake accelerograms. The recorded earthquakes are selected arbitrarily. In the next step, the nine parameters required to depict a particular ground motion are found out for all the 100 ground motions in the database. The probability distributions are created for the parameters of all the earthquake motions. Now the parameters required for the stochastic ground motion model to simulate the artificial ground motions are obtained from these distributions. The Monte Carlo simulation is used to generate an ensemble of ground motions.

The expression to calculate the ground acceleration $\hat{x}(t),$ at any time t is given as

$$\hat{x}(t) = q(t) \sum_{(i=1)}^{k} s_i(t) u_i, t_k \ \leq t < t_{k+1} \tag{10}$$

where $q(t)$ is the modulating function at time t and u_i is the standard random normal variable. A modified version of the Housner and Jennings model [1] using the modulating function is given as

$$\begin{aligned} q(t) &= 0, && t \ \leq T_0 \\ q(t) &= \sigma_{\max}\left(\frac{t - T_0}{T_1 - T_0}\right)^2, && T_0 < t \ \leq T_1 \\ q(t) &= \sigma_{\max}, && T_1 \leq t \ \leq T_2 \\ q(t) &= \sigma_{\max}\exp\left[-\alpha(t - T_2)^{\beta}\right], && T_2 \ \leq t \end{aligned} \tag{11}$$

This model has six parameters $T_0, T_1, T_2, \sigma_{\max}, \alpha$ and β which obey the conditions $T_0 < T_1 < T_2$ $0 < \sigma_{\max},$ $0 < \alpha$ and $0 < \beta$. The T_0 denotes the start time of the process, T_1 and T_2 denote the start and end times of the strong-motion phase with root mean square (RMS) amplitude, $\sigma_{\max},$ and α and β are the parameters that shape the decaying end of the modulating function. The value of β is taken as 1 and $k = \text{int}\left(\frac{t}{\Delta t}\right)$ where Δt is the time step taken for discretizing the model. The filter function is given as

$$s_i(t) = \frac{h[t - t_i, \theta(t_i)]}{\sqrt{\sum_{j=1}^{k} h^2\left[t - t_j, \theta\left(t_j\right)\right]}}, \quad \leq t < t_{k+1,}\ 0 < i \leq k \tag{12}$$

Any damped single- or multi-degree-of-freedom linear system that has differentiable response can be selected as the filter, i.e.

$$\begin{aligned} h[t - \tau, \theta(\tau)] = {} & \frac{\omega_f(\tau)}{\sqrt{1 - \zeta_f^2(\tau)}} \exp\left[-\zeta_f(\tau)\omega_f(\tau)(t - \tau)\right] \\ & \times \sin\left[\omega_f(\tau)\sqrt{1 - \zeta_f^2(\tau)}(t - \tau)\right], \tau \leq t \\ & h[t - \tau, \theta(\tau)] = 0, \text{ otherwise} \end{aligned} \tag{13}$$

which represents the pseudo-acceleration response of a single-degree-of-freedom linear oscillator subjected to a unit impulse, in which τ denotes the time of the pulse and $\theta(\tau) = \left[\omega_f(\tau), \zeta_f(\tau)\right]$ is the set of parameters of the filter with $\omega_f(\tau)$ denoting the natural frequency and $\zeta_f(\tau)$ denoting the damping ratio, both dependent on the time of application of the pulse. The $\omega_f(\tau)$ influences the predominant frequency of the resulting process, whereas $\zeta_f(\tau)$ influences its bandwidth. The predominant frequency of an earthquake ground motion tends to decay with time. Therefore,

$$\omega_f(\tau) = \omega_0 - (\omega_0 - \omega_n)\frac{\tau}{t_n} \tag{14}$$

where t_n is the total duration of the ground motion, ω_0 is the filter frequency at time $t_0 = 0$ and ω_n is the frequency at time t_n. For a typical ground motion, $\omega_n < \omega_0$. Thus, the two parameters ω_0 and ω_n describe the time-varying frequency content of the ground motion.

3.1 Determination of Model Parameters

The nine parameters of the stochastic ground motion model are found out for each of the earthquakes in the database. The two additional parameters that are required are the time duration T_{n} and the time steps Δt. The T_n is known from the time history, and Δt is taken as 0.02 s for all the earthquakes. The six parameters required for the modulating function can be obtained by minimizing the difference between the cumulative energy of the recorded ground motion and the cumulative energy of the fitted ground motion. Using the same method of optimization, the parameters in the filter depicting the predominant frequency of the ground motion are obtained by minimizing the difference between the cumulative count of negative maxima and positive minima of the target and the model. The parameters in the filter that depict the bandwidth of the ground motion are obtained by minimizing the difference between the cumulative number of zero-level up-crossings of the target and the model.

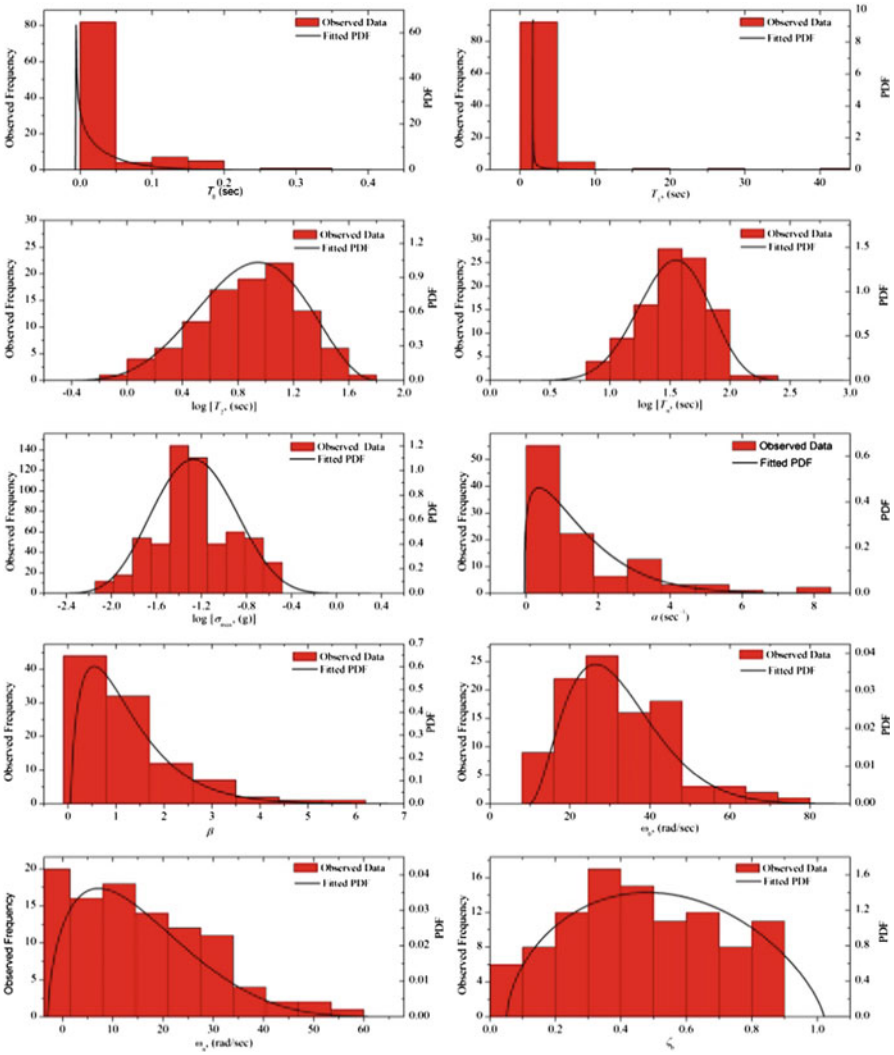

Fig. 3 PDF of parameters superimposed on observed normalized frequency diagrams

3.2 Distribution of Model Parameters and Ground Motion Simulation

After identifying the model parameter values by fitting to each of the recorded ground motion in the database, a probability distribution is assigned to the sample of values of each parameter. Now there are 100 sets of parameters representing the 100 earthquakes. The time step Δt is kept constant for all the 100 earthquakes. The distribution models are assigned to each of the ten parameters. It is found that the data of all the ten parameters are effectively fitted by β distribution. Figure 3

shows the normalized frequency diagrams of the fitted model parameters for the entire dataset with the fitted probability density functions (PDFs) superimposed.

A cluster of earthquake ground motions is produced. This is done by randomly selecting the parameters of the stochastic ground motion model. Initially 10,000 samples of each parameter are arbitrarily chosen from the distributions of the particular parameter. From this pool of samples, 5,000 sets of parameters which satisfy the conditions are chosen. Using these 5,000 sets of parameters, 5,000 artificial ground motions are generated. This cluster of earthquakes which represents a completely random choice of ground motions is used in the response analysis of the base-isolated building.

4 Stochastic Response of an Isolated Building

The stochastic response of the base-isolated building is evaluated by using direct Monte Carlo simulations. The uncertainty in the characteristics of the ground motion is considered, and all the structural input parameters are considered as deterministic. The response quantities of interest are the absolute peak value of the acceleration at the top floor, hereinafter simply referred as top floor acceleration, and the peak value of the isolator displacement hereinafter simply referred as isolator displacement. To perform the response analysis, a total of 5,000 artificial earthquakes are simulated as described before. Deterministic analysis is performed for each simulation, and their corresponding response quantities are evaluated. The deterministic results are then processed to find the peak values, root mean square (RMS) values and distributions of the response quantities. While calculating the responses, the parameters of the structure are kept unchanged. The top floor acceleration is found to be fitted effectively by using β distribution, and the isolator displacement is effectively fitted by generalized Pareto distribution. The PDFs of the response quantities are plotted and superimposed with their observed frequency diagrams as shown in Fig. 4. The mean and standard deviation of the top floor acceleration are 0.158 and 0.097 g, respectively. The mean and standard deviation of the isolator displacement are 5.873 and 6.981 cm, respectively. For the considered parameters, the extreme top floor acceleration is found to be 0.89 g, and the extreme isolator displacement is found to be 92 cm. Their corresponding RMS values are 0.185 g and 9.122 cm.

5 Reliability Analysis of the Base-Isolated Building

The term ‘reliability’ of a structural system may be defined as the probability of satisfactory performance under the given environmental conditions. Past experience shows that apparently conservative designs (based on the traditional ‘factor of safety concept’) are not always safe against failure. Reliability analysis offers a

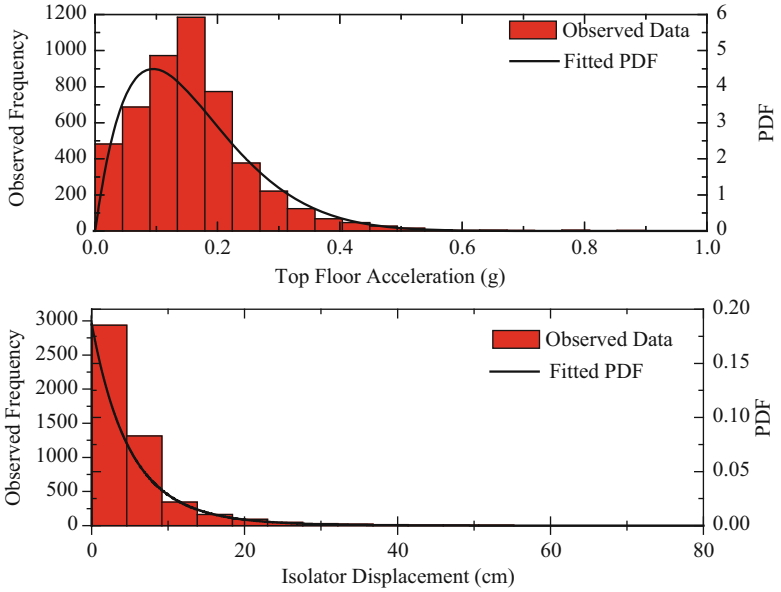

Fig. 4 PDF of response quantities superimposed on observed normalized frequency diagrams

more rational way to evaluate the stability of structural systems by explicitly accounting for uncertainties associated with material properties and loading, environmental conditions and modelling errors. The simplest reliability model involves two resultant variables, called load effect (S) and resistance (R). These resultant variables are usually functions of several random variables $X_1, X_2, \ldots, X_n$. For example, with reference to stability of cantilever retaining wall, S is the net lateral force (causing sliding), and R is the net resisting force. The limit state function associated with the sliding failure can be expressed as

$$M = R - S = g(X_1, X_2, ..., X_n) \tag{15}$$

where M is referred to as the safety margin which is a random variable and a function $g(X)$ of the basic variables X_i. The condition $g(X) < 0$ implies failure, while $g(X) > 0$ implies stable behaviour. The boundary, defined by $g(X) = 0$, separating the stable and unstable states is called the limit state boundary.

Mathematically the probability of failure P_f can be simply defined as follows:

$$P_f = \int \ldots \int_{g(X) < 0} f_{\bar{X}}(x_1, x_2, ..., x_n)\ dx_1, dx_2, \ldots dx_n \tag{16}$$

where $f_X\ (x)$ is the joint probability density function of all the basic variables (JPDF). This JPDF may be visualized as a hyper-geometrical space with unit

volume, and P_f denotes the function of that volume which lies in the failure domain $g(X) < 0$. There are several computational difficulties in computing the value of P_f as defined above, and hence, the problem is numerically addressed by alternative approximate methods, such as Monte Carlo simulation (MCS). Furthermore, the statistical data for the basic variables is generally limited in practice to second-order statistics (mean and standard deviation), and the correlations among the variables are also not well known. In reliability analysis, a popular alternative procedure to address such problems is by the 'first-order' and 'second-order' reliability methods (FORM and SORM).

The reliability index can be defined as the distance from the origin ($M = 0$) to the mean μ_M, measured in standard deviation units. Alternatively, it is the measure of the probability that the safety margin M will be less than zero. Reliability index is defined as,

$$\beta = \frac{\mu_M}{\sigma_M} \tag{17}$$

If M is a linear function of basic variables that are normally distributed, then M is also normally distributed, whereby the probability of failure is related to reliability index as

$$P_f = \Phi(-\beta) \tag{18}$$

The mean-value-based reliability index has the drawback that its value changes when the limit state function (Eq. 15) is expressed as an equivalent, but nonlinear function. For example, $M = R - S$ and $M = (R/S) - 1$ will give different values of β. This problem of 'lack of invariance' can be resolved, by transforming the X variables into an equivalent set of uncorrelated standard unit normal U variables. In this transformed 'U- space', the reliability index β is given by the shortest distance from the origin to the surface defining the failure function, g (U). The point of intersection of this line with the failure surface is termed as 'design point'. The nonlinear failure function can be conveniently approximated by its tangent plane at the 'design point', and the corresponding method of finding β is referred to as first-order reliability method (FORM).

In this chapter, as the available statistics are restricted to second-order properties and the basic variables are assumed to be uncorrelated, the following transformation from the X- space to U- space is applicable:

$$U_i = \frac{X_i - \mu_{x_i}}{\sigma_{x_i}} (i = 1,\ 2,\ \ ...,\ n) \tag{19}$$

The problem of computing β by FORM is essentially an optimization problem, and many techniques have been developed to achieve this in the literature. The algorithm proposed by Rackwitz and Fiessler [7] is particularly convenient to apply in FORM with feature of converting nonnormal random variables to equivalent normal variables.

5.1 Monte Carlo Simulation Method

In the MCS method, each random variable is sampled several times to represent its real distribution according to its probabilistic characteristics. A set of such numbers reflects one possible realization of the problem itself. Solving the problem deterministically for each realization is known as a simulation cycle. Using a large number of simulation cycles enables the generation of the overall probabilistic characteristics of the problem. After repeated simulations, one can assess the sensitivity of the system response to variation in the parameters. Each continuous variable is replaced by a large number of discrete values generated from the underlying distribution; these values are used to compute a large number of values of function M and its distribution.

Let N_f be the number of simulation cycles when $g(X)$ is less than zero, and let N be the total number of simulation cycles. Therefore, an estimate of the probability of failure can be expressed as

$$P_f = \frac{N_f}{N} \tag{20}$$

5.2 Numerical Example

The probability of failure for the five-storey base-isolated building is evaluated considering the following limit state function:

$$h(X) = 0.3 - a_i \tag{21}$$

where $h(X)$ is the limit state function associated with the top floor acceleration response of the building and a_i is the peak acceleration of the top floor in g evaluated considering the stochastic nature of the input ground motion. A value of 0.3 g is taken as the allowable acceleration at the top floor for the building under consideration. Then, the probability of failure is defined as

$$P_f = P[h(X) \leq 0] \tag{22}$$

The probability of failure is evaluated via Monte Carlo simulation by determining the number of realizations with $h(X) < 0$ and dividing that number by the total number of simulations. The convergence of the probability of failure is demonstrated in Fig. 5 where the isolator parameters are $T_b = 2.0$ s, , $q = 2.5$ cm, $\zeta_b = 0.1$ and $D = 40$ cm. The figure also depicts the probability of failure evaluated using FORM. It is seen that the FORM has also provided a reasonably good approximation as compared to the MCS.

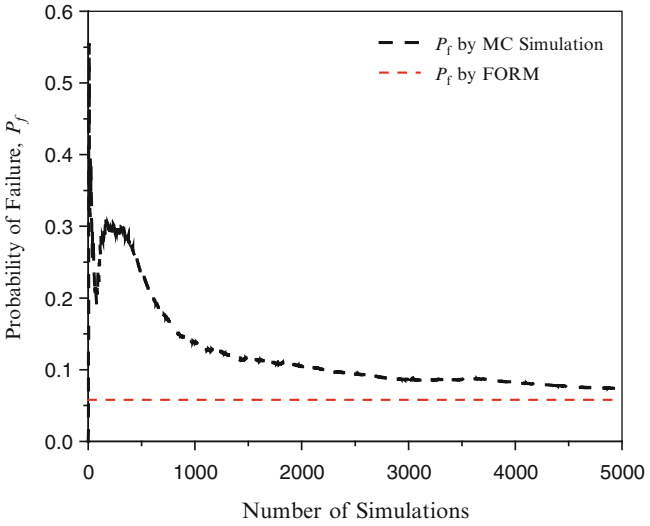

Fig. 5 An example of convergence of probability of failure for the isolation system

6 Conclusions

Base isolation is the most powerful tool in earthquake engineering pertaining to the passive structural vibration control technologies. In this study, a database to use in line with the probabilistic ground motion model is created using the 100 recorded earthquake motions. Using the ground motion model and Monte Carlo simulation (MCS), 5,000 artificial acceleration time histories are generated and used to carry out the stochastic response analysis of the five-storey base-isolated building. In order to carry out the seismic reliability analysis, the top floor acceleration response statistics are used in the performance function considering 0.3 g as a maximum allowable acceleration, and the probability of failure is evaluated. The MCS is also a convenient and accurate method for calculating the probability of failure associated with any of the response statistics. The probability of failure evaluated using the FORM is fairly in good agreement with the value obtained by the MCS.

References

1. Housner GW, Jennings PC (1964) Generation of artificial earthquakes. J Eng Mech (ASCE) 90:113–150
2. Jacob MC, Marburg S, Matsagar VA (2010) A probabilistic method to generate artificial earthquake ground motions. In: 14th symposium on earthquake engineering, Roorkee, India
3. Jangid RS, Datta TK (1995) Seismic behavior of base-isolated buildings: a state-of-the-art review. Struct Build 110(2):186–203

4. Kelly JM (1986) Aseismic base isolation: review and bibliography. Soil Dyn Earthq Eng 5 (4):202–216
5. Naeim F, Kelly JM (1999) Design of isolated structures, from theory to practice. Wiley, New York
6. Rezaeian S, Kiureghian AD (2008) A stochastic ground motion model with separable temporal and spectral nonstationarities. Earthq Eng Struct Dyn 37:1565–1584
7. Rackwitz R, Fiessler B (1978) Structural reliability under combine random load sequences. Comput Struct 9:489–494
8. Wen YK (1976) Method for random vibrations of hysteretic systems. J Eng Mech (ASCE) 102:249–263

Seismic Evaluation of Existing Unreinforced Masonry Building

Debranjan Sar and Pradip Sarkar

Abstract It is well known that masonry buildings suffer a great deal of damage during earthquakes, leading to significant loss of lives. Almost 75% of the fatalities, attributed to earthquake in the last century, are caused by collapse of buildings of which the greatest portion (more than 70%) is due to collapse of masonry buildings. A majority of the tenements in India are unreinforced masonry (URM) buildings that are weak and vulnerable even under moderate earthquakes. On the other hand, a cursory glance through the literature on earthquake-resistant structures reveals that a bulk of research efforts is on RC structures. Clearly there is a great need to expend more effort in understanding masonry buildings subjected to earthquake-induced dynamic loads.

In this chapter, an unreinforced masonry building located in Guwahati is considered for seismic evaluation. The process of seismic evaluation involves linear static and nonlinear static (pushover) analysis. The seismic evaluation has been done initially by calculating demand-to-capacity ratios (DCRs) for each wall segment using linear static and dynamic analyses. A prerequisite for pushover analysis is the definition of the possible locations and types of the plastic hinges that might develop along the span of each element. The walls in the building modelled as equivalent frame elements with appropriate hinge properties as per FEMA 273. Results of nonlinear analysis show that building is globally safe as per ATC-40 capacity spectrum method but the building is unable to achieve target displacements calculated as per FEMA 356 displacement coefficient method. However, linear analysis shows that some wall segments cross the permissible shear stresses.

Keywords Seismic evaluation • Unreinforced masonry • Demand-to-capacity ratio • Pushover analysis • Plastic hinge • Shear stress

D. Sar (✉) • P. Sarkar
National Institute Technology Rourkela, Orissa, India
e-mail: debranjans@gmail.com; sarkar.pradip@gmail.com

S. Chakraborty and G. Bhattacharya (eds.), *Proceedings of the International Symposium on Engineering under Uncertainty: Safety Assessment and Management (ISEUSAM - 2012)*,
DOI 10.1007/978-81-322-0757-3_88,

1 Introduction

Over the last two decades, the loss of lives and economic losses due to moderate to large earthquakes worldwide have been significant. The recent earthquakes in Sikim (18 September 2011), Kashmir (8 October 2005), Bhuj (26 January 2001) and other earthquakes of the past have exposed the seismic vulnerability of load-bearing unreinforced masonry buildings, many of which have been severely damaged. Surveys and analyses conducted in some cities located in earthquake prone zones in India have revealed that most of the existing unreinforced masonry buildings do not meet the earthquake-resistant requirements of the latest Indian code [4]. Also, the design code does not spell out any specific requirement for earthquake resistance URM buildings. This chapter is an effort to address the assessment of seismic vulnerability of existing URM buildings.

In this chapter, an existing URM building from Guwahati, India (zone V), is presented as a case study. The building was analysed using equivalent static method and response spectrum method [4] followed by pushover analysis [1,3]. It was found that, based on the linear analysis, the building does not satisfy the requirements of the current IS code [5]. Of course the nonlinear pushover analysis results reveal that the building has sufficient strength and ductility at global levels.

2 Building Description

An existing load-bearing unreinforced masonry building located in Guwahati (seismic zone V) is presented in this chapter. Figure 1 shows the typical floor plan and 3D computer model of the building. It is a two-storey residential building

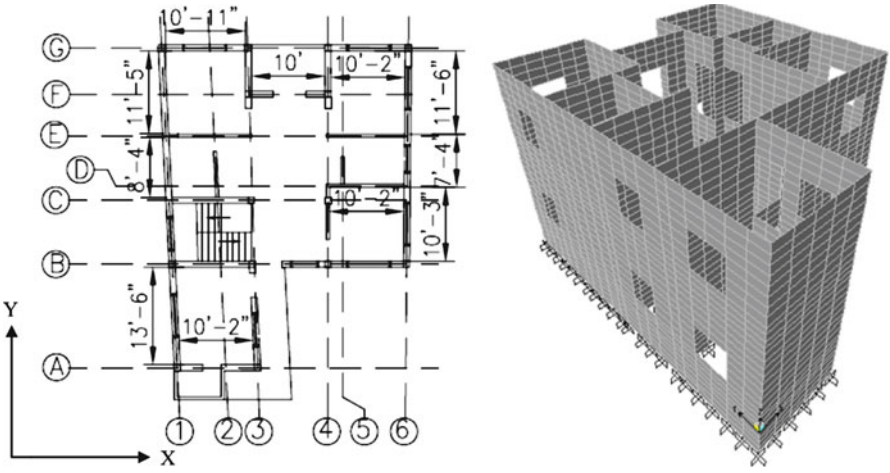

Fig. 1 Typical floor plan with the gridlines and 3D computer model of the building

Table 1 Material constants used for the orthotropic wall panel

E_b/E_m	E_1 (MPa)	E_2 (MPa)	E_3 (MPa)	G_{12} (MPa)	G_{23} (MPa)	G_{31} (MPa)	ν_{12}	ν_{23}	ν_{31}
3	4,694	4,464	4,237	2,344	1,710	1,942	0.144	0.139	0.130

(2 × 3.2 m height from the ground level) with door and window openings. Plan dimensions of the building are 11.4 m × 9.5 m. Standard brick of size 230 mm × 110 mm × 75 mm and mortar grade of M1 [5] were used for the construction of the building using Flemish garden wall bond [6]. The building is approximately 5 years old. Thickness of all the outer walls is 230 mm, and all inner walls are of 110 mm thick. The slabs are 150 mm thick for all the floor levels in the buildings. Visual inspection did not reveal any deterioration in buildings. The subsoils were assumed to be medium (type II) as geotechnical data were not available. Walls were supported on 350-thick and 1,000-mm-deep brick wall.

3 Structural Modelling

The analytical models of the buildings include all components that influence the mass, strength and stiffness. The nonstructural elements and components that do not significantly influence the building behaviour were not modelled.

3.1 Modelling for Linear Analysis

A three-dimensional linear elastic computer model of the building has been developed using the computer program [8]. Walls are modelled using plate elements with orthotropic properties. Orthotropic material properties of the masonry wall were taken from Jurina and Peano [7] and presented in Table 1. These values of elastic properties correspond to the brick-to-mortar Young's modulus ratio is equal to three. Each wall panel is divided into small finite element meshes for convergence. Face wall and cross wall are connected properly at the junction. For dynamic analyses, the mass of the slab was lumped at the centre of mass location at each floor level. This was located at the design eccentricity (based on [4]) from the calculated centre of stiffness. Design lateral forces at each storey level were applied at the centre of mass locations independently in two horizontal directions.

End of the walls at the foundation was modelled as fixed support at the top of the foundation considering compacted hard soil above foundation. The structural effect of slabs due to their in-plane stiffness is taken into account by assigning 'diaphragm' action at each floor level. The mass/weight contribution of slab is modelled separately on the supporting walls. Staircase is not modelled for their stiffness, but its mass was considered in the static and dynamic analyses. The design

spectrum for medium soil specified in [4] was used for the analyses. The effect of soil-structure interaction was ignored in the analyses. The first 20 modes were considered for the dynamic analysis, which gives more than 80% mass participation in both the horizontal directions. The SRSS method of modal combination was used for the dynamic analysis.

3.2 Modelling for Nonlinear Analysis

Modelling walls with plate element performs well in linear analysis, but it is difficult to model nonlinear element properties with the plate modelling. Hence, the building was modelled with equivalent frame (line) element for the nonlinear analysis. The whole building was modelled as combination of one-dimensional piers and spandrels. The wall portion in between two openings is considered as pier, and the portion above and below the opening is considered as spandrel. Width of pier is taken as clear distance between adjacent openings, and depth of the pier is taken as thickness of wall. Depth of spandrel is taken as depth of wall segment available above or below opening, and thickness is taken same as wall thickness. Young's modulus of the material is suitably modified in this model to match the elastic modal properties of the building. All other material constants kept similar to that of brick masonry. All the frame elements (piers and spandrels) are modelled with nonlinear properties at the possible yield locations.

In the implementation of nonlinear static (pushover) analysis, the model must account for the nonlinear behaviour of the structural elements. In this chapter, a point-plasticity approach is considered for modelling nonlinearity, wherein the plastic hinge is assumed to be concentrated at a specific point in the frame member under consideration. Pier elements in this study were modelled with shear (V2 and V3) hinges at possible plastic regions under lateral load (i.e. both ends of the piers). The normalised force-deformation relations and the acceptance criteria for the hinges were obtained from [2]. The force-deformation relations were taken as symmetric in the positive and negative sides of the shear-force axis. The force-deformation relation and the acceptance criteria for plastic hinge deformation in the piers and spandrels sections are shown in Fig. 2.

4 Results and Discussions

The building model was analysed using equivalent static method (linear static method) and response spectrum method (linear dynamic method) according to [4]. Pushover analysis (nonlinear static method) was also carried out. The pushover analysis provides an insight into the structural aspects which control the performance during earthquakes. It also provides data on the strength and ductility of a building. The analyses were done by using the finite element analysis software, SAP2000. All the three analyses expose various design weaknesses that are present in a building.

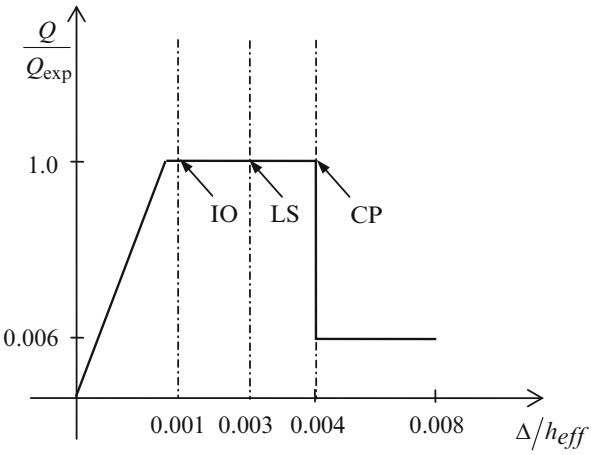

Fig. 2 Typical force-deformation relations for plastic hinge (FEMA 273)

Table 2 Time periods and modal participation for the first three modes

		Mass participation ratio (%)	
Mode	Natural period (s)	UX	UY
1	0.075	43	19
2	0.069	22	46
3	0.054	02	04

Table 3 Comparison of base shear

	$V_x(kN)$	$V_y(kN)$
Equivalent static $(\overline{V_B})$	575.8	575.8
Response spectra (V_B)	236.94	237.52
$\overline{V_B}/V_B$	2.43	2.42

To evaluate the performance of this building, a performance-based approach was adopted. The performance-based approach identifies a target building performance level under an anticipated earthquake level. The building performance is broadly categorised under the levels of (a) collapse prevention, CP, (b) life safety, LS, and (c) immediate occupancy, IO. The two commonly used earthquake levels are design basis earthquake (DBE) and maximum considered earthquake (MCE). For the present buildings, CP under MCE was selected as the safety objective.

Table 2 provides the period and the predominant direction of vibration for the first three modes of the building as obtained from the modal analysis of the elastic model. The table also shows the percentage of mass participation for each of the three modes. It is clear from the table that all the three modes are coupled translational-torsional mode. This is due to the irregular shape of the building in plan and irregular opening distribution in the wall. As the base shear found in response spectrum analysis (V_B) is lesser than design base shear $(\overline{V}_B)$ as per [4], shear stress demand from response spectrum analysis was scaled up by a factor equal to the ratio of the two base shears $(\overline{V}_B/V_B)$. Table 3 shows the comparison between (V_B) and $(\overline{V}_B)$.

Table 4 Deficient walls in the building

Wall grid		Shear strength (MPa)	Equivalent static analysis		Response spectrum analysis	
			Shear demand (MPa)	DCR	Shear demand (MPa)	DCR
X-panels						
Ground floor walls	B3-B4	0.12	0.30	2.5	0.29	2.0
	D4-D6	0.14	0.21	1.5	0.23	1.6
	E1-E3	0.14	0.23	1.6	0.25	1.9
	F3-F4	0.12	0.35	3.0	0.37	3.2
1st floor walls	B3-B4	0.12	0.26	2.4	0.24	2.1
	D4-D6	0.14	0.14	1.2	0.12	1.1
	E1-E3	0.14	0.14	1.2	0.11	1.0
	F3-F4	0.12	0.30	2.9	0.26	2.5
Y-panels						
Ground floor walls	A3-B3	0.15	0.21	1.4	0.25	1.7
	B4-C4	0.13	0.19	1.4	0.20	1.5
	B6-D6	0.14	0.41	2.9	0.49	3.5
	G1-E1	0.12	0.29	2.3	0.26	2.2
1st floor walls	A3-B3	0.15	0.21	1.7	0.16	1.3
	B4-C4	0.13	0.13	1.2	0.09	0.8
	B6-D6	0.14	0.34	2.8	0.31	2.6
	G1-E1	0.12	0.19	1.7	0.17	1.6

The absolute shear demand for each wall segment was calculated from elastic analyses for the load combinations given in [4] and compared with the corresponding capacities in terms of demand capacity ratio (DCR). DCR refers to the ratio of the shear stress demand to the shear stress capacity for a wall segment. Shear capacity for the brick masonry walls was calculated [5] as follows:

$$f_s = 0.1 + \frac{f_d}{6} \tag{1}$$

where f_s is shear strength (in MPa) and f_d is the compressive stress acting on the wall (in MPa) due to dead load. For each wall segment, maximum demand was calculated by equivalent static and response spectrum methods, and thereby DCR calculated for all wall segments. For typical walls, shear stress demand and capacities were tabulated in Table 4. This table shows that a number of wall segments do not satisfy the code criteria as the corresponding DCR values exeed 0.9. To include the deterioration of the structural material, a lesser DCR (less than 1.0) is taken as the criterion for code compliance. But for the present building, maximum wall segments exeeds the permissible limit of DCR value.

The storey drift for every storey due to the design lateral force, with partial load factor of 1.0, is calculated. For both directions, inter-storey drift is within the code limitation of 4%. Figure 3 shows storey drift in both directions when design seismic force is applied in the respective direction.

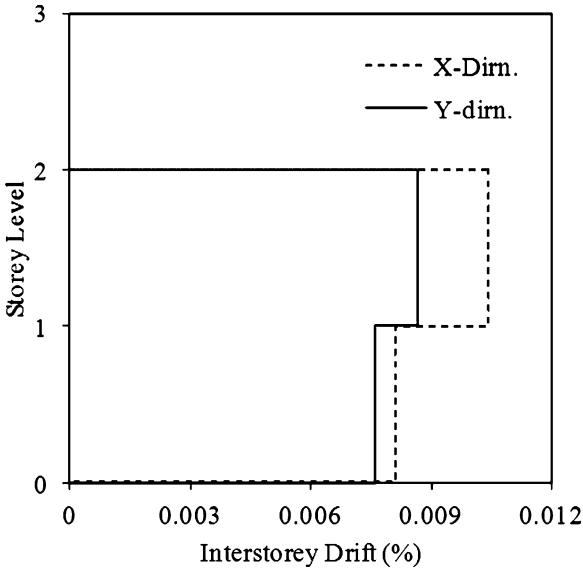

Fig. 3 Storey drifts for design seismic base shear

Pushover analysis is done for the gravity loads (DL + 0.25LL) incrementally under load control. The lateral pushover analysis (in X- and Y-directions) was followed after the gravity pushover, under displacement control. The building is pushed in lateral directions until the formation of collapse mechanism. The pushover curve (base shear vs. roof displacement) is obtained in X- and Y-directions and presented in Fig. 4. Pushover curve shows that the base shear capacities of the building along X- and Y-directions are 1,217 kN (i.e. 60% of total weight) and 1,142 kN (i.e. 58% of total weight), respectively. This figure shows that the building strength comfortably reaches the design base shear force ($\bar{V}_B = 575.8$ kN) in both directions. Maximum roof displacements along X- and Y-directions are 2.05 mm (0.028% of the building height) and 1.81 mm (0.024% of the building height), respectively.

Target displacements for the building were calculated as per FEMA-356 and presented in Table 5. This table shows that the building does not attain the target displacement recommended by FEMA in any of the two orthogonal directions. Formation of the hinges during pushover analysis shows that the failure of the building is due to the failure of the ground storey columns and subsequent formation of storey mechanism.

In a pushover analysis, when the demand spectrum is plotted along with the capacity spectrum in an acceleration displacement response spectrum (ADRS) format, the two curves may meet to give a performance point. Capacity spectrum here corresponds to the base shear versus roof displacement curve. This approach is to check the performance of the building as per capacity spectrum method given in ATC-40.

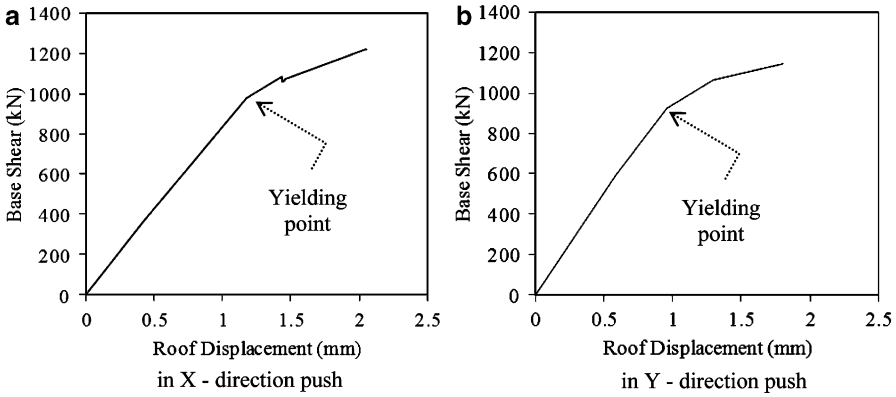

Fig. 4 Pushover curve of the building (**a**) in X-direction push (**b**) in Y-direction push

Table 5 Target displacement (mm) for the building (FEMA-356)

	Life safety (LS)	Collapse prevention (CP)	Displacement undergone
X-direction	2.44	2.87	2.05
Y-direction	2.02	2.38	1.81

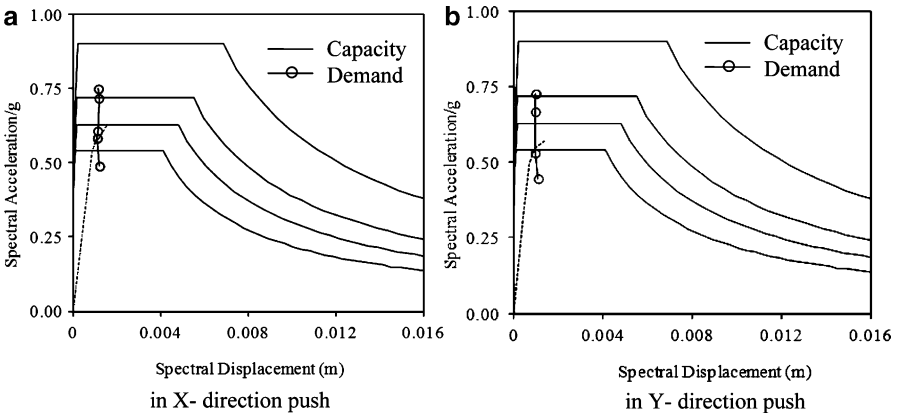

Fig. 5 Capacity and demand spectrum under MCE (**a**) in X-direction push (**b**) in Y-direction push

The zone factor (Z) for Guwahati is taken as 0.36. The demand spectrum for MCE is obtained from peak ground acceleration (PGA) of 0.36 g. The demand spectrum is plotted with $C_a = 0.36$ g, $C_v = 1.36 \times 0.36$ g and 5% initial damping. The demand spectrum is compared with the capacity spectrum and is shown in Fig. 5. The performance point is achieved in this case which is the point at which

Table 6 Status of performance point push-X (MCE)

Quantity	Value	Quantity	Value
Base shear (kN)	1,074 (56%W)	Roof displacement(mm)	1.49 (0.02%H)
Spectral acceleration, S_a (m/s^2)	0.578	Spectral displacement, S_d (mm)	1.11
Effective time period, T_{eff} (s)	0.088	Effective damping, β_{eff}	0.116 (11.6%)

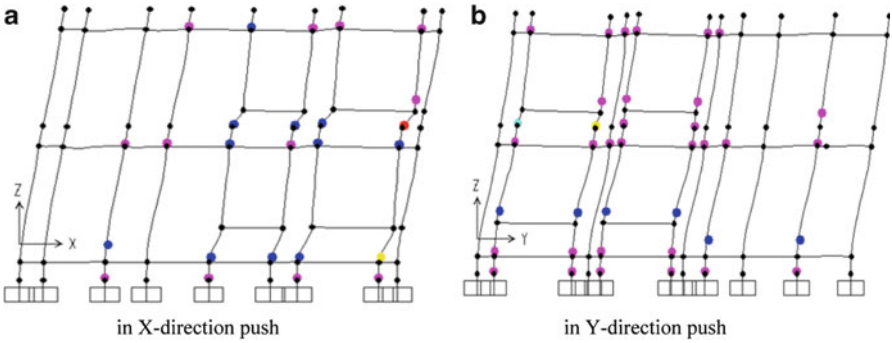

Fig. 6 Formation of hinges at performance point (**a**) in X-direction push (**b**) in Y-direction push

demand and capacity meets. The base shear, roof displacement, spectral acceleration, spectral displacement, effective time period and effective damping corresponding to the performance point are given in Table 6. For the present building, pushover analysis in both directions gave a performance point. So the global performance of the building is acceptable as per ATC-40 capacity spectrum method. So the building does not need retrofitting in a global sense, but some of the wall segments need local retrofitting as plastic hinges on those sections are going beyond life-safety limit. The formation of hinges at performance point in a typical frame is shown in the Fig. 6.

5 Conclusions

This chapter illustrates the methodology adopted for the seismic evaluation of two-storeyed unreinforced masonry buildings. Summarised results of a case study are presented. The use of pushover analysis as a tool of evaluating the seismic performance is illustrated. The main conclusion from the study is that the performance-based evaluation is a rational tool for seismic evaluation of unreinforced masonry buildings. Pushover analysis is an elegant method for visualising the damage state of a building.

References

1. ATC 40 (1996) Seismic evaluation and retrofit of concrete buildings, vol 1. Applied Technology Council, Redwood City
2. FEMA 273 (1997) NEHRP guidelines for the seismic rehabilitation of buildings. American Society of Civil Engineers, Washington, DC
3. FEMA 356 (2000) Prestandard and commentary for the seismic rehabilitation of buildings. American Society of Civil Engineers, Washington, DC
4. IS 1893 Part 1 (2002) Indian standard criteria for earthquake resistant design of structures. Bureau of Indian Standards, New Delhi
5. IS 1905 (1987) Code of practice for structural use of un-reinforced masonry. Bureau of Indian Standards, New Delhi
6. IS 2212 (1991) Brick work – code of practice. Bureau of Indian Standards, New Delhi
7. Jurina L, Peano A (1982) Characterization of brick masonry stiffness by numerical modelling and in situ flat-jack test results. In: Proceedings of the sixth international brick masonry conference. Rome, pp 177–188, 16–19 May 1982
8. SAP 2000 (2009) Integrated software for structural analysis and design, version 14.0. Computers & Structures, Inc., Berkeley

Identification of Night-Time Severe Crash Pattern Using Data Mining Technique

Ranja Bandyopadhyaya and Sudeshna Mitra

Abstract India has the second largest road network in the world. The national and state highways are high-speed facilities connecting all parts of the country. About 65% of freight and 80% of passenger traffic are carried by the roads. The road building and improvement projects "National Highway Development Program (NHDP)" and "Pradhan Mantri Gram Sadak Yojana (PMGSY)", funded by the Government of India, have led to rapid growth in highways, and more and more people are choosing to use these high-speed road facilities. However, coupled with growth of vehicular traffic, the number of road traffic accidents, including fatal and severe injury accidents, has been rising over the last decade. This makes road safety a very serious issue in India and needs to be addressed with utmost priority.

The traffic accidents may be seen as random events triggered by various factors. These factors govern the occurrence as well as severity of crashes. A variety of road safety measures are undertaken in recent years to improve the country's road safety records. One such measure is to identify and rank "unsafe locations" in order of gravity of risk hazard, so that improvement efforts can be targeted optimally with the available limited resources. Other measure is to identify factors that trigger repeated severe injury and fatal accidents, which can enable undertaking overall safety measures to improve the safety performance of the road system.

It is seen from the accident history data of Indian highways that a considerable number of fatal and severe injury crashes occur during evening and night for which inadequate lighting may be responsible. During evening the traffic volume is high, and mostly people returning from office and business use the facility. The evening traffic in highways consists mostly of passenger cars, buses and motorcycles. The traffic volume at night is quite low, and mostly lorries and containers use the highway facility at late hours. The work aims to find causal factors and patterns of night-time accidents in Indian highways using data mining techniques.

R. Bandyopadhyaya • S. Mitra (✉)
Department of Civil Engineering, Indian Institute of Technology Kharagpur, Kharagpur 721302, India
e-mail: b_ranja@yahoo.co.in; sudeshna@civil.iitkgp.ernet.in

S. Chakraborty and G. Bhattacharya (eds.), *Proceedings of the International Symposium on Engineering under Uncertainty: Safety Assessment and Management (ISEUSAM - 2012)*,
DOI 10.1007/978-81-322-0757-3_89,

Twelve-hour night-time data, divided into six 2-h intervals, of a stretch of National Highway (NH-6) from Kolaghat to Bally is used for the analysis. The location type (segment or intersection), accused vehicle involved, victim vehicle involved and traffic volume of each type of vehicle during the 2-h period are used to find the period most vulnerable to fatal and severe injury accidents and the pattern of night-time severe and fatal accidents.

Keywords Crash patterns • Pattern mining • Highway safety

1 Introduction and Background

India's road network is the second largest in the world. The national highways (NH), mostly two lane and undivided, make up about 2% of total road network but carry nearly 40% of the total road traffic. The National Highway Authority of India is now upgrading the highways to multilane-divided high-speed road facility.

The road crash rate, injury rate and casualty rate have been rising rapidly in India over the last decade, and the country accounts for about 9.5% of the total 1.2 million fatal crashes in the world. Among these, 25% of total crashes, 34% of fatal crashes and 28% of injury crashes occur on national highways (Sundar committee report). Evidence also shows that road traffic crashes are on increasing trend in India. To reduce this trend, it is important to identify the factors causing repeated crashes and also those causing higher severity and fatal crashes on Indian highways. A considerable volume of work has been done in the developed countries in the past to identify high crash locations and recommendation of countermeasures for improvement. Identification of such location is mostly done by analysing crash history data along with other traffic regulatory information and road geometric information.

Among some of the relevant studies to identify critical locations and finding factors that influence high crash, work by Kononov [1], Montella [2] and Pande and Abdel-Aty [3] are noteworthy. For example, Kononov [1] proposed a pattern recognition algorithm for detection of hotspots and suggested that roadway conditions and geometric and pavement design-related elements are primarily responsible for triggering crashes. Thus, improving road conditions can help to develop more effective roadway safety improvement strategies. A study by Montella [2] identified general safety issues in roadway element, *viz*. alignment, cross section, markings, longitudinal rumble strips, pedestrian crosswalks, delineation, signs, pavement, roadside and accesses are among the most significant factors responsible for crash occurrence.

Pande and Abdel-Aty [3] studied rear-end crashes in segments in congested as well as free flow conditions. They developed a framework for real-time detection of causes of "crash prone" conditions for rear-end crashes by identifying the traffic and geometric factors significantly associated with such crashes. The crash data and data for average speed, occupancy and volume over 30-s periods on each through

travel lanes (in both directions having a total of 69 loop detector stations spaced out at nearly half-mile intervals) was obtained from Orlando area I-4 corridor. They used data mining techniques, *viz*. Kohonen clustering algorithm, classification tree, multilayer perceptron (MLP), and normalized radial basis function (NRBF) neural networks, with Enterprise Miner software from the SAS Institute, for prediction of rear-end crashes in free flow and congested flow conditions. They found that approximately three-quarters of the rear-end crashes could be identified 5–10 min before their occurrence with only 33% positive decisions (*i.e*. crash warnings). They opined that a reasonable number of warnings given to drivers, based on the proposed strategy, can play a critical role in proactive traffic management. However, the frequency and impacts of such warnings on driver behaviour should be carefully estimated before the measures are implemented. They also suggested that variable speed limit strategies be developed to reduce the risk of rear-end crashes.

Pande and Abdel-Aty [4] presents a data mining-based approach to identify potential lane-change-related freeway crashes, *i.e*. sideswipe crashes and angle crashes on inner lanes of the freeway. The researchers found that the location-specific characteristics and intensity of lane changes, measured in terms of overall average flow ratio (OAFR), are not significant crash causing parameters. The variables found significantly associated with lane-change-related crashes were average speeds upstream and downstream of the crash site, average differences between adjacent lane occupancies upstream of the crash site, and standard deviation of volume and speed downstream. These significant variables were used as inputs to classification models based on two neural network architectures, *viz*. an MLP model with four hidden neurons and an NRBF model with three hidden neurons. A hybrid model, created by combining these two models, performed better than the individual models in terms of crash identification over the validation data set. The researchers recommended this hybrid model to assess the risk of a lane-change crash between two loop detector stations on the freeway. Through an online application of this hybrid model, the risk of a lane-change-related crash may be continuously estimated between any two loop detector stations, provided the data from all three lanes are available at those stations. Based on the measure of risk, *i.e*. the posterior probability output from the model, decision can be made about warning the motorists on the freeway. They suggest that the frequency and impacts of such warnings/messages on driver behaviour need to be assessed through further research.

Chang and Wang [5] aimed to model the injury severity of an individual involved in a traffic crash (*i.e*. no injury, injury and fatality). They used 20 predictor variables to predict the qualitative target variable of injury severity level and identify the important patterns among them. These predictor variables included temporal characteristics (*e.g*. time of crash), highway/environmental characteristics (*e.g*. light condition, speed limit), driver/vehicle characteristics (*e.g*. vehicle type) and crash variables (*e.g*. collision type, contributing circumstance). They used the complete 2001 traffic crash data for Taipei, Taiwan. Individual crash data containing information on the injury severity level of each involved individual, time of crash (*e.g*. month, date, hour), involved driver (*e.g*. age, gender and driver

sobriety at the time of crash) and involved vehicle (*e.g.* vehicle type) were studied. Data on roadway geometrics (*e.g.* divided or undivided), weather conditions (*e.g.* clear, rain or fog) and pavement surface conditions (*e.g.* wet or dry) were also considered. Crash-related data included information on the contributing circumstance, driver/vehicle actions (*e.g.* passing, left turning) and collision types. Other important data included restraint systems used by the rider and passenger at the time of the crash and roadway illumination. They used non-parametric tree-based CART (classification and regression tree) model to analyse the risk factors that can influence the injury severity in traffic crashes. As the severity outcome is discrete, a classification tree instead of a regression tree was developed. The results indicated that the most important variable associated with crash severity is the vehicle type. The model identified pedestrians, motorcycle and bicycle riders as the most vulnerable groups on the road. Collision type, contributing circumstance and driver/vehicle action were also found to be critical in determining injury severity in traffic crashes.

Montella et al. [6] conducted an exploratory analysis of pedestrian crashes to identify predominant crash patterns. They identified the causes of fatal pedestrian crashes with the help of classification trees and association rules of data mining using 56,014 pedestrian crashes occurred in Italy between 2006 and 2008. Crash attributes, *viz.* area, road type, lighting, weather, pavement, pedestrian gender, pedestrian age, pedestrian outcome, vehicle type, PTW (two-wheeler) type, vehicle driver gender, vehicle driver age, vehicle driver outcome, alignment and crash severity are used for identifying inherent crash patterns for fatal pedestrian crashes. Apriori algorithm was used to discover associations. Statistical software *Statistica Data Miner V8.0* was used for analysis. The response variables were severity, involved vehicle and alignment. The rest were the consequent or causes of the response.

In India, road traffic crash data may be obtained from FIR (First Information Reports) complaints recorded at police stations. Each FIR crash record details the crash attributes, *viz.* severity (fatal, major injury or minor injury), vehicles involved, time of crash and type of collision. These details may be used for identifying strong associations between crash severity levels and other crash-related attributes and can help in predicting crash patterns. The crash patterns for severe crashes or any attribute repeatedly occurring in crash data may be seen as factors causing such crashes repeatedly in Indian highways. These factors can be considered as potential hazards to the safety performance of a road facility in general and highways in particular and may be eliminated by identifying areas of improvement. Use of low-cost countermeasures, focus on safety campaign or stricter law enforcement can ultimately help to improve the overall safety performance of the road system.

With this objective, the study aims to:

1. Map the inherent pattern of night-time crashes in the section of highway road chosen for study
2. Identify the factors contributing to night-time crashes

2 Methodology

Pattern mining or identification of frequent patterns of occurrence of a particular event can help to predict the preconditions of the event. The frequent patterns are item-sets, subsequences or substructures that appear in a data set with frequency no less than a user-specified threshold. It may be used for finding inherent regularities in data and is used for association, correlation and causality analysis, pattern analysis, associative classification and cluster analysis and data warehousing. Its practical application areas include basket data analysis, cross-marketing, catalogue design, sale campaign analysis, Web log (click stream) analysis, and DNA sequence analysis. It discloses an intrinsic and important property of data sets.

In this study, the frequent pattern of fatal and severe injury crashes is identified using *apriori technique* of pattern mining. The crash history information containing detailed information about the crash severity, crash location type (segment or intersection), vehicle involvement (accused and victim), crash time (month, day and time of the day) and the crash type is used for the study. The factors, *viz*. crash type, time, location type and vehicles involved that strongly correlated with fatal crashes and strongly correlated with severe injury crashes are identified from the data set. The strong correlation is measured with the support (*i.e*. percentage occurrence of antecedent factors and consequent severity together in the data set), confidence (ratio of support and marginal probability of antecedent factors) and a correlation measure (which shows positive or negative correlation of antecedent factors). The detailed methodology given below is taken from Han and Kamber [7].

3 Apriori Algorithm

Apriori method is one of the scalable mining methods along with frequent pattern growth and vertical data format approach. A scalable data mining technique is one having the characteristics of incremental learning, decremental learning, variable addition, variable deletion, scenario testing, real-time operation, in-line operation, distributed processing and parallel processing. Apriori is the name given to a downward closure property among frequent k-item-sets that says that a k-item-set is frequent only if all of its subitem sets are frequent. This implies that frequent itemsets can be mined by first scanning the database to find the frequent 1-itemsets, then using the frequent 1-itemsets to generate candidate frequent 2-itemsets and check against the database to obtain the frequent 2-itemsets. This process iterates until no more frequent k-item-sets can be generated for some k. This is the essence of the Apriori algorithm and its alternative. The Apriori algorithm has two steps, *viz*. self-joining and pruning. The Apriori pruning principle states that if there is any itemset which is infrequent, its superset should not be generated.

For example, if $L_3 = \{abc, abd, acd, ace, bcd\}$,
Self-joining: $L_3 * L_3$

```
                abcd from abc and abd
                acde from acd and ace
Pruning:
                acde is removed because ade is not in L3
        C4 = {abcd}
```

In this algorithm, two probabilities are defined, *viz*. a support (s) and confidence (c). The support is given by the probability of both antecedent (A) and consequent (B) occurring together in the database, as shown in Eq. 1 below:

$$\text{Support} = P(A \cup B) \tag{1}$$

Confidence is given by the ratio of the support over the marginal probability of the antecedent (A), as shown in Eq. 2 below:

$$\text{Confidence} = \frac{P(A \cup B)}{P(A)} \tag{2}$$

The support and confidence measures alone may not be sufficient at filtering out uninteresting association rules. So a correlation measure can be used to objectively augment the support-confidence framework for association rules. The correlation rules take the form of antecedent (A) implies consequent (B) and have three parameters, *viz*. support, confidence and correlation, as shown in the Eq. 3 below:

$$A \Rightarrow B[\text{Support, Confidence, Correlation}] \tag{3}$$

This shows that the correlation rule is measured not only by the support and confidence but also by the correlation between the item sets A and B. Two measures of correlation are generally used, *viz*. lift and cosine. The lift is a simple measure of finding the correlation between the occurrence of antecedent (A) and consequent (B) given by Eq. 4:

$$\text{lift}(A, B) = \frac{P(A \cup B)}{P(A)P(B)} \tag{4}$$

The occurrence of item-set A is independent of the occurrence of item-set B if

$$P(A \cup B) = P(A)P(B)$$

If the above relation does not hold good, then it may be said that A and B are dependent and correlated as events. So if the resulting value of lift is less than 1, then the occurrence of A is negatively correlated with the occurrence of B. If the resulting value is greater than 1, then A and B are positively correlated, *i.e*. the occurrence of one implies the occurrence of the other. If the resulting value is equal

to 1, then A and B are independent, and there is no correlation between them. Lift may also be calculated from Eqs. 5 or 6:

$$\text{lift}(AB) = \frac{P(B/A)}{P(B)} \tag{5}$$

Or

$$\text{lift}(A,B) = \frac{\text{conf}(A \Rightarrow B)}{\sup(B)} \tag{6}$$

The above relation is also referred as the lift of the association (or correlation) rule $A \rightarrow B$. In other words, it assesses the degree to which the occurrence of one *lifts* the occurrence of the other. The other correlation measure is the cosine. For two item-sets A and B, the cosine measure is defined as in Eq. 7 below:

$$\text{cosine}(A,B) = \frac{P(A \cup B)}{\sqrt{P(A) \times P(B)}} = \frac{\sup(A \cup B)}{\sqrt{\sup(A) \times \sup(B)}} \tag{7}$$

The cosine measure can be viewed as a harmonized lift measure. The formulae for lift and cosine are similar except that for cosine; the square root is taken on the product of the probabilities of A and B in the denominator. This is an important difference, however, because by taking the square root, the cosine value is only influenced by the supports of A, B and $A \cup B$, and not by the total number of transactions.

4 Data

In this study, 12-h night-time (6 PM to 6 AM) crash records for 3 years (2007, 2008 and 2009) over a 70-km stretch of National Highway (NH-6) in India is used for analysis. NH-6 is a four-lane divided highway with raised median. This is not a limited access facility and functions similar to a multilane suburban highway with no interchanges at intersections. This 70-km stretch, between Kolaghat and Bally, fall in Howrah district of West Bengal. The crash records of National Highway-6 (NH-6) are obtained from FIR from seven police stations, *viz*. Bagnan, Uluberia, Panchla, Sankrail, Bally, Domjur and Liluah. The crash history records contain details of location type, time of occurrence of crash, type of collision and vehicles involved in the crash. In total, 522 night-time crash records were obtained and used for the analysis. The volume of bus, lorry, car and motorcycle in the hour of crash are obtained at particular crash time, and the correlation between accused and victim vehicles of crashes are studied with the hourly traffic volume.

5 Results and Discussions

The traffic data is analysed to find strong association rules with apriori algorithm using *Weka 3.7.5*. The strong associations are obtained between crash severities and different attributes, *viz*. vehicles involved in the crash, time of the day the crash is taking place, location type (segment or intersection) and the collision type. The rules along with their support, confidence and correlation (measured in terms of lift and cosine measure) are also shown in the rule tables. The antecedent factors identified by association rule mining are represented diagrammatically in Fig. 1.

The rules with minimum support of 2.5%, minimum confidence as 0.4 and minimum lift (correlation measure) as 1.1 is listed as strong association rules. The cosine measure calculated for the rules varies from 0.19 to 0.56. The lift correlation measure shows positive correlation between antecedents and consequent crash severity (fatal or major injury) for all rules. The cosine measure does not give very good correlation value. The correlation measures usually depend on the inherent data set. The correlation between crashes being fatal when pedestrian is hit by lorry is intuitively positively correlated. There remains a question as to which correlation measure performs better in this case.

The 12-h night-time crash data is divided into six 2-h periods. This data consist of the time of accident in close 2-h period, the accused vehicle, the victim vehicle and severity of accidents. The pattern mining of the 12-h night-time crash data showing some important rules related to hit-and-run fatal accidents which often go unreported are given below:

Rule 1: accused vehicle = unknown victim vehicle = pedestrian 61 → severity = fatal 57 < conf:(0.93) > lift:(1.87) lev:(0.05) [26] conv:(6.1)

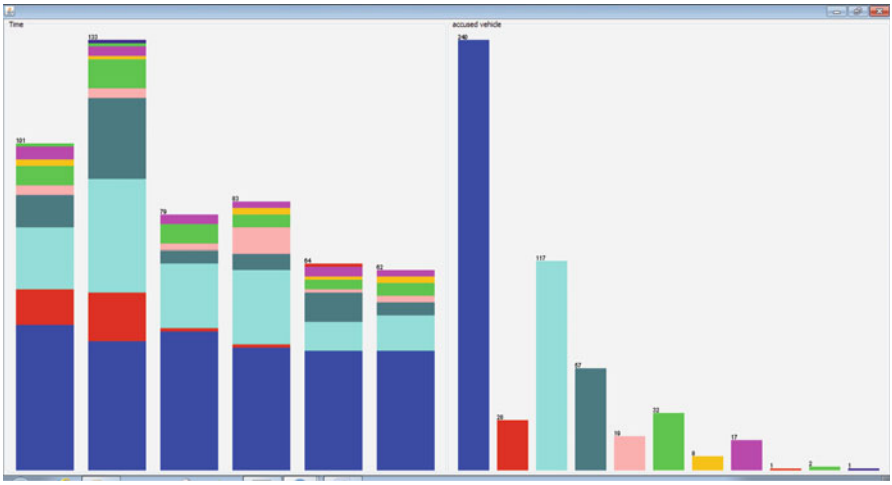

Fig. 1 Pattern of vehicles accused at different times of night

Rule 2: accused vehicle = unknown 117 → accident type = hit-and-run 86 < conf:(0.74) > lift:(2.05) lev:(0.08) [43] conv:(2.34)
Rule 3: accused vehicle = unknown accident type = hit-and-run 86 → severity = fatal 74 < conf:(0.86) > lift:(1.72) lev:(0.06) [31] conv:(3.31)
Rule 4: victim vehicle = pedestrian accident type = hit-and-run 113 → severity = fatal 94 < conf:(0.83) > lift:(1.66) lev:(0.07) [37] conv:(2.83)
Rule 5: victim vehicle = pedestrian severity = fatal 117 → accident type = hit-and-run 94 < conf:(0.8) > lift:(2.24) lev:(0.1) [51] conv:(3.12)

The top five strong rules obtained from pattern mining of crash data show that majority of night-time fatal crashes are caused by unknown vehicles. Thus, it can be concluded that a considerable number night-time accidents are not reported on time and the accused vehicle escape without reporting the accident.

Looking closer to the pattern of accused vehicles (Fig. 1) in each of the two periods, we can see that lorry accidents are frequent throughout the night. The slot between evening 6:00 PM and 8:00 PM experiences maximum number of accidents. The frequency of accidents decreases from 8:00 PM to 10:00 PM but is also very high. Night from 10:00 PM to 12:00 AM and morning from 2:00 AM to 4:00 AM experience relatively lesser frequent accidents. The maximum unreported accidents or hit-and-run accidents occur between evening 6:00 PM and 8:00 PM.

It can be also observed that unknown unreported accidents are quite frequent between 8 PM and 2:00 AM.

Index number:

Accused vehicle: 1– lorry, 2 – motorcycle, 3 – unknown, 4 – car, 5 – n/a, 6 – minilorry, 7 – pickup van, 8 – bus, 9 – tracker, 10 – auto 11 – pedestrian
Time: 1 – N 8:00 PM to 10:00 PM, 2 – N 6:00 PM to 8:00 PM, 3 – N 12:00 AM to 2:00 AM, 4 – N 4:00 AM to 6:00 AM, 5 – N 10:00 PM to 12:00 AM, 6 – N 2:00 AM to 4:00 AM

A few more strong association rules that could be mined from the night-time crash data are listed below:

Rule 1: accused vehicle = unknown victim vehicle = pedestrian accident type = hit-and-run 54 → severity = fatal 50 conf:(0.93)
Rule 2: victim vehicle = pedestrian accident type = hit-and-run 113 → severity = fatal 94 Sconf:(0.83)
Rule 3: accident type = hit-and-run volume lorry/h = L-57.5 34 → severity = fatal 27 conf:(0.79)
Rule 4: time = N – 20–22 accident type = hit-and-run volume lorry/h = L-57.5 34 → severity = Fatal 27 conf:(0.79)
Rule 5: accident type = hit-and-run volume bus/h = B-32.5 volume lorry/h = L-57.5 34 → severity = fatal 27 conf:(0.79)
Rule 6: accident type = hit-and-run volume lorry/h = L-57.5 volume M/C/h = M-44 34 → severity = fatal 27 Supp (0.77), conf:(0.79)
Rule 7: Time = N – 20–22 accident type = hit-and-run volume bus/h = B-32.5 volume lorry/h = L-57.5 34 → severity = fatal 27 conf:(0.79)

Rule 8: Accident type = hit-and-run volume bus/h = B-32.5 volume lorry/h = L-57.5 volume M/C/h = M-44 34 → severity = fatal 27 conf:(0.79)
Rule 9: Time = N – 20–22 accident type = hit-and-run volume bus/h = B-32.5 volume lorry/h = L-57.5 volume M/C/h = M-44 34 → severity = fatal 27 conf:(0.79)
Rule 10: Accident type = hit-and-run volume bus/h = B-32.5 volume lorry/h = L-57.5 volume M/C/h = M-44 Car/h = C-126 34 → severity = fatal 27 Supp (0.76), conf:(0.79)
Rule 11: Time = N – 18–20 accused vehicle = unknown volume lorry/h = L-46 35 → severity = fatal 27 conf:(0.77)

The *S%* is the support percentage, *C* is the confidence, and *L* (Lift) and Co (Cosine) measures are the correlation measures of the rules obtained.

6 Conclusions and Recommendations

Detailed study of night-time crash history data reveals that certain factors such as collision type, type of victim and accused vehicles and the time of crash occurrence govern the severity level of a crash. The rules or close associations of different attributes as obtained from this pattern mining help us gain insight about fatal and severe injury crash occurrence on national highways. The findings also help us adopt proactive measures to improve safety not only for the study highway but also for highways of similar functional classes elsewhere. The conclusions that can be drawn from detailed pattern study of crash data are:

1. A majority of night-time fatal crashes are caused by unknown vehicles. Thus, it can be concluded that a considerable number night-time accidents are not reported on time and the accused vehicle escape without reporting the accident. Looking at the traffic volume during the night, it may not be too wrong to assume that the unnamed accused vehicles are mostly lorries.
2. The maximum unreported accidents or hit-and-run accidents occur between evening 6:00 PM and 8:00 PM. Looking at the traffic volume during this time, it may be said that most unreported accidents during this time may be bus or motorcycle.
3. Unknown unreported accidents are also quite frequent between 8 PM and 2:00 AM.
4. Lorry accidents are frequent throughout the night.
5. The slot between evening 6:00 PM and 8:00 PM experiences maximum number of accidents. The frequency of accidents decreases from 8:00 PM to 10 PM but is also very high.
6. Night from 10:00 PM to 12:00 AM and morning from 2:00 AM to 4:00 AM experience relatively lesser frequent accidents.

Looking closer at the traffic volume at night, the following observations can be made:

1. Evening from 6 PM to 8 PM has equal volume of bus and lorry. Car and motorcycle traffic is higher in this period.
2. Night from 8 PM to10 PM have relatively lesser bus volume and motorcycle volume. While the car volume remains more or less constant, the lorry volume increases during this period.
3. Night from 10 PM to12 midnight the bus and motorcycle volumes are very low. Lorry volume increases further, and the car volume decreases considerably.
4. From midnight to 2 AM the highways are used predominantly by lorry. Few cars can be seen.
5. Night from 2 AM to 4 AM the traffic volume decreases, and mostly lorries use the highway.
6. Morning from 4 AM to 6 AM the traffic increases slightly but lorry is still predominant.

Based on these observations, the major recommendation will be better enforcement and patrolling during night-time. Provision of road side phone booths to call nearby police station or hospital may also be very effective in fast arrival of required services at crash scene.

7 Limitations

The pattern mining approach identifies inherent pattern from the available historical database. This study is conducted with 522 crash records which may not be exhaustive to suggest a very clear pattern. Though some useful pattern could be identified, this limited data size may tend to bias the association rules.

Acknowledgement The authors would like to thank Mr Jinu Anchaniland and Mr.Satish Mahato, M. Tech, Department of Civil Engineering, IIT Kharagpur, for their help in data collection and tabulation.

References

1. Kononov J (2002) Identifying locations with potential for accident reductions, Transportation research record 1784. TRB, National Research Council, Washington, DC, pp 153–158
2. Montella A (2005) Safety reviews of existing roads: quantitative safety assessment methodology, Transportation research record 1922. TRB, National Research Council, Washington, DC, pp 62–72
3. Pande A, Abdel-Aty M (2006) Comprehensive analysis of the relationship between real-time traffic surveillance data and rear-end crashes on freeways, Transportation research record 1953. TRB, National Research Council, Washington, DC, pp 31–40

4. Pande A, Abdel-Aty M (2006) Assessment of freeway traffic parameters leading to lane-change related collisions. Accid Anal Prev 38:936–948
5. Chang YL, Wang HW (2006) Analysis of traffic severity: an application of non parametric classification tree techniques. Accid Anal Prev 38:1019–1027
6. Montella A (2011) Data mining techniques for exploratory analysis of pedestrian crashes. Transportation Research Board, Washington, DC. http://amonline.trb.org/12jjvk/1,last. Accessed 29 Aug 2011
7. Han J, Kamber M (2006) Data mining concepts and techniques, 2nd edn. Morgan Kaufmann, San Francisco, pp 259–265

Landslides Induced Damages Due to Recent Sikkim Earthquake: Strategies for Geotechnical Intervention

Chandan Ghosh

Abstract An earthquake measuring M6.8 on Richter scale occurred on September 18, 2011 in the Sikkim–Nepal border (27.723°N, 88.064°E) region. It was widely felt in all the northeastern states of India, West Bengal, Bihar, Uttar Pradesh, Haryana and Rajasthan, including capital city Delhi. National highways and state highways including the rural connectivity in the Chungthang, Lachung and Lachen area have been snapped. Several aftershocks accompanied with incessant rainfall were causing further distress in the relief and rescue operations. As per information received, while BRO (GREF) cleared debris at more than 20 spots along NH31A up to Gangtok within 20 h, followed by road to Mangan, the North District HQ., via Dikchu in 3 days, road to Nathula, the Chinese border, by October 2, and from Mangan to Chungthang by October 18, it will take more time to restore normal road traffic up to Lachung and further north. It is reported that roads so cleared for traffic have not been yet found fit for carrying heavy machineries to many hydroelectric power (HEP) project sites, thus resulting in inordinate delay in their target achievements.

Keywords Sikkim earthquake • Landslides induced damages • Geotechnical intervention • Slope stabilisation • Anchored earth • Geosynthetics application

1 Introduction

A moderate earthquake of M6.8 on Richter scale hit the North Sikkim–Nepal border on September 18 at 6:10 PM (IST). The epicentre lies in a seismically known and active belt called Alpide–Himalayan seismic belt. The main shock was

C. Ghosh (✉)
National Institute of Disaster management, Ministry of Home Affairs, Government of India, IIPA Campus, New Delhi 110 002, India
e-mail: cghosh24@gmail.com

S. Chakraborty and G. Bhattacharya (eds.), *Proceedings of the International Symposium on Engineering under Uncertainty: Safety Assessment and Management (ISEUSAM - 2012)*,
DOI 10.1007/978-81-322-0757-3_90,

followed by a few significant aftershocks located by the national seismological network, maintained by India Meteorological Department (IMD) and 16 more scientific organisations of the country. IMD recorded 2 aftershocks of M5.0 and M4.5 within 2 h and another of M4.2 at 3:21 AM on September 19. Indian army helicopters ferried rescuers and dropped food and supplies to still-inaccessible villages in Sikkim, a sparsely populated and almost entirely mountainous region. At least 91 people were killed in the earthquake. Most of the deaths occurred in Sikkim, with reports of fatalities in and near Singtam in the East Sikkim district. Several buildings collapsed in Gangtok [1].

The earthquake activity in the NE region is due to the Indian plate diving (thrusting) beneath the Eurasian plate. Sikkim is spread out on the Himalayan mountain range with two main thrust faults, the Main Boundary Thrust (MBT) and Main Central Thrust (MCT) crossing the state (Fig. 1). Continuous thrusting of

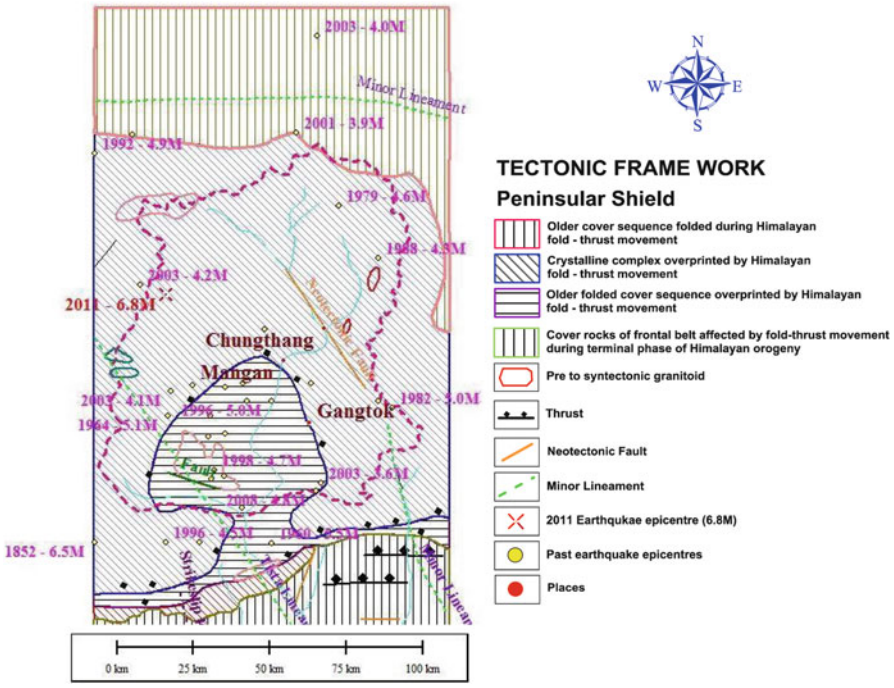

Fig. 1 Seismo-tectonic features of Sikkim Himalaya

the Indo-Australian plate against the Eurasian plate has made most parts of the Himalayan collision zone seismically active. Sikkim is a part of this zone; therefore, it had been a moderately active seismic region in historical times. Significant earthquakes in the region in the last 50 years include the 19 November 1980 Sikkim earthquake of *M*b 6.0 and 21 August 1988 Bihar–Nepal earthquake of *M*b 6.5. Thus, Sikkim is located in seismic zone IV of the Indian seismic zoning map, with the expected maximum intensity of shaking as VIII on the MSK scale. This region has experienced relatively moderate seismicity in the past, with 18 earthquakes of M5 or greater over the past 35 years within 100 km of the epicentre of the September 18 event. The largest of these was a M6.1 earthquake in November of 1980, 75 km to the southeast.

The entire Himalayan belt is one of the most seismically active regions in the world. In the last 110 years, four great earthquakes (magnitude equal to or greater than 8.0) have occurred along this subduction zone causing large-scale damage in the surrounding areas 5 and 6. These are the 1897 Shillong (*M* 8.0), 1905 Kangra (*M* 7.8 to *M* 8.0), 1934 Bihar–Nepal (*M* 8.1) and 1950 Assam (*M* 8.5) earthquakes. The area between the 1934 and 1950 events (Sikkim falls in this region) stands out as a seismic gap that has not produced any major earthquake in the historical times. Another known seismic gap is in the area between the 1905 and 1934 events. There is a high probability of a major event in these seismic gaps in near future (Fig. 2). It has been reported that there were large-scale damages (intensity VII and above) in Sikkim after the 1897 and 1934 events. It may be mentioned here that even smaller earthquakes of 1980 (Sikkim, M 6.0) and 1988 (Bihar–Nepal, M 6.5) have caused damage in Sikkim. Therefore, there is possibility of widespread damage in the state during another major event in the seismic gap regions near Sikkim.

1.1 Earthquake-Induced Damages

The secretariat building, Sikkim press building, education, health and police headquarters in Gangtok suffered severe damage. More than 34,000 buildings in Sikkim such as multistorey RCC buildings, monasteries, hospitals, schools, Gumpas, Panchayat Ghars and public health centres have suffered various degrees of damages. Urban water supply and drainage schemes in Gangtok irrigation channels and PMGSY's village roads and rural water supplies in various districts have also been adversely affected. The earthquake claimed 60 human lives in Sikkim, including 16 at the Teesta Stage III hydroelectric power project site, 719 persons injured and also caused substantial loss to livestock. It shook for more than 30 s at intensity MSK VII, triggered landslides and caused extensive damages to houses and infrastructures. Wide-scale damages were also reported from neighbouring countries like Nepal, Bhutan, Tibet and Bangladesh.

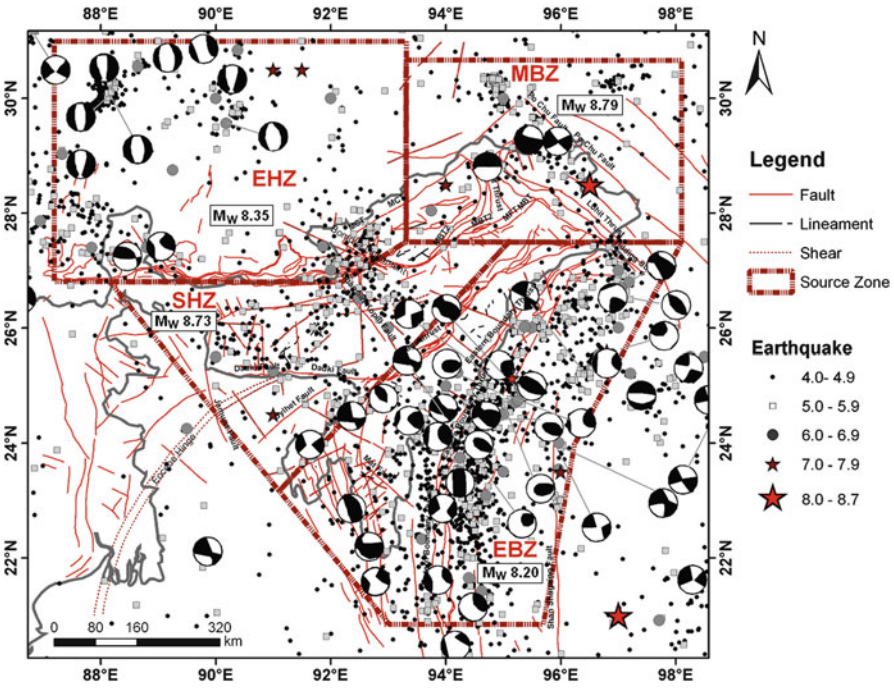

Fig. 2 Seismo-tectonic activities of Sikkim and adjoining region [2]

Though the life loss was not much, the impact of this earthquake in terms of (a) direct and indirect economic loss to nation, (b) expenses to be incurred for mass scale reconstruction and rehabilitation measures, (c) affecting tourism industry and (d) setback to developmental perspectives of the affected area needs thorough assessment, and the outcome should find a space in the 12th plan document of Planning Commission, which is under formulation stage now.

1.2 Landslides Due to Earthquake

The National Highway 31A has suffered landslides at over 21 places, over a cumulative length of 700 m. It was reported by director general of Border Roads Organisation and chief secretary of Sikkim that the road could be opened for traffic by 19 Sept. 2011. The NDRF personnel who are stranded at Bagdogra will be able to reach Sikkim once the road is opened for traffic. (At 1:30 p.m. information has been received that NH31A is functional till Singtam, 29 km short of Gangtok).

The damage of road from Gangtok to Nathula (61 km) is yet to be assessed fully. The first 24 km of road has been surveyed so far showing 12 landslides and severe damage to the road formation over a cumulative stretch of 90 m. Restoration of this road is unlikely to take place immediately, as indicated by DG, BRO (on 1st October 2011, this stretch of the road is reported to be OK).

The third important road in Sikkim which is affected badly is North Sikkim Highway from Gangtok to Chungthang (95 km). About 400 m of road formation has been damaged due to 16 landslides. Restoration of this road too is likely to take some time.

1.3 Augmentation of Seismological Studies

1. Seismic microzonation of Sikkim state, which was carried out under DST funding in 2006, requires status monitoring and road map with particular motivation towards their practical application in the new construction and land use planning for the entire state and similar exercise to be extended to all seismically high-risk areas in northeast
2. National network of seismic instrumentation, strong motion recording and data processing in the NE region need for upgradation and R & D for effective early warning system (EWS) in the NE region. Despite having more than 30 seismic stations in place in the NE region, the country is yet to bring out rational earthquake information dissemination through information media for common public.
3. Seismological data so far being collected at IMD, New Delhi, needs upgradation to their quality and acceptability across the world, which is possible only when these limitations shall be highlighted in the Indian scientific diaspora. [On 14 October 2011, Hon'ble Central Minister of Earth Sciences released a manual for microzonation study for the entire country. Application of the same for seismic design has been highlighted in the panel discussion. It is emphasised that damage statistics following Sikkim earthquake 2011 must be compared with existing microzonation map of Sikkim.]

1.4 Action Plan

All major roads and landslide-prone areas must be surveyed in association with BRO, PWD, forest department and sustainable landslides mitigation measures such as reinforced earth retaining wall, soil nailing by rock bolts/wooden piles, slope stabilisation by anchored earth, geosynthetic retaining wall, gabion walls, rock fall protection by geonetting, jhora training works by slope stitching and shotcreting, to name a few.

2 Construction-Induced Vulnerability (Fig. 3)

Fig. 3 Ongoing Barrage construction site at Sirwani, near Singtam, Sikkim state, along with 26 km tunnel for hydropower generation by Lanco Infratech Limited

3 Roads Made for Development: Issues of Sustainability and Technical Know-How

Road blocks due to earthquake-induced landslides cleared in jet-speed, showing prowess of BRO, but their sustainability and timeline to normalcy is point of serious concern to the proponents of various industry and power projects in the region (Figs. 4-1, 4-2, 4-3, and 4-4).

4 Menace of Earthquake-Induced Landslides and Impact on Power Projects

Based on the preliminary survey of affected area and analysing the situation, it is recommended that (Fig. 5):

1. Measures for systematic damage as well as vulnerability assessment survey along with suggestive timelines for carrying out specific task of repair,

Fig. 4-1 Road clearance made up to Mangan, North Dist. HQ., in 3 days time after the earthquake, but long-term performance measures not ensured, thus affecting work of power projects

Fig. 4-2 Road widening along NH31A near Ranipool is on but technical feasibility of taming cut slope as seen here are very much local and pristine

Fig. 4-3 Controling measures around the Bagthang waterfalls in the form of buttressed retaining walls are no way effective in preventing landslides. The road has no culvert or x-drains. Boulders are constant threat to unwary travellers

Fig. 4-4 Landslides caused severe trouble to dwindling infrastructures services and utilities. Once again restoration of the same has hardly any technology in place

Fig. 5 An aerial view of Teesta III hydropower project site partially damaged in Sunday's earthquake in Chungthang, India, Wednesday, Sept. 21, 2011, and aerial view of massive landslides triggered by the earthquake along Gangtok–Mangan highway (Source AP/Altaf Qadri)

retrofitting and rehabilitation framework. Expert teams are to be formed by involving various national agencies/companies/organisations in coherence with the aims and objective of government organisations such as NDMA, NIDM and MHA and state government agencies.

2. Development/upgradation of Indian standards and guidelines dealing with earthquake-resistant design of buildings on slopes, landslides and rock fall protection measures by modern techniques such as geosynthetics reinforced earth, soil nailing, anchored earth, geonetting and bioengineering.
3. Vulnerability assessment exercise for all hydroelectric power generation projects in the NE.

4. Strategies for pre and post event data collection and further instrumentation of the affected area for understanding unique tectonic features by reputed Indian organisations such as NGRI, GSI, IMD, NEIST, WIHG, IIG and IITs.
5. Establishment of more number of *earthquake- and landslide-resilient helipads* in the seismic zone V area (covering 12% of Indian land mass) and provision of satellite and WLL telephones with defined emergency communication protocol.
6. To provide a forum *for interchanging of ideas and views* pertaining to earthquake risk mitigation, capacity building of mason, architect, engineers, town planners, contractors and other stakeholders.
7. The *performance check of the existing conventional earth retaining* structures such as gravity retaining wall and cantilever wall against earthquake-induced vibration. *A* brain *storming workshop* for all those organisations involved in the hill road construction and maintenance highlighting efficacy of modern techniques based on the on-site assessment of damage patterns and mitigating them through a pilot project along NH31A.
8. *Workmanship, supervision and construction* methods must be revised in the form of strict regulation and implementation drives. Thus, strict adherence to prescribed standards, of construction materials and processes is essential in assuring an earthquake-resistant building. Regular testing of materials to laboratories, periodic training of workmen at professional training houses and on-site evaluation of the technical work are elements of good quality control.
9. Upgradation of present seismic zonation of Sikkim and adjoining areas to *zone V*, i.e. same as rest of the NE India.

5 Conclusions

It is important to find out vulnerabilities of roads on hill slopes as well as portending scenarios of road widening works, multi-storey buildings juxtaposed on steep slopes with little or no breathing space and dwindling lifeline infrastructures in hilly terrain. As post earthquake measures, simple guidelines for crack repair and treatment along with name of products and companies; restoration and strengthening methodology; and applicability of some sustainable technology in landslide mitigation, including bioengineering methods for slope stabilisation, anchored earth and geosynthetics application, to name a few, are essential.

References

1. Ghosh C, Parkash S (2011) Sikkim earthquake 2011 – a roadmap for resurrection. A report submitted to the Ministry of Home Affairs, Govt. of India, New Delhi, 100 p
2. Nath SK, Thingbaijam KKS, Raj A (2008) Earthquake hazard in Northeast India – a seismic microzonation approach with typical case studies from Sikkim Himalaya and Guwahati city. J Earth Syst Sci 117(S2):809–831

Crucial Role of Transportation System in the Socioeconomic Development of the Nation in the Context of Safety Assessment and Management

B.K. Dam and A.K. Chakraborty

Abstract India is one of the largest democratic countries with second largest population in the world. Transportation system with adequate infrastructure contributes to the index of pace of socioeconomic development. Different modes of transportation prevailing the country, gradual changes, diversifications, and growth were reviewed. Importance of related infrastructures commensurate with the requirement of the society from time to time was discussed. With the introduction of policy of liberalization and globalization adopted two decades back demanded rapid growth of all kinds of transportation for faster movement of traffic from one place to the other. Modern and scientific approach was conceived to build infrastructures of international standard. Foreign investments and participation of international traders and businessmen in this country needed requisite developed infrastructures, but at the same time safety, security, and efficient management of the transportation systems are to be ensured in every sphere. Critical scientific studies and assessment of the deficiencies of different systems need to be analyzed carefully. Administrative and managerial steps should be conceived to avoid any undesirable incidents and to ensure safety in every domain of their functions. In this chapter transportation systems, constrains, limitations, safety, security, and efficient management were highlighted.

Keywords Airways • Waterways • Railways • Rapid transit system • Tramways • Highways

B.K. Dam
Public Works Department, Government of West Bengal, Kolkata, India
e-mail: barundam@gmail.com

A.K. Chakraborty (✉)
Civil Engineering, Bengal Engineering and Science University, Shibpur, Howrah 711 103, India
e-mail: arunchakraborty@mailcity.com

S. Chakraborty and G. Bhattacharya (eds.), *Proceedings of the International Symposium on Engineering under Uncertainty: Safety Assessment and Management (ISEUSAM - 2012)*,
DOI 10.1007/978-81-322-0757-3_91,

1 Introduction

In the pre-independence era under the legacy of British Empire and colonial rule of two centuries, the transportation system was developed with a view to run the administration from their angle but was not popular and helpful for Indians. Transportation system of India has been developed since independence with priority. Emphasis was given for the infrastructural development related to transportation. Various time-bound programs were included in the 5-year plans, but with passage of time, the demand of the modern pace of socioeconomic development is inevitable in the changed context of globalization and international competitiveness. Subsequent many plans and programs were framed from time to time and implemented. The most effective radical changes were initiated in late 1990s when ambitious plans and programs were framed with massive investment both from national and international financial institutions. The entire program was coordinated by the planning commission and different relevant ministries for successful implementation. World Bank and Asian Development Bank were the highest international contributors to the gigantic schemes for infrastructural development apart from a number of international financial institutions from Japan, Sweden, and many other countries. Substantial part of the project cost was deployed for safety assessment and effective management to avoid any undesirable disaster.

2 Mode of Transportation System

Transportation system may be broadly classified as follows:

1. Airways
2. Waterways
3. Surface transport
   (a) Railways
   (b) Rapid transit system
   (c) Tramways
   (d) Highways

3 Airways

Indian aerospace for civil aviation was mainly utilized by Indian Airlines and Air India as government undertaking till the end of 1980s except the foreign airlines. Indian Airlines was mainly responsible for domestic connectivity, whereas Air India was meant for international destinations. Revolutionary

changes took place during the last two decades in the diversification of airways in the private sectors. Large number of private airlines gradually immerged into Indian aerospace to provide more connectivity across the country. Due to induction of some of the private airlines, viz., Sahara, Kingfisher, Jet, SpiceJet, and IndiGo, substantial growth in air traffic was observed but could not achieve requisite level of rapid movement and connectivity. Due to deficiencies in various infrastructures of airports, high cost of operation forced the airlines to shift their original decisions to provide economic fares to popularize domestic air transportation. In the international scenario, many of the foreign airlines withdrew their services from some parts of the country including metropolitan cities due to lack of economic viability. "Air India" survived with ups and downs with the support of the government.

Safety and security regulations prescribed by the International Civil Aviation Organization should always be ensured for operation. Any slightest deviation may inflict disastrous destiny including loss of human lives. Prevailing environment of insurgency may lead to any uncertainty in the smooth operation in airways.

3.1 Domestic Airlines in India

Domestic airlines started operation during the British regime as far back as 1929, but most of the airlines served for a short period. These airlines have got their limitation to serve as mass transportation media even in postindependence era; many private airlines started their operation but due to various factors they could not survive. The latest main operators in domestic airspace and are defunct domestic airlines as follows:

List of main operators at present:

- Air India
- Air India Express
- IndiGo
- Jet Airways
- JetLite
- Jet Konnect
- Kingfisher Airlines
- SpiceJet

Defunct domestic airlines in India:

About 31 number of domestic airlines operated between 1929 and 2010. Duration of operation varied widely due to various reasons, e.g., economic viability and increase in expenditure for operation. Fuel cost, taxes, and maintenance cost of aircraft jumped from time to time which inflected inconveniences for the operations.

3.2 International Airlines in India

Since the world has turned into a global village, it has become easier for people, living in extreme corners of the world, to connect to their loved ones as well as increase their business network, without much of a hassle. Thanks to the booming civil aviation industry—it has helped people travel to the nook and corners of the world, within just few hours. As a part of this global village, India is also witnessing a steep increase in the number of passengers, traveling to and from the country via air. The prominent international airlines have been carrying on their operations in India, mainly because of the fact that they attract people in India, largely the business and leisure travelers.

At present 60 international airlines are operating in India, connecting numerous international destinations.

3.3 Safety Assessment and Management of Airways

- Various parameters related to safety of air transportation should be assessed carefully in all steps of planning, implementation, and operation.
- Not only safety assessment to be studied meticulously to identify specific snag where the safety and security is in danger but also safety audit is to be conducted.
- In airways international regulations of ICAO and IATA relating to aircraft and airport infrastructure, maintenance management should be rigidly followed. Slightest deviation may lead to fatal accident.
- Operational staff should be well trained and accustomed to latest rules in force.
- The pilots and copilot should have long experience of flying and accustomed to the mechanism of the relevant aircraft.
- The airports handling the aircraft should be fully equipped and furnished with requisite infrastructure—the runway pavements should be strictly as per specifications to handle the type of aircraft operated in the airport, and any deterioration should be mended promptly. Radar facilities should be adequate to cover the desired airspace. The visibility in all conditions of weather should be maintained with proper lighting and other arrangements.
- Metrologic advance information system should be developed in the airport. Air traffic control personnel should be very efficient and prompt to interact and communicate the pilots.
- Security in all spheres including rigorous checking of the passenger and their belonging to be enforced without loopholes.
- Management of the individual airlines should be vigilant to check all activities of their organization. Deficiency in any corner should be made up and restored instantaneously. Any indiscipline in the organization should be dealt with firmly.
- Pilots should be conversant with “air bumping zones” and fly carefully when passing through bumping zones.

- Pilots should follow the correct path, altitude, considering the visibility, navigability, and weather conditions.
- In the airports prompt through checking of aircraft, tire pressure, refueling, cleaning on landing, and ground engineer should indicate OK for next fling.
- In the context of global insurgency in recent years, security forces and fire brigade should be alert at the airport to handle any undesirable situation. Well-trained commando forces should be stationed in the airport and deployed in case of hijacking.

4 Waterways

India has 11 major sea ports—Kandla, Mumbai, Nhava Sheva, Marmagao, New Mangalore and Kochi on the west coast and Kolkata, Haldia, Visakhapatnam, Paradip, Chennai, and Tuticorin on the east coast. These ports are under the administrative control of Ministry of Surface Transport. Gross tonnage of cargo handled by Mumbai, Visakhapatnam, Chennai, and Tuticorin is significant in comparison to other ports in India.

There are three government-owned shipping corporations; the most important was the Shipping Corporation of India. There were a large number of private shipping companies, a number of which are defunct now. In mid ninetys, all shipping companies operating a total of 443 vessels amounting to 6.3 million gross registered tons and represented 1.7% of the world total tonnage.

4.1 Inland Waterways

India has about 14,500 km of navigable waterways, which consist of the Ganges–Bhagirathi–Hooghly rivers, the Brahmaputra, the Barak river, the rivers in Goa, the backwaters in Kerala, inland waters in Mumbai, and the deltaic regions of the Godavari–Krishna rivers. About 44 million tons of cargo is moved annually through these waterways using mechanized vessels and country boats.

- *National Waterway 1*: Allahabad–Haldia stretch of the Ganges–Bhagirathi –Hooghly river of total length 1,620 km was declared as National Waterway 1 (NW-1) in the year 1986.
- *National Waterway 2*: Sadiya–Dhubri stretch of the Brahmaputra river of total length 891 km was declared as National Waterway 2 (NW-2) in the year 1988.
- *National Waterway 3*: Kollam–Kottapuram stretch of West Coast Canal and Champakara and Udyogamandal canals of total length 205 km was declared as National Waterway 3 (NW-3) in the year 1993.
- *National Waterway 4*: Kakinada–Pondicherry stretch of canals and Kaluvelly tank, Bhadrachalam–Rajahmundry stretch of river Godavari, and

Wazirabad–Vijayawada stretch of river Krishna of total length 1,095 km were declared as National Waterway 4 (NW-4) in the year 2008.

- *National Waterway 5*: Talcher–Dhamra stretch of rivers, Geonkhali–Charbatia stretch of East Coast Canal, and Charbatia–Dhamra stretch of Matai river and Mahanadi delta rivers of total length 620 km were declared as National Waterway 5 (NW-5) in the year 2008.
- *National Waterways 6:* It is a proposed waterway between Lakhipur and Bhanga of river Barak.

Six National Waterways were declared since 1986, and improvement plans were framed to induce better navigability and carrying capacity of passenger vessels and goods cargo. But unfortunately the plans and programs were not fully materialized and target was not achieved. Most of the Indian rivers pass through alluvial planes and siltation takes place during the rainy season. Indian rivers and canals are not lined and protected structurally and are susceptible to bank erosion leading to the raising of bed level. Since most of the rivers do not have the safe cleansing velocity, the siltation cannot be avoided resulting hindrances to the safe navigability of the vessels. Indian reverie ports have been suffering from this problem affecting their turnout and economic viability for their survival.

4.2 Safety Assessment and Management of Waterways

- Watercrafts should be maintained regularly and crews should be careful during sailing through tidal water and rough weather; they should be conversant to the weather forecast valid for the period of sailing especially to a long distance, and they should take proper measures to overcome the unfavorable conditions. Even they could postpone the journey whenever the situation demands.
- Prior assessment should be made regarding the safe navigability of the river ports. Depth of water should be calculated for the passage of heavily loaded ships. Attempt should be made to keep the riverbed navigable by dredging offshore; mooring should be adopted either in the sea or where the draft of water is sufficient. Goods are transferred to the lighter vessels and carried to the port to avoid any undesirable incident.
- Bank protection with high guide on either side of the rivers to avoid overflow and inundation of the adjoining land causing flood.
- Big reservoir may be constructed and impounded with dams to conserved water which can be utilized for hydropower generation and irrigation during lean season.
- Weather forecast should be communicated to the sailors and advanced warning should be given as precautionary measures.
- Red alert should be given when the river spates and crosses danger level and evacuation of the people of anticipated locality.

- Centralized control room should be operated round the clock to assess the flood situation and to mitigate any eventuality.
- Disaster management team should be ready and equipped to meet any situation.

5 Railways

Indian Railways is a departmental undertaking of the Government of India, which owns and operates most of India's rail transport. It is overseen by the Ministry of Railways of the Government of India having its own independent budget.

Indian Railways has 114,500 km (71,147 miles) of total track over a route of 65,000 km (40,389 miles) and 7,500 stations. It has the world's fourth largest railway network after those of the United States, Russia, and China. The railways traverse the length and breadth of the country and carry over 30 million passengers and 2.8 million tons of freight daily. It is the world's second largest commercial or utility employer, with more than 1.36 million employees. As for rolling stock, IR owns over 240,000 (freight) wagons, 60,000 coaches, and 9,000 locomotives.

Railways were first introduced to India in 1853. By 1947, the year of India's independence, there were 42 rail systems. In 1951, the systems were nationalized as one unit, becoming one of the largest networks in the world. IR operates both long distance and suburban rail systems on a multi-gauge network of broad, meter, and narrow gauges. It also owns locomotive and coach production facilities.

The existing Indian Railway Establishment was reorganized curtailing the jurisdiction of big establishments like Eastern Railway, South Eastern Railway, Northern Railway, Western Railway, and Southern Railway, emerging new zonal railways during 2002–2003 for efficient management and better administrative control.

The following is the present status of different zones of Indian Railways with their headquarters:

Central (Mumbai), East Central (Hajipur), East Coast (Bhubaneswar), Eastern (Kolkata), North Central (Allahabad), North Eastern (Gorakhpur), North Western (Jaipur), Northeast Frontier (Guwahati), Northern (Delhi), South Central (Secunderabad), South East Central (Bilaspur), South Eastern (Kolkata), South Western (Hubli), Southern (Chennai), West Central (Jabalpur), Western (Mumbai), and Kolkata Metro (Kolkata)

Major production units of Indian Railways are as follows:

Chittaranjan Locomotive Works, Diesel Locomotive Works (Varanasi), Diesel-Loco Modernization Works (Patiala), Integral Coach Factory (Chennai), Rail Coach Factory (Kapurthala), and Rail Wheel Factory (Bangalore)

Apart from the above units, there are a number of production units of coaches, locomotives, and wagons in both public and private sector. Maintenance of carriage, wagons, and locomotives is done by the railway units located in various parts of the country.

New proposals of various production units at different locations have been implemented in recent years. Faster passenger and freight transportation have been conceived by increasing the speed of the trains, viz., Rajdhani originated from state capitals connected to Rajdhani, Delhi. Duronto nonstop trains between two terminal stations and Shatabdi fast-moving trains were introduced between short-distance terminals. Luxurious tourist trains Palace on Wheels, The Golden Chariot, Heritage on Wheels, The Royal Orient train, Fairy Queen, and Deccan Odyssey were introduced to enhance tourism and to attract foreign tourists. The speeds of the trains largely depend on the condition of the rail tracks and the soil condition of the terrain through which the rail track passes. Wooden Sal timber sleepers have been replaced by the precast concrete sleepers as good quality Sal timber is not available in large quantities. Soil stabilization needs to be done in stretches where poor quality of soil is encountered with suitable admixture, additives with modern mechanized means.

Dedicated freight corridor have been planned for faster movement of goods, wagons, rakes with a view to competitive economic haulage of goods transportation by roads.

5.1 Safety Assessment and Management of Railway

- In recent years, safety and security of railway transportation is at stake; insurgency is one of the main factors to the smooth running of railways.
- Regular maintenance of track circuit, points and crossings, and signals should be ensured for smooth operation.
- Manual faults can be avoided with proper training of the running staffs and assessment of their IQ and alertness level.
- Unmanned level crossings often induce fatal accidents. In major crossings with highways crossing should be made with road over bridge in collaboration with highway authority.
- Sufficient protection force should be deployed in long-distance running trains for the security of the passengers.
- Railway engineer should inspect the track regularly, and any shorts of minor distress should be corrected immediately.
- Railway management at all level including general manager of individual zonal railway should be vigilant to assess all relevant parameters of safety and to take action if needed.

5.2 Rapid Transit System in Metropolitan Cities in India

Rapid mass transportation system is essential in the congested metro cities either by underground tube or overhead elevated carriageways. Schemes are already implemented in Kolkata, Delhi, and Chennai.

5.3 Cities that Have a Metro System

Kolkata Metro, Chennai Mass Rapid Transit System, and Delhi Metro

Kolkata Metro carries about 5 Lakh commuters, whereas Delhi Metro carries about 1,600,000 passengers daily.

5.4 Metro Systems Under Construction

Namma Metro, Mumbai Metro, Rapid Metro Rail Gurgaon, Jaipur Metro, Chennai Metro, Navi Mumbai Metro, Hyderabad Metro, and Kochi Metro

Metro system around the world

Fifty-three countries have developed rapid transit system for mass transportation in their major and thickly populated cities. Many of the countries have metro system in a number of cities. London underground is the oldest metro started in 1863 having a length of 250 miles and 11 lines. New York City Subway was established in 1870 with 209 miles and 422 number of stations. Shanghai Metro was started in 1995 with the longest network of 264 miles. Beijing Subway started functioning in 1969 having length of 208.8 miles.

5.5 Safety Assessment and Management of Rapid Transit System

- In some system, the electrified track circuit is exposed and vulnerable to accident. Research and innovative design should be made to insulate the electrical circuit to avoid any disaster.
- Screen cover should be introduced for safety and protection.
- Efficient management and well-trained man power should be introduced in the metro system.
- Computerized signaling and interlocking system to run the frequent services.

5.6 Tramways

The Calcutta Tramways Company (1978) Limited (CTC) is a West Bengal, government-run company which runs trams in Kolkata (formerly known as Calcutta) and buses in and around Kolkata. The Kolkata tram is the oldest operating electric tram in Asia, running since 1902.

Trams were the brainchild of the then Viceroy of India, Lord Curzon. His motives were to ensure better public transport for the native people, better passage of goods from ports and dockyards to their respective destinations, and rapid

mobilization of police contingents to sites of anti-British protests. Thus, trams were the first mode of police transportation in Calcutta since police cars, vans, buses, lorries, and armored cars were not introduced until 1917.

Anti-tram sentiment began about 1955 and spread around the world. Many countries (both developed and developing) began closing their tram systems, and India was no exception. Tram service closed in Kanpur in 1933, Chennai in 1955, Delhi in 1962, and Mumbai in 1964. Kolkata's network survived, but in a truncated form.

5.7 Safety Assessment and Management of Tramways

- Truck circuit of tramways should be segregated from the main carriageway to avoid interruption of smooth movement of main vehicular traffic.
- Electrical power transmission system to run the trams should be well protected to avoid hazard.
- Truck circuit and tram crossings should be well maintained to avoid derailment.

5.8 Highways

India is a vast country with diversity of land, people, languages, cultural heritages, and religion, with singular entity with national integration. Roads and highways contribute significantly toward integrity through easy accessibility and exchange of cultural wealth throughout the length and breadth of the country. No other mode of transportation except highways can serve to any furthest point of destination. Railways were the most popular mode of transportation even three decades back both for passenger and goods transportation in India. With the rapid growth of highway infrastructures, road transport gradually became competitive and viable. During the 5-year plans, much emphasis was given for the growth of road network in the country. Twenty-Year Road Development Plan was finalized in the year 1941 (known as Bombay Plan) but implementation was not as the desired level. Another 20-year plan was chocked out known as Nagpur Plan in 1961. The plan conceived target of different categories of roads for time-bound implementation. But when the progress of plan was reviewed, there was a big shortfall in achieving the target.

India has a road network of over 3.314 million km (2.059 million miles) of roadway, making it the third largest road network in the world. At 0.66 km of highway per square kilometer of land, the density of India's highway network is slightly higher than that of the United States (0.65) and far higher than that of China's (0.16) or Brazil's (0.20). As of 2002, only 47.3% of the network consisted of paved roads. India, in its past, had not allocated resources to build or maintain its road network. This has changed in the last 15 years, with major efforts currently underway to modernize the country's road infrastructure. India plans to spend

approximately US$70 billion by 2013 to modernize its highway network. As of October 2011, India had completed and placed in use over 14,000 km of recently built 4-lane highways connecting many major manufacturing centers and commercial and cultural centers. Some of the major projects that are being implemented include the National Highways Development Project, Yamuna Expressway, and the Mumbai–Pune Expressway.

According to recent estimates by Goldman Sachs, India will need to invest US $1.7 trillion on infrastructure projects over the next decade to boost economic growth. In an effort to accomplish this, the Government of India is attempting to promote foreign investment in road projects by offering financial incentives such as toll rights to developers.

Indian road network	
Major district roads	470,000
National highways/expressways	66,754
Rural and other roads	2,650,000
State highways	128,000
Total (approx)	3,314,754

As of February 2008, out of the total length of 7,000 km of completed highways, 14% had 4 or more lanes and about 59% had 2 lanes or are double laned, while the rest (27%) of the national highway network had single or intermediate lane. In addition, by 2008, India had awarded numerous contracts on a public–private partnership and build–operate–transfer model to expand its nationwide road network.

As of September 2011, India had completed and placed in use the following newly built highways:

- 5,829 km of its 4-lane Golden Quadrilateral highway
- 5,831 km of its 4-lane North–South and East–West Corridor highway
- 330 km of 4-lane port connectivity highways
- 1,342 km of 4-lane inter-capital highways
- 945 km of 4-lane bypass and other national highways

The above 14,277 km of highways connect most of the major manufacturing centers, commercial, and cultural cities of India.

5.8.1 Rural and Other Roads

The rural roads in India form a substantial portion of the Indian road network. For the development of these rural roads, Pradhan Mantri Gram Sadak Yojana (PMGSY) (or "Prime Minister Rural Roads Scheme") was launched in December 2000 by the Indian government to provide connectivity to unconnected rural habitations. These roads are constructed and maintained by the village panchayats. Their total length in 2005 was 2,650,000 km, which was about 80% of all types of roads in India .

5.9 The Project Is Composed of the Following Phases

- Phase I: The Golden Quadrilateral (GQ; 5,846 km) connecting the four major cities of Delhi, Mumbai, Chennai, and Kolkata. This project connecting four metro cities would be 5,846 km (3,633 mi). Total cost of the project is Rs.300 billion (US$6.8 billion), funded largely by the government's special petroleum product tax revenues and government borrowing. As of February 2011, the project is almost complete, with 5,821 km (3,617 mi) of the intended 5,846 km (3,633 mi) having been 4 lane.
- Phase II: North–South and East–West corridors comprising national highways connecting four extreme points of the country. The North–South and East–West Corridor (NS–EW; 7,300 km) connecting Srinagar in the north to Kanyakumari in the south, including spur from Salem to Kanyakumari (via Coimbatore and Kochi) and Silchar in the east to Porbandar in the west. Total length of the network is 7,300 km (4,500 mi). As of August 2011, 79.4% of the project had been completed and 12.7% of the project work is currently at progress [2]. It also includes port connectivity and other projects—1,157 km (719 mi). The final completion date was on February 28, 2009 at a cost of Rs.350 billion (US$8 billion), with funding similar to Phase I.
- Phase III: The government recently approved NHDP-III to upgrade 12,109 km (7,524 mi) of national highways on a build–operate–transfer (BOT) basis, which takes into account high-density traffic, connectivity of state capitals via NHDP Phases I and II, and connectivity to centers of economic importance. Contracts have been awarded for a 2,075 km (1,289 mi).
- Phase IV: The government is considering widening 20,000 km (12,000 mi) of highway that was not part of Phase I, II, or III. Phase IV will convert existing single-lane highways into 2 lanes with paved shoulders. The plan will soon be presented to the government for approval.
- Phase V: As road traffic increases over time, a number of 4-lane highways will need to be upgraded/expanded to 6 lanes. The current plan calls for upgrade of about 5,000 km (3,100 mi) of 4-lane roads, although the government has not yet identified the stretches.
- Phase VI: The government is working on constructing expressways that would connect major commercial and industrial townships. It has already identified 400 km (250 mi) of Vadodara (earlier Baroda)–Mumbai section that would connect to the existing Vadodara (earlier Baroda)–Ahmedabad section. The World Bank is studying this project. The project will be funded on BOT basis. 334- km (208- mi) expressway between Chennai and Bangalore and 277-km (172- mi) expressway between Kolkata and Dhanbad have been identified, and feasibility study and DPR contract have been awarded by NHAI.
- Phase VII: This phase calls for improvements to city road networks by adding ring roads to enable easier connectivity with national highways to important cities. In addition, improvements will be made to stretches of national highways that require additional flyovers and bypasses given population and housing

growth along the highways and increasing traffic. The government has not yet identified a firm investment plan for this phase. The 19- km (12- mi) long Chennai Port–Maduravoyal Elevated Expressway is being executed under this phase.

The Indian government has set ambitious plans for upgrading of the national highways in a phased manner in the years to come. The details are as follows:

- 4-laning of 10,000 km (6,200 mi) (NHDP Phase III) including 4,000 km (2,500 mi) that has been already approved. An Accelerated Road Development Programme for the North Eastern region
- 2-laning with paved shoulders of 20,000 km (12,000 mi) of national highways under NHDP Phase IV
- 6-laning of GQ and some other selected stretches covering 6,500 km (4,000 mi) under NHDP Phase V
- Development of 1,000 km (620 mi) of express ways under NHDP Phase VI
- Development of ring roads, bypasses, grade separators, service roads, etc. under NHDP Phase VII

5.10 Safety Assessment of Transportation System and Efficient Management

In any transportation system safety and security is the foremost criteria for its efficient function.

Severity of accidents can be minimized by proper Traffic Safety Management.

- Speed of vehicles is directly related to the severity of the accidents. Speed should be regulated as per standard norms. Speed can be controlled by displaying signage with speed limit installed at different focal points of the highways. Speed measurement techniques are enoscope, radar speed meter, laser speed meters, piezoelectric sensors, video image processing, speed breakers, and posting of speed limit signs. Rumble strips are some of the means by which the speed can be controlled. Video cameras are installed on the road side in advanced countries like the UK and the USA to regulate and assess the speed limit violations.
- Traffic problems and their direct impact: unusual congestion during peak hours, increase in running time of vehicles, abnormal delay in reaching destination, increasing vehicle operating cost, increase in pollution level, loss of man hours, other causes create problem to smooth running of traffic, reduction in capacity of carriageway, tremendous increase in vehicle population, bad riding quality of the road surface, encroachment of footpath, parking of vehicles on the carriageway, commercial activities on the side of the carriageway, water logging on the roads during monsoon, poor drainage conditions, etc.

- In major highways dedicated lane should be earmarked for safety management. Intelligent transport system should be developed in congested cities for traffic management and guidance. GPS indicator installed in the vehicle will guide safe riding to destinations.

5.11 Implementation of Traffic Management System

Rigid enforcement of traffic rules adequate training to the police force controlling traffic, expansion of congested cities to its periphery, decentralization of CBD to other parts of the cities, development of satellite township, segregation of slow moving traffic, improvement of geometrics, scientific renovation of road intersections, proper time phasing of traffic signals.

Regulatory technique (RT): unidirectional traffic, reverse streets and lanes, turning movement restrictions, closing side street

Traffic control devices (TCD): traffic signs, road markings, traffic signals, barricades, intersection channelization, delineators, studs

Traffic segregation technique (TST): pedestrian grade separations, central dividers, footpath railing

Demand management technique (DMT): parking restrictions, parking toll

Police public interaction technique: education to bring about awareness, traffic booths, and road users

6 Conclusion

Transportation system is one of the most important and vital infrastructure for economic and social development of any country. In this new millennium, we face great challenge ahead to meet the fast growing needs of all kinds of traffic in all the system of transportation. Fast movement from one end of the country to the other and international destinations is extremely important for the sovereignty, economic development, and international relations. In the present worldwide scenario of insurgency and restlessness, safety of any system of transportations is the first and foremost criterion to ensure smooth movement. Authorities, organizations, and administrations of relevant system of transportation should always be alert and sufficiently active to create a congenial environment for free and safe movement.

References

1. A report from "IRF-Basic road statistics data 2001 updated up to 2010", Washington DC, 2001
2. Chakraborty SS, Bahadur AP & SP (1998) Innovative safety devices for urban stretches of National Highways. In: International seminar on highway safety devices and management, organized by Indian Road Congress, held in New Delhi, 6–7 Nov 1998
3. Dam BK (1998) Traffic management system developed to combat acute transport problems of Calcutta Metropolis. Published in Proceedings of international seminar on highway safety devices and management, organized by Indian Road Congress, held in New Delhi
4. "Wikipedia", the free encyclopedia
5. Wolf Peter Zeplin (2000) Chairman of the experts group for road safety devices, Washington, DC, Keynote address on "Safety devices, standards and specifications"

Uncertainty in Predicting Bearing Capacity of Piles in Sand Using SPT Data

K.K. Kudmetha and A. Dey

Abstract SPT is the most common testing methodology adopted in the field to gain idea about the stratigraphic profile at a site. The same is also employed directly or indirectly to determine the bearing capacity of proposed foundations. The present study aims at understating the usage of various correlations devoted to the correction of the field SPT data and their subsequent use in conjunction to the various correlations to determine the bearing capacity of pile foundation in sand. In this regard, a MATLAB code has been developed that can be used as ready-reference software to obtain the bearing capacity of the pile foundation in sand depending on the correction factor and bearing capacity correlations. Ten different forms of SPT correction correlation and six different bearing capacity correlations have been used in various combinations to reveal their effect on the determined bearing capacity, and the results of the same have been reported in the study. The degree of scatter in the output has been determined as an indirect measure to the degree of uncertainty in the usage of various correlations. The outcome of the present study can be further extended for reliability analysis of the usage of the correlations.

Keywords Pile bearing capacity • SPT test • Correction factor • Standard deviation • Degree of scatter

1 Introduction

Foundations are defined as that part of the structure that aids in the transfer of loads from the superstructure to the soil, and vice versa. In other words, foundations provide the basis of soil-structure interaction mechanism. Based on the depth of embedment, foundations are generally classified as *shallow foundations* and *deep*

K.K. Kudmetha (✉) • A. Dey
Department of Civil Engineering, IIT, Guwahati, India
e-mail: kudmetha@iitg.ac.in; arindam.dey@iitg.ernet.in

S. Chakraborty and G. Bhattacharya (eds.), *Proceedings of the International Symposium on Engineering under Uncertainty: Safety Assessment and Management (ISEUSAM - 2012)*,
DOI 10.1007/978-81-322-0757-3_92,

foundations. Among the deep foundations, due to its frequent usage, *pile foundations* form a large fraternity. Although used for eons, the detailed mechanism of the pile behavior, the load transfer mechanisms, and the determination of their bearing capacity are still fuzzy. Several researchers over the time have proposed several correlations to determine the bearing capacity of pile foundations depending on the soil and pile parameters. Many of the theoretical approaches suffered from the lack of proper understanding of the load transfer and failure mechanisms of pile and hence, on many occasions, failed to provide reasonable or agreeable results. Therefore, attention had been reverted to the semiempirical approaches, wherein based on several experiments on different types of soil, the bearing capacity of piles has been expressed as correlations of pile bearing capacity as a function of soil and pile parameters. With time, the extent of the experiments has increased, and further variations have been studied by different researchers. This attempt has led to the existence of several correlations. Since these semiempirical methods are restrained in their applicability, bounded by the domains of the experiment carried out to develop the correlation, it is easily comprehendible that these methods are not universal and cannot be single-handedly applied to any soil condition. This renders fuzziness in the decision to be taken by a field engineer about the choice of the correlation to be adopted for a particular case. This chapter aims in highlighting this fuzziness described and establishes the same as a background of a consolidated reliability study.

2 Bearing Capacity of Piles Using Penetration Data

Several researchers have proposed several theories to estimate the bearing capacity of pile foundations in sandy soil using mechanics of statics [6]. Few correlations have also been proposed for estimating the pile bearing capacity using dynamic methods. In spite of the mechanistic approaches, the most popular method of estimating the bearing capacity of piles still pertains with the use of penetration test data, either standard penetration test (SPT) or cone penetration test (CPT).

The standard penetration test (SPT) is a common in situ testing method used to determine the subsurface soil profile and their geotechnical engineering properties. The details of N value can be referred to any standard geotechnical engineering textbook. The output of SPT is described in terms of blow counts corresponding to a certain penetration. If the SPT is carried out on sandy soil, the N value provides an indication of the relative density of the subsurface soil, and it is used in empirical geotechnical correlation to estimate the approximate shear strength properties of the soils. The SPT is conducted normally at 2.5 ft (75 cm) to 5 ft (150 cm) intervals. The intervals may be increased at greater depths if necessary. Figure 1 depicts a typical example of the representation of SPT data.

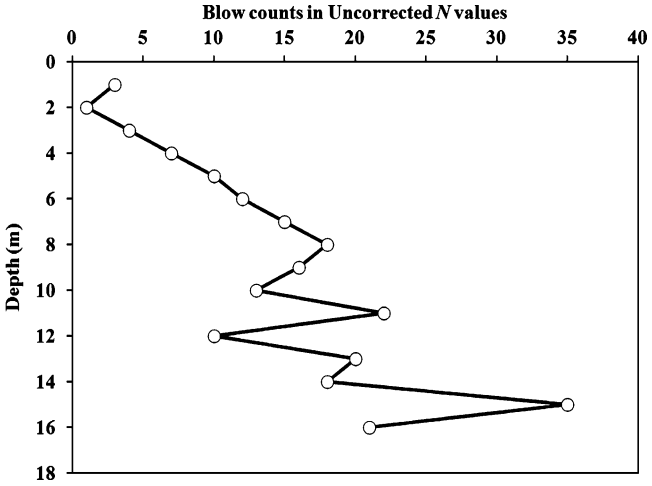

Fig. 1 Typical SPT data

2.1 Corrections on SPT Data

Four types of corrections that are normally applied to the uncorrected *N* values are:

1. Correction due to overburden pressure
2. Hammer efficiency correction
3. Drill rod, sampler, and borehole corrections
4. Dilatancy correction

It has been observed by several researchers that among the various corrections, the overburden correction has the most significant effect on the modification of the *N* value. A description of the same is provided enlisting a number of propositions by various researchers.

2.1.1 Correction Due to Overburden Pressure

The standard penetration number *N* is commonly used to correlate several physical parameters of soil. In granular soils, the standard penetration number is largely affected and dependent on the effective overburden pressure, σ'_o.The SPT correction factor C_N is defined as the ratio of the SPT resistance measured at a given effective vertical stress level σ'_o to the resistance measured at a standard stress level $(\sigma'_o)_{\text{ref}}$, usually the atmospheric pressure which is equal to 96 kN/m^2. This recommended correction factor is essential because penetration resistance is known to increase with depth (in most cases) and at a constant vertical effective stress, penetration

increases approximately as the square of relative density D_r (Meyerhof 1957). This is expressed as

$$N = D_r^2(a + bp') \tag{1}$$

where a and b are material-dependent factors and p' is the mean effective stress. Equation 3 is often expressed as a function of the effective vertical stress σ'_o since σ'_o can be estimated with reasonable accuracy at any given site.

The general expression for the correction factor C_N is expressed as

$$C_N = \frac{N_{\text{cor}}}{N} = \frac{D_r^2(a + b * 100)}{D_r^2(a + bp')} = \frac{\frac{a}{b} + 100}{\frac{a}{b} + p'} \tag{2}$$

The influence of effective overburden pressure σ'_o can then be expressed by a depth correction factor C_N. Several correlations have been proposed by various researchers that are illustrated as follows:

Correlation by Liao and Whitman [5]

$$C_N = 9.78\sqrt{\frac{1}{\sigma'_o}} \quad \sigma'_o \text{ in } kN/m^2, \qquad C_N = \sqrt{\frac{1}{\sigma'_o}} \quad \sigma'_o \text{ in ton/ft}^2 \tag{3}$$

Correlation by Skempton [9]

$$C_N = \frac{n}{1 + 0.01\sigma'_o} \quad \sigma'_o \text{ in } kN/m^2$$
$$(n = 2 \text{ for Loose Sands, } n = 3 \text{ for Dense Sands}) \tag{4}$$

Correlation by Cubrinovski and Ishihara (1999)

Cubrinovski and Ishihara (1999) proposed a correlation between the uncorrected N value, effective overburden pressure, and the relative density of granular soil that is expressed as

$$D_r(\%) = \left[N\left(0.23 + \frac{0.06}{D_{50}}\right)^{1.7}\left(\frac{98}{\sigma'_o}\right)/9\right]^{0.5}(100) \tag{5}$$

where σ'_o = effective overburden pressure in kN/m^2 and D_{50} = sieve size through which 50% of soil will pass (mm). A graphical correlation between the corrected SPT values and the relative density of sand had also been established as tabulated below (Table 1).

Table 1 Approximate relationship between corrected N value and relative density of sand

Corrected standard penetration number (N_{cor})	Relative density, D_r (%)
0–5	0–5
5–10	5–30
10–30	30–60
30–50	60–95

Correlation by Wolff (1988)

The drained or effective angle of friction of granular soils (ϕ') has also been correlated to the standard penetration number. Peck et al. (1974) proposed a correlation between N_{cor} and ϕ' in a graphic form, which was approximated as (Wolff 1988)

$$\phi'(\text{deg}) = 27.1 + 0.3N_{cor} - 0.00054N_{cor}^2 \tag{6a}$$

Schmertmann (1975) also provided a correlation for N versus σ'_o, which was modified by Kulhawy and Mayne (1990), and the approximated correlation is expressed as

$$\phi' = \tan^{-1}\left[N \Big/ \left\{12.2 + 20.3\left(\frac{\sigma'_o}{p_a}\right)\right\}\right]^{0.34} \tag{6b}$$

where p_a = atmospheric pressure (same units as σ'_o).

Correlation by Peck, Hansen, and Thornburn (1974)

$$C_N = 077\log\left(\frac{2000}{\sigma'_o}\right) \quad \sigma'_o \text{ in } kN/m^2 \qquad C_N = 077\log\left(\frac{20}{\sigma'_o}\right) \quad \sigma'_o \text{ in ton/ft}^2 \tag{7}$$

Correlation by Teng [10]

$$C_N = \frac{50}{10 + \sigma'_o} \quad \sigma'_o \text{ in psi} \tag{8}$$

Correlation by Bazaraa (1967)

$$C_N = \left\{\frac{4}{1 + 2\sigma'_o}, \sigma'_o \leqslant 1.5; \qquad \frac{4}{3.25 + 0.5\sigma'_o}, \sigma'_o > 1.5 \right. \qquad \sigma'_o \text{ in ksf} \tag{9}$$

Correlation by Seed (1976)

$$C_N = 1 - 1.25\log 10(\sigma'_o) \quad \sigma'_o \text{ in ton/ft}^2 \tag{10}$$

Correlation by Tokimastu and Yoshimi [11]

$$C_N = \frac{1.7}{0.7 + \sigma'_o} \quad \sigma'_o \text{ in kN/cm}^2 \tag{11}$$

Correlation of Clayton (1993)

$$C_N = \frac{143}{43 + \sigma'_o} \quad \sigma'_o \text{ in kN/m}^2 \tag{12}$$

This correlation is valid only for over-consolidated sands.

3 Determination of Pile Bearing Capacity Using SPT Data

SPT investigation is one of the common and most frequently adopted in the field in addendum to the borehole stratigraphic investigation. Due to its simplicity of execution (apart from the difficulty in repeatability), a field engineer finds the method to be one of the most amiable and reliable one. Hence, the use of SPT data for the determination of pile bearing capacity has been one of the largely adopted techniques. The same is carried out by two main approaches – direct and indirect methods. *Direct methods* apply *N* values with some modification factors. *Indirect SPT methods* employ a friction angle and undrained shear strength values estimated from measured data based on different theories. Among the two, the direct methods are more accepted among the field engineers for the ease of computations.

In the present study, the following SPT-based direct methods have been employed to predict the pile bearing capacity in sandy soil. Hence, the excessive pore water pressure generated during the test has been ignored, and therefore, the results may not be reliable in low-permeable soils such as clays and silts. Since design procedures mainly involve considering the long-term capacity of piles, SPT data generally is only applicable for sands or non-cohesive granular soils. However, as per necessity, the effect of pore water pressure can be incorporated with ease in the study. Table 2 provides the main aspects of each of the direct methods incorporated in the study.

Based on the discussion presented above, it is understandable that various combinations of correlations for correction factor and bearing capacity will yield different estimates of bearing capacity. This might result in considerable scatter and initiate fuzziness in the minds of the user about the choice and reliability of the correlations to be applied to an unknown problem. In order to investigate the mentioned possibility, a MATLAB code has been developed and various aspects are scrutinized. The following section furnishes the detail of the same.

Table 2 SPT direct methods for prediction of pile bearing capacity in the present study

Method	Unit base and unit shaft resistance	Remarks
Meyerhof [6]	$Q_b(\text{MPa}) = 40N_b(\frac{L}{D}) \leqslant 4p_aN_b$	Failure criterion: minimum slope of load-movement curve
	N_b: average of N between 10D above and 5D below pile base	Energy ratio for N: 55%
	$Q_s(\text{kPa}) = n_sN_s$	Low-disp. piles: $n_s = 1$
		High-disp. piles: $n_s = 2$
Briaud (1985)	$Q_b(\text{MPa}) = 19.7p_a(N_b)^{0.36}$	Failure criteria: penetration of pile head equal to 10% of pile diameter (D)
	N_b: average of N between 10D above and 5D below pile base	
	$Q_s(\text{kPa}) = pL\left(0.01p_a(\overline{N_{60}})^{0.29}\right)$	
Aoki and De'Alencar [1]	$Q_b(\text{MPa}) = (\frac{k}{1.75})N_b$	Failure criteria: van der Veen method
	N_b: average of three value of SPT blows around pile base	Energy ratio for N: 70%
	$Q_s(\text{kPa}) = (\frac{ak}{3.5})N_s$	For sand: $a = 14$ and $k = 1$ For clay: $a = 60$ and $k = 0.2$
Shioi and Fukui [8]	$Q_b(\text{MPa}) = \left(1 + 0.04\frac{L}{D}\right)N_b \leqslant 0.3N_b$	Energy ratio for N: 55%
	$Q_s(\text{kPa}) = n_sN_s$	$n_s = 2$ for sand and 10 for clay
Bazaraa and Kurkur (1986)	$Q_b(\text{MPa}) = n_bN_b$	$n_s = 2 \sim 4$
	N_b: average of N between 1D above and 3.75D below pile base, $N_b \leq 50$	$n_b = 0.06 \sim 0.2$
	$Q_s(\text{kPa}) = n_sN_s$	

4 Algorithm of the Developed Software

A user-controlled MATLAB code is developed to investigate the problem stated above incorporating the different expressions for correction factors and axial bearing capacity (expressed as a summation of tip and shaft bearing capacity). The algorithm of the code is briefly stated as follows:

- The user is requested to provide the effective unit weight of soil and the pile parameters (length and diameter of the pile).
- Based on basic theory of soil mechanics, the effective overburden stress is determined using the unit weight and the depth of the soil element.
- The overburden pressure of sand is used to determine the correction factor based on the correlations earlier.
- These different correction factors as determined from various correlations are used to determine the corrected SPT N value.
- The corrected SPT N values are used to obtain the ultimate pile tip and pile shaft capacity considering the empirical correlations as described earlier.
- The pile bearing capacity is evaluated as a summation of the ultimate tip capacity and the shaft capacity.
- The steps described above is repeated for different correction expressions and bearing capacity equations and is used to plot the envelope curves for correction

factors versus depth, uncorrected and corrected SPT values versus depth, and bearing capacity of piles determined from different expressions for each of the correction expressions.

5 Results and Discussions

5.1 *Analysis of Correction Factors*

Figure 2 depicts the variation of the correction factors with depth as obtained using the various correlation factors as detailed earlier. The following conclusions are drawn:

- The correlation by Teng [10] equation plots to the right of all the other correction factors simply because its reference stress level $(\sigma'_o)_{\text{ref}}$ is at approximately 311 kN/m^2, whereas the other curves are standardized at 107 kN/m^2. The use of different stress levels for standardization of the SPT *N* value does not present a conflict, as long as empirical correlations associated with each are consistently applied.
- The correlation for correction factor by Bazaraa (1967) has a slope discontinuity at depth of 4 m which has a stress level of 72 kN/m^2 (≈1.5 ksf as mentioned earlier).
- In the correlations presented by Clayton (1993) and Seed (1976), the correction factors are very conservative especially at high overburden pressures.

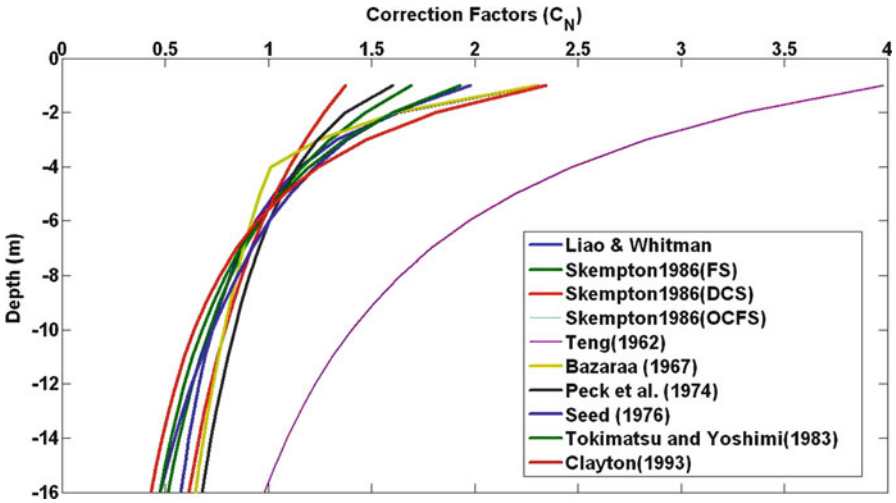

Fig. 2 Correction factor vs. depth

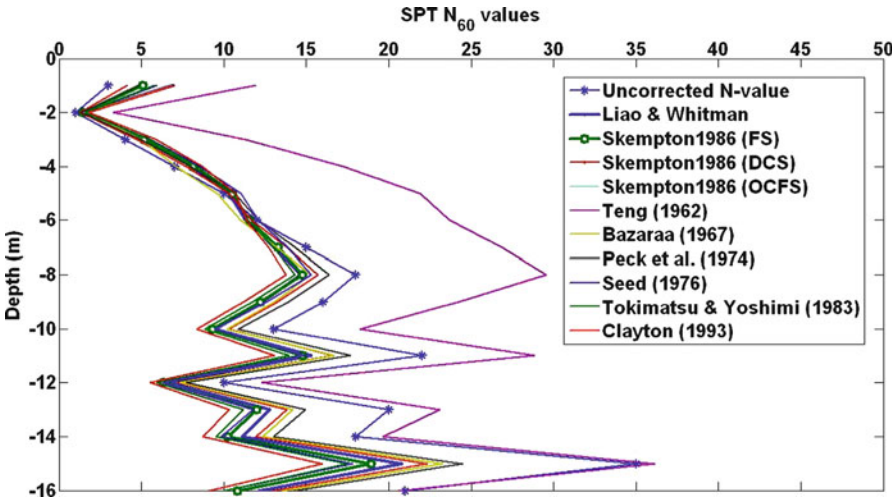

Fig. 3 Typical SPT test data and the corresponding corrected values

- The correction factor as proposed by Seed (1976) correction factor becomes negative for $\sigma'_o > 675$ kN/m^2 (6.3 tsf).
- The correction factor presented by Tokimatsu and Yoshimi [11] is based on Meyerhoff (1957) and is somewhat conservative for $\sigma'_o > 107$ kN/m^2 (1 tsf). Tokimatsu and Yoshimi [11] concluded that this is justified because of a reduction in the energy reaching the SPT sampler for the longer rod lengths and depths corresponding to higher values of σ'_o

It is recommended that the Teng [10] correction factor should be phased out of usage because its standard stress level is set too high at $(\sigma'_o)_{\text{ref}} = 311$ kN/m^2 (2.9 tsf). It is also recommended that the Seed (1976) and Tokimatsu and Yoshimi [11] correction factors should be used only after proper judgment or at least be restricted for use to $\sigma'_o \leqslant 161$ kN/m^2 (1.5 tsf)

5.2 Typical Uncorrected (N) and Corrected SPT Results (N_{cor})

Figure 3 depicts the result of application of different correlations of correction factor on an uncorrected SPT result to obtain the corrected SPT values (N_{cor}). The SPT result represents the borehole stratigraphic test carried out for the identification of soil profile for the construction of New Student House at Campobasso, Molise, Italy. From the figure it is observed that the N_{cor} obtained using the correction factors by Teng [10] does not provide satisfactory and reliable results, the reason for which has been described earlier. Hence, it is advisable that such this particular expression might not be suitable enough for the subsequent determination

of the bearing capacity of piles. However, this aspect needs further investigation in terms of the reliability of each of the above methods.

It is also understandable from the figure that the scattering among the corrected N values is more and increasing with depth, while at lower depths (~<7–10 m), a nearly distinct cluster is formed. At this depth level, the overburden stress ranges from 126 to 180 kN/m^2. This also conforms to the limiting stress level as mentioned by several researchers referred earlier wherein they have considered a limiting stress level of 1.5 tsf (≈160 kN/m^2). Hence, it is comprehendible that for piles of shorter length, the use of different correction factors would lead to a reliable estimation of the bearing capacity of the pile from a particular expression for bearing capacity. However, for piles of larger length, estimated bearing capacity may not be sufficiently reliable owing to the larger degree of scattering with increasing depth. A further insight to this aspect is investigated and has been reported in a subsequent section with relation to standard deviation of the results.

It is observed that at a depth lower than 2 m, the corrected N values are quite scattered. This refers to a stress level of 36 kN/m^2 (≈0.01 tsf). Although a conclusive explanation for this scattering cannot be drawn, this can be explained from the geotechnical engineering point of view wherein the top 1.5–2 m of soil layer is always neglected from any sort of bearing capacity calculation. It is also well illustrated by the fact the shallow foundations are always placed beyond a depth of 2–2.5 m. The top layer of the soil is always considered as a disturbed zone that is significantly affected by the weathering, erosion, and tension crack formation. Hence, these superficial anomalies might affect the degree of reliability of corrected N values and hence might result in the depicted scattering. However, the same cannot be concluded for a pile of larger length owing to the increasing scattering of the cluster of corrected SPT values with depth. The following section would provide further insight concerning this proposition.

5.3 Variation of Bearing Capacity of Piles

Based on the above SPT data, a hypothetical problem is considered wherein the bearing capacity of a pile $(L = 8\ m,\ D = 1\ m)$ is determined considering combinations of the different correlations of correction factor and correlations for bearing capacity (as in Table 2).

5.3.1 Choice of Bearing Capacity Correlations

A theoretical experiment has been carried to study the effect of choice of the various bearing capacity correlations while using a particular correlation of correction factor. A significant variation in the bearing capacity is observed as shown in Fig. 4, which depicts two typical variations of bearing capacity using the correlation for correction as proposed by Liao and Whitman [5] and Tokimatsu and Yoshimi [11]. It can be observed from the figures that there is a significant variation in the

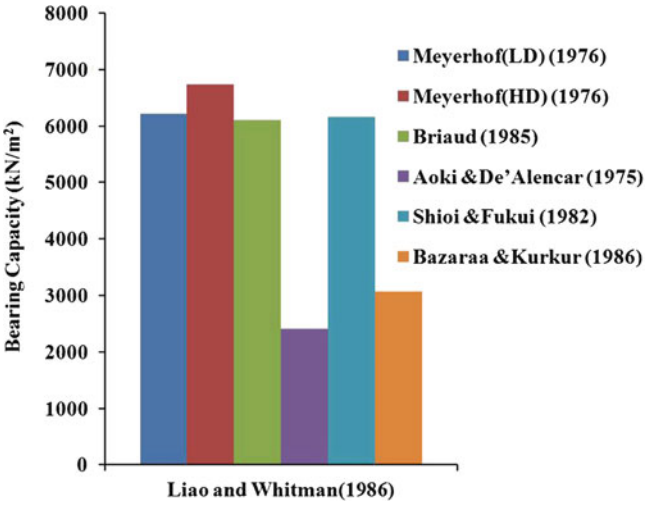

Fig. 4 Typical variation of bearing capacity due to the choice of different bearing capacity correlations for a particular correlation for SPT correction

bearing capacity if the choice of bearing capacity correlation is different. For the two typical cases depicted, the difference between the maximum and minimum magnitude of the obtained bearing capacity was found to be 4,320 and 4,100 kN/m^2, respectively. The quantitative estimation of the variation of the bearing capacity will be tabulated in the later part of the section to highlight its variation depending on the choice of the correlation expression.

5.3.2 Choice of Correlations for SPT Corrections

A theoretical investigation has also been carried out to highlight the effect of choice of the correlations of SPT correction on the bearing capacity of pile foundation considering a particular bearing capacity expression. The same is depicted in Fig. 5. It is observed from the figure that a considerable variation exists in the magnitude of the determined bearing capacity if different correlation of correction factor is taken into account even while using a particular bearing capacity equation.

5.3.3 General Comment on the Variation of Bearing Capacity of Pile Foundation

From the above two discussions, it is followed that the bearing capacity of a pile foundation will vary depending on the choice of correlation for SPT correction and bearing capacity correlation. In the present study, as described earlier, ten sets of correlation for SPT correction have been chosen, each of which is used with each of the six sets of bearing capacity correlations. Hence, total 54 sets of data are analyzed and the result of the same are depicted in Fig. 6. In the figure, the bearing

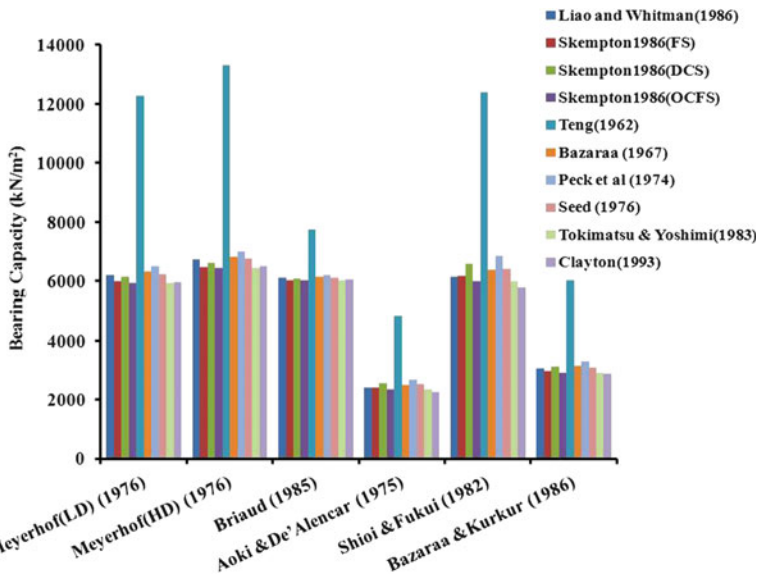

Fig. 5 Variation of bearing capacity due to the choice of different correlation for SPT correction for particular bearing capacity correlations

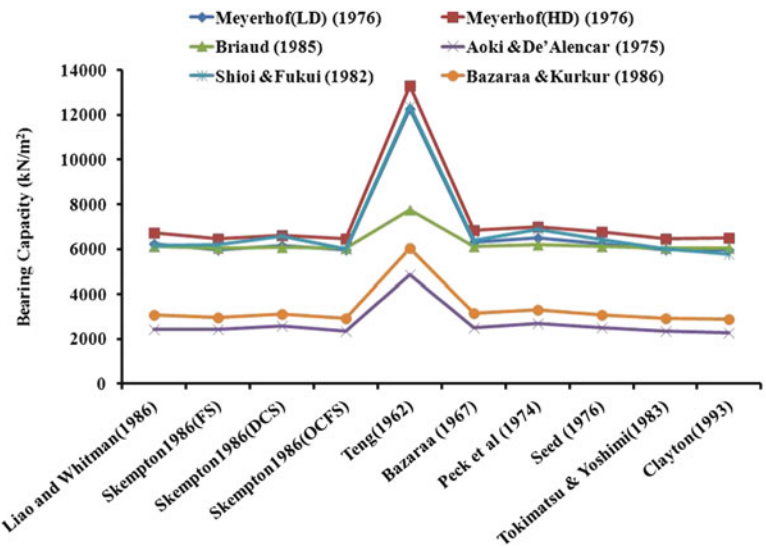

Fig. 6 Variation of bearing capacity for various combinations of SPT correction correlations and bearing capacity correlations

capacity of pile foundation is plotted against different sets of SPT correction correlations, and an envelope of curve is produced considering six sets of bearing capacity expressions. The variation in the magnitude of the bearing capacity is self-indicative. The quantitative estimation of the same is enumerated in Table 3. It is

Table 3 Quantitative variation of bearing capacity of pile foundation using SPT investigations

Correlations for SPT correction	Bearing capacity of pile foundation ($kN.m^2$)	Bearing capacity correlations										
		Meyerhof (LD) [6]	Meyerhof (HD) [6]	Briaud (1985)	Aoki and De'Alencar [1]	Shioi and Fukui [8]	Bazaraa and Kurkur (1986)	Diff	Dev of diff with max value (%)	Dev of diff with min value (%)	Mean value	Std dev
	Liao and Whitman [5]	6216.43	6729.59	6110.92	2410.24	6153.34	3063.96	4319.35	64.18	179.21	5114.08	1866.15
	Skempton [9] (FS)	5981.10	6473.65	6029.64	2420.31	6186.74	2972.76	4053.34	62.61	167.47	5010.70	1809.23
	Skempton[9] (DCS)	6146.98	6621.13	6071.15	2567.16	6578.43	3113.93	4053.97	61.23	157.92	5183.13	1836.15
	Skempton [9] (OCFS)	5946.36	6452.54	6025.31	2350.25	5998.22	2921.87	4102.29	63.58	174.55	4949.09	1809.83
	Teng [10]	12274.48	13318.92	7735.03	4852.93	12385.70	6032.19	8466.00	63.56	174.45	9433.21	3669.29
	Bazaraa (1967)	6326.49	6823.84	6136.28	2498.41	6390.13	3160.53	4325.43	63.39	173.13	5222.62	1879.03
	Peck et al (1974)	6507.10	7006.30	6190.18	2678.86	6863.18	3290.88	4327.43	61.76	161.54	5422.75	1919.43
	Seed (1986)	6234.13	6759.22	6121.68	2514.00	6421.67	3082.88	4245.22	62.81	168.86	5188.93	1872.89
	Tokimatsu and Yoshimi [11]	5946.36	6452.54	6025.31	2350.25	5998.22	2921.87	4102.29	63.58	174.55	4949.09	1809.83
	Clayton (1993)	5963.27	6492.36	6040.83	2269.08	5777.40	2883.02	4223.28	65.05	186.12	4904.33	1829.06
	Difference	6328.12	6866.38	1709.72	2583.84	6608.30	3149.17					
	Dev of diff with max value (%)	51.56	51.55	22.10	53.24	53.35	52.21					
	Dev of diff with min value (%)	106.42	106.41	28.38	113.87	114.38	109.23					
	Mean value	6754.27	7313.01	6248.63	2691.15	6875.30	3344.39					
	Std dev	1948.63	2118.41	525.24	768.85	1961.67	952.72					

Table 4 Comparison of the standard deviations for piles of different length considering all correlation of SPT correction factors

		Correlations of bearing capacity					
Pile length		Meyerhof (LD) [6]	Meyerhof (HD) [6]	Briaud (1985)	Aoki and De'Alencar [1]	Shioi and Fukui [8]	Bazaraa and Kurkur (1986)
Including Teng [10]	7 m	1709.02	1859.12	515.58	812.84	2076.25	959.85
	11 m	2521.24	2763.47	562.75	757.47	1930.58	993.69
Excluding Teng [10]	7 m	139.19	139.01	48.33	93.12	248.10	105.33
	11 m	459.46	472.65	113.34	244.12	638.11	236.82

observed from the table that the estimated standard deviations are quite high. For a statistical set of data, standard deviation is a measure of the degree of scattering in the data; the more the standard deviation, the higher is the degree of scattering. Hence, from this study, it is revealed that the bearing capacity of the pile foundation calculated using the various combinations of correlations of SPT correction and bearing capacity results in a scattered output, which indirectly points out to the degree of uncertainty in the obtained result.

5.3.4 Bearing Capacity of Piles of Different Lengths

Another aspect of the theoretical investigation in the present study dealt with the estimation and comparison of the bearing capacities of piles of different length. The basic idea is to get visualization on the degree of scattering of the output data when two different pile lengths are considered, keeping in mind that the scattering of the corrected N values increased at larger depths. For this investigation, two piles of different lengths (7 and 11 m) were chosen. The results, in terms of the standard deviations, are enumerated in the following tables. Table 4 provides the standard deviations for a particular bearing capacity correlation considering all the correlations for SPT correction. The results do not reveal a clear picture about the degree of scattering when compared for different lengths of piles; for few bearing capacity correlations, standard deviation increased with the length of pile, while for some others, it is decreased. Since it has already been elaborated that the scattering in the corrected N value increased with depth (Fig. 3), the degree of scattering for pile of longer length should also increase. However, the following table does not reveal so. The probable reason for this might be due to the inclusion of the correlation proposed by Teng [10] in the estimation of standard deviation that has affected the result of the same. It has already been shown earlier that the correlation proposed by Teng is an out-of-phase expression that does not fit in the jargon of other correlations (Fig. 2).

6 Conclusions

From the various theoretical investigations carried out, the following significantly important outcomes have been observed and reported as follows:

- The correlation for SPT correction factor proposed by Teng [10] is found to be largely out of phase with the other correlations possibly due to the high value of the reference stress level, nearly three times than the others.
- The scatter in the corrected N values is found to increase progressively with the increase in the depth. Within a depth of 7–10 m from the surface, the corrected values seemed to form a cluster that is conformational with the limiting stress condition assumed by several researchers. This phenomenon also indicates that for piles of length lesser than 8 m or so, any of the correction factor correlation can be used to obtain the bearing capacity using a particular bearing capacity correlation. However, owing to the larger degree of scatter at larger depths, the above-mentioned hypothesis is not applicable to piles of larger lengths.
- Bearing capacities of pile foundation for various combination of the SPT correction and bearing capacity correlations have been determined, and the standard deviation of the output dataset have been estimated for different sets of the correlations. From the observation of the outcomes, it is concluded that there exists significant degree of scatter in the calculated results and hence creates an uncertainty and fuzziness toward confident application of a correlation to an unforeseen problem.

References

1. Aoki N, De'Alencar D (1975) An approximate method to estimate the bearing capacity of piles. In: Proceeding of the fifth Pan-American conference on soil mechanics and foundation engineering, Buenos Aires, Argentina, pp 367–376
2. Briaud JL, Tucker LM (1988) Measured and predicted axial capacity of 98 piles. J Geotech Eng ASCE 114(9):984–1001
3. Das BM (1998) Principal of geotechnical engineering, 5th edn. ITP, Boston
4. Das BM (1999) Principles of foundation engineering. Brooks/Cole Publishing Company, Pacific Grove
5. Liao SS, Whitman RV (1986) Overburden correction factors for sand. J Geotech Eng ASCE 112(GT3):373–377
6. Meyerhof GG (1976) "Bearing capacity of settlement of pile foundations" The eleventh Terzaghi lecture. ASCE J Geotech Eng 102(GT3):195–228
7. Murthy VNS (1996) Principles and practices of soil mechanics and foundation engineering. Marcel-Dekker, New York
8. Shioi Y, Fukui J (1982) Application of N-value to design of foundation in Japan. In: Proceeding of the second European symposium on penetration testing, Amsterdam, vol 1, pp 159–164
9. Skempton AW (1986) Standard penetration test procedures and the effects in sands of overburden pressure, relative density, particle size, ageing and over consolidation. Geotechnique 36:425–447
10. Teng WC (1962) Foundation design. Prentice-Hall, Inc., Englewood Cliffs
11. Tokimatsu K, Yoshimi Y (1983) Empirical correlation of soil liquefaction based on SPT N-value and fines content. Soils Found 23(4):56–74

Author Index

S. Chakraborty and G. Bhattacharya (eds.), *Proceedings of the International Symposium on Engineering under Uncertainty: Safety Assessment and Management (ISEUSAM - 2012)*,
DOI 10.1007/978-81-322-0757-3,

D

L

T